

PROPERTY OF:

NASA SP-11

50234

*Proceedings of the*

**NASA-UNIVERSITY**

**CONFERENCE ON THE**

**SCIENCE AND TECHNOLOGY**

**OF SPACE EXPLORATION**

*Volume 2*

Reproduced From  
Best Available Copy

DISTRIBUTION STATEMENT A

Approved for Public Release

Distribution Unlimited

20011116 066

CHICAGO, ILLINOIS

NOVEMBER 1-3, 1962



NASA SP-11



*Proceedings of the*  
NASA-UNIVERSITY  
CONFERENCE ON THE  
SCIENCE AND TECHNOLOGY  
OF SPACE EXPLORATION

*Volume 2*

PROPERTY OF:  
ADPTIAS LIBRARY

CHICAGO, ILLINOIS      NOVEMBER 1-3, 1962



**December 1962**  
**Office of Scientific and Technical Information**  
**NATIONAL AERONAUTICS AND SPACE ADMINISTRATION**  
**Washington, D.C.**

---

For sale by the Superintendent of Documents, U.S. Government Printing Office, Washington 25, D.C. - - - - - Price \$3.00

# Contents

## SESSION M

### CHEMICAL ROCKET PROPULSION

*Chairman: Walter T. Olson*

INTRODUCTION.....	Page 3
WALTER T. OLSON	
37. FLUID PHYSICS OF LIQUID PROPELLANTS.....	7
DONALD L. NORED and EDWARD W. OTTO	
38. NEW PROBLEMS ENCOUNTERED WITH PUMPS AND TURBINES..	23
MELVIN J. HARTMANN and CALVIN L. BALL	
39. RECENT ASPECTS OF ROCKET COMBUSTION RESEARCH.....	37
GERALD MORRELL and RICHARD J. PRIEM	
40. CURRENT RESEARCH AND DEVELOPMENT ON THRUST CHAM- BERS.....	43
EDMUND R. JONASH and WILLIAM A. TOMAZIC	
41. DYNAMICS AND CONTROL OF CHEMICAL ROCKETS.....	53
JOHN C. SANDERS and LEON M. WENZEL	
CONCLUDING REMARKS.....	57
WALTER T. OLSON	

## SESSION N

### NUCLEAR PROPULSION

*Chairman: David S. Gabriel*

INTRODUCTION.....	61
DAVID S. GABRIEL	
42. ADVANCED CONCEPTS FOR NUCLEAR ROCKET PROPULSION.....	63
FRANK E. ROM and ROBERT G. RAGSDALE	
43. NUCLEAR PHYSICS OF SOLID-CORE GAS-COOLED ROCKET PRO- PULSION REACTORS.....	77
DONALD BOGART and EDWARD LANTZ	
44. FLUID FLOW AND HEAT TRANSFER PROBLEMS IN NUCLEAR ROCKETS.....	87
HERMAN ELLERBROCK, JOHN N. B. LIVINGOOD, and DAVID M. STRAIGHT	
45. PROBLEMS IN DYNAMICS AND CONTROL OF NUCLEAR ROCKETS..	117
JOHN C. SANDERS, HERBERT J. HEPPLER, JR., and CLINT E. HART	

## SESSION O

### POWER FOR SPACECRAFT

*Chairman: Newell D. Sanders*

46. POWER FOR SPACECRAFT.....	125
NEWELL D. SANDERS, CHARLES A. BARRETT, DANIEL T. BERNATOWICZ, THOMAS P. MOFFITT, ANDREW E. POTTER, JR., and HARVEY J. SCHWARTZ	

## CONTENTS

### SESSION P

#### ELECTRIC PROPULSION

*Chairman: Wolfgang E. Moeckel*

	Page
INTRODUCTION.....	153
WOLFGANG E. MOECKEL	
47. SPECIAL REQUIREMENTS ON POWER GENERATION SYSTEMS FOR ELECTRIC PROPULSION.....	157
SEYMOUR LIEBLEIN	
48. (a) GENERATION OF THRUST—ELECTROTHERMAL THRUSTORS..	167
JOHN R. JACK	
(b) GENERATION OF THRUST—ELECTROMAGNETIC THRUSTORS..	171
GEORGE R. SEIKEL	
(c) GENERATION OF THRUST—ELECTROSTATIC THRUSTORS.....	177
WARREN D. RAYLE	
49. ADVANCED CONCEPTS.....	183
EDMUND E. CALLAGHAN	

### SESSION Q

#### AERODYNAMICS

*Chairman: Laurence K. Loftin, Jr.*

50. AERODYNAMIC PROBLEMS OF LAUNCH VEHICLES.....	193
ROBERT W. BOSWINKLE, JR.	
51. LOW-SPEED AERODYNAMIC RESEARCH RELATED TO THE LAND- ING OF SPACE VEHICLES.....	203
JOHN P. CAMPBELL	
52. THE AERODYNAMICS OF HYPERSONIC CRUISING AND BOOST VEHICLES.....	215
MITCHEL H. BERTRAM, DAVID E. FETTERMAN, JR., and JOHN R. HENRY	
53. AERODYNAMIC AND HEATING PROBLEMS OF ADVANCED RE- ENTRY VEHICLES.....	235
ROBERT L. TRIMPI, FREDERICK C. GRANT, and NATHANIEL B. COHEN	

### SESSION R

#### GAS DYNAMICS

*Chairman: Alfred J. Eggers, Jr.*

54. GAS DYNAMICS PROBLEMS OF SPACE VEHICLES.....	251
H. JULIAN ALLEN	
55. RECENT INFORMATION ON HYPERSONIC FLOW FIELDS.....	269
ALVIN SEIFF	
56. RECENT DEVELOPMENTS IN THE CHEMISTRY AND THERMO- DYNAMICS OF GASES AT HYPERVELOCITIES.....	283
THOMAS N. CANNING	
57. RECENT DEVELOPMENTS IN MASS, MOMENTUM, AND ENERGY TRANSFER AT HYPERVELOCITIES.....	291
GLEN GOODWIN and JOHN T. HOWE	

## CONTENTS

### SESSION S

#### PLASMA PHYSICS AND MAGNETOHYDRODYNAMICS

*Chairman: Adolf Busemann*

	Page
58. RELATIONS BETWEEN AERODYNAMICS AND MAGNETOHYDRODYNAMICS.....	305
ADOLF BUSEMANN	
59. FUNDAMENTALS OF PLASMA INTERACTION WITH ELECTRIC AND MAGNETIC FIELDS.....	313
ROBERT V. HESS	
60. THE ELECTRIC DRAG FORCES ON A SATELLITE IN THE EARTH'S UPPER ATMOSPHERE.....	337
GEORGE P. WOOD	
61. PLASMA FREQUENCY AND RADIO ATTENUATION.....	347
PAUL W. HUBER and CLIFFORD H. NELSON	
62. SURVEY OF PLASMA ACCELERATOR RESEARCH.....	361
MACON C. ELLIS, JR.	

### SESSION T

#### LABORATORY TECHNIQUES

*Chairman: Leonard D. Jaffe*

63. TECHNIQUES FOR ACHIEVING STEADY-STATE TEMPERATURES ABOVE 1,500° C.....	385
HOWARD E. MARTENS	
64. HIGH-VACUUM TECHNIQUES FOR RESEARCH.....	391
JACK L. TAYLOR	
65. TECHNIQUES FOR LABORATORY STUDIES OF MODERN MAGNETISM.....	411
FLOYD B. HUMPHREY	
66. GENERATION OF MAGNETIC FIELDS BY FLUX COMPRESSION IN SUPERCONDUCTORS.....	429
DANIEL D. ELLEMAN	

### SESSION U

#### MATERIALS

*Chairman: John E. Duberg*

67. SPACE ENVIRONMENT AND ITS EFFECTS ON MATERIALS.....	439
DON D. DAVIS, JR.	
68. NONMETALLIC MATERIALS FOR SPACECRAFT.....	451
GEORGE F. PEZDIRTZ	
69. ABLATION MATERIALS FOR ATMOSPHERIC ENTRY.....	461
LEONARD ROBERTS	
70. FLOW AND FRACTURE PROBLEMS IN AEROSPACE VEHICLES....	469
RICHARD H. KEMP	
71. HIGH-STRENGTH MATERIALS RESEARCH.....	477
HUBERT B. PROBST	

**CONTENTS**

*SESSION V*

*STRUCTURES*

*Chairman: Richard R. Heldenfels*

	Page
72. RESEARCH, DESIGN CONSIDERATIONS, AND TECHNOLOGICAL PROBLEMS OF STRUCTURES FOR LAUNCH VEHICLES.....	487
HARRY L. RUNYAN and ROBERT W. LEONARD	
73. RESEARCH, DESIGN CONSIDERATIONS, AND TECHNOLOGICAL PROBLEMS OF STRUCTURES FOR WINGED AEROSPACE VEHICLES.....	499
ELDON E. MATHAUSER	
74. RESEARCH, DESIGN CONSIDERATIONS, AND TECHNOLOGICAL PROBLEMS OF STRUCTURES FOR PLANETARY ENTRY VEHICLES.....	511
ROGER A. ANDERSON	
75. RESEARCH, DESIGN CONSIDERATIONS, AND TECHNOLOGICAL PROBLEMS OF STRUCTURES FOR SPACECRAFT.....	521
GEORGE W. BROOKS	

**SESSION M**

**Chemical Rocket Propulsion**

***Chairman,* WALTER T. OLSON**

DR. WALTER T. OLSON is Chief of the Chemistry and Energy Conversion Division of the NASA Lewis Research Center. Appointed to the Lewis staff in 1942, he has conducted, supervised and reported research on fuels and combustion programs for turbojet, ramjet, and rocket engines. Dr. Olson has also served as a consultant to the Department of Defense and the U.S. Air Force. He was graduated from DePauw University in 1939 with a B.S. degree in Chemistry, earning his M.S. and Ph. D. degrees in Chemistry and Chemical Engineering from Case Institute of Technology in 1940 and 1942, respectively. Dr. Olson is an Associate Fellow of the Institute of the Aerospace Sciences, a Director of the Combustion Institute and a member of the American Chemical Society and the American Rocket Society.

# Introduction

By WALTER T. OLSON

The status of some of the key technology of the chemical rocket system is reviewed in this Session. In this review it is hoped that (1) the current problems in this technology will be revealed, (2) the fundamental physical principles involved in these problems will be made apparent, and (3) the directions in which solutions probably will lie will be indicated.

A sonde, satellite, space probe, or manned spacecraft requires for its mission a specified amount of kinetic energy, more often expressed as a velocity. With regard to rocket-propulsion, the speed imparted to the payload depends on just two items: the energy per pound of propellant and the amount of propellant that is carried. The former is specific impulse, is expressed as seconds, and is dependent on propellant chemistry; the latter is mass ratio and is dependent on vehicle design. Figure 1 shows the relations. For example, an RP-1 (kerosene)—liquid-oxygen engine in a vehicle in which 92 percent of the initial weight is consumable could provide a velocity to the payload of 27,000 feet per second (92 percent is a number that is commensurate with several large vehicles using this propellant). If the thrusting is done near the earth, 32.2 feet per second must be deducted for each second of burning. About 10,000 feet per second must be deducted for a 5-minute launch because of work against gravity; therefore, 17,000 feet per second is the net velocity for this example. Other corrections can be ignored for the present purposes.

Of course, one rocket vehicle can be made the payload on another, larger vehicle—by staging—to build up the ultimate flight velocity needed.

The inherent simplicity and instant readiness of solid propellants makes them useful for many applications: launching of smaller satel-

lite payloads, as in Scout; orbital changes or injection, as in Echo, Tiros, or Surveyor; stage separation and emergency escape, as in Mercury, Gemini, and Apollo. Their great value in the military mission need not be detailed.

Over the years since the first asphalt—potassium perchlorate and double-base powders, the specific-impulse performance of solids has risen from about 180 pounds per pound per second to values for today's composite propellants of about 245 seconds (on a 1000-lb/sq in. chamber pressure basis). Further gains, however, are difficult. Expenditures of many millions of dollars in the last half dozen years in an attempt to find new ingredients for higher specific impulse have made specific-impulse values of the order of 300 seconds appear possible, but probably at the expense of the physical properties of the grain. Best gains in the performance of solid rockets have come from improving the mass ratio. Innovations such as high-tensile steels, cases wound from high-tensile glass filaments, and composite structures for nozzles have boosted propellant loadings to as much as 0.87 to 0.91 of the vehicle gross weight.

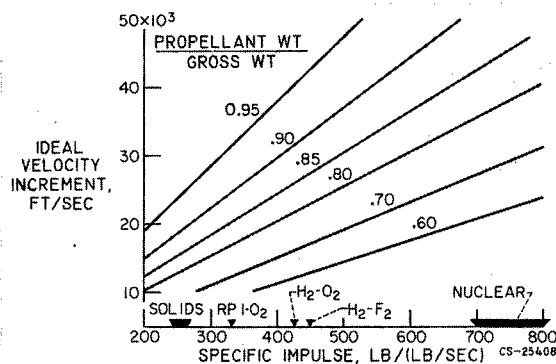


FIGURE 1.—Rocket vehicle performance.



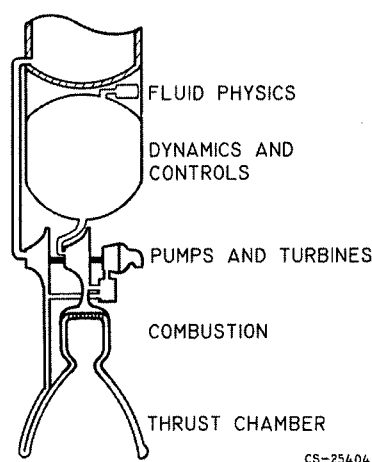
## CHEMICAL ROCKET PROPULSION

Not shown on figure 1, but performing in the range between solids and RP-1—liquid oxygen, are propellants like nitric acid and alkyl-hydrazine mixtures. Having the advantage of being liquids at room temperatures, they are useful in space rockets like Agena, the Mariner course-correction engine, and the lunar excursion module of Apollo.

The higher end of performance including even reasonably stable chemicals, is represented by hydrogen-oxygen and hydrogen-fluorine. Addition of metals like beryllium or lithium to these systems improves the specific impulse, but this approach requires a very high weight fraction of hydrogen, which makes a poor density for the system, and also adds the complexity of feeding and burning metal.

For reference, the coming first generation of nuclear heat-transfer rockets is shown, with performance at 700 seconds for hydrogen at 2672° F to 800 seconds at 3500° F. With a propellant density about one-fifth to one-twentieth that of chemical rockets, with an inherently heavier powerplant, and with the necessity of shielding, nuclear heat-transfer rockets as presently conceived have a long, rough, and expensive road before they will be able to compete in performance with chemical rockets. Propellant fractions will certainly have to exceed 0.75 of gross weight. Therefore, chemical rocket systems will be used for a long time, and it is vital to the space program that they be made as efficient and reliable as possible.

The particular propellants to which the discussion of this Session are directed are RP-1—



CS-25404

FIGURE 3.—Chemical rocket.

liquid oxygen and hydrogen-oxygen, although much of what is presented is broadly applicable to more than these propellants alone. Time does not permit detailed discussion of other liquids or of solids. Furthermore, these propellants are prominent in the several principal engine programs of NASA as seen in figure 2. These engines are vital to many of our foreseeable space flights, particularly manned flights.

The H-1 engine is an outgrowth of the Thor and Atlas engines; a cluster of eight of these engines drives the Saturn C-1 booster. The F-1 engine is currently in development and will power launch vehicles for manned lunar flight. The three hydrogen-oxygen engines are for various upper stages of lunar vehicles. They signify a heavy reliance of the NASA space program on hydrogen-oxygen. Consequently, a large technology effort is progressing on this combination, which should have its first successful flight in the Centaur vehicle, powered by two of the A-3 chambers. The J-2 engine, in development, is for upper stages of Saturn for manned lunar flight. The M-1 engine is for still larger launch vehicles.

Figure 3 shows the five topics of the chemical rocket discussed in this Session: fluid systems, pumps and turbines, combustion, thrust chambers, and dynamics and controls. The physical principles, the understanding and mastery of which are vital to successful engineering of rocket-propulsion systems, are discussed.

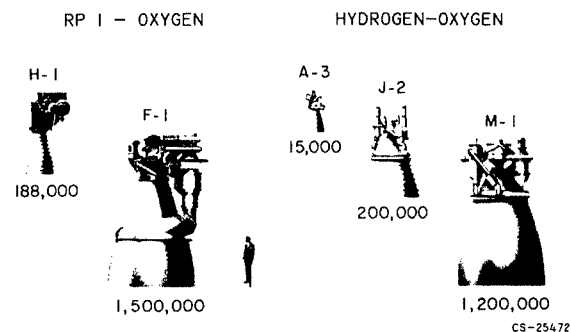


FIGURE 2.—NASA chemical rocket engines and pounds of thrust produced.

## INTRODUCTION

## BIBLIOGRAPHY

- GRELACHI, C. J. and TANNENBAUM, S.: Survey of Current Storable Propellant. ARS Jour., vol. 32, no. 8, Aug. 1962, pp. 1189-1195.
- OLSON, WALTER T.: Problems of High Energy Propellants for Rockets. Rocket and Missile Technology, Chem. Eng. Prog. Symposium (Am. Inst. Chem. Eng.), ser. 33, vol. 57, 1961, pp. 28-37.
- SEIFERT, H. S.: Twenty-Five Years of Rocket Development. Jet Prop., vol. 25, no. 11, Nov. 1955.
- SUTTON, GEORGE P.: Rocket Propulsion Elements. Second ed., John Wiley & Sons, Inc., 1956.
- The Chemistry of Propellants. Combustion and Propulsion Researches and Reviews. AGARD, Pergamon Press, 1960.
- Jet Propulsion Engines. Vol. XII of High Speed Aerodynamics and Jet Propulsion, Princeton Univ. Press, 1959.
- Liquid Propellants Handbook, vols. 1 to 3, and LPIA Abstracts, 1958 to Present. Liquid Propellant Info. Agency, Appl. Phys. Lab., Johns Hopkins Univ.
- Propellant Manual. SPIA/M-2, Feb. 1961, and SPIA Abstracts. Solid Propellant Info. Agency, Appl. Phys. Lab., Johns Hopkins Univ.
- Rocket Motor Manual. SPIA/M-1, vols. 1 and 2, Sept. 1962, SPIA, Appl. Phys. Lab., Johns Hopkins Univ.

## 37. Fluid Physics of Liquid Propellants

By Donald L. Nored and Edward W. Otto

DONALD L. NORED, an Aerospace Scientist at the Lewis Research Center, is engaged in program planning and design studies for pressurization systems and fluid components in the Apollo Propulsion Office. He has worked on advanced propulsion facility design and operation, high-energy-propellant rocket engine development, and vehicle systems studies. Mr. Nored received his B.S. degree in Chemical Engineering from Texas Technological College in 1955. He is a member of the American Rocket Society and the American Institute of Chemical Engineers and is a registered Professional Engineer of the State of Ohio.

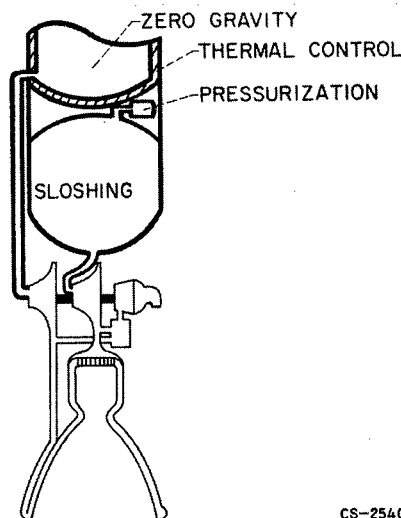
EDWARD W. OTTO is Head of the Fluid Systems Section of the Lewis Research Center. He has specialized in propulsion systems dynamics and controls and is currently engaged in the study of the behavior of liquids in a zero-gravity environment. Mr. Otto is a graduate of Iowa State University, where he received his B.S. degree in Mechanical Engineering in 1944. He is a member of Pi Tau Sigma and Phi Kappa Phi.

### INTRODUCTION

The use of liquid propellants in chemical rocket engine propulsion systems, while quite common, has necessitated the solution of a number of problems peculiar to rocket vehicles. Two relatively new areas of application, however, have presented new fluid physics problems. These areas are (1) the use of cryogenic propellants in general and (2) the use of liquid propellants in a space vehicle. This discussion treats these two new areas of application by reviewing the various attendant problems and indicating the extent of present knowledge.

Figure 37-1, showing a typical liquid bipropellant rocket vehicle, indicates those areas directly concerned with the physics of the fluid systems. These fluid systems are composed of the tankage for the liquid propellants, associated internal baffles and diffusers, insulation surrounding the tanks, and the pressurization system. Also included are the necessary lines, control components, and heat exchangers. The problems existing in such systems may be di-

vided into two categories: those pertaining to the powered phases of a mission and those pertaining to the coast phases. Pressurization and sloshing of propellants are the two problem



CS-25406

FIGURE 37-1.—Problem areas in typical liquid propellant rocket fluid systems.

areas of interest during the powered phases, while thermal control and effects of zero gravity are of interest during coast.

### PRESSURIZATION

The first major problem area, pressurization, exists whether the vehicle is pressure-fed or pump-fed since a pressurization system of some kind will always be required. Such a pressurization system can become a large part of vehicle dry weight for those space vehicles utilizing cryogenic propellants for the following reasons:

(1) Liquid hydrogen has a low density, hence the tanks will be large, and a resultant large amount of pressurant will be required.

(2) There will be a drastic drop in the temperature of the incoming pressurizing gas; thus, the final gas density will be high, and even more gas will be required.

The largest problem encountered in the field of pressurization is the accurate prediction of pressurant requirements. Such prediction is difficult because of the complex transient physical and thermodynamic processes occurring within the propellant tank. These processes are shown in figure 37-2.

The heat-transfer processes of primary importance are the heat transferred to the walls, heat transferred to the liquid, and heat transferred to the ullage space vapor and gas by the incoming pressurizing gas. The mode of internal heat transfer to the walls and liquid is some form of free convection; thus, the geometry of the tank becomes important. The heat trans-

ferred to the ullage gas and vapor is dependent on the mixing occurring and hence is a function of diffuser design (i.e., inlet gas distribution), propellant vapor density changes, and pressurant density changes. Heat transfer from the external environment, from the wall to the liquid, and by axial conduction is generally quite small during the expulsion period but of extreme importance during coasting periods.

The mass transfer within the tank occurs by condensation and evaporation at the liquid interface and wall interface. Generally, it is assumed that mass transfer, while significant in small tanks, becomes quite small as tank size increases. Recent data taken on Saturn tanks, however, indicate that such mass transfer may be larger than is generally assumed. In any event, the analytical prediction of mass transfer is perhaps the most difficult task in determining pressurant requirements. The transient nature of the processes occurring, as well as the unknown pressurant and vapor distribution throughout the ullage space, are only two of the reasons for the task being difficult. Future mathematical models based on analytical studies must of necessity include considerations of mass transfer, with experimental tests being required to establish the actual magnitude and mode of such mass transfer, especially for large tanks.

Because of the transient nature of the various processes, with system parameters varying in both time and space, temperature stratification occurs during expulsion. The stratification within the liquid causes a warm layer of liquid to form at the interface, although the temperature of the bulk of the liquid remains relatively constant. Temperature stratification that occurs within the ullage space varies from the warm liquid temperature at the interface to the gas inlet temperature at the top of the tank. There are also concentration gradients throughout the ullage space of the inlet pressurant, pressurant used in previous expulsions, and propellant vapor. These gradients are dependent upon diffusion effects and degree of mixing, variables not subject to ready analysis, as well as history effects (i.e., time of pressurization prior to expulsion, heat transfer during coast,

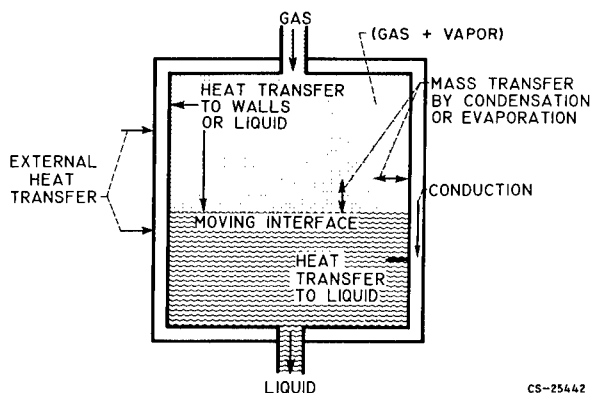


FIGURE 37-2.—Heat- and mass-transfer processes affecting pressurization during expulsion.

venting during coast, pressurant added in previous firings of the engine system, etc.).

As can be appreciated, an analytical approach to the problem of predicting pressurant requirements is extremely difficult. In general, the variables affecting the heat- and mass-transfer processes, and thus influencing pressurant requirements, are (1) pressurant type and state, (2) propellant type and state, (3) propellant tank characteristics, (4) expulsion characteristics, (5) history of the tank and contents, (6) slosh, vortexing, and diffuser design, and (7) gravity field. Several methods have been advanced for predicting pressurant requirements; however, they are limited in application, particularly for space vehicles, either because of simplifying assumptions or because many of the variables are neglected. Better methods, of a more generalized nature and verified by representative experimental data, will be required in the future in order that realistic space vehicles may be designed.

Another problem concerning pressurization systems is the selection of a particular system. The general requirements for a pressurization system for a space vehicle always include: (1) lightweight and (2) high reliability, and depending upon the mission, may include (3) restart capability, (4) instant readiness, (5) long-term compatibility with the propellants, and (6) variable flow capability. Since a multitude of systems exist that potentially meet these requirements, some type of classification is required for the process of selection. If systems are classified according to source of pressurizing fluid, there are only four major classes. Roughly in order of decreasing system weight and increasing system complexity, the classes of systems are those that use

- (1) Stored gases
- (2) Evaporated propellants
- (3) Evaporated nonpropellants
- (4) Products of a chemical reaction

The first class is one of the most common, being used in some form in most of the present-day liquid-propellant rocket vehicles. Stored helium systems typical of this class have high reliability; compatibility is not a problem; and there is a backlog of experience on components.

Some of the parameters influencing the weight of the system are: (1) storage temperature, (2) storage pressure, (3) type of gas expansion, and (4) material used for the storage tank.

The second class, using evaporated propellants, is the next most common type of system. This type of system has been used on several pump-fed vehicles where the liquid, usually liquid oxygen, is tapped off downstream of the pump, vaporized in some convenient heat exchanger, and then used to pressurize the propellant tank from which it was obtained. Systems for pressure-fed vehicles have not been developed to any extent, but they offer great potential in weight savings (especially for liquid hydrogen) and should be studied further.

Evaporated-nonpropellant systems, the third class, have not been tested extensively. Indeed, only two types of systems could be contemplated as being useful for cryogenics, those using liquid helium and liquid nitrogen. Each of these has certain disadvantages, however, that would generally preclude their use.

The last class, systems using products of a chemical reaction, perhaps offers the greatest potential in future weight savings. Gas generators to generate gaseous products for use in pressurizing storable propellant tanks have been developed and flown. Another method, having undergone a small amount of testing recently, involves the injection of a hypergolic (spontaneously ignitable) fluid into one of the propellant tanks. This permits the reaction to occur within the tank. The method is attractive for the liquid-hydrogen tank in particular, since vaporized liquid hydrogen, if obtainable, has a lower gas density than the reaction products. Although the method is basically simple, it does present problems of control, especially of temperature.

The selection of a system from the four classes for a particular space vehicle depends not only on the requirements just discussed, but also on the tradeoffs involved with other systems. The development of the more advanced systems, particularly in the areas of controls, heat exchangers, components, and materials, will be desirable in order to give a more valid basis for the tradeoffs involved.

## SLOSHING OF PROPELLANTS

The second major problem area influencing the use of liquid propellants in rocket vehicles is propellant sloshing. Oscillations may result, for example, from the attitude control system and can exert forces and moments on the vehicle that cause a shift in the center of gravity. Figure 37-3 shows a schematic of a vehicle undergoing sloshing. The propellant sloshing exerts side forces which, at a maximum, may reach a force approximately equal to one-quarter of the apparent weight of the propellant. These side forces not only increase structural loads on the tankage and supports, but also require thrust-vector control from the rocket engine. In extreme cases, critical disturbances to the stability of the vehicle may occur. Furthermore, when sloshing occurs, the pressurization gas entering the tank may be cooled more rapidly, and thus more gas would be required. Still another effect might be the exposure of the outlet to vapor. This would result in vapor entering the flow systems, where it could have disastrous effects. The alleviation or elimination of sloshing is, therefore, extremely desirable.

Figure 37-4 shows the slosh-force parameter as a function of the frequency parameter for a half-full spherical tank. These parameters are nondimensionalized and are independent of tank size or density of the liquid. The solid curve represents the theoretical results for un-

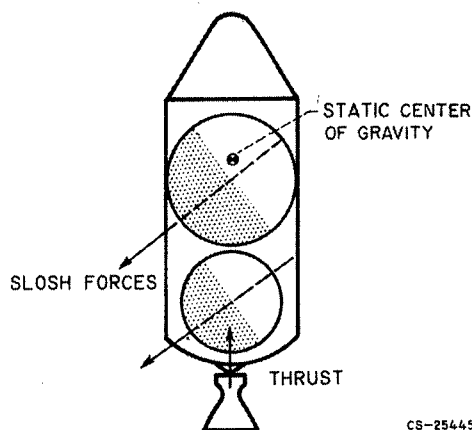


FIGURE 37-3.—Forces exerted on vehicle during sloshing.

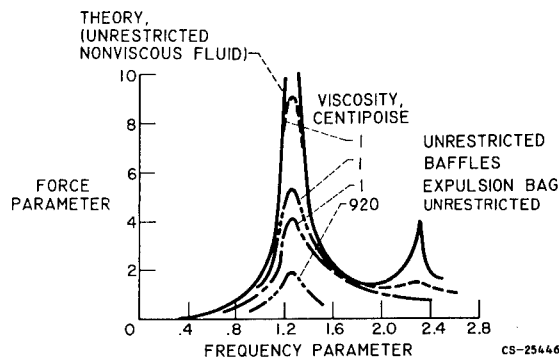


FIGURE 37-4.—Effects of control devices on slosh forces in half-full spherical tank.

restricted nonviscous sloshing. The effects of various methods of slosh control are shown, and they are best compared at the first natural frequency at which the largest slosh forces arise. The first natural frequency is the point at which the excitation and fundamental frequencies of the contained liquid are equal.

The most common method to date of controlling sloshing is by placing baffles within the tank. While effective, these are seen to be the worst of three available methods. The second method utilizes a continuous surface film, such as obtained by expulsion bags or diaphragms. This method is more effective than baffles, but involves problems of compatibility, leakage, venting, fabrication, and other mechanical difficulties, particularly for large tanks. Since expulsion bags also permit displacement of liquids under zero gravity, however, such an approach has been used for relatively small-scale propellant tanks—slosh control being gained as a secondary feature. The third method is the most effective and involves increasing the viscosity of the liquid; for the case shown in figure 37-4, the viscosity was increased from 1 to 920 centipoise. Successful attempts have been made at increasing the viscosity of so-called Earth storable propellants by gelling the propellants and making a thixotropic material out of the liquid; however, very little progress has been made in such gelling for cryogenic propellants. Indeed, the gelling of cryogenics remains as one of the few fields in which large advances may still be made.

### THERMAL CONTROL OF PROPELLANTS

The third major problem area is thermal control of the propellants. For cryogenic liquids the incoming thermal energy must be minimized since such heat input will cause propellant heating, vaporization, and a resulting loss of propellant by venting. Unless these losses are small, the potential advantages of using cryogenic propellants will vanish.

The sources of propellant heating may be either internal or external with respect to the space vehicle, as indicated by figure 37-5. The space vehicle is assumed to comprise four sections. The payload section contains the instrumentation and guidance equipment and must be maintained at a temperature on the order of  $520^{\circ}$  R. The liquid-oxygen section requires a temperature of approximately  $163^{\circ}$  R, while the liquid-hydrogen tank must be maintained at approximately  $37^{\circ}$  R; the engine temperature will depend on the type of engine system. These temperatures may vary somewhat, depending upon the pressure of the propellant, the type of instrumentation, and the specific design of the vehicle, but the relative order of magnitude will remain the same.

Heating due to internal sources is caused by thermal radiation between the various components of the vehicle and by conduction through propellant lines and structural supports. The possible external sources of heat are the sun, the planets and their moons, and the galaxies. Heat is transferred between the vehicle and these sources solely by thermal radiation. The largest external heat flux encountered by a space

vehicle within our solar system is usually that which originates from the sun. The heat flux received from a planet results partly from planetary radiation and partly from reflected solar radiation. This planetary heat flux becomes greater as the planet is approached, and, in some cases, could become of the same order of magnitude as the solar heat flux. Galactic heating is negligibly small and is usually ignored.

In general, interstage conduction is controlled by using minimum areas and low-conductivity materials for all components attached to the tank. Thus, the major problem of heat input is one of proper control of thermal radiation due both to internal and external sources. Various methods of control of thermal radiation are available, and they may be classified as orientation, coatings, and insulations.

By proper orientation of the vehicle certain sections can shade other sections. For example, the payload could be pointed toward the sun, thus acting as an effective external sun shadow shield for the rest of the vehicle. Also, arrangement is important since the oxygen tank could act as a shadow shield for the hydrogen tank, protecting it against internal thermal radiation from the payload. In any case, however, some other method of thermal radiation control must still be employed since such arrangement or orientation will leave at least one section at too high a temperature for effective use.

Various inorganic or organic coatings are available which, by the proper balance of emissivity and absorptivity, permit some equilibrium temperature to be attained by the surface on which the coating is applied. The lowest temperature obtainable, however, by presently available coatings, is still much higher than the temperatures of the cryogenic liquids. Hence, while useful, coatings will not alone provide the proper temperature environment and must be supplemented by other methods of thermal radiation control.

The best means of control is the use of insulations. Figure 37-6 shows a comparison of various insulations that are useful for space vehicles. The product of apparent thermal conductivity and density is used as the means of

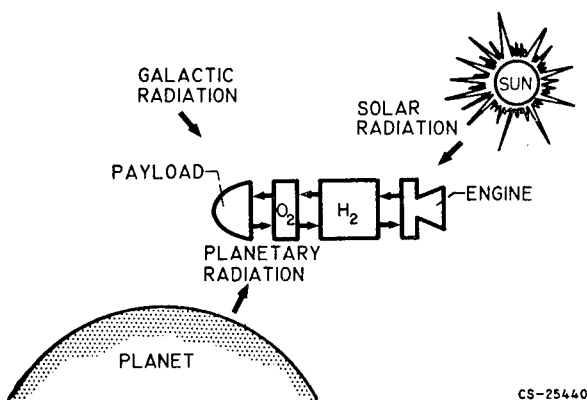


FIGURE 37-5.—Sources of heat input to cryogenic vehicle in space.

## CHEMICAL ROCKET PROPULSION

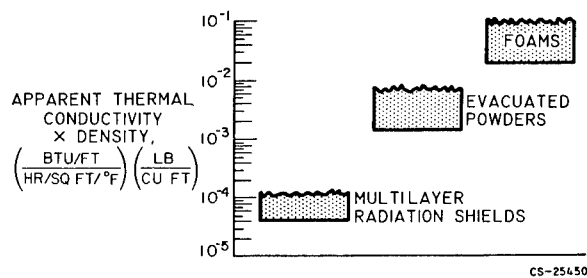


FIGURE 37-6.—Comparison of insulations for space applications.

comparison since this product arises when the basic heat-transfer equation for conduction is modified to reflect insulation weight. Optimum insulation occurs when this product is a minimum. The apparent thermal conductivity is determined from measurements of the net heat flux across a thickness of insulation, and thus includes conduction, radiation, and convection if applicable. Foams are typical of those insulations that restrict the flow of heat primarily by means of low thermal conduction alone. Evacuated powder-type insulations not only have low conduction and very little convection, but also reduce the radiant energy transfer and thus result in a much lower apparent thermal conductivity than foams. At present, however, the best of the insulations consists of parallel, thermally isolated, reflected shields. Such shields are more effective than powders in reducing radiant heat transfer, and thus are better insulations for thermal control of propellants under space conditions. If close together, these shields are commonly called foils. The so-called superinsulations consist of reflective foils separated by very low-conduction materials.

In use, foams are relatively easy to apply to the vehicle tanks but give high weights of insulation required. The powders require a rigid jacket around the tank for correct placement, which increases the weight and causes problems of settling and the occurrence of voids. Foils also have an installation problem, as compressive loads reduce their efficiency. Trade-offs, therefore, between the various insulations must be made for each particular mission, as well as for the proper use of each of the methods of thermal control. At present, however, the effects of compressive loads, and techniques of design, such as fastening, supporting, and evac-

uation, require more work before valid trade-offs may be performed.

## EFFECTS OF ZERO GRAVITY

The final problem area to be discussed concerns the effects of weightlessness (i.e., zero gravity) on the liquid propellants. Weightlessness will be encountered by space vehicles during orbital or space missions, and a knowledge of the final equilibrium liquid-vapor interface configuration will be needed to solve the problems of effective tank venting and proper pump inlet design. Furthermore, a knowledge of the modes of heat transfer to stored propellants during periods of weightlessness will also be needed.

### Control of Interface

For effective control of the liquid-vapor interface the various forces predominating in a zero-gravity environment must be understood. Such forces are generally intermolecular in nature; that is, they are relatively small, are exerted over a short range, and are independent of the gravitational field. One such force that should persist in zero gravity is the surface tension of the liquid, or, a property associated with surface tension, the contact angle at which the liquid meets the solid surface (measured in the liquid). Another consideration for a zero-gravity environment actually is based on the observed characteristic of systems to assume a state of minimum energy when external forces are removed. This would suggest that the interfaces, if free to move, would assume some

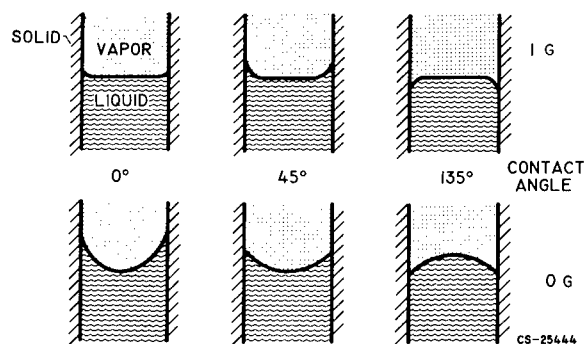


FIGURE 37-7.—Interface configurations in cylindrical container as function of gravity field and contact angle.



spherical shape, this being the shape representative of minimum energy.

Figure 37-7 indicates the effect of combining these two conditions for liquid in a cylindrical container. Both the 1-g and zero-g configurations are shown, for a range of contact angles. For the 1-g case the contact angle of the liquid is observed in the meniscus at the liquid-solid interface. Upon entering the zero-gravity state, the contact angle will be preserved, and the liquid-vapor interface, being free to move, will adjust itself until a constant curvature surface is reached. In an enclosed container, of course, the actual shape of the liquid surface would not only be determined by contact angle preservation and considerations of minimization of energy, but also by the shape of the container and the amount of liquid in the container.

To verify the reasoning used in this analysis many experimental tests have been conducted at the Lewis Research Center, primarily in a 2.25-second-free-fall drop tower. These tests have verified the predictions in every detail. Selected photographs taken from motion-picture data (using high-speed photography) for a typical test drop are shown in figure 37-8. This figure shows a 100-milliliter glass sphere with a liquid- to tank-volume ratio of 40 percent. The liquid in this case is ethyl alcohol, which has a contact angle of zero and is thus representative of the cryogenic fluids. The photographs represent the conditions at 1 g and the equilibrium conditions for zero g. It can be seen that, at 1 g, the alcohol rests in a pool at the bottom of the sphere. The liquid surface is essentially flat. The meniscus is concave, and the liquid contacts the wall at an angle of  $0^\circ$ . During the zero-g period, the liquid begins to rise along the wall, and the liquid surface becomes curved. At the equilibrium condition the result is a completely wetted tank wall with a spherical vapor bubble in the interior of the liquid.

The results of the experimental studies, as previously indicated, have tended to verify the prediction that the total surface energy is minimized in zero gravity. In order to provide further verification, a definitive analytical model was studied. This model used a geometry consisting of a hollow tube suspended

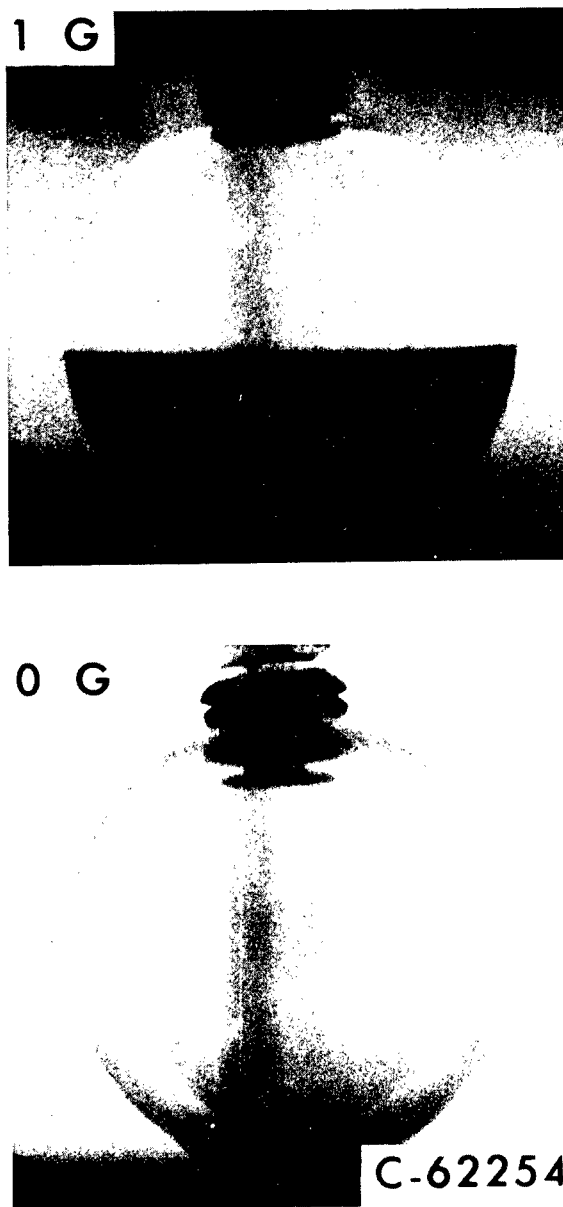
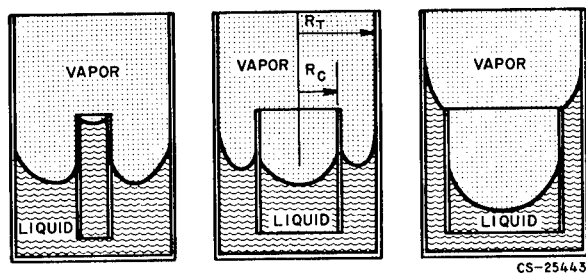


FIGURE 37-8.—Interface configurations of wetting liquid in spherical container at normal gravity and during weightlessness. Tank 40 percent full.

within a cylindrical tank, aligned with the vertical axis, and being open to the liquid at both top and bottom. An analysis of this configuration, solving for the minimization of surface energy, indicated that for liquids with contact angles less than  $90^\circ$  the liquid will rise in the tube if the tube radius is less than one-half the tank radius, will remain level if the tube radius is equal to one-half the tank radius, and



(a)  $R_c < \frac{1}{2} R_T$ . (b)  $R_c = \frac{1}{2} R_T$ . (c)  $R_c > \frac{1}{2} R_T$ .

FIGURE 37-9.—Effect of tube radius on interface configuration for wetting liquid in cylindrical container.

will fall if the tube radius is greater than one-half the tank radius.

Experimental tests have been conducted with wetting liquids in a similar geometry, in which the tube radius was varied and the direction of liquid motion was observed as the experiment was subjected to zero gravity. Results of these experiments are summarized schematically in figure 37-9 for a liquid with a contact angle of  $0^\circ$ . Sketches of the interface configurations are shown after equilibrium conditions in zero gravity have been reached. Three tube radii ( $R_c$ ) were used, being respectively less than, equal to, and greater than one-half the tank radius ( $R_T$ ). These experiments verified the previous analysis in every detail and provided proof that the solid-liquid-vapor system will tend to assume a configuration of minimum free surface energy when placed in a weightless environment.

#### APPLICATIONS

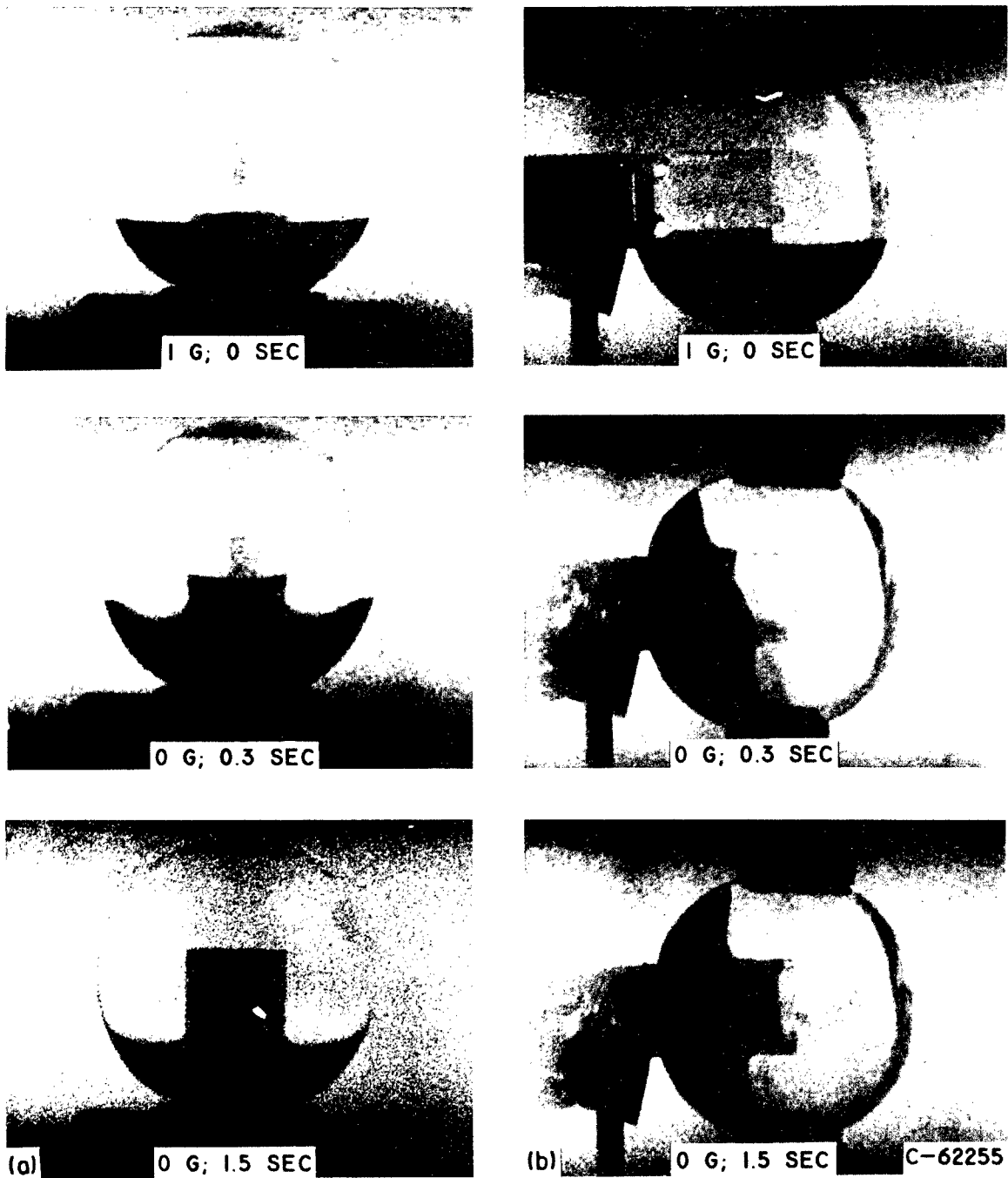
As a result of these fundamental studies, it appears that the tank systems can be designed by using suitable internal baffling to position the liquid-vapor interface properly. The principal requirements of an interface control system in a propellant tank are that it maintain a quantity of liquid over the pump inlet, and, if venting is necessary, that it maintain the main ullage volume over the vent. The capillary tube geometry employed in the minimum-surface-energy studies appears to provide a satisfactory interface configuration in that it locates liquid over the pump inlet if such a pump inlet is placed at the bottom of the capillary tube and

vapor over the vent if the vent is located above the tube.

The configuration of the liquid-vapor interface in zero gravity, obtained with a standpipe geometry for two orientations of the container, is shown in figure 37-10. This figure shows a 100-milliliter glass sphere with a liquid- to tank-volume ratio of 30 percent. Again ethyl alcohol (containing a dye for ease of photography) is used in order to duplicate cryogenic liquids having a contact angle of zero. The capillary tube (or standpipe) has a tube diameter of 33 percent of sphere diameter and a relative height of 60 percent. The photographs in figure 37-10(a) indicate the ability of the liquid to fill the standpipe and the vapor to form over the vent (if located above the standpipe) for the case in which the sphere enters zero gravity at an angle of  $0^\circ$  between the gravity vector and the axis of the standpipe. Figure 37-10(b) is similar, except that the sphere enters zero gravity at an angle of  $90^\circ$ , and again the ability to position the liquid and vapor bubble is shown. Such ability, however, is very time dependent, and for low fillings a relatively long period of time is required to properly position the vapor bubble after zero gravity has been entered at a high angle to the initial gravity vector.

The standpipe geometry encounters difficulties in positioning the vapor bubble over the vent at high fillings, however, when the vapor bubble is small. If the standpipe is made relatively high, there is danger that the bubble could become trapped in the annular space following an adverse acceleration. A geometry that avoids entrapment of the vapor bubble and urges it to the vicinity of the vent or, conversely, pumps the liquid to the bottom of the tank would be desirable. Liquid can be pumped by capillary forces from one end of a tank to the other if tapered geometry is used and suitable return paths are provided. This principle may be employed to overcome some of the difficulties encountered with standpipes at high fillings. The application of this principle to a spherical tank is shown in figure 37-11. The tapered section is formed in this case by offsetting a second sphere within the first. The geometry is now such that the vapor bubble obtains its

FLUID PHYSICS OF LIQUID PROPELLANTS



- (a) Initial position,  $0^\circ$  between gravity vector and standpipe.  
 (b) Initial position,  $90^\circ$  between gravity vector and standpipe.

FIGURE 37-10.—Movement of wetting liquid in capillary tube ullage control geometry.

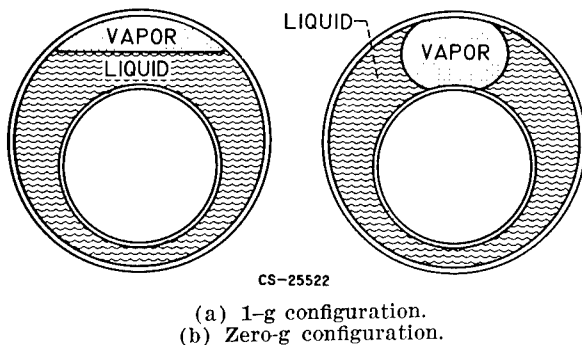


FIGURE 37-11.—Application of tapered section principle to spherical tank.

most nearly spherical shape under the vent but cannot become completely spherical even for fillings of 95 percent. The result is the movement of the bubble to the vent from any starting position. The ability of this geometry to move the vapor bubble is shown in figure 37-12; the vapor bubble is initially 90° away from the vent but is pumped toward the vent by capillary action when zero gravity is entered. In this experiment, the outer sphere has a volume of 100 milliliters. The inner sphere is 60 percent of the diameter of the outer sphere, which forms a tapered annular section around the inner sphere. The liquid is again ethyl alcohol, and the liquid- to tank-volume ratio is 95 percent.

While the experiments to date have indicated that the liquid-vapor interface can be adequately controlled, two questions remain to be answered. The scaling parameter of time must be further studied, and the amount of acceleration to disrupt a surface under zero gravity must be known. Acceleration disturbances (crew movement, orientation maneuver, etc.) may cause the liquid and vapor to be improperly oriented, and thus an unknown length of time may be required for proper positioning.

#### Heat Transfer

Another problem on which further research is needed is that of heat transfer under weightless conditions. The mechanism of heat input to a tank under space conditions corresponds to that of a classical pool-boiling situation, the various regions of which are shown in figure 37-13 for a 1-g field. The coordinates are heat

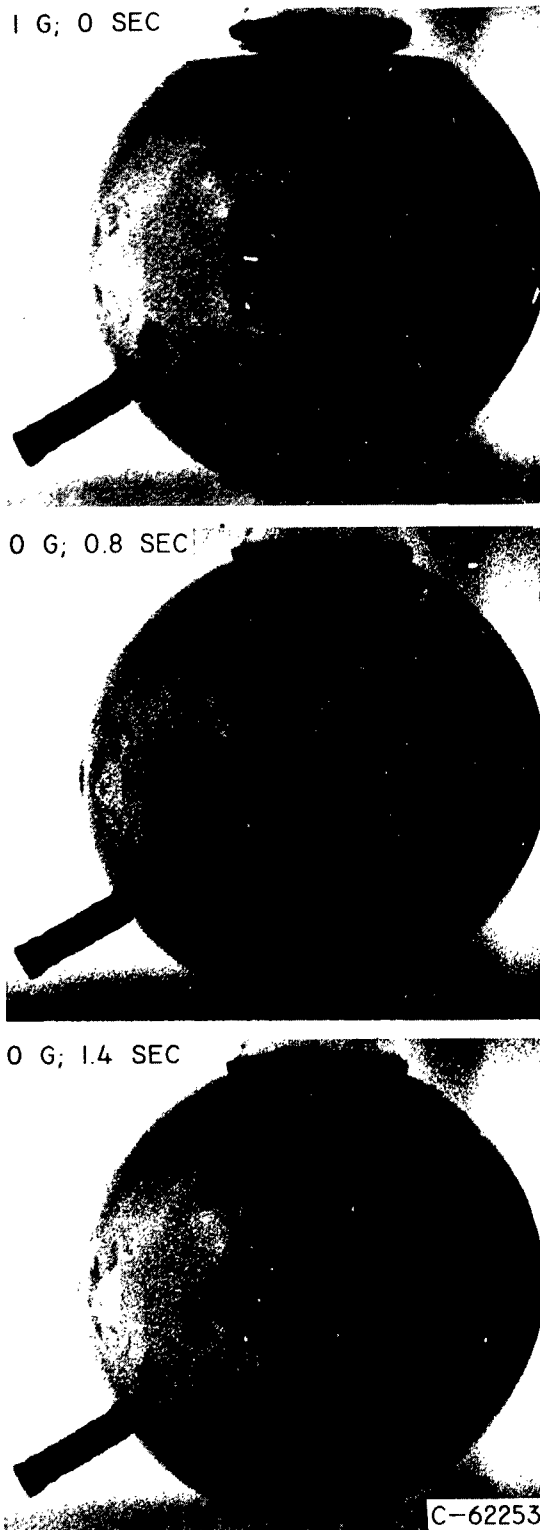


FIGURE 37-12.—Movement of vapor bubble in tapered-section ullage control geometry. Initial position, 90° from vent; wetting liquid.

flux plotted as a function of temperature difference.

The heat-transfer regions start with conduction at very low flux, and, as flux is increased, progress through convection and nucleation, and finally, at very high flux, to the mechanism of film boiling. The regions of convection and nucleation may be substantially affected by the loss of gravity. Convection currents should certainly be absent in a zero-gravity environment, although residual currents might persist for some time; however, the nucleation picture is less clear. The velocity of bubbles through the liquid depends on the gravity field. If the velocity becomes zero because of loss of buoyancy, the nucleation region may be replaced by a film mechanism of boiling. This situation would be predicted by a proposed nucleation concept that is gravity dependent. A nucleation model has been proposed, however, which is independent of gravity in that bubbles are removed from the surface by a flow field set up around the bubble because of its rate of expansion. If this model is correct, the nucleation region should be relatively unaffected by a zero-gravity environment, and this region would probably extend down to cover the convection region.

A series of experiments using liquid hydrogen has been performed by General Dynamics/Astronautics in which the heat transfer in the nucleate range as a function of temperature difference was measured at 1-g and zero-g conditions. Results of this study are shown in figure 37-14. These results indicate that zero

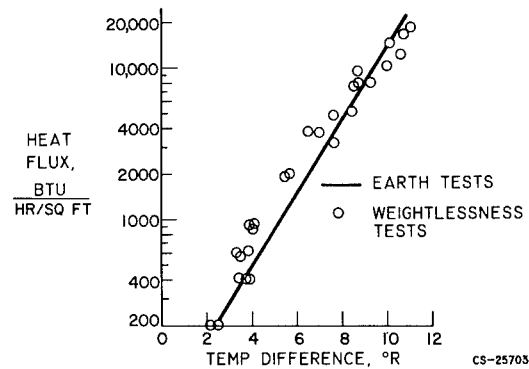


FIGURE 37-14.—Comparison of 1-g and zero-g liquid-hydrogen heat-transfer characteristics for nucleate boiling range. Small, directly heated metal specimens in pool of liquid hydrogen.

gravity has little effect on heat transfer in the nucleate region, which supports the nucleation model that is independent of gravity. The scaling parameter of time, however, among others, is probably quite important in these experiments, and much more work in this area is needed in order to extend our knowledge of heat transfer processes to the zero-gravity situation.

The primary effect of the heat-transfer mechanism for cryogenic liquids is the pressure rise within the container. This problem could be serious in a long term coasting situation. In a normal gravity field, convection currents and high bubble velocities cause most of the heat to be delivered to the gas space, which causes an abnormal pressure rise and thus excessive venting. The heat sink capacity of the liquid, which is considerable in the case of cryogenic propellants, is lost. In a zero-gravity field, if the conduction and nucleation regions are replaced by a film process, again most of the heat will be delivered to the gas, and the heat sink capacity of the liquid will be lost. If the gravity-independent nucleation concept is correct, however, the nucleation continues, but at reduced bubble velocity. Thus more time is available for bubbles to condense as they move through the liquid, more heat is delivered to the liquid, and a lower pressure rise results. Since the available data tend to support the gravity-independent nucleation concept, it would appear that less pressure rise will be experienced in zero gravity than under normal

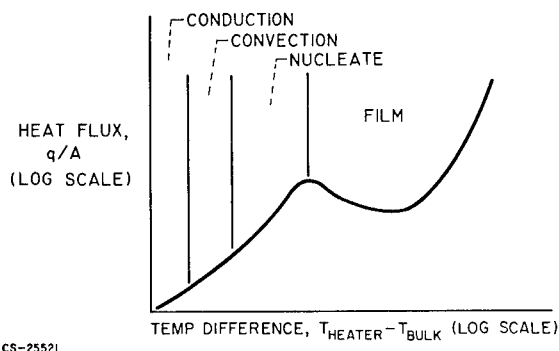


FIGURE 37-13.—Typical pool boiling characteristics for 1-g field.

gravity. The magnitude of this effect is still relatively unknown, however, and warrants further study.

### CONCLUDING REMARKS

In summary, four problem areas primarily involving the use of cryogenic liquids in space vehicles have been briefly discussed. Some answers exist for these areas, but further work, of both a fundamental and an applied nature, is required. In particular, more detailed in-

formation is needed on the physical and thermodynamic properties for the liquids of interest. Furthermore, the areas of heat and mass transfer need better definition under conditions peculiar to a space vehicle.

The problem areas of fluid physics as outlined are not the only areas of interest today, and, as space flights become more ambitious, even more areas requiring study will appear. Indeed, the successful operation of space vehicles must depend upon future solutions to these and other problems.

## BIBLIOGRAPHY

### Pressurization

- ARPACI, V. S., and CLARK, J. A.: Dynamic Response of Fluid and Wall Temperatures During Pressurized Discharge for Simultaneous, Time-Dependent Inlet Gas Temperature, Ambient Temperature, and/or Ambient Heat Flux. Vol. 7 of *Advances in Cryogenic Eng.*, K. D. Timmerhaus, ed., 1961, p. 419.
- ARPACI, V. S., CLARK, J. A., and WINER, W. O.: Dynamic Response of Fluid and Wall Temperatures During Pressurized Discharge of a Liquid from a Container. Vol. 6 of *Advances in Cryogenic Eng.*, K. D. Timmerhaus, ed., Plenum Press, 1960, p. 310.
- BOWERSOCK, D. C., GARDNER, R. W., and REID, R. C.: Pressurized Transfer of Cryogenic Liquids. Vol. 4 of *Advances in Cryogenic Eng.*, K. D. Timmerhaus, ed., Plenum Press, 1958, p. 342.
- BOWERSOCK, D. C., and REID, R. C.: An Analytical Method for Estimating Gas Requirements in the Pressurization and Transfer of Cryogenic Fluids. Vol. 6 of *Advances in Cryogenic Eng.*, K. D. Timmerhaus, ed., Plenum Press, 1960, p. 261.
- CLARK, J. A., VAN WYLEN, G. J., and FENSTER, S. K.: Transient Phenomena Associated with the Pressurized Discharge of a Cryogenic Liquid from a Closed Vessel. Vol. 5 of *Advances in Cryogenic Eng.*, K. D. Timmerhaus, ed., Plenum Press, 1959, p. 467.
- COXE, E. F., and TATOM, J. W.: Analysis of the Pressurizing Gas Requirements for an Evaporated Propellant Pressurization System. Vol. 7 of *Advances in Cryogenic Eng.*, K. D. Timmerhaus, ed., Plenum Press, 1961, p. 234.
- FENSTER, S. K., VAN WYLEN, G. J., and CLARK, J. A.: Transient Phenomena Associated with the Pressurization of Liquid Nitrogen Boiling at Constant Heat Flux. Vol. 5 of *Advances in Cryogenic Eng.*, K. D. Timmerhaus, ed., Plenum Press, 1959, p. 226.
- GLUCK, D. F., and KLINE, J. F.: Gas Requirements in Pressurized Transfer of Liquid Hydrogen. Vol. 7 of *Advances in Cryogenic Eng.*, K. D. Timmerhaus, ed., Plenum Press, 1961, p. 219.
- KAPLAN, C.: Selection of Pressurization System for Storable Liquid Propellant Rocket Engines. *ARS Jour.*, vol. 31, no. 6, June 1961, pp. 786-793.
- NEIN, M. E., and HEAD, R. R.: Experiences with Pressurized Discharge of Liquid Oxygen from Large Flight Vehicle Propellant Tanks. Vol. 7 of *Advances in Cryogenic Eng.*, K. D. Timmerhaus, ed., 1961, p. 244.
- SCHMIDT, A. F., PURCELL, J. R., WILSON, W. A., and SMITH, R. V.: An Experimental Study Concerning the Pressurization and Stratification of Liquid Hydrogen. Vol. 5 of *Advances in Cryogenic Eng.*, K. D. Timmerhaus, ed., Plenum Press, 1959, p. 487.
- SUTTON, J. F., et al.: Main Propellant Tank Pressurization System Study and Test Program. Rep. ER-4728, Lockheed Aircraft Corp., Marietta, Georgia, Feb. 1961.
- VAN WYLEN, G. J., FENSTER, S. K., MERTE H., JR., and WARREN, W. A.: Pressurized Discharge of Liquid Nitrogen from an Uninsulated Tank. Vol. 4 of *Advances in Cryogenic Eng.*, K. D. Timmerhaus, ed., Plenum Press, 1958, p. 395.
- WALSH, THOMAS J., HIBBARD, R. R., and ORDIN, PAUL M.: Dillution of Liquid Oxygen when Nitrogen is Used for Pressurization. NACA RM E58AO3a, 1958.

## FLUID PHYSICS OF LIQUID PROPELLANTS

Anon.: Main Propellant Tank Pressurization System Study and Test Program. Rep. ER-5238, Lockheed Aircraft Corp., Marietta, Georgia, Aug. 1961.

Anon.: Main Propellant Tank Pressurization System Study and Test Program. Rep. ER-5296, vol. III. Lockheed Aircraft Corp., Marietta, Georgia, Dec. 1961.

### Sloshing

ABRAMSON, H. NORMAN, and RANSLEBEN, GUIDO E., JR.: A Note on the Effectiveness of Two Types of Slosh Suppression Devices. Tech. Rep. 6, Southwest Res. Inst., June 15, 1959.

ABRAMSON, H. NORMAN, and RANSLEBEN, GUIDO E., JR.: A Note on Wall Pressure Distributions During Sloshing in Rigid Tanks. Tech. Rep. 5, Southwest Res. Inst., June 15, 1959.

ABRAMSON, H. NORMAN, and RANSLEBEN, GUIDO E., JR.: Simulation of Fuel Sloshing Characteristics in Missile Tanks by Use of Small Models. Tech. Rep. 7, Southwest Res. Inst., Apr. 25, 1960.

BAUER, HELMUT F.: Fluid Oscillations in a Circular Cylindrical Tank. Rep. DA-TR-1-58, Army Ballistic Missile Agency, Apr. 18, 1958.

BAUER, HELMUT F.: Fluid Oscillation in a Cylindrical Tank with Damping. Rep. DA-TR-4-58, Army Ballistic Missile Agency, Apr. 23, 1958.

BAUER, HELMUT F.: Propellant Sloshing. Rep. DA-TR-18-58, Army Ballistic Missile Agency, Nov. 5, 1958.

BUDIANSKY, BERNARD: Sloshing of Liquids in Circular Canals and Spherical Tanks. Jour. Aero/Space Sci., vol. 27, no. 3, Mar. 1960, pp. 161-173.

COLE, HENRY A., JR., and GAMBUCCI, BRUNO J.: Tests of an Asymmetrical Baffle for Fuel Sloshing Suppression. NASA TN D-1036, 1961.

LAMB, HORACE: Hydrodynamics. Sixth ed., Dover Pub., 1945.

LEONARD, H. WAYNE, and WALTON, WILLIAM C., JR.: An Investigation of the Natural Frequencies and Mode Shapes of Liquids in Oblate Spheroidal Tanks. NASA TN D-904, 1961.

MCCARTY, JOHN LOCKE, LEONARD, H. WAYNE, and WALTON, WILLIAM C., JR.: Experimental Investigation of the Natural Frequencies of Liquids in Toroidal Tanks. NASA TN D-531, 1960.

MCCARTY, JOHN LOCKE, and STEPHENS, DAVID G.: Investigation of the Natural Frequencies of Fluids in Spherical and Cylindrical Tanks. NASA TN D-252, 1960.

O'NEILL, J. P.: An Experimental Investigation of Sloshing. STL-TR-59-0000-09960, Space Tech. Labs., Inc., Mar. 4, 1960.

STEPHENS, DAVID G., LEONARD, H. WAYNE, and SILVERIA, MILTON A.: An Experimental Investigation of the Damping of Liquid Oscillations in an Oblate Spheroidal Tank With and Without Baffles. NASA TN D-808, 1961.

STOFAN, ANDREW J., and ARMSTEAD, ALFRED L.: Analytical and Experimental Investigation of Forces and Frequencies Resulting from Liquid Sloshing in a Spherical Tank. NASA TN D-1281, 1962.

STOFAN, ANDREW J., and PAVLI, ALBERT J.: Experimental Damping of Liquid Oscillations in a Spherical Tank by Positive-Expulsion Bags and Diaphragms. NASA TN D-1311, 1962.

### Thermal Control

BALLINGER, J. C.: Environmental Control Study of Space Vehicles, Pt. 1. Rep. ERR-AN-004, General Dynamics/Astronautics, Mar. 9, 1960.

BALLINGER, J. C.: Environmental Control Study of Space Vehicles, Pt. 2. Rep. ERR-AN-004, General Dynamics/Astronautics, Nov. 1, 1960.

BALLINGER, J. C.: Environmental Control Study of Space Vehicles, Pt. 2. Supp. A, Rep. ERR-AN-016, General Dynamics/Astronautics, Dec. 31, 1960.

BALLINGER, J. C.: Environment Control Study of Space Vehicles, Pt. 2, Supp. B, Rep. ERR-AN-016, General Dynamics/Astronautics, Jan. 20, 1961.

BALLINGER, J. C.: Environmental Control Study of Space Vehicles, Pt. 3. Rep. ERR-AN-051, General Dynamics/Astronautics, Dec. 31, 1960.

BURRY, R. V., and DEGNER, V. R.: Liquid-Propellant Storage Evaluation for Space Vehicles. Fourth Symposium on Ballistic Missile and Space Tech., Aug. 1959.

CHRISTIANSEN, R. M., HOLLINGSWORTH, M., JR., and MARSH, H. N., JR.: Low Temperature Insulating Materials. 1959 Cryogenic Eng. Confer., Sept. 2-4, 1959.

CRAMER, KENNETH R.: Orbital Storage of Cryogenic Fluids. TN 58-282, WADC, Oct. 1958.

## CHEMICAL ROCKET PROPULSION

- CORNOG, ROBERT: Temperature Equilibria in Space Vehicles. Proc. Am. Astronautical Soc., Western Regional Meeting, Aug. 18-19, 1958.
- CUNNINGHAM, F. G.: Earth Reflected Solar Radiation Input to Spherical Satellites. NASA TN D-1099, 1962.
- CUNNINGHAM, F. G.: Power Input to a Small Flat Plate from a Diffusely Radiating Sphere, with Application to Earth Satellites. NASA TN D-710, 1961.
- DRISCOLL, D. G.: Cryogenic Tankage for Space Flight Applications. 1959 Cryogenic Eng. Conf., Sept. 2-4, 1959.
- GAZLEY, CARL, JR., KELLOGG, W. W., and VESTINE, E. H.: Space Vehicle Environment. Jour. Aero/Space Sci., vol. 26, no. 12, Dec. 1959.
- GLASER, PETER E., ed.: Aerodynamically Heated Structures. Prentice-Hall, Inc., 1962.
- GOLDMAN, D. T., and SINGER, S. F.: Radiation Equilibrium and Temperature. Proc. of VII Int. Astronautical Cong. (Rome), Sept. 17-22, 1956.
- HELLAR, GERHARD: Thermal Control of the Explorer Satellites. Paper 834-59, ARS, 1959.
- HNDLICKA, MILO P.: Engineering Aspects of Heat Transfer in Multilayer Reflective Insulation and Performance of NRC Insulation. 1959 Cryogenic Eng. Conf., Sept. 2-4, 1959.
- JOHNSON, FRANCIS S.: Satellite Environment Handbook. Stanford Univ. Press, 1961.
- JOHNSON, FRANCIS S.: The Solar Constant. Jour. of Meteorology, vol. 11, no. 6, Dec. 1954, pp. 431-439.
- KREITH, F.: Radiation Heat Transfer and Thermal Control of Spacecraft. Pub. 112, Eng. Exp. Station, Oklahoma State Univ., Apr. 1960.
- OLIVIER, J. R., and DEMPSTER, W. E.: Orbital Storage of Liquid Hydrogen. NASA TN D-559, 1961.
- SCOTT, RUSSELL B.: Cryogenic Engineering. D. Van Nostrand Co., Inc., 1959.
- SMOLAK, G. R., and KNOLL, R. H.: Cryogenic Propellant Storage for Round Trips to Mars and Venus. Paper 60-23. Inst. Aero. Sci., 1960.
- SMOLAK, GEORGE R., KNOLL, RICHARD H., and WALLNER, LEWIS E.: Analysis of Thermal-Protection Systems for Space-Vehicle Cryogenic-Propellant Tanks. NASA TR R-130, 1962.
- WOOD, GEORGE P., and CARTER, ARLEN F.: The Design Characteristics of Inflatable Aluminized-Plastic Spherical Earth Satellites with Respect to Ultraviolet, Visible, Infrared and Radar Radiation. Paper 59-AV-38, ASME, 1959.

## Zero Gravity

- ADAM, NEIL KENSINGTON: The Physics and Chemistry of Surfaces. Oxford Univ. Press, 1941.
- ADAMSON, ARTHUR W.: Physical Chemistry of Surfaces. Intersci. Pub., 1960. Aerophysics Group: June-August Progress report for the Combined Laboratory and KC-135 Aircraft Zero-G Test Program. Rep. AE61-0871, Convair Astronautics, Sept. 5, 1961.
- ALEXANDER, A. E.: Surface Chemistry. Longmans, Green, and Co., 1951.
- BARTWELL, F. E.: Wetting of Solids by Liquids. Colloid Chem., vol. III, Chem. Catalog Co., Inc., 1931.
- BENEDIKT, E. T.: Dynamics of a Liquid Spheroid Under the Action of Cohesive Forces. Rep. ASRL-TM-60-10, Norair Div., Northrop Corp., Sept. 1960.
- BENEDIKT, E. T.: General Behavior of a Liquid in a Zero or Near Zero Gravity Environment. Rep. ASG-TM-60-9Z6, Norair Div., Northrop Corp., May 1960.
- BENEDIKT, E. T.: Scale of Separation Phenomena in Liquids Under Conditions of Nearly Free Fall. ARS Jour., vol. 29, no. 2, Feb. 1959, pp. 150-151.
- BERNETT, M. K., and ZISMAN, W. A.: Relation of Wettability by Aqueous Solutions to the Surface Constitution of Low-Energy Solids. Jour. Phys. Chem., vol. 63, no. 8, Aug. 1959, pp. 1241-1246.
- BIKERMANN, J. J.: Surface Roughness and Contact Angle. Jour. Phys. and Colloid Chem., vol. 54, no. 5, May 1950, pp. 653-658.
- BRAZINSKY, IRVING, and WEISS, SOLOMON: A Photographic Study of Liquid Hydrogen at Zero Gravity. NASA TN D-1107, 1961.
- BURDON, R. S.: Surface Tension and the Spreading of Liquids. Cambridge Univ. Press (London), 1940.
- CALLAGHAN, EDMUND E.: Weightlessness. Machine Design, vol. 34, no. 24, Oct. 11, 1962, pp. 156-161.
- CASSIE, A. B. D.: Contact Angles. Discussions of Faraday Soc., no. 3, 1948, pp. 11-16.



# FLUID PHYSICS OF LIQUID PROPELLANTS

- DUPRE, ATHANASE: *Memoirs of the Mechanical Theory of Heat*. Nos. 5, 6, and 7, *Ann. Chim. et Phys.*, 1866-1868.
- FORSTER, H. K., and ZUBER, N.: Growth of a Vapor Bubble in a Superheated Liquid. *Jour. Appl. Phys.*, vol. 25, Apr. 1954, pp. 474-478.
- FOWKES, FREDERICK M., and HARKINS, WILLIAM D.: The State of Monolayers Adsorbed at the Interface Solid-Aqueous Solution. *Jour. Am. Chem. Soc.*, vol. 62, no. 12, Dec. 1940, pp. 3377-3386.
- GAUSS, CARL FRIEDERICH: *Principia Generalia Theoriae Figurae Fluidorum in Statu Aequilibril*. Gottingen, 1830.
- GERATHEWOHL, SIEGFRIED J.: Zero-G Devices and Weightlessness Simulators. Pub. 781, Nat. Acad. Sci.-Nat. Res. Council, 1961.
- GIBBS, J. WILLARD: *Collected Works*. Vol. 2. Longmans, Green, and Co., 1928.
- GLASSTONE, SAMUEL: *Textbook of Physical Chemistry*. Second ed., D. Van Nostrand Co., Inc., 1946, pp. 481-483.
- GOOD, ROBERT J., and GIRIFALCO, L. A.: A Theory for Estimation of Surface and Interfacial Energies. III. Estimation of Surface Energies of Solids from Contact Angle Data. *Jour. Phys. Chem.*, vol. 64, no. 5, May 1960, pp. 561-565.
- GOODRICH, F. C.: The Mathematical Theory of Capillarity, I; II; III. *Proc. Roy. Soc. (London)*, ser. A, vol. 260, no. 1303, Mar. 21, 1961, pp. 481-509.
- GREGG, S. J.: Hysteresis of the Contact Angle. *Jour. Chem. Phys.*, vol. 16, no. 5, May 1948, pp. 549-550.
- GURNEY, C.: Surface Forces in Liquids and Solids. *Proc. Phys. Soc. (London)*, sec. A, no. 358, vol. 62, Oct. 1, 1949, pp. 639-648.
- HARKINS, WILLIAM D.: *The Physical Chemistry of Surface Films*. Reinhold Pub. Corp., 1952.
- HARKINS, WILLIAM D., and LOESER, E. H.: Surfaces of Solids. XIX Molecular Interactions Between Metals and Hydrocarbons. *Jour. Chem. Phys.*, vol. 18, no. 4, Apr. 1950, pp. 556-560.
- JONES, EDWARD W.: What Does "Weightlessness" Really Mean? *Space/Aero.*, vol. 38, no. 5, Oct. 1962, pp. 65-67.
- KOENIG, FREDERICK O.: On the Thermodynamic Relation Between Surface Tension and Curvature. *Jour. Chem. Phys.*, vol. 18, no. 4, Apr. 1950, pp. 449-459.
- LANGMUIR, IRVING: The Constitution and Fundamental Properties of Solids and Liquids, I. *Jour. Am. Chem. Soc.*, vol. 38, no. 11, Nov. 1916, pp. 2221-2295.
- LAPLACE, PIERRE SIMON: *Mecanique Celeste*, Supplement to Tenth Book, 1806.
- LI, T.: Cryogenic Liquids in the Absence of Gravity. Vol. 7 of *Advances in Cryogenic Eng.*, K. D. Timmerhaus, ed., Plenum Press, 1962, pp. 16-23.
- LI, TA: Liquid Behavior in a Zero-G Field. Rep. AE 60-0682, Convair-Astronautics, Aug. 1960.
- M McNUTT, JAMES E., and ANDES, GEORGE M.: Relationship of the Contact Angle to Interfacial Energies. *Jour. Chem. Phys.*, vol. 30, no. 5, May 1959, pp. 1300-1303.
- MERTE, H., and CLARK, J. A.: Boiling Heat Transfer Data for Liquid Nitrogen at Standard and Near-Zero-Gravity. Vol. 7 of *Advances in Cryogenic Eng.*, K. D. Timmerhaus, ed., 1961, p. 546.
- MILLER, N. F.: The Wetting of Steel Surfaces by Esters of Unsaturated Fatty Acids. *Jour. Phys. Chem.*, vol. 50, no. 4, July 1946, pp. 300-319.
- NEINER, J. J.: The Effect of Zero Gravity on Fluid Behavior and System Design. TN 59-149, WADC, Apr. 1949.
- PARTINGTON, J. R.: *An Advanced Treatise on Physical Chemistry*. Vol. II. Longmans, Green, and Co., 1951, pp. 134-207.
- PETRASH, DONALD A., ZAPPA, ROBERT F., and OTTO, EDWARD W.: Experimental Study of the Effects of Weightlessness on the Configuration of Mercury and Alcohol in Spherical Tanks. NASA TN D-1197, 1962.
- PLATEAU, J. A. F.: *Statique Experimentale et Theorique des Liquides*. 1873.
- POISSON, SIMEON DENIS: *Nouvelle Theorie de L'Action*. 1831.
- RAYLEIGH: *Collected Scientific Papers*. Vol. VI. Cambridge Univ. Press (London), 1920.
- REYNOLDS, W. C.: Hydrodynamic Consideration for the Design of Systems for Very Low Gravity Environments. Tech. Rep. LG-1, Dept. Mech. Eng., Stanford Univ., Sept. 1961.
- REYNOLDS, WILLIAM C.: Behavior of Liquids in Free Fall. *Jour. Aero/Space Sci.*, vol. 26, no. 12, Dec. 1959, pp. 847-848.

## CHEMICAL ROCKET PROPULSION

- ROHSENOW, W. M.: A Method of Correlating Heat-Transfer Data for Surface Boiling Liquids. Trans. ASME, vol. 74, 1952, p. 969.
- SCHOLBERG, HAROLD M., and WETZEL, W. W.: Some Observations on the Theory of Contact Angles. Jour. Chem. Phys., vol. 13, no. 10, Oct. 1945, p. 448.
- SHAFRIN, ELAINE G., and ZISMAN, WILLIAM A.: Constitutive Relations in the Wetting of Low Energy Surfaces and the Theory of the Retraction Method of Preparing Monolayers. Jour. Phys. Chem., vol. 64, no. 5, May 1960, pp. 519-524.
- SHERLEY, J. E., and MERINO, F.: The Final Report for the General Dynamics/Astronautics Zero-G Program Covering the Period from May 1960 Through March 1962. Rep. AY62-0031, General Dynamics/Astronautics, Aug. 15, 1962.
- SHERLEY, JOAN: Evaluation of Liquid Behavior in a Zero-G Field Using Free Floating Technique. Convair-Astronautics, 1960.
- SHUTTLEWORTH, R.: The Surface Tension of Solids. Proc. Phys. Soc. (London), sec. A, vol. 63, no. 365, May 1, 1950, pp. 444-457.
- SHUTTLEWORTH, R., and BAILEY, G. L. J.: The Spreading of a Liquid Over a Rough Solid. Discussions of Faraday Soc., no. 3, 1948, pp. 16-21.
- SIEGEL, ROBERT: Transient Capillary Rise in Reduced and Zero-Gravity Fields. Paper 60-WA-201, ASME, 1960.
- STEINLE, HANS: Heat Transfer in a Zero-G Field. Convair-Astronautics, 1960.
- USISKIN, C. M., and SIEGEL, R.: An Experimental Study of Boiling in Reduced and Zero Gravity Fields. Paper 60-HT-10, ASME-AIChE, 1960.
- WASHBURN, E. ROGER, and ANDERSON, ELMER A.: The Pressure Against Which Oils Will Spread on Solids. Jour. Phys. Chem., vol. 50, no. 5, Sept. 1946, pp. 401-406.
- YARNOLD, G. D.: Understanding Surface Tension. Contemporary Phys., vol. 1, no. 4, Apr. 1960, pp. 267-275.
- YARNOLD, G. D., and MASON, B. J.: The Angle of Contact Between Water and Wax. Proc. Phys. Soc., sec. B, vol. 62, pt. 2, Feb. 1949, pp. 125-128.
- YARNOLD, G. D., and MASON, B. J.: A Theory of the Angle of Contact. Proc. Phys. Soc., sec. B, vol. 62, pt. 2, Feb. 1949, pp. 121-125.
- YOUNG, THOMAS: Essay on the Cohesion of Fluids. Roy. Phil. Trans., Dec. 20, 1805, pp. 65-87.
- YUST, WALTER, ed.: Surface Tension. Encyclopaedia Britannica, Inc., vol. 21, 1947, pp. 593-602.

## 38. New Problems Encountered With Pumps and Turbines

By Melvin J. Hartmann and Calvin L. Ball

MELVIN J. HARTMANN is Head of the Pump Section of the Fluid System Components Division of the NASA Lewis Research Center. He has conducted and supervised research in the field of turbomachinery. Mr. Hartmann earned his B.S. degree in Mechanical Engineering from the University of Nebraska in 1944. He is a member of the Institute of the Aerospace Sciences.

CALVIN L. BALL, Aerospace Scientist at the NASA Lewis Research Center, is conducting research on turbomachinery, primarily involving pumps for cryogenic fluids that are applicable to rocket engines. Mr. Ball attended Michigan College of Mining and Technology and received his B.S. degree in Mechanical Engineering in 1956. He is a member of the American Society of Mechanical Engineers.

### INTRODUCTION

As the missions in the space program become more difficult, a wide range of new requirements are placed on all components of both chemical and nuclear rocket engine systems. The advent of manned space flight has resulted in stringent requirements on the reliability of all rocket components in an effort to eliminate catastrophic engine failure. The trend toward larger booster engines and higher engine operating pressures has required increased size and pressure producing capability of the turbopump units. The smaller thrust engines used to provide thrust in space as well as in landing and rendezvous maneuvers require that the turbopumps perform satisfactorily over a wide range of thrust levels (engine throttability) and, in addition, provide multiple restart capability. The pumping systems for these engines must respond nearly instantaneously to demands of the control system even though the propellants may have been stored for long periods in the space environment. For some of the new engines there is the requirement that the pump accept the propellants from the tank at or near their boiling points.

Further complexities exist in the development of pumping machinery for future rocket engines. Statistics have indicated that about one-third of the effort in a rocket engine development program is devoted to the turbopump. Because the development of the turbopump is a long process, it is often necessary to establish many of the engine parameters long before turbopump test data are available. If the turbopump does not achieve the performance assumed in establishing engine performance parameters, a complete redesign involving expensive and critical time delays may be necessary. In the past this problem has been handled by overdesigning the turbopump to meet possible deficiencies. Because of the new requirements placed on the turbopump, design parameters are being pushed closer and closer to limitations set by the present state of technology. Therefore, there no longer exists sufficient margin for overdesigning to satisfy possible deficiencies showing up in the development phase. As a result, it is necessary to improve pump design techniques to meet the increased requirements with assurance that a suitable turbopump will result.

## CHEMICAL ROCKET PROPULSION

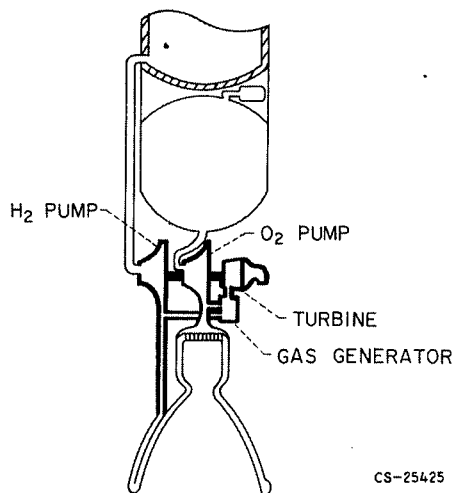


FIGURE 38-1.—Chemical-rocket pumps and turbine.

From figure 38-1, some of the general functions and requirements of the turbopump in a chemical rocket system may be inferred. In general, the propellant must be moved from the low-pressure tank to the high-pressure engine system. The propellants are usually stored at low pressures for minimum tank weight, and boiling or cavitation may occur in the fluid system wherever the pressure is further reduced by velocity increase. The pump must be capable of ingesting such vapor and still increasing the pressure of the propellants. Furthermore, the propellants must be delivered to the engine without pressure or flow fluctuations that could result in a thrust fluctuation or possible destructive engine instabilities. The power for pumping the propellant must be developed by a turbine. The exhaust from the turbine develops a relatively small thrust, and thus the flow through the turbine must be minimized to avoid a sizable reduction in engine specific impulse, the energy release in pound-seconds per pound of propellant.

This paper covers three topics pertinent to the turbopump:

- (1) Pumping under cavitating conditions
- (2) Flow stability in high-pressure pumps
- (3) Turbine drives with high-energy propellants

The discussion mainly concerns hydrogen or hydrogen-oxygen turbines and pumps. It is applicable, in general, to modern turbomachinery

for all rocket propellants and to both chemical and nuclear rocket systems.

### PUMPING UNDER CAVITATING CONDITIONS

In general, when the pump must operate with the inlet fluid very near the boiling condition, vapor forms in the pump inlet. The formation of vapor bubbles and their subsequent collapse as the fluid is exposed to boiling or vapor pressure in low-pressure regions of the flow is referred to as cavitation. The inlet portion of the pump must be capable of increasing the pressure to suppress the boiling even when the flow contains some vapor. Several methods of approaching the cavitation problem are illustrated in figure 38-2. In the upper left sketch of figure 38-2 an inducer stage is added to the pump. This stage is designed to operate under cavitating conditions and increases the pressure sufficiently above the vapor pressure so that the main-stage pump is not affected by cavitation. This can also be thought of as a prepumping stage raising the pressure in the line ahead of the main pump rather than increasing the pressure in the entire tank to suppress boiling. The lower left sketch illustrates an inducer stage ahead of an axial-flow pump. The upper right sketch illustrates a pump in which the inducer is integral with the main stage of the pump. In this type of pump the design must avoid interactions between the

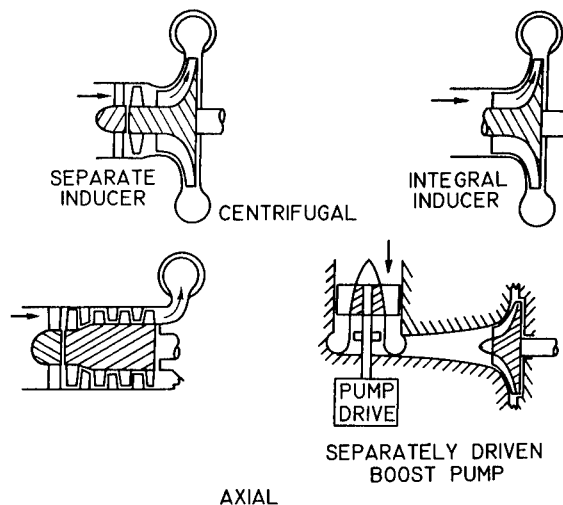


FIGURE 38-2.—Pump and inducer configurations.

cavitation and the blade loading necessary to obtain high pump pressure rises. In each of these three configurations either a separate inducer or an inducer portion of the pump is utilized to obtain energy addition or pressure rise even under cavitating conditions. In each case the inducer is operated at pump speed. If the inlet conditions are too close to fluid vapor pressure to obtain the necessary suction performance in this manner, it is necessary to add a low-speed booster pump ahead of the high-speed pump. Such a configuration is shown in the lower right sketch of figure 38-2. The booster pump may be driven by a variety of devices, including gears, an electric motor, and gas or hydraulic turbines. Whether a high-speed or low-speed cavitating pump inducer is utilized, it is necessary to understand the vapor formation within the pump rotor and to find ways to minimize the formation of vapor and the effect of these vapor formations on the pressure production capability of the pump.

Vapor forms when the low-pressure regions of a pump rotor are at or below fluid vapor pressure. The low-pressure regions exist in vortices formed with tip or corner flows and on the low-pressure portion of the pump blades. Figure 38-3 shows two pump blades rotating in the downward direction with the relative flow entering from the left. The high- and low-pressure portions of the blade are indicated by plus and minus signs. The integrated difference in these pressures reflects the level of energy addition to the pumped fluid. As a result of this pressure difference there is a flow in the

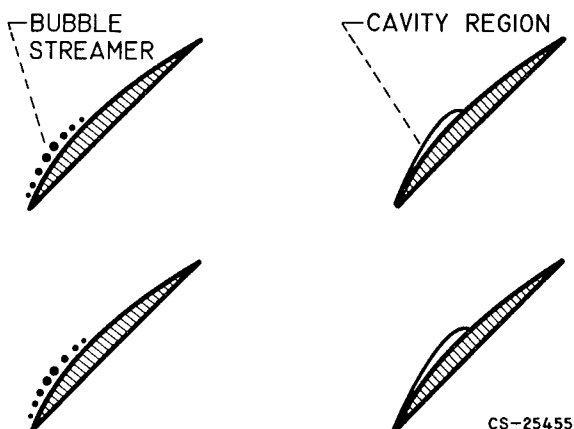


FIGURE 38-4.—Vapor formation at blade surface.

clearance space, as indicated in the lower left sketch of figure 38-3. At the intersection of the crossflow and the through flow, a vortex is formed. The center of this tip vortex forms a line at an angle to the inducer blade depending on the relative velocity of the through flow and the crossflow. The center of this vortex is a low-pressure region in which vapor first forms. As the inlet pressure is lowered further, vapor forms in the region of the crossflow and closes in the region between the blade and the tip vortex and thus completely obscures the view of the vaporous regions on the low-pressure surface of the inducer blade.

The vapor formation on the blade surface can only be observed by viewing the inducer from the upstream direction. In this manner a view under the tip vortex can be obtained. The blade surface cavitation forms in one of two configurations shown in figure 38-4. The right sketch illustrates a cavity region forming on the blade leading edge and closing on the low-pressure surface of the blade. This type of vapor formation occurs when vapor pressure first occurs some small distance back from the blade leading edge, streamers of bubbles occur along the low-pressure surface of the blade. This latter type of vapor configuration is illustrated in the left sketch of figure 38-4. Under normal operating conditions very little difference in performance exists as a result of the type of blade surface cavitation, but rather is determined by the degree of cavitation.

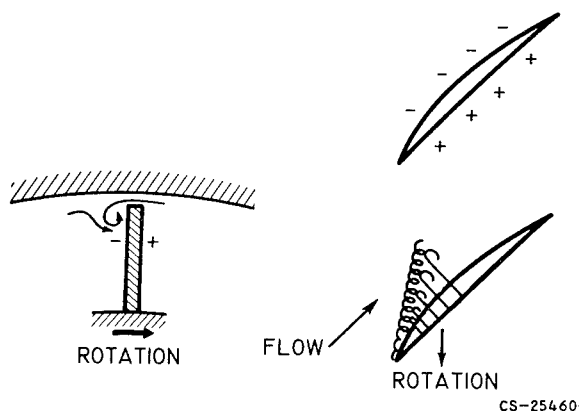
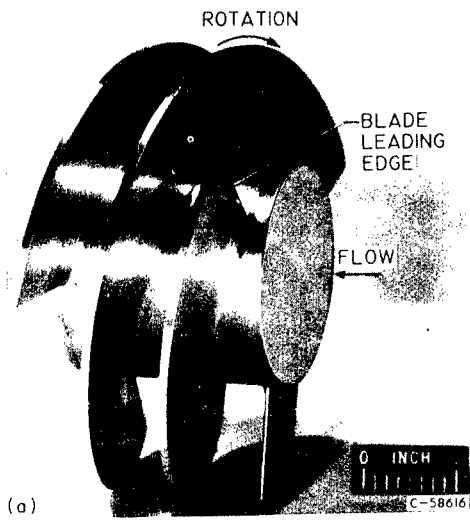


FIGURE 38-3.—Vortex formed because of flow through tip clearance space.

# CHEMICAL ROCKET PROPULSION



(a)



(b)



(c)



(d)



(e)



(f)

In either case, the vapor region is very close to the blade surface, and the blade surface pressure is very nearly fluid vapor pressure.

Basic research on cavitation can be done most easily and inexpensively in water with verification tests using the actual propellants. A series of photographs illustrating a pump inducer and the various types of vapor formation that are observed in water is shown in figure 38-5. The helical inducer that was operated in the Lewis water tunnel with a transparent housing is shown in figure 38-5(a). The directions of rotation and flow are indicated in the photograph. The orientation of the inducer blades to the flow is similar in the following five photographs, selected to illustrate the cavitation configuration discussed in connection with the sketches in figures 38-3 and 38-4.

The photograph shown in figure 38-5(b) illustrates the formation of cavitation vapor in the center of the tip vortex. The side of the inducer blade being viewed is the low-pressure surface. Thus, the cross-flow is normal to the blade toward the lower right direction, and it causes the tip vortex to form as shown. Over the forward portion of the blade some vapor forms in the crossflow, and the tip vortex appears nearly attached to the blade. Vapor is then confined to a narrow region of the vortex. When this process is viewed as a movie, there is a slight oscillatory motion of the tip vortex. Figure 38-5(c) illustrates the tip vortex and crossflow vapor formation as the inlet pressure is lowered toward fluid vapor pressure. The blade tip and the tip vortex form the edges of the vaporous region. Under these conditions the vapor extends to only about  $\frac{1}{4}$  inch from the outer housing. Any surface cavitation that may exist on the low-pressure surface of the blade is not visible unless the camera is placed in a more forward position so that a view under this tip cavitation can be obtained.

Figure 38-5(d) was selected to show the formation of streamers of vapor bubbles on the low-pressure surface of the pump inducer blade. (White tufts of yarn used to indicate tip eddy flows are shown on the inside of the transparent housing. These yarn tufts are not significant to this discussion and should not be of concern.) The streamers of bubbles appear to start at various points on the blade surface some distance behind the blade leading edge and exist at all radii. The number of streamers and the length of the streamers increase as the inlet pressure is lowered toward fluid vapor pressure. When streamer cavitation is viewed as a movie, streamers seem to appear and disappear at random, even though overall cavitation conditions appear to be constant.

Figures 38-5(e) and (f) were selected to illustrate a cavity region on the low-pressure surface of the pump inducer blade. The cavity begins at the blade leading edge and extends some distance along the blade. Lowering the inlet pressure toward fluid vapor pressure increases the length of the surface cavity. The surface of the cavity is "dimpled" in such a manner as to reflect light as bright points. The closure of the cavity also appears very bright because of the light reflection. When surface cavitation is viewed as a movie, the cavity closure point is noted to oscillate slightly forward and backward along the blade. With either type of surface cavitation the vapor formation is confined to a relatively narrow region from the blade suction surface with an estimated thickness comparable to blade thickness.

It is necessary to relate the vapor formation as inlet pressure is lowered toward fluid vapor pressure to the blade pressure distributions that control the energy addition to the pumped fluid. The sketch in figure 38-6 shows two blades moving downward with the relative flow from the lower left. The torque force being exerted on the fluid is related to the summation of the pressure difference on the high- and low-pressure blade surfaces. In this sketch a vaporous region is shown to exist on the low-pressure surface of the blade. Tip vortex cavitation is not shown since this constitutes a blockage effect on the through flow rather than a major effect on the blade pressure distribution (especially if the


- 
- (a) Orientation of helical inducer.
  - (b) Formation of tip vortex cavitation.
  - (c) Cavitation in tip vortex and crossflow region.
  - (d) Cavitation appearing as streamers on blade low-pressure surface.
  - (e) Blade surface cavity at moderate inlet pressure.
  - (f) Blade surface cavity at lower inlet pressure.

FIGURE 38-5.—Visual studies of cavitation on pump inducer in Lewis water tunnel.

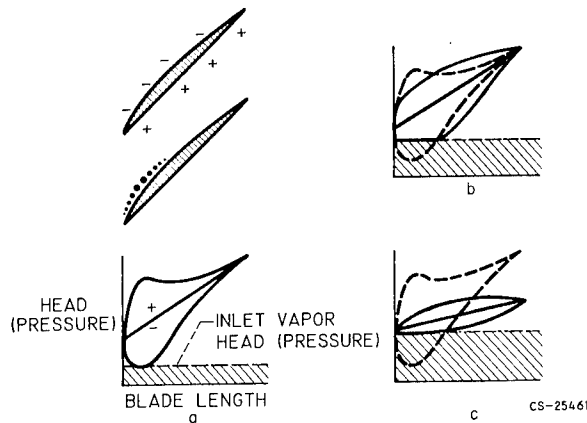


FIGURE 38-6.—Effect of cavitation on blade pressure distribution.

flow some small distance away from the blade tip is considered). The pressure distribution along the length of an inducer blade is sketched in figure 38-6(a). The mean pressure line at the inlet represents the inlet static pressure. The large pressure difference (high- to low-pressure blade surface) near the inlet is due to some angle of incidence between the inlet flow and blade mean angle. The pressure difference gradually decreases as the mean pressure approaches the discharge pressure. The cross-hatched region is the region below fluid vapor pressure. Pressure distributions of this general nature were utilized for pump inducer blades, and performance was not affected when the lowest blade surface pressure was at vapor pressure. In fact, in operation the inlet pressure can be lowered so that the indicated low-pressure point will be well below vapor pressure (assuming that the pressure distribution remains the same) before changes in performance are experienced. As the inlet pressure is lowered, the portion of the pressure distribution curve that would fall below the fluid vapor pressure line (as indicated by dashed lines in fig. 38-6(b)) probably does not exist. If the pump inducer is to continue to deliver the fluid to the discharge pressure, it is necessary for the pressure difference over the blade to increase in the rearward portion of the blade (solid lines), and for the total pressure loading to be sufficient to achieve the required head rise. Thus the inducer can continue to maintain the discharge pressure or head rise as long as the overall pres-

sure loading can be maintained by redistribution rearward as the inlet pressure is lowered toward vapor pressure. This process can continue as long as the pressure gradient at the rear of the low-pressure blade surface can be achieved. When the fluid can no longer be delivered at the desired discharge pressure, the energy addition (area within the pressure loading diagram) decreases. This condition is illustrated in figure 38-6(c), and under these conditions the inducer will produce only a small head rise. The original or noncavitating blade pressure distribution is shown as a dotted line in figures 38-6 (b) and (c). The area of the pressure loading distributions represented by the solid line of figure 38-6(b) is meant to be essentially the same as that shown by the dotted curve. It should be noted that vapor formation just begins at the inlet pressure shown in figure 38-6(a) and that the length of vapor formation will increase from figure 38-6(b) to 38-6(c), as noted in figure 38-5.

The pressure loading diagrams can be related to pump inducer performance by comparison with figure 38-7. In this figure the head developed is plotted against the head above vapor pressure at the suction side of the pump. Condition A, where vapor first occurs on the inducer blade, on the solid curve exists at a sizable pressure above vapor pressure. It can be noted that tip vortex cavitation exists at inlet pressures well above point A. The vapor cavity continues to grow without affecting the inducer head produced as the inlet pressure is

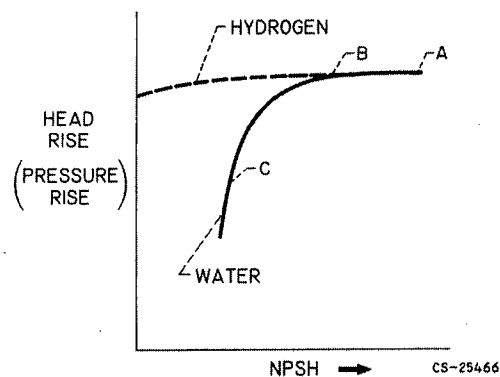


FIGURE 38-7.—Cavitation performance of pump inducer in water and in liquid hydrogen.



lowered to B. At lower inlet pressures corresponding to point C the pump inducer head rise falls off very rapidly. From the comparison it is concluded that the flow model description is suitable for inducers operating in water (solid line in fig. 38-7).

The cavitation performance of a given inducer in hydrogen may be vastly different from that obtained in water, as indicated by figure 38-7. As the inlet pressure was lowered at some point, the inducer head developed in water dropped off rather rapidly. In hydrogen, however, the head produced did not decrease drastically, even though the inlet pressure was reduced to vapor pressure (NPSH=0). An additional concept must be introduced into the blade loading diagram considerations to account for this large fluid property effect encountered with liquid hydrogen. These concepts are illustrated in figure 38-8. The sketch on the left shows the pressure distribution previously discussed at an inlet pressure just above that at which a performance loss would be experienced. It is believed that this is the type of performance encountered with water. The inlet static pressure is shown slightly higher than the inlet fluid vapor pressure. The inlet head, or total head, must be higher to account for the fluid velocity head at the pump inlet. (The term NPSH, inlet head above inlet fluid vapor pressure, is usually used to describe the inlet performance and is indicated in fig. 38-8.) On the other hand, other fluids, such as hydrogen, indicate a marked tendency to maintain some of the pressure loading below the inlet vapor pressure level. Several possible effects can occur to allow this low-pressure region to exist:

(1) lower local fluid vapor pressure as a result of temperature drop due to fluid evaporation, (2) vapor and liquid with relatively similar densities and thus a relatively large pressure gradient that can be supported by a vaporous region, (3) fluid tension effects that retard the tendency to cavitate, and (4) rates of phase change relatively different between fluids.

One or more of these effects or others not indicated may occur to allow the blade pressure to drop below the fluid inlet vapor pressure. The net result is that the inlet pressure can be lowered further without experiencing a loss in head producing capability. The right sketch in figure 38-8 illustrates a case where the tank head and vapor pressure are coincidental. The amount that the inlet pressure can be lowered without reaching the limiting pressure gradient or the effectiveness of the pressure diagram that must exist below the inlet vapor pressure is a result of the thermodynamic properties of the fluid and thus is termed thermodynamic suppression head (TSH), as illustrated in figure 38-8. It is likely that the TSH effects are present in all fluids, but they are relatively small in water and relatively large in a fluid such as hydrogen. It may be feasible to incorporate the TSH effect into the equations for suction specific speed  $S_s$  and blade operating cavitation number  $k$  in the following manner:

Suction specific speed:

$$S_s = \frac{N\sqrt{Q}}{(\text{NPSH})^{3/4}} \approx \frac{N\sqrt{Q}}{(\text{NPSH} + \text{TSH})^{3/4}}$$

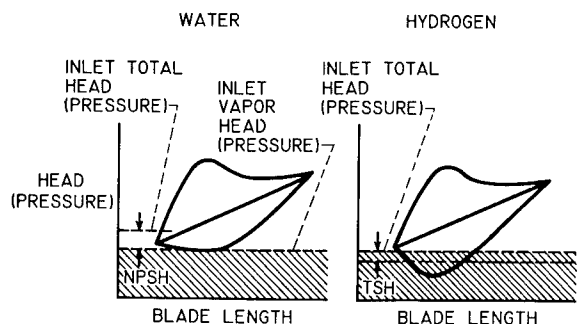
where  $N$  is rotational speed in rpm, and  $Q$  is the flow rate in gallons per minute.

Effective cavitation number:

$$k = \frac{h_s - h_{vp}}{1/2\rho(V_1')^2} \approx \frac{h_s - h_{vp} + \text{TSH}}{1/2\rho(V_1')^2}$$

where  $h_s$  and  $h_{vp}$  are the fluid static head and fluid vapor head at the inlet, respectively, and  $1/2\rho(V_1')^2$  is the inlet relative velocity head.

It can be noted that for the performance produced in hydrogen as shown in figure 38-7 the suction specific speed term is infinity and the cavitation number becomes zero or negative, none of which are meaningful unless appropriate fluid property effects (TSH) are included.



CS-25456

FIGURE 38-8.—Fluid property effects on blade-loading distribution.

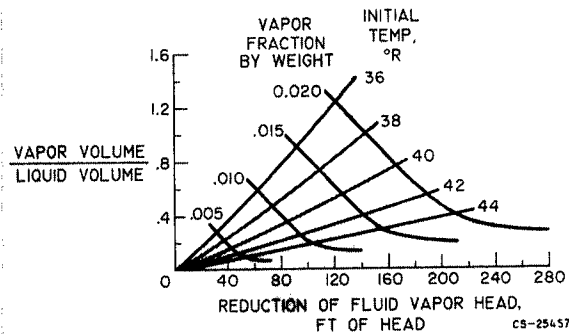


FIGURE 38-9.—Reduction of fluid vapor head due to hydrogen thermodynamic properties.

A thermodynamic chart that illustrates the basis for the difference in cavitation performance between liquid hydrogen and water is shown in figure 38-9. This theoretical plot shows the thermodynamic changes that occur when evaporation of part of the fluid reduces the vapor pressure and temperature of the liquid-vapor mixture. The ratio of vapor volume to liquid volume is plotted against the reduction in fluid vapor head that occurs for evaporation from several initial liquid-hydrogen temperatures. Contours of the corresponding constant vapor weight fractions are also indicated. The interesting conclusion from this chart concerns the large reduction in fluid vapor pressure that can be achieved with a relatively small amount of evaporation. For example, if only 0.016 of the weight fraction of a quantity of hydrogen adjacent to the low-pressure surface of the blade were evaporated from an initial temperature of 36° R, equal volumes of liquid and vapor would result in the local region, and the local vapor pressure would be reduced about 100 feet below that of the fluid generally. This local reduction in vapor head corresponds approximately to the low-pressure curve shown in figure 38-8, the average of which corresponds approximately to the value of TSH. This analytical approach appears to be at least qualitatively useful in explaining the phenomenon. The required vaporization can occur locally in the region where vapor head reduction is specifically needed without subjecting the entire flow passage to a large volume of vapor. The amount of TSH achieved from this process depends on how effectively the various factors are

utilized on the pressure loading diagram of a given pump blade design.

Better understanding of the hydrodynamic principles and the internal flow conditions during cavitation is necessary. Further research to determine definitive values of the hydrodynamic and thermodynamic interactions during cavitation will allow the designer to take full advantage of these principles.

### HIGH-PRESSURE PUMP STABILITY

The problem of pump flow stability will be approached by noting the effects illustrated in figure 38-10. The variation in head rise with flow is shown in the upper left sketch of figure 38-10. At some low flow value the pump and system operated with violent pressure fluctuations and are said to have been stalled. Even in what appears to be a good region of flow, however, the pump head rise varied with time, as shown in the upper right sketch. The ratio of peak-to-peak variation in pressure head to the head rise in general  $H_{p-p}/\Delta H$  varies with both the flow rate and the suction head above vapor pressure in the manner indicated by the lower sketches in figure 38-10. These pressure fluctuations are a result of unsteady flow configurations such as flow eddies. If the flow eddy exists near the pump discharge, and thus affects energy addition, the variation with  $Q$  can be expected to be a major factor. On the other hand, if the eddy condition exists near the inlet and can interact with cavitation, the variation shown with inlet head above vapor pressure can be expected to be large.

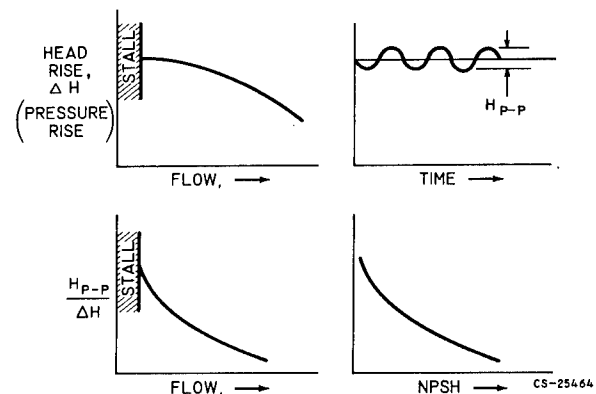
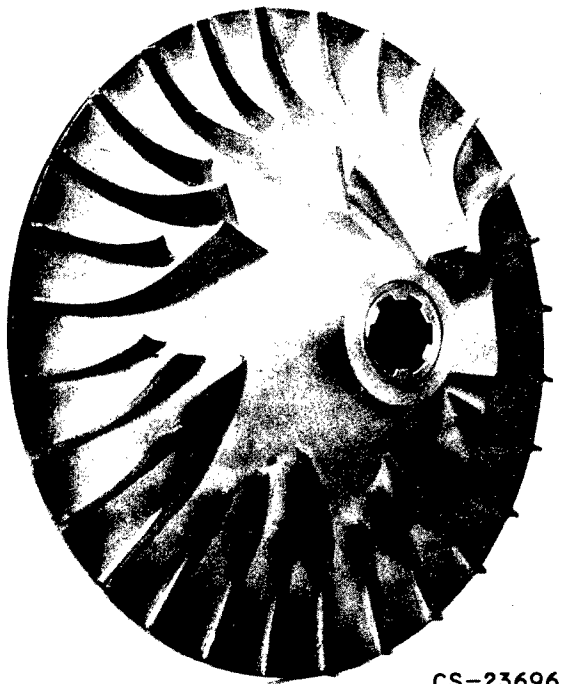


FIGURE 38-10.—Pump discharge pressure fluctuations due to unsteady flow conditions.

## NEW PROBLEMS ENCOUNTERED WITH PUMPS AND TURBINES

Before discussing the internal flow conditions which may affect pump stability, it would be well to describe the overall characteristics of hydrogen pumps. The pump shown in figure 38-11 is a research hydrogen pump rotor under investigation at the Lewis Research Center. When operated at 40,000 rpm (tip speed of about 1100 ft./sec) the power required to drive this rotor is of the order of 6000 horsepower. The pressure rise from inlet to outlet



CS-23696

FIGURE 38-11.—Large flow hydrogen pump rotor.

under the conditions described is about 1000 pounds per square inch. High pressure and velocity gradients within the pump rotor are necessary to achieve this large transfer of energy from the rotor to the pumped fluid. The following discussion will consider the effects of excessive flow gradients within the pump rotor, and some of the methods of avoiding excessive flow gradients will also be indicated.

The velocity distribution between blades on a pump rotor is illustrated by the sketches in figure 38-12. The blades are presumed to be rotating to the right so that the high- and low-

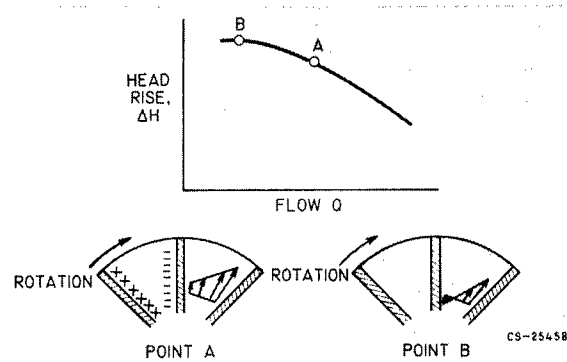
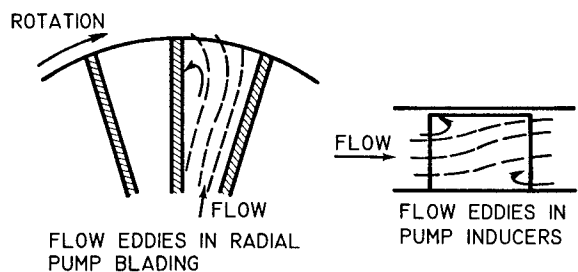


FIGURE 38-12.—Effect of passage pressure and velocity distribution on pump performance.

pressure surfaces of the blade are as indicated in the figure. A mean flow velocity exists near the passage center, a high velocity is associated with the low-pressure surface, and a low velocity is associated with the high-pressure blade surface. Such a velocity variation is necessary to achieve the energy transfer to the pumped fluid. At a slightly reduced flow, however, or in another design in which the mean velocity is reduced but a similar velocity distribution from blade to blade is required, the low-velocity flow may be reduced to zero or reversed flow may occur. The sketch on the right in figure 38-10 indicates a case in which reverse flow occurs over a portion of the passage. Such regions of reverse flow result in the formation of a flow eddy as illustrated by the flow streamlines shown in figure 38-13 (left sketch). If the flow eddies are of sufficient size, they may become unsteady. This unsteadiness may result from pressure fluctuations originating in the system external to the pump or those associated with the rotor blades passing the volute tongue. In this manner the small pressure fluctuations

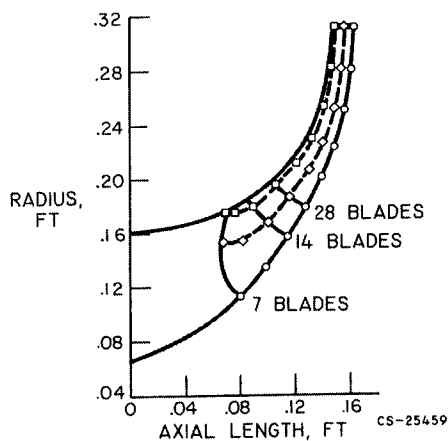


CS-25465

FIGURE 38-13.—Aspects of unsteady flow in pump rotors.

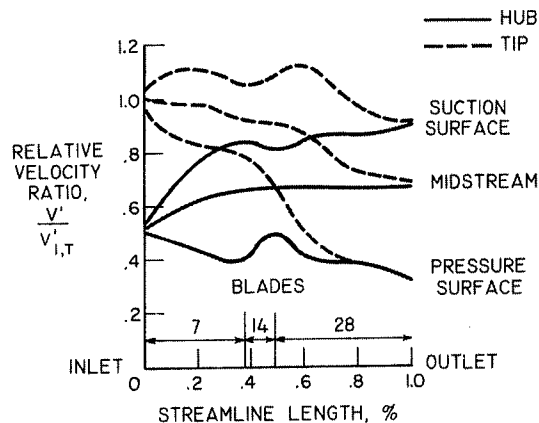
in the system may become amplified as a result of unsteady eddy flow conditions within the pump.

The right sketch in figure 38-13 shows a flow eddy that can occur in an inducer or axial-flow pump stage. The flow distribution at the rotor discharge must be such that, with the radial distribution of energy addition and flow losses, simple radial equilibrium exists. This usually requires that there be a radial outward shift of mass flow as the inducer is operated at reduced flow rates. The result is the formation of a flow eddy as shown at the discharge of the rotor hub. The accompanying streamline curvature can result in a simultaneous flow eddy near the rotor tip at the inlet. This type of flow eddy can also be involved in causing pressure fluctuations in a pump rotor similar to those described previously. Flow eddies can be avoided in design if additional blades are added to reduce the blade-to-blade velocity variation indicated in the left sketch of figure 38-13 or if the through flow velocity is increased to avoid zero flow velocities. In the case of the axial-flow configuration it may be necessary to reduce the overall loading to avoid premature flow eddies. The design restrictions resulting from these considerations may reduce the potential overall pump performance or efficiency but may be the compromises necessary to obtain stable operation over the desired flow range.



(a) Flow streamlines in plane of axis.

FIGURE 38-14.—Impeller velocity gradients calculated by stream-filament solution.



(b) Blade-to-blade solution.

FIGURE 38-14 (Concluded).—Impeller velocity gradients calculated by stream-filament solution.

One of the approximate theoretical methods of determining velocity distributions within an impeller is the stream-filament method. This method was utilized in the design of the pump rotor shown in figure 38-11. The calculated streamline flow and the velocity distribution on the blades are shown in figure 38-14(a). The streamlines are calculated in the axial plane by the previously mentioned stream filament solution. This assumes that the flow is at the blade angle and is symmetrical in the axial plane. It is assumed that the pressure varies linearly from blade to blade about the mean of the passage. By this approximation, which has been shown to be reasonably good for many cases, the blade surface velocities are calculated as shown in figure 38-14(b). The mean velocity at the rotor tip is shown to decrease slightly. The high- and low-velocity surfaces of the blade are displayed above and below the mean passage velocity. The rotor hub velocity is somewhat lower than the tip velocity. The low blade surface velocity along the hub can be kept from becoming zero by the addition of splitter vanes at several stations through the impeller. A mathematical relation between eddy size and flow stability is not as yet available except that it is known that pumps which experimentally exhibit large pressure fluctuations also indicate extensive eddy regions when this type of solution is used to calculate internal velocity distributions.

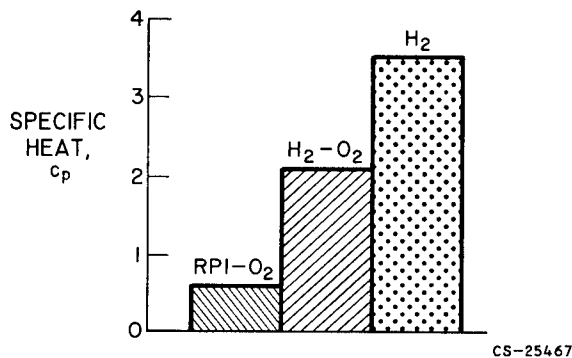


FIGURE 38-15.—Specific-heat comparison for turbine drive gases.

### TURBINES FOR HIGH ENERGY

Hydrogen pumps require high power levels to move the liquid to the high-pressure engine. This results because a low-density fluid such as liquid hydrogen requires pumps of very high head rise (for a given pressure rise) and power is proportional to head rise. Compensating for this is the fact that hydrogen-rich gases have a very high heat content. This is illustrated in figure 38-15, where the specific heat of RPI (kerosene) oxygen, hydrogen-oxygen, and pure hydrogen gas are compared. The  $H_2$ - $O_2$  contains  $3\frac{1}{2}$  times the thermal energy of RPI- $O_2$  and the  $H_2$  contains about six times the thermal energy of RPI- $O_2$ . The problem becomes one of obtaining turbine geometry that extracts these high specific energies at reasonable turbine efficiency.

Turbine efficiency is shown in figure 38-16 plotted against the turbine speed-work parameter. A decrease in this speed-work parameter occurs as more energy is extracted from a

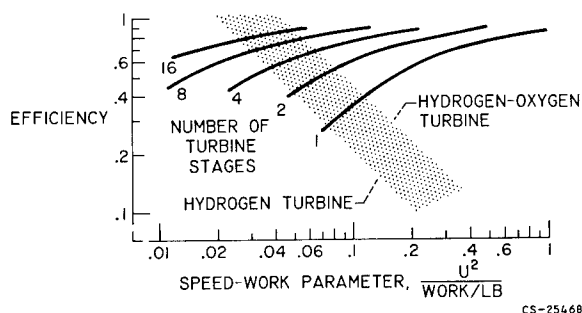


FIGURE 38-16.—Turbine-efficiency considerations for high-energy propellants.

given mass of working fluid passing through the turbine. Thus, as shown by figure 38-15, a single-stage turbine experiences a decrease in efficiency as more specific energy of the working fluid is extracted. An approximate region of performance of a turbine for hydrogen-oxygen gas is indicated as well as the anticipated performance of a hydrogen gas turbine. The turbine performance curves for different numbers of stages are anticipated as a result of reducing the work extracted in each stage. The contours for the various propellants are only meant to indicate that, if reasonable turbine efficiencies are to be obtained, it is necessary to use a considerable number of turbine stages for the high-energy propellants.

In practice the achievement of the performance levels indicated in figure 38-14 requires the use of a sophisticated aerodynamic as well as mechanical design. Both the stators and the rotors must utilize a three-dimensional design technique similar to that described in the previous sections. The blade-surface diffusion must be controlled to suitable limits. The previous discussion shows that the turbine requirements cannot be met with a simple unsophisticated design.

The need for multistage turbines also results in increased mechanical problems. For example, large thrust unbalances can be encountered that must be handled by thrust bearings or balance pistons. Critical speeds of the running gear may occur in the region of design speed as a result of the larger rotating masses. The pressure drop over these multistage turbines may be very large and thus be accompanied by a very large expansion in flow area or blade height through the turbine. The value of obtaining high turbine efficiency is emphasized by the fact that the propellant bleed rate for turbine drive is inversely proportional to turbine efficiency. Since the drive fluid must be hydrogen-rich to hold the temperature to levels that the rotating parts can tolerate and the turbine exhaust is low in propulsive energy, a low turbine efficiency will result in a large increase in hydrogen tank size and a decided decrease in overall specific impulse. Because of the low density of hydrogen, the tankage and

system are large and heavy. Each pound of hydrogen carried into space must be utilized to its fullest extent.

### SUMMARY OF DISCUSSION

The following summarizes the material presented on problem areas of turbomachinery:

1. Three areas were discussed as typical of the high level of design sophistication required in modern turbomachinery. These areas were

a. The effect of cavitation on blade loading distributions

b. The relation of pump pressure fluctuations to flow stability within the pump

c. The desirability and complexity of multistage turbines

2. The discussion pointed out the necessity for extensive design efforts with particular efforts to understand the internal flow processes involved. This has become necessary because:

a. In a rocket engine system the turbomachinery must be closely integrated with

the other components. Turbopump efficiency affects propellant tank size and specific impulse, suction performance affects tank pressurization requirements and weight, and unstable operation could cause instabilities in many other components of the system.

b. The development of a rocket engine is a stepwise process. Thus, if the turbopump does not perform as anticipated, extensive system changes may be necessary.

c. In general, changes in the turbopump can result in extensive space program delays. In order to avoid such delays, it is often necessary to limit the changes, and this results in performance and/or reliability sacrifices.

3. Pumping machinery for our modern rocket engines cannot be considered an "off the shelf item." Because of the interrelation between turbopump characteristics and those of the engine system, it is necessary to design a turbopump for a given engine system rather than adapt an existing unit.

### BIBLIOGRAPHY

#### Design of Cavitating Pump Inducers

MONTGOMERY, JOHN C.: Analytical Performance Characteristics and Outlet Flow Conditions of Constant and Variable Lead Helical Inducers for Cryogenic Pumps. NASA TN D-583, 1961.

ROSS, C. C., and BANERIAN, GORDON: Some aspects of High-Suction Specific-Speed Pump Inducers. Trans. ASME, vol. 78, no. 8, Nov. 1956, pp. 1715-1721.

SANDERCOCK, DONALD M., SOLTIS, RICHARD F., and ANDERSON, DOUGLAS A.: Cavitation and Noncavitation Performance of an 80.6° Flat-Plate Helical Inducer at Three Rotational Speeds. NASA TN D-1439, 1962.

STRIPLING, L. B.: Cavitation on Turbopumps, pt. 2. Paper 61-WA-98, ASME, 1961.

STRIPLING, L. B., and ACOSTA, A. J.: Cavitation in Turbopumps, pt. 1. Paper 61-WA-62, ASME, 1961.

#### Fluid Effects on Cavitation

HOLLANDER, A.: Thermodynamic Aspects of Cavitation in Centrifugal Pumps. ARS Jour., vol. 32, no. 10, Oct. 1962, pp. 1594-1595.

JACOBS, R. B., MARTIN, D. B., VAN WYLEN, G. J., and BIRMINGHAM, B. W.: Pumping Cryogenic Liquids. NBS Rep. 3569.

SALEMAN, VICTOR: Cavitation and NPSH Requirements of Various Liquids. Trans. ASME, ser. D, Jour. Basic Eng., vol. 81, 1959, p. 167.

STAHL, H. A., and STEPANOFF, A. J.: Thermodynamic Aspects of Cavitation in Centrifugal Pumps. Trans. ASME, vol. 78, 1956, p. 1691.

WILCOX, WARD W., MENG, PHILIP R., and DAVIS, ROGER L.: Performance of an Inducer-Impeller Combination at or Near Boiling Conditions for Liquid Hydrogen. Paper presented at Cryogenic Eng. Conf., Los Angeles (Calif.), Aug. 14-16, 1962.

#### Pump Internal Flow Design Consideration

HAMRICK, JOSEPH T., GINSBURG, AMBROSE, and OSBORN, WALTER M.: Method of Analysis for Compressible Flow through Mixed-Flow Centrifugal Impellers of Arbitrary Design. NACA Rep. 1082, 1952. (Supersedes NACA TN 2165).

#### **NEW PROBLEMS ENCOUNTERED WITH PUMPS AND TURBINES**

- OSBORN, WALTER M., SMITH, KENNETH J., and HAMRICK, JOSEPH T.: Design and Test of Mixed-Flow Impellers. VIII—Comparison of Experimental Results for Three Impellers with Shroud Redesigned by Rapid Approximate Method. NACA RM E56L07, 1957.
- SMITH, KENNETH J., and HAMRICK, JOSEPH T.: A Rapid Approximate Method for the Design of Hub Shroud Profiles of Centrifugal Impellers of Given Blade Shape. NACA TN 3399, 1955.
- WU, CHUNG-HUA: A General Theory of Three-Dimensional Flow in Subsonic and Supersonic Turbo-machines of Axial-, Radial-, and Mixed-Flow Types. NACA TN 2604, 1952.

#### **Turbine Design Considerations**

- GINSBURG, AMBROSE, HARTMANN, MELVIN, and STEWART, WARNER: Review of Problems Encountered in Turbomachinery Design for Advanced Propulsion Systems. Paper 62-AV-23, ASME, 1962.
- STEWART, W. L.: A Study of Axial-Flow Turbine Efficiency Characteristics in Terms of Velocity Diagram Parameters. Paper 61-WA-37, ASME, 1961.
- STEWART, WARNER L.: Analytical Investigation of Multistage-Turbine Efficiency Characteristics in Terms of Work and Speed Requirements. NACA RM E57K22b, 1958.

#### **Text Books**

- SHEPARD, D. G.: Principles of Turbomachinery. The MacMillan Co., 1956.
- SPANNHAKE, WILHELM: Centrifugal Pumps, Turbines, and Propellers. The Technology Press, M.I.T., 1934.
- STEPANOFF, A. J.: Centrifugal and Axial-Flow Pumps. Second ed., John Wiley & Sons, Inc., 1957.
- VAVRA, M. H.: Aero-Thermodynamics and Flow in Turbomachines. John Wiley & Sons, Inc., 1960.
- WISLICENUS, G. F.: Fluid Mechanics of Turbomachinery. McGraw-Hill Book Co., Inc., 1947.

## 39. Recent Aspects of Rocket Combustion Research

By Gerald Morrell and Richard J. Priem

GERALD MORRELL, *Chief of the Chemical Rocket Fundamentals Branch at the Lewis Research Center, has specialized in the fields of heat transfer, combustion, hydrodynamics, gas dynamics, and chemistry. He earned his B.S. degree in Chemical Engineering from Wayne State University in 1943, and his M.S. degree in Chemical Engineering from the University of Michigan in 1948. Mr. Morrell is a Senior Member of the American Rocket Society, an Associate Fellow of the Institute of Aerospace Sciences, a Member of the American Institute of Chemical Engineers, and a licensed professional engineer of the State of Ohio. He received the Rockefeller Public Service Award in 1957.*

DR. RICHARD J. PRIEM, *Head of the Rocket Combustion Section at the NASA Lewis Research Center, is currently working in research on combustion and fluid flow studies. A native of Mayville, Wisconsin, Dr. Priem attended the University of Wisconsin, where he earned his B.S., M.S., and Ph. D. degrees.*

In the broadest sense, all forms of combustion are similar because they involve the reaction of a reducing agent (fuel) and an oxidizing agent to produce reaction products with the liberation of heat. Such a broad concept can be useful in bringing together the results of diverse researches, but is of little value in guiding a particular program of research, because the boundary conditions determine the rate-limiting steps. It is these boundary conditions that guide the research worker in the selection of theoretical and experimental approaches to the goal of understanding or, at least, characterization. The specialization of combustion research or research, in general, arises when attention is confined to a particular set of boundary conditions.

If the case of a combustion wave propagating through initially premixed gases, or the equivalent, a stabilized wave in a flowing system is considered, the problem is in the realm of classical flame studies that have occupied the attention of researchers for many decades. The results of these studies are basic to all other areas of combustion research, since in this case it is

the chemistry that is rate limiting. Consider next a different boundary condition of initially unmixed gases. This produces a diffusion flame in which the overall conversion rate is governed by mixing rather than by chemical kinetics. A still more complicated set of boundary conditions is provided by initially unmixed liquid or solid reactants. Rocket-combustion research is concerned with problems arising out of this set of conditions. In addition to flame chemistry and gas phase mixing, other processes should be considered such as phase transitions, heat and mass transfer between phases, hydrodynamics of atomization, liquid mixing, viscoelastic behavior, and condensed phase reactions. There are, of course, many ways of approaching a complicated set of competing and sequential processes. At the NASA Lewis Research Center, two complementary approaches are being followed. (1) An attempt is made to devise simplified conceptual models of the combustion system that can give quantitative predictions of system behavior from the conservation equations; the predictions then must be checked experimentally. (2) Individual rate processes are



studied with the hope that increased knowledge will enable generation of more realistic models. Of course, this kind of research also stands by itself, since the results, ideally, represent a net gain in the understanding of a variety of physical and chemical processes.

For this presentation, one example of each approach to learning is discussed in detail. The first example is concerned with the interesting phenomenon of combustion resonance and, in particular, with the question of the magnitude of disturbance that leads to instability or resonance burning.

Under certain conditions that are not yet well understood, one or more acoustic modes of the combustor may be excited to large amplitudes. For combustors with large length-to-diameter ratios, the axial mode is usually observed, while for small length-to-diameter ratios the transverse or spinning transverse modes are more apt to occur. These waves interact with the combustion processes to produce large variations in the local heat-release rates. From a practical standpoint, the results are often deleterious: increased heat flux rates can cause wall failures and the vibration may induce structural failures. The transverse modes are especially severe with respect to the first type of failure.

Another common mode of instability is that produced by the coupling of combustor pressure variations with those in the feed system. The characteristic time for these oscillations is determined by the filling time of the combustor. This form of instability will be discussed in the paper by J. C. Sanders.

The geometric model chosen for analysis of the transverse mode is shown in figure 39-1.

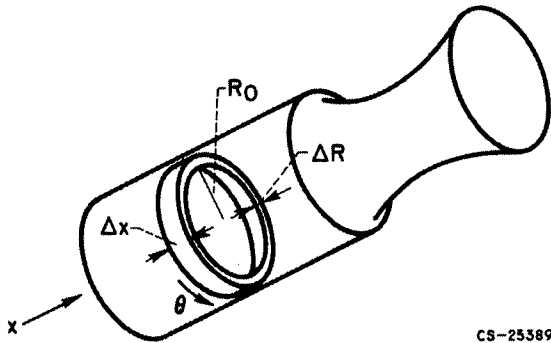


FIGURE 39-1.—Model used for instability analysis.

An annular section of a cylindrical combustor is imagined, a pressure or velocity disturbance of finite magnitude is introduced at one location, and the growth (or decay) of the wave is computed as it travels along the annulus. Simultaneous solutions of the conservation equations and an expression for the burning rate are required. The equation for conservation of momentum is

$$\frac{\partial}{\partial t}(\rho \vec{v}) = -\vec{\nabla} \cdot (\rho \vec{v} \cdot \vec{v}) - g \vec{\nabla} P - \vec{\nabla} : \tau + \vec{W} v_i$$

According to this equation the accumulation of momentum is the sum of the convective flow term, the viscous dissipation term, and the mass addition term. In nondimensional form the equation becomes

$$\begin{aligned} \frac{\partial}{\partial t^*} \left( \frac{P^*}{T^*} \vec{v}^* \right) = & -\vec{\nabla}^* \cdot \left( \frac{P^*}{T^*} \vec{v}^* \cdot \vec{v}^* \right) - \left[ \frac{1}{\gamma} \right] \vec{\nabla}^* P^* \\ & - \left[ \frac{\mu_0}{R \rho_0 V_0} \right] \vec{\nabla}^* : \vec{\tau}^* + \left[ \frac{R w_0}{\rho_0 V_0} \right] w^* \vec{v}_i^* \end{aligned}$$

where  $\rho$  is gas density,  $\vec{v}$  is gas velocity,  $v_i$  is liquid velocity,  $w$  is the local instantaneous burning rate,  $P$  is pressure,  $V_0$  is velocity of sound,  $R$  is radius,  $\mu$  is viscosity, and the subscript 0 refers to steady-state conditions. The second parameter on the right side is a Reynolds number based on the velocity of sound, and the third parameter is analogous to Damkohler's first similarity group.

The equation for average burning rate is

$$m = \left[ \frac{1 + \left( \frac{w_0}{w_f} \right)_{ST}}{1 + \left( \frac{w_0}{w_f} \right)} \right] \frac{\mathcal{K} (P_0/300)^{0.5}}{\mathcal{A}^{0.3} (1 - T_r)^{0.2} \left( \frac{\kappa_m}{0.003} \right)^{1.5} \left( \frac{V_j}{1200} \right)^{0.8}}$$

where  $w_o$  and  $w_f$  are oxidant and fuel flow rates, respectively,  $T_r$  is reduced liquid temperature,  $\mathcal{A}$  is the ratio of combustor cross-sectional area to nozzle cross-sectional area ( $A_c/A_t$ ),  $\kappa_m$  is mass-medium drop size,  $V_j$  is injection velocity, and  $\mathcal{K}$  is a constant that depends on liquid properties. This equation is applicable to steady-state vaporization, and its use here indicates two of the

major assumptions in the development: (1) vaporization is the rate-controlling process, and (2) the response of the process to a disturbance is quasi-steady state. The second assumption is especially serious, but in the absence of data on the time variation of vaporization it is the best that can be done now.

The parameters mentioned in connection with the nondimensional momentum equation are converted to rocket nomenclature as follows:

Burning Parameter:

$$\frac{Rw_0}{\rho_0 V_0} = \frac{Rm}{\mathcal{A}} \sqrt{\left(\frac{2}{\gamma-1}\right)^{\frac{\gamma+1}{\gamma-1}}}$$

$$\mathcal{L} \equiv \frac{Rm}{\mathcal{A}}$$

Dissipation Parameter:

$$\frac{\mu_0}{\rho_0 R V_0} = \frac{\mu_0 c^*}{R P_0 g} \sqrt{\left(\frac{2}{\gamma-1}\right)^{\frac{\gamma+1}{\gamma-1}}}$$

$$\mathcal{J} \equiv \frac{\mu_0 c^*}{R P_0 g}$$

where  $m$  is the fractional liquid consumption per unit length; and  $c^*$  is characteristic velocity  $P_0 A_g / \dot{W}$  where  $\dot{W}$  is total mass flow rate. The  $\mathcal{L}$  term represents the steady-state intensity of combustion, while the  $\mathcal{J}$  term represents the viscous damping. The general stability diagram that results from the solution of the equations is shown in figure 39-2, where nondimensional wave amplitude is plotted as a function of the  $\mathcal{L}$  factor for several values of the relative gas velocity with respect to the liquid

phase. Here  $\Delta v$  is  $\frac{|\vec{v} - \vec{v}_l|}{V_0}$ . The  $\mathcal{J}$  factor does

not appear, because for the one-dimensional case considered boundary-layer effects and other damping processes are negligible. The lower curves in the figure represent the threshold values of disturbance amplitude that will result in wave amplification; the upper band represents the equilibrium amplitude of the wave. Several interesting points are immediately apparent. No matter what flow conditions are imposed, there is always a minimum in the threshold amplitude that increases with an increase in relative velocity ( $\Delta v$ ). This

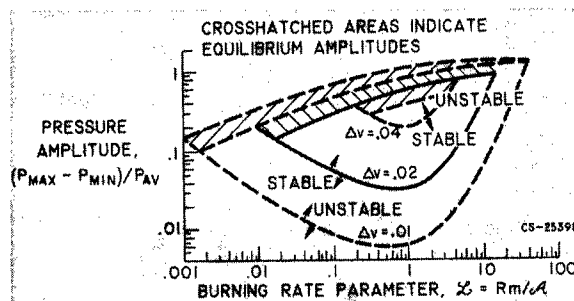


FIGURE 39-2.—Stability plot for vaporization model with various velocity differences.

implies that low contraction ratio combustors would be most stable providing that some way were available to keep the liquid phase from accelerating to gas velocity. The minimums, which occur in a small range of  $\mathcal{L}$  values, indicate a region of space-heating rates that should be avoided for maximum stability. The most interesting feature is that the theory predicts absolute stability at sufficiently high heating rates. Qualitatively, this means that if the axial momentum becomes sufficiently large, all disturbances will be damped. Currently an experiment is being initiated to check this conclusion. A toroidal combustor several feet in diameter will be employed, which has been designed to obtain values of  $\mathcal{L}$  well into the stable region. In the absence of definitive data, however, it might be useful to examine qualitatively the relation between  $\mathcal{J}$  and  $\mathcal{L}$  for available reactor data. Such a relation is shown in figure 39-3, where vaporization has been assumed to control the burning process.

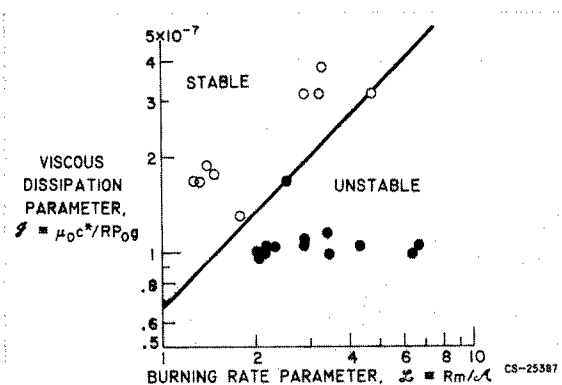


FIGURE 39-3.—Stability plot based on fuel-jet breakup by a shock wave.

It is possible to obtain a clear separation of stable and unstable combustors. If the theory is correct, there should be a second stable region for values of  $\mathcal{L}$  much larger than those shown in the figure. This empirical plot indicates that the assumption of a single slow rate process may be valid for describing the stability of a complex system.

The second example of research is concerned with measuring the rate of atomization of a liquid jet by a transverse shock wave. Interest in this question stems from the elementary notion that, in vaporization-limited combustion, a velocity disturbance or steady-state wave that produced a rapid increase in liquid surface area could be amplified and driven.

To simplify matters, study of the phenomenon has been made in the absence of combustion and in a shock wave rather than an oscillating flow. A schematic diagram of the experimental arrangement is shown in figure 39-4. A variable-length high-pressure section provides gas flows of varying duration, and the atomization is recorded by both frame and streak photographs. Examples of the data are shown in figure 39-5. It appears that at least two modes of breakup occur: (1) a deformation into sheets of liquid, and (2) atomization by streaming from the liquid surface. The theoretical model chosen for examination is a boundary layer on a flat plate of liquid as an approximation of the streaming phenomenon. The rate of atomization is then given by the product of boundary-

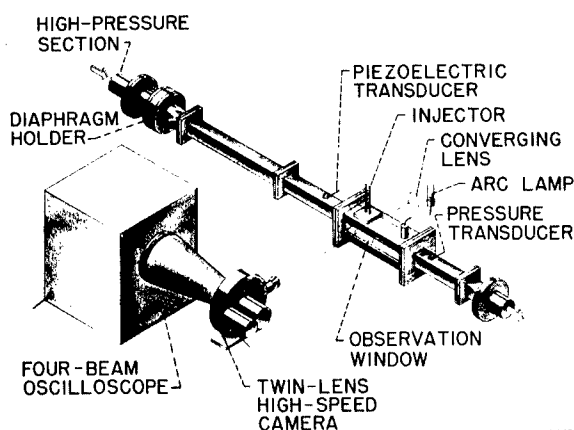
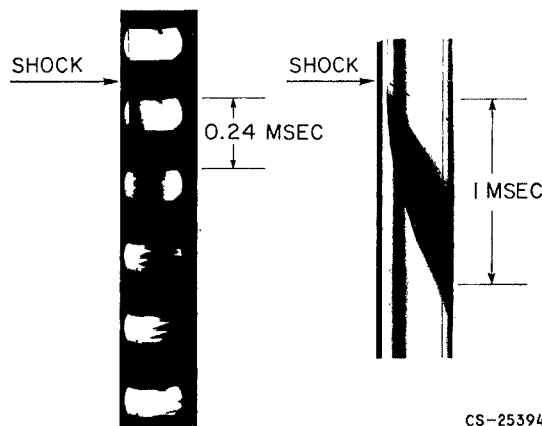


FIGURE 39-4.—Schematic diagram of experimental arrangement.



CS-25394

FIGURE 39-5.—Examples of photographic data of jet breakup. Shock velocity,  $1655 \pm 5$  feet per second; gas velocity,  $732 \pm 5$  feet per second; jet diameter, 0.052 inch.

layer thickness and velocity evaluated at the rear edge of the sheet. On the basis that surface tension determines the stable length of a liquid sheet, it can be shown that the length should be a function of Weber number and the square root of Reynolds number. The actual expression for maximum length (derived from streak pictures) is

$$\frac{L}{2R_0} = 1 + 2 \frac{We_0}{\sqrt{Re_0}}$$

where  $R_0$  is the initial radius of the jet;  $We_0$  is the Weber number  $R_0 u^2 \rho / \sigma$  where  $u$  is the gas velocity behind the shock wave relative to the liquid,  $\rho$  is gas density, and  $\sigma$  is interfacial tension; and  $Re_0$  is the Reynolds number  $R_0 u \rho / \mu$  where  $\mu$  is gas viscosity. This linear relation is the simplest one that describes the data. The boundary-layer thickness and velocity were determined by solving von Kármán's momentum equations with a modified Sanborn-Kline laminar velocity profile for both the gas and liquid phases. The final equation is

$$t_b = 0.536 \left( \frac{\rho_l}{\rho_g} \right)^{2/3} \left( \frac{\mu_g}{\mu_l} \right)^{1/3} \frac{R_0}{u} \sqrt{\frac{Re_0}{1 + 2 \frac{We_0}{\sqrt{Re_0}}}}$$

where  $t_b$  is the time for complete atomization and the other terms have their usual significance with the subscripts  $g$  for the gas phase and  $l$  for

# RECENT ASPECTS OF ROCKET COMBUSTION RESEARCH

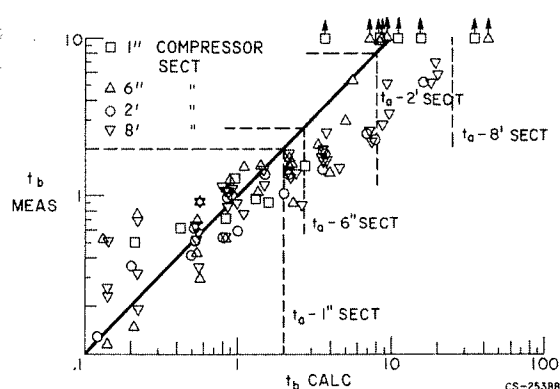


FIGURE 39-6.—Comparison of experimental and calculated atomization times based on boundary-layer theory.

the liquid phase. In figure 39-6, the measured values of breakup time are compared with the calculated values. The arrows indicate incomplete breakup, and the dashed boundaries are the limits of gas flow duration for the corresponding length of high-pressure section. Although the agreement is far from perfect, the model appears to be basically correct. Experiments with other fluids are required to test the theory adequately and certainly the effects of ambient pressure and combustion need to be evaluated. Some of these experiments are now being conducted. Figure 39-7 shows a plot similar to the one in figure 39-3 but with the fractional burning rate evaluated in terms of jet atomization. Such an empirical plot hardly represents a test of the theory, but it does show again that a single rate-limiting process may be used to describe the response of a combustion system to a disturbance.

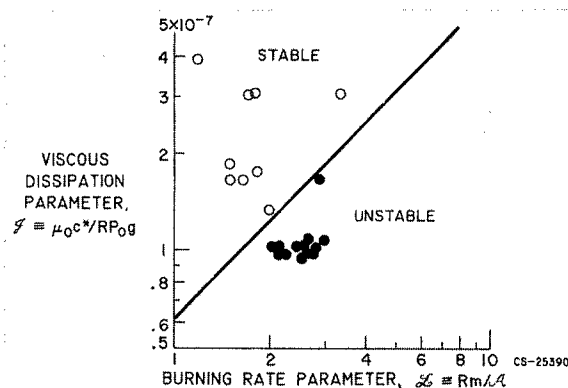


FIGURE 39-7.—Stability plot based on steady-state propellant vaporization.

Much more research is needed on the processes of rocket combustion, not only to satisfy scientific curiosity but also to make a contribution to the need for ever-increasing reliability. Experimental and theoretical work on more realistic system models would certainly be desirable. The physics and chemistry of many other rate processes need thorough investigation, especially the response of the processes to a disturbance. At low combustion pressures, chemical kinetics might be expected to become the dominant factor, while at very high pressures the unburned phase may become supercritical, and turbulent mixing could be an important process. For fuels and oxidants that react on contact, interfacial liquid-phase-reaction kinetics may be important. Consideration of initially solid reactants involves the study of gas-solid reactions. These considerations are only illustrative of the many challenges awaiting the researcher in combustion theory and practice.

## BIBLIOGRAPHY

*The following references are pertinent to the present discussion:*

- MORRELL, G.: Critical Conditions for Drop and Jet Shattering. NASA TN D-677, 1961.
- MORRELL, GERALD: Breakup of Liquid Jets by Transverse Shocks. Eighth Symposium (International) on Combustion, The Williams & Wilkins Co., 1962, pp. 1059-1068.
- PRIEM, R. J., and MORRELL, G.: Application of Similarity Parameters for Correlating High Frequency Instability Behavior of Liquid Propellant Combustors. Progress in Astronautics and Rocketry. Vol. 6—Detonation and Two-Phase Flow, Academic Press, 1962, pp. 305-320.
- PRIEM, RICHARD J., and GUENTERT, DONALD C.: Combustion Instability Limits Determined by a Nonlinear Theory and a One-Dimensional Model. NASA TN D-1409, 1962.

## CHEMICAL ROCKET PROPULSION

PRIEM, RICHARD J., and HEIDMANN, MARCUS F.: Propellant Vaporization as a Design Criterion for Rocket-Engine Combustion Chambers. NASA TR R-67, 1960.

*For alternative approaches to the study of unstable combustion the following references are recommended:*

CROCCO, L., and CHENG, S. I.: Theory of Combustion Instability in Liquid Propellant Rocket Motors. AGARD Monograph 8, Butterworths Sci. Pub. (London), 1956.

CROCCO, L., HARRJE, D. T., and REARDON, F. H.: Transverse Combustion Instability in Liquid Propellant Rocket Motors. Jour. Am. Rocket Soc., vol. 32, no. 3, Mar. 1962, pp. 366-373.

McCLURE, F. T., HART, R. W., and BIRD, J. F.: Acoustic Resonance in Solid Propellant Rockets. Jour. App. Phys., vol. 31, no. 5, May 1960, pp. 884-896.

*Recommended general references on combustion are:*

LEWIS, B., and VON ELBE, G.: Combustion, Flames, and Explosions of Gases. Academic Press, Inc., 1951.

LEWIS, B., PEASE, R. N., and TAYLOR, H. S., eds.: Combustion Processes. Vol. II of High Speed Aerodynamics and Jet Prop., Princeton Univ. Press, 1956.

PENNER, S. S.: Chemistry Problems in Jet Propulsion. Pergamon Press, 1957.

PROPULSION CHEMISTRY DIVISION: Basic Considerations in the Combustion of Hydrocarbon Fuels with Air. NACA Rep. 1300, 1957.

SURUGUE, J., ed.: Experimental Methods in Combustion Research, AGARD, Pergamon Press, 1961.

VON KÁRMÁN, T.: Fundamental Equations in Aerothermo-Chemistry. AGARD, Selected Combustion Problems, II. Butterworths Sci. Pub. (London), 1956.

## 40. Current Research and Development on Thrust Chambers

By Edmund R. Jonash and William A. Tomazic

EDMUND R. JONASH is currently Chief of the Apollo Propulsion Office at the NASA Lewis Research Center. He has specialized in research of reciprocating engine fuels, turbojet engine fuels, turbojet engine combustion, and chemical rockets. A native of Kenton, Ohio, Mr. Jonash received a B.S. degree in Chemical Engineering from Massachusetts Institute of Technology in 1944. Mr. Jonash is a member of the American Rocket Society.

WILLIAM A. TOMAZIC, an Aerospace Scientist at the NASA Lewis Research Center, has specialized in the field of chemical rocket thrust chambers. A native of Cleveland, Ohio, Mr. Tomazic received his B.S. and M.S. degrees in Mechanical Engineering from Case Institute of Technology. He is a member of Tau Beta Pi and the American Rocket Society.

### INTRODUCTION

A million pounds of thrust for large boosters, a few ounces of thrust for attitude control systems—this is the range in size of thrust chambers that are under development today. Basic operating principles are the same for all sizes. The state of the art, however, is such that optimum thrust-chamber designs cannot be scaled from one size to another, and each new rocket engine procurement requires an extensive development program that is heavily dependent on cut-and-try experimental tests to meet system performance requirements.

The present state of the art of the chemical rocket thrust chamber, its principal problems and how they are being solved today are described herein. The areas of research and development that are required to provide the necessary improvements in system performance and operating characteristics to meet tomorrow's needs are indicated.

The thrust chamber illustrated in figure 40-1 is typical of a liquid-bipropellant rocket, in which the fuel and oxidizer are pumped into a propellant injector located at the forward end of the thrust chamber. The propellants are

sprayed into the combustion chamber from many small orifices distributed over the face of the injector; they then vaporize, mix, ignite, and burn to produce high-temperature gases that are expanded through the nozzle to give thrust. This process occupies a total of some 3 to 4 milliseconds from injection of the propellants to ejection of the gases from the nozzle. Gas temperatures in the combustion zone vary

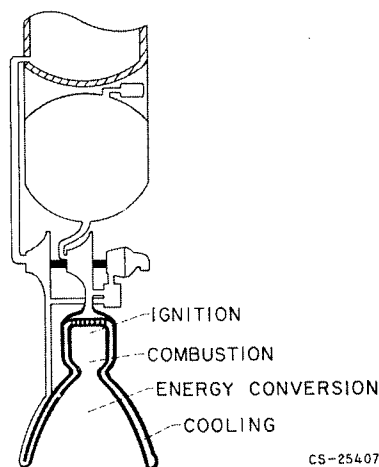


FIGURE 40-1.—Thrust chamber of chemical rocket.

## CHEMICAL ROCKET PROPULSION

from 5000° to 8000° F depending upon the propellants used; pressures in current engines vary, with design, from 50 to 1000 pounds per square inch absolute.

The principal requirements of the thrust chamber are satisfactory ignition, stable and efficient combustion, maximum conversion of thermal to kinetic energy in the nozzle, and adequate cooling to maintain structural integrity of the chamber. These requirements are discussed in some detail. Some additional requirements are frequently involved but they are not discussed. These requirements include thrust vector control, which is necessary to provide control of vehicle direction and stability; hot-gas generation for supplying the turbopump drive turbine; and energy source for heating propellant-tank pressurizing gases.

### IGNITION

Ignition in the chemical rocket must be reliable, reproducible, and rapid. Reliability is an obvious requirement. Reproducibility in terms of reaction time is particularly important in multiengine clusters in order that all engines start uniformly and no excessive thrust unbalances are produced. Ignition must be rapid to avoid accumulation of unburned propellants, which upon finally reacting will result in a high-pressure pulse. This pulse may be severe enough to rupture the chamber or trigger destructive combustion instabilities.

With hypergolic propellants, satisfactory ignition means providing for proper mixing of the propellants so that reaction may begin rapidly and smoothly. With nonhypergolic propellants, it means not only mixing the propellants, but also providing a separate energy source sufficient to initiate reaction. Various ignition energy sources have been used; some are illustrated in figure 40-2. Electrical-spark ignition systems have been used to produce ignition and, in fact, are used in restartable rocket systems that are currently under development. These systems are similar in principle to those used in reciprocating engines but must operate at a much higher energy level to assure satisfactory ignition. The principal problems inherent in such systems are assuring the presence of an inflammable mixture in the

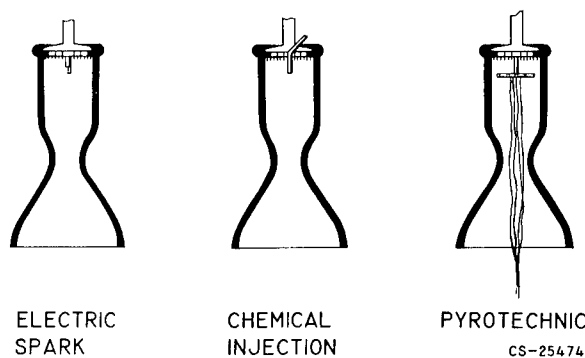


FIGURE 40-2.—Ignition techniques for nonhypergolic propellants.

very localized area of energy release of a spark and providing adequate cooling of the spark plug during engine operation. A second method commonly used for rocket ignition is the injection of a chemical that is spontaneously inflammable with one of the two main propellants. The ignition propellant is introduced simultaneously with the appropriate main propellant. Reaction is initiated. The other main propellant is then injected and reacts, completing the ignition sequence. The ignition propellant may be injected separately into the combustion chamber, as illustrated in figure 40-2. Sometimes it has been introduced as a "slug" of liquid directly within one of the propellant feed systems; the slug is initially isolated from the propellants by frangible diaphragms. The third system shown in figure 40-2 is the pyrotechnic, which is simply a solid-propellant charge located near the injector. The solid propellant charge is ignited by an electric pulse. The resulting combustion provides the energy source for main-propellant ignition. For rocket systems requiring but one start, the pyrotechnic method has been favored because of its simplicity and reliability. The charge can be designed to provide a large excess of energy, and this energy can be distributed over a substantial volume of the chamber. A major problem encountered in use has been damage to the thrust-chamber walls by the burning solid charge. The scheme is not applicable to systems requiring multiple starts. Two additional ignition methods are catalysts and propellant additives. These methods are, as yet, only laboratory curiosities that require

much more research and development effort before they can be considered for application. Promising research has been conducted on ozone bifluoride ( $O_3F_2$ ) as an additive for liquid oxygen to induce hypergolic ignition with hydrogen. Laboratory experiments have indicated that ozone bifluoride concentrations as low as 1 part in 2000 are sufficient to provide ignition. The nature of the reactions involved has not been determined, and the practical applicability of this technique has not yet been defined. Research in this area is continuing. Platinum has been considered as a potential catalyst for hydrogen-oxygen ignition. This area, although promising, has been little explored. Research into the nature of catalyzed reactions at very low temperatures ( $40^\circ$  to  $140^\circ$  R) is required.

In general, ignition systems have been developed to a satisfactory level of reliability to meet the requirements of rocket systems now in use. There has not yet been enough experience, however, in deep-space propulsive flights to assure that these same systems are adequate for the more sophisticated missions now planned. Also, the introduction of the high-thrust engine intensifies the problem of igniting a large volume of propellant mixture in a controlled fashion that will assure establishing stable combustion conditions. The introduction of man into our rocket-propelled flights imposes greatly increased reliability requirements on critical components such as the ignition system. Additional effort is required to define better the potential capabilities of some of the more advanced systems that have been investigated. Passive systems such as additives and catalysts warrant particular attention in the laboratory since such systems have potentially higher reliabilities. Most of the effort must be concentrated on hydrogen-oxygen since a very large part of our space propulsion development is committed to this combination.

### COMBUSTION EFFICIENCY

The potential space mileage from a chosen propellant combination is represented by its theoretical specific impulse. How well this potential is translated into actual performance is a function of two principal factors, combustion

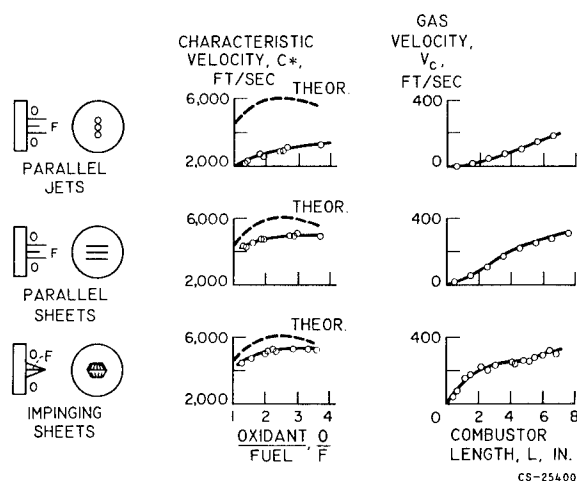


FIGURE 40-3.—Effect of injector element design on performance.

efficiency and exhaust-nozzle efficiency. Combustion efficiency is most dependent on the design of the propellant injector. A number of basic injector designs have been evolved during the course of development of our current engines; within these basic designs, thousands of variations in details are frequently tested before a satisfactory design is achieved. Some of these basic designs are illustrated in figure 40-3: (1) parallel jets that yield poorly atomized streams of propellant and do not promote cross mixing of the fuel and oxidant streams, (2) parallel sheets that are produced by pairs of fuel-on-fuel and oxidant-on-oxidant impinging jets and give improved atomization but still limited mixing, and (3) fuel-on-oxidant impinging jets that promote both mixing and atomization. The first set of curves shows the effect of injector design on the characteristic velocity, which is a measure of combustion efficiency. As might be expected, improvements in atomization and mixing reflect directly in improved performance, with experimental results ultimately approaching the theoretical maximum. The next set of curves of gas velocity and combustor length verify this improvement by showing that with improved atomization and mixing, combustion takes place more rapidly, that is, closer to the injector. These data were obtained with a liquid-oxygen-hydrocarbon propellant combination.



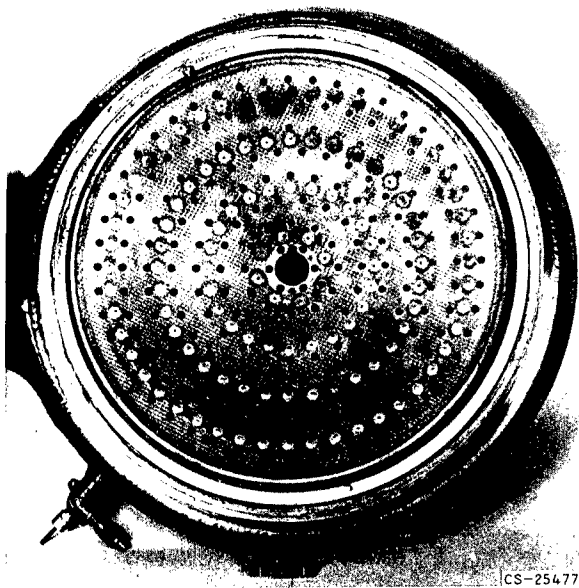


FIGURE 40-4.—Multielement 15,000-pound thrust injector.

In addition to its function in atomizing and mixing the propellants efficiently, the injector must provide a uniform distribution of mixture over the cross section of the chamber in order to make maximum use of the combustion space. Thus, injectors generally incorporate a large number of individual elements. As an example, figure 40-4 shows the face of an injector for a 15,000-pound thrust chamber; this injector contains 216 fuel and oxidant elements. If a 1,500,000-pound-thrust system were scaled up from this injector on a logical basis of constant thrust per element, 21,600 elements would be required. The fabrication of such injectors for a large rocket-engine development program would be extremely time consuming and expensive.

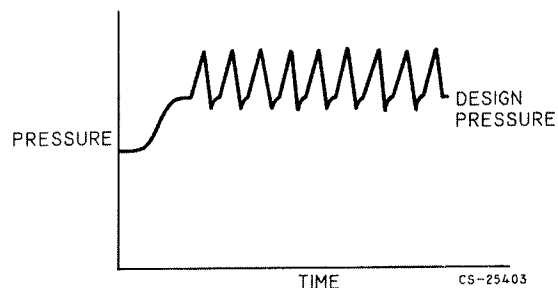
Two vital needs are evident: (1) quantitative criteria for injector design to reduce the number of injectors required to be investigated in a development program, and (2) simpler designs capable of higher thrust per element without sacrifice in performance. These needs will be even more critical in the development of propulsion systems that include a throttling capability, since such systems may utilize more complex, variable-geometry injection elements. The manned lunar landing is an outstanding ex-

ample of a mission requiring this kind of increased operational flexibility.

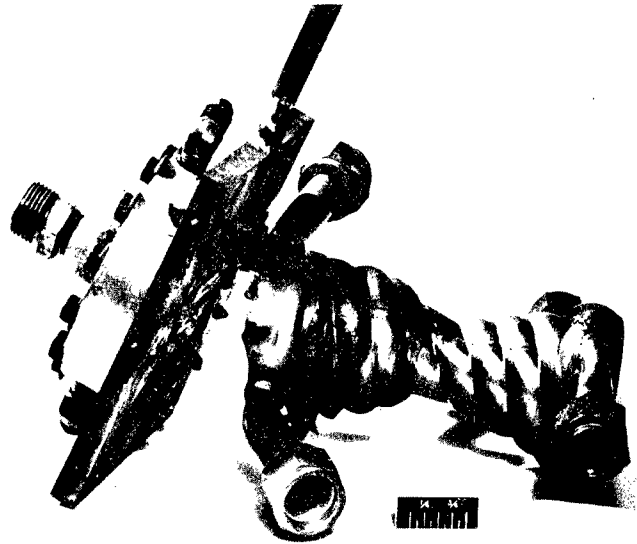
### COMBUSTION INSTABILITIES

If combustion efficiency were the only consideration, the choice of injector design would be reasonably straightforward; however, two other important requirements of the thrust chamber become involved: combustion stability and thrust-chamber durability. Experience indicates that thrust chambers with injectors providing high performance are frequently prone to combustion instabilities. The paper by Gerald Morrell and Richard J. Priem discussed fundamental studies of combustion instability. Some practical aspects of the problem are discussed briefly herein.

As has been noted, there are two principal kinds of instability, low-frequency "chugging" and high-frequency "screaming." Chugging is discussed in relation to control systems in the paper by John C. Sanders and Leon M. Wenzel. The most troublesome and least understood kind of combustion instability is the high-frequency screaming. The effect of such instabilities on thrust-chamber operation is illustrated in figure 40-5. Shown in figure 40-5(a) is a pressure trace typical of these oscillations. The frequency is inversely proportional to the chamber and in most applications is greater than 1000 cps. The predominant mode of damage is not a direct result of the pressure excursions, but rather it is a result of the scrubbing action of the oscillating gases causing very large increases in heat-transfer rate at the thrust-



(a) Chamber pressures with screaming.  
FIGURE 40-5.—High-frequency instability.



CS-25403

(b) Failure resulting from screaming.

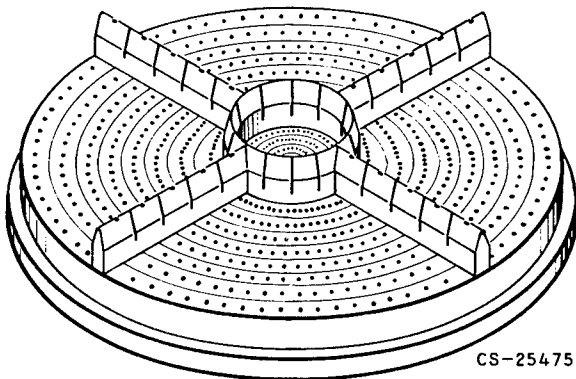
FIGURE 40-5 (Concluded).—High-frequency instability.

chamber wall. A failure resulting from screaming in a laboratory thrust-chamber unit is shown in figure 40-5(b). The "burnout" occurred at the face of the injector, and the burn patterns indicated a rotary motion of the wave front. The severity of the heat-transfer increase is indicated by the fact that burnout occurred in approximately  $\frac{1}{2}$  second with a water-cooled chamber designed to provide a substantial cooling margin under stable combustion conditions.

One remedy for this mode of oscillation that has been widely investigated experimentally is the use of baffles on the face of the injector to

compartment and break up the rotary motion. Figure 40-6 depicts an injector combining radial baffles and a circular, centrally located baffle. The radial baffles are intended to prevent tangential oscillations while the circular baffle is intended to prevent radial oscillations. The number of baffles, their design, and their dimensions are all parameters that thus far must be determined experimentally.

Other possible means of eliminating or alleviating destructive high-frequency oscillations include variations in injector element patterns and thrust-chamber wall contours. These design "fixes" generally require prolonged and costly cut-and-try experimentation; and, while they should receive considerable attention in our future thrust-chamber research, what is needed above all is a precise theoretical model of the entire combustion process that will account for the combustion-oscillation characteristics as well as the combustion-efficiency characteristics. Research of the type described in the preceding paper is directed toward the achievement of such a model. The complexity and diversity of this problem are such that a great deal of imaginative research, both analytical and experimental, must be conducted in order to expedite its solution.



CS-25475

FIGURE 40-6.—Injector with baffles.

# EXHAUST NOZZLE

The exhaust nozzle converts the thermal energy resulting from combustion into kinetic energy and, hence, into thrust by expanding the combustion gases to high velocity. In the atmosphere the degree of conversion is limited, since a conventional rocket nozzle cannot expand gas to velocities corresponding to pressures below ambient without incurring an overall thrust loss. In space there is no fundamental limit to expansion, since the ambient pressure is essentially zero.

The effect of altitude, or ambient pressure, on nozzle performance is illustrated in figure 40-7. Specific impulse in pounds thrust per pound flow per second as a function of altitude is shown for two nozzles, one with an expansion area ratio of 13, the other with an expansion area ratio of 50. The propellant combination is liquid oxygen-kerosene. At low altitudes, the large nozzle overexpands the working fluid to the extent that considerable thrust and, hence, specific impulse is lost. In practice, the loss is less than shown on this curve. At some point the flow no longer remains attached to the wall of the nozzle, flow separation occurs and the thrust loss due to a negative pressure differential is reduced. At higher altitudes, the more complete expansion possible with the larger nozzle yields considerably higher performance. Thus, there are two entirely different problems in the design of this component. One is concerned with the rocket engine operating in an Earth-launch trajectory. Since the engine will traverse a broad range of ambient pressures,

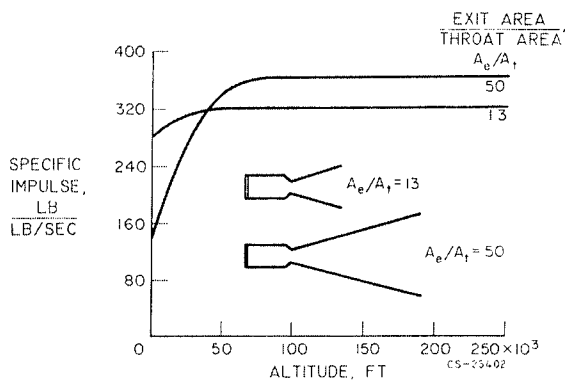


FIGURE 40-7.—Effect of altitude on nozzle performance.

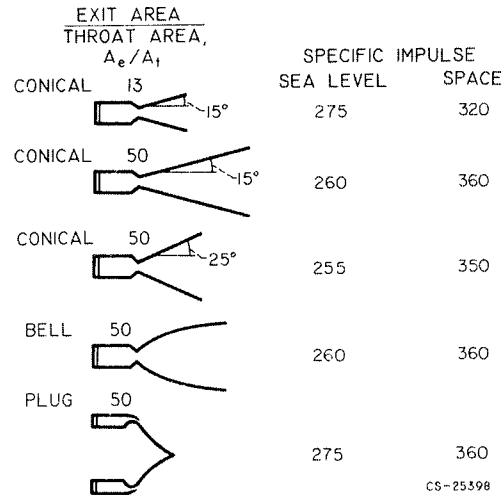


FIGURE 40-8.—Nozzle configurations and performance.

it cannot be designed to provide ideal expansion throughout its flight. A compromise design must be chosen to maximize the integrated impulse over the intended trajectory. The problem prompts investigation of potentially more flexible nozzle designs that may allow near-optimum expansion over a wider pressure range. For propulsion in space, the nozzle is designed to achieve the highest degree of expansion possible within the size envelope allowable in the vehicle and without imposing overall weight penalties on the vehicle.

Some design approaches that have been taken in the development of high performance, lightweight rocket nozzles are illustrated in figure 40-8. The first and second designs represent the low- and high-area-ratio nozzles of the preceding figure. These are 15° conics with sea-level and space specific-impulse values as noted. One approach to decreasing the size and the weight of the large-area-ratio space nozzle is to increase the divergence angle, as represented by the third design. Because of the increased divergence, there is a larger non-axial component of thrust produced by the existing gas; hence, some performance is lost. The fourth design is the contoured or "bell" nozzle. The contouring allows expansion performance at a given area-ratio equivalent to the 15° conical nozzle, but at only 75 to 80 percent of the length. Exit divergence loss is minimized in this design.

The last design is the "plug" nozzle, which essentially allows free expansion of the gases. It not only provides a very short length, but also it has the added advantage of selfadjustment of the exhaust flow to the ambient pressure conditions. Its performance tends to match that of a high-area-ratio nozzle at high altitude and that of a low-area-ratio nozzle at low altitudes. Thus, it represents an approach to the ideal booster nozzle. Some promising experimental work has been accomplished with this design; the disadvantages are found primarily in physical hardware problems. Severe wall-cooling problems result from the fact that the maximum heat-transfer rate, which occurs in the throat region, is also in the region of maximum surface area. Large amounts of cooling, or superior cooling techniques, would be required to assure adequate durability of this design.

In addition to the plug nozzle, a number of other promising designs have been proposed to improve off-design performance, weight, and size. These designs include shrouded, annular, reverse-flow, and expansion-deflection nozzles. Further theoretical analyses may evolve still others. High-thrust booster engines and high-area-ratio space engines alike have ever increasing needs for more compact, lighter weight nozzles.

One final factor affecting nozzle performance is the extent of chemical recombination. Experience has shown that all nozzles suffer, in varying degrees, losses in performance that result from the less than maximum recombination of the highly dissociated combustion gases. The actual loss is a function of the propellants used, the combustion conditions, and the nozzle-design factors. The problem is not yet amenable to design approaches. Present tech-

nology has not provided us with adequate means of measuring or characterizing the chemical kinetic processes occurring during expansion so that possible solutions may be evolved. The need for basic research on chemical recombination, particularly under low-pressure conditions, is clear.

## DURABILITY

The last principal thrust-chamber requirement, durability, is closely related to nozzle design, combustion efficiency, and combustion stability. Large nozzles, and in particular some unconventional designs, impose increased cooling demands. Injectors that promote rapid combustion for high efficiency create injector and wall-cooling problems. Combustion instabilities can result in destructive levels of wall heat flux.

The four primary methods of cooling the walls of a thrust chamber are illustrated in figure 40-9. The first method is regenerative cooling, whereby one of the propellants, generally the fuel, flows through coolant passages in the wall of the thrust chamber prior to being injected into the combustion chamber. The second cooling method is ablation. The ablation process is basically one of dissipation of heat from the boundary layer by the decomposition and/or melting and vaporizing of the wall materials. While the regenerative chamber achieves equilibrium during operation, the ablative chamber continues to be eaten away and, hence, is a duration-limited system.

Most rocket thrust chambers that are in use today or are under development utilize one of these first two cooling methods. The third cooling method is radiation. The chamber wall in this case is a single thickness of high-temperature metal. Heat absorbed from the combustion process is radiated to space. The last method, the heat sink, has little application other than in research installations. The walls of a heat-sink chamber are made heavy enough to provide a sufficient heat capacity so that, for short duration operation, wall temperatures do not exceed the design limits.

Two additional basic methods of cooling are available to the thrust-chamber designer: (1) film cooling the wall by introducing a fraction

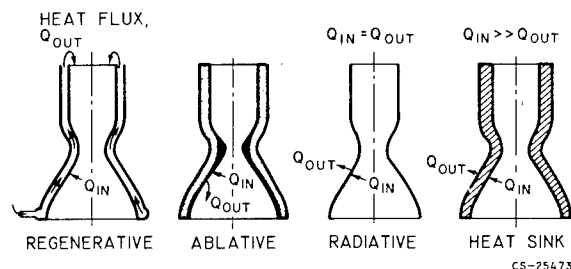


FIGURE 40-9.—Thrust-chamber cooling techniques.

of the flow of one propellant near the wall, and (2) transpiration cooling by introducing a part or all of one propellant through a porous liner in the chamber. Both methods tend to incur serious performance penalties and, hence, have not been used to any extent as a primary cooling scheme. Film cooling in particular, however, is frequently applied to augment the primary cooling scheme.

Most of the current research on regeneratively cooled chambers has been directed toward the application of hydrogen for cooling of hydrogen-oxygen thrust chambers. This fuel is an excellent coolant because of its high heat capacity and because it does not decompose as do some fuels, for example, hydrazine. Because of these excellent cooling capabilities, hydrogen-oxygen thrust chambers that are now under development could be designed rather conservatively. The coolant is, in general, more than adequate for the job. Two areas of future activity, however, will involve greatly increased heat-flux conditions; the cooling margin will diminish, and more precise predictions of the heat-transfer characteristics will be required. In particular, local rather than overall heat transfer and transient as well as steady-state conditions will need consideration. One of these areas is the hydrogen-fueled, nuclear heat-transfer rocket; the other is the compact, high-pressure, high-thrust chemical rocket. Figure 40-10 is a plot of the relative value of heat-transfer coefficient for hydrogen against the ratio of wall to bulk-coolant temperature. The different curves represent cor-

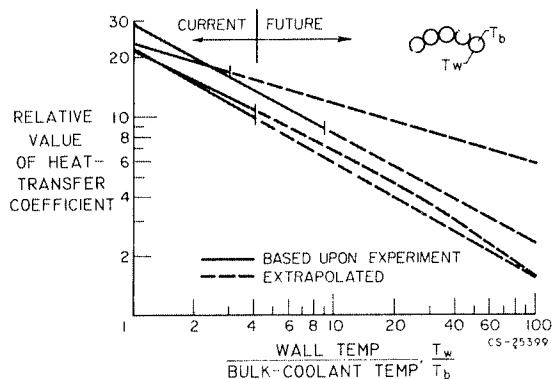


FIGURE 40-10.—Heat-transfer correlations over a range of wall-to-bulk-coolant temperature ratios.

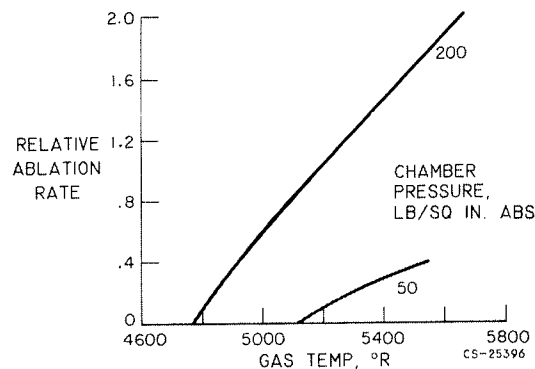


FIGURE 40-11.—Thrust-chamber ablation rates.

relations by different experimenters. The solid portions of the curves represent the ranges of experimental data; the dash portions represent the extrapolations. For temperature ratios currently encountered, the correlations represented predict about the same value of heat-transfer coefficient. The nuclear rocket and the high-pressure chemical rocket, however, will involve coolant-side heat transfer at wall-to-bulk-coolant temperature ratios that are well beyond the experimental conditions. The cooling potential of hydrogen at these very high heat-transfer rates must be precisely determined. Tube-type heat-transfer experiments under boiling and nucleate boiling conditions are needed. Also, the cooling requirements of these high heat-flux applications are not yet sufficiently well understood. The achievement of precise methods of predicting local as well as overall heat-flux rates will require analytical studies coupled with high heat-flux thrust-chamber tests.

The durability of an ablatively cooled thrust chamber is represented by its ablation rate, the rate at which material is removed from the wall. The variation of ablation rate with gas temperature and combustion pressure is illustrated in figure 40-11. It can be seen that ablation rate increases rapidly as temperature is increased and that higher pressures also result in higher ablation rates. These data imply that the application of ablation cooling may be restricted to relatively low-pressure systems. While such systems are feasible for low-thrust application, they become impractical for high thrust appli-

## CURRENT RESEARCH AND DEVELOPMENT ON THRUST CHAMBERS

cations. For example, the design of a 50-pounds-per-square-inch booster engine of 1,500,000-pounds thrust would require a combustion chamber with a diameter of about 14 feet. The temperature effect on ablation cannot be easily circumvented by design since high performance generally means high gas temperatures.

Much of the ablative material technology that is in use today for rocket engines has stemmed from atmospheric reentry hardware developments. The conditions are so different that optimum materials for the reentry condition are not necessarily also optimum for the rocket chamber walls. Therefore, considerably more effort needs to be expended on materials research specifically for rocket thrust chambers in an effort to develop ablative materials that are better able to withstand higher gas temperatures and higher pressures.

Radiation cooling is also restricted to special applications that involve low heat flux conditions, for example, nozzle extensions and very-low-pressure combustion systems. Surface temperatures of a radiation-cooled chamber are above the melting points of many of the more conventional alloys. The kinds of materials that must be considered include molybdenum, tungsten, and tantalum; fabrication techniques for these materials must be advanced if they are to be applied to thrust chambers. Even at wall temperatures well below the melting point of the material, durability can be considerably reduced by rapid corrosion of the walls. This problem calls for research on high-temperature

protective coatings. Such coatings must withstand thermal shocks and vibrations.

## SUMMARY

This brief review of the state of the art of the chemical-rocket thrust chamber has considered its principal requirements: ignition, combustion, exhaust-nozzle expansion, and durability. In each of these areas, the hardware technology required to produce satisfactory systems for today's needs is generally available. Additional research and development, however, is required to provide a better understanding of the processes involved so that new requirements can be met without repeating a multitude of cut-and-try experiments. Many areas exist where improved performance and increased operational flexibility would be highly desirable and, in fact, will be necessary for sophisticated space missions.

The kinds of problems that have been discussed relate to a number of basic fields of study. Analytical and experimental research is needed on ignition processes, including catalysis; the physics of propellant atomization and mixing; combustion dynamics; fluid flow and heat transfer under high-heat-flux conditions, nozzle aerodynamics, and high-temperature materials with particular emphasis on ablative compositions. This research is most urgently needed for the development of hydrogen-oxygen rocket systems but should also recognize potential future applications of other high-energy propellant combinations such as hydrogen-fluorine.

## BIBLIOGRAPHY

*The following is a bibliography of selected references pertaining to the liquid-propellant rocket thrust chamber.*

- AUBIE, CARMON M.: A Study of Injection Processes for Liquid Oxygen and Gaseous Hydrogen in a 200-Pound-Thrust Rocket Engine. NACA RM E56125a, 1956.
- BLOOMER, HARRY E., ANTI, ROBERT J., and RENAS, PAUL E.: Experimental Study of Effects of Geometric Variables on Performance of Contoured Rocket-Engine Exhaust Nozzles. NASA TN D-1181, 1962.
- CAMPBELL, C. E., and FARLEY, J. M.: Performance of Several Conical Convergent-Divergent Rocket-Type Exhaust Nozzles. NASA TN D-467, 1960.
- CONNORS, JAMES F., CUBBISON, ROBERT W., and MITCHELL, GLENN A.: Annular Internal-External-Expansion Rocket Nozzles for Large Booster Applications. NASA TN D-1049, 1961.
- CURREN, ARTHUR N., PRICE, HAROLD G., JR., and DOUGLASS, HOWARD W.: Analysis of Effects of Rocket-Engine Design Parameters on Regenerative-Cooling Capabilities of Several Propellants. NASA TN D-66, 1959.

## CHEMICAL ROCKET PROPULSION

- FARLEY, JOHN M., and CAMPBELL, CARL E.: Performance of Several Method-of-Characteristics Exhaust Nozzles. NASA TN D-293, 1960.
- FEILER, CHARLES E., and YEAGER, ERNEST B.: Effect of Large-Amplitude Oscillations on Heat Transfer. NASA TR R-142, 1962.
- GORDON, SANFORD, and MCBRIDE, BONNIE J.: Theoretical Performance of Liquid Hydrogen with Liquid Oxygen as a Rocket Propellant. NASA MEMO 5-21-59E, 1959.
- GREGORY, JOHN W., and STRAIGHT, DAVID M.: Ignition of Hydrogen-Oxygen Rocket Combustor with Chlorine Trifluoride and Triethylaluminum. NASA TN D-684, 1961.
- HEIDMANN, M. F., and BAKER, LOUIS, JR.: Combustor Performance with Various Hydrogen-Oxygen Injection Methods in a 200-Pound-Thrust Engine. NACA RM E58E21, 1958.
- HENDRICKS, R. C., GRAHAM, R. W., HSU, Y. Y., and FRIEDMAN, R.: Experimental Heat Transfer and Pressure Drop of Liquid Hydrogen Flowing Through a Heated Tube. NASA TN D-765, 1961.
- LADANYI, DESZO, J. and MILLER, RILEY O.: Comparison of Ignition Delays of Several Propellant Combinations Obtained with Modified Open-Cup and Small-Scale Rocket Engine Apparatus. NACA RM E53DO3, 1953.
- LOVELL, J. CALVIN, SAMANICH, NICK E., and BARNETT, DONALD O.: Experimental Performance of Area Ratio 200, 25 and 8 Nozzles on JP-4 Fuel and Liquid-Oxygen Rocket Engine. NASA TM X-382, 1960.
- MALE, THEODORE, KERSLAKE, WILLIAM R., and TISCHLER, ADELBERT O.: Photographic Study of Rotary Screaming and Other Oscillations in a Rocket Engine. NACA RM E54A29, 1954.
- NEU, RICHARD F.: Injection Principles for Liquid Oxygen and Heptane Using Nine-Element Injectors in an 1800-Pound-Thrust Rocket Engine. NACA RM E57E13, 1957.
- PRIEM, RICHARD J., and HEIDMANN, MARCUS F.: Propellant Vaporization as a Design Criterion for Rocket-Engine Combustion Chambers. NASA TR R-67, 1960.
- RAO, G. V. R.: Recent Developments in Rocket Nozzle Configurations. ARS Jour., vol. 31, no. 11, Nov. 1961, p. 1488.
- RIEHL, W. A., PERKINS, HAROLD, STOKER, CHARLES S., and KIRSHENBAUM, A. D.: Ozone Fluoride for Rocket Propulsion, ARS Jour., vol. 32, no. 3, Mar. 1962, p. 384.
- ROBBINS, WILLIAM H.: Analysis of the Transient Radiation Heat Transfer of an Uncooled Rocket Engine Operating Outside Earth's Atmosphere. NASA TN D-62, 1959.
- ROLLBUHLER, R. JAMES, and STRAIGHT, DAVID M.: Ignition of a Hydrogen-Oxygen Rocket Engine by Addition of Fluorine to the Oxidant. NASA TN D-1309, 1962.
- RUPE, JACK H.: A Correlation Between the Dynamic Properties of a Pair of Impinging Streams and the Uniformity of Mixture-Ratio Distribution in the Resulting Spray. Progress Rep. 20-209, Jet Propulsion Laboratory, Pasadena, Calif., Mar. 1956.
- SIEVERS, GILBERT K., TOMAZIC, WILLIAM A., and KINNEY, GEORGE R.: Theoretical Performance of Hydrogen-Oxygen Rocket Thrust Chambers. NASA TR R-111, 1961.
- SUTTON, GEORGE P.: Rocket Propulsion Elements. Second ed., John Wiley & Sons, Inc., 1956.

# 41. Dynamics and Control of Chemical Rockets

By John C. Sanders and Leon M. Wenzel

JOHN C. SANDERS is Technical Consultant for Development in the Advanced Development and Evaluation Division of the NASA Lewis Research Center. Currently concerned with nuclear rocket research, he has specialized in aircraft and spacecraft powerplants and propulsion systems with particular emphasis on application of controls to these systems. He attended Virginia Polytechnic Institute, receiving B.S. and M.S. degrees in Mechanical Engineering in 1936 and 1937, respectively. He is a member of the American Society of Mechanical Engineers and the Institute of the Aerospace Sciences.

LEON M. WENZEL, Aerospace Scientist at the NASA Lewis Research Center, is currently working on the application of large hydrogen-oxygen rocket engine systems and on systems analysis. He graduated from Ohio Northern University with a B.S. degree in Electrical Engineering in 1954.

## INTRODUCTION

Some of the problems will be examined herein that arise when a complete propulsion system is assembled. The problems discussed are dynamic ones—the problems of system stability and control. In the interest of brevity, the problems will be illustrated by reference chiefly to the hydrogen-oxygen rocket. After describing some possible rocket systems and some of the necessary control functions, the study will delve into dynamic properties of components of rocket systems that influence system stability and control. Then some of the effects of component dynamics on system stability, design, operation, and control will be illustrated.

## DESCRIPTION OF COMPLETE ROCKET SYSTEMS

One of the rocket systems where pumps are used to supply propellants to the combustion chamber is shown in figure 41-1. The heat picked up by the hydrogen as it circulates through the coolant jacket of the combustion chamber and nozzle is sufficient to drive a turbine. The gas exhausted by the turbine is then injected into the combustion chamber. This

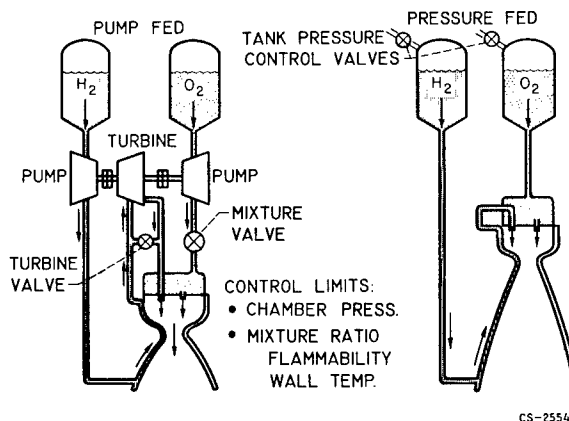


FIGURE 41-1.—Two flow systems for a chemical rocket.

pumping arrangement is called the topping cycle. Control in the topping cycle is achieved by manipulation of the turbine valve to regulate thrust and the mixture valve in the oxygen propellant line to maintain desired mixture ratio.

A pressure fed engine is also shown in figure 41-1. The pressure in the propellant tanks is sufficient to force the two propellants through the injector into the combustion chamber. The hydrogen is first circulated through the coolant



## CHEMICAL ROCKET PROPULSION

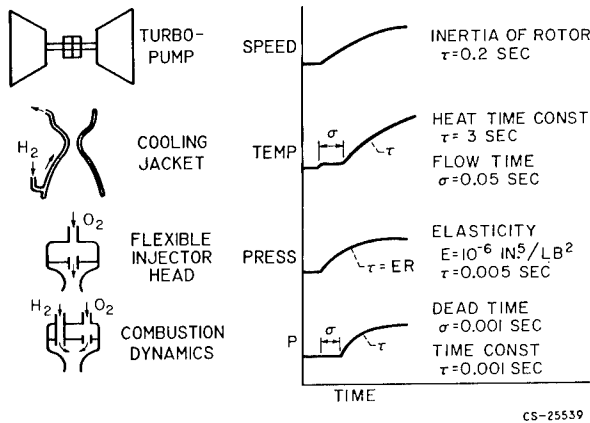


FIGURE 41-2.—Dynamics of components of a rocket system.

jacket. In the pressure-fed engine the pressures in the supply tank can be regulated to yield the desired chamber pressure and mixture ratio.

Among the control limits are chamber pressure (which is proportional to thrust), mixture ratio, and turbopump speed. High chamber pressure and high turbopump speed can cause injuriously high material stresses, and even rupture. Limits on mixture ratio are flammability limits and high gas temperature near stoichiometric mixture, which can cause overheating of the walls of the combustion chamber.

### DYNAMICAL ELEMENTS OF ROCKET

Four of the elements of the rocket that contribute significantly to system dynamics are shown in figure 41-2. First is the turbopump. Its inertia causes a comparatively slow response of pump speed to a disturbance. The cooling jacket introduces the characteristic dynamics of a heat exchanger, which may be simplified to a rough approximation containing a heat-transfer term and a flow term. The elasticity of the injector is significant to high frequency stability, as are the combustion dynamics, herein described in terms of dead time and time constant.

### COMBUSTION DYNAMICS

The properties of combustion dynamics and their significance in determining flow system stability are illustrated in figure 41-3. The figure shows that, if a step change in oxygen

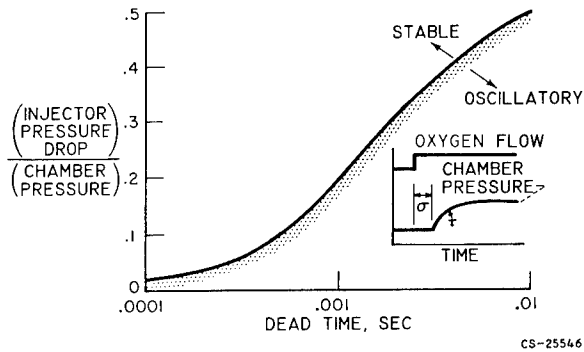


FIGURE 41-3.—Destabilizing effect of dead time on propellant flow system. Time constant, 0.001 second.

flow is introduced, the chamber pressure shows no change for a period  $\sigma$ , called the dead time. Then the pressure rises with a characteristic time constant  $\tau$ . The dead time, which is associated with the drop atomization, mixing, and ignition, is more disastrous and less understood than the time constant, which is like an aerodynamic filling time.

The effect of this dead time on stability is shown in figure 41-3. In general, as the dead time increases, the injector pressure drop required to ensure stable propellant flow increases, thereby increasing the required supply pressure.

Operating conditions that influence dead time are shown in figure 41-4. The dead time is shown to decrease with increasing chamber pressure and decreasing oxidant-fuel ratio. It is possible that the injection velocity of the liquid propellant (oxygen, since the hydrogen is heated in the cooling jacket) is more significant than chamber pressure.

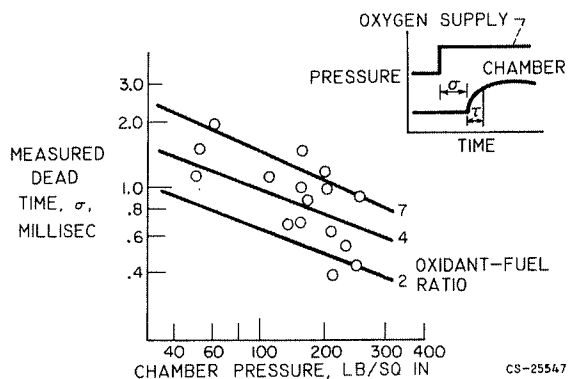


FIGURE 41-4.—Control dynamics of a rocket combustion chamber using hydrogen-oxygen propellant.

It is worthy to note the extremely short dead time for the hydrogen-oxygen propellant combination. Kerosene and other nonhypergolic storable propellants have dead times five times as great. With hydrogen-fluorine, on the other hand, the dead time has been immeasurably small. Thus, the order of stability from stable to unstable is: hydrogen-fluorine, hydrogen-oxygen, storable nonhypergolic.

### STABILITY OF PRESSURE-FED ENGINE

One of the instances where instability plagues the propellant system is while "throttling" or reducing the thrust of a pressure-fed engine. This propensity to oscillate is the result of the low injector pressure drop encountered at low thrust. The injector pressure drop had been set at a low value even at full thrust to avoid tank pressure and high tank weight.

The stability bounds, shown as a function of throttle range for a selected rocket, are presented in figure 41-5. The throttle range is the ratio of maximum thrust to minimum thrust. In each curve, operation at oxygen pressure drop below the curve will result in oscillation at the minimum thrust.

An interesting feature of the figure is that reducing hydrogen injector pressure drop can be achieved by a moderate increase in oxygen pressure. Such a trade is desirable since the hydrogen tank is larger, and weight savings are realized at the lower tank pressure. The

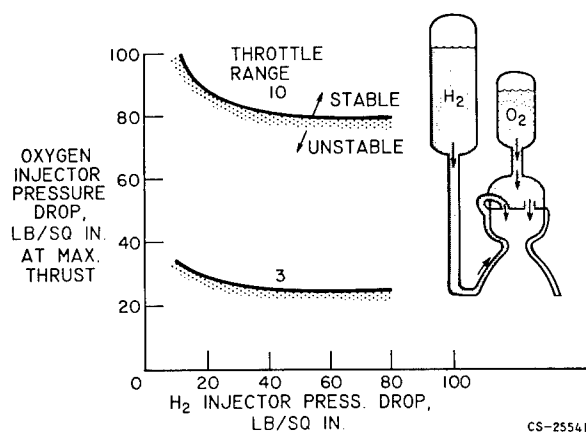


FIGURE 41-5.—Injector flow stability limits of hydrogen-oxygen engine. Dead time, 0.001 second; time constant, 0.00085 second; elasticity,  $10^{-6}$  inch<sup>5</sup> per pound<sup>2</sup>.

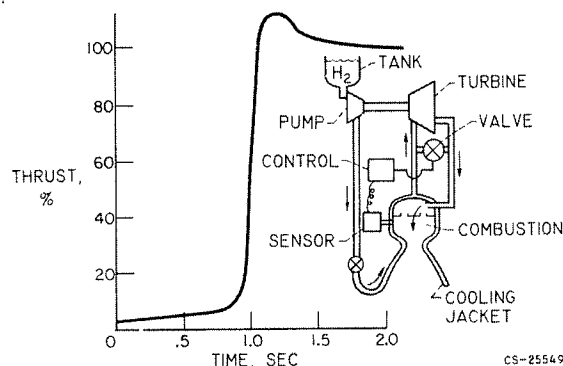


FIGURE 41-6.—Startup of a hydrogen-oxygen rocket-topping cycle (oxygen not shown).

reason for the insensitivity of stability limits to hydrogen injection pressure drop is the heating of the hydrogen in the coolant passages before injection. Also shown is the fact that high oxygen pressure drop must accompany large throttle ratio if stability is to be achieved. Throttle ratios as high as 10 have been obtained in tests.

### STARTUP OF PUMP-FED ENGINE

The startup transient of the pump-fed engine is influenced by pump inertia, turbine torque, and particle passage time through the coolant jacket more than by combustion-chamber dynamics. An idea of the quickness of acceleration may be obtained from Figure 41-6. The rapidity with which the thrust approaches maximum shows that an accurate, quick-acting control is needed to prevent going to such high overload that damage is incurred. Control frequency responses up to 10 cycles per second are needed.

### THRUST MANIPULATION WITH PUMP-FED ROCKET

Once the rocket has been started, the problems arise of manipulating the thrust to desired values quickly and stably. In the problem of injector system instability previously discussed, additional problems associated with the pump are encountered. Two of these pump problems are pump stall and flow instability resulting from a static characteristic of the pump.

These problems are illustrated in Figure 41-7, where deceleration from full thrust at point

## CHEMICAL ROCKET PROPULSION

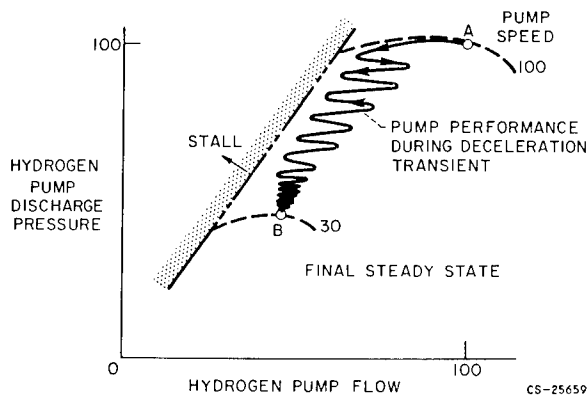


FIGURE 41-7.—Oscillations in a rocket flow system induced by pump flow characteristics.

A to a lower thrust at point B was attempted. A rather severe oscillation was induced, and the stall limit was approached with a dangerously small margin. The cause of the oscillation was traced to the slope of the pump pressure delivery characteristic at constant speed. A positive slope produces a less stable flow system than does a negative one. Inspection of Figure 41-7 shows that the deceleration transient caused the pump to operate in a less stable positive slope region. Furthermore, at the lower thrust level, point B, the steady-state operating point is in a less stable operating region (more positive slope of pump character-

istic) than point A. Throttling to an even lower operating point than B could have resulted in failure of the system to even reach steady state. The results shown were obtained from an analog computer study that simulated an actual experience.

Thus, the figure shows that oscillation of the entire flow system can be induced by a positive slope of the pump characteristic and that the steady-state throttling range can also be limited by the same pump characteristic.

## FURTHER WORK NEED ON CHEMICAL ROCKETS

The technology of control and dynamics of chemical rockets is far advanced as a result of long intensive research and development. Dynamics of combustion, however, are worthy of further investigation, although many investigators have worked in this field. Only in the very simple chemicals has the knowledge of dynamics reached a degree of usefulness, and even here the dynamics at low pressure are not thoroughly developed. Certain knowledge of the dynamics of storable propellants useful for course corrections and of attitude control of a space vehicle would improve the capability to modulate the thrust, and thereby enhance the usefulness of these propellants.

## BIBLIOGRAPHY

- DRAIN, DANIEL I., SCHUM, HAROLD J., and WASSERBAUER, CHARLES A.: Relations of Combustion Dead Time to Engine Variables for a 20,000-Pound-Thrust Gaseous-Hydrogen-Liquid-Oxygen Rocket Engine. NASA TN D-851, June 1961.
- HURRELL, HERBERT G.: Analysis of Injection-Velocity Effects on Rocket Motor Dynamics and Stability. NASA TR R-43, 1959.
- OTTO, EDWARD W., and FLAGE, RICHARD A.: Experimental Studies of Combustion Chamber and Feed System Stability During Throttling of a Regeneratively Cooled Liquid Hydrogen-Fluorine Rocket Engine. Paper 246B, SAE, Oct. 10-14, 1960.

# Concluding Remarks

By Walter T. Olson

For a somewhat detailed picture of certain key technology in the chemical-rocket field, it is necessary to discuss one thing at a time. In real life, however, things usually do not happen one at a time. Thus, the importance of viewing a propulsion system as a system must be stressed.

In order to achieve needed reliability in future high-performance systems of increasing sophistication, high quality must be specified and designed into all components at inception. Problems arising from unfavorable interactions of components also must be avoided. The paper by John C. Sanders and Leon M. Wenzel has detailed some examples in system dynamics; some further examples selected from past occurrences and experiences are: (1) The pump blades should not stimulate or excite resonant frequencies in such tender parts as an injector face. (2) The state and the flow rate of gas to drive a turbopump must be controlled to keep the pump flows within the stall and the surge limits of the pumps; and, to complicate matters, the pump delivery, in turn, may be affecting the gas flow to the turbine. (3) The cooling passages of a thrust chamber must accommodate the local heat transfer, which, in turn, is strongly a function of the combustion pattern produced by the injector design. (4) Propellant-flow lines can be harmfully in tune or safely out of tune with fluctuating gas pressure

in the combustor. (5) Pump design must allow for enough delivery pressure to ensure enough pressure drop for cooling needs and for injection with stable combustion.

Reliability is a quality in the initial concept of the complete system and its parts. The designs and systems that are being and will be created are too intricate and specialized, and the performance of their components is too interrelated for uninformed tinkering. A development must start right, not just because subsequent attempts at fixes may be costly and time consuming, but also because fixes may be impossible.

There is a continuing need for emphasizing training in the basic principles of engineering and science, so that even while working on a specialty the engineer or scientist will have a broad, interdisciplinary point of view. The scientists and engineers that are trained for the future must have the ability to see the problems of whatever they undertake with clarity and completeness. Such comprehension comes by use of the fundamental principles of physics, chemistry, mechanics, metallurgy, electricity, etc., to create a conceptual quantitative model of the device or the system. Both high-quality components and their harmonious blending come from an understanding and appreciation of the physical processes and phenomena at work in a particular operation.

SESSION N

## **Nuclear Propulsion**

*Chairman, DAVID S. GABRIEL*

---

DAVID S. GABRIEL, *Chief of the Advanced Development and Evaluation Division of the NASA Lewis Research Center, received his B.S. degree in Mechanical Engineering from the University of Akron in 1943, and did graduate work in Aeronautical Engineering at Case Institute of Technology.*

*He has participated in directing research on turbines and rotating machinery, turbojets, ramjets, chemical rockets, and nuclear rockets and power conversion systems. He is a member of the Institute of the Aerospace Sciences and the New York Academy of Science.*

# Introduction

By David S. Gabriel

The nuclear rocket engine is believed by many to be the most important space powerplant for the near future. Some of the reasons for this belief are illustrated by figure 1.

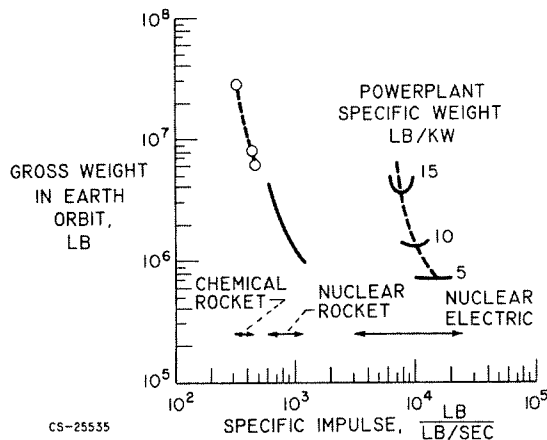


FIGURE 1.—Manned Mars mission with a seven-man crew and two-man surface exploration. Round-trip time, 420 days.

In figure 1 are shown the vehicle requirements for a seven-man trip to Mars in a little over 1 year flight time for three types of spacecrafts: chemically propelled, nuclear-rocket propelled, and nuclear-electric propelled. The ordinate is the weight of the vehicles in the Earth orbit (300 miles) required for the mission. About 25 times as much weight is required on the ground to boost these vehicles into orbit. The specific-impulse range for chemical rockets is from 300 to 450 and for nuclear rockets, from 700 to 1000 seconds. Electric propulsion provides much greater impulse, but, although not shown here, at a considerable sacrifice in ratio of thrust to weight. It is

apparent that a rather fantastic reduction in launch weight is possible with nuclear rockets compared with chemical rockets. Because, for nuclear-electric systems, it is not now known how light these systems can be built, three curves are shown for various system weights. From current information, 5 pounds per kilowatt is extremely light and probably will not be achieved without some unforeseen breakthrough. The more likely range is 10 to 15 pounds per kilowatt. These results are, of course, highly dependent on the particular mission. A different one would give a different answer. At least for this type of highly energetic short-time trip, typical of many of great interest to us, nuclear rockets and nuclear electric systems are highly competitive, and neither is clearly superior to the other. Further, it is evident that even if very lightweight electrical systems are developed, the gains to be expected are not spectacular. For very-long-term missions such as a trip to Pluto, the electric rocket is comparatively better. The nuclear rocket is, therefore, clearly a superior powerplant to the chemical rocket and at least competitive with nuclear electric systems for many future missions. For these reasons, a great urgency is felt for nuclear-rocket development.

Nuclear rockets require high-flow, high-pressure turbopumps, exhaust systems capable of withstanding heat loads in excess of any present system, and specialized instruments for the measurement of not only pressure, temperature, and flow, but also of nuclear environment. The design and development of reactors with impulses in the range previously mentioned introduce the requirement of very high power density in order to keep weight within reason. This

necessity aggravates the usual problems in both nucleonics and heat transfer and, in turn, introduces the problem of maximum material temperature of the order of 4000° to 6000° F and minimum hydrogen temperatures around -400° F. Structures and materials must survive extreme environments. The control of the reactor and its associated systems is a very difficult problem, particularly in off-design condi-

tions. The mating of the reactor to the vehicle creates interaction problems. Overlying all these problem areas are the difficulties caused by a high-nuclear-radiation environment.

Not all of these areas will be discussed in the following four papers, however. These papers are concerned primarily with the problems of nucleonics, heat transfer, control, and overall performance.



## 42. Advanced Concepts for Nuclear Rocket Propulsion

By Frank E. Rom and Robert G. Ragsdale

FRANK E. ROM, *Chief of the Nuclear Propulsion Concepts Branch of the NASA Lewis Research Center, attended Cornell University where he received his B.S. and M.S. degrees in Mechanical Engineering in 1946 and 1948, respectively. Mr. Rom has been active in research on nuclear propulsion systems for aircraft and rockets. He is the chairman of the Nuclear Propulsion Committee of the American Rocket Society and a member of the Nuclear Applications Panel of the Institute of Aerospace Sciences.*

ROBERT G. RAGSDALE, *Aerospace Scientist in heat-transfer research at the NASA Lewis Research Center, is currently working on experimental tests of hydrodynamic mixing, radiation heat transfer, and system evaluation of a coaxial flow gaseous nuclear rocket. He received his B.S. and M.S. degrees in Chemical Engineering from Purdue University in 1950 and 1951, respectively.*

### INTRODUCTION

The use of the nuclear rocket offers about a tenfold reduction in interplanetary spacecraft weight when compared with chemical rockets (refs. 1, 2, 3, and 4). With such a great potential gain in view, the nation is currently developing the first flyable nuclear-rocket engine. The reactor for this engine is composed of high-temperature materials that serve to heat the hydrogen propellant. A schematic drawing of a solid-core heat-transfer-type nuclear rocket showing the principle of the nuclear-rocket engine is shown in figure 42-1. The fission energy is liberated within solid materials of which the reactor core is composed. This heat is then transferred from the solid-core materials to hydrogen as it flows through the heat-transfer passages. The hydrogen is stored in a propellant tank and then is pumped through the nozzle walls for cooling purposes. It is also passed through the reflector regions and any other parts that require cooling. On leaving the reflector, the hydrogen flows through the passages of the reactor core where

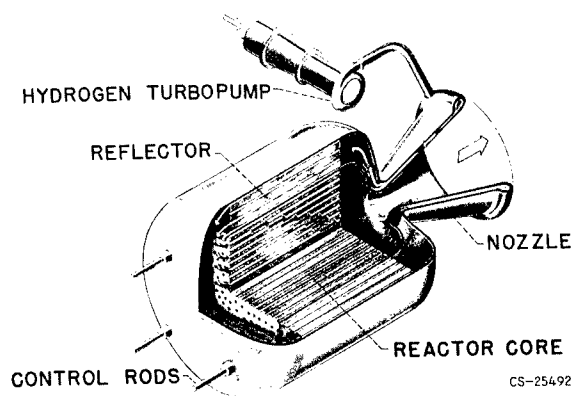


FIGURE 42-1.—Solid-core heat-transfer-type nuclear rocket.

it is heated to as high a temperature as the core materials will stand. The high-temperature hydrogen is then exhausted through a convergent-divergent nozzle to produce thrust.

Since nuclear rockets eject mass to produce thrust, the only reason for considering nuclear systems for rocket propulsion is that they have the potential for producing a higher specific impulse than chemical rockets.

## NUCLEAR PROPULSION

The specific impulse that may be attained by nuclear rockets is shown in figure 42-2, where specific impulse is plotted as a function of hydrogen temperature. For reference purposes, the specific impulse of advanced hydrogen-oxygen rockets such as those that will power the Centaur and the upper stages of the Saturn C-5 is over 400 pounds per pound per second. The temperature capability of the materials of which the nuclear reactor is constructed will limit hydrogen temperatures to less than 6000° F or specific impulses of about 1000 pounds per pound per second. This limit is determined by the strength of reactor-core materials operating at temperatures approaching their melting points. Beyond this limit, reactors in which the fissionable material is in the gaseous form and heats hydrogen by direct contact or by thermal radiation must be envisioned. In this case, specific impulses up to 3000 pounds per pound per second may be possible.

There is considerable interest in specific impulses greater than 1000 pounds per pound per second, even though a tenfold advantage in spacecraft weight has been obtained over chemical systems at that value. Further increases in specific impulse will, of course, produce greater weight savings. Perhaps it may be more important to take advantage of the greater flexibility in performing interplanetary missions that higher specific impulse can give. For example, the use of solid-core nuclear rockets limits the departure time for a 460-day round trip to Venus to about 1 month every 2 years.

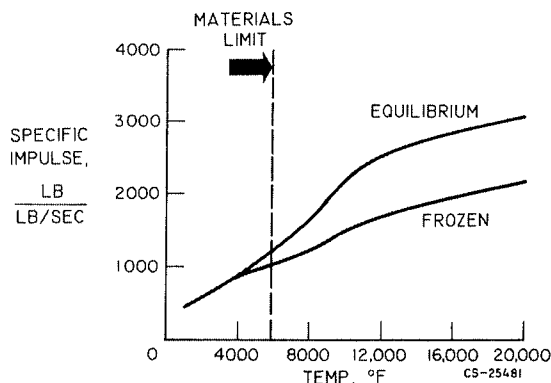


FIGURE 42-2.—Specific impulse of hydrogen as a function of temperature.

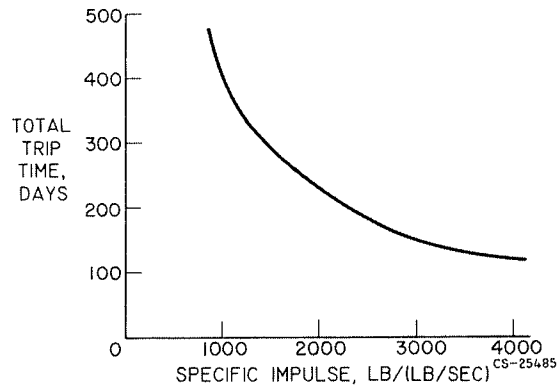


FIGURE 42-3.—Effect of specific impulse on mission time.

For a specific impulse of 2000 pounds per pound per second, departures during about 8 months out of every 2 years would be possible. A further benefit of higher specific impulse is that it will permit much shorter trip times for a given spacecraft weight as illustrated in figure 42-3, which shows the total trip for a 7-man Venus mission as a function of specific impulse. The weight of the spacecraft that is launched from an Earth orbit is fixed at 1.7 million pounds. The data in this figure apply only for high-thrust systems; that is, where the thrust-to-weight ratio of the spacecraft is greater than 0.10. Lower thrust-to-weight ratios will increase the trip time appreciably. Materials-limited nuclear rockets can accomplish this mission in about 450 days. A gaseous-core nuclear rocket with a specific impulse of 3000 pounds per pound per second could accomplish this mission in one-third the time or about 150 days.

In the following discussion, both solid-core and gaseous-core advanced nuclear-rocket concepts are considered. In the case of the solid-core nuclear rocket, the chief problem is to achieve the highest hydrogen temperature within the limits of the melting points of the most refractory materials. For the gaseous-core reactor, the chief problems are associated with schemes whereby hydrogen is heated by gaseous fissionable material without excessive fuel loss and without melting down the walls that contain gases at temperatures far beyond the melting point of solids.

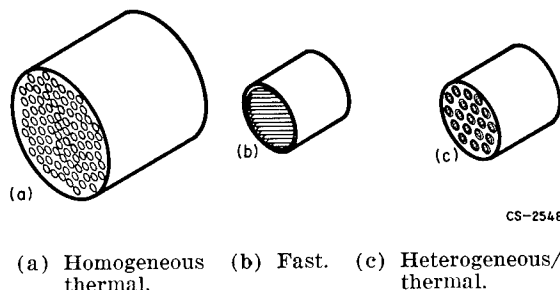
### ADVANCED SOLID-CORE REACTORS

First, consider advanced "solid-core" nuclear-rocket concepts that heat hydrogen by contact with high-temperature solids. The main objective in this case is to find which of the materials or combinations of materials found in nature can be made to produce the highest operating temperature and, hence, the highest specific impulse. In addition, reactor concepts that have the greatest probability of being successfully developed into highly reliable powerplants in the most economical and efficient manner must be found. Finally, there is always an interest in achieving the smallest size and weight.

#### Reactor Types

Some of the reactor types considered for nuclear-rocket use are shown in figure 42-4, namely, homogeneous thermal, fast, and heterogeneous thermal. The advantages and disadvantages are given in table 42-I.

*Homogeneous thermal reactor.*—In this reactor, the fissionable material is intimately mixed with a neutron-moderating material. The heat of fission is thus liberated in the moderator and is removed by the hydrogen propellant that flows through an array of coolant passages, which can be visualized as holes passing from one end of the reactor to the other. The highest temperatures in the reactor occur in the moderator, hence, the name "hot moderator". In addition to being capable of slowing down neutrons, the moderator must also be capable of operating at high temperatures. Graphite and beryllium oxide are the only two materials that



CS-25486

FIGURE 42-4.—Nuclear-rocket reactors.

can reasonably serve this dual function. Graphite has the poorer moderating properties of the two, and therefore its use leads to larger core dimensions and weight. On the other hand, beryllium oxide is limited to operating temperatures of at least 1000 degrees Fahrenheit less than that of graphite. Since specific impulse is of the utmost importance, graphite is really the only contender. The use of graphite, however, requires a protective coating on the heat-transfer passages to prevent chemical reaction with hydrogen.

*Fast reactors.*—This type of reactor is composed of all fuel-bearing material, schematically considered as an array of fueled plates for heat-transfer surfaces with no moderator. Fast reactors can be made very small (ref. 5) and can use the best available high-temperature fuel-bearing materials. The largest drawback stems from the fact that nuclearwise fast reactors are less efficient than moderated systems, and a great deal more fissionable material is required for criticality. This leads to more difficult materials problems, since the volume of

TABLE 42-I.—Characteristics of Three Types of Nuclear-Rocket Reactors

Reactor type	Homogeneous thermal (hot moderator)	Fast (no moderator)	Heterogeneous thermal (cooled moderator)
Moderating material	Graphite Beryllium oxide	None	Water Heavy water Beryllium Beryllium oxide Metallic hydrides
Fuel-bearing material	Coated graphite Beryllium oxide	Refractory metals (W, Mo) Carbides (ZrC, HfC, TaC)	Refractory metals ( $W^{184}$ , Mo) Coated graphite Carbides (ZrC)

## NUCLEAR PROPULSION

fissionable material must be about equal to the total volume of all other materials in the core. Unfortunately, since fissionable compounds are not very satisfactory as structural or heat-transfer materials, they must be contained within a refractory material such as tungsten, molybdenum, or the carbides of zirconium, hafnium, or tantalum. Development of satisfactory fuel elements that contain 50 volume percent of fissionable material without penalizing high-temperature performance is difficult. This major problem area of fast-reactor concepts requires a great deal of research on materials and techniques for achieving the high fuel loadings.

*Heterogeneous thermal reactors.*—In this reactor, the fissionable material is separated from the moderator and contained in a refractory fuel-bearing material that provides the heat-transfer surfaces. The moderator is independently cooled and, therefore, can be maintained at a lower temperature than the fuel elements. Relatively low-temperature operation permits consideration of such moderating materials as water, heavy water, beryllium, beryllium oxide, and metallic hydrides. The fuel-bearing material can be any of the best high-temperature materials such as tungsten, molybdenum, graphite, or low neutron absorbing ceramics such as zirconium carbide. Fuel loadings of 15 to 20 volume percent are sufficient. The heterogeneous reactor does involve

the complication of requiring a cooling system for the moderator. In addition, the relatively cold moderator must be thermally insulated from the high-temperature fuel-element regions, and in the case of tungsten, it must be enriched in the tungsten 184 isotope (ref. 6). The homogeneous thermal and the fast reactors appear, at least in concept, to be the simplest since fuel-bearing material constitutes the entire core. The heterogeneous thermal reactor seems to have the greatest potential for producing the high specific impulse, since the relatively low fuel concentrations required are expected to permit the fuel bearing materials to operate nearer to their melting points.

### Fuel-Element Materials

Table 42-II shows the properties of the most refractory materials available. Shown here are graphite, which sublimates at 7000° F, tungsten, the most refractory metal, which melts at 6170° F, and the most refractory ceramics which are the carbides of hafnium and tantalum, which melt at 7030° F and 7020° F, respectively. These materials can be utilized as fuel elements by adding a suitable uranium compound. Uranium dioxide, the most refractory of all uranium compounds (m.p. 5000° F, ref. 7) can be used with tungsten. Unfortunately in the case of hafnium and tantalum carbides, a solid solution forms with uranium carbide. Thus,

TABLE 42-II.—*Properties of Refractory Materials*

Material	Melting point, °F	Tensile strength at 5000° F, psi	Creep strength at 5000° F, psi <sup>a</sup>	Thermal conductivity, (Btu)(in.)/(ft <sup>2</sup> )(hr)(°F)	Linear expansion coefficient, 10 <sup>-6</sup> in./in. (°F)	Modulus of elasticity, 10 <sup>6</sup> lb/in. <sup>2</sup>	Hydrogen reaction	Evaporation rate at 5000° F, mls/hr	Compatible fuel material	Other limits
Graphite...	7000 (sublimes)	1000 to 6000	10 to 800...	140 at 5000° F	2.75 up to 4000° F (ATJ).	1.4 to 2.0 at 4000° F	>2800° F..	30	UC <sub>2</sub> ....	UC <sub>2</sub> melts at 4535° F
Tungsten ..	6170.....	<sup>b</sup> 3000 to 7000	1000.....	920 at 5000° F	3.6.....	1 to 10.....	None.....	0.1	UO <sub>2</sub> ....	-----
Hafnium carbide	7030.....	<sup>c</sup> 2500 at 4000° F	-----	260 to 310 at 4000° F	2.88 up to 4000° F	79.....	>4840° F..	3	UC.....	-----
Tantalum carbide	7020.....	<sup>c</sup> 6000 at 4000° F	-----	275 at 4000° F	3.05 up to 4000° F	-----	>4630° F..	0.6	UC.....	Loses carbon above 4000° F

<sup>a</sup> Creep rate, 10<sup>-5</sup> inch per inch per minute.

<sup>b</sup> One-half of measured bend strength.

<sup>c</sup> For tensile test strain rate of 0.02 to 2.0 inch per inch per minute.

the melting point of a 50-50 mixture of 50 percent hafnium carbide and 50 percent uranium carbide is only about 5750° F compared with 7030° F, the melting point of hafnium carbide alone.

The tensile strength of graphite given for a temperature of 5000° F varies from 1000 to 6000 pounds per square inch depending on its grade and density (ref. 8). The tensile strength of tungsten varies from 3000 to 7000 pounds per square inch depending on the rate of applying the load (refs. 9 and 10). The highest temperature for which the strengths of the carbides have been measured is 4000° F. At this temperature, the tensile strength was assumed to be one-half of the measured strength in bending. The values for hafnium carbide and tantalum carbide at 4000° F are 2500 and 6000 pounds per square inch, respectively (refs. 11 and 12).

Since the fuel-element materials are subjected to loads for finite periods of time, creep strength is of great importance. The creep strengths are presented at 5000° for a creep rate of  $10^{-5}$  inch per inch per minute, which corresponds to an elongation of about 1/2 percent in 10 hours. The creep-rate values for graphite depend on grain orientation, density, and grade and range from 10 to 800 pounds per square inch (ref. 13). Tungsten has a value of 1000 pounds per square inch (ref. 14).

Values of thermal conductivity vary from 140 Btu per hour per square foot per degrees Fahrenheit per inch for graphite (ref. 15) up to 920 for tungsten (ref. 16). The thermal conductivity of hafnium carbide was obtained from reference 12. The value for tantalum carbide was obtained from reference 17. The coefficients of linear expansion were obtained from references 16 and 17. The modulus of elasticity was obtained from references 16, 17, and 18. Further data on properties of refractory materials can be found in reference 11.

A strong hydrogen reaction with graphite begins at 2800° F (ref. 19); therefore, protective coatings are essential when graphite is used. Hydrogen does not react with tungsten, but hafnium and tantalum carbides do react at temperatures of 4840° and 4630° F, respectively (ref. 20).

The evaporation rate of graphite at 5000° F in a vacuum is 30 mils per hour (ref. 21). The use of sound coatings on graphite should reduce the evaporation rate to the rate of evaporation of the coating material. Because it is usually desirable to minimize coating thicknesses, low evaporation rates of suitable coating materials are of extreme importance: tungsten has the lowest rate at 0.1 mil per hour (ref. 22). Tantalum and hafnium carbides have intermediate rates (refs. 21 and 23).

Uranium carbide ( $UC_2$ ) melts at 4535° F (ref. 24) and would be expected to affect adversely the properties of graphite fuel elements at higher temperatures. Tantalum carbide loses carbon above about 4000° F with the resultant formation of  $Ta_2C$ . The use of tantalum carbide would be limited to applications where relatively short life is adequate. The data presented in the table are for refractory materials with no uranium compounds added. Much less data are available for these materials when they contain fuel compounds. Supplying these data represents a major field for continued research.

On the basis of data presented in the table, tungsten may be expected to have the greatest potential for producing the highest specific impulse attainable by solid-core nuclear rockets. Whether or not this potential will be realized can only be determined by extensive experimental investigations.

#### Solid-Core Reactor Studies

A portion of the nuclear-rocket program at Lewis involves the study of advanced solid-core-reactor concepts and their problems. This work is aimed at pushing forward the technology of nuclear-rocket reactors and providing some degree of insurance for the nation's nuclear-rocket program. In developing a new engine based on a relatively advanced technology, success is not assured for any chosen approach to the problem. Within the limits of resources available, alternate or backup approaches must be undertaken. In a limited way, the program at Lewis on advanced solid-core nuclear rockets is such a backup effort, even though the main emphasis is on providing the technology for the development of the ultimate solid-core nuclear rocket.

## NUCLEAR PROPULSION

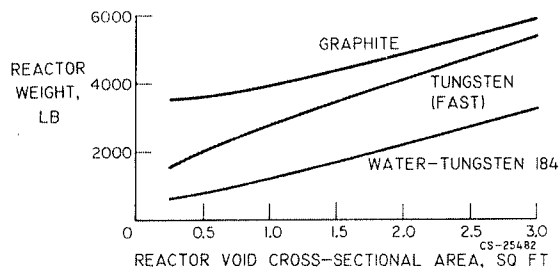


FIGURE 42-5.—Nuclear-rocket reactor weight as a function of reactor void cross-sectional area.

*Reactor-weight comparison.*—A study has been made of the three reactor types described earlier to help determine the selection of the most promising avenues of research. Figure 42-5 shows one of the results of this investigation. Reactor core plus reflector weight is plotted as a function of reactor void cross-sectional area. (A 1000 megawatt reactor requires about 1 sq ft of flow area.) The graphite reactor, which represents the best of the homogeneous-thermal type, is the heaviest. The fast-tungsten reactor, which assumes a 50-50 volume ratio of tungsten and uranium dioxide, is lighter than the graphite reactor. The lowest curve is the best that can be done with heterogeneous-reactor cores. Water was found to be the best of the moderators considered. Tungsten enriched in the tungsten 184 isotope was considered to have the best potential for high-temperature performance, because it has the desirable structural properties of metal and its use requires a lower percentage of uranium dioxide to be contained within the fuel-element material. It should be emphasized that the weight of the reactor is only one criterion for the selection of a reactor for nuclear rockets. The importance of high temperature materials has already been discussed. Consideration must also be given to the mechanical aspects of the core design. In other words, does a reactor design exist that is practical and can be developed in a reasonable fashion?

*Reactor design problems.*—Some typical reactor-core-design problems arising in advanced concept studies can be illustrated by using the tungsten-water-moderated reactor as an exam-

ple. The reactor shown schematically in figure 42-6 consists of an aluminum tank of water with an array of aluminum tubes joining the end header plates. It is very similar in principle to the heat-transfer-reactor experiment number 1 (ref. 25), which was used to heat air for a turbojet powerplant, and the ML-1 reactor (refs. 26 and 27), which is used to heat gas for a mobile powerplant unit. The tubes provide space for fuel elements and flow passages for the hydrogen. First, the hydrogen passes through the regeneratively cooled nozzle, then through a water-to-hydrogen heat exchanger to remove the heat generated by neutron and gamma radiation and any other heat that may be absorbed by the water, then through the fuel elements located within the aluminum tubes. The heated hydrogen is then expanded through the nozzle to produce thrust. The sketch in the figure indicates how insulation is provided to reduce the heat transferred from the high temperature elements to the water. The fuel elements are supported by a continuous tungsten tube that runs the full length of the core. The space between this tube and the aluminum tank is filled with stagnant hydrogen. This is accomplished by venting the downstream end to the reactor exit region and sealing the upstream portion. A molybdenum radiation shield is also

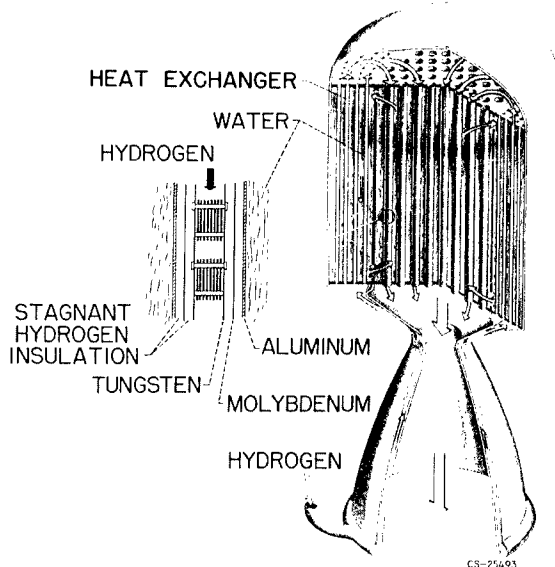


FIGURE 42-6.—Tungsten-water-moderated reactor concept.

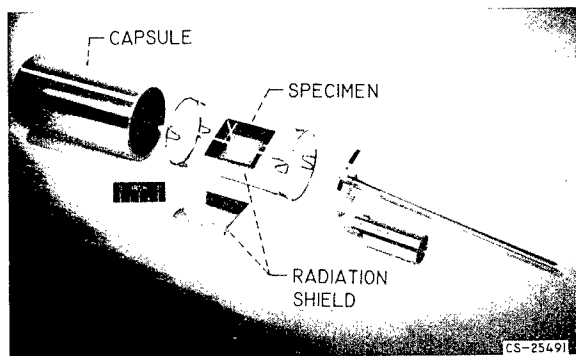


FIGURE 42-7.—In-pile capsule experiment.

shown. A hydrogen thickness of less than  $\frac{1}{8}$  inch is sufficient to reduce the heat flow to less than 1 percent of the reactor power.

The most important problems of this or any other reactor concept employing tungsten are the fueled materials and the fuel-element structure. The question is can suitable fueled-tungsten material be made and can this material retain fissionable material such as uranium dioxide at temperatures of the order of 5000° F for periods of up to 10 hours with no loss or attack by hydrogen? Once a suitable material is obtained, a fuel-element structure that supplies the required heat-transfer surfaces and flow passages must be designed and evaluated. The fuel-element structure, indicated schematically by flat plates (fig. 42-6), must be capable of withstanding very high heat-transfer rates and large aerodynamic loads at high temperatures with a minimum of stress to avoid creep or distortion. The fuel element must be capable of withstanding severe thermal cycling loads corresponding (1) to reactor startups and shut-downs required for space missions, and particularly (2) for economical development of highly reliable powerplants, where a very large number of tests must be performed to demonstrate reliable operation.

*Experimental investigations.*—Experimental investigations are required to determine the performance limits of the fuel-element materials and proposed fuel-element structures because of the lack of fundamental data and understanding of the complex structures usually encountered. Analytical procedures are used as tools to correlate or extrapolate experimental data.

In-pile capsule tests (fig. 42-7) have been and are being conducted in materials-testing reactors to evaluate fueled materials. The test specimen shown is a fueled plate 1 inch square and about  $\frac{1}{32}$  inch thick made by powder-metallurgy techniques. It contains fully-enriched uranium (235) dioxide. It is surrounded by a box of molybdenum that forms a radiation shield. Tungsten wires suspend the specimen and shield within the central region of the capsule. The heat generated by fissions is removed by radiation to the water-cooled capsule walls. After the capsule is sealed and evacuated, it is inserted into a test hole next to the testing reactor, where the specimen is heated by the fissioning uranium contained therein. Tests such as these are used to establish the ability of the fueled material to retain fissionable compounds at any desired temperature level. In addition, the effects of fuel burn-up and radiation damage can be ascertained. This type of test can also be used to obtain rapid and inexpensive evaluation of a wide range of fueled materials to determine their potential and for research aimed at improving the properties of the materials considered.

These tests cannot determine the effect of flowing hydrogen, high heat-transfer rates or aerodynamic loads on fuel-element geometries. Such problems can be investigated by electrically heating sample fuel elements and subjecting them to the hydrogen flow rates and heat-transfer rates to be encountered in the reactor. Study of the effects of simultaneous

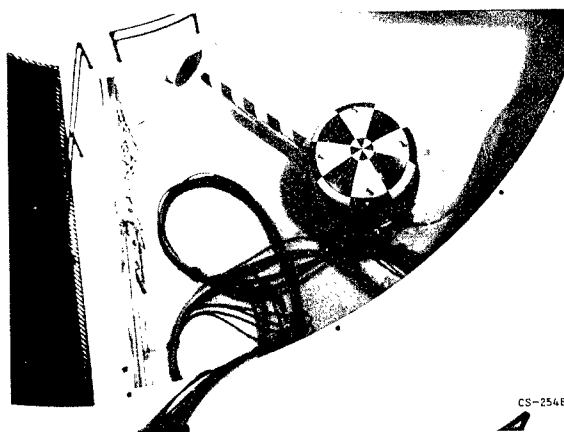


FIGURE 42-8.—Fuel-element-experiment facility in Plum Brook reactor.

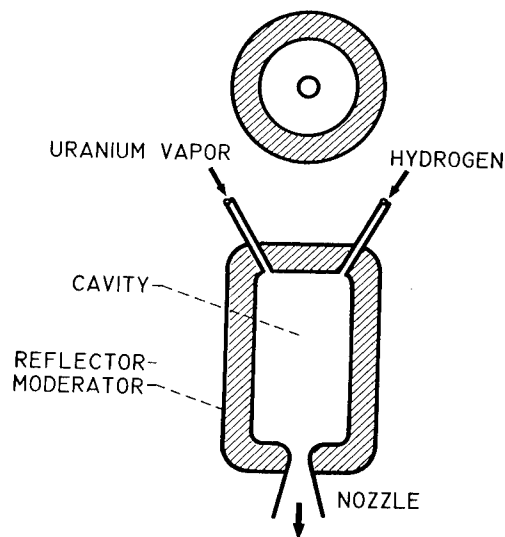
fission heating and aerodynamic loads can be made during flow tests run on fuel elements that are placed within a testing reactor. Figure 42-8 shows a model of the NASA Plum Brook Reactor Facility with a fuel-element test loop about to be inserted into the core. The ends of the test holes, which are directly adjacent to the reactor, are shown as the flanged pipes. The test fuel element is located within the snout of the fuel-element test loop. The tank houses the pumps and heat exchangers necessary to flow the helium coolant. This loop, which is now under construction, is designed to operate with the test fuel element to produce 100 kilowatts of power.

### GASEOUS-CORE REACTORS

The problems of attaining the ultimate performance of solid-core reactors basically limited by the melting temperature of solid materials have been discussed briefly. Now consider gaseous-reactor concepts, where the aim is to bypass the materials limit and to produce hydrogen temperatures of 10,000 to 20,000° F. with specific impulses up to 3000 pounds per pound per second. This is accomplished by maintaining nuclear fuel in the reactor as a gas rather than as a solid.

#### Basic Concept

The fundamental concept of a gas-core reactor is shown in figure 42-9. The nuclear fuel in gaseous form is contained in a reactor cavity that is externally moderated and reflected. The reactor is made critical by increasing the pressure of the fissionable gas. The heat generated by the fissioning gas can be used to heat hydrogen by direct mixing. The heated mixture is then ejected through a nozzle to produce thrust. The weight-flow ratio of fissionable material to hydrogen, of course, is limited by various considerations. For example, if the cost of the fissionable material is limited to the cost of hydrogen for an orbital launch interplanetary space mission, the fissionable-material flow would be about  $\frac{1}{35}$  of the hydrogen mass flow (assuming that hydrogen placed in orbit costs \$200 per pound, while fissionable material costs \$7,000 per pound.) A less severe limit arises from the increase of propellant

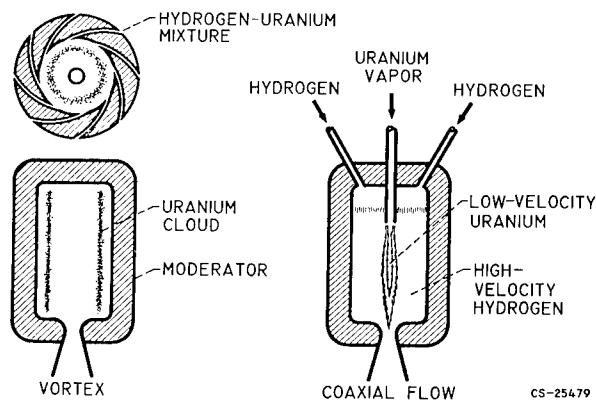


CS-25483

FIGURE 42-9.—Gaseous-cavity reactor.

average molecular weight; a 1-to-1 flow ratio would yield a specific impulse equal to 70 percent of that of pure hydrogen. For a ratio of 1 to 35 or less the effect on specific impulse is less than 3 percent. For a mass flow ratio of 1 to 35, the hydrogen pressure would be about 4000 times greater than the fissionable-material pressure because of the low molecular weight of hydrogen compared with that of uranium or plutonium. Under rather ideal conditions, the required partial pressure of fissionable material for criticality is of the order of 25 pounds per square inch (ref. 28). The total pressure in the cavity, therefore, would be of the order of 100,000 pounds per square inch!

Clearly some scheme is required to circumvent the pressure dilemma. If the uranium



CS-25479

FIGURE 42-10.—Gaseous-cavity-reactor concepts.



could be caused to recirculate so that its residence time relative to the hydrogen would be increased by a factor of 100, the pressure level would be reduced by this ratio.

Figure 42-10 illustrates two gaseous-reactor concepts. The scheme on the left uses a vortex to increase the residence time of the uranium (refs. 29 and 30). A mixture of hydrogen and

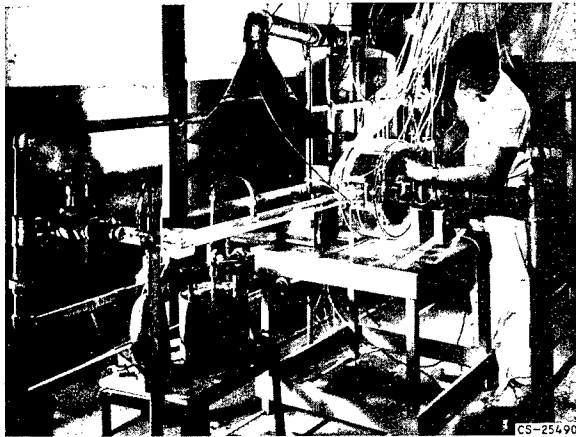


FIGURE 42-11.—Two-fluid vortex experiment.

uranium vapors is introduced tangentially into a cavity. The resultant centrifugal field set up will tend to throw the uranium atoms toward the walls, since they are heavy relative to the hydrogen. The radial-velocity component of the gas flowing through the reactor will try to drag the uranium with it. The hydrogen is heated as it diffuses through the resulting uranium cloud. If the flow rate is too high, the centrifugal forces on the uranium atoms will be overcome, and the uranium will be blown out. The limitation of this system appears to be the low flow rates that are permissible. In the scheme on the right, the uranium and hydrogen are introduced in separate streams in a coaxial fashion (ref. 31). The uranium must flow at a lower velocity than the hydrogen to maintain a reasonable uranium-to-hydrogen weight-flow ratio. Here the hydrogen is heated by thermal radiation from the fissioning uranium gas in the cavity center. In both reactor concepts, the hydrogen must contain a material to render it essentially opaque to radiation at temperatures below about 10,000° F. Above this temperature, hydrogen absorbs radiation by itself.

Other schemes have been proposed for gaseous reactors. Some utilize electromagnetic forces to increase the residence time of uranium (ref. 32), others use a multiple array of vortex tubes (ref. 29). Another scheme is called a "glo-plug" system (ref. 33), which, in principle, is similar to the coaxial-flow system except that a transparent hydrogen-cooled tube separates the uranium from the hydrogen. The problem of providing a transparent tube for the "glo-plug" system seems very formidable. The plasma-core concept requires very large magnetic-field strengths (ref. 32).

The hydrodynamics of the gaseous-vortex reactor has received considerable attention (refs. 34, 35, and 36). A bromine-vapor-air experimental vortex system is shown in figure 42-11 (ref. 30). A bromine-air mixture is introduced tangentially into a transparent vortex chamber. The radial concentration profiles of bromine are measured by light-absorption techniques. Attempts to predict the observed data using one-dimensional analyses for two-component flow have not been too successful (ref. 30). Recent investigations (refs. 35 and 36) suggest that the flow pattern in a vortex is much more complex compared with the models that have been used for analyses. Realistic analyses must consider the influences of turbulence and end-wall boundary-layer flow. A similar set of experiments run with a coaxially flowing bromine-air system is shown in figure 42-12. In this case analysis agrees very well with experimental results for both laminar and turbulent situations. Typical data are shown in figure 42-13 for laminar- and turbulent-flow regimes.

The results of these hydrodynamics experiments are used to verify or check theoretical predictions that are used as a basis for determining performance of real gaseous reactors. Inasmuch as the gases in the real situation are quite different and the tests are isothermal, such experiments must be extended to other gases and heating must be provided to increase further the confidence in theoretical estimates.

Analytical investigations are being conducted for the coaxial system, where flow and radiation heat transfer are considered simultaneously (ref. 37). This analysis has predicted the effective absorptivity required to prevent melting

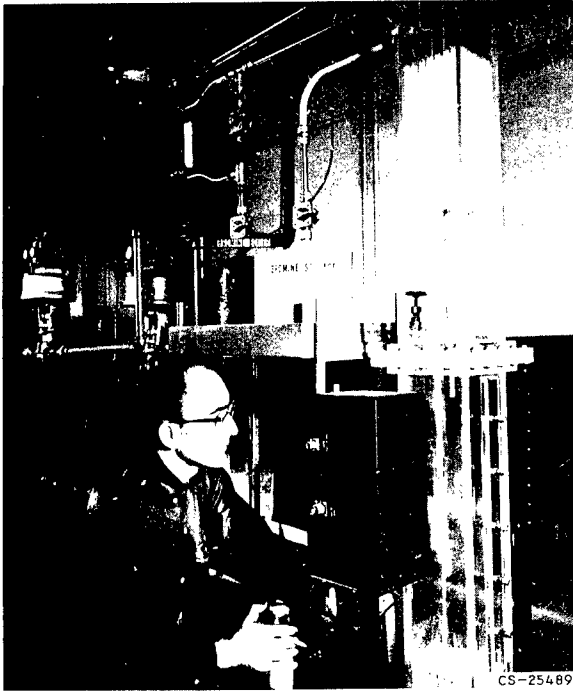


FIGURE 42-12.—Coaxial-flow experiment.

down the cavity walls. The use of seeding material such as graphite dust has been suggested to increase the thermal radiation absorption of the hydrogen, and some basic transmissivity measurements have been reported (ref. 38).

The results of reference 38 are summarized in figure 42-14. The conclusions indicate that the transmissivity of carbon-particle clouds is relatively independent of wavelength for 0.2 to 1.0 micron radiation and that the exponential dependency on concentration predicted by Beer's law exists. These data were all obtained at room temperature, however, and additional information at elevated temperatures and pressures including the chemical interaction with hydrogen is required. Currently, experiments are being conducted on the radiation absorption of seeded gases in flowing systems. Figure 42-15 shows the test apparatus used in these experiments. An arc about 2 feet long with a power of about 250 kilowatts is struck between the electrodes and is stabilized in a nitrogen vortex. The arc supplies a source of radiant thermal energy. Flowing coaxially in an annular region outside the arc tube is a stream of gas that can be seeded with dust particles. The

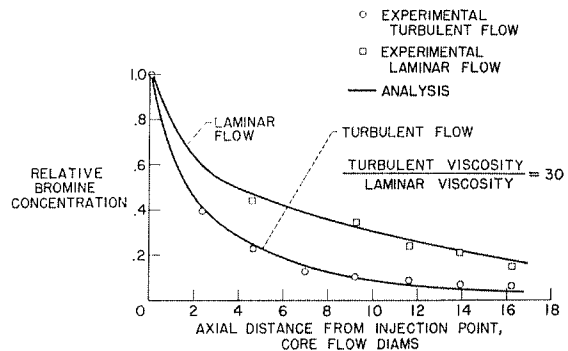


FIGURE 42-13.—Air-bromine coaxial-flow experimental data.

energy transmitted through the gas with and without seeding is measured to determine the effect of seeding.

Very little work has been done or is under way in the area of criticality of gaseous reactors. The importance of this research stems from the fact that the operating pressure of gaseous-reactor concepts is directly determined by the critical-mass requirements of cavity reactors with unusual three-dimensional fuel distributions. These distributions arise from the hydrodynamics of fuel-separation schemes and nonuniform temperature distributions. Early work on criticality of cavity reactors has considered the case of uniform fuel distributions in spherical one-dimensional geometries (refs. 39, 40, and 41). This work has been extended at Lewis to two-dimensions where nonuniform radial fuel distribution has been considered (refs. 42 and 43).

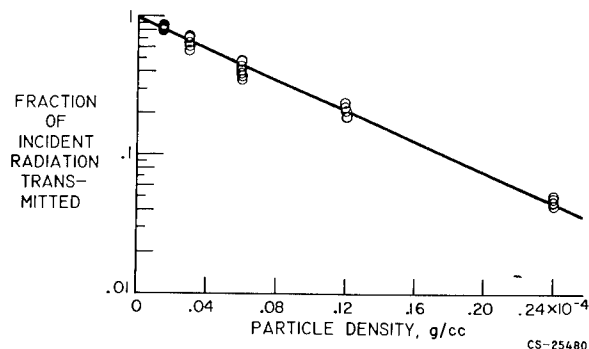


FIGURE 42-14.—Spectral transmissivities of carbon particles. Particle diameter, 0.15 micron; radiation wavelength, 0.2 to 1.0 micron; radiation path length, 10 centimeters.

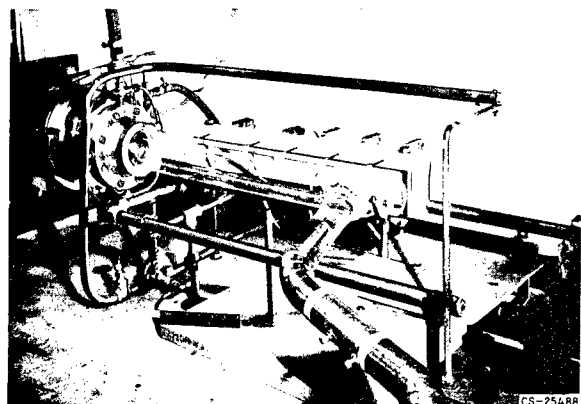


FIGURE 42-15.—Thermal-radiation-absorption experiment.

Because the potential performance of gaseous-nuclear rockets is far beyond that of advanced solid-core systems, the necessary research to determine feasibility should be vigorously pursued. The degree to which gaseous reactors can realistically attain their potential requires a great deal of work in the fundamental fields of gaseous radiant heat

transfer, nucleonics, and hydrodynamics, and especially in their interaction.

### CONCLUDING REMARKS

A limited amount of work is under way on the problems of both advanced solid-core and gaseous-core nuclear-rocket reactors. As the goals of our space program expand, the importance of nuclear rockets will become increasingly recognized. Therefore, the necessary technology needed to develop reliable nuclear rockets for manned interplanetary flight must be expanded as quickly as possible so that a solid foundation on which to base decisions to develop powerplants will exist. Most important among the things to be done in the study of solid-core reactors is the experimental evaluation of fueled materials and reactor concepts. In the study of gaseous reactors, the problems of hydrodynamics associated with increasing the residence time of the fuel, gaseous heat transfer by thermal radiation, and criticality of gaseous cores are the most pressing.

### REFERENCES

1. HIMMEL, S. C., DUGAN, J. F., JR., LUIDENS, R. W., and WEBER, R. J.: A Study of Manned Nuclear-Rocket Missions to Mars. Paper 61-49, Inst. Aerospace Sci., Inc., 1961.
2. HIMMEL, S. C., DUGAN, J. F., JR., LUIDENS, R. W., and WEBER, R. J.: Nuclear-Rocket Vehicles for Mars and Venus Missions. Paper presented at ARS/ORNL Space-Nuclear Conf., Gatlinburg (Tenn.), May 1961.
3. JOHNSON, PAUL G., and ROM, FRANK E.: Perigee Propulsion for Orbital Launch of Nuclear Rockets. NASA TR R-140, 1962.
4. ROM, FRANK E., LIETZKE, ARMIN F., and JOHNSON, PAUL G.: Small Nuclear Rockets for Space Missions. Nucleonics, vol. 20, no. 11, 1962.
5. COOPER, RALPH S.: Fast Reactor Rocket Engines-Criticality. Nuclear Sci. and Eng., vol. 13, no. 4, Aug. 1962, pp. 355-365.
6. LEVIN, S. A., HATCH, D. C., and VON HALLE, E.: The Separation of Tungsten-184. Rep. KOA-865, Paper presented at ARS/ORNL Space-Nuclear Conf., Oak Ridge Gaseous Diffusion Plant, Union Carbide Nuclear Co.
7. WISNYI, L. G., and PIJANOWSKI, S. W.: The Thermal Stability of Uranium Dioxide. KAPL-1702, Knolls Atomic Power Lab., Nov. 1, 1957. (Available from Office Tech. Services, U.S. Dept. Commerce, Wash., D.C.)
8. Anon.: Tensile Strength—Graphite: Some Mechanical Properties of Graphite at Elevated Temperatures. Jour. App. Phys., vol. 22, no. 5, 1951, pp. 593-600.
9. Anon.: Tensile Strength—Tungsten: Memo. 157, Defense Metals Info. Center, Sept. 11, 1962, p. 20.
10. SIKORA, PAUL F., and HALL, ROBERT W.: Effect of Strain Rate on Mechanical Properties of Wrought Sintered Tungsten at Temperatures Above 2500° F. NASA TN D-1094, 1961.
11. BRADSHAW, WANDA D., and MATTHEWS, CLAYTON O.: Properties of Refractory Materials: Collected Data and References. LMSD-2466, Missile Systems Div., Lockheed Aircraft Corp., Jan. 15, 1959.

# NUCLEAR PROPULSION

12. SANDERS, WILLIAM A., CREAGH, J. W. R., ZALABAK, C., and GANGLER, J. J.: Preliminary Investigation of the Fabrication and Properties of Hafnium Carbide. Paper presented at Tech. Conf. on High Temperature Materials, AIME, Apr. 26-27, 1961.
13. Graphite Creep Strength: Research and Development on Advanced Graphite Materials. TN 61-18, WADD, Apr. 1961.
14. GREEN, WALTER V.: Short-Time Creep-Rupture Behavior of Tungsten at 2250° to 2800° C. Trans. AIME, vol. 215, no. 6, Dec. 1959, pp. 1057-1060.
15. Materials Symposium, Sept. 13-15, 1961: ASD Tech. Rep. 61-322, p. 71.
16. BARTH, V. D.: Physical and Mechanical Properties of Tungsten and Tungsten-Base Alloys. DMIC Rep. 127, Defense Metals Info. Center, Battelle Memorial Inst., Mar. 15, 1960.
17. NEEL, D. S., and PEARS, C. D.: Southern Research Inst., Nov. 1960.
18. Investigation of Graphite Bodies. TR 59-706, WADC, Apr. 1960, p. 58.
19. MACMILLAN, DONALD P.: High Temperature Materials for Rocket Reactors. Nucleonics, vol. 19, no. 4, Apr. 1961.
20. MAY, CHARLES E., and HOEKSTRA, PAUL D.: Stability of Refractory Compounds in Hydrogen Between 4500° and 5000° F, and Their Compatibility with Tungsten. NASA TN D-844, 1961.
21. Anon.: Carbonization of Plastics and Refractory Materials Research, pt. 1. TR 60-646, WADD, Feb. 1961, p. 50.
22. DUSHMAN, S.: Vacuum Technique. John Wiley & Sons, Inc., 1949.
23. Anon.: Carbonization of Plastics and Refractory Materials Research. Fifth Quarterly Prog. Rep., General Electric Co., Mar. 30, 1960.
24. Anon.: Progress in the Development of Uranium Carbide-Type Fuel. BMI-1554, Battelle Memorial Inst., Nov. 17, 1961.
25. Anon.: Heat Transfer Reactor Experiment No. 1. APEX-904, Flight Prop. Lab. Dept., General Electric Co.
26. LISIN, A. V., and MONTGOMERY, H.: Application of the ML-1 Reactor to a Nuclear Rocket Experiment. Rep. AN-232, Aerojet General Nucleonics, Aug. 1960.
27. Anon.: Preliminary Hazards Summary Report for the ML-1 Nuclear Powerplant. Rep. IDO-28537, Aerojet General Nucleonics, Apr. 22, 1959.
28. ROM, FRANK E.: Advanced Reactor Concepts for Nuclear Propulsion Astronautics, vol. 4, no. 10, Oct. 1959, pp. 20-22; 46-50.
29. KERREBROCK, JACK L., and MEGHREBLIAN, ROBERT V.: Vortex Containment for the Gaseous-Fission Rocket. Tech. Release 34-205, Jet Prop. Lab., C.I.T., Sept. 1961.
30. RAGSDALE, ROBERT G.: NASA Research on the Hydrodynamics of the Gaseous Vortex Reactor. NASA TN D-288, 1960.
31. WEINSTEIN, HERBERT, and RAGSDALE, ROBERT G.: A Coaxial Flow Reactor—A Gaseous Nuclear-Rocket Concept. Preprint 1518-60, Am. Rocket Soc., Inc., 1960.
32. SPENCER, D. F.: Thermal and Criticality Analysis of the Plasma Core Reactor. Tech. Rep. 32-189, Jet Prop. Lab., C.I.T., Jan. 1962.
33. Anon.: A Summary of Douglas Research in Advanced Propulsion Systems. Rep. SM-41961, Douglas Aircraft Corp., June 1962.
34. ROSENZWEIG, MARTIN L., LEWELLEN, W. S., and KERREBROCK, JACK L.: The Feasibility of Turbulent Vortex Containment in the Gaseous Fission Rocket. Preprint 1516A-60, Am. Rocket Soc., Inc., 1960.
35. RAGSDALE, ROBERT G.: Applicability of Mixing Length Theory to a Turbulent Vortex System. NASA TN D-1051, 1961.
36. KENDALL, JAMES M., JR.: Experimental Study of a Compressible, Viscous Vortex. Tech. Rep. 32-290, Jet Prop. Lab., C.I.T., June 1962.
37. EINSTEIN, THOMAS H.: Radiant Heat Transfer to Absorbing Gases Enclosed in a Circular Pipe with Conduction, Gas Flow, and Internal Heat Generation. (NASA TR to be publ.)
38. LANZO, CHESTER D., and RAGSDALE, ROBERT G.: Experimental Determination of Spectral and Total Transmissivities of Clouds of Small Particles. NASA TN D-1405, 1962.
39. SAFONOV, G.: Externally Moderated Reactors. Vol. 12—Reactor Physics. Paper 625, Proc. Second United Nations Int. Conf. on Peaceful Uses of Atomic Energy (Geneva), 1958, pp. 705-718.
40. BELL, GEORGE I.: Calculations of the Critical Mass of  $UF_6$  as a Gaseous Core with Reflectors of  $D_2O$ , Be, and C. LA-1874, Los Alamos Sci. Lab., Feb. 1955.

**ADVANCED CONCEPTS FOR NUCLEAR ROCKET PROPULSION**

41. PAXTON, H. C., and ORNDORFF, J. D.: Group N-2. Prog. Rep. for Oct. 21-Nov. 20, 1960, Los Alamos Sci. Lab., 1960.
42. RAGSDALE, ROBERT G., and HYLAND, ROBERT E.: Some Nuclear Calculations of  $U^{235}$ -D<sub>2</sub>O Gaseous-Core Cavity Reactors. NASA TN D-475, 1961.
43. HYLAND, ROBERT E., RAGSDALE, ROBERT G., and GUNN, EUGENE J.: Two-Dimensional Criticality Calculation of Gaseous-Core Cylindrical Cavity Reactors. NASA TN D-1575, 1962.

# 43. Nuclear Physics of Solid-Core Gas-Cooled Rocket Propulsion Reactors

By Donald Bogart and Edward Lantz

DONALD BOGART, *Chief of the Reactor Physics Branch, NASA Lewis Research Center, has specialized in the fields of thermodynamics, nuclear engineering and reactor physics. Mr. Bogart earned a B.S. degree in Mechanical Engineering from Cooper Union in 1943 and an M.S. degree in Mechanical Engineering from Case Institute of Technology in 1948. He is a member of the American Nuclear Society.*

EDWARD LANTZ, *Aerospace Scientist at the NASA Lewis Research Center, is presently working in the field of nuclear propulsion and power research. He attended Case Institute of Technology, where he received his B.S. degree in Physics in 1949. In 1960 he received his M.S. degree in Physics from Union College. He is a member of the American Nuclear Society, American Rocket Society and Sigma Xi.*

## SUMMARY

The design of a nuclear-rocket reactor that will produce maximum propellant-gas temperature for limited core-material temperature requires successful integration of the mechanical, thermal, and nuclear aspects of a complex problem. The strong interaction of the three-dimensional heat generation with heat transfer to the propellant requires "tailoring" of reactor composition and geometry. The techniques used are zoning of uranium concentration, metering of gas flow through fuel-element cooling passages, core-moderator zoning, and judicious use of reflectors.

Control systems should encompass sufficient excess reactivity to start, shutdown, and restart a nuclear-rocket engine without introducing severe power distortions.

Herterogeneous moderated reactors that use tungsten, which exhibits neutron resonance absorption, require that fuel-element-moderator lattices be optimized to produce maximum neutron multiplication.

## INTRODUCTION

A considerable effort has been mobilized during the past few years for the development of a nuclear-rocket engine. The engine contains a solid-core reactor that directly heats a gaseous

hydrogen propellant. During its operating life of a few hours, the reactor should be capable of power densities of about 2 megawatts per liter and produce hydrogen exit temperatures near 4500° R. At these operating conditions, construction and support of reactor fuel elements pose extremely difficult mechanical-design problems. The strength of materials becomes marginal at anticipated core-operating temperatures, but some strength is required to withstand the forces of the hydrogen flow without excessive creep.

If acceptable hydrogen temperatures are to be obtained for limited core-material temperatures, the mechanical, thermal, and nuclear design aspects of the reactor have to be thoroughly integrated.

Some aspects of reactor physics are presented that are exploited by the reactor designer to permit the use of available high-temperature materials to advantage. Techniques are discussed for adjusting heat-generation distributions in the core to obtain maximum possible

gas temperature. Required reactor excess reactivity and general methods for its control are briefly discussed. Finally, the problem of fuel-element-moderator-lattice optimization in heterogeneous tungsten reactors is presented. The objective of finding the best fuel-element spacings that produce maximum neutron multiplication is illustrated by calculations of tungsten-water lattices.

### REACTOR CRITICALITY

The spectra of reactor criticality can be observed conveniently by the variation of critical mass of a reactor as a function of its size as various diluents are added to fissionable material. Such a variation is presented in figure 43-1 in which the critical mass in kilograms of uranium 235 is plotted against the radii of bare homogeneous spheres of fully enriched uranium containing several diluting materials. The critical condition implies a balance between neutrons produced by fission and neutrons lost by absorption and leakage.

The anchor point is the undiluted ball of uranium 235, which is about 8.5 centimeters in radius, that is critical with about 48 kilograms. This is a true fast reactor, since the neutron spectrum in the core is essentially that of the prompt fission neutron spectrum. Of course, in the rocket application, uranium metal, which melts at  $2550^{\circ}\text{R}$ , cannot be used; however, compounds such as uranium carbide or uranium oxide, which melt at temperatures of  $4950^{\circ}\text{R}$

and  $5550^{\circ}\text{R}$ , respectively, are desirable. Although these uranium compounds have poor structural properties, they may be incorporated with graphite or tungsten, which still have some structural strength as  $5000^{\circ}\text{R}$  is approached.

Refer to figure 43-1 and note that initial dilution of uranium with graphite causes the critical mass to increase at first. This is the result of the neutron spectrum shifting so as to increase nonproductive absorption in uranium. As more graphite is added, a point is reached where decreasing neutron leakage causes the critical mass to decrease, resulting in the peak reversal. Additional graphite now begins to act as a moderator, and the neutron spectrum approaches thermal equilibrium with the temperature of the carbon atoms; at thermal energies the neutrons see a large fission cross section and critical mass decreases to the low reversal point. Further addition of moderator causes the size and critical mass to increase, since the uranium atoms are already being used with maximum effectiveness and the additional moderator acts as a neutron poison.

The same characteristics are shown by the addition of water as the moderator, except that the unusually excellent slowing-down properties of hydrogen in water cause rapid neutron thermalization. The low reversal point of the thermal core shown in figure 43-1 is obtained at relatively small size and with small critical mass.

The criticality curve for natural tungsten as the diluent starts out similar to that for graphite, but since tungsten is ineffective as a moderator, the critical mass can be expected to increase as shown. The data of figure 43-1 were taken from a correlation of experimental and analytical criticality data presented in reference 1.

Of course, any real core must contain propellant-gas heating passages and be cylindrical instead of spherical. In addition, in a water-moderated core the high-temperature metallic fuel elements have to be thermally insulated from the water. If the metal is tungsten, it is desirable to use a mixture of separated tungsten isotopes that have low resonance capture for neutrons during the slowing-down process. This subject is discussed in detail later in connection with heterogeneous moderated cores.

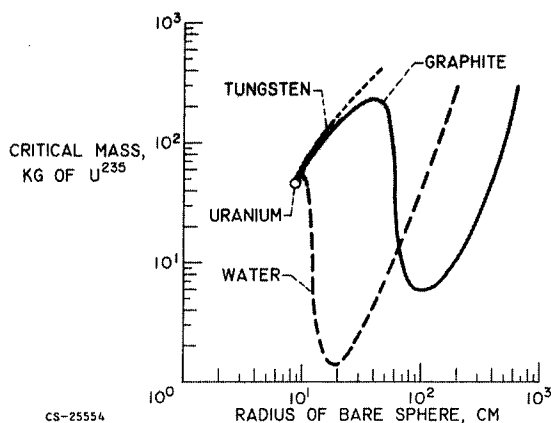


FIGURE 43.1.—Critical masses of homogeneous bare spheres of uranium 235 with diluents.

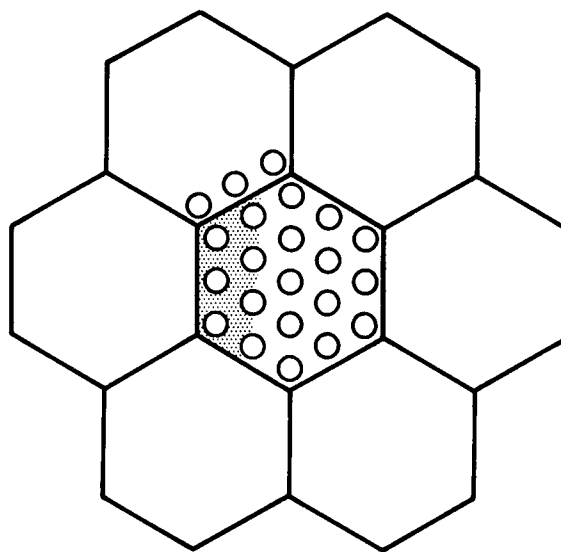
## SOLID-CORE GAS-COOLED ROCKET PROPULSION REACTORS

Fast-spectrum reactors, characterized by the tungsten-diluent curve in figure 43-1, are sensitive to the introduction of gas passages; in particular, hydrogen gas introduces peculiar reactivity effects. Core-uranium loadings rise rapidly requiring fuel elements that contain much higher metallurgical uranium concentrations than those required for moderated systems; however, fast-spectrum reactors can use natural tungsten and other thermal neutron-absorptive materials that are less absorptive at high neutron energies.

### HEAT-GENERATION DISTRIBUTIONS

Reference neutron-flux distributions  $\varphi$  in a schematic homogeneous cylindrical core are shown in figure 43-2. The core has axial cooling channels and may have thick or thin neutron reflectors on the sides and ends of the core. Slowing down and diffusion of neutrons to the boundaries result in a bare core taking on a radial flux of  $J_0$  Bessel variation as shown. For a core with a side reflector, reflected neutrons contribute an added component near the radial core-reflector interface region. The axial flux takes on a cosine distribution in a bare core; an added component due to a thin front reflector is shown.

The heat released in every unit volume of the core is the product of the local neutron flux, uranium concentration, and fission cross section. This product integrated over all neutron energies provides a measure of the local heat-release rate. Since the neutron fluxes and flux



CS-25556

FIGURE 43-3.—Typical fuel-element array for homogeneous core.

spectra vary from unit volume to unit volume in the core, the heat-release rate varies in a unique three-dimensional way. What the reactor designer desires is for every unit volume of the core to be releasing as much heat as the materials will stand. These objectives require cylindrical reactors to have a radial heat-release rate that is uniform or flat, and an axial heat-release rate that heats up the propellant gas to the desired exit temperatures without exceeding limiting material temperatures and thermal stresses within the core.

The basic building blocks of the reactor are the fuel elements, which for a typical homogeneous honeycomb core look like the array shown in figure 43-3. All the fuel elements have some fixed uranium composition, and the generated heat is removed by thermal conduction to the many small cooling channels that axially pierce the element. In order to approach a flat radial heat generation with such elements, the uranium concentration may be altered from one element to another. Variation of the heat generation axially would require the elements to be segmented and each segment to have a different uranium composition. Gradients in heat generation across a given element can be accommodated by regulating the propellant mass flow through the individual cooling channels.

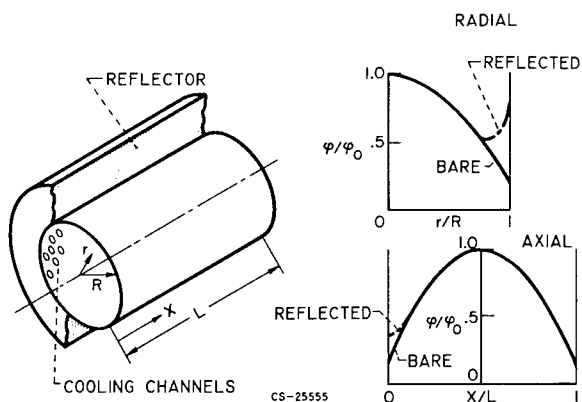


FIGURE 43-2.—Reference neutron fluxes in homogeneous cylindrical core.



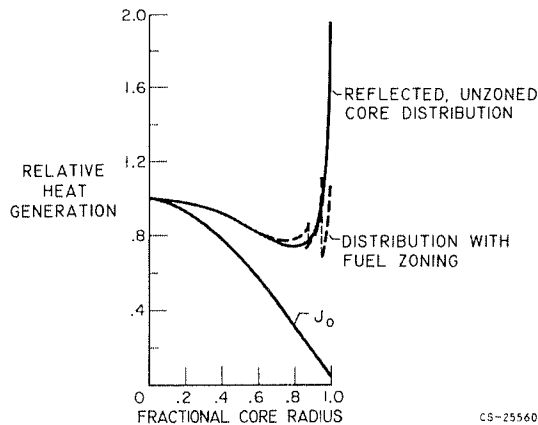


FIGURE 43-4.—Radial heat-generation distributions.

These methods of literally “tailoring” the heat-generation distributions in a cylindrical reactor are illustrated.

#### Radial Heat-Generation Distribution

The radial heat-generation distribution at the midplane of a homogeneous cylindrical graphite reactor using a beryllium side reflector is shown in figure 43-4. The beryllium reflector admirably produces a large thermal neutron flux that spills over from the reflector into the core. These thermal neutrons, which encounter a core loaded with uranium, produce sharp peaks in heat release, as shown by the upper solid curve in figure 43-4. The peak produced at the core-reflector interface is about twice that of the heat-release rate at the core center. This so-called “thermal spike” is intolerable and may be reduced by nonuniform radial distribution of fuel that would have to be continuously variable to produce a flat radial distribution.

A practical compromise is achieved by using several uranium concentrations in radial zones of the core. The results for three such zones are shown by the dashed curve of figure 43-4. Large heat-release variations are still present in short radial distances, but these can be accommodated by nonuniform propellant mass flow in the cooling holes that hopefully keep the maximum graphite temperatures within acceptable limits. This calls for solving a rather tricky problem of orificing gas flows through parallel

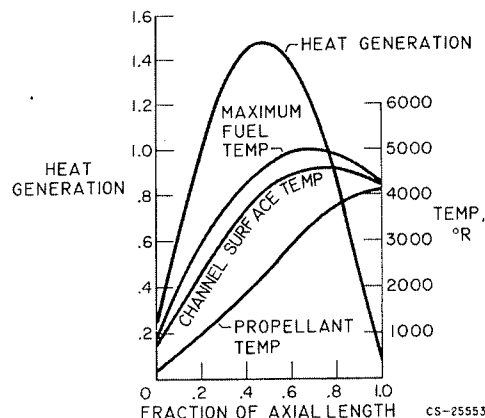
passages with variable heat inputs and with a given overall pressure drop.

Of course, if there were no side reflector, the radial heat-generation distribution would be given a  $J_0$  Bessel function shown as the bottom curve in figure 43-4. Its drooping character could never be compensated for by nonuniform uranium distribution. Without a side reflector, this resulting distribution severely penalizes the total power output of the reactor.

#### Axial Heat-Generation Distribution

The increase in propellant gas temperature as it passes through the core is proportional to the integral of the axial heat release. The fuel surface temperature at any axial position is higher than the gas temperature by a temperature difference that is directly proportional to the heat release at that point. The shape of the axial heat-generation curve is, therefore, an important factor in determining gas exit temperature for a maximum fuel temperature. It is here that reactor physics and heat transfer are very intimately related.

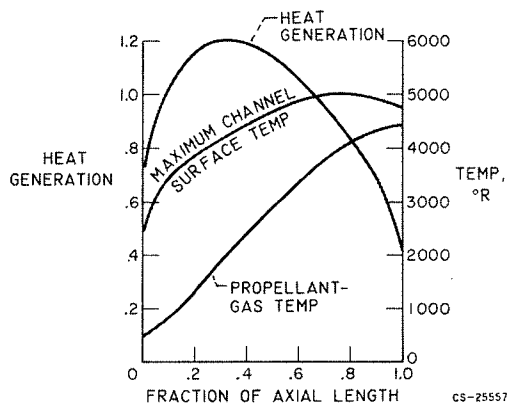
A typical axial heat-generation curve for a homogeneous core is shown in figure 43-5(a). This distribution is for a reactor with uniform axial uranium concentration and a thin front reflector. The axial heat generation is very closely a cosine function. The thin front reflector alters the cosine shape slightly. The curve for the propellant-gas temperature rises monotonically through the core. The cooling-



(a) Uniform core with top reflector.

FIGURE 43-5.—Axial distributions.

## SOLID-CORE GAS-COOLED ROCKET PROPULSION REACTORS



(b) Fuel-zoned core with top reflector.

FIGURE 43-5.—Concluded. Axial distributions.

channel-surface and maximum-fuel-temperature curves reach a peak well before the end of the cooling channel is reached. In this example, a gas exit temperature of about 4100° R is achieved with a maximum fuel-element temperature of 5000° R.

The axial situation shown in figure 43-5(a) is not the best but is the distribution that exists for reactors in which axial fuel zoning is not employed. An example of a better axial distribution is shown in figure 43-5(b), which employs segmented axial fuel elements. This particular core used a metallic fuel element made in small axial segments so that fuel may be axially zoned. In addition, a thicker front reflector has been employed. In this case, the axial heat-generation distribution is far from a cosine function; it reaches a peak in the front half of the core. Since the fuel element is metallic and has good thermal conductivity, the maximum-fuel and cooling-channel-surface temperatures are practically the same. In this case, a gas exit temperature of 4500° R is calculated for a maximum fuel temperature of 5000° R.

In summation, it has been shown that core designs to produce maximum gas temperature for a limited material temperature require zoning of uranium concentration, delicate metering of gas flow through fuel-element cooling passages, and judicious use of reflectors.

Proved neutron-diffusion and heat-transfer theories have provided good first approximations to core design problems. In conjunction with separate criticality and flow experiments,

further design refinements may be built into the reactor; however, what cannot be answered by these approaches are the effects of interaction of the mechanical, thermal, and nuclear aspects as design conditions are approached. The question remains whether or not the core structure will hold up at the high temperatures under the combined thermal stresses resulting from nonuniform internal heat generation and other stresses resulting from the forces of the hydrogen flow.

## REACTOR-CONTROL CONSIDERATIONS

The control system requirements for nuclear-rocket reactors are unique because of the short operating time (of the order of an hour), which results in small fuel burnup and fission product buildup. Therefore, provision for fuel burnup, which is the largest part of required excess reactivity in conventional power reactors, is unnecessary in the rocket reactor.

Reactivity is required to place the rocket reactor on fairly short startup periods and to compensate for the large rise in temperature which the liquid hydrogen and reactor must experience. In addition, positive shutdown requires that the control system ensure subcriticality by a safe margin. Finally, since it is desirable for the reactor to be restarted several times to execute its mission, some loss of fuel from the core must be anticipated and allowed for.

Most control devices introduce absorbers to compete with the fuel for neutrons. The best absorbers are materials with high capture cross section for thermalized neutrons such as boron, cadmium, or hafnium. As shown in figure 43-6, these absorptive materials can be placed in conventional push-pull control rods in the core of a thermal reactor or placed on one side of rotating control drums in the side reflector of thermal or intermediate spectrum reactors. The drums are shown in the figure at the half-way position.

In homogeneous cores, it is convenient to use rotating cylindrical control drums in the side reflector; however, both control rods and rotating drums introduce distortion in the local power generation. Consider the radial distri-

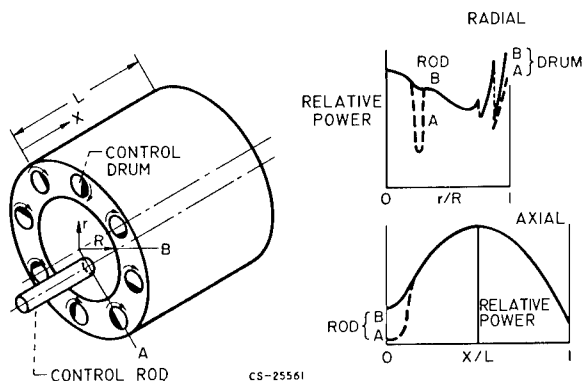


FIGURE 43-6.—Power distortion due to control devices.

butions along direction A, which passes through the rod and drum position, and direction B, which avoids the local flux perturbation. The rotating drums perturb the power distributions near the core-reflector interface by partial insertion of poison as shown in the radial distribution of figure 43-6. This introduces a scalloped circumferential power distribution that must be considered in the thermal design. In the same manner, the push-pull control rods depress the fluxes around the partly inserted rod in both the radial and axial directions, as shown in figure 43-6.

From an engineering viewpoint, the reflector control system is convenient in that the rotating drums are located in a cooled reflector; however, the reflector is a region of relatively low statistical importance and many large control drums are required. In a thermal core, the same control could be accomplished by smaller rods within the core but with attendant difficult cooling problems. For larger homogeneous cores, the side reflector becomes less important, and methods other than reflector control are necessary.

Control for heterogeneous reactors like the water-moderated core opens many new avenues of approach because of the accessibility of the moderator. For example, the use of liquid-poison passages or gas passages in the low-temperature water moderator of the core looks interesting. Such control techniques should be independent of the size of the core. Of course, several methods of control are usually possible for any reactor depending on the specific design.

## HETEROGENEOUS MODERATED REACTORS

As mentioned earlier, in order to use the efficient water moderator, the high-temperature fuel elements have to be insulated and separated from the water. This results in a heterogeneous core arrangement that introduces peculiar reactor physics problems, which are discussed in connection with the tungsten-water-moderated core. The use of the most refractory metal, tungsten, in a moderated reactor introduces the problem of neutrons escaping resonance capture during slowing down.

The total cross section for natural tungsten in the slowing down energy region is shown in figure 43-7 (ref. 2). The four major isotopes, tungsten 182, 183, 184, and 186, exhibit large absorptive resonant cross sections in the region below a kilovolt. Tungsten 186 has an especially large resonance at about 20 electron volts, which is shown in the figure with a change of scale. The most abundant isotope, tungsten 184, is relatively free of absorptive resonances so that tungsten enriched in tungsten 184 is desirable. Fission neutrons born in the Mev energy region make collisions with water and must bypass this resonance region by spending most of the slowing down time in the water and not in the tungsten. The fraction of fission neutrons starting out that slow down past the resonance region is known as the resonance escape probability.

Shown in figure 43-8 is a representative heterogeneous core region consisting of an array of lattice cells of the high-temperature tungsten fuel elements in insulated water-

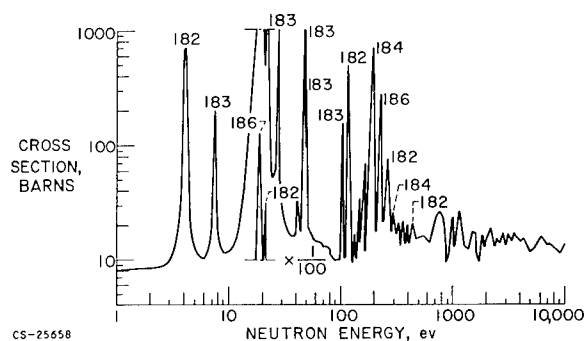
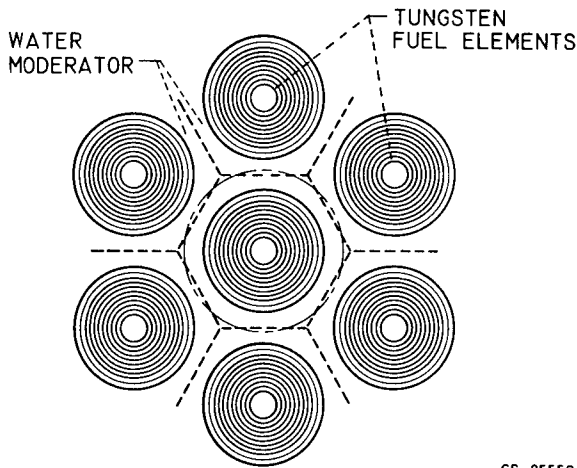


FIGURE 43-7.—Tungsten total cross section in slowing-down energy region.

# SOLID-CORE GAS-COOLED ROCKET PROPULSION REACTORS

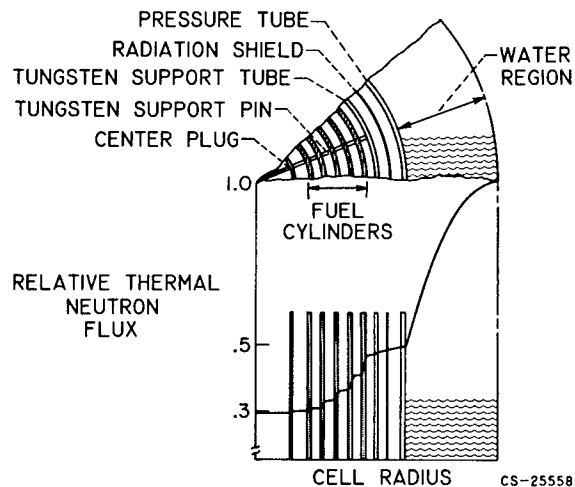


CS-25559

FIGURE 43-8.—Typical fuel-element array for heterogeneous core.

moderator regions. Tungsten enriched in the tungsten 184 isotope may be used to avoid excessive resonance capture while neutrons slow down in the water regions. The thermalized neutrons that have bypassed the resonance capture energies then diffuse into the individual fueled region from the water to produce the bulk of the fissions. For ease in calculation, the equivalent cylindrical cell shown in figure 43-8 is studied, and the flux variation in the lattice cell is determined.

The variation of the thermal-neutron flux in this individual cell is plotted against cell radius in figure 43-9. The separate fuel and water regions may be seen. This illustrative fuel element contains five concentric fueled tungsten



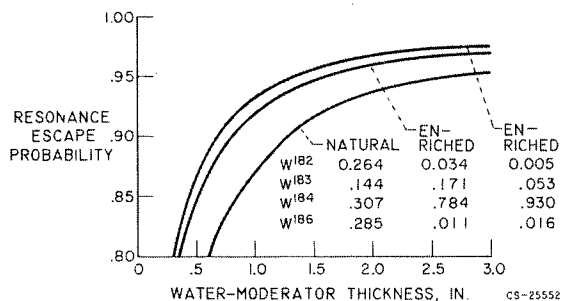
CS-25558

FIGURE 43-9.—Lattice cell of heterogeneous core.

cylinders supported by an unfueled tungsten tube. Hydrogen flow is guided by this support tube and tungsten center plug. The insulating spaces between the tungsten support tube and the moderator pressure tube have a thermal-radiation shield and stagnant hydrogen to keep the water container cool. The thermal neutron flux is seen to fall rapidly in the water region and through the successive fueled cylinders.

In order to achieve the required exit gas temperature, a heat-generation tailoring job must be done. Because the metallic fuel elements are individual, the fuel loadings in the various fuel cylinders may be varied to permit each one to operate at its maximum temperature. The thermal design may be aided further by varying the heat-transfer spacings between fuel cylinders. Once again there appears the complex interplay between the nuclear, thermal, and mechanical aspects of the problem. Once an acceptable fuel-element configuration is determined, it is convenient for all the fuel elements of the core to be identical. Variations in gross radial heat generation from one fuel element to another can be tailored by small changes in moderator thickness called moderator zoning; however, it must be remembered that water captures thermal neutrons and too large a water thickness in the lattice will waste neutrons. Alternately, if the water thickness is too small, not enough neutrons will bypass the tungsten while slowing down and escape resonance capture.

The effects of resonance capture in tungsten enriched in varying degrees in the tungsten 184 isotope is shown in figure 43-10. Here the



CS-25552

FIGURE 43-10.—Resonance capture in enriched tungsten for tungsten slabs 0.10 inch thick in water.

## NUCLEAR PROPULSION

resonance escape probability is plotted against water thickness. Recall that the resonance escape probability is the fraction of fission neutrons starting to slow down that escape tungsten resonance absorption and become thermal neutrons. These results are for lattice cells containing tungsten slabs 0.100 inch thick based on analytical and experimental data presented in reference 3. The enrichment varies from natural tungsten that contains 30.7 percent tungsten 184 to separated isotopic mixtures containing 78.4 and 93.0 percent of tungsten 184.

It may be seen that resonance escape increases for larger water thicknesses. For any given water thickness, separation of tungsten 184 significantly increases the resonance escape probability. Enrichment in tungsten 184 also reduces the thermal-neutron absorption cross section and results in less competition with the uranium to improve the neutron multiplication factor of the lattice cell. The multiplication factor  $K$  is simply the number of neutrons produced by fission per neutron absorbed in the cell. Since resonance escape is increasing for larger water spacings because of better bypassing of resonances even though more thermal neutrons are wasted by absorption in water, an optimum neutron multiplication factor  $K$  exists for the fueled lattice cell; that is, there is some water thickness for a given fuel cell for which  $K$  is a maximum. The resultant multiplication factor for tungsten-fuel slab lattices containing 0.10 inch of natural or separated tungsten and a concentration of uranium 235 of about 10 percent by weight is shown in figure 43-11.

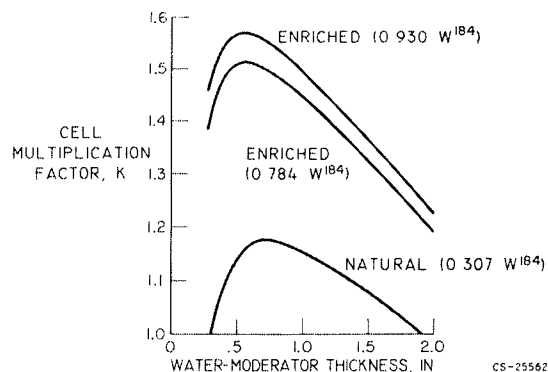


FIGURE 43-11.—Multiplication factor for tungsten fuel cell for tungsten slabs 0.10 inch thick in water.

ure 43-11. It may be seen that  $K$  reaches a peak at 1.18 for natural tungsten, but for tungsten enriched in tungsten 184,  $K$  can be greater than 1.50. These peak values occur for water thickness between 0.5 and 1.0 inch.

Since the cell multiplication factor is a measure of the reactivity for an infinite number of these cells, the excess above unity must be used for neutrons to be lost by leakage from a finite critical reactor size. It follows that a natural tungsten reactor would have to be very much larger than an enriched tungsten reactor. Tungsten 184 enrichment further provides excess reactivity for use in fuel and moderator zoning that is so necessary to achieve desirable heat-generation distributions in any reactor.

## CONCLUDING REMARKS

The strong interaction between the three-dimensional heat generation and heat transfer in nuclear-rocket reactors has been illustrated. It has been seen that both homogeneous and heterogeneous reactors must be tailored to approach maximum gas exit temperatures for a given maximum core material temperature. Techniques such as fine-scale fuel zoning and nonuniformly sized cooling passages in fuel elements are applied; on the gross scale, the use of reflectors and moderator zoning in the core are exploited.

A nuclear rocket control system must have a sufficient amount of controlled excess reactivity to start and maintain criticality throughout the required operating time and to restart the engine after it has been shut down. The thermal design of the core must consider the power distortions introduced by partly inserted control devices.

These design techniques may be applied analytically, since neutron-diffusion and heat-transfer processes are reasonably well understood, and digital computers can handle the elaborate problem. Separate criticality and flow experiments may further improve the design. Even with the known properties of materials at temperatures of interest, however, the basic question remains of whether or not a nuclear-rocket reactor design will perform satisfactorily as rated conditions are ap-

#### SOLID-CORE GAS-COOLED ROCKET PROPULSION REACTORS

proached. The question remains because the complex interaction of the mechanical, thermal, and nuclear aspects of the design cannot be fully analyzed.

At the present time, the development of a

nuclear-rocket reactor must telescope a large number of uncertainties into every hot-reactor experiment. A great deal more must be learned before nuclear-rocket reactors may be adequately and reliably designed.

#### REFERENCES

1. PAXTON, H. C.: Correlations of Experimental and Theoretical Critical Data. Rep. LAMS-2537, Los Alamos Sci. Lab., May 15, 1961.
2. HUGHES, D. J., and SCHWARTZ, R. B.: Neutron Cross Sections. Rep. BNL-325, Brookhaven Nat. Lab., July 1, 1958.
3. SCHNEIDER, HAROLD, LEVITT, LEO, and SROUB, KEVIN J.: A Monte Carlo Study of Resonance Escape Probability in Heterogeneous Slab Lattices Containing Resonant Absorbers and Scatterers. NASA TN D-1184, 1962.

## 44. Fluid-Flow and Heat-Transfer Problems in Nuclear Rockets

By Herman H. Ellerbrock, John N. B. Livingood, and David M. Straight

HERMAN H. ELLERBROCK, *Chief of the Nuclear Propulsion Branch of the NASA Lewis Research Center, has specialized in research on heat transfer and propulsion. He joined the NACA staff, NASA's predecessor, in 1930. Mr. Ellerbrock received his B.S. degree in Mechanical Engineering from Johns Hopkins and his M.S. degree from Case Institute of Technology. He is an Associate Member of the Institute of the Aerospace Sciences, a Senior Member of the American Rocket Society, and a member of the New York Academy of Sciences and Sigma Xi.*

DR. JOHN N. B. LIVINGOOD, *currently working on nuclear rocket heat-transfer and flow problems, has been a member of the NASA Lewis Research Center staff for 16 years. He is a member of the American Mathematical Society and Phi Beta Kappa and is listed in American Men of Science and Who's Who in World Aviation. He received his A.B. degree from Gettysburg College and his A.M. and Ph. D. degrees from the University of Pennsylvania.*

DAVID M. STRAIGHT, *Aerospace Scientist at the NASA Lewis Research Center, is presently working in nuclear propulsion and power system research. In his 19-year career at Lewis, he has worked in research on fuel-feed systems, turbojet and rocket ignition and starting, rocket combustion, and flow dynamics of cryogenic systems. Mr. Straight holds a B.S. degree in Mechanical Engineering from Northeastern University and is an Associate Fellow of the Institute of the Aerospace Sciences.*

### INTRODUCTION

Deep-space probes and interplanetary travel require the successful development of the nuclear rocket. The use of nuclear rockets will permit such missions with lower takeoff weight and in shorter time than would be required if only chemical rockets were used. For these reasons, numerous scientists and engineers are actively engaged in a search for solutions to the many problems connected with the successful development of the nuclear rocket. This discussion is restricted to some of the typical heat-transfer and flow problems encountered in the development of the nozzle and the nuclear reactor and of progress being made in attempts to solve these problems.

The solutions to numerous reactor-core problems must be known before a successful nuclear rocket can be developed. For cores consisting of fuel modules with solid fuel elements, an accurate knowledge of the module temperature gradients is important. These values depend on the material, the type of passage configuration, passage size, etc. Some typical fuel-module temperatures for a given configuration, with allowance for different void fractions (or passage sizes), are presented herein. The effects of modifying the fuel distribution are also included. With a knowledge of fuel-module temperature gradients, core stresses can be calculated in order to determine whether the core is mechanically satisfactory. The state of the

art of calculating these stresses is briefly discussed.

Another important core problem is encountered during reactor cool down. The amount of cooling required to overcome the afterheat may be so low that laminar flow exists and conditions become favorable for the well-known "flow excursion" or "static instability" to occur. A discussion of this problem is included.

For safe operation of the reactor, it is desirable to have the hydrogen propellant enter the reactor core in the gaseous phase. Since the hydrogen is stored in the liquid phase in the storage tank, the hydrogen must pass through the two-phase state somewhere in the system during reactor startup. For chemical rockets, in which startup times are of the order of 1 to 2 seconds, no problem is encountered; for nuclear rockets, in which startup times may be of the order of 20 to 30 seconds, serious problems may be caused by the two-phase flow. In addition, any flow or pressure instabilities or maldistributions of the hydrogen can cause local hot spots in the core and create problems for the control system that regulates the coolant flow, the pressure, and the reactor power of the engine system.

Since current two-phase hydrogen heat-transfer and flow knowledge is inadequate for nozzle and reactor design, an experimental program is in progress at the Lewis Research Center to augment the existing information. A résumé of the present state of knowledge, a description of experimental apparatus being used to augment fluid-flow and heat-transfer knowledge for the reactor, and presentation of some results of tests will be given. Single heated tubes (steady state), single unheated tubes (transient), nozzle sectors, and simulated reflector pieces with parallel unlike passages are all included in the Lewis program. Moreover, the test sections are of sufficient length that the gaseous phase of the hydrogen is achieved within the tube and experimental data for gaseous hydrogen are also included.

Since a typical reflector contains numerous different size coolant passages, the problems of flow maldistribution and detrimental pressure oscillations must also be investigated and solved. Oscillatory-flow data for hydrogen

flow through the unheated and the heated tubes and frames from motion pictures of flow distribution for the multiple-hole reflector pieces are presented; a discussion of current knowledge on these subjects is included. Information obtained from these investigations should also apply to the nozzle.

Current plans indicate the nuclear reactor will probably be started in or near an Earth orbit. As a consequence, the effects of low or zero gravity on flow and heat transfer must be known. A brief discussion of the problem is presented.

Current nozzle design procedures involve the specification of a wall temperature. The gas-side heat-transfer coefficient is then estimated, and the heat flux to the wall calculated. A coolant-side heat-transfer coefficient is then obtained by iteration, such that the desired wall temperature is attained. This procedure is carried out at local positions along the nozzle. Unfortunately, methods of achieving reliable predictions of the gas-side heat flux are not yet available; a status report on methods now used will be given.

## REACTOR CORE

The final design of a reactor involves an iteration among the results obtained from nuclear, temperature, and stress calculations. The nuclear calculations result in several geometries that could be used and that will give the required reactivity. After the temperatures and stresses are calculated for the reactor parts resulting from these geometries, the dimensions of the final reactor parts are chosen.

The reactor core poses the largest problem of heat removal and existing high temperatures during operation. This problem may be illustrated by a comparison of heat-release rates of modern-day steam boilers with those of proposed reactors for nuclear rockets. A boiler has a typical heat-release rate of 40,000 Btu per hour per cubic foot, while a nuclear-rocket reactor could have a typical heat-release rate of 400,000,000 Btu per hour per cubic foot, a 10,000-fold increase.

In addition to these problems during full operation, another type of problem exists for the period of reactor cool down. The require-



ment of a nuclear rocket for a given space mission would most likely be a startup, full operation, shutdown, coast, and then a restart. During the coast period after shutdown, removal of the reactor afterheat would be necessary. During this cool-down phase, the flow rate is gradually decreased, and in the process of diminishing this flow rate there arises the problem of flow excursion, which will be explained in greater detail in one of the following sections.

### Thermal-Stress Considerations

The order of magnitude of thermal stress is, in general, given by

$$\sigma_{th} \sim \frac{E\alpha\Delta T}{1-\nu} \quad (1)$$

where  $\Delta T$  is considered to be the maximum temperature difference existing between any two points in the material. (All symbols are defined in the appendix.) The entire integrity of the core is coupled to the maximum temperature existing within the material and to the temperature gradient across a given member. Two determining factors involved with these parameters are power density and distance between points of maximum temperature difference. The dependence on these factors is shown, for simplicity, in the steady-state temperature equation for uniform power generation in a slab:

$$T_{\max} - T_w = \frac{Q_v \delta^2}{2k} \quad (2)$$

Both  $T_{\max}$  and  $T_{\max} - T_w$  must be controlled to within allowable limits. Obviously,  $T_{\max}$  must be less than the melting point of the material and  $T_{\max} - T_w$  must be compatible with allowable thermal stresses. These thermal stresses are a function of heat generation, which determines the temperature gradient, and of material properties.

Equation (1) as shown merely indicates the basic parameters involved with thermal stresses; it is not a complete representation. The geometry of a reactor is usually reduced to a simplified representative part, for which thermal-stress equations can be derived. The adequacies of these equations as applied to the entire structure can be verified only by actual operation.

The types of stress usually calculated are elastic stresses, although in the high-temperature range of operation plastic flow undoubtedly will occur. Designing for this plastic flow is acceptable, but existing loads on members must be accurately known. The other items that must be known are stress-rupture data and the required material properties at high temperatures. At present, these high-temperature data are relatively scarce.

### Effect of Geometry on Temperature

For nuclear rockets, the maintenance of as small a size as possible is desirable; that is, for a given reactor power, the value of power density will usually be the maximum allowable from a size determination. Equation (2) shows that for a fixed value of  $Q$ , the temperature difference could still be reduced by a factor of 4 by reducing the distance  $\delta$  by a factor of 2. The maximum temperature is also reduced by the amount of the decrease of the temperature difference.

For a given reactor size of high-power rating, maximum temperatures and thermal stresses can thus be controlled by a choice of reactor geometries consisting of a fine structure; that is, all distances  $\delta$  are kept to a minimum. A reactor consisting of concentric rings of both fuel elements and moderator, for example, could be made to operate in a safe region of thermal stress by splitting these rings into as small a thickness as could be fabricated.

Some typical reactor geometry configurations are shown in figure 44-1. Figures 44-1(a) and (b) show typical fine-structure geometries with possible methods of arranging the coolant passages. By assuming symmetry and uniform heating, the temperature distribution in each shaded segment can be calculated as explained in reference 1. Figures 44-1(c) and (d) show other arrangements of fuel and moderator where again symmetry may be assumed and relaxation methods may be used to calculate internal temperatures. The concentric ring type of arrangement that was mentioned previously is shown in figure 44-1(e).

Of the various geometries shown in figure 44-1, the first two are of the most importance

# NUCLEAR PROPULSION

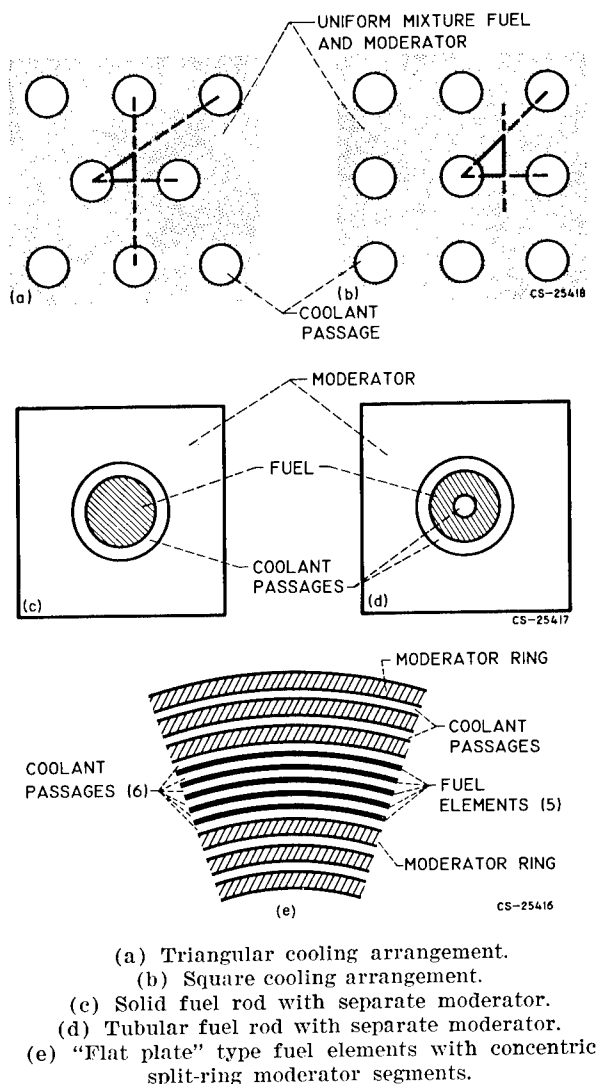


FIGURE 44-1.—Typical reactor geometry configurations.

herein. This homogeneous type of structure is now readily amenable to adjustment of hole size and spacing to arrive at optimum temperatures. The temperature distribution and the conduction heat-transfer characteristics of the material will depend upon the ratio of the spacing between passage centers to the passage diameter. Equations that give the temperature at every point in the material for both the triangular and the square arrays are presented in reference 1.

The surface temperature of the cooling passage is assumed to be constant around the circumference. Results of reference 1 show that for very large spacings the heat removal is

essentially uniform around the periphery, which indicates little influence of the presence of neighboring cooling passages. As these spacings get closer, nonuniformities of heat removal appear, and the temperature distribution around a passage is influenced by neighboring passages more in a square array than in a triangular array. The most important difference between the two arrays, however, is that the hot-spot temperature for a square array will always exceed that for a triangular array for fixed values of heating rate, spacing, and passage diameter.

The actual effect of varying coolant-passage size on maximum temperature and on temperature gradient is shown in figure 44-2. The temperatures were calculated for a typical reactor with graphite assumed to be the predominant material with a geometrical arrangement the same as the triangular array of figure 44-1(a). The core void fraction was kept constant and a cosine distribution was assumed for the heat generation in the axial direction. The fact that reactor power and therefore coolant-flow rate were the same for each geometry resulted in the same coolant temperatures. This procedure makes possible a direct comparison on a geometrical basis alone.

The finer geometry resulting from smaller hole sizes produced a dramatic difference in maximum temperatures and temperature gradients. The maximum temperature of approximately 6400° R for the 0.15-inch-diameter hole geometry was reduced to about 5200° R

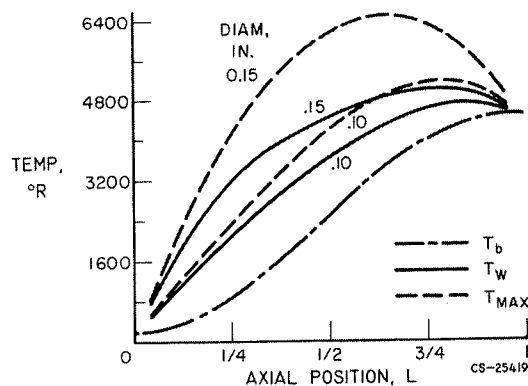


FIGURE 44-2.—Effect of coolant-passage diameter on temperature gradient and maximum temperature (20 percent void).

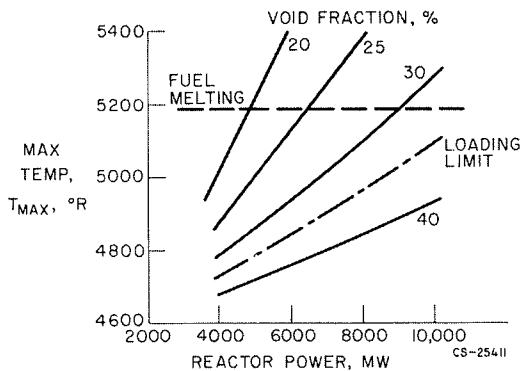


FIGURE 44-3.—Effect of void fraction on maximum temperature. Inlet bulk gas temperature, 200° R; outlet bulk gas temperature, 4500° R; diameter, 0.1 inch.

by using 0.10-inch-diameter holes. Maximum temperature differences were reduced from about 1600° to about 600° R in going to the smaller passages.

As stated in the discussion, these calculations were for a fixed core void fraction and two different hole sizes. The result of varying void fraction for a fixed hole size is shown in figure 44-3. For a reactor power of 6000 megawatts, for example, the maximum temperature is reduced by 500° R in going from a 20- to a 30-percent void. For even higher powers, a 30-percent void results in possible allowable temperatures, whereas a 20-percent void obviously would not even permit the attainment of these higher powers.

Using the results of such curves as those in figures 44-2 and 44-3 allows the calculation of thermal stresses if formulas are available. A maximum allowable stress therefore establishes the geometry sizing required. The introduction of nuclear considerations such as maximum allowable void fraction for criticality (dash-dot line) and of limitations on possible fuel melting (dashed line) then results in a final core choice that is compatible with all factors concerned. Each of these limitation lines is merely representative and may actually be located elsewhere for the core geometry investigated.

In addition to using fine geometrical configurations to reduce maximum temperatures, fuel loading may be distributed so as to reduce

hot spots by reducing the power density in certain locations while increasing it in others. When acceptable temperatures have been achieved, nucleonic, mechanical, and volume aspects must be reconsidered. This redistribution of fuel will have some definite limit presented by each of these factors.

#### Status of Knowledge of Heat Transfer

As the gaseous hydrogen flows through the reactor, its temperature increases from several hundred degrees to about 4500° R or more. Over this wide range of temperatures, the calculation of heat-transfer coefficients becomes questionable. Many investigators have studied gaseous-hydrogen heat transfer, but the individual experiments have usually been limited to wall temperatures below 2600° R; some helium tests have been run at higher wall temperatures (5000° R), but use of such results would not include effects of hydrogen dissociation and variation in fluid properties. Furthermore, most existing correlations are for overall average values rather than local values. Apparently, gaseous-hydrogen heat-transfer data must be augmented for conditions like those prevailing in a reactor core before any conclusive assurance on hydrogen heat-transfer calculation procedures applicable to the core becomes possible.

#### Flow Excursions

Several effects should be considered in an evaluation of the flow distribution and stability through the core during the cool-down phase of operation. Although the effects of characteristics are somewhat interrelated, they are listed as follows for purposes of discussion:

- (1) Distribution of core radial temperature
- (2) Variation in velocity head of coolant approaching core passages
- (3) Probability of operation in transition region from turbulent to laminar flow during cool-down phase
- (4) Prediction by pressure-drop equations that at a given pressure drop a passage may have either of two flow rates with a constant heat input

The core radial temperature profile predicted for design-point operation will not be valid dur-

ing the cool-down phase of operation, and the profile will be exaggerated by the actual flow characteristics. The pressure drop in the hotter passages will tend to be greater, and as the pressure drop is set by the pressure in the inlet and the outlet plenums, the pressure drop can be satisfied only by lower flow rates in the hot passages, which aggravates the condition.

As lower flow rates are considered during the cool down, the second effect becomes more prominent. As the flow rate decreases, the effectiveness of flow-distributing baffles or screens decreases, which could permit a variation in the velocity of the coolant approaching the various core passages and result in additional temperature variation across the core.

The reduced flow rates of cool down would also produce the third effect. The frictional pressure drop through a passage is a function of Reynolds number and depending on the magnitude of the number is expressed in one of two ways. The transition region of values of Reynolds number ranges from 2000 to 10,000 and in this region either the laminar-flow or the turbulent-flow friction factor could be applied. In considering a group of parallel passages, a prediction of whether the flow will be laminar or turbulent in the various passages is nearly impossible if the pressure drop and inlet conditions are such as to establish flow in the transition region. This case will lead to flow maldistribution and to flow oscillations if conditions are such as to permit random tubes to alternate between laminar and turbulent flow. The change in temperature of the coolant as it passes through the passage further compounds this effect by making it possible for flow to enter the passage at a Reynolds number safely in the turbulent range and to leave safely in the laminar range.

The fourth effect is illustrated in figure 44-4. The equation of pressure drop in a uniformly heated tube was written and analyzed. For a given pressure drop, two flow values were possible. A digital-computer program was written at Lewis to evaluate this equation over a range of values. Figure 44-4 presents a series of lines representing the variation of pressure drop with flow rate, each with a constant heat input along the length of the passage. The lower series of curves represents the corresponding

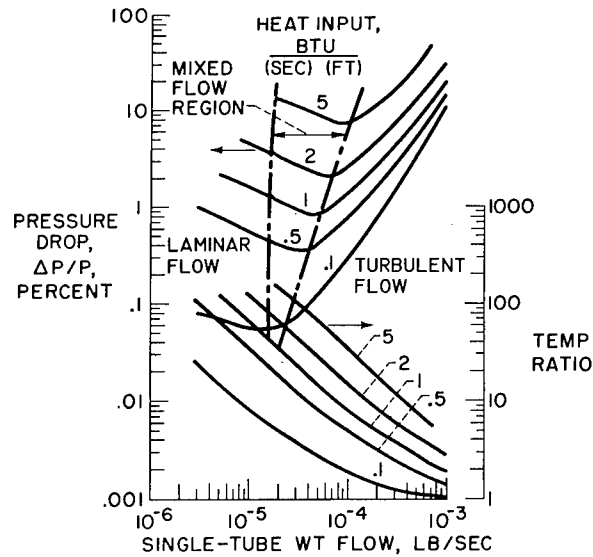


FIGURE 44-4.—Core flow stability.

outlet- to inlet-temperature ratios for the various heat inputs. These computed data have a common inlet pressure and temperature. The transition region between all-laminar and all-turbulent flow is indicated between the dash-dot lines. Figure 44-4 indicates, for example, at 2-percent pressure drop and a heating rate of 1 Btu per second per foot that a flow excursion could occur from  $6.2 \times 10^{-6}$  to  $1.45 \times 10^{-4}$  pound per second, which is an increase in flow by a factor of 23. The corresponding temperature ratios for these flows, as indicated by the lower curves in figure 44-4, are 100 and 6, respectively. If the core-inlet temperature were  $150^\circ \text{ R}$ , the corresponding core-outlet temperatures would be  $15,000^\circ$  and  $900^\circ \text{ R}$  at the low and the high flow rates, respectively. This relation can indeed predict serious problems in flow distribution and the related problems of thermal stresses and material failure. In addition, flow excursions could occur in a given passage as the flow cycled back and forth between the two possible flow rates. A similar relation for flow in a capillary tube is presented in reference 2, in which it is indicated that the low flow case is unstable and that the high flow case is stable.

In summarizing the cool-down problem, it must be concluded that current considerations indicate a serious problem and that further analysis and experiments are required; possibly intermittent bursts of coolant at relatively high flow rates should also be considered.

## REFLECTOR

A knowledge of the hydrogen state as a function of time is essential in the startup transient. One such typical history is shown in figure 44-5

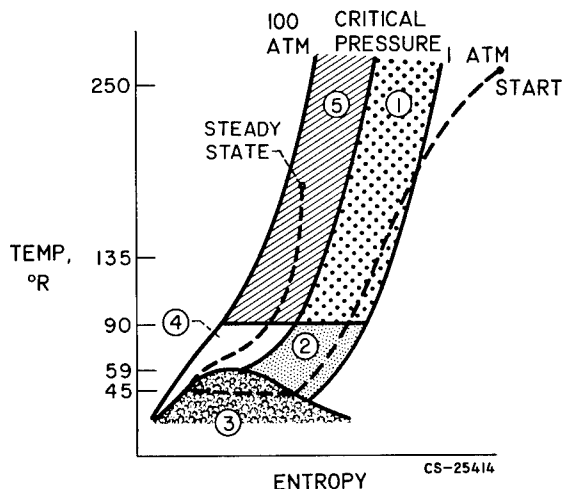


FIGURE 44-5.—Hydrogen state at reflector inlet during startup.

for the reflector inlet, in which time increases in the direction from the starting point to the steady-state full-power point. At startup, the hydrogen enters the reflector in a gaseous state (region 1) and at subcritical pressure. As time increases and the hydrogen temperature at the reflector inlet is reduced to about 90° R, a transition region (region 2) extending to the saturation line is encountered. Then the entering condition reaches the two-phase state and remains in this region (region 3) until the other leg of the saturation curve is met. Region 4, which is supercritical, is then encountered; this region near the saturation line is another transition region. The supercritical gaseous phase begins at about 90° R (region 5). Steady-state operation takes place in region 5. Hence, transition or pseudo-two-phase and two-phase heat transfer are all encountered at the reflector inlet, depending upon time after startup.

## Stable Flow

*Two-phase hydrogen flow and heat transfer.*—The presence of two-phase hydrogen flow through the reflector at some time during startup is indicated in figure 44-5. As the hydrogen

entering the reflector in the two-phase state moves along the reflector passages, it picks up additional heat and an increase in quality results. Even after 100-percent quality is attained, the hydrogen may not yet be in the gaseous state, but in the pseudo-two-phase state. Both two-phase and pseudo-two-phase heat transfer and flow will be discussed in this section.

Many investigations of two-phase or boiling fluids, especially in the nucleate boiling range, have been conducted. Data for hydrogen in the film boiling region, however, are limited. Some are presented in reference 3. In the reflector, the magnitude of the difference between the wall and the bulk temperatures is such that film boiling takes place. Film boiling is therefore of prime interest in reflector studies.

The following paragraphs give the status of knowledge of heat-transfer and fluid-flow correlation equations, the need for more data for reactor design and study, and experimental work in progress at the Lewis Research Center related to this subject.

**Status of knowledge:** According to reference 4, reliable methods for predicting two-phase heat-transfer coefficients are unavailable, because several different kinds of boiling region exist, heat transfer in these regions is affected in different ways by a variety of variables, and flow patterns in two-phase mixtures are not yet established. Some correlations have been proposed for restricted ranges of variables, but to date their limits of applicability are unknown. Moreover, the importance of local conditions is becoming more pronounced. The problem is reviewed in reference 5.

A study of isothermal pressure drop for two-phase flow in a horizontal tube showed that turbulent-flow data for a number of fluids could be correlated on the basis of a dimensionless parameter (ref. 6):

$$\chi_{tt} = \left( \frac{1-x}{x} \right)^{0.9} \left( \frac{\rho_g}{\rho_l} \right)^{0.5} \left( \frac{\mu_l}{\mu_g} \right)^{0.1} \quad (3)$$

The Martinelli parameter  $\chi_{tt}$  represents the ratio of shearing forces in the two fluid phases; since only isothermal pressure drops were considered, no momentum pressure drop was included. This parameter, as will be discussed

later, has been used in several proposed heat-transfer correlations for two-phase flow. These correlations, according to reference 4, are formulated in terms of single-phase heat-transfer coefficients for the liquid and thereby imply that the liquid is in contact with the surface. Consequently, there is no assurance that such a correlation would be applicable for cases in which the gas phase is in contact with the surface. Reference 4 also states that  $\chi_{tt}$  depends on vapor density, which in turn is a function of two-phase pressure drop; since two-phase pressure drop depends on the local density of the mixture, an iteration process is required to obtain  $\chi_{tt}$  and the two-phase heat-transfer coefficient.

The parameter  $\chi_{tt}$  was used in reference 7 to correlate two-phase heat-transfer data for water flowing through a vertical tube. Local heat-transfer coefficients were obtained for the nucleate boiling region during circulation vaporization in a long vertical copper tube. The heat flux contributed by nucleate boiling was apparently additive to the convection heat flux. Although this information was not used in the correlation procedure in reference 7, it has been suggested as an alternative method of correlating nucleate boiling data (see ref. 8). Other suggested correlations are discussed in reference 9.

Nucleate boiling heat transfer for five organic liquids flowing by natural circulation through a vertical single tube was correlated with the aid of  $\chi_{tt}$  (ref. 10). Separation of the effects of convection and nucleate boiling by calculating a convection coefficient in terms of a liquid coefficient and  $\chi_{tt}$  and applying a nucleate boiling correction factor to the convection coefficient to obtain the two-phase heat-transfer coefficient was attempted in reference 10. The correction factor used varied with the radius of the minimum-size stable bubble and the laminar film thickness.

Reference 3 reports heat-transfer and pressure-drop data for hydrogen flowing under forced convection through a vertical heated tube. In these experiments, the fluid model consisted of a liquid core and a gaseous annulus in contact with the wall. These conditions are opposite to those observed in reference 6; reference 3, however, shows that a two-phase heat

correlation can be obtained by use of the  $\chi_{tt}$  parameter. The parameter  $\chi_{tt}$  was originally used to correlate pressure-drop data for isothermal conditions and for the nucleate boiling region; it correlated heat-transfer two-phase hydrogen data in the film boiling region for a nonisothermal case. Data were also obtained for hydrogen at supercritical pressure just above and below critical temperature.

In reference 11 are defined five regions into which hydrogen is arbitrarily divided in order to investigate its cooling capabilities. One of these is the two-phase region (region 3 in fig. 44-5), in which the correlation equation of reference 12 was used. The part of region 4 (fig. 44-5) between the saturation line and about 90° F and between the critical pressure line and the 100-atmosphere line is a so-called pseudo-two-phase region, and heat-transfer data for this region are correlated by means of a modified or pseudo  $\chi_{tt}$ . The 90° F limit attached to this region is used because it is at about this temperature that the specific heat of hydrogen attains its maximum value; this value corresponds to the temperature above which the transport and specific-heat properties of hydrogen appear to be unaffected by the critical temperature condition (see ref. 11). Reference 12 gives a good discussion of boiling and near-critical heat transfer.

Local heat-transfer data are presented in reference 13 for bulk boiling of water in vertically upward forced flow. These data were correlated by means of  $\chi_{tt}$  and a boiling (or Stermann) number  $Bo$ . For low values of the boiling number, the local heat-transfer coefficient is a function of  $\chi_{tt}$  alone; for large values of the boiling number, the local heat-transfer coefficient becomes independent of  $\chi_{tt}$  (ref. 13).

In reference 14, the use of a two-phase Reynolds number for correlating two-phase heat-transfer data is proposed. One such number is found from

$$Re_{TP} = Re_{SP, l} \left( 1 - x + x \frac{\mu_l}{\mu_g} \right)$$

where

$$Re_{SP, l} = \frac{\rho_l u_{l, in} D}{\mu_l}$$

The model contained a gaseous core and a liquid annulus; for a liquid core and a gaseous

annulus,  $Re_{SP,g}$  may be required. A plot of  $Nu_g$  against  $Re_{TP}$  correlates film boiling hydrogen heat-transfer data very well.

Data for the heat transfer to hydrogen in the liquid, nucleate and film boiling, and gaseous regions under forced convection have been obtained in electrically heated stainless-steel tubes (ref. 15). These data covered velocities from 25 to 55 feet per second, inlet bulk temperatures from 40° to 57° R, outlet bulk temperatures from 40° to 147° R, inlet pressures from 28 to 213 pounds per square inch absolute, heat fluxes from 0.01 to 6 Btu per second per square inch, and wall temperatures from 51° to 1505° R. The two-phase data were correlated at Los Alamos Scientific Laboratory by use of  $Re_t$ ,  $Pr_t$ ,  $\rho_t/\rho$ , and  $T_w/T$ ; the resulting correlation equation is unpublished, to the best of the authors' knowledge. The absence of subscripts on  $\rho$  and  $T$  appearing in the denominators of the two fractions leaves doubt as to what the basis for these terms should be. Since the correlation is for two-phase flow, these quantities might conceivably be based on mean fluid conditions and hence include quality.

The static-pressure drop for two-phase flow in a horizontal pipe for isothermal conditions led Martinelli to the discovery of the parameter  $\chi_{tt}$  (ref. 6). The final correlation equation given in reference 6 predicts the static-pressure drop per unit length for two-phase flow in terms of that for gaseous flow and  $\chi_{tt}$ ; in the limiting case, as the gas-flow rate approaches 0, the equation reduces to that for liquid flowing alone. In reference 3, for hydrogen flow through a heated tube, it was found that the viscous shear forces at the wall could be neglected and that the two-phase pressure drop could be determined from the one-dimensional pressure drop due to momentum change alone.

According to reference 11, most of the pressure drop in the pseudo-two-phase region reported was due to change in momentum; however, some frictional drop also existed. It was concluded that both pressure losses should be calculated for the pseudo-two-phase region, but that sufficient information was not yet available for the appropriate selection on the non-isothermal friction factors. Such factors, however, are expected to be appreciably smaller

than the isothermal values; the friction data of reference 16 verify this expectation.

Experimental investigations at subcritical pressure: Few experimental data for the pseudo-two-phase region are available. Some data for the two-phase region were presented in reference 3; these data were determined for heated vertical tubes with inside diameters of 0.495 and 0.313 inch and for steady-state conditions. Since both these two diameters are considerably larger than a typical reflector passage, and since it had not yet been ascertained as to what effect diameter might have on two-phase and pseudo-two-phase heat-transfer correlations, a test program was initiated at the Lewis Research Center to consider tubes of 0.188-inch diameter and 52-inch length; this size approximates a typical reflector passage.

The test program was set up to include both transient and steady-state investigations; according to figure 44-5, the reflector operates in both ranges. One of the objectives of the program was to determine whether the same correlation or different correlations are required for steady-state and transient data.

Both unheated and heated tubes were included. Tube-inlet pressures from 22 to 46 pounds per square inch absolute and weight-flow rates from 0.002 to 0.022 pound per second were considered. The heated tubes were supplied with up to 6 kilowatts of electrical power. Wall temperatures varied from 100° to 500° R.

Apparatus and test procedure: A schematic diagram of the liquid-hydrogen heat-transfer facility is shown in figure 44-6. A hydrogen-supply Dewar is shown on the right of the fig-

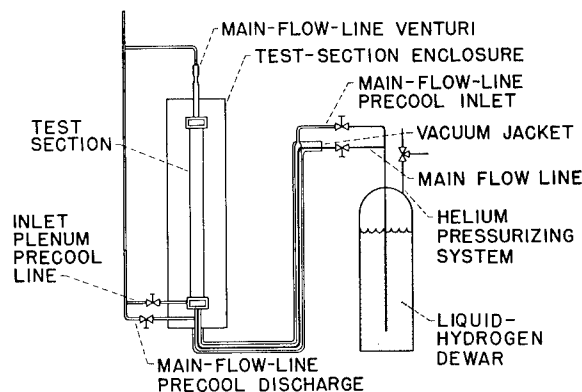


FIGURE 44-6.—Schematic diagram of liquid-hydrogen heat-transfer facility.

ure. The main hydrogen flow line connecting the Dewar to the test section is surrounded by two annuli; the inner annulus precools the main flow line and the outer annulus, maintained at a high vacuum, minimizes external heat leaks. The test sections, complete with inlet and outlet plenums, were contained in a large test-section enclosure that could be evacuated to prevent external heat leaks. A Venturi was located in the vent pipe for flow-measurement purposes. The locations of the various valves are also indicated in figure 44-6.

A photograph of the single-tube test section with three equally spaced electric heaters installed for steady-state runs is presented in figure 44-7. Insulation was wrapped around the

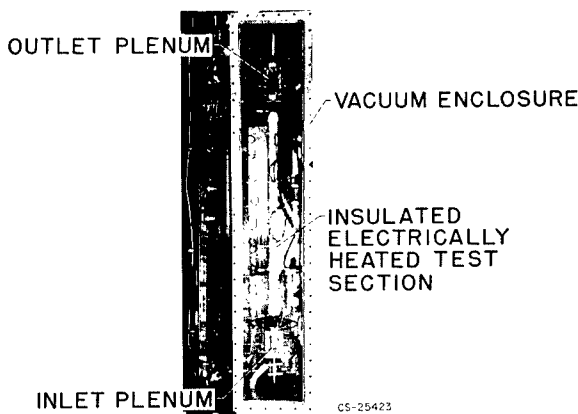


FIGURE 44-7.—Heated test section installed in heat-transfer facility.

assembly to reduce external heat leaks. Figure 44-8 is a closeup view of the inlet plenum of the test section in which the transparent window and instrumentation techniques can be more clearly seen. The unheated-tube installation is the same as that for the heated tube except that no heaters or power supply lines were used.

Aluminum was chosen as a material because its thermal diffusivity is similar to that of material, such as beryllium, generally used in reactor reflectors. The tube size (0.75-in. outer diameter and 0.188-in. inner diameter) was chosen to simulate the ratio of material volume to flow area typical of reflector geometries.

Facility instrumentation consisted of supply Dewar pressure (pressurized with helium gas),

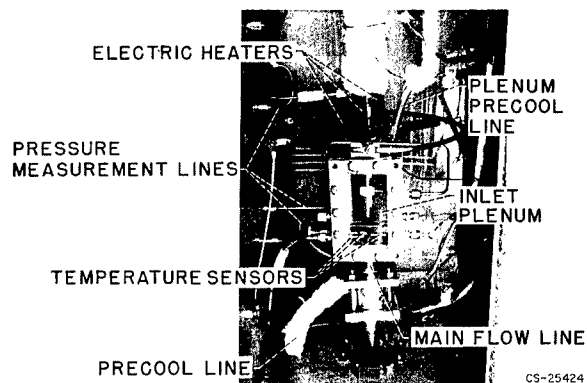


FIGURE 44-8.—Inlet plenum, heated test section, and associated equipment.

precool line temperature, liquid-level indicators in the Dewar, Venturi flow measurement at the exit end of the test section, and electric power when used for the heated test section. The inlet and the outlet plenums of the test sections were monitored by high-speed cameras, so that the quality of the hydrogen entering and leaving the test section could be appraised.

A schematic diagram of the test-section instrumentation used for single-tube experiments, typical for both heated and unheated tubes, is shown in figure 44-9. The pressure and the temperature of the hydrogen were measured in the inlet and the outlet plenums. The tube wall temperature was measured at four radial positions at each of 10 stations along the 52-inch length of the tube. The local pressure of the hydrogen was also measured at the 10 stations.

The output signals from the temperature sen-

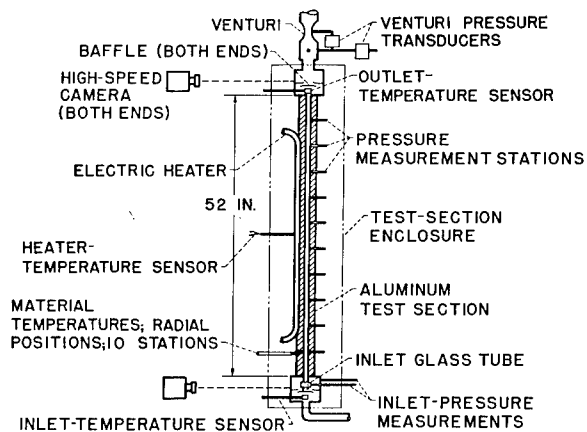


FIGURE 44-9.—Schematic diagram of instrumentation on heated test section.



sors and pressure transducers used for sensing the test variables were passed through appropriate signal-conditioning electronic equipment and readout was on direct-writing recording oscillographs or on magnetic tape that was then automatically processed to obtain the data.

Details of typical pressure- and temperature-instrumentation installation methods are presented in figure 44-10. Considerable difficulty

differences in contact thermal resistance between the thermocouple bead and the test section and the influence of the material that holds the thermocouple in place. Two thermocouple-installation methods that were used are shown in figure 44-10. Neither one, however, was satisfactory for precise measurements of radial profiles. For transient tests, in which the test section was cooling down with time, the slope of indicated temperature with time was consistent and the heat-flow rate based on this method was accurate within  $\pm 5$  percent.

The procedure for test operation is given in the following discussion: The hydrogen-supply Dewar was filled with liquid hydrogen (99+ percent para-hydrogen) from large transportable delivery Dewars through a transfer system incorporated in the test stand. Prior to a run, the flow line connecting the supply Dewar to the test section was precooled by flowing liquid hydrogen in an annulus surrounding the main flow line under control by the precool valves shown in figure 44-6. The test-section-inlet plenum chamber, which supplies hydrogen to the test section, was also precooled by flowing hydrogen through the main line and out the plenum precooling valve. The test section was kept warm during the precooling process by a reverse purge of warm helium gas through the test section that was also vented from the system through the plenum precooling valve. The flow from both precooling systems and the test-section flow were all vented through a common vent stack to the atmosphere.

During a run, an automatic timer controlled the valves, valve positions, data recorders, and camera over preselected time periods.

The operating procedures for both the heated and the unheated tubes were generally the same, except that recording instruments were turned on before test-section flow started for the unheated-tube runs and after flow and power were stabilized for the heated-tube steady-state runs.

Description of data-reduction methods: A brief summary of the calculations made in correlating the two-phase-flow data for the unheated tube follows: (This study is for transient heat transfer.) The flow rate  $\dot{w}$  was determined at the vent Venturi located down-

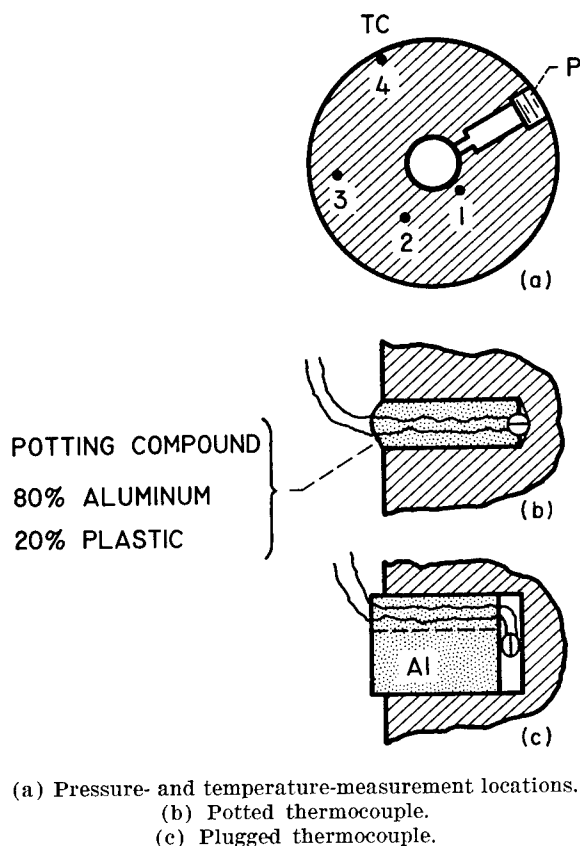


FIGURE 44-10.—Typical pressure- and temperature-instrumentation installation on test sections.

was encountered in obtaining accurate temperature measurements of the test-section material. Calculated radial-temperature profiles from a transient-conduction heat-transfer digital-computer program indicated a maximum radial gradient of about  $10^\circ \text{R}$  from the inner to the outer wall of the test section.

Comparison of individual experimental thermocouple measurements indicated that each thermocouple measurement could vary by as much as  $\pm 15^\circ$  (average deviations about  $\pm 5^\circ$ ), which resulted in an erratic measurement of radial gradient. This variation is a result of

stream of the test section proper. The standard Venturi equation and the data recorded at the Venturi were used; an iteration on the Venturi discharge coefficient was performed until calculated and calibrated values agreed to within 0.2 percent. The test-section inlet quality of the fluid was obtained with the aid of motion-picture photographs taken of the inlet glass tube. From the photographs, a value of the inlet velocity of the mixture was determined. This value, together with the glass-tube passage area and the calculated flow rate, yielded an inlet mixture density. This density, together with measured inlet pressure, permitted the reading of inlet quality from a chart in reference 17.

The heat input to the hydrogen from a section of the tube of axial length  $\Delta l$  was obtained from

$$Q_{\Delta l} = W_m c_{p_m} \frac{\Delta T_m}{\Delta t}$$

where

$$W_m = \frac{\pi}{4} \rho_m \Delta l (D_o^2 - D_i^2)$$

The term  $c_{p_m}$  was evaluated at the third radial temperature measured at the station at the midpoint of the section of length  $\Delta l$ , and  $\Delta T_m / \Delta t$  was taken as the temperature gradient at this position. A typical plot of  $T_m$  against time of the type that was used to determine the gradients is shown in figure 44-11. The third radial

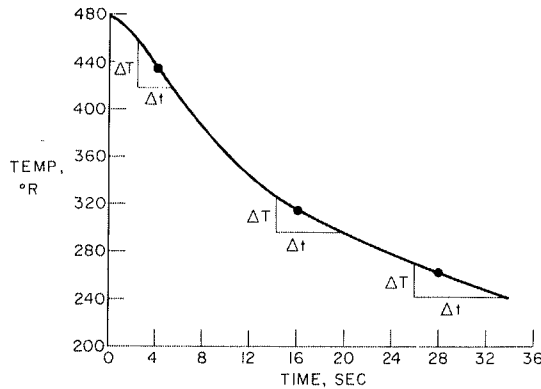


FIGURE 44-11.—Typical variation of tube-wall temperature with time in single unheated tubes.

position corresponds closely to the center of mass. The value of the local experimental heat-transfer coefficient was found from

$$h_{\text{exp}} = \frac{Q_{\Delta l}}{A_s (T_w - T_b)}$$

where

$$A_s = \pi D_i \Delta l$$

and  $T_w$  is the inner wall temperature.

The local fluid quality was evaluated from

$$x = x_i + \sum \Delta x$$

where

$$\Delta x = \frac{Q_{\Delta l}}{\dot{w} \lambda}$$

The heat of vaporization  $\lambda$  was determined at the local pressure with the aid of reference 17.

The initial attempt at correlating two-phase heat-transfer data was to follow the procedure in reference 3; other attempts will be made in the future. Since the tube diameter of reference 3 differed from that for which the data herein were obtained, calculation of the parameters required for the chosen correlation method was necessary because the correlation equation of reference 3 may not apply to other tube diameters. In fact, other investigators have already made use of the boiling or Stermann parameter to account for diameter changes. In addition, the data of reference 3 were for steady-state heat flow; hence, the correlation of  $Nu_{\text{exp}} / Nu_{\text{calc}}$  against  $\chi_{tt}$  is used herein. The parameter  $\chi_{tt}$  has already been defined by equation (3); values of  $\chi_{tt}$  were obtained by use of this equation. The values of  $Nu_{\text{exp}}$  were obtained from

$$Nu_{\text{exp}} = \frac{h_{\text{exp}} D_i}{k_f}$$

and  $h_{\text{exp}}$  has already been discussed. The value of  $Nu_{\text{calc}}$  was obtained from the equation used in reference 3:

$$Nu_{\text{calc}} = 0.023 (Pr_f)^{0.4} (Re_{TP})^{0.8}$$

The value of  $Re_{TP}$ , as in reference 3, was found from

$$Re_{TP} = \frac{\dot{w}}{A_t} \frac{D_i \rho_{fm}}{\mu_f \rho_b}$$

and the densities required for this evaluation from

$$\rho_{fm} = \frac{1}{\frac{x}{\rho_{pg,f}} + \frac{1-x}{\rho_{l, sat}}}$$

and

$$\rho_b = \frac{1}{\frac{x}{\rho_{g, \text{sat}}} + \frac{1-x}{\rho_{l, \text{sat}}}}$$

The two-phase Reynolds number was defined, according to reference 11, to account for film-density changes incurred over a large range of qualities from the near-gaseous to the near-liquid values. As the fluid approaches the gaseous phase, the Reynolds number becomes the same as the usual gaseous Reynolds number.

For the pseudo-two-phase region, the procedure suggested in reference 11 for supercritical conditions might be applicable for subcritical conditions. The procedure employs the use of a light and a heavy species and bases property values for the heavy species on the melting temperature of the fluid and for the light species on the bulk temperature. The correlation is of the form  $Nu_{\text{exp}}/Nu'_{\text{calc}}$  against  $x'_{it}$ , where

$$x'_{it} = \left( \frac{1-x'}{x'} \right)^{0.9} \left( \frac{\mu_{\text{melt}}}{\mu_{pg, f}} \right)^{0.1} \left( \frac{\rho_{pg, f}}{\rho_{\text{melt}}} \right)^{0.5}$$

$$Nu'_{\text{calc}} = 0.023 (Pr_f)^{0.4} (Re'_{TP})^{0.8}$$

$$Re'_{TP} = \frac{\dot{m} D_i \rho'_{fm}}{A_i \mu_f \rho'_b}$$

$$\rho'_b = \frac{1}{\frac{x'}{\rho_{pg, b}} + \frac{1-x'}{\rho_{\text{melt}}}}$$

$$\rho'_{fm} = \frac{1}{\frac{x'}{\rho_{pg, f}} + \frac{1-x'}{\rho_{\text{melt}}}}$$

The value of  $x'_{it}$  may be determined as follows: The equation for  $\rho'_b$  may be solved for  $x'$ . In order to determine the numerical value of  $x'$ , the values of  $\rho_{pg, b}$  and  $\rho_{\text{melt}}$  can be found from tabulated or graphical hydrogen data and the value of  $\rho'_b$  can be determined by use of Goodwin's iteration. This iteration requires the assumption of a value of specific volume and calculation until an output specific volume agrees with the input specific volume.

In order to apply this procedure to the subcritical cases, properties for the light species might be evaluated at the wall or the film tem-

perature and for the heavy species, at the saturation temperature for either gas or liquid. To date, these attempts have not been made for a sufficient amount of data to permit any further comment.

Steady-state heat transfer was investigated by use of heated tubes. A brief description of the method of correlation for these tests follows. Steady-state conditions were obtained by manipulating flow rate and electric power to the heaters until thermocouples imbedded in the test section gave a steady reading. About 20 seconds after a stable condition was visually determined, the 15-second recording of run conditions was made.

All the steady-state tests were made with subcooled hydrogen entering the test section. The inlet flow lines and inlet plenum were precooled, and the supply Dewar was vented to the atmosphere. After stabilization, the Dewar was pressurized to obtain the desired flow conditions. Subcooling from 1.6° to 7.5° R was achieved; these values were obtained by taking the difference between the measured and the saturated temperatures for the measured fluid pressure.

The heat input to the hydrogen was determined from

$$Q_T = \dot{m} \Delta H$$

The flow rate was obtained in the same way as that for the unheated tube, and the change in enthalpy was determined from measured inlet and outlet pressures and temperatures. Since the heaters were shorter than the test section, calculations of the heat entering the hydrogen from these unheated sections were made by use of the conduction equation:

$$Q = kA \frac{\Delta T}{\Delta l'}$$

where  $\Delta T$  was the difference in measured temperatures in the heated and the unheated lengths and  $\Delta l'$  was the distance between the end of the heater and the temperature sense point in the unheated section. The rate of heat addition to the hydrogen along the heated section of the tube was determined by subtracting the two conduction rates from  $Q_T$ . This heat addition was then assumed to be distributed uniformly along the heated tube length. Incremental lengths along the heated tube were taken be-

tween instrumentation points. The lengths required to bring the hydrogen from the subcooled state to a saturated liquid and from a saturated liquid to a saturated gas were calculated by use of inlet enthalpy, flow rate, and heat rate per unit length.

The experimental heat-transfer coefficients were obtained from

$$h_{\text{exp}} = \frac{Q_{\Delta l}}{A_i(T_w - T_b)}$$

where  $T_w$  was taken as the average value between the measured end points of the incremental length  $\Delta l$ . The remainder of the calculations were made in the same way as those for the unheated tube.

Both momentum and friction pressure drops were included to calculate pressure drop for these two regions. The momentum pressure drop, for each incremental length, was obtained from

$$\Delta p_{\text{mom}} = \frac{G^2}{g} \left( \frac{1}{\rho_{\text{out}}} - \frac{1}{\rho_{\text{in}}} \right)$$

where  $G = \dot{m}/A_i$  and  $\rho_{\text{in}}$  and  $\rho_{\text{out}}$  are evaluated for each incremental length from the entering enthalpy, the pressure, and reference 17. The frictional pressure drop was determined from

$$\Delta p_{\text{frict}} = \frac{0.184}{\left( \frac{GD_i T_b}{\mu_f T_f} \right)^{0.2}} \left( \frac{T_b}{T_f} \right) \left( \frac{l}{D} \right) \left( \frac{G^2}{2g\rho_{\text{av}}} \right)$$

Here

$$\rho_{\text{av}} = \frac{\rho_{\text{in}} + \rho_{\text{out}}}{2}$$

for the respective increment.

Results: Figure 44-12 shows a plot of  $Q/A_s$  against  $T_w - T_b$  for the unheated tests. Since published hydrogen data show the peak nucleate boiling point at a value of  $T_w - T_b \approx 4^\circ$  and the data on figure 44-12 indicate a value of  $T_w - T_b$  ranging from  $100^\circ$  to  $400^\circ$ , the statement that film boiling predominates in the reflector passages is confirmed.

The two-phase heat-transfer data for both the heated and the unheated tubes are shown in figure 44-13. The ordinate consists of the ratio of the experimental Nusselt number to the calculated Nusselt number times the boiling number to the  $-0.4$  power; the abscissa is the Mar-

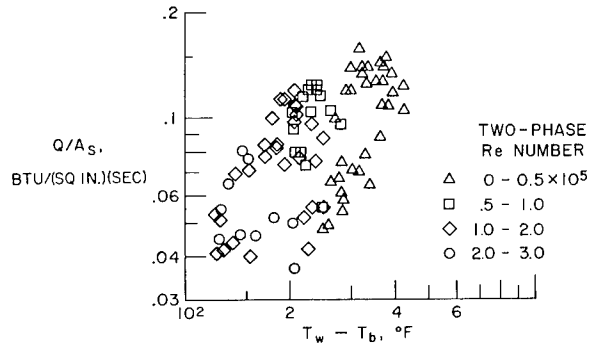


FIGURE 44-12.—Typical hydrogen convective-film-boiling heat-transfer data.

tinelli parameter. The exponent on the boiling number was determined empirically from the experimental data. Superimposed on the slide are some steady-state data from reference 3. The correlation curve was determined for the unheated-tube data and the data of reference 3; the heated-tube data fall into the same general pattern, but slightly higher; this difference may be attributed to the uncertainty in the determination of heat input into the tube. Only the total heat to the tube was measured, and the assumption was used that this heat was uniformly distributed.

A plot of the ratio of experimental Nusselt number to a calculated Nusselt number against  $\chi_{tt}$  is presented in reference 3. When the data of the current experiments were plotted on this basis, the data separated into groups according to the boiling number in a manner similar to that presented in reference 13. The heat-transfer rate was more dependent on  $\chi_{tt}$  at low values of boiling number than at high ones (ref. 13). The use of the boiling number in the correlation should thus improve the two-phase heat-transfer correlation.

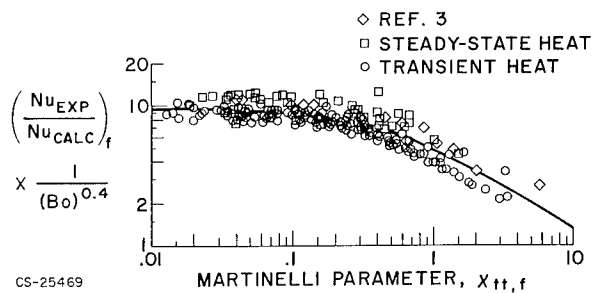


FIGURE 44-13.—Two-phase hydrogen-flow heat-transfer correlation.

A first attempt to apply the boiling number to the data in a simple manner resulted in the correlation presented in figure 44-13. Although this correlation appears satisfactory because it reduced an original  $\pm 60$ -percent spread to a  $\pm 25$ -percent maximum spread for two different sets of data, it should be considered as only the beginning of the investigation. The study of liquid- and gaseous-interface geometries and the degree of wall wetting during two-phase flow with heat addition, together with the establishment of an improved model based on visual observations, might yield more information on this subject. The theory developed in reference 13, for example, is based on a wetted wall with bulk boiling in forced flows; the wall- to bulk-temperature ratios in the current experiments (fig. 44-12), however, indicate film boiling.

A plot of experimental against calculated two-phase pressure data is shown in figure 44-

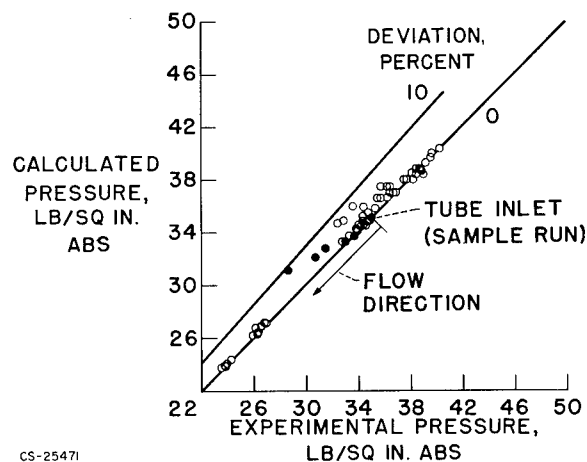


FIGURE 44-14.—Transient two-phase hydrogen-flow pressure drop.

14; data from several runs with the unheated tube are shown. A sample run is marked with an arrow that indicates the direction from the tube inlet. The calculated absolute pressures at the tube entrance are matched with the experimental values for the calculations. As the flow proceeds up the tube, the calculated pressures become larger than the measured pressures; in other words, the calculated pressure drops are lower than the experimental pressure drops. The shearing forces between the liquid and the gaseous layers were not included in the

calculations. Martinelli (ref. 6) correlated isothermal pressure-drop data for a gaseous core and a liquid annulus by including shearing forces between the liquid and the gaseous phases. If this procedure applies to the present model (liquid core and gaseous annulus), the pressure drop caused by these shearing forces should be included, and the absolute value of the calculated pressure would be reduced. This should give better agreement between calculated and experimental pressures along the tube length.

*Gaseous-hydrogen flow and heat transfer.*—During the initial phases of startup, gaseous hydrogen is present in the reflector at subcritical pressure, as shown in figure 44-5. Steady-state operation in the gaseous region at supercritical pressure is also shown in this figure. In fact, even if two-phase hydrogen enters the reflector, somewhere along the reflector passage the hydrogen enters the gaseous phase. The following discussion reviews the current status of knowledge for gaseous flow and heat transfer and describes current Lewis tests involving gaseous-hydrogen flow and heat transfer.

Status of knowledge: Reference 11 presents a list of correlation equations, with pertinent limits, presented by various investigators for gaseous-phase hydrogen (and, in certain cases, helium). These equations were taken from references 16, 18, 19, and 20. Most of them are for an average heat-transfer coefficient for the entire test section and of the general form

$$Nu = C(Re)_{ref}^a (Pr)_{ref}^b \left(\frac{l}{D}\right)^c$$

The coefficients and exponents vary from investigation to investigation; some of the proposed correlations contain a wall- to bulk-temperature ratio raised to different powers. A comparison of data from references 16, 18, 19, and 20 is presented in reference 11; the data were extrapolated over a range of values of  $T_w/T_b$  from less than 10 up to 100. The data of reference 18, extrapolated, show a different trend with  $T_w/T_b$  from those of references 16, 19, and 20; this difference might result from the fact that the original data of reference 18 covered temperature ratios from 1.5 to 2.8 and the extrapolation to a value of 100 may not be ac-

curate. The other three sets of data indicate fairly good agreement in their trends with  $T_w/T_b$ . The respective curves are close, although not perfectly correlated.

Reference 11 also proposes that local coefficients may be correlated by use of the equation

$$Nu_f = 0.021 Re_f^{0.8} Pr_f^{0.4}$$

This equation was applied to hydrogen data and worked well for the test section except for regions near the entrance and the exit. For entrance and exit regions, some alterations are required.

Local heat fluxes are plotted against  $T_w - T_b$  in reference 21 for hydrogen flowing through a 0.194-inch-diameter heated tube for hydrogen at pressures from 680 to 1344 pounds per square inch absolute and at values of  $T_w/T_b$  from 1.36 to 16.5. At a value of  $T_w - T_b$  of about 500° R, an abrupt change in the slope of the line through the data occurred; two distinct correlation equations were therefore obtained, one for  $T_w - T_b < 500°$  R and one for  $T_w - T_b > 500°$  R, with property values based on bulk temperature. These results appear in the form

$$Nu = C Re_b^{0.8} Pr_b^{0.4} \left( \frac{T_w}{T_b} \right)^d$$

where  $C$  and  $d$  differ for the two regions. The explanation for the existence of these two correlations for this set of data is given in reference 21 and is repeated herein. At low heat fluxes, the unit heat flux is proportional to a fractional power of the temperature driving force ( $Q/A < 1$  Btu/(sec) (sq. in) and  $T_w - T_b < 500°$  R). At higher heat fluxes, the unit heat flux is proportional to the first power of the temperature driving force. A relation seems to exist between the first correlation (for low heat fluxes) and a transition region, according to reference 21.

In reference 18, hydrogen data is compared with the helium data of reference 20 by means of the correlation

$$Nu = 0.027 Re^{0.8} Pr^{0.4}$$

where all properties are based on wall temperature. These sets of data were for comparable conditions: For  $H_2$ ,  $l/D = 42.6$  and 67 and  $T_w/$

$T_b = 1.5$  to 2.8; for He,  $l/D = 60$  and  $T_w/T_b = 1.8$  to 3.9. This correlation was satisfactory, since the same data did not correlate when plotted in reference 11 against  $T_w/T_b$ , but correlated well in reference 18. The statement made previously relative to the extrapolation of the data of reference 18 is confirmed.

The preceding discussion indicates that at least two correlations for local gaseous-hydrogen heat-transfer data have been successful. Both are of the form

$$Nu = C Re^{0.8} Pr^{0.4}$$

where in one case  $C = 0.021$  and fluid properties are based on film temperatures and in the other case  $C = 0.027$  and fluid properties are based on wall temperatures.

The pressure drop in the gaseous region must include both momentum and frictional losses. The general pipe equation useful for this determination is available in almost any advanced fluid-mechanics textbook.

Experimental investigations at subcritical pressure: It was previously stated that even when two-phase hydrogen enters the test section, the gaseous phase will be attained at some point farther up the tube. Hence, data for the gaseous region were obtained from the same tests that supplied the two-phase data. Consequently, the test program and the ranges in variables are the same as those discussed for the two-phase state.

Description of data-reduction methods: The method used for obtaining the heat input to the hydrogen for the gaseous data is the same as that used for the two-phase-flow data for both the transient and the steady-state experiments. The temperature and the other properties of the hydrogen required for correlations, however, had to be obtained from accumulated total enthalpy gain of the hydrogen from the tube entrance (which was supplied with liquid hydrogen), local measured pressures, and available hydrogen-property tabulations. Data reduction was accomplished by means of a digital-computer code including a subroutine containing the hydrogen properties for the transient experiments and by hand calculations for the heated-tube steady-state experiments. Values of density, Reynolds number, Prandtl num-

ber, and experimental Nusselt number were all calculated three times on the basis of bulk, film, and wall temperatures of the hydrogen. With this information, the data could be plotted according to the various heat-transfer correlations available. Friction, momentum, and total-pressure drops were also computed by the digital code.

Results: Local heat-transfer data for gaseous-hydrogen points above  $90^\circ \text{ R}$  were plotted as  $Nu_{\text{exp}}/Pr^{0.4}$  against  $Re$  for bulk, film, and wall conditions, but the results indicated considerable scatter. The next attempt to correlate the data used equations from the literature (summarized in ref. 11), which were successful for the case of supercritical pressures and temperatures greater than  $90^\circ \text{ R}$ , which is region 5 in figure 44-5. Most of these equations include wall- to bulk-temperature ratios and an  $l/D$  term and use overall bulk or average temperature for fluid-property evaluation. Defining the  $l$  in the equation posed a problem since liquid hydrogen entered the test section. The following model was assumed: As hydrogen flows up the tube, the liquid is converted to gas in the two-phase region. When all liquid is evaporated and warmed to  $90^\circ \text{ R}$ , the gas region is assumed to begin and  $l$  is the distance from this point to the end of the tube. Uniform velocity distribution is also assumed at this point.

With these assumptions, the best correlation to date, shown in figure 44-15, uses the equation of reference 16. Data for both the steady-state (heated-tube) and transient runs are shown, as well as the line representing the equation of reference 16. The data points show

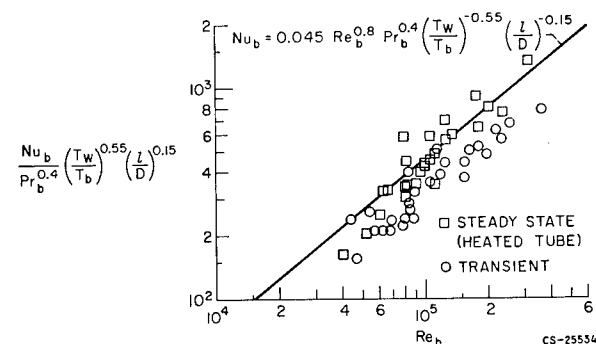
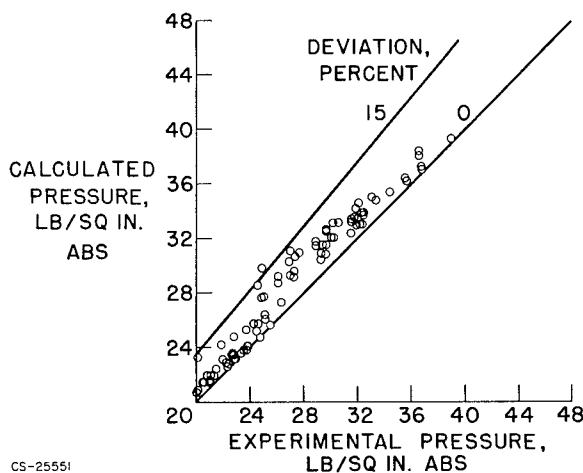


FIGURE 44-15.—Heat-transfer correlation for gaseous hydrogen. Bulk gas temperatures,  $>90^\circ \text{ R}$ ; pressure, 1 to 3 atmospheres.



CS-25551

FIGURE 44-16.—Transient gaseous-hydrogen-flow pressure drop.

that the heated-tube results are again somewhat higher than the transient points, such as was the case in the two-phase-flow heat-transfer data.

Calculated pressure is plotted against experimental pressure for the gaseous region in figure 44-16. Calculated pressures are shown to be larger than experimental pressures. Investigation revealed that the experimental friction factors were larger than those calculated in the usual way by use of the von Kármán equation. This difference in friction factor apparently accounts for the discrepancy in the pressure data. A more careful study of friction factors may be in order, especially since low friction pressure losses exist with hydrogen and two-phase flow precedes the gaseous region in the tube.

### Oscillatory Flow

It has previously been stated that during reactor startup two-phase flow occurs somewhere in the rocket flow system. For safe operation of the rocket, stable flow conditions must prevail. Consequently, an investigation of possible two-phase-flow oscillations in the system is necessary to find methods for determining whether stable or unstable flows will exist in a system. From such knowledge, stable systems can be designed.

Pressure oscillations are generated by the boiling process during two-phase flow. Particles of liquid vaporize and cause pressure surges; the vapor is condensed when cooled by

surrounding liquid and this condensation causes pressure decreases. These processes occur at random rates, and a spectrum of frequencies of pressure perturbations results.

In recent years, many attempts have been made to predict circumstances leading to parallel channel instabilities. In 1938, unstable operation was reported whenever the steady-state pressure-drop-flow curve exhibited a negative slope (ref. 22). More recently, pronounced flow oscillations were observed in a series of parallel channels in which the steady-state pressure-drop-flow curve exhibited a positive slope (ref. 23). In reference 23, the criteria for flow instabilities were attained in terms of initial fluid conditions, channel geometry, and heat-flux distribution. Other investigators have also been active in this field.

Flow oscillations have recently been observed at the Lewis Research Center in some of the two-phase hydrogen heat-transfer tests conducted for single tubes. Some gross effects observed in these tests will be presented later. Existing methods for determining characteristics of the oscillations, such as amplitude, for example, are available and will be used to compare theoretical results with the experimental data being obtained. A brief résumé of some of these approaches is given subsequently.

*Status of knowledge.*—According to unpublished information from Los Alamos Scientific Laboratory, a simple spring-mass model that included a dashpot and a forcing function resulted in the successful simulation of the amplitudes of pressure oscillations obtained during an experimental run. The damping coefficient and hence the amplitude of the pressure oscillations varied with the cube of the passage diameter. The use, of course, of a spring model for determining oscillations depends upon the degree of nonlinearity of the system.

Flow oscillations were analyzed in reference 23 by considering the four basic transient equations for two-phase flow in a heated channel: energy, continuity, state, and momentum. Perturbations were applied to the variables and the resulting equations were integrated in the flow direction. The channel enthalpy profile was assumed to be of the same shape (but not necessarily the same level) as

if steady-state operation existed. A second-order transfer function relating heat flux and inlet flow perturbations was obtained; from this transfer function, the criteria of flow instabilities in terms of initial fluid conditions, channel geometry, and heat flux distribution were determined. Comparison with data showed that this analysis could predict coolant conditions at the inception of flow oscillations and the frequency of the oscillations.

Another type of analysis was used in reference 24 to study a two-phase natural-circulation system. An exact solution of equations expressing mass and energy conservation for a channel subjected to a cyclic variation was obtained by use of a Lagrangian coordinate model. Channel pressure drop was predicted by numerical integration; from a Nyquist diagram, channel stability was investigated. No slip flow or uniform-heat-flux profile is required for this method.

Another method of analysis was presented in reference 25. Differential equations for the transient conservation laws in the fluid and metal and heat-transfer conditions at the fluid metal interface were used to obtain difference equations (without perturbations). These equations permitted determination of fluid conditions and metal temperatures at a discrete number of points in the channel and a discrete number of times during a transient. The equations were solved on a digital computer to determine fluid conditions in response to arbitrary time variations in heat-generation rate, plenum to plenum pressure drop, and inlet enthalpy. Channel oscillatory tendencies could then be predicted by determining flow as a function of time after a small step increase in heat generation. Advantages of this approach over those of references 23 and 24 are also given in reference 25.

A number of responses to step inputs were calculated at different heat fluxes near those where oscillations occurred in the heated channel experiments with boiling water. At heat fluxes slightly less than the flux required for oscillating flow, the calculated response to the step change (1 percent of steady-state heat flux) showed a slightly overdamped response. When the heat flux was equal to the experi-



mental condition, the response was slightly underdamped, but the oscillations converged rapidly to the new steady-state operating condition. When a larger heat flux was used in the calculations (e.g., a flux of 1.15 times the experimental flux), the system oscillated with continually increasing amplitude. The oscillating mass velocity (flow) curves had the appearance of sine waves until large amplitudes were reached, when the shape of the curves was distorted because of the increasing significance of nonlinear effects. The equations, however, in no case predict a sustained oscillation of constant amplitude, which is often encountered in two-phase-flow experiments (refs. 23 and 25).

A certain amount of flow or pressure variation with time or "noise" is always present in two-phase-flow systems. If the damping ratio is small (low friction), the existing noise will be greatly amplified when the frequency of the "noise" approaches the natural frequency of the system. This phenomenon is probably occurring in many of the experimental observations.

The need for more theoretical work is required in the study of these flow oscillations in order to predict when they will occur and their magnitude in complex systems. Experimental data with hydrogen should then be obtained and analyzed to confirm the calculations.

*Flow stability during experiments.*—Flow oscillations have been recorded during the single-tube experiments. A typical pressure trace of one type of oscillation measured at one of the static-pressure locations along the test section during a transient run is presented in figure 44-17. At the beginning of the run (time, 0), high-amplitude oscillations existed; these oscillations persisted during the run until about 16.3 seconds later (fig. 44-17), at which point the amplitude was quickly damped; evidence of the frequency, however, still persisted. The resonant frequencies, in general, decreased during the transient runs. The flow rate at the test-section exit for the run shown in figure 44-17 oscillated  $\pm 25$  percent about the mean value at the beginning of the transient, and the inlet liquid hydrogen had three degrees of subcooling.

Some of the instabilities were traced to oscillation sources in the flow system and means

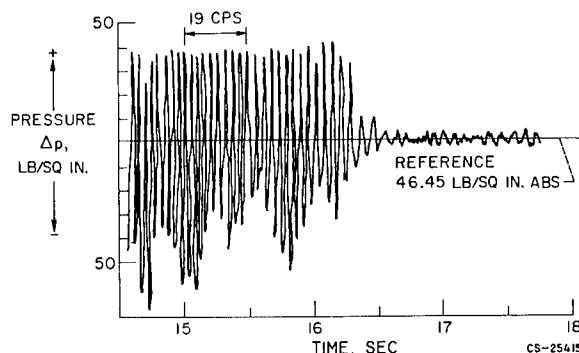


FIGURE 44-17.—Pressure-data trace of oscillating-flow transient run.

were found to eliminate them. An initial criterion based on the frequency of the flow oscillations has been established for conditions that will produce oscillations greater or less than a selected value of frequency. The criterion for grouping the runs according to frequency will be discussed first, and then a model representative of the flow oscillation sources in the system will be described and discussed.

The trend that developed during the heated-tube experiments is illustrated in figure 44-18. The dashed line separates the data into regions having higher (unstable) or lower (stable) frequencies than 2 cycles per second. If the liquid entering the test section is subcooled less than  $2^\circ$  to  $21\frac{1}{2}^\circ$  R and if there is sufficient heat input to attain an outlet- to inlet-velocity ratio in excess of 350, low-frequency runs will be attained. Conversely, when the entering fluid is more subcooled and the heat rate is insufficient to attain the high velocity ratios, the flow rate oscillates at higher frequencies.

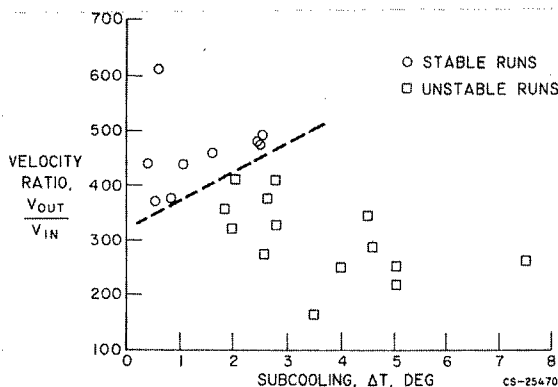


FIGURE 44-18.—Variation of subcooling with velocity ratio.

It was operationally possible during heated-tube experiments to decrease the frequency of the flow oscillations either by decreasing the amount of subcooling in the inlet plenum or by increasing the test-section heat input, which increased the velocity ratio.

This information should be considered as a status report on experiments and analysis now

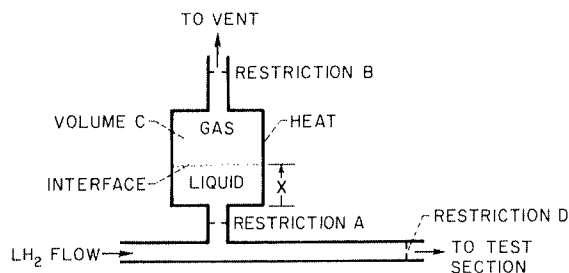


FIGURE 44-19.—Model of oscillator in system.

being performed and is presented primarily to cultivate interest in a recurring and unexplained phenomenon. The terms velocity ratio and subcooling will probably be replaced by more pertinent parameters, and amplitude will probably be used as a criterion instead of frequency.

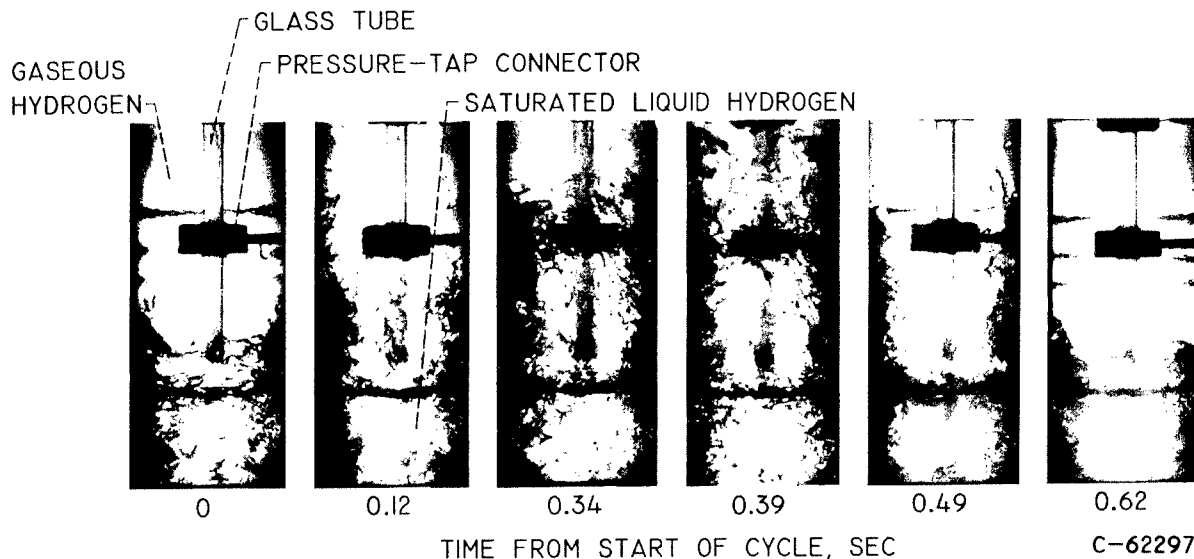
Sources of oscillation in the system can be described by the model shown in figure 44-19. As the pressure rises in the liquid-hydrogen

flow line, liquid flows through restriction A into volume C. The liquid is vaporized in the volume because of heat addition. The phase change in the volume results in an increase in pressure; first liquid and then gas are forced back into the liquid flow line through the restriction A. When the pressure in the volume approaches the line pressure, liquid may again enter volume C. Initially, the remaining gas in the volume will be cooled, with a further decrease in pressure, which will allow more liquid to enter the volume. When the evaporation rate and the resulting increase in pressure balance the line pressure, the flow through the restriction reverses and the cycle continues.

This phenomenon is cyclical (i.e., the distance X to the interface is periodic with time) and affects the mass-flow rate in the main flow line by alternately bleeding off liquid to volume C and then returning liquid and then gas to the flow line. The flow variations are then reflected as system pressure oscillations if there is a restriction downstream of the flow oscillator, such as restriction D.

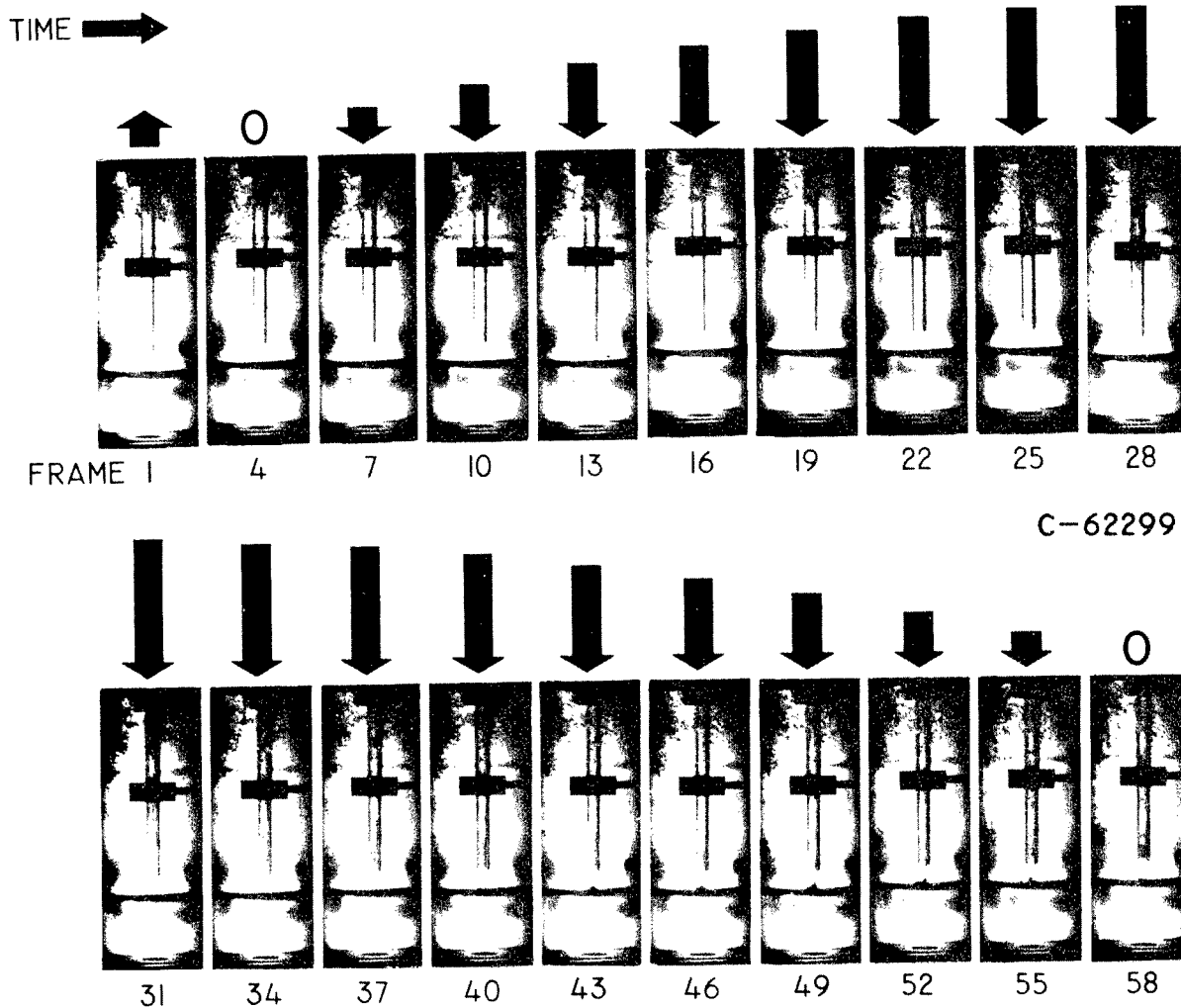
A mathematical model that assumes that the evaporation rate is proportional to the liquid column height X has been shown to be unstable.

Two points in the Lewis flow system were similar to the model. One was a T in the trans-



(a) Inlet-plenum oscillation.

FIGURE 44-20.—Enlargement of frames from high-speed motion pictures of oscillating hydrogen flow.



(b) Test-section oscillation. Arrows indicate relative flow velocity.

FIGURE 44-20 (Concluded).—Enlargement of frames from high-speed motion pictures of oscillating hydrogen flow.

fer line, where the hydrogen was diverted to the precooling annulus, and the other was the volume surrounding the glass tube at the entrance to the test section.

High-speed motion pictures were taken of the inlet plenum that supplied hydrogen to the test section. At least two forms of oscillation were identified. Enlargements of photographs taken during two runs showing the two oscillating modes are presented in figure 44-20. In figure 44-20(a), the saturated liquid level rises and falls in the inlet plenum and the volume of gas surrounding the glass tube varies with time in a periodic manner. In figure 44-20(b), the inlet plenum is full of subcooled liquid hydrogen and the flow in the glass tube varies in such

a periodic manner (19 cps) that the flow actually reverses during part of the cycle as shown. Static-pressure measurements along the tube for this type of oscillation showed high-amplitude variations such as illustrated in figure 44-17. Also observed in the photographs were a few small bubbles that originated from a small amount of nucleate boiling in the upper part of the chamber and from the "breathing" of the instrumentation pressure lines connected to the chamber (fig. 44-20(b)).

The technique of removing the oscillations from the test-section inlet plenum and the T in the system consisted merely of allowing sufficient flow through restriction B (fig. 44-19) that no meniscus could form or that if it did

form the gas generated would be vented out at a rate that held the meniscus fixed with time.

When this model has been thoroughly analyzed mathematically and verified by experimental data, the approach can be applied to other parts of the flow system. During the experiments, only the test section, not the rest of the flow system, has been instrumented. In particular, a question arises as to whether the pressure-tap lines in the lower plenum and along the test section are acting as oscillators and generating the flow oscillations.

### Maldistribution of Flow

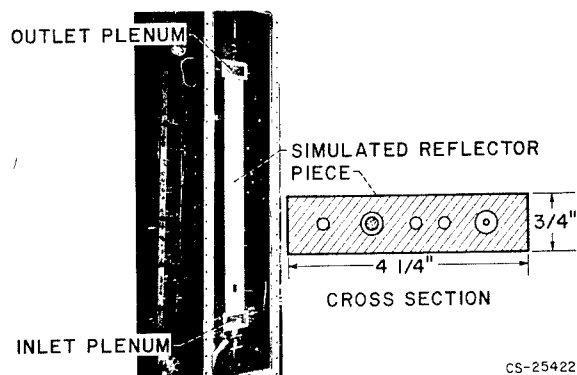
One of the most important problems encountered in reactor design is the prevention of maldistribution of flow. Since both the reactor reflector and the reactor core contain numerous different-size parallel coolant passages, and since the power generation throughout a typical reactor is nonuniform, the maldistribution problem becomes even more severe. The different-size passages (with different surface areas) receive various amounts of heat from different volume elements, and hence the flow rates in the passages must be different in order to maintain the same outlet pressure for each passage. Since most methods of reactor control tend to change the pattern of heat generation, an extra difficulty is encountered. According to reference 26, the designer must therefore be prepared to sacrifice potentially achievable coolant-outlet temperatures by allowing for substantial differences between the maximum (design) and the average coolant-outlet temperature or to incorporate such devices as orifices to counteract flow maldistribution and thus increase the average coolant-outlet temperature at the expense of increased pressure drop. The following sections will give some indication of the Lewis effort in this vital area of flow maldistribution.

*Description of typical reflector.*—A typical reflector might consist of several annular segments of a selected reflector material with coolant passages between the sectors and between the outermost sector and the pressure shell. Numerous coolant holes would also probably be required in the annular regions. In many reactors, the control devices are located in the

reflector. Additional holes and annular flow passages in the control devices will be required for such cases since the control devices would also have to be cooled. A typical reflector will thus contain numerous coolant passages of different diameters and annuli of different sizes; adequate flow distribution among these many passages must be maintained.

*Power distribution in the reflector.*—According to reference 27, about 5 percent of the total heat release in the reactor takes place in the reflector and the pressure shell. The sources of this reflector heat are neutron leakage from the core and gamma radiation. These heat sources decrease in importance as the distance penetrated in the reflector from the core increases; that is, the greater the distance from the core within the reflector, the smaller is the neutron and gamma attenuation. In a typical reflector consisting of two annular rings and a pressure shell, it was estimated that about 3 percent of the total reactor heat release occurred in the inner reflector annulus, about 2 percent in the outer reflector annulus, and about 1 percent in the pressure shell. These are average values, and because of the change in energy attenuation through these pieces, passages in the individual pieces do not all receive the same amount of heat. In fact, even for two similar passages, the one receiving the greater heat input will undergo a greater change in momentum pressure drop, and hence the two passages will have different temperatures and flow rates, which leads to the flow-maldistribution problem.

*Theoretical background.*—When an appreciable change in density occurs in the coolant as it flows through a reactor, the distribution of fluid among parallel passages may be affected by a number of things. An analytical study of the variations in outlet fluid temperatures and maximum tube-wall temperatures resulting from nonuniformity of heat flux, mass-flow rate, tube shape, or tube dimensions among the members of a group of flow passages is presented in reference 26. All these factors are interrelated and dependent upon the physical properties of the coolant. Analytical expressions for partial derivatives that measure flow variations are determined for a number of situations and are applied to the study of water



CS-25422

FIGURE 44-21.—Simulated reflector piece for maldistribution studies.

flowing through a system at supercritical pressure. In the example, if one tube should receive 1 percent more heat than its neighbors, the fluid outlet temperature would be  $67^{\circ}\text{F}$  hotter, the wall temperature would be increased  $80^{\circ}\text{F}$ , and the flow rate reduced 3.75 percent.

*Experimental apparatus.*—In order to study reflector heat transfer and flow maldistribution during reactor startup, a simulated aluminum reflector segment was used. A photograph of the test section installed in the test facility and a sketch of the cross section, including the hydrogen passages (circular and annular), are shown in figure 44-21.

Contemplated instrumentation for a typical passage will include that for inlet and outlet plenum temperatures and pressures, static pressures along the tube, and tube-exit pressure. From the exit total and static pressures, the relative flow rates can be determined. Metal temperatures at several planar locations will also be obtained. Cameras will be provided to photograph the inlet and outlet plenums.

*Calculation of reflector design parameters.*—One of the objectives of the test program is to compare experimental parameters, such as individual passage flow rates, bulk temperatures, heat-transfer coefficients, pressure drops, and metal temperatures with purely analytical calculated values. The design of workable reactors for nuclear rockets requires the ability to predict these parameters accurately.

The largest contributor to the difficulty of making these predictions is the interdependence of metal temperatures and coolant temperatures. As previously mentioned, for flow

systems with multipassages, variations in heat flux into the fluid produce maldistribution of flow in the passages. The calculation of this heat flux under both transient and steady-state conditions is dependent upon the metal temperatures, which in turn are dependent upon the boundary conditions (fluid temperature and heat-transfer coefficient) existing at a given axial location.

For one passage and the material surrounding it, iteration techniques are thus required to obtain material and coolant temperatures that are compatible, in terms of heat flux, out of the material and into the coolant. If this situation is compounded with several passages that must be handled simultaneously, a very complex mathematical procedure is definitely required.

The procedure that would be required for a part of a possible reflector design will be described so that this complexity may be illustrated more clearly. The reflector segment being considered, which for cooling and fabrication purposes could conceivably be divided into an inner and an outer reflector section surrounded by the pressure vessel, is represented in figure 44-22. A cooled control rod is considered as being located in the outer reflector section.

If the control rods are assumed to be evenly spaced, symmetry can then be used to reduce the complication of calculations. Figure 44-23 shows this symmetrical section and indicates how this section can be further broken down into individual symmetrical parts. These parts are still related through the same boundary conditions at adjoining coolant passages. For temperature solutions, each symmetrical part can be divided into nodal points, and calcula-

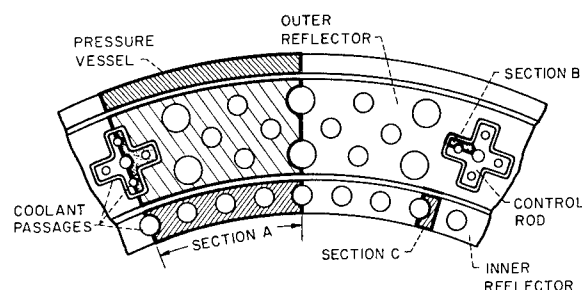


FIGURE 44-22.—Typical reflector segment showing symmetric arrangement of individual parts.

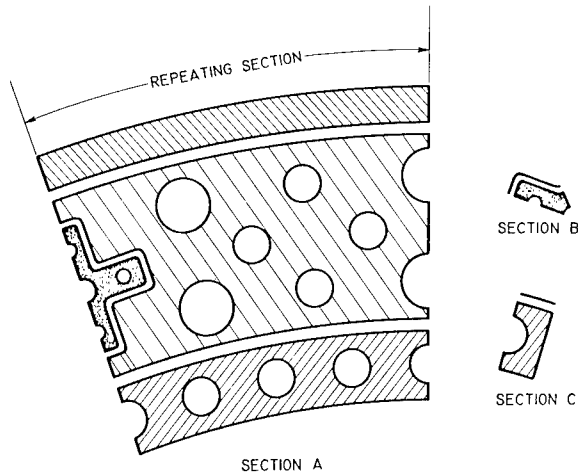


FIGURE 44-23.—Individual symmetric parts within symmetric system.

tions can be made that utilize the appropriate equation listed in figure 44-24.

High-speed-electronic-computer programs can be and have been set up to solve these heat-transfer equations for a three-dimensional body. As discussed in the preceding paragraphs, however, necessary input to this type of program is the boundary conditions (coolant temperature and heat-transfer coefficient). Other programs can be written to calculate these values, but part of the required input for these programs is heat flux into the coolant. Iteration between these two types of programs could result in final numbers. Ideally, both programs would be combined into one large overall program. Either approach results in the previously men-

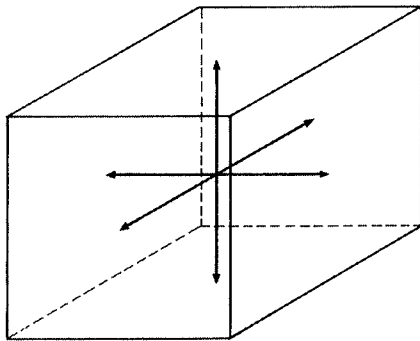


FIGURE 44-24.—Typical nodal point. Applicable equations for calculating metal temperatures are as fol-

lows: transient,  $\nabla^2 T = \frac{1}{\alpha} \frac{dT}{dt}$ ; steady state,  $\nabla^2 T = 0$ .

tioned complex mathematical procedure. Even with the use of high-speed computers, the time to perform these calculations becomes rather lengthy and correspondingly expensive. This calculation procedure, however, will be used until an improved method becomes available.

*Experimental results from reflector segments.*—A few preliminary experimental transient runs with the simulated reflector segment shown in figure 44-21 have been made with liquid nitrogen and liquid hydrogen as the fluid. These experiments demonstrate a problem in multiple-parallel-passage geometries that was not mentioned in the preceding paragraphs.

In an actual system, the flow passes through the nozzle cooling passages before it enters the reflector, and often there are abrupt changes in flow direction at such interface locations as the connection between the nozzle and the reflector. During the startup transient, gas and then liquid enter the reflector (see fig. 44-5) from the nozzle coolant-passage discharge.

The experiments were run with the fluid, first gas and then liquid, entering the inlet plenum at a position  $90^\circ$  to the flow direction in the test section; a structure that approximately simulated a mechanical support structure found in an actual system was included.

Enlargements of high-speed motion pictures showing views of the test-section inlet are shown in figure 44-25. The photographs show liquid nitrogen entering the inlet plenum, impinging on the diagonal structural member, flowing around the end of it, and then into the upper half of the chamber in which the nitrogen entered the five cooling passages. Near the beginning of the transient, gross maldistribution occurred because of the presence of the structural member, which threw most of the liquid into test-section passages at the right side of the photographs. Much of this maldistribution could be avoided by more careful engineering design; the phenomenon, however, indicates another fundamental problem. Any passage that happens to have more liquid flowing through it initially than through any other passage during the start transient (when the reflector material is cooling down) will tend to continue to have more liquid flowing through it because that part of the reflector system will be colder than the

FLUID-FLOW AND HEAT-TRANSFER PROBLEMS

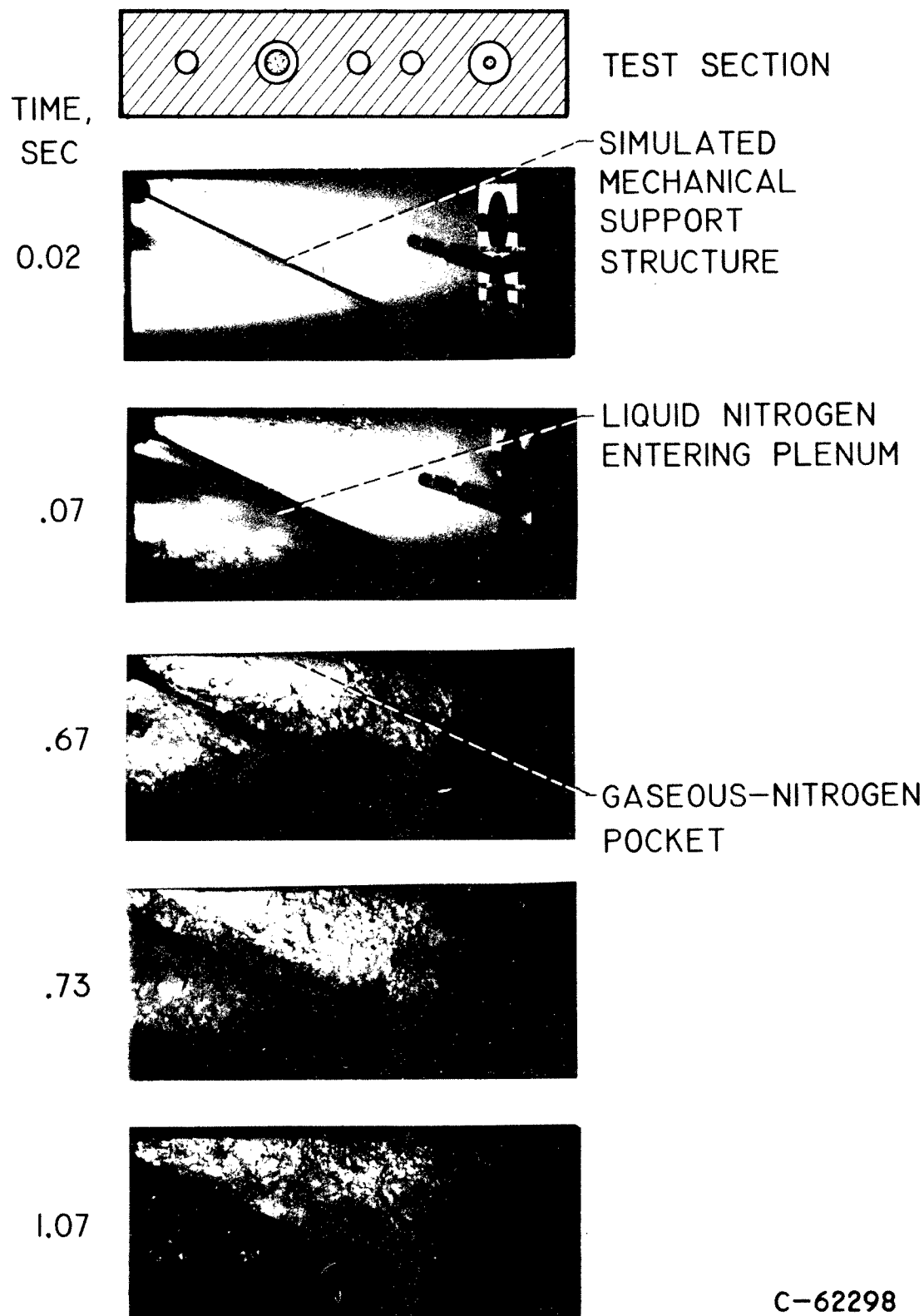


FIGURE 44-25.—Enlargements of high-speed motion pictures of inlet plenum of simulated reflector piece showing flow phenomena during startup transient.

other parts. This factor complicates the calculations of reflector geometries and requires knowledge of the initial flow distribution in the system.

#### Force or Gravity Effects

The use of the nuclear rocket is proposed for deep-space probes and interplanetary travel. For such missions, a rocket capable of several restarts is necessary. Since the initial rocket startup will probably take place in an Earth orbit and subsequent starts will occur in space, knowing what effects a low- or zero-gravity condition will have on the rocket flow system, especially during startup, is essential. This, of course, involves a knowledge of boiling heat transfer under low-gravity conditions.

Numerous investigations into low-gravity effects have been and are being made. According to reference 3, nucleation and the rate of bubble growth are not affected by a reduction in the gravitational force field; the rate of vapor removal, however, depends upon the nature of the force field. In forced convection flow, the velocity gradients are highest near the solid surface. Bubbles in this region are subjected to lift forces and tend to travel toward the tube center. The vapor, concentrated in the high-velocity region, moves at a faster rate than it would under a uniform distribution. The result is that the mean velocity of the vapor is larger than that of the liquid. The ratio of these mean velocities is the slip velocity  $u_g/u_l$ . Reference 3 further states that in the bubble-flow region, the slip velocity exceeds the value of 1, which is the slug-flow-region value for this factor in a low-gravity field.

Under force fall, a definite decrease in heat flux occurs in all boiling regions except perhaps the nucleate boiling region (ref. 28). This conclusion was based on short-time force-fall tests of boiling heat transfer to liquid nitrogen at atmospheric pressure from a 1-inch-diameter copper sphere. One possible explanation for the fairly large heat fluxes obtained in these short-time tests has been offered: The momentum of the liquid set up by the action of vapor departing from the sphere during 1-g conditions may continue to sweep vapor from the vicinity of the sphere under the zero-gravity conditions. This situation would be most pro-

nounced in film boiling. In addition, this well-defined maximum heat flux in saturated liquid nitrogen under zero-gravity conditions may be linked to the dynamics of bubble formation and growth; that is, the hydrodynamic forces of bubble growth far overpower the buoyant forces.

Many other zero-gravity investigations of nucleate and pool boiling, with various fluids, have been made. Many have been limited to the study of the flow phenomena of fluids contained within a sphere or Dewar. The problem of concern in the nuclear rocket, however, deals with a flowing system. One such investigation for a water system was reported in reference 29. A forced-flow water heat-transfer apparatus using a resistance-heated tube was flown in an airplane for a 15-second near-zero-gravity test. The test was conducted to determine whether a zero-gravity environment influenced the nature of two-phase-flow patterns; such changes would be observed in the heat-transfer results. An instability, initiated by a momentary interruption of flow, forced the transition from a highly subcooled bubbly flow to a slug-type phenomenon that resulted in a 16-percent increase in local heat-transfer coefficients.

Not only must the effects of low gravity on flow and heat transfer be known, but the effects of high-gravity fields are also of interest, since the nuclear rocket will pass through such environments in its proposed missions. Not many investigations in this area have been made. Pool boiling of distilled water at approximately atmospheric conditions up to 21 g's has been tested (ref. 30). The influence of acceleration was greatest in heat fluxes up to 50,000 Btu per hour, where a transition in the convective mechanism apparently took place. The acceleration decreases the value of  $T_w - T_{sat}$  required for a given flux. Above this heat flux, a reversal of the effect of acceleration on  $T_w - T_{sat}$  was observed. Data of reference 31 agree with those of reference 30.

As noted previously, the nuclear-rocket low-gravity problem deals with a flowing system. Reference was made to one such investigation using water. An experiment is currently being planned at Lewis that will involve a hydrogen



flowing system. The multiple-passage reflector simulation shown in figure 44-21 is being prepared for insertion into a so-called drop package. This package will be dropped from a drop tower, and a free fall of about 2 seconds will be attained. Recorded data and motion pictures taken during this test will be compared with similar data obtained for the same test section in a 1-g experiment.

One phenomenon that might be expected is that the initial flow distribution into a multiple-passage test section might be different in a zero-gravity environment than in other gravity fields. Maldistribution of flow in the passages as previously discussed may therefore be different.

### NOZZLE

The design of a regeneratively cooled rocket nozzle is based on calculation of a balance between the heat flux from the hot gas to the nozzle wall and from the nozzle wall to the coolant. Such calculations require accurate estimates of heat-transfer coefficients on both the hot gas and the coolant sides of the nozzle. In addition, accurate estimates of coolant pressure drop are also necessary. An excellent review of the nozzle-design problem and the shortcomings of current nozzle-design methods is given in reference 12.

A nozzle design is usually determined for full-power operating conditions. Startup times for nuclear rockets, however, are much longer than those for chemical rockets, and the serious problem of possible choking in the cooling passages at the nozzle throat during startup must not be overlooked. The tapered cooling passages have minimum cross-sectional area at the throat. A nozzle intended for use on a nuclear rocket should therefore be designed for full-power operating conditions and then for possible choking at startup. A redesign may then be required.

Current design methods are dependent upon the hot-gas-side heat flux, and to date adequate methods for estimating this flux are not available. Two methods are currently being used, but each has discrepancies. The first uses a turbulent-flow heat-transfer correlation that assumes a constant coefficient for the entire nozzle and uses the local diameter; this method

is an adaptation of the correlation originally determined for a constant-diameter pipe in which there are no appreciable axial pressure gradients. The determination of the Reynolds number for use in the correlation equation, moreover, involves a term  $\rho_s V_s$  that may be calculated in two ways, a one-dimensional or a three-dimensional determination of  $\rho_s V_s$  at the wall. Reference 12 explains discrepancies encountered in these calculations and how they differ for conical or bell-shaped nozzles. The

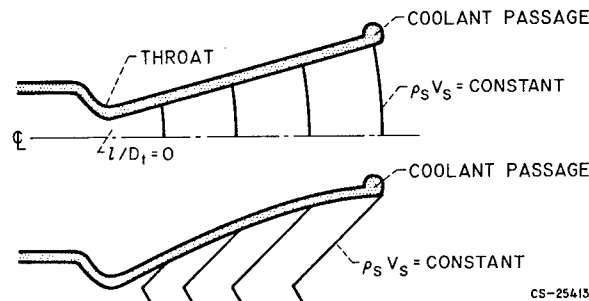


FIGURE 44-26.—Surfaces of constant  $\rho_s V_s$  for typical conical and bell nozzles.

lines of constant  $\rho_s V_s$  for typical conical and bell-shaped nozzles are shown in figure 44-26, taken from reference 12. No essential difference exists between a one-dimensional calculation (a point on the centerline) and a three-dimensional calculation (a point at the wall) for the conical nozzle. On the other hand, for the bell-shaped nozzle, a considerable difference in the one- and the three-dimensional calculated values of  $\rho_s V_s$  will exist. The three-dimensional procedure has been recommended for bell-shaped nozzles.

The second approach to gas-side heat-flux calculations involves boundary-layer solutions. For turbulent flow, only approximate boundary-layer solutions exist. Two distinct approaches to this type of solution are also currently employed. The first case assumes that the boundary-layer thickness is zero at the core end of the nozzle; the second case assumes that there is a finite boundary-layer thickness at this point.

A comparison of calculated and experimental values of heat-transfer coefficient for the bell-shaped nozzle is presented in figure 3 of reference 12 and is summarized for several locations along the nozzle as follows:

## NUCLEAR PROPULSION

Location along nozzle, $l/D_r$	Comparison of calculated with experimental heat-transfer coefficients			
	Turbulent-flow solution		Boundary-layer solution	
	One-dimensional determination	Three-dimensional determination	Case 1	Case 2
-1.9	40 percent low -----	40 percent low -----	30 percent low	45 percent low
0	Good -----	Good -----	35 percent high	16 percent high
>.5	50 percent low -----	23 percent low -----	35 percent high	16 percent high

The degree of accuracy varies with distance from the nozzle throat. The turbulent-flow correlation underestimates experimental data in both the convergent and the divergent sections of the nozzle and agrees with experimental data at the throat. The largest discrepancy (50 percent) is in the divergent section. The boundary-layer solutions underestimate experimental data by as much as 45 percent in the convergent part of the nozzle and overestimate the experimental data by as much as 35 percent in the divergent part of the nozzle. Experimental data are required in order to determine the type of variation that the coefficient in the turbulent-flow correlation should follow.

The preceding discussion illustrates inadequacies in nozzle design heat-transfer relations. For nuclear rockets, in which nozzle-throat heat fluxes may be twice those for chemical rockets, and in which nozzle wall temperatures may be limited to 1600° or 1800° F and temperature differences greater than 2000° F are required between the nozzle wall and the hot gas, the nozzle cooling and design problem become more severe. Hot-gas-side nozzle heat transfer must be more thoroughly investigated.

Coolant-side heat transfer is similar in both

nozzle and reflector, and the latter has been discussed in some detail in a preceding section.

### CONCLUDING REMARKS

Core, reflector, and nozzle heat-transfer and flow problems that require solutions before adequate nuclear rockets can be designed are presented. Core problems, such as maintaining allowable temperatures and calculating thermal stresses, are included. Core flow-stability problems are also discussed. Reflector two-phase- and gaseous-hydrogen heat-transfer and pressure-drop correlations are illustrated with experimental data. Examples of oscillations and maldistributions in the reflector and discussion of gravitational effects on flow and heat transfer are included. Limitations of nozzle-design methods are reviewed.

A careful investigation of the aforementioned problems revealed that adequate knowledge is not yet available for the determination of satisfactory solutions. More intensive research in such areas as oscillatory flow, maldistribution of flow, two-phase flow, nozzle heat transfer, stress-calculation methods, etc. is urgently needed before improved nuclear rockets can be designed.

APPENDIX—SYMBOLS

$A$	area	$\nu$	Poisson's ratio
$a$	constant	$\rho$	density
$Bo$	boiling number, $(Q/A_s)/(\lambda \dot{w}/A_i)$	$\rho_s$	nozzle stream density
$b$	constant	$\sigma_{th}$	thermal stress
$C$	constant	$\chi_{tt}$	Martinelli parameter
$c$	constant	<i>Subscripts:</i>	
$c_p$	specific heat	av	average
$D$	diameter	$b$	bulk
$d$	constant	calc	calculated
$E$	Young's modulus	exp	experimental
$f$	frequency	$f$	film
$G$	mass-flow rate, $\dot{w}/A_i$	$fm$	film mean (for two phase)
$g$	gravitational constant	frict	friction
$H$	enthalpy	$g$	gas
$h$	heat-transfer coefficient	$i$	inner
$k$	thermal conductivity	in	in
$l$	length	$l$	liquid
$\Delta l'$	distance between end of heater and temperature sense point in unheated section	$\Delta l$	incremental length
$Nu$	Nusselt number, $hD_i/k$	$m$	metal
$Pr$	Prandtl number	max	maximum
$p$	pressure	melt	melting point
$Q$	heat-flow rate	mom	momentum
$Re$	Reynolds number	$o$	outer
$T$	temperature	out	out
$t$	time	$pg$	perfect gas
$u$	velocity	ref	reference
$V_s$	nozzle stream velocity	$SP$	single phase
$W$	weight	$s$	surface
$\dot{w}$	flow rate	sat	saturated
$X$	distance to interface	$T$	total
$x$	quality	$t$	nozzle throat
$\alpha$	coefficient of linear expansion	$TP$	two phase
$\delta$	distance between $T_{max}$ and $T_w$	$v$	per unit volume
$\lambda$	heat of vaporization	$w$	wall
$\mu$	viscosity	<i>Superscript:</i>	
		'	pseudo-two-phase quantities

REFERENCES

1. SPARROW, E. M.: Temperature Distribution in an Internally-Cooled Heat-Generating Solid. Jour. Heat Transfer, ser. C, vol. 82, Nov. 1960, pp. 389-393.
2. BUSSARD, R. W., and DELAUER, R. D.: Nuclear Rocket Propulsion. McGraw-Hill Book Co., Inc., 1958.
3. HENDRICKS, R. C., GRAHAM, R. W., HSU, Y. Y., and FRIEDMAN, R.: Experimental Heat Transfer and Pressure Drop of Liquid Hydrogen Flowing through a Heated Tube. NASA TN D-765, 1961.
4. ZUBER, NOVAK, and FRIED, ERWIN: Two-Phase Flow and Boiling Heat Transfer to Cryogenic Liquids. ARS Jour., vol. 32, no. 9, Sept. 1962, pp. 1332-1341.
5. COLLIER, J. G.: A Review of Two-Phase Heat Transfer. CE/R-2496, British AERE, 1958.
6. MARTINELLI, R. C., ET AL.: Isothermal Pressure Drop for Two-Phase Two-Component Flow in a Horizontal Pipe. Trans. ASME, vol. 66, no. 2, Feb. 1944, pp. 139-151.
7. DENGLE, C. E., and ADDOMS, J. N.: Heat Transfer Mechanism for Vaporization of Water in a Vertical Tube. Heat Transfer Symposium, Louisville (Ky.), vol. 52, no. 18, 1956, p. 95.
8. KREITH, FRANK: Principles of Heat Transfer. International Textbook Co., 1961.
9. TIMMERHAUS, K. D., DRAYER, D. E., and DEAN, J. W.: An Experimental Investigation of Over-All Heat Transfer Coefficient for Condensing and Boiling Hydrogen Films. Paper presented at Int. Heat Transfer Conf., Boulder (Colo.), Aug. 28-Sept. 1, 1961.

# NUCLEAR PROPULSION

10. GUERRIERI, S. A., and TALTY, R. D.: A Study of Heat Transfer to Organic Liquids in Single-Tube Natural-Circulation Vertical-Tube Boilers. Heat Transfer Symposium, Louisville (Ky.), vol. 52, no. 18, 1956, p. 69.
11. HENDRICKS, R. C., GRAHAM, R. W., HSU, Y. Y., and MEDEIROS, A. A.: Correlation of Hydrogen Heat Transfer in Boiling and Supercritical Pressure States. ARS Jour., vol. 32, no. 2, Feb. 1962, pp. 244-251.
12. BENSER, W. A., and GRAHAM, R. W.: Hydrogen Convection Cooling of Rocket Nozzles. Preprint 62-AV-22, ASME, 1962.
13. SCHROCK, V. E., and GROSSMAN, L. M.: Forced Convection Boiling in Tubes. Nuclear Sci. Eng., vol. 12, 1962, pp. 474-481.
14. GROOTHUIS, H., and HENDAL, W. P.: Heat Transfer in Two-Phase Flow. Chem. Eng. Sci., vol. 2, 1959, p. 212.
15. CORE, T. C., HARKEE, J. F., MISRA, B., and SATO, K.: Heat Transfer Studies. Aerojet-General Corp., Sept. 1959.
16. WOLF, H., and MCCARTHY, J. R.: Heat Transfer to Hydrogen and Helium with Wall to Fluid Temperature Ratios to 11.09. Abs. 100, Presented at AIChE Meeting, (Wash., D.C.), Dec. 4-7, 1960.
17. RÖDER, HANS M., and GOODWIN, ROBERT D.: Provisional Thermodynamic Functions for Para-Hydrogen. TN 130, NBS, Dec. 1961.
18. MCCARTHY, J. R., and WOLF, H.: Forced Convection Heat Transfer to Gaseous Hydrogen at High Heat Flux and High Pressure in a Smooth Round, Electrically Heated Tube. ARS Jour., vol. 30, Apr. 1960, pp. 423-425.
19. WRIGHT, C. C., and WALTERS, H. H.: Single Tube Heat Transfer Tests, Gaseous and Liquid Hydrogen. TR 59-423, WADC, Aug. 1959.
20. TAYLOR, MAYNARD F., and KIRCHGESSNER, THOMAS, A.: Measurements of Heat Transfer and Friction Coefficients for Helium Flowing in a Tube at Surface Temperatures up to 5900° R. NASA TN D-133, 1959.
21. THOMPSON, W. R., and GEERY, E. L.: Heat Transfer to Cryogenic Hydrogen at Supercritical Pressures. Vol. 7 of Advances in Cryogenic Eng., 1962, pp. 391-400.
22. LEDINEGG, M.: Instability of Flow During Natural and Forced Circulation. Die Wärme, vol. 61, 1938, pp. 891-898.
23. QUANDT, E. R.: Analysis and Measurement of Flow Oscillations. Preprint 27, AIChE-ASME, 1960.
24. WALLIS, G. B., and HEASLEY, J. H.: Oscillations in Two-Phase Flow Systems. Trans. ASME, ser. C, Jour. Heat Transfer, vol. 83, 1961, pp. 363-369.
25. MEYER, J. E., and ROSE, R. P.: Application of a Momentum Integral Model to the Study of Parallel Channel Boiling Flow Oscillations. Trans. ASME, ser. C, Jour. Heat Transfer.
26. GRUBER, ALAN R., and HYMAN, SEYMOUR C.: Flow Distribution Among Parallel Heated Channels. AIChE Jour., vol. 2, no. 2, 1956, pp. 199-205.
27. GLASSTONE, SAMUEL: Principles of Nuclear Reactor Engineering. D. Van Nostrand Co., Inc., 1955.
28. MERTE, H., and CLARK, J. A.: Boiling Heat Transfer Data for Liquid Nitrogen at Standard and Near/Zero-Gravity. Paper presented at Cryogenic Eng. Conf., Ann Arbor (Mich.), Aug. 1961.
29. PAPELL, S. STEPHEN: An Instability Effect on Two-Phase Heat Transfer for Subcooled Water Flowing under Conditions of Zero Gravity. Paper Presented at Am. Rocket Soc., Inc. Space Power Systems Conf., Santa Monica (Calif.), Sept. 1962.
30. MERTE, HERMAN, Jr., and CLARK, J. A.: Pool Boiling in an Accelerating System. Trans. ASME, ser. C, Jour. Heat Transfer, vol. 83, no. 3, 1961, pp. 233-241.
31. COSTELLO, C. P., and TUTHILL, W. E.: Effects of Acceleration on Nucleate Pool Boiling. Paper Presented at AIChE-IMI Meeting, Mexico City, June 1960.

## 45. Problems in Dynamics and Control of Nuclear Rockets

By John C. Sanders, Herbert J. Heppler, Jr., and Clint E. Hart

JOHN C. SANDERS is Technical Consultant for Development in the Advanced Development and Evaluation Division of the NASA Lewis Research Center. Currently concerned with nuclear rocket research, he has specialized in research on aircraft and nuclear powerplants and propulsion systems with particular emphasis on application of controls to these systems. He attended Virginia Polytechnic Institute, receiving B.S. and M.S. degrees in Mechanical Engineering in 1936 and 1937, respectively. He is a member of the American Society of Mechanical Engineers and the Institute of the Aerospace Sciences.

HERBERT J. HEPPLER, JR., is Head of the Nuclear Rockets and Control Section of the NASA Lewis Research Center. He is currently working on nuclear rocket engines for NERVA and other advanced concepts, particularly in the field of controls and applications of propulsion devices and systems analysis. Mr. Heppler is a graduate of the University of Detroit where he received a B.S. degree in Electrical Engineering in 1951.

CLINT E. HART, Aerospace Scientist in the Nuclear Rocket Dynamics and Controls section at the Lewis Research Center, has performed experimental work on the dynamics and control of turbojet engines and analytical studies on the dynamics and control of chemical and nuclear rocket systems and components. He received his B.S. degree in Electrical Engineering from the University of Michigan in 1948.

The problems and the behavior of a complete nuclear rocket, and, in particular, problems in control, are considered herein. Topics covered are damage limits, performance, stability dynamics, startup, and control selection. Listing of fields where further research and development would be helpful is presented.

### NUCLEAR-ROCKET FLOW SYSTEM

One possible nuclear-rocket flow system is shown in figure 45-1 together with an indication of the control problems. This system is called the hot bleed cycle because the power to drive the pump is derived from hot gas extracted at high pressure from the reactor outlet region.

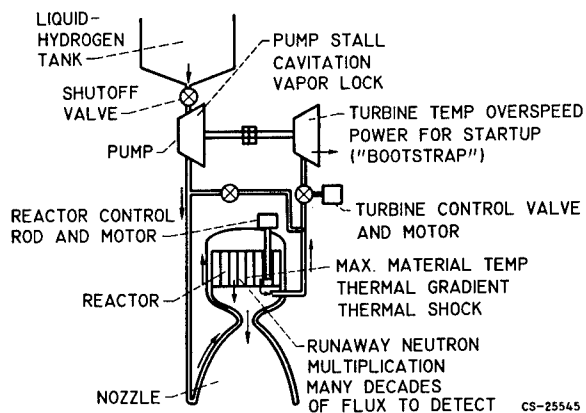


FIGURE 45-1.—Control problem areas and operational limits.

## NUCLEAR PROPULSION

One of the most important operational limits the control must observe is the rate of neutron multiplication; this rate should be slow enough that the control can always move quickly enough to avoid a runaway multiplication. This control function is most stringently demanded in the startup maneuver. Reference 1 presents a good exposition of some of the problems of reactor control for the maneuver of raising the neutron flux from source level to a level that produces significant heat in the reactor.

A second control requirement is that the maximum gas temperature be obtained without damage to the material of the reactor. This control function is most important because the specific impulse is proportional to the square root of the gas temperature, and, consequently, the highest temperature that will not damage the reactor is desired.

Within the core are additional limitations on engine operation. Thermal gradients induce high stresses or may result in hot spots at higher temperature than the material can stand. Similarly, quick changes in temperature can induce high thermal shock stresses.

Another control problem associated with the core is the wide range of neutron flux (10 decades) that must be sensed for safe control.

In regard to the other parts of the system, the pump is limited in operating condition to avoid stall and possible damage during startup. Cavitation within the pump can cause erosion and damage and perhaps lead to a "vapor lock," which is the presence of a large enough quantity of gas in the liquid to impair the pumping capability of the pump. Such a condition can arise in starting if the pump and the lines have not been chilled down. Also, it can occur near the end of powered flight when the propellant that has picked up heat in the tank enters the pump.

### A CONTROL SYSTEM

One possible control system would utilize measurement of reactor outlet gas temperature, reactor outlet pressure, and neutron flux to manipulate turbine valve and control rod. Figure 45-2 is a block diagram of this control scheme. Such a control would fulfill most of the required functions, provided a dependable tem-

perature sensor was available. Also, the flux sensor must provide a good enough signal to permit rapid calculation of the rate of change of flux, particularly during startup.

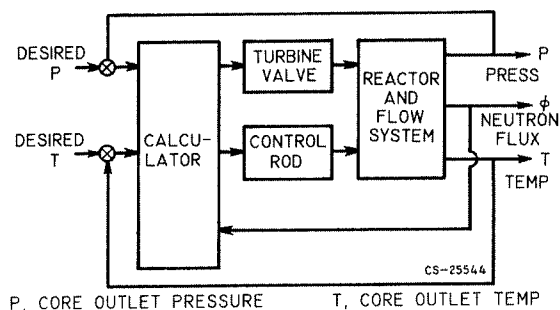


FIGURE 45-2.—A control for maximum power operation of a nuclear rocket.

Selection of the computer functions for dispatching commands to the valve and control rod is aided by a knowledge of the dynamical behavior of the components of the system.

### DYNAMICS OF REACTOR AND FLOW SYSTEM

For control stability purposes (accurate, fast controls may suffer from instability), the dynamical relations among the manipulated and output variables may be expressed in terms of steady-state gain and frequency response. The gains are derived from a steady-state calibration, such as shown in figure 45-3. Here the

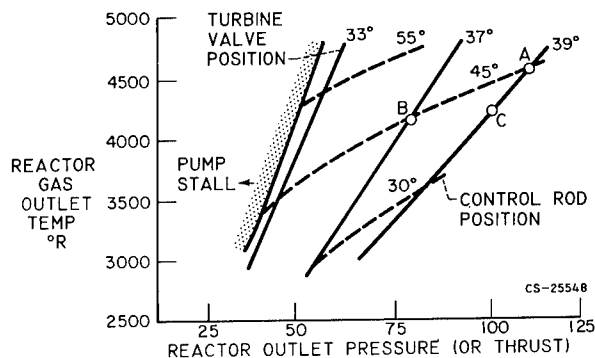


FIGURE 45-3.—Control parameters near maximum power for a nuclear rocket.

steady-state settings of turbine valve and control rod to generated selected value of gas temperature and reactor pressure are shown. The gains about point A in the map are as follows:

# DYNAMICS AND CONTROL OF NUCLEAR ROCKETS

	Valve	Rod
$\partial P/\partial \theta$ , percent/percent-----	1.1	0.7
$\partial T/\partial \theta$ , °R/percent-----	14	21

Incidentally, figure 45-3 gives a view of some damage limits and their relation to controls. Directly observable are the maximum temperature limit and the conditions of pump stall. Derivable from this data is a function of thermal gradient; this gradient increases with pressure at a selected temperature.

An alternate map, replacing temperature with reactor neutron flux, could be prepared for use in the event that sensing of neutron flux proves to be more reliable than temperature sensing.

Of great interest to the control designer is the strong effect of the flow system on the reactor power. For illustration, if the turbine valve is closed from 39° to 37° while the reactor control rod is held fixed at 45°, the pressure and temperature are reduced (when an increase in temperature might be expected). This strong reverse effect almost equals the effectiveness of the control rods and is explained by the large effect of hydrogen in the reactor on its reactivity. Here, then, is a significant difference between this reactor system and others commonly studied. The effect of hydrogen in the core is to make the system less stable (run-away rather than oscillatory) than a reactor in which the coolant does not influence the nucleonic processes.

The time-varying portion of the dynamic relations among control variables is shown in figure 45-4. The information is in the con-

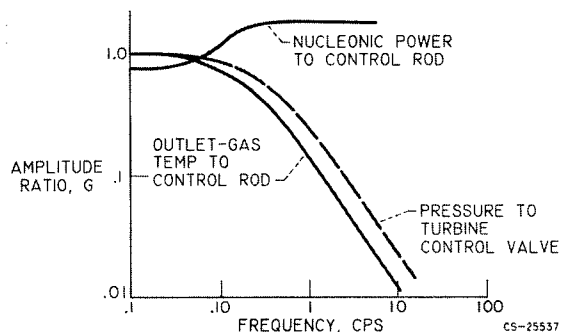


FIGURE 45-4.—Frequency responses among control variables for a nuclear rocket.

venient frequency-response form. This frequency-response information is combined with the steady-state gains to give a complete dynamic description through the following relation:

$$\frac{\theta_{out}}{\theta_{in}} = KG$$

where

$G$  frequency (or time) variant portion of the description

$K$  steady-state gain

$\theta_{out}$  change in output function being observed

$\theta_{in}$  change in input function being disturbed

The response of nucleonic power to control rod position, shown in figure 45-4, is not unlike published reactor behavior, such as shown by Schultz in reference 1. The high-frequency dynamics, above 10 cycles per second, are governed by the mean neutron lifetime between generations and are, therefore, related to the degree to which the reactor is moderated. At low frequency, below 1 cycle per second, the behavior of the nucleonic power differs somewhat from the published literature because the interaction of the hydrogen with the nucleonic process is significant.

Of considerable interest is the fact that, although the system is quite complex, including pump, turbine, heat exchangers, and so forth, the responses of pressure and temperature are reasonably described by a single time constant. Phase measurements show a similar result.

The time constants of the flow system vary approximately inversely as the flow rate. Thus, it is possible to estimate the dynamics at other than maximum power. This approximation is not good for extension down to startup; also, some of the high-frequency dynamics of the reactor are not closely related to the flow system.

## DYNAMICS IN STARTUP REGIME

In the startup transient, several dynamical properties not observable at high power must be considered. Some of these properties arise from the phase change of hydrogen from gas

## NUCLEAR PROPULSION

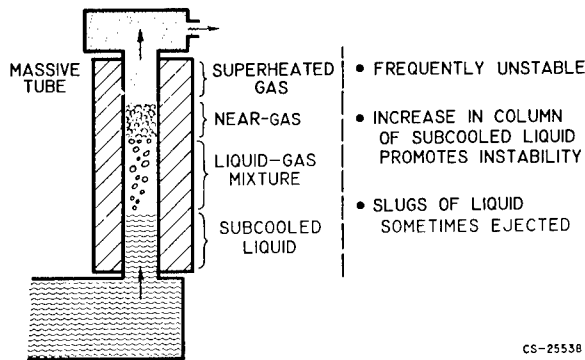


FIGURE 45-5.—Dynamic model of evaporation in cooling jacket.

to liquid at low pressure. The boiling of hydrogen while flowing through a tube has been observed to be quite oscillatory in many instances. This problem is illustrated in figure 45-5. The change from all liquid to a mixture of a liquid and vapor and thence to some sort of gas is accompanied by momentum pressure drop that is a function of the flow, which is, in turn, a function of pressure drop. Several modes of severe oscillation are possible and have been observed. Oscillations violent enough to cause ejection of slugs of liquid from the exit even when the steady-state heat balance would indicate superheated gas have been observed.

Flow instability due to inadvertent stall of the pump is an occurrence that can be introduced by inadequate control of flow and power during startup. Attempt to start flow before the pump is adequately cooled is also a source of unstable flow.

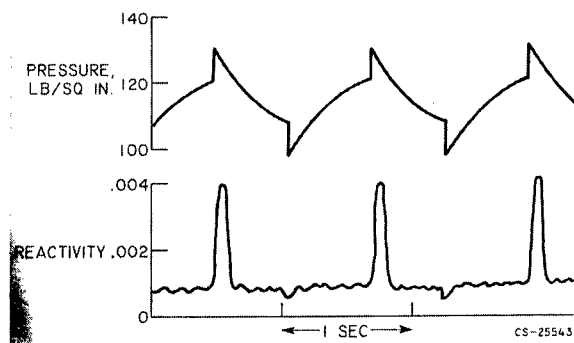


FIGURE 45-6.—An estimated flow oscillation and reactivity excursion.

The dynamics of unstable flow are of great concern because the periodic ingestion of large amounts of hydrogen into the reactor could cause severe and perhaps runaway transients in reactivity. A rough estimate has been made to show the effect on reactor period of a severe oscillation in flow such as might be induced by pump stall. The results are shown in figure 45-6. In this instance sharp spikes in period occur, reaching the dangerously short period of 1 second. Only slight more reactivity would produce periods of milliseconds and possible destruction.

### CONTROL DURING STARTUP

One control scheme for conducting the engine from a condition where hydrogen has been admitted to the core to a terminal condition of full

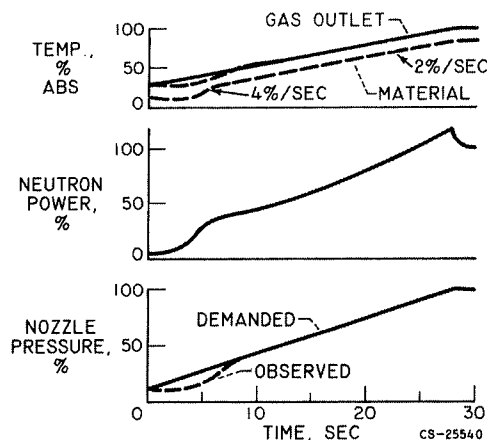


FIGURE 45-7.—Example startup transient.

power would be to use the control of figure 45-2, imposing thereon demanded pressure and temperature scheduled with time. (This system is not necessarily the best or recommended.) The program calls for a linear rise in temperature to maximum temperature in 28 seconds; the linearity is desired to minimize thermal shock. A schedule in pressure to avoid stall and to reach full thrust in 28 seconds is also used. These schedules of demanded pressure and temperature and the calculated behavior of the system are shown in figure 45-7.

The resultant performance shows inadequacy of the control at the start and gives a very rapid



rise in flux corresponding to a dangerously short period and subsequent rapid rate of rise of material temperature, more than twice the desired rate. Similar results have been published for a somewhat different nuclear rocket system by Mohler and Perry (ref. 2).

Thus, the results shown here illustrate that careful selection of the control is needed to avoid trouble in the early part of the startup. Modern control theory appears to be quite adequate at high power near maximum thrust.

Another thought induced by the foregoing results is the possible consequence of simultaneously imposed flow instability and improper control. Such a combination could produce more severe reactor and pump excursions than shown.

#### SENSOR PROPERTIES THAT INFLUENCE CHOICE OF CONTROL

The control system of figure 45-2 depends upon a temperature sensor that is dependable and accurate in a severe environment of up to 5000° R, intense nuclear radiation, and high flow velocities. A temperature sensor meeting these requirements may not be developed for a long time, and other means of control will be sought.

One alternative might be to use the neutron flux sensor to measure the nucleonic power, and, since nozzle pressure is measured, the mean gas temperature can be inferred. This system is particularly attractive since the neutron detector is used to measure nucleonic power and to control the reactor from source level up to a power level where the temperature sensor gives a readable and accurate signal.

The primary difficulty in using the neutron detector to control at maximum power is that it is not accurate enough. This inaccuracy is due not as much to the inaccuracies in the instrument itself as to the nonuniformity of the neutron flux field in regions where the detector might be located. Presence of volumes of hydrogen, changes in control rod position, and many other disturbing factors cause considerable uncertainty in the relation between the flux at a selected point and the reactor nucleonic

power. Furthermore, the reactor that is used in a space vehicle will never have been operated at high power before flight; thus calibration is made very uncertain. If a good temperature sensor is not created, however, the neutron detector system could be used, but reduction of maximum temperature to allow for error would be necessary.

#### SOME PROBLEMS NEEDING FURTHER WORK

As may be seen, treatment of the problems of dynamics and controls in the nuclear rocket is in an embryonic state, and much progress is yet needed. Most of the problems are of a general nature, applicable to a variety of possible designs of nuclear rockets. Some of these problems that could be explored further by independent investigation are mentioned in the following paragraphs.

A reliable temperature sensor capable of surviving in hydrogen at 4000° to 5000° R for 1 hour is urgently needed. Fast response time, less than 1-second time constant, would simplify the control system using the sensor.

A neutron flux detector that could be calibrated accurately to 1 percent could be used in a control system that does not need the temperature sensor. The source of error here seems to be the spatial variability of the neutron flux field in the vicinity of the detector. The calibration difficulty is compounded by the fact that the particular reactor used in a space mission will never have been operated at power prior to the mission.

A statement of the dynamic properties of hydrogen boiling while flowing through an evaporator tube is needed. Progress is being made, but considerably more work is needed, both in experimental observation and in theory.

The mathematical tools used to select optimum control functions should be extended to fit a particular class of large-scale disturbances in nonlinear systems. The particular case is for a dynamical system having square-law relations among some of its parameters (i.e., flow to pressure drop). Current linear techniques seems to be satisfactory for transients around maximum flow.

---

## **NUCLEAR PROPULSION**

### **REFERENCES**

1. SCHULTZ, M. A.: Control of Nuclear Reactors and Power Plants. McGraw Hill Book Co., Inc., 1955.
2. MOHLER, RONALD R., and PERRY, JOSEPH E., JR.: Nuclear Rocket Engine Control. Nucleonics, vol. 19, no. 4, April, 1961, pp. 80-84.

SESSION O

## **Power for Spacecraft**

*Chairman,* NEWELL D. SANDERS

## 46. Power for Spacecraft

By Newell D. Sanders, Charles A. Barrett, Daniel T. Bernatowicz, Thomas P. Moffitt,  
Andrew E. Potter, Jr., and Harvey J. Schwartz

NEWELL D. SANDERS is Chief of the newly organized Space Power Generation Division at the NASA Lewis Research Center, responsible for the advanced developments in nuclear, chemical, and solar power systems for spacecraft. He is a graduate of Virginia Polytechnic Institute, where he received B.S. and M.S. degrees in Mechanical Engineering in 1936 and 1937, respectively. Joining NACA, NASA's predecessor, in 1938, Mr. Sanders has done research on engine fuels, jet engine research instrumentation, aircraft noise, and computer techniques. He recently returned from NASA Headquarters, where he worked for the past four years in the formation and management of space programs. He is an Associate Fellow of the Institute of the Aerospace Sciences, a Senior member of the American Rocket Society, and a member of the Institute of Radio Engineers.

CHARLES A. BARRETT is an Aerospace Scientist at the NASA Lewis Research Center. While at Lewis, he has specialized in research in high-temperature metallurgy. Mr. Barrett received his B.S. degree in Metallurgical Engineering and his M.S. degree in Physical Metallurgy from Case Institute of Technology.

DANIEL T. BERNATOWICZ, currently conducting research on nuclear electric powerplants for space vehicles, is Head of the Nuclear Systems Section of the NASA Lewis Research Center. A native of Worcester, Massachusetts, Mr. Bernatowicz earned his B.S. degree in Mechanical Engineering from Worcester Polytechnic Institute in 1952, and his M.E. in Aeronautical Engineering from Case Institute of Technology in 1958. He is a member of the American Society of Mechanical Engineers.

THOMAS P. MOFFITT of the Turbodrives Section of the NASA Lewis Research Center, has specialized in the field of gas-turbine aerodynamics and currently is doing research in the field of alkali-metal-turbine aerodynamics. He earned his B.M.E. degree from Marquette University in 1951. For three years he taught thermodynamics and fluid mechanics at the United States Naval Academy. He is a member of Tau Beta Pi and Pi Tau Sigma.

DR. ANDREW E. POTTER, JR., is Head of the Reaction Kinetics Section of the NASA Lewis Research Center. A graduate of the University of Florida in 1948 with a Bachelor's degree, he obtained his Ph. D. from the University of Wisconsin in 1953. Dr. Potter has specialized in combustion, solar energy, and upper atmosphere chemistry. He is currently conducting research on the photochemistry of cometary atmospheres, thin-film photovoltaic effects, and ozone releases in the upper atmosphere. Earlier this year, the Cleveland Technical Societies Council presented Dr. Potter the Junior Technical Achievement Award.

HARVEY J. SCHWARTZ, *Aerospace Technologist at the NASA Lewis Research Center, is currently active in research on fuel cells, batteries, and other areas of electrochemical energy conversion. He attended Case Institute of Technology, receiving his B.S. degree in Chemical Engineering in 1954. He is a member of the American Rocket Society and the American Institute of Chemical Engineers.*

### INTRODUCTION

NEWELL D. SANDERS. The electric-power requirements for spacecraft may be classed in two categories, power for auxiliary systems and power for electric propulsion. Examples of the first category are the requirements established by life support, attitude and course control, scientific measurements, and communications systems. These requirements for auxiliary power systems face us today. The demands of electric propulsion are in the future but because of the great size and stringent requirements on these systems, their development will be difficult and lengthy.

Sources of energy that are available to spacecraft are chemical sources, the sun, and nuclear energy from reactors or isotopes. Energy from these sources may be converted to useful electric power by devices or techniques, such as fuel cells, thermodynamic engines, photovoltaic effect, thermionics, and thermoelectricity.

Certain aspects of the interrelation of power requirements, energy sources, and conversion techniques are discussed in this paper.

### MISSIONS ILLUSTRATING REQUIREMENTS

DANIEL T. BERNATOWICZ. Up to now the electric-power systems used in NASA space missions have differed little in basic character. The power required on board most satellites and space probes launched to date has been less than a few tens of watts. This power has been supplied by solar cells with batteries for peak

power demands and for storage for dark periods. For future missions, the diversity among the power systems will be more striking than the similarity. One of the principal factors influencing this diversity is the wide range of power level required. Figure 46-1 shows anticipated maximum requirements for nonpropulsive and propulsive electric power plotted against calendar year. The nonpropulsive power needs grow about a thousandfold in 10 years, from less than 100 watts for early satellites to several hundred kilowatts in the early 1970's. Power requirements for electric propulsion start at about 60 kilowatts for unmanned probes to the planets and extend well above 1 megawatt for manned interplanetary missions.

A few examples will illustrate the need for this wide spectrum of power. Typical of the small solar-powered satellites is Explorer XII

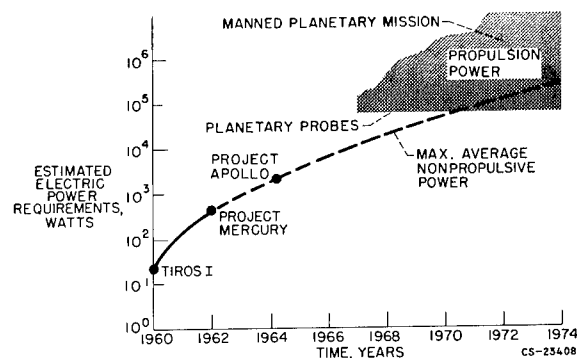


FIGURE 46-1.—Anticipated nonpropulsive and propulsive space-power requirements.

## POWER FOR SPACECRAFT

(fig. 46-2), which was launched in August 1961 to study the zones of energetic particles around the Earth. Solar cells mounted on the four panels furnished about 20 watts of power.

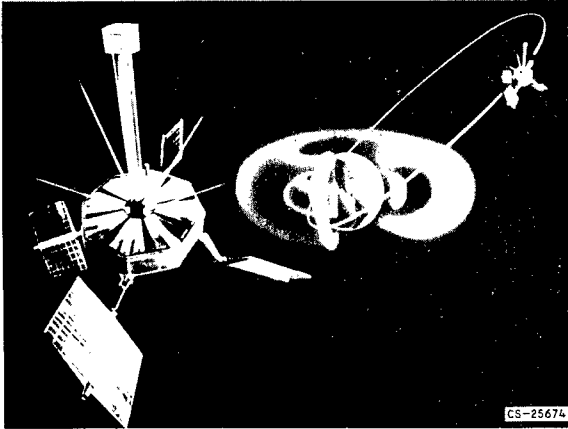


FIGURE 46-2.—Explorer XII.

A mission requiring a few kilowatts of power is Apollo, the objective of which is the landing of men on the Moon in this decade (fig. 46-3). The main power supply will be hydrogen-oxygen fuel cells providing an average power of about 2 kilowatts for 2 weeks. Two of the three astronauts will land on the Moon in a lunar excursion module. The power system for the landing module has not been selected, but it may be a fuel cell or a chemically fueled engine. It must supply several hundred watts for a period of up to 1 week.

An application requiring 20 kilowatts or more of power is the orbiting space platform,

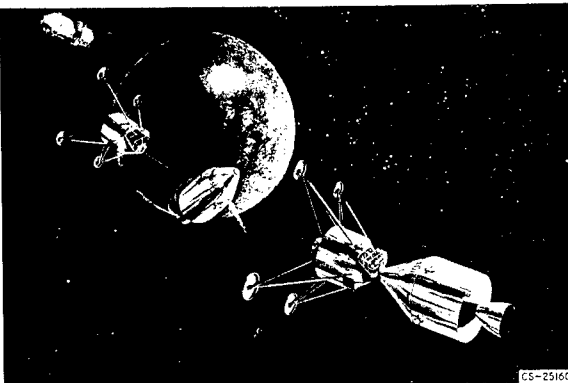


FIGURE 46-3.—Apollo vehicle.

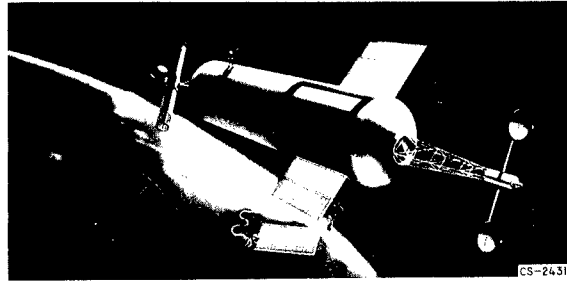


FIGURE 46-4.—Orbiting space laboratory. Estimated power requirement, 60 kilowatts; booster, Saturn C-5; gross weight, 200,000 pounds.

one concept of which is shown in figure 46-4. Because the useful life will have to be at least 1 year, a nuclear or solar power system will be selected. The figure shows men assembling a radiator for rejecting the waste heat from a nuclear powerplant.

When exploration of the distant parts of the solar system is undertaken, even unmanned vehicles may require huge powers. Figure 46-5

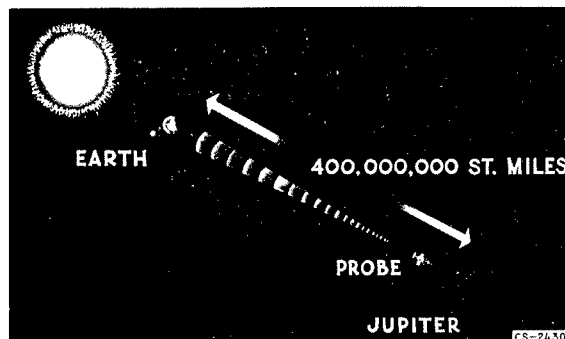


FIGURE 46-5.—Unmanned television probe of Jupiter. Estimated power requirement, 1 megawatt.

shows an unmanned probe to Jupiter for which the power requirement may be as high as 1 megawatt in order to send television pictures back to Earth.

The application that imposes the most difficult requirements on the powerplant is electric propulsion. Figure 46-6 shows one concept of a manned, electrically propelled, interplanetary spacecraft. The most prominent part of an electrically propelled vehicle is the radiator, which rejects the waste heat from the powerplant. For the vehicle shown, the total radiating area is 10,000 to 20,000 square feet. At the near end of the vehicle are the nuclear reactor

and shield. Behind them is the electrical generating machinery and the radiator. At the far end of the vehicle are the living quarters and the electric propulsors. The length of the vehicle is about 600 feet.

A round trip to Mars will take  $1\frac{1}{2}$  to 2 years and the powerplant will have to provide 10 to 30 megawatts of power continuously for this period. Furthermore, the powerplant will have



FIGURE 46-6.—Manned, electrically propelled, interplanetary spacecraft. Estimated power requirement, 10 to 30 megawatts.

to be very lightweight. Only nuclear power systems can fulfill these requirements.

### SOLAR CELLS

A. E. POTTER, JR. All scientific satellites that require power for more than a few months rely on solar photovoltaic cells. Silicon cells have been used exclusively up to the present, although other cell materials, such as gallium arsenide, may eventually be used. Although they are well suited for space use, solar cells could be improved in several areas. In this section are discussed some of these problem areas, specifically, radiation damage to solar cells and the complexity and weight of large solar-cell power systems.

An important problem facing the designer of solar-cell power systems intended to operate in space is radiation damage to the solar cells. The ultimate limit to the lifetime of spacecraft powered by solar cells is set by radiation damage, which occurs principally in the Van Allen belt. The procedure in the past has been to protect the solar cell by covering it with a quartz or sapphire window 10 to 30 mils thick. This protective covering has been sufficient to prolong the lifetime of the unshielded cell in

the heart of the Van Allen belt from a few days to months or years. This lifetime is sufficient for most purposes. The situation however, has been changed by the U.S. high-altitude nuclear detonation, Starfish, on July 9, 1962. This explosion injected large numbers of energetic electrons into the magnetic field of the Earth and formed a new radiation belt around the Earth. The altitude and the contours of the new radiation belt greatly resemble the natural Van Allen radiation belt. A significant difference between the old natural belt and the new artificial belt superimposed on it is that the new belt has about ten times as many energetic electrons as the old one. The new electrons are disappearing rapidly at low altitudes, but very slowly at high altitudes. The mean lifetime of the artificial belt is estimated to be between 10 and 100 years. Since the density of energetic electrons has increased by an order of magnitude, the lifetime of solar cells in the artificial radiation belt (which for convenience is called the new Van Allen belt herein) has decreased by an order of magnitude. Furthermore, this state of affairs is not temporary but will continue for a decade or more. The effect of the nuclear blast on solar-cell lifetime is shown in figure 46-7, where the lifetime (defined herein as the time required for solar-cell output to drop 25 percent) of an unshielded solar cell in the heart of the radiation belt is compared before and after the blast. Lifetime was reduced a factor of 10 by the nuclear blast. The reduction in cell lifetime was shown 3 days after the nuclear detonation, when the British satellite Ariel ceased to operate because of radiation damage

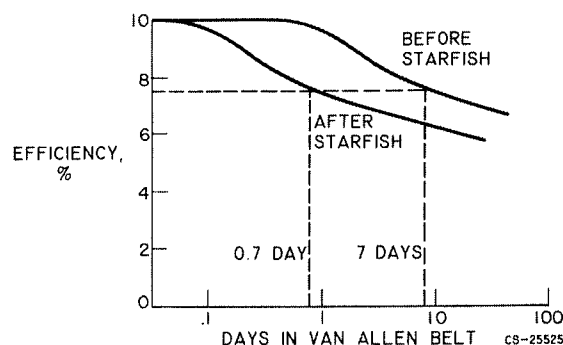


FIGURE 46-7.—Effect of nuclear detonation Starfish on lifetime of unshielded p-n solar cells.

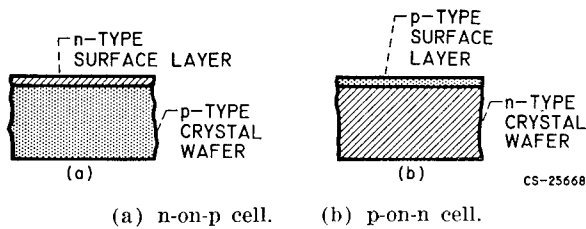


FIGURE 46-8.—The p-on-n and n-on-p type solar cells.

to the solar power supply. Shortly after, two other satellites ceased to operate for this same reason.

There are two ways in which this problem can be solved. The quartz or sapphire shield covers could be thickened. To be effective, however, they become so thick as to make the power system extremely heavy. A better solution is to use more radiation-resistant solar cells. Joseph Mandelkorn, formerly of the Signal Corps, now at Lewis, has discovered how to make radiation-resistant solar cells. These new cells are called n-on-p cells to distinguish them from the older p-on-n cells commonly manufactured. These two types of cells are illustrated in figure 46-8. The old silicon cell, the p-on-n cell, is made by diffusing boron into the surface of an n-type silicon crystal wafer to make a p-type layer on the wafer surface. Hence, a p-on-n cell. The new n-on-p cells are made by diffusing phosphorous into the surface of a p-type silicon crystal so as to make an n-type layer on the surface. Hence, an n-on-p cell. The radiation resistance of the new cells is shown in figure 46-9. In the figure, the lifetime in the heart of the artificial radiation belt for the old p-on-n cells is compared with that for the new n-on-p cells. The lifetime of the new cells is more than an order of magnitude longer than the old cells. Therefore, the lifetime of the new cells in the new radiation belt is comparable to the lifetime of the old cells before the nuclear detonation. The Bell Telstar satellite is equipped with these new cells, and its long lifetime is directly attributable to this fact. It is intended that future U.S. satellites shall be equipped with the new n-on-p cells. Meanwhile, our research on radiation-resistant solar cells continues. Possibilities that seem promising at present are as follows:

(1) Gallium arsenide solar cells: These cells appear definitely to be very resistant to

radiation damage, but are difficult to make with useful conversion efficiencies.

(2) Superpure silicon cells: Use of very pure silicon may make cells more resistant to radiation damage.

(3) Thin-film cadmium sulfide cells: These cells, while of low efficiency, seem to be resistant to radiation damage.

There are many potential uses for large solar-cell power supplies that yield 1 kilowatt or more of electric power. The fabrication of large solar-cell arrays, however, is both difficult and costly principally because of the small size of the cells. Cells are available in areas of only a few square centimeters. Hence, many thousands must be wired together to produce large amounts of power. It has been estimated that 30,000 cells would be required to make a 1-kilowatt array, and that the labor involved in assembling the array would cost in excess of a half-million dollars. Naturally, such an array is complex. Such complexity is very undesirable for any system intended to operate for years in space.

In addition to complexity, large solar-cell power systems are heavy. The silicon cells alone are quite lightweight, but by the time the cells have been shielded from radiation damage, wired together, and placed on a support the weight has increased considerably. An optimistic estimate of the weight of a 1-kilowatt solar-cell array is 100 pounds. A smaller weight would be very desirable.

A further difficulty with large solar-cell arrays is that of packaging them in rockets. Some means is required of folding the array

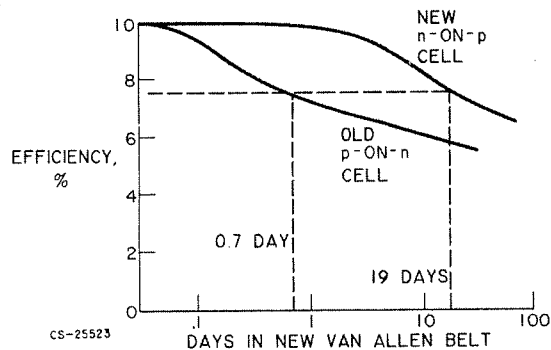


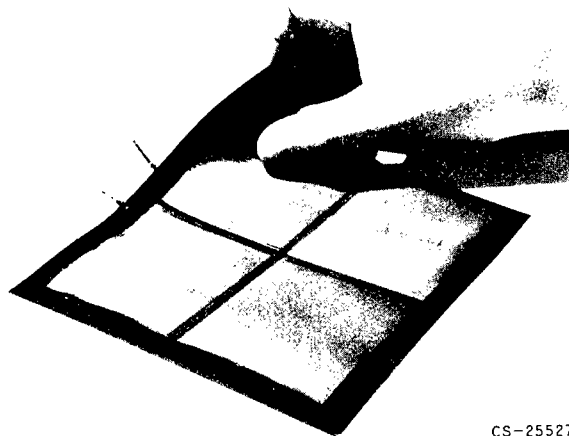
FIGURE 46-9.—Lifetimes in new Van Allen belt for unshielded p-on-n and n-on-p solar cells.



into a small volume for launch, followed by deployment of the array when orbit is achieved. Further undesirable complexity is introduced by this requirement.

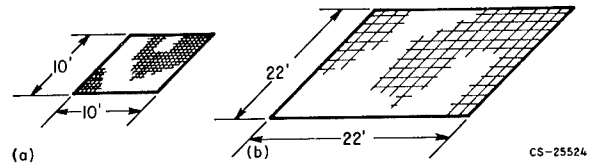
A possible solution to the problems of complexity and weight may be found in the development of large-area thin-film photovoltaic cells. Such cells can be made by evaporation of thin layers of semiconductors onto thin flexible metal or plastic substrates. The familiar selenium cell as used in lightmeters is an example of a photovoltaic cell that is made in this way. Other materials, such as silicon, cadmium sulfide, cadmium telluride, or gallium arsenide can also be used. Thin-film cells are characteristically of low efficiency, not more than a few percent. Because they can be made very thin, however, they are lightweight. Another important advantage gained from the thinness is flexibility. Flexible cells can be rolled up or folded into small volumes suitable for rocket payloads. An additional major advantage of the thin-film cells is the simplicity with which large areas can be made. Evaporation processes are easily adaptable to making very large areas in a single operation. This possibility should greatly reduce the complexity and cost of a large power supply.

Research on such cells is being done at Lewis and is also being sponsored by NASA at non-government organizations. Work is going on with both gallium arsenide and cadmium sulfide



CS-25527

FIGURE 46-10.—Flexible thin-film cadmium sulfide photovoltaic cell.



(a) Silicon cell array. (b) Cadmium sulfide cell array.

FIGURE 46-11.—Comparison of 1-kilowatt silicon solar-cell panel with 1-kilowatt cadmium sulfide film solar-cell panel.

film cells. Promising thin-film cadmium sulfide cells have been made by the Harshaw Company. An example of one of these cells is shown in figure 46-10. This cell is about 6 inches square and has an efficiency of about 1.5 percent. It is thin (about 0.008 in.) and flexible. Cells of this kind have been made with efficiencies of over 2.5 percent. At the present state of the art, thin-film cadmium sulfide solar cells that are 2 percent efficient, flexible, and lightweight (weighing approximately 70 lb/kw of power output) can be made in large numbers. The unshielded lifetime of such cells is estimated at 100 to 1000 days in the heart of the new radiation belt.

It is interesting to compare a large silicon solar-cell array with a large cadmium sulfide film cell array. This is done in figure 46-11. A 1-kilowatt silicon cell array will weigh of the order of 100 pounds and occupy an area of about 100 square feet. About 30,000 cells are required. A 1-kilowatt cadmium sulfide film cell array will weigh about 70 pounds and occupy an area of about 500 square feet. The larger area is required because of the low efficiency of the cells. About 2000 film cells 6 inches square are required. It appears that significant savings in weight and complexity of large arrays can be achieved with the use of cadmium sulfide film cells. The larger area required for the film-cell array is offset by the fact that the film cells are flexible enough that folding into small volumes for launch appears possible. This problem of storage in the rocket with subsequent deployment in space, however, is a major one that must be solved before large power supplies are practical.

Solar-cell arrays are unique in that they provide power at a constant level and only in sunlight. If large peaks of power, or operation in

## POWER FOR SPACECRAFT

darkness are required, batteries must be used for energy storage. These batteries may weigh as much as the solar-cell array itself. Therefore, an important problem area for solar-power supplies is the energy-storage system.

### BATTERIES

**HARVEY J. SCHWARTZ.** In almost every space vehicle launched to date, batteries have been used for energy storage. This energy storage capability is used in several ways.

Secondary batteries, that is, those which may be recharged, like the battery in an automobile, are used in combination with solar cells for orbiting satellites. The orbital paths of these vehicles pass from sunshine to shade on each trip around the Earth. The solar panels supply power during the sun portion of the orbit and additional energy to recharge the batteries. During the shade period, battery power is expended.

Primary batteries, those which are used once and then discarded, as a flashlight cell, supply all the power requirements of the Mercury capsule in manned orbital flight. Batteries are used to supply power for instrumentation, telemetry, communications, and general capsule housekeeping.

Batteries also find application where surges of power are required. Typical of this application is the Ranger vehicle shown in figure 46-12. Here, the solar panels are the main source of power. Battery power is used during the launch phase of the mission and for deployment and orientation of the solar panels. The batteries are then recharged and maintained in a charged state until required to meet peak power-load conditions later in the mission. Thus, batteries are actually used to supplement

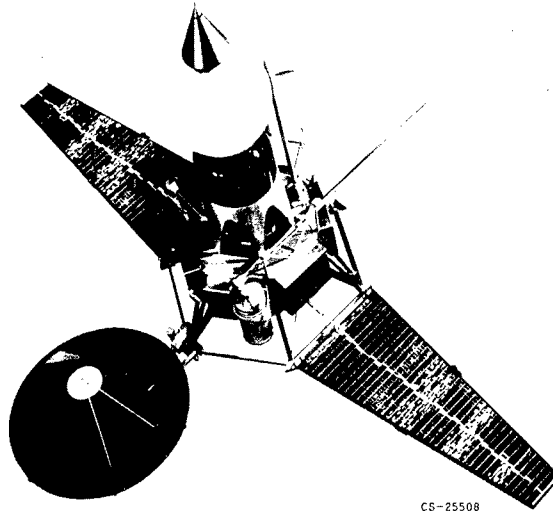


FIGURE 46-12.—Ranger 3 spacecraft.

the power output of the solar array, which results in a smaller, lighter power system.

Smaller and lighter are key words in the design of power systems for space use. The energy densities available from conventional batteries operated at low discharge rates are compared in table 46-I. Several significant points are evident from this table. The most commonly used batteries for space purposes are alkaline electrolyte cells that use nickel-cadmium, silver oxide-cadmium, and silver oxide-zinc as the electrode reactants. Of concern here are energy outputs ranging from 15 to 80 watt-hours for each pound of battery carried on the mission. In addition, a great difference exists in the ability of these cells to withstand the repeated charge-discharge cycling required for secondary-battery applications.

In selecting the proper cell for a particular mission requirement, it is necessary to consider

TABLE 46-I.—*Energy Densities Available from Conventional Batteries*

System	Primary battery			Secondary battery	
	Power density, watt-hr/lb			Actual power density, watt-hr/lb	Shallow discharge life, cycles
	Theory	Actual	Expected maximum		
Zinc-silver oxide, Zn/KOH/AgO.....	193	80	95	40	80-100
Silver-cadmium, AgO/KOH/Cd.....	118	33	40	30	2000-3000
Nickel-cadmium, NiO OH/KOH/Cd.....	99	17	20	7-10	1000-11, 000

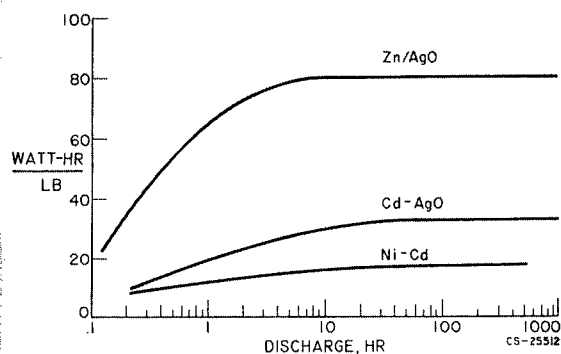


FIGURE 46-13.—Variation of primary-cell capacity with discharge rate at a temperature of 80° F and a voltage drop of 20 percent.

factors other than capacity and cycle life. Characteristics such as storage life, temperature stability, and the effect of discharge rate on capacity must be considered. In general, increases in temperature or discharge rate will decrease capacity and cycle life. Likewise, increasing the depth of discharge beyond the design level will limit cycle life in a secondary battery. One such effect, the variation of capacity with discharge rate is illustrated in figure 46-13. Here, the capacity in watt-hours per pound is plotted against the discharge time, which is the time required to discharge to 80 percent of the initial potential. Capacity is lowest at the high discharge rate portion of the curve and reaches a maximum value at discharge times from 10 to 100 hours.

The problem areas in conventional batteries are readily apparent. Efforts are being made to produce cells with increased capacity under rapid deep discharge conditions, better shelf life, and more favorable charge-discharge characteristics over extended cycling. In addition, new systems that have theoretical energy densities of 500 to 2500 watt-hours per pound are being explored. Realization of only a small fraction of these yields will be marked improvement over today's batteries.

Batteries are not exotic power sources, but they will continue to play an important role in space-power systems. They will be used, even when far more advanced power systems become available. They offer a safe reliable power source for use prior to startup of the main system, for meeting transient load peaks in mis-

sion power profiles, and for emergency power supplies.

### RADIOISOTOPE POWER SUPPLIES

A. E. POTTER, JR. When small amounts of power are required for longer times than available from chemical batteries and solar cells cannot be used, radioisotope heat sources are useful. Radioisotope heat sources may be combined with a thermoelectric converter to produce a source of electric power suitable for use in space. The odd-numbered Snap (Systems for nuclear auxiliary power) generators are this type of power supply. For example, Snap-3 is a 3.3-watt generator, which uses polonium 210 as the heat source and lead telluride elements as the thermoelectric converter. Radioisotope-thermoelectric generators have the disadvantage that they are heavy, 1000 pounds or more per kilowatt, and hence, are not useful for large powers.

A novel idea for the use of radioisotopes is the radioisotope balloon for generation of high voltages. This device is discussed in the paper by Edmund E. Callaghan.

### FUEL CELLS

HARVEY J. SCHWARTZ. If a battery is the power system of today, the fuel cell will be the power system of tomorrow's missions. This is pointed out clearly by the fact that NASA has selected fuel-cell power systems for both the Gemini and Apollo missions.

A fuel cell is an electrochemical device in which the reactants and the reaction products are not stored within the case as they are in a battery. In a fuel cell, reactants are stored separately and fed continuously to the electrodes, and the reaction product is removed continuously. As long as these processes continue, power is generated.

Fuel cells may be classified in a number of ways. There are primary cells, in which fuel and oxidant are continuously used up, and regenerative systems, in which the reaction product is dissociated to regenerate the reactants. Systems may be classified as low-, medium-, or high-temperature according to the cell operating temperature involved. Electrolytes may be aqueous solutions (27 percent potassium hy-

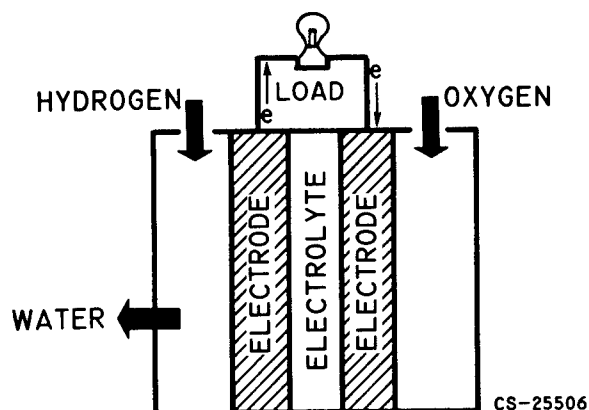
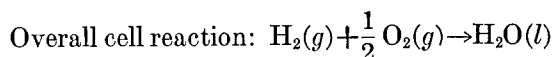
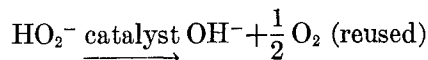
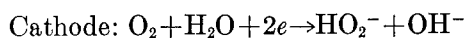
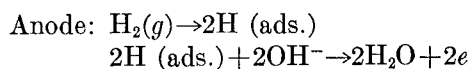


FIGURE 46-14.—Typical hydrogen-oxygen fuel cell.

dioxide is typical), solid electrolytes such as ion-exchange membranes, or fused salts. Electrolytes that are liquids may reside freely between the electrodes or be retained in a suitable matrix. In regenerative systems, the required dissociation may be achieved by adding either thermal, electrical, or photochemical energy.

Primary systems using hydrogen and oxygen as reactants are of greatest interest today. The reason is simple: We know the most about these systems and they work the best. A typical hydrogen-oxygen fuel cell is shown in figure 46-14. A single cell looks much like a battery. It consists of a pair of electrodes between which is an electrolyte. The electrolyte must be not only an ionic conductor but also an electronic insulator. The gases are admitted to their respective electrodes and ionize. Electrons are released at the hydrogen electrode, travel through an external

load to do useful work, and then return to the cell at the oxygen electrode. The simplified individual electrode reactions for an alkaline cell are as follows:



These reactions differ slightly for acid electrolyte cells, but the overall reaction,  $\text{H}_2 + \text{O}_2 \rightarrow \frac{1}{2} \text{H}_2\text{O}$ , remains the same.

It would appear then that all hydrogen-oxygen fuel cells should be the same. They do share common problems of rejecting the heat formed during cell operation and removing the reaction product water.

There are a large number of possible combinations of electrolyte, electrodes, and operating conditions that can be combined to form a workable hydrogen-oxygen fuel cell. Each combination leads to different solutions to the problems cited before. To illustrate this point, consider the ion-exchange membrane fuel-cell system being developed by the General Electric Company for the Gemini mission and the modified Bacon-type fuel-cell system designed by Pratt & Whitney Aircraft Company for the Apollo mission. A comparison of these two systems is given in table 46-II.

TABLE 46-II.—Comparison of Hydrogen-Oxygen Fuel-Cell Systems

Type of system.....	Modified Bacon cell (Apollo).....	Ion exchange membrane cell (Gemini)
Operating temperature, °F.....	500	140
Operating pressure, lb/sq in. gage.....	60	>10
Electrolyte.....	Concentrated potassium hydroxide (solution)	Cation exchange membrane (solid)
Electrodes.....	Sintered dual-porosity nickel.....	Woven metal screen
Operating current density, amp/sq ft.....	200	40
Water removal.....	Evaporation into circulating gas stream	Capillary transport
Heat rejection.....	Circulating gas stream.....	Circulating coolant to individual cells

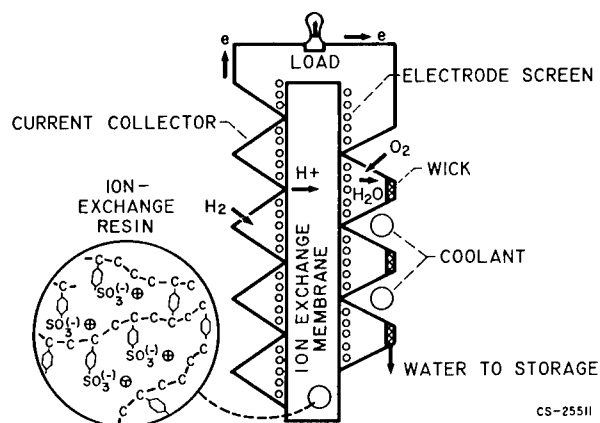


FIGURE 46-15.—Ion-exchange-membrane cell for space application.

The values shown in the table are representative of these systems but are not necessarily design points for the respective missions.

The ion-exchange-membrane fuel cell designed for space use is shown in figure 46-15. The electrolyte consists of a solid ion-exchange resin; a sulfonated polystyrene is shown. The resin has the property of selectivity; it transports cations and does not transfer anions. Hydrogen gas ionizes at its electrode; the ions formed travel through the electrolyte, and then combine with oxygen to form water at the oxygen electrode. Heat is removed by circulating a liquid coolant to each cell. A woven cloth wick is placed in the channel of each oxygen-electrode current collector. Since the water formed has an appreciable vapor pressure at the cell operating temperature, water vapor is transported to the wick, where it condenses.

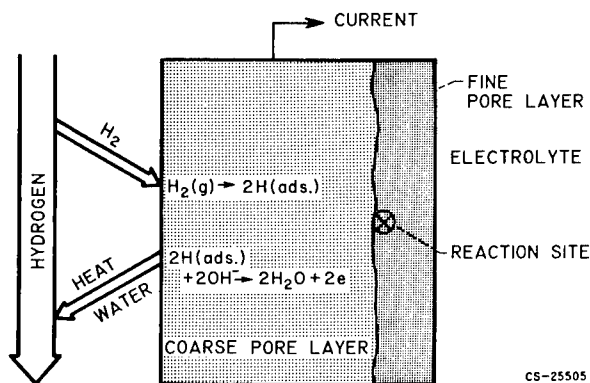


FIGURE 46-16.—Hydrogen electrode processes in Bacon-type fuel cell.

Capillary forces then remove the water to storage.

The modified Bacon-type fuel-cell system to be used on the Apollo mission is a medium-temperature system. The electrolyte, a highly concentrated potassium hydroxide solution, is contained between sintered porous nickel electrodes. In this alkaline cell, water is formed at the hydrogen electrode, and the heat- and mass-transfer operations occur here as shown in figure 46-16. Excess hydrogen gas is circulated past the back face of the porous electrode. Water formed by the cell reaction is evaporated into the gas stream. The stream is cooled to condense the water and the two phases are then separated. Water is pumped to storage while the gas stream is recirculated.

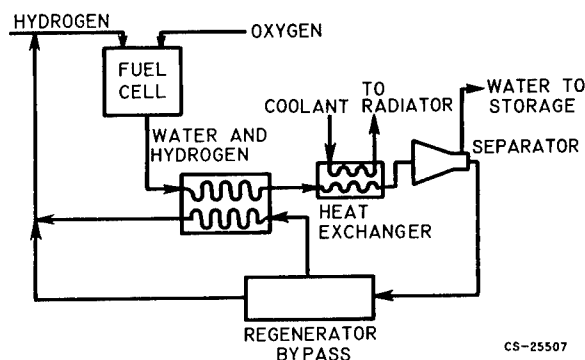


FIGURE 46-17.—Schematic representation of Bacon-type fuel-cell system.

A schematic diagram of the Bacon-type system is shown in figure 46-17. The hot, moist hydrogen stream leaving the cell warms the recirculating gas stream and thus conserves heat. The stream is cooled to condense the water; the waste heat is transferred by a coolant to a space radiator for rejection. The two phases are then separated in a rotating separator capable of operating at zero gravity. The circulating gas serves as a means of transferring heat to the system radiator.

As different as these systems are, they offer the same advantages for their respective missions. The weight of the system and fuel required is considerably less than the weight of the batteries needed to produce the same power output. In addition, both systems are capable of producing potable water as a byproduct,

which can be consumed by the astronauts. This byproduct yields a savings of several hundred pounds of payload on a mission of the Apollo type. Since the Apollo mission as originally conceived called for landing of the fuel cell on the lunar surface, a medium-temperature system has definite advantage with respect to heat rejection. The Gemini mission permits use of a low-temperature fuel cell. Advantage can therefore be taken of the lighter weight offered by the ion-exchange membrane system.

Other types of fuel cells are under active investigation. Regenerative fuel cells are of interest. In these cells a simple energy source such as heat, light, or electricity is used to dissociate the cell product to reactants for recirculation. Since fuel cells offer a higher energy density than batteries, they may some day replace batteries as an energy storage means for orbiting satellites. Electricity from the solar array could be used to electrolyze the water formed during the shade part of the orbit when the fuel cells are in use.

Another interesting facet of electrochemical power generation is the biological generator. Biochemical fuel cells have received much publicity in the popular press lately. While it is unlikely that the results obtained to date justify the amount of attention received, biological systems may some day find use where long life, very-low-power output systems are required.

Fuel cells offer attractive power systems where moderate power outputs are required over periods of days to several weeks. They offer a simple static generating device with highly efficient fuel utilization. They will continue to be important over the next several years.

#### CHEMICALLY FUELED ENGINES

**DANIEL T. BERNATOWICZ.** Several types of chemically fueled engines are being considered for applications similar to those for fuel cells. The weight of these engines is estimated to be considerably less than the weight of the fuel cells, but they are less efficient and, therefore, consume more reactants. For periods of operation up to a few days, the combined weight of engine and reactants is estimated to be less than that of a fuel cell and its react-

ants. An engine could be used as a stand-by power unit to provide power while repairs are made on the main power system, as the main power supply on a vehicle like the Apollo lunar landing module, or as a portable power unit during lunar surface operations, for example, for digging postholes.

#### SOLAR HEAT COLLECTORS

**NEWELL D. SANDERS.** Stored chemical energy is not generally practical as a sustaining power source where the mission duration exceeds 2 weeks because of the great weight of reactants required. Examples of the longer duration missions are orbiting laboratories, manned lunar bases, and communications and weather satellites. The lifetimes of these missions are measured in months or years. For these and similar missions, solar and nuclear power are needed.

Perhaps the most important problem connected with the use of solar energy is the collection of the energy. The Sun's radiation at the Earth's orbit amounts to 125 watts per square foot. The efficiency of conversion may lie in the range between 3 percent to better than 15 percent. To produce 5 kilowatts, the Sun's energy must be collected from an area lying in the range of several hundred to more than 1000 square feet. The launching of such large-area reflectors can be accomplished only by using folding structures which can be placed in small packages for launching and later deployment in space.

The use of thin-film solar cells on a flexible support, as described earlier, is a very promising technique for producing power in the range of several tens of kilowatts. If good new ideas are forthcoming concerning deployment and orientation of acres of this material, power in the megawatt range may be possible.

Collectors that concentrate the Sun's energy are required for thermodynamic or thermionic power systems as they are now conceived. A folding collector for the 3-kilowatt Sunflower system is shown in figure 46-18. The diameter is 32 feet. It consists of rigid petals made of 3-mil aluminum skin bonded to a 1/2-inch honeycomb core. The inner surface is formed to a paraboloid and is polished. The assembled

## POWER FOR SPACECRAFT

mirror focuses the Sun's image into the mercury boiler (not shown) of the power-generating system. The petals are hinged to the frame at the center and can be folded into a 10-foot-diameter shroud for launching. The specific weight of this collector is 0.26 pound per square foot. It is being made by the Thompson Ramo Wooldridge Corporation.

A smaller 10-foot-diameter folding petal reflector using a truss-and-skin-type structure is also being constructed by the Ryan Company. Its specific weight is 0.37 pound per square foot.

A small 4-foot-diameter folding Fresnel reflector has been made by the Allison Division

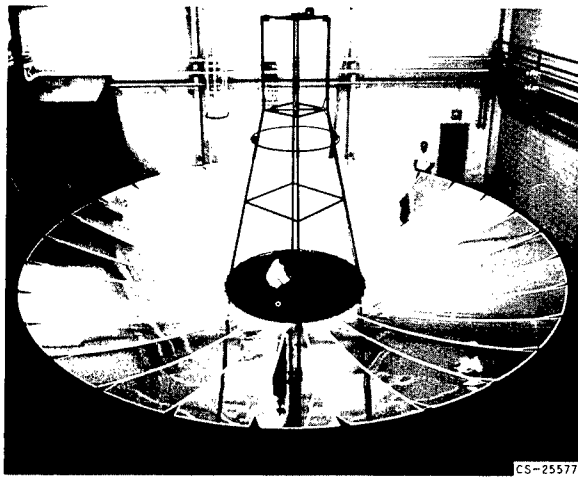


FIGURE 46-18.—Furlable petal collector of aluminum foil bonded to honeycomb core.

of General Motors. The Fresnel reflector resembles a serrated flat plate. This flat shape eases the problem of folding and storing and the serrations give rigidity to the reflector. The Allison unit is made by depositing nickel on a master and then coating the reflecting surface with aluminum. Its specific weight is 0.46 pound per square foot.

Collectors made of flexible inflatable plastic films are especially attractive because of the potential capability of very large size and small storage volume during launch. Figure 46-19 shows such a collector made by Goodyear. It consists of segments or gores made of preshaped Mylar envelopes. The bundle at the bottom of the photograph illustrates the size of the collapsed unit. After launching into space, a



FIGURE 46-19.—Inflatable rigidized collector of foam-backed aluminized Mylar.

foaming plastic is injected into the gores and the collector is caused to take the desired shape. The rigid foam maintains the extended shape of the collector. The collector shown here is 10 feet in diameter and the specific weight is estimated to be 0.2 pound per square foot for a 30-foot collector.

The accuracies of the collectors, just discussed, are expected to be satisfactory when the collectors are used with heat engines operating at relatively low temperatures near 1300° F. In the case of thermionic conversion devices, however, much higher temperatures are required and reflectors of much greater accuracy are needed. Small fixed reflectors might be de-

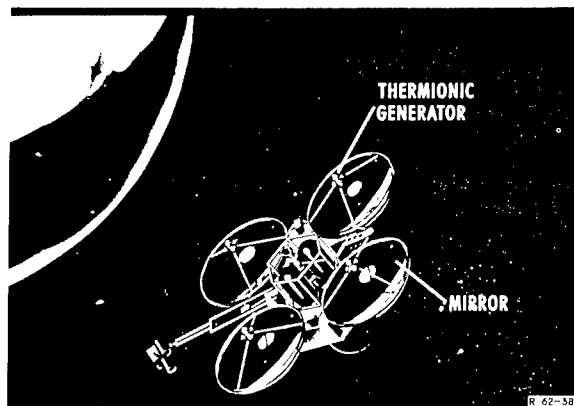


FIGURE 46-20.—Solar thermionic power system.

veloped with the desired accuracy. A 9½-foot rigid metal mirror is under development by the Electro-Optical Systems Company. Several of these mirrors might be clustered as shown in figure 46-20 to give the desired power.

In addition to the highly accurate shape required for the high-temperature systems, accurate pointing systems are required.

### NUCLEAR REACTORS FOR SPACE POWER

CHARLES A. BARRETT. A promising heat source, especially in the kilowatt and megawatt range, for a Rankine cycle system is an alkali-metal, cooled nuclear reactor. In most of the current concepts, a reactor loop is coupled to the Rankine cycle working loop through the heat exchanger.

Fortunately for the space program, alkali-metal reactor technology has been developed for various military and commercial applications so that it can be readily adapted for space nuclear powerplants. These reactors fall into two general classes: (1) a low-temperature system with a fluid-out temperature as high as 1400° F and (2) a high-temperature system with a fluid-out temperature close to 2000° F. The cores in such reactors are quite small; they range from less than 1 foot in diameter (if spherical cores are used) in the lower-temperature reactors to almost 2 feet in the advanced reactors.

The low-temperature system uses either a sodium-potassium alloy or sodium as the coolant and conventional alloys such as stainless steels and nickel-base alloys as the cladding and piping material. The fuel and moderator material is also fairly conventional. A major problem in such systems is to keep the oxygen and carbon contamination low enough in the reactor fluid that corrosion and subsequent plugging is not a problem. This involves proper purification analysis and handling of the alkali metal prior to loading the system and generally trapping the impurities in the metal or gettering the impurities while the system is in operation. Sources of contaminants within the system such as carbon in high-carbon steels must also be minimized. Because the problem can be so severe, continual monitoring of the system, usually by a plugging meter, is neces-

sary. If such precautions are taken, these systems are very reliable. Current commercial powerplants are using this general type of reactor, such as Hallam in Nebraska and Fermi in Michigan, which are designed for many years' operation (though attended)—much longer than the 10,000 hours for space power systems. The original Sea Wolf submarine reactor was also this same type and was operated successfully to design conditions.

Another problem at temperatures above 1200° F, unique to the space powerplant reactors that are to be hydride moderated, is dissociation of the hydride moderator into free hydrogen. Some sort of coating is required to minimize diffusion.

The advanced alkali-metal reactor was designed originally for the now defunct Aircraft Nuclear Propulsion program and was still in an early state of development. The originally designed lifetime was much shorter—of the order of 1000 hours. Because of the very high operational temperatures, a new fluid, lithium, had to be used as the reactor coolant. Because operating temperatures were close to 2000° F, conventional alloys had neither the strength nor corrosion resistance to hold up for even a few hours. In a sense this was fortunate because the system was forced to use and develop the refractory metal columbium (chosen mainly because of its low capture cross section for thermal neutrons) which was a rare metal up to that time, 1956. It appeared that columbium had sufficient strength and corrosion resistance but also some limitations, which made development of such a system lengthy and costly. This advanced reactor now rechristened Snap-50, although quite promising, is far from being truly operational.

Another possibility would be to use gas-cooled reactors with either helium or argon as the coolant. Little work has been done by the AEC on developing small compact gas-cooled reactors. Most of the development has been done on very large reactors for very high power levels. Scaling down both in size and power to compete with liquid-metal-cooled reactors does not seem likely at this time.

The obvious problem in using a nuclear reactor, especially where human beings might be



in proximity, is that of shielding them from harmful radiation. The design of such a system must take this into consideration. The required shield is very heavy. Its weight approaches 20 percent of the system weight. Wide separation of crew and reactor helps to minimize shield weight.

Additional radiation-hazard problems are associated with launch and rendezvous. These problems must be considered in the selection of the power system.

### LOW-POWER RANKINE CYCLE SYSTEMS

THOMAS P. MOFFITT. Either a reactor or a solar heat source can be used for the Rankine power conversion system. Figure 46-21 is a schematic diagram of a typical Rankine cycle utilizing a reactor as the heat source. The example shown is a two-loop system: a liquid loop using a liquid metal as the heat-transport fluid between the reactor and the boiler, and a two-phase loop where a liquid metal is vaporized, expanded through the turbine producing power, condensed in the radiator, and pumped back to boiler pressure by the condensate pump.

The main advantage of the Rankine cycle is that high conversion efficiencies are obtainable, because both heat-transfer processes can be made to take place at essentially constant temperature. The cycle can thus approach Carnot efficiency, which is the theoretical limit between any two given temperatures.

The reliability and life requirements of this type of system are very stringent. The equip-

ment may have to run for years with unattended operation. The principal disadvantages of the Rankine cycle are related to the life problem. These disadvantages are the use of corrosive liquid metals as working fluids and the necessity of using rotating components in the conversion system. The implied problems become more acute with increasing temperatures, which are desired for the high-power systems of the future.

Although the Rankine cycle is attractive in the multimewatt range, it is competitive in the relatively low-power level, the multikilowatt range.

Systems under development in the low-power range include both nuclear and solar heat sources. Snap-2, which is a nuclear Rankine system, uses NaK, a sodium and potassium alloy, as the reactor coolant liquid. The NaK, then, is the heat source to boil mercury, which drives the mercury-vapor turbine. It is designed to produce 3 kilowatts of electric power and operate with a maximum NaK temperature of 1200° F at the reactor outlet. The only other nuclear Rankine space powerplant under development is Snap-8, which is similar to Snap-2, but is to produce 30 kilowatts of electric power and operate at a higher reactor-outlet temperature, 1300° F compared with 1200° F for Snap-2. An example of a solar Rankine space cycle system under consideration is Sunflower, which is shown in figure 46-22. The system utilizes a solar collector to concentrate solar energy to a mercury boiler. Because Sunflower must operate continuously in the sun or shade, a stored heat source is required to boil the mercury during shadow time. Lithium hydride is used for this purpose. The boiler is contained within the lithium hydride thermal storage medium, which absorbs the collected heat during sun time and transfers its latent heat of fusion to the mercury while it freezes during shadow time. The system is to produce 3 kilowatts of electric power and to operate at a maximum mercury-vapor temperature of 1250° F. The mercury technology and alternator from Snap-2 are to be used in Sunflower with minor changes in the power-conversion system.

In the development of the Snap-2 and Snap-8 systems, several major problems have arisen

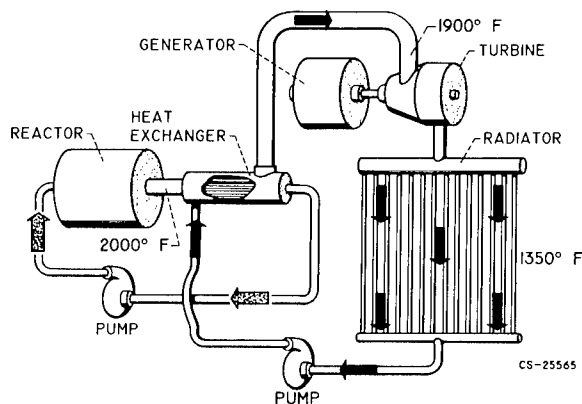


FIGURE 46-21.—Rankine cycle space power system.

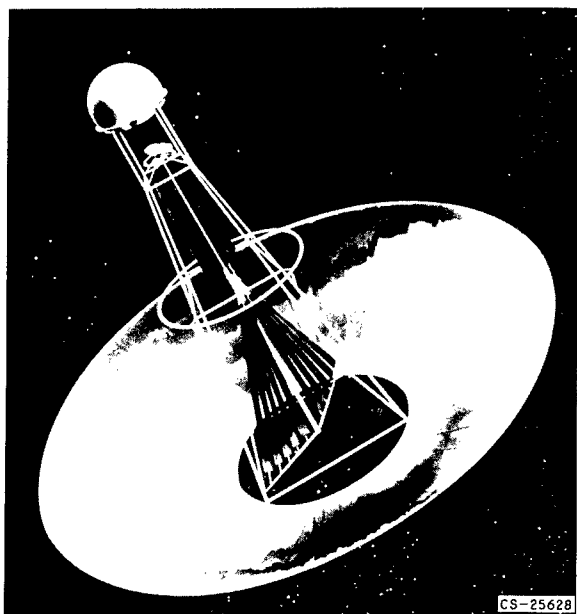


FIGURE 46-22.—Sunflower.

that were either unforeseen or of unforeseen severity. These problems are generally related to (1) bearing integration into a complex thermal package, (2) containment-material problems involving corrosion and system contamination, and (3) boiling heat transfer as affected by tube wetting, temperature, and pressure-drop distribution.

### BRAYTON CYCLE SYSTEMS

DANIEL T. BERNATOWICZ. Another cycle being given serious consideration is the regenerative Brayton cycle. Figure 46-23 depicts schematically a Brayton cycle space power-

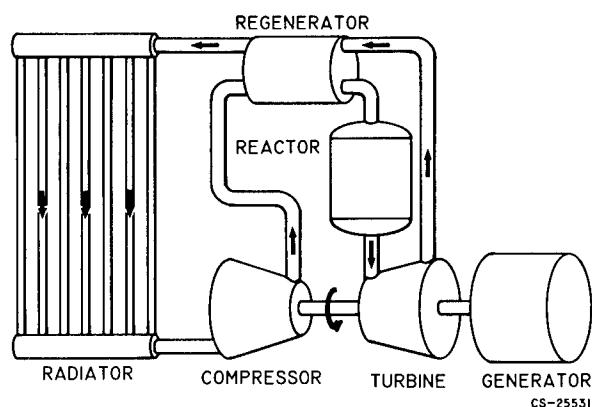


FIGURE 46-23.—Regenerative Brayton cycle space power system.

plant. In the Brayton cycle the working fluid remains gaseous throughout the cycle. Cold gas is compressed in the compressor and passes through a regenerator in which it is preheated by gas from the turbine exhaust. The gas is then heated to its maximum temperature in the reactor and is expanded through a turbine that drives the compressor and an electrical generator. The gas then passes through the regenerator, where it gives up some of its heat to the gas leaving the compressor. More heat is given up in the radiator, and this heat is radiated to space. The cold gas enters the compressor and passes through the cycle again.

A nuclear reactor is shown as the heat source; gas passes through the reactor core. If a gas-cooled reactor is not suitable, a liquid-metal-cooled reactor could be used, with the liquid metal heating the gas in a heat exchanger. Also, a solar or chemical heat source could be used if either fitted the application better.

For the same temperature limits the Brayton cycle is less efficient and requires a larger radiator than the Rankine cycle. For comparable performance, the Brayton cycle system must operate with a higher maximum temperature and would impose more difficult requirements on the heat source. The Brayton cycle is also very sensitive to compressor and turbine performance and pressure losses in the system, more so than the Rankine cycle. The Brayton cycle system is estimated to weigh more than the Rankine cycle system. For nonpropulsive power applications, however, the weight of the powerplant, although important, is not of overriding importance. The absence of zero-gravity problems with a single-phase fluid, the lack of corrosion if an inert gas is used, and the large backlog of experience with turbomachinery suggest that quick development of a reliable Brayton system may be possible. A decision on whether to use a Brayton system will depend on the penalties in system weight and radiator size and on the ease of development relative to a Rankine system.

### POWER FOR ELECTRIC PROPULSION

DANIEL T. BERNATOWICZ. It was pointed out earlier that very lightweight long-lived powerplants capable of furnishing tre-

mendous amounts of power will be required for electric propulsion of manned interplanetary spacecraft. Before these powerplants and associated problems are described, an indication of why there is enough interest in electric propulsion to warrant undertaking such a difficult course is appropriate.

The basic motivation can be seen from a simple consideration of rocket propulsion. Chemical rockets expel a large mass of material at moderate velocities. As the missions become more difficult, the mass of propellant becomes a very large fraction of the mass of the entire vehicle. Obviously, the way to improve the situation is to increase the velocity of the expelled propellant, but in ordinary rockets the velocity is limited by the temperature to which the propellant can be raised. For a given temperature limit, the velocity is higher for propellants of low molecular weight. One improvement over ordinary chemical rockets is the nuclear rocket, in which hydrogen is heated by a nuclear reactor and expelled. In this system, the maximum velocity is limited by the temperature that the reactor can tolerate.

Charged particles can be electrically accelerated to very high velocities, up to near the speed of light. With electric acceleration, the propulsion problem takes on different aspects. Because the kinetic energy in the exhaust rises as the square of the velocity and the thrust only as the first power, the power added to the stream per pound of thrust increases linearly with velocity. In order that the power requirements be reasonable, low-thrust rockets can be used, and the mission objectives must be achieved by operating the thrusters for very long periods, perhaps continuously throughout the mission. In fact, for practical vehicles the thrust is so low that the acceleration is only  $10^{-3}$  to  $10^{-4}$  g. Such vehicles must be launched into orbit by chemical or nuclear rockets and then will proceed to the planets using electric propulsion.

Figure 46-24 shows the results of a study of a mission to send seven men to Mars. A nuclear-rocket vehicle is compared with an electrically propelled vehicle, both starting from an orbit around Earth. Initial gross weight of the vehicle is presented against the time required to perform the mission. For a mission time of

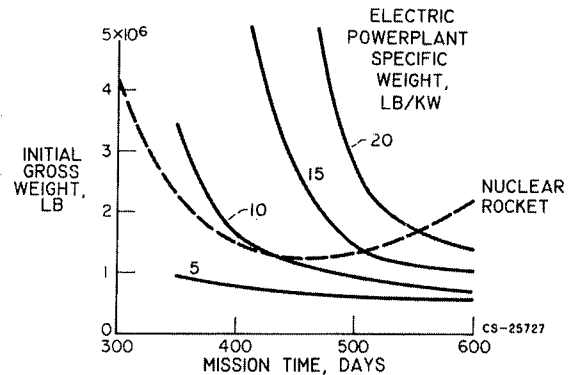


FIGURE 46-24.—Study of seven-man mission to Mars.

about 450 days, the powerplant specific weight must be 10 pounds per kilowatt or less to be superior to the nuclear rocket. If longer mission times can be tolerated, heavier powerplants can be used. Then, however, the powerplant must operate for a longer period of time and the low specific weights are more difficult to achieve. The power level required is 10 to 30 megawatts.

The specific weights shown in this figure are extremely low. The specific weights of systems under development, for example, Snap-2, Snap-8, and Sunflower, range from 70 to 250 pounds per kilowatt. Although enough information is not available to make accurate weight calculations for the advanced systems, studies indicate that such low weights may be possible, but only after enough technology is acquired to permit highly refined engineering design. Only two systems look attractive for this application, the nuclear Rankine turbogenerator system and the thermionic reactor system.

#### HIGH-POWER RANKINE CYCLE SYSTEMS

**THOMAS P. MOFFITT.** Consider the high-power Rankine conversion system utilizing a reactor as the heat source. Such a closed cycle can reject waste heat to space only by radiation, which is an inefficient method from area considerations. Furthermore, the best systems available must reject more than 75 percent of the reactor thermal power as waste heat. Consequently, the radiators for large power systems become massive and may constitute up to 50 percent of total system weight. Therefore, a system is required to maintain this weight with-

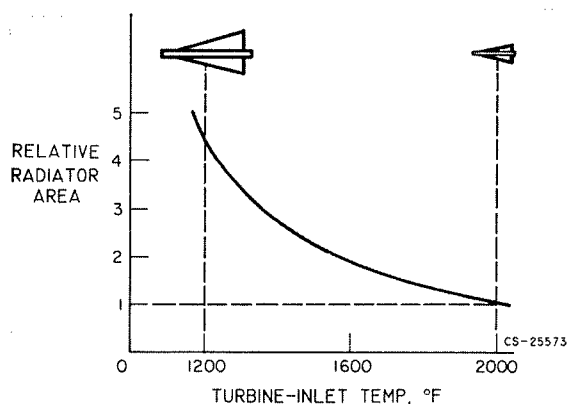


FIGURE 46-25.—Effect of turbine-inlet temperature on radiator area.

in reason. Of the systems available, the Rankine cycle turboelectric system is the only one likely to yield lightweight systems in the near future. The principal unknown in the field of radiator design is the meteoroid damage and protection required. This subject is discussed in the paper by Seymour Lieblein.

The necessity of minimizing radiator weight specifies certain requirements on the system:

(1) The system must operate at extremely high temperatures, 2000° F and higher. Figure 46-25 shows the effect of turbine-inlet temperature on relative radiator area, which is the parameter used to describe radiator weight. More than a fourfold difference in area exists between turbine-inlet temperatures of 1200° and 2000° F. This difference is due to the fact that radiation area is inversely proportional to the fourth power of the absolute radiation temperature. This fact, then, indicates the need for high system temperatures to achieve low system weight. The upper limit on temperature would be limited by either the reactor or the rotating components within the turbine.

(2) The system must use alkali metals as the working fluid. These metals appear to be the most attractive fluids from considerations of such things as heat-transfer characteristics, critical temperature, vapor pressure, and thermodynamic properties.

(3) Refractory-based alloys must be used as the fluid-containment material. At the extreme temperatures involved, the refractories appear to be the best materials to retain strength prop-

erties and also afford corrosion resistance to the alkali metals.

These requirements greatly magnify and generate new problems not encountered in the development programs under way in the low-power field, such as the Snap programs previously discussed. The problems result mostly from the higher temperatures involved and cover both the heat-transfer processes and the rotating components of the Rankine conversion system.

### Heat Transfer

Although the alkali metals have long been recognized for their excellent heat-transfer characteristics, the data resulting from their use have been largely restricted to single-phase liquid flow at temperatures below 1600° F.

Of more significance is the lack of data for two-phase heat transfer, notably forced-flow boiling. In the nucleate boiling regime, where very high heat fluxes are obtainable, the only data available are for nonflowing or pool boiling at temperatures less than 1600° F. Even here, the data can be scattered as much as an order of magnitude. There are no known data available for film boiling of the alkali metals, nor for the critical heating rate in the transition from nucleate to film boiling.

The two-phase problem is further complicated by the requirement of zero-g operation in space. Such problems as flow stability, phase separation, and keeping the desired phase on the heat-transfer surface are magnified. Techniques under investigation include the use of twisted ribbons and wires to sling the liquid phase outward to the heater surface, the generation of vapors by flashing centrifugal separators, and the use of liquid condensers.

There are extensive research programs under way at government laboratories, universities, and within the industry. These projects are expected to provide much high-temperature heat-transfer data in the next 2 to 3 years.

### Rotating Components

*Turbine.*—There are three parameters associated with the turbine that have a gross effect on the radiator weight. These parameters are turbine-inlet temperature, turbine efficiency,

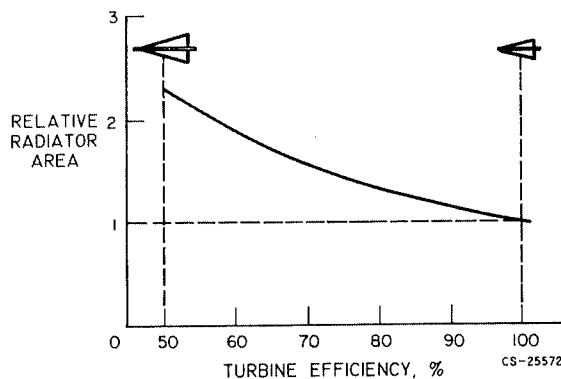


FIGURE 46-26.—Effect of turbine efficiency on radiator area.

and the condition of the vapor entering the turbine. It has previously been shown that more than a four fold difference in radiation area exists with an 800° F difference in turbine-inlet temperature, which indicates the need for high turbine temperatures.

The effect of turbine efficiency on radiator area is shown in figure 46-26. This figure shows the change in required relative radiator area for constant system power output at varying turbine efficiencies. As turbine efficiency increases from 50 to 100 percent, radiator area decreases by a factor of about 2½. In view of the massive size of the radiator, it is apparent that high-performance turbines are a prerequisite to lightweight systems.

The condition of the vapor as it enters the turbine has an important effect upon the radiator weight. The vapor can either be superheated above its boiling temperature, or it can

be saturated, that is, at its boiling temperature. At the saturated condition, the vapor will start to condense as soon as the pressure drops during the turbine expansion process. For a fixed limiting turbine-inlet temperature, figure 46-27 shows the effect of using saturated or superheated vapor at the turbine inlet. A radiator area value of 1 represents a condition of saturated vapor at the turbine inlet. Increasing superheat from the saturated-vapor condition has a marked effect. For example, reducing turbine moisture at the exit from 14 to 4 percent by use of superheated vapor increases the radiator area by a factor of 1.5. Therefore, it appears desirable to use saturated or nearly saturated vapor at the turbine inlet.

The requirements on the turbine of high temperature, high efficiency, and wet-vapor operation impose many severe turbine design problems if good performance and high reliability are to be achieved.

A major factor affecting system reliability is the choice of proper materials of construction. Long-time strength properties are required for the refractory metals considered as containment material. In addition, if different materials are used in the rotating machinery system (shaft, bearings, rotors), a bimetallic condition will exist that could result in severe mass-transfer problems. Since little or no information exists on material long-time strength, corrosion resistance, and fabricability, many problems remain to be solved.

There are additional problems. For example, as the temperature and life requirements increase, allowable design stress decreases. Consequently, turbine-blade speeds must be reduced below present limits. This speed reduction results in an increase in the number of turbine stages required to produce high efficiencies. Although the associated increase in turbine weight may not significantly affect gross system weight, such factors as bearing alignment, clearance allowance for thermal expansion, and moisture-removal techniques become more complex. Figure 46-28 illustrates the moisture formation within the turbine if the condensate is not removed as it forms. As noted, approximately 14 percent liquid, by weight, may be present in the turbine exhaust. The turbine blade material must be able to resist the erosion

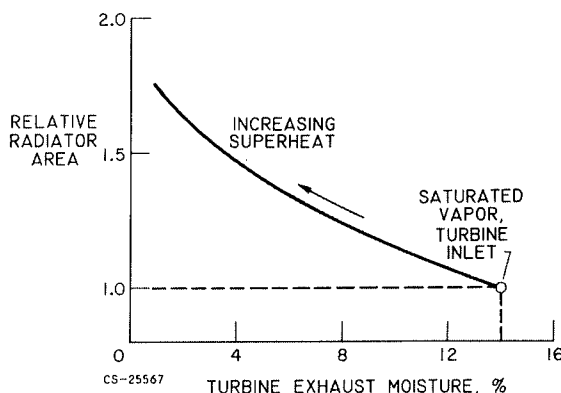


FIGURE 46-27.—Effect of superheat on radiator area.

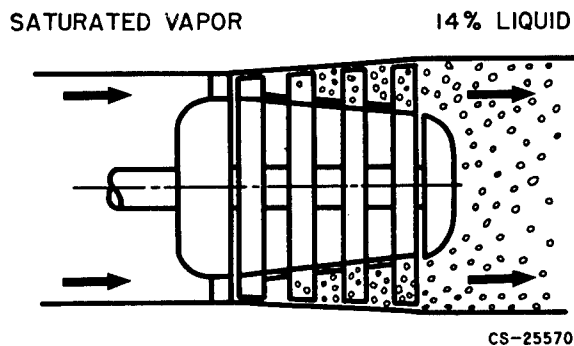


FIGURE 46-28.—Moisture formation within turbine with no moisture removal.

damage that can be caused by the impinging liquid droplets. Condensation, in addition to affecting turbine life by erosion, also causes reduced turbine performance. The performance loss has been estimated at 1 to 1.5 percent for each 1 percent of liquid present.

The state of technology for alkali-metal-vapor turbines may be summarized as follows:

- (1) There are no performance data available for vapor turbines, nor are there any data on moisture damage or its effect on performance.
- (2) There is very limited experience on two-phase flow of the alkali metals in the engineering-size facilities required for component investigations.
- (3) The vapor-property data required for the turbine-design phase are extremely limited.

The present research programs include two experimental vapor turbines operating at intermediate temperatures (1600° F), one to be tested at Lewis and the other by the General Electric Company. These studies will cover areas such as turbine design and performance, moisture formation and removal, moisture erosion damage, and turbine-life characteristics. A research study is also being conducted by the Atomic Energy Commission on the effects of alkali-metal erosion on materials.

**Pumps.**—The functions performed by pumps in closed-loop systems include the circulation of high-temperature liquids and the raising of pressure to the level required by other components in the system. In the vapor loop of the system, the working fluid experiences a change

of phase, and a condensate pump must be used that is capable of pumping the alkali metal at or near boiling conditions. Under these conditions, the liquid will form vapor bubbles (or cavitate) in the pump impeller passages when its pressure is reduced below the vapor pressure corresponding to the inlet temperature. This formation and collapsing of the vapor bubbles can result in severe cavitation damage to the pump parts. The combination of pump cavitation damage and liquid-metal corrosion imposes a severe design problem for condensate pumps requiring long life reliability.

The cavitation problem can be alleviated by moving the condensate away from its boiling point before the pump impeller inlet. One of two methods, or a combination of these methods, may be used. First, the condensate can be subcooled below its boiling temperature by the addition of heat-transfer area in the radiator. Figure 46-29 shows the effect of subcooling on additional radiator-area requirements. Approximately 200° to 300° R of subcooling is required to substantially remove the condensate away from boiling for the alkali metals of interest. Required radiator size must, then, be increased about 8 percent. The second method of moving the condensate away from its boiling point is to prepressurize the liquid above the vapor pressure corresponding to the inlet temperature. Figure 46-30 shows a schematic diagram of a typical inducer used for such a purpose. The inducer is designed to gently raise the pressure of the incoming liquid above vapor pressure before entering the impeller passages. This type of pump has potential, but its effectiveness in liquid-metal pumps has yet to be determined. Another method of prepressurizing the liquid is presented in figure 46-31, which shows a combination jet centrifugal pump used to boost the inlet pressure by a mo-

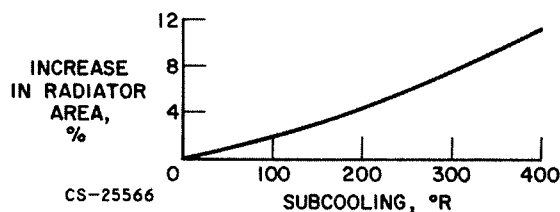


FIGURE 46-29.—Effect of subcooling on radiator area.

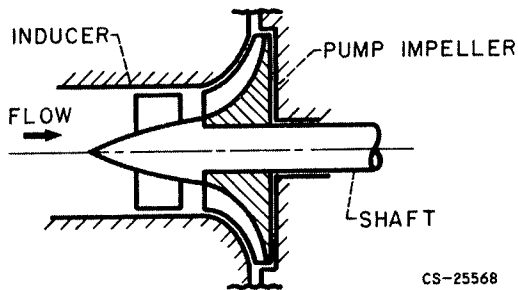


FIGURE 46-30.—Typical inducer for prepressurizing liquid.

mentum exchange with high-pressure liquid from the centrifugal-pump discharge. Approximately half of the flow through the centrifugal pump is recirculated through the jet pump. Even with this device, some radiator subcooling will be required to prevent cavitation in the jet pump.

The state of technology for alkali-metal condensate pumps is as follows:

(1) Experience has been primarily for single-phase-flow circulating pumps operating at intermediate temperatures (1500° F).

(2) Only very limited performance data exist for condensate pumps operating under cavitating conditions with alkali metals.

(3) There is no information on the interaction of cavitation damage and alkali-metal corrosion.

(4) No accurate method exists for predicting cavitation damage rate, even for simple fluids such as water.

Figure 46-32 shows an example of one of the many projects under way to investigate cavitation in condensate pumps. This particular test

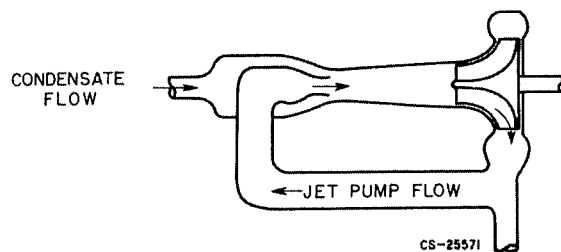


FIGURE 46-31.—Typical jet centrifugal pump for prepressurizing liquid.

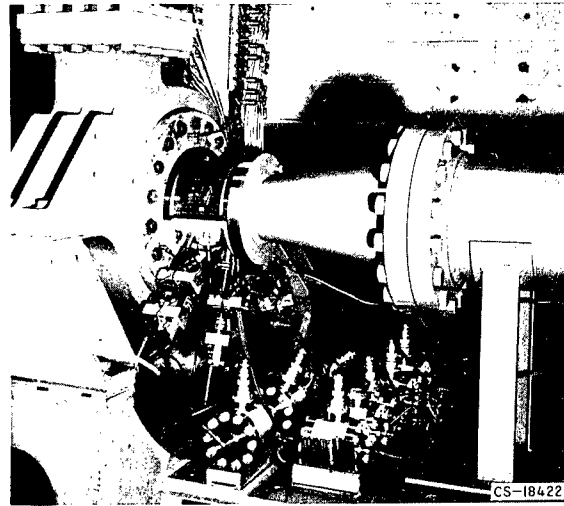


FIGURE 46-32.—Pump inducer operated in Lewis water tunnel.

rig uses water as the test fluid. A transparent casing is used in conjunction with a synchronous light source and camera to study cavitation as affected by operating conditions.

#### MATERIALS FOR RANKINE CYCLE SYSTEMS

**CHARLES A. BARRETT.** The three principal materials problem areas for nuclear Rankine systems are the reactor, the boiler, and the radiator. In the low-temperature systems (typified by Snap-2 and Snap-8), the reactor and the radiator do not appear to be a major problem. In this system, the mercury boiler presents the problem. A boiler alloy must combine suitable strength, weldability, and fabricability along with good corrosion resistance to boiling mercury on the inside and sodium-potassium from the reactor on the outside. The problem of corrosion is not only the eating away of the wall in the boiler but also the carryover of corrosion products to small passages downstream in the system, such as bearing passages. Figure 46-33 indicates the possible magnitude of this problem. The figure shows boiling reflux corrosion capsules, which were machined from three conventional alloys that were of interest as a Snap-8 boiler material. Figure 46-33(c) is the high-strength, highly alloyed, ductile, cobalt superalloy HS-25. In the center is

# POWER FOR SPACECRAFT

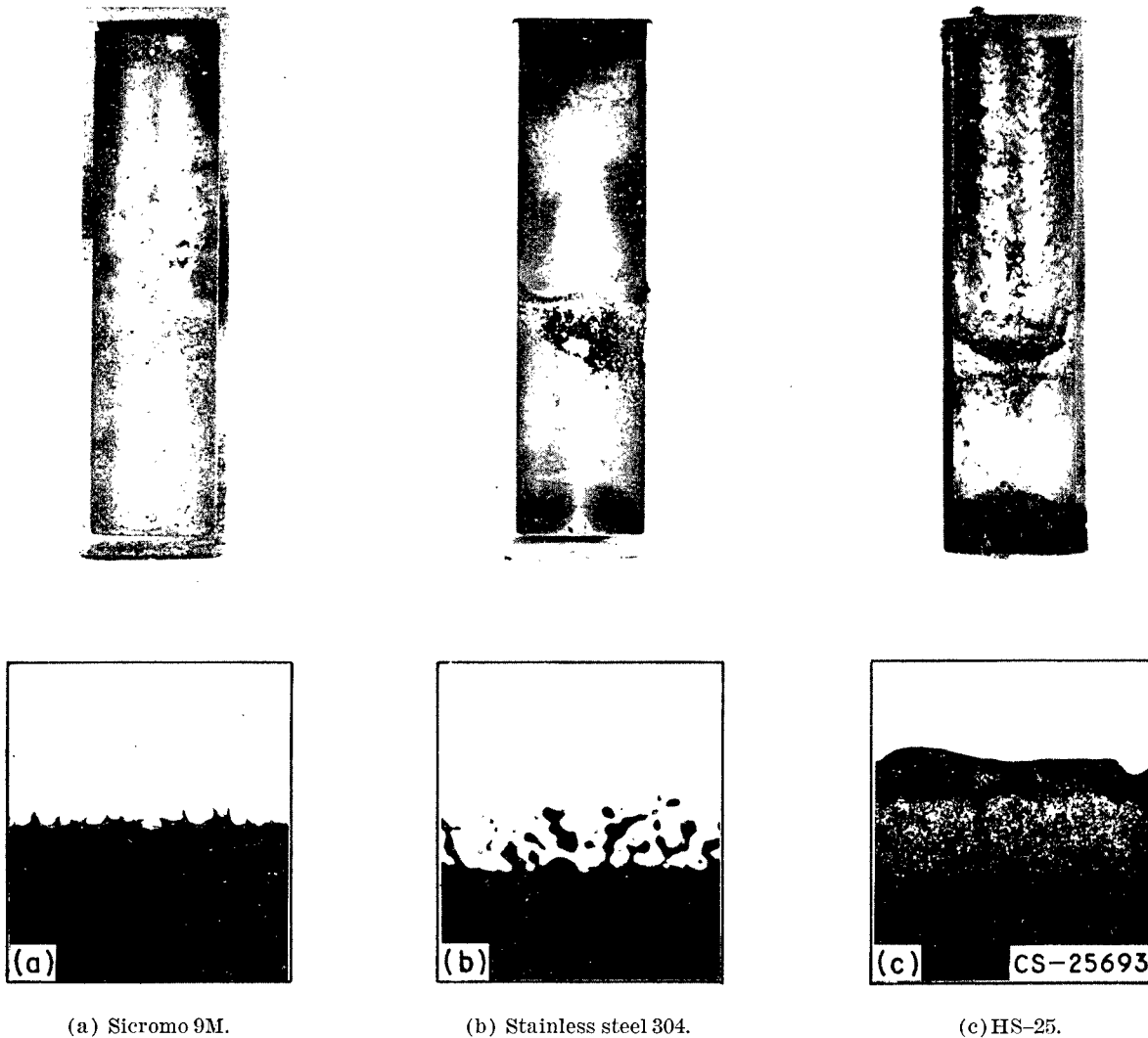


FIGURE 46-33.—Mercury compatibility capsules after 1000 hours at 1200° F.

the conventional austenitic stainless steel 304. In figure 46-33(a) is the high-chromium martensitic boiler alloy Sicromo 9M. These capsules are approximately 2 inches long and  $\frac{1}{2}$  inch in diameter with a 40-mil wall. The capsules were etched on the inside and then filled approximately one-third full with high-purity mercury. They were then evacuated and sealed under high vacuum by an electron beam welder. The capsules were then placed in small furnaces and heated for 1000 hours at 1200° F. There is a slight gradient of 20° to 40° F between the boiling interface and the tops of the capsule. The liquid region quickly becomes saturated with the more soluble elements such as nickel and chromium. The vapor condenses on the

cooler top part of the capsule and runs down the wall. This virgin liquid continuously leaches out the more soluble elements and builds up a deposit at the boiling interface. This buildup is greatest in the heavily alloyed HS-25, less so in the 304, and very low in the 9M.

The photomicrographs below each capsule in figure 46-33 are cross sections in the heavily leached condensing areas at an original magnification of 250 diameters. The white portion is the unetched metal and its lower edge is the mercury-metal interface. The porous area in the HS-25 photomicrograph is the heavily leached area. The 304 stainless steel shows more of a grain-boundary-type leaching, while the 9M is much less attacked. The 9M still would



generate some buildup, and its creep strength is too low to be used in the boiler.

Although these capsule studies cannot truly simulate the corrosion conditions in an actual boiler, they do indicate that these and similar alloys are quite corrosion prone with mercury.

It was hoped that conventional alloys such as these general-type steels or superalloys could be used as boiler-tube alloys in such systems. The experimental indications, however, are that too large an amount of corrosion products is generated. The present approach, therefore, is to use refractory-metal-lined boilers (such as columbium or tantalum), which by their very nature are virtually insoluble in mercury and generate no corrosion products. This refractory alloy must be clad with stainless steel, however, for suitable strength and compatibility with the reactor materials and fluid. The major problems in this clad-boiler concept are the making of reliably bonded, clad, stainless steel—refractory-metal tubing and the ease and reliability of welding such tubing.

In the advanced system with reactor operating temperatures close to 2200° F and boiler temperatures close to 2000° F, the reactor, the boiler, and the radiator all present formidable problems. In such systems the reactor will set the upper limit. At the present state of the art, a reactor-fluid outlet temperature of 2000° F to the boiler seems reasonable.

For these very high temperatures, none of the conventional stainless steels or nickel- or cobalt-base alloys are satisfactory. An upper-limit temperature of 1500° F is set not by low strength or excessive corrosion but rather by excessive vaporization in the vacuum of space.

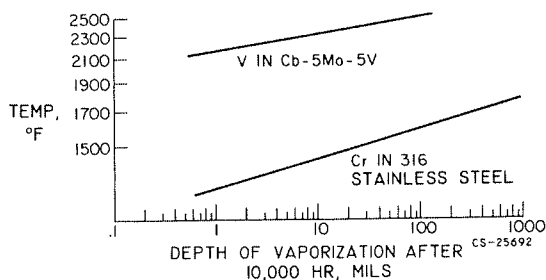


FIGURE 46-34.—Calculated depth of vaporization depletion for typical high-temperature alloys in space. Ideal solution and nondiffusion control assumed.

This effect is shown in figure 46-34. Virtually all the conventional high-temperature alloys contain chromium for oxidation resistance in air. In vacuum, however, chromium has an extremely high vapor pressure, above 1500° F. In an alloy, it would tend to diffuse to the surface and evaporate (or boil away) provided that it was not combined somehow—perhaps as a carbide. Even if chromium could be eliminated, the evaporation temperature of iron and nickel at 1800° F is close to that of chromium at 1500° F, and this proximity would tend to place a temperature limit here. The lower theoretical curve in figure 46-34 is typical for any chromium-containing alloy and shows that for 10,000 hours at 1500° F, 100 mils of chromium would be depleted; this amount is greater than any contemplated boiler-wall thickness.

The advantage of using the refractory metal columbium is also shown on figure 46-34. One of the advantages of the refractory metals<sup>1</sup> is their very low vapor pressures at 2000° F. As long as columbium, for example, is alloyed with other refractory metals or metals such as zirconium, hafnium, or vanadium, evaporation is not a problem. The curve in the figure shows that vanadium in a columbium alloy (again assuming ideal solution and nondiffusion control) would not give 100 mils depletion in 10,000 hours until a temperature of 2500° F was considered. For this reason, as well as strength and corrosion considerations, the refractory metals and their alloys are necessary in the reactor and the boiler. For overall system compatibility, the same metals may have to be used in the radiator also, even though its use temperature may be as low as 1300° F.

Fortunately, the old Aircraft Nuclear Propulsion Program (ANP) developed a suitable high-temperature, compact liquid-metal reactor using the refractory metal columbium. The reliability of such a reactor for the long 10,000-hour life along with adequate corrosion resistance must be proven.

The advanced boiler presents a formidable problem. It involves literally thousands of feet of high-quality, small-diameter, thin-

<sup>1</sup> Refractory metals may be arbitrarily defined as the transition metals columbium, tantalum, molybdenum, tungsten, and rhenium with melting points over 4000° F, exclusive of the platinum group metals.

# POWER FOR SPACECRAFT

walled tubing that must be butt welded in suitable locations to make numerous helixes and then attached to a header with many high-reliability welds. The alloy to be used is still in doubt. Presumably columbium—1-percent-zirconium alloy will be used as tubing because a great deal of fabrication and corrosion experience was obtained with it during the ANP program. There is some question of whether it has the long-time creep strength and corrosion resistance needed for space power systems. There may be an embrittlement problem on welding also. Other refractory-metal alloys based on columbium and tantalum are currently being developed which, supposedly, have better overall tubing properties than columbium—1-percent-zirconium alloys. These alloys must still be further evaluated.

A major problem with columbium and tantalum alloys (as with all refractory metal alloys) is not only that they oxidize catastrophically at elevated temperatures, so that they cannot be tested in air unless coated or clad, but also that they dissolve large quantities of gases like oxygen when exposed at high temperatures. They are "getters" and essentially act as pumps to pick up these gases. These gases change the properties of the alloys drastically, change their fabricability, weldability, creep strength, and resistance to alkali-metal corrosion. The main problem in testing these alloys is to provide conditions under which their properties are not being altered by their test environment. This probably means testing in ultrahigh vacuums, which is not only expensive but, because so few test facilities are available, gives rise to long delays in securing design data. In addition, the turbine problem exists for which long-time detailed corrosion, erosion, and especially creep-rupture data must be obtained.

Strength curves for refractory metal alloys are shown in figure 46-35. The lower curve is for the columbium tubing alloy columbium—1 zirconium and is shown in comparison with the cobalt-base alloy HS-25. Most of the advanced tubing alloys fall between the columbium-1-zirconium and the tantalum-10-tungsten alloys. It shows that the hoop stress gen-

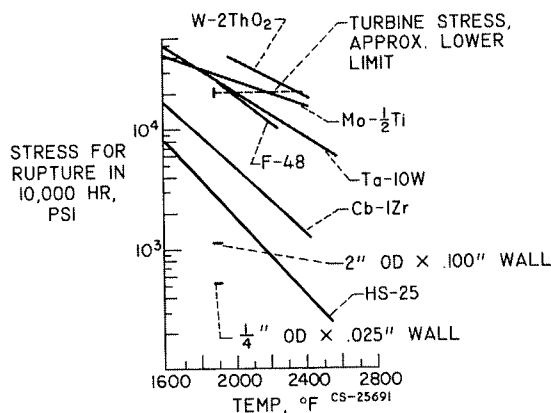


FIGURE 46-35.—Strength requirements for advanced space power systems. Turbine hoop stress at temperature of 1900° F. for potassium.

erated in the boiler at 1900° F by potassium should not cause rupture of two possible sizes of boiler tubing in 10,000 hours. These curves are extrapolated from short-time data (from 100 to 300 hr) and from higher level stress data. The data must be verified for long times and low stresses before they can be used in an actual system.

More important than rupture data are low-stress creep data, which must be obtained for tubing alloys before they can be used.

The dashed line at 20,000 psi represents a turbine stress, and here a whole new class of very-high-strength refractory metals are needed. Fortunately, high-strength tungsten and molybdenum alloys can also be considered. These alloys, because of their limited ductility and fabricability, as yet have not been considered for tubing. Here, also, long-time rupture and creep data are very meager.

Even the existing data for columbium and tantalum alloys are questionable, for it is not known how the environment affected the results. Obviously, a detailed testing program is needed, not only in ultrahigh vacuum but eventually in the alkali-metal environment.

Compounding the problem of contaminating the refractory alloy is that of contaminating the alkali metal, which must be purified, analyzed, and transferred all under high vacuum wherever possible to minimize the pickup of deleterious gases.

In summary, in the advanced systems an entire new technology exists that involves alkali metals and refractory metals where a contamination-free environment is an absolute must. For the alkali metals, such as potassium, rubidium, and cesium, there is little purification, analyzing, and handling experience. High-reliability tubing using tantalum- and columbium-base alloys is still in an early state of development. It will also be necessary to run complicated corrosion and component test loops, which as yet have not been run successfully, even at lower temperatures under easier test conditions. Obviously, a great deal of research is needed before such a system can be seriously considered.

Additional materials problems exist in the pump and alternator, along with bearing problems in the various rotating components.

Finally, the radiator presents, for the advanced system, the third major problem area. Here must be fabricated literally thousands of feet of refractory-metal-alloy tubing (columbium or perhaps vanadium base) over which is clad a bumper-finned material of pyrolytic graphite or beryllium, both extremely brittle and difficult to fabricate and of uncertain compatibility with columbium or vanadium. Producing a reliable radiator of several thousand square feet of this combination of material, with the numerous brazed or welded joints having the required reliability, is extremely difficult. For this reason, the radiator appears to be the most severe problem in the advanced system, at least from a materials standpoint.

### THERMIONIC CONVERTERS

A. E. POTTER, JR. As stated previously, another technique for converting reactor thermal energy to electric power involves the use of thermionic converters. The essential features of a thermionic converter are shown in figure 46-36. It consists of a high-temperature electron-emitting surface (the cathode) and a lower-temperature electron-collecting surface (the anode). The number of electrons boiling off the hot emitter is greater than the number from the cooler collector, so that a charge builds up on the collector. This charge or voltage can

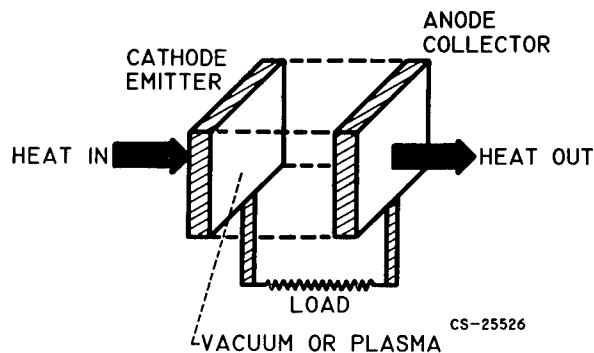


FIGURE 46-36.—Thermionic converter.

be used to drive current through an external load.

The thermionic converter has several attractive features for space power. It can be quite efficient, converting up to 17 percent of heat to electricity. It is small and compact. It operates at high temperatures, 2000° to 3000° F. High operating temperatures for heat engines working in space are a great advantage, since high temperatures mean small and lightweight radiators.

Although the principle of the device is old—Edison held the first patent on a thermionic generator—it is only recently that practical converters have been made, and the device is not yet completely perfected. The bulk of the research on thermionic converters has been aimed at improving efficiency. The principal route to improvement of efficiency has been to reduce space charge between the electrodes. Space charge limits current flow between the electrodes. Two good methods of reducing space charge have emerged. One is to reduce spacing between the electrodes to less than 0.004 inch. This reduces space charge, but makes the device difficult to fabricate in large sizes. Another way of reducing space charge is to introduce cesium vapor between the electrodes. This procedure seems to be the most useful method yet devised, although research is continuing to find still other ways of reducing space charge. Another route to improved efficiency is to reduce heat losses by conduction through the sealing material and radiation losses across the electrode gap. Choice of electrode materials having the proper work functions is also important in achieving highest efficiencies. When

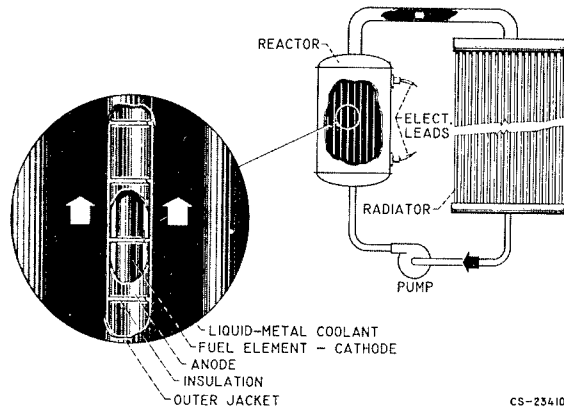
properly used, cesium vapor plays a dual role, not only suppressing space charge, but also adjusting the work function of the collector to a suitably low value by means of partial absorption of cesium on the collector surface.

The remainder of research in thermionics can be classified as research on the lifetime of the device. Some of the problems are the following. Evaporation of electrode material from the emitter and its subsequent deposition on the collector can eventually build up needlelike deposits, which can short out the device. If cesium is used to suppress space charge and control work function, it corrodes the sealing materials and may eventually cause a leak. If no cesium is used and close-spaced electrodes are employed to suppress space charge, creep and flow of the electrodes will eventually alter the spacing from its optimum value. The general problem of maintaining the device in operation for 10,000 to 20,000 hours at 2000° to 3000° F is a difficult problem. Progress is slow, although some 3000° F converters have been operated for 1000 hours.

When the practical difficulties associated with the use of the thermionic converter are overcome, it seems likely that its major use in space will be in conjunction with a very-high-temperature nuclear reactor to provide power in the megawatt range.

#### THERMIONIC-REACTOR POWER SYSTEM

**DANIEL T. BERNATOWICZ.** Several ways exist in which thermionic converters can be incorporated into a system, but the most promising way is to put the converters into the reactor core, integral with the fuel elements. Figure 46-37 is a schematic diagram of a thermionic reactor system. Cylindrical thermionic converters are connected in series and are stacked inside tubes. The central region of each converter is filled with nuclear fuel. The surface of the fuel can is the emitting surface. Coaxial with the emitter is the collector, and the space between the electrodes is filled with low-pressure cesium vapor. Between the wall of the containment tube and the collector is a layer of electrically insulating material to prevent short circuiting of the converters. Heat generated in the nuclear fuel maintains the emitter



CS-23410

FIGURE 46-37.—Thermionic-reactor power system.

at a high temperature. The collector is cooled by conduction through the insulator and the tube wall. The tube wall is cooled by a liquid metal, which probably will be lithium.

Several hundred of these tubular thermionic fuel elements are assembled into a reactor core. Liquid-metal coolant is pumped through the core assembly and the heat is rejected in a radiator.

Because only the fuel and the emitter operate at the maximum temperature, it is reasonable to expect that this system can operate at higher temperatures than the Rankine cycle system, in which the liquid metal and the turbine are exposed to the maximum temperature. Also, the small number of moving parts in the thermionic system suggests high reliability. If an electromagnetic pump, which is composed only of static elements, is used, moving parts are needed only in auxiliary equipment, such as the reactor control system.

Studies of the thermionic systems as well as the Rankine cycle system are based on information inadequate to justify a selection of one system over the other at this time. Weight estimates, however, indicate that the thermionic system may be lighter than the Rankine cycle system.

Although the potential for the thermionic system is high, difficult problem areas and serious deficiencies in knowledge and technology are recognized. The very feature that makes the thermionic reactor system appear so attractive, that is, that the heat source and the energy conversion device are closely integrated, com-

pounds the engineering problems. Information on nuclear fuels, seal and insulator materials, and fabricating techniques is not sufficient to assure that the converters can operate reliably for years at high temperature under the intense radiation in the reactor core. Also, little work has been done on systems of converters. Several thousand converters will be connected in a series-parallel network in the system described here. Because of reactor heat-generation characteristics, there will be a variation in temperature among the converters. How seriously this variation will affect the performance of the system as a whole has not been established. There may also be electric oscillations or large stray currents in such a large network. Furthermore, thermionic converters are low-voltage d-c devices. Power conditioning equipment will be needed to raise the voltage to the several thousand volts d-c required by the electric propulsors. The weight of this equipment may be a substantial part of the total weight. Nevertheless, the high performance that may be possible for the thermionic reactor system certainly justifies undertaking the solution of these many problems.

#### **CONCLUDING REMARKS**

NEWELL D. SANDERS. The long durations of space missions place severe requirements upon space power systems. Trips to the planets will take 1 or 2 years or perhaps more. Elaborate satellites such as those being planned

for communication, weather observation, and space stations are expensive to build and launch. A long life, at least a year, is a requirement with respect to economy and practical operation.

This requirement of a long life without attention has a profound effect upon the course of development. Many paths may be pursued in the initial laboratory and bench investigations of components and breadboard systems. A tremendous gap exists, however, between the bench proof of performance and the actual achievement of a flyable power system with the desired lifetime. The development cost involved in crossing the gap is measured in tens of millions of dollars for even the simplest systems. In the case of the very large multimewatt systems, the development cost will be hundreds of millions.

Because of the great cost and the drain on technical manpower, unwise choices of systems for development will impede seriously the space program. Technical information is absolutely necessary for making these decisions. The technical information must be provided by a broad-based program of research and preliminary development in critical areas.

In the light of the foregoing discussion and because of the many unsolved technological problems that were discussed in earlier portions of the paper, it is concluded that a healthy program of supporting research is absolutely necessary to a successful program of space power development.

**SESSION P**

## **Electric Propulsion**

***Chairman, WOLFGANG E. MOECKEL***

---

WOLFGANG E. MOECKEL, *Chief of the Electromagnetic Propulsion Division of the NASA Lewis Research Center, is currently concerned with most of NASA's research on electric propulsion systems suitable for advanced space missions, as well as studies in plasma physics, magnetics, and space-environment simulation. Among his contributions to research are the use of aerodynamic heating to propel aircraft at hypersonic speeds and the optimization study of low-thrust propulsion systems for space missions. He attended the University of Michigan where he received his B.S. degree in 1944. In 1961, Mr. Moeckel received the Arthur S. Fleming Award, which is given annually to men under 40 who have made outstanding contributions in Federal Government Service. He is an Associate Fellow in the Institute of Aeronautical Sciences, a Senior Member of the American Rocket Society, and a member of the American Physical Society.*

# Introduction

By Wolfgang E. Moeckel

The NASA program of research and development in the field of electric propulsion is aimed at eventual use of electric rockets for propulsion of unmanned and manned space vehicles, primarily for interplanetary missions. There are several other promising applications, such as control of the orientation and orbit of Earth satellites and propulsion of lunar supply vehicles, but many mission studies have shown that electric propulsion is most attractive for missions beyond the Moon.

This attractiveness, however, depends on the attainment of certain goals with regard to weight and performance. Perhaps the most critical of these goals is that of developing electric-power generation systems with low enough weight per unit electric power produced and with long enough lifetime. Many of the problems involved in developing such systems have already been discussed, but one of the most difficult, namely, the radiation of waste heat, will be discussed in one of the following papers.

The importance of low specific powerplant weight is illustrated in figures 1 and 2. Figure 1 shows the payload ratio as a function of

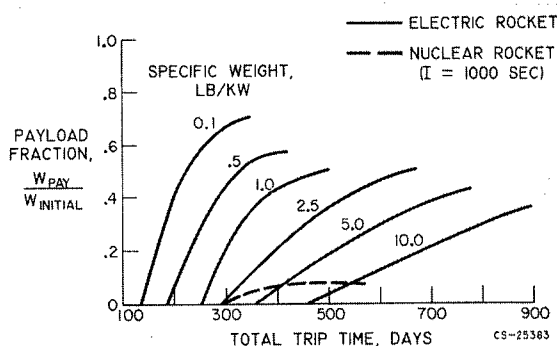


FIGURE 2.—Payload ratio for Mars round trip. Time at Mars, 50 days.

trip time for scientific probe missions to Mars and to Jupiter. In this payload ratio, the initial weight is that of the electrically propelled vehicle launched into a low Earth orbit; and the payload is the weight, exclusive of electric power, delivered into the Mars or Jupiter orbit. For electrically propelled vehicles, no additional power supply is required for communication and payload operation, so that the actual payload advantage of electrically propelled vehicles is correspondingly enhanced by the amount of weight that would be required to provide adequate nonpropulsive power with other propulsion systems. For many space-probe missions, the availability of large amounts of electric power should prove to be invaluable in increasing the amount and the variety of data that can be accumulated and transmitted in a single mission. Among the possibilities, for example, is continuous television transmission from a mobile vehicle on the surface of Mars or Venus.

Figure 1 shows that reasonable payloads can be carried to Mars and Jupiter with specific weights as high as 50 pounds per kilowatt. These specific weights are in terms of pounds of powerplant weight per kilowatt of power in the

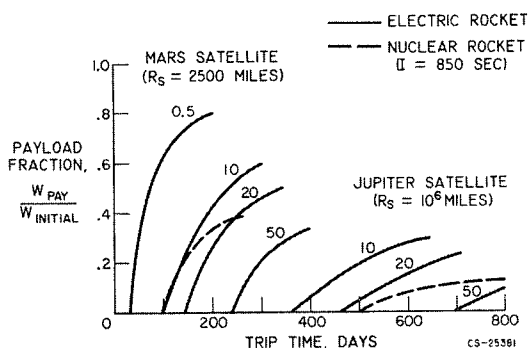


FIGURE 1.—Interplanetary probe missions. (Numbers beside curves are specific weight, lb/kw.)



# ELECTRIC PROPULSION

propulsive jet. They therefore include the inefficiencies of the electric rocket (also called thruster) in converting electric power into jet power. The specific weights of the power generation system (in lb/electric kw) are the values shown in this figure divided by the thruster power efficiency. The figure shows that large reductions in trip time are possible as specific weight is reduced.

Shown for comparison are values of the payload ratio obtainable with a nuclear rocket with a specific impulse of 850 seconds and a powerplant weight about 10 percent of the initial vehicle weight. The nuclear rocket is competitive with electric propulsion systems having specific weights greater than 10 to 20 pounds per kilowatt for the Mars trip and somewhat higher for the Jupiter mission if the required electric powerplant for the payload and communication is neglected. A similar comparison for the more difficult Mars round-trip mission is shown in figure 2. This mission corresponds approximately to a manned exploration expedition except that the payload in the case shown has been assumed to be fixed, whereas for an actual manned mission, supply consumption en route and the abandonment of the Mars landing vehicle should be considered. These more detailed calculations, however, yield the same relative weights as those given in figure 2, where results are given in terms of ratios that are independent of absolute size. The conclusion to be reached from figure 2 is that manned missions to Mars can be accomplished with greater payload ratios (less initial weight) with electric rockets than with nuclear rockets if powerplant specific weights of the order of 10 pounds per kilowatt can be attained. Nuclear rockets, however, can achieve shorter total mission time unless the specific weight of electric rockets is reduced to 5 pounds per kilowatt or less.

Figures 1 and 2, then, illustrate the goals of electric propulsion systems with regard to specific weight, i.e., less than 50 pounds per kilowatt for interplanetary probes, and less than 10 pounds per kilowatt for the higher-power manned interplanetary missions of the more distant future. The figures also show the very large savings in trip time that are possible

if specific weight can be greatly improved. The very low values of specific weight shown in figures 1 and 2 may be considered academic with regard to power generators now under development. Mr. Edmund Callaghan, however, discusses two propulsion systems for which values of specific weight in the range of 1 pound per kilowatt or less appear theoretically possible.

The specific weights discussed are, as mentioned before, the weights per kilowatt of jet power. If the efficiency of the thruster in converting electric power into jet power is very high, these values are close to those for the weight per kilowatt of electric power generated. An inefficiency in the thruster effectively degrades the specific weight of the entire propulsion system. Another performance goal in electric propulsion research is therefore high efficiency in conversion of electric power into thrust.

As will be pointed out in subsequent papers, the efficiency of electric thrusters is a strong function of the specific impulse, or jet velocity, produced. Consequently, the range of specific impulse required for contemplated space missions must be known. As shown in table I, this range can be determined roughly from the total impulse required for the mission and the allowable ratio of propellant weight to initial weight. For satellite orientation and orbit control, the total impulse, even for several years of operation, can be quite low, but the propellant ratio must also be low. For the remaining missions,

TABLE I.—*Specific Impulse Range for Electric Propulsion Missions*

Mission (constant-thrust)	Typical total impulse, $a \Delta$ , sec	Typical specific impulse, $^a I$ , sec
Satellite orbit control.....	30-100	300-5000
Mars and Venus orbiters.....	1000-3000	2000-6000
24-Hr satellite orbit.....	500	1000
Mars and Venus round trips.....	2500-6000	5000-12,000
Jupiter orbiter (10 <sup>6</sup> mile orbit)	3000	6000

$$^a I = \frac{F}{\dot{W}_p} = \frac{Ft/W_o}{W_p/W_o} = \frac{a \Delta}{W_p/W_o} = \frac{\text{total impulse}}{\text{propellant ratio}}$$

## INTRODUCTION

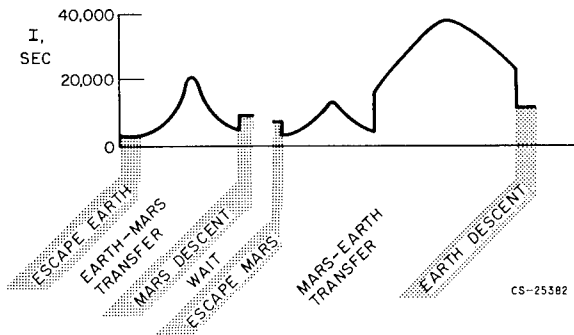


FIGURE 3.—Specific impulse program for constant-power Mars round trip. Total trip time, 500 days; specific powerplant weight, 10 pounds per kilowatt.

where electric rockets are the primary propulsion system, propellant weight ratios in the neighborhood of 0.5 are allowable. Table I shows that, for constant-thrust missions, a large range of specific impulses from below 100 to over 10,000 seconds is needed.

Shown in figure 3 are the specific impulses required during a round-trip Mars mission. These values are for a particular family of trajectories for which the total power is constant, but specific impulse and thrust are allowed to vary. Trajectories of this type are somewhat more efficient with regard to propellant consumption for a given trip time than constant-thrust trajectories. Figure 3 shows that, to follow such trajectories, thrustors that can operate efficiently over a very wide range of specific impulse from 2000 through 40,000 seconds are needed.

Table I and figure 3 show that the further goal of electric propulsion research should be to develop thrustors that can operate with high efficiency over a range of specific impulses from below 1000 to above 40,000 seconds. It is doubtful whether such a range can be covered efficiently with a single type of thrustor. Consequently, research is proceeding on several varieties of electric thrustor, which will be described subsequently.

Another major goal of electric propulsion research is a very long, reliable operating lifetime for all components of the system. The difficulty of achieving this goal for lightweight power-generation equipment was discussed in the Space Power Session. These problems are reviewed and elaborated upon by Mr. Lieblein, particularly with regard to the radiator prob-

lem for systems that use a closed thermodynamic cycle. The need for long lifetimes with electric propulsion systems stems mainly from the fact that they are basically low-thrust systems. Since the power delivered by the jet is the product of thrust and jet velocity, it is evident that, for any given power level, thrust decreases as jet velocity or specific impulse increases. Furthermore, for a closed thermodynamic cycle, the weight required to generate a given power level is much greater than for open cycles such as in chemical or nuclear rockets. Consequently, thrust is reduced and weight is increased to achieve the high specific impulses possible with electric propulsion systems. Thus to achieve a given total impulse (thrust multiplied by propulsion time) needed for a mission requires greater propulsion time as thrust is reduced and weight is increased. Typically, for specific weights of the order of 10 pounds per kilowatt at 10,000 seconds specific impulse, the ratio of thrust developed to weight of the powerplant is of the order of  $5 \times 10^{-4}$ . These low thrust-weight ratios require that thrust be applied for months, or almost continuously, throughout an interplanetary mission. Lifetimes of the order of 1 year are therefore a goal in electric propulsion research.

To summarize these goals, extensive use of electric propulsion for space missions requires development of power-generation equipment with specific weights less than 50 pounds per kilowatt for unmanned probe missions and less than 10 pounds per kilowatt for manned interplanetary missions.

Also required are thrustors capable of operating at high efficiency (greater than 70 percent, e.g.) over a range of specific impulses from 1000 to over 10,000 seconds. Also, all components of the electric propulsion system should operate reliably for periods of time of the order of 1 year or longer.

## SYMBOLS

$a_o$	$F/W_o$
$F$	thrust, lb
$I$	specific impulse, sec
$R_s$	radius of satellite orbit
$t$	time, sec
$W_o$	initial vehicle weight, lb
$W_p$	propellant weight, lb
$\alpha$	specific powerplant weight, lb/kw

# 47. Special Requirements on Power Generation Systems for Electric Propulsion

By Seymour Lieblein

SEYMOUR LIEBLEIN, *Chief of the Flow Processes Branch of the NASA Lewis Research Center, is currently involved in research on waste-heat rejection systems for space powerplants. He received his B.S. degree in Mechanical Engineering from the City College of New York in 1944 and his M.S. degree in Aeronautical Engineering from Case Institute of Technology in 1952. He received the NACA Exceptional Service Medal in 1957 for his work in jet engine and compressor research. Mr. Lieblein is a member of the Institute of the Aerospace Sciences, the American Society of Mechanical Engineers, the American Rocket Society, and the American Astronomical Society.*

## INTRODUCTION

In the preceding paper, Mr. Moeckel describes briefly the long-range electric propulsion missions contemplated by NASA. In the Space Power Session, power generation systems and some of the problems involved in their development for space application are discussed in general. A further discussion of the powerplants required specifically for long-range interplanetary missions in which electric rockets are used is presented herein.

The requirements placed on powerplants for advanced electric propulsion missions can best be summarized as shown in figure 47-1 for the sake of reiteration. Powerplant specific weight in pounds per kilowatt of jet power is plotted against total trip time for equal payloads for electric rockets and nuclear rockets for several missions. Values below each curve indicate the electric rocket to be superior. The lower the power-plant weight, the shorter is the total trip time required for each mission. In particular, extremely low powerplant weights by present standards are required for manned round-trip interplanetary missions with electric rockets.

In summary, power levels from around 600 kilowatts up to 50 megawatts are required; specific weights of the order of 10 pounds per kilowatt or less up to 50 pounds per kilowatt must be achieved; and operating lifetimes from 100 to 800 days have to be considered. In addition, extreme emphasis must be placed upon powerplant reliability to achieve continuous unattended operation for the duration of the mission. In this respect, reduction of powerplant weight is doubly important in that reduced weight leads to shorter trip times, which,

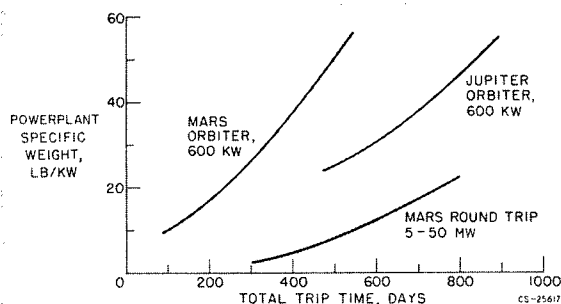


FIGURE 47-1.—Electric powerplant specific weight for equal payload weight for nuclear rocket and electric rocket.

in turn, leads to a better chance of achieving the desired reliability.

Electric powerplants suitable for interplanetary missions are discussed, and a brief review of the various problem areas involved in their development is given herein. In particular, a detailed discussion of the problems involved in the dissipation of waste heat, namely the radiator problem, is given with particular reference to the question of protection against impact from meteoroids. It is believed that the radiator currently constitutes the largest obstacle in the achievement of low weight and long-time operation for these powerplants.

## POWER GENERATION SYSTEM

### General Characteristics

(1) For the long mission times and low specific weights required for interplanetary missions, it is clear that a nuclear reactor power source must be used. Therefore, the powerplant must be started in orbit because of safety considerations.

(2) The systems must operate on closed thermodynamic cycles; cycle efficiencies are therefore governed by Carnot considerations. Furthermore, considerable amounts of waste heat must be continuously rejected, and since thermal radiation is the only mechanism for the rejection of waste heat in space, large radiating surface areas will be required.

(3) In view of the need for high cycle efficiency and low radiator area, high operating temperatures must be utilized. The use of these temperatures results in problems in the selection of materials and working fluids.

To date, the type of powerplant system that appears most attractive for long-range missions is the nuclear turbogenerator power conversion system. As is discussed previously, the nuclear thermionic and magnetohydrodynamic converter systems have also been proposed to achieve the low weights required for advanced missions. These systems contain no moving parts; however, they do need higher operating temperatures in order to produce the same cycle efficiencies as the turbogenerator systems. In addition, since they are closed cycles, they will also require waste-heat removal, and the basic

radiator problem remains. In general, the thermionic and magnetohydrodynamic systems have not reached the state of development that the turbogenerator has. Accordingly, attention is centered on the turbogenerator system.

### Rankine Cycle Turbogenerator

The basic elements of the turbogenerator system based on a Rankine vapor cycle are illustrated in figure 47-2. Heat from the reactor is supplied to the boiler where working fluid is vaporized. The vapor then drives the turbine, which, in turn, powers the generator producing the desired electric-power output. The vapor exhausting from the turbine is then condensed in a condenser-radiator where its heat of condensation is given up to space by thermal radiation. The condensate is then returned to the circuit through a pump. Inasmuch as condensation of vapor is involved, heat rejection occurs at a constant temperature. For this type of cycle, an alkali metal working fluid, such as potassium, cesium, rubidium, or sodium, is required to keep the fluid pressures at reasonable values for the temperatures involved.

As is indicated previously, the Brayton cycle using an inert gas such as helium or argon has also been proposed in an effort to circumvent the alkali metal corrosion and two-phase flow problems of the Rankine cycle. Since single-phase flow is involved in the gas cycle, however, radiation occurs at a decreasing temperature from radiator inlet to outlet. Radiators for gas cycles, therefore, have a greater surface area

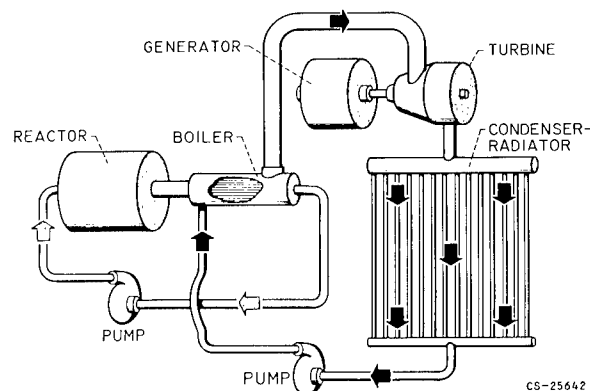


FIGURE 47-2.—Rankine cycle space power system.

requirement than those for the corresponding Rankine cycle. For this and other reasons, the gas cycle will not be considered in this discussion.

For the Rankine vapor cycle, there is a further degree of freedom in how the vapor from the turbine is condensed, as shown in figure 47-3. In figure 47-3(a) is shown the direct condenser in which vapor from the turbine passes directly into the radiator and is condensed in the radiator tubes.

In the second method (fig. 47-3(b)), called the heat-exchanger condenser, a form of heat exchanger similar to the shell and tube type is used to condense the vapor. Subcooled liquid

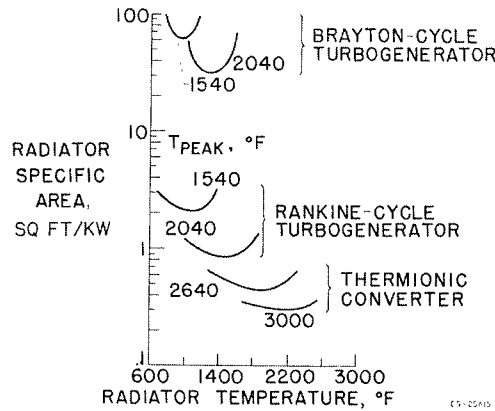


FIGURE 47-4.—Radiator-specific-area requirements for several power-conversion systems.

upper curves are for the Brayton cycle, the center curves are for the Rankine cycle, and the lower curves represent the thermionic converter. Obviously rather substantial radiator areas are required for these systems. For example, for a Rankine cycle turbogenerator, between 1000 and 2000 square feet of isothermal surface area might be required for every megawatt of desired power output. Such large surface areas can result in complex problems for the powerplant system such as structural complications; difficulties in system startup due to large heat capacity; and, finally and most important, high vulnerability to damage from impact with meteoroids.

An example of a radiator configuration currently being considered for electric rocket systems is given in figure 47-5. This type is referred to as the fin-and-tube radiator and is the

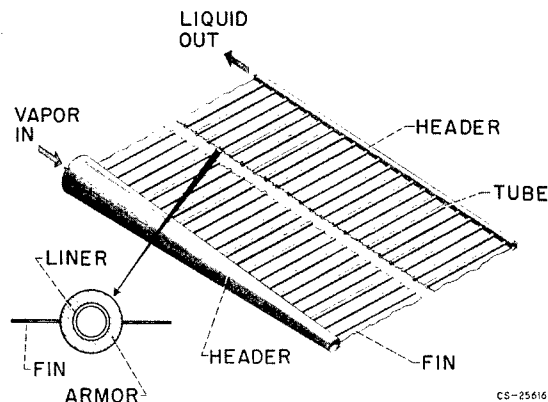


FIGURE 47-5.—Fin-and-tube radiator.

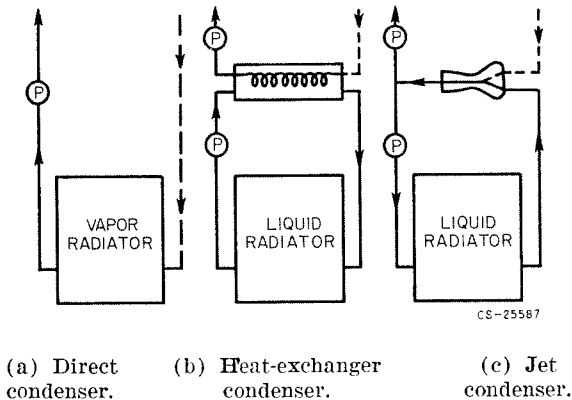


FIGURE 47-3.—Condensing methods for Rankine cycle.

is provided by a circuit that passes through an all-liquid radiator.

In the third method (fig. 47-3(c)), vapor from the turbine is physically mixed with subcooled liquid, which is obtained from an all-liquid radiator circuit. Part of the mixed condensate is returned to the cycle and the remainder to the liquid radiator loop. There are various advantages and disadvantages associated with these three condensing systems, and they are currently under intensive study.

### Radiator Characteristics

As far as radiator characteristics are concerned, typical surface area requirements will be considered first. Figure 47-4 shows specific radiator area in terms of electrical output power against radiator temperature for fixed values of peak cycle temperature. The

general type being used in low-power-level designs such as Snap 2 and 8. In this configuration for a direct radiator, vapor from the turbine entering the header is distributed to a large number of parallel finned tubes. The vapor condenses within these tubes, and the heat of condensation is radiated to space from the outer surfaces of the tubes and the fins between them. The condensate is then collected in a header and returned to the cycle.

A typical fin-and-tube construction is indicated in the lower part of the figure. The tube is shown to be composed of an inner liner of refractory material to contain the corrosive liquid-metal working fluid. Around the liner is a sleeve of armor sufficiently thick to stop an impacting meteoroid particle. Conducting fins that act as extended heat-transfer surfaces are spaced between the tubes. Radiators for all-liquid circuits will be similar in configuration except that the inlet header and the tube diameters will be smaller.

Fin-and-tube radiators can be used in a large number of configurations for integration with the vehicle. Some are shown in figure 47-6. For the flat-plate type of radiator, means must be provided for packaging the radiator during launch and unfolding before startup in orbit. The cylindrical type can be used if the radiator forms part of the vehicle outer skin; conical shapes can also be used in this respect. Finally, a modification of the flat-plate radiator that can be utilized is the triform configuration. This configuration can also fit within the confines of the launch vehicle skin.

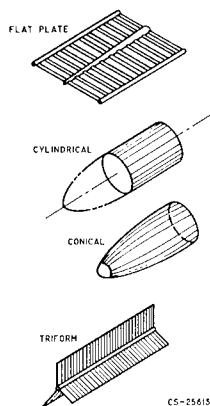


FIGURE 47-6.—Fluid radiator configurations.

### Weight Breakdown

Inasmuch as specific weight is the crucial item for interplanetary applications, the weight breakdown for the components of the power-plant system is of great interest. Representative values for the weight breakdown for a 1-megawatt-level Rankine cycle using the tubular radiator configuration illustrated herein are shown in the following table:

Component	Percent of total weight
Reactor and shielding (unmanned)---	15-20
Primary loop (pump, boiler, piping) -	5-10
Turboalternator and power conditioning-----	20-25
Heat-rejection system (condenser, unsegmented radiators)-----	40-50
Other-----	10-15

It should be noted that the large weight percentage associated with the radiator may also be typical of other closed-cycle power generating systems. Unfortunately, as will be shown later, this largest weight contribution also constitutes the greatest area of uncertainty in current design techniques.

Analysis of tubular radiators indicates that the specific weight involved in the protective armor tends to increase as power level and surface area are increased. Furthermore, most of the weight of the radiator is contained in the protective armor for high-power-level applications (ref. 1). Figure 47-7 shows the variation of tubular radiator weight in pounds per square foot of surface area as a function of sur-

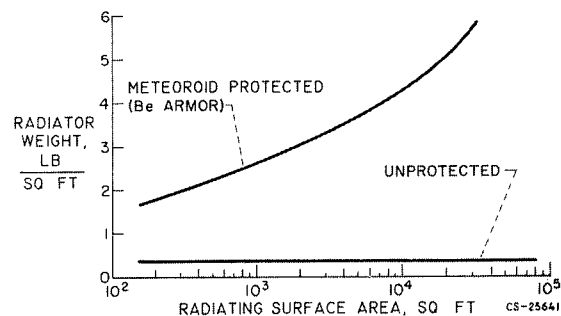


FIGURE 47-7.—Effect of meteoroid protection on radiator weight.

face area for a meteoroid-protected and an unprotected radiator for a typical Rankine cycle. It is seen that, in the megawatt range where thousands of square feet of surface are required, the armor protection can well constitute over three-fourths of the weight of the radiator. It is important, therefore, that the question of the meteoroid hazard and the protection required to defeat it be investigated further.

### METEOROID PROTECTION

Present knowledge of meteoroid characteristics (ref. 2) comes primarily from photographic and radar observations of meteors striking the Earth's atmosphere and also from limited data taken from satellites and ballistic-rocket experiments. It is believed that about 80 percent of the meteoroids are sporadic in nature and that only 20 percent appear as showers whose location and time of occurrence are reasonably predictable. More than 90 percent of meteoroids are believed to be of cometary origin with densities ranging from 0.05 to 3.5 grams per cubic centimeter (av., 0.6g/cc). The remaining few percent are asteroidal in origin with densities ranging from 3.5 to 8.0 grams per cubic centimeter. For each category, the density tends to vary with the mass of the meteoroid particle.

Most of the meteoroids lie near the plane of the ecliptic and are in direct orbits similar to that of the Earth. Velocities with respect to the Earth range from 11 to 72 kilometers per second and with respect to a vehicle radiator,

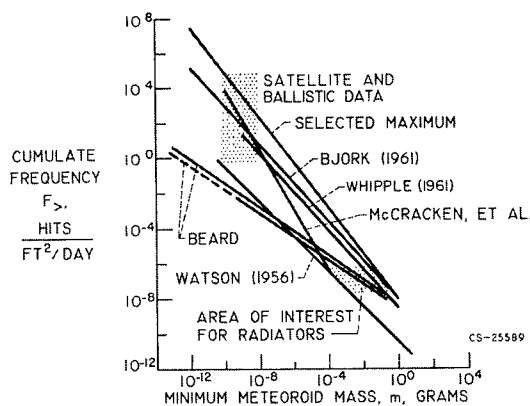


FIGURE 47-8.—Meteoroid mass-frequency distribution.

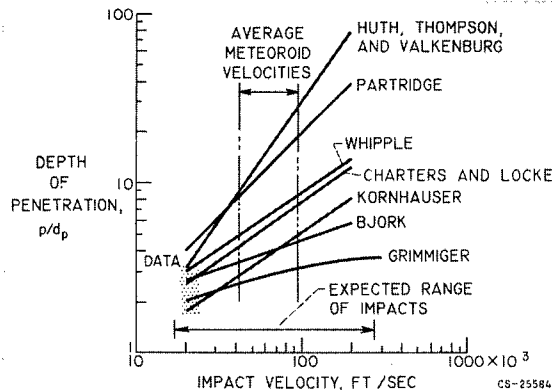


FIGURE 47-9.—Comparison of penetration theories.

from 0 to 84 kilometers per second. Maximum velocities can therefore occur up to around 250,000 feet per second (av., 90,000 ft/sec). The meteoroids vary in structure from a solid to a matrix form and in size from a micron up to several miles in diameter. Fortunately, however, the very large sizes are very infrequent near Earth.

Information on the number of hits likely to be encountered in space is shown in figure 47-8. Here the cumulative frequency in number of hits per square foot of surface per day is plotted as a function of the minimum meteoroid mass in grams. Also shown are various estimates of this mass frequency distribution as obtained by several investigators. The region of data in the upper left was obtained from satellite and ballistic experiments. The dotted area on the right shows the area of interest for large space radiators. It is important to note here that a wide range of frequency distributions is obtained such that there is an uncertainty of several orders of magnitude for the flux distribution in the range of interest.

There is a corresponding uncertainty in the depth of penetration that results from impact with meteoroids as indicated in figure 47-9 as an example. The depth of penetration expressed as a ratio of the penetration depth  $p$  to the diameter of the impacting particle  $d_p$  is plotted as a function of impact velocity  $V$  for several penetration theories as obtained by various investigators (for same target and pellet). Hypervelocity impact data have been obtained in the laboratory, but only at relatively low

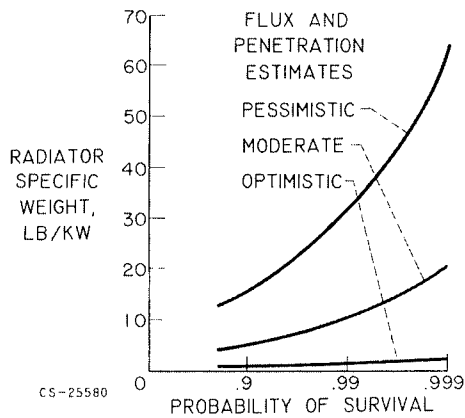


FIGURE 47-10.—Radiator weight estimates for 1-megawatt Rankine cycle.

velocities as shown in the figure. It is clear that there is a wide range of variation in depth of penetration at the expected velocities of meteoroids.

The indicated uncertainties in both the flux distribution and the depth of penetration will be reflected in a corresponding uncertainty in the protection required for space radiators as illustrated in figure 47-10. Here radiator specific weight in pounds per kilowatt of electric power output is plotted as a function of probability of survival. Also plotted are three estimates of weight depending upon whether a pessimistic, optimistic, or moderate (as currently used) interpretation of the available flux and penetration data is used. The curves show that a wide range of estimated weights can be obtained for the required protection. A resolution of the uncertainties involved in the meteoroid hazard to space radiators must therefore be obtained.

Figure 47-10 represents the degree of uncertainty involved in the required protection against simple puncture from impacting meteoroids. Other damage mechanisms, however, may exist in radiator configurations. For example, spalling can occur on the inside surfaces of the fluid-carrying tubes. The nature of the spalling phenomenon is indicated in figure 47-11. In the upper part of the figure are results of hypervelocity impact into a thick target on the right and into a thin "bumper" plate on the left. On the right is the deep crater resulting from the impact into the thick

target; on the left the bumper plate has dispersed the pellet material over a wide area of the back plate. For both plates, however, as shown in figure 47-11(b), even though puncture did not occur, material was spalled or chipped off the back side of the plate. Spalled material in radiator tubes can be just as serious as a puncture. Protection for space radiators may therefore be somewhat more complex than indicated by the simple penetration relations shown earlier.

Since depth of penetration depends on target material, the weight of a fin-tube radiator will depend to a large extent upon the material that is used for the armor protection (ref. 3). This is illustrated in figure 47-12, a plot of radiator specific weight as a function of radiator temperature for a typical Rankine cycle for a 1-megawatt power output at a peak temperature of 2000° F. Meteoroid protection was computed according to a moderate estimate of the meteoroid hazard for a no-puncture probability of 0.9 for 500 days. It can be seen that a wide range of weights can be obtained for different armor materials. Beryllium appears to be the best for producing a minimum weight. Fabrication and bonding problems, however, may exist for this material. It should also be noted that, since beryllium is unusable at temperatures higher than around 1400° F because of strength and sublimation characteristics, the use of higher radiator temperatures will actually involve a large increase in weight if it is necessary to use other armor materials such as stainless steel, columbium, or molybdenum.

#### APPROACHES TO METEOROID PROBLEM

In view of the critical nature of the meteoroid hazard and the uncertainties involved in designing for it, the designer is faced with adopting various approaches to the problem:

(1) First, of course, he would like a better determination of meteoroid characteristics radiators. For this he would like an intensified determination of meteoroids characteristics from radar and photographic observations from more significant space satellite experiments, and from laboratory hypervelocity firings into actual radiator sections at operating conditions. Efforts along these lines are currently under



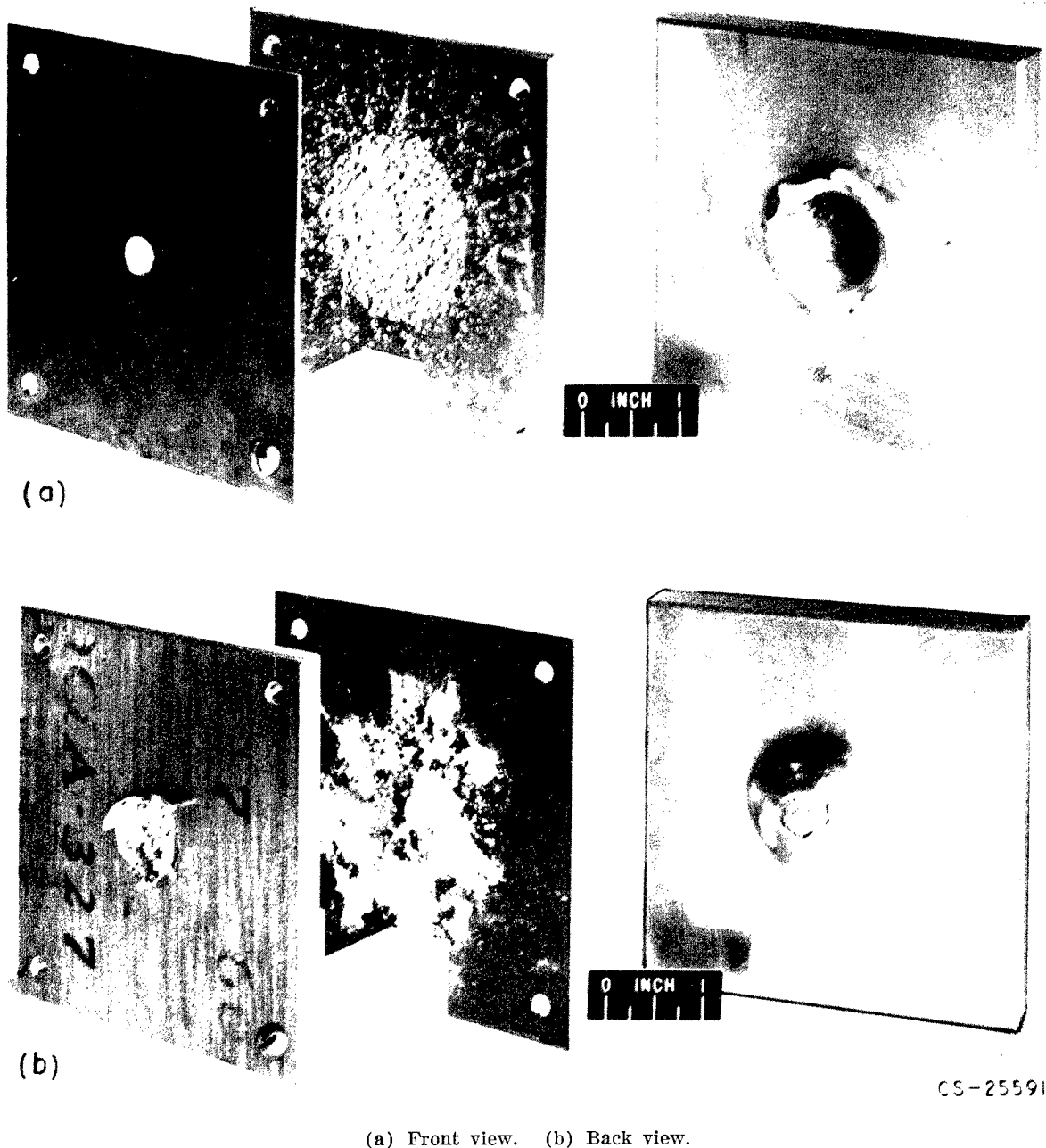


FIGURE 47-11.—Impact on soft aluminum targets. Aluminum pellet diameter, 3/16 inch; velocity, 18,500 feet per second.

way, and improved information should be forthcoming.

(2) Radiator area and vulnerability can also be reduced by increasing peak cycle temperatures as shown in figure 47-4. However, if temperatures become very high, it may no longer be possible to use lightweight armor materials such

as beryllium, and, as shown previously, no net gain in weight will occur. In addition, the higher temperatures may involve further difficulties with respect to material strength and corrosion.

(3) Various techniques for self-sealing and repairing are possible. In view of the com-

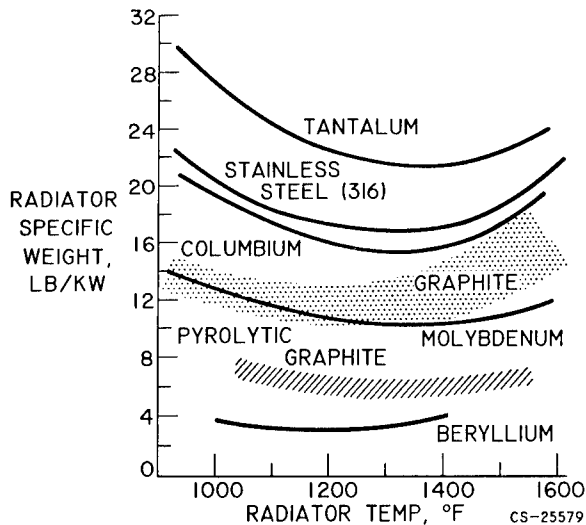


FIGURE 47-12.—Radiator specific weight for various thin and armor materials for a typical 1-megawatt Rankine cycle.

plexities involved in such techniques, however, the prognosis for successful development does not appear optimistic at the moment.

(4) A more promising approach to reducing radiator vulnerability, especially for manned missions where high survival probabilities are required, is in the concept of segmented or redundant radiators. In this technique, the radiator is divided into a large number of independent segments that can be isolated from the rest of the system in the event of a puncture. The theoretical potential for weight saving resulting from the use of this concept (ref. 4) is shown in figure 47-13. Plotted is a weight function against number of isolatable segments for two survival probabilities of 0.9 and 0.999. The calculation assumes that three-fourths of the segments will survive at the end of the mission. As shown by this figure, segmenting can either provide a reduced weight for a given probability or, and this is perhaps more important for a manned mission, it can provide for a large increase in survival probability without an excessive increase in weight, as would be the case for a single-segment radiator. The curves shown in the figure, however, are highly optimistic in that they present only the weights of the radiator tubing. Additional complications and weight penalties will be involved because of the segmenting system, the additional

headers, pumps, and other components. Furthermore, the effectiveness of segmenting will also depend on the type of condensing system used, since cutoff valving and leak detection devices may be required.

(5) In another approach the designer can try to determine the best geometric configuration for his radiator to provide the maximum protection for the least weight and complexity. Several fin-tube geometries are illustrated in figure 47-14. On the left are some configurations that embody primarily the armor sleeve approach. The two configurations shown on the right are more typical of the bumper application. In these configurations, the bumper or shield is displaced from the tube surface in order to fragment an impacting particle and spread its energy over a wider area on the tube. A thinner armor sleeve or tube wall can therefore be tolerated. These configurations, however, suffer from the disadvantage that they also present an impedance to the outward flow of heat. Comparative estimates of the relative effectiveness of these geometries are needed.

(6) Another approach to reducing meteoroid vulnerability is the use of controlled orientation of the radiator. As was indicated earlier, meteoroids are not isotropic in space in that they tend to be concentrated nearer the plane of the ecliptic and in the direction of the Earth's movement around the Sun. It may be possible, therefore, to take advantage of these directional characteristics of meteoroids by using a radiator orientation that would result in a lower required armor thickness (ref. 2). The potential gains of controlled orientation are illus-

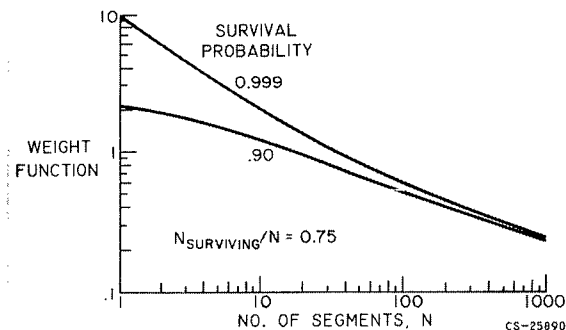


FIGURE 47-13.—Effect of segmenting on radiator panel weight.

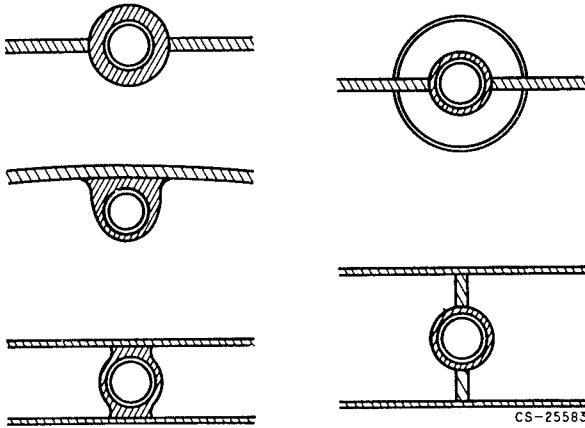


FIGURE 47-14.—Fin-and-tube geometries.

trated in figure 47-15, which is a plot of the ratio of armor thickness required for an oriented radiator  $t_o$  to that for an unoriented radiator  $t_u$  (isotropic flux) as a function of a design parameter  $J$ . The design parameter  $J$  involves the meteoroid flux distribution, the variation of depth of penetration with impact velocity, and the angle of impact. Curves are plotted for several radiator orientations sketched in the upper part of the figure. For a plate radiator oriented parallel to the plane of the ecliptic, shown as Case I, a 45-percent reduction in required armor thickness can result in the region of interest.

(7) Finally, there is the potential of producing a low-weight radiator system through the use of a nonfluid type of radiator, which utilizes a moving-belt or rotating-disk concept. In principle, these radiator systems show promise

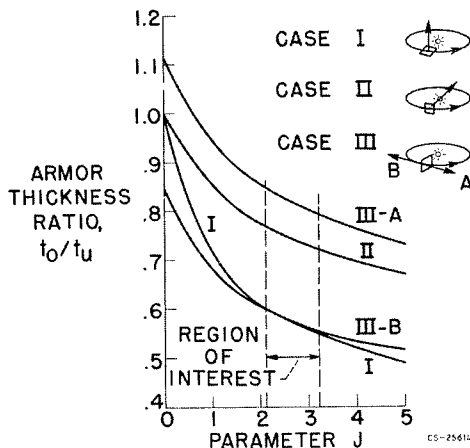


FIGURE 47-15.—Effect of spatial orientation on required armor thickness.

of reduced weight because they present much smaller areas vulnerable to meteoroid impact than tubular radiators. Some of the concepts considered in this respect are illustrated in figure 47-16.

Figure 47-16(a) shows the rotating-disk concept (ref. 5) in which rotating disks are placed between banks of tubes and receive their heat by radiation from these tubes. Then, as the disks rotate, the waste heat is radiated to space. Since a large number of rows can be stacked vertically as shown in the figure, meteoroid pro-

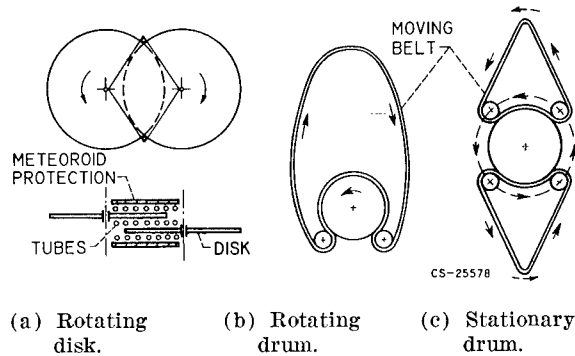


FIGURE 47-16.—Nonfluid radiator configurations.

tection will be required only at the ends of the stack, and, therefore, the protection weight can be considerably reduced.

Moving-belt configurations (refs. 6 and 7) are shown in figures 47-16 (b) and (c). In 47-16(b) are a thin moving belt and a rotating drum, which receives the cycle working fluid. Heat is picked up from the drum by means of conduction between the belt and the drum. The heat is then radiated to space as the belt passes through the loop and returns to the drum at a lower temperature. In a second concept (fig. 47-16(c)) the drum can be held stationary, and the belt can be made to rotate around the drum by means of powered rollers. In this version, the principle of heat transmission from the fluid to the drum to the moving belt is the same. The exposed surface area of the drums, which is the vulnerable area in these configurations, will be less than the exposed surface area of a corresponding tubular radiator.

Complex mechanical, structural, and heat-transfer problems are recognized to exist for

## ELECTRIC PROPULSION

these nonfluid radiator systems. If the problems inherent in these configurations can be overcome, however, this type of radiator system could be useful.

### CONCLUDING REMARKS

This paper has attempted to present some of the special requirements placed upon electric powerplants by the various advanced missions for interplanetary travel with electric rockets. Stringent requirements with respect to powerplant specific weight and long-time reliability

were indicated. For closed-cycle systems such as the Rankine turbogenerator, the heaviest system component was estimated to be the waste-heat rejection system. It was also seen that accurate estimates of the weights of suitable electric powerplants are difficult to make because of the large uncertainties involved in the protection required against meteoroid impact for the waste heat radiators. Considerable effort will therefore be required to resolve the uncertainties involved and permit the development of lightweight reliable radiator systems.

### REFERENCES

1. KREBS, RICHARD P., WINCH, DAVID M., and LIEBLEIN, SEYMOUR: Analysis of Megawatt Level Direct Condenser-Radiator. Paper 2545-62, ARS Space Power Systems Conf., 1962.
2. LOEFFLER, I. J., LIEBLEIN, SEYMOUR, and CLOUGH, NESTOR: Meteoroid Protection for Space Radiators. Paper No. 2543-62, ARS Space Power Systems Conf., Sept. 25-28, 1962.
3. DIEDRICH, JAMES H., and LIEBLEIN, SEYMOUR: Materials Problems Associated with the Design of Radiators for Space Powerplants. Paper No. 2535-62, ARS Space Power Systems Conf., Sept. 25-28, 1962.
4. ENGLISH, R. E. and GUENTERT, D. C.: Segmenting of Radiators for Meteoroid Protection. ARS Jour., Aug. 1961, pp. 1162-1164.
5. WEATHERSTON, R. C.: The Radiation Amplifier—A New Approach to Heat Rejection from Space Powerplants. Paper 62-73, Inst. Aero., Sci., Inc., 1962.
6. WEATHERSTON R. C., and SMITH, W. E.: A New Type of Thermal Radiator for Space Vehicles. Paper 60-78, Inst. Aero., Sci., Inc., 1960.
7. BURGE, H. L.: Revolving Belt Space Radiator. ARS Jour., vol. 32, no. 3, Aug. 1962, pp. 1243-1248.

## 48(a). Generation of Thrust—Electrothermal Thrustors

By John R. Jack

JOHN R. JACK, *Head of the Electrothermal Section of the NASA Lewis Research Center, has conducted research on aerodynamic loads, boundary-layer heat transfer and transition, and electrothermal rockets. Mr. Jack received his B.S. degree in 1946 from Kent State University, and his M.S. degree in 1948 from Carnegie Institute of Technology.*

### INTRODUCTION

As Mr. Moeckel noted in his introduction, a specific impulse of the order of 1000 seconds is adequate for several space missions within the gravitational field of the Earth. This specific impulse can be achieved readily with fairly good efficiency by an electrothermal thrust generator. In such a device the propellant is heated electrically before being expanded in a conventional convergent-divergent nozzle.

The effort at the Lewis Research Center in the electrothermal propulsion field is in three areas: (1) the investigation of complete engine configurations, (2) propellant heat-transfer effects, and (3) the investigation of suitable propellants.

### ENGINE CONFIGURATIONS

There are two electrothermal propulsion schemes under investigation. The first of these approaches is shown schematically in figure 48(a)-1. This experimental arc jet consists of a cathode and an anode, which also serves as a convergent-divergent nozzle. In operation an arc is struck between the two electrodes. The propellant flows through and around the arc, where it is heated to very high temperatures, and is then expanded through the nozzle to produce thrust.

Arc jet research is being conducted at various research establishments on both alternating- and direct-current units. Currently a 30-kilo-

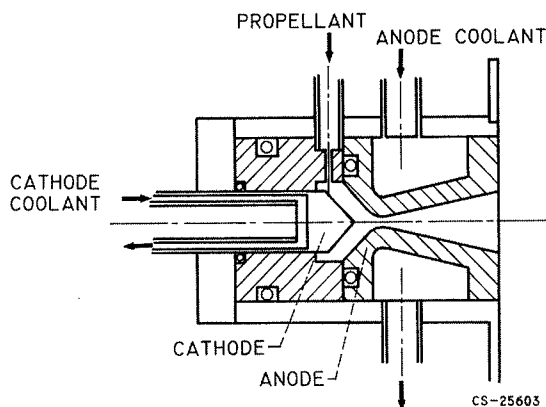


FIGURE 48(a)-1.—Arc-heated thrust device.

watt unit using hydrogen yields a specific impulse of about 1000 seconds, a thrust of  $\frac{1}{2}$  pound, and efficiencies of approximately 40 percent. The main problem areas associated with this type of thruster are: (1) the choice of a suitable propellant to increase efficiency and to meet space storage requirements, (2) the demonstration of electrode life to meet lifetime requirements, and (3) the development of better regenerative and radiation cooling techniques.

The second electrothermal device of interest is shown in figure 48(a)-2. It is an experimental resistance-heated hydrogen rocket designed for a thrust of 1 pound and a specific impulse of 1000 seconds. Its principle of operation is based upon using an electrically powered, resistance-heated heat exchanger to bring

## ELECTRIC PROPULSION

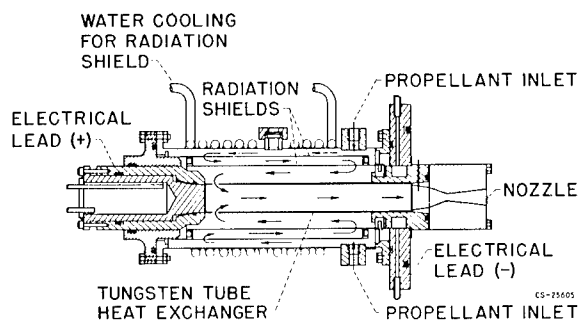


FIGURE 48(a)-2.—30-Kilowatt tungsten tube electrothermal propulsion engine.

the propellant up to the temperature required to produce the desired engine performance. A detailed discussion of this engine may be found in references 1 and 2.

This propulsion approach offers several potentially attractive features. Among them are:

- (1) High efficiency
- (2) Long life and good reliability
- (3) Simple matching to a power supply (this device can operate equally well on either alternating or direct current)
- (4) Simple starting technique
- (5) Variable thrust

There are two disadvantages associated with this engine. First, since its operation requires a metal heat exchanger, it is temperature limited; consequently, the specific impulse is limited to approximately 1100 seconds. Second, this engine must use hydrogen for a propellant to achieve a specific impulse of 1000 seconds; therefore, the space storage of hydrogen is a problem.

A typical set of experimental thrust data for a resistance-heated hydrogen jet is shown in figure 48(a)-3 for a propellant flow rate of  $10^{-3}$  pound per second. The thrust increases from a cold-flow value of 0.25 pound to a value of 0.73 pound at an input power of 38 kilowatts. Since the propellant flow rate is  $10^{-3}$  pound per second, the specific impulse increases from 250 to 730 seconds. Also presented in figure 51(a)-3 is the calculated thrust based upon one-dimensional gas-flow theory for the gas stagnation temperature at a given power input and nozzle geometry. Experiment and theory are in good agreement. The amount of thrust to be expected in a space environment is also presented.

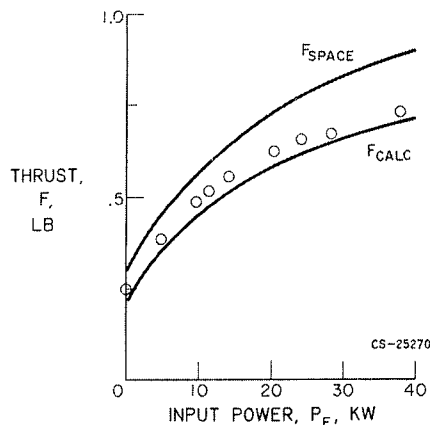


FIGURE 48(a)-3.—Variation of thrust with input power. Propellant weight flow,  $10^{-3}$  pound per second.

At the highest input power, the thrust to be expected for space operation is 0.9 pound, and the corresponding specific impulse 900 seconds. The vacuum specific impulse of 900 seconds should not be considered an upper limit because this value is based upon a heat-exchanger temperature of  $4600^{\circ}$  R and a gas stagnation temperature of  $4100^{\circ}$  R. Both of these temperatures can be increased so that a vacuum specific impulse of 1000 seconds may be obtained.

The flow through the engine is quite uniform, so that studies of a more fundamental nature may be made using the engine as a source of high-temperature hydrogen.

### PROPELLANT HEAT-TRANSFER EFFECTS

Two propellant characteristics affect the performance of an electrothermal thrust generator. The first is heat loss to the engine walls by convection. This characteristic is very important because it affects engine performance and ultimately limits thruster performance. This limitation arises for regenerative cooling because the heat capacity of a propellant at a given engine wall temperature is limited, and, for radiation cooling, because the engine wall material has an operating temperature limit.

A preliminary analysis of this problem has been made for complete regenerative and radiation cooling utilizing hydrogen and helium as propellants (ref. 3). The results for regenerative cooling with hydrogen are shown in figure 48(a)-4. The maximum specific impulse ob-

## GENERATION OF THRUST—ELECTROTHERMAL THRUSTORS

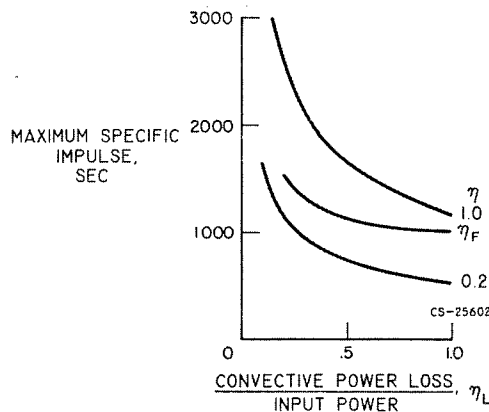


FIGURE 48(a)-4.—Maximum specific impulse with regenerative cooling. Propellant, hydrogen; pressure, 1 atmosphere; wall temperature, 5400° R.

tainable is presented as a function of the amount of heat or power to be recovered regeneratively. Results are presented for three overall engine efficiencies:  $\eta=0.2$ , a low experimental efficiency;  $\eta=1.0$ , the maximum engine efficiency; and  $\eta=\eta_F$ , the maximum efficiency to expect if the flow is frozen ( $\eta_F$  is the frozen flow efficiency and will be discussed in a subsequent section). If the flow is frozen and a typical power loss ratio of  $\eta_L=0.2$  is used, it is found that the maximum specific impulse obtainable with regenerative cooling is of the order of 1500 seconds.

Figure 48(a)-5 illustrates what is expected for radiation cooling with hydrogen as a propellant. In this case, the maximum specific im-

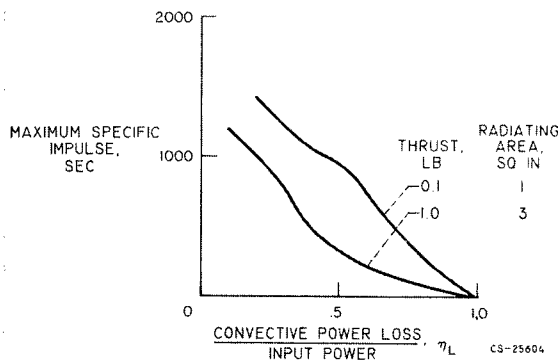


FIGURE 48(a)-5.—Maximum specific impulse with radiation cooling. Propellant, hydrogen; pressure, 1 atmosphere; wall temperature, 5400° R;  $\eta = \eta_F (1-\eta_L)$ .

pulse is a function of the thrust level, so two typical thrusts have been used, 0.1 and 1.0 pound. The radiating areas used are estimated values appropriate for the thrust levels considered. Assuming again a power loss ratio of  $\eta_L=0.2$ , the maximum specific impulse attainable at a thrust level of 1.0 pound is approximately 1100 seconds, whereas that found for a thrust level of 0.1 pound is about 1500 seconds. Thus radiation cooling appears more attractive at the lower thrust levels.

## SUITABLE PROPELLANTS

As noted previously, hydrogen presents a severe space storage problem, and it is desirable to search for a propellant that yields comparable performance and yet is easily stored. Pos-

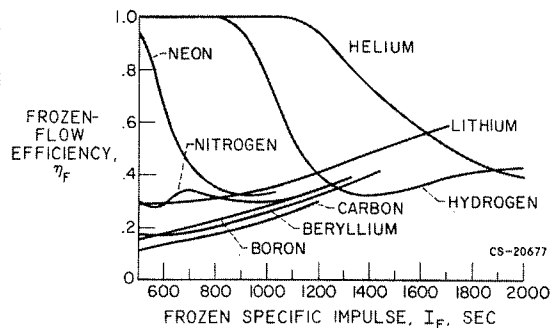


FIGURE 48(a)-6.—Frozen flow efficiencies for various propellants. Pressure, 1 atmosphere.

sible propellants for electrothermal thrusters may be evaluated by considering the second propellant characteristic affecting engine performance. Because of the high temperatures encountered, the propellant dissociates and ionizes, and, if it does not recombine in the nozzle, an energy loss is experienced which decreases the engine performance. Experience to date has indicated that little recombination can be expected, so that the propellant flow can be considered frozen. As a result, the ideal engine efficiency is equal to the frozen-flow efficiency, and propellants may be compared in terms of this parameter. The frozen-flow efficiency is defined as the ratio of the power available for thrust to the total power imparted to the propellant; it is also a measure of the amount of power invested in dissociation and ionization.

Figure 48(a)-6 shows a typical comparison obtained from an analytical study (ref. 1). The frozen-flow efficiencies for eight possible propellants are presented as a function of specific impulse for a pressure level of 1 atmosphere. At a specific impulse of 1000 seconds, helium and hydrogen have considerably better efficiencies than any of the other propellants considered. At specific impulses greater than 1600 seconds, lithium is better than either helium or hydrogen.

Although the better propellants discussed here have good efficiency in the specific impulse range of interest, each has associated with it space storage or feed problems; it is thus desirable to look further at other possible propellants. Some possibilities are water, ammonia, ethane, methane, and lithium hydride. These propellants have been studied, and a comparison of frozen-flow efficiencies is shown in figure 48(a)-7.

For specific impulses of about 1000 seconds, hydrogen still yields a better efficiency than any of the noncryogenic propellants considered. It appears, however, that both lithium hydride

and water may possibly yield a comparable efficiency and should be given more consideration. For specific impulses of the order of 1200 seconds, both lithium and ammonia are better than hydrogen, and ethane and methane seem promising.

### CONCLUDING REMARKS

During the past few years the research conducted on electrothermal thrusters has narrowed considerably the gap existing between the research model and the flyable prototype. The lifetime of engine components, initially measured in minutes, has now been extended to weeks. Specific impulses, originally measured at a few hundred seconds, have been pushed up into the 1000- to 1500-second range. In fact, it now appears feasible to design a thruster having the desired performance characteristics and a fairly good conversion efficiency.

Despite the many advances made, however, there still remain several major problem areas that require additional research effort before the overall capability of an electrothermal thruster can be fully realized. For example, electrodes and heat exchangers that are reliable and can meet mission lifetime requirements must be demonstrated. Noncryogenic propellants that indicate the possibility of yielding good performance and yet could be easily stored in space should be given considerable attention. In conjunction with a propellant investigation, the local convective heating rates should be measured because these will determine the type and characteristics of the cooling system finally employed. Continued research in these areas should ultimately prove very profitable and lead to the development of an efficient and reliable electrothermal thrust unit.

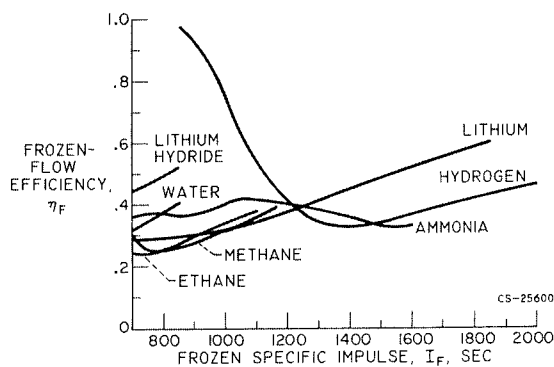


FIGURE 48(a)-7.—Frozen flow efficiencies for several noncryogenic propellants. Pressure, 1 atmosphere.

### REFERENCES

1. JACK, JOHN R.: Theoretical Performance of Propellants Suitable for Electrothermal Jet Engines. NASA TN D-682, 1961.
2. JACK, JOHN R.: NASA Research on Resistance Heated Hydrogen Jets. Third Symposium on Advanced Propulsion Concepts, AFOSR and General Electric Co. (Cincinnati).
3. JACK, JOHN R.: Regenerative and Radiation Cooling of Electrothermal Thrust Generators. Paper 61-97-1791, Am. Rocket Soc., Inc., 1961.



## 48(b). Generation of Thrust—Electromagnetic Thrustors

By George R. Seikel

GEORGE R. SEIKEL, *Head of the Plasma Flow Section of the Lewis Research Center, is currently conducting research on the fundamentals of flowing plasma and the possibility of utilizing plasma thrustors for interplanetary electric propulsion systems. He received his B.S. degree in Aeronautical Engineering in 1955 and his M.S. degree in Engineering Mechanics in 1957 from the University of Notre Dame. In September 1961, Mr. Seikel was a delegate to the International Atomic Energy Agency Conference on Plasma Physics and Controlled Nuclear Fusion Research conducted in Salzburg, Austria.*

### INTRODUCTION

The general principle of acceleration in all electromagnetic thrustors is essentially the same as that in ordinary electric motors. As illustrated in figure 48(b)-1, if in an electric conductor, be it a wire or a plasma, a current  $\vec{j}$  flows in the presence of a magnetic field  $\vec{B}$ , an electromagnetic body force is produced on the conductor. The body force  $\vec{F}$  is equal to the vector or cross product of the current and the magnetic field. The direction of the force is perpendicular to both  $\vec{j}$  and  $\vec{B}$ , as illustrated by the right-hand rule. In electromagnetic thrustors, it is this  $\vec{j} \times \vec{B}$  body force that is used to act on the plasma propellant.

### PLASMA PROPELLANT

The general properties of the plasma propellant are as follows:

(1) The plasma is composed of three constituents: electrons, ions, and neutrals. This distinction is exceedingly important since most of the physics is involved with the simultaneous dealing with three different things. In fact, a great deal of confusion can often be eliminated if the species can be individually treated.

(2) The plasma charged particle density is sufficiently high that approximate charge neutrality exists throughout the fluid, except in thin sheaths at all boundaries. Large departures from charge neutrality can exist only over a distance termed the Debye length. The Debye length is, however, always much less than the accelerator characteristic length. The sheaths at the boundaries have thicknesses of the order of a Debye length.

(3) Nonequilibrium effects predominate in the plasma. The mere fact that large currents flow in the plasma guarantees velocity nonequilibrium, for a current requires that electrons are moving relative to ions. Electrons with velocities relative to the ions of one-thousandth of the speed of light would not be unusual. Similarly, ion slip may exist;

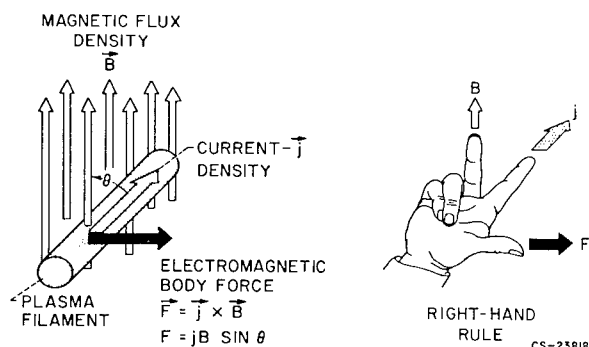


FIGURE 48(b)-1.—Electromagnetic body force on a plasma current filament.

that is, an insufficient number of collisions may be present to prevent the ions from slipping through the neutrals. With regard to thermal equilibrium, to expect to be able to do more than assign different temperatures to each of the plasma constituents is usually unreasonable. Even a constituent may not be in self-equilibrium; that is, its particles do not have a Maxwellian particle distribution. Typically, a plasma propellant may have an electron temperature of  $100,000^\circ\text{K}$ , while the ions and neutrals are essentially at room temperature.

(4) By metallic standards, the ordinary or scalar conductivity of the plasma propellant is low. Even for a fully ionized plasma, an electron temperature of  $5,000,000^\circ\text{K}$  is required to obtain a conductivity equal to that of copper. Typical plasma propellants have electron temperatures of less than a few hundred thousand  $^\circ\text{K}$  and, thus, have conductivities slightly less than that of carbon, which is used to make resistors. Because of the large energy required to elevate the electron temperature, however, utilizing these low-conductivity plasmas for propulsion applications is desirable.

(5) Hall effects predominate in the accelerators; that is, the currents and the electric fields in the plasma are not parallel. This is a necessary consequence of efficient accelerator operation, since the ratio of the useful work to the Joule heating is either less than, or of the order of, the Hall parameter  $\omega_c\tau_-$  (where  $\omega_c$  is the electron cyclotron frequency  $eB/m_-$ , and  $\tau_-$  is the mean time for an electron to lose its momentum to the ions or neutrals).

### PLASMA ACCELERATION

There are theoretically two methods of efficiently accelerating a plasma. One method is to heat the plasma and convert the random energy of the hot propellant into kinetic energy in a nozzle. If a physical nozzle is employed, it is a pure electrothermal device of the general class described by Mr. John R. Jack in the previous paper. If a magnetic nozzle is employed, the accelerator may be classed as an indirect electromagnetic device; that is, no work is done with the electromagnetic body force, but it is utilized

to transfer the forces between the plasma and the accelerator structure. The alternative method of accelerating the plasma is to use directly the electromagnetic body force  $\vec{j} \times \vec{B}$  to add kinetic energy to the plasma.

Consider the plasma acceleration process from a multifluid point of view; that is, what is happening to the electrons, the ions, and the neutrals? Note that the electrons have more than enough thermal energy to be expelled at any specific impulse of interest to electric propulsion, and the primary method of accelerating neutrals is by collisions with ions. Thus, in any plasma acceleration process the chief concern is the mechanism for accelerating the ion plasma constituent.

### TYPES OF ELECTROMAGNETIC ACCELERATORS

A large number of devices use the electromagnetic body force to accelerate a plasma propellant; one convenient method of classification is on the basis of the type of electric power utilized—direct current, alternating current, radio-frequency, or pulsed. Such a division is descriptive and permits estimation of the required power conditioning systems. Power sources presently being developed utilize alternators to generate the electric power. Thus, the minimum power conditioning requirement for d-c accelerators is that the power be rectified; a-c accelerators may be able to operate directly from the alternators. Estimates indicate that up to 100-kilocycle systems appear possible without serious penalties in alternator weight or efficiency. Radio frequency systems would require both rectification and vacuum tubes to condition the power and, thus, have competitive disadvantages in power-conditioning-system efficiency and weight. The pulsed systems require efficient charging circuits and capacitive power storage. Recent advances in capacitor technology indicate that sufficiently light capacitors appear imminent.

A cursory description of some of the plasma accelerator configurations presently being investigated by the Lewis Research Center is given and references to some other devices are cited in the following section. Additional discussion is presented in the paper by Mr. Macon C. Ellis, Jr.

## GENERATION OF THRUST—ELECTROMAGNETIC THRUSTORS

### D-C Accelerators

The type of d-c accelerators under investigation range from the direct relatively low-impedance segmented crossed-field accelerators (refs. 1 to 4), to the relatively high-impedance Hall current accelerators (refs. 5 to 10), to the indirect nonequilibrium magnetically contained electrothermal accelerator (refs. 11 and 12).

*Hall current ion accelerator.*—Figure 48(b)-2 schematically depicts the Hall current ion accelerator (ref. 8), which is annular in geometry. The applied electric field is utilized to accelerate directly the ions produced by the discharges. The applied radial magnetic field is sufficiently weak that it does not affect the ion motion, but is sufficiently strong to be dominant in determining the electron motion. In such a situation the current of the electrons diffusing upstream in the accelerator is substantially less than the azimuthal electron drift or Hall current. Since it is this Hall current that appears to provide the electromagnetic acceleration force, and only the much smaller diffusion electron current and ion current are supplied by the power source, the device has a relatively high impedance. This device is analogous to an ion engine with no space-charge limitations on the ion flux. Since only the ion plasma constituent is accelerated, the accelerator cathode also serves as a neutralizer. Only very preliminary performance data have been obtained for such devices, but the results are promising.

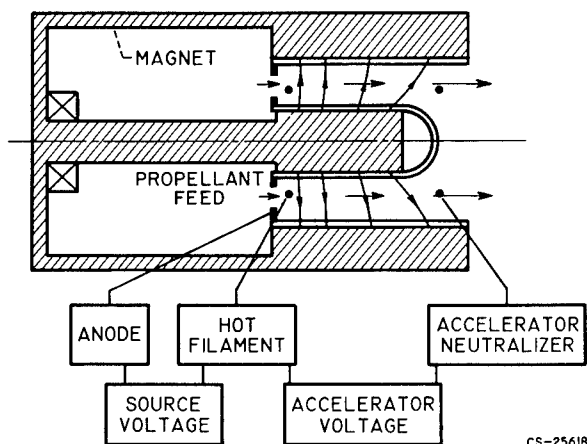


FIGURE 48(b)-2.—Hall current ion accelerator.

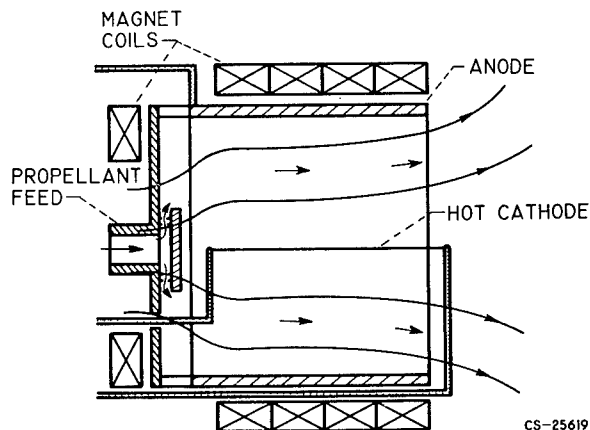


FIGURE 48(b)-3.—Nonequilibrium magnetically contained electrothermal thruster.

*Nonequilibrium electrothermal magnetically contained accelerator.*—Figure 48(b)-3 schematically depicts a nonequilibrium electrothermal magnetically contained accelerator (ref. 12). It consists of a heated filament, a cylindrical anode, and a varying axial magnetic field. In low-density discharges of this type, the electric power is directly added to the random energy of the plasma electrons. The high-energy electrons ionize the propellant, and, as the plasma's electron gas expands out of the device, its random electron energy is converted to direct energy. Since there can be no divergence of current, however, the electrons drag the ions along. Physically, this is accomplished by an axial electric field that the plasma itself builds. This field retards the electron's expansion, accelerates the ions, and causes an azimuthal electron Hall current to flow that provides the electromagnetic reaction force on the accelerator. The energy added to the ions is at the expense of the random electron energy. The expansion process is controlled by the magnetic nozzle action of the spatially varying magnetic field. Preliminary performance of a 200-watt thruster with argon as the propellant has yielded power efficiencies of the order of 20 percent at a specific impulse of 1500 seconds.

### A-C Accelerators

All d-c accelerators require that electrodes be in contact with the plasma. This possible limitation of life can be circumvented by a-c electrodeless accelerators that utilize induction

## ELECTRIC PROPULSION

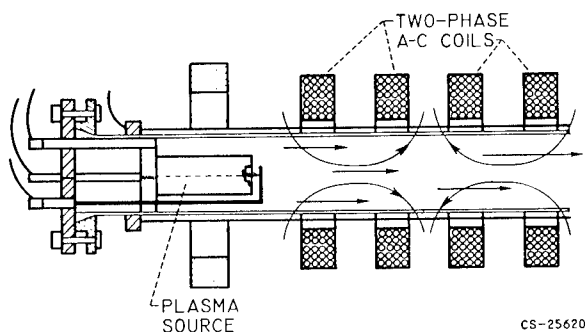


FIGURE 48(b)-4.—Traveling magnetic wave plasma engine.

coupling; however, the coupling efficiency must be good. A number of electrodeless accelerators are being investigated (refs. 13 to 18). One such device, the traveling magnetic wave accelerator (ref. 16), is schematically depicted in figure 48(b)-4. The plasma produced in the plasma source diffuses into the accelerator and is accelerated by the moving magnetic wave produced by the polyphase coil system. The operation is analogous to a polyphase induction motor. As the magnetic wave moves through the plasma, an azimuthal current is induced. The interaction of this current with the magnetic wave produces an electromagnetic body force tending to drag the plasma with the wave. The body force acts on the plasma's electrons, which transfer the force to the ions through an induced axial polarization or Hall electric field (ref. 10).

### Pulsed Accelerators

The efficiency of plasma accelerators tends to increase with power level. The pulsed accelerators, or guns (refs. 19 to 23), attempt to capitalize on this fact by utilizing instantaneous power levels above 100 megawatts. Final versions of such thrusters would have pulsing rates of 100 to 1000 pulses per second and pulse durations of a few microseconds. The chief problem in such systems is in obtaining a sufficiently tight coupling to the gun. Useful power addition to the plasma terminates in less than the first half cycle of the discharge. This places stringent requirements on obtaining low-inductance capacitors and low-inductance circuits at breakdown. An experiment (ref. 23) on one of the most interesting of these accelerators, the

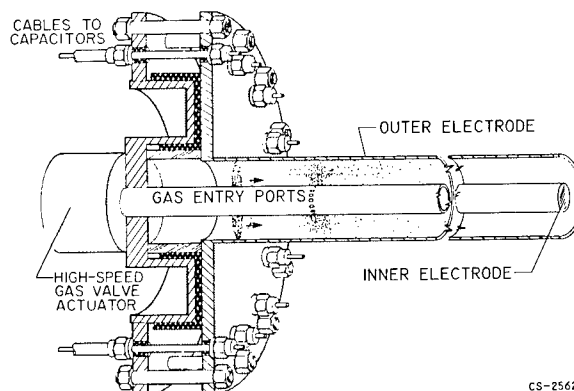


FIGURE 48(b)-5.—Coaxial plasma gun.

coaxial plasma gun, is schematically depicted in figure 48(b)-5. In this gun the low-inductance capacitor bank is discharged before the coaxial pair of electrodes. The radial current sheet interacts with the azimuthal magnetic field created by the current flowing in the electrodes to provide the electromagnetic acceleration force. This force acts on the electrons, which are coupled to the ions by the induced axial-electric field (ref. 24). Typical experiments utilize pulsed propellant injection, but in final systems the pulsing rate may be adequate to permit continuous propellant flow. Experiments may or may not use switching between the capacitors and the gun. Such devices are polarity sensitive, and operation is superior if the center electrode is the initial cathode (ref. 25). Performance to date of such a gun has yielded efficiencies as high as 30 percent at a specific impulse of 5000 seconds.

### CONCLUSIONS

In conclusion, although many interesting and attractive schemes are being investigated for electromagnetic propulsion applications, none of these devices has as yet demonstrated the performance required for an actual propulsion mission. On the other hand, no fundamental obstacles have been discovered that would prevent the eventual achievement of this goal. The chief problems in the development of such devices have primarily been the lack of fundamental knowledge of plasma physics and the lack of sufficient plasma diagnostic techniques to evaluate adequately the experiments being performed. Thus, it is actually in these areas that

## GENERATION OF THRUST—ELECTROMAGNETIC THRUSTORS

the major effort has been devoted, and in which substantial contributions are being made.

Potentially, electromagnetic accelerators should be able to provide rugged, relatively small thrusters capable of above megawatt power levels. Efficiencies should be competitively attractive, at least in the lower specific

impulse range of from 1000 to 5000 seconds. Potentially high efficiency in this range of specific impulses is due to the possibility of efficient utilization of the plasma's ions. Since in such devices the ionization and acceleration processes can be integral, the ions can be accelerated as they are produced.

## REFERENCES

1. CARTER, A. F., WOOD, G. P., SABOL, A. P., and WEINSTEIN, R. H.: Experiments in Steady-State High-Density Plasma Acceleration. *Engineering Aspects of MHD*, Ed. Mannel and Mather, Columbia Press, 1961.
2. DEMETRIADES, S. T., and ZIEMER, R. W.: Energy Transfer to Plasmas by Continuous Lorentz Forces. Preprint 2002-61, Am. Rocket Soc., Inc., 1961.
3. BLACKMAN, V. H., and SUNDERLAND, R. J.: The Experimental Performance of a Crossed-Field Plasma Accelerator. Preprint 2633-62, Am. Rocket Soc., Inc., 1962.
4. WAX, S.: Hall Type MHD Space Propulsion Device. Res. Rep. 62-111-600-R1, Westinghouse Res. Lab., May 1962.
5. HESS, R. V.: Experiments and Theory for Continuous Steady Acceleration of Low Density Plasmas. Vol. 1, Proc. XIth Int. Astronautical Conf., Julius Springer (Vienna), 1961, pp. 404-411.
6. PATRICK, R. M., and POWERS, W. E.: A Magnetic Annular Arc. Res. Rep. 129, Avco-Everett Res. Lab., May 1962. (See also *Physics of Fluids*, Oct. 1962.)
7. CANN, G. L., BUHLER, R. D., TEEM, J. M., and BRANSON, L. K.: Magnetogasdynamic Accelerator Techniques, Final Rep., Electro-Optical Systems, Inc., Nov. 1961. (Contract No. AF 40(600)-939.)
8. SEIKEL, G. R., and RESHOTKO, E.: Hall Current Ion Accelerator. *Bull. Am. Phys. Soc.*, vol. 7, no. 6, June 1962.
9. SALZ, F., MEYERAND, R. G., and LARY, E. C.: Ion Acceleration in a Gyro-Dominated Neutral Plasma Experiment. *Bull. Am. Phys. Soc.*, vol. 7, no. 7, Aug. 1962.
10. JANES, G. S., and WILSON, T.: Electrostatic Acceleration of Neutral Plasmas—Momentum Transfer Through Magnetic Fields. Third Symposium on Advanced Propulsion Concepts, Cincinnati, Ohio, Oct. 1962.
11. MEYERAND, R. G., JR., SALZ, F., LARY, E. C., and WALCH, A. P.: Electrostatic Potential Gradients in a Nonthermal Plasma. Paper No. 47, Fifth Int. Conf., Ionization Phenomena in Gases, Munich, 1961.
12. DOMITZ, STANLEY: Low-Pressure dc Plasma Source. *Bull. Am. Phys. Soc.*, vol. 7, no. 6, June 1962.
13. COVERT, E. E., and HALDEMAN, C. W.: The Traveling Wave Pump. *ARS Jour.*, vol. 31, no. 9, Sept. 1961, pp. 1252-1259.
14. JANES, G. S.: Magnetohydrodynamics Propulsion. Res. Rep. 90 (AFOSR TN 60-955), Avco-Everett Res. Lab., Aug. 1960.
15. PENFOLD, A. S.: Traveling Wave Plasma Accelerators. Preprint No. 2130-61, Am. Rocket Soc., Inc., 1961.
16. JONES, R. E., and PALMER, R. W.: Traveling Wave Plasma Engine Program at NASA Lewis Research Center. Third Symposium on Engineering Aspects of Magnetohydrodynamics, Univ. of Rochester, Mar. 1962.
17. BARGER, R. L., BROOKS, J. D., and BEASLEY, W. D.: The Design and Operation of a Continuous-Flow Electrodeless Plasma Accelerator. NASA TN D-1004, 1962.
18. MILLER, D. B., GLOERSEN, P., GIBBONS, E. F., and BEN DANIEL, D. J.: Cyclotron Resonance Propulsion System. Third Symposium on Engineering Aspects of Magnetohydrodynamics, Univ. of Rochester, Mar. 1962.
19. KUNEN, A. E., and McILLROY, W.: The Electromagnetic Pinch Effect for Space Propulsion. ARS—Northwestern Gas Dynamics Symposium, Northwestern Univ., Aug. 1959.
20. MARSHALL, JOHN, JR.: Performance of a Hydromagnetic Plasma Gun. *Physics of Fluids*, vol. 3, 1960, p. 134.

#### **ELECTRIC PROPULSION**

21. LOVEBERG, R., GOODING, T., and HAYWORTH, B.: The Use of a Coaxial Gun for Plasma Propulsion. General Dynamics—Astronautics. Final Report, 1962. (Contract NAS 5-1139.)
22. GLOERSEN, P., GOROWITZ, B., HOVIS, W. A., Jr., and THOMAS, R. B.: An Investigation of the Properties of a Repetitively Fired Two-Stage Coaxial Plasma Engine. Third Symposium on Engineer Aspects of Magnetohydrodynamics, Univ. of Rochester, Mar. 1962.
23. MICHELS, C. J., and RAMINS, P.: Survey of Coaxial Plasma Gun Performance with Various Propellants. Int. Coaxial Plasma Gun Symposium, Case Inst. of Tech., Sept. 1962.
24. BURKHARDT, L. C., and LOVEBERG, R.: Current Sheet in a Coaxial Plasma Gun. Physics of Fluids, vol. 5, no. 3, Mar. 1962, p. 341.
25. KECK, J. C.: Current Distribution in a Magnetic Annular Shock Tube. Physics of Fluids, vol. 5, no. 5, 1962, p. 630.

## 48(c). Generation of Thrust—Electrostatic Thrustors

By Warren D. Rayle

WARREN RAYLE, *Chief of the Advanced Concepts Branch at the NASA Lewis Research Center, has specialized in electric propulsion. He attended Case Institute of Technology, receiving his B.S. degree in Chemical Engineering in 1948. He is a member of the American Rocket Society.*

### INTRODUCTION

The electrostatic thruster, as exemplified by the ion rocket, is not a new concept. For example, Oberth (ref. 1) discussed such a system in 1929. A fair amount of theoretical examination had been given to the idea well in advance of the first space flights. Not, however, until shortly before those flights, or the brink of the space age, did the serious development of the associated technology commence. Under the auspices of the Department of Defense as well as NASA, this development has now been carried to the point where prototype devices that might be suitable for some space applications are available.

This discussion has as its purpose (1) to outline the fundamental processes integral to electrostatic propulsion, (2) to describe the main categories of such thrusters and their current status, and (3) to point out a few possible future developments which might change the present emphasis in electric propulsion research. This paper is not a comprehensive survey of the field. The reader seeking more detailed and comprehensive information is directed to the existing literature, especially references 2 to 5.

### ELECTROSTATIC PROPULSION FUNDAMENTALS

Figure 48(c)-1 is a schematic diagram of an electrostatic thruster. The three processes integral to the cycle are (1) the generation of charged particles, (2) their acceleration, and

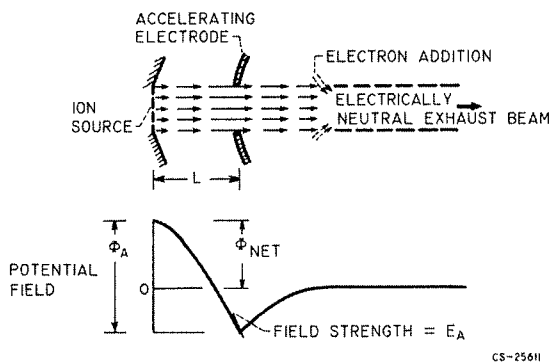


FIGURE 48(c)-1.—Electrostatic thruster.

(3) the neutralization of the resultant beam. As shown, the ions are accelerated beyond the velocity desired and then decelerated. This process permits greater ion current densities and also prevents electrons from being drawn back into the ion source. In the development of an electrostatic thruster, the primary goals are high efficiency, thrust-to-weight ratio, and durability. The thrust-to-weight ratio is directly dependent on the attainable thrust density, that is, the thrust per unit area. The maximum current density which an electrostatic accelerator will accept is calculable and is implied in figure 48(c)-1 by the potential gradients being shown as zero at the source. Such limiting currents have been calculated for a wide variety of configurations (ref. 6). The maximum thrust density has also been shown to depend on the electric field at the accelerator

## ELECTRIC PROPULSION

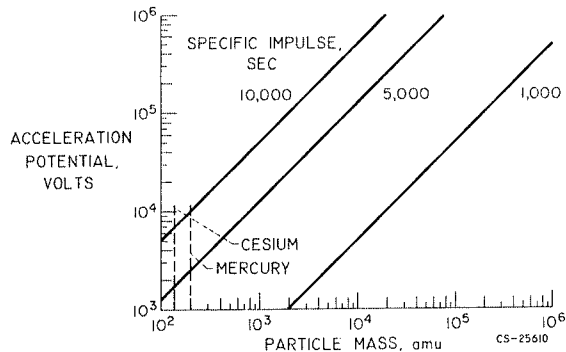


FIGURE 48(c)-2.—Singly charged particle acceleration.

(refs. 2 and 7), which, in turn, is approximated by the ratio of the accelerating potential to the acceleration length.

The net accelerating potential required to obtain a given specific impulse varies, as shown in figure 48(c)-2, with the particle mass. Singly charged particles are assumed. A convenient number to remember is 10 volts per atomic mass unit, which corresponds to a specific impulse of about 4500 seconds. For particles such as cesium or mercury ions, the required accelerating potentials are then on the order of 1000 to 2000 volts. With such a small accelerating potential, acceleration lengths of less than 1 millimeter would be quite feasible if electric breakdown were the only limiting factor. Other difficulties are encountered in attempting to fabricate and operate such a delicate structure. A major consideration is the probable operating life.

An alternative approach to obtaining high thrust densities is through the use of heavier particles. A 100,000 atomic mass unit particle requiring 1 megavolt of acceleration permits accelerating lengths between 0.1 and 1 meter.

The accelerator limits are thus seen to be rather clearly delineated. Ion or charged-particle sources are currently of two principal varieties. One source is known as contact ionization and depends on the fact that some of the alkali metals, notably cesium, have ionization potentials so low that they may lose an electron on contact with a high-work-function surface such as tungsten. Contact ionization would be an extremely efficient method for the production of ions if it were not for the requirement

that the tungsten be kept hot in order to prevent the accumulation of a layer of cesium and the consequent reduction of the work function of the surface.

The second system involves the bombardment of the propellant atoms with electrons. This system is not specific to any single propellant, but is in theory able to produce ions of many different materials. The efficiency of this system is a function of many factors but has been shown to be relatively attractive for fairly heavy ions.

The neutralization of the charged-particle beam is a subject to which considerable analytical and experimental effort has been devoted. It is easily demonstrated that neutralization of ion beams can be accomplished inside vacuum tanks. Less easy is the task of proving conclusively that a similar result can be obtained in space where the beam is semi-infinite. Some mechanism must be postulated whereby the mean or drift velocities of the ions and electrons can be synchronized. Analysis is continuing and, in addition, an experiment is being readied whereby actual operation of two types of ion engine will be attempted in space.

### PRESENT STATUS OF THREE TYPES OF THRUSTOR

Ion engines in the operational prototype stage include the contact engine in which cesium is used as the propellant and the electron-bombardment engine in which mercury is used. A third type, the colloidal-particle engine, is less advanced. Although the first two engines may be considered to have had their potentialities well demonstrated, future work is required to

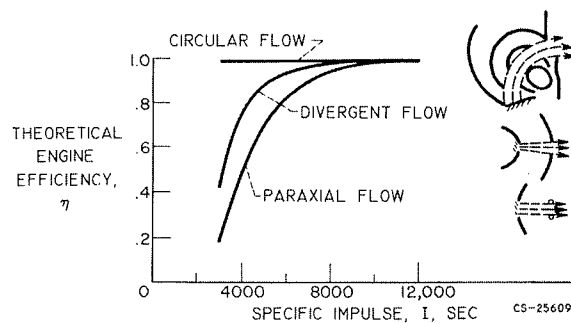


FIGURE 48(c)-3.—Theoretical efficiency of contact-ionization engines.



# GENERATION OF THRUST—ELECTROSTATIC THRUSTORS

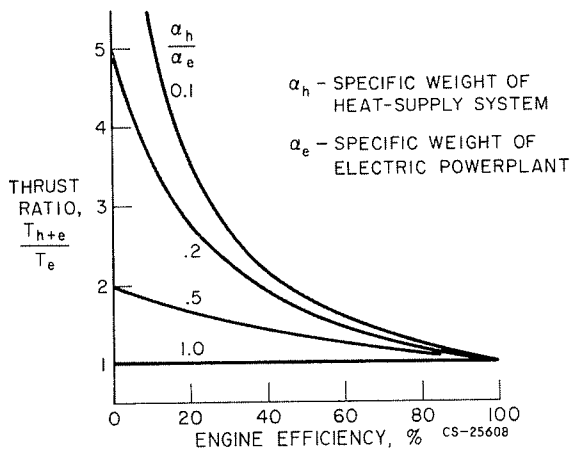


FIGURE 48(c)-4.—Ion-engine thrust gains with direct heat supply. Constant total weight and specific impulse.

improve the factors of thrust-to-weight ratio, efficiency, and durability.

In the contact ion engine, the principal source of energy loss is the heat radiated from the hot ion emitter. To some extent the accelerating electrodes can serve as radiation shielding to reduce this loss. Figure 48(c)-3 (from ref. 2) shows how greatly this might increase efficiency if the only radiation loss is assumed to be directly from the emitter to empty space; radiation falling on the accelerator is assumed to be perfectly reflected to the emitter. Compared with the "standard" paraxial-flow engine, the divergent-flow engine with its increased emitter current density is a substantial improvement. In a curved-beam configuration, the emitter radiation has no straight-line path of escape, and the efficiency calculated according to these assumptions approaches 100 percent.

Inasmuch as the principal source of loss is from the heat radiated by the emitter, the next logical question is whether there might not be a more effective (i.e., lighter) system for providing this heat. If, for example, the powerplant incorporates a very-high-temperature nuclear reactor, it might easily be possible to transfer the heat directly rather than first converting it to electric power. A separate nuclear reactor that would serve only to heat the emitter might even be considered. In figure 48(c)-4 is shown the effect of using a separate heat supply. The value 0.2 might be about

right for the ratio of specific weights of the heat supply to the electric powerplant. As should be expected, the gains in engine output at a fixed specific impulse and total powerplant weight become greater at the lower engine efficiencies.

The electron-bombardment engine of the type invented and developed by Mr. Harold R. Kaufman at the Lewis Research Center is shown as a cutaway version in figure 48(c)-5. Mercury vapor is admitted to the ion chamber at a controlled rate. The hot cathode in the center emits electrons, which are attracted to the peripheral anode. An axial magnetic field extends the electron paths increasing the probability of ionizing collision. In operation the chamber is filled with a dilute plasma from which ions are extracted by a high potential difference impressed across the pair of perforated plates labeled "screen" and "accelerator." The principal sources of power loss include the heating power to the filament, the "discharge" power between filament and anode, and the power to maintain the magnetic field. Work under way is aimed at reducing each of these.

The electron-bombardment engine differs in one very important respect from the contact-ion engine. The propellant utilization—the fraction of the total propellant flow that becomes ionized and accelerated into the beam—is substantially less than 100 percent. Correct-

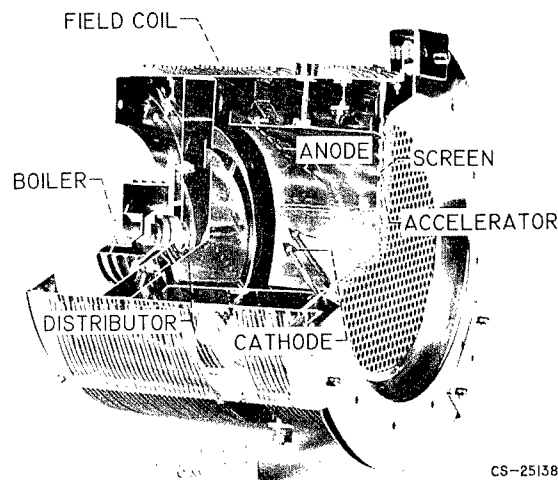


FIGURE 48(c)-5.—Electron-bombardment ion engine.

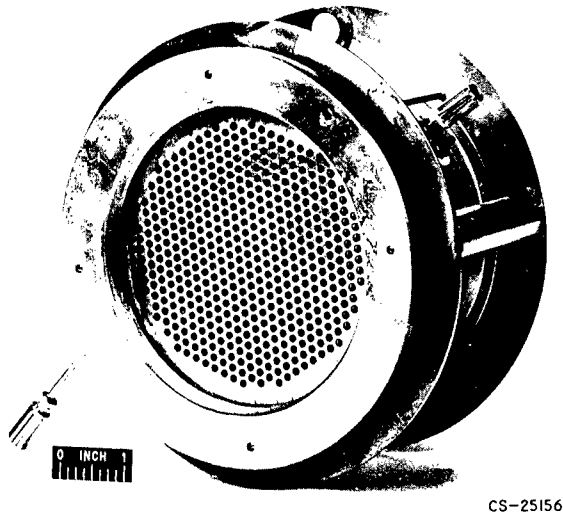


FIGURE 48(c)-6.—Permanent-magnet engine.

ing the efficiency and the specific impulse for this factor is easy enough; the problem arises from the neutral atoms going through the accelerator structure. A number of these neutrals will undergo charge exchange with the fast ions and fall into the accelerator. Ensuing erosion of the accelerator will then impose a durability limit on the entire system. Data have been obtained (ref. 8) which indicate that this charge-exchange process is indeed the primary contributor to the accelerator impingement and that the erosion is proportional thereto. It then follows that the life expectancy of a particular engine can be fairly well calculated in advance and that long life may require the engine to operate inefficiently or at a low thrust-to-weight ratio. Kaufman (ref. 8) shows that lifetimes of approximately 1 year (10,000 hr) may be predicted from current accelerator types with a thrust-to-weight ratio for the thruster alone of about 0.001. A more severe problem may be the durability of the cathode. To date the main effort has involved the use of elemental (tantalum or tungsten) cathodes. Work now in progress with low-work-function cathodes should reduce power requirements and also promise extended cathode life.

In figure 48(c)-6 is shown an engine with permanent magnets in place of the field coil. The magnets are in contact with sheets of ferromagnetic material at the front and the back of the engine; thus the requisite weak field is in-

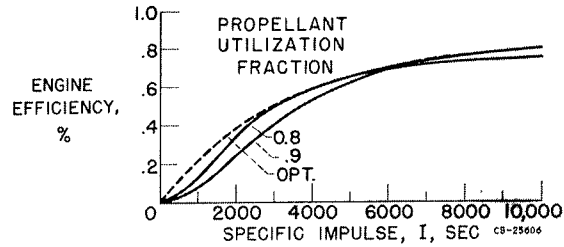


FIGURE 40(c)-7.—Engine efficiency.

duced throughout the ionization chamber. Not only does this procedure eliminate the power requirement of the field coil, but also, because it reduces by one the number of separate power supplies, simplifies and lightens the power-conditioning equipment. The weight of this engine corresponds closely to the weight of the equivalent configuration with field coil.

The efficiencies obtainable from an electron-bombardment engine according to Kaufman's estimates are shown in figure 48(c)-7. These estimates were obtained by a realistic combination of the ingredients which have been separately determined. Permanent magnets were assumed, as were low-temperature cathodes. The optimum propellant utilization varies with specific impulse; the estimated efficiency attains only about 80 percent even at 10,000 seconds. By some standards, the efficiencies at the lower specific impulses are high. Nevertheless there seems to be room for improvement.

The efficiency estimates might be compared with some others, as in figure 48(c)-8. Here the curve for the bombardment engine and the curve calculated for the divergent-flow engine

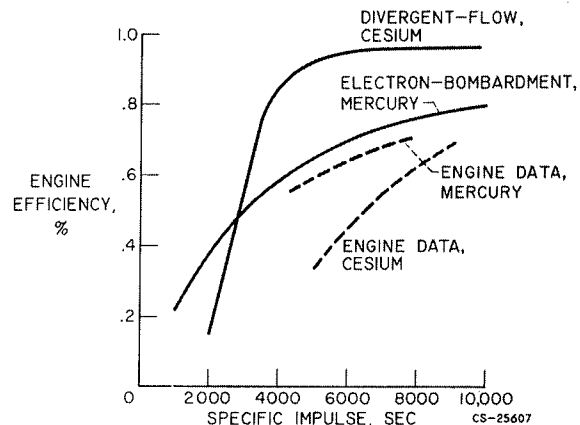


FIGURE 48(c)-8.—Estimates of ion-engine efficiencies.

## GENERATION OF THRUST—ELECTROSTATIC THRUSTORS

are compared with some actual data for existing engines. The mercury engine data approach quite closely the estimates of attainable performance. The cesium engine data fall far short of the predicted divergent-flow engine performance. If the predictions are soundly based, some very substantial improvements in the low specific impulse range may be obtained. It should be pointed out that the divergent-flow curve is entirely theoretical; no engine data for such a configuration are available at this time.

The third category of electrostatic thruster offers distinct promise for high efficiency in the low-specific-impulse region. Although its development is in an embryonic state, the colloid rocket, which uses particles of 100,000 atomic mass units or more may perform as well at low specific impulse as does the electron-bombardment engine at high specific impulse. The possibilities of this propulsion system have been discussed frequently during the past 5 years. Difficulties have been encountered in the production, charging, and acceleration of such tiny particles. A typical particle diameter might be about 40 angstroms. One frequent problem is the production of atomic or molecular ions, which, at the high accelerating voltages, consume much more power than their thrust is worth. Progress has been reported by Norgren (ref. 9). His process is the condensation of low-density vapor in an expanding nozzle. Figure 48(c)-9 shows both an electron photomicrograph of a sample of such colloids and also the particle-size distribution measured therefrom. The peak of the distribu-

tion occurs at about 0.009 micron. The particles were charged and accelerated, although only to 30 kilovolts, which gives an effective specific impulse of about 420 seconds. The progress with the colloid rocket is promising both because of the ability to provide high efficiency at low specific impulse and of a possible application with an advanced powerplant that gives megavolt potentials directly. This application is discussed by Mr. Edmund E. Callaghan.

### FUTURE CONTINGENCIES

The existing thrusters of both the cesium-tungsten and the electron-bombardment engine types will, of course, continue to be improved. The colloid rocket will be explored until its potentialities are more rigorously defined. Aside from such straight-line extrapolations, what may the future hold for electric propulsion? A great deal of effort is currently being devoted to powerplant development. The interface area between powerplant and thruster, which contains the power conditioning and control equipment, has as yet received little concentrated attention. Such equipment will be subject to most stringent requirements as to weight and reliability. Further, the type of powerplant output may well be different from that which is now being designed. System optimization may demand that the characteristics of the thruster be compromised in the interest of compatibility with other components. The possibility of a powerplant's yielding megavolts directly has certainly stimulated interest in the colloid engine wherein such voltages might be directly employed. A high-temperature nuclear turbogenerator system could similarly stimulate research in the cesium-tungsten engine with the heat-transfer system for the emitter.

Despite the vast number of missions that have been calculated, it should not be assumed that the field is exhausted. Special mission requirements may bring about the need for "non-conventional" electric thrusters. Already, as Mr. W. E. Moeckel has shown, the Jupiter mission might require a duration (and durability for the thruster) of about twice the current target of 10,000 hours. Such durability requirements may demand new approaches.

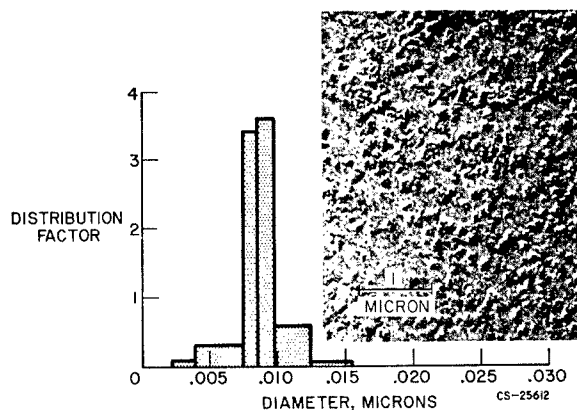


FIGURE 48(c)-9.—Particle distribution of mercurous chloride.

## ELECTRIC PROPULSION

### REFERENCES

1. OBERTH, H.: *WEGE ZUR RAUMSCHIFFFAHRT*, R. OLDENBOURG, Munich, 1929, pp. 409-423.
2. MICKELSEN, WILLIAM: Comparative Performance of Electrostatic Rocket Engines, Paper 62-74, IAS, 1962.
3. MICKELSEN, WILLIAM R.: Electric Propulsion for Space Flight, *Aerospace Eng.*, vol. 19, no. 11, Nov. 1960, pp. 6-11; 36.
4. FORRESTER, A. T., and SPEISER, R. C.: Cesium-ion Propulsion. *Astronautics*, Oct. 1959, p. 34.
5. STUHLINGER, E.: Possibilities of Electric Space Ship Propulsion. *Proc. Fifth Int. Astronautical Cong.*, 1954, pp. 100-119.
6. LOCKWOOD, DAVID L., MICKELSEN, WILLIAM R., and HAMZA, VLADIMIR: Analytic Space-Charge Flow and Theoretical Electrostatic Rocket Engine Performance. Paper 2400-62, Am. Rocket Soc., Inc., 1962.
7. LANGMUIR, DAVID B.: Problems of Thrust Production by Electrostatic Fields. *Vistas in Astronautics*. Vol. II. Pergamon Press, 1959, pp. 191-218; discussion, p. 218.
8. KAUFMAN, H. R.: The Electron-Bombardment Ion Rocket. *Third Symposium on Advanced Propulsion Concepts*, Cincinnati, (Ohio), Oct. 2-4, 1962.
9. NORGREN, C. T.: Onboard Colloidal Particle Generator for Electrostatic Engines. Paper 2380-62, Am. Rocket Soc., Inc., 1962.

## 49. Advanced Concepts

By Edmund E. Callaghan

EDMUND E. CALLAGHAN, *Assistant Chief of the Electromagnetic Propulsion Division at the NASA Lewis Research Center, has specialized in research on icing problems, heat transfer, noise, turbulence, and cryogenics and currently is concerned with magnetics. In December 1961 he received the NASA Superior Achievement Award for outstanding accomplishment in his field. Mr. Callaghan attended Rensselaer Polytechnic Institute, where he received his B.S. degree in Aeronautical Engineering in 1943. He is a member of the Institute of the Aerospace Sciences and the American Physical Society.*

The need for ever increased payloads and decreased trip times has been emphasized by previous papers. Experience indicates that each major step forward requires development of some new power source. A prime example of this is the gas turbine, which has, to a great extent displaced the piston engine in air travel. Therefore, "advanced concepts" really means the study and development of energy sources that can be adapted to propulsion devices.

First, a propulsion concept, proposed in reference 1, which is based on a radioisotope electrogenerator integrated with a colloidal particle electrostatic engine will be considered briefly. Emphasis will be placed primarily on the electrogenerator since the colloidal particle electrostatic engine has been discussed previously by Mr. Warren Rayle. Secondly, the concept of a thermonuclear rocket will be explored. Since a wide variety of scientific and space uses of intense magnetic fields is anticipated, NASA research program on magnetics (ref. 2), low-temperature physics, superconductivity, and other related programs will be discussed in some detail.

Figure 49-1 illustrates the general mode of operation of a direct nuclear electrogenerator cell. Charged particles are emitted by a decaying radioisotope. Some of these particles will reach the collector, and the potential or charge

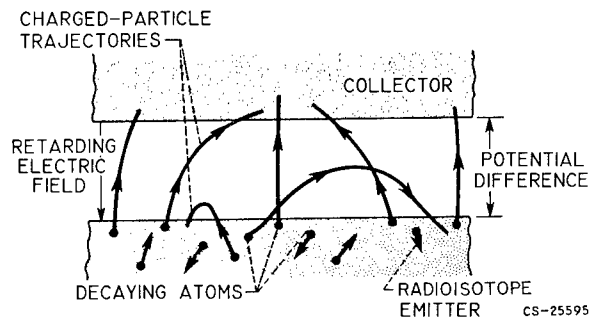


FIGURE 49-1.—Radioisotope electrogenerator cell.

will gradually build up until there is a sufficiently large potential difference between the collector and the emitter to prevent any further particles from reaching the collector. In this manner, a cell or voltage generating device is formed. In actual use an external load would be connected between the collector and emitter to complete the circuit for the flow of charge.

Not all the nuclear energy is converted to electricity. The random direction of emission of the particles causes some to have an insufficient velocity component oriented parallel to the field; thus, these particles do not reach the collector and fall back into the emitter. Since particles lose energy on passage through matter and the fuel layer cannot be infinitesimally thin and still produce power, particles emitted below the fuel layer surface lose energy

## ELECTRIC PROPULSION

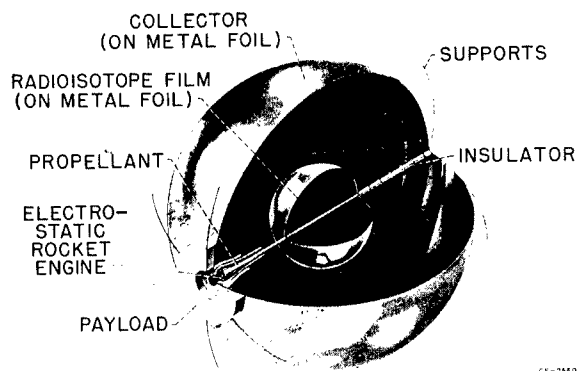


FIGURE 49-2.—Design study of 500-kilowatt electrostatic propulsion system with direct nuclear electro-generator.

in the fuel layer. In addition, any excess energy of the particle when it reaches the collector is dissipated on penetration into the surface. In all cases where energy is lost in the emitter or collector, it is transformed into heat; this results in reduced efficiency and a heat disposal problem.

Design studies have been made of several conceptual spacecraft (ref. 1) using the ideas outlined herein and in Mr. Rayle's paper. One of these concepts is shown in figure 49-2. A spherical configuration has been assumed with an alpha-emitting radioisotope film located on the surface of the inner sphere; the outer sphere acts as the collector. In this concept the outer collector is floated at space electric potential, and the inner sphere then carries a negative charge. In order to evaluate this particular concept, i.e., to estimate its specific weight, it was decided to study an electrogenerator of 500-kilowatt capability. The radioisotope chosen was polonium 210, although cerium 144 would probably serve equally well. The collector for this case is about 135 feet in diameter, and the inner emitter diameter is about 45 feet. The radioisotope total mass required is about 30 pounds. Detailed design studies show a total system weight for the integrated electrogenerator and propulsion system of about 265 pounds or a specific powerplant weight of about  $\frac{1}{2}$  pound per kilowatt.

Recent studies have shown that the size of the system can be easily scaled downward to power levels of the order of 30 kilowatts with-

out any increase in specific system weight. This makes the system of considerable interest for interplanetary space probes. The use of cerium instead of polonium would require radiation shielding of the payload package. For a typical configuration, this represents an additional weight of perhaps 1200 pounds, which would give a specific system weight of 3 pounds per kilowatt. Since this represents an order-of-magnitude reduction in specific weight over current systems and, hence, greatly enhanced emission capabilities, it becomes important to study the physics and engineering problems associated with the development of such a spacecraft.

Basic physics problems exist in regard to (a) whether particles will knock electrons out of the support foil and cause local shorts, (b) the flux distribution of particles coming out of the support foil, (c) the sputtering of the collector and emitter support materials, (d) and high voltage breakdown between the collector and emitter. Some of the engineering problems to be solved are the packaging of the isotope during launch and the dissipation of its high heat output. The mere obtaining of large quantities of radioisotopes other than cerium may be a serious problem. There are the problems of integrity of the package if the mission is aborted, the production of lightweight insulators with small leakage, and the development of methods for depositing and attaching isotopes in thin films to the emitter surface.

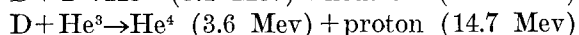
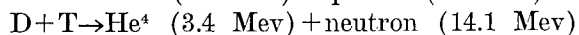
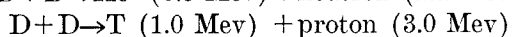
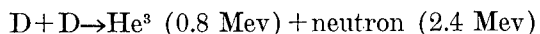
Study has been started on some of these problems, but as yet the problems have not been investigated thoroughly. Several small experiments to investigate some of the basic physics problems are under way.

The next advanced concept to be considered is the fusion engine. Considerable effort has already been expended on the development of fusion power. This program, known as Project Sherwood, is being conducted by the Atomic Energy Commission with the express aim of obtaining a controlled thermonuclear reaction. In principle, what must be done is understood, but the problems are difficult. When it is considered that fusion is similar to building and maintaining a small sun, the difficulties are quite apparent.

The principle of achieving thermonuclear fusion reactions is well known; all that is necessary is to cause the atomic nuclei of light elements to collide with sufficient energy. The problem is that "sufficient energy" means that high enough relative velocities must be achieved to overcome the electrostatic repulsion that tends to keep the nuclei apart, and to achieve these velocities a plasma must be created with temperatures of the order of tens or hundreds of millions of degrees Kelvin. At these temperatures the nuclei move about randomly with high enough velocities to combine and release sufficient amounts of energy to enable the reaction to be self-sustaining.

It is clear then that the two major problems are (1) to heat a plasma of light elements to a sufficiently high temperature to cause fusion and (2) to contain the plasma without the use of material walls. The AEC work on both plasma containment by magnetic bottles and plasma heating by a wide variety of methods has not been specifically aimed at a space propulsion system. With this in mind, therefore, some typical fusion reactions will be considered.

As shown by the following equations, two deuterium nuclei fuse together to produce either helium 3 and a neutron or tritium and a proton. These two reactions have an equal probability of occurrence. A deuterium nucleus and a tritium nucleus combine to produce helium 4 and a neutron, and a deuterium nucleus combines with helium 3 to produce helium 4 and a proton. Of interest here is the extremely high energy of the reaction products.



The major task, therefore, is to examine these reactions and to determine how they can best be utilized in space. It is evident, for example, that the last two reactions release far more energy than either of the deuterium reactions (about 18 Mev compared with 3 or 4 Mev). Consider further that the deuterium-tritium reaction produces a helium 4 nucleus and a neutron, whereas the deuterium-helium 3 reaction produces a helium 4 nucleus and a proton, both

of which are positively charged. If the use of deuterium-tritium is studied as an energy source, most of the available energy is in the neutrons that escape the magnetic bottle. The high-energy neutrons must be trapped in thick and massive shields and their energy removed as heat. This brings about the usual thermodynamic problems associated with the utilization of a heat source in space. Either this heat must be used directly to heat a propellant or it must be converted to electricity and thence into an electrical propulsion system. Studies reported in reference 3 show no substantial gains as compared with an ordinary fission reactor. Therefore, the  $D-He^3$  reaction is left, the products of which are charged particles and, hence, can be contained magnetically. If for the moment the problem of plasma heating is ignored and the necessary conditions are assumed to be created, the problem of magnetic containment must be considered. Early studies of thermonuclear propulsion showed that ordinary electromagnets, for example, of copper operating at room temperature, were far too massive for any practical use in space. Later studies in which cryogenically cooled magnets were used to decrease resistivity resulted in substantial gains, but such systems did not show any marked improvements over other space power and propulsion systems that were already being developed. In the last several years tremendous advances have been made with superconducting materials and superconducting magnets. In fact, in the laboratory, fields of the order of 90 kilogauss have been achieved with superconducting magnets. Even more spectacular gains will probably be made in the future. In any event, the use of superconducting magnets for plasma containment is a distinct possibility, and the conceptual design of a thermonuclear rocket is based on their use.

It should be emphasized that it is not as yet known how to build a thermonuclear reactor but that enough is known about the kinds of energy releases to analyze the possible propulsion implications for advanced space missions.

The basic elements of a propulsion system using  $D-He^3$  as a fuel are shown in figure 49-3. This figure illustrates one of the many concepts explored at the Lewis Research Center (ref. 3).

## ELECTRIC PROPULSION

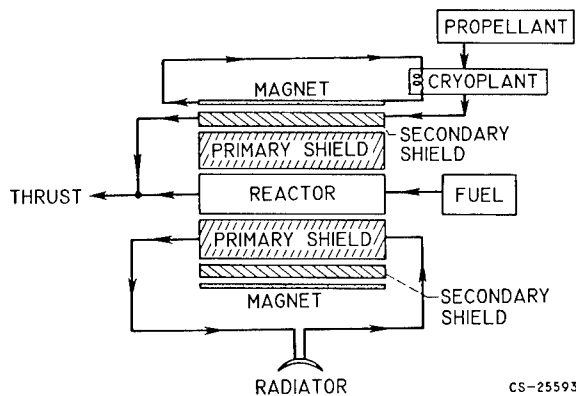


FIGURE 49-3.—Final two-shield system for a reaction.

The view shown is a cross section of a cylindrical system using a solenoidal magnet. For a device such as envisioned here, magnetic fields of the order of 100,000 gauss in the center and 200,000 gauss at the ends are required to contain the plasma and to keep the overall size to reasonable values.

For an assumed reactor whose total power output is 100 megawatts, the total size of the reactor is found to be only 50 centimeters in diameter and 250 centimeters long for the conditions chosen.

Note in the figure that several shields have been placed between the reactor and the magnet. These shields are necessary since a  $D-He^3$  plasma radiates gamma rays, which, if allowed to impinge on the superconducting magnet, would cause excessive heat loads that must be removed at the extremely low temperature ( $4^\circ K$ ) at which the magnet operates. For the particular device that will be discussed, liquid hydrogen is used as a propellant that is heated in the secondary shield and mixed with the reaction products and expelled to produce thrust. The use of a propellant separate from the fuel is necessary in order to produce the thrusts and specific impulses that are more nearly optimum for interplanetary flights. It should be pointed out that very little is known about the mixing and expulsion of gases at the temperatures involved. This is an area that is currently of great interest in plasma physics.

Although the superconducting magnet will not generate any heat by internal resistance, some heat will be generated by the residual gamma rays that pass through both the primary

and secondary shields. This heat must be removed by the cryoplant. For the conceptual design it has been assumed that the magnet is cooled by liquid helium and that the heat from gamma-ray absorption in the magnet is handled by the cryoplant, which rejects its heat to the liquid-hydrogen propellant. The heat generated in the primary shield is rejected to space directly. It could, of course, be used to generate auxiliary power for nonpropulsive applications aboard the spacecraft.

Any analysis of a system such as this is dependent on a large number of variables. For the configuration shown and in the range of specific impulses of interest, specific powerplant weights considerably less than 1 pound per kilowatt and thrust-to-weight ratios of the order of 0.004 pound of thrust per pound of propulsion system weight appear to be achievable (ref. 3). Since these values, like those for the isotope cell system, are at least an order of magnitude better than electric propulsion systems currently under development, it is clear that thermonuclear propulsion offers exciting possibilities for the conquest of space if and when the reaction is achieved.

The question arises then as to what is being done to solve the many problems that are involved. The two principal stumbling blocks are plasma heating to thermonuclear temperatures and containment. As mentioned before, the AEC has a large effort covering many phases of controlled thermonuclear reactions. At the Lewis Research Center, work is being done on magnetics as related to containment (ref. 2) and on plasma heating, as well as on a wide area of plasma physics. Currently a large experiment is being set up that uses a heating method called "ion cyclotron resonance," which was first analyzed in reference 4. Radio frequencies are used to excite ions to very high temperatures. Several preliminary experiments using this technique are under way, and the results to date are quite promising.

Although strong magnetic fields are essential for the fusion process, their applications to other areas may be even more fruitful. Obvious applications of such fields are in magnetohydrodynamic power generation, magnetic nozzles, and the magnetic shielding of spacecraft from



high-energy charged particles. Because of these interests, the remainder of this paper will be devoted to discussing the Lewis program in magnetics.

Magnetohydrodynamic power generation is a particularly interesting concept since it avoids some of the problems associated with rotating power equipment at extremely high temperatures. It does, however, have unique problems of its own and appears to be feasible for space only if the required magnetic field can be generated by using superconductors.

The concept of shielding interplanetary spacecraft from high-energy particles by using superconducting magnets has been explored by several investigators. It appears that for large interplanetary vehicles an order-of-magnitude weight savings may be possible as compared with the usual mass shielding.

Perhaps even more important are the wholly scientific aspects of high fields. For example, studies are being made of the biologic effects of extremely high fields, particularly as related to cancer.

The achievement of intense magnetic fields for steady-state operation and over reasonably large volumes is in itself a considerable accomplishment. Space applications add the additional requirements of light weight and low power consumption.

It has become increasingly evident that minimum power, both for the magnet and indeed for the total system, can be achieved only by means of cryogenics. One of the goals is to construct

and operate large cryogenically cooled magnets made of both normal and superconducting materials and to apply these magnets to the applications previously mentioned.

This kind of an activity requires the availability of an electric power source for magnet coils and large quantities of cryogenic fluids. The power source is a homopolar machine. This is an interesting device that uses liquid brushes of a sodium-potassium mixture and is capable of producing upwards of 200,000 amperes at 15 volts for 1 minute. It can be operated at 2.2 megawatts or less continuously and is currently being used to power two water-cooled magnets with fields up to 110,000 gauss.

For cryogenic fluids, a helium liquefier of 100-liter-per-hour capacity is available, and a liquid-neon system with 60-liter-per-hour capability will soon be ready. It is necessary, of course, that both of these gases be recaptured after they have served as coolants and have been vaporized. For example, a large plastic bag is used for helium storage, as shown in figure 49-4. This bag is an inflatable structure; the outer shell is held up by air pressure, and the inner bag holds the helium. This kind of system can achieve greatly reduced costs over metal tanks.

In order to develop either superconducting or cryogenic magnets, the characteristics of applicable materials in the presence of both low temperatures and high magnetic fields must be studied. Figure 49-5 shows a 100-kilogauss water-cooled magnet into which a helium Dewar has been lowered. Provisions have been made to pump on the Dewar, which reduces the helium vapor pressure and, hence, achieves temperatures down to about  $1^{\circ}$  K. A working volume in the Dewar of about  $\frac{3}{4}$  inch in diameter by 12 inches high is available. A larger system, which provides fields over 100 kilogauss with a working volume of 3 inches in diameter by 12 inches high, is also being used. Both these facilities are used for studies of effects of strong fields and low temperatures. Of particular interest, however, are the superconducting properties of such materials as niobium-tin and niobium-zirconium alloys. These have been studied, and a number of small superconducting magnets have been constructed.

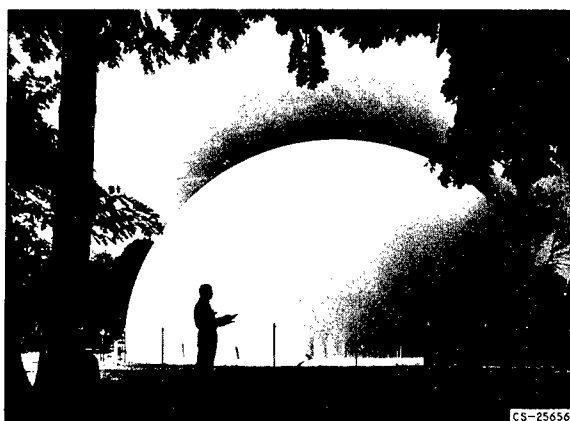


FIGURE 49-4.—Helium storage bag.

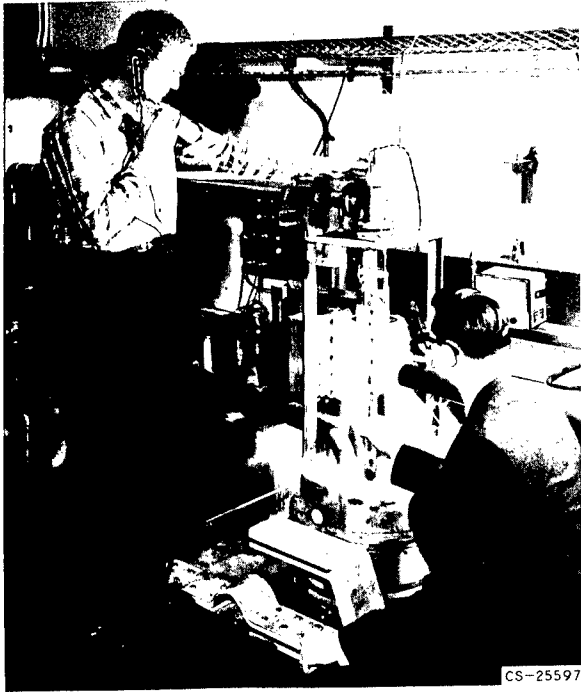


FIGURE 49-5.—Magnetoresistance and superconductivity test apparatus.

In the area of superconductivity, a wide variety of research problems requires solution. One of the most interesting of these problems is the "training effect." A superconducting magnet of niobium-zirconium alloy will "learn" to build higher and higher fields. Each time it is operated, the wires will carry successively higher currents and, hence, produce higher fields until a maximum is reached. Another effect, which is not yet understandable, is the fact that the maximum current a given superconducting wire will carry decreases with increasing length.

At the current state of the art many metallurgical problems exist. Material properties, supposedly the same, will vary from sample to sample. It is quite difficult to achieve reproducible results with niobium-tin magnets.

If the construction of cryogenic but nonsuperconducting magnets is considered, it is well known that the electrical resistance of materials decreases with decreasing temperature. At low temperatures, however, two effects are encountered that are normally negligible at room temperature. When the temperature is reduced

sufficiently and the lattice structure of the material becomes relatively stable, the regularity of the lattice becomes important. Regularity of the lattice can be achieved by using very-high-purity materials. The second effect is called magnetoresistance and is due to the magnetic field in which the conductor lies. If both low temperatures and very pure materials are used, the magnetoresistance effect dominates. For the construction of cryogenic coils it is desirable to choose a material that has a minimum magnetoresistance in the presence of high fields. Studies have shown that either very pure aluminum or sodium gives the minimum total resistance at low temperatures and in high fields.

Based on this information and on a series of heat-transfer studies, a large magnet is being constructed that will provide fields up to 200 kilogauss for several minutes (ref. 5). Several single experimental coils have been constructed; one is shown in figure 49-6. This coil has a bore of 12 inches and an outer diameter of over 3 feet. The coil is made of a spiral wrap of very high purity aluminum (99.9983 percent) laminated to stainless steel. Small stainless-steel separators are used to transfer the forces and to provide cooling passageways. The size of the outer restraining hoop indicates the kinds of stresses anticipated; 200-kilogauss fields will give stresses equivalent to an internal gas pressure of about 25,000 pounds per square inch.



FIGURE 49-6.—Liquid-neon-cooled coil.

Cooling is accomplished by nucleate boiling of the cryogenic fluid in which the coil is placed. Tests have been conducted in both nitrogen and hydrogen. In the final configuration a stack of 12 of these coils will be cooled by liquid neon to provide a field of 200 kilogauss. This magnet should be very useful for studies of various physical phenomena in intense fields. Further in the future a magnetic-mirror machine using 36 coils will be constructed. This machine should provide a central field of 100 kilogauss with end mirrors of 200 kilogauss and will be used in fundamental studies of plasma heating and containment.

To summarize briefly, two proposed conceptual propulsion systems that appear to give far greater mission capability than others that are under development have been reviewed. Both, however, have serious problems that must be solved before any real feasibility can be demonstrated. A wide variety of uses is anticipated for intense magnetic fields for future space, ground, and scientific applications. In space, however, it will probably be necessary to achieve these fields using superconducting systems. Experience at Lewis and other laboratories throughout the country is disclosing exciting new possibilities for superconductors.

#### REFERENCES

1. LOW, CHARLES A., JR., and MICKELSEN, WILLIAM R.: An Electrostatic Propulsion System with a Direct Nuclear Electrogenerator. *Aerospace Eng.*, Dec. 1962.
2. CALLAGHAN, EDMUND E.: Magnetic Research at NASA. *High Magnetic Fields*, John Wiley & Sons, Inc., pp. 420-426.
3. ENGLERT, GERALD W.: Study of Thermonuclear Propulsion Using Superconducting Magnets. Third Ann. Conf. on Eng. Magnetohydrodynamics, Univ. Rochester, Mar. 28-29, 1962.
4. STIX, THOMAS H.: Generation and Thermalization of Plasma Waves. *Physics of Fluids*, vol. 1, no. 4, July-Aug. 1958.
5. LAURENCE, JAMES C., and BROWN, GERALD V.: A Large Liquid-Neon-Cooled Electro Magnet. *High Magnetic Fields*, John Wiley & Sons, Inc., pp. 170-179.

**SESSION Q**

## **Aerodynamics**

***Chairman,* LAURENCE K. LOFTIN, JR.**

---

LAURENCE K. LOFTIN, JR., is Assistant Director of the NASA Langley Research Center. He received his B.S. degree in Mechanical Engineering from the University of Virginia in 1943.

As Assistant Director, Loftin directs and guides research activities of the Aero-Physics Division, the Aero-Space Mechanics Division, and the Full-Scale Research Division. He initiated establishment of a space station research program at Langley and set up committees which conducted early studies in the field of space vehicle rendezvous. He is widely known for his research work in the fields of airfoils, high-lift devices, boundary-layer problems, and transonic flutter. Of particular importance was his pioneering work on the use of the variable-density feature of the transonic blowdown tunnel to accelerate the accumulation of transonic flutter information. Mr. Loftin is consultant and adviser to Government and industry in a wide variety of advanced research and development fields. He is an Associate Fellow of the Institute of the Aerospace Sciences.

# 50. Aerodynamic Problems of Launch Vehicles

By Robert W. Boswinkle, Jr.

ROBERT W. BOSWINKLE, JR., *Head, Aeroelasticity Branch, Dynamic Loads Division, NASA Langley Research Center*, received his Bachelor of Science degree in Aeronautical Engineering from Purdue University in 1943, and his Master of Aeronautical Engineering degree from the University of Virginia in 1952. He joined the Langley staff after graduation from Purdue. Boswinkle has done extensive work in fluid mechanics and in the aerodynamic design of wind tunnels. Considered an expert in the field of aircraft flutter, he presently heads a professional staff engaged in a broad experimental and theoretical research program on the aeroelastic problems of spacecraft and aircraft from subsonic to hypersonic speeds. In this work, many new techniques have been devised for the study of flutter, buffet, and gust response. He is author or coauthor of numerous NASA technical publications on research that he has conducted at Langley. He is an Associate Fellow of the Institute of the Aerospace Sciences; Secretary, Hampton Roads Section of the Institute of the Aerospace Sciences; and a member of the Engineers' Club of the Virginia Peninsula.

## SUMMARY

The airflow about a launch vehicle causes problems which may affect the entire vehicle or may affect only localized areas; the problems can occur when the vehicle is on the launcher as well as during flight. Specific problems discussed include local steady-state loads, overall steady-state loads, buffet, ground wind loads, base heating, and rocket-nozzle hinge moments.

## INTRODUCTION

Figure 50-1 indicates the subject under discussion—the aerodynamic problems of launch vehicles—and provides an orientation for the subject. Aerodynamics is shown as the hub of a wheel which has three spokes. The spokes are attached to the rim at points labeled inertia, elasticity, and heat. Aerodynamics alone and in combination with one or more of the items shown on the rim represents separate areas of investigation wherein the airflow about a launch vehicle may be an important factor. For example, the different spokes represent the areas of dynamics, aeroelasticity, and aerothermody-

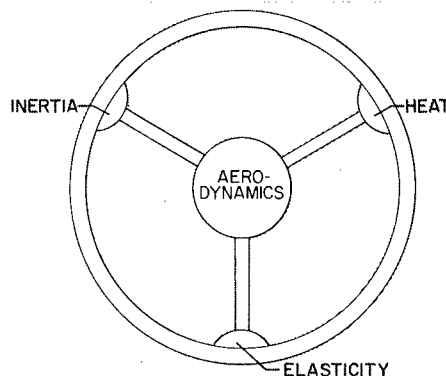


FIGURE 50-1.—Aerodynamic problems of launch vehicles.

namics. The whole wheel represents the broad area of aerothermoelasticity.

A very large number of specific problems are represented by this diagram. Only a few of the problems, as shown figure 50-2, have been chosen for discussion herein. A typical large launch vehicle is shown at the right of the fig-

- LOCAL STEADY-STATE LOADS
- OVERALL STEADY-STATE LOADS
- BUFFET
- GROUND WIND LOADS
- BASE HEATING
- NOZZLE HINGE MOMENTS

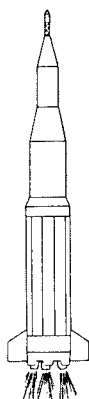


FIGURE 50-2.—Problems to be discussed.

ure. The treatment is directed more toward the problems of large launch vehicles than toward small ones; however, much of the discussion also applies to small launch vehicles.

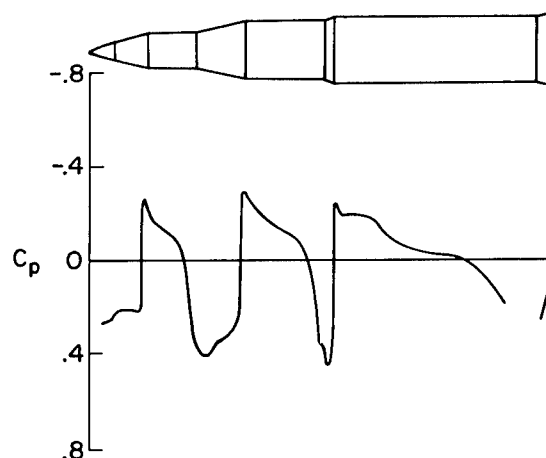
### SYMBOLS

$C_p$	pressure coefficient, $\frac{p-p_\infty}{q}$
$C_{p, \text{peak}}$	peak negative pressure coefficient
$f$	frequency
$M$	Mach number
$p$	local static pressure
$p_\infty$	free-stream static pressure
$q$	free-stream dynamic pressure
$\bar{V}(x)$	steady wind velocity
$V(x, t)$	unsteady wind velocity
$V_{\text{WIND}}$	horizontal wind velocity
$\alpha$	angle of attack
$\sigma_M$	root-mean-square bending moment
$\Phi$	power=spectral density

### LOCAL STEADY-STATE LOADS

The first subject to be discussed is local steady-state aerodynamic loads. Figure 50-3 shows the distribution of pressure coefficients over a typical vehicle. The Mach number is 1.3 and the angle of attack is zero. Negative pressure coefficients, which indicate pressures below ambient, are shown above the horizontal axis.

Note that large changes in pressure occur in the regions of the flares. Both negative and positive pressure-coefficient peaks are obtained, and these peaks represent concentrated local loads. The negative pressure-coefficient peaks

FIGURE 50-3.—Pressure distribution.  $M = 1.3$ ;  $\alpha = 0^\circ$ .

occur at each corner where the flow is required to expand.

The peak negative pressure coefficient near the first corner of a different nose cone is shown as a function of Mach number in figure 50-4. The dynamic pressure is also shown as a function of Mach number for a typical trajectory. The local load is proportional to the product of  $C_p$  and  $q$  as shown by the solid curve. It may be seen that the local load at a Mach number of 0.8 is about four times higher than the load at maximum dynamic pressure.

The local load is a particularly important factor in the design of secondary structures, such as insulation panels or fairings. Several vehicle failures have occurred because local loads near a corner were underestimated. The assumption has been made in several instances that all aerodynamic loads are a maximum at the maximum dynamic-pressure condition. These data indicate the error of such an assumption.

Figure 50-5 again shows the variation of pressure coefficient with Mach number. The configuration is a cone-cylinder. During launch the Mach number continually increases and the Mach number scale may be thought of as a time scale. Maximum negative pressure coefficients at transonic speeds occur near the corner as indicated by the solid curve. In interstage sections of launch vehicles and also in adapter sections behind payloads, of which this configuration might be an example, the volume

## AERODYNAMIC PROBLEMS OF LAUNCH VEHICLES

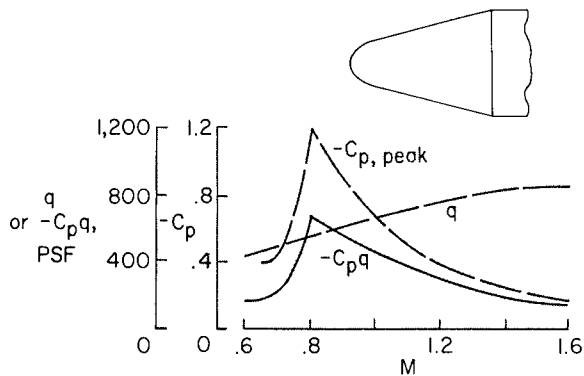


FIGURE 50-4.—Maximum local load for typical cone-cylinder.

enclosed is often vented to the external flow. A vent located at the corner, at point A, might reduce the net local load across the skin at point A to very low values. However, it may be seen that if the internal pressure is maintained at the value plotted here for point A, the net pressure difference across the skin at point B would be the difference between the two curves, and the local loads might become large at point B. Thus in the very important problem of locating vents, a detailed knowledge of the variation of the pressure with Mach number is required.

### OVERALL STEADY-STATE LOADS

Figure 50-6 introduces the subject of overall steady-state loads. The Mach number and dynamic pressure are plotted as functions of altitude for an example trajectory. The velocity

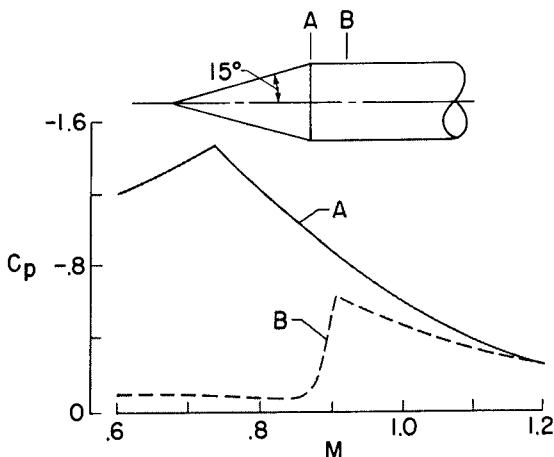


FIGURE 50-5.—Local load for cone-cylinder.

of horizontal winds which the vehicle might encounter is shown also as a function of altitude. This variation of wind velocity with altitude is about an average of the different profiles used for design purposes (ref. 1). The response of an elastic vehicle to varying horizontal winds is discussed briefly in reference 1; in the present paper, only the steady-state aspects of the problem are considered.

The horizontal winds cause the vehicle to fly at an angle of attack. Note that the maximum dynamic pressure occurs at about the same altitude as the maximum horizontal winds so that the maximum dynamic pressure and maximum

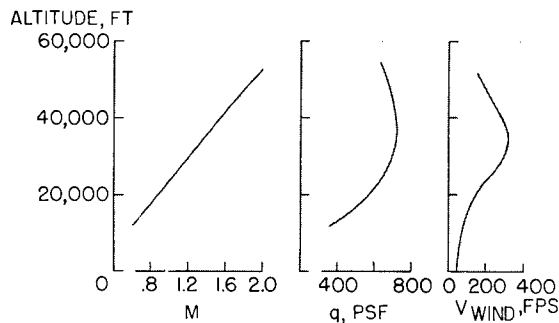


FIGURE 50-6.—Example launch-vehicle flight characteristics.

angle of attack occur at about the same time. As will be shown subsequently, the effect of angle of attack is to produce a bending moment along the vehicle length. The bending moment is nearly proportional to the product of dynamic pressure and angle of attack so that the maximum bending moments will be obtained in this region. The Mach number for large launch vehicles is usually between 1.5 and 2.0. This is a very important load condition for the design of the vehicle structure. Thus, maximum bending moments generally occur at supersonic Mach numbers, and maximum local loads (discussed previously) usually occur at high subsonic Mach numbers.

Figure 50-7 shows the pressure distribution obtained on a vehicle at an angle of attack of  $8^\circ$  for the top and bottom surfaces. As just discussed, the angle of attack might be caused by horizontal winds. The vehicle shown in figure 50-7 is the same as that shown in figure 50-3 and the Mach number again is 1.3. These



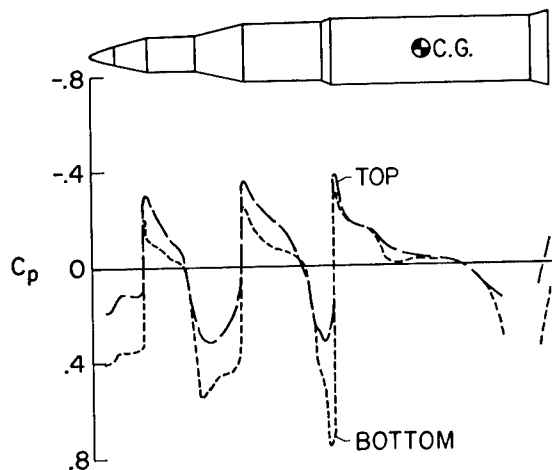


FIGURE 50-7.—Pressure distribution.  $M = 1.3$ ;  $\alpha = 8^\circ$ .

data indicate that at each point along the vehicle length there is an upward force on the vehicle. To calculate the pitching-moment distributions along the vehicle length, the vertical component of the pressure force is integrated circumferentially and longitudinally. Typically, for a vehicle without fins at the base, a nose-up pitching moment is obtained about the vehicle center of gravity for positive angles of attack. The pitching moment is counteracted by the stabilization system, which for example, might be swiveling rocket nozzles. The two opposing moments produce the bending moment in the vehicle.

Thus, accurate determination of the bending-moment distribution, as well as the local loads discussed previously, requires an accurate determination of the pressure distribution. No completely satisfactory theoretical method exists for computing the pressure distributions throughout the required Mach number and angle-of-attack ranges. Slender-body, shock-expansion, and piston theories give trends for some conditions, but the theoretical treatment is grossly inadequate. In practice, most designers have a collection of load distributions obtained experimentally for various shapes, and these data are used in preliminary design. For final verification, wind-tunnel studies of the configuration are often made and add more data to the collection. A much more satisfactory situation would be to have a reliable theoretical method of predicting pressure, particularly at transonic speeds.

Figure 50-8 illustrates another aspect of the need for accurate prediction of the pressure distributions. A typical vehicle is shown at the left of the figure. The upper curve is the predicted center-of-pressure location on the vehicle obtained by use of theory and the generalized experimental data available. The middle curve is the center-of-pressure location as measured in wind-tunnel studies. The center of gravity of the vehicle, shown by the bottom curve, varies with burning time. With the center of pressure ahead of the center of gravity, the vehicle is aerodynamically unstable. It may be seen that somewhat greater instability was predicted than was measured. An engine-swiveling requirement for automatic stabilization, based on the analytical prediction, would yield a considerably conservative design. The problem of attitude stabilization for large guided vehicles is discussed in reference 2.

#### BUFFET

Buffet is simply pressure oscillations caused by separated flow. The greatest buffet problems occur at transonic speeds where shock interactions with the separated flow augment the pressure fluctuations. Often buffet produces the greatest loads at the same locations and conditions where the local steady-state loads

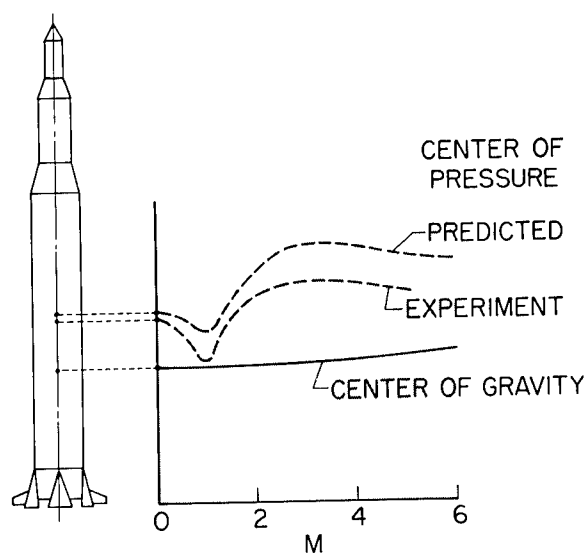


FIGURE 50-8.—Static stability.

# AERODYNAMIC PROBLEMS OF LAUNCH VEHICLES

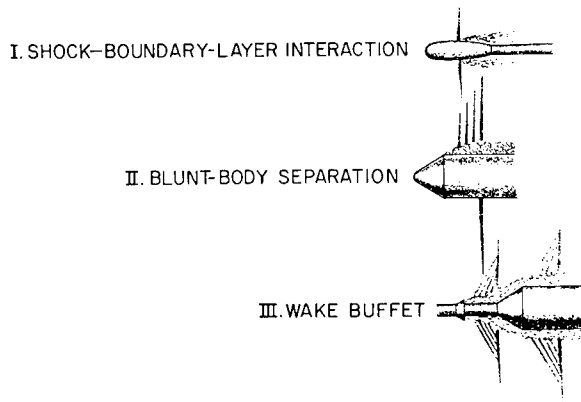


FIGURE 50.9.—Types of buffet flow on launch vehicles.

are a maximum. Three types of buffet which have been observed are shown in figure 50-9.

Shock-boundary-layer interaction buffet is often obtained on hammerhead configurations of the type shown. The flow resembles that over thick airfoils at transonic speeds.

Blunt-body separation buffet is characterized by unstable flow at the shoulder of a blunt cone-cylinder. At subsonic Mach numbers the flow is separated at the corner and at supersonic speeds it is attached. At Mach numbers just below one, the flow is alternately separated and attached.

Abrupt protuberances cause an unsteady wake which impinges on downstream parts of the vehicle and causes wake buffet. It is this type of buffet which appears to have caused the failure of the first Mercury-Atlas vehicle. Sub-

sequent vehicles were strengthened and no further structural problems have been encountered.

As shown in figure 50-10, different types of buffet may have considerably different characteristics. These power spectra of the pressures show that the energy of the wake buffet is distributed over the frequency range, while most of the energy of the shock-boundary-layer interaction buffet is concentrated at low frequencies. These two types of buffet would be expected to cause considerably different elastic responses of the structure. With the buffet energy concentrated at low frequencies, overall bending modes might be excited. With distributed buffet energy, local response of the structure might be excited.

Before model buffet data such as these can be applied with confidence to full-size vehicles, the scaling relationships must be derived and verified experimentally. Simple dimensional considerations would indicate, for example, that the buffet frequency spectrum would be shifted to higher frequencies as the model scale is reduced. Buffet-pressure studies have been conducted with models which differed only in size, and the scaling laws based on the simple dimensional considerations appear to have been verified.

Since buffet is suspected to be the cause of several vehicle failures, a wind-tunnel study program on buffet pressures has been undertaken. (References 3 and 4 present results obtained to date.) The value of this buffet-pressure program is well recognized; however, considerable difficulty exists in applying the buffet-pressure data to the structural design. The obvious approach is to use experimental buffet pressures as force inputs in a dynamic analysis of the structure; however, the task of obtaining sufficiently detailed experimental data and of making the calculations appears to be overwhelming.

Figure 50-11 illustrates an alternate to such a response analysis. The two models (ref. 5) are a hammerhead configuration and a blunted cone-cylinder. The models had the same dynamic and elastic properties and were supported in a wind tunnel in such a way that they were free to respond in their elastic free-free bending modes. The response of the models

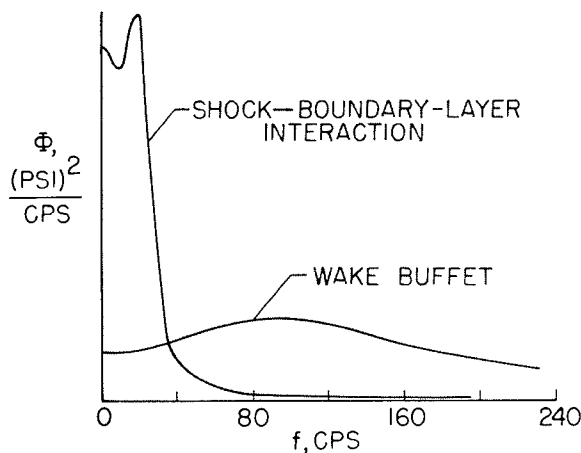


FIGURE 50-10.—Pressure power spectra; transonic wind-tunnel results.

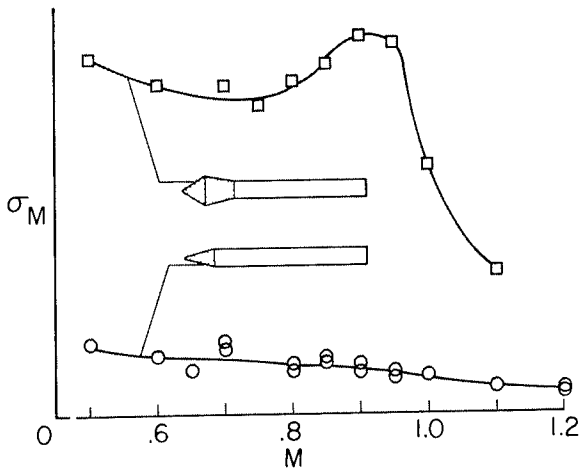


FIGURE 50-11.—Effect of nose shape on buffet response.

was measured in terms of the root-mean-square bending moment as a function of Mach number. Thus, the aeroelastic models were used as wind-tunnel analogues to measure the response directly. The low-level response for the cone-cylinder model is believed to be caused primarily by wind-tunnel turbulence. The much higher level response of the hammerhead configuration is due to buffeting produced by the reflex frustum.

Figure 50-12 shows the power spectra of the bending moment for the same two models at a Mach number of 0.90. Naturally, the data for the cone-cylinder model are at a very low level. Of considerable interest is that the response for the hammerhead configuration was primarily in the first two bending modes, and each mode

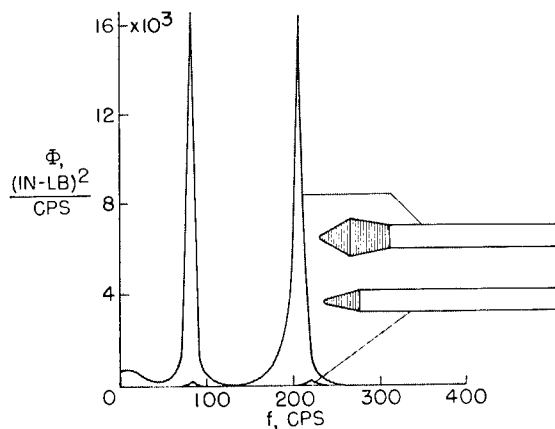


FIGURE 50-12.—Bending-moment power spectra.  
 $M = 0.90$ ;  $\alpha = 0^\circ$ .

contributed about equally to the total response. The technique of using aeroelastic models for buffet-response studies such as these has been used previously for aircraft wings (ref. 6). In aircraft wing models the simulation of only the first elastic wing mode usually sufficed. However, it appears from this result that at least two elastic modes must be simulated for launch-vehicle models.

To date no flight data have been available for correlation with the wind-tunnel response measurements. Correlation will have to be shown, of course, before the technique can be considered reliable for prediction of buffet response. It is anticipated that models might be satisfactory for predicting overall bending response; however, the prediction of localized response of panels might require structural replica models at small scale and might therefore be infeasible. Meanwhile, additional emphasis is needed on analytical solution of the buffet loads, using power-spectral approaches for very simple shapes.

Figure 50-12 may also be referred to in connection with another aspect of vehicle response. The sharpness of the peaks indicates that the total of the structural and aerodynamic damping was low for both modes. In fact, negative aerodynamic damping was measured in the first mode at slightly greater Mach numbers, and this situation is of concern because of the possibility that sustained or divergent oscillations of the vehicle may be produced. However, in most applications, the magnitude of any negative aerodynamic damping is very small compared with the positive damping usually provided by the structure, the thrust-vector control system, and the liquid fuel so that sustained or divergent oscillations of the vehicle have not yet materialized as a major problem.

#### GROUND WIND LOADS

The ground wind-loads problem is introduced in figure 50-13. The launch vehicle is shown on the launch pad during prelaunch operations. The horizontal wind is considered to consist of a steady wind vector which varies both with time and with height above the ground. The unsteady part is due to gusts and turbulence. The winds produce a steady drag

## AERODYNAMIC PROBLEMS OF LAUNCH VEHICLES

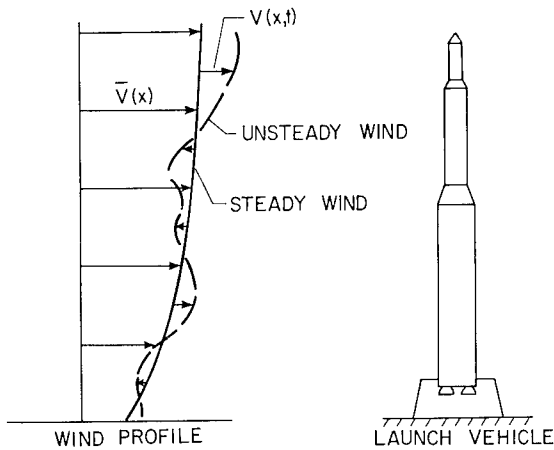


FIGURE 50-13.—Launch vehicle exposed to ground winds.

deflection and oscillatory deflections in both the lateral and drag directions. The deflections cause problems in structural strength, guidance alignment, and flight-instrumentation checkouts. The problem is of sufficient importance that design or operations changes have been required for several vehicles.

The oscillatory lateral deflections are caused primarily by the steady wind vector and no satisfactory analytical technique exists for predicting the input aerodynamics, even for two-dimensional cylinders. Wind-tunnel studies of models (refs. 7 and 8) are therefore required for lateral load predictions. Figure 50-14 shows such a model used in reference 9. On the right is shown the Scout vehicle and on the left, the dynamically and elastically scaled 15-percent wind-tunnel model. The model, complete with simulated launch tower, is shown

mounted in the wind tunnel. The accuracy with which ground wind response to steady winds can be simulated in wind tunnels is a moot question because of a lack of response data on full-scale vehicles which could be used for comparison with wind-tunnel data. Thus, a need exists for improving the analytical prediction methods for steady winds and for obtaining response data for full-scale vehicles.

The oscillatory drag deflections, caused primarily by the unsteady wind vector, can probably be handled analytically by using power-spectral density techniques (ref. 10). The handicap has been the lack of power-spectra information on winds near the ground. The small amount of data available have been obtained, for the most part, with conventional wind-measuring devices which are not responsive to the higher wind frequencies that can represent important dynamic load inputs to the vehicle. Thus, a need exists to determine the ground-wind properties in greater detail. A fast response anemometer under development for this purpose is described in reference 11.

## BASE HEATING

Figure 50-15 illustrates the base-heating problem (refs. 12 to 15). The base of a launch vehicle which has a cluster of four rocket nozzles is shown. At high altitudes the rocket exhausts plume and intersect. Trailing shock waves are formed at the intersection of the jets. The energy of the air near the jet boundaries is too low to allow the flow to move back through the shock waves, so the flow reverses and flows toward the base of the vehicle. It escapes by flowing laterally across the base. At high altitudes, this recirculated flow of hot

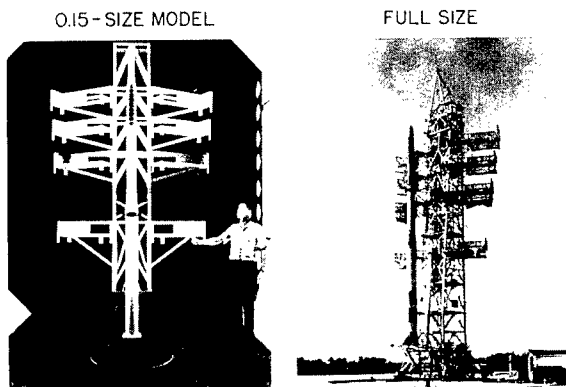


FIGURE 50-14.—Scout vehicles.

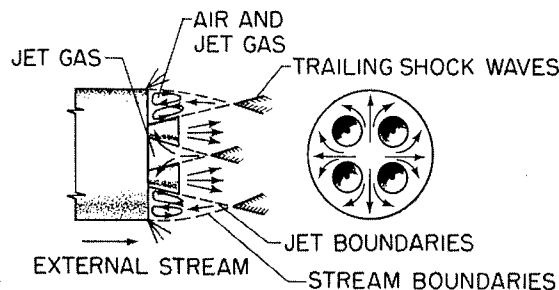


FIGURE 50-15.—Base flow for clustered nozzles.

exhaust gases reaches supersonic velocities and can cause severe damage to surfaces which are not heat protected.

The intersection of the jet exhaust with the external stream also produces trailing shock waves and a reversed flow. In this case, oxygen from the external stream combined with the fuel-rich exhaust produces a combustible mixture which could lead to burning in the base region. A much more likely source of base burning, however, is from the exhaust of the turbines which pump the propellants, since the

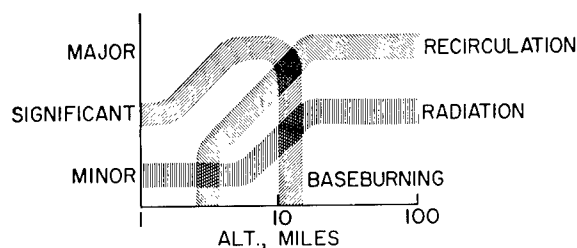


FIGURE 50-16.—Sources of base heating for clustered nozzles.

turbine exhaust is even more fuel-rich than the rocket jets.

The significance of the sources of base heating as a function of altitude in miles is shown qualitatively in figure 50-16. This figure is based on information from reference 14. Recirculation of the hot exhaust gases is indicated to be a major problem into space. At lower altitudes the jets plume less, the trailing shock strength decreases, and less of the hot gases is recirculated. At still lower altitudes, the jets do not intersect, and act instead as ejectors in pulling the external stream over the base to produce base cooling rather than heating. Base burning is indicated to be a major problem at altitudes from 3 to 10 miles. At higher altitudes, the lack of oxygen precludes combustion. Radiation is shown as the third source of base heating. Much of the radiation comes from afterburning of the rocket jet downstream of the nozzle.

Base-heating problems are generally studied by use of scaled models in wind tunnels and altitude chambers. Considerable work remains to be done in improving model-testing techniques.

## NOZZLE HINGE MOMENTS

Figure 50-17 introduces the subject of the aerodynamic hinge moments on swiveling rocket nozzles. The bases of two Saturn vehicles are shown; both vehicles utilize swiveling nozzles to produce thrust-vector control.

For the C-1 Block I vehicle shown at the left, the H-1 engines are contained within the periphery of the booster and relatively large shrouds extend over the nozzles. Consequently there is very little impingement of the external flow on the nozzles.

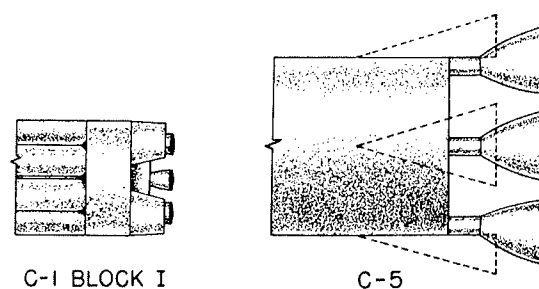


FIGURE 50-17.—Base regions of Saturn vehicles.

However, with the C-5 vehicle, the center lines of the outer F-1 engine nozzles lie nearly on the booster periphery. If no shrouds are used, the external stream impinges on a large area of the nozzles. This impingement produces very large hinge moments which lead to impractically large actuators in order to overcome the hinge moments. Elaborate backup structure would also be required for the actuator. Large shrouds may be used to shield the nozzles from the external flow, but the shroud loads then become large, and excessive backup structure is required for the shrouds. In addition, the base drag of the vehicle becomes large and the recirculation of exhaust gases at the base can become a serious problem. A probable solution is to use a shroud of moderate length, perhaps about as shown by the dashed lines, and to use scoops to guide airflow into the base area. A proper arrangement can reduce hinge moments as well as recirculation and base drag.

## AERODYNAMIC PROBLEMS OF LAUNCH VEHICLES

Wind-tunnel studies are used for predicting the nozzle hinge moments since present theories are inadequate for prediction of the complicated flow field behind the base of a launch vehicle. It would probably not be profitable to expend a great deal of effort in developing a theoretical method because the problem is so dependent on the details of the configuration and the operating conditions. However, the problem is an interesting example of the many

different kinds of aerodynamic problems encountered in the design of launch vehicles.

### CONCLUDING REMARKS

In conclusion, some of the aerodynamic problems of launch vehicles have been discussed. The importance of the problems has been cited and areas where additional work is required have been indicated.

### REFERENCES

1. RUNYAN, HARRY L., and LEONARD, ROBERT W.: Research, Design Considerations, and Technological Problems of Structures for Launch Vehicles. NASA University Conference, 1962. (Paper no. 72 in this compilation.)
2. GEISSLER, ERNST D.: Problems in Attitude Stabilization of Large Guided Missiles. *Aerospace Eng.*, vol. 19, no. 10, Oct. 1960, pp. 24-29, 68-71.
3. COE, CHARLES F.: Steady and Fluctuating Pressures at Transonic Speeds on Two Space-Vehicle Payload Shapes. NASA TM X-503, 1961.
4. COE, CHARLES F.: The Effects of Some Variations in Launch-Vehicle Nose Shape on Steady and Fluctuating Pressures at Transonic Speeds. NASA TM X-646, 1962.
5. HANSON, PERRY W., and DOGGETT, ROBERT V., Jr.: Wind-Tunnel Measurements of Aerodynamic Damping Derivatives of a Launch Vehicle Vibrating in Free-Free Bending Modes at Mach Numbers From 0.70 to 2.87 and Comparisons With Theory. NASA TN D-1391, 1962.
6. HUSTON, WILBER B., RAINEY, A. GERALD, and BAKER, THOMAS F.: A Study of the Correlation Between Flight and Wind-Tunnel Buffeting Loads. NACA RM L55E16b, 1955.
7. BUELL, DONALD A., and KENYON, GEORGE C.: The Wind-Induced Loads on a Dynamically Scaled Model of a Large Missile in Launching Position. NASA TM X-109, 1959.
8. EZRA, A. A., and BIRNBAUM, S.: Design Criteria for Space Vehicles To Resist Wind Induced Oscillations. [Preprint] 1081-60, American Rocket Soc., Apr. 1960.
9. JONES, GEORGE W., JR., and GILMAN, JEAN, JR.: Measured Response to Wind-Induced Dynamic Loads of a Full-Scale Scout Vehicle Mounted Vertically on a Launching Tower. NASA TN D-757, 1961.
10. BOHNE, QUINTIN R.: Power Spectral Considerations on the Launch Pad. Proc. Nat. Symposium on Winds for Aerospace Vehicle Design. Vol. I. Air Force Surveys in Geophysics, No. 140 (AFCRL-62-273(I)), Mar. 1962.
11. REED, WILMER H., III, and LYNCH, JAMES W.: A Simple Fast Response Anemometer. Presented at Conference on Low Level Winds (El Paso-Dallas, Texas), Aug. 7-9, 1962. (Sponsored by the U.S. Army Missile Support Agency and the American Meteorological Soc.)
12. SCHUELLER, CARL F.: Interactions Between the External Flow and Rocket-Exhaust Nozzle. Paper no. 59-133, Inst. Aeronautical Sci., Oct. 1959.
13. GOETHERT, B. H.: Base Flow Characteristics of Missiles With Cluster-Rocket Exhausts. *Aero/Space Eng.*, vol. 20, no. 3, Mar. 1961, pp. 28-29, 108-117.
14. GOETHERT, B. H.: Base Heating Problems of Missiles and Space Vehicles. [Preprint] 1666-61, American Rocket Soc., Mar. 1961.
15. BEHEIM, MILTON A., and OBERY, LEONARD J.: Wind Tunnel Studies of Booster Base Heating. Paper no. 62-166, Inst. Aerospace Sci., June 1962.

# 51. Low-Speed Aerodynamic Research Related to the Landing of Space Vehicles

By John P. Campbell

JOHN P. CAMPBELL, Assistant Chief, Aero-Space Mechanics Division, NASA Langley Research Center, attended the U.S. Naval Academy and graduated from Auburn University, receiving a Bachelor of Science degree in Aeronautical Engineering in May 1939. Campbell, who joined the Langley staff in November 1939, is recognized as a leading specialist in the field of research with dynamic models and has been instrumental in the development of free-flight model testing techniques at Langley.

Campbell plans and directs low-speed aerodynamic research dealing with VTOL and STOL aircraft, conventional aircraft, and spacecraft landing configurations. He has authored or co-authored some 35 research reports and has represented the NASA in making presentations at technical conferences and before various high-level groups in this country and at international symposiums held in Brussels, Madrid, Toronto, and London.

At Auburn, he was elected to Tau Beta Pi and Phi Kappa Phi honorary fraternities and he is a member of the Engineers' Club of the Virginia Peninsula.

## SUMMARY

Aerodynamic research results related to the low-speed approach and landing of space vehicles are presented. Two basic types of space vehicles are covered: those designed for vertical or near-vertical descent (which require some auxiliary device for landing) and those which perform glide landings. Spacecraft discussed include nonlifting bodies (such as the Mercury spacecraft), low-lift-drag-ratio lifting bodies, fixed-geometry glide-landing types similar to the Dyna-Soar, and variable-geometry glide-landing types which involve a change in configuration between reentry and landing. Aerodynamic characteristics are also presented for auxiliary landing aids which may replace the parachute for some recovery applications. These landing aids include the steerable parachute, the rotor-chute, and the parawing which is being developed for use in the Gemini recovery system.

## INTRODUCTION

The landing of all space vehicles recovered to date has been accomplished by means of para-

chutes which are relatively simple, well-proven, and reliable devices that will, no doubt, continue to be used for space-vehicle recovery in the future. Since the parachute is inherently limited to an essentially vertical and uncontrolled descent, however, other means of performing space-vehicle landings involving controlled gliding flight are also being developed to give the astronaut greater latitude in the choice of a landing site. It is the purpose of this paper to present some recent aerodynamic research results related to the various means of landing space vehicles, with particular emphasis on those means which involve the performance of glide landings.

Table 51-I shows the types of space vehicles and auxiliary landing aids to be considered, grouped into two general categories: those designed for vertical or near-vertical descent and

# AERODYNAMICS

TABLE 51-I.—Types of Vehicles and Landing Aids

	Vertical landing		Glide landing
	Zero $L/D$	Low $L/D$ ( $<1$ )	Moderate $L/D$ ( $>3$ ).
Reentry vehicles.	Nonlifting bodies.	Lifting bodies.	Fixed geometry. Variable geometry.
Auxiliary landing aids.	Parachute.	Steerable parachute.	Parawing. Rotorchute.

those which perform glide landings. The vertical-landing reentry vehicles can be classed either as nonlifting bodies, such as the Mercury spacecraft, or as low-lift-drag-ratio lifting bodies. Both of these types require some form of auxiliary device for landing. Glide landing vehicles are considered to be those which have a large enough value of subsonic lift-drag ratio (greater than about 3 or 4) to permit safe glide landings to be made consistently. These vehicles may be either fixed-geometry types, such as the Dyna-Soar, or variable-geometry types which involve a change in configuration between reentry and landing.

## SYMBOLS

$L$	lift, lb
$D$	drag, lb
$C_L$	lift coefficient, $\frac{\text{Lift}}{qS}$
$C_N$	normal-force coefficient, $\frac{\text{Normal force}}{qS}$
$C_D$	drag coefficient, $\frac{\text{Drag}}{qS}$
$C_m$	pitching-moment coefficient, $\frac{\text{Pitching moment}}{qS\bar{c}}$
$C_n$	yawing-moment coefficient, $\frac{\text{Yawing moment}}{qSb}$
$C_l$	rolling-moment coefficient, $\frac{\text{Rolling moment}}{qSb}$
$q$	dynamic pressure, lb/sq ft; pitching velocity, radians/sec
$S$	wing area, sq ft
$b$	wing span, ft
$\bar{c}$	mean aerodynamic chord, ft
$\alpha$	angle of attack, deg
$\beta$	angle of sideslip, deg
$\phi$	angle of bank, deg
$\dot{\alpha}$	rate of change of angle of attack, radians/sec
$p$	rolling velocity, radians/sec
$r$	yawing velocity, radians/sec; rotor radius, ft
$\delta_a$	aileron deflection, deg
$\delta_r$	rudder deflection, deg

$V$	free-stream velocity, ft/sec
$V_v$	rate of descent, ft/sec
$z$	vertical distance from center of gravity to wing pivot, ft
$W$	weight, lb
$I_x$	moment of inertia about X-axis, slug-ft <sup>2</sup>
$I_z$	moment of inertia about Z-axis, slug-ft <sup>2</sup>
$P$	period of oscillation, sec
$T_{1/2}$	time to damp to one-half amplitude, sec

$$\begin{aligned}
 C_{L_\alpha} &= \frac{\partial C_L}{\partial \alpha} & C_{N_\alpha} &= \frac{\partial C_N}{\partial \alpha} & C_{m_\alpha} &= \frac{\partial C_m}{\partial \alpha} \\
 C_{n_\beta} &= \frac{\partial C_n}{\partial \beta} & C_{l_\beta} &= \frac{\partial C_l}{\partial \beta} & C_{l_p} &= \frac{\partial C_l}{\partial \frac{pb}{2V}} \\
 C_{n_r} &= \frac{\partial C_n}{\partial \frac{rb}{2V}} & C_{n_p} &= \frac{\partial C_n}{\partial \frac{pb}{2V}} & C_{m_q} &= \frac{\partial C_m}{\partial \frac{qc}{2V}} \\
 C_{m_\alpha} &= \frac{\partial C_m}{\partial \alpha} & C_{l_\alpha} &= \frac{\partial C_l}{\partial \alpha} & C_{l_\alpha} &= \frac{\partial C_l}{\partial \alpha} \\
 C_{n_\delta_r} &= \frac{\partial C_n}{\partial \delta_r}
 \end{aligned}$$

Subscripts:  
MAX maximum  
DYN dynamic

## NONLIFTING BODIES

It may be recalled that astronauts Glenn and Carpenter both experienced unstable oscillations of their Mercury spacecraft after expending all their control fuel during the final subsonic portion of descent, and it was necessary in both cases to deploy the drogue parachute early in order to stabilize the spacecraft. (See refs. 1 and 2.) An illustration of this form of dynamic instability is presented in figure 51-1 which shows the oscillations obtained in free-flight tests of a Mercury-type spacecraft model in the Langley 20-foot free-spinning tunnel. The angle of attack measured in the plane of the oscillation is plotted against full-scale time for



# RESEARCH RELATED TO THE LANDING OF SPACE VEHICLES

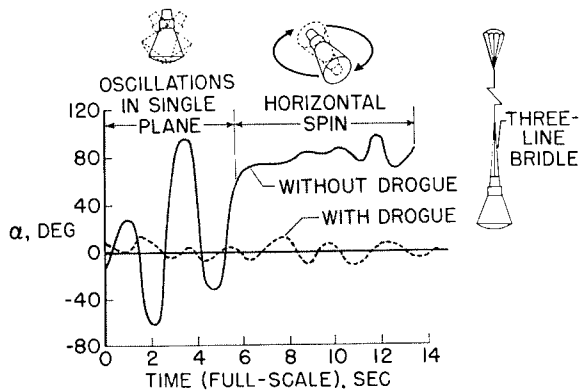


FIGURE 51-1.—Dynamic stability of nonlifting vehicle.

the model with and without a drogue parachute installed. The oscillation for the model without the drogue is very unstable and builds up quickly to very large angles, after which the model starts a horizontal spinning motion at high angles of attack. With the drogue deployed, however, the amplitude of the oscillation is restrained to an acceptably small value. These model tests apparently predicted quite well the character of the oscillations experienced on the full-scale Mercury spacecraft. (The drogue of the full-scale spacecraft was deployed in both cases before the horizontal spinning motion could develop.)

Some of the important aerodynamic parameters involved in this dynamic stability problem of blunt-faced Mercury-type spacecraft are shown in figure 51-2. Plotted against angle of attack (from  $0^\circ$  to  $180^\circ$ ) are shown low-speed test data for the parameters  $C_{N\alpha}$  (which is roughly equivalent to  $C_{L\alpha}$ , the lift-curve slope),  $C_{m\alpha}$  (the static-longitudinal-stability parameter), and  $C_{m\dot{q}} + C_{m\dot{\alpha}}$  (the damping-in-pitch parameter). The data show that at  $0^\circ$  angle of attack, which represents vertical descent with the blunt face down, the value of  $C_{N\alpha}$  is negative, indicating a reversed lift-curve slope, the value of  $C_{m\alpha}$  is also negative, indicating positive static stability, and the damping parameter  $C_{m\dot{q}} + C_{m\dot{\alpha}}$  is positive, indicating negative damping of any pitching motion that develops. This combination of parameters, which results from the separated flow condition behind the blunt face of the spacecraft, is primarily responsible for the unstable oscillations obtained in flight.

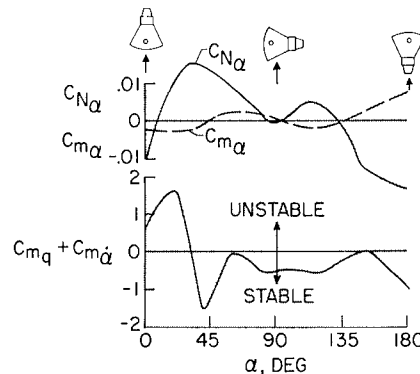


FIGURE 51-2.—Stability parameters of nonlifting vehicle.

Research has shown that these characteristics are not peculiar to the particular Mercury configuration but are common to all bluff-body nonlifting configurations of this general type which descend vertically with the blunt face down.

## LIFTING BODIES

Three examples of lifting-body configurations are shown in figure 51-3. These lifting-body vehicles may be considered to bridge the gap between the vertical-descent and glide-landing types since they can be designed to have subsonic lift-drag ratios from less than 1 to as high as 4 or 5. The configuration in the upper left-hand part of figure 51-3 is a blunt half-cone, which has an  $L/D$  less than 1 and therefore requires some auxiliary landing device. Configurations of this general type are usually quite stable in their steep subsonic descent and do not experience the unstable oscillations ob-

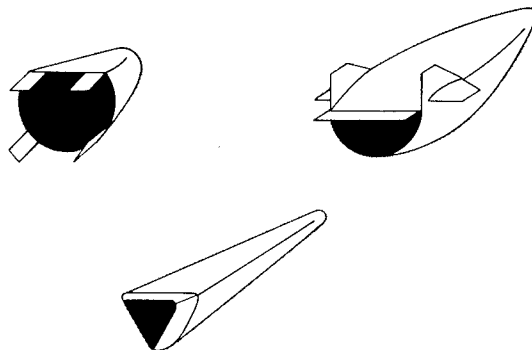


FIGURE 51-3.—Lifting-body vehicles.

tained with the blunt-faced Mercury-type spacecraft. The other two configurations shown in this figure are slender half-cone and pyramid shapes which can, by proper design, achieve lift-drag ratios high enough for performing glide landings. In order to obtain these values of  $L/D$ , careful use must be made of boattailing to reduce the large base area of the bodies. (See ref. 3.)

### GLIDE-LANDING VEHICLES

#### Subsonic Lift-Drag Ratio

Figures 51-4 and 51-5 illustrate what can be done to increase the subsonic  $L/D$  of both lifting-body and winged reentry vehicles. Figure 51-4 shows the maximum subsonic  $L/D$  for a variety of configurations plotted against a non-dimensional volume parameter (volume to the two-thirds power divided by wing area). The results shown are for trimmed conditions and a small amount of longitudinal stability. These data show that, as would be expected, the higher values of  $L/D$  are associated with the winged configurations which have the least fuselage and wing volume for a given wing area, whereas the lower values are associated with the lifting bodies which have the greater volume-to-wing-area ratios. These data were obtained at low Reynolds numbers; a few tests at higher Reynolds numbers have indicated that  $L/D$  values for the corresponding full-scale reentry vehicle in some cases may be as much as 0.5 to 1.0 greater than these values. The configurations illustrated in figure 51-4 were designed primarily with the hypersonic flight

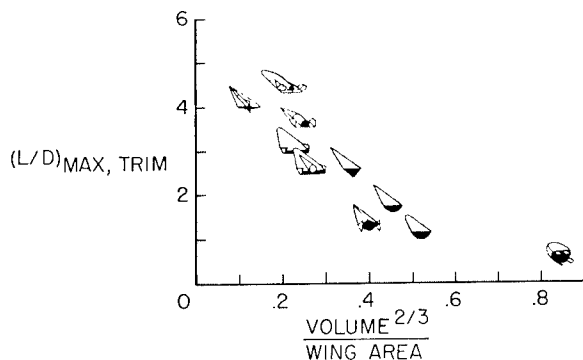


FIGURE 51-4.—Maximum lift-drag ratio. Trimmed conditions.

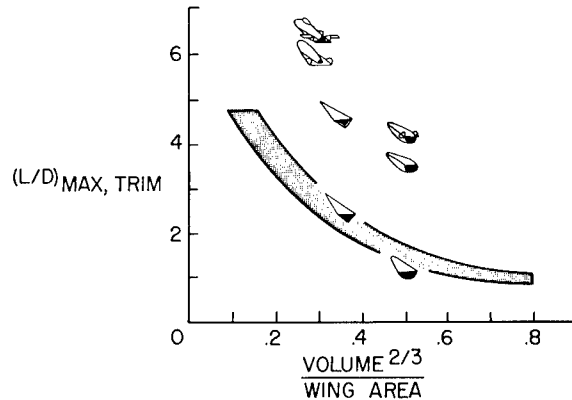


FIGURE 51-5.—Configurations designed for higher lift-drag ratio. Trimmed conditions.

condition in mind and with little or no attention given to obtaining a good subsonic  $L/D$ . Despite this, some of the winged configurations have a fairly good subsonic  $(L/D)_{MAX}$ .

Figure 51-5 shows that substantial increases in subsonic  $L/D$  for both winged and lifting-body vehicles can be attained when some effort is made to design the vehicles for the low-speed case. The shaded area represents the region in which the  $(L/D)_{MAX, TRIM}$  values for the configurations of figure 51-4 were located. Boattailing the base of the half-cone and pyramid-shaped vehicles increased the  $L/D$  values substantially. Adding control surfaces to the half-cone vehicle resulted in a further increase in  $L/D$ . In the case of one winged reentry configuration, an  $(L/D)_{MAX}$  of about 6 was obtained when the configuration was specially modified to achieve high  $L/D$  at low speeds. With these modifications, this configuration had a thick, highly cambered wing and a teardrop fuselage with a small base area. The hypersonic  $L/D$  was reduced by these changes, but the hypersonic  $L/D$  values for the half-cone and pyramid-shaped vehicles were relatively unaffected by boattailing. Another method for obtaining high  $L/D$  for landing is the use of a variable-geometry vehicle, such as the one shown at the top of figure 51-5, which has a subsonic  $(L/D)_{MAX}$  of about 7.

#### Variable-Geometry Vehicles

Some subsonic aerodynamic data for the variable-geometry vehicle shown in figure 51-5 are

# RESEARCH RELATED TO THE LANDING OF SPACE VEHICLES

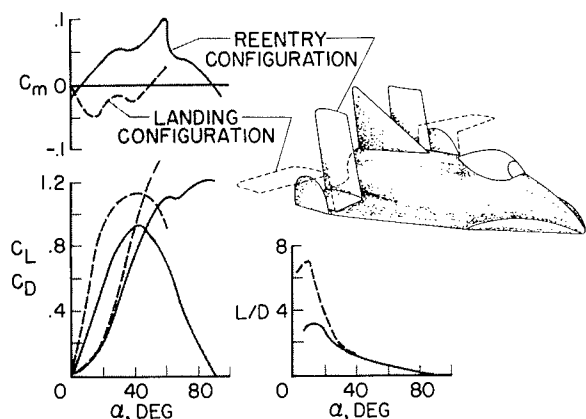


FIGURE 51-6.—Aerodynamics of variable-geometry vehicle.

presented in figure 51-6. (See refs. 4 and 5 for additional information.) In the reentry configuration, the wing tips of this vehicle are folded up to protect them from high heating rates during reentry at high angles of attack. For landing, the surfaces are folded down. The pronounced increase in  $L/D$  produced by extending the surfaces is shown in the plot at the lower right. The pitching-moment plot at the upper left illustrates the basic principle of the variable-geometry concept. In the reentry configuration with the wing tips retracted, the vehicle is designed to have zero pitching moment at an angle of attack of about  $90^\circ$  so as to be trimmed for vertical or near-vertical descent. The negative slope of the pitching-moment curve at  $\alpha=90^\circ$  indicates static longitudinal stability for this condition; but, like the blunt-faced Mercury-type vehicles discussed earlier, this configuration has a negative lift-curve slope and negative damping in pitch at an angle of attack of  $90^\circ$  and, consequently, has an unstable pitching oscillation in subsonic vertical descent. In the landing configuration, the extended surfaces provide longitudinal stability and trim in the low angle-of-attack range. This variable-geometry configuration is, of course, only one of many possible variable-geometry schemes which have been considered.

## Stability and Control of Glide-Landing Vehicles

Some of the effects of wing sweep on the stability and control characteristics of glide-landing reentry vehicles with highly swept

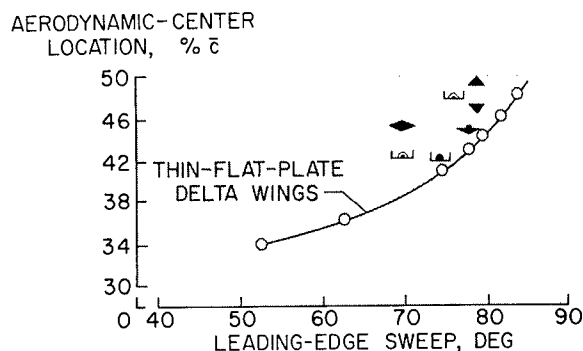


FIGURE 51-7.—Aerodynamic-center location at low subsonic speed.

wings are presented in figures 51-7 to 51-10. Figure 51-7 shows the variation of aerodynamic-center location with leading-edge sweep for thin-flat-plate delta wings. The aerodynamic center must, of course, be aft of the center of gravity for longitudinal stability. The data indicate that there is a systematic variation in aerodynamic-center position with sweep approaching the theoretical value of 50 percent  $\bar{c}$  at  $90^\circ$  sweep. Also shown in figure 51-7 are the aerodynamic-center locations for several reentry vehicles as given by symbols showing their cross-sectional views. These data indicate that a rearward (or stabilizing) shift in aerodynamic center generally results when the wing is very thick, when a large fuselage is added, or when wing-tip vertical tails are used.

For this same series of thin-flat-plate delta wings, figure 51-8 shows the variation with sweep angle of the effective-dihedral parameter  $C_{i\theta}$ , the damping-in-roll parameter  $C_{l_p}$ , and the ratio of the yawing moment of inertia to the rolling moment of inertia  $I_z/I_x$ . Although these data are for thin delta wings at a lift coefficient of 0.60, the trends shown are considered to be generally representative of highly swept reentry configurations for a fairly wide lift-coefficient range. As the sweep angle increases, the effective dihedral ( $-C_{i\theta}$ ) increases to very large values, the damping in roll ( $-C_{l_p}$ ) drops off and even becomes unstable at the higher angles, and the ratio of yawing inertia to rolling inertia becomes very large. This combination of changes leads to a lightly damped Dutch roll oscillation and, as would be expected with a high yawing inertia

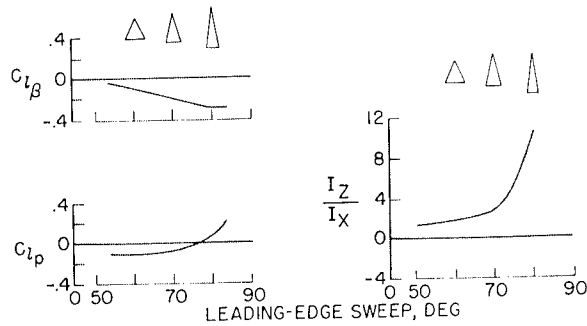


FIGURE 51-8.—Aerodynamic and inertia parameters of thin delta wings.  $C_L=0.60$ .

and low rolling inertia, the oscillation is almost a pure rolling motion about the body  $X$ -axis. (See ref. 6.)

An illustration of the Dutch roll stability problem for a typical highly swept, glide-landing reentry vehicle is presented in figure 51-9. In the left-hand plots, the calculated period and damping of the Dutch roll oscillation for subsonic flight are plotted against angle of attack.

The decrease in the damping parameter  $\frac{1}{T_{1/2}}$  with increasing angle of attack indicates a reduction in Dutch roll damping to unsatisfactorily low values at angles of attack around  $30^\circ$ . In model flight tests of this configuration in the Langley full-scale tunnel, a very lightly damped oscillation, involving primarily a rolling motion about the body axis, was obtained.

Research has indicated that a very effective means of obtaining satisfactory Dutch roll damping with highly swept reentry vehicles of this type is to use a roll-rate damper, that is, an automatic stabilization device which operates the roll control in response to rate of roll. The plot on the right-hand side of figure 51-9 shows the relative effect of roll and yaw dampers for this reentry configuration. The damping factor  $\frac{1}{T_{1/2}}$  is plotted against values of the damping-in-roll derivative  $-C_{l_p}$ , the damping-in-yaw derivative  $-C_{n_r}$ , and the cross derivative  $C_{n_p}$  (yawing moment due to rolling velocity). These results show that an increase in  $-C_{l_p}$  (representing the use of a roll damper) produced a large increase in the damping of the Dutch roll oscillation, whereas an increase in  $-C_{n_r}$

(representing the use of a yaw damper) produced only a very small increment of damping. Another point of interest here is that the derivative  $C_{n_p}$  also has a large effect on the damping. This effect can be significant in cases where the ailerons used for roll damping produce large yawing moments. In such cases, the damper will produce  $C_{n_p}$  as well as  $C_{l_p}$ ; and the  $C_{n_p}$  contribution will be stabilizing when the yawing moments are adverse and destabilizing when the yawing moments are favorable.

Figure 51-10 presents some information on directional stability which indicates that highly swept reentry configurations are not likely to experience directional stability problems. Plotted against sweep angle are values of two directional stability parameters,  $C_{n_\beta}$  and  $(C_{n_\beta})_{DYN}$ , for the same series of thin-flat-plate delta wings covered earlier. The values of the static directional stability parameter  $C_{n_\beta}$  are low and become negative at the higher sweep angles. On the other hand, the dynamic directional stability parameter  $(C_{n_\beta})_{DYN}$ , which is defined as  $C_{n_\beta} - C_{l_\beta} \frac{I_z}{I_x} \sin \alpha$ , increases rapidly

to large positive values at high sweep angles because of the large positive increases in  $I_z/I_x$  and negative increases in  $C_{l_\beta}$ . It has generally been found that the parameter  $(C_{n_\beta})_{DYN}$  is a better criterion for directional divergence than the static stability parameter  $C_{n_\beta}$ . For example, it has been found possible to fly airplane models with large negative values of  $C_{n_\beta}$  as

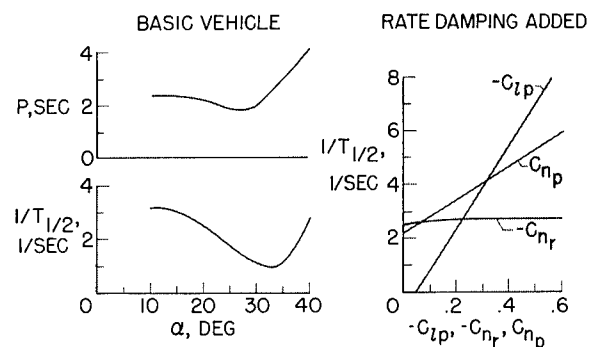


FIGURE 51-9.—Dutch roll stability. Glide-landing reentry vehicle.

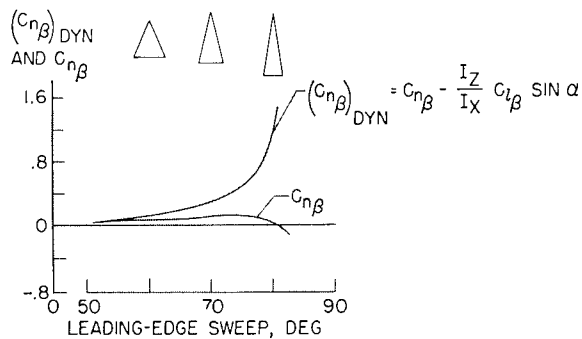


FIGURE 51-10.—Directional stability parameters of thin delta wings.  $C_L=0.60$ .

long as  $(C_{n\beta})_{\text{DYN}}$  remains positive. It would appear, therefore, that directional-divergence problems are not likely to be experienced with highly swept reentry vehicles because of their large values of effective dihedral and large ratios of yawing inertia to rolling inertia.

It has been found, however, that directional problems can be encountered with such configurations because of the adverse yawing moments produced by aileron control. This point is illustrated by the data of figure 51-11. The upper part of the figure shows the ratio of yawing moment to rolling moment produced by aileron deflection  $C_{n\delta_a}/C_{l\delta_a}$  for two reentry configurations—one having wing-tip vertical tails and the other a single center vertical tail. The data show that aileron deflection produced small favorable yawing moments over most of the angle-of-attack range for the configuration with the center tail but produced large adverse yawing moments for the wing-tip tail configuration. The large adverse aileron yawing moments are associated with the large induced loads produced on the vertical-tail surfaces by differential deflection of the ailerons. The plot at the bottom of figure 51-11 shows that the rudder effectiveness  $C_{n\delta_r}$  remained about constant with angle of attack for the center-tail model, but decreased with increasing angle of attack for the model with the wing-tip tails and became practically zero at an angle of attack of  $40^\circ$ .

The significance of these results was clearly shown in model flight tests of the wing-tip tail configuration. It was not possible to fly the model with ailerons-alone control because the

large adverse yawing moments produced by the ailerons resulted in directional divergences. At the lower angles of attack these yawing moments could be counteracted by the use of rudder control, and successful flights could be made. At the higher angles of attack where the rudder effectiveness had dropped off appreciably, however, the adverse yawing moments produced large yawing motions and the model became uncontrollable. It appears that configurations of this type with wing-tip tails will need a powerful rudder control and may require interconnection of the ailerons and rudders for satisfactory lateral control at subsonic speeds.

#### AUXILIARY LANDING AIDS

Since the conventional parachute has been under development for so long and its characteristics generally understood, it will not be discussed in this paper except to point out that the Mercury recovery system involves the use of main and reserve parachutes of the ring-sail type which are deployed first in a reefed condition to minimize the opening shock loads. These are rather porous parachutes which provide a relatively stable descent.

An interesting development of the conventional parachute that has been receiving some attention is the steerable parachute which is intended to provide enough maneuvering capability to afford some choice of landing site. One example of the steerable parachute is illustrated in figure 51-12. This is a flapped parachute which was tested in the Ames 40- by 80-foot tunnel. (See ref. 7.) The flap was formed

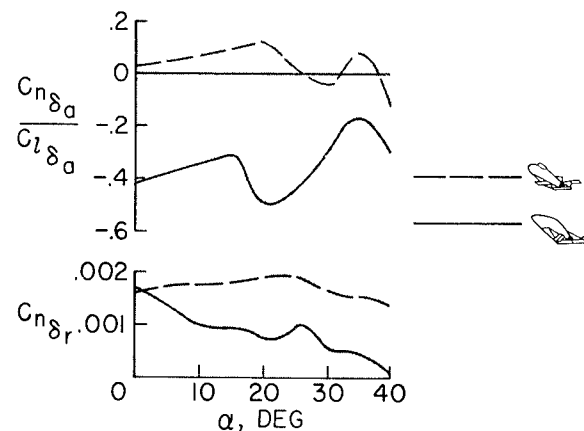


FIGURE 51-11.—Lateral control parameters.

## AERODYNAMICS

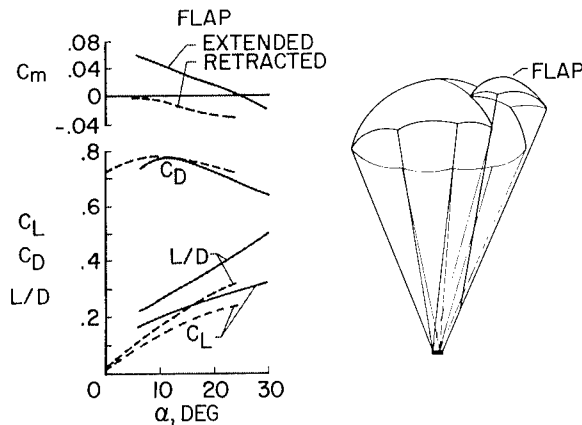


FIGURE 51-12.—Aerodynamics of steerable parachute.

by allowing a portion of the skirt to deflect upward as illustrated in the sketch. The pitching-moment data in the upper left-hand plot show that extending the flap caused the parachute to trim at an angle of attack of about  $25^\circ$  (compared with  $0^\circ$  with the flap retracted). At this angle of  $25^\circ$  with flap extended, an  $L/D$  of about 0.4 or 0.5 was obtained. This result indicates that the flap does provide a limited amount of glide-path control.

### Parawing Recovery Systems

A recovery device which provides a much greater degree of maneuvering capability is the parawing which is now being developed for use in the Gemini program as a replacement for the parachute. (See refs. 8 and 9.) Figure

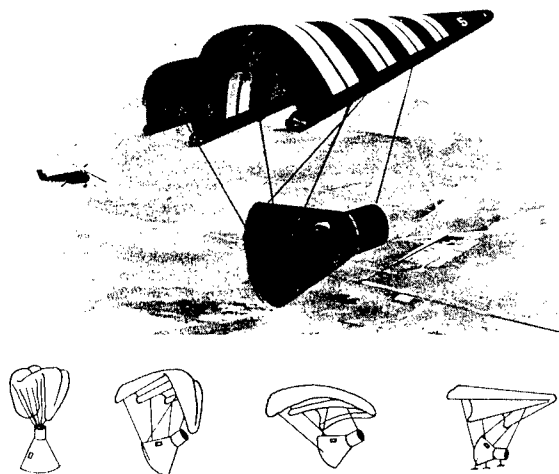


FIGURE 51-13.—Parawing recovery system.

51-13 is an artist's conceptual drawing of the Gemini parawing recovery system. This illustration is not accurate in all details but does serve to illustrate the system. It is anticipated that the glide capability provided by such a system will greatly increase the chances of reaching a safe landing site. But it is generally agreed that in order to provide greater capability than the parachute, the parawing will almost certainly be a more complex system and is also likely to have more aerodynamic problems than the parachute. Maneuvering of the parawing vehicle is accomplished by differential lengthening and shortening of the fore-and-aft lines for pitch control and of the wing-tip lines for roll control. In other words, the center of gravity of the system is effectively shifted to provide control moments. The main structural members of the parawing—the keel and leading edges—are inflatable tubes which are stowed in the deflated condition prior to deployment.

The proposed deployment sequence for the Gemini recovery system, illustrated schematically at the bottom of figure 51-13, involves a carefully timed series of steps including release of the stowed parawing, inflation of the keel and leading edges, and extension of all the supporting lines. Research to date has indicated that careful attention must be given to parawing deployment to insure success since a slight error in rigging or timing may lead to serious stability and trim problems which could prevent a successful recovery.

Figure 51-14 presents some low-speed aerodynamic data obtained in tests of a large-scale model of a parawing with a thick rounded leading edge generally similar to that being considered for the Gemini recovery system. In this figure are shown various coefficients and parameters plotted against the angle of attack of the keel from negative to large positive angles. It should be noted that the lift curve is very nonlinear near zero lift between angles of attack of about  $-5^\circ$  and  $15^\circ$ . This is the range in which the fabric of the parawing goes slack, resulting in a fabric flapping problem which may be experienced even up to angles of attack of  $20^\circ$  or  $25^\circ$  in some cases in the form of a trailing-edge flutter. It is of interest to note that at an angle of attack of  $55^\circ$  and a lift

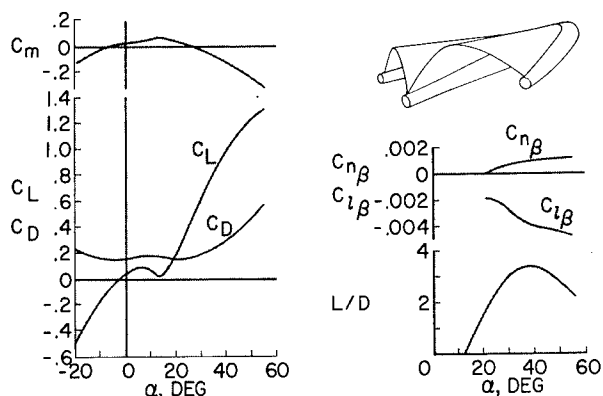


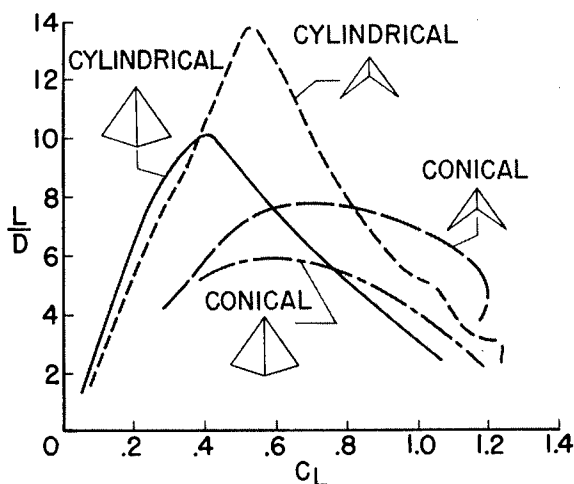
FIGURE 51-14.—Aerodynamics of parawing.

coefficient of about 1.3 the wing has not yet stalled. In the plot at the top of figure 51-14 it can be seen that the pitching-moment curve has a normal stable slope at angles of attack above about  $15^\circ$ , but below this angle the parawing is statically unstable. Research has indicated that this instability at low angles of attack, which is an inherent characteristic of the parawing because the fabric goes slack, can be a serious problem and may under some conditions even result in a tendency to enter an end-over-end tumbling motion. It thus appears desirable to operate the parawing at all times well away from this critical low-angle-of-attack range in order to avoid this problem.

The upper plot in the right-hand side of figure 51-14 shows small positive directional stability ( $C_{n\beta}$ ) and a large value of effective dihedral ( $-C_{l\beta}$ ) which are typical values for parawings. As for dynamic lateral stability, the Dutch roll damping observed in parawing flight tests to date has been generally satisfactory, but there have been some cases of poor Dutch roll damping when very large destabilizing bodies such as boosters were suspended beneath the parawing.

The plot at the bottom right-hand side of figure 51-14 shows that a maximum  $L/D$  of about 3.5 was obtained at an angle of attack of almost  $40^\circ$ . This is a typical value for parawing configurations tested to date with large inflatable leading edges. It is possible to realize considerably higher values of  $L/D$  by going to configurations with smaller leading edges, higher aspect ratio, and changes in the wing canopy shape as indicated in figure 51-15.

This figure presents data for parawings with rigid, streamlined leading edges having two different aspect ratios (2.8 and 6), and two different canopy shapes which may be called conical and cylindrical. With the conical canopy shape, which has been used on most parawings to date, the canopy assumes the shape of a portion of the surface of a cone; whereas with the cylindrical canopy, the canopy assumes the shape of a portion of a cylinder having its axis parallel to the keel. The long-dash—short-dash curve shows a maximum  $L/D$  of about 6 for the aspect-ratio-2.8 conical-canopy wing. The fact that the  $L/D$  of this wing is higher than that for the wing of figure 51-14 is attributed primarily to its smaller, more streamlined leading edges. The long-dash line shows that increasing the aspect ratio of the conical-canopy wing to 6 causes an increase in  $L/D$  to almost 8. Changing to the cylindrical-canopy shape increases the  $L/D$  to 10 for the aspect-ratio-2.8 wing and to almost 14 for the aspect-ratio-6 wing. It should be pointed out that these large increases in  $L/D$  are obtained at the expense of a somewhat more complicated structure and that more information is needed on these higher  $L/D$  configurations before it can be determined how practical they will be. In any event, one important conclusion that can be drawn from these data is that it should eventually be possible by careful design and development to increase the  $L/D$  of parawing re-

FIGURE 51-15.— $L/D$  values for parawings with conical and cylindrical surfaces.

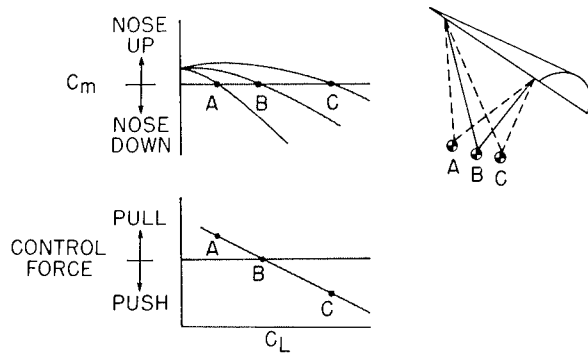


FIGURE 51-16.—Parawing longitudinal control.

covery systems considerably above the value of about 3.5 expected for Gemini.

The basic characteristics of parawing longitudinal control by center-of-gravity shift are illustrated in figure 51-16. The upper plot in this figure shows the pitching-moment curves resulting when the center of gravity is shifted forward from B to A or rearward from B to C. When the center of gravity is shifted forward to trim at a lower lift coefficient (point A), an increase in stability is also obtained as indicated by the increased slope of the curve. Conversely, there is a reduction in stability when the parawing is trimmed to the higher lift coefficient (point C). Presented in the plot at the lower left is a typical variation of control force with lift coefficient which shows that the stick forces are unstable—that is, a pull force is required for trim at the lower lift coefficients and a push force at the higher lift coefficients. (Additional information on parawing control forces is presented in ref. 9.) Because the stick forces are unstable and also rather large for a parawing large enough to carry the Gemini spacecraft, a powered control system is indicated for such applications.

Figure 51-17 illustrates the parawing lateral control, which is obtained by a lateral center-of-gravity shift that also corresponds to a banking of the wing for control. The formula and sketch at the upper left indicate that the net rolling-moment coefficient produced is not only a function of the lift coefficient and the distance the lift vector passes from the center of gravity but is also affected by the factor in parentheses which includes the effective dihedral parameter  $-C_{l\beta}$ , the directional stability parameter  $C_{n\beta}$ ,

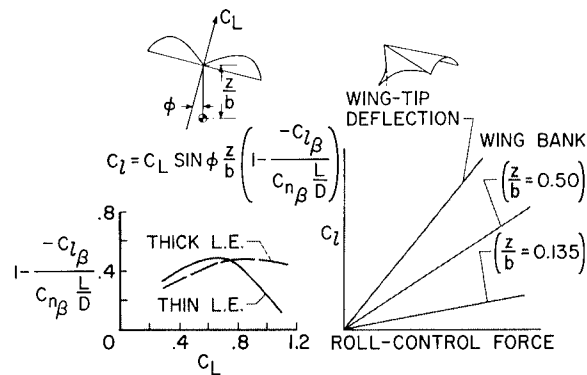


FIGURE 51-17.—Parawing lateral control.

and the lift-drag ratio  $L/D$ . This factor is used to account for the fact that a wing-bank control produces adverse yawing moments which act through the stability parameters to effectively reduce the rolling moment. At the lower left, values of this factor for parawings with thick and thin leading edges are shown plotted against lift coefficient. The factor never gets larger than about 0.5 and, in the case of the thin-leading-edge parawing, drops to about 0.1 at the higher lift coefficients. A zero value of the factor would, of course, indicate no control effectiveness.

In the plot on the right of figure 51-17, the roll-control forces experienced with the wing-bank control are compared with those for a wing-tip control which may be considered equivalent to an aileron control on a conventional wing. Two values of  $z/b$  are shown for the wing-bank control, the value of 0.50 corresponding to that used on the Gemini parawing recovery system and the value of 0.135 being a value used on one research configuration. The point to be made from this plot is that for a given rolling moment, the control forces with a wing-bank control system will be considerably higher than those with an aileron-like wing-tip control. Here again, it appears that a powered system is required to operate the wing-bank control on a Gemini-sized parawing.

A photograph of a parawing research vehicle built and flown at the NASA Flight Research Center at Edwards, Calif., is shown in figure 51-18. The vehicle is towed to altitude by an airplane and then cut loose to glide back to earth while performing various studies of parawing flight characteristics. Control is achieved



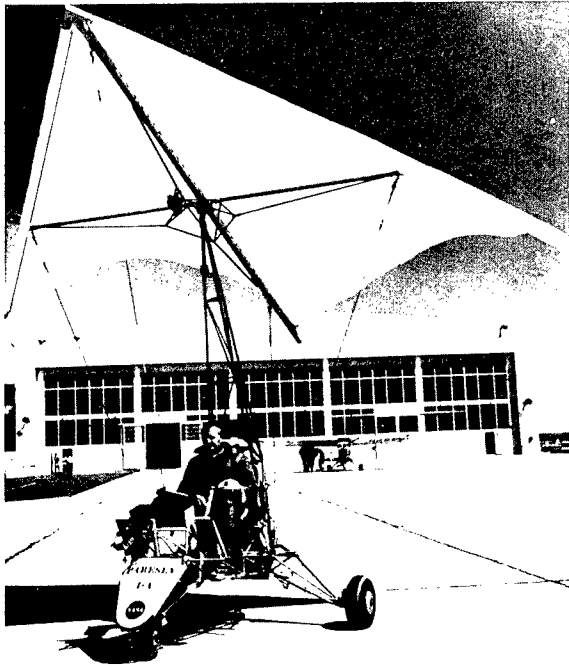


FIGURE 51-18.—NASA parawing research vehicle.

by tilting the wing with respect to the fuselage hanging underneath. Although some stability and control problems have been encountered in these tests, the results have been generally encouraging and have proved the feasibility of performing satisfactory flared landings with a parawing. Checkout flights will be made in the vehicle by some of our astronauts in the near future to provide some preliminary experience with a parawing vehicle having some of the same flight characteristics as the Gemini recovery system.

### Rotor Recovery System

Figure 51-19 presents some information on a rotor recovery device, sometimes called a rotorchute. In this scheme, the rotor blades are stowed in some manner during reentry and are then extended for landing. The attractiveness of the rotorchute lies in its capability for both gliding and vertical flight with the ability to

perform flared landings with essentially zero vertical and horizontal ground speed. Figure 51-19 shows calculated values of  $(L/D)_{MAX}$  for a spacecraft-rotorchute recovery system having a gross weight of 8,000 pounds with disk loadings varying from about 4 to 16 lb/ft<sup>2</sup>. For the disk loading of 16 lb/ft<sup>2</sup>, the blades would not need to be folded except at the root; whereas for the disk loading of 4 lb/ft<sup>2</sup>, a fold in the middle of the blades would also be required. The values of  $(L/D)_{MAX}$  increase from about 2 to 4 as the disk loading is reduced. Experience to date with power-off helicopter landings indicates that flared landings of rotorchutes with a disk loading of 4 lb/ft<sup>2</sup> could be made fairly easily, but with a disk loading of 16 lb/ft<sup>2</sup> they would be extremely difficult to perform unless some automatic features were incorporated.

### CONCLUDING REMARKS

Perhaps the principal significance of the information presented in the paper is that when a parachute is replaced by a glide-landing reentry vehicle or a glide-landing recovery device in order to give the astronaut greater latitude in the choice of a landing site, additional problems in low-speed aerodynamics are introduced, and careful attention must be given to the solution of these problems to insure a safe landing at the end of each space mission.

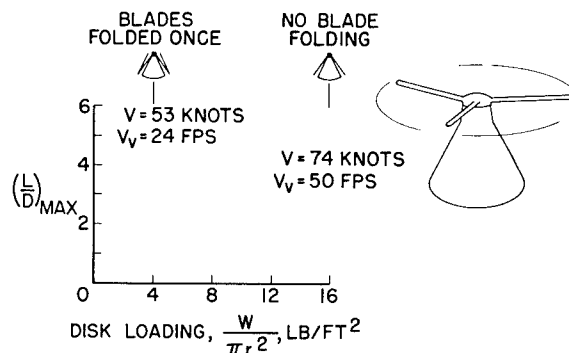


FIGURE 51-19.—Rotor recovery device.  $W=8,000$  lb.

## AERODYNAMICS

### REFERENCES

1. ANON.: Results of the First U.S. Manned Orbital Space Flight February 20, 1962. Manned Spacecraft Center, NASA.
2. ANON.: Results of the Second U.S. Manned Orbital Space Flight May 24, 1962. NASA SP-6, 1962.
3. WARE, GEORGE M.: Low-Subsonic-Speed Static Stability of Right-Triangular-Pyramid and Half-Cone Lifting Reentry Configurations. NASA TN D-646, 1961.
4. STAFF OF LANGLEY FLIGHT RESEARCH DIVISION (compiled by Donald C. Cheatham): A Concept of a Manned Satellite Reentry Which Is Completed With a Glide Landing. NASA TM X-226, 1959.
5. WARE, GEORGE M.: Low-Subsonic-Speed Static Longitudinal Stability and Control Characteristics of a Winged Reentry-Vehicle Configuration Having Wingtip Panels That Fold Up for High-Drag Reentry. NASA TM X-227, 1960.
6. PAULSON, JOHN W., and SHANKS, ROBERT E.: Investigation of Low-Subsonic Flight Characteristics of a Model of a Hypersonic Boost-Glide Configuration Having a 78° Delta Wing. NASA TN D-894, 1961. (Supersedes NASA TM X-201.)
7. GAMSE, BERL, and YAGGY, PAUL F.: Wind-Tunnel Tests of a Series of 18-Foot-Diameter Parachutes With Extendable Flaps. NASA TN D-1334, 1962.
8. ROGALLO, FRANCIS M.: Paraglider Recovery Systems. Presented at IAS Meeting on Man's Progress in the Conquest of Space (St. Louis, Mo.), Apr. 30-May 1-2, 1962.
9. JOHNSON, JOSEPH L., JR.: Low-Speed Wind-Tunnel Investigation To Determine the Flight Characteristics of a Model of a Parawing Utility Vehicle. NASA TN D-1255, 1962.

## 52. The Aerodynamics of Hypersonic Cruising and Boost Vehicles

By Mitchel H. Bertram, David E. Fetterman, Jr., and John R. Henry

MITCHEL H. BERTRAM, *Head of the Hypersonic Aerodynamics Section, Aero-Physics Division, NASA Langley Research Center*, received his Bachelor of Science degree in Aeronautical Engineering in August 1946 from New York University, Bronx, New York. Bertram is an authority in the field of hypersonic aerodynamics and especially in the field of boundary-layer interaction effects and effect of nose and leading-edge blunting. He was a member of the team at the Langley Research Center which in 1947, did research in the first regularly operating hypersonic tunnel in this country and perhaps the world. This team pioneered much of the ground which today forms the foundation of United States knowledge at very high speeds. Bertram is author of many NASA publications and has served as a reviewer of numerous papers for technical publications. He has been a frequent consultant to industrial and university representatives. He is an Associate Fellow of the Institute of the Aerospace Sciences and a member of the Hypersonics Committee of the American Rocket Society.

DAVID E. FETTERMAN, JR., *Aero-Space Engineer, Hypersonic Branch, Aero-Physics Division, NASA Langley Research Center*, received his Bachelor of Science degree in aeronautical engineering from Pennsylvania State University in June 1952. Fetterman joined the Langley staff in June 1952 and has been working in the fields of aerodynamic performance—stability and control. He is author of several NASA technical reports on research which he has conducted at Langley. He is a member of the Institute of the Aerospace Sciences, Tau Beta Pi, and Sigma Tau honorary fraternities.

JOHN R. HENRY, *Assistant Head, Internal Aerodynamics Branch, Aero-Physics Division, NASA Langley Research Center*, received his Bachelor of Science degrees in mechanical and aeronautical engineering in 1942 from the University of Michigan. Henry joined the Langley staff after graduation and has specialized in the fields of internal flow, supersonic and hypersonic air-breathing propulsion, and hypersonic air inlets. He is author or co-author of 13 NASA technical reports on research which he has conducted at Langley.

### SUMMARY

The problems of efficient hypersonic flight of boost-glide and air-breathing vehicles are reviewed for the areas of aerodynamics, stability and control, heating, and air ingestion. The application of classical hyper-

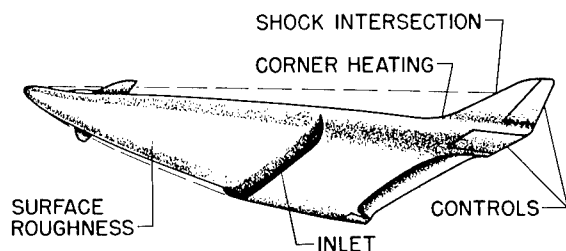
sonic solutions to this class of vehicles is shown although these solutions cannot always be applied without extensive modification. Particular attention is given to the problems of interference between major vehicle components and the internal flow problems of air breathers.

## INTRODUCTION

In the development of an efficient hypersonic vehicle, all of the classic problems associated with lower speed aircraft must be resolved together with the additional problems imposed by the more severe environment encountered at hypervelocities.

Pictorially, figure 52-1 shows some of the aerodynamic problem areas that might be important to a given hypersonic vehicle. A review of the present technology as applied to these problems plus that of providing a machine with high lift-drag ratios is the subject of this paper. As a larger problem area, the airplane must be trimmable and the provision of stability about all three axes is desirable. Another general problem is that of predicting the aerodynamic heating to all parts of the vehicle. This problem not only includes predictions on smooth skins, leading edges, and nose, but also the effects of both production-type and temperature-induced surface roughnesses or distortions. Where surfaces intersect, the so-called "corner problem" occurs and the effect on heating, for example, must be evaluated. Similarly, for the case of a shock which intersects parts of the airplane, flaps or fins used for control will have separate heating and viscous problems.

In a vehicle with provision for air-breathing propulsion such as the one shown here, another set of problems must be solved. The inlet, which is the main concern here, must be able to accept large quantities of air in as precompressed a form as possible. At the same time,



- TRIM AND STABILITY
- AERODYNAMIC HEATING

FIGURE 52-1.—Aerodynamic problem areas.

the inlet lip and surfaces must survive the high heating rates to which they will be exposed and further compress the air for use by the propulsion system.

## SYMBOLS

$\bar{c}$	wing mean aerodynamic chord, ft
$C_{D,\min}$	minimum drag coefficient
$C_L$	lift coefficient
$C_{L\alpha}$	lift-curve slope at zero angle of attack
$C_m$	pitching-moment coefficient
$c_{p,w}$	specific heat of gas at wall temperature, $\frac{\text{ft}^2}{\text{sec}^2 - ^\circ\text{F}}$
$D$	drag, lb
$h$	heat-transfer coefficient; height
$I_{sp}$	specific impulse, sec
$L$	lift, lb
$L/D$	lift-drag ratio
$l$	length, ft
$M$	Mach number
$M_c$	Mach number at which combustion occurs
$N_{St}$	Stanton number
$p$	static pressure, psf
$q$	free-stream dynamic pressure, psf
$R$	Reynolds number
$r$	radius, ft
$S$	wing planform area, sq ft
$T_w$	wall temperature, $^\circ\text{R}$
$V$	volume, cu ft
$V_{\text{orbital}}$	satellite velocity, fps
$V_\infty$	free-stream velocity, fps
$W$	weight, lb
$x$	linear distance from nose apex or leading edge for two-dimensional wings
$y$	spanwise distance measured from corner
$\alpha$	angle of attack, deg
$\delta$	control deflection angle, deg
$\epsilon$	emissivity
$\Lambda$	leading-edge sweep angle, deg
$\varphi$	angle of ray through wing vertex measured from center line, deg
$\rho_o$	density of gas at sea level, slugs/ft <sup>3</sup>

## Subscripts:

Body	body length
$c$	wing root chord; capture
$f$	tip flap
$\text{inf}$	value for infinite cylinder
$j$	jet exit
$\text{max}$	maximum
$n$	nose
$\infty$	free stream
$t$	throat
$i$	inviscid
$w$	wall

# HYPERSONIC CRUISING AND BOOST VEHICLES

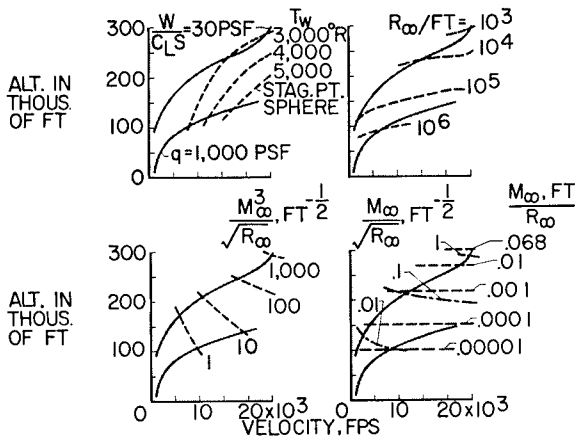


FIGURE 52-2.—Glider environment.

## VEHICLE OPERATING ENVIRONMENT

At this point, it is instructive to examine the environment in which the hypothetical vehicle will be functioning. In figure 52-2 the solid lines outline the velocity-altitude corridor in which the vehicle must fly. The lower line represents a limitation imposed by the maximum load that the structure will support and the upper line indicates an altitude above which aerodynamic lift fails to support the airplane weight. The lower limit may be somewhat pessimistic but the upper limit is believed to be overly optimistic. For the purposes of this paper, they suffice.

The upper left-hand corner of figure 52-2 illustrates how aerodynamic heating can further limit the extent of the flight corridor. Assume that the nose of the vehicle is a sphere of radius 1 foot. If this sphere is radiation cooled, the temperature limitations of the material composing the sphere determine the path which the vehicle must follow so that the sphere remains intact.

The radius of a sphere required to maintain a given radiation equilibrium temperature at arbitrary dynamic pressures may be obtained by equating the classic equations for radiative heat transfer to those for aerodynamic heating. In this case Lees' approximate equation for the aerodynamic heating at the stagnation point of a sphere was used. (See ref. 1.) The result for planetary atmosphere, in general, is as follows:

$$r = \frac{3.05 \times 10^3}{\epsilon^2 \rho_o \left( \frac{V_{orbital}}{1000} \right)^6} \frac{\left[ \left( \frac{V_\infty}{1000} \right)^2 - \frac{2c_{p,w}}{1000} \frac{T_w}{1000} \right]^2}{(T_w/1000)^8} q \quad (1)$$

and for the earth atmosphere specifically

$$r = \frac{0.00436}{\epsilon^2} \frac{\left[ \left( \frac{V_\infty}{1000} \right)^2 - 12 \frac{T_w}{1000} \right]^2}{(T_w/1000)^8} q \quad (2)$$

By assuming various equilibrium wall temperatures that must be maintained with a surface emissivity of 0.8, the dashed lines were obtained. If the wall temperature of the spherical nose has to be as low as 3000° R, the maximum velocity is limited to about 15,000 feet per second. If a higher performance material is assumed, a neck opens in the corridor, although the allowable range of flight altitudes is limited. This condition occurs in the neighborhood of a Mach number of 20. If through advances in material technology the wall temperature of the spherical nose could be allowed to rise to 5000° R, a much lower altitude trajectory can be followed by the glider.

The other curves in figure 52-2 which intersect the flight corridor are concerned mainly with viscous effects. In the upper right-hand corner are shown curves along which various unit Reynolds numbers would be obtained. If vehicles with lengths on the order of 100 feet are of the proper size to be considered, when the numbers shown here are multiplied by 100 it is indicated that extensive regions of turbulent flow will probably occur on the vehicle over much of the corridor.

In the lower left-hand corner are shown curves for various values of the hypersonic interaction parameters  $M_\infty^3/\sqrt{R}$  at a length of 1 foot. This parameter determines the importance of effects induced by thick hypersonic laminar boundary layers. These are the boundary-layer "displacement" or "self-induced" effects. (See refs. 2 and 3.) The larger the value of  $M_\infty^3/\sqrt{R}$  the more important are the self-induced effects. It is clear that viscous effects involving thick boundary layers can be important in the same region that heating is critical, that is, in the region of a Mach number of 20.

The lower right-hand section of figure 52-2 contains parameters which are a form of the Knudsen number and indicate the regime of flow as outlined by Tsien. (See ref. 4.) The values of these parameters indicate that the main interest lies in the continuum flow region within the flight regime. It is only at the extreme altitudes that low-density effects might be significant. The more recent work of Probst (ref. 5) on the delineation of the flow regimes for blunt bodies also gives this result.

## PERFORMANCE AND STABILITY

### Effect of Vehicle Shape on Lift-Drag Ratio

The importance of high lift-drag ratios for low to moderate hypersonic speeds has long been recognized. (See ref. 6.) The vehicle shapes that constitute the best approaches to obtaining high lift-drag ratios are still prime food for controversy. As shown in figure 52-3, three main vehicle types have been considered—the flat top or body suspended below wing, the flat bottom or body mounted above wing, and the intermediate shape which has the body symmetrically arranged on the wing. The principle of the flat-top type which utilizes favorable interference was independently suggested by several investigators. (See refs. 7 to 10.) This wing-body arrangement in its various forms utilizes upwash and pressure lift on the wing due to the body to obtain increased aerodynamic efficiency. Because of the behavior of the body pressure field with flight speed, optimum aerodynamic efficiency for these

configuration types is Mach number limited. The flat-bottom type was proposed mainly as a means to put the body into a more shielded region and thus decrease the heating load on the configuration.

Linearized theory indicates the maximum lift-drag ratio of symmetrical wings is a function of the lift-curve slope divided by the minimum drag coefficients. Data for  $(L/D)_{\max}$  obtained by Clarence A. Syvertson, Hermilo R. Gloria, and Michael F. Sarabia at the Ames Research Center and William O. Armstrong and Charles L. Ladson at the Langley Research Center on the various random configuration types over a range of Mach and Reynolds numbers are shown as a function of  $C_{L\alpha}/C_{D,\min}$  in figure 52-3. The solid line represents the prediction of linearized theory and the data arrange themselves about this line. In general, at the higher values of  $L/D$  the flat-top types have the highest maximum lift-drag ratios; the flat bottom, the lowest; and the symmetrical types, intermediate values. At the lower values of  $L/D$ , for example, about 4, the differences in  $L/D$  between the various shapes tends to disappear on this plot.

If a constant value of  $(L/D)_{\max}$  is examined, for example 5, a large range of the parameter  $C_{L\alpha}/C_{D,\min}$  is covered. What this means, however, in terms of available volume and the accompanying wing area which affects the structural efficiency remains to be determined. In figure 52-4 the details of the vehicle configurations which generated this particular value of  $(L/D)_{\max}$  are shown. The lift-drag ratios of these configurations are shown in figure 52-5 as a function of the much used volumetric efficiency parameter, that is, volume to the  $2/3$  power divided by the vehicle planform area. Note that the vehicle on the far right has a planform area less than 30 percent of that of the configuration on the far left even though the bodies of the two configurations are identical. Some penalty, however, accrues to the lift coefficient as the volumetric efficiency is increased as shown at the top of this figure. In proceeding from the lowest volumetric efficiency configuration to the highest, there is a loss of about 30 percent in lift coefficient.

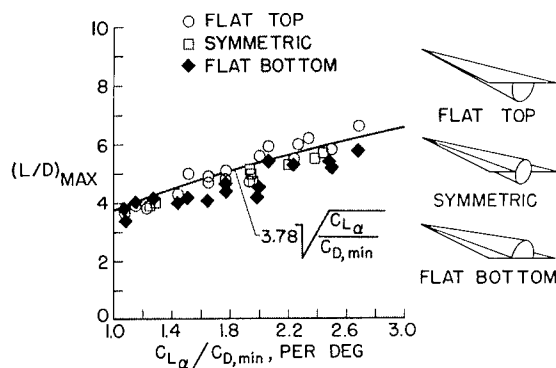


FIGURE 52-3.—Configuration comparison on basis of aerodynamic efficiency.  $M_\infty = 3$  to 10.

# HYPERSONIC CRUISING AND BOOST VEHICLES

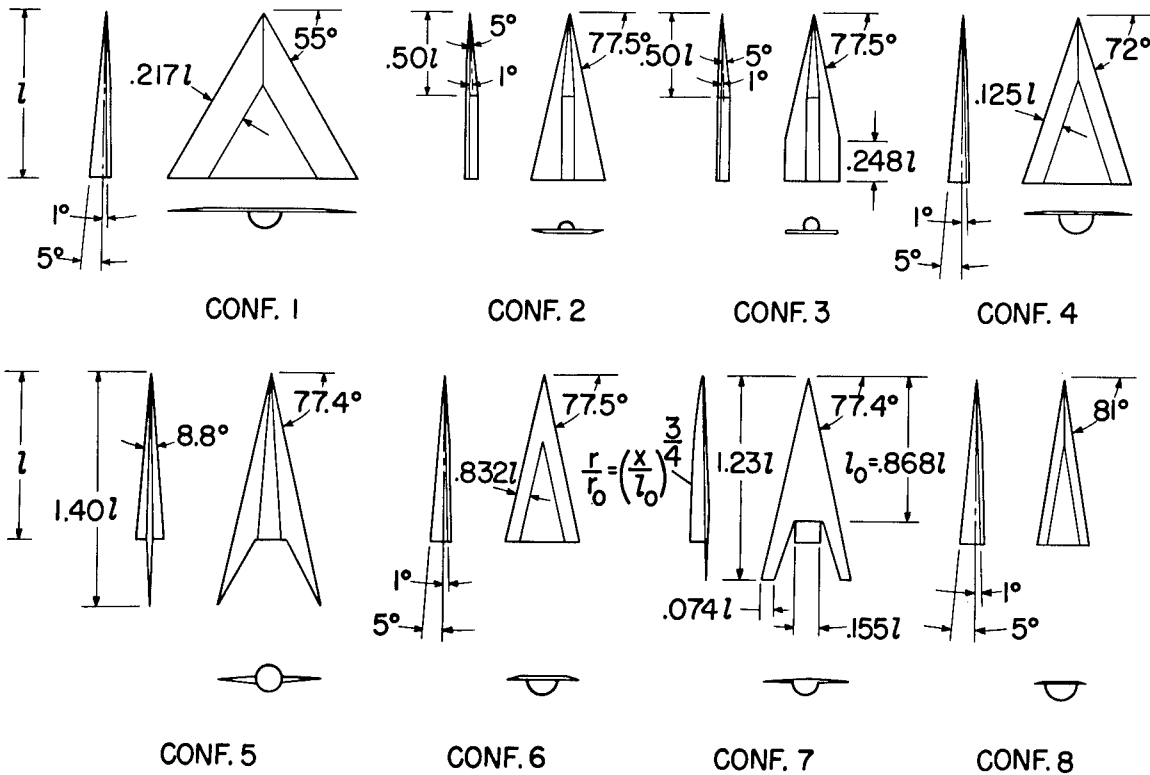


FIGURE 52-4.—Details of configurations used in aerodynamic efficiency study.

These data are for essentially constant body length. If results for other constraints such as constant volume or constant planform area were to be evaluated, the Reynolds numbers would have to be adjusted accordingly. Table 52-I gives volume, planform area, and length under the various geometric constraints as a ratio to its value for configuration 1. Note that, when the configurations are adjusted to constant body

volume, the body length does not vary greatly over this range of configurations.

It should be noted that any inference from figure 52-5 that  $(L/D)_{\max}$  is relatively independent of volume should be avoided. Actually, data not included herein indicate that for a given wing planform and wing-body orientation, an increase in volume can significantly lower the  $(L/D)_{\max}$  capability of a configuration. The data of figure 52-5, however, indicate that this result is not necessarily true when a variety of configurations are considered so that apparently a great deal more flexibility in configuration design is available to the aerodynamicist than was previously realized.

In the comparison, a wide range of volumetric efficiencies is covered by a number of miscellaneous shapes. Of course, one problem is to provide the volume distribution in such a way as to allow a proper weight distribution. For these purposes, a cone is poor. The second configuration from the right, where the body is a  $3/4$  power shape, is an improvement over a cone in regard to volume distribution. This

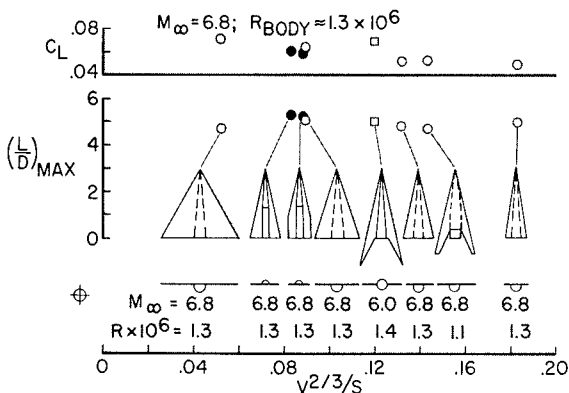


FIGURE 52-5.—Volumetric efficiency variation at a given  $(L/D)_{\max}$ .

# AERODYNAMICS

TABLE 52-I.—Geometric Properties of Configurations With Various Constraints

Configuration	$\frac{V^{2/3}}{S}$	Constant body length		Constant body volume		Constant planform area	
		$V/V_1$	$S/S_1$	$l/l_1$	$S/S_1$	$l/l_1$	$V/V_1$
1-----	0.052	1	1	1	1	1	1
2-----	.083	.50	.38	1.26	.61	1.62	2.11
3-----	.088	.50	.36	1.26	.57	1.67	2.33
4-----	.089	1	.56	1	.56	1.33	2.37
5-----	.120	1.24	.49	.93	.42	1.43	3.64
6-----	.132	1	.38	1	.38	1.61	4.22
7-----	.143	1.97	.55	.80	.35	1.35	4.80
8-----	.183	1	.28	1	.28	1.91	6.93

configuration type will now be examined further.

The body for this configuration was arranged on a fixed wing in three different ways: (1) with the body suspended below the wing as presented previously, (2) with the body above the wing, and (3) with the same volume distribution but with a circular cross section arranged symmetrically on the wing. Experimental results for these configurations are shown in figure 52-6. At Mach number 6.8, the flat-top and the midbody arrangements have about the same value of  $(L/D)_{\max}$  and are clearly superior in this respect to the flat-bottom arrangement. At Mach number 9.6, however, the value of  $(L/D)_{\max}$  is decreased and the flat-top and flat-bottom arrangements appear about equal, some superiority being exhibited for the midbody arrangement.

Based on the reasoning in terms of momentum considerations on which the flat-top development is based, this result might not be

expected since it indicates a high efficiency for the midbody. Actually, these results indicate inadequacies in the knowledge of predicting optimum aerodynamically efficient configurations with volumetric and linear-dimension constraints and the penalties incurred by operation at off-design conditions. Much additional work must be accomplished on a larger and more complex variety of configurations before sufficient information is in hand to allow competent preliminary designs of practical configurations. For instance, the merged-wing-body design appears theoretically promising but essentially no experimental information on this type is now available. Unfortunately, because of the com-

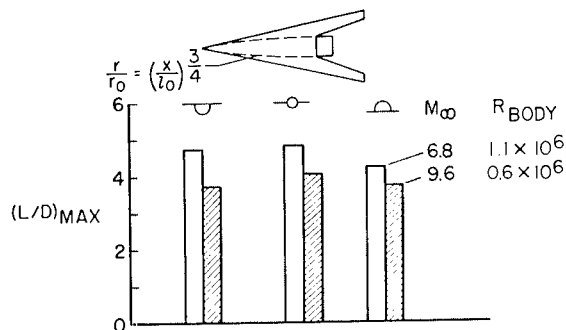


FIGURE 52-6.—Effect of wing location on  $(L/D)_{\max}$  of high-volume configuration.

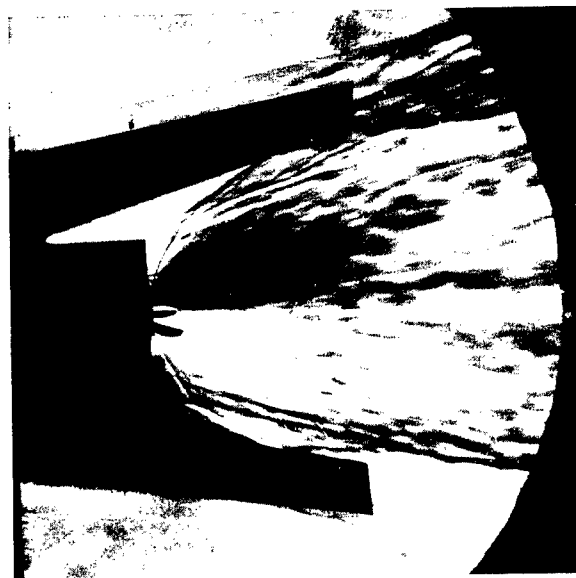


FIGURE 52-7.—Jet expansion in base of configuration 7.  $p_1/p_\infty = 467$ ;  $M_\infty = 6.8$ ;  $R_{\text{Body}} = 4 \times 10^5$ .



plex interfering flow fields that occur over even the simplest of these configurations, experimental research must be depended upon to provide the necessary information since theoretical treatment is not reliable at present.

If air inlets have to be provided, research will have to determine how this capability can be provided with minimum aerodynamic penalty. One of the problems of integrating propulsion and airframe is shown in figure 52-7. A schlieren photograph of tests at a Mach number of 6.8 illustrates the potential interference between the jet exhaust field and the aft portion of a wing when the jet is highly expanded as at high altitudes. The jet boundary also induces a separated-flow region over the aft portion of the fuselage which could also significantly affect vehicle stability.

#### Effect of Trim and Directional Stability on $(L/D)_{\max}$

It should be noted that the foregoing data were primarily obtained on simple wing-body combinations with no provisions for nose or leading-edge blunting, longitudinal trim, or directional stability. In general, these complications will tend to reduce  $(L/D)_{\max}$  values below those previously shown; however, some information is available which indicates that trim penalties need not be excessive. These results were obtained at a Mach number of about 6.8 and are shown in figure 52-8. On the left of the figure the pitching-moment and the lift-drag ratio characteristics for the  $3/4$  power body configuration, previously discussed, are shown for a representative center-of-gravity position at 46-percent mean aerodynamic chord. Data are presented for both the flat-top and flat-bottom versions of this configuration. The data indicate that the flat-top configuration trims ( $C_m=0$ ) near  $(L/D)_{\max}$  with no longitudinal control deflection necessary; thus, the trim penalty on  $(L/D)_{\max}$  for this configuration is essentially zero. On the other hand, the data for the flat-bottom version of the same configuration produces the negative pitching moments (characteristic of flat-bottom types) which must be overcome for trim with a negative control deflection if conventional trailing-edge controls are employed. Since negative control deflection

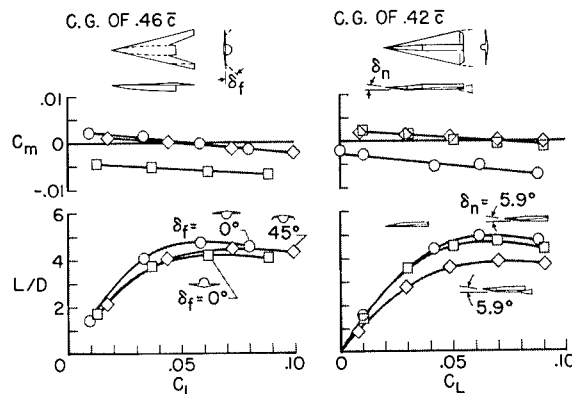


FIGURE 52-8.—Effect of trim and directional stability on  $(L/D)_{\max}$ .  $M_{\infty}=6.8$ .

implies primarily a loss in lift, it also implies a decrease in  $(L/D)_{\max}$  at trim for the flat-bottom types. However, a significant loss in  $L/D$  is not necessary; this fact is indicated by the data obtained by Robert W. Rainey at the Langley Research Center for the flat-bottom configuration shown at the right on figure 52-8. On this model, provisions were made for deflection of the forward portion of the nose. With the nose portion undeflected, the characteristic negative pitching-moment variation with lift coefficient results. With the nose portion deflected to give positive lift, however, the altered pitching-moment characteristics are similar to those of the flat-top configuration (on the left of fig. 52-8) so that trim is now obtained with only a slight reduction in  $(L/D)_{\max}$ . Trailing-edge controls were also included on this configuration but, since the control area was insufficient to provide trim at  $(L/D)_{\max}$ , these results have not been included. The trends of the data, however, indicated that, with this control alone, significant trim penalties in  $(L/D)_{\max}$  could be expected. The effects on trimmed  $(L/D)_{\max}$  of providing directional stability to these configurations are shown by the additional data included in figure 52-8. In order to provide directional stability, the wing tips of the configuration on the left-hand side of figure 52-8 were turned down  $45^\circ$  and wing-tip fins were added to the configuration on the right. In both cases these modifications had small effects on the resulting pitching-moment characteristics but significantly lowered the  $(L/D)_{\max}$  at trim.

## HEAT TRANSFER

## Heat Transfer to Lower Surface of Delta Wing

In order to present a clear picture of the overall distribution of heat-transfer rates and their relation to the external flow fields, the first part of this discussion will be based on fully laminar data at  $M_\infty=9.6$  obtained by James C. Dunavant at the Langley Research Center. Consider the sharp-leading-edge delta wing; it is geometrically simple but should still indicate the general behavior of the heat transfer to a blunt wing far from the leading edge. Figure 52-9 shows the trend of heat transfer with angle of attack for points along the center line of a flat delta wing. The results are presented in the form of the laminar flat-plate correlating parameter (Stanton number times the square root of Reynolds number based on distance from the nose) with fluid properties evaluated at free-stream conditions.

Up to an angle of attack of about  $20^\circ$ , the heat transfer increases with angle of attack about as expected for a flat plate, as shown by the solid curve in figure 52-9 labeled "strip theory." At higher angles of attack, the data depart from the strip theory trend and approach the dashed curve predicted by crossflow theory, which regards the wing as a succession of independent spanwise strips in two-dimensional crossflow. The crossflow approach neglects effects of the chordwise component of the flow. A more refined and more nearly correct approach is given by the streamwise divergence

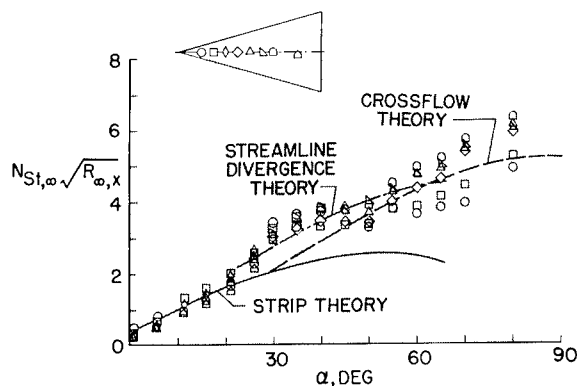


FIGURE 52-9.—Heat transfer to the center line of a delta wing over angle-of-attack range from  $0^\circ$  to  $90^\circ$ .  $\Lambda=75^\circ$ ;  $M_\infty=9.6$ .

theory shown by the dot-dashed line which fits the data well. (See ref. 11.) Above an angle of attack of about  $60^\circ$ , the wing shock is curved and the correlation based on a single characteristic length, the distance from the nose, can be expected to break down.

The effect of turbulent flow is a larger unknown than that of laminar flow previously considered. As noted earlier, over a large part of the flight corridor the Reynolds numbers are high enough that considerable regions of turbulent flow might be anticipated on the vehicle. Heat-transfer data have been obtained by James C. Dunavant of the Langley Research Center over a wide range of Reynolds number on the same delta wing on which the results shown in figure 52-9 were obtained. These data however were taken at a Mach number of 6.8 and an angle of attack of  $16^\circ$ . In figure 52-10 only data on the center line of the flat delta wing are shown. The data were obtained at a stagnation temperature of about  $650^\circ\text{F}$  and a skin temperature of about  $100^\circ\text{F}$ .

The data are laminar up to a Reynolds number of about 400,000 as indicated by a comparison with laminar theory (Monaghan T' method, ref. 12). The flow is then transitional to a Reynolds number of about  $10^6$  and appears to be fully turbulent above this value of Reynolds number. The data of the highest Reynolds numbers show good agreement with the turbulent theory (Van Driest, ref. 13) even though the turbulent theory assumes turbulent flow from the leading edge.

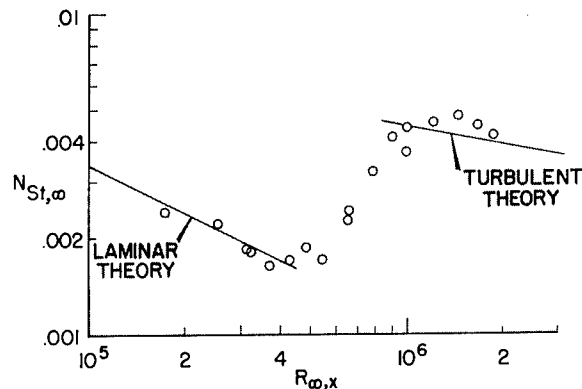


FIGURE 52-10.—Heat transfer on center line of delta wing. Sharp leading edge;  $\Lambda=75^\circ$ ;  $M_\infty=6.8$ ;  $\alpha=16^\circ$ .

The surface flow patterns obtained by James C. Dunavant corresponding to the heat-transfer data are shown in figure 52-11. These are tracings of oil-flow streak patterns formed by flowing lubricating oil impregnated with carbon black at a Mach number of 9.6. The patterns are shown in  $15^\circ$  increments from  $0^\circ$  to  $60^\circ$ . At the far left on figure 52-11 the pattern for zero angle of attack is shown. Here the surface flow is directed toward the center line of the wing because of the pressure gradient induced by the thick laminar boundary layer. This case was considered in some detail in reference 14 and additional information is given in a following section. With increasing angle of attack as shock loss effects start to predominate, the flow at the surface turns out from the center as shown in the three figures to the right. At an angle of attack of  $15^\circ$  the flow is away from the wing center line but still comes in across the leading edge. At an angle of attack of  $30^\circ$  the flow has turned out to such an extent that in the sense of the airflow direction the geometric leading edge has become a trailing edge. An interesting feature of the flow at an angle of attack of  $30^\circ$  is the appearance of a parting line at about  $12^\circ$  from the center line of the wing. At an angle of attack of  $45^\circ$  the flow is very close to radial in the center region of the wing and above this angle of attack the parting line is not a feature of the surface flow lines. At an angle of attack of  $60^\circ$  the flow lines which for the most part were more or less straight at lower angles of attack appear to be hyperbolic in nature. It may be seen that the patterns show conical symmetry at angles of attack of  $30^\circ$  and greater.

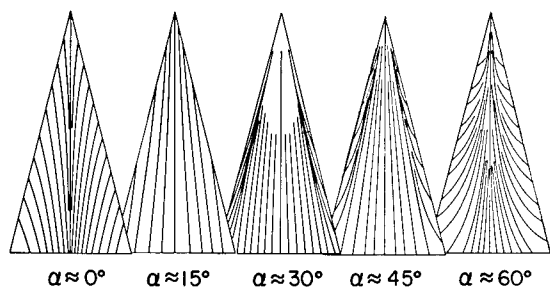


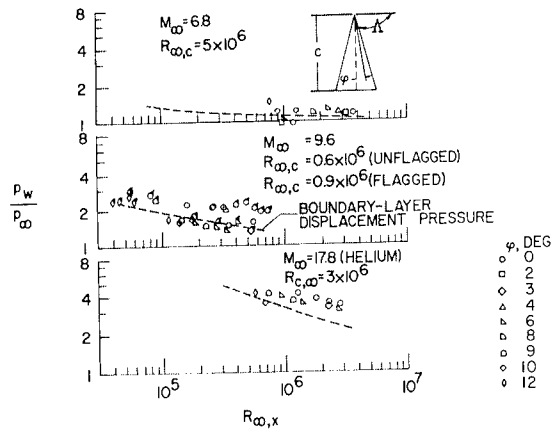
FIGURE 52-11.—Lower-surface flow patterns on flat delta wings.  $\Lambda=75^\circ$ ;  $M_\infty=9.6$ .

Much of the problem of predicting the heat transfer to a delta wing over a wide range of angle of attack is the changing flow pattern with angle of attack. Simple approaches to predicting the heat transfer will only be successful if the flow pattern peculiar to the angle-of-attack range under consideration is taken into account. For high  $L/D$  vehicles, it is the low angle-of-attack range that is generally of interest.

At low Reynolds numbers and high Mach numbers thick laminar boundary layers may have large effects on local pressure, skin friction, and aerodynamic heating. How these boundary-layer self-induced effects affect the chord force on a delta-wing configuration was shown in figure 5 of reference 15. The configuration analyzed was actually configuration 4 of the present paper (see fig. 52-4) tested at a Mach number of 9.6. Some additional information is now available on the local pressure and heat transfer to a delta wing at an angle of attack of  $0^\circ$ .

Consider first the  $\alpha=0^\circ$  flow pattern presented in figure 52-11. The boundary-layer induced-pressure gradient has caused the low-energy air in the boundary layer near the surface to flow toward the center of the wing and to pile up along the center line. However, because of this very gradient, the streamlines external to the boundary layer must be away from the center of the wing. The angle between the surface flow direction and the external streamline increases with increasing Mach number. (See ref. 14.)

Pressures and heat transfer measured on a  $75^\circ$  sweep delta wing at three hypersonic Mach numbers by James C. Dunavant are shown in figure 52-12. Mach number 6.8 and 9.6 data are from tests in air and the Mach number 17.8 data are from tests in helium. The pressure data shown in figure 52-12(a) show reasonable agreement with the theoretical two-dimensional boundary-layer displacement pressures. However, the result is different for the heat-transfer data shown in figure 52-12(b) which were obtained at essentially the same three Mach numbers as the pressures. The heat-transfer results, shown in terms of the laminar correlation parameter (Stanton number times the



(a) Pressures.

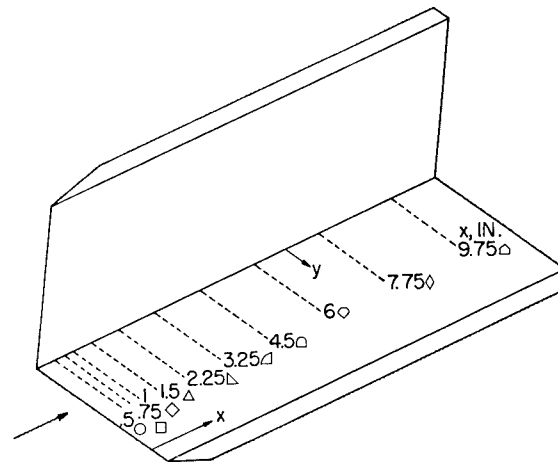
FIGURE 52-12.—Variation of pressure and heat transfer with Mach number.  $\Lambda = 75^\circ$ ; flat sharp-edge delta wing;  $\alpha \approx 0^\circ$ .

square root of Reynolds number based on tunnel test-section static conditions), are plotted against Reynolds number based on streamwise distance from the leading edge. At a Mach number of 6.6, the data in general group around the theory but the data in the region of the wing near the center line tend to lie below the theory (ref. 16). At Mach numbers of 9.6 and 17.8, the heat transfer is increased above the value from constant-pressure strip theory for the points nearest the leading edge. This increase is due to boundary-layer induced pressures. There is, however, a dropoff in the value of the heat-transfer parameter with distance from the leading edge, and at the farthest

distances from the leading edge there is a large discrepancy between data and theory. The deviation between theory and data increases with increasing Mach number and is attributed to the flow of low-energy air in the boundary layer toward the center line of the wing.

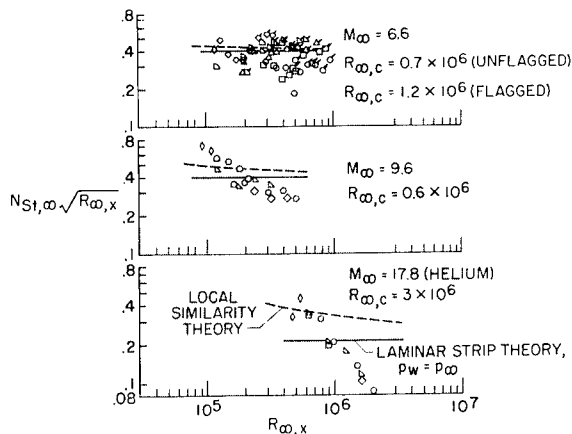
### Corner Heating

As mentioned early in this paper, a corner problem exists wherever two surfaces which form part of the airplane intersect at an angle. For example, this could be the intersection of a wing with a body or a fin and could be an internal or an external corner. A knowledge of corner effects on local pressures and heating is



(a) Sketch of model.

FIGURE 52-13.—Heat transfer to a  $90^\circ$  corner at a Mach number of 8.



(b) Heat transfer.

FIGURE 52-12.—Concluded.

clearly necessary. Actually, not a great deal of work has been done on corner effects. Gersten in reference 17 summarizes the results obtained in incompressible flow. Stainback's results for pressure and heat transfer at a Mach number of 5 (ref. 18) are compromised by what appears to be tunnel interference. The Princeton results (ref. 19) give pressure measurements in a corner and the recent Boeing results (ref. 20) give both pressure and heat-transfer results at a Mach number of 16. Some recent heat-transfer data obtained by P. Calvin Stainback in the Langley Mach 8 variable-density tunnel on a simple  $90^\circ$  corner model are shown in figure 52-13. Each of the plates making up the model (fig.

52-13(a)) had a span of 4 inches and an overall length of 11 inches. The leading edges were unswept and sharp. Instrumentation extended from close to the corner to 2 inches from the corner. The symbols shown for the given values of longitudinal distance  $x$  are the coding used in figure 52-13(b).

Based on the incompressible results, the data in the form of the laminar heat-transfer correlating parameter were plotted against angular spacing from the corner as shown in figure 52-13(b) for the model surfaces aligned with the flow. Data at two unit Reynolds numbers are shown, one of which is roughly 40 times the other. At the lowest unit Reynolds number the correlation on the basis of the parameters used is believed to be good. At large values of  $y/x$  where the corner does not influence the flow, the laminar flat-plate theory (ref. 12) closely predicts the level of heat transfer except for the stations closest to the leading edge. The increased heat transfer at these stations is attributed to boundary-layer displacement effects.

As the corner is approached, there is at first a general dip in the heat-transfer level. This dip occurs ahead of the free-stream location of the Mach wave from the vertical plate (vertical dashed line). Closer to the corner, there is a rapid increase in heat transfer to a peak roughly 40 percent greater than in the undisturbed flow far from the corner. Approaching the corner after the peak, there is a decrease in heat transfer as predicted by reference 21. Reference 21,

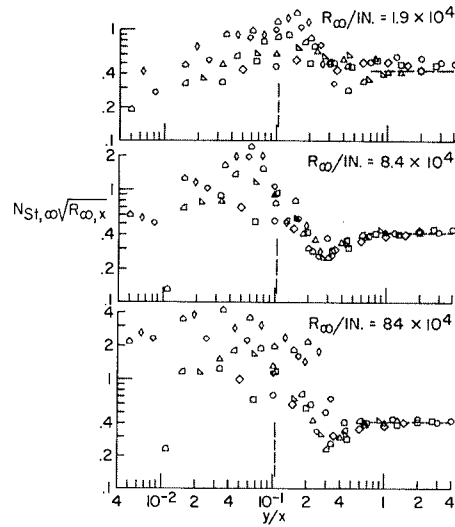


FIGURE 52-13.—(c) Model yawed 5°.

however, predicts only a uniform decrease from the flat-plate value to 0 in the corner. The general shape of the curve is similar to that obtained from local shear variations in a corner in incompressible turbulent flow. (See ref. 17.)

At the higher unit Reynolds number in figure 52-13(b), the description is much the same except that the stations farthest back on the model show evidence of transition. At the rear stations there is evidence that the turbulent flow is inhibited as the corner is approached, since the data from these stations close to the corner fair into similar data obtained at the more forward stations.

Because of the success in correlating the data with the surfaces aligned with the flow, the same approach was taken with the results obtained at 5° yaw. In the yaw case, it is the vertical surface that is at an angle of attack of 5° and the horizontal instrumented surface is at an angle of attack of 0° although the leading edge has been rotated 5°. These data are shown in figure 52-13(c). The laminar flat-plate correlating parameter (Stanton number times square root of Reynolds number) is shown as a function of angular spacing from the corner. The correlation is good where the corner does not influence the flow (that is, large  $y/x$ ) and laminar flat-plate theory closely predicts the level of heat transfer in this region. As the corner is approached, there is at first a general dip in the heat-transfer level. This dip occurs ahead of

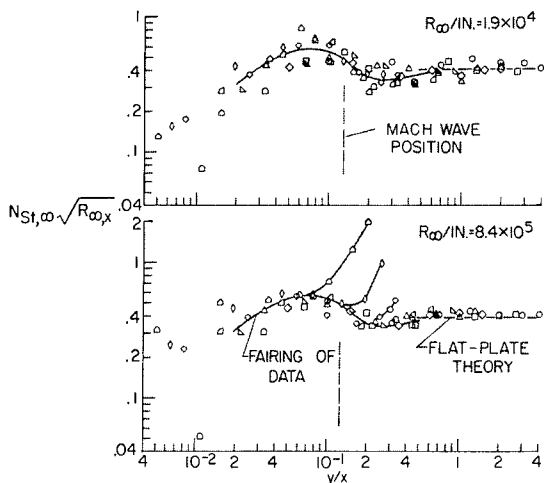


FIGURE 52-13.—(b) Model aligned with flow.

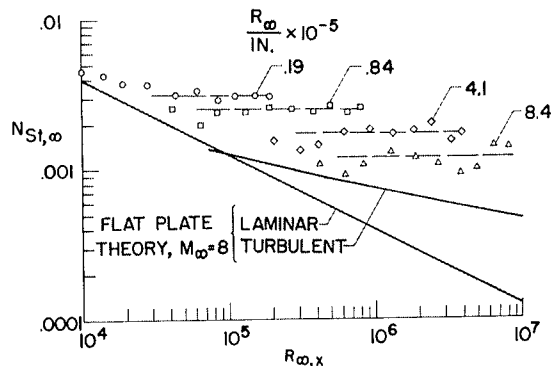


FIGURE 52-14.—Peak values of corner heating at a Mach number of 8 and with 5° yaw.

the free-stream location of the shock from the yawed plate shown by the vertical dashed line. Closer to the corner, there is a rapid increase in heat transfer to a peak generally much greater than in the undisturbed flow far from the corner.

The data in the high heating region close to the corner obviously do not correlate in the parametric form shown. The peak values of heating in the form of Stanton number alone were then taken and plotted against the Reynolds number based on distance from the leading edge at which this peak heating occurred. The data in this form are presented in figure 52-14. For reference purposes, laminar and turbulent flat-plate theory for a Mach number of 8 are included in this figure. The level of this flat-plate theory would be somewhat raised if the pressure increase behind a shock caused by a 5° deflection was taken into account.

At a given unit Reynolds number the peak heat-transfer coefficient is more or less independent of Reynolds number based on  $x$ -distance. The horizontal dashed lines are arbitrary fairings of these data at the various unit Reynolds numbers. The peak Stanton number, however, does decrease with an increase in unit Reynolds number. Thus some interesting results have been obtained but, as yet, the information is incomplete. For one thing, the peak heat-transfer coefficient is a function of a dimensional quantity. The pressure results corresponding to these heat-transfer data are not yet available and, when obtained, may aid in evaluating these results. The available infor-

mation would still be meager because practical leading edges would be blunted, probably swept, and may not meet at a 90° angle. Even less has been done on the external corner than on the interior corner. This is a problem that needs a great deal of future study.

### Shock Impingement

Not much work has been done on shock-impingement effects as a separate problem although some of the results of corner investigations are probably applicable. Ivan E. Beckwith at the Langley Research Center has obtained some heat-transfer and pressure results on a rod protruding from a 8° wedge as shown in figure 52-15. The circular rod was swept back 60° from a normal to the free-stream flow direction. The measurements, when comparison is made with previous work (ref. 22), showed the flow over the rod, including the stagnation point, to be turbulent. No effect of the shock impingement can be detected in either the stagnation-line pressure or heat-transfer measurements. An appreciable increase in pressure and heat transfer can be found in the vicinity of the juncture of the rod and wedge. At least part of this increase can be attributed to the oblique shock which occurs near the base, although some boundary-layer separation may complicate the picture.

It would appear that for these conditions, shock-impingement effects were not important;

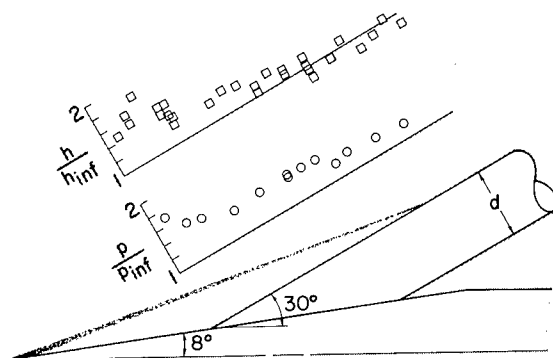


FIGURE 52-15.—Effect of shock impingement on swept-cylinder stagnation-line pressures and heat transfer at  $M_{\infty}=4.15$  and  $R_{\infty}d=1.7 \times 10^6$ .

however, much more work needs to be done before a definitive answer can be given. Experiments need to be made at higher Mach numbers, at various shock strengths and sweep, and for laminar and turbulent boundary layers.

### Heating on Surface Distortions

In previous considerations of aerodynamic heating, the experimental data were obtained on smooth models. In the case of actual vehicles, however, the skin may be significantly irregular. Such irregularities may be the result of structures choice and the high heating rates and temperatures to which the vehicle surface is subjected. A recent experimental program at the Langley Research Center represented distortions to the surface in an idealized way. One main group of these irregularities represented a distortion as a single sine wave on a basically flat plate. Part of this work is presented in reference 23 for the laminar case; however, some turbulent data have also been obtained. These aerodynamic heating data are shown in figure 52-16 for concave and convex sine wave shapes on a flat plate with a sharp leading edge at an angle of attack of  $20^\circ$ . The convex shape is the mirror image of the concave shape and the length of the wave was  $7\frac{1}{2}$  times the depth or height of the wave. The thickness of the boundary layer just ahead of the sine wave shape was small compared with the depth or height of the wave. The data are shown in terms of the aerodynamic heating parameter

(Stanton number) as a function of Reynolds number based on distance from the leading edge. For each wave the data on the left of the figure represent results at a unit Reynolds number about one fourth that of the data on the right. The open symbols represent data obtained on a flat plate at locations the same as those for the distortion. The flat-plate data at the lower unit Reynolds number are laminar whereas those at the higher unit Reynolds number range from transitional to turbulent in nature.

With laminar flow over the concavity the flow separates a short distance after it turns to enter the concavity. The local heating drops under the separation, reaches a minimum, increases again, and reaches a peak of about 4 times the flat-plate value at about the point where reattachment occurs. For the turbulent case, the flat-plate heating is increased and the peak heating on the concavity is about 3 times the flat-plate turbulent values.

The convex sine wave shows a considerably increased peak heating. In this case for the laminar-flow results, separation due to the bump extends well ahead of the distortion and, at about the point of reattachment on the sine wave, the heat transfer peaks to a value about 17 times that on the flat plate. For the turbulent case, the peak increase in heating is only about  $3\frac{1}{2}$  times the flat-plate value.

These results are only part of the story because representative data would also include the case where the surface irregularity height or depth is of the same order to much thinner than the turbulent boundary layer as well as covering a large range of Mach number. Much more needs to be learned about surface irregularity effects.

### Heat Transfer to Blunt Nose and Leading Edges

Up to this point no detailed consideration has been given to the blunt nose and leading edges. Actually, studies of these blunt shapes have been part of the literature for some time now and are already textbook material. Some of the sources of our knowledge of blunt-nose heat transfer will be pointed out.

Beckwith's theoretical work (ref. 24) together with experimental and further theoretic-

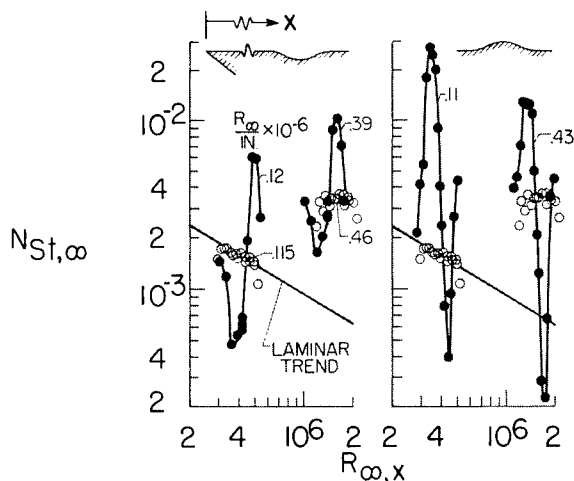


FIGURE 52-16.—Heating distribution on sine wave shapes. Sharp leading edge;  $M_\infty = 6.8$ ;  $\alpha = 20^\circ$ .

cal work by Feller, Eggers, and Goodwin and their colleagues (refs. 25 to 27) showed the advantage of sweep in reducing the heat-transfer rates to blunt leading edges. The effect of sweep on the leading-edge heat transfer was further refined by Reshotko and Beckwith. (See ref. 28.) Lees introduced the concept of the frozen distribution of heat transfer over blunt bodies and thus simplified the problem of extrapolating the results of experiment. (See ref. 29.)

The well-known work of Fay and Riddell assessed the effects of equilibrium dissociation and gave correlation equations for the numerical results. (See ref. 30.) In later work which included the effects of transpiration cooling on the heat transfer to a yawed cylinder, Beckwith postulated that the stagnation-point heat-transfer parameter might be more dependent on the viscosity law assumed than on whether dissociation occurs. (See ref. 31.) Based on complete solutions of the boundary-layer equations for a dissociated gas in equilibrium, Cohen and Beckwith found this to be the case. (See ref. 32.)

Transition to turbulent flow on yawed cylinders has been investigated by Beckwith and Gallagher at a Mach number of 4 (See refs. 22 and 33.) They found streamline curvature to cause premature transition in many cases. The theory in reference 33 provides a means of evaluating the turbulent heat transfer on a yawed cylinder. By use of Cohen's theory (ref. 34), the heat transfer on a variety of blunt shapes with turbulent flow may be evaluated.

### PROPULSION CONSIDERATIONS

As previously mentioned, air-breathing propulsion is being considered for high  $L/D$  hypersonic vehicles, primarily because of its inherent advantage of high thrust per unit fuel flow or specific impulse. This section of the paper will be devoted to a brief consideration of air-breathing engines from the aerodynamicist's point of view. Several types of engines would be required to utilize air-breathing propulsion over a wide range of flight speeds as illustrated in figure 52-17 by a bar-graph type of presentation. The total length of each bar denotes the probable applicable speed range for

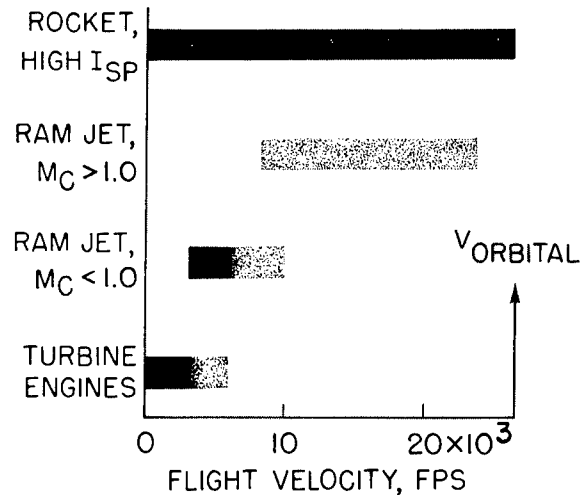


FIGURE 52-17.—Engine operating ranges.

each of the engines selected for illustration. The dark areas correspond to what may be attained with current technology, whereas the light areas would require extensions of the state of the art and extensive research in some cases. A turbojet engine could be used up to a velocity of 3,000 fps, at which point a ramjet with subsonic combustion velocities would take over and operate to some higher velocity (in the 6- to 10,000-fps range). At this point the ramjet employing supersonic combustion velocities would become effective and operate to the highest practical velocity. The high-impulse rocket is presented to indicate that it would be used to supplement air breathing in areas where air breathing proves to be marginal or not possible. In order to avoid duplication of hardware, the combination of two or more of these engines into a single unit appears to be practical. In some instances novel engine cycles are being investigated which may fulfill special mission requirements more efficiently. Extensive discussions of these considerations are given in the literature. (For example, see refs. 35 and 36.) Most of the lower speed engines which employ subsonic combustion are beyond the basic research stage; the remaining problems relate to the development of suitable hardware.

The concept of a ramjet engine which employs supersonic combustion velocities has excited a great deal of interest in the last few years since it offers the potential of operation



to high hypersonic speeds. (See refs. 35 and 37.) The practical realization of the concept requires the successful completion of much basic research, which is a matter of interest to universities as well as to the National Aeronautics and Space Administration. Consequently, the ramjet engine will be discussed briefly, particularly with regard to the aerodynamic aspects of the inlet.

Several features of the engine, which are directly related to supersonic combustion chamber velocities, are fundamental to its potential operation at high hypersonic speeds. The pressures and temperatures in the combustion chamber can be made low enough to bring the structural problem within reason. In addition, the combustion chamber pressures and temperatures can be maintained at levels where large amounts of dissociation of combustion products are avoided. In comparison with a subsonic combustion ramjet, the reduced amount of compression in the inlet and reduced expansion in the nozzle will result in higher performances for these components; however, these advantages will be offset somewhat by the higher entropy gains caused by combustion at supersonic velocities.

A diagrammatic cross section of the engine configuration is presented in figure 52-18 for the purpose of outlining the problem areas. If the aerodynamic design of the inlet is considered, boundary-layer growth is so rapid at high speeds that the throat of the inlet will be entirely filled with boundary layer. No research has been done on the effects of shocks on boundary layers under real-gas conditions. Leading edges will have to be blunted to avoid overheating, which will affect both the boundary-layer transition characteristics and the

compression field. (See refs. 38 to 42.) The inclusion of boundary-layer bleeds or variable geometry in the design will introduce serious heating problems.

With regard to the rest of the engine, a great deal of research must be done on the combustion chamber to determine methods of obtaining proper fuel mixing with a minimum entropy gain (ref. 43) and to evaluate the combustion process in general. One of the critical problems associated with the nozzle is the requirement that the flow of exhaust products have a high degree of recombination. As mentioned previously, this problem can be controlled to a certain extent by the amount of compression in the inlet design. An overall problem of great importance is the cooling requirements for the entire engine and vehicle. Hydrogen fuel is an excellent heat sink; however, the required cooling at the high-speed end of a flight may require fuel-air ratios greater than stoichiometric and thus impair the specific impulse.

For the purpose of this paper the aerodynamic design of the inlet for a supersonic combustion ramjet was studied by computing two-dimensional point designs for several flight speeds. Table 52-II provides the input assumptions for the computations. To simplify the problem the initial shock was assumed to turn the flow  $9^\circ$  and all succeeding shocks  $3^\circ$ . The schedule of inviscid velocity reduction in the inlets was selected from studies similar to that of reference 35. The inviscid compression fields were computed by assuming a real gas and using references 44 to 48. Real-gas boundary-layer calculations were made by modifying the equations of reference 49 for laminar flow and those of reference 50 for turbulent flow. Turbulent boundary layers were assumed to have a  $1/7$  power velocity profile. The boundary-layer parameters of reference 51 were modified to real-gas values. Inlet total-pressure recoveries and kinetic-energy efficiencies were based on a one-dimensional equivalent flow at the inlet throat obtained from conservation of mass, momentum, and energy considerations similar to those of reference 52. Real-gas properties were obtained from reference 53. Boundary-layer growth was computed along the main compression surface only. In order to deter-

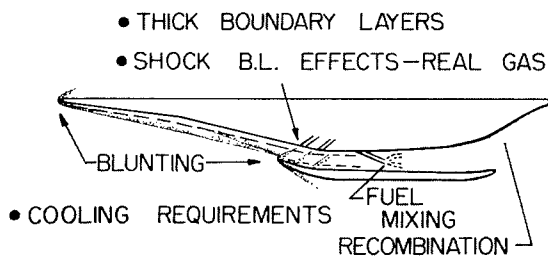


FIGURE 52-18.—Supersonic combustion ramjet problem areas.

# AERODYNAMICS

**TABLE 52-II.—Assumptions Used in Supersonic Combustion Ramjet Inlet Performance Calculations**

[Geometric capture height upstream of initial shock, 35 feet; turning angle of initial shock, 9°; turning through all other shocks, 3°; flow at inlet throat parallel to vehicle axis within 6° or less; and wall temperature, 2,000° F.]

Flight Mach number	Flight altitude, ft	Flight velocity, fps	Inviscid velocity reduction, fps	Total turning in compression field, deg
8	$97.0 \times 10^3$	$7.98 \times 10^3$	1495	48.5
12	136.0	12.85	1065	30.2
16	170.0	17.70	839	21.2
20.6	200.0	21.40	720	17.0

mine a representative overall value of kinetic-energy efficiency, the sum of the losses in kinetic-energy efficiency due to the boundary-layer growth on the internal surface of the cowl and due to side-wall and corner effects was assumed to be equal to the loss in kinetic-energy efficiency computed for the boundary-layer growth along the main compression surface. The computed values of kinetic-energy efficiency were corrected for the reduction in total enthalpy produced by heat transfer through the walls on the assumption that the fuel would be used as the coolant and that the heat would be returned to the combustion chamber.

The geometric proportions computed for the inlet designs for inviscid, laminar, and turbulent flow are presented in figure 52-19. As indicated by the sketch, the geometric walls were

determined by adding the boundary-layer displacement thicknesses to the inviscid-flow-field contours. For all laminar flow, figure 52-19 shows that the throat height is not significantly larger than the inviscid throat height because of the large capture height and Reynolds numbers assumed. For all turbulent flow, the throat height is considerably larger than the inviscid case on the high-speed end; in the actual case, the curve probably would fall between the laminar and turbulent results since there would have to be some length of run of laminar flow. These results clearly show the need for reliable methods for predicting the location of transition. Furthermore, the wide variation in required throat height obtained with changes in flight velocity indicates that variable geometry will be necessary unless the amount of compression is reduced at the lower speeds with some sacrifice in thrust.

Figure 52-19 also indicates that the required distance from the leading edge to the cowl lip  $l_c$  varies about 25 percent over the flight-velocity range. Although this variation would be modified by changes in the angle of attack with flight speed, fixed geometry probably will either introduce additive drag or subject the inlet to conditions where the shock enters the cowl and impinges on the boundary layer producing boundary-layer interaction effects. The most significant implication derived from the results given in figure 52-19 is that extensive trade-off analyses are required to determine the most practical designs incorporating either fixed geometry or a minimum of variable geometry.

The overall performance in terms of kinetic-energy efficiency computed by methods outlined

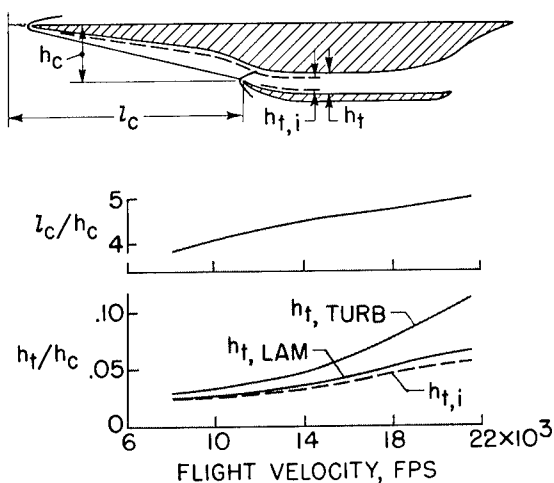


**FIGURE 52-19.—Effect of velocity on inlet geometry.**

## HYPERSONIC CRUISING AND BOOST VEHICLES

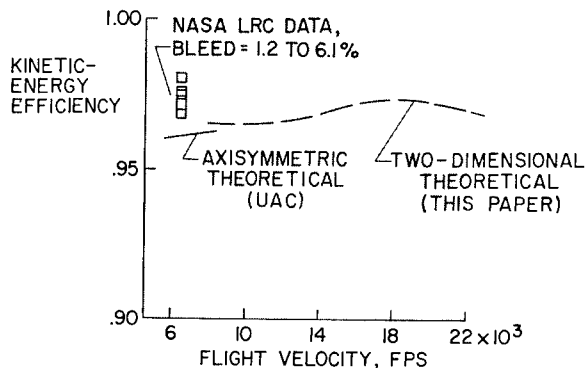


FIGURE 52-20.—Inlet efficiency.

previously is presented in figure 52-20. In order to attack significance to values of kinetic-energy efficiency, it should be realized that at speeds on the order of 20,000 fps, values of efficiency of approximately 90 percent are low enough to eliminate any thrust potential. Therefore, the efficiency must be substantially above the 90-percent level to obtain efficient operation. Figure 52-20 shows that the general level of efficiency obtained in the analysis of this paper is about 97 percent; the shape of the curve faired through the computed points has little significance because of the somewhat arbitrary assumptions of values for the flight trajectory and the amount of compression in the inlets. Theoretical performances for an axisymmetric inlet design computed by McLafferty and presented in reference 54 agree in general magnitude with the results of this paper. The experimental data points given in figure 52-20 represent wind-tunnel data for a two-dimensional inlet taken at a Mach number

of 6.8 for several different arrangements of boundary-layer bleed and for several bleed quantities. The favorable effect of the boundary-layer bleed on the performance is believed to be the reason for the experimental efficiencies being higher than the theoretical curves.

From the preceding discussion one can deduce that a 1-percent increase in kinetic-energy efficiency would produce significant increases in thrust, particularly at high hypersonic speeds. Therefore, effort should be directed toward increasing the level of kinetic-energy efficiency by developing more efficient compression-field designs and by reducing viscous effects to a minimum.

### CONCLUDING REMARKS

A great deal of information exists that is applicable to the high lift-drag ratio vehicle. However, much of this information is somewhat preliminary and is of the type that suggests further investigation rather than being directly usable. This discussion attempted to point out the many avenues of research which have to be more thoroughly explored before a better grasp of the total problem is in hand. Although this work will necessarily rely heavily on an experimental approach, because of the complexities involved, the theoretical aspects of the problem should also be pursued with equal vigor. Fortunately, much of this experimental work can be done at present in the conventional relatively cold facilities which have been available for some time; however, evaluation of the effects of a hypervelocity environment will eventually have to be made.

### REFERENCES

1. LEES, LESTER: Recovery Dynamics—Heat Transfer at Hypersonic Speeds in a Planetary Atmosphere. Space Technology, ch. 12, Howard Seifert, ed., John Wiley & Sons, Inc., 1959, pp. 12-01—12-20.
2. LEES, LESTER, and PROBSTEN, RONALD F.: Hypersonic Viscous Flow Over a Flat Plate. Rep. No. 195 (Contract AF 33(038)-250), Aero. Eng. Lab., Princeton Univ., Apr. 20, 1952.
3. BERTRAM, MITCHEL H.: Boundary-Layer Displacement Effects in Air at Mach Numbers of 6.8 and 9.6. NASA TR R-22, 1959. (Supersedes NACA TN 4133.)
4. TSIEN, HSUE-SHEN: Superaerodynamics, Mechanics of Rarefied Gases. Jour. Aero. Sci., vol. 13, no. 12, Dec. 1946, pp. 653-664.
5. PROBSTEN, RONALD F.: Shock Wave and Flow Field Development in Hypersonic Re-Entry. ARS Jour., vol. 31, no. 2, Feb. 1961, pp. 185-194.

# AERODYNAMICS

6. EGGERS, ALFRED J., JR., ALLEN, H. JULIAN, and NEICE, STANFORD E.: A Comparative Analysis of the Performance of Long-Range Hypervelocity Vehicles. NACA Rep. 1382, 1958. (Supersedes NACA TN 4046.)
7. FERRI, ANTONIO, CLARKE, JOSEPH H., and CASACCIO, ANTHONY: Drag Reduction in Lifting Systems by Advantageous Use of Interference. PIBAL Rep. 272 (Contract No. AF 18(600)-694), Polytechnic Institute of Brooklyn, May 1955.
8. EGGERS, A. J., JR., and SYVERTSON, CLARENCE A.: Aircraft Configurations Developing High Lift-Drag Ratios at High Supersonic Speeds. NACA RM A55L05, 1956.
9. ROSSOW, VERNON J.: A Theoretical Study of the Lifting Efficiency at Supersonic Speeds of Wings Utilizing Indirect Lift Induced by Vertical Surfaces. NACA RM A55L08, 1956.
10. EGGERS, A. J., JR.: Some Considerations of Aircraft Configurations Suitable for Long-Range Hypersonic Flight. Presented to Symposium on Hypersonic Flow (Univ. of Bristol, England), Apr. 6, 1959. (Sponsored by Colston Res. Soc.)
11. VAGLIO-LAURIN, ROBERTO: Laminar Heat Transfer on Blunt-Nosed Bodies in Three-Dimensional Hypersonic Flow. WADC Tech. Note 58-147, ASTIA Doc. No. AD 155 588, U.S. Air Force, May 1958.
12. MONAGHAN, R. J.: On the Behavior of Boundary Layers at Supersonic Speeds. Fifth International Aeronautical Conference (Los Angeles, Calif., June 20-23, 1955), Inst. Aero. Sci., Inc., 1955, pp. 277-315.
13. VAN DRIEST, E. R.: The Problem of Aerodynamic Heating. Aero. Eng. Rev., vol. 15, no. 10, Oct. 1956, pp. 26-41.
14. BERTRAM, MITCHEL H., and HENDERSON, ARTHUR, JR.: Recent Hypersonic Studies of Wings and Bodies. ARS Jour., vol. 31, no. 8, Aug. 1961, pp. 1129-1139.
15. BERTRAM, MITCHEL H., and HENDERSON, ARTHUR, JR.: Effects of Boundary-Layer Displacement and Leading-Edge Bluntness on Pressure Distribution, Skin-Friction, and Heat Transfer of Bodies at Hypersonic Speeds. NACA TN 4301, 1958.
16. BERTRAM, MITCHEL H., and FELLER, WILLIAM V.: A Simple Method for Determining Heat Transfer, Skin Friction, and Boundary-Layer Thickness for Hypersonic Laminar Boundary-Layer Flows in a Pressure Gradient. NASA MEMO 5-24-59L, 1959.
17. GERSTEN, K.: Corner Interference Effects. Rep. 299, AGARD, North Atlantic Treaty Organization (Paris), Mar. 1959.
18. STAINBACK, P. CALVIN: An Experimental Investigation at a Mach Number of 4.95 of Flow in the Vicinity of a 90° Interior Corner Alined With the Free-Stream Velocity. NASA TN D-184, 1960.
19. BOGDONOFF, S. M., and VAS, T. E.: A Preliminary Investigation of the Flow in a 90° Corner at Hypersonic Speeds. Part I—Flat Plates With Thin Leading Edges at Zero Angle of Attack. D143-978-013 (ARDC TR 57-202, AD 150 023), Bell Aircraft Corp., Dec. 1957.
20. MILLER, D. S., HIJMAN, R., REDEKER, E., JANSSEN, W. C., and MULLEN, C. R.: A Study of Shock Impingements on Boundary Layers at Mach 16. Proc. 1962 Heat Transfer and Fluid Mechanics Inst. (Univ. Wash.), F. Edward Ehlers, James J. Kauzlarich, Charles A. Sleicher, Jr., and Robert E. Street, eds., Stanford Univ. Press, June 1962, pp. 255-278.
21. BLOOM, MARTIN H., and RUBIN, STANLEY: High-Speed Viscous Corner Flow. Jour. Aerospace Sci., vol. 28, no. 2, Feb. 1961, pp. 145-157.
22. BECKWITH, IVAN E., and GALLAGHER, JAMES J.: Local Heat Transfer and Recovery Temperatures on a Yawed Cylinder at a Mach Number of 4.15 and High Reynolds Numbers. NASA TR R-104, 1961. (Supersedes NASA MEMO 2-27-59L.)
23. BERTRAM, M. H., and WIGGS, M. MARGARETTE: Effect of Surface Distortions on the Heat Transfer to a Wing at Hypersonic Speeds. Paper No. 62-127, Inst. Aerospace Sci., June 1962.
24. BECKWITH, IVAN E.: Theoretical Investigation of Laminar Heat Transfer on Yawed Infinite Cylinders in Supersonic Flow and a Comparison With Experimental Data. NACA RM L55F09, 1955.
25. FELLER, WILLIAM V.: Investigation of Equilibrium Temperatures and Average Laminar Heat-Transfer Coefficients for the Front Half of Swept Circular Cylinders at a Mach Number of 6.9. NACA RM L55F08a, 1955.

# HYPERSONIC CRUISING AND BOOST VEHICLES

26. EGGERS, A. J., JR., HANSEN, C. FREDERICK, and CUNNINGHAM, BERNARD E.: Theoretical and Experimental Investigation of the Effect of Yaw on Heat Transfer to Circular Cylinders in Hypersonic Flow. NACA RM A55E02, 1955.
27. GOODWIN, GLEN, CREAGER, MARCUS O., and WINKLER, ERNEST L.: Investigation of Local Heat-Transfer and Pressure Drag Characteristics of a Yawed Circular Cylinder at Supersonic Speeds. NACA RM A55H31, 1956.
28. RESHOTKO, ELI, and BECKWITH, IVAN E.: Compressible Laminar Boundary Layer Over a Yawed Infinite Cylinder With Heat Transfer and Arbitrary Prandtl Number. NACA Rep. 1379, 1958. (Supersedes NACA TN 3986.)
29. LEES, LESTER: Laminar Heat Transfer Over Blunt-Nosed Bodies at Hypersonic Flight Speeds. Jet Propulsion, vol. 26, no. 4, Apr. 1956, pp. 259-269, 274.
30. FAY, J. A., and RIDDELL, F. R.: Theory of Stagnation Point Heat Transfer in Dissociated Air. Jour. Aero. Sci., vol. 25, no. 2, Feb. 1958, pp. 73-85, 121.
31. BECKWITH, IVAN E.: Similar Solutions for the Compressible Boundary Layer on a Yawed Cylinder With Transpiration Cooling. NASA TR R-42, 1959. (Supersedes NACA TN 4345.)
32. COHEN, NATHANIEL B., and BECKWITH, IVAN E.: Boundary-Layer Similar Solutions for Equilibrium Dissociated Air and Application to the Calculation of Laminar Heat-Transfer Distribution on Blunt Bodies in High-Speed Flow. Presented at the Second International Heat Transfer Conference (Boulder, Colo.), Aug. 28-Sept. 1, 1961.
33. BECKWITH, IVAN E., and GALLAGHER, JAMES J.: Experimental Investigation of the Effect of Boundary-Layer Transition on the Average Heat Transfer to a Yawed Cylinder in Supersonic Flow. NACA RM L56E09, 1956.
34. COHEN, NATHANIEL B.: A Method for Computing Turbulent Heat Transfer in the Presence of a Streamwise Pressure Gradient for Bodies in High-Speed Flow. NASA MEMO 1-2-59L, 1959.
35. FERRI, ANTONIO: Possible Directions of Future Research in Air-Breathing Engines. Combustion and Propulsion Fourth AGARD Colloquium on High Mach Number Air-Breathing Engines, A. L. Jaumotte, A. H. Lefebvre, and A. M. Rothrock, eds., Pergamon Press (New York), 1961, pp. 3-15.
36. ZIPKIN, M. A., and NUCCI, L. M.: Composite Air-Breathing Systems. Combustion and Propulsion Fourth AGARD Colloquium on High Mach Number Air-Breathing Engines, A. L. Jaumotte, A. H. Lefebvre, and A. M. Rothrock, eds., Pergamon Press (New York), 1961, pp. 16-36.
37. DUGGER, GORDON L.: Comparison of Hypersonic Ramjet Engines With Subsonic and Supersonic Combustion. Combustion and Propulsion Fourth AGARD Colloquium on High Mach Number Air-Breathing Engines, A. L. Jaumotte, A. H. Lefebvre, and A. M. Rothrock, eds., Pergamon Press (New York), 1961, pp. 84-119.
38. MOECKEL, W. E.: Some Effects of Bluntness on Boundary-Layer Transition and Heat Transfer at Supersonic Speeds. NACA Rep. 1312, 1957. (Supersedes NACA TN 3653.)
39. BRINICH, PAUL F., and SANDS, NORMAN: Effect of Bluntness on Transition for a Cone and a Hollow Cylinder at Mach 3.1. NACA TN 3979, 1957.
40. BERTRAM, MITCHEL H.: Exploratory Investigation of Boundary-Layer Transition on a Hollow Cylinder at a Mach Number of 6.9. NACA Rep. 1313, 1957. (Supersedes NACA TN 3546.)
41. SEIFF, ALVIN, and WHITING, ELLIS E.: Calculation of Flow Fields From Bow-Wave Profiles for the Downstream Region of Blunt-Nosed Circular Cylinders in Axial Hypersonic Flight. NASA TN D-1147, 1961.
42. SEIFF, ALVIN, and WHITING, ELLIS E.: A Correlation Study of the Bow-Wave Profiles of Blunt Bodies. NASA TN D-1148, 1962.
43. PETERS, C. E., and WEHOFFER, S.: Constant Area Mixing of Non-Isoenergetic Coaxial Compressible Streams. AEDC-TR-61-18 (Contract No. AF 40(600)-800 S/A 24(61-73)), Arnold Eng. Dev. Center, Jan. 1962.
44. MINZNER, R. A., CHAMPION, K. S. W., and POND, H. L.: The ARDC Model Atmosphere, 1959. Air Force Surveys in Geophysics No. 115 (AFCRC-TR-59-267), Air Force Cambridge Res. Center, Aug. 1959.
45. AMES RESEARCH STAFF: Equations, Tables, and Charts for Compressible Flow. NACA Rep. 1135, 1953. (Supersedes NACA TN 1428.)

# AERODYNAMICS

46. HILSENATH, JOSEPH, BECKETT, CHARLES W., ET AL.: Tables of Thermal Properties of Gases. NBS Cir. 564, U.S. Dept. Commerce, 1955.
47. ANON.: Handbook of Supersonic Aerodynamics. NAVORD Rep. 1488 (vol. 5), Bur. Ord., Aug. 1953.
48. HUBER, PAUL R.: Tables and Graphs of Normal-Shock Wave Parameters at Hypersonic Mach Numbers and Selected Altitudes. NACA TN 4352, 1958.
49. MONAGHAN, R. J.: An Approximate Solution of the Compressible Laminar Boundary Layer on a Flat Plate. R. & M. No. 2760, British A.R.C., 1956.
50. ECKERT, E. R. G.: Engineering Relations for Heat Transfer and Friction in High-Velocity Laminar and Turbulent Boundary-Layer Flow Over Surfaces With Constant Pressure and Temperature. Trans. A.S.M.E., vol. 78, no. 6, Aug. 1956, pp. 1273-1283.
51. PERSH, JEROME, and LEE, ROLAND: Tabulation of Compressible Turbulent Boundary Layer Parameters. NAVORD Rep. 4282 (Aeroballistic Res. Rep. 337), U.S. Naval Ord. Lab. (White Oak, Md.), May 1, 1956.
52. WYATT, DE MARQUIS D.: Analysis of Errors Introduced by Several Methods of Weighting Nonuniform Duct Flows. NACA TN 3400, 1955.
53. MOECKEL, W. E., and WESTON, KENNETH C.: Composition and Thermodynamic Properties of Air in Chemical Equilibrium. NACA TN 4265, 1958.
54. McLAFFERTY, GEORGE H.: Hypersonic Inlet Studies at UAC Research Laboratories. Rep. M-2000-113, United Aircraft Corp., Dec. 1959. (Also available as Combustion and Propulsion Fourth AGARD Colloquium on High Mach Number Air-Breathing Engines, A. L. JAUMOTTE, A. H. LEFEBVRE, and A. M. ROTHROCK, eds., Pergamon Press (New York), 1961, pp. 138-155.)

## 53. Aerodynamic and Heating Problems of Advanced Reentry Vehicles

By Robert L. Trimpi, Frederick C. Grant, and Nathaniel B. Cohen

ROBERT L. TRIMPI is Head of Reentry Physics Branch, Aero-Physics Division, NASA Langley Research Center. He received his Bachelor of Science degree in Mechanical Engineering in 1948 from Cornell University and his Master of Science degree in Aeronautical Engineering the following year. Mr. Trimpi, who joined the Langley staff in August 1949, has earned a national reputation as an authority on reentry heating, unsteady flow, real-gas flow, and heat conduction problems. He serves as a consultant on advanced technical problems in areas of reentry heating and unsteady flow, and he has produced many important contributions in basic flow phenomena. His theoretical investigations cover a variety of fields, and his publications include the subjects of supersonic inlet instability, hypersonic heat transfer, shock-tube attenuation, unsteady boundary layers, three-dimensional real-gas shock waves and flow fields, and transient aerodynamic heating of multilayer skins.

FREDERICK C. GRANT, Aero-Space Engineer, Reentry Physics Branch, Aero-Physics Division, NASA Langley Research Center, received his Bachelor of Science degree in aeronautical engineering from Massachusetts Institute of Technology in September 1947. He earned a Master of Arts degree in Physics from the College of William and Mary in August 1962. Grant joined the Langley staff in December 1947 as an aeronautical engineer and has been active in the fields of experimental and theoretical aerodynamics and flight mechanics. He is author or co-author of 16 technical publications on research he has conducted at Langley.

NATHANIEL B. COHEN, Assistant Head, Reentry Physics Branch, Aero-Physics Division, NASA Langley Research Center, received his Bachelor of Science degree in aeronautical engineering from the Polytechnic Institute of Brooklyn, Brooklyn, New York, in June 1950. He earned his Master of Science degree in aeronautical engineering from the University of Virginia in June 1956. Since joining Langley, he has been active in the fields of shock-tube research and boundary-layer and convective-heat-transfer theory. He developed a theory of laminar heat transfer in equilibrium air at flight velocities up to 41,000 feet per second. Working with Robert L. Trimpi, he developed a theory and carried out supporting experiments for shock-wave attenuation in a shock tube. Mr. Cohen is a member of the Institute of the Aerospace Sciences, and the American Rocket Society, and belongs to Tau Beta Pi and Sigma Xi honorary fraternities. He is author or co-author of 10 NASA technical publications on research he has conducted at Langley.

## AERODYNAMICS

### SUMMARY

Reentry of manned lifting vehicles at parabolic (escape) velocity and reentry of unmanned nonlifting planetary probes at hyperbolic velocities are considered. A brief discussion is presented of the necessity of lift and lift modulation for the manned return; and the heating problems of aerodynamic and reaction controls are illustrated. Spatial and temporal convective and radiation heating distributions are predicted for a lifting spacecraft of the Apollo class.

Radiation heating will be the dominant mode for early planetary probes which, because of weight limitations, will be unmanned and will enter the atmosphere on nonlifting trajectories. The effect of vehicle shape on heating is first discussed for no-mass-loss (constant profile) vehicles. A section on reentry of high-mass-loss vehicles includes a preliminary study of the effects of (a) heat of sublimation on limiting entry velocity; (b) ratio of payload to total weight on limiting entry velocity; and (c) the size and total weight of a reentry vehicle necessary to return a specific payload to earth at a given high reentry velocity.

### INTRODUCTION

Familiarity with near circular or satellite reentry is widespread as a result of the recent flights of the Mercury spacecraft. In this paper some of the aerodynamic and heating aspects of reentry from more advanced missions are discussed. The first part is concerned with parabolic reentry with emphasis on the manned lunar mission, and the second part with the unmanned reentry of high-speed planetary probes.

### SYMBOLS

$A$	reference area
$C_D$	drag coefficient
$C_H$	total energy transfer coefficient, $H/\frac{1}{2} m_E V_E^2$
$C_L$	lift coefficient
$D$	drag
$d$	vehicle diameter
$G$	acceleration in earth gravitational units
$H$	total heat absorbed by vehicle during reentry
$L$	lift
$l$	vehicle reference length
$m_E$	mass of vehicle at start of reentry
$m_f$	mass of vehicle at end of reentry
$Q$	heat of sublimation, Btu/lb
$q$	heating load per unit area, $\int \dot{q} dt$
$\dot{q}$	heating rate per unit area
$\dot{q}_{stag}$	stagnation-point heating rate per unit area
$R$	radius of curvature of front surface of vehicle
$r_b$	radius of body
$s$	distance along surface from axis
$t$	time
$V$	velocity

$V_E$	entrance velocity
$(V_E)_l$	limiting entrance velocity
$W$	vehicle weight, lb
$w$	vehicle density, lb/cu ft
$y$	altitude
$\alpha$	angle of attack
$\gamma_E$	entrance angle
$\rho$	density
$\delta$	flap-deflection angle
$\eta$	heat-transfer coefficient, $\dot{q}/\frac{1}{2} \rho_\infty V_\infty^3$
$\theta_c$	semicone angle
$\phi$	roll angle

#### Subscripts:

$\infty$	ambient conditions ahead of vehicle
MAX	maximum
$l$	limiting value
$C$	convective
$ER$	equilibrium radiative
$NER$	nonequilibrium radiative

### REENTRY AT PARABOLIC VELOCITY

For the lunar mission the reentry velocity is parabolic and is about 36,500 feet per second at an altitude of 400,000 feet, which may be considered the outer edge of the atmosphere for aerodynamic effects. In this case, in contrast to that of the nonlifting Mercury spacecraft, a lifting capability is highly desirable. The use of lift can reduce the severity of certain reentry problems. In figure 53-1 is shown the effect of  $L/D$  on the reentry corridor height (ref. 1). This height, illustrated in the inset, is the difference between the vacuum perigees of the overshoot and undershoot boundaries. The

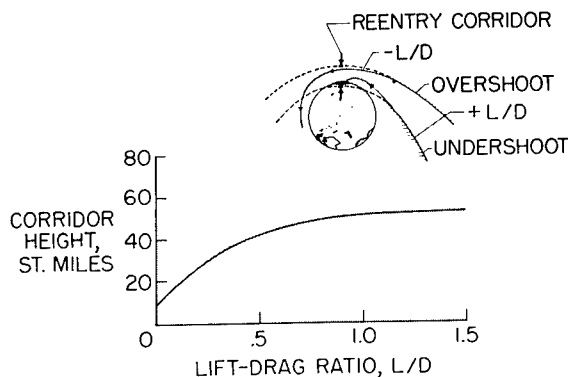


FIGURE 53-1.—Variation of reentry corridor height with lift-drag ratio.

$$V_E = 36,500 \text{ feet per second; } \frac{W}{C_D A} = 50 \text{ lb/sq ft.}$$



overshoot boundary in this case assumes a constant negative  $L/D$  during pull-up, with subsequent later modulation as required under the restriction that the trajectory never has an ascending phase; that is,  $dy/dt \leq 0$  (ref. 2). The undershoot boundary assumes constant positive  $L/D$  during pull-up with a maximum deceleration of  $10G$ . Note the appreciable gains in reentry corridor as  $L/D$  first increases from 0 up to approximately  $1/2$  with diminishing gains thereafter. At  $L/D=0$ , the corridor is about 10 miles deep; at  $L/D=1/2$ , it has become about 40 miles deep, and at  $L/D=1.5$ , it has only increased to 50 miles.

The accessible landing area, or "footprint" as it is popularly called (ref. 3), increases significantly with  $L/D$  (fig. 53-2). The longitudinal range is approximately proportional to  $L/D$  and the lateral range varies roughly as  $L/D$  raised to a power between  $1\frac{1}{2}$  and 2. Note that the landing area for  $L/D=1/2$  covers a major section of the continental United States.

The maximum deceleration during reentry from a given space orbit may also be significantly reduced by the application of lift. With a fixed lifting capability the air loads are reduced by using the lift force to decrease the flight-path angle continually to the horizontal and thus to lower the rate of density increase with time. If the lifting capability is variable, further peak-load reduction is possible by use of a change in attitude to reduce the resultant force. Details on this subject are given in references 4, 5, and 6.

The low lift-drag ratios that are sufficient for parabolic reentry may be obtained through

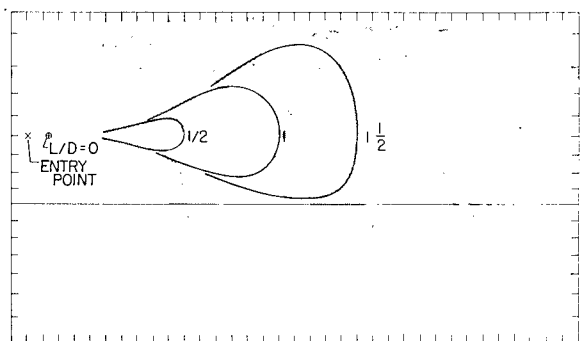


FIGURE 53-2.—Variation of accessible landing area with lift-drag ratio for parabolic reentry.

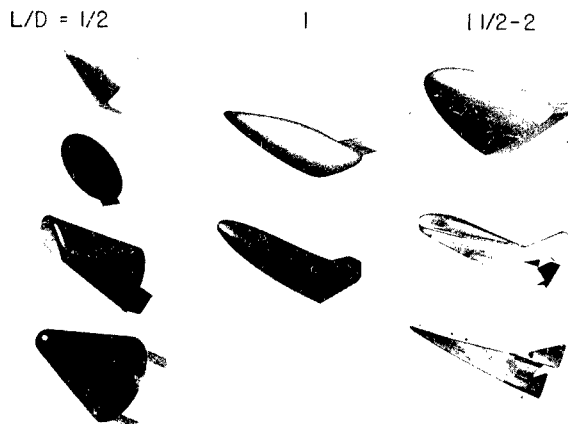


FIGURE 53-3.—Hypersonic lift-drag capability of reentry shapes.

a variety of shapes (fig. 53-3). In the three columns are illustrative shapes having  $L/D$ 's at high velocity of  $1/2$ , 1, and  $1\frac{1}{2}$  to 2. The first column consists of blunt spacecraft types trimmed by internal packaging to place the center of gravity so that  $L/D=1/2$  for the pull-up phase of reentry. The aerodynamic controls would be used for modulation after the pull-up. For these shapes the subsonic  $L/D$  is so low that auxiliary landing aids (parachutes or paragliders) are required.

Increased  $L/D$  capability is obtained, in general, by making the configuration more wing-like. The configurations with a hypersonic  $L/D \approx 1$  have a subsonic  $L/D$  in the neighborhood of 4 and so are able to land horizontally without any auxiliary aids. The shapes for  $L/D=1\frac{1}{2}$  to 2 appear more like conventional airplanes, and include the Dyna-Soar configuration for missions at satellite speed.

The  $L/D$  capability is very expensive in terms of vehicle weight. Configurations with higher values of  $L/D$  are not illustrated in figure 53-3, because analyses have shown that at an  $L/D$  somewhere between  $1\frac{1}{2}$  and 2, the weight of the ablation material required for heat protection from a parabolic reentry appears to be prohibitive. However, vehicles in this  $L/D$  range may be used for orbital missions by employing radiation-cooled surfaces.

The trade-off between  $L/D$  and weight is naturally dictated by the mission requirements. Studies are now in progress for various super-

circular missions utilizing  $L/D \approx 1$  vehicles. This is the maximum  $L/D$  which appears feasible for parabolic reentry using present ablation techniques.

For the Apollo manned lunar mission which is planned for more or less ideal conditions, an  $L/D \approx 1/2$  appears sufficient in terms of corridor height, landing area, and G alleviation. Studies of such parabolic reentry vehicles have shown that although the critical heating problems are found at different parts of the vehicle for different shapes, the magnitude of the total heat load during reentry varied only moderately with vehicle shape, with the blunt spacecraft having a lower total heat load for most trajectories than the other  $L/D \approx 1/2$  shapes illustrated. However, this factor was not the deciding factor in the choice of the Apollo reentry module; several other factors, such as the structural advantages of a symmetric body, ease of integration of the reentry module with the service module and launch vehicle, the packaging of components so that the center of gravity would permit the desired trim, the more direct applicability of experience gained from the Mercury, Gemini, and similar projects, determined the selection of a blunt reentry module for the Apollo mission.

Although the pull-up phase of the Apollo reentry is now visualized as a constant  $L/D$  maneuver, modulation is to be exercised immediately after the pull-up. Figure 53-4 shows two methods of modulation for obtaining the required orientation of the lift vector, namely, pitch modulation with varying  $C_L$

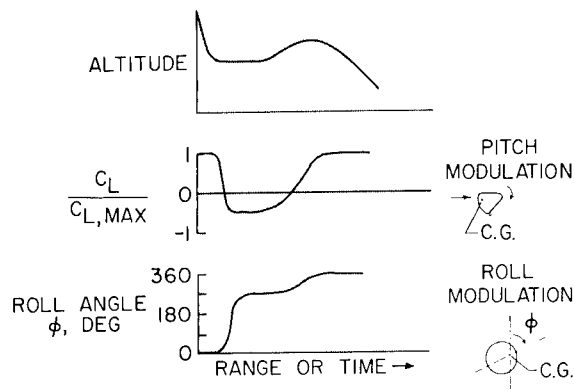


FIGURE 53-4.—Simplified examples of pitch and roll modulation.

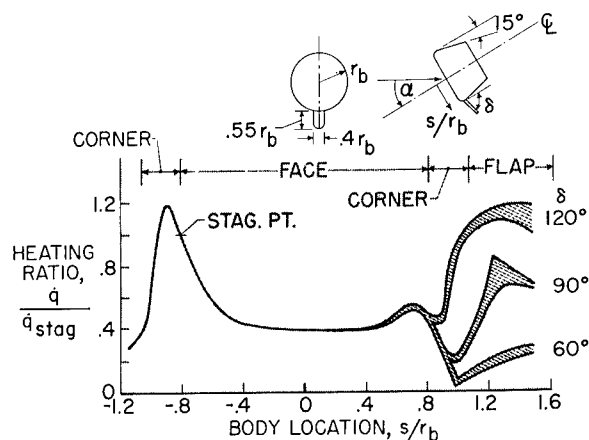


FIGURE 53-5.—Chin-flap heating on flat-faced model.  $M=8$ ;  $\alpha=30^\circ$ .

and  $C_D$  or roll modulation at constant  $L/D$ . At the top of the figure is a plot of altitude as a function of time (or range) for a typical reentry from the middle of the corridor and having a landing point near the center of the footprint. Immediately after completion of the pull-up maneuver in this typical reentry, negative lift is required and is obtained by either pitching to negative angle of attack or rolling at least  $90^\circ$ , respectively, in the two cases. More gradual changes are subsequently required until the reentry finally terminates in a positive-lift equilibrium glide. Not illustrated are the various maneuvers required for additional lateral or longitudinal ranges such as those discussed in references 3 and 7. Note that a rapid variation in lift and vehicle orientation is required at the time of peak dynamic pressure at the bottom of the pull-up.

Control heating problems are evident in both of these modulation techniques. The heating problems of a "chin" flap on a flat-faced body of revolution with rounded corners are depicted on figure 53-5. These data were obtained in the Langley Mach 8 hypersonic tunnel at a free-stream Reynolds number, based on model diameter, of  $0.22 \times 10^6$ . This Reynolds number is representative of parabolic reentry for full-scale vehicles at altitudes near 230,000 feet. The ratio of local heating along the plane of symmetry to the stagnation-point heating is plotted as a function of body location. The shaded bands for the flap heating represent the spanwise data variation at a particular position

$s/r_b$  on the flap. The flap heating has a peak approximately 20 percent of the stagnation-point value for  $\delta=60^\circ$ . At  $\delta=120^\circ$ , the local heating exceeds the stagnation-point value, and in addition the heating on the body itself ahead of the flap has been increased from under 10 percent of the stagnation value to 100 percent. This last increase is due to the interaction of the shock wave generated by the flap with the flow over the face of the model. Additional information on flap heating may be found in reference 8. Flap heating problems (such as those illustrated) plus the large hinge moments required for rapid attitude change under high dynamic-pressure conditions have led to the conclusion that modulation by roll control using reaction jets is more desirable.

However, reaction jets are not without interference heating problems. Figure 53-6 is a sketch illustrating the results of a temperature-sensitive-paint test for such interference heating. In this technique a model is coated with a paint which changes color with temperature. The model is then suddenly inserted into the test airstream and the color changes are recorded photographically. The heating patterns shown were obtained in the Langley Mach 8 variable-density tunnel with a cold jet located  $90^\circ$  from the plane of symmetry and exhausting upward nearly tangential to the surface (roll jet) or perpendicular to the surface (yaw jet). Note the localized high heating rates (indicated on the sketch by the shaded areas) due to the interaction between the cold reaction jets and the afterbody flow.

At present there is no theory to describe this interaction heating phenomena adequately. However, the rolling moments required are simply inertial and thus are not sensitive to the high dynamic pressures. Furthermore, the other jets, such as pitch and yaw jets, are used only for minor variations in attitude or to counteract the cross coupling of the roll jets and are located away from the windward side. Consequently, these jets will be operative only a small fraction of the time and the heating problem can be handled by adding a little extra heat protection in these critical areas. An experimental investigation is in progress at the

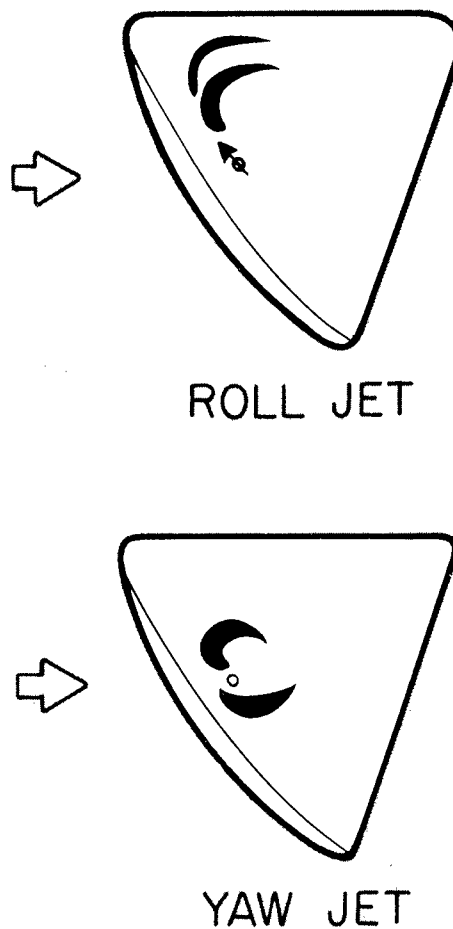


FIGURE 53-6.—Effect of reaction controls on afterbody heating of lunar module.

Langley Research Center to study this problem further.

Another problem associated with reaction jets is the heating to the jet nozzle cavities during the long times when the jets are not operative. This problem is similar to the heating of cavities discussed in references 9 and 10.

The theoretically predicted heating history of the stagnation point of a 12-foot-diameter lunar reentry module during a 3,500-nautical-mile reentry is shown in figure 53-7. For this prediction, the location of the stagnation point and the stagnation-point velocity gradient were obtained from pressure measurements in the

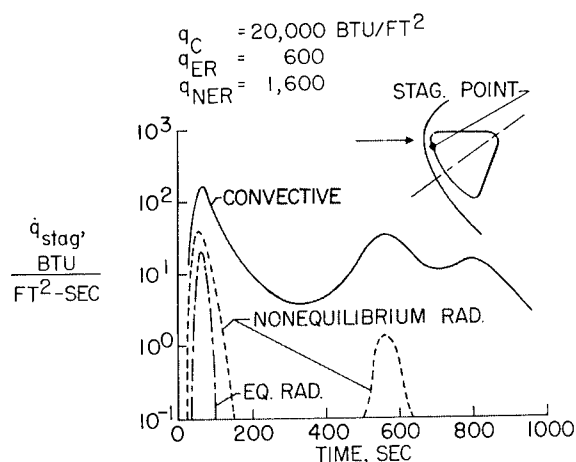


FIGURE 53-7.—Stagnation point heating history for 12-foot-diameter lunar reentry module.

Langley Mach 8 variable-density tunnel. These experiments were necessary because of the lack of a simple adequate theory suitable for configurations in which the stagnation point is located near the rounded corner of an otherwise blunt body at angle of attack. The convective heating  $\dot{q}_c$  was computed by the two-dimensional method of reference 11 for real air in thermochemical equilibrium. Nonequilibrium radiation was computed by use of the data of references 12, 13, and 14 and includes a simple model for the profile of radiation intensity behind the shock wave. The nonequilibrium radiation arises from the very high temperatures (as high as about  $60,000^\circ \text{K}$ ) which occur just behind the shock wave when all the thermal energy is essentially in the translational and rotational modes excited by a very few molecular collisions. The thermal and chemical relaxation which follows as more collisions take place reduces the temperature toward the equilibrium value, which is of the order of  $12,000^\circ \text{K}$  at parabolic entry speed. The nonequilibrium radiation is truncated when the relaxation process has not had sufficient time for completion before the gas has left the stagnation region and started to flow around the body. The nonequilibrium phenomena are discussed more fully in reference 15, as well as in the aforementioned references. Equilibrium radiation  $\dot{q}_{ER}$  was computed from the correlation of reference 16 (based on the absorption coefficients of ref. 17) and a shock shape which was determined by

correcting the shape obtained in the  $M=8$  tunnel tests at low density ratios to account for the high density ratios of actual flight. Note that the detachment distance shown in figure 53-7 is exaggerated. More elaborate methods, such as that of reference 18, are available, but these are not uniformly valid for arbitrary shapes and rely on a prior knowledge of certain parameters, such as sonic-point location on the body.

For this trajectory, the stagnation-point convective heating rate and load dominate over the radiative heating rate and load; this result is generally true for lunar reentry. The total radiative load to the stagnation point  $q_{ER} + q_{NER}$  indicated on figure 53-7 is only 10 percent of the total convective load  $q_c$  for the case illustrated. The equilibrium radiation is very low because the vehicle remains at high altitude (above 200,000 ft) for much of this long-range trajectory. For trajectories of shorter range, the peak equilibrium radiation would be somewhat increased while the peak nonequilibrium value would remain essentially unchanged. The dominant convective peak is about one order of magnitude higher than that experienced at the stagnation point of the Mercury spacecraft. The three peaks in convective heating result from a moderate skip after the first pull-up and two subsequent pull-up maneuvers for this trajectory.

The theoretical distribution of heating rate on the lunar reentry module in the plane of symmetry is presented in figure 53-8 for the time of peak stagnation point heating during

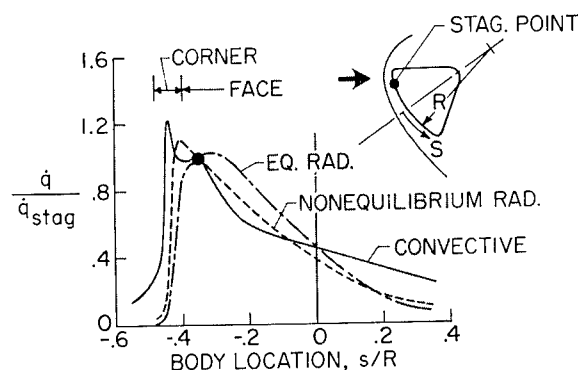


FIGURE 53-8.—Center-line heating rate distribution for lunar reentry module.

the reentry shown in figure 53-7. The convective distribution was predicted from a local similarity theory of reference 19 for laminar two-dimensional flow with the real-air boundary-layer results of reference 11. Other theories (refs. 20 and 21) would predict distributions not differing significantly from that shown. Streamline divergence effects (refs. 22 and 23) are not included but should be negligible. Again the Mach 8 variable-density tunnel (ideal gas) pressure distribution was employed. The implication that such a pressure distribution can be used for the prediction of high-velocity heat-transfer distributions is based on the insensitivity of pressure distribution to gas properties and Mach number for blunt forebodies at high Mach number. The heat-transfer theory, itself, is valid for real air in equilibrium. Well-defined experiments are still not available for real air at high enthalpies to validate these methods on asymmetric shapes.

The peak convective heating rate occurs on the rounded corner because of the high local pressure gradient combined with the occurrence here of sonic flow. The convective heating rate decreases rapidly beyond this peak as the flow progresses around to the windward afterbody (on which the heating rates are roughly only 10 percent of the stagnation value). A more gradual decrease is apparent down along the module face, and of course the leeward portions of the afterbody will experience even lower heating rates than will the windward portions. The predictions of afterbody heating are not on too firm ground, especially away from the windward ray, because of the effects of separation and reattachment. Cold-tunnel data obtained in the absence of real-gas effects but with sting or strut support interference is of questionable value in this case. In addition, transition to turbulent flow may be a factor during pull-up for steeper entry angles and this phenomenon is still not well understood.

The peaks in radiative heating are also located at points other than the stagnation point; the nonequilibrium peak is nearer the corner and the equilibrium peak is a short distance down the face. At each point the nonequilibrium radiation was assumed equal to that

emanating from behind a plane two-dimensional shock wave having an incident velocity equal to the local normal component of the free-stream velocity. This approximation appears reasonable when the relaxation length is small compared with the detachment distance, as is the case at peak heating in this trajectory. The nonequilibrium peak on the body thus is located where the bow shock is normal to the free stream—in this case near the corner. The equilibrium radiation distribution was estimated by assuming that each point on the body center line is irradiated by a semi-infinite slab of gas having an emission coefficient equal to the average of the value just behind the local oblique shock and the value at the surface. The slab thickness is given by the local detachment distance and was determined from the Mach 8 variable-density tunnel shock shape scaled to high-speed flight as discussed previously. Thus the peak in this curve on the face below the stagnation point results from the condition that the larger detachment distance more than compensates for the decreased emission coefficients. More elaborate methods for calculations of this type can be made if a knowledge of the flow-field properties and emission-coefficient variation across the shock layer is available. (See refs. 24 and 25.)

In order to design the reentry-module heat protection system, it is necessary that the distribution of heating rate be known away from as well as on the plane of symmetry. Various approximate methods are available. For example, if the surface streamlines and pressure distributions are known, the three-dimensional methods of references 22 and 23 are applicable as long as crossflow is small. Alternately, on the plane through the module center line normal to the plane of symmetry, it has been found that the heat-transfer distribution is adequately predicted by the distribution at zero angle of attack normalized to the value at the center line at angle of attack. Below this plane, the heat transfer on the forebody is roughly constant, and above this plane interpolation may be used to estimate the heating distribution.

The radiative heating histories and distributions do not account for either the absorption of incident radiation by the products of ablation

from the heat shield or for any reradiation from these ablation products to the front face or afterbody. The absorption problem has been investigated (ref. 26) in an overall manner but little appears to have been done on the problem of radiation from the ablation products.

The status of the convective-heating predictions for the manned lunar module might be summed as follows: For the forebody where the heating loads are greatest, predictions appear to be reaching the point where each new refinement to the distribution results in only a small percentage change in the total heat load. In regard to the afterbody, the case is far from settled, but the heating level is so low that even doubling the presently predicted level would change the module heat load by only about 20 percent. However, ablators have a low efficiency for these low heating rates on the afterbody. Thus the afterbody is more important when viewed from weight considerations than when viewed from heating-load considerations. Furthermore, if heating protection for the afterbody were to be provided through reradiation from the hot surface, uncertainty by a factor of 2 in heating rate would result in a 20-percent uncertainty in skin temperature, which could be very significant. Experiments are being conducted on this problem but data obtained in cold tunnels with sting supports is questionable. Finally, although the forebody radiative heating may be uncertain within a factor of 2 (refs. 17, 27, and 28), the design of the forebody heat shield is not critically affected because the contribution of radiation to the total load is so small (about 10 percent).

#### ENTRY OF PLANETARY PROBES

When the entry of planetary probes is considered, it is found that the velocities encountered are significantly above parabolic. The velocity range of interest for the near future is indicated in figure 53-9. This figure is a plot of the minimum earth entry velocity (for no retrorocket braking) which occurs after a return from Venus or Mars with a given transit time. The minimum-energy (Hohman) transfer velocities are only slightly in excess of parabolic (38,000 feet per second) but require long trip times (259 days for Mars and 146 days for

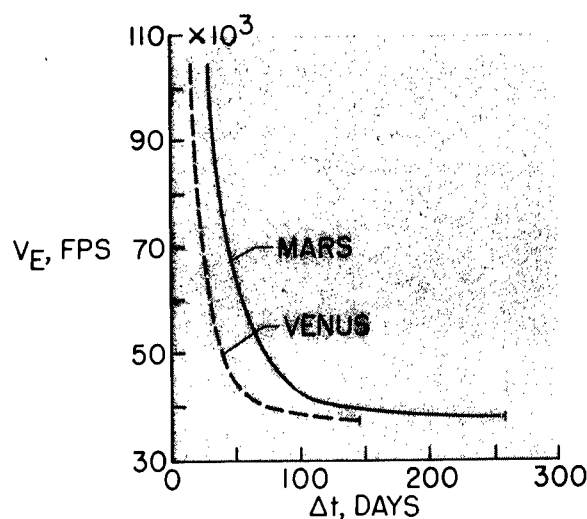


FIGURE 53-9.—Minimum Earth entry velocity as a function of transit time from Mars and Venus.

Venus). In order to reduce this time by a factor of 4, entry velocities of about 50,000 feet per second are required, and to reduce the transit time from Mars to 1 month would require a velocity of 100,000 feet per second.

The principal consideration for such high velocities is the added care which must be given to radiative heating. This fact is evident in figure 53-10 where the total heating load to a 2-foot-diameter sphere in vertical entry is plotted against entry velocity. Contours are also indicated for values of the energy transfer coefficient  $C_H$ , which is the ratio of the total heat load during reentry to the kinetic energy of the

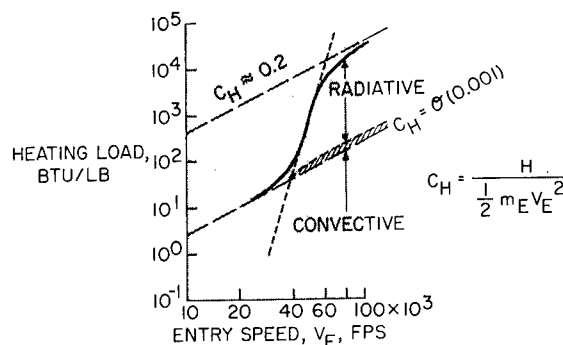


FIGURE 53-10.—Heating load variation with entry speed for 2-foot-diameter sphere.

$$\gamma_E = -90^\circ; \frac{W}{C_D A} = 50 \text{ lb/sq ft.}$$

vehicle at start of reentry. The convective heating contribution has a  $C_H$  of the order of  $1/1000$ . The shaded area for  $V_E > 40,000$  feet per second represents the present uncertainty in predicting convective heating due to ionization effects on the thermal conductivity of air (refs. 11 and 29 to 32). The short-dashed line is an optically thin adiabatic approximation for the equilibrium radiation heating based on reference 16. The total-heat-load curve deviates from this approximation when the effects of optical thickness and energy loss due to radiation become significant (refs. 33 and 34). The radiative contribution is two orders greater than the convective contribution at the high velocity end of the curve and approaches  $C_H \approx 0.2$ , an approximate upper limit at high velocities found in reference 35, in which blackbody radiation was assumed and energy loss was accounted for in an approximate manner. This result is consistent with the highest values of radiative heating rates in reference 33, which were about  $1/4$  to  $1/3$  of the oncoming fluid kinetic energy flux ( $1/2 \rho \infty V_\infty^3$ ) for velocities up to 60,000 feet per second.

Slenderizing the reentry vehicle is one obvious way of alleviating the radiation heating. This possibility is illustrated in figure 53-11 which shows self-illuminated frames from high-speed motion pictures obtained by Jim J. Jones and John A. Moore in the Langely pilot expansion tube (reference 36). The two parts of the figure are reproduced to a scale such that the dotted outlines of the models shown have the same

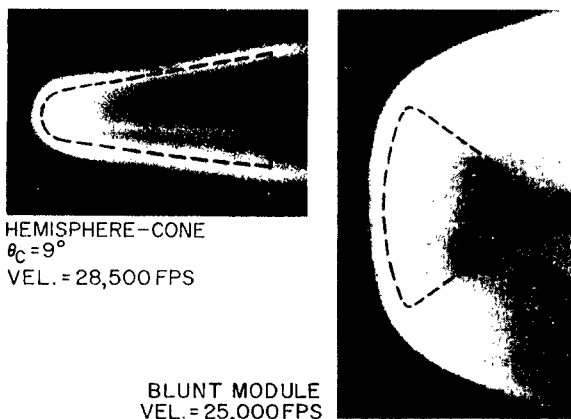


FIGURE 53-11.—Radiation from models in expansion tube.

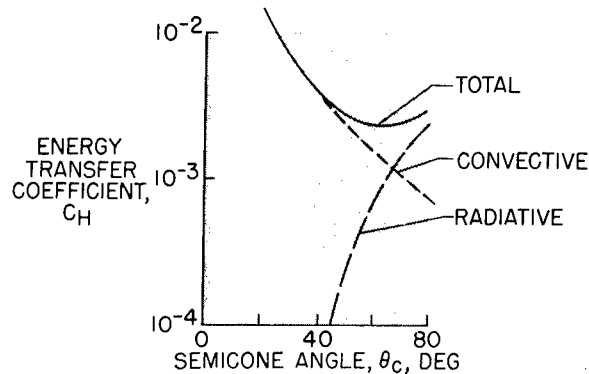


FIGURE 53-12.—Heating load variation with  $\theta_c$  for 2-foot-diameter pointed cones.  $V_E = 45,000$  feet per second;  $\lambda_E = -90^\circ$ ;  $W/C_{DA} = 50$  lb/sq ft.

volume. The radiation from the blunter model is much more intense, even though the velocity is much lower (ambient densities are approximately equal).

Since the local radiation intensity varies mainly as the local normal component of the free-stream velocity, further gains in radiative heating can be realized by pointing the blunt nose of the cone. However, elimination of the blunt nose will result in increased convective heating. Figure 53-12 shows the variation with cone angle of radiative, convective, and total heating for a sharp cone. The case illustrated is that of a 2-foot-base-diameter cone with  $V_E = 45,000$  feet per second,  $\gamma_E = -90^\circ$ , and  $W/C_{DA} = 50$  pounds per square foot. (The density of the reentry vehicle thus must change with cone angle.) In this instance, a minimum in the total load appears at  $\theta_c \approx 60^\circ$ . The value of  $\theta_c$  for minimum heating is, of course, different for other initial conditions and depends upon the radiation model assumed. (See refs. 37 and 38.)

In the preceding discussions of this paper it has been assumed that even though ablation heat shields were employed, the mass loss and vehicle profile change were negligible. Nevertheless, with very high reentry speeds, conditions resulting in high mass loss can arise, and such cases will be considered in the remainder of this paper. These high-mass-loss results are excerpted from a recent analysis made by F. C. Grant of the Langley Research Center, as yet

unpublished. The analytical model for this study is shown in figure 53-13. Mass loss is assumed to occur only at the front faces of the cone and cylinder; whereas the sphere loses mass uniformly over its entire surface. Although investigations of such shrinking spheres have been previously made by others (refs. 35, 39, 40, and 41), the sphere is included for completeness. Newtonian drag is assumed for entry into an exponential density atmosphere with a scale height (height for change of a factor  $e$  in density) of about 25,200 feet. The reentry is steep with a straight-line trajectory and the gravitational force neglected (ref. 42). The final mass  $m_f$ , which might consist of payload instrumentation plus an allowance for structure and other weights, is so located that it generates no aerodynamic forces. The heating rate per unit area follows the law  $\dot{q} = \eta (\frac{1}{2} \rho_\infty V_\infty^3)$ , where  $\eta$  is assumed constant during reentry. An upper boundary of  $\frac{1}{2}$  for  $\eta$  appears reasonable. If radiation is the predominant heating mode, then at most  $\frac{1}{2}$  of the total energy flux will be radiated toward the body and  $\frac{1}{2}$  will be radiated back into the atmosphere ahead of the vehicle. (The case of the absorption of this forward radiation by the atmospheric gases ahead of the shock, which then approach the vehicle with increased energy, is not considered herein but is discussed in ref. 37.) In reference 33 the theoretical predictions of  $\eta$  on a one-dimen-

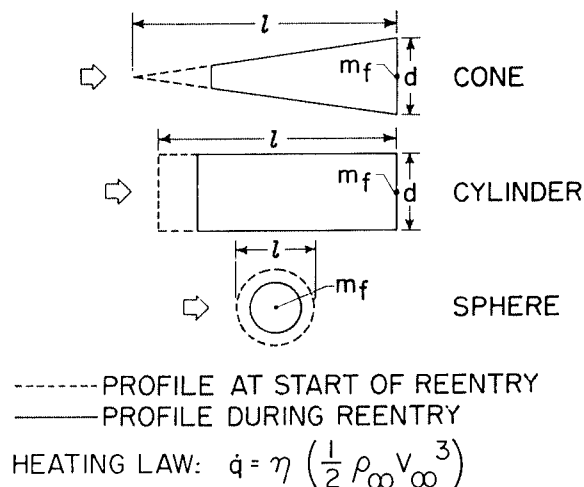


FIGURE 53-13.—Model used for high-speed high-mass-loss analysis.

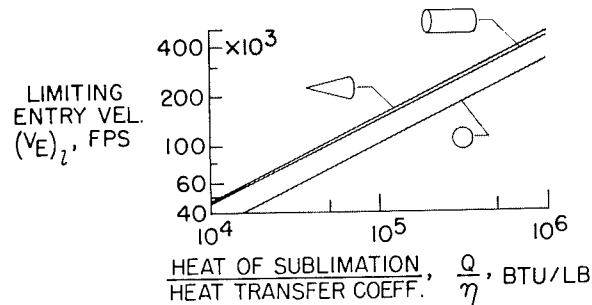


FIGURE 53-14.—Effect of heat of sublimation and heat-transfer coefficient on  $(V_E)_l$ .

$$\frac{m_f}{m_E} = 0.125; \theta_c \approx 8.5^\circ.$$

sional basis for velocities up to 60,000 feet per second are less than approximately  $\frac{1}{4}$  for altitudes below 100,000 feet, which is the limit of the altitude range of interest for this analysis.

Before this matter is discussed further, it should be noted that although the cones are shown to be sharp in the illustrations, the assumption is made that an arbitrarily small initial bluntness exists, which will then grow rapidly as a result of radiation heating. Reference 38 discusses the possibility of special body contouring in order to realize the appreciable gains of a body which can retain a pointed shape during mass loss.

The next problem to be discussed is concerned with the effect of certain parameters on the limiting entry velocity  $(V_E)_l$ . This velocity is defined as that entry velocity which will cause ablation during reentry of all the mass of the vehicle with the exception of the final mass  $m_f$ . The variation of  $(V_E)_l$  with the quotient  $Q/\eta$  (heat of sublimation divided by heat-transfer coefficient) is plotted in figure 53-14 for a final mass ratio  $m_f/m_E = 0.125$ . The cone angle  $\theta_c = 8.5^\circ$  so that heating of the conical flanks is negligible. The heat of sublimation is employed rather than the effective heat of ablation because radiation is the predominant heating mode during the period of high mass loss for the reentries considered. The difference between the heat of ablation and heat of sublimation may be considered then to block the convective heating. At a given value of  $Q/\eta$ , the limiting velocity is nearly the same for the cone and cylinder while that of the sphere is 50 percent



# PROBLEMS OF ADVANCED REENTRY VEHICLES

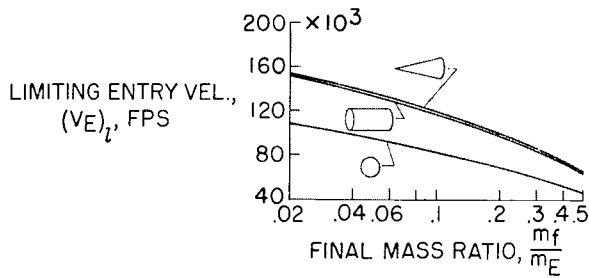


FIGURE 53-15.—Effect of final mass ratio on  $(V_E)_l$ .

$$\frac{Q}{\eta} = \frac{15,000}{1/4} = 60,000 \text{ Btu/lb; } \theta_c = 8.5^\circ.$$

smaller. The limiting velocity varies as the square root of  $Q/\eta$ .

The effect of final mass ratio on limiting velocity is shown in figure 53-15. The value of  $Q/\eta = 15,000/(1/4) = 60,000$  Btu per pound (selected for illustration) is composed of values of  $Q$  representative of the heat of sublimation for graphite together with a conservative value of  $1/4$  for  $\eta$ . As expected,  $(V_E)_l$  decreases as the final mass ratio increases; however, even for this conservative value of  $Q/\eta$ , velocities of 70,000 feet per second are possible with mass fractions of  $1/2$ .

The data in figures 53-14 and 53-15 indicate that very high limiting entry speeds are possible with substantial final mass fractions and that the pointed cones and cylinders are superior to the sphere. However, one of the prices that must be paid for such reentries appears in figure 53-16, which is a plot of maximum decel-

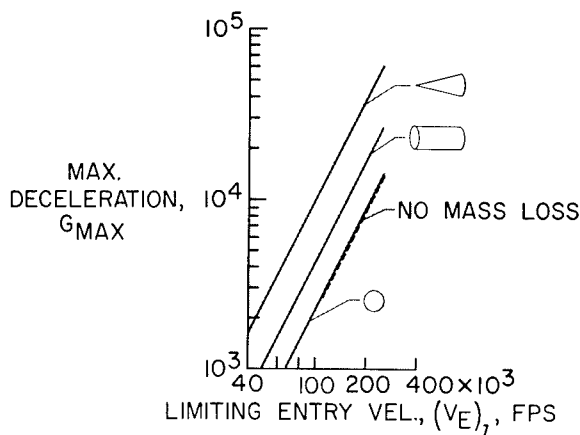


FIGURE 53-16.—Relation between  $G_{max}$  and  $(V_E)_l$ .

$$\frac{m_f}{m_E} = 0.125; \theta_c \approx 8.5^\circ.$$

eration, in earth gravitational units, as a function of  $(V_E)_l$ . The  $G$ -magnitude is extreme, ranging from  $10^3$  to  $10^5$ , and varies as the square of the entry velocity. Much higher loadings are experienced by the cone and cylinder than by the sphere. For the case of zero mass loss at an entry velocity equal to  $(V_E)_l$ , the maximum deceleration is nearly identical to that of the high-mass-loss sphere. After a quick inspection of this curve it is obvious that such reentries will be unmanned.

An interesting point regarding figures 53-14, 53-15, and 53-16 should be mentioned. First, there is no dependency of  $(V_E)_l$  on the size ( $i$ ) of the vehicle. This independence results from the fact that in these figures no restriction was placed on the lower extent of the atmosphere; that is, the atmosphere has been assumed to increase exponentially as the altitude decreases until the vehicle has completed its deceleration without regard to the final altitude. Of course, when the practical boundary condition that the vehicle must have finished its deceleration before impact with the earth's surface is imposed, then the size of the vehicles becomes limited since the  $G$ -pulse occurs at lower altitudes for larger  $i$ . Inasmuch as the velocity ultimately has an exponential decay with altitude, the deceleration never vanishes completely. Thus, some convention must be adopted to define the end of the deceleration pulse. In this paper the limiting size will be defined as that value of  $i$  which puts the peak  $G$  point at 1 and 2 scale heights above sea-level for the cones and cylinders, respectively. The vehicles are then so limited in size that the velocity at sea level is less than 1,000 feet per second for the cones and 150 feet per second for the cylinders at  $m_f/m_E = 1/2$ . For smaller values of  $m_f/m_E$ , smaller sea-level velocities occur. The values of 1,000 and 150 feet per second are for a  $Q/\eta$  value of 60,000 Btu per pound, but may be readily scaled to other  $Q/\eta$  values since all velocities scale as  $\sqrt{Q/\eta}$ .

This limiting vehicle size is shown in figure 53-17 for the cone ( $\theta_c = 8.5^\circ$ ) and cylinder. The sphere is not shown because it has negligible size under the aforementioned impact-velocity restrictions. The curves are drawn for  $Q/\eta = 60,000$  Btu per pound, and a material density  $w$  of 140 pounds per cubic foot, a value

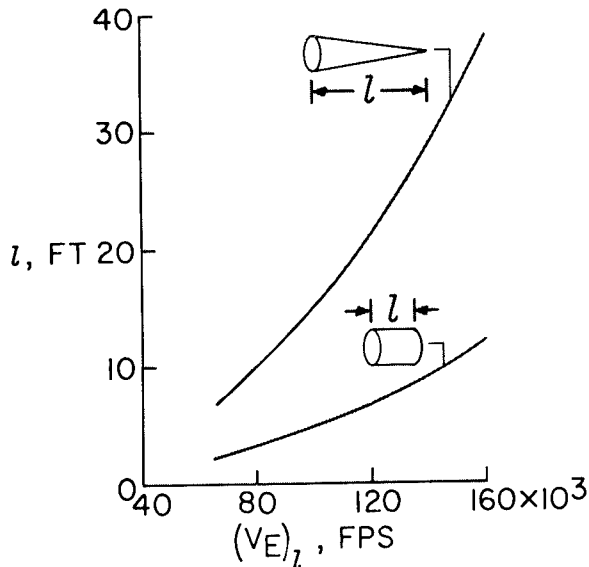


FIGURE 53-17.—Limiting size for deceleration before impact.  $w=140$  lb/cu ft;  $Q/\eta=60,000$  Btu/lb;  $\theta_c=8.5^\circ$ .

also typical of graphite. The value of the final mass fraction  $m_f/m_E$  varies along these curves with the lower values occurring at the higher velocities. At  $(V_E)_l=100,000$  feet per second, the limiting length of an  $8.5^\circ$  cone is 15 feet.

The weights (sizes) required to return a specified final weight to earth after entry from a particular limiting velocity are illustrated in figure 53-18. Curves are drawn for cylinders of  $d/l=0.3$ , 0.6, and 1.2 and for the cone with  $\theta_c=8.5^\circ$  ( $d/l=0.3$ ). Again the impact velocity is restricted and values of  $Q/\eta=60,000$  Btu per pound and a density of 140 pounds per cubic foot are used. The ticks on the curve give the gross vehicle weight at start of reentry. If curves of these gross entry weights were to be cross plotted one would find that the cone is

only slightly more efficient (smaller entry weight for given final weight) than the cylinders. For cylinders at a given  $(V_E)_l$ , the  $d/l$  must increase as the final weight increases because  $l$  and  $m_f/m_E$  are constant; and at a given final weight, the  $d/l$  ratio decreases with increasing  $(V_E)_l$ . A typical example using this figure would show that a 2,000-pound final weight could be reentered at about 65,000 feet per second using a graphite cylinder with a  $d/l=1.2$ . The entry vehicle would have a gross weight of 4,000 pounds, a diameter of 2.8 feet, and a length of 2.3 feet. The  $w/C_D A$  would vary from 310 to 155 during reentry.

The estimates of this high-mass-loss analysis indicate that sizable payload fractions can be recovered after the reentry of unmanned high-speed planetary probes having gross weights and sizes compatible with future launch vehicles. However, the final optimization and sophistication of these reentry probes must be preceded by further knowledge and detailed studies of the radiative and convective heating at these extreme speeds.

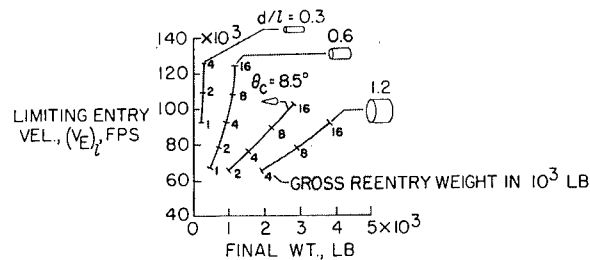


FIGURE 53-18.—Limiting entry velocity and final weight for deceleration before impact.

$$\frac{Q}{\eta} = \frac{15,000}{1/4} = 60,000 \text{ Btu/lb; } w = 140 \text{ lb/cu ft.}$$

## REFERENCES

1. CHAPMAN, DEAN R.: An Analysis of the Corridor and Guidance Requirements for Supercircular Entry Into Planetary Atmospheres. NASA TR R-55, 1960.
2. BARADELL, D. L.: Range Control During Initial Phases of Supercircular Reentries. Thesis submitted to Virginia Polytechnic Institute in Partial Fulfillment of the Requirements for the Degree Master of Science in Aerospace Engineering, May 1962.
3. BECKER, J. V., BARADELL, D. L., and PRITCHARD, E. B.: Aerodynamics of Trajectory Control for Reentry at Escape Speed. *Astronautica Acta*, vol. VII, 1961, pp. 334-358.

# PROBLEMS OF ADVANCED REENTRY VEHICLES

4. LEES, LESTER, HARTWIG, FREDERIC W., and COHEN, CLARENCE B.: The Use of Aerodynamic Lift During Entry Into the Earth's Atmosphere. *ARS Jour.*, vol. 29, no. 9, Sept. 1959, pp. 633-641.
5. GRANT, FREDERICK C.: Importance of the Variation of Drag With Lift in Minimization of Satellite Entry Acceleration. NASA TN D-120, 1959.
6. GRANT, FREDERICK C.: Analysis of Low-Acceleration Lifting Entry From Escape Speed. NASA TN D-249, 1960.
7. BARADELL, DONALD L.: Lateral Range Control by Banking During Initial Phases of Supercircular Reentries. NASA TN D-1511, 1962.
8. JONES, ROBERT A.: Heat-Transfer and Pressure Distributions on a Flat-Face Rounded-Corner Body of Revolution With and Without a Flap at a Mach Number of 8. NASA TM X-703, 1962.
9. BERTRAM, MITCHELL H., FETTERMAN, DAVID E., JR., and HENRY, JOHN R.: The Aerodynamics of Hypersonic Cruising and Boost Vehicles. NASA University Conference, 1962. (Paper No. 55 of present compilation.)
10. CHARWAT, A. F., DEWEY, C. F., JR., ROOS, J. N., and HITZ, J. A.: An Investigation of Separated Flows—Part II: Flow in the Cavity and Heat Transfer. *Jour. Aerospace Sci.*, vol. 28, no. 7, July 1961, pp. 513-528.
11. COHEN, NATHANIEL B.: Boundary-Layer Similar Solutions and Correlation Equations for Laminar Heat-Transfer Distribution in Equilibrium Air at Velocities up to 41,000 Feet Per Second. NASA TR R-118, 1961.
12. CAMM, J. C., KIVEL, B., TAYLOR, R. L., and TEARE, J. D.: Absolute Intensity of Non-Equilibrium Radiation in Air and Stagnation Heating at High Altitudes. Res. Rep. 93 (AFBMD TR 60-184), AVCO-Everett Res. Lab., Dec. 1959.
13. TEARE, J. D., GEORGIEV, S., and ALLEN, R. A.: Radiation from the non-equilibrium Shock Front. Res. Rep. 112, AVCO-Everett Res. Lab., Oct. 1961.
14. CANNING, THOMAS N., and PAGE, WILLIAM A.: Measurements of Radiation from the Flow Fields of Bodies Flying at Speeds up to 13.4 Kilometers Per Second. Presented to the Fluid Mechanics Panel of AGARD (Brussels, Belgium), Apr. 3-6, 1962.
15. CANNING, THOMAS N.: Recent Developments in the Chemistry and Thermodynamics of Gases at Hypervelocity. NASA University Conference 1962. (Paper No. 59 of present compilation.)
16. THOMAS, P. D.: Air Emissivity and Shock Layer Radiation. *Jour. Aerospace Sci. (Readers Forum)*, vol. 29, no. 4, Apr. 1962, pp. 477-478.
17. MEYEROTT, R. E., SOKOLOFF, J., and NICHOLLS, R. W.: Absorption Coefficients of Air. Rep. No. LMSD 288052, Lockheed Aircraft Corp., July 1960.
18. KAATTARI, GEORGE E.: Predicted Shock Envelopes About Two Types of Vehicles at Large Angles of Attack. NASA TN D-860, April 1961.
19. BECKWITH, IVAN E., and COHEN, NATHANIEL B.: Application of Similar Solutions to Calculation of Laminar Heat Transfer on Bodies with Yaw and Large Pressure Gradient in High-Speed Flow. NASA TN D-625, 1961.
20. LEES, LESTER: Laminar Heat Transfer Over Blunt-Nosed Bodies at Hypersonic Flight Speeds. *Jet Propulsion*, vol. 26, no. 4, Apr. 1956, pp. 259-269, 274.
21. KEMP, NELSON H., ROSE, PETER H., and DETRA, RALPH W.: Laminar Heat Transfer Around Blunt Bodies in Dissociated Air. *Jour. Aero/Space Sci.*, vol. 26, no. 7, July 1959, pp. 421-430.
22. VAGLIO-LAURIN, ROBERTO: Laminar Heat Transfer on Three-Dimensional Blunt Nosed Bodies in Hypersonic Flow. *ARS Jour.*, vol. 29, no. 2, Feb. 1959, pp. 123-129.
23. BECKWITH, IVAN E.: Similarity Solutions for Small Cross Flows in Laminar Compressible Boundary Layers. NASA TR R-107, 1961.
24. WICK, BRADFORD H.: Radiative Heating of Vehicles Entering the Earth's Atmosphere. Presented to the Fluid Mechanics Panel of AGARD (Brussels, Belgium), Apr. 3-6, 1962.
25. ANON.: Study of Thermal Radiation Associated with Non-Equilibrium Flow in the Apollo Flight Regime. Doc. No. AERL 62-702, Ser. A (Contract No. NAS 9-156), AVCO-Everett Res. Lab., Sept. 1962.
26. HOWE, JOHN THOMAS: Shielding of Partially Reflecting Stagnation Surfaces Against Radiation by Transpiration of an Absorbing Gas. NASA TR R-95, 1961.
27. KIVEL, B., and BAILEY, K.: Tables of Radiation From High Temperature Air. Res. Rep. 21 (Contracts AF 04(645)-18 and AF 49(638)-61), AVCO Res. Lab., Dec. 1957.

# AERODYNAMICS

28. BREENE, R. G., JR., and NARDONE, MARIA: Radiant Emission from High Temperature Equilibrium Air. R61SD020, Space Sci. Lab., Gen. Elec. Co., May 1961.
29. ADAMS, MAC C.: A Look at the Heat Transfer Problem at Super-Satellite Speeds. [Preprint] 1556-60, American Rocket Soc., Dec. 1960.
30. HOSHIZAKI, H.: Heat Transfer in Planetary Atmospheres at Super-Satellite Speeds. ARS Jour., vol. 32, no. 10, Oct. 1962, pp. 1544-1551.
31. SCALA, SINCLAIRE M., and WARREN, WALTER R.: Hypervelocity Stagnation Point Heat Transfer. ARS Jour., vol. 32, no. 1, 1962, pp. 101-102.
32. FAY, JAMES A.: Hypersonic Heat Transfer in the Air Laminar Boundary Layer. Presented at AGARD Hypersonic Specialists' Conference (Brussels, Belgium), Apr. 3-6, 1962.
33. YOSHIKAWA, KENNETH K., and CHAPMAN, DEAN R.: Radiative Heat Transfer and Absorption Behind a Hypersonic Normal Shock Wave. NASA TN D-1424, 1962.
34. KENNET, H., and STRACK, S. L.: Stagnation Point Radiative Transfer. ARS Jour., vol. 31, no. 3, Mar. 1961, p. 370.
35. RIDDELL, FREDERICK R., and WINKLER, HOWARD B.: Meteorites and Re-Entry of Space Vehicles at Meteor Velocities. ARS Jour., vol. 32, no. 10, Oct. 1962, pp. 1523-1530.
36. TRIMPL, R. L.: A Preliminary Study of a New Device for Producing High-Enthalpy, Short-Duration Gas Flows. For presentation at Second National Hypervelocity Techniques Symposium (Denver, Col.), March 19-20, 1962.
37. ALLEN, H. JULIAN: Hypersonic Aerodynamic Problems of the Future. Presented to the Fluid Mechanics Panel of AGARD (Brussels, Belgium), Apr. 3-6, 1962.
38. ALLEN, H. JULIAN: Gas Dynamic Problems of Space Vehicles. NASA University Conference, 1962. (Paper No. 57 of present compilation.)
39. ÖPIK, ERNST J.: Physics of Meteor Flight in the Atmosphere. Interscience Publishers, 1958.
40. HOPPE, J.: Die physikalischen Vorgänge beim Eindringen meteorische Körper in die Erdatmosphäre. Astronomische Nachrichten, vol. 262, 1937, pp. 169-198.
41. HANSEN, C. FREDERICK: The Erosion of Meteors and High-Speed Vehicles in the Upper Atmosphere. NACA TN 3962, March 1957.
42. ALLEN, H. JULIAN, and EGGERS, A. J., Jr.: A Study of the Motion and Aerodynamic Heating of Ballistic Missiles Entering the Earth's Atmosphere at High Supersonic Speeds. NACA Rep. 1381, 1958.

SESSION R

## **Gas Dynamics**

*Chairman,* ALFRED J. EGGERS, JR.

DR. ALFRED J. EGGERS, JR., *Chief, Vehicle-Environment Division of the NASA Ames Research Center, has contributed novel aircraft and lifting reentry concepts, and has made basic contributions to hypersonic flow theory and the understanding of spacecraft motion and heating during atmosphere entry. He has also developed specialized research equipment such as hypersonic wind tunnels and an atmosphere entry simulator. The fundamental aerodynamic principle on which the RS-70 Mach 3 airplane is based was conceived by him. Dr. Eggers earned his B.A. degree at the University of Omaha in 1944, and his M.S. and Ph.D. degrees from Stanford University in 1949 and 1956, respectively. He was presented the Arthur S. Flemming Award in 1956, the Junior Chamber of Commerce Ten Outstanding Young Men Award in 1957, and the Sylvanus Albert Reed Award of the IAS in 1962. Dr Eggers is a member of the Scientific Advisory Board of the USAF, Fellow of the Institute of the Aerospace Sciences, and a member of the American Rocket Society, Sigma Xi, Tau Beta Pi, and the American Association for the Advancement of Science.*

## 54. Gas Dynamics Problems of Space Vehicles

By H. Julian Allen

H. JULIAN ALLEN is Assistant Director of the NASA Ames Research Center. Mr. Allen earned a B.A. degree from Stanford University, 1932 (engineering), and a degree in aeronautical engineering from Stanford in 1935. He is a recipient of the following awards and honors: Sylvanus Albert Reed Award of the Institute of the Aerospace Sciences (1955); Distinguished Service Medal of NACA (1957); delivered Wright Brothers Lecture for the Institute of the Aerospace Sciences (1957); Airpower Trophy of the Air Force Association (1958).

Mr. Allen is author of numerous papers on aerodynamics of atmosphere entry vehicles and ballistic missiles and on design of wind tunnels and research facilities. He is the originator of the concept of using bluntness to reduce heating of atmosphere entry vehicles; he developed supersonic theory for predicting forces and flows about bodies at angles of attack, contributed and guided the experimental investigation of heat transfer and boundary-layer development at supersonic speeds, and conceived and applied new research techniques and equipment including novel supersonic wind-tunnel nozzles, methods for visualizing airflows at supersonic speeds, and the flight-test technique of firing gun-launched models upstream through supersonic wind tunnels. He is a Fellow of the Institute of the Aerospace Sciences, a Senior Member of the American Rocket Society, and a member of Sigma Xi.

### INTRODUCTION

Many space science investigations could be considered under the heading of gas dynamics. Problems concerned with the solar wind and with the interaction of planetary magnetic field with the flow of charged particles in space, while they belong in the broad sense under this province, are more appropriately treated elsewhere in this conference. Flows involved with neutral free molecules which determine the surface sputtering and the life of near-Earth satellites are certainly in the domain of gas dynamics. The present state of knowledge concerning such flows is poor despite the fact that they have long been a subject of much interest.

Moreover, the so-called slip flow regime of gas flow is even less well understood. However, for lack of time, we have concentrated in this session of the conference on continuum flow problems since they are most often the gas-dynamic problems of critical importance in the space flight field. Some of the major problems have already been discussed earlier in the conference. Those discussed in this session are confined to the atmosphere entry of space vehicles with particular reference to aerodynamic heating. It is the purpose of this opening paper to discuss, first, the trajectories and speeds of entry vehicles which are of interest at present and for the future and, second, the nature of some of the problems entailed.

## NEAR EARTH SPACE VEHICLE PROBLEMS

When it is required to recover intact on the Earth's surface a near-Earth space probe, it can readily be shown that to effect the landing, aerodynamic braking is far more efficient from the weight standpoint than is retrorocket braking. It is well to review the fundamentals of this aerodynamic braking process. Consider for simplicity the case wherein gravity acceleration can be neglected compared to the deceleration due to drag. Then the flight trajectory is a straight line and the equation of motion is approximately

$$m \frac{dV}{dt} = -\frac{1}{2} C_D \rho V^2 A \quad (1)$$

where

- $m$  vehicle mass
- $t$  time
- $V$  velocity
- $C_D$  drag coefficient
- $\rho$  air density
- $A$  characteristic area of the body

If, for simplicity, it is assumed that the enthalpy of the air is very large compared to the surface temperature of the vehicle and that the rate of radiation of heat from the vehicle to space can be neglected in comparison with the aerodynamic heating rate—assumptions appropriate for high speeds of entry—then the heat input rate is given by

$$\frac{dH}{dt} = \frac{1}{2} C_H \rho V^3 A \quad (2)$$

where

- $H$  heat input
- $C_H$  heat-transfer coefficient

Combining equations (1) and (2) gives

$$dH = -\frac{C_H}{C_D} m V dV = -\frac{C_H}{C_D} m \frac{dV^2}{2} \quad (3)$$

Now let us consider the case for which the ratio of heat transfer to drag coefficient is constant and assume first that the vehicle mass is constant corresponding to the case in which a heat sink is employed to absorb the aerodynamic heat generated. Then the total heat in-

put from entry velocity,  $V_E$ , to landing is

$$H = \int_{V=V_E}^0 dH = \frac{C_H}{C_D} \frac{m V_E^2}{2} \quad (4)$$

Now let us consider the mass to be the sum of coolant mass,  $m_c$ , the payload,  $m_p$ , and any extraneous mass,  $m_e$ , and let the heat capacity of the heat sink per unit mass expressed in kinetic energy units be  $\xi$ . Then the coolant mass is simply

$$m_c = \left[ \frac{C_H V_E^2 / 2 C_D \xi}{1 - (C_H V_E^2 / 2 C_D \xi)} \right] (m_p + m_e) \quad (5)$$

To minimize the mass of the heat sink, then, attention must be paid to the following: The extraneous mass of the entry vehicle must be kept to a minimum (i.e., to that required for structural support in the vehicle, etc.), the heat capacity per unit mass,  $\xi$ , should be as large as possible, and the ratio of heat transfer to drag coefficient as small as possible. For velocities up to Earth circular (satellite) speed, at least, the heat-transfer process is essentially one of convection within the boundary layer. The minimum ratio of heat-transfer coefficient to drag coefficient is then generally obtained (ref. 1) by using a body shape having as high a drag coefficient as is possible, consistent with other demands.

Let us now, for comparison, consider the case wherein we replace the heat sink with an ablative heat shield which is vaporized by the aerodynamic heating experienced. One advantage long recognized for the ablative shield is that the total aerodynamic heat which can be absorbed is greatly increased by virtue of the latent heat of vaporization involved in the ablation process. A second advantage of the ablative shield (see, e.g., refs. 2 to 5) is that the issuing vapor fends off the air near the body surface within the boundary layer so as to reduce the heat-transfer coefficient itself. The reduction is approximately in the ratio (ref. 5)

$$\frac{1}{1 + (KV^2/\xi_v)} \quad (6)$$

where  $K$  depends on the molecular weight of the vapor and upon whether the boundary layer is laminar or turbulent (typically  $K$  varies in the



range 0.3 to 0.1), and  $\zeta_v$  is the total energy per unit mass required to vaporize the ablator. This advantage is greater the greater the speed.

Another advantage not generally appreciated is that as the heat shield is vaporized it is automatically jettisoned; therefore, the ensuing heat load is diminished by the continuous reduction of unnecessary body mass. Thus in equation (2)

$$\frac{dH}{dt} = -\zeta_v \frac{dm}{dt} = -\frac{1}{2} C_H \rho V^3 A \quad (7)$$

Combining this with the motion equation gives

$$\frac{dm}{m} = \left( \frac{C_H}{C_D \zeta_v} \right) V dV \quad (8)$$

so that if the quantity in parentheses is assumed to be essentially constant, then the mass,  $m$ , at any time when the speed is  $V$ , is related to the entry mass,  $m_E$ , and the entry speed,  $V_E$ , by

$$m = m_E e^{\frac{C_H}{2C_D \zeta_v} (V^2 - V_E^2)} \quad (9)$$

The coolant mass required is therefore

$$m_c = \left( \frac{1 - e^{-\frac{C_H V_E^2}{2C_D \zeta_v}}}{e^{-\frac{C_H V_E^2}{2C_D \zeta_v}}} \right) (m_p + m_e) \quad (10)$$

which corresponds to that derived for the heat sink as equation (5).

Figure 54-1 gives the ratio of coolant mass to the payload mass (assuming the extraneous mass is zero) for an ablative heat shield obtained from equation (10) and, for comparison, the optimum corresponding ratio for a heat-sink shield (eq. (5)). For this comparison no advantage of reduced  $C_H$  and increased  $\zeta$  is taken for an ablative shield in order to demonstrate the advantage of continuous mass loss due to ablation. The advantage of reducing mass by vapor jettisoning is, of course, small for our present day entry vehicles, but it will become more and more important as speed is increased. In fact, it should be noted that for the heat sink, the payload vanishes when

$$\frac{C_H V_E^2}{2C_D \zeta} = 1 \quad (11)$$

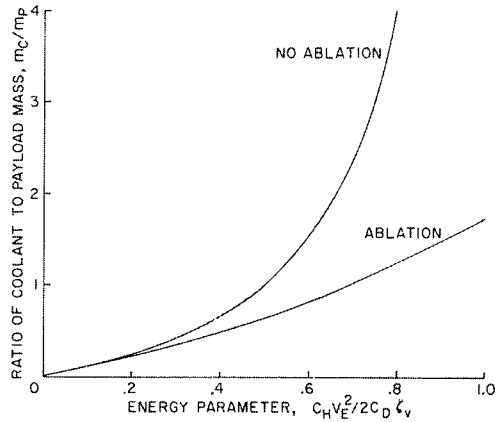


FIGURE 54-1.—Coolant mass requirements for ablative and nonablative heat shields.

but for the ablative shield the payload will not vanish regardless of the value of the ratio although for large values the fraction of total entry mass which may be payload will be uneconomically small. It is clear that the advantages for the ablating heat shield are overwhelming. In the remainder of this paper, accordingly, it is assumed that the heat shields will always be of the ablative type.

Up to this point we have considered only aerodynamic heating aspects of the entry problem. Let us turn our attention to the question of loads since, for many cases of interest, loads are a vital consideration. Again neglecting gravity the motion equation is

$$m \frac{dV}{dt} = -\frac{1}{2} C_D \rho V^2 A \quad (12)$$

The trajectory is a straight line for which

$$dt = -\frac{dy}{V \sin \gamma} \quad (13)$$

where  $y$  is the altitude and  $\gamma$  is the angle between the flight path and the local horizontal. The air density, moreover, may be related to the altitude by the approximation

$$\rho = \rho_0 e^{-\beta y} = \rho_0 \bar{\rho} \quad (14)$$

where

$\rho_0$  sea-level density  
 $\beta$  a constant

Thus, equation (13) becomes

$$\frac{dV}{V} = \frac{C_D \rho_0 A}{2m \sin \gamma} e^{-\beta y} dy = - \left[ \frac{C_D \rho_0 A}{2\beta m \sin \gamma} \right] d\bar{\rho} \quad (15)$$

which upon integration, assuming the bracketed term is constant, yields

$$\text{where} \quad \left. \begin{aligned} V &= V_E^{-1/2 B \bar{\rho}} \\ B &= \frac{C_D \rho_0 A}{\beta m \sin \gamma} \end{aligned} \right\} \quad (16)$$

is known as the ballistic parameter.

The deceleration can be determined from equations (16) and (12) from which the unique result is obtained that if the maximum deceleration is attained before impact with the Earth (which is always the case for a vehicle that is to land intact), it is independent of the altitude at which it occurs and independent of the shape or mass of the body. The maximum value is

$$\left( \frac{dV}{dt} \right)_{\max} = - \frac{\beta V_E^2 \sin \gamma}{2e} \quad (17)$$

where  $e$  is the Napierian base.

For vertical entry at Earth parabolic (escape) speed, 11.2 km/sec, the maximum deceleration is about 330 g, twice the value at Earth circular speed. Such large loads although usually permissible for instrument payloads are not acceptable for most animate payloads. As indicated by equation (17), these large decelerations can be avoided only by entering the atmosphere along a path which is nearly tangential with respect to the Earth's surface. This simple equation cannot usually be used, however, since the permissible decelerations—and this is particularly the case for manned vehicles—are not large relative to the acceleration of gravity, which is contrary to the assumption that gravity effects could be neglected. Moreover, aerodynamic lift will generally be employed to tailor the trajectory for reasons evident later. Chapman (ref. 6) has analyzed the loading problem that includes both gravity and lift in its formulation, and the numerous facets of the manned-flight problem have been treated in current literature (e.g., refs. 7 to 10).

Reduced to its essence, the problem of minimizing aerodynamic loads can be satisfactorily handled by:

(a) Stretching the total time required for entry so as to reduce the average deceleration required.

(b) Employing lift or variable drag to keep maximum decelerations near the average, or to change the trajectory after entry if the initial one would promote unacceptable decelerations.

The trajectories of interest are shown on figure 54-2 as those which are more or less tangential to the Earth surface at the beginning of entry as opposed to the near vertical entry which might be appropriate for vehicles carrying instruments only. An essential difficulty with the manned-vehicle trajectory is that the farther the vehicle goes from the Earth, the more accurate its guidance must be prior to atmosphere entry to assure that its path does not travel through levels in the atmosphere where the air is so dense that there would be intolerable decelerations. The trajectory for which the permitted maximum deceleration is reached has been termed the "undershoot" trajectory. For vehicle entry at speeds greater than the Earth parabolic speed the problem is enhanced since, then, in addition, the path must pass at the other extreme through air sufficiently dense to guarantee "capture" of the vehicle by the atmosphere. That is to say, for this path the vehicle will enter and then leave the atmosphere but the exit velocity must not exceed parabolic speed or the vehicle will be lost to space. Generally the situation will have to be more restricted than has been indicated, for even if

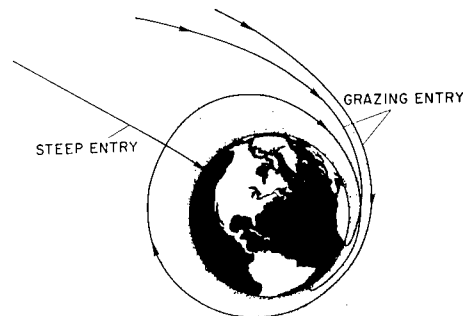


FIGURE 54-2.—Trajectories for entry into Earth's atmosphere from space.

the exit velocity is less than parabolic speed, the ensuing trajectory will entail repeated passes through the atmosphere until the speed falls below satellite speed. These digressions should not permit the manned vehicles to pass through the Van Allen radiation belts unless shielding from the lethal effects of this radiation is provided. It is usually assumed, a priori, that multiple pass entry is to be avoided. The high altitude trajectory which just meets the requirements of minimum allowed deceleration has been termed the "overshoot" trajectory.

Control of lift permits alleviation of these problems in the following ways: For some entry trajectories which would entail excessive load, lift forces directed away from the Earth can be used to alter the path during entry to reduce the loads to acceptable values. On the other hand other trajectories which would provide insufficient deceleration to effect recovery in a single pass can be corrected to a single pass entry by lift forces directed toward the Earth. Figure 54-3 shows the entry corridor permitted as a function of the lift-drag ratio available for a maximum deceleration of 10 g for entry at Earth parabolic speed. The assumption here is that the lift-drag ratio is a constant for any particular trajectory. If modulation of this ratio is permitted, the incremental improvement in the corridor limits can be increased by the order of 50 percent.

Control of drag can also be used to increase the corridor height. However, lift control has the advantage that it easily permits lateral path

changes near the end of the entry as landing is approached and thus assists in maneuvering to a landing point.

The introduction of lift or variable drag, in any event, complicates the problem of aerodynamic stability and requires provision for aerodynamic control. In addition, it introduces new and often objectionable facets to the problem of aerodynamic heating. The entry vehicles with relatively flat trajectories experience lower convective heat rates but for longer times. Often advantage is gained from the lower Reynolds numbers characteristic of the flatter trajectories in that laminar boundary-layer flow can be enjoyed where otherwise turbulent flow would exist. For such cases a marked reduction in heat-transfer coefficient is realized, particularly with ablative heat shields since the effect of vaporization is markedly more beneficial in reducing the heat-transfer rate in the laminar case. On the other hand, with overshoot trajectories the Reynolds number may be so low that the laminar convective heat-transfer coefficient, which varies inversely as the square root of Reynolds number, may become excessively high. In these cases although the heat-transfer rates will be decreased, the integrated heat load will be increased. This trend is shown in figure 54-4 which compares the calculated convective heating history with time for a vehicle (which for simplicity is assumed to be spherical) in vertical descent with the same vehicle in grazing trajectories at the undershoot and overshoot limits. Clearly, the integrated

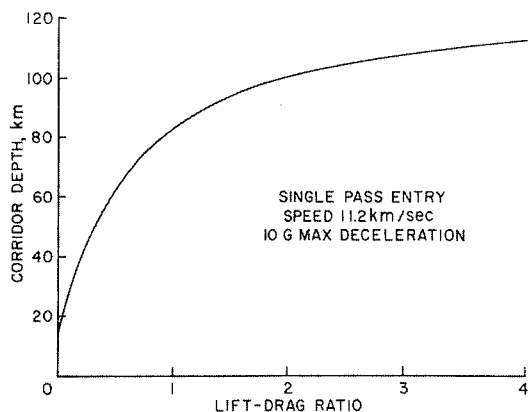


FIGURE 54-3.—Effect of lift-drag ratio on corridor depth.

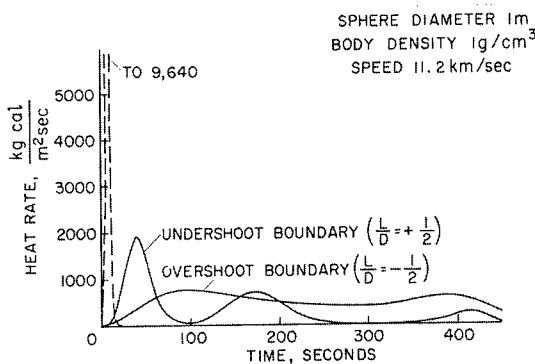


FIGURE 54-4.—Stagnation point convective heat rate for lifting spheres in grazing descent.

input for the overshoot trajectory exceeds that for the others.

All in all, the convective heating problems with the manned entry vehicles are more troublesome than those for vehicles designed for steep entry. The steep-entry vehicles always experience very high convective heating rates but for short total heating time which is a desirable state of affairs for ablative heat shields. The manned vehicles at undershoot conditions experience fairly high heat rates for reasonable short times which again makes ablative shields desirable. In overshoot conditions the lower heat rates and the longer time periods promote an increase in the absorption of heat within the ablative shield. In such cases, many otherwise suitable ablative shields will be weakened unacceptably or will soften and flow excessively. In fact, the optimum heat shields for overshoot trajectories usually are those which act in part as heat sinks and in part as radiators of heat. Thus for the manned entry vehicle, compromise in the heat-shield design is required.

Up to this point the tacit assumption has been made that convective heating constitutes the total. This is very nearly the case for entry at ballistic missile speeds, but as speed is increased, there is another source of heating which gains rapidly in importance with increase in speed. Consider a body in continuum flow at hypersonic speed. The air in the region between the shock wave and the body is drastically slowed down relative to the body in the compression process. The high kinetic energy of the stream is then almost entirely converted to heat. The translational, rotational, and vibrational modes are thus excited and, at sufficiently high speed, the energy will be enough, in fact, to dissociate and ionize a large fraction of the air in this compressed gas region. These atomic and molecular species become important sources of radiation which serve to promote additional surface heating of the entry vehicle. A chain of processes is required to establish thermodynamic and chemical equilibrium between the gas species during and following the compression transient. However, the time required for individual processes varies depending upon the reaction involved; hence, the amount of radia-

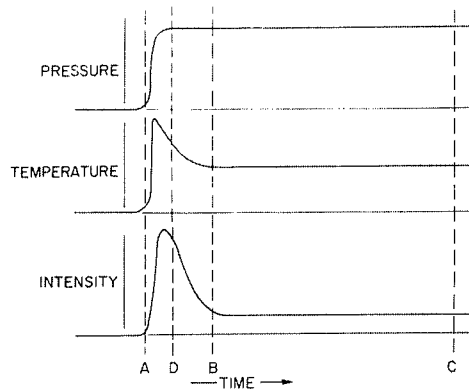


FIGURE 54-5.—Pressure, temperature, and radiation intensity history during shock compression.

tion emitted from elemental volumes within the gas cap is a function of the transient time. Therefore the intensity of radiation per unit volume is not constant within the gas cap but varies along streamlines. The radiative process can be visualized by reference to figure 54-5. During the initial compression immediately following A the temperature attains values approaching those corresponding to an ideal molecular gas since the translational modes of excitation of molecules are rapidly excited. As energy is diverted to the less rapid excitation of the rotational and vibrational modes and then to the relatively slow processes of molecular dissociation and to ionization, the temperature falls with time, as indicated. The early excitation of the various rotational and vibrational modes promotes the appearance and the strong upsurge of the radiation which follows the initial decline in temperature. As energy is then diverted to dissociation and ionization, the drop in temperature causes a subsidence of the radiation level until, in a short time, an equilibrium radiation level is established. By following an element of volume along a streamline, we may envision its changes of time dependent radiation intensity. If the air density in the gas cap is low, the time scale can be such that the body surface may be in the position marked B. The radiation will then be principally from the air which is not in equilibrium. On the contrary, if the gas cap density is high, the whole of the transient behavior will occur in a much shorter time and, hence, effectively farther from the body. In this case C will rep-

represent the position of the body so that the radiation received may be well approximated by the equilibrium value as the integrated mean, provided the density is not so high that strong reabsorption of the radiation occurs within the gas layers. Reabsorption reduces the radiative heating from the value it would otherwise have.

In order to predict radiation effects and to understand experimental radiation data it is obvious that the aerodynamicist must now have much more than a passing acquaintance with the various disciplines of high-temperature physics. The gas dynamics of radiative systems has for some time been a field of interest to the astrophysicist concerned with the internal construction of stars and the radiation from them. The pioneering work of Homer Lane, Emden, and Eddington established a field of investigation that has now reached an advanced state of development (see, e.g., refs. 11, 12, and 13).

An intensive effort, both theoretical and experimental, has been made in recent years to understand the phenomenon of air radiation as it applies to atmosphere entry of space vehicles (see, e.g., refs. 14 to 18). The phenomenon is complex and far from completely understood from theoretical aspects. Moreover, the experimental investigations have not been carried far enough within the regimes of speed, air density, and body size to permit rigorous formulation of scaling laws or accurate appraisals of the levels of the equilibrium and nonequilibrium components of radiation in all cases of interest. What is known quantitatively of the entry radiative heating problem is the subject of a paper to follow, so the remarks here will be restricted to a discussion of the general aspects of the radiative heating problem and the relation of the radiative to the convective contributions for bluff bodies.

With reference to the nonequilibrium radiation, the chemical and excitation processes that occur are nearly all binary reactions (ref. 14). The time required for such reactions is inversely proportional to frequency of collisions. Therefore the thickness of the nonequilibrium layer varies inversely with density. On the other hand, the local magnitude at corresponding locations varies directly as the density. Thus for an arbitrary entry body the total none-

quilibrium radiation is independent of density, although it is a function of velocity and is proportional to the cross-sectional area of the body and to its shape. The nonequilibrium contribution to the heat-transfer coefficient for a body of given shape is therefore

$$C_{H_n} = \frac{dH/dt}{\frac{1}{2}\rho V^3 A} \sim \frac{\varphi(V) A}{\frac{1}{2}\rho V^3 A} \sim \frac{\Phi(V)}{\rho} \quad (18)$$

where  $\varphi$  and  $\Phi$  are functions of flight speed.

With reference to the equilibrium radiation, this contribution is not only a function of velocity but also of density. For parabolic entry speed or less and for near normal bow shock compression the experimental data indicate this contribution varies approximately as the density to the 1.7 power. In addition, the total radiation emitted by the gas cap of an entry body is proportional to the volume of the gas cap which, in turn, is proportional to the body volume (i.e.,  $A^{3/2}$ ) at any given speed. Thus the equilibrium radiation contribution to the heat transfer is

$$C_{H_e} = \frac{dH_e/dt}{\frac{1}{2}\rho V^3 A} \sim \frac{\psi(V)\rho^{1.7}A^{1.5}}{\frac{1}{2}\rho V^3 A} \sim \Psi(V)\rho^{0.7}A^{0.5} \quad (19)$$

where  $\psi(V)$  and  $\Psi(V)$  are functions of flight speed.

The convective heat-transfer contribution is dependent upon whether the flow is laminar or turbulent in the boundary layer and whether vapor ablation occurs, but, at hypersonic speeds, the magnitudes are in question (refs. 19, 20, and 15). For laminar flow, as is well known (e.g., see ref. 21) the heat-transfer coefficient is inversely proportional to the square root of Reynolds number; while in turbulent flow, the Reynolds number dependence is much reduced. The attenuation of the heat transfer due to vapor blowing within the boundary layer is a function of velocity but not density. Thus the convective heat-transfer coefficient is

$$C_{H_c} \sim F(V)\rho^{-\frac{n}{2}}A^{-\frac{n}{4}} \quad (20)$$

where  $F(V)$  is a function of flight speed and the exponent  $n$  is unity for laminar flow but much smaller than unity for turbulent flow.

Now it was noted earlier that the level of heat input is determined by the ratio of heat-

transfer coefficient,  $C_H$ , to the drag coefficient,  $C_D$ . For bluff bodies the drag coefficient at hypersonic speeds in continuum flow is essentially independent of speed and density. Thus summing the components

$$\frac{C_H}{C_D} \sim \Phi(V)\rho^{-1} + \Psi(V)\rho^{0.7}A^{0.5} + F(V)\rho^{-0.5n}A^{-0.25n} \quad (21)$$

From this proportionality it is clear that  $C_H/C_D$  attains a minimum for some value of air density, for if the density is increased from this value, the equilibrium radiation increases  $C_H/C_D$  more than the sum of the convection and nonequilibrium radiation decreases it, and conversely.

To illustrate this compensating influence of density, figure 54-6 shows the estimated values of the total ratio of heat-transfer coefficient to drag coefficient and the individual contributions from the several heating sources as a function of altitude for an ablating sphere of 1 meter radius moving at a speed of 10 km/sec.<sup>1</sup>

These curves are shown as solid lines where the estimate is reasonably reliable. The dotted portions indicate that the estimate is unreliably high for the following reasons:

(a) Convective Heating.

Between the slip flow regime and the free molecule regime an estimate which assumes

<sup>1</sup> The convective heat transfer is that for a nonablating surface so that these results are applicable only for a heat-sink type of heat shield.

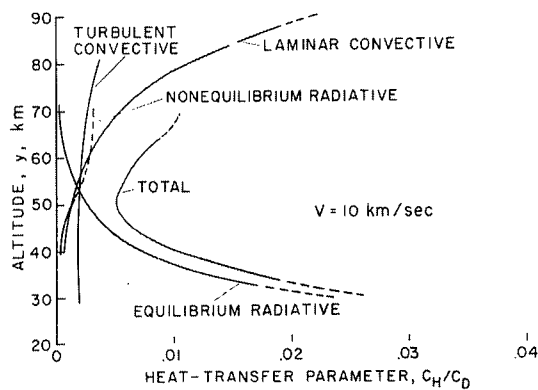


FIGURE 54-6.—Estimates of total and component heat-transfer coefficients for a sphere at 10 km/sec.

laminar continuum flow (eq. (20)) yields values which increase indefinitely as density is decreased. Clearly, the ratio cannot exceed a value of about one-half since, by Reynolds analogy, if all the drag of the body were due to frictional forces, only one-half of the heat generated could enter the body. The other half must be retained by the air in the wake. In fact, in free-molecule flow a similar limitation exists. Suppose the collision of the moving body surface with the stationary air molecules were to release all of the collision energy to the body. The mass of air involved in the collisions is in unit time

$$\rho VA \quad (22)$$

The total rate of release of energy, then, is

$$\frac{(\rho VA) V^2}{2} = \frac{\rho AV^3}{2} \quad (23)$$

so that  $C_H$  cannot exceed unity. On the other hand, the drag force experienced by the body in this case is simply the momentum exchange

$$(\rho VA) V = \rho V^2 A \quad (24)$$

That is, for such an energy release the drag coefficient must be 2; hence, the same limit for  $C_H/C_D$  of one-half is obtained.

(b) Radiative Heating.

Here, again, an upper bound for  $C_H/C_D$  is indicated, for suppose all of the energy

$$DV = \left( \frac{C_D}{2} \rho V^2 A \right) V = \frac{C_D}{2} \rho V^3 A \quad (25)$$

were to appear as radiant energy in the gas cap. If the one-half is radiated forward to space then only the other half of this energy is accepted by the body; hence,

$$\frac{1}{2} \left( \frac{C_D \rho V^3 A}{2} \right) = \frac{C_H}{2} \rho V^3 A \quad (26)$$

or

$$\frac{C_H}{C_D} = \frac{1}{2} \quad (27)$$

There are, in addition, other limiting factors which serve to reduce the individual radiative contributions.

## (1) Nonequilibrium radiation

In equation (18) all the nonequilibrium radiation is assumed to be released to the body when, in fact, if the collision proceeds at such a slow rate that the air passes through the compression region and expands to low density and temperature before the nonequilibrium radiant energy release is complete, the radiation will be prematurely quenched and the radiant energy release is less than estimated. This situation is equivalent to the case where the body position in figure 54-5 is *D*. This limiting phenomenon is thus a truncation process.

Another factor which serves to limit the nonequilibrium radiation is termed "collision limiting" (ref. 15). This occurs when the air density in the gas cap is so low that there are not enough collisions to maintain the population of particles in excited states against the drainage by radiation. Present estimates are that effects of collision limiting occur as altitude exceeds about 50 km.

## (2) Equilibrium radiation

In equation (19) for equilibrium radiation each layer of the gas within the gas cap is tacitly assumed to be nearly transparent to the radiation from neighboring layers. As air density is increased, the gas becomes less and less transparent to its own radiation. Thus when strong absorption exists, the radiative heat, as noted earlier, must diminish from what it would be for an essentially transparent gas under the same conditions, and if the air density becomes sufficiently high, the gas cap radiates essentially as a black body at the equilibrium temperature corresponding to the density within the gas cap.

Let us now return to a discussion of the relative importance of the radiative and convective contribution to aerodynamic heating during entry in the speed range of near-Earth space vehicles ( $7 \text{ km/sec} < V < 11 \text{ km/sec}$ ). For a manned vehicle the sphere of 1 meter radius might be considered representative and for entry at Earth parabolic speed the maximum radiative heating would occur approximately at the speed of 10 km/sec when the altitude of the flight trajectory would be of the order of 60 km. At this speed and in this altitude range (fig. 54-6), the combined radiative heating is

somewhat higher than the convective contribution. For the whole of the flight trajectory, however, the convective contribution would well outweigh the radiative since the convective heat-transfer coefficient is not greatly affected by change in speed. The levels of the radiative contributions are very sensitive to speed and so drop rapidly in the later stages of the entry trajectory.

For grazing trajectories, had we assumed a somewhat lower entry speed, the total radiative contribution, because of its extreme sensitivity to speed, would have been markedly reduced. On the contrary, an increase of entry speed above parabolic speed by a few kilometers per second will reverse this state of affairs.

For entry vehicles in steep descent, the speed is relatively greater at lower altitudes than it would be for a grazing trajectory. The equilibrium radiative heat transfer therefore tends to dominate the convective transfer even at parabolic speeds.

It was noted earlier that when convective processes only are important in aerodynamic heating, the heating problem for an ablative heat shield is related to the materials involved. When, in addition, radiative processes become important the relationship becomes so intimate that one cannot treat the one without full consideration of the other. It is worthwhile to note here two of the more important considerations that must be given to the cross coupling which occurs: First, certain ablative materials that have excellent qualities when convective transfer is the sole source of heating are not attractive, per se, when radiative heating is superimposed. Quartz, for example, is transparent to a wide range of radiative wavelengths and, in the presence of strong radiation, transmits this radiation to the structure supporting it, which, clearly, is most undesirable. Another material, having a similar characteristic, though it is not obvious at first thought, is a polytetrafluoroethylene known as "Teflon." This material is opaque to visual radiation at temperatures up to  $600^\circ \text{K}$ . A phase change occurs then and the material becomes transparent. Of course, the transparency fault can generally be corrected by introducing additives during manufacture which will promote opacity. Another

solution which suggests itself would be to introduce, as an additive, small flakes of highly reflective metals so oriented as to reflect the radiation back out of the shield. If the transmissivity of the base material and the reflectivity of the additive were both high, such a composite might serve to reduce the heating component resulting from gas radiation. This solution has, to my knowledge, never been attempted. In keeping with this approach, Howe (ref. 22) has suggested the use of ablative materials which are opaque in the vapor state. He noted that the vapors of common materials will not provide such characteristics except to a trivial degree. His idea is a novel one, however, and deserves further consideration. Second, some ablative materials contain chemical constituents which, in the vapor state, can become sufficiently excited that they add to the radiative heat input when the flow enthalpy and total heating rate are high. Carbonaceous materials are offenders in this regard.

From the foregoing discussion of aerodynamic heating and of the reaction of materials to it, we can conclude on the basis of our present knowledge that advance to Earth hyperbolic speed brings us to a new regime, a regime in which considerations of radiative heating will dictate the philosophy of design for entry vehicles. The change in point of view will have a more far reaching influence on the course of hypersonic aerodynamics, I believe, than is immediately apparent.

#### THE DEEP SPACE VEHICLE—PROBLEMS OF THE FUTURE

Space vehicles of the future which will become of increasing interest are those intended for journeys to distant points in the solar system. It will be desired to return to Earth some which are unmanned as well as those which are manned. Since it is anticipated that aerodynamic drag will be employed to brake the approach to Earth, the likely speed of the approach prior to entry to the atmosphere is of first concern to the aerodynamicist in that it fixes the scope of interest.

For vehicles intended for journeys to our neighboring planets, Mars and Venus, it is well known that if one employs a near-minimum

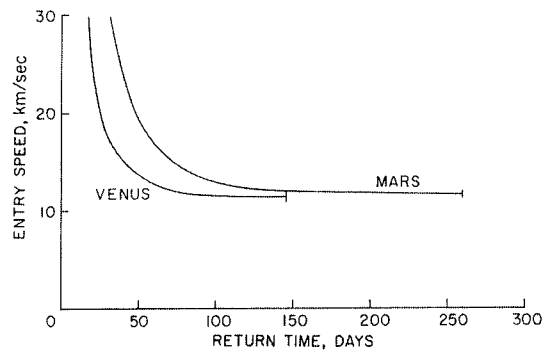


FIGURE 54-7.—Earth entry speed for minimum transit time from Mars and Venus.

energy trajectory—that is, by essentially following the Hohmann transfer ellipses—the speed of return to Earth need not be much in excess of Earth parabolic speed. The question therefore arises, “What is to be gained by employing higher speed vehicles?” The answer is simply that near-minimum energy trajectories are too time consuming as indicated in figure 54-7. A reasonably short transit time will not only be usually desired for its own sake but can effect reductions in total vehicle mass at take-off in many cases. Shorter transit time, for example, decreases the masses involved in life support systems, in radiation shielding when accumulative exposure is a pertinent factor, and in structure required to resist, with some specified probability, the damage resulting from meteoroid impact. With reference to Earth return of such unmanned vehicles as those intended for scientific probing of the vicinity of the Sun, the aerodynamicist must contend with the entry speeds shown in figure 54-8. In short, for future vehicles we may find entry speeds far in excess of Earth parabolic speed to be of interest.

Let us turn now to the subject of aerodynamic loads imposed on vehicles in Earth atmosphere entry. For instrument payloads, as discussed earlier, steep entry trajectories are usually desired. At the higher speeds characteristic of the deep space vehicles, however, the loads may well be limiting considerations. This is apparent from the magnitude of the decelerations shown in figure 54-9.



$$G = \frac{V_{\text{lim}}^2}{gR} - 1 = \frac{V_{\text{lim}}^2}{V_s^2} - 1 \quad (29)$$

where  $V_{\text{lim}}$  is the limiting speed and  $V_s$  is the Earth satellite speed. The limiting speed is therefore

$$V_{\text{lim}} = V_s \sqrt{G+1} = 7.9 \sqrt{G+1} \text{ km/sec} \quad (30)$$

Of course, this limiting speed is an unrealistic upper bound since no drag is assumed to occur and thus the entry time is indefinitely long. These results establish the fact that for manned vehicles when transit times for space journeys become very short, it will be necessary to resort to rocket braking, at least in part, to effect an Earth landing.

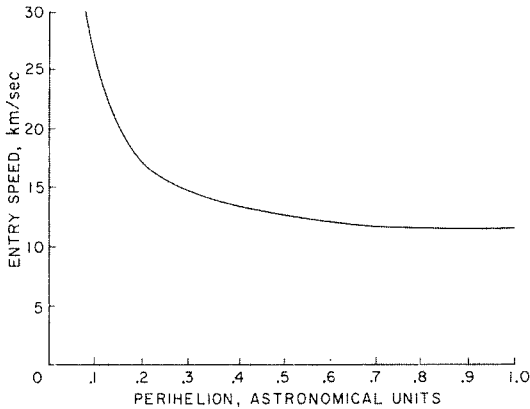


FIGURE 54-8.—Earth entry speed for a solar probe.

For manned vehicles the restrictions are considerable. If one assumes that decelerations must be limited to ten times the Earth gravity acceleration, then even if with the maximum benefit of lift (i.e.,  $L/D \rightarrow \infty$ ), the entry corridor height attainable, as shown in figure 54-10, would vanish at an entry speed of 26 km/sec. This limiting entry speed is determined in the following way: The lift force directed toward the Earth must equal the centrifugal force less the gravitational pull or

$$L = \frac{mV^2}{R} - mg \quad (28)$$

where  $R$  is the Earth radius. Hence if  $G$  is the multiple of Earth gravitational acceleration permitted

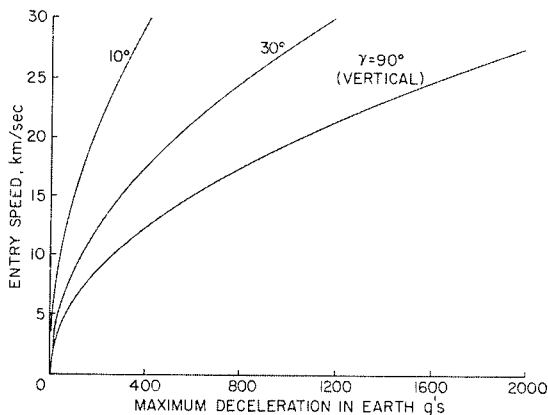


FIGURE 54-9.—Maximum decelerations as a function of Earth entry speed and entry angle.

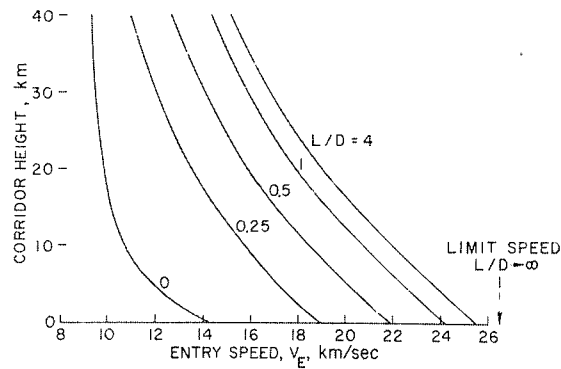


FIGURE 54-10.—Entry corridor height as a function of entry speed and vehicle lift-drag ratio.

Many interplanetary journeys will, of course, entail landings on planets other than Earth, so that gas dynamic problems associated with high-speed entry into such atmospheres form a new field of interest in hypersonic gas dynamics. Chapman (ref. 6) has given consideration to the problem of such entries. Generally, the aerodynamic loads follow the same functional relations with velocity and atmospheric density as for entry into the Earth's atmosphere but the change in atmospheric properties and, in some cases, the change in planet size and mass must be taken into account. Pertinent approximate characteristics for some near-Earth planets and for Titan, a satellite of the planet Saturn which has an atmosphere, are given in table 54-I.

# GAS DYNAMICS

TABLE 54-I.—*Approximate Characteristics of Some Planetary Bodies and Titan*

Planet	Orbit radius from Sun, km	Planet radius, km	Atmosphere density scale factor $\rho^{-1}$ , km	Surface gravity acceleration, m/sec <sup>2</sup>	Surface satellite speed, km/sec	Surface parabolic speed, km/sec	Atmosphere density at surface, kg/m <sup>3</sup>	Principal atmospheric gases
Venus----	$1.082 \times 10^8$	$0.619 \times 10^4$	6. 1	8. 53	7. 27	10. 26	$2 \pm 1$	CO <sub>2</sub> , N <sub>2</sub>
Earth----	$1.495 \times 10^8$	$0.637 \times 10^4$	7. 16	9. 806	7. 90	11. 17	1. 225	N <sub>2</sub> , O <sub>2</sub>
Mars----	$2.278 \times 10^8$	$0.340 \times 10^4$	18	3. 73	3. 56	5. 03	. 1	N <sub>2</sub> , CO <sub>2</sub>
Jupiter----	$7.876 \times 10^8$	$6.96 \times 10^4$ (?)	18	25. 8(?)	42. 4(?)	59. 9(?)	-----	H <sub>2</sub> , CH <sub>4</sub>
Titan----	$14.25 \times 10^8$	$0.210 \times 10^5$	30	2. 16	2. 13	3. 01	-----	CH

TABLE 54-II.—*Approach Speed and Deceleration*

Planet	Speed for Hohmann transfer from Earth, km/sec	10 g limit speed, km/sec	Deceleration for vertical entry with Hohmann transfer, Earth g
Venus-----	10. 5	25. 7	340
Earth-----	(11.2) parabolic speed	26. 2	(329) for parabolic entry speed
Mars-----	5. 8	18. 6	35
Jupiter-----	60. 2	92. 9	3780
Titan-----	6. 4	14. 5	26

Generally, atmosphere entry decelerations for grazing trajectories and entry corridor heights for Venus and Jupiter are about the same as for Earth. For Titan and Mars, entry is far easier to effect from the loads standpoint. For grazing trajectories, the limit speed for magnitude of deceleration equal to 10 Earth gravity accelerations as well as the minimum speed of approach corresponding to Hohmann transfer is given in table 54-II.

The last column of table 54-II gives the deceleration in Earth g units for vertical atmosphere entry. Again Mars and Titan represent a one order magnitude reduction in loading compared to Venus and Earth (listed for Earth parabolic speed) vertical entry. Note that for vertical descent, Jupiter entry is one order magnitude more difficult than Earth entry contrary to the case for grazing entry. Steep approach to that large massive planet will be troublesome.

Let us now return to the subject of aerodynamic heating. As noted earlier, at speeds exceeding Earth parabolic speed, radiation of the air in the compressed atmosphere ahead of a blunt entry body is expected to become the principal contributor to the aerodynamic heating. Thus, in contrast with the aerodynamic

heating at the lower speeds where convective heating dominates so that the ratio of heat-transfer coefficient to drag coefficient can be kept small and essentially independent of the speed, the heat to drag ratio now apparently increases rapidly with increase in speed; that is to say, the fraction of the total kinetic energy per unit of vehicle mass which appears as heat to the vehicle increases with speed. But this total energy per unit of mass itself increases as the square of speed; hence, it is clear that the magnitude of the aerodynamic heating with increased speed soon reaches such alarming proportions that the fraction of vehicle mass which can be allocated to the payload becomes economically untenable.

What, if anything, can we hope to do to make more efficient entry possible at the higher speeds? This question answers itself if we but review the past developments. In the speed range of ballistic missiles, the heating during atmosphere entry was essentially all convective heating. The least ratios of heat-transfer coefficient to drag coefficient were obtained with very blunt shapes. Now for higher speed entry we must answer the question, "What shapes will provide the minimum ratio of heat-transfer to drag coefficient when both radiative and

convective heating occur and the radiative heating tends to dominate?"

The answer which has occurred to me, and probably to others as well, is that we must concede some ground on convective heating if by so doing we can drastically reduce the radiative heating. To attain this end, a conical body looks attractive. As shown in figure 54-11, a conical bow shock reduces the air speed normal to the wave to  $V \sin \theta_w$  in contrast to  $V$  for a severely blunt body. Of course, the drag coefficient for the conical body is less than that for the blunt body but the radiative heating should be considerably less, since it is so very speed sensitive, so that a net gain may be possible.

An analysis of this problem for entry into the Earth's atmosphere has been undertaken by my colleague Mr. Alvin Seiff and me. To date the case for the laminar boundary layer and for ablative heat shields has been completed, and it has been assumed that the conical shape is maintained during ablation—a critical assumption as will be discussed later. Some of the results to follow are most instructive. Let us define a mean value of heat-transfer coefficient,  $\bar{C}_H$ , so that

$$\frac{\bar{C}_H}{C_D} = \frac{\int_{-\infty}^{\infty} \frac{1}{2} C_H \rho V^3 dt}{\frac{m_E V_E^2}{2}} \quad (31)$$

The value  $\bar{C}_H/C_D$  is the fraction of the total vehicle kinetic energy at atmosphere entry

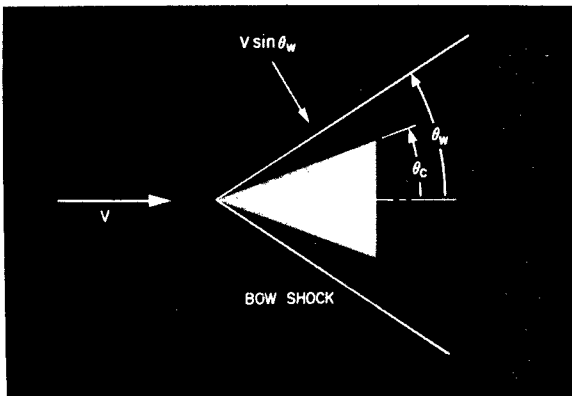


FIGURE 54-11.—Velocity vectors for conical bodies.

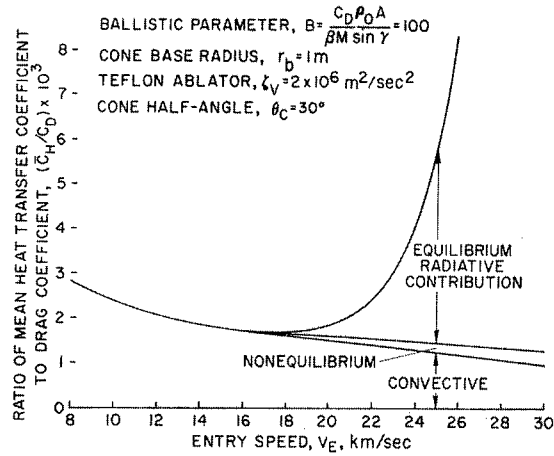


FIGURE 54-12.—Ratio of mean heat-transfer coefficient to drag coefficient for one cone half-angle.

which must appear in the form of heat to the vehicle.

It may be related directly to mass loss due to surface ablation,  $m_a$ , by

$$m_a = \frac{\bar{C}_H}{C_D \zeta_v} \left( \frac{m_E V_E^2}{2} \right) \quad (32)$$

On figure 54-12 is shown the variation of  $\bar{C}_H/C_D$  as a function of entry speed for one arbitrary case in which

$$\left. \begin{array}{l} \text{Cone half-angle; } \theta_c = 30^\circ \\ \text{Ballistic parameter; } B = \frac{C_D \rho_0 A}{\beta m \sin \gamma} = 100 \\ \text{Cone base radius; } r_b = 1\text{m} \\ \text{Teflon ablator, specific energy of ablation; } \zeta_v = 2 \times 10^6 \frac{\text{m}^2}{\text{sec}^2} \end{array} \right\} \quad (33)$$

These particular values are not pertinent to the following discussion—rather this case should be viewed as a typical one to show the trends with speed and the contributions to the total of the convective, the nonequilibrium radiative, and the equilibrium radiative components. As seen, for entry speeds up to about 16 km/sec, the convective heating contribution dominates, indicating the very effective suppression of radiative heat transfer provided by the cone flow field. The decrease of  $\bar{C}_H/C_D$  with speed in the low-speed regime is principally a

result of the effect of blowing of the ablated vapor within the boundary layer in reducing the convective transfer. When radiative heating does become important with increasing speed, it rapidly dominates. The nonequilibrium radiative contribution is relatively unimportant—a result which may be regarded as a general one.

Figure 54-13 shows the effect of varying the cone half-angle, other factors being equal. The advantage of choosing the optimum cone-angle from the envelope curve for the particular entry speed of interest is apparent. Figure 54-14 shows the envelope curves for various values of the ballistic parameter. The results shown indicate that the smallest ballistic parameter is best.

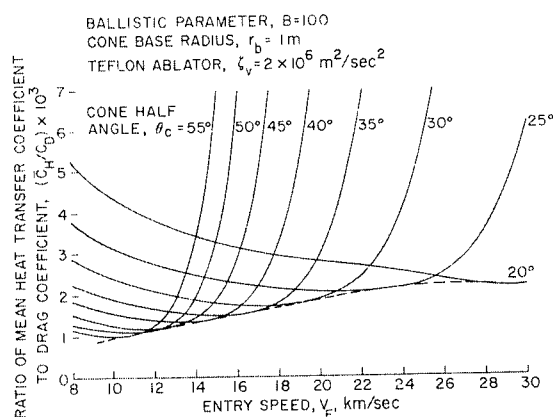


FIGURE 54-13.—Ratio of mean heat-transfer coefficient to drag coefficient as a function of cone half-angle.

However, it should be recalled that laminar flow only was assumed for these calculations and, in reality, one cannot expect to maintain laminar boundary layers to arbitrarily high Reynolds numbers. If we limit the Reynolds number to  $10^7$  based on local conditions—which at present seems an upper limit of what appears to be a reasonably safe value—then the least values for the ratio of mean heat transfer to drag coefficient are as indicated by the heavy solid line. The fraction of the total kinetic energy at entry to the atmosphere which must be accepted as heat energy by the heat shield can apparently be kept to low values even at entry speeds well in excess of earth parabolic speed.

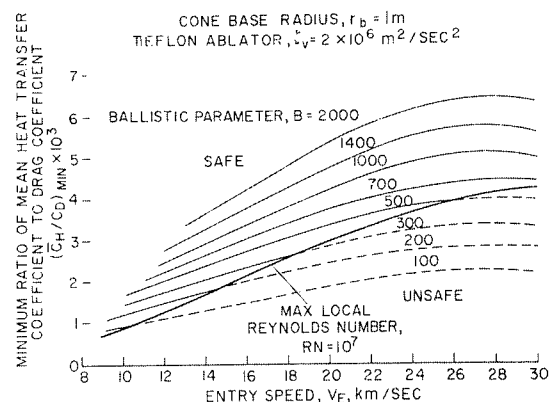


FIGURE 54-14.—Minimum ratio of mean heat-transfer coefficient to drag coefficient for various values of ballistic parameters.

Figure 54-15 gives the optimum cone half-angles as a function of speed. The optimum angles are not small even for very high entry speeds. It is of some interest to note that at the optimum condition the analysis indicates that the convective heat transfer constitutes between 85 percent and 90 percent of the total.

The corresponding ratios of ablated mass to entry mass are shown on the curve marked "Teflon ablator" in figure 54-16. It appears that one could keep the ablated mass loss to 10 percent or less to speeds up to 15 km/sec with Teflon (or equivalent ablative materials such as nylon or polyethylene). For higher entry speeds an improved ablator is needed. Graphite looks particularly appealing.

Now, it will be remembered that the foregoing analysis was predicated upon the assump-

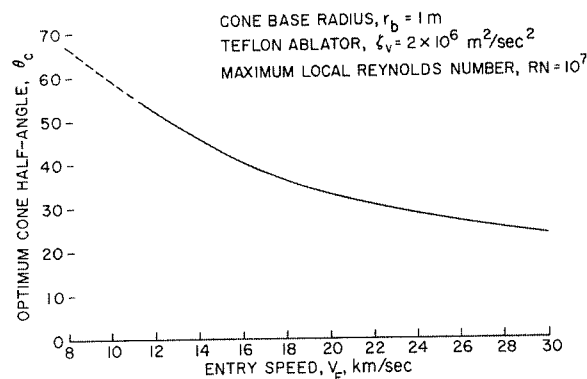


FIGURE 54-15.—Optimum cone half-angles as a function of entry speed.

# GAS DYNAMICS PROBLEMS OF SPACE VEHICLES

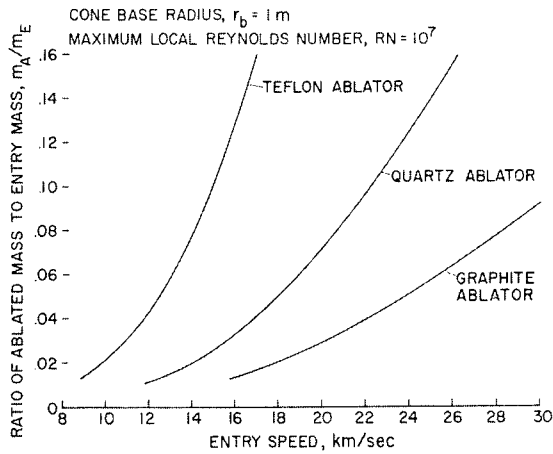


FIGURE 54-16.—Ratio of ablated mass to entry mass as a function of entry speed.

tion that the conical vehicle remained conical during entry. The local heat transfer varies greatly over the surface, being large at the cone apex and small near the base. For an ablative shield for which the heat of ablation is uniform over the surface, the ablation, accordingly, would be nonuniform over the surface. A shape which was conical at entry would become blunted by the large convective heat transfer at the apex. Then the radiative contribution would maintain this flattened forward face which would grow as the entry trajectory progressed (see ref. 23). Thus the ratio of heat-transfer coefficient to drag coefficient and, in turn, the ratio of ablated mass to entry mass would exceed those we have given previously. This increase in ablation would not be great if the entry speed were only moderately larger than Earth parabolic speed. However, it would certainly be excessive, if not overwhelming, at the highest entry speeds we have considered. The question then arises: What can be done to prevent excessive nose flattening from occurring? Several remedies suggest themselves. The more attractive of these are the following: One is to feed a solid-ablator rod (e.g., a graphite rod) of small radius through a hole at the apex at a programmed rate equal to the rate of ablation so that growth of a flattened face over the remainder of the body can be prevented. Another is to expel a suitable ablating liquid, such as water, through an ori-

fice at the apex which could accomplish the same result. A third is to employ a near conical shape which prior to entry is cusped at the apex so as to delay the radial rate of growth of the flat face. This last alternate would probably not be as effective as the other two, but it avoids the need to program the rate of feed of ablation material. In any event it does not appear that this problem is an unsurmountable one for entry speeds up to 20 km/sec or so, but the required mass loss will exceed in some degree the amounts which were previously indicated in figure 54-16.

One final problem which, I believe, will bear investigation concerns the effects that the gas compression process in shock waves will have on the flow field about aerodynamic bodies when the enthalpy is extremely high, such as in the case for meteoric bodies, for example, at maximum entry speeds (50 to 70 km/sec for Earth). At these speeds a pointed body is blunted almost immediately. A gas cap of a blunt body, such as shown in figure 54-17(a), at the lower hypersonic speed radiates energy mostly in the long wavelength end of the spectrum. The fraction of this gas cap energy which radiates away from the body is only very minutely absorbed in the neighboring air layers ahead and to the side of the body. One can ignore, then, the effects of the radiation on the oncoming stream of air (i.e., in effect, one assumes the radiation is absorbed at infinity). As flow speed is increased, the principal radiation of the gas cap energy moves to shorter and shorter wavelengths until at very high speeds practically all the energy is radiated at such short wavelengths that a substantial fraction can be absorbed in air layers directly ahead of the body. Thus, preheating of the air ap-

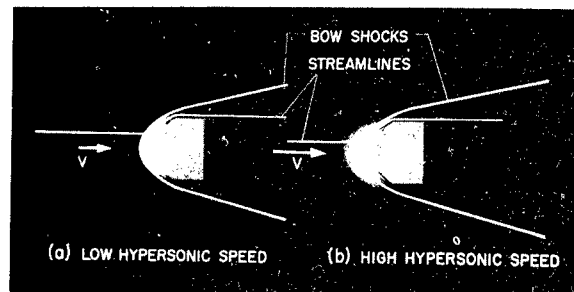


FIGURE 54-17.—Blunt bodies in hypersonic flow.

proaching the body occurs and, accordingly, the gas cap energy increases since it must accept this preheated air as the flow progresses. It appears that one effect of such "radiation trapping" is that the body must now accept more than half the energy radiated from the gas cap. Also, the air flow is no longer a usual hypersonic one since the gas ahead of the body, although moving at speed greater than that of pressure propagation, is now forewarned of the presence of the body. Moreover, the energy contained in each elemental volume can no longer be treated as constant, by virtue of the transfer of radiant energy from element to element within the flow.

Analyses concerned with prediction of temperatures and pressures within the Earth's atmosphere due to the sudden release of nuclear energy (see, e.g., ref. 24) indicate that when radiation absorption in neighboring layers becomes an important consideration, the ionization process itself brings new facets to the problem. The numerous liberated electrons, because they have a much greater mobility than the heavy particles, tend to be segregated from the main gas cap mass. Thus the flow becomes a charge-separated one so that additional flow changes are expected. In 1957, Sen and Guess (ref. 25) formulated an analysis of shock wave structure for conditions under which radiation mean free path is small and the so-called Roseland approximation term can be used. The similar work of V. A. Prokofiev (ref. 26) is particularly enlightening. He shows that a

rather dramatic thickening of the shock wave can result. To keep his mathematics and physics within bounds, Prokofiev neglected viscosity and heat conduction and treated only hydrogen and argon. His calculations, which are already rather complex, thus fail to push knowledge as far as we would like but the effects of radiation, as well as ionization, are demonstrated conclusively. My colleague, Dr. Max Heaslet, after reviewing these analyses has found that our physical knowledge has been materially improved since these earlier works appeared so that it would seem that a reanalysis is in order. He is undertaking such an analysis at this time.

However, without knowing what shock thickening is characteristic for air in very high enthalpy flows we can, in any event, describe the possible effects of such thickening. Suppose, as indicated in figure 54-17(b), the shock thickness, as indicated by the shading, becomes comparable with the dimensions of the body. The presence of the body will then be felt in the flow ahead of it by about this thickness. The stream lines will therefore resemble those we normally associate with subsonic flows, but clearly will be of a far more complex nature.

In summary, only a few of the hypersonic problems which will need solutions in the future have been treated. The advance in flight speeds and the introduction of gas media other than the air will introduce a host of new ones. Many of these requiring both analytical and experimental study are most fitting as fields of interest for our university research staffs.

## REFERENCES

1. ALLEN, H. JULIAN, and EGGERS, A. J., JR.: A Study of the Motion and Aerodynamic Heating of Ballistic Missiles Entering the Earth's Atmosphere at High Supersonic Speeds. NACA Rep. 1381, 1958. (Supersedes NACA TN 4047.)
2. GROSS, JOSEPH F., MARSON, DAVID J., and GAZLEY, CARL, JR.: General Characteristics of Binary Boundary Layers With Application to Sublimation Cooling. Rand Rep. P-1371, May 8, 1958, Aug. 1, 1958 (rev.).
3. ROBERTS, LEONARD: Stagnation-Point Shielding by Melting and Vaporization. NASA Rep. 10, 1959.
4. LEES, LESTER: Convective Heat Transfer With Mass Addition and Chemical Reactions. Presented at the Third Combustion and Propulsion Colloquium, AGARD, NATO, Palermo, Sicily, Mar. 17-21, 1958.
5. ADAMS, MAC C.: Recent Advances in Ablation. ARS Journal, vol. 29, no. 9, Sept. 1959, pp. 625-632.
6. CHAPMAN, DEAN R.: An Approximate Analytical Method for Studying Entry Into Planetary Atmospheres. NACA TN 4276, 1958.

# GAS DYNAMICS PROBLEMS OF SPACE VEHICLES

7. LEES, LESTER, HARTWIG, FREDERIC W., and COHEN, CLARENCE B.: The Use of Aerodynamic Lift During Entry Into the Earth's Atmosphere. Space Technology Lab. Rep. GM-TR-0165-00519, Nov. 1958.
8. EGGERS, ALFRED J.: The Possibility of a Safe Landing. Space Technology, ch. 13, Howard S. Seifert, ed., John Wiley and Sons, New York, 1959.
9. CHAPMAN, DEAN R.: An Analysis of the Corridor and Guidance Requirements for Supercircular Entry Into Planetary Atmospheres. NASA TR R-55, 1960.
10. LEVY, LIONEL L., JR.: An Approximate Analytical Method for Studying Atmosphere Entry of Vehicles With Modulated Aerodynamic Forces. NASA TN D-319, 1960.
11. KOURGANOFF, V.: Basic Methods in Transfer Problems; Radiative Equilibrium and Neutron Diffusion. Oxford, Clarendon Press, 1952.
12. UNSÖLD, ALBRECHT: Physik der Sternatmosphären, mit besonderer Berücksichtigung der Sonne. Second ed., Julius Springer (Berlin), 1955.
13. AMBARTSUMYAN, V. A., ed. Theoretical Astrophysics. Pergamon Press, New York, 1958.
14. CAMM, J. C., KIVEL, B., TAYLOR, R. L., and TEARE, J. D.: Absolute Intensity of Non-Equilibrium Radiation in Air and Stagnation Heating at High Altitudes. Avco-Everett Research Laboratory RR-93, Dec. 1959.
15. ROSE, PETER H.: Reentry From Lunar Missions. Preprint no. 7, Lunar Flight Symposium, Amer. Astronaut. Soc., Denver, Colo., Dec. 29, 1961.
16. PAGE, WILLIAM A., CANNING, THOMAS N., CRAIG, ROGER A., and STEPHENSON, JACK D.: Measurements of Thermal Radiation of Air From the Stagnation Region of Blunt Bodies Traveling at Velocities up to 31,000 Feet Per Second. NASA TM X-508, 1961.
17. KIVEL, B., and BAILEY, K.: Tables of Radiation From High Temperature Air. Avco-Everett Research Lab. RR-21, Dec. 1957.
18. MEYEROTT, R. E.: Radiation Heat Transfer to Hypersonic Vehicles. Lockheed Aircraft Corp., LMSD 2264-R1, Sept. 1958.
19. FAY, J. A., and RIDDELL, F. R.: Theory of Stagnation Point Heat Transfer in Dissociated Air. Jour. Aero. Sci., vol. 25, no. 2, Feb. 1958, pp. 73-85, 121.
20. SCALA, SINCLAIRE M., and WARREN, WALTER R.: Hypervelocity Stagnation Point Heat Transfer. General Electric Missile and Space Vehicle Dept. Rep. R61SD185, Oct. 1961.
21. HAYES, WALLACE D., and PROBSTEN, RONALD F.: Hypersonic Flow Theory. (Applied Mathematics and Mechanics. Vol. 5.) Academic Press, New York, 1959.
22. HOWE, JOHN THOMAS: Radiation Shielding of the Stagnation Region by Transpiration of an Opaque Gas. NASA TN D-329, 1960.
23. TRIMPI, ROBERT L., GRANT, FRED C., and COHEN, NATHANIEL B.: Aerodynamic and Heating Problems of Advanced Reentry Vehicles. NASA-University Conference Report, 1962.
24. BETHE, HANS A., FUCHS, KLAUS, HIRSCHFELDER, JOSEPH O., MAGEE, JOHN L., PEIERLS, RUDOLPH E., and VON NEUMANN, JOHN: Blast Wave. Los Alamos Scientific Laboratory LA-2000, Aug. 1947, U.S. Dept. of Commerce, Washington, D.C., distributed March 1958.
25. SEN, HARI K., and GUESS, ARNOLD W.: Radiation Effects in Shock-Wave Structure. Phys. Rev., vol. 108, no. 3, Nov. 1957, pp. 560-564.
26. PROKOFIEV, V. A.: Consideration of the Effect of Emission of Radiation in the One-Dimensional, Stationary Flow of a Monatomic Gas. Uchenye Zapiski Moskovskogo Gosudarstvennogo Universiteta, Mekhanika, 172, pp. 79-124, 1952. (Translation by University Microfilms, Inc., Ann Arbor.)

## 55. Recent Information on Hypersonic Flow Fields

By Alvin Seiff

ALVIN SEIFF is chief of the Supersonic Free-Flight Wind Tunnel Branch, NASA Ames Research Center. He earned a B.S. degree from the University of Missouri in 1942 (chemical engineering). He is interested in hypersonic aerodynamics and manned space flight. Mr Seiff was associated with the development of first atomic bomb at Oak Ridge; he developed free-flight testing technique for hypersonic research; he was first to point out the effects of wall temperature on skin friction of supersonic turbulent boundary layers; he performed early studies on transition to turbulence in supersonic boundary layers; and he contributed to the development of concepts of manned lunar flight. He is an Associate Fellow of the Institute of the Aerospace Sciences. Mr. Seiff was a physics instructor at the University of Tennessee from 1946 to 1948.

### SUMMARY

This paper attempts to summarize some of the significant recent developments in the description and understanding of hypersonic flow fields. Topics discussed include the blast-wave theory, and the more exact description of pressures and bow-wave shapes to which it is applicable; Newtonian impact theory, with emphasis on its limitations; calculation of flow fields with detached bow shock waves by numerical solution of the equations of motion, with emphasis on stream-tube methods; shockwave standoff distance for hemispheres as given by theory and experiment; secondary flow fields embedded within hypersonic shock layers; hypersonic flow of gases other than air; and one-dimensional shock waves with energy exchange by radiative transfer. The treatment of these topics is necessarily brief, but an effort is made to stress important conclusions, and to present references where available to permit the reader to obtain more detailed information.

### INTRODUCTION

The past five years have seen some notable progress in the understanding of hypersonic gas flows. This progress has not been so much a matter of one or two brilliant discoveries but, instead, a general advancement contributed to by many investigators. The two most formidable and practically important problems of hypersonic flow—flow with a detached bow wave

and the flow of real gases at elevated temperatures—have both given ground to a considerable degree. While the detailed understanding of these problems and the final description is always accomplished theoretically, the important role of experiment in defining the importance of various effects and in pointing out the existence of new effects should not be underestimated. It is significant that experimental facilities have made rapid strides within this same time period, increasing their speed capabilities by a factor of approximately 3, and now reaching speeds in the range of 36,000 to 40,000 ft/sec.

Although flow in the vicinity of a blunt nose is frequently viewed as *the* hypersonic flow problem, other problems are of interest and have received attention, including the flow field downstream of a blunt nose, such as would occur along a cylindrical surface preceded by a blunt nose, or in the wake of a blunt-nosed entry body; flow over stabilizing surfaces and controls; and flow over pointed cones. Recently, interest has developed also in the hypersonic flow of gases other than air. Several of these topics will be discussed at least briefly in this paper.



The theoretical methods which have been applied to these problems include some approximate methods, one of which, blast-wave theory, deserves special mention as an important first-order description of the basic hypersonic flow phenomenon, although, as will be seen, it is not quantitatively accurate at the present state of its development. The Newtonian impact theory, certainly the most widely used theory for hypersonic flow, must also be considered. A more general appreciation of the limitations of this theory is needed. Because of its simplicity, it has been somewhat wantonly applied in the recent past to problems where it is not applicable; as with any other theory, it is important to understand where the impact theory can and cannot be used.

The more exact methods of solutions applied to the blunt-body problem and to real-gas flow problems, in general, are invariably numerical solutions of the equations of motion, usually performed with an electronic computer. Although a number of techniques have been applied to obtaining these solutions, emphasis will be given to one of these, the mathematically simple stream-tube methods.

#### BLAST-WAVE THEORY, BOW WAVE PROFILES, AND AXIAL PRESSURE DISTRIBUTIONS

Let us begin our detailed considerations by examining the broad picture of hypersonic flow downstream of a blunt nose as given by the blast-wave theory. It will be of interest to compare this picture with experimental information and the results of more exact theory. The blast-wave theory, developed by G. I. Taylor in England and by L. I. Sedov in the U.S.S.R. (refs. 1 and 2), was originally written to consider the problem of the strong shock wave (generated, for example, by a nuclear explosion) and resulting disturbance within the wave. This problem was idealized by these authors to the case of a gas with a constant ratio of specific heats,  $\gamma$ , and the strong shock-wave approximations were employed. The application of blast-wave theory to hypersonic flow problems was suggested by W. Hayes, who pointed out that the radial growth of a cylindrical blast wave with time could be related to the rate of growth with distance behind the nose

of the bow shock wave generated by a blunt-nosed body in hypersonic flow. The case of a cylindrical blast wave was treated in this country by S. C. Lin (ref. 3), who applied Hayes' transformation to obtain the following equations for the bow-wave profile and the axial pressure distribution for a constant  $\gamma=1.4$ .

$$\frac{r_s}{d} = 0.80 C_D^{1/4} \left( \frac{x}{d} \right)^{1/2} \quad (1)$$

$$\frac{p}{p_\infty} = 0.0692 \frac{C_D^{1/2} M_\infty^2}{x/d} \quad (2)$$

The first equation predicts that the bow wave will be a paraboloid of revolution. Two characteristics of this equation should be noted. One is that the bow waves described are insensitive to nose shape, depending only on the one-fourth power of the drag coefficient. Second, the equation is deficient in that the waves do not approach their known asymptotic slope, the tangent of the Mach angle, except at infinite Mach number. The second equation gives the interesting result that pressure on a cylindrical body following a blunt nose is a rapidly increasing function of Mach number, predicting, e.g., a pressure of  $13.8 p_\infty$  at  $M_\infty=20$  for a point 2 diameters behind a nose with a drag coefficient of 1. From the standpoint of the cylindrical explosion, this high pressure may be explained by saying that the energy of the explosion is at this station confined to such a cross section as to maintain the high pressure. An aerodynamicist might prefer to say that the high pressures of the nose region have carried over onto the cylinder.

The work of Sedov (ref. 2) and that of Sakurai (ref. 4 reviewed and summarized in ref. 5) indicates that the constant coefficients in Lin's equations (1) and (2), which are restricted to  $\gamma=1.4$ , are more properly functions of  $\gamma$ . These coefficients are also given in general form for any constant value of  $\gamma$  in reference 6.

But how accurate are these predictions? In figure 55-1 a comparison with experiment and more exact theory is shown. In figure 55-1(a) Lin's equation is compared with a correlation formula given by Van Hise (ref. 7) for a gas with constant  $\gamma=1.4$ . The Van Hise formula is based on a correlation of pressure distributions

# RECENT INFORMATION ON HYPERSONIC FLOW FIELDS

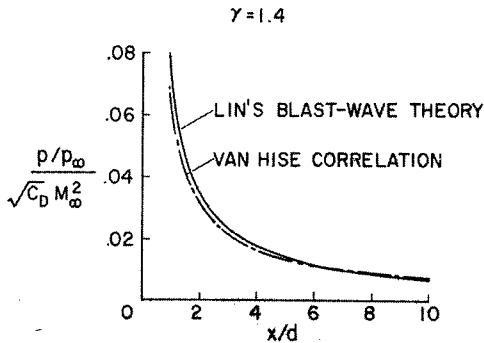


FIGURE 55-1 (a).—Pressure distributions given by blast-wave theory and exact theory for very high Mach number.

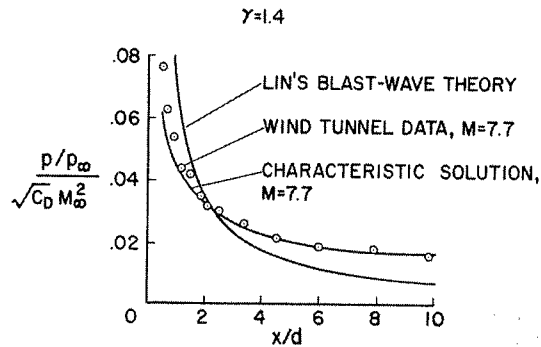


FIGURE 55-1 (b).—Pressure distributions given by blast-wave theory, experiment, and exact theory at  $M_\infty = 7.7$ .

obtained by the method of characteristics for pointed bodies, shown in figure 55-2. The Mach numbers are for the most part, greater than 20, and the data plotted are restricted to the region beginning approximately four nose lengths downstream of the shoulder. The agreement between Lin's formula and Van Hise's correlation is exceptional. In figure 55-1(b) the blast-wave pressure distribution is compared with a wind tunnel experiment for a Mach number of 7.7 (ref. 8). While these data and the characteristics solution performed by Inouye and Lomax for the same conditions as the experiment (ref. 9) show the type of behavior called for by blast-wave theory, agreement is not quantitative. This may perhaps be a consequence of the Mach number being too low. In figure 55-1(c), the blast-wave theory is compared with a real-gas flow-field solution for a speed of 20,000 ft/sec (ref. 10). Again,

agreement is only qualitative, perhaps because of a violation of the assumption of constant  $\gamma = 1.4$ . This is a representative current picture of comparisons of the blast-wave pressure distribution with experiment and more exact theory—it is qualitatively correct, but quantitatively frequently in appreciable error. The basic description of the flow field provided by blast-wave theory is correct, however, to a first order of approximation, and the validity of the view that the blunt-nosed body at hypersonic speed may be considered as a cylindrical explosion phenomenon is confirmed.

Also shown in figure 55-1(c) is a predicted bow wave compared with an experimental bow wave at a Mach number of 15. About the same type of comparison is obtained as in the case of the pressure distributions. If the waves are made to start at the same origin, the theoretical wave intersects and passes through positions

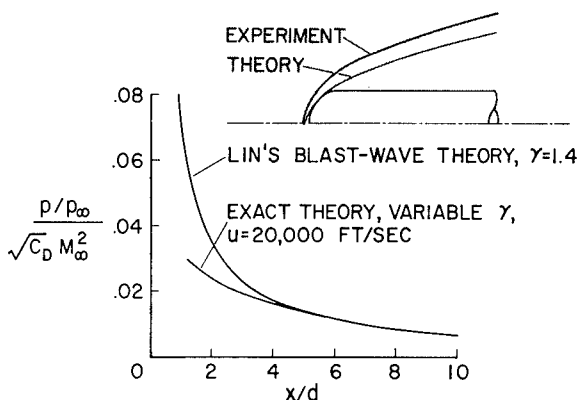


FIGURE 55-1 (c).—Pressure distributions given by blast-wave theory and exact theory for real air.

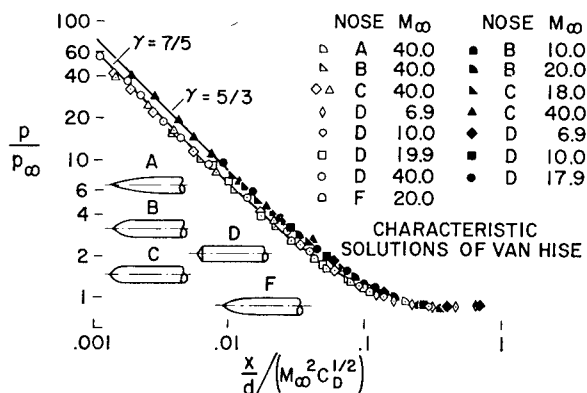


FIGURE 55-2.—Correlation of body-surface pressures by use of blast-wave variables.

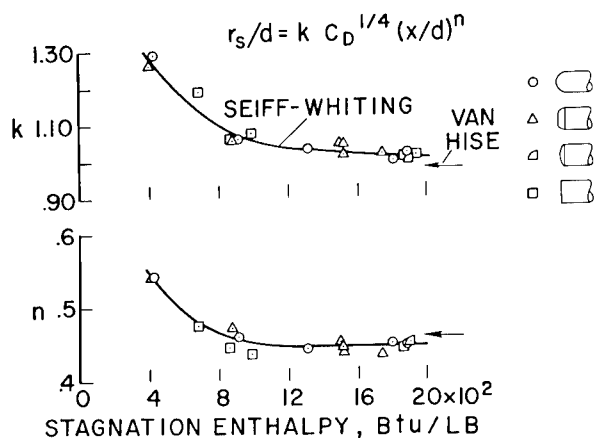


FIGURE 55-3.—Correlation of bow-wave profiles by use of blast-wave variables.

occupied by the body, which is clearly impossible. However, it is found that the form indicated by blast-wave theory for the wave equation is very suitable for describing experimental shock waves, with only minor alterations in the coefficients and exponents. The latter can, in fact, be correlated as a function of a stream total enthalpy (ref. 11). Such a correlation is shown in figure 55-3. It is particularly noteworthy that the one-fourth power dependence on drag coefficient successfully brings together data from the set of blunt noses shown in the figure, which show appreciable variations in both wave profile and drag coefficient. Although the exponents and the coefficients obtained differ importantly from the theoretical values for quantitative purposes, they are of the theoretical magnitude.

The above correlations are restricted to the region "not too close" to the body nose. In the nose region, as noted above the hemispheres, the theoretical bow wave intersects and passes through the body nose. Experimentally, the wave profile in the nose region is smooth and continuous and never intersects the surface. A detailed comparison of the blast-wave shock profile and some experimental nose-region profiles is shown in figure 55-4 for a pair of highly blunt noses. Since the experimental bow-wave profiles necessarily lie outside the theoretical, it may be said that the wave growth in this region is forced by the nose profile, rather than being allowed to take the "natural" growth curve of a cylindrical blast wave.

It is interesting that a two-line fit to the shock-wave coordinate data on logarithmic paper yields a very adequate description of the wave ordinates in this figure (ref. 11). The nose-region power law expression for the bow wave has a smaller exponent than that for the downstream region. The exponent tends to be further reduced by decreasing the shock-wave standoff distance. This may be interpreted as an approach to a step wave, for which the exponent would be zero. Where the theory is violated as a result of the nose forcing the rate of wave growth, the pressures predicted must also be in error and only become valid 2 or 3 diameters downstream.

In the region to which blast-wave theory may be applied, the following technique has been used to obtain the flow-field properties throughout the disturbed flow with considerably improved accuracy over blast-wave theory (ref. 12). The bow-wave profile is taken from the correlations described by figure 55-3. A pressure distribution in the radial direction mathematically similar to that given by blast-wave theory is assumed. The value of the static pressure at the bow wave is calculated from the wave slope, and the body surface pressure is determined from a numerical integration to satisfy continuity of flow through the cross section considered. This technique is comparatively easy to apply and has in some cases led to excellent agreement with the results of more exact calculations, as shown in figure 55-5. The profiles of density, temperature, and velocity ob-

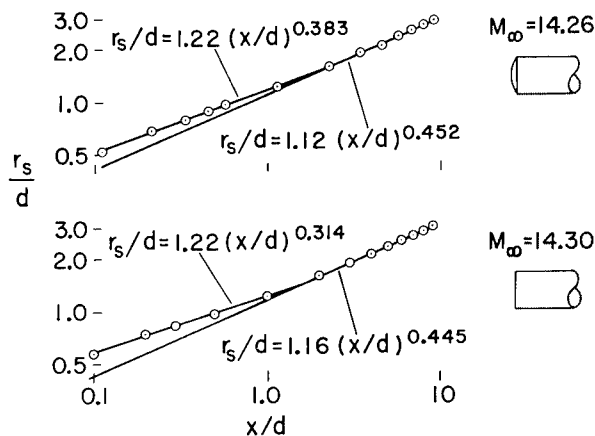


FIGURE 55-4.—Relation of nose region and downstream bow waves of very blunt bodies.

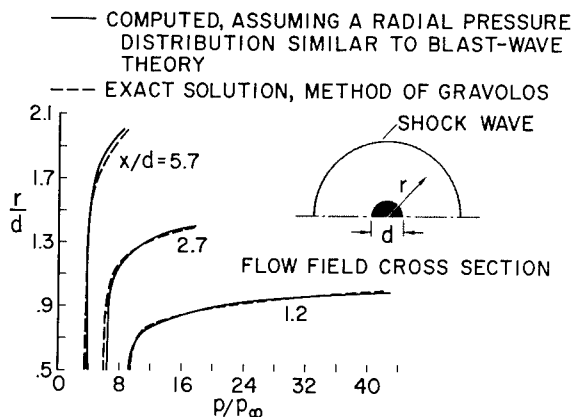


FIGURE 55-5.—Improvement of the blast-wave solution by use of correlated experimental shock wave.

tained in this case are in as good agreement with exact theory (from ref. 10) as the pressure profiles shown. It should be expected, however, that whenever the form of the pressure distribution in the cross section differs from that given by blast-wave theory, the accuracy of the computed properties would deteriorate.

## FLOW IN THE NOSE REGION OF BLUNT-NOSED BODIES

### Limitations of Newtonian Impact Theory

Turning now to consideration of the flow in the nose region of blunt-nosed bodies, we may begin by noting that this is the problem to which the Newtonian impact theory most properly applies. The flow described by impact theory is one in which the component of free-stream momentum normal to the body surface is lost while the component parallel to the surface is unchanged. This condition is most nearly realized in a thin disturbance layer where the flow direction is of necessity approximately parallel to the body surface. Since the predominant mechanism for altering the free-stream momentum is the bow shock wave, which for a thin disturbance layer is approximately parallel to the surface, and since it is a known property of oblique shock waves that the component of velocity parallel to the wave is unaffected by the wave, the basic conditions for impact flow obtain when the shock or disturbance layer is thin. A corollary to this state-

ment is that the basic conditions for impact flow are not satisfied unless the shock layer is locally thin and the shock wave approximately parallel to the body surface, since it cannot then be assumed that the component of momentum parallel to the surface is the same as that in the free stream.

It has long been recognized that a thin shock layer is not necessarily a uniform pressure layer normal to the body surface, since curvature of the surface dictates that the streamlines be curved and that pressure gradient exist normal to the flow direction. For convex surfaces, the pressure immediately behind the shock wave must be higher than that at the body surface. Early investigators tried to define a centrifugal-force correction to be applied to the impact theory (see, e.g., ref. 13). However, it is not correct to assume that the impact theory gives the pressure immediately behind the shock wave, for two basic reasons: (1) The shock-wave angle is, in general, greater than the body surface angle at corresponding points; and (2) even if the wave angle rather than the body angle were used in the impact pressure equation, the pressure coefficient would be in error by a factor  $1 - \rho_\infty / \rho_2$  because the momentum normal to the wave is not entirely lost at the wave. Thus, an essential shortcoming of centrifugal-force corrections is that the pressure to be corrected, that immediately behind the shock wave, is not obtained from simple impact theory. Experience has shown that these corrections are not in general successful, and the simple impact theory is to be preferred over the corrected theories. Furthermore, detailed investigations made by more exact theories show that the pressure differences from the body to the shock wave are not usually as large as 20 percent of the body surface pressure.

The impact theory equation for pressure coefficient,  $C_p = 2 (\sin \theta)^2$ , is now ordinarily modified by replacing the coefficient 2 by the pitot pressure coefficient  $C_{pt}$  to obtain  $C_p = C_{pt} (\sin \theta)^2$ . The latter form, conventionally referred to as modified Newtonian theory, insures that the pressures will be correct at and in the vicinity of the flow stagnation point.

Even in the case of the blunt-nosed body, conditions arise in which the impact theory fails

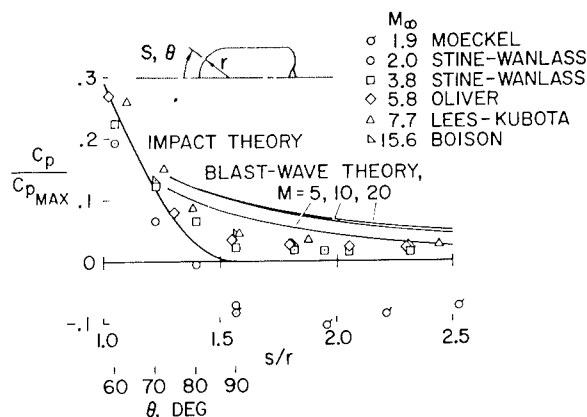


FIGURE 55-6(a).—Deviation from impact theory of pressures near the base of hemispheres.

to give the pressure distribution accurately. Two of these are illustrated in figure 55-6. (Experimental data in this figure are from refs. 8 and 14 through 17.) The first is the case of a hemisphere cylinder at high Mach number. The modified impact theory, which is by definition exact at the stagnation point, gives the pressure distribution correctly to at least  $45^\circ$  surface angle from the stagnation point. At the higher angles shown in the left part of this figure, and on the cylindrical afterbody, the errors of the theory, expressed as percent of the measured pressures, become large. A deviation of the data from the theory obviously means that the theoretical assumptions are not being met. The shock wave at these stations is departing from parallel to the surface and is gradually moving away, just as the pressures are gradually beginning to disagree. It is interesting to see how the region of the impact theory, the nose region, gives way to the region of the blastwave theory as the experimental data make a transition from one to the other. As the Mach number is increased, the level of pressures on the back part of the hemisphere tends to increase. The impact theory does not, then, give the high Mach number limit of the pressure distribution on a hemisphere.

For the region of departure of the pressure data from impact theory, it has been observed by Lees and Kubota (ref. 8) that Prandtl-Meyer expansion equations relating stream angle to pressure can be used to estimate the pressures.

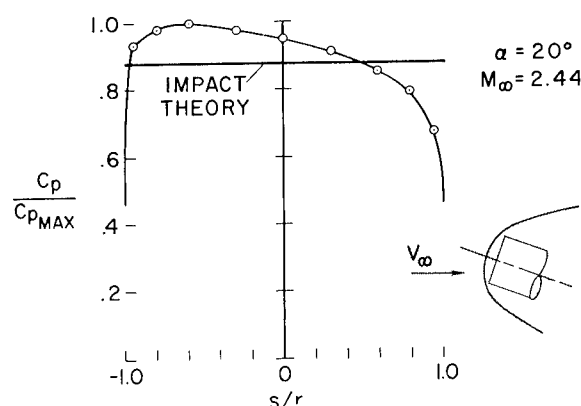


FIGURE 55-6(b).—Deviation from impact theory of pressures on a flat face at angle of attack.

The second example in figure 55-6(b) is of interest and importance to entry vehicles which, like the Mercury and Apollo, have essentially flat faces. The impact theory predicts for this case a uniform pressure over the face, as shown. Experiment (unpublished wind-tunnel measurements by Stalder and Seiff) shows an appreciable variation in pressure, which is maximum near the leading corner, as might be expected intuitively. This failure of the theory is again attributable to an inadequate description of the shock wave, which should ideally be plane and parallel to the face. A more realistic shock-wave profile is shown sketched. It is interesting that the eccentricity of the experimental pressure distribution is responsible for a thin disk being statistically stable in flight with its flat face normal to the flight direction.

#### More Exact Theory

Since the impact theory is unfortunately unable to quantitatively describe in all cases the flow over a blunt nose, more exact theories are required. Certainly, fundamental interest in such flows also leads to more detailed investigations. This problem has attracted much interest and attention in the last 10 years, and a number of methods of attack have been described and applied. These have been well summarized in the textbook on Hypersonic Flow Theory by Hayes and Probstein (ref. 6), and it will not be the purpose of the present paper to repeat this summary. The writer would, however, like to indicate what in his opinion is

the present state of this field of investigation, and to point out some of the significant developments.

It is important to note, for example, that all presently available solutions which may be referred to as exact are numerical solutions, rather than explicit functional solutions, for the flow variables. Also, the methods of solution may be classified in three groups: (1) those that seek to integrate the complete equations of motion, given the body shape; (2) those that specify a shock shape and numerically integrate the equations of motion to define the flow field and the body shape; and (3) the so-called stream-tube methods. The first group considers perhaps the most difficult problem. One of the essential boundaries of the flow, the shock wave, is initially unknown in shape and position. Computational difficulties arise near the sonic line, and the computations are, in general, quite complex and intricate. Accordingly, very few solutions by these techniques have been published. The second group, by specifying the shock wave, and finding the body shape as a result of the computation, raises the objection that one cannot directly solve the problem of a particular body shape which may be of immediate interest. Also, for certain ranges of conditions, the body shape is very sensitive to small changes in the shock-wave shape. This is particularly true for nearly flat faced bodies. Computational difficulties initially associated with this approach have been overcome at least for the case of the ideal gas (refs. 18 and 19).

The third method, the stream-tube method, has an essential simplicity which is at once appealing and surprising—surprising because the inherent difficulty of the blunt-body problem has become almost an axiom of our time. The principles which must be understood to apply the stream-tube method are elementary. The method is, like the others, somewhat laborious and requires iteration. It also runs into numerical accuracy difficulties for the nearly flat body, which apparently poses problems for all known methods of solution.

In the stream-tube method (see fig. 55-7), one-dimensional flow equations are applied to the individual stream tubes and the following assumptions are made:

$$(r_b + y_s \cos \theta)^2 = 2y_s^2 \int_0^1 \frac{\rho}{\rho_\infty} \frac{u}{u_\infty} (\cos \alpha) \left( \frac{r_b}{y_s} + \frac{y}{y_s} \cos \theta \right) d \frac{y}{y_s}$$

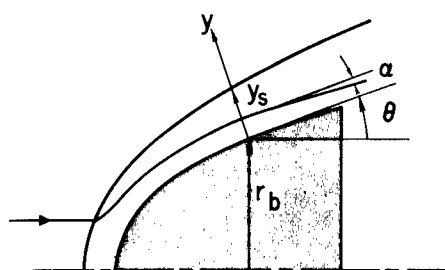


FIGURE 55-7.—Stream-tube method.

(1) The flow in each stream tube is isentropic downstream of the bow wave and has the entropy determined by the free-stream conditions and the shock-wave angle where the stream tube crosses the bow shock wave.

(2) The total enthalpy in each stream tube is a constant and equal to the free-stream total enthalpy.

(3) The pressure gradient normal to the stream tube is determined by the stream-tube curvature and is given by  $\frac{\partial p}{\partial y} = \frac{\rho u^2}{R}$ .

The Rankine-Hugoniot equations are applied at the bow wave to determine conditions immediately behind the wave. An equation of state, which for a real gas may take the form of a Mollier diagram or other graphical or tabular presentation of the relationship between the state variables, is also required.

Solutions are found at a preselected number of stations along the body surface, such as the one indicated in figure 55-7. The procedure is iterative and begins with a first approximation to the surface pressure distribution and the bow-wave shape and standoff distance. The assumed bow wave and pressure distribution are improved in successive iterations until a completely consistent set of values is obtained. The next approximation to the shock-wave contour is obtained by determining its normal distance from the body surface at each station and connecting the points so obtained. The normal distance of the shock wave from the surface must

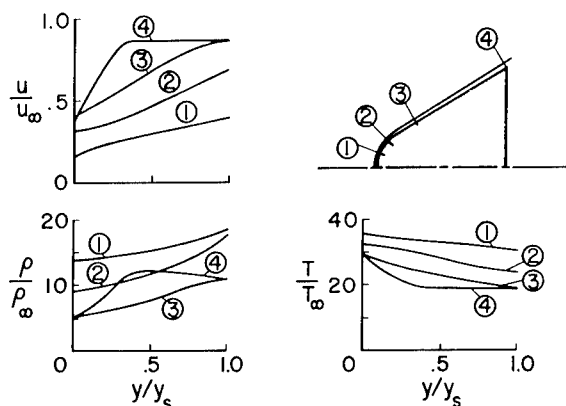


FIGURE 55-8.—Flow field computed by stream-tube method;  $\mu_\infty = 33,000$  ft/sec; altitude = 171,500 ft.

be that required to satisfy continuity of flow through the station under consideration, according to the equation shown in figure 55-7.

Solutions have been obtained by this method, with some minor variations, by a number of authors, including Maslen and Moeckel (ref. 20) and Gravalos, Edelfelt, and Emmons (ref. 21). One which has not been previously published by the present author is shown in figure 55-8, for a round-nosed  $30^\circ$  half-angle cone at a flight velocity of 33,000 ft/sec and an altitude of 171,500 feet. The shock-wave position and shape shown in the figure are drawn approximately to scale. In obtaining this solution, the cosine of the streamline inclination to the surface was taken equal to 1, and two iterations were performed to obtain a good approximation to the final shock shape. The state properties of real air at equilibrium were employed. Results of interest include the extreme thinness of the shock layer over the entire surface; the comparatively large variations within this thin layer of velocity, temperature, and density resulting from bow-wave curvature over the spherical nose; and the correspondence of flow properties in the outer part of the flow over the conical surface to pure conical flow properties at the same flight conditions.

Three-dimensional hypersonic blunt-body flows, such as those over spherical segment noses at angle of attack, have also been studied by use of stream-tube methods. Additional assumptions employed in reference 22 for this case include the following: (1) The bow shock

wave is made up of circular arc segments, meeting in tangent intersection at the point where the shock wave is perpendicular to the stream; (2) The surface streamlines are radial to the stagnation point; and (3) The average mass flow per unit area at a given station is the average of the values at the bow wave and the body surface. With these assumptions, solutions are obtained which compare closely enough with experimental observations to be considered very useful.

### Shock-Wave Standoff Distance

A quantity which has frequently been used for comparison of various theories and for comparing theories with experiment is the shock-wave standoff distance at the stagnation point, since a good quality schlieren or shadowgraph picture provides this information. The standoff distance also has practical importance for radiative heat transfer from the gas to the surface, since it determines the volume of gas available to radiate. It is now well known that the standoff distance is determined by mass conservation considerations, since, as was discussed in connection with the stream-tube methods of flow analysis, the mass flow passing between the body surface and the bow wave at any given station must match that crossing the bow wave inside that station. The principal variable affecting the mass flow ratio,  $\rho_1 u_1 / \rho_\infty u_\infty$ , is the gas density ratio,  $\rho_1 / \rho_\infty$ , since the velocity ratio is at high speeds relatively unaffected by speed, dissociation, etc. Hence, the shock-wave standoff distance for any given configuration is correlated in terms of the density ratio across the shock wave on the stagnation streamline. This type of correlation and a comparison of various theories and experiments is shown in figure 55-9 for hemispherical noses. It can be seen that the experimental points, from references 23, 24, and 19, and exact theoretical points, from references 19 and 25, define a dependence of standoff distance on density ratio that is essentially independent of other test variables. An approximate theory of Serbin (ref. 26) that fits the more exact theories very well has been included. The experimental data are observed to scatter somewhat more than do the various theories. This scatter can probably be attrib-

uted to two principal causes—light refraction effects distorting the body position, and failure of the flow to obtain complete chemical and thermodynamic equilibrium, particularly at the lower density ratios. The Van Dyke theoretical points are for a series of Mach numbers, increasing toward the origin. The Wick-Kaattari line is also for a range of flight conditions extending approximately up to the escape speed from earth. The Seiff point is from the solution figure 58-8. In the range of density ratio from 0 to 0.2, these collected data can be very well represented by the linear equation,  $\delta/R_n = 0.78 \rho_\infty/\rho_1$ . According to reference 25, this figure is applicable not only to complete hemispheres but also to spherical segments with arc half angles greater than about  $39^\circ$ .

It is important to note that shock waves in monatomic gases, such as helium, are limited to density ratios greater than 0.25, which is the density ratio for a normal shock wave in ideal air at a Mach number of 3.16. Hence, the bow shock wave in helium tests will never approach closer to the body than it does in air at a Mach number of 3.16.

Shock-wave angles in cone flow are analogous to shock-wave standoff distances in blunt-body flow. It is appropriate to refer to the angle between the bow wave and the surface as the shock-wave standoff angle. This angle is determined by mass flow considerations and may be estimated on this basis (ref. 27).

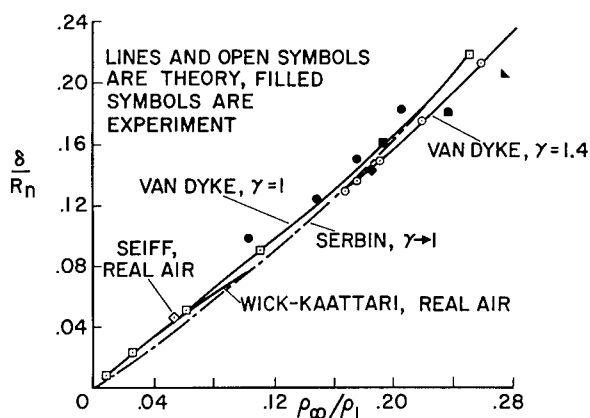


FIGURE 55-9.—Correlation of shock wave standoff distance with density ratio at the shock wave for spheres.

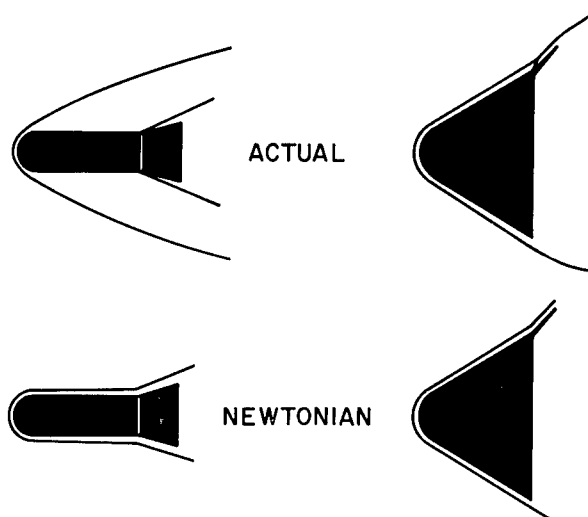


FIGURE 55-10.—Hypersonic flow configurations.

### THREE FURTHER TOPICS

#### Embedded Flows

Most early considerations of hypersonic flow did not include within their scope complex effects such as are conventionally considered in airplane design including wing-body interference. However, it is now clear that such effects can and do arise. It is particularly necessary to consider the flow-field interference when an aerodynamic element, such as a stabilizer or control, is located in a supersonic region of a hypersonic disturbance field. Two examples of such flows are indicated schematically in figure 55-10. The flow configuration, as it is now known, is shown in the upper part of the figure, while that predicted according to impact theory is shown in the lower part. On the left, two differences between the flow configurations may be noted: (1) The degree to which the bow shock wave confines the disturbed flow to a thin layer is far less for the actual flow than the Newtonian, and (2) since the flow approaching the stabilizer is supersonic, it generates a secondary shock wave, an embedded flow field. On the right, the actual bow shock wave meets the requirements for Newtonian flow, but since the surface Mach number at the base is supersonic, again, an embedded shock wave occurs on the flap.

The existence of the embedded flow field clearly indicates that the pressures on the de-



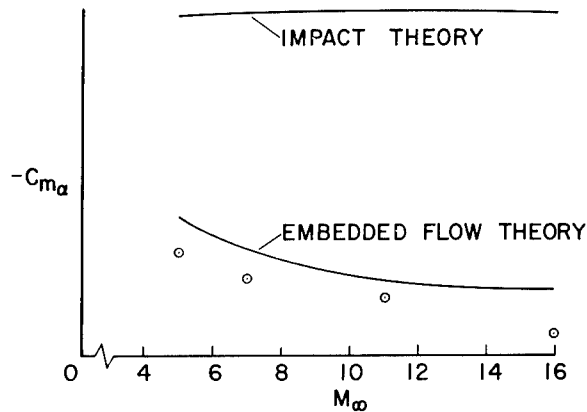


FIGURE 55-11.—Hypersonic flight stability of blunt-nosed flare-stabilized bodies.

flected surface must be analyzed in terms of the local conditions ahead of that surface. In reference 28, the use of a Newtonian approximation based on local flow conditions ahead of the flare or flap is proposed. Available data show that the accuracy obtained by this approach is about the same as the Newtonian theory normally obtains when applied to usual blunt-body problems. This type of calculation can be used to estimate pressures, normal force, and stability.

The interactions under discussion produce some large and surprising effects. For example, in the case of bodies like those shown at the left in figure 55-10, stability variations with Mach number occur in the hypersonic range, where it has conventionally been assumed that Mach number effects would not occur. One example of this is shown in figure 55-11. A comparison of the measured stability with impact theory and with embedded flow theory shows that impact theory is grossly in error, while the embedded impact flow model gives a reasonable approximation to the stability. In the case of the flap problem shown by the sketches on the right in figure 55-10, the effects obtained are illustrated in figure 55-12. A large variation in surface pressure on the flap with distance from its leading edge is calculated to result from variations in local flow variables through the shear layer on the parent body presented in figure 55-8. Surface pressure coefficients approach 5 compared to the Newtonian maximum of 2, because of the more efficient compression process utilizing two shock waves

of lower strength rather than the single strong shock-wave process. As is well known, isentropic compression of the free stream would yield pressure coefficients in the hundreds and thousands at hypersonic speeds. A comparison of figures 55-11 and 55-12 shows that in one case, Newtonian theory overestimates the pressures, and in the other case, underestimates them. In both cases, the errors are serious.

With the impact flow model, the effects under present consideration would not occur. The question may legitimately be asked, "Would these flow configurations tend to go to the Newtonian limit at sufficiently high speed?" The answer, as the present writer sees it, is no. Both from empirical observations and from the theoretical arguments of Oswatitsch (ref. 29), it is known that the distribution of local Mach numbers in the flow field becomes invariant with Mach number at high supersonic speeds. Hence, a locally supersonic Mach number will remain locally supersonic, and it follows that a concave corner will generate an embedded shock wave at all flight speeds, however high. Also, in light of the blast-wave theory, the bow-wave configuration shown in the upper left of figure 55-10 will continue to be the type of wave configuration at indefinitely high speed, although it may tend to approach the body somewhat as gaseous dissociation becomes complete behind the shock wave and ionization becomes appreciable, both of which effectively lower the ratio of specific heats. For conditions where the principal bow wave intersects the flap or control, Newtonian flow may be obtained on the flap in the outer portions.

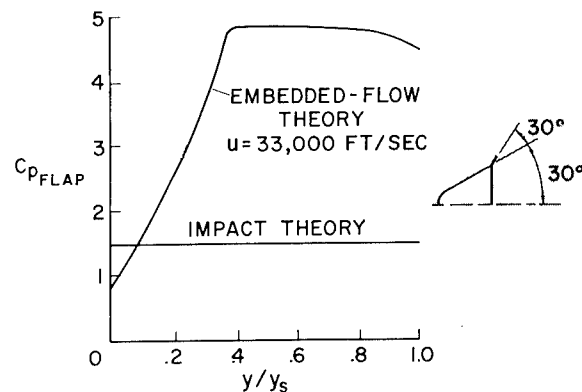


FIGURE 55-12.—Embedded flow on a flap control.

## Flows in Other Gases

Most recently, interest has developed in gas flows involving gases other than air. This is stimulated by (1) a desire to use test gases which do not liquefy when expanded to high Mach numbers, such as helium, and (2) interest in entries into the atmospheres of the planets Mars and Venus which atmospheres are usually assumed to consist predominantly of mixtures of nitrogen and carbon dioxide. The importance of the gas composition depends on which flow-field properties are under consideration and on the body shape. For cases where the Newtonian approximation is valid, pressure distribution and force produced will not depend significantly on the gas employed, since Newtonian pressure equation is independent of all gas characteristics. It may be noted, however, that air flows will tend to approach the Newtonian condition more closely than helium flows because of the thinner shock layers in air.

It has also been shown that air and helium flow will differ systematically in the regime where blast-wave theory applies, on cylinders behind blunt noses. It can be seen in figure 55-2 that afterbody pressures behind blunt noses are 10 to 15 percent higher in helium than in air, and it is also found (ref. 7) that the

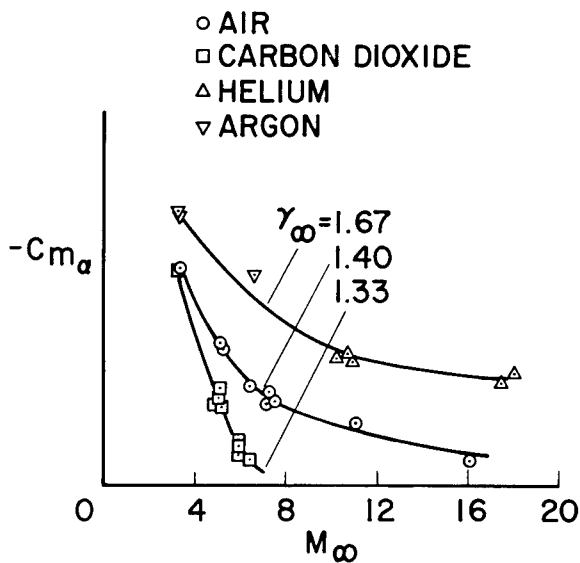


FIGURE 55-13.—Flight stability of in four gases of a blunt-nosed flare-stabilized body.

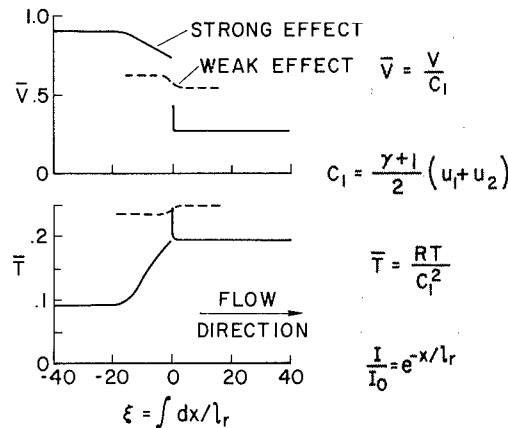


FIGURE 55-14.—Normal shock wave with radiative energy exchange.

bow-wave radius of cross section is roughly 5 percent greater in helium than in air.

Configurations which generate embedded flow fields will apparently be especially sensitive to gas composition. This is shown in figure 55-13 by a collection of data from reference 30 for a flare-stabilized blunt-nosed body. These effects on static stability are surprisingly large. They are predictable as to trend, at least, by the same method employed in the preceding figure. These results give indication of interesting problems yet to come in the gas dynamics of other gas mixtures.

## Flow With Radiative Energy Exchange

A classical assumption of gas dynamics has been the assumption of constant energy on streamlines outside of the boundary layer. The consideration of gases which are luminescent as a result of compression processes in the flow field has brought a realization that energy exchange must be allowed. Normally, one thinks first of energy loss by radiation from the high temperature gases near a stagnation point. There will, of course, also be regions of the flow for which there is a net gain in energy by radiation absorption. This is true, for example, of the gas immediately ahead of a strong shock wave.

These problems have been considered in references 31 and 32 and are also the subject of a recent study by Heaslet and Baldwin at Ames Research Center. Some results from their study are shown in figure 55-14. The problem

considered was the one-dimensional normal shock wave in a radiating and absorbing gas. Distributions of temperature and velocity, in dimensionless form, are shown as a function of dimensionless distance in the flow direction. The physical coordinate,  $dx$ , is divided by the local mean free path for absorption and integrated to obtain  $\xi$ . Two cases are shown, a weak effect, corresponding to a weak shock wave and low radiation levels, and a strong effect, corresponding to a strong shock wave and high radiation levels. The weak effect case shows a spreading out of the shock wave so that no discontinuous jump occurs in velocity or temperature. The shock wave is diffused over a distance of about four radiation mean free paths. This is analogous to the effects of viscosity or thermal conductivity in diffusing the shock surface. In the strong effect situation, the velocity shows a definite discontinuity, but also shows an upstream influence due to radiation ahead of the shock wave to a distance of about 20 mean free paths of the radiation. The temperature distribution also shows a discontinuity—an adiabatic, inviscid shock wave—and a very local overshoot jump immediately behind the wave. Although the overshoot resembles a relaxation-induced effect, nonequilibrium conditions were not included in this study, so the overshoot is purely a result of the radiative energy exchange. The over-all temperature and velocity changes obey the Rankine-Hugoniot equations and hence match the corresponding values for the case of no radiative energy exchange. Further studies in flows with radiative energy exchange will certainly be of interest and importance at very high flight speeds.

### CONCLUDING REMARKS

In this review, we have attempted to touch on some of the significant quantitative results available pertaining to hypersonic flow fields. Needless to say, it has not been possible within this brief note to describe in sufficient detail all of the important work which has been done, and some very interesting and competent investigations have had to be dismissed with just a few words. Much useful quantitative work

has been done within the last 10 years. In fact, it is true that most of today's quantitative knowledge of hypersonic flow is a product of that period.

It is somewhat of a gamble to try to predict what direction future work should or will take. One thing is certain, consideration will be given to still higher flight speeds. The phenomenon of departure from adiabatic flow has been mentioned as a future problem area. The characteristics of highly ionized flow fields will also have to be considered and evaluated. A problem that is receiving attention, but still has not been resolved to a few simple conclusions, is that of flow with nonequilibrium chemistry and thermodynamics, which tends to occur at high flight altitudes. In addition, a practically endless set of questions awaits us in the study of the dynamics of gases other than air. It seems that the next 10 years can easily be as interesting and as challenging as the 10 years just past.

### SYMBOLS

$C_D$	drag coefficient
$C_p$	pressure coefficient, $\frac{p-p_\infty}{q_\infty}$
$C_{m_\alpha}$	static stability coefficient
$d$	body diameter
$M$	Mach number
$p$	pressure
$q$	dynamic pressure, $\frac{1}{2} \rho u^2$
$r$	radius of cross section
$R$	radius of curvature
$s$	distance along surface from stagnation point
$T$	temperature
$u$	air velocity
$x$	axial coordinate
$y$	coordinate normal to body surface
$\alpha$	angle of attack, or angle between streamline and body surface (fig. 55-7)
$\delta$	shock-wave standoff distance at stagnation point
$\gamma$	adiabatic exponent, ratio of specific heats
$\rho$	air density
$\theta$	surface angle relative to free stream direction
$\xi$	dimensionless coordinate in flow direction, figure 55-14

#### Subscripts:

$\infty$	in the undisturbed free stream
1	behind the bow shock wave
$b$	body
$n$	body nose
$s$	at the shock wave
$t$	total

REFERENCES

1. TAYLOR, GEOFFREY: The Formation of a Blast Wave by a Very Intense Explosion. Proc. Roy. Soc. London. Ser. A, vol. 201, no. 1065, 1950, pp. 159-186.
2. SEDOV, L. I. (Maurice Holt, ed., trans.): Similarity and Dimensional Methods in Mechanics. Gostekhizdat, SSSR. Third ed. 1954, fourth ed. 1957. Academic Press (New York), 1959.
3. LIN, S. C.: Cylindrical Shock Waves Produced by Instantaneous Energy Release. Jour. Appl. Phys., vol. 25, no. 1, 1954, pp. 54-57.
4. SAKURAI, A.: On the Propagation and Structure of the Blast Wave. I. Jour. Phys. Soc. Japan, vol. 8, 1953, pp. 662-669. II. Jour. Phys. Soc. Japan, vol. 9, 1954, pp. 256-266.
5. LUKASIEWICZ, J.: Hypersonic Flow-Blast Analogy. AEDC-TR-61-4., Arnold Engineering Development Center, Air Force Systems Command, June 1961.
6. HAYES, WALLACE D., and PROBST, RONALD F.: Hypersonic Flow Theory. Academic Press (New York), 1959.
7. VAN HISE, VERNON: Analytic Study of Induced Pressure on Long Bodies of Revolution With Varying Nose Bluntness at Hypersonic Speeds. NASA TR R-78, 1961.
8. LEES, LESTER, and KUBOTA, TOSHI: Inviscid Hypersonic Flow Over Blunt-Nosed Slender Bodies. Jour. Aero. Sci., vol. 24, no. 3, March 1957, pp. 195-202.
9. INOUE, MAMORU, and LOMAX, HARVARD: Comparison of Experimental and Numerical Results for the Flow of a Perfect Gas About Blunt-Nosed Bodies. NASA TN D-1426, 1962.
10. FITZGIBBON, SHEILA: Lines of Constant Pressure, Density, and Temperature for Real Gas in the Supersonic Flow Field About a Hemisphere-Cylinder. Program Information Release 116-248, General Electric Co., Aug. 1960.
11. SEIFF, ALVIN, and WHITING, ELLIS E.: A Correlation Study of the Bow-Wave Profiles of Blunt Bodies. NASA TN D-1148, 1962.
12. SEIFF, ALVIN, and WHITING, ELLIS E.: Calculation of Flow Field From Bow-Wave Profiles for the Downstream Region of Blunt-Nosed Circular Cylinders in Axial Hypersonic Flight. NASA TN D-1147, 1961.
13. GRIMMINGER, G., WILLIAMS, E. P., and YOUNG, G. B. W.: Lift on Inclined Bodies of Revolution in Hypersonic Flow. Jour. Aero. Sci., vol. 17, no. 11, Nov. 1950, pp. 675-690.
14. MOECKEL, W. E.: Experimental Investigation of Supersonic Flow With Detached Shock Waves for Mach Numbers Between 1.8 and 2.9. NACA RM E50D05, 1950.
15. STINE, HOWARD A., and WANLASS, KENT: Theoretical and Experimental Investigation of Aerodynamic-Heating and Isothermal Heat-Transfer Parameters on a Hemispherical Nose With Laminar Boundary Layer at Supersonic Mach Numbers. NACA TN 3344, 1954.
16. OLIVER, R. E.: An Experimental Investigation of Flow Over Simple Blunt Bodies at a Nominal Mach Number of 5.8. CIT MEMO no. 26, June 1955.
17. BOISON, J. CHRISTOPHER: Experimental Investigation of the Hemisphere-Cylinder at Hypervelocities in Air. AEDC-TR-58-20, Arnold Engineering Development Center, Air Research and Development Command, Nov. 1958.
18. VAN DYKE, MILTON D.: The Supersonic Blunt-Body Problem—Review and Extension. Jour. Aero/Space Sci., vol. 25, no. 8, Aug. 1958, pp. 485-496.
19. VAN DYKE, MILTON D., and GORDON, HELEN D.: Supersonic Flow Past a Family of Blunt Axisymmetric Bodies. NASA TR R-1, 1959.
20. MASLEN, S. H., and MOECKEL, W. E.: Inviscid Hypersonic Flow Past Blunt Bodies. Jour. Aero. Sci., vol. 24, no. 9, Sept. 1957, pp. 683-693.
21. GRAVALOS, F. G., EDELFELT, I. H. and EMMONS, H. W.: The Supersonic Flow About a Blunt Body of Revolution for Gases at Chemical Equilibrium. TIS R58SD245, General Electric Missile and Space Vehicle Dept., June 1958.
22. KAATTARI, GEORGE E.: Predicted Shock Envelopes About Two Types of Vehicles at Large Angles of Attack. NASA TN D-860, 1961.
23. SEIFF, ALVIN, SOMNER, SIMON C., and CANNING, THOMAS N.: Some Experiments at High Supersonic Speeds on the Aerodynamic and Boundary-Layer Transition Characteristics of High-Drag Bodies of Revolution. NACA RM A56105, 1957.

# GAS DYNAMICS

24. PAGE, WILLIAM A., CANNING, THOMAS N., CRAIG, ROGER A., and STEPHENSON, JACK D.: Measurements of Thermal Radiation of Air From the Stagnation Region of Blunt Bodies Traveling at Velocities Up to 31,000 Feet Per Second. NASA TM X-508, 1961.
25. WICK, BRADFORD H.: Radiative Heating of Vehicles Entering the Earth's Atmosphere. Paper presented to the Fluid Mechanics Panel of Advisory Group for Aeronautical Research and Development, Brussels, Belgium, April 3-6, 1962.
26. SERBIN, HYMAN: Supersonic Flow Around Blunt Bodies. Jour. Aero. Sci. Readers' Forum, vol. 25, no. 1, Jan. 1958, pp. 58-59.
27. STEPHENSON, JACK D.: A Technique for Determining Relaxation Times by Free-Flight Tests of Low-Fineness-Ratio Cones; With Experimental Results for Air at Equilibrium Temperatures Up to 3440° K. NASA TN D-327, 1960.
28. SEIFF, ALVIN: Secondary Flow Fields Embedded in Hypersonic Shock Layers. NASA TN D-1304, 1962.
29. OSWATITSCH, KLAUS: Similarity Laws for Hypersonic Flow. Tech. Note no. 16, Institutionen för Flygteknik, Kungl. Tekniska Högskolan, Stockholm, 1950.
30. SMITH, WILLARD, G., and PETERSON, WILLIAM P.: Free-Flight Measurement of Drag and Stability of a Blunt-Nosed Cylinder With a Flared After-body in Air and Carbon Dioxide. NASA TM X-642, 1961.
31. PROKOFIEV, V. A.: Consideration of the Effect of Emission of Radiation in the One-Dimensional, Stationary Flow of a Monatomic Gas. Uchenye Zapiski Moskovskogo Gosuderstvennogo Universiteta, Mekhanika, 172, 79, 1952.
32. CLARKE, JOHN F.: Radiation-Resisted Shock Waves. Sudaer no. 121, Stanford University Dept. of Aeronautics and Astronautics, Feb. 1962.

# 56. Recent Developments in the Chemistry and Thermodynamics of Gases at Hypervelocities

By Thomas N. Canning

THOMAS N. CANNING is Chief of the Hypervelocity Ballistic Range Branch, NASA Ames Research Center. He earned a B.A. degree from Stanford University in 1943 and an M.S. degree from Stanford in 1947 (mechanical engineering). Mr. Canning developed a mechanical analog for studying the dynamic stability of aircraft; he contributed to understanding of supersonic flows about bodies with fins; he devised novel techniques for hypersonic research on blunt bodies including boundary-layer transition, dynamic stability, and gas-cap radiation; he directed research on hypervelocity impact as applied to meteoroid hazard of spacecraft. Mr. Canning is affiliated with Sigma Xi.

## INTRODUCTION

The day has long since passed when the aerodynamicist working on problems of hypersonic flight could ignore the effects of fundamental physical changes that occur in air at high temperatures. The successive complications that arise beyond those presented by ideal gases, which have translational and rotational degrees of freedom, result from vibration, electronic excitation, dissociation, formation of new molecules, and ionization. The varying rates at which these phenomena occur produce additional complications. The fundamentals of at least a part of these processes are well in hand; for example, the thermodynamic properties of air and other gas mixtures at elevated temperatures may be calculated with great precision.

## THERMODYNAMIC AND CHEMICAL PROPERTIES

The details of the calculations and the fundamental spectroscopic work on which the entire theoretical model is based are beyond the scope of the present paper, but an outline of the steps involved may be useful. Emission and absorp-

tion spectra of constituents, such as those presented in reference 1, are used to calculate the molecular constants and, subsequently, the partition functions of the atoms and molecules of the particular system in question. The equilibrium constants used for calculating the chemical balance of all anticipated reactions are derived, in turn, from the partition functions. These calculations and the final calculations of chemical reactions are quite laborious, but can be performed, even for complex mixtures, on modern digital computing machines (e.g., ref. 2).

One illustration of results of such computations (as yet unpublished) is shown in figure 56-1. Here the mole fractions of the less common species present in hot mixtures of  $\text{CO}_2$  and  $\text{N}_2$  are shown as functions of the proportions of  $\text{CO}_2$  and  $\text{N}_2$  before heating. The reason for selecting this pair of gases was that the atmospheres of Venus and Mars may be composed principally of these two gases. Of particular interest is the production of considerable cyanogen and free carbon, which might result in a significant increment of radiative heating of bodies entering such atmospheres.

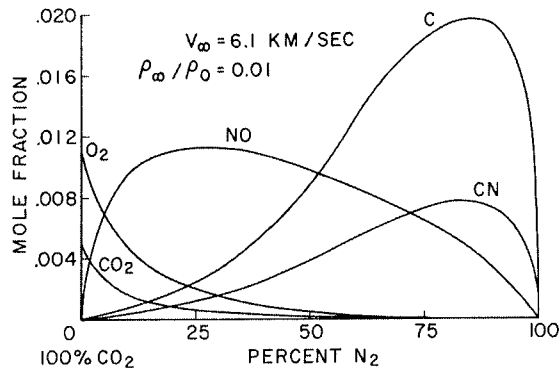


FIGURE 56-1.—Minor-constituent mole fractions behind a normal shock wave in mixtures of nitrogen and carbon dioxide.

### TRANSPORT PROPERTIES

The results of the calculations of thermodynamic and chemical properties are straightforward and quite precise, and probably will not require important revision. On the other hand, the transport properties, thermal conductivity, viscosity, Prandtl number, and Lewis number, are not as secure because the details of collisions of the gas particles are not well known.

Efforts have been made, nonetheless, to estimate for engineering purposes the transport properties of air (e.g., Hansen, ref. 3). Some experimental shock tube measurements of thermal conductivity of air have been obtained by Peng and Ahtye (ref. 4). Maecker (ref. 5) has reported conductivity measurements in arc-heated nitrogen.

Peng and Ahtye used the hot stagnant column of gas at the end of a shock tube as shown in figure 56-2. The flow in the shock tube is produced by rupturing a diaphragm, not shown, which separates the driver gas, usually helium, from the driven gas, air. A strong shock wave traverses the length of the air chamber and accelerates the air to high speed. Since the shock tube is closed, the air is stopped by the tube end, and a shock wave passes back through the air producing a hot stagnant region. The equilibrium temperature and density of this air may be accurately calculated from the shock velocity and pressure records. After reflection of the shock wave from the end plate, which contains a thin-film resistance thermometer, there is a transient heat flux from the hot air into the

plug. Although the heat-flow rate diminishes rapidly with time, the temperature of the gage surface remains constant at that intermediate temperature to which it jumped, as shown in the inset sketch, until turbulence from the driver gas introduces forced convection. At this time the heat-transfer rate increases and the gage temperature rises. The amount of the temperature jump at the gage surface is a direct measure of the air conductivity integrated over the temperature range between that at the gage surface and the highest air temperature. This feature of the experiment makes the results insensitive to small changes in conductivity at high temperatures because the high resistance to heat flow in the cool air next to the gage tends to dominate the process. Therefore only the integrated theoretical conductivity may be compared to the experimental results.

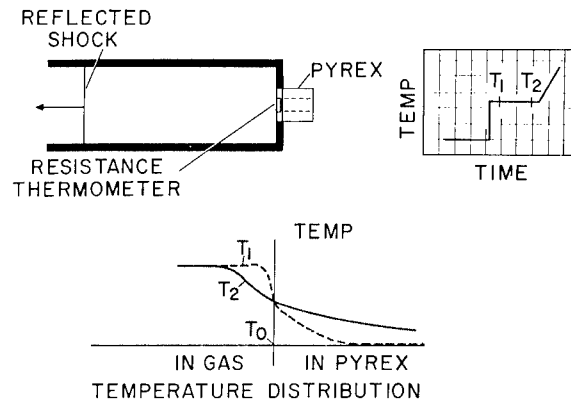


FIGURE 56-2.—Schematic diagram of measurement of integrated thermal conductivity of air in a shock tube.

The integrated thermal conductivity determined experimentally by Peng and Ahtye (ref. 4) is presented in figure 56-3, in the nomenclature of that paper, for comparison with the predictions of Hansen. The agreement observed is quite satisfactory. Any other measurement of heat transfer from gases or liquids to walls also may be used to evaluate the effective conductivity, provided the correct model for heat transfer is used in analyzing the data. Thus the multitude of published shock-tube measurements of heat transfer to models exposed to moving gas, as opposed to the stag-

nant gas samples used by Peng and Ahtye, also may be used to evaluate effective conductivity. The attractive feature of the stagnant-air tests is the simplicity and exactness of the heat-transfer model.

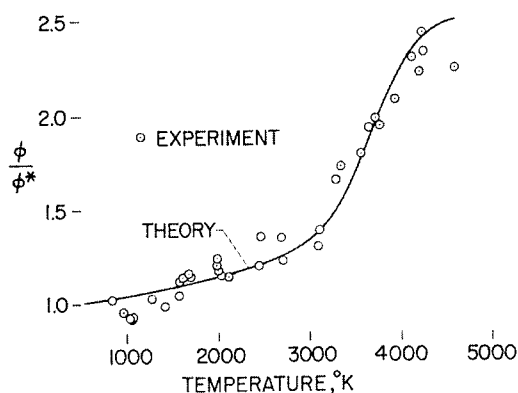


FIGURE 56-3.—Comparison of experimental and theoretical integrated thermal conductivity of shock-heated air.

A radically different experimental approach to this problem which yielded local values of conductivity at high temperature was made by Maecker (ref. 5). He measured the temperature distributions in and near an arc in nitrogen and related the derived gradient at a particular radius to the energy flux from the volume within that radius. The experimental arrangement is shown in figure 56-4. A steady direct-

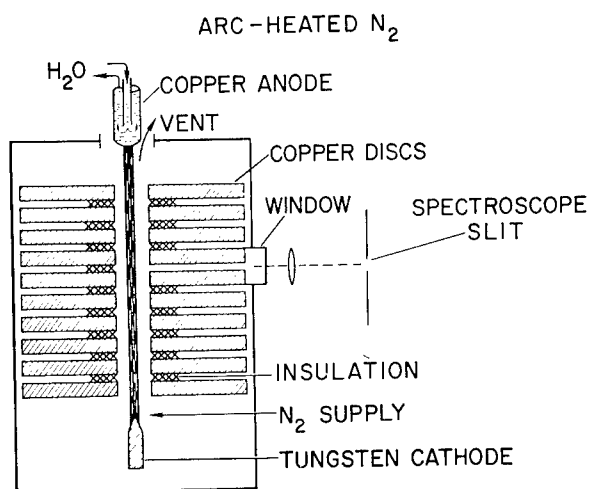


FIGURE 56-4.—Schematic diagram of measurement of local conductivity of nitrogen in an arc.

current arc is struck between cathode and anode along a slender channel through a series of cooled copper discs. When steady conditions were obtained, the energy flux per unit of arc length was determined by measuring the arc current and the voltage drop between adjacent insulated copper discs. Since the gas bulk velocity in the apparatus was low, the mechanism of heat flux to the walls was assumed to be laminar conduction (including diffusion of reactive gases) and not forced convection. Radiative effects were also small.

Temperature distributions deduced from emission spectra are presented in figure 56-5.

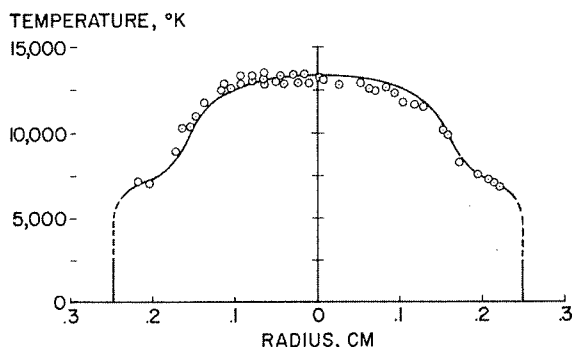


FIGURE 56-5.—Spectrographically measured temperature distribution in and near a direct-current arc in nitrogen.

The low temperature derivatives near the center attest to the exceedingly high thermal conductivity; similarly, the flat portion at 6000° K shows a peak in conductivity. The quantitative results of these tests in  $N_2$  are shown in figure

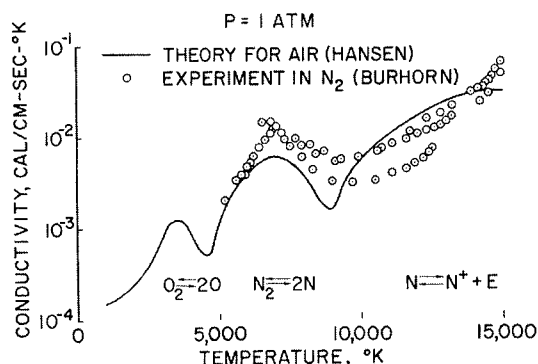


FIGURE 56-6.—Variation of thermal conductivity of nitrogen and air with temperature.



56-6 for comparison with Hansen's prediction for air. The peaks of conductivity correspond to temperature ranges where the rate of formation of the new products noted in the figure with increasing temperature is a maximum. If Hansen's calculations are repeated for pure nitrogen, the peak at 3000° K disappears.

The reason for interest in the thermal conductivity of air and other gases arises naturally from the problem of estimating the aerodynamic heat loads on hypervelocity bodies. Some of the consequences of differing conductivity at high temperatures are discussed by Goodwin (ref. 6).

### RADIATIVE PROPERTIES

Another consequence of the excitation of internal degrees of freedom is that if the excited particles return to lower energy states, spontaneously, rather than by virtue of collisions with other particles, they emit radiant energy. At high speeds, this radiation becomes an important part of the heat transferred to body surfaces. In addition to the radiation from hot air within the shock layer, we observe copious radiation from material ablated from heat shields as well. Most of the work done to date by NASA, however, concerns the radiation from air.

The theory of emission of radiant energy from thermally excited atoms and molecules has long been under intensive study and is the subject of many papers. Several such papers (refs. 7, 8, and 9), which are in only reasonable agreement, give values of emissivity of air in chemical and thermodynamic equilibrium at high temperatures for a wide range of densities. These papers are based, in turn, on earlier studies of the chemical constituents of air under the required conditions and on investigations of the particular processes controlling the amount and spectrum of the radiation due to each constituent. The details of these estimates are beyond the scope of the present paper, but predictions from reference 8 of the total radiation per unit volume are shown in figure 56-7 for a broad range of density and velocity. Results derived from references 7 and 9 agree, for the most part within a factor of 2, with those shown in figure 56-7.

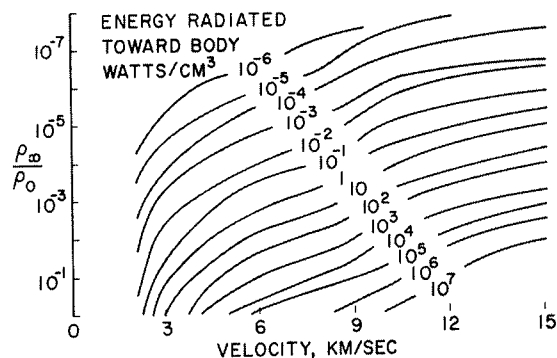


FIGURE 56-7.—Stagnation point equilibrium radiation.

Most of the experimental and theoretical air-radiation work done by industrial and university researchers (e.g., refs. 7-10) has been based on shock tube work while most of that done by NASA at Ames has been done in ballistic-range facilities, reference 11.

The facilities used for the ballistic investigations include small-caliber light-gas guns having muzzle velocities up to 10 kilometers per second. The models are fired into still air or into countercurrent air streams generated by shock-tube-driven wind tunnels having stream velocities up to 5 km/sec. A combined velocity of 13.4 km/sec has been obtained in one facility.

Observations of the radiation from the shock layers of the models are made with photomultiplier tubes; for measurements of the total emitted radiation, broad-band phototubes were used. In most tests several calibrated phototubes were fitted with various narrow-bandwidth optical filters for determining the spectral distribution of the radiation. Figure 56-8 shows schematically the manner in which the models were viewed by the photomultiplier tubes. The inset in this figure is a self-illuminated photograph of the model taken with a Kerr-cell camera with an exposure time of 50 nanoseconds (0.05 microsecond). The velocity of the model relative to the camera for this particular example was 7.9 km/sec. Also shown in the figure is a typical oscilloscope trace of the output of a phototube. The trace records radiation from the hot-gas cap of the model and then of the wake.

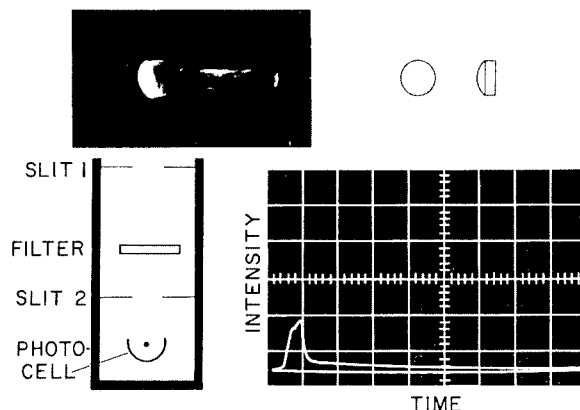
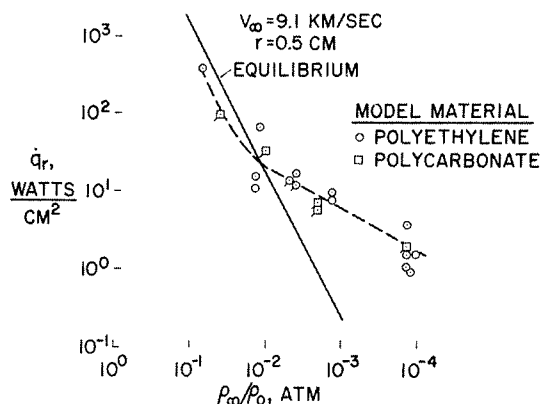


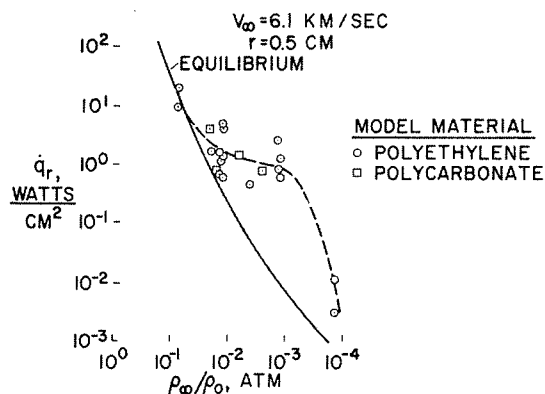
FIGURE 56-8.—Schematic diagram of measurement of radiation from shock layer and wake of hypervelocity projectiles.

Some of the experimental results from the ballistic-range tests are shown in figure 56-9(a), (b), and (c) where the experimentally deduced



(b) Polyethylene and polycarbonate.

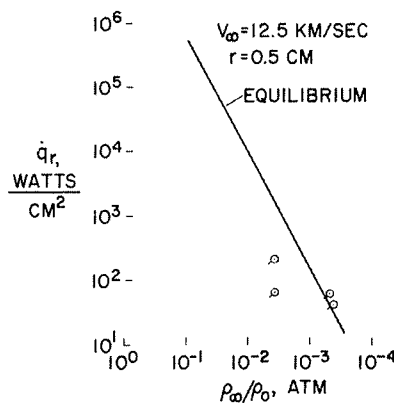
of important thickness lies between the shock-wave front and the region where the gas is in equilibrium. In one-dimensional flow behind a strong shock wave, it may be argued, following reference 12, that the temperature varies in



(a) Polyethylene and polycarbonate.

FIGURE 56-9.—Total stagnation-point radiative heating on plastic models.

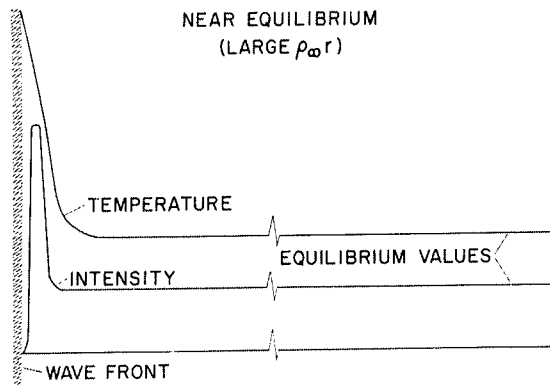
radiative flux on the stagnation regions of the test bodies is compared with predictions based on shock-tube work shown as solid lines. Clearly, the observed radiation exceeds the theoretical levels at ambient densities less than  $10^{-2}$  atmospheres for this model scale at the two lower velocities. The excess radiation is believed to result from nonequilibrium effects which arise because of the finite reaction rates in the disturbed flow field. If the air density becomes low enough, the chemical reaction rates are slowed to such an extent that a reaction zone



(c) Polyethylene only.

a manner such as that sketched in figure 56-10(a). In an exceedingly short distance behind the wave front, the translational temperature reaches a higher than equilibrium value, close to that which would be achieved by a perfect gas. Subsequently, the air relaxes toward thermodynamic and chemical equilibrium, and the temperature reduces to the equilibrium value. In this transient period, collisions produce excited particles that decay to lower states and emit radiation, apparently at rates related to the higher than equilibrium temperatures ex-

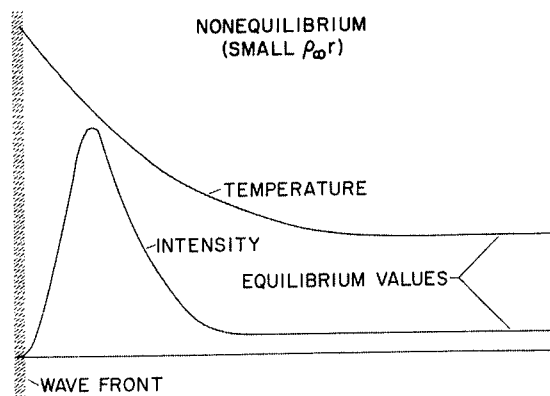
isting in this nonequilibrium gas layer. The radiative intensity therefore reaches a value greater than the equilibrium intensity and then reduces to the lower equilibrium value as the gas flows back from the shock front and relaxes to the equilibrium state. In contrast to the high density case depicted in figure 56-10(a), the situation for a lower gas density is depicted in



(a) Near equilibrium (large  $\rho_{\infty} r$ ).

FIGURE 56-10.—Schematic diagram of temperature and radiation as functions of distance behind a strong shock wave.

figure 56-10(b). The relaxation process requires a longer flow distance to achieve completion because the collision rate is reduced if the density is reduced. It can then be seen that greater and greater fractions of the shock layer in front of a body are out of equilibrium and radiate at greater-than-equilibrium radiation levels as the density of the gas in the shock layer is reduced.



(b) Nonequilibrium (small  $\rho_{\infty} r$ ).

According to the theory of reaction kinetics, the reaction rates for binary collision processes (which are thought to be controlling in the present case) vary directly with the gas density. On the other hand, the time available for the reactions to occur varies directly with the linear dimension of the flow field. Therefore, if one holds the product of these two quantities constant, that is  $\rho_{\infty} r = \text{constant}$  where  $\rho_{\infty}$  is free-stream density and  $r$  is a characteristic length of the body, such as the nose radius), the degree of completion of the chemical processes should remain similar between tests made at widely differing scales.

The abrupt reduction at still lower densities noted at 6.1 km/sec is believed to result from one, or a combination of, three effects: first, the reaction rates become so slow that the nonequilibrium radiation does not achieve its full strength before the gas expands around the body; second, the rate of depletion of the excited states by spontaneous decay to lower levels becomes important relative to the collision rate which produces the excited particles (i.e., it is self-extinguishing), and third, the viscous boundary layer becomes so thick that convection to the body reduces the shock-layer temperature and hence the radiation.

One further problem in assessing the importance of radiative heating is to predict and measure the spatial distribution over bodies of interest. The prediction of radiation distribution has been attacked by calculating the density and temperature variations within the disturbed flow fields with well-known mathematical techniques, such as those discussed in reference 13. The results of such calculations plus the existing data on the radiation from air in thermochemical equilibrium, references 7, 8, and 9, provide the groundwork for the desired estimates. Experimental verification of these estimates is presently being sought in ballistic-range tests. The experimental apparatus is illustrated in figure 56-11. An orifice plate is imaged, by means of a lens and mirror, into the path of a model which is fired along the range center line. As the projectile flies by, its image traverses the plate and is scanned by one orifice in each column. Behind each column of orifices is placed a thin strip of lucite which acts as a

wave guide for the received light. The strip conducts the light to a photomultiplier for

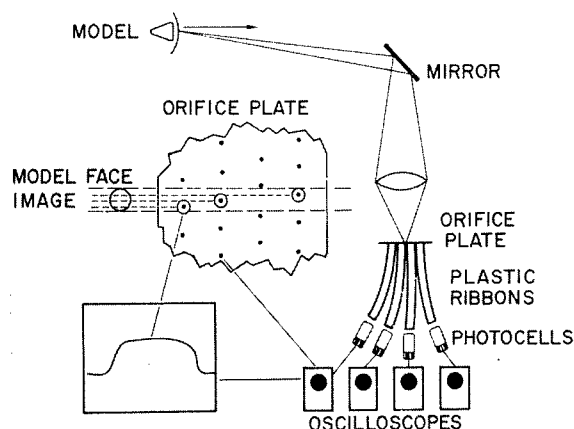


FIGURE 56-11.—Schematic diagram of image dissector for measuring radiation distribution in flow fields of hypervelocity projectiles.

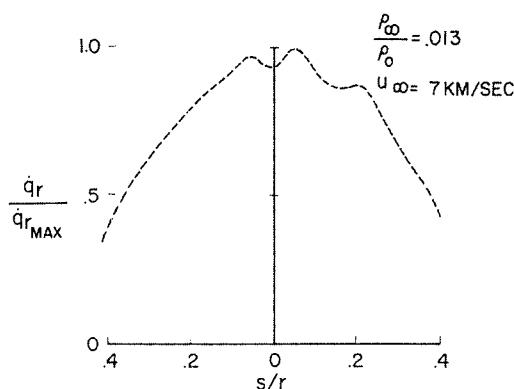


FIGURE 56-12.—Distribution of radiation from the shock layer of a blunt polyethylene projectile.

measurement and recording by an oscilloscope. The instrument sketched yields three or four traces on each test. (The vertical spacing of orifices is such that the image can pass between two holes in one column and hence yield no data.) This instrument was devised only recently and has yielded few data. One output trace showing a nearly diametric scan across a spherical model face is shown in figure 56-12.

### CONCLUDING REMARKS

All phenomena resulting from high temperatures and their practical ramifications could hardly be treated, even casually, in one paper. The implications of ionization on the thermodynamics and on the attenuation and reflection of microwave energy (the communications blackout and radar cross-section effects) are being studied intensively at many research facilities, academic, industrial, and government. Some of these problems are discussed by Huber (ref. 14). The intense radiation of ultraviolet light by gases behind the bow shock may be absorbed in the flow region ahead of the shock and may produce, in effect, a subsonic-type "warning" to the air that a body is approaching. Study of this complication has begun, as mentioned by Allen (ref. 15), but much work remains to be done.

To bring this discussion full circle, it should be stated that the continued progress in this type of work must be based on more complete understanding of the fundamental properties of the particles, such as collision cross sections, and of the processes which control reaction rates. Only with such theoretical and experimental groundwork will improved understanding and prediction of the observed phenomena be possible.

### REFERENCES

1. HERZBERG, G.: *Molecular Spectra and Molecular Structure. I. Spectra of Diatomic Molecules.* D. Van Nostrand Co., 1950.
2. ZELEZNIK, FRANK J., and GORDON, SANFORD: A General IBM 704 or 7090 Computer Program for Computation of Chemical Equilibrium Compositions, Rocket Performance, and Chapman Jouguet Detonations. NASA TN D-1454, 1962.
3. HANSEN, C. FREDERICK: Approximations for the Thermodynamic and Transport Properties of High-Temperature Air. NASA TR R-50, 1959.
4. PENG, TZY-CHENG, and AHTYE, WARREN F.: Experimental and Theoretical Study of Heat Conduction for Air Up to 5000° K. NASA TN D-687, 1961.

#### GAS DYNAMICS

5. MAECKER, H.: Properties of Nitrogen Up to 15,000° K. AGARD Rep. 324, September 1959.
6. GOODWIN, GLEN, and HOWE, JOHN T.: Recent Developments in Mass, Momentum, and Energy Transfer at Hypervelocities. Paper presented at the NASA-University Conference, Chicago, Illinois, Nov. 1-3, 1962.
7. MEYEROTT, R. E., SOKOLOFF, J., and NICHOLLS, R. W.: Absorption Coefficients of Air. LMSD 288052, Lockheed Aircraft Corp., 1959.
8. KIVEL, B., and BAILEY, K.: Tables of Radiation From High Temperature Air. Res. Rep. 21, AVCO-Everett Res. Lab., 1957.
9. BREENE, R. G., NARDONE, MARIA, RIETHOF, T. R., and ZELDIN, SAYDEAN: Radiance of Species in High Temperature Air. Gen. Electric Space Sciences Lab., July 1962.
10. TREANOR, CHARLES E., and MARRONE, PAUL V.: The Effect of Dissociation on the Rate of Vibrational Relaxation. Cornell Aeronautical Lab., Inc., Rep. QM-1626-A-4, Feb. 1962.
11. CANNING, THOMAS N., and PAGE, WILLIAM A.: Measurements of Radiation From the Flow Fields of Bodies Flying at Speeds Up to 13.4 Kilometers Per Second. NASA Paper presented to Fluid Mechanics Panel of Advisory Group for Aeronautical Research and Development, Brussels, Belgium April 3-6, 1962.
12. CAMM, J. C., KIVEL, B., TAYLOR, R. L., and TEARE, J. D.: Absolute Intensity of Non-equilibrium Radiation in Air and Stagnation Heating at High Altitudes. Res. Rep. 93, AVCO-Everett Res. Lab., 1959.
13. SEIFF, ALVIN: Recent Information on Hypersonic Flow Fields. Paper presented at the NASA-University Conference, Chicago, Illinois, Nov. 1-3, 1962.
14. HUBER, PAUL W.: Plasma Frequency and Radio Attenuation. Paper presented at the NASA-University Conference, Chicago, Illinois, Nov. 1-3, 1962.
15. ALLEN, H. JULIAN: Gas-Dynamic Problems of Space Vehicles. Paper presented at the NASA-University Conference, Chicago, Illinois, Nov. 1-3, 1962.

# 57. Recent Developments in Mass, Momentum, and Energy Transfer at Hypervelocities

By Glen Goodwin and John T. Howe

*GLEN GOODWIN is Chief of the Heat Transfer Branch, NASA Ames Research Center. He earned a B.S. degree from the University of Washington in 1942 (mechanical engineering). He was a U.S. delegate in 1960 to the International Institute of the Aerospace Sciences Conference. Mr. Goodwin is a pioneer in gas dynamics of high-speed rarefied flows; he developed fundamental concepts of hypersonic aerodynamic heating used in design of vehicles such as the X-15; he has directed analytical studies of the chemical state of the flow about reentry vehicles and its dependence on flight trajectory; and he has developed laboratory equipment for producing high-enthalpy rarefied flows. Mr. Goodwin is a member of Sigma Xi.*

## INTRODUCTION

The transfer of energy, mass, and momentum by the convective process to surfaces of high-speed vehicles has been studied intensively for many years. A large body of information has been accumulated on the behavior of boundary-layer flows in the speed range where air can be treated as an ideal diatomic gas. The high reentry speeds of space vehicles have introduced complications into these transfer processes which were not considered by the classical boundary-layer theory. These complications are: the interaction with the boundary-layer flows of dissociation and recombination, of ionization and radiation, and of foreign gases from ablation materials. It is the main purpose of this paper to review the effects of these complications on the convective energy transport process and to point out some of the many problem areas which still remain to be solved.

This paper emphasizes the studies of heating rates needed by the space program; skin friction has not been treated directly because the motion of the space vehicles is largely controlled by the

pressure drag and not by skin friction. Also, any analysis which treats heat transfer must first solve the momentum equation, and therefore, yields the surface shear forces.

## HEAT TRANSFER IN DISASSOCIATED AIR

The first complications to appear as vehicle speeds increase are dissociation and recombination. These phenomena have been treated extensively in the literature and, in particular, in the early papers of Lees and of Fay and Riddell (refs. 1 and 2). The stagnation region of a bluff body is important since it generally has the highest heating rate and is the simplest region to analyze. It is, therefore, interesting to compare the predicted and measured heating rates on the stagnation region of bluff bodies for the speed range where dissociation and recombination are the dominant new phenomena. This comparison is presented in figure 57-1. On the figure are plotted the heating rate normalized with respect to the body nose radius and the stagnation region pressure as a function of the difference between the total enthalpy and

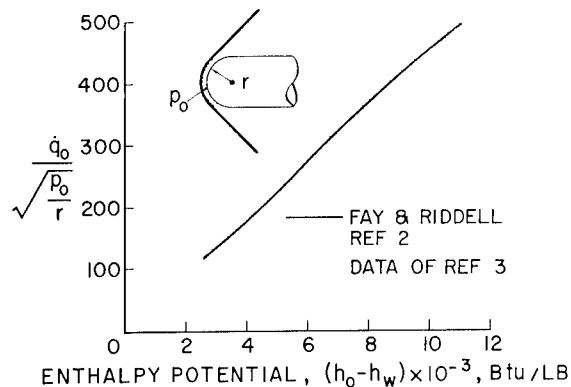


FIGURE 57-1.—Stagnation region heating—equilibrium dissociation.

the enthalpy of the wall. The solid-line curve on the figure is the heating rate predicted by Fay and Riddell (ref. 2). The shaded area represents shock tube data of reference 3. Notice that, although there is scatter in the data, the agreement between the theory and the measurements is reasonably good. A large number of measurements have been made in this enthalpy range (see refs. 4 to 6), and the general conclusion is that the prediction method of Fay and Riddell is adequate in this speed range.

Lees, in reference 1, pointed out that the heat-transfer distribution over the body at high Mach numbers could be expressed as a fraction of the stagnation heating, this fraction being mainly a function of the position along the body. A comparison of measured heating rates with the prediction of Lees for hemisphere-cylinder bodies is shown in figure 57-2. On this figure are plotted the heating rates at various positions along the body divided by the value at the stagnation point. Two sets of data are shown here. Shock tube data from reference 6 are shown as the circular symbols, and these are mostly confined to the forward region of the body. Note that the agreement with Lees' prediction is quite good. To the right of the chart is a data point representing a series of measurements at various enthalpy levels of the heating rate downstream of the shoulder of the hemisphere cylinder. Again, the theory of Lees predicts the data quite well.

In order to use Lees' theory, the details of the inviscid flow over the body must be known, but the flow fields over bodies with relatively

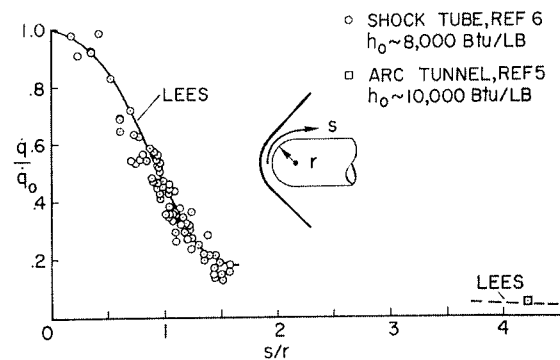


FIGURE 57-2.—Heating rate distribution.

complicated shapes cannot be easily analyzed. It is possible, however, to measure these flow details and the resulting heating rate experimentally in a conventional high Mach number wind tunnel. The distribution of the heating rate over the body determined by the wind-tunnel tests using a cold gas can then be extrapolated to high enthalpy flows using Lees' theory. My colleague John Reller has verified this method experimentally in the Ames shock tunnel to enthalpy levels of approximately 6,000 Btu/lb, which corresponds to a flight speed of approximately 12,000 ft/sec.

The two figures previously discussed have illustrated the case where the disassociation and recombination time is very short compared to the time the fluid is in the vicinity of the body; hence, the chemical reaction rates can be considered to be in equilibrium everywhere in the flow field. High heating rates are encountered at high altitudes by manned entry vehicles because the deceleration forces must be kept to tolerable levels. The combination of low density, in which the chemical reaction times are long, and high flight speeds is the condition for which one would expect the dissociation and recombination to be out of equilibrium. If the flow time is very short compared with the chemical reaction time, the chemical reactions can be considered frozen. For this condition, energy is transferred to a surface by normal convection and by atoms which diffuse through the boundary layer and recombine on the surface. The question then arises as to the effec-

tiveness of surfaces in promoting the recombination of atoms. On figure 57-3 are shown the stagnation region heating for the case where the boundary layer flow is chemically frozen. Plotted on this chart is the heating rate divided by its equilibrium value, as a function of the total stream enthalpy. Fay and Riddell have shown that if all of the atoms which diffuse to the wall recombined upon it, there would be little change in the gross heating rate to the surface whether the boundary air be frozen or be in equilibrium. This is indicated by the horizontal line. The solid-line curve labeled no recombination at the wall represents the convective portion of the heating from the frozen boundary layer, and the difference between the two curves represents the energy carried by the atoms. Silicon monoxide has a low catalytic efficiency and allows only a small fraction of the atoms to recombine. The data points shown on the figure were obtained on a silicon monoxide surface in a stream of nitrogen gas at sufficiently low pressures and high enthalpy to insure a frozen flow (see ref. 7).

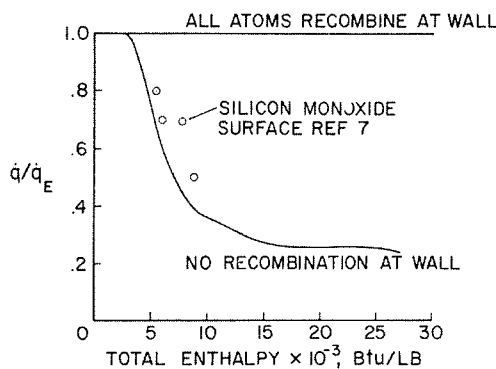


FIGURE 57-3.—Stagnation region—frozen boundary layer.

The reduction in measured heating rate agrees reasonably well with that predicted for the case where no atoms recombined upon the wall. Most metallic surfaces, however, have high catalytic efficiency, and data obtained on copper surfaces lie near the equilibrium value. The question arises as to whether ablating materials will exhibit a high or a low catalytic efficiency for this interesting phenomenon to be exploited. Teflon mass losses measured in a

high-enthalpy stream of frozen nitrogen (ref. 5) are about the same as those measured in a stream in equilibrium. This indicates either that teflon has a high catalytic efficiency or that the introduction of teflon vapors into the boundary layer speeds up the recombination reaction. It is interesting to speculate whether or not ablation materials could be found which have a low surface catalysis and, therefore, would receive considerably less incoming heat than surfaces which have been tested.

An important regime to be considered is flight at velocities and altitudes where the boundary layers are neither completely frozen nor in equilibrium. The correlation method presented in reference 8 allows one to determine whether a body is in an equilibrium, a frozen, or a nonequilibrium flight regime when the flight velocity, altitude, and vehicle size are specified. The method essentially is based upon estimating the chemical reaction time compared to the diffusion time of the atoms across the boundary layer. However, this method has not been checked experimentally.

## IONIZATION AND RADIATION

As flight speed increases above about 30,000 ft/sec., ionizing reactions take place in the stagnation region flow field. Whether or not the presence of ions and electrons in the flow has a strong influence on convective heat transfer has been the subject of considerable argument. Intuitively, one might feel that the highly mobile electrons would increase the transport of energy by diffusion. Figure 57-4

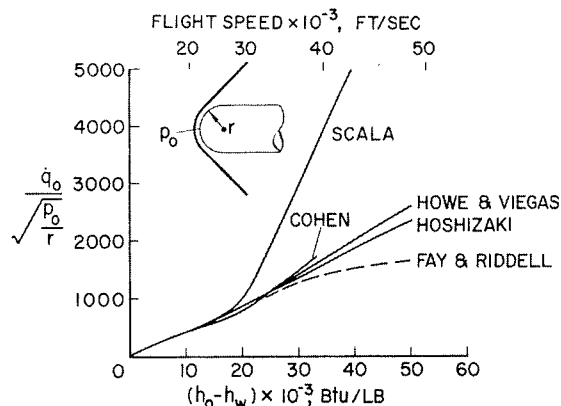


FIGURE 57-4.—Convective heat transfer with ionization.



shows the result of several theoretical efforts to predict the influence of ionization on convective heat transfer in the stagnation region of bluff bodies. Scala (ref. 9) predicts a sharp increase in convective heating at speeds above 30,000 ft/sec. The results of Hoshizaki<sup>1</sup> (ref. 4), Cohen<sup>1</sup> (ref. 10), and Howe and Viegas<sup>1</sup> (ref. 11) indicate that there is no strong ionization effect on convection. The result of Fay and Riddell (ref. 2) for Lewis number of unity is shown for reference, although ionization was not considered in their analysis. Analyses by Pallone and van Tassel (ref. 12), and by Adams (ref. 13) also predict little effect of ionization on convection. Thus, we have a striking difference between the results of Scala and those of other investigators. It appears that the difference in the theoretical results can be attributed to the different methods of treating the transport of energy of reacting species. In particular, the difference appears to be in the total thermal conductivity used by Scala compared to that used by the other investigators. Most of the other investigators have used the transport properties calculated by Hansen in reference 14. A comparison of various calculated transport properties is presented by Fay in reference 15. Theoretical and experimental work in this area is needed to allow the theoretical differences to be reconciled.

Since the theoretical work has not completely settled the question of the effects of ionization on the heating rate, it is of interest to examine the experimental results obtained in this speed range. The comparison is shown on figure 57-5 which uses the same coordinate system as the theoretical comparison. The shock tube experiments of Warren (ref. 16) are in substantial agreement with the Scala theory, while those of Offenhartz (ref. 17), Rose (ref. 3), Stankevics and Rose (ref. 18), and Hoshizaki<sup>2</sup> are in substantial agreement with the other theories (typified by Howe and Viegas). It is much more difficult to determine the reasons for the differences in experimental results than in the theoretical results. Here corrections must be

<sup>1</sup> Compared for a stagnation pressure of one atmosphere; however, little effect of pressure level is evident.

<sup>2</sup> In a private communication, Hoshizaki gives results slightly modified from those of reference 4.

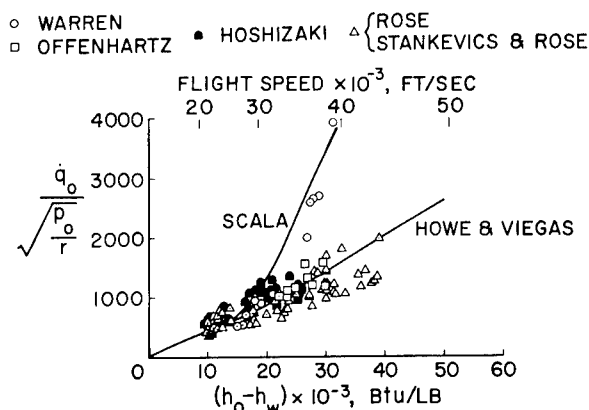


FIGURE 57-5.—Convective heating—comparison with experiment.

made for radiation from the test gas and shock tube driver gas. There is some question concerning the duration of steady-state test time and, of course, questions pertaining to instrumentation. At present, the experimental differences are unresolved, but it is emphasized that these data are very new and the problem is being actively worked on.

In all of the previous discussion, no mention has been made of another phenomenon that influences heat transfer to a large extent at severe flight conditions—a coupling which exists between convection, which is principally a boundary layer effect and gaseous radiation from the flow outside the boundary layer. An analysis by Howe and Viegas (ref. 11) of the entire stagnation region flow field from the body surface to the bow shock wave includes the effects of transport of energy by conduction, diffusion, and radiation in the flow equations. Their results as they affect convective heat transfer (for a stagnation pressure of 1 atm) are shown in figure 57-6. The dashed line represents the convective heat transfer when radiation is neglected in the flow equations. This line is relatively insensitive to changes in nose radius or pressure level and represents a general result when radiative coupling is neglected. The fan of solid lines represents the convective heat transfer when radiation losses from the shock layer are included in the flow equations. It is seen that the effect of radiative coupling reduces the convective heat transfer by about 1/2 for a body having a 5-foot nose radius.

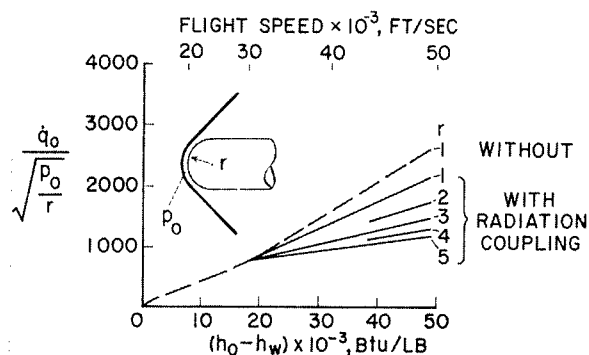


FIGURE 57-6.—Convective-radiative interaction—stagnation region.

Attempts to predict the coupling effect by simple methods have not met with success. The boundary-layer concept apparently breaks down when radiative coupling effects are considered, and the entire flow field must be analyzed. Indeed, flow fields are not clearly divided into a viscous region and an isoenergetic inviscid region characteristic of the lower speeds. This breakdown of the boundary-layer concept has also been shown to occur when the flow is not in chemical equilibrium. (See, e.g., ref. 19.) Generally, it seems that when high speeds occur at high altitudes or when radiation is the predominant form of energy transfer, boundary-layer concepts should be applied with caution.

#### HEATING RATE IN REGIONS OF SEPARATED FLOW

The preceding section of the paper has been concerned with attached flows; however, the understanding of separated flows has become important because heat transfer to a vehicle surface under a separated flow is frequently less than that to a corresponding attached flow. The Mercury and Apollo spacecraft, for example, take advantage of this fact, and a relatively large portion of the surface of these vehicles is in the separated flow field. An early analysis by Chapman (ref. 20) of the average heating in a cavity covered by a steady separated laminar boundary layer indicated that the average heating rate to the bottom of the cavity should be approximately  $\frac{1}{2}$  of its attached flow value. The prediction of this analysis was later confirmed experimentally at moderate Mach num-

bers. (See refs. 21 and 22.) Later measurements of heating rates to the base of three-dimensional bodies, shaped somewhat like the Mercury spacecraft, have been made at high Mach numbers. The results of a typical test are shown in figure 57-7 wherein the heating rate referred to the forward stagnation-point value is shown as a function of the position along the afterbody. The test was conducted in helium at a Mach number of 15. The solid line curve is the prediction of Chapman, mentioned earlier. It can be seen that this prediction agrees reasonably well with the data and indicates that the early work of Chapman can be used at high Mach numbers. In the test, the flow did not reattach on the afterbody.

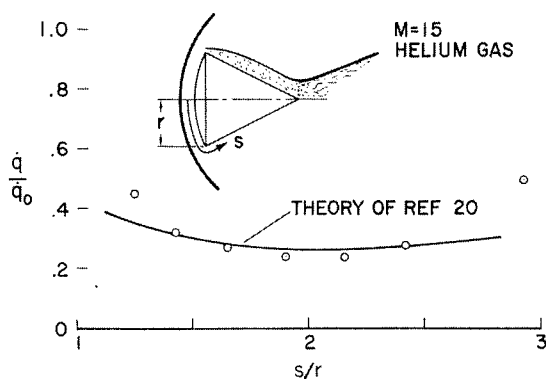


FIGURE 57-7.—Heating in separated region—laminar flow.

When the model in this particular test was positioned at an angle of attack sufficient to cause flow reattachment, the heating rate rose. In fact, the heating rate in the reattached region was higher than that corresponding to a completely attached flow. This is an expected result and has been treated analytically in reference 23 for the case where the flow reattachment angle was perpendicular to the solid surface. In essence, when the separated flow reattaches, it produces a region of high local pressure gradient on the surface, and the high boundary-layer growth rate in this area produces high local heating rates. In the same free stream these reattachment heating rates can be higher than those on a stagnation region of a bluff body with a nose radius roughly equal to the separation length.

The distribution of heating rate along a separated region is generally not analytically predictable at the present time because of our inability to specify the flow details (eddy currents, vortex systems, and flow steadiness) in the separated region. The method of reference 23 will allow heating-rate distributions to be calculated in the separated region if the main features of the flow within the region can be specified. Another problem in this general area that has received little or no attention, at least to the author's knowledge, is that of the effectiveness of transpiration or ablation cooling in a region of separated flow. These are important problems, and certainly worthy of study.

#### THE EFFECTS OF FOREIGN GASES ORIGINATING FROM SOLID SURFACES ON BOUNDARY-LAYER FLOWS

The preceding portion of this paper has treated clean air flows over reentry bodies but, in practice, the air is almost never uncontaminated. Ablation cooling systems emit a wide variety of foreign gases, and these end up in the boundary layer and in the wake of the body. Generally, little is known about the type or quantity of gas that will be given off by an ablation cooling system because of the types of materials which appear attractive as ablators. These materials are generally mixtures of plastics concocted to achieve a real or fancied result. At the present time, the problem is generally handled by measuring some gross system response, either the amount of material burned away after a timed exposure to a known heating rate or the temperature rise of a portion of a substructure protected by the particular ablation material under study. Some rational results can be obtained, however, on the effect of foreign gases on boundary-layer flows by measuring the change in the heating rate or skin friction resulting from transpiring measured amounts of gases of known properties and composition through porous model surfaces. The results of one such study made by C. Pappas of Ames are shown in figure 57-8. On this figure is plotted the heating rate divided by its value for no transpiration as a function of the transpiration flow rate per unit area times the

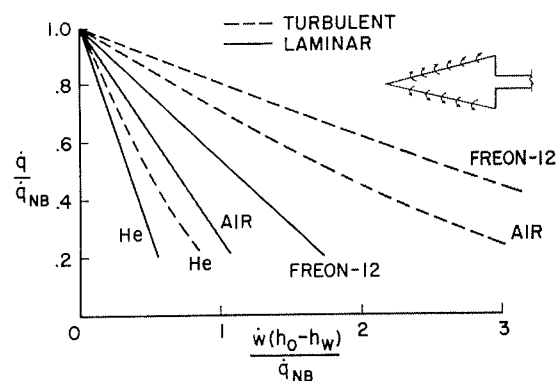


FIGURE 57-8.—Effect of foreign gas transpiration on heating rate.

driving enthalpy potential divided by the heating rate for zero transpiration. This particular coordinate system is used because it accounts for the major effects of Mach number and Reynolds number on test results of this type. For a particular flight condition, the abscissa is proportional to the weight flow of the foreign gas transpired through the porous surface. Two sets of results are shown. The solid lines are for the behavior of a laminar boundary layer, and the dashed lines are for the behavior of a turbulent boundary layer. The results of the laminar-flow tests will be examined first. Three gases were transpired: helium, a light gas having a molecular weight of 4; air, having a molecular weight of 29; and freon, a heavy gas having a molecular weight of 121. Notice generally that the light gases are more effective than the heavy gases in reducing the heating rate, and a large reduction in heating rate results from rather small transpiration rates. Typically the ratio of the mass-flow rate of the transpired gas to the mass-flow rate of the free stream per unit area is about 0.001.

The turbulent boundary layer results are not so dramatic as the laminar flow results, but the trends are similar.

At very high blowing rates from ablating surfaces the heating rates do not go to zero as indicated by a simple extrapolation of the results shown on figure 57-8. For laminar flow, high blowing rates cause transition and, for turbulent flow, high blowing rates appear to destroy boundary-layer character of the flow. It is, therefore, difficult to make any general

statements about the asymptotic values of the heating rate for very large blowing rates. Some work has been done along this line, however, and is reported in reference 24. These test results were obtained indirectly from the ablation of teflon and they show an asymptotic heating rate for laminar flow of approximately 0.18 of its no-blowing value. Work is needed to extend transpiration test results to other gases and to higher enthalpy flows.

### TURBULENT BOUNDARY LAYER AT HIGH ENTHALPIES

Theoretical predictions of the behavior of a turbulent boundary layer have depended largely upon experiment to evaluate critical assumptions, fundamentally, because the turbulent boundary layer is a more complicated phenomenon than the laminar boundary layer, and no complete solutions to the turbulent boundary-layer equations have been obtained. Progress that has been made generally resulted from transformations such as those given in reference 25 which allow one to transform turbulent compressible boundary-layer equations into their equivalent incompressible form. These transformations are valuable in that they allow the well-known low velocity profiles and the matching point between the laminar sublayer and the outer turbulent layer to be extrapolated to the compressible flow case. However, these methods give no hint of the effect of increasing stream enthalpy level on the skin friction or the heat transfer.

Historically, the effects of temperature or enthalpy level on the heating rate and skin friction produced by turbulent boundary layers have been handled by a method analogous to that used to correlate skin friction and heating rate from turbulent flows in pipes. This method uses a reference temperature intermediate between the wall surface and the bulk of the fluid at which to evaluate the fluid properties to account for temperature level effects. For the case of undissociated air at relatively high Mach numbers, the reference temperature method has been used successfully in aerodynamics to correlate experimental results of skin friction and heating rate. The methods are described and compared with experiments in references 26 and

27. At still higher flight speeds where dissociation becomes important, Eckert, reference 28, has suggested evaluating the fluid properties at a reference enthalpy, which lies intermediate between the enthalpy at the wall and the enthalpy of the gas at the boundary-layer edge. The details of this method are given in reference 29, but it is, in essence, similar to the older reference temperature method. These methods, as crude as they are, do a reasonably good job of correlating experimental data. They are, however, disappointing in the sense that they do not shed any real understanding on the basic changes in the turbulent transport mechanism with increasing enthalpy. A typical set of experimental data is compared with the reference enthalpy method on figure 57-9. On this figure are plotted the heating rate divided by the  $(R)^{4/5}$ , which is the parameter used for low-speed turbulent boundary layer flows to account for the Reynolds number variation of the data. This parameter is plotted as a function of the total stream enthalpy. The circular points are experimentally measured values of this parameter obtained in a shock tube and reported in reference 30. The reference enthalpy method of Eckert is shown as the solid-line curve. Notice that the data generally fall below the prediction as is characteristic of this method when applied at lower enthalpies; that is, the method generally is conservative and overestimates the heating rate somewhat. However, it has been found extremely useful for engineering applications.

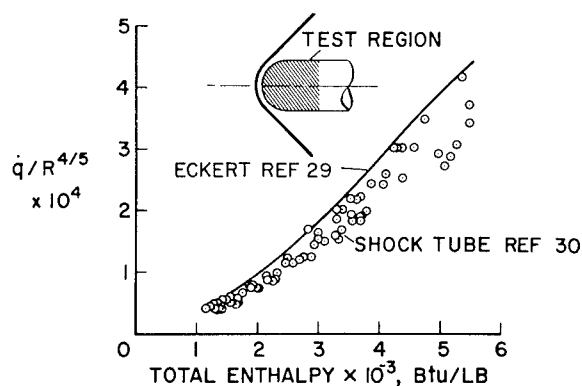


FIGURE 57-9.—Heating in turbulent flow at high enthalpy.

Further progress in the field of predicting heat-transfer rate or skin friction produced by a turbulent boundary layer awaits the development of experimental apparatus capable of producing high enthalpies at sufficiently high pressures to produce a fully developed turbulent flow.

Another problem area essentially unsolved even for low speed is the prediction of the point of transition between a laminar and a turbulent flow. Probably no other area of research in aerodynamics has received so much attention from so many people. In spite of the large amount of work expended on this subject, only a few general rules have emerged. These rules were stated by Osborne Reynolds and have remained essentially unchanged up to the present time. The rules are that if the Reynolds number is less than about 1 million, the flow will probably be laminar; if the Reynolds number is greater than approximately 10 million, then the flow will generally be turbulent. If the Reynolds number of the flow lies between these two rather generous boundaries, then the flow will be laminar, transitional, or turbulent, depending upon the particulars, the discussion of which is outside the scope of this paper. Generally, the body surface roughness, the pressure gradient, the wall temperature, and the history of the flow as it proceeds over the body influence the transition. The situation is further complicated when the enthalpy of the flow is increased. At the present time, transition information must be collected from flight tests which are expensive and which do not lead to generalizations. The ballistic range has proven a very useful tool to study transition at lower speeds, and the development of techniques to detect transition in the newer ballistic range shock tunnels would allow this problem to be studied at the higher speeds of present interest.

Yet another complication is introduced when foreign gases are ablated into the boundary layer. Results obtained from porous cones tested in wind tunnels over a relatively wide Mach number range with various foreign gases transpired through the surface give some hint as to the influence of this phenomenon on transition. These tests have indicated that the in-

troduction of a foreign gas into the boundary layer reduces the Reynolds number of transition; however, the Reynolds number of transition does appear to reach an asymptotic value beyond which further surface blowing has little effect. In the particular set of tests reported in reference 31, this asymptotic value of the transition Reynolds number was about 1.75 million, as compared to a transition Reynolds number of 3.3 million on the same body without transpiration.

### HEATING RATES IN PLANETARY ATMOSPHERES

Currently planned entry into the atmosphere of the nearby planets emphasizes the need for research in gases other than air. The atmospheres of the two planets nearest the earth, Mars and Venus, consist of mixtures of nitrogen and carbon dioxide, but the particular composition of these atmospheres is not known with great precision at present; however, it is interesting and informative to compare the heat-transfer results in pure carbon dioxide and see whether they are greatly different from those experienced in air.

It is known (see refs. 32 and 33) that carbon dioxide dissociates at relatively low temperatures and that the recombination of carbon monoxide back to its carbon dioxide state is a very slow process. The temperatures at which carbon monoxide and nitrogen dissociate are not greatly different. It is reasonable to conclude, therefore, that the fluid contained in the boundary layers of vehicles flying in atmospheres rich in carbon dioxide and nitrogen will have as their main constituents nitrogen, carbon monoxide, and atomic oxygen at the lower speeds and the atomic products of the dissociation of these gases at higher speeds. The collision diameters and molecular weights of the  $\text{CO}_2$ - $\text{N}_2$  mixtures are similar to air at elevated temperatures; therefore, it is reasonable to expect that the transport properties will be similar. Hoshizaki (ref. 4) has made this comparison and finds that the viscosity and total thermal conductivity are not too different. Using these transport properties, he solved the laminar boundary layer equations for the stagnation region of a blunt body in carbon dioxide and found that the heating rates should not differ

from those predicted for air by more than about 10 percent. It is interesting now to compare the measured and predicted heating rates in carbon dioxide with those in air to see whether these predictions are borne out. These comparison is shown on figure 57-10 where the heating rate is plotted as a function of the difference between the total enthalpy and the wall enthalpy. Two theoretical lines are shown. The upper line is the theory of Scala (ref. 34), and the lower line is the theory of Hoshizaki (ref. 4). Shown on the figure also are the various measurements that have been made. The lower set of points was obtained in a free-flight range and is described in detail in reference 35. The middle set of points was obtained by Rutowski and Chan, reference 36. The data represented by the circular points were obtained in the General Electric Hypervelocity Shock Tube. It can be seen that up to about 25,000 ft/sec the experimental data agree quite well with either prediction; at the higher speeds the data lie intermediate between the two theories. Also shown on the chart as a shaded area is the air data taken from figure 57-4, and it can be seen that it agrees with the carbon dioxide data reasonably well. It appears then, that to a first approximation the heating rates in carbon dioxide are about the same as the heating rates for air.

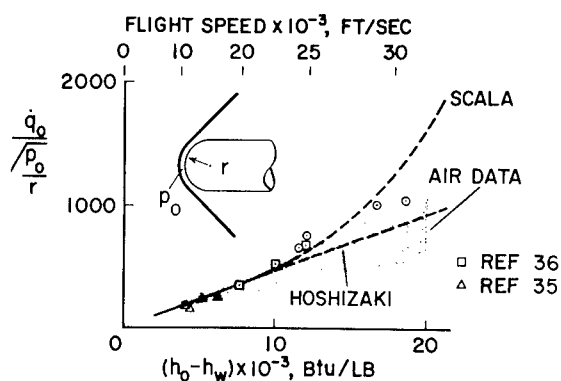


FIGURE 57-10.—Comparison of heating rate in air and carbon dioxide.

There is no information, to the authors' knowledge, of heating-rate distribution over a body in carbon dioxide or in carbon dioxide and nitrogen mixtures. However, based on the

similarity of the transport properties and the considerations outlined by Lees in reference 37, one would not expect marked deviation from the results obtained with air. This conjecture, however, should most certainly be checked experimentally.

### RÉSUMÉ

The primary points of this survey are:

(1) Methods are generally available which account reasonably well for the behavior of the laminar attached boundary layer up to speeds corresponding to the onset of ionization.

(2) Although the effect of ionization on convective heat transfer has yet to be determined conclusively, most of the theoretical and experimental results indicate that the effect is small.

(3) The structure of the flow field loses the appearance of a boundary layer joined to an isoenergetic inviscid region.

(a) at high altitude because of chemical effects and

(b) at high speed because of radiative transport.

The conclusion is that at these conditions the entire flow field should be analyzed without dividing it into a boundary layer and an isoenergetic inviscid shock layer.

(4) Heating rates to the stagnation region of bluff bodies in carbon dioxide are essentially the same as those in air.

(5) The largest area of uncertainty in flow-field analysis is concerned with the effects of contamination on energy transport phenomena. In particular, the influence of the high enthalpy on the thermochemistry and of ionization on the flow field containing foreign gases needs intensive investigation.

(6) Experimental and theoretical work needs to be done on transition and on the turbulent boundary layer in high enthalpy flows.

### SYMBOLS

$h$	static enthalpy, Btu/lb
$M$	Mach number
$p$	pressure, atm
$q$	heating rate, Btu/ft <sup>2</sup> sec
$r$	nose radius, ft

# GAS DYNAMICS

$R$	Reynolds number based on edge properties	<i>Subscripts:</i>
$s$	coordinate along body measured from stagnation point, ft	$E$ equilibrium
$w$	mass rate of injection, lb/sec ft <sup>2</sup>	$NB$ no blowing
		$O$ stagnation conditions
		$w$ conditions at the wall

## REFERENCES

1. LEES, L.: Laminar Heat Transfer Over Blunt-Nosed Bodies at Hypersonic Flight Speeds. *Jet Propulsion*, vol. 26, no. 4, April 1956, pp. 259-269, 274.
2. FAY, J. A., and RIDDELL, F. R.: Theory of Stagnation Point Heat Transfer in Dissociated Air. *Jour. Aero. Sci.*, vol. 25, no. 2, Feb. 1958, pp. 73-85, 121.
3. ROSE, P. H., and STARK, W. I.: Stagnation Point Heat-Transfer Measurements in Dissociated Air. *Jour. Aero. Sci.*, vol. 25, no. 2, Feb. 1958, pp. 86-97.
4. HOSHIZAKI, H.: Heat Transfer in Planetary Atmospheres at Super-Satellite Speeds. *ARS Journal*, vol. 32, no. 10, Oct. 1962, pp. 1544-51.
5. VOJVODICH, NICK S.: The Performance of Ablative Materials in a High-Energy, Partially Dissociated Frozen Nitrogen Stream. NASA TN D-1205, 1962.
6. KEMP, NELSON H., ROSE, PETER H., and DETRA, RALPH W.: Laminar Heat Transfer Around Blunt Bodies in Dissociated Air. *Jour. Aero/Space Sci.*, vol. 26, no. 7, July 1959, pp. 421-430.
7. WINKLER, ERNEST L., and GRIFFIN, ROY N., JR.: Effects of Surface Recombination on Heat Transfer to Bodies in a High Enthalpy Stream of Partially Dissociated Nitrogen. NASA TN D-1146, 1961.
8. GOODWIN, GLEN, and CHUNG, PAUL M.: Effects of Nonequilibrium Flows on Aerodynamic Heating During Entry into the Earth's Atmospheres from Parabolic Orbits. *Advances in Aero. Sci.*, vol. 4, Pergamon Press, New York, 1961, pp. 997-1018.
9. SCALA, SINCLAIRE M., and WARREN, WALTER R.: Hypervelocity Stagnation Point Heat Transfer. Gen. Elec. Space Sci. Lab., R61SD185, 1961.
10. COHEN, NATHANIEL B.: Boundary-Layer Similar Solutions and Correlation Equations for Laminar Heat-Transfer Distribution in Equilibrium Air at Velocities up to 41,000 Feet per Second. NASA TR R-118, 1961.
11. HOWE, J. T., and VIEGAS, J. R.: Solutions of the Ionized Radiating Shock Layer Including Reabsorption and Foreign Species Effects and Stagnation Region Heat Transfer. Prospective NASA TR, 1963.
12. PALLONE, A., and VAN TASSELL, W.: Stagnation Point Heat Transfer for Air in the Ionization Regime. *ARS Journal*, vol. 32, no. 3, March 1962, pp. 436-7.
13. ADAMS, MAC C.: A Look at the Heat Transfer Problem at Super-Satellite Speeds. ARS Paper No. 1556-60, American Rocket Society, New York, December 1960.
14. HANSEN, C. FREDERICK: Approximations for the Thermodynamic and Transport Properties of High-Temperature Air. NASA TR R-50, 1959.
15. FAY, JAMES A.: Hypersonic Heat Transfer in the Air Laminar Boundary Layer. Presented at Hypersonic Specialists Conference, AGARD, Brussels, Belgium, 1962.
16. WARREN, W. R., ROGERS, D. A., and HARRIS, C. J.: The Development of an Electrically Heated, Shock Driven Test Facility. Second Symposium on Hypervelocity Techniques, Denver, 1962.
17. OFFENHARTZ, E., WEISBLATT, H., and FLAGG, R. F.: Stagnation Point Heat Transfer Measurements at Super Satellite Speeds. *Jour. of the Royal Aero. Soc.*, vol. 66, no. 613, January 1962, p. 54.
18. STANKEVICS, J. O. A., and ROSE, P. H.: Measurements of Stagnation Point Heat Transfer in Partially Ionized Air. Paper to be presented at IAS Meeting, January 1963.
19. CHUNG, PAUL M.: Hypersonic Viscous Shock Layer of Nonequilibrium Dissociating Gas. NASA TR R-109, 1961.
20. CHAPMAN, DEAN R.: A Theoretical Analysis of Heat Transfer in Regions of Separated Flow. NACA TN 3792, 1956.
21. LARSON, HOWARD K.: Heat Transfer in Separated Flows. *Jour. Aero/Space Sci.*, vol. 26, no. 11, November 1959, pp. 731-738.
22. CHAPMAN, DEAN R., KUEHN, DONALD M., and LARSON, HOWARD K.: Investigation of Separated Flows in Supersonic and Subsonic Streams With Emphasis on the Effect of Transition. NACA TN 3869, 1957.

# MASS, MOMENTUM, AND ENERGY TRANSFER AT HYPERVELOCITIES

23. CHUNG, PAUL M., and VIEGAS, JOHN R.: Heat Transfer in the Reattachment Zone of Separated Laminar Boundary Layers. NASA TN D-1072, 1961.
24. LUNDELL, JOHN H., WINOVICH, WARREN, and WAKEFIELD, ROY M.: Simulation of Convective and Radiative Entry Heating. *Advances in Hypervelocity Technique*, Plenum Press, New York, 1962, pp. 729-748.
25. VAGLIO-LAURIN, ROBERTO: Turbulent Heat Transfer on Blunt-Nosed Bodies in Two-Dimensional and General Three-Dimensional Hypersonic Flow. *Jour. Aero/Space Sci.*, vol. 27, no. 1, January 1960, pp. 27-36.
26. SOMMER, SIMON C., and SHORT, BARBARA J.: Free-Flight Measurements of Turbulent-Boundary-Layer Skin Friction in the Presence of Severe Aerodynamic Heating at Mach Numbers from 2.8 to 7.0. NACA TN 3391, 1955.
27. TENDELAND, THORVAL: Effects of Mach Number and Wall-Temperature Ratio on Turbulent Heat Transfer at Mach Numbers from 3 to 5. NASA TR R-16, 1959.
28. ECKERT, ERNEST R. G.: Survey on Heat Transfer at High Speeds. WADC Technical Report 54-70, 1954.
29. ECKERT, ERNST R. G.: Survey of Boundary Layer Heat Transfer at High Velocities and High Temperatures. WADC Technical Report 59-624, 1960.
30. ROSE, PETER H., ADAMS, MAC C., PROBSTEIN, RONALD F.: Turbulent Heat Transfer on Highly Cooled Blunt Nosed Bodies of Revolution in Dissociated Air. *Heat Transfer and Fluid Mechanics Institute*, 1958, pp. 143-155.
31. PAPPAS, CONSTANTINE C., and OKUNO, ARTHUR F.: Measurements of Skin Friction of the Compressible Turbulent Boundary Layer on a Cone with Foreign Gas Injection. *Jour. Aero/Space Sci.*, vol. 27, no. 5, May 1960, pp. 321-333.
32. RAYMOND, J. L.: Thermodynamic Properties of Carbon Dioxide to 24,000° K with Possible Application to the Atmosphere of Venus, RM-2292, The Rand Corporation, November 1958.
33. STEINBERG, MARTIN, and DAVIES, WILLIAM O.: The Oxidation of Carbon Monoxide Behind Shock Waves. ARL Tech. Rep. 60-312, Armour Research Foundation, December 1960.
34. SCALA, S. M.: Heating Problems of Entry into Planetary Atmospheres from Supercircular Orbiting Velocities. General Electric Space Science Laboratory, R61SD176, 1961.
35. YEE, LAYTON, BAILEY, HARRY E., and WOODWARD, HENRY T.: Ballistic Range Measurements of Stagnation-Point Heat Transfer in Air and in Carbon Dioxide at Velocities up to 18,000 Feet per Second. NASA TN D-777, 1961.
36. RUTOWSKI, R. W., and CHAN, K. K.: Shock Tube Experiments Simulating Entry into Planetary Atmospheres. LMSD-288139, Lockheed Missiles and Space Co., January 1960.
37. LEES, LESTER: Convective Heat Transfer with Mass Addition and Chemical Reactions. Paper presented at Third Combustion and Propulsion Colloquium, AGARD, NATO Palermo, Sicily, 1958. Pergamon Press (California Institute of Technology, Pub. 451).



**SESSION 5**

**Plasma Physics and Magnetohydrodynamics**

*Chairman, ADOLF BUSEMANN*

DR. ADOLF BUSEMANN, born in Lübeck, Germany, has been a member of the research staff of the Langley Research Center of the National Aeronautics and Space Administration since April 1947. He completed his undergraduate and graduate work at the Technical College at Braunschweig, Germany, graduating as an engineer in 1924 and receiving his doctorate in engineering in 1925. He started his career as an engineer at the Kaiser Wilhelm Institute (now the Max Planck Institute) in Göttingen, Germany, and later became chief engineer of the Institute. While conducting research for 6 years, Dr. Busemann also studied under Dr. L. Prandtl, renowned scientist and wind-tunnel designer, who at that time was director of the Kaiser Wilhelm Institute.

In April 1931, Dr. Busemann began a 4-year period as a lecturer on the subjects of heat transfer, hydrodynamics, and aerodynamics in the Engine Laboratory of the Technical College at Dresden, Germany. Returning to Braunschweig in 1935 Dr. Busemann served as chief of the Gas Dynamics Division of the Aeronautical Research Laboratory until the Allied occupation 10 years later.

Following a period as a research consultant in England during 1946 and 1947, Dr. Busemann accepted an invitation in 1947 from the United States Government to come to this country and continue his career as a research scientist. At Langley Research Center, Dr. Busemann conducts original research in magnetofluid-dynamics and aerodynamics, and he acts as a consultant with the NASA on gas dynamical problems and related subjects. Dr. Busemann has authored more than 100 technical papers that have been published. He was one of two German scientists invited to deliver technical papers at the Volta Congress on high-speed aerodynamics held in Rome, Italy, in 1935. His paper was the first to propose the use of swept wings in the design of high-speed aircraft. He was elected a foreign member of both the Max Planck Association for the Advancement of Science, Germany, and the Academy of Science in Turin, Italy. He received the Carl Bosch Award for Advancement in Aeronautical Science in 1944, and is a member of the International Academy of Astronautics in Paris, France.

A resident of 18 East Southampton Avenue, Hampton, Va., Dr. Busemann became a naturalized citizen of the United States in ceremonies conducted in Norfolk, Va., on November 11, 1954. Members of his family, all of whom are now American citizens, include his wife, Mrs. Magda Krage Busemann, and three married daughters.

# 58. Relations Between Aerodynamics and Magnetohydrodynamics

By Adolf Busemann

## SUMMARY

Although aerodynamics is approaching a state of perfection, at least in connection with turbulence, some important parts have not been completed. For example, magnetohydrodynamics, or the combination of aerodynamics and electromagnetic forces in electrically conductive fluids or ionized gases (called plasma), is a rather young science. Interesting results for technical or for astronomical application are known, but many controversies are still going on. One of the more obvious reasons that some of the results touch on a new version of very old problems is seen in the fact that under equal conditions, hydrodynamic forces and magnetic forces have opposite sign and thus reverse the situation when the magnetic field strength becomes predominant.

## INTRODUCTION

The main objective of the presentations on plasma physics and magnetohydrodynamics is to demonstrate its importance for its proper placement within the university curriculum. To a certain extent this new subject is an outgrowth of aerodynamics, which has been developing to maturity not only since before man began to fly but also as the range of flying speeds has been extended throughout the subsonic and transonic range to supersonic or even hypersonic velocities. When I started my career with supersonic speeds, this speed regime could still be regarded as a quiet corner of purely academic interest where motivation and satisfaction rely on scientific curiosity and accomplishment. It may be forgotten under the glamour added by progress in aeronautics that there was enough incentive and that there were enough natural difficulties in this part of the continuum of mechanics to create a frontier spirit among those early workers on this subject. While we are entering space in the eternal demand to increase the speed of human transportation, the prospect of leaving the air

and traveling through vacuum could be taken as the turning of the tide against aeronautics in retaliation for her murder of other means of transportation during the time that air travel was on the rise.

Space, however, is still not empty. The upper atmosphere under the sun's direct radiation is ionized and forms layers that change from day to night and are detected by the reflection of radio waves. Farther out, the universe is not empty either. It is filled with ionized particles that sometimes become passively entangled in magnetic fields, sometimes actively create them, and sometimes pull them along. This concept of the space environment not only is part of modern astronomy, but its development indicates one of the early nuclei around which a large portion of today's magnetohydrodynamics grew. The particle densities and the magnetic-field intensities are, of course, small compared with those on the earth's surface. Still, having no stronger competitors, their drag deserves first importance for extended space travel. With regard to the future of magnetohydrodynamics from this angle alone, the applicability to engineering which aerodynamics possessed in such a high degree as part of man's early dream of flying seems to fade out in the thin air. Combining its efforts with electromagnetism, however, aerodynamics is also engaged in making a greater dream of mankind a reality, the dream of tapping the very sources of energy which drive our universe. A great deal of research is directed toward developing the "fusion" engine, a kind of atomic diesel engine, in which a mixture is compressed beyond its threshold of stability and fuses into new products while a large energy differential derived from the combination process is being released. Ordinary materials cannot be used

to confine and compress these mixtures because they are unable to withstand the high temperatures involved. Therefore, only magnetic fields seem to be able to serve as the actual walls for confining, compressing, and ducting the mixtures although the problem remains of cooling the electric conductors, the backbones of magnetic fields. Magnetic fields have to be trained to accomplish the task of initiating the fusion, and they are the first ones present during the extraction of the energy during the expansion and have to transmit the energies to the proper destination.

In a problem of such dimensions, there is no doubt that frontier spirit in combination with glamour will remain for quite a while. All nostalgic feelings of aerodynamicists who see their field of research growing up to maturity or completion are premature; there will be in magnetohydrodynamics a second generation of researchers working in a similar way on similar problems and extending again the opportunities for a balanced theoretical and experimental approach that they learned to appreciate and that, in turn, formed their thinking.

In the belief that progress goes hand in hand with thorough understanding, regardless of how little may be accomplished at the beginning, and that experimental verification is needed to provide assurance of a proper approach, half of this session will be devoted to the theoretical, academical, or pedagogical aspect of the subject and the other half to the practical problems in a short survey. Since magnetohydrodynamic theory is such a complicated and extensive subject, not even the fundamentals can be covered in a paper of this length. The purpose here is to display the many facets of this new subject and to give cross-connections to more familiar results in order to show some of the life hidden underneath its surface.

### SYMBOLS

$B_0$	magnetic field strength
$F$	force
$F_h$	hydrodynamic force
$F_m$	magnetic force
$I$	electric current
$V$	flow velocity
$v$	wave speed
$\mu$	permeability

$\rho$	density
$\Gamma$	circulation

### HISTORY OF AERODYNAMICS AND ELECTRODYNAMICS

No one can predict the future of a new branch of science nor the time it will take to grow to maturity. There is no better example for learning this lesson than to compare the history of aerodynamics and electrodynamics. Wind and water are easily noticed with our own senses. Their capacity to work for mankind by driving mills and sailboats is ancient knowledge. Still, aerodynamics was not completely developed as a reasonable science prior to early flight. It more or less accompanied, with mutual support, the development of flight within the last 50 years.

Electric and magnetic fields are, as such, invisible and they did not reveal the electrodynamic forces much earlier than 1820 when Oersted discovered them. About 50 years later, in 1873, Maxwell was able to complete the electromagnetic-field theory in a form ready to give useful results. Not only is the short time remarkable, but also the fact that scientists of that time borrowed hydrodynamic pictures to interpret their invisible fields until electrodynamics learned to stand on its own feet and abandoned the attempt to call itself hydrodynamics of the ether.

Many aspects of electricity, for instance electronics and semiconductors, came much later and had a fantastic growth by themselves. Ionization, although one of the older branches dating from electrostatic times in Geissler tubes, needed further study and required a higher vacuum to simplify confusing findings. Occupied with such investigations of ionized gases in the General Electric Research Laboratory in Schenectady, Irving Langmuir in 1928 found it necessary to distinguish rather sharply between two fundamentally different states. He gave names to these extreme states by saying: "Except near the electrodes, where there are *sheaths* containing very few electrons, the ionized gas contains ions and electrons in about equal numbers so that the resultant space charge is very small. We shall use the name *plasma* to describe this region containing balanced charges of ions and electrons." (See ref. 1, p. 112.)

Plasma and sheaths are, since that time, seen as separable parts rather than extreme states on either end of a natural transient. In about the same manner, Ludwig Prandtl in 1904 mastered the basic problem of hydrodynamics of low friction by distinguishing between what he called the friction layer at the body walls—it became famous under the name boundary layer—and the potential flow farther out. Langmuir's name plasma for the ionized-gas state of balanced charges has been adopted for the whole science and it is not always contrasted with the sheaths on the electrodes. Contrary to that first distinction, it is now permissible to say that a Mercury spacecraft surrounds itself with a plasma sheath during its reentry into the earth's atmosphere. Its effect on radio communication need not be mentioned since the prolonged reentry of Astronaut Scott Carpenter in the MA-7 spacecraft is well remembered because this missing communication created, at least for the public, many minutes of uncertainty about his landing. Plasma is now used to designate a further state of matter, beyond solid, liquid, or gaseous, when temperatures are high enough to ionize the molecules or when density is low enough to prevent ions and electrons from recombining in triple collisions. It has been speculated that more than 90 percent of all matter in the universe is in this new plasma state.

Magnetohydrodynamics as a name does not indicate its relation to plasmas but rather its applications for stirring molten metals or for pumping mercury or other electrically conductive liquids. However, incompressibility is not considered necessary for use of the term. Plasma physics is almost synonymous with magnetohydrodynamics. Different names are also created, and sometimes preferred, when it is felt that magnetohydrodynamics emphasizes either incompressibility or the presence of magnetic fields too much. Examples of such names are magnetoaerodynamics, magnetofluid-dynamics, and electrofluid-dynamics.

### REACTIONS ON SINGULARITIES

In the historical introduction contrasting slow and rapid development of hydrodynamics with electrodynamics, some of the striking differences between the two fields were not specified. Neither are these differences pointed out

in many books concerned with only one of these two subjects.

In an idealized fluid, one must deal with point singularities in sinks and sources as well as with line singularities of the vortex type. Magnetic fields also have point singularities, such as north and south poles, as well as line singularities of the vortex type if the line is a conductor of electric currents. Both types of singularities are in complete analogy with respect to the field structure and with respect to being indicative of forces exerted by the fields. With all this analogy and the additional information that the energy in flow fields and magnetic fields is positive and proportional to the square of the field intensity, it comes as a shock when one learns that the forces are, in both cases, equal except for a systematic reversal of the sign. An attraction force changes to a repulsion force and vice versa. If the forces were made to build up field energy when a north pole is removed from a south pole, the force has to be an attraction force. If a vortex is removed from one of opposite circulation while building up the velocity field, the sign has to be an attraction again. But it seems that there are responsible forces which really cooperate in the formation of field energy. Then there are irresponsible forces doing just the opposite from what is needed and thus, exactly speaking, introducing a doubled difference for someone to resolve. The amusing part of the problem is that neither the hydrodynamic nor the electrodynamic forces are responsible altogether, but that each field has one kind of singularity that is responsible and another one that is irresponsible in dealing with the field energy. As figure 58-1 shows for point

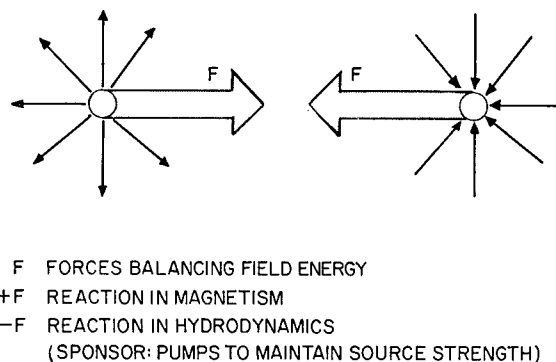


FIGURE 58-1.—Forces between point singularities (poles of opposite sign).

singularities, it is the magnetic pole which has the proper sign; the hydrodynamic sinks and sources rely on pumps to maintain the source strength against nonsteady pressure differences accompanying the movements of sinks and sources. Figure 58-2 shows that in the case of line singularities, the fluid vortices have responsible forces—the basic elements of airfoil theory—whereas the magnetic vortices have irresponsible forces and rely on induced electromotive forces against the electric currents flowing in the vortex core to sponsor the doubled amount of missing field energy.

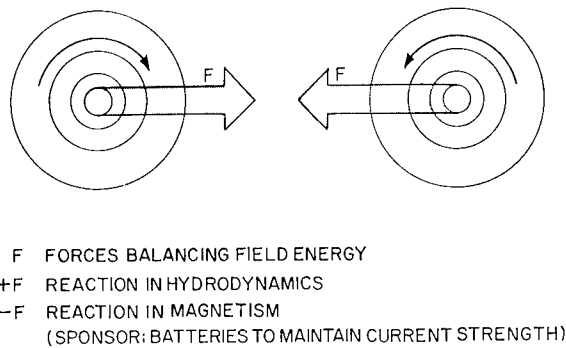


FIGURE 58-2.—Forces between line singularities (vortices of opposite sign).

It may seem for the student rather a nuisance that his memory rules for forces on singularities get hopelessly mixed up when he enters the second field after acquaintance with the first one. The physics of the combined hydrodynamic and magnetic vortices around the same core, however, takes advantage of the reversed signs for the creation of free vortices. These combinations have identical velocity and magnetic fields and lose the expected resulting force by compensating the hydrodynamic force with the magnetic field force.

### LIMIT OF INFINITE CONDUCTIVITY

In order to set the stage for an easy application of this field combination, the two components must first be brought to a more comparable state of idealization. The fluid for simple vortex laws has to be of vanishing viscosity. The magnetic field in which currents are representing the magnetic vortices would show equally reduced dissipations if one goes to the

limit of infinite conductivity or vanishing resistivity in the plasma. For ordinary fluids, this requirement applies to the opposite end of the conductivity scale since these fluids really are of very moderate conductivity. As concerns applications for plasmas so hot that ordinary materials cannot be used as confinement walls, it is indeed reasonable to say that the electrical conductivity may be near infinity. Plasma in the universe will also have high values of electrical conductivity in many astronomical applications and the limit of infinite conductivity can well serve as first approximation.

Any fluid moving through a magnetic field creates electric induction wherever it crosses magnetic lines. Infinite conductivity raises currents so large with any small amount of induction that the new magnetic field superimposed on the original one by the presence of the new currents is of the same order as the original field. It is, therefore, easier to deal with the total field than with its parts. The total field is now not allowed to create any induction by fluid elements crossing magnetic lines. The result is that the original magnetic lines appear to follow the fluid. Similarly, the free forces on the electric currents in the magnetic fields correspond to the magnetic field deformation and are, therefore, visible without regard to the electric currents inside the plasma. The limit of infinite conductivity is such a great simplification that everybody takes the magnetic field itself as being swallowed by the fluid and thus it has to be distorted with the fluid while exerting its reactions on account of the deformations directly to the fluid. Such a story is easy to learn and is for the main part correct.

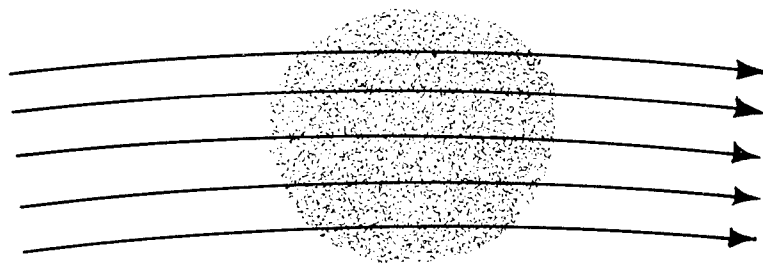
There are a couple of exceptions connected with the fact that electric currents have to be closed. An induction field which drives electric currents in a one-way sense with no possibility of returning is not benefited by the infinite conductivity of the fluid. Such a frustrated induction field permits a certain slip of the magnetic lines through the plasma. It occurs when all magnetic lines are being replaced by similar lines while the magnetic flux is conserved. The more specific rule for the plasma clinging to the magnetic lines is, therefore, stated as follows: All elements once connected with a cer-

tain magnetic line remain always on a common line and any magnetic tube formed by magnetic lines inside the fluid has to carry the same flux for all times. The fluid of infinite conductivity which swallowed a magnetic field at birth stays with this field for life, but the identity of the lines is not guaranteed.

The confinement of a limited volume of plasma by the sole presence of a magnetic field is now not as sure as when the elements were obliged to cling to the identical magnetic line. There are, however, more refined methods whereby this lack of identity of magnetic lines may be overcome. A simple method is to use the fact that the magnetic flux is conserved. A plasma originating outside any magnetic field will, therefore, be trapped between strong fields as shown in figure 58-3 under confinement (a). A more sophisticated way of trapping the plasma is to identify the magnetic lines by their shape. In a ring of plasma, the regular mag-

netic lines would be circular and concentric to the axis of the ring. If a special spool around the ring causes the magnetic lines to wiggle in a steady shape so that they miss their connection after one full turn, it is possible to increase the distance of miss from the center to the outside. Such magnetic lines make many turns inside the ring before they ever close. The important part in this pattern is that there are different knots in different magnetic lines and a family born on one of them cannot jump to any other one as a substitute. These magnetic lines are topologically different and that means that they can be identified by shape.

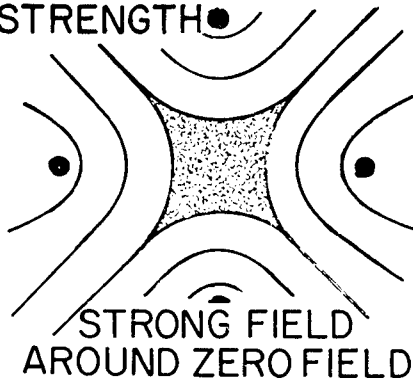
The problem of confinement is a very good example of scientific education connected with plasma physics. There is a great deal of geometrical orientation in our three-dimensional space that can be learned in this application. The stability of configurations is another good exercise in mechanics of three-dimensional field



PLASMA CLINGING TO MAGNETIC LINE PATTERN  
BUT NOT TO THE SAME LINE

### CONFINEMENT

(a) DIFFERENCE IN FIELD  
STRENGTH



(b) DIFFERENCE IN FIELD SHAPE

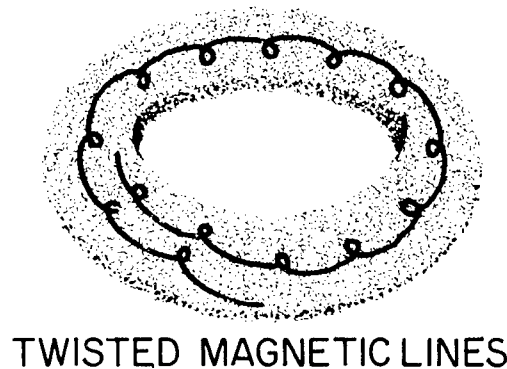


FIGURE 58-3.—Limit of infinite conductivity.

patterns. Although the education in these disciplines will remain as time goes on, the fact that the confinement problem is not solved yet has, at the present time, the added attraction of finding new tricks in acts of jailbreaking of the plasma. The fight of human ingenuity against the eternal laws of nature is still going on. Reassurance can be gained not only from the fact that mankind has always won this fight, but also from the natural examples of good confinement in astronomy and in the Van Allen belts around the earth.

### FREE MAGNETOHYDRODYNAMIC VORTICES

With reference to the two-dimensional incompressible problem of free magnetohydrodynamic vortices, a parallel magnetic field of the intensity  $B_0$  may be assumed to extend far beyond the region of interest where it is not affected by the local distortions. The plasma that is far out plays the role as the identification service for all the magnetic lines concerned. Under these conditions, the simple trapping of plasma by identical magnetic lines can be applied. Before our interest starts, a moving body may have created a single vortex in its wake in the same manner as it created a vortex in pure aerodynamics. This idea gets full plausibility when one first considers a very weak magnetic field and a fast start of a body with a sharp trailing edge as indicated in figure 58-4. No matter how weak we may assume the magnetic field to be for this purpose, the vortex left alone in the fluid of infinite electrical conductivity cannot wind up the magnetic lines of the given magnetic field  $B_0$  forever. The final

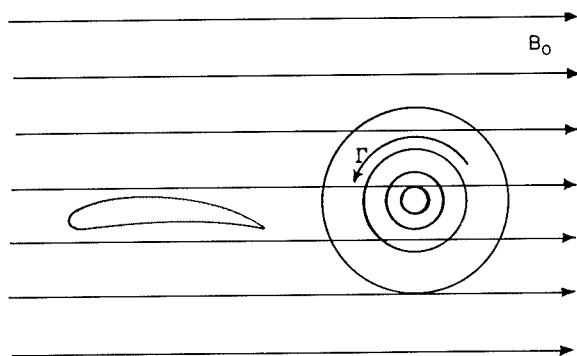


FIGURE 58-4.—Free hydrodynamic vortex with superimposed magnetic field.

state should be an arrangement of magnetic lines coinciding with steady streamlines around the vortex. Circular magnetic lines are easily achieved if an electric current  $I$  is assumed perpendicular to the plane of figure 58-5, com-

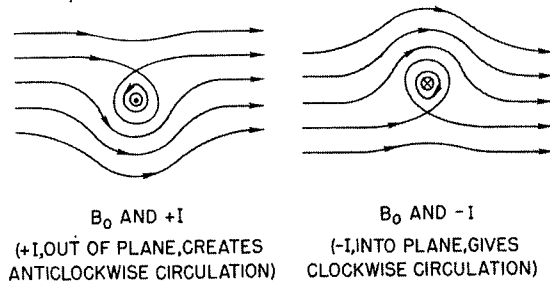


FIGURE 58-5.—Magnetic field patterns (parallel and circulatory).

ing out or going into the plane of this figure. Any finite current cannot overpower the parallel magnetic field  $B_0$  completely and, therefore, has a stagnation point some distance from the location of the current, where circular lines change to passing lines. Two such configurations are drawn in figure 58-5, one for current out of the plane and the other for current into the plane. A resting fluid vortex is not able to show similar lines in the pattern of its streamlines. If the vortex is permitted to move, then two equal steady streamline patterns are possible as in figure 58-6.

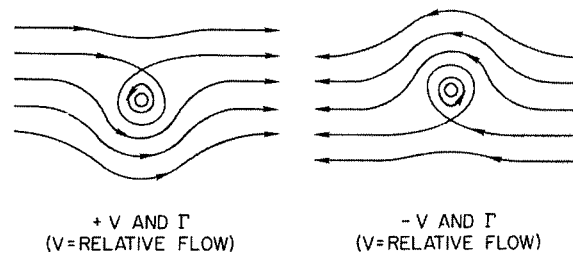


FIGURE 58-6.—Steady streamlines (parallel and circulatory).

There were, however, very valid reasons for Helmholtz to postulate that free vortices do not move with respect to their surrounding fluid neighborhood. The vortex singularity superimposed to a parallel motion would create lifting forces which a free vortex could not



absorb for any length of time. The concept of a free vortex staying within its original neighborhood of fluid particles is actually the concept of a force-free singularity, and the feature to rest within the fluid was the only way to satisfy this demand. In combinations of opposing magnetic and hydrodynamic forces, there is a much larger variety of force-free superpositions as long as an outside magnetic field is given. There is even a force-free combination with identical magnetic lines and steady streamlines if the vortex is allowed to move with a certain speed parallel to the imposed magnetic field  $B_0$ . (Compare fig. 58-5 with fig. 58-6.) Since due to the fixing of a conventional sign to the direction of the magnetic field there is still the choice of matching a clockwise or an anticlockwise magnetic field with the anticlockwise circulating vortex, the same velocity of the vortex may be taken either up or down the direction of the magnetic field. A corotating magnetohydrodynamic vortex is free of a resulting force traveling against the magnetic field vector. (See fig. 58-7.) A contrarotating free vortex has to move with the magnetic field vector  $B_0$ . Actually the condition that the electric currents have to be closed will split any fluid vortex into two magnetohydrodynamic free vortices of one-half the circulation strength but superimposed with either a magnetic circulation of the same or the opposite sign to travel in opposite directions with respect to the resting fluid and guided by the direction of the imposed magnetic field  $B_0$ .

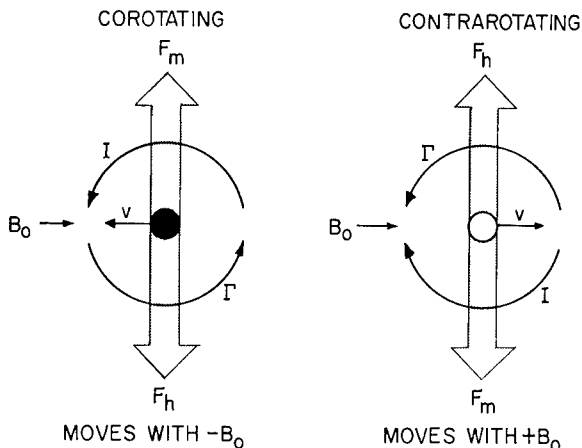


FIGURE 58-7.—Force-free combinations.

## ALF VÉN WAVES

The splitting of a former free vortex into two halves, a corotating and a contrarotating free magnetohydrodynamic vortex, opens the curtain for a play with a foursome of free magnetohydrodynamic vortices for the same magnetic field strength, having either clockwise or anticlockwise fluid circulation combined with either clockwise or anticlockwise magnetic circulation. How do they behave with each other? The completely reversed ones are either corotating or contrarotating free vortices. They are known to move together either against or with the magnetic field. The fact that, say, the corotating vortices walk together does not indicate that they have the slightest effect on each other. On the contrary, whatever the added fluid velocity would try to do, when one vortex is close to the other one, the added magnetic field strength is intended to undo. And so they walk together in complete disregard of each other as long as any distribution of corotating free magnetohydrodynamic vortices is separated from the contrarotating ones. The same holds true as long as contrarotating vortices are among themselves, the true meaning of "co" or "contra" being only a magnetic sign convention in the first place. The constant velocity and the dull neutral stability of any group of corotating or contrarotating free vortices in separation are best known in an arrangement of infinitesimal strength along lines perpendicular to the magnetic field. (See fig. 58-8.)

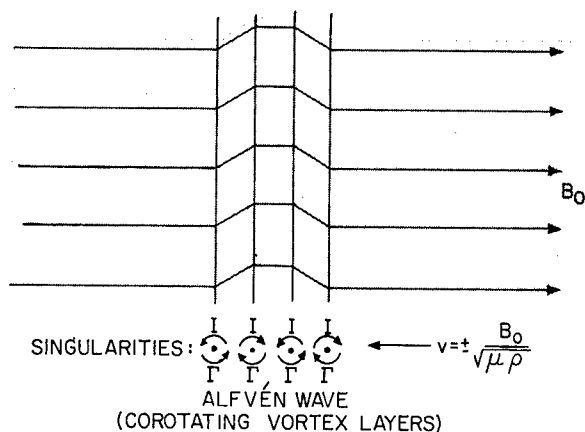


FIGURE 58-8.—Alfvén waves.

Such an arrangement represents the shear wave perpendicular to the magnetic lines and travels according to its discoverer Alfvén with the so-called Alfvén speed up or down the direction of the given magnetic field.

### COMPRESSIBLE PLASMAS

This free movement of the fluid in the shear wave demonstrates two changes, one for each of the cooperating sciences. The clinging of plasma to the magnetic lines makes their usual propagation speed, the speed of light, very much slower. The structure added to the fluid by being connected to magnetic lines gives restoring forces to deformations which had none before. It also adds to the volume changes a new pressure, the magnetic pressure difference, in case the compressibility is considered and is not applied to compressions in the direction of the magnetic lines. The plasma enters, with the help of the magnetic field, the mechanics of a solid able to resist volume and shape changes but with a very obvious anisotropy according to the line structure of the magnetic field. Shear and compression waves of the Alfvén type, in combination with the acoustic waves, form a pattern of two waves for every direction with respect to the magnetic field direction. Depending upon the strength of the magnetic field, the given speed of a body moving through the plasma can be subsonic or supersonic as well as of either the sub-Alfvén or super-Alfvén types. At large Alfvén speed (the body speed being of the sub-Alfvén type), the vortices created by the body may get ahead of the body and form the surprising forward wake predicted by the theory. There are many new flow patterns possible for the flow past bodies in magnetohydrodynamics. The sharp trailing edge, one of the significant points in subsonic flow for con-

trol of lift without large corrections on account of the viscosity, lost its importance for supersonic speeds and is still a controversial factor concerning its ability to control lift at sub-Alfvén speeds when a part of the shed vortices march ahead of the body instead of staying behind.

### MUTUAL INTERACTIONS OF FREE VORTICES

By separating the two groups of corotating and contrarotating vortices, a great simplicity was gained since they ignored each other's presence within either of these groups. A last remark about what happens when both groups are together may give reassurance that whatever has been suppressing the interaction between the members of each group has doubled the interest a member of one group takes in a member of the other group. The interaction, however, is complicated by the fact that when two members of the different groups are left in the vicinity of one another for any length of time, creation of new vorticity of both kinds, the corotating and the contrarotating, can be expected. (See ref. 2.) The other speakers will introduce you to many more items of the magnetohydrodynamics and plasma physics field.

Seeing the future with the eyes of the aerodynamicist, I should like to conclude that there is a continuation for almost any phase of pure aerodynamics, with great variety already under study at the very opening of the door to this combined field. Many problems apparently solved by a purely aerodynamic approach have to be reconsidered either directly from the beginning or, when higher Alfvén speeds indicate the predominance of the magnetic field strength, a "no" may turn into a "yes" when two partners cooperate who in spite of their great similarity have opposite ideas about the sign of forces.

### REFERENCES

1. LANGMUIR, IRVING: Oscillations in Ionized Gases. Vol. 5 of the Collected Works of Irving Langmuir, C. Guy Suits, ed., Pergamon Press (New York), c. 1961, pp. 111-120.
2. BUSEMANN, ADOLF: On the Kármán Vortex Street in Magnetofluidynamics. Proc. Aerospace Scientific Symposium of Distinguished Lecturers in Honor of Dr. Theodore von Kármán on his 80th Anniversary. Sponsored by the Air Force Office of Scientific Research. Inst. Aero. Sci., 1962.

# 59. Fundamentals of Plasma Interaction With Electric and Magnetic Fields

By Robert V. Hess

ROBERT V. HESS, *Head, Plasma Physics Section, Aero-Physics Division, NASA Langley Research Center, received his Bachelor of Science and Master of Science equivalent from the Vienna (Austria) Institute of Technology in 1938. He studied Fluid Flow at the Massachusetts Institute of Technology in 1939. Since joining the Langley staff in November 1944, Hess has specialized in magnetoplasmadynamics, plasma acceleration, and gasdynamics. He was the first to give analytic expression of three-dimensional subsonic flow effects depending on wing aspect ratio; he predicted novel interaction effect of explosion wave with hot ground layer, subsequently experimentally confirmed. He invented a new type of chemical plasma used for telemetering experiments and electric power generation and invented a new type of plasma accelerator using Hall currents. He is author of many NASA publications on research he has conducted at Langley. Hess is a member of the Scientific Research Society of America (RESA).*

## SUMMARY

The fundamental aspects of the interaction of plasmas with electric and magnetic fields are treated through specific examples from actual problems of research. For instance, the dielectric behaviour of a plasma in a strong magnetic field which applies to capacitive energy storage and Alfvén waves is discussed. The equations of motion of electrons and ions in a plasma including collisions and space charge effects are unified. The plasma is treated as a single fluid with velocity, current, and various transport properties, such as electrical conduction. The single-fluid approach is applied to a variety of methods of steady plasma acceleration and to the acceleration of ions in a plasma. Collision processes and electrical conduction are given for fully and partially ionized plasmas with and without a magnetic field. Their effect on voltage current characteristics of electrical discharges in the presence of magnetic fields is discussed for a variety of experiments. Examples of turbulent electrical conduction are given.

## INTRODUCTION

Textbooks dealing with the fundamentals of plasmas in magnetic fields draw largely on examples from thermonuclear fusion problems, where problems of leakage or diffusion of a plasma across the confining magnetic field are of major concern. Since our major concern is that of plasma acceleration for which the use of electric fields crossing magnetic fields is important, our problems deal frequently with electrical conduction across a magnetic field rather than with diffusion. In this paper, an attempt is made to present the fundamentals of plasma physics up to the latest findings from this viewpoint. It will turn out that problems of anomalous, or "turbulent", electrical conduction across magnetic fields may be encountered, from which comparisons may be made with anomalous or "turbulent" diffusion processes across

magnetic fields which are of prime concern to the whole field of plasma physics.

The plan of the paper is to obtain a general picture through a discussion of many specific examples of plasmas interacting with electric and magnetic fields. In a broad sense, one can, however, distinguish between the pure kinetics and dynamics of such interactions and the plasma physics of actual electrical discharges in magnetic fields.

### SYMBOLS

An arrow above a symbol indicates a vector quantity. Quantities are expressed in the rationalized mks system of units.

$B$	magnetic flux density
$c$	speed of light
$\bar{c}$	mean thermal velocity
$C_1, C_2, C_3, C_4$	constants
$D$	diffusion coefficient
$\frac{D(\ )}{dt}$	substantial derivative, $\frac{\partial(\ )}{\partial t} + v \cdot \text{grad}(\ )$
$d$	Debye length
$E$	electric field strength
$E^* = E + v \times B$	
$e$	electronic charge
$H$	magnetic intensity
$j$	current density per unit area
$k$	Boltzmann's constant
$l$	length
$m$	mass
$n$	particle density per unit volume
$P$	polarization
$p$	pressure
$Q$	collision cross section
$r$	radius
$s$	displacement
$T$	temperature
$v$	velocity
$\alpha$	turbulent coefficient
$\beta$	geometric factor
$\epsilon$	permittivity
$\lambda$	mean-free path
$\mu$	permeability
$\rho$	density
$\nu$	collision frequency
$\sigma$	conductivity
$\tau$	collision time, $1/\nu$
$\omega$	cyclotron frequency

Subscripts:

$x, y, z$  and  $r, \theta, x$  refer to directions in Cartesian and cylindrical coordinates, respectively

$c$	coulomb
$D$	drift
$e$	electron
$i$	ion
$L$	Larmor
$n$	neutral
$0$	free space

$p$	plasma
$i, e$	ion-electron
$i, n$	ion-neutral
$e, n$	electron-neutral
$\perp$	perpendicular to the direction of . . .
turb	turbulent
osc	oscillations in plasma
Superscript:	
$f$	finite electrodes

### FUNDAMENTAL DIFFERENCES IN EFFECTS OF ELECTRIC AND MAGNETIC FIELDS

The plasma contains approximately an equal number of electrons and ions and is thus on the whole electrically neutral. The electric field exerts equal forces on the charged particles whose directions of motion are, however, opposed. These forces cancel and, as a result, an electric field in itself cannot exert a force on the plasma as a whole. A magnetic field, on the other hand, has the quality that when stationary, it cannot put energy into the plasma but merely exerts forces on it for which reactions can be measured on the magnetic coils. Since a magnetic field exerts a force on a plasma, a moving magnetic field can be expected to do work on the plasma or put energy into it. Because, however, it is actually the electric field which puts energy into the plasma, the magnetic field will put energy into the plasma or its motion through the intermediary of an electric field. It was established experimentally by Faraday and from a broader point of view by Maxwell and Einstein that a moving magnetic field is equivalent to a combination of stationary electric and magnetic fields.

### I. KINETICS AND DYNAMICS OF PLASMAS IN ELECTRIC AND MAGNETIC FIELDS

#### Behavior of Electrons and Ions in Constant Electric and Magnetic Fields

The most fundamental case to be discussed deals with charged particles accelerated by a constant electric field in the presence of a constant magnetic field. The equation of motion of the charged particle, for example, of an ion, is then, according to basic texts such as references 1 to 11:

$$m_i \frac{d\vec{v}_i}{dt} = e\vec{E} + e(\vec{v}_i \times \vec{B}) \quad (1)$$

The first term on the right-hand side in equation (1) is the well-known electrostatic force. Since the magnetic force does not impart energy, it is normal to the velocity  $\vec{v}$  of the particle and to the magnetic field  $\vec{B}$ . In order to absorb the reaction to the force on the particles, the magnetic field  $\vec{B}$  has to be deformed. Then,  $\vec{B}$  designates the deformed field. First, an even simpler problem is treated. Assume that after the particle has attained a velocity, the electric field is removed. Then,  $m_i \frac{d\vec{v}_i}{dt}$  is the centrifugal force which balances the magnetic force  $e(\vec{v}_i \times \vec{B})$  which, since it is always normal to the particle velocity, produces a curvature in particle path without change in its absolute velocity and kinetic energy. From this force balance

$$m_i \frac{v_i^2}{r_{L,i}} = e|v_i|B \quad (2)$$

the radius of gyration  $r_{L,i}$  (sometimes called Larmor radius) is obtained as is the angular frequency  $\omega_i = v_i/r_{L,i}$  (sometimes called cyclotron frequency)

$$\left. \begin{aligned} r_{L,i} &= \frac{m_i v_i}{eB} \\ \omega_i &= \frac{eB}{m_i} \end{aligned} \right\} \quad (3)$$

The rotation of the negative electrons is opposed to that of the positive ions. The direction of rotation is based on fundamental experimental facts.

Suppose now that the electric field  $E$  is imposed. The following particle motion results (fig. 59-1):

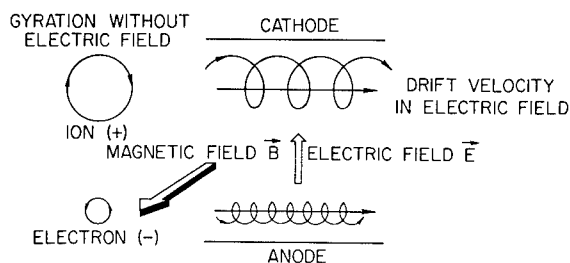


FIGURE 59-1.—Graphical representation of motions of electrons and ions.

A physical explanation for the particle drift perpendicular to the electric and magnetic field can be given as follows. The electric field accelerates ions and electrons in opposite directions and, as a result of the force balance, only energy is put into the system. The positive ions are attracted by lower or negative potential, which would be at the cathode in a discharge, and are accelerated in the direction of the electric field; whereas, the negative electrons are accelerated in the direction opposed to the electric field. The ions thus reach their maximum velocity on top and the electrons on the bottom. As a result, their Larmor radii are a maximum in this region and a minimum on the opposite side. This behaviour results in a drift normal to the electric and magnetic fields. The force exerted by the magnetic field has thus accelerated both ions and electrons in one direction normal to the electric field. The magnetic field has thus converted the energy input of the electric field, which acts in opposite directions on the electrons and ions of the plasma, into an unbalanced force in one direction.

While this description gives a good qualitative physical picture, it does not bring out the great simplicity of the motion and does not determine the value of the drift velocity. When drift velocity is attained, the acceleration of the particles normal to  $\vec{E}$  and  $\vec{B}$  is zero; thus

$$\vec{v}_D = \frac{\vec{E} \times \vec{B}}{B^2} \quad (4)$$

where for  $\vec{E}$  perpendicular to  $\vec{B}$ ,  $v_D = \frac{E}{B}$ . An observer moving with the drift velocity will detect no electric field and he will see only particles circling in the magnetic field.

#### Meaning of Simple Case for Practical Acceleration of a Collisionless Plasma

It was shown that the acceleration to drift velocity of particles gyrating in a strong magnetic field is due to different effects of the imposed electric field on each side of the circular motion. The minimum time for plasma acceleration would thus be, on the average, the reciprocal of the cyclotron frequency of the

heavier ions, whose mass predominates in the plasma. Correspondingly, the minimum distance of acceleration is, on the average, of the order of a Larmor radius. The neglect of collisions is justified for a plasma like the present one, which consists of only charged particles, that is, a fully ionized plasma, not only when the density is low but also when the temperature is high, as is discussed subsequently. The collisionless cases discussed herein are not merely playthings of the theoretician but are of great importance for plasma interactions with magnetic fields in space and in thermonuclear devices. The above collisionless acceleration has been approached in thermonuclear devices like the Ixion (refs. 12 and 13, sections 1 and 2), where the plasma is put into rotation in very short bursts. The use of such a system for continuous, steady plasma acceleration does not seem promising unless the losses of the highly ionized plasma to the walls are kept small like in the Ixion, where the electric and magnetic field configuration permits both confinement and acceleration of the plasma.

#### Collisionless Plasma Acceleration Described in Terms of Energy Input

When the drift velocity normal to the electric and magnetic field is attained, no current will flow in the direction of the electric field. As a result, a steady electric field cannot put energy into the plasma, since

$$\text{Input Rate of Energy Density} = \vec{j} \cdot \vec{E} \quad (5)$$

with

$$\vec{j} = ne(\vec{v}_i - \vec{v}_e)$$

Equation (5) indicates that for zero  $\vec{j}$  the input ratio of energy density is zero. Of course, energy can be put into a plasma with collisions because, as is well known, collisions permit the particles to break through the magnetic field. It is also well known that energy can be put into plasma with or without collisions by an electric field alone without the presence of a magnetic field. But in the presence of a steady magnetic field the electric field  $\vec{E}$  must vary to permit an energy input. As indicated at the

beginning of this paper, a variation of magnetic fields could also produce collisionless plasma acceleration. The study of the acceleration, however, of a collisionless plasma in a steady magnetic field, aside from applying to the present case, introduces many truly basic aspects of plasmas in magnetic fields.

#### Dielectric Properties of Plasma in a Magnetic Field

The current due to variation of  $\vec{E}$  in a steady magnetic field can be obtained from a balance of the  $\vec{j} \times \vec{B}$  force per unit volume with the accelerating force  $\rho \frac{D\vec{v}}{dt}$ ; thus (from basic texts)

$$\rho \frac{D\vec{v}}{dt} = \vec{j} \times \vec{B} \quad (6)$$

The field strength  $\vec{E}$  is assumed to change slowly so that  $\vec{v}$  is at no time far removed from the drift velocity  $\frac{\vec{E} \times \vec{B}}{B^2} = \frac{E_{\perp}}{B}$ ; the subscript  $\perp$  indicates perpendicular to the direction of drift motion. Solving for  $\vec{j}$  gives

$$\vec{j}_{\perp} = \frac{\rho}{B^2} \vec{B} \times \frac{D\vec{v}}{dt} = \frac{\rho}{B^2} \frac{DE_{\perp}}{dt} \quad (7)$$

The quantity  $\rho/B^2$  is the product of the permittivity of free space times the dimensionless susceptibility characterizing the dielectric. Using  $B^2/2\mu_0$  as magnetic pressure and  $1/\mu_0\epsilon_0$  as the speed of light squared,

$$\frac{\rho}{B^2} = \frac{\rho\epsilon_0}{B^2} = \frac{\rho c^2}{B^2} \epsilon_0$$

A better physical picture is obtained by noting

$$\frac{\rho}{B^2} \vec{E} = n\vec{P} = ne\vec{l} \quad (8)$$

where

$$\rho = n_e m_e + n_i m_i$$

and in a plasma  $n_e \approx n_i$ . Thus, the problem is concerned with a polarization which equals a charge times the average separation of a plasma with  $n$  particles per unit volume. This polariza-

tion is to be distinguished from the more familiar microscopic polarization of bound charges. The average charge separation in this case is limited to the sum of the Larmor radii, using the drift velocity; thus, as noted especially in reference 6,

$$r_{L,i} + r_{L,e} = \frac{m_i v_i}{eB} + \frac{m_e v_e}{eB} = \frac{m_i + m_e}{e} \frac{E}{B^2} \quad (9)$$

Since the mass of the ions is much larger than that of the electrons, the displacement of the ions predominates. Subsequently, space-charge displacement effects will be shown in the plasma without a magnetic field, with effects of electrons predominant.

The existence of such dielectric effects of a plasma in the presence of an electric and magnetic field has very important practical consequences. It becomes possible to store electrical energy in motion, most conveniently in rotation; this energy is

$$\frac{\rho}{B^2} \frac{E^2}{2} = \frac{1}{2} \rho v_D^2 \quad (10)$$

Such a device has been actually used as a "Hydromagnetic Capacitor" (ref. 14).

Perhaps even more significantly from a basic viewpoint the existence of a dielectric effect for a plasma in the presence of a magnetic field introduces the possibility of waves in the plasma. The electric field, of course, need not be externally imposed but is related to velocity perturbations. The well-known Alfvén waves, as is pointed out by Dr. A. Busemann in paper number 58 of this volume, can use the magnetic field either for propagation of transverse waves by using the magnetic field lines as if they were strings or for propagation of longitudinal waves by using the magnetic pressure instead of the gas pressure. Existence of such waves has great practical influence in the behavior of plasmas in a magnetic field, both in the laboratory and in space. The possibility of amplification of such waves has played a great role in the stability consideration of magnetically confined plasmas and for the study of collisionless shocks related to thermonuclear situations or to the mechanisms for the onset of the effect of solar storms on the earth's environment.

### Simplified Analysis of Plasma Behavior Including Collisions and Space-Charge Effects

It has been shown so far that the electrons and ions have their displacement restricted in the presence of a magnetic field and electric field. But even without the magnetic field, restrictions on their motions exist. The most important ones are those due to collisions with each other and with neutral particles and the restriction of motion due to attractive electrostatic forces between positive and negative particles. As a result of these restrictions to their motions, the complicated particle motions in a plasma can be lumped for many practical purposes as those of a single fluid.

Since ordinary nonionized particles also have collisions but not electrostatic attraction effects, the latter will be treated in some detail. Their importance for the understanding of plasma behavior cannot be overemphasized. The electric fields built up by charge separation are given by Gauss's law or Poisson's equation as given in reference 15:

$$\text{div } \vec{D} = \epsilon_0 \text{div } \vec{E} = e(n_i - n_e) \quad (11)$$

Putting numbers into equation (11) indicates that differences of  $n_i - n_e$  of  $10^9$  particles/cm<sup>3</sup> in a plasma of  $10^{14}$  particles/cm<sup>3</sup> will build up very large electric fields which couple the particle motion. In the first very good approximation, it may thus be assumed that  $n_i \approx n_e$  and use of Poisson's equation may be avoided, whereas the electric fields produced in the plasma by charge separation are considered.

With the foregoing physical picture in mind, the equations of motion for the individual particles are considered. The more fundamental equations of kinetic theory like the Boltzmann, Fock-Planck, and Vlasov equations are avoided; also, the collision terms are expressed simply through a friction force which varies linearly with the collision frequency  $\nu$  and with the difference between the particle velocities.

The balance of forces for electrons and ions are written as:

Electron force:

$$\begin{aligned} n_e m_e \frac{d\vec{v}_e}{dt} + \text{grad } p_e + n_e m_e \nu (\vec{v}_e - \vec{v}_i) \\ = -n_e e (\vec{E} + \vec{v}_e \times \vec{B}) \end{aligned} \quad (12)$$

Ion force:

$$n_i m_i \frac{D\vec{v}_i}{dt} + \text{grad } p_i - n_i m_e v (\vec{v}_e - \vec{v}_i) = n_i e (\vec{E} + \vec{v}_i \times \vec{B}) \quad (13)$$

The friction force between ions and electrons and electrons and ions is obviously the same. This relationship is more evident, perhaps, when written in the full form  $\left( \frac{\text{Friction force}}{\text{Volume}} \right)$

$$v n \frac{m_i m_e}{m_i + m_e} (\vec{v}_e - \vec{v}_i) \quad (14)$$

The reason for the appearance of  $m_e$  is that  $m_e \ll m_i$  and thus in the center-of-mass system of the colliding particles, the heavier ions will be near to stationary with mainly the electrons being influenced by the friction.

The motion of the plasma may be expressed as a single fluid by defining the density  $\rho$  from the mass balance

$$\rho = n_e m_e + n_i m_i = \rho_e + \rho_i \quad (15)$$

and the velocity of the center of mass  $\vec{v}$  from the momentum balance

$$(n_e m_e + n_i m_i) \vec{v} = n_e m_e \vec{v}_e + n_i m_i \vec{v}_i \quad (16)$$

Also, the current density  $\vec{j}$  may be expressed as

$$\vec{j} = e(n_i \vec{v}_i - n_e \vec{v}_e) \quad (17)$$

with

$$\text{grad } p = \text{grad } (p_e + p_i) \quad (18)$$

Adding equations (12) and (13) and substitution from equations (15), (16), (17), and (18) gives the equation of motion

$$\rho \frac{D\vec{v}}{dt} = \vec{j} \times \vec{B} - \text{grad } p \quad (19)$$

Subtracting equations (12) and (13) with use of equations (15) to (18) and neglecting for the moment the differences in the time derivatives of the velocities results in, since  $n_i = n_e$ ,

$$\frac{m_e v}{e} \vec{j} = n e (\vec{E} + \vec{v} \times \vec{B}) - \vec{j} \times \vec{B} + \text{grad } p_e \quad (20)$$

This force balance can be written in the form

$$\vec{j} = \sigma (\vec{E} + \vec{v} \times \vec{B}) + \frac{e}{m_e v} (\text{grad } p_e - \vec{j} \times \vec{B}) \quad (21)$$

where  $\sigma = \frac{ne^2}{m_e v}$  is the electrical conductivity; equation (21) is often called the "generalized Ohm's law."

It must be emphasized that the electric field  $\vec{E}$  is either externally applied or is built up inside the plasma due to space-charge separation. The measurement of the electric field inside a plasma can be a very important diagnostic tool in determining regions of magnetic interaction. In reference 15 the equations of motion of the neutral particles are included and the importance of space charge in plasma acceleration is emphasized. Before equation (21) is applied to practical cases, a few remarks about the neglected time derivatives of the velocity are appropriate. For simplicity, only the difference between the partial time derivatives is considered because this difference has more general significance. In order to bring out the main effect, collisions and other terms except the  $\vec{E}$  term in the force balance of equations (12) and (13) are neglected; then,

$$n e \vec{E} = \frac{m_e}{e} \frac{\partial \vec{j}}{\partial t} \quad (22)$$

$$\frac{\partial \vec{j}}{\partial t} = \frac{ne^2}{m_e} \vec{E} \quad (23)$$

It is useful to remember that  $\vec{j}$  is proportional to a velocity which, of course, is the time derivative of a displacement  $\vec{s}$ . Thus, the equation takes the general form (ref. 3)

$$m_e \frac{\partial^2 \vec{s}}{\partial t^2} = e \vec{E} \quad (24)$$

which is the equation for a free vibration with a restoring force  $e\vec{E}$ . The electric fields due to charge separation are in turn given by Poisson's equation. The polarization per unit volume due to charge separation can be obtained for an oscillating electric field in the form

$$n \vec{P} = n e \vec{s} = \frac{-ne^2}{m_e \omega_{ce}^2} \vec{E} \quad (25)$$



This leads to the natural frequency of oscillation (the so-called plasma frequency)

$$\omega_p = \left( \frac{ne^2}{m_e \epsilon_0} \right)^{1/2} \quad (26)$$

Note that in contrast to the Alfvén waves, where the oscillations of ions are predominant, in the electrostatic waves the oscillations of the lighter electrons are more important. For the propagation of electromagnetic waves through the plasma sheath discussed subsequently in paper number 61 of this volume, these electrostatic effects are essential in changing the dielectric effect of free space but are neglected here and with them the use of Poisson's equation. These waves are, of course, also very important for thermonuclear and solar phenomena and stability considerations of plasma confinement. They also play a part in possible plasma wave amplifiers.

Now, it would be very convenient to express what has been neglected in terms of length. Such a length is easily formed by dividing the mean thermal velocity by  $\omega_p$

$$\frac{\bar{c}}{\omega_p} \approx \left( \frac{kT}{m_e} \right)^{1/2} \left( \frac{m_e \epsilon_0}{ne^2} \right)^{1/2} \approx \left( \frac{kT \epsilon_0}{ne^2} \right)^{1/2} \approx d \quad (27)$$

The Debye length  $d$  has many interpretations, such as the distance where the thermal energy equals the electrostatic energy stored due to charge separation. Of course, it is also interpreted as a sheath or a region near a plasma boundary where large deviations from charge equality occur. It must be emphasized that this distance, while very useful, is not a magic length, but it has stood the test of time.

Since, in the plasma, charge equality is approximately preserved, equations (15) to (21) describing the behavior of a plasma apply to dimensions of ionized gases in excess of the Debye length. In addition, the definition of plasma requires that the dimensions characteristic of processes in the plasma (like the mean-free path and the gyration radii of electrons and ions) are larger than the Debye length

$$\lambda > d$$

and

$$r_{L,e} \text{ and } r_{L,i} > d$$

For a collisionless plasma in the presence of a magnetic field, in addition, the mean-free path must be larger than both ion and electron gyration radii

$$\lambda > r_{L,i} > r_{L,e} \quad (28)$$

It is frequently convenient to express this inequality in terms of cyclotron frequencies and the reciprocal of the collision frequency  $\nu$ , that is, in terms of the collision time  $\tau$ . The collision time  $\tau$  is given usually by the ratio of the mean-free path and the mean thermal velocity  $\bar{c}$ . Thus, the product  $\omega\tau$  becomes, by using equation (3) for  $\omega$  and the Larmor radius,

$$\omega\tau \approx \frac{eB}{m} \frac{\lambda}{\bar{c}} = \frac{\lambda}{r} \quad (29)$$

As a result, the previously given inequality approximately corresponds to

$$(\omega\tau)_e > (\omega\tau)_i > 1$$

#### Acceleration of a Fully Ionized, Collisionless Plasma Produced by a Magnetic Piston

The rest of the paper is chiefly concerned with examples using plasmas in steady electric and magnetic fields. But first an example is given that is important for unsteady acceleration. The simplest case appears to be that of a moving magnetic field pushing a highly ionized collisionless plasma like a magnetic piston.

Under such conditions the  $\vec{j} \times \vec{B}$  force per unit volume will be balanced by a pressure gradient,  $\text{grad } p$ , which establishes itself at the boundary of the plasma. This concept is a highly simplified version of a traveling-wave accelerator. The unsteady problem has thus been changed into a steady equilibrium case in the reference system of the moving magnetic field (fig. 59-2).

The equilibrium equation as given in basic texts such as references 1 to 11

$$\vec{j} \times \vec{B} = \text{grad } p \quad (30)$$

can be solved for the azimuthal current  $\vec{j}_\theta$ , which consists principally of electrons

$$\vec{j}_\theta = \frac{\vec{B} \times \text{grad } p}{B^2} \quad (31)$$

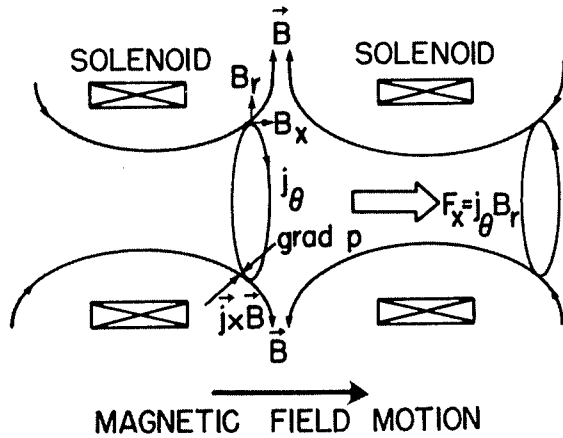


FIGURE 59-2.—Acceleration with moving magnetic piston.

For the collisionless case, using the condition that the velocity of the plasma relative to the magnetic field is zero, the force balance version of the “generalized Ohm’s law” in equation (20) becomes

$$ne\vec{E} - \vec{j} \times \vec{B} + \text{grad } p_e = 0$$

Using the previous equilibrium equation (30), since

$$p_i + p_e = p$$

Then

$$ne\vec{E} = -\text{grad } p_i \quad (32)$$

Thus, the ions are kept in the magnetic field by space-charge electric fields due to electron attraction. It should be noted that in a stationary reference system, fixed to the apparatus, the electrons will pull the ions as the magnetic piston moves by. Let us contrast this case with constant magnetic field  $\vec{B}$  and pressure gradient  $\text{grad } p$  with the previously discussed case of constant  $\vec{B}$  and electric field  $\vec{E}$ . In the latter case the electric field drives electrons and ions in opposite directions and thereby establishes a current. In the presence of the magnetic field, both particles move, however, in the normal direction to both fields, so that the current in the steady state approaches zero.

In the presence of a pressure gradient the particles, however, attempt to move in the same direction. The magnetic field forces them to move normal to it and to the pressure gradient in azimuthal directions opposed to each other.

Thereby a steady current can be established. Of course, the more precise counterpart to the electric-field case is the situation where a moving plasma stream is trying to cross a magnetic field, and the charged particles are forced to move in opposite azimuthal directions forming an induction current. When the effect of collision is small and magnetic-field strength is assumed constant, the rate of input of kinetic energy would equal the rate of work done by the  $\vec{j} \times \vec{B}$  force in stopping the plasma. In this case where a pressure gradient balances  $\vec{j} \times \vec{B}$ , the forces are already balanced. A discussion of finer points in this problem are included in reference 6, section 3.

Since the term “magnetic pressure” is frequently used in connection with plasma confinement, this term is discussed next. In order to define magnetic pressure the Maxwell equation (or Ampere’s law)

$$\vec{j} = \text{curl } \vec{H} \quad (33)$$

has to be introduced. This equation expresses the magnetic field due to a given current. Inserting equation (33) into equation (30) yields, for magnetic lines of zero curvature, with  $\vec{B} = \mu \vec{H}$

$$\text{grad } p + \frac{1}{2\mu} \text{grad } B^2 = 0$$

or

$$p + \frac{B^2}{2\mu} = \left( p + \frac{B^2}{2\mu} \right)_{\text{ext}} \quad (34)$$

When the plasma is truly confined by the external magnetic field the external pressure must be zero, and

$$p + \frac{B^2}{2\mu} = \left( \frac{B^2}{2\mu} \right)_{\text{ext}} \quad (35)$$

#### Steady Plasma Acceleration With Currents Across Electrodes

For the sample cases of plasma acceleration with currents across electrodes the electron pressure gradients may be neglected and attention is given to the currents which are predominantly due to electron motion. The generalized Ohm’s law may then be written in the form (see refs. 15 and 16 and eq. (21)):

$$\vec{j} = \frac{ne^2}{m_e \nu_e} (\vec{E} + \vec{v} \times \vec{B}) - \frac{e}{m_e \nu_e} (\vec{j} \times \vec{B})$$

To put the equation into a more convenient form, an expression for the collision frequency must be given. In the present approximation it equals the ratio of the mean thermal velocity  $\bar{c}$  to the mean-free paths  $\nu = \bar{c}/\lambda$  or the often used collision time  $\tau = \lambda/\bar{c}$ .

The generalized Ohm's law can be written in the form

$$\vec{j} = \sigma \left[ E^* - \frac{\omega_e \tau_e}{\sigma B} (\vec{j} \times \vec{B}) \right] \quad (36)$$

where  $\omega_e = \frac{eB}{m_e}$  is the cyclotron frequency of the electrons in the magnetic field, and

$$\vec{E}^* = \vec{E} + \vec{v} \times \vec{B}$$

Solving this equation explicitly for  $\vec{j}$  gives

$$\vec{j} = \frac{\sigma}{1 + (\omega\tau)_e^2} \left[ \vec{E}^* - \frac{(\omega\tau)_e}{B} (\vec{E}^* \times \vec{B}) + \frac{(\omega\tau)_e^2}{B^2} (\vec{E}^* \cdot \vec{B}) \vec{B} \right]$$

For  $\vec{E}^*$  perpendicular to  $\vec{B}$  the last term drops out and the expression becomes

$$\vec{j} = \frac{\sigma}{1 + (\omega\tau)_e^2} \left[ \vec{E}^* - \frac{(\omega\tau)_e}{B} (\vec{E}^* \times \vec{B}) \right] \quad (37)$$

In Cartesian coordinates, with  $z$  in the direction of the externally imposed magnetic field the  $x$ - and  $y$ -components become

$$j_x = \frac{\sigma}{1 + (\omega\tau)_e^2} [E_x^* - (\omega\tau)_e E_y^*] \quad (38)$$

and

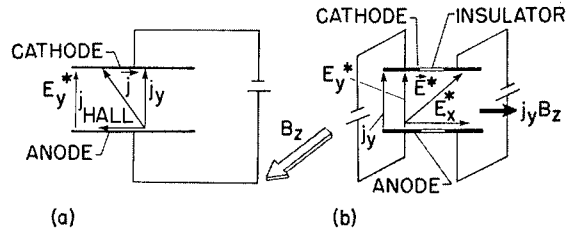
$$j_y = \frac{\sigma}{1 + (\omega\tau)_e^2} [E_y^* + (\omega\tau)_e E_x^*] \quad (39)$$

It is a well established fact that two major possibilities exist:

(a) The first possibility is illustrated on the left side of figure 59-3. The current is permitted to flow between theoretically infinite electrodes; then no space charge will build up inside the plasma as the charges are free to flow. As a result,  $E_x^* = 0$  and

$$\left. \begin{aligned} j_x &= -\frac{\sigma(\omega\tau)_e E_y^*}{1 + (\omega\tau)_e^2} \\ j_y &= \frac{\sigma E_y^*}{1 + (\omega\tau)_e^2} \end{aligned} \right\} \quad \left| \frac{j_x}{j_y} \right| = (\omega\tau)_e \quad (40)$$

The  $x$ -component of the current is the so-called Hall current. Note that neither the  $x$ - nor  $y$ -components of the current actually constitute a particle trajectory.



$$\left. \begin{aligned} E_x^* &= 0 \\ \left| \frac{j_x}{j_y} \right| &= (\omega\tau)_e \quad (20); \\ j_x &= 0 \\ j_y &= \sigma E_y^* \\ E_x^* &= (\omega\tau)_e E_y^* \end{aligned} \right\} \quad (21)$$

(a) Long electrodes.  
(b) Short and segmented electrodes.  
FIGURE 59-3.—Plasma acceleration with currents across electrodes.

(b) The second possibility is shown on the right side of figure 59-3. The current is not permitted to flow in the  $x$ -direction, that is  $j_x = 0$ , by making short electrodes or by segmenting them and connecting with separate power supplies. The  $\vec{j} \times \vec{B}$  force is now in the  $x$ -direction.

$$j_y = \sigma E_y^*$$

and

$$E_x^* = (\omega\tau)_e E_y^* \quad (41)$$

Thus, an electric field due to space-charge separation builds up in the flow direction. Its function is to slow down the electrons which want to move ahead and speed up the ions by mutual space-charge effects so that both move at the same velocity in the axial direction. Details about this approach of plasma acceleration with researchers and companies connected with its development is discussed by M. C. Ellis in paper number 62 of this volume.

### Influence of Collisions in Fully and Partially Ionized Plasmas

If figure 59-1 is compared with figure 59-3(a), it is seen that under the influence of collisions a steady current is established at the angle whose tangent is equal to  $(\omega\tau)_e$ . The electrons have, through collisions, established a steady motion across the magnetic field. What has happened to the ions?

The effects of the friction force on the ions have been actually neglected in the equations (12) and (13) for fully ionized plasmas. The reason is that although the ions and electrons experience the same friction force, the effect of friction on the light electrons will be much larger than the effect on the much heavier ions. In other words, since the ions are so much heavier, the center of mass moves approximately with the ion velocity and thus the effect of friction on the ion motion is negligible. The light electrons, on the other hand, can be influenced to such an extent that the friction force can balance the accelerating force in the electric field, so that a steady electron current is produced. The small magnitude of the influence of the electrons on the ion motion is also evidenced by the ratio

$$\frac{\omega_i \tau_{i,e}}{\omega_e \tau_{e,i}} = \frac{eB \cdot m_e}{m_i \cdot eB} = \frac{m_e}{m_i}$$

Since the collision time between ions and electrons  $\tau_{i,e}$  must equal the collision time between electrons and ions  $\tau_{e,i}$ , the ratio equals that of the cyclotron frequencies, which in turn is equal to the inverse ratio of the masses. In the presence of neutral atoms, the friction forces and collision times between electrons and ions are no longer balanced and different results are obtained.

As a result of this small influence of friction on the motion of the ions in a fully ionized plasma, the ions will follow their tendency toward drift motion normal to electric and magnetic fields more or less in the same fashion as in the collisionless case in figure 59-1. However, in view of the fact that the ion Larmor radius is very much larger than that of the electrons, it can be assumed that when the ion Larmor radius is also much larger than the distance between the electrodes, the ions move

essentially straight across the electrodes. Under such conditions the steady electric field can put energy into the electrons, which accelerate the ions by collisions and space-charge effects. (See figs. 59-3(a) and 59-3(b).)

Now, a few brief remarks will be made on the effects of collisions on partially ionized plasma acceleration. Since neutral atoms have about the same mass as the ions, the motion of the ions can now be strongly influenced in contrast to that of the fully ionized case. The accelerating force and the friction force can balance to give a steady ion velocity. While an additional equation has to be included (refs. 8, 15, and 17) to take account of the collisions of ions and neutrals, there are no more fundamental fine points involved than those already introduced in the fully ionized case. Briefly, the influence of "ion slip" with respect to the neutrals adds to the generalized Ohm's law in equation (21) a term, for  $m_i = m_n$ ,

$$\frac{2\tau_{i,n}}{m_i m_e} (\vec{j} \times \vec{B}) \times \vec{B}$$

The loss due to this term is obtained from the scalar product with  $\vec{j}$ . For  $\vec{j}$  perpendicular to  $\vec{B}$ , this term becomes (ref. 15, eq. (A-4)) and also ref. 8, eq. (6-28)):

Ion-slip loss	Joule loss
$\frac{2\tau_{i,n}}{m_i m_e} j^2 B^2$	$\frac{j^2}{\sigma}$

(42)

In contrast to the well-known Joule loss  $j^2/\sigma$ , the ion-slip loss is thus proportional to the square of the accelerating force per unit volume  $\vec{j} \times \vec{B}$ . The ratio of Joule loss to ion-slip loss is

$$2\omega_e \tau_{e,i} \omega_i \tau_{i,n} \quad (43)$$

In view of the undesirability of these extra losses for plasma acceleration, conditions are usually tailored so as to keep them small. This can be done in a partially ionized plasma by going to relatively high densities where  $\tau_{i,n}$  becomes small, or by using a fully ionized gas where  $\tau_{i,n}$  goes to zero because of a scarcity of neutrals. Fully ionized plasmas are, of course, more easily produced at low densities.

The so-called *EM* (electromagnetic) region (refs. 18 and 19) is frequently mentioned in con-

nection with plasma acceleration. This region applies to fully ionized plasmas and is defined as that region where the ion Larmor radius is larger than the dimensions of the apparatus. The mean-free path is also assumed to be larger than the apparatus dimensions so that even the electrons cannot be influenced by collisions. The ions can only be accelerated by space-charge effects. The name *EM* thus refers to the case where only electric and magnetic effects act in the plasma acceleration. Evidently, it is impossible to have a steady acceleration under precisely these conditions, since as previously pointed out, no energy can be supplied to the plasma for the collisionless steady acceleration. However, from a practical viewpoint, a few collisions will alleviate this condition.

The *EM* concept can, however, be applied precisely to a time-dependent plasma acceleration and, as will be shown subsequently, to the acceleration in the direction of the electric field of ions in a plasma in steady electric and magnetic fields.

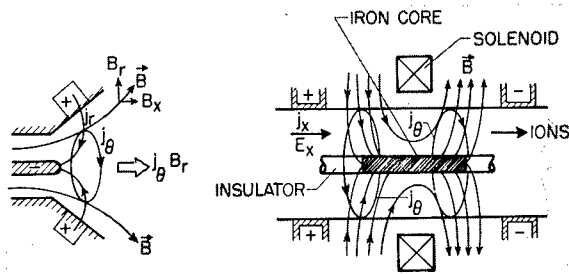
#### Acceleration Using Hall Currents

Two cases are shown in figure 59-4. Since in case (a) the current has a horizontal component the  $\vec{j} \times \vec{B}$  force will be partly against the wall, and this effect increases with increasing that current component. The question thus arises whether one could not use the undesirable Hall current component as the driving current for the  $\vec{j} \times \vec{B}$  force per unit volume. Two ways of accomplishing this result exist and are discussed in paper number 62 of this volume by Ellis. A discussion of a few fundamental questions in such arrangements is of interest. In both cases the arrangement of electric and magnetic fields will be such as to have the Hall current component in the azimuthal direction with a radial magnetic field component to give the  $\vec{j} \times \vec{B}$  force per unit volume.

Briefly, in the first arrangement (fig. 59-4(a)) the Hall current  $j_\theta$  is produced by interaction of a radial electric field  $E_r$  and an axial magnetic field component  $B_z$ ; it subsequently interacts with the radial magnetic field component  $B_r$  to give the  $\vec{j} \times \vec{B}$  force. This mechanism of Hall current acceleration was first discussed

by the writer in reference 20. Most of the further experimental and theoretical developments have been made in some ingenious experiments and analyses at AVCO by R. Patrick and W. Powers (refs. 21 and 22) and by personnel of the NASA Langley Research Center (refs. 15 and 23). It should be emphasized that figure 59-4(a) represents only one possible version of this Hall accelerator. Others are discussed in paper number 62 of this volume. An analysis of the Hall accelerator in figure 59-4(a) with emphasis on the physics of the mechanism is given in reference 24.

In the acceleration method in figure 59-4(b) the azimuthal Hall currents  $j_\theta$  are produced by interaction of the axial electric field  $E_z$  and the radial electric field  $B_r$ . This magnetic field  $B_r$  together with  $j_\theta$  provides the driving force per unit volume. The acceleration is analyzed in some detail in the next section, as also are details about the magnetic-field distribution in figure 59-4(b).



(a) Plasma Hall accelerator.

(b) Ion Hall accelerator.

FIGURE 59-4.—Acceleration of plasma and ions in plasma with Hall currents.

Several questions arise the answers to which are extremely useful in clearing up the differences in the actions of electric and magnetic fields. First, how can the Hall current which is actually a blind current component provide a  $\vec{j} \times \vec{B}$  force? The answer is that the current component is called blind only because it is normal to the axial electric field through which energy is put into the electron current in the direction of the electric field. However, through the magnetic field an electron current component in the azimuthal direction is produced. This component can interact with the radial magnetic field to provide

a  $\vec{j} \times \vec{B}$  force per unit volume for acceleration. The azimuthal component of the electron current will, of course, also provide added Joule losses. This effect is evident by performing a scalar vector multiplication with  $\vec{j}$  for the generalized Ohm's law (eq. (21)); then, with  $\vec{E}^* = \vec{E} + \vec{v} \times \vec{B}$ ,

$$\vec{j} \cdot \vec{E} - (\vec{j} \times \vec{B}) \cdot \vec{v} = \frac{j^2}{\sigma} + \frac{(\omega\tau)_c}{\sigma B} (\vec{j} \times \vec{B}) \cdot \vec{j} \quad (44)$$

where the last term is zero. However, it is the total current density which provides Joule losses. Detailed studies in reference 24 indicate, however, that the efficiency of Hall accelerators based on these simple effects should be as high as that of the basic crossed-field accelerator. If it is assumed in reference 24 for the accelerator in figure 4(a) that current density and magnetic field are the same as  $j_\theta$  and  $B_r$  in the Hall current accelerator, then the Hall current which provides the driving force is higher than the current between the electrodes. The Hall current accelerators offer further possibilities of reduction in losses by plasma containment away from walls by magnetic fields as in a magnetic nozzle. This effect is rather large in the configuration of reference 22 (similar to that of fig. 4(a)), where bulging current paths maintain a plasma in a supersonic magnetic nozzle. The final design will probably be a combination of Hall acceleration and magnetic-nozzle effects. The low efficiencies calculated in reference 25 are based on the choice of a configuration of electrodes and magnetic fields where in the limit of large  $(\omega\tau)_c$  the current across the electrodes cannot cross the magnetic field lines. Thus dissipation rather than acceleration is mostly obtained. With proper choice of configuration (ref. 24), this problem can be avoided with resulting higher efficiencies.

#### Theory for Acceleration of Ions in a Plasma With Hall Currents

In the conventional ion accelerator, the ions are accelerated in the absence of electrons and as a result, according to Childs law, the ion current is limited by space-charge effects. A discussion of such acceleration is given in paper number

48(c) "Electrostatic Thrusters" by Warren D. Rayle. One way to overcome the space-charge limitations for conventional electrostatic ion accelerators is to accelerate the ions inside of a plasma in the presence of electrons. Naturally, as in the conventional ion accelerator, the ions emerging from the accelerator must be neutralized by electrons.

The concept of ion acceleration in plasmas was first described in the work of A. Bratenahl, S. Janes, and A. Kantrowitz from AVCO (ref. 26) as a means for boosting the acceleration in a traveling wave accelerator through superposition of an axial electric field. No direct mention was made of the action of azimuthal Hall currents. The classification of this system of ion acceleration under Hall current accelerators has emerged only gradually. A. Sutton in a review of plasma accelerators (ref. 25) discussed a Hall current accelerator with longitudinal electric field and compared its efficiency with that of a conventional crossed-field accelerator. The physical aspects of this system as an ion accelerator and of the motion of the electrons, however, were not brought out. Detailed descriptions of the acceleration as a steady Hall current ion accelerator with axial electric field and radial magnetic field were given at a meeting on magnetoplasma dynamics held at the Langley Research Center in April 1962, where discussions of Hall current ion accelerators were given by G. R. Seikel and E. Reshotko from the NASA Lewis Research Center, by G. L. Cann from Electro-Optics, Inc. and by R. V. Hess, J. R. Sevier, and R. N. Rigby from the Langley Research Center. At a later date, results of their investigations appeared as references 27 to 29. F. Salz, R. G. Meyerand, and E. C. Lary from United Aircraft have performed fundamental experiments coupled with analysis on such a system (refs. 30 and 31). So have Janes, Dotson, and Wilson from AVCO (ref. 19). J. S. Luce and J. W. Flowers from Oak Ridge National Laboratory have discussed use of an energetic arc confined in an axial magnetic field for ion acceleration in a plasma (ref. 32). Some communications from J. S. Luce, now with Aerojet General, Nucleonics, point to certain common features with ion Hall accelerators.

The following analysis of the Hall current ion accelerator is of a similar form as that given by the writer and J. Sevier at the meeting on magnetoplasma dynamics held at the Langley Research Center, with added remarks concerning the physical mechanism. Assuming the use of a fully ionized gas and steady state acceleration, that is  $\vec{E}$  and  $\vec{B}$  constant, the "generalized Ohm's law" explicitly expressed in terms of the current density  $\vec{j}$  (eq. (37)) is

$$\vec{j} = \frac{\sigma}{1 + (\omega\tau)_e^2} \left[ \vec{E}^* - \frac{(\omega\tau)_e}{B} (\vec{E}^* \times \vec{B}) \right] \quad (45)$$

Expressing  $\vec{j}$  in coordinate form yields

$$j_\theta = \frac{\sigma}{1 + (\omega\tau)_e^2} [v_z B_r - (\omega\tau)_e (E_x - v_\theta B_r)] \quad (46)$$

and

$$j_x = \frac{\sigma}{1 + (\omega\tau)_e^2} [(E_x - v_\theta B_r) + (\omega\tau)_e v_z B_r] \quad (47)$$

The  $\vec{j} \times \vec{B}$  force per unit volume is

$$j_\theta B_r = \frac{\sigma B_r}{1 + (\omega\tau)_e^2} [v_z B_r - (\omega\tau)_e (E_x - v_\theta B_r)] \quad (48)$$

It is indicated that in addition to the axial motion  $v_z$ , the possibility of a rotational motion  $v_\theta$  exists. For the present purpose this rotational motion is ignored by assuming that the Larmor radius of the ions is much larger than the length of acceleration. If this were not the case, other methods would have to be tried to prevent the ions from going into azimuthal drift motion normal to  $E_x$  and  $B_r$ , since the azimuthal Hall current would tend to be sacrificed. The direction of rotation can be reversed by making the ions travel through reversing magnetic fields as indicated, for example, in figure 59-4(b). The  $j_\theta B_r$  force per unit volume is in the same direction for reversed  $B_r$ , since  $j_\theta$  is also reversed. Use of one to several magnetic field reversals through arrangement of several solenoids to form a series of magnetic cusps is discussed in references 19 and 27 to 29. The nature of acceleration for large values of  $(\omega\tau)_e$  is of interest. Then, assuming  $v_\theta \rightarrow 0$ ,

$$j_\theta \rightarrow \sigma \left[ \frac{v_z B_r}{(\omega\tau)_e^2} - \frac{E_x}{(\omega\tau)_e} \right] \quad (49)$$

and

$$j_x \rightarrow \sigma \left[ \frac{E_x}{(\omega\tau)_e^2} + \frac{v_z B_r}{(\omega\tau)_e} \right] \quad (50)$$

Using the expression

$$\sigma = \frac{ne^2}{me} \tau_e$$

there results

$$j_\theta \rightarrow -ne \frac{E_x}{B_r} \quad (51)$$

and

$$j_x = ne(v_{i,x} - v_{e,x}) = nev_x \quad (52)$$

Now  $v_x$  is the velocity of the center of mass, which for a fully ionized plasma is, as can be seen from equation (16), essentially the velocity of the ions. The current  $j_x$  is proportional to the difference in the velocities of ions and electrons; thus,

$$j_x = ne(v_{i,x} - v_{e,x}) \rightarrow nev_{i,x}, \text{ thus } v_{e,x} \rightarrow 0 \quad (53)$$

Also, since the ion velocity in the azimuthal direction is assumed to be zero,

$$j_\theta = ne(v_{i,\theta} - v_{e,\theta}) \rightarrow -nev_{e,\theta} \quad (54)$$

For the sake of completeness the equation of motion, which for the fully ionized plasma is about the same as that for the ions, is given:

$$nm_i \frac{Dv_{i,x}}{dt} = (\vec{j} \times \vec{B})_x = -j_\theta B_r = neE_x \quad (55)$$

Let us summarize the results. The equations of motion for the fully ionized plasma as a whole and of the individual particles yield in the collisionless limit of large  $(\omega\tau)_e$  and correspondingly large  $(\omega\tau)_i$  values the following results. The velocity of the electrons  $v_e$  in the axial direction approaches zero (eq. (53)) and the full drift velocity is attained in the azimuthal direction (eqs. (51) and (54)). The magnetic field exerts a force per unit volume  $-j_\theta B_r$  (eq. (55)), which nearly stops the electron motion; thus in the center of mass system which moves with the ions this force points in the positive direction. The axial current is a pure ion current (eq. (53)). The acceleration of the ions is in the direction of the axial electric field (eq. (55)).

The magnetic field by nearly stopping the axial electron motion has performed the func-

tion of unbalancing the equal and opposite forces on the electrons and ions exerted by the axial electric field. The electric field, which usually puts only energy into the plasma, can now put momentum in the plasma through the ions.

The very fundamental question arises as to what is the true function of the magnetic field and the  $j_\theta B_r$  force per unit volume in providing a thrust on the apparatus. Since a thrust constitutes an integrated effect of the forces acting in the system, it does not matter where the electrons are stopped in the apparatus, as long as they are being stopped so that the directed energy of the ions can be used for thrust. To bring out certain fundamentals, assume for the moment that the plasma is fully ionized and collisionless. If no magnetic field were applied, a thrust would be obtained by having the axial motion of the electrons stopped by the anode, while the ions escape through the cathode. Without a magnetic field the electrons can gain very high velocities in the electric field and would cause considerable energy loss and thus a reduction in efficiency. The possibility, of course, exists of using the anode as the ion source so that the actual waste of energy is greatly reduced, since the ions have to be produced somewhere.

The avoiding of a possible energy loss is, however, only one reason for the use of the magnetic field. Another lies in the fact that without the magnetic field it is difficult to build up a potential inside of the plasma, which is necessary to accelerate the ions. The reason is that since charge continuity must be preserved, for electrons and ions,

$$n_e e v_r = C_1$$

and

$$n_i e v_i = C_2$$

their respective charge densities will be high when their velocities are low and low when their velocities are high. As a result large differences in charge densities will exist near the electrodes. Thus the Debye distance  $d$  (eq. (27)) is small, and the plasma beyond a reasonable multiple of this distance will be shielded from the voltage drop across the electrodes. In other words, the voltage drop will be restricted to thin sheaths near the electrodes and the ion accelera-

tion, as well as the electron acceleration, occurs inside the sheaths. As a result, the ions could lose some axial thrust at the cathode.

The function of the magnetic field is to distribute the voltage drop over the whole plasma. This is accomplished by slowing down the electrons so that, according to the laws of charge continuity, the charge density of the electrons can build up. Thus, in a manner of speaking, a sheath is distributed along the axial direction of the accelerator furnishing a distributed potential drop for accelerating the ions. This distributed potential drop is not in conflict with the definition of a plasma, where  $n_e \approx n_i$ . The reason is that, as pointed out in the discussion of Gauss's law (eq. (11)), only a very small percentage of charge unbalance, as compared with the total charge concentration, is necessary to produce large electric fields inside of the plasma.

Words of caution are necessary in relating the stopping of the electrons in the axial direction by the magnetic field to the establishment of a charge distribution, which in turn yields the electric fields for ion acceleration inside of the plasma. If one were to state merely that the charges are stopped without stating how they are stopped, the law of charge continuity would offer no answer to the nature of the charge distribution. A determination of the magnetic field configuration to yield the optimum charge distribution for ion acceleration would require simultaneous solution of the equations of motion of the ions, Gauss's law, and the law of charge continuity.

The question has also been asked whether the Hall ion accelerator is a  $j \times \vec{B}$  accelerator or an electrostatic accelerator. For the collisionless case where  $\vec{j} \times \vec{B}$  and  $n_e \vec{E}$  are equal, this becomes a question of semantics. Of course, it must be kept in mind that without magnetic field, the electric field  $\vec{E}$  would not be properly distributed in the plasma.

Where collision losses, especially those due to ionizing collisions, are included, the electrostatic effect will no longer be a direct measure of ion acceleration, since the electric field or the voltage drop across the electrodes must also overcome these losses. The  $j_\theta B_r$  force per unit



volume will be a true indicator of the accelerating force on the system. The losses are discussed subsequently in the section "Voltage-Current Characteristics of Hall Ion Accelerator."

### PLASMA PHYSICS OF ELECTRICAL DISCHARGES IN MAGNETIC FIELDS

Thus far, the kinematics and dynamics of plasmas in electric and magnetic fields have been treated. In the sections that follow emphasis will be given to the effect of a magnetic field on the electrical conductivity, ionization, and complete discharge characteristics.

#### General Effect of Magnetic Field on Electrical Conductivity

If the Hall current is permitted to flow (fig. 3(a)), the current between electrodes is given by equation (40)

$$j_y = \frac{\sigma E_y^*}{1 + (\omega\tau)^2}$$

The conductivity is thus effectively reduced by the factor shown in equation (40). Take the case of large magnetic fields where  $(\omega\tau)_e \gg 1$  and use  $\sigma$  in the form

$$\sigma = \frac{n_e e^2}{m\nu}$$

without a magnetic field, where  $\nu = 1/\tau$ . With  $\omega = eB/m_e$ , then with a magnetic field,

$$\sigma_{B\perp} = \frac{m_e n_e \nu}{B^2} \quad (56)$$

The current density in a strong magnetic field is

$$j_y = \frac{n_e m_e}{B^2} \nu E_y^*$$

Thus the dielectric storage effect is again found in a strong magnetic field (eq. (7)), this time for the electrons and modified by collisions.

It is evident that in the presence of a strong magnetic field an increase in collision frequency  $\nu$  will help the electrical conduction by reducing the dielectric storage effects, whereas without the magnetic field an increase in  $\nu$  lowers the conduction. In other words without collisions

the electrons would be forced to go into drift motion normal to the electric and magnetic fields and collisions help them to move in the direction of the electric field.

#### Electrical Conductivities in Partially and Fully Ionized Plasmas Without Magnetic Fields

The collision frequency in the electrical conductivity  $\sigma$  can be expressed in the form

$$\nu = \frac{\bar{c}}{\lambda} = \bar{c}(n_n Q_{e,n} + n_e Q_{e,i}) \quad (57)$$

where  $\bar{c}$  is the mean thermal velocity,  $\lambda$  the mean free path as defined in reference 10, page 105,  $n_n$  and  $n_e$  are the concentrations of neutrons and electrons,  $Q_{e,n}$  the collision cross section of electrons with neutral atoms, and  $Q_{e,i}$  the collision cross section of electrons and ions. The value of  $Q_{e,n}$  is very difficult to determine theoretically as it depends on the detailed electric structure of the atom. Since the positive and negative charges are balanced in an atom, the electron will have to approach very closely to feel the presence of the atom. Analysis of the interaction requires a quantum mechanics approach which may become very complicated; thus one often relies on experiments. The electrons and ions act as single poles and, as such, they can also make fairly close collisions, but the long-range effect of large-angle scattering effects due to many small-angle scattering effects can become very important in a plasma where many particles are present.

The elementary electrostatic laws inherent to the short-range as well as long-range electrostatic interactions are next briefly discussed. For the detailed picture, see, for example, reference 7 (page 249), and reference 1; for a simplified version, see reference 2. The force between two charges is inversely proportional to the square of the distance and the mutual potential is inversely proportional to the distance. At the point of closest approach of the charges their distance is of the order of the effective radius of the charge influence. The collision cross section is of course proportional to the square of this radius. As a result the collision cross section is inversely proportional to the square of the potential energy. Expressing the interaction in terms of thermal energy instead

of potential energy yields the result that the so-called "Coulomb" collision cross section

$$Q_c \propto \frac{1}{T^2} \quad (58)$$

is inversely proportional to the square of the temperature. Since the mean thermal velocity  $\bar{c}$  is proportional to  $T^{1/2}$  (eq. (27)), the collision frequency for a given ionized particle density  $n_c$  is

$$\nu_c \propto \frac{n_c}{T^{3/2}} \quad (59)$$

For a partially ionized plasma, when the collisions of electrons and neutrals predominate, for a given  $n_n$  and  $Q_{c,n}$ ,

$$\nu_n \propto n_n T^{1/2} \quad (60)$$

The constancy of  $Q_{c,n}$  is thereby a carry-over from the elastic-sphere approach of kinetic theory. Actually,  $Q_{c,n}$  may decrease or increase with temperature, in a temperature range before coulomb collisions become important (related for example to the Ramsauer effect, ref. 33, which requires a quantum-mechanics explanation). For the present purpose  $Q_{c,n}$  is assumed to be independent of temperature; this condition would also hold for the billiard ball approach of classical kinetic theory.

It must be strongly emphasized that use of the collision cross section  $Q_{c,i}$  for fully ionized plasmas does not necessarily imply that the plasma has to be fully ionized. This is especially true if a plasma tends to become ionized at comparatively low temperatures and thus the collision cross section between electrons and ions begins to dominate when the percentage of ionization is very small.

The conductivity  $\sigma$  for Coulomb collisions is

$$\sigma_c = \frac{n_c e^2}{m \nu} \propto T^{2/3} \quad (61)$$

whereas, for collisions of electrons with neutral atoms,

$$\sigma_n \propto \frac{n_c}{n_n} T^{-1/2} \quad (62)$$

For the Coulomb conductivity the concentration of charged particles thus has cancelled out, ex-

cept for a weak dependence in a logarithmic term related to the long range interaction effects, this term is not included here, but can be found in the basic texts (réf. 1 to 11).

The fact that the Coulomb conductivity depends only weakly on the particle density is not surprising if classical kinetic theory for a gas consisting only of one species of atoms is considered. There, the transport coefficients such as viscosity or thermal conductivity are independent of density but solely dependent on temperature. It can be considered that for charged particles or Coulomb interactions the particles act alike in spite of their different masses because the interaction effects are based on the like charges of the particles.

#### Electrical Conductivity of Fully and Partially Ionized Plasmas in Magnetic Fields

As shown in equation (56), the conductivity of a plasma across a magnetic field  $B$  is given by

$$\sigma_{B\perp} = \frac{m_e n_c \nu}{B^2}$$

For a fully ionized plasma, if  $\nu_c$  is taken from equation (59)

$$(\sigma_{B\perp})_c \propto \frac{n_c^2}{T^{3/2}} \frac{1}{B^2} \quad (63)$$

whereas for a partially ionized plasma with  $\nu_n$  taken from equation (60)

$$(\sigma_{B\perp})_n \propto \frac{n_c n_n}{B^2} T^{1/2} \quad (64)$$

assuming that the collision cross section  $Q_{c,n}$  remains constant with varying  $T$ . Note that the coulomb conductivity across the magnetic field,  $(\sigma_{B\perp})_c$ , depends now also on the charged particle density. The magnetic field by acting differently on electrons and ions, has reduced the effect of equality of particles with like charges, on which was based the strong dependence of  $\sigma_c$  on temperature.

#### Effect of Finite Extensions of Electrodes on Electric Conductivity in Magnetic Fields

In AVCO's work (ref. 34) the interesting result was shown that if the magnetic field

lines are made to extend beyond the electrode region, the currents will not flow straight across the magnetic field but will bulge in the direction of the magnetic field lines. The bulging of the current is related to the fact that the electrons like to move (in a corkscrew motion) along the magnetic lines when there are comparatively few corresponding collisions, that is  $(\omega\tau)_e$  is considerably larger than 1. The ratio of the azimuthal Hall current density to the radial current density is as in the case of infinite electrodes (eq. 40))

$$\frac{j_\theta}{j_r} = (\omega\tau)_e$$

For the limiting case of very short electrodes, the radial current density is credited to F. J. Fishman in the appendix of reference 34.

$$j_r = \frac{\sigma E_r}{\sqrt{1 + (\omega\tau)_e^2}} \quad (65)$$

for infinite electrodes. For very strong magnetic fields this implies

$$j_r \rightarrow \frac{\sigma E_r}{\omega\tau} = \frac{ne}{B} E_r \quad (66)$$

The electrical conductivity normal to the magnetic field thus becomes independent of collisions in this limit and is the same for fully and partially ionized plasmas (using the superscript  $f$  for finite electrodes).

$$(\sigma_{B\perp})^f = \frac{ne}{B} \quad (67)$$

Then,  $j_r = \frac{nm_e\omega E_r}{B^2}$ , where the dielectric effect in a strong magnetic field again makes its appearance.

One should be reminded that also for diffusion in magnetic fields important effects are introduced by finite dimensions of the apparatus, related to the tendency of electrons to move along magnetic lines for high values of  $(\omega\tau)_e$ . This so-called Simon diffusion (for example, refs. 9 and 22) has, however, different reasons from those discussed here.

### Conductivity and Voltage Current Characteristics of Electrical Discharges in Magnetic Field

The development of the expressions for electrical conductivity show that aside from its direct dependence on the magnetic field it depends also on the electron concentration  $n_e$  (or on the ratio of  $n_e/n_n$ , where  $n_n$  is the concentration of neutral atoms) and the temperature. The form of the dependence, however, depends on the magnetic field.

No mention has been made of the possible variation of these parameters under variation of electric field. Such a constancy of the parameters can be enforced, for practical cases, by introducing, into the crossed electric and magnetic fields, a plasma of a given ionization whereby the function of the discharge is just to keep the parameters constant. Furthermore, it could be assumed that the cathode is thermionically emitting so that only slightly higher electric fields are required to produce the electrons necessary for ionization.

From a practical viewpoint it is not only of interest that these parameters are constant but how much energy need be supplied by the electric field to keep them constant. Also, it is important to know how each parameter varies with an increased energy input; for example, it is of great practical importance how the electron concentration  $n_e$  may be increased without excessive increase in the temperature  $T$ .

Much useful information about the behavior of a discharge can be gained from its voltage-current characteristics. Since no attempt will be made to develop a general theory on this involved matter, examples from some recent research developments at NASA and elsewhere will be given.

### Voltage Plateaus for Widely Differing Discharges in Magnetic Fields

Experiments have shown that a large number of arc discharges without magnetic fields have negative voltage-current characteristics. This result is due to the fact that when the discharge just begins to become ionized, very rapid ionization processes can occur; these processes increase  $n_e$  very rapidly so that the discharge may require only a low temperature and low electric field or voltage to furnish an increased current.

As the ionization of the plasma increases and the electrical conductivity changes from that of a partially ionized plasma (eq. (62))

$$\sigma \propto \frac{n_e}{n_n} T^{-1/2}$$

to that of a more highly ionized plasma, where the Coulomb collisions predominate (eq. (61))

$$\sigma_c \propto T^{3/2}$$

The voltage must increase, therefore, to increase the current when the increase in temperature is not large. The existence of a positive voltage-current characteristic for discharges with predominant Coulomb collisions has been observed in reference 35 at atmospheric pressure and in reference 21 at pressures from 10 to 100 mm Hg at very high currents. In view of the fact that, in changing from a partially to a more highly ionized plasma, the voltage-current characteristic can change from negative to positive, a voltage plateau can occur without a magnetic field.

Arc discharges in fairly well ionized plasmas of pressures from 1 to 100 mm Hg in magnetic fields up to 13,000 gauss with currents up to 270 amperes have been produced in experiments by W. Grossmann, Jr., at the Langley Research Center. The electric field is in the radial and the magnetic field in the axial direction. In these experiments a constant voltage with increasing current was observed. Measurements by researchers at AVCO (ref. 34) and at Langley for a similar discharge indicate the existence of Hall currents. For both experiments using tungsten cathodes uniform disk discharges were observed; more about these results are given in paper number 62 of this volume by M. C. Ellis. A report on the existence of the voltage plateau and its possible interpretation was given in a joint paper by W. Grossmann and the writer (ref. 23). In AVCO's work the existence of a "voltage plateau" was not explicitly recognized. It can, however, be obtained by replotting figure 8 in reference 34. A brief analysis, performed by Philip Brockman at the Langley Research Center, using the assumption that a large share of the power goes into rapid ionization has indicated this same result.

Since the plasma is fairly well ionized the question arises: how can the ionization affect the conductivity and the voltage-current characteristics, since the Coulomb conductivity without the magnetic field shows only a temperature dependence? As indicated from the expressions of the conductivity in a magnetic field in the Coulomb range (eq. (63))

$$(\sigma_{B\perp})_c \propto \frac{n_e^2}{T^{3/2}} \frac{1}{B^2}$$

or for the finite electrode case (eq. (67))

$$(\sigma_{B\perp})^f \propto \frac{n_e}{B}$$

in the presence of the magnetic field, an increase in ionized particles can affect the conductivity. Thus, a voltage plateau with increasing current due to rapid ionization processes can occur.

It should be emphasized that voltage plateaus have been also observed under vastly different conditions. For example, the well-known Alfvén-Fahleson voltage plateau (refs. 36 and 37) in an apparatus of similar geometry occurs for very low densities under conditions where the ion Larmor radius is smaller than the gap between electrodes. As a result the ions perform azimuthal drift motion normal to the radial electric field and the axial magnetic field. The electron currents are assumed to be small. The ions transfer their drift energy via the electrons which in turn use it to rapidly ionize the neutral atoms. The latter move slowly in view of their collisions with the apparatus wall. (See also analysis in ref. 38.)

The reason for the voltage plateau in the present case is vastly different since the ions are not set into collisionless drift motion, the densities being much higher. The energy for ionization is fed into the plasma directly by the electrons. A detailed analysis of this discharge including radiation effects and possible nonequilibrium ionization effects due to electron temperatures in excess of atom temperatures is being performed by H. Hassan at North Carolina State College under contracts to NASA. (For a discussion of such nonequilibrium effects, see ref. 39.)

The voltage plateau noted by both the Alfvén-Fahleson research and by research at

Langley are related to rapid ionization processes in plasmas. The energy is fed rapidly into ionization, while the ionization is still too low to put the plasma as a whole in rotation. Once the ionization becomes high enough and begins to be saturated, energy can be put into accelerating the plasma with a resultant voltage increase and the establishment of a positive voltage-current characteristic.

Recently a voltage plateau was also reported for a fully ionized rotating plasma in the Ixion (ref. 12, part II). The reasons for this voltage plateau are vastly different. Apparently the rotating plasma reaches a velocity limit due to friction with the walls. As a result it can no longer be accelerated and the voltage reaches a plateau.

#### Voltage-Current Characteristics of Hall Ion Accelerator

In the discussion of the Hall ion accelerator a fully ionized collisionless plasma was assumed corresponding to values  $(\omega\tau)_c$  approaching infinity. For practical situations, of course,  $\tau$  is finite. To analyze the effects of collisions one could adopt the viewpoint that the ionized plasma has been freely provided and that not much energy is required to maintain it. Since the matter of concern here is with fully ionized, almost collisionless plasmas for ion acceleration, if possible with a negligible amount of neutral atoms, the operation must be at considerably lower pressures than 1 mm Hg. While it is often easier to produce higher ionization at low pressures just because there is less gas to ionize, it is also more difficult to maintain it because of greater losses to the walls unless, of course, the plasma is kept away from the walls with magnetic fields. In the basic experiment performed by R. N. Rigby (ref. 29) of the Langley Research Center and continued by R. H. Weinstein, a radial magnetic field was imposed across an axial discharge (with the use of a flux concentrator in the center as shown in the schematic drawing in fig. 59-4(b)). The purpose was to see what happens when the  $j\theta B_r$  interaction is optimized with a pure radial magnetic field  $B_r$  with expected penalties in losses. A similar configuration was used in

reference 31, however, without reversed magnetic fields along the axis.

From the previous discussion better understanding of the practical implications in relaxing the collisionless fully ionized state is possible. For this case the only energy required is that for accelerating the ions. No energy is supplied by the axial electric field to the azimuthal electron current  $j_\theta$  because without elastic collisions and without requirements on the electrons to perform ionizing or inelastic collisions, they do not require an energy input in the steady state. In order to provide steady energy for ionization an axial current will, however, need to exist. Through it some energy is also fed into heat, some of which is lost to the wall.

In the experiments, which will be discussed in more detail by M. C. Ellis (paper number 62 of this volume), an increase of voltage was required for a current increase. The slope of the voltage-current characteristic increases with increasing magnetic field and decreasing pressure. The slopes are too steep to suggest the effect of axial or azimuthal velocity (through  $v_x B_r$  or  $v_\theta B_r$ ) responsible for the main effect in the increase of  $E_x$  (see eqs. (46) and (47)). The increasingly positive voltage-current characteristic with increasing magnetic field can be obtained from equations (63) and (64) for the conductivity  $\sigma$  by assuming that the electron concentration  $n_e$  and the temperature  $T$  do not vary much as voltage and current are increased.

The important fact is that if approximately constant values of  $n_e$  and  $T$  can be shown to exist over a wide variety of slopes of the voltage-current characteristics, the slopes will be solely a function of the magnetic field. (Of course careful measurements of  $n_e$  and  $T$  over a wide variety of conditions are important.) Assuming that the discharge covers the same cathode area for increasing magnetic field, the electric field-current density characteristic can be substituted for the voltage-current characteristics. There follows, when no current bulging is possible as in the Hall ion accelerator, with  $(\sigma_{B\perp})_c$  from equation (63):

$$\frac{E_x}{j_z} = \frac{1}{(\sigma_{B\perp})_c} \propto B^2$$

Experiments in the low pressure range at high  $(\omega\tau)_e$  indicate a slope proportional to  $\vec{B}$ . This could be the result of current bulging along the magnetic field lines, since using the conductivity from equation (67) would result in

$$\frac{E_x}{j_x} = \frac{1}{(\sigma_{B\perp})^f} \propto B_r$$

However, the experimental arrangement in the Hall ion accelerator does not encourage current bulging. Thus, there must be different reasons for the linear dependence on  $\vec{B}$  of the slope of the voltage-current characteristic. They will be discussed in the following section.

First, a few remarks about the significance of Hall current measurements are important. As previously mentioned the voltage gradient or electric field  $E_x$  along the axis of the device is no longer responsible solely for the acceleration of the ions but must also furnish the energy to overcome losses due to ionization or heating. The electric field along the axis and the voltage drop across the electrodes will thus be higher than that required for acceleration. A measurement of the voltage variation along the axis will as a consequence not be an explicit measure of the directed energy put into the ions. The  $j_\theta B_r$  force per unit volume, however, actually represents the true accelerating force. Measurement of the Hall current in the azimuthal direction thus is desirable for a knowledge of the distribution of accelerating forces along the accelerator. Measurements of both  $j_\theta$  and  $E_x$  can, of course, furnish important information concerning the losses. Hall current measurements have been performed by R. N. Rigby (ref. 29) and have been continued by R. H. Weinstein, J. Burlock, and T. M. Collier of the Langley Research Center.

#### Effect of "Plasma Turbulence" on Electrical Conductivity and Voltage-Current Characteristics in a Magnetic Field

The problem of "turbulent" or anomalous diffusion has become one of the most critical problems of plasma physics. (It is noteworthy that the turbulence in plasmas is not the same process as in fluids). On its avoidance depends the success of thermonuclear fusion. The prob-

lem is essentially that whenever deviations from a quiescent plasma state occur, the tendency exists for a diffusion more rapid across the magnetic field than that determined by the classical result (see refs. 1 to 11)

$$D_{B\perp} = \frac{D}{1 + (\omega\tau)_e^2} \quad (68)$$

where  $D$ , the diffusion coefficient, say for electrons, can be expressed by

$$D = C_3 \lambda \bar{c} = C_3 \lambda^2 \nu \quad (69)$$

in the presence of a strong magnetic field by making the proper substitutions

$$D_{B\perp} = \frac{D}{(\omega\tau)_e^2} = \frac{1}{\frac{e^2 \lambda^2}{m^2 c^2}} \frac{D}{B^2} = C_3 r_{L,e}^2 \nu \quad (70)$$

It has now been found (refs. 1 to 11) that for anomalous or turbulent diffusion, the diffusion is inversely proportional to  $\vec{B}$

$$(D_{B\perp})_{\text{turb}} = C_4 \frac{D}{B} \quad (71)$$

instead of being inversely proportional to  $B^2$ . This relation is the so-called Bohm diffusion. The reason for such behavior is, roughly, that amplified oscillations occur in the plasma and produce electric fields normal to the magnetic lines; as a result a drift motion occurs across the magnetic field. Since such drift motion is inversely proportional to  $\vec{B}$  (and proportional to  $\vec{E}$ ), a diffusion coefficient inversely proportional to  $\vec{B}$  instead of  $B^2$  is established.

It has long been known that discharges across magnetic fields can maintain much higher currents than would be expected on the basis of the classical law that suggests a conductivity inversely proportional to  $B^2$ . The operation of the PIG (Phillips Ionization Gage) discharge at low pressures has shown such behavior (see also refs. 40 and 41 for more recent work). A study of a PIG discharge with radial electric and axial magnetic fields was made at the Langley Research Center (ref. 15), and the mechanism for oscillations was studied. In the axial discharges with radial magnetic fields, oscilla-

tions were observed by researchers at AVCO (ref. 19), at United Aircraft (refs. 30 and 31), and at the Langley Research Center (ref. 29).

For determination of the "turbulent" electrical conduction in a discharge crossing a magnetic field, the voltage-current characteristic again offers a very useful tool. For turbulent conduction oscillating electric fields can build up in the azimuthal direction superposed on the Hall current (refs. 15 and 42, for a possible amplification mechanism), which together with the radial magnetic field permit a drift of the electrons along the axial direction. As a result the axial current is given by

$$\left. \begin{aligned} j_x &= \alpha \beta n_e e \frac{E_x}{B_r} \\ j_x &= (\sigma_{B\perp})_{\text{turb}} E_x \end{aligned} \right\} \quad (72)$$

with

$$(\sigma_{B\perp})_{\text{turb}} = \frac{\alpha \beta n_e e}{B_r} \quad (73)$$

This expression is found in reference 43 (see also ref. 44). (In these references  $\vec{B}$  is axial and  $\vec{E}$  is radial.) In this expression the nature of the drift is included by the inverse proportionality of the electrical conductivity to  $B_r$ . The effect of the azimuthal electric field oscillations producing the enhanced conduction across  $B_r$  is included by a factor  $\alpha$ ; the factor  $\beta$  depends on the particular geometry.

Assuming that  $n_e$ ,  $\alpha$  and  $\beta$  do not vary much with increasing currents, the slope of the voltage characteristic is then

$$\frac{E_x}{j_x} \propto B_r \quad (74)$$

This fits the variation of the slope of the voltage-current characteristics in the Hall ion accelerator for low pressures given in reference 29. Such fit was also found by researchers at AVCO (ref. 19) and United Aircraft (ref. 31). It thus appears that we are dealing with turbulent electrical conduction.

The question arises of how to reduce this turbulence. One way as pointed out in reference 19 is to use truly well-ionized plasmas. Then the magnitude of axial electron currents to maintain the energy input through the axial

electric field is reduced. The axial electric field required to feed the ionization energy into the plasma, feeds it also into the oscillations. Thus, for proper injection of a fully ionized fast moving plasma the possibility exists of keeping the oscillations and the turbulence down. Another way is to operate a Hall accelerator at higher pressures as is done for the Hall accelerators with radial electric fields. Such an approach is also used for the Hall ion accelerator by G. Cann (ref. 28) and in some of the configurations used at the Langley Research Center. Another possibility arises by using a time-dependent reversal of the radial magnetic field with resulting reversal of the azimuthal electron motion to delay the growth of instabilities. This concept is suggested by recent experiments in ref. (45), indicating that instabilities of a magnetically confined discharge could be delayed by rapid current reversals; this, however, would be detrimental to propulsion. A many-phase traveling magnetic field rotating around the annulus would cut down the occurrence of zero magnetic field, but it may also prevent the electrons from oscillating back and forth if they are tied to the rotating magnetic field. The use of externally imposed waves has also been suggested.

Finally, attention should be drawn to the coincidence that the slope of the voltage-current characteristic for turbulent electrical conductivity (eq. (73)) is inversely proportional to  $\vec{B}$ , but the slope for nonturbulent conductivity with current fringing along the magnetic lines (eq. (67)) is also inversely proportional to  $B$ , but for vastly different reasons. In this connection details of the experimental arrangement in reference 43, for which turbulent conduction and diffusion laws have been established, is of interest. A highly ionized plasma is produced in an axial discharge which is confined by an axial magnetic field. Perpendicular to this field a small current is drawn to an auxiliary ring electrode. Since the ring electrode is of finite dimension, a slight possibility exists of some current bulging in the direction of the magnetic field lines, although the other electrode is the long discharge plasma. In references 43 and 44, however, the turbulent noise level is also

checked and apparently the theory of turbulent conduction or diffusion is well established. It is also of interest that in reference 43 a current actually drawn from the main plasma is used to check the effects of plasma turbulence in the presence of a magnetic field. The implication is given that similar turbulent laws should apply to diffusion across the magnetic field. The idea is that although there exist differing mechanisms for the production of turbulence, the actual effect of the fully developed turbulence should give a voltage-current slope inversely proportional to  $\bar{B}$ . Since there are a variety of macroscopic and microscopic amplification mechanisms (see discussion on stability in ref. 7 and ref. 46) in the plasma with different individual character, the final answer is not yet

quite clear although large-scale turbulence is known to decay to small-scale turbulence.

### FINAL REMARKS

The purpose of this paper is mainly to point out that a profound knowledge of the deeper implications of known aspects of plasma physics or measurement techniques is necessary before experimental results can be attributed to anomalous effects. The history of plasma physics is full of such situations. On the other hand, once new effects are discovered they can be found in many situations; the field of plasma "turbulence" is a good example. On both counts the role of the university which combines teaching with research is of great importance.

### REFERENCES

1. SPITZER, LYMAN, JR.: Physics of Fully Ionized Gases. Interscience Publ., Inc. (New York), 1956.
2. GLASSTONE, SAMUEL, and LOVBERG, RALPH H.: Controlled Thermonuclear Reactions. D. Van Nostrand Co., Inc., c.1960.
3. CHANDRASEKHAR, S. (S. K. TREHAN, compiler): Plasma Physics. The Univ. of Chicago Press, c.1960.
4. LINHART, J. G.: Plasma Physics. Interscience Publ., Inc. (New York), 1960.
5. ROSE, DAVID J., and CLARK, MELVILLE, JR.: Plasmas and Controlled Fusion. The M.I.T. Press and John Wiley & Sons, Inc., c.1961.
6. ANON.: Notes on Plasma Dynamics, M.I.T., Aug. 1959.
7. WANDEL, C. F., ed.: International Summer Course in Plasma Physics, 1960. Risø Rep. No. 18, Danish Atomic Energy Comm., Nov. 1960, pp. 119-248.
8. COWLING, T. G.: Magnetohydrodynamics. Interscience Publ., Inc., (New York), 1957.
9. SIMON, ALBERT: An Introduction to Thermonuclear Research. Pergamon Press (New York), 1959.
10. KENNARD, EARLE H.: Kinetic Theory of Gases. McGraw-Hill Book Co., Inc., 1938.
11. ECKER, G.: Electrode Components of the Arc Discharge. Reprinted from *Ergebnisse der Exakten Naturwissenschaften*, Bd. XXXIII, Springer-Verlag (Berlin), 1961.
12. BAKER, D. A., HAMMEL, J. E., and RIBE, F. L.: Rotating Plasma Experiments. I. Hydromagnetic Properties. *The Physics of Fluids*, vol. 4, no. 12, Dec. 1961, pp. 1534-1548.
13. BAKER, D. A., and HAMMEL, J. E.: Rotating Plasma Experiments. II. Energy Measurements and the Velocity Limiting Effect. *The Physics of Fluids*, vol. 4, no. 12, Dec. 1961, pp. 1549-1558.
14. EBEL, M. E., KROLL, N. M., et al.: Plasma Propulsion Studies—Summer, 1959. LA-2408 (Contract W-7405-ENG. 36), Los Alamos Sci. Lab., Univ. of California, Aug. 3, 1960.
15. ANDERSON, OSCAR, BARKER, WILLIAM R., et al.: Hydromagnetic Capacitor. *Jour. Appl. Phys.*, vol. 30, no. 2, Feb. 1959, pp. 188-196.
16. HESS, R. V., BURLOCK, J., SEVIER, J. R., and BROCKMAN, P.: Theory and Experiments for the Role of Space-Charge in Plasma Acceleration. *Electromagnetics and Fluid Dynamics of Gaseous Plasma*. Vol. XI of Microwave Res. Inst. Symposia Ser., Polytechnic Press of Polytechnic Inst. of Brooklyn, c.1962, pp. 269-305.
17. KEMP, NELSON H., and PETSCHKE, HARRY E.: Two-Dimensional Incompressible Magnetohydrodynamic Flow Across an Elliptical Solenoid. Res. Rep. 26, AVCO Res. Lab., Apr. 1958.



# PLASMA INTERACTION WITH ELECTRIC AND MAGNETIC FIELDS

17. WOOD, GEORGE P., CARTER, ARLEN F., LINTZ, HUBERT K., and PENNINGTON, J. BYRON: A Theoretical Treatment of the Steady-Flow, Linear, Crossed-Field, Direct-Current Plasma Accelerator for Inviscid, Adiabatic, Isothermal, Constant-Area Flow. NASA TR R-114, 1961.
18. KANTROWITZ, ARTHUR R., and PETSCHKE, HARRY, E.: An Introductory Discussion of Magnetohydrodynamics. Res. Rep. 16, AVCO Res. Lab., May 11, 1957.
19. JANES, G. S., DOTSON, J., and WILSON, T.: Electrostatic Acceleration of Neutral Plasmas—Momentum Transfer Through Magnetic Fields. Presented at Third Symposium on Advanced Propulsion Concepts (Cincinnati, Ohio), Oct. 2-4, 1962. (Sponsored by U.S. Air Force and Gen. Elec. Co.)
20. HESS, ROBERT V.: Experiments and Theory for Continuous Steady Acceleration of Low Density Plasmas. Vol. I of Proc. XIth Int. Astronautical Cong., Carl W. P. Reuterswärd, ed., Springer-Verlag (Vienna), 1961, pp. 404-411.
21. POWERS, W. E., and PATRICK, R. M.: A Magnetic Annular Arc. Engineering Aspects of Magnetohydrodynamics, Clifford Mannal and Norman W. Mather, eds., Columbia Univ. Press, 1962, pp. 5-18.
22. PATRICK, R. M., and POWERS, W. E.: Plasma Flow in a Magnetic Annular Arc Nozzle. Presented at Third Symposium on Advanced Propulsion Concepts (Cincinnati, Ohio), Oct. 2-4, 1962. (Sponsored by U.S. Air Force and Gen. Elec. Co.)
23. GROSSMANN, WILLIAM, Jr., and HESS, ROBERT V.: Existence of a Voltage Plateau for a Discharge Crossed With a Magnetic Field at Elevated Pressures. Presented at the Summer Meeting, American Phys. Soc. (Seattle, Wash.), Aug. 27, 1962.
24. SEVIER, JOHN R., HESS, ROBERT V., and BROCKMAN, PHILIP: Coaxial Hall Current Accelerator Operation at Forces and Efficiencies Comparable to Conventional Crossed-Field Accelerators. ARS Jour. (Tech. Notes), vol. 32, no. 1, Jan. 1962, pp. 78-80.
25. SUTTON, GEORGE W., and GLOERSEN, PER: Magnetohydrodynamic Power and Propulsion. Magnetohydrodynamics, Ali Bulent Cambel, Thomas P. Anderson, and Milton M. Slawsky, eds., Northwestern Univ. Press (Evanston, Ill.), c. 1962, pp. 243-268.
26. BRATENAH, A., JANES, G. S., and KANTROWITZ, A. R.: Plasma Acceleration in the Electromagnetic Region II. Bull. American Phys. Soc., ser. II, vol. 6, no. 4, June 22, 1961, p. 379.
27. SEIKEL, G. R., and RESHOTKO, E.: Hall Current Ion Accelerator. Bull. American Phys. Soc., ser. II, vol. 7, no. 6, June 19, 1962, p. 414.
28. CANN, G. L., TEEM, J. M., BUHLER, R. D., and BRANSON, L. K.: Magnetogasdynamics Accelerator Techniques. AEDC-TDR-62-145 (Contract No. AF 40(600)-939), Arnold Eng. Dev. Center, July 1962.
29. RIGBY, ROBERT NORRIS: Some Physical Properties of an Axial Electric Arc in a Radial Magnetic Field. M. S. Thesis, The College of William and Mary in Virginia, 1962.
30. LARY, E. C., MEYERAND, R. G., Jr., and SALZ, F.: Ion Acceleration in a Gyro-Dominated Neutral Plasma—Theory. Bull. American Phys. Soc., ser. II, vol. 7, no. 7, Aug. 27, 1962, p. 441.
31. SALZ, F., MEYERAND, R. G., Jr., and LARY, E. C.: Ion Acceleration in a Gyro-Dominated Neutral Plasma—Experiment. Bull. American Phys. Soc., ser. II, vol. 7, no. 7, Aug. 27, 1962, p. 441.
32. LUCE, J. S., and FLOWERS, J. W.: The High Specific Impulse, Arc-Ion System. ORNL-3031 (Contract No. W-7405-eng-26), U.S. Atomic Energy Comm., Apr. 21, 1961.
33. MASSEY, H. S. W., and BURHOP, E. H. S.: Electronic and Ionic Impact Phenomena. The Clarendon Press (Oxford), 1952.
34. POWERS, WILLIAM E., and PATRICK, RICHARD M.: Magnetic Annular Arc. The Physics of Fluids, vol. 5, no. 10, Oct. 1962, pp. 1196-1206.
35. BUSZ, G., and FINKELNBURG, W.: Thermische Lichtbögen hoher Temperatur und niedriger Brennspannung. Z. Phys., Bd. 138, Heft 2, 1954, pp. 212-225.
36. ALFVÉN, H.: Collision Between a Nonionized Gas and a Magnetized Plasma. Magneto-Fluid Dynamics, F. N. Frenkiel and W. R. Sears, eds., Pub. 829, Nat. Res. Council, Nat. Acad. Sci., 1960, pp. 710-713.
37. FAHLESON, ULF V.: Experiments With Plasma Moving Through Neutral Gas. The Physics of Fluids, vol. 4, no. 1, Jan. 1961, pp. 123-127.
38. LIN, SHAO-CHI: Limiting Velocity for a Rotating Plasma. The Physics of Fluids, vol. 4, no. 10, Oct. 1961, pp. 1277-1288.
39. HURWITZ, H., JR., SUTTON, G. W., and TAMOR, S.: Electron Heating in Magneto-hydrodynamic Power Generators. ARS Jour., vol. 32, no. 8, Aug. 1962, pp. 1237-1243.

# PLASMA PHYSICS AND MAGNETOHYDRODYNAMICS

40. KAUFMAN, HAROLD R.: The Electron-Bombardment Ion Rocket. Presented at Third Symposium on Advanced Propulsion Concepts (Cincinnati, Ohio), Oct. 2-4, 1962. (Sponsored by U.S. Air Force and Gen. Elec. Co.)
41. BINGHAM, R. L., CHEN, F. F., and HARRIES, W. L.: Preliminary Studies of a Reflex Arc. MATT-63 (Contract AT(30-1)-1238), Plasma Phys. Lab., Princeton Univ., Feb. 1, 1962.
42. BUNEMAN, O.: Instability of Electrons Drifting Through Ions Across a Magnetic Field. Tech. Rep. No. 251-1 (Contract AF49(638)-660), Stanford Electronics Labs., Stanford Univ., July 20, 1961.
43. YOSHIKAWA, S., and ROSE, D. J.: Anomalous Diffusion of a Plasma Across a Magnetic Field. *The Physics of Fluids*, vol. 5, no. 3, Mar. 1962, pp. 334-340.
44. YOSHIKAWA, SHOICHI: Electrical Conductivity of a Turbulent Plasma. *The Physics of Fluids*, vol. 5, no. 10, Oct. 1962, pp. 1272-1277.
45. RUGGE, HENRY F., and PYLE, ROBERT V.: Instability of the Positive Column of an AC Discharge in a Magnetic Field. *Bull. American Phys. Soc. Abstract D12. Ser. II*, vol. 7, no. 7, Aug. 27-29, 1962, p. 442.
46. KADOMTSEV, B. B.: Turbulent Loss of Particles From a Discharge in a Strong Magnetic Field. *Soviet Physics—Tech. Phys.*, vol. 6, no. 10, Apr. 1962, pp. 882-888.

*AUTHOR'S NOTE: After this paper was presented at the conference, the 4th Annual Meeting of the Division of Plasma Physics of the American Physical Society was held in Atlantic City, N.J., from November 28 to December 1, 1962, where further instability mechanisms in crossed electric and magnetic fields were suggested by Albert Simon from General Atomic and by G. Briffod, M. Gregoire, and C. Manus, Centre d'Etudes Nucleair de Saclay, France. In the latter paper, also, interesting experiments for the onset of the instabilities were shown. At this meeting, also, recent Hall current measurements were discussed in a paper by R. V. Hess, R. N. Rigby, and R. H. Weinstein of the NASA Langley Research Center, with emphasis on the use of the Hall currents for the measure of the onset and existence of turbulent conduction.*

# 60. The Electric Drag Forces on a Satellite in the Earth's Upper Atmosphere

By George P. Wood

GEORGE P. WOOD, *Head, Magnetohydrodynamics Section, Aero-Physics Division, NASA Langley Research Center, received his Bachelor's and Master's degrees in Physics from the University of Mississippi and also did graduate work at the Johns Hopkins University. Wood joined the Langley staff as a junior physicist in July 1940. He is recognized as an international authority on optical interferometric observation of flows and in magnetohydrodynamics. He has specialized in heat transfer, optical interferometric study of transonic and supersonic flows, and magnetohydrodynamics. He published the first paper in the United States dealing with aerodynamic heating at supersonic speeds and was the first to achieve steady-state crossed-field acceleration of high-density plasma. He is author of 25 NASA technical publications on research he has conducted at Langley.*

## SUMMARY

A theoretical study has been made of the electric drag forces acting, as a result of the electric charge on the sphere, on a spherical satellite in free-molecule flow in the upper atmosphere. The analysis has been applied to a 4-meter-diameter earth satellite at an altitude of 1,500 kilometers. The calculations have yielded charge-density distribution and potential distribution in the sheath, the ion trajectories, the increased ion-impact drag, the ion-scattering drag, and the induction drag due to the earth's magnetic field. These three electric drags total about  $3\frac{1}{2}$  percent of the drag of the uncharged sphere for average conditions between maximum and minimum of sunspot activity. The percentage would be approximately doubled at the maximum and approximately halved at the minimum.

## INTRODUCTION

This paper describes one of the applications of plasma physics and magnetohydrodynamics in space research.

One of the uses of artificial earth satellites is the determination of the density of the upper reaches of the earth's atmosphere. Explorer

IX (1961 Delta 1) is a satellite that was placed into orbit by the NASA in February of 1961 for the purpose of measuring the density of the atmosphere. It is a 12-foot-diameter hollow lightweight sphere that was constructed of two layers of thin plastic and two layers of aluminum foil and was inflated after being placed in orbit. This satellite is rather large, yet of small mass, and its orbit is considerably affected by the aerodynamic drag exerted by the atmosphere. From the observed effect of this drag on the orbit, the density of the atmosphere at least at the altitude of perigee, which is about 700 kilometers, can be inferred.

The upper atmosphere of the earth, however, is a plasma, and electrostatic and electromagnetic interactions can take place between the plasma and the satellite, the outer layer of which is a metal and carries a charge. These interactions cause drags on the satellite that are additional to the conventional aerodynamic drag that occurs in an un-ionized environment. Although these additional drags may turn out

to be small, as they do in the present case, it seems advisable to calculate them in order to be able to take them into account in the determination of atmospheric density.

A number of papers are available on the subject of the electric drag of satellites (refs. 1 to 8). Some of the analyses apply, however, only to charged bodies that are small compared to a Debye length, and for an altitude of 1,500 kilometers (the altitude used herein as an example) the Debye length is only 3 centimeters. In some of the analyses the satellite is assumed to be charged to many tens of volts, whereas in the case to be considered herein the potential of the satellite is only a fraction of a volt. Some of the published works treat only one of the three electric drags. In others, the concepts themselves are erroneous. (A comprehensive and useful review of the subject is given in ref. 9.) It therefore seemed advisable to perform the analysis and computation in such a way that the results are applicable to the average altitude of Explorer IX. The present analysis applies to satellites that are large compared to a Debye length (a satellite diameter of 4 meters is used) and that are at altitudes high enough that free-molecule flow obtains (an altitude of 1,500 kilometers is used). A more extensive treatment has been given in reference 10.

### SYMBOLS

$B$	magnetic induction, webers/m <sup>2</sup>
$e$	charge on singly ionized positive ion, coulombs
$i$	current, amperes
$j$	current density, amperes/m <sup>2</sup>
$k$	Boltzmann's constant, joules/°K
$l$	length, m
$m$	mass, kg

$n$	number density, m <sup>-3</sup>
$Q$	charge, coulombs
$r, \theta, \psi$	spherical coordinates
$T$	temperature, °K
$U$	nondimensionalized potential, $e\phi/kT$
$v$	velocity, m/sec
$x, y, z$	Cartesian coordinates
$\epsilon$	permittivity, farads/m
$\zeta$	nondimensionalized length, $r/\lambda_D$
$\eta$	transformed coordinate, $\log_e \frac{\zeta}{\zeta_s}$
$\lambda_D$	Debye length, $\left(\frac{\epsilon k T}{n_e e^2}\right)^{1/2}$
$\sigma$	conductivity, mhos/m
$\phi$	potential, volts

### Subscripts:

$e$	electron
$i$	ion
$\infty$	ambient
$s$	satellite

### DESCRIPTION OF ELECTRIC DRAGS

A satellite experiences electrostatic drags because it acquires a charge. At an altitude of 1,500 kilometers, the principal constituent of the atmosphere is helium. For average conditions over a solar cycle, one-fourth of the helium atoms are ionized by radiation from the sun in the far ultraviolet. The number density of electrons and of ions is equal and both are at the same temperature. (See table 60-I, which shows conditions at an altitude of 1,500 kilometers.) The satellite velocity is greater than the ion velocity; therefore, the satellite sweeps up the ions. The electrons, on the other hand, being of small mass and being tied to the lines of force of the earth's magnetic field, spiral in very small circles around these lines and, having much greater velocity than the satellite, impinge on the satellite at a higher rate than

TABLE 60-I.—Conditions at an Altitude of 1,500 Kilometers

		Ions	Electrons
Mass density, kg/m <sup>3</sup> .....	$2 \times 10^{-16}$		
Number density, m <sup>-3</sup> .....	$3 \times 10^{10}$	$7 \times 10^9$	$7 \times 10^9$
Temperature, °K.....	1,300	1,300	1,300
Magnetic flux density, weber/m <sup>2</sup> .....	$2.3 \times 10^{-5}$		
Debye length, m.....	$3 \times 10^{-2}$		
Satellite velocity, m/sec.....	$7 \times 10^3$		
Thermal velocity, m/sec.....		$3 \times 10^3$	$2 \times 10^5$
Mean free path, m.....		$4 \times 10^2$	$3 \times 10^4$
Radius of gyration, m.....		3	$5 \times 10^{-2}$
Revolutions/collision.....		10	$8 \times 10^4$

# ELECTRIC DRAG FORCES ON A SATELLITE IN UPPER ATMOSPHERE

the ions. The satellite therefore quickly builds up a negative charge and a negative potential of such magnitude that the rates of impingement of ions and electrons become equal. At an altitude of 1,500 kilometers, charged particle densities and velocities are such that this negative potential is 0.4 volt.

The ultraviolet portion of the sun's radiation can also cause photoelectrons to be emitted from the surface of the satellite, but because the aluminum surface is not really clean and is oxidized, the photocurrent at this altitude can only reduce the equilibrium charge on the satellite toward zero. In order to obtain a maximum value for the electric drag, the effects of photoemission were neglected. This condition would correspond either to a dirty surface or to the satellite's being in the earth's shadow. The calculations were therefore made for a negative potential of 0.4 volt on the satellite.

Three electric drag forces can act on a satellite. Two of these forces are electrostatic in nature and are identified herein as Coulomb drags. The third is electromagnetic and is termed the induction drag. One of the Coulomb drags is due to the increase in the rate at which ions impinge on the satellite (and thus mechanically transfer momentum to it) because of the Coulomb forces between the charge on the satellite and the charges on the ions. This phenomenon is illustrated in figure 60-1 for the case of no magnetic field. Because of the negative charge on the satellite, the cross section for ion impingement is increased. When, however, the satellite is crossing the lines of force

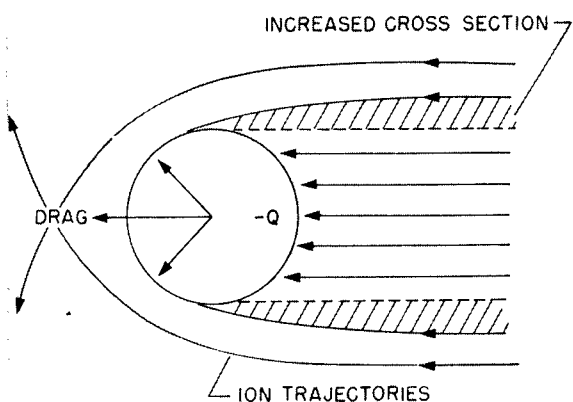


FIGURE 60-1.—Coulomb drags (without magnetic field).

of the earth's magnetic field, a voltage gradient is induced in the satellite, which thus becomes polarized. Thus, the increase in the cross section for ion impingement is not symmetrical about the satellite. This condition is shown in figure 60-2.

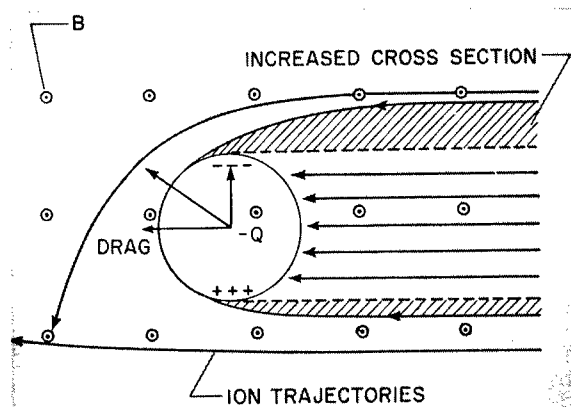


FIGURE 60-2.—Coulomb drags (with magnetic field).

The second Coulomb drag is due to the fact that ions whose trajectories are affected by the electrostatic force but which do not actually impinge on the satellite are deflected or scattered and thus exert a force on the satellite. This type of drag is illustrated in figure 60-1 for the case of no magnetic field. The force between the ion and the satellite varies in both direction and magnitude but can be illustrated qualitatively by a single force as shown. The resultant of the forces exerted by all the scattered ions is a force in the drag direction. When the earth's magnetic field is taken into account, the scattering is no longer symmetrical, as is shown in figure 60-2. The resultant force vector due to scattering of ions can in this case be resolved into two components, one along the drag direction and one in the lateral direction.

Induction drag occurs only when a magnetic field is involved and can be qualitatively described as follows. (See fig. 60-3.) Ions impinge preferentially on the portion of the front of the satellite that is more negative, and electrons traveling along the magnetic lines of force impinge most copiously on the portion of the two sides that is more positive. The positive ions and the negative electrons have to combine, so there is a flow of electrons in the satellite

which is equivalent to a positive current as shown. The well-known electromagnetic force on a current in a magnetic field is the vector product of the current density and the magnetic flux density  $j \times B$  per unit volume. This force has a component in the lateral direction and a component in the drag direction.

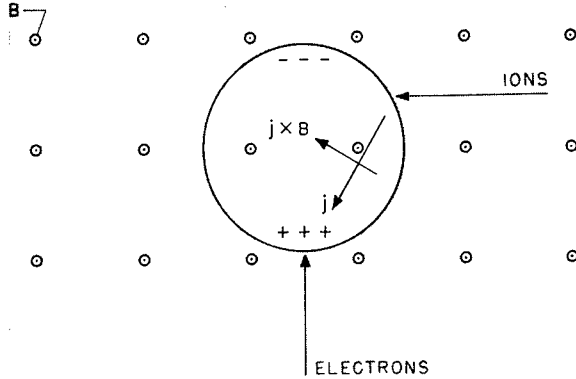


FIGURE 60-3.—Induction drag.

### CALCULATION OF SHEATH

The foregoing discussion indicates that, before these three electric drags can be calculated, a knowledge of the trajectories of the ions is required. The ion trajectories are found by solving the equations of motion of the ions. Solving the equations of motion requires in turn a knowledge of the electric potential distribution around the satellite. The electric field of the satellite does not extend to infinity but is limited to a few tens of centimeters by a sheath that forms around the satellite. It is the potential distribution in this sheath that is required. To find it, ion and electron density distributions in the sheath are needed.

Because the ions are very massive as compared with the electrons, the ion density in the sheath can, as a good first approximation, be considered to be constant and equal to that outside the sheath. Most of the redistribution of charge density in the sheath is made by the electrons.

The electrons in the undisturbed atmosphere can be taken to be in thermodynamic equilibrium, as was verified by measurements taken with Explorer VIII (1960 Xi 1). Then if the satellite surface were a perfect reflector of

electrons, the electrons in the sheath would be distributed according to the Boltzmann law; thus,

$$n_e = n_{e,\infty} \exp\left(\frac{e\phi}{kT}\right)$$

But since the satellite surface is an almost perfect absorber of electrons, those electrons that initially have sufficient kinetic energy to reach the surface are not reflected, and of course no electrons come through the satellite from the other side to replace them. The Boltzmann distribution must therefore be modified near the satellite surface to account for this deficit in the distribution of receding electrons. The modification is effected in the following manner. At any point in the sheath at which the potential is  $\phi$ , the electrons that have velocities toward the surface of the satellite have a Maxwellian distribution with velocities ranging from zero to infinity, but their number density is reduced by the Boltzmann factor  $\exp\left(\frac{e\phi}{kT}\right)$ . The electrons that have velocities

away from the surface, which are those that have been reversed in direction by the potential field, are reduced in number density by the Boltzmann factor and have only that part of a Maxwellian distribution that extends from  $-\sqrt{\frac{2e(\phi-\phi_s)}{m_e}}$  to zero. Those missing from the Maxwellian distribution were intercepted by the surface. The electron density at the point where the potential is  $\phi$  is then

$$\begin{aligned} n_e &= n_{e,\infty} \exp\left(\frac{e\phi}{kT}\right) \sqrt{\frac{m_e}{2\pi kT}} \\ &\quad \int_{-\sqrt{\frac{2e(\phi-\phi_s)}{m_e}}}^{\infty} \exp\left(\frac{m_e v^2}{2kT}\right) dv \\ &= \left[ \frac{1}{2} + \frac{1}{2} \operatorname{erf} \sqrt{\frac{e(\phi-\phi_s)}{kT}} \right] n_{e,\infty} \exp\left(\frac{e\phi}{kT}\right) \end{aligned}$$

The right-hand side of this equation is the Boltzmann distribution modified by the expression in the brackets.

The potential distribution and the charge-density distribution in the sheath were found by solving Poisson's equation

$$\nabla^2 \phi = \frac{e}{\epsilon} (n_e - n_i)$$

Dimensional quantities were made nondimensional as follows: Distance from the center of the satellite  $r$  was expressed in terms of Debye lengths, potential in terms of temperature (in volts), and number density in terms of ambient number density. Poisson's equation in spherical coordinates then becomes

$$\frac{1}{\xi^2} \frac{\partial}{\partial \xi} \left( \xi^2 \frac{\partial U}{\partial \xi} \right) + \frac{1}{\xi^2 \sin \theta} \frac{\partial}{\partial \theta} \left( \sin \theta \frac{\partial U}{\partial \theta} \right) = e^U \left[ \frac{1}{2} + \frac{1}{2} \operatorname{erf} \sqrt{U - U_{\theta=\pi/2} - \frac{(v_s \times B) r_s}{kT} \cos \theta_s} \right] - 1$$

The ohmic voltage gradient  $j/\sigma$  is not taken into account in this equation because it is negligible as compared with the polarizing voltage gradient  $v_s \times B$ . The orientation of the coordinate systems used for the calculation of the sheath is shown in figure 60-4. These coordinate systems are fixed in the satellite. The boundary conditions for the sheath are:

$$U = 0 \text{ at } \xi = \infty \text{ (actually used was } \xi = 20)$$

$$U = U_{\theta=\pi/2} + \frac{(v_s \times B) r_s}{kT} \cos \theta_s \text{ at } \xi = \xi_s$$

$$\frac{\partial U}{\partial \theta} = 0 \text{ at } \theta = 0, \pi$$

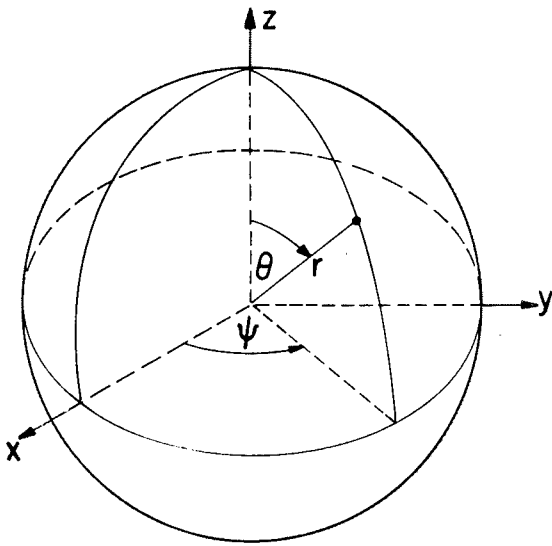


FIGURE 60-4.—Spherical and Cartesian coordinate systems.

This last boundary condition is based on the assumption that the wake has a negligible effect on the sheath on the front half of the satellite and that the sheath can therefore be calculated as though it were symmetrical about the  $z$ -axis. The region of the sheath, an area bounded by circular arcs, was transformed into a rectangular area by the substitution

$$\eta = \log_e \frac{\xi}{\xi_s}$$

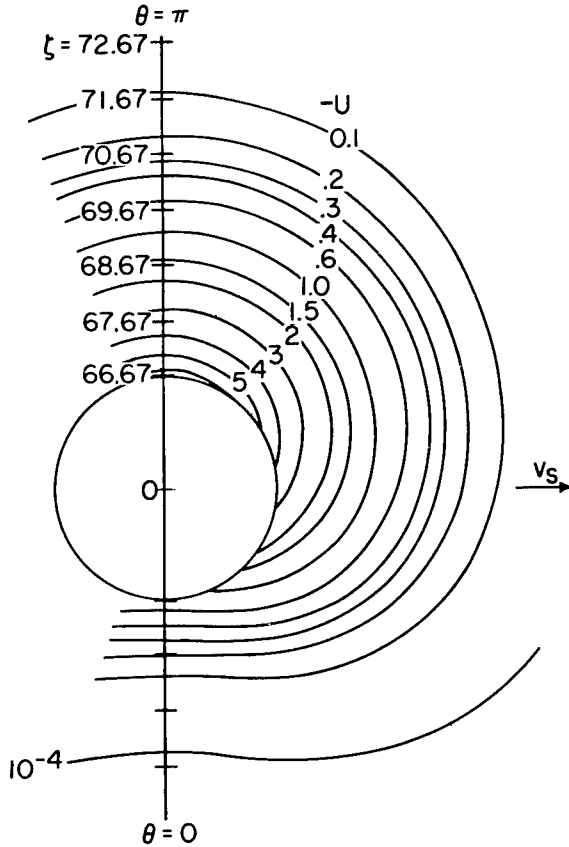
With this substitution, Poisson's equation becomes

$$\frac{\partial^2 U}{\partial \eta^2} + \frac{\partial U}{\partial \eta} + \frac{\partial^2 U}{\partial \theta^2} + \cot \theta \frac{\partial U}{\partial \theta} = r_s^2 e^{2\eta} \left\{ e^U \left[ \frac{1}{2} + \frac{1}{2} \operatorname{erf} \sqrt{U - U_{\theta=\pi/2} - \frac{(v_s \times B) r_s}{kT} \cos \theta_s} \right] - 1 \right\}$$

(The angle  $\theta_s$  is the angle defining the point on the satellite surface which projects along the direction of the earth's magnetic field lines to the point where the potential is  $U$ .) This equation was written as a system of difference equations which were solved simultaneously for a network of 51 by 51 mesh points by an iteration procedure on an IBM 7090 electronic data processing system. One hundred twenty iterations were found to be sufficient.

The results for the potential  $U$  in the sheath are shown in figure 60-5, where contours of constant  $U$  are drawn. It should be emphasized that, since the radius of the satellite is so much greater than the thickness of the sheath ( $r_s = 66.67 \lambda_D$ ), it was necessary, in order to be able to show the structure of the sheath, to use vastly different distance scales for the two regions, inside and outside of the satellite. The ratio of the scales is 1 to 33.33. The results for the charge density  $\frac{(n_i - n_e)}{n_{i,\infty}}$  in the sheath are given in figure 60-6, which shows contours of constant charge density. (Here again different scales were used for the satellite and the sheath.) It can be seen that the retarding action of the negative charge on the satellite, together with the absorption of electrons that contact the surface, results in very much reduced electron number densities very close to the surface. The thickness of the sheath is shown by figure 60-5 to depend on the local value of

(NOTE DIFFERENCE IN SCALES INSIDE AND OUTSIDE OF SPHERE)


 FIGURE 60-5.—Contours of potential  $U$  in the sheath.

the potential on the satellite surface and to vary from about 0.8 to 1.5 Debye lengths, if the edge of the sheath is taken to be the location of  $1/e$  of the surface potential. Since the sheath on the front half of the satellite has symmetry about the  $z$ -axis (the vertical axis in the plane of the paper in figs. 60-5 and 60-6), three-dimensional surfaces of constant potential and constant charge density can be generated by rotating these figures about that axis.

#### CALCULATIONS AND RESULTS FOR ION TRAJECTORIES

The trajectories of the ions were found from a solution of the Lagrangian form of the equations of motion,

$$\ddot{\zeta} - \zeta \dot{\theta}^2 - \zeta \sin^2 \theta \dot{\psi}^2 + \frac{e^2 n_{i,\infty}}{\epsilon m_i} \frac{\partial U}{\partial \zeta} = 0$$

(NOTE DIFFERENCE IN SCALES INSIDE AND OUTSIDE OF SPHERE)

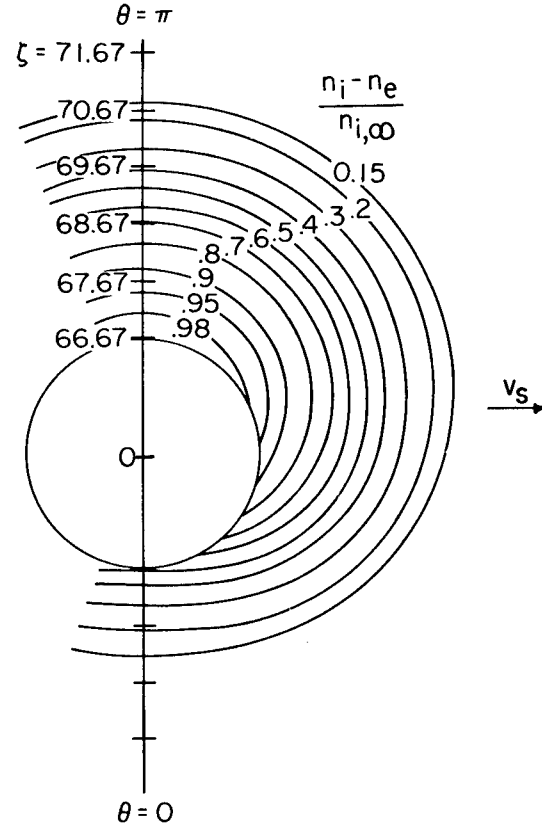


FIGURE 60-6.—Contours of constant charge density in the sheath.

$$\zeta^2 \ddot{\theta} + 2\zeta \dot{\zeta} \dot{\theta} - \zeta^2 \cos \theta \sin \theta \dot{\psi}^2 + \frac{e^2 n_{i,\infty}}{\epsilon m_i} \frac{\partial U}{\partial \theta} = 0$$

$$\zeta^2 \sin^2 \theta \dot{\psi} = \text{Constant}$$

where the dots over symbols denote differentiation with respect to time. The two derivatives of potential ( $\partial U / \partial \zeta$  and  $\partial U / \partial \theta$ ) that appear in these equations had been calculated and stored in the process of calculating the potential and the charge density in the sheath. They were used in solving these equations numerically on the IBM 7090 electronic data processing system. A fifth-order integration routine that employed a fourth-order Runge-Kutta method was used. Each interval was computed by two complete half-interval steps and comparison was made with the whole interval step for accuracy agreement.



# ELECTRIC DRAG FORCES ON A SATELLITE IN UPPER ATMOSPHERE

Typical results are shown in figure 60-7 for the most negative ( $-0.72$  volt) and the least negative ( $-0.076$  volt) regions on the sphere. The trajectories shown are in the plane  $\psi = \pi/2$ . It is only for this condition that the ion trajectories are planar and are not unreasonably difficult to calculate. The trajectories appear to agree qualitatively with those calculated by Jastrow and Pearse (ref. 1). For the low satellite potential used herein, comparatively few ions are deflected from the sheath into the wake. Again, this result is in general agreement with the results in reference 1.

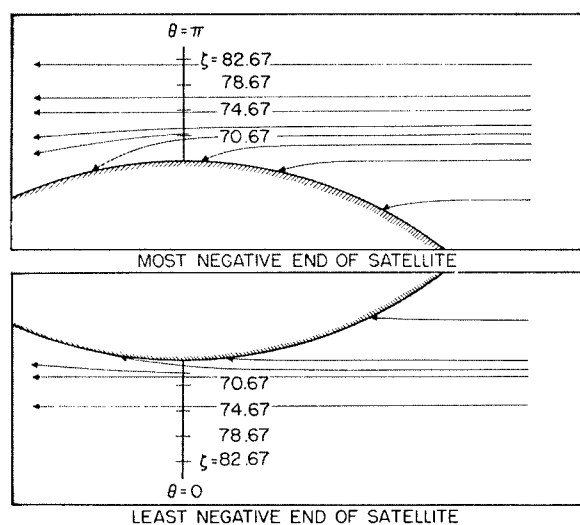


Figure 60-7.—Ion trajectories.

## CALCULATION OF COULOMB DRAG

On the basis of the results obtained in the preceding section, the portion of the Coulomb drag of a 4-meter sphere at 1,500 kilometers due to ion scattering has been estimated and shown to be not more than 0.05 of 1 percent of the drag of the uncharged sphere. The portion of the Coulomb drag due to increased ion impringement is calculated from the effective cross-sectional area of the satellite for ion impingement. This effective area, obtained from the calculated trajectories, is shown in figure 60-8. It is 10 percent larger than the projected area of the sphere. The degree of ionization obtained from table 60-I is 23 percent. Therefore the Coulomb drag due to

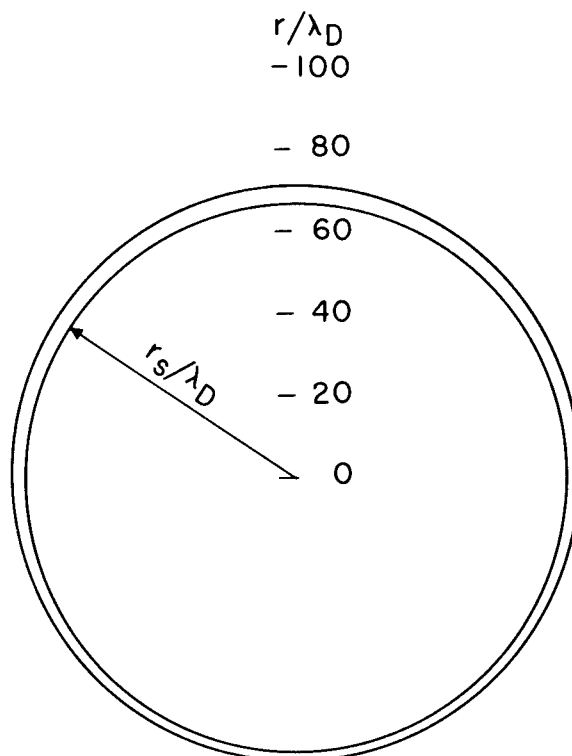


FIGURE 60-8.—Cross section for ion impact.

increased ion impacts is 2.3 percent of the drag of the uncharged sphere.

The conditions in the atmosphere at an altitude of 1,500 kilometers that were used herein are presumably close to average conditions over a cycle of sunspot activity. At sunspot maximum, when the degree of ionization is about twice as large as average, the ratio of the Coulomb drag to the drag of the uncharged sphere would be approximately twice as great as at average conditions. At sunspot minimum, where the degree of ionization is about half that used herein, the ratio of Coulomb to uncharged-sphere drag would be approximately half that shown here.

## CALCULATION OF INDUCTION DRAG

The method used herein for calculating induction drag is the following. First, the current in the satellite normal to  $B$  must be obtained; to obtain this current, the satellite is considered to be divided into circular elements or rings centered on an axis perpendicular to the directions of both satellite velocity and magnetic flux as shown in figure 60-9. From

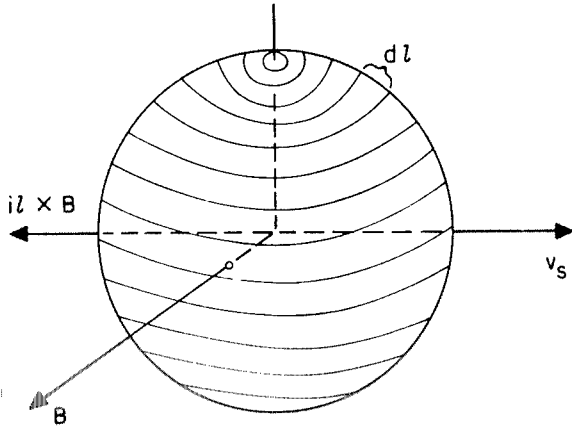


FIGURE 60-9.—Geometry for calculation of induction drag.

the trajectories of the ions, the ion current to the first element is obtained. The electron current to that element is given by the well-known kinetic-theory differential expression for the flux of particles crossing a surface in one direction (with velocities normal to the surface between  $v$  and  $v+dv$ ) integrated between the kinetic-energy limits of  $-\epsilon\phi_s$  and  $\infty$ ; that is, the electron current density to the spherical surface is

$$j_e = en_{e,\infty} \left( \frac{kT}{2\pi m_e} \right)^{1/2} \sin \theta \cos \psi \exp \left( \frac{\epsilon\phi_s}{kT} \right)$$

The net current to the first element is then the difference between the ion current and the electron current to that element. This net current has to flow into the second element, from which this net current plus the net inflow of ion and electron current from the plasma into the second element has to flow into the third element, and so on. Any current flow in the plane of a circular element can be ignored because, for it,  $i \times B$  is not in the drag direction. The total induction drag is obtained by summing for all elements the product  $i(dl \times B)$ .

The magnitude of the induction drag was found to change very little if, instead of using the actual ion trajectories to determine the ion current to the different elements, the satellite is assumed to run into a stationary ion gas. The ion current density to the spherical surface is thus

$$j_i = n_{i,\infty} e v_s \sin \theta \sin \psi \quad 0 \leq \psi \leq \pi$$

The net current flowing downward at each one of the circular elements where the polar angle is  $\theta$  is

$$\begin{aligned} i &= \int_0^\theta \int_0^{2\pi} (j_i - j_e) r_s^2 \sin \theta \, d\psi \, d\theta \\ &= 2n_{i,\infty} e v_s r_s^2 \left( \frac{\theta}{2} - \frac{\sin 2\theta}{4} \right) \\ &\quad - 4n_{e,\infty} e r_s^2 \left( \frac{kT}{2\pi m} \right)^{1/2} \exp \left( \frac{\epsilon\phi_{\theta=\pi/2}}{kT} \right) \\ &\quad \int_0^\theta \sin^2 \theta \exp (\alpha \cos \theta) \, d\theta \end{aligned}$$

where

$$\alpha = \frac{e B r_s v_s}{kT} \approx 2.85$$

From this the induction drag is found to be

$$\begin{aligned} \int i(dl \times B) &= \int i B r_s \sin \theta \, d\theta \\ &= B r_s^3 \left\{ n_{i,\infty} e v_s \left( \pi + \frac{2}{3} \right) \right. \\ &\quad \left. - 4n_{e,\infty} e \left( \frac{kT}{2\pi m} \right)^{1/2} \exp \left( \frac{\epsilon\phi_{\theta=\pi/2}}{kT} \right) \right. \\ &\quad \left. \int_0^\pi \left[ \int_0^\theta \sin^2 \theta \exp (\alpha \cos \theta) \, d\theta \right] \sin \theta \, d\theta \right\} \end{aligned}$$

From this expression the induction drag is found to be  $1.8 \times 10^{-9}$  newton, or 1.2 percent of the drag of the uncharged sphere. This is the induction drag calculated for the velocity vector  $v_s$  and the magnetic vector  $B$  normal to each other. In general, the angle between these two vectors will be less than  $\pi/2$  and the induction drag will accordingly be less.

### CONCLUDING REMARKS

The potential and the charge distribution in the sheath on a 4-meter-diameter sphere and the drag of the sphere resulting from its electric charge have been calculated for an altitude of 1,500 kilometers. The results are perhaps more accurate than any previously obtained.

The Coulomb drag due to scattering has been shown to be essentially zero. The Coulomb

# ELECTRIC DRAG FORCES ON A SATELLITE IN UPPER ATMOSPHERE

drag due to increased ion impingement is shown to be 2.3 percent of the drag of the uncharged sphere at average conditions during a solar cycle. The percentage would be approximately doubled for the degree of ionization prevailing at the maximum of the solar cycle of sunspot activity and would be approximately halved at the minimum. These values for Coulomb drag are obtained without taking account of photoemission. If photoemission has the ex-

pected effect for an aluminum surface, these values would be decreased. They can therefore be taken to be upper limits which occur when the satellite is in the earth's shadow.

The induction drag due to the electric generator action of the satellite has been shown to be 1.2 percent of the drag of the uncharged sphere for the orientation for which the induction drag is a maximum.

## REFERENCES

1. JASTROW, R., and PEARSE, C. A.: Atmospheric Drag on the Satellite. *Jour. Geophys. Res.*, vol. 62, no. 3, Sept. 1957, pp. 413-423.
2. CHOPRA, K. P., and SINGER, S. F.: Drag of a Sphere Moving in a Conducting Fluid in the Presence of a Magnetic Field. Reprint from 1958 Heat Transfer and Fluid Mechanics Institute. Stanford Univ. Press, pp. 166-175.
3. KRAUS, LESTER, and WATSON, KENNETH M.: Plasma Motions Induced by Satellites in the Ionosphere. *The Physics of Fluids*, vol. 1, no. 6, Nov.-Dec. 1958, pp. 480-488.
4. CHANG, H. H. C., and SMITH, M. C.: On the Drag of a Spherical Satellite Moving in a Partially Ionized Atmosphere. *Jour. British Interplanetary Soc.*, vol. 17, no. 7, Jan.-Feb. 1960, pp. 199-205.
5. JEFIMENKO, OLEG: Effect of the Earth's Magnetic Field on the Motion of an Artificial Satellite. *American Jour. Phys.*, vol. 27, no. 5, May 1959, pp. 344-351.
6. BEARD, DAVID B., and JOHNSON, FRANCIS S.: Charge and Magnetic Field Interaction with Satellites. *Jour. Geophys. Res.*, vol. 65, no. 1, Jan. 1960, pp. 1-7.
7. WYATT, P. J.: Induction Drag on a Large Negatively Charged Satellite Moving in a Magnetic-Field-Free Ionosphere. *Jour. Geophys. Res.*, vol. 65, no. 6, June 1960, pp. 1673-1678.
8. DAVIS, A. H., and HARRIS, I.: Interaction of a Charged Satellite with the Ionosphere. NASA TN D-704, 1961.
9. CHOPRA, K. P.: Interactions of Rapidly Moving Bodies in Terrestrial Atmosphere. *Rev. Modern Phys.*, vol. 33, no. 2, Apr. 1961, pp. 153-189.
10. HOHL, FRANK, and WOOD, GEORGE P.: The Electrostatic and Electromagnetic Drag Forces on a Spherical Satellite in a Rarefied Partially Ionized Atmosphere. For presentation at Third International Symposium on Rarefied Gas Dynamics (Paris, France), June 26-30, 1962. (NASA)

# 61. Plasma Frequency and Radio Attenuation

By Paul W. Huber and Clifford H. Nelson

PAUL W. HUBER, *Head, Plasma Applications Section of the Aero-Physics Division, NASA Langley Research Center*, received his Bachelor of Science degree in Electrical Engineering from Ohio Northern University in May 1942. Joining Langley after graduation, Huber has specialized in the general field of research dealing with real-gas-flow properties. Some of the contributions in this field have included early measurements of vibrational heat-capacity lag in various gases, early measurements of pressure versus time and boundary-layer development in shock tubes, the first direct measurement of Mach stem development and surface effects for spherical blast waves, and the first direct measurement of radio-frequency wave attenuation in a specifiable plasma. Huber is a member of the American Rocket Society. He is author of numerous NASA publications and has presented symposium papers and published journal papers.

CLIFFORD H. NELSON, *Head, Measurement Research Branch, Instrument Research Division, NASA Langley Research Center*, received his Bachelor of Science degree in Electrical Engineering from the University of Washington in June 1938. Nelson is active in the development of flight instrumentation for airborne and space vehicles and techniques for transmitting data by telemetry. He has specialized in the development of techniques for determining the properties of the plasma sheath surrounding space vehicles during atmospheric entry. He is presently investigating the problems of radio telemetry blackout associated with this plasma sheath. Earlier, Nelson was responsible for the development and application of a line of self-contained recording instruments used in flight research with piloted aircraft up to and including the X-15. This array of flight instrumentation has been unequalled on the basis of accuracy and reliability of operation and has received international recognition through the AGARD publications. Nelson is a member of the Instrument Society of America and the Engineers' Club of the Virginia Peninsula.

## SUMMARY

The problem of radio-frequency attenuation due to the interaction of an electromagnetic wave and a plasma layer is reviewed with particular attention to that aspect dealing with communications during the reentry phase of space-flight missions. The need for concerted effort on the problem is first brought out by the projection of radio blackout data from current missions to that of second-generation missions. The electromagnetic plasma parameters are discussed in relation to their influence on the wave propagation

properties. It is shown that theoretical models of wave-plasma interaction (absorption and reflection) can be synthesized to approximate the reentry plasma-layer problem, which is interaction with relatively dense plasmas having gradients of finite extent with respect to a signal wavelength. Comparison of flight results with those obtained with a simplified conceptual model is presented. Finally, various means by which the attenuation problem may be alleviated or circumvented are reviewed and the capabilities for laboratory and flight model tests are outlined.

## INTRODUCTION

Almost everyone is familiar with one radio attenuation problem associated with reentry from space flight, this of course being the Mercury-Atlas radio blackout period experienced by the Astronauts. It was observed in these missions that there was a period of a few minutes in which communications both from and to the capsule were totally obstructed by the ionization layer formed about the body during the reentry phase of the mission (ref. 1). Although this was by no means the first time such a phenomenon has been observed, it did nevertheless serve to dramatically reemphasize the importance of the problem and, indeed, to substantiate the current factual as well as conceptual thinking to a surprising degree.

It had been previously established, from many tests of unmanned vehicles and from evaluation of gross theoretical models of the electromagnetic-wave-plasma interaction problems, that radio interference effects can and do exist in both the boost and reentry phases and can compromise the operational, not to mention the psychological, aspects of space flight. The really disturbing part about the situation is that for the second-generation space-flight missions, such as Apollo and other planned space and planetary probes, these effects appear to be greatly magnified in the light of present technology, so that data systems as well as monitoring and command systems may be seriously impaired. In some instances, however, tracking by means of radar may be improved (ref. 2). It is well, then, to review and examine the present status of knowledge and technology in regard to radio attenuation with a view toward delineation of the problem areas and avenues which might be pursued in the hope for solutions.

The general flight blackout problem can be briefly reviewed by first examining the data from Mercury space-flight missions. Figure 61-1 illustrates the relationship of the plasma layer or ionization layer with respect to the vehicle, its aerodynamic flow field, and the communications system. The plasma layer is located between the surface of the vehicle and the main shock wave, and not only does it completely surround the body but it may extend to

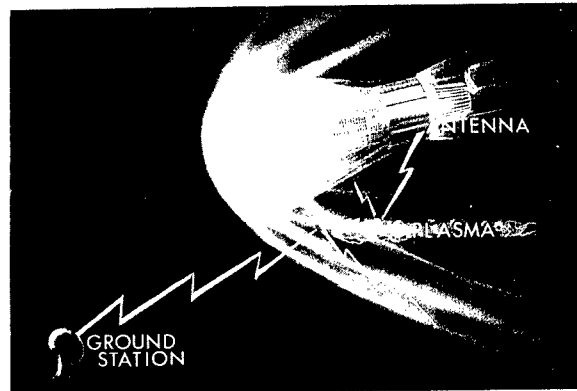


FIGURE 61-1.—Signal blackout due to plasma layer.

a distance of many body dimensions behind the vehicle. The important point to be noted is that the radio-frequency (RF) signals both from the capsule and from the ground are reflected and/or absorbed by the plasma layer which is thus acting as a shield to obstruct communications from both directions.

Figure 61-2 shows the velocity-altitude spectrum in which this signal impairment is manifested for the Mercury spacecraft VHF voice telemetry as well as the C-band radar-beacon signal. The upper shaded region is an experience curve gained from a variety of other flight experiments. A possible Apollo path is shown by the dashed curve for comparison. The Mercury beacon signal was not completely blacked out but was greatly attenuated for the short period shown. The VHF signal was blacked out completely for a few minutes, in which time the capsule traversed a distance measured in hundreds of miles. For the Apollo curve shown in this figure, the beacon signal would be cer-

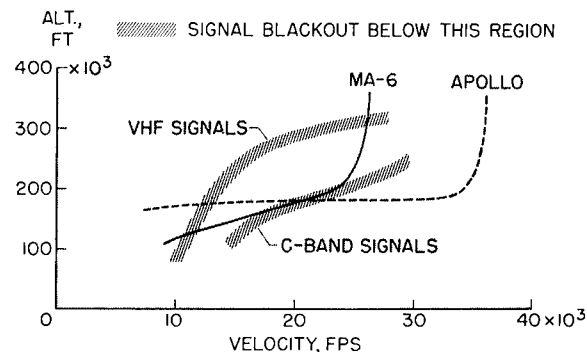


FIGURE 61-2.—Radio frequency blackout regions for Mercury-Atlas communications.

tainly blacked out completely and the VHF blackout period would be expressed in terms of thousands of miles traversed by the capsule. Lack of communications during such a lengthy period could very well mean a greatly increased requirement for the onboard navigation and flight evaluation system, which in turn is measured in increased payload or decreased mission capability, not to mention reliability.

### SYMBOLS

$B$	magnetic induction
$c_0$	speed of light
$E$	electric field intensity, $r + js$
$e$	charge on electron
$f$	signal frequency
$k$	propagation parameter, $\alpha + j\beta$
$k_1$	value of propagation parameter in uniform plasma
$m$	mass of electron
$N$	concentration
$n$	index of refraction
$Q$	average effective momentum transfer cross section for electron-particle collision
$R$	amplitude of reflected wave
$T$	amplitude of transmitted wave
$r$	real part of $E$
$s$	imaginary part of $E$
$t$	time
$V$	real part of $(k/k_0)^2$
$W$	imaginary part of $(k/k_0)^2$
$w_e$	mean thermal velocity of electrons
$x, y, z$	space coordinates
$\alpha$	phase parameter
$\beta$	attenuation parameter
$\Delta$	thickness of shock layer
$\lambda$	wavelength
$\nu$	electron collision frequency
$\phi$	angle of incidence
$\omega$	angular signal frequency, $2\pi f$
$\omega_b$	cyclotron frequency, $\frac{eB}{mc_0}$
$\omega_p$	plasma frequency, $\left[ \frac{4\pi e^2 N_e}{m} \right]^{1/2}$
<i>Subscripts:</i>	
$b$	dependent on $B$
$e$	electron
$i$	particle other than electron
$o$	in vacuum
$p$	plasma
$\parallel$	$E$ vector parallel to plane of incidence
$\perp$	$E$ vector perpendicular to plane of incidence
$\infty$	semi-infinite homogeneous plasma with $N_e$ discontinuous at boundary
1, 2	designate particular values of $y$

### CHARACTER OF PLASMA LAYER

In order to study some of the fundamental aspects of the interaction of electromagnetic (E.M.) waves and plasmas, in particular, plasmas of the type associated with blunt-body reentry into an earth or planetary atmosphere, the reentry plasmas must first be defined or characterized. It is necessary to know both the magnitude and spatial extent of plasma properties during reentry. The determination of the shock-layer flow field, and hence plasma properties, about blunted bodies in hypersonic flow is indeed a complex mixture of disciplines. These disciplines include hypersonic aerodynamics, high-temperature thermodynamics, multicomponent chemical kinetics, and viscous ablating flow, even for the simpler continuum-flow concept of primary interest. Although it is not within the scope of this presentation to review these theoretical methods, suffice it to say that only a very limited number of such computations have been made for highly blunted bodies and these are either restricted to the nose region or are for thermochemical equilibrium and/or inviscid flow (refs. 3 to 6). Such results do, however, provide a good indication of the influence of the various flight parameters on the plasma characteristics and serve as inputs for first-order radio attenuation estimates. There are few, if any, direct experimental plasma measurements available for application to this problem. The general character of the plasma in the shock layer, as based on present knowledge (ref. 3), is illustrated in figure 61-3. The plots show the spatial variation of the electromagnetic plasma parameters—free electron concentration and electron collision frequency—along a path normal to the body surface for an aft location on a blunted body at a possible reentry flight condition. Note particularly the nonlinear, nonmonotonic variation of  $N_e$ , the peak value of  $N_e$ , and the relatively constant value of  $\nu$ . It might also be noted that the only part of the layer which is of particular consequence with regard to RF attenuation is that part with a value of  $N_e$  higher than approximately  $10^6 \text{ cm}^{-3}$ . The number  $10^6$  is of significance in that this is about the maximum electron concentration in the ionosphere (refs. 7 to 9) through which, of course,

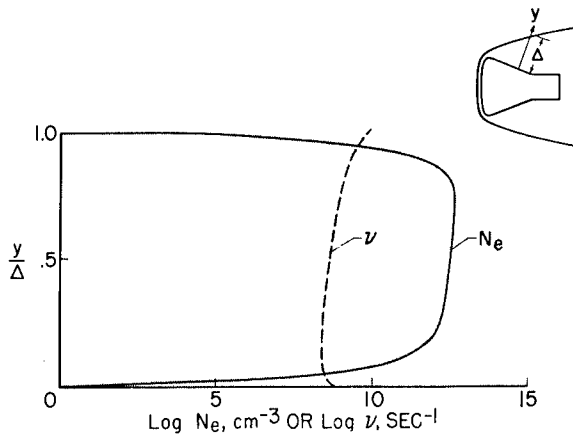


FIGURE 61-3.—Typical variation of electromagnetic parameters in shock layer.

any space communications system must be capable of transmitting a priori.

Since the reentry plasma layer has been defined, at least in qualitative fashion, the problem of electromagnetic wave interaction with this plasma can now be considered. Probably the best way to do this is to look first at the simplest type of an interaction, bringing out the important plasma parameters and their influence on the wave propagation nature. It should then be possible to consider the influence on the propagation of the various nonidealities which comprise the actual plasma-wave model and, thereby, attempt to synthesize a more comprehensive picture of the problem.

#### PLASMA PROPERTIES FOR ELECTROMAGNETIC WAVE INTERACTIONS

From a solution of Maxwell's equations for the simplest interaction, that of a plane wave in a uniform plasma, expressions can be derived to show the perturbations on the electromagnetic wave due to the presence of the plasma—that is, propagation characteristics in the plasma as compared, for example, with propagation characteristics in a free-space medium. By using also the equation of motion of an electron in an infinite uniform plasma undergoing harmonic oscillation (the ions may be considered stationary for RF frequencies), it can be further shown that there is a parameter known as plasma frequency which defines a range in the wave frequency spectrum in which these

perturbations are not small (refs. 8 and 10 to 13). It is this range—where signal frequency is of the order of or less than the property called plasma frequency—that is of particular interest. Within this range, a significant part of the wave electric energy can become transformed into electron kinetic energy and thus alter the wave characteristics. The result is manifested by displacement currents and conduction currents in the plasma, depending furthermore upon the rate at which electrons can collide with other particles in the plasma and the strength of any imposed magnetic field. (Radiation damping due to electron oscillation is negligible for RF frequencies.) Therefore, the plasma properties for wave propagation—that is, the index of refraction and attenuation coefficient—are expressible in terms of the parameters: plasma frequency, collision frequency, and magnetic-field strength.

Since the plasma-frequency parameter is the most important of the plasma properties, it is discussed first. This parameter is also called characteristic frequency and sometimes critical frequency and is a convenient lumped parameter having the dimensions of frequency. However, it is an inherent property of the plasma. For example, consider in an infinite plasma that some of the electrons are displaced from their equilibrium position in the plasma due to the application of some force on the electron. A restoring space charge field is then created which, if the displacing force is suddenly removed, causes the electrons to oscillate about their equilibrium at a frequency proportional to the plasma frequency. The value of the restoring field (and the plasma frequency) is dependent exclusively on the free electron concentration in the plasma—that is, the number of free electrons in a unit of volume. It is intuitively obvious that, when the exciting frequency (signal frequency) becomes equal to this characteristic frequency of oscillation, the electromagnetic properties of a plasma may exhibit marked changes, as indeed they do.

The other important plasma property is called electron collision frequency and is representative of the rate at which electrons interact with other particles in the plasma. (See refs. 11 and 14 to 17.) This property indicates the

lossy or dissipation properties of the plasma resulting from the transport of electron energy. These electron interactions may be binary with neutral species or ions, or with several particles concurrently, and may be elastic or inelastic, all depending on the thermal and state properties of the plasma and the strength of the electromagnetic wave.

It is well to point out that the reentry plasmas which are of importance to RF attenuation generally fall into the category of weakly ionized, dense gases—that is, most of the particles are neutral atoms and molecules and a relatively small fraction are free electrons and ions, but the density of electrons and rate of electron collisions are relatively high.

### SIMPLE INTERACTION MODEL

The simplest type of wave-plasma interaction is illustrated in figure 61-4 where a plane wave propagating in free space is normally incident upon a semi-infinite uniform plasma. The boundary in this model is a discontinuous jump from the free-space values to the plasma values of the propagation parameters. After impingement of the incident wave upon the plasma, two waves are generated: one propagated into the plasma (the transmitted wave) and the other reflected away from the plasma. The following properties of these waves may be determined from the solutions appropriate to this model (ref. 13):

$$n = \frac{\alpha c_0}{\omega} = \left[ \frac{V + \sqrt{V^2 + W^2}}{2} \right]^{1/2}$$

$$\frac{\beta c_0}{\omega} = \left[ \frac{-V + \sqrt{V^2 + W^2}}{2} \right]^{1/2}$$

where

$$V = 1 - \left[ \left( \frac{\nu}{\omega_p} \right)^2 + \left( \frac{\omega}{\omega_p} \right)^2 \right]^{-1/2}$$

$$W = \frac{\nu}{\omega} \left[ \left( \frac{\nu}{\omega_p} \right)^2 + \left( \frac{\omega}{\omega_p} \right)^2 \right]^{-1/2}$$

$$R_{\infty}^2 = \frac{(\alpha_o - \alpha)^2 + (\beta_o - \beta)^2}{(\alpha_o + \alpha)^2 + (\beta_o + \beta)^2}$$

$$\omega_p = 2\pi(8970)\sqrt{N_e}$$

$$\nu = \bar{w}_e \sum_i N_i Q_i$$

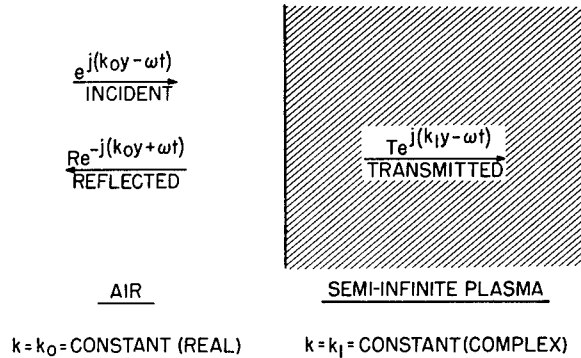


FIGURE 61-4.—Simple wave-plasma model (semi-infinite uniform plasma).

In these equations the propagation parameters, index of refraction (or phase constant) and the extinction (or attenuation) coefficient, are seen as functions of the plasma frequency and collision frequency at a given signal frequency. The reflection coefficient for this semi-infinite type of reflection is seen also as a function of the plasma properties. For this wave-plasma model only one reflection occurs, and the strength of the reflected wave is constant in time and space. The transmitted wave, however, is weakened due to absorption in the plasma for each unit of plasma thickness traversed. In each element of plasma, a portion of the wave electric energy is lost to electron kinetic energy which, when equilibrated, appears as an increase in the thermal energy of the plasma, although this increase is of a thermally negligible amount. The fractional loss of wave energy, however, is by no means negligible over a large portion of the wave frequency spectrum as can be illustrated by a plot such as that shown in figure 61-5 which is similar to a sketch in reference 18. It is seen that, for wave frequencies much less than the plasma frequency, the plasma is highly reflective and almost all the energy is reflected away. In such a case the plasma acts like a conductor; penetration of the wave into the plasma is small, and equivalent displacement currents in the plasma act to change only the index of refraction. At the other end of the spectrum ( $\omega > \omega_p$ ) where the signal frequency is very high, the plasma is completely transparent to the wave (acts as a good dielectric) and no consequential effects are noted. In the intermediate frequency region,



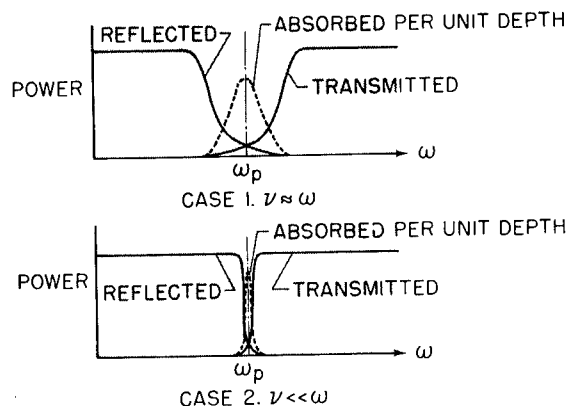


FIGURE 61-5.—Influence of parameters on wave propagation.

however, the situation is quite mixed, depending, in addition to the plasma frequency, upon the value of the electron collision frequency. In this frequency regime, the plasma is like a lossy dielectric and some of the wave energy is reflected back and the remaining energy is lost by plasma absorption. The region where  $\omega \approx \omega_p$  is frequently referred to as the cutoff region. It is seen, therefore, from these results that the most important plasma parameter for determination of wave propagation characteristics is the plasma frequency or, in the most explicit terms, the free-electron concentration.

Figures 61-6 and 61-7 show in normalized form the explicit dependence of absorption per unit plasma thickness and of the reflection on the electromagnetic plasma parameters for the simple wave-plasma model. To be noted in figure 61-6 (from ref. 19) is the interesting result that for very low frequencies the absorption loss falls off. If, therefore, the reflection losses

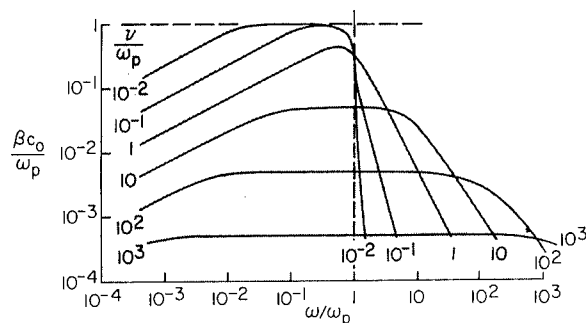


FIGURE 61-6.—Normalized plane-wave attenuation in a uniform plasma.

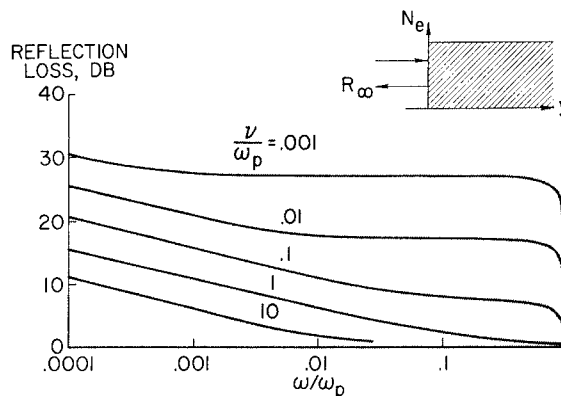


FIGURE 61-7.—Signal loss due to reflection at semi-infinite plasma interface.

are not too great, the use of very low frequency (as well as very high frequency) is suggested.

### NONUNIFORM, FINITE-THICKNESS MODELS

It is interesting to consider the effect of replacing the abrupt change of properties at the air-plasma interface with a more gradual and continuous change. The general problem of wave propagation at normal incidence through a nonuniform plasma has been formulated by John S. Evans of the Langley Research Center (see ref. 20) and involves numerical integration, through the plasma layer, of the following equations:

$$\frac{d^2 r}{dy^2} + k_0^2 (rV - sW) = 0$$

$$\frac{d^2 s}{dy^2} + k_0^2 (sV + rW) = 0$$

where  $r$  and  $s$  are the real and imaginary parts, respectively, of the electric vector. The numerical integration of the propagation equations is done by using the Runge-Kutta method on an IBM 7090 electronic data processing system. Such a program can be used to find the transmitted and reflected wave strengths for any pathwise variation of plasma properties whether discontinuous or gradual, but, of course, the number of integration steps is dependent upon the magnitude of the gradients. An analytical method (ref. 21) has also been developed which is applicable to special types of plasma property variations (linear ramps and combinations of ramps and uniform plas-

mas) for transmission at normal incidence. Solutions are obtained in the form of complex Airy functions and numerical evaluation performed by a machine. Since the results of these two programs are compatible, they are not separately discussed but are used hereinafter to illustrate effects of plasma nonuniformity. Figure 61-8 shows such an effect on the reflected wave strength for a linear variation of properties from free-space to plasma values. It is seen from this figure that the reflected power drops markedly from the discontinuous-jump value when the ramp length (linear region) increases to a fraction of the signal wavelength, the effect being only weakly dependent on the plasma absorptivity for the shorter ramp lengths. It can be also shown that gradients other than the linear ramp gradient produce effects generally similar to those shown in this figure, but such details as these are not discussed herein. With regard to the absorption properties, it can be shown that for gradients in the plasma the absorption is generally closely evaluated by summation or integration of the local absorption coefficients along the propagation path, the gradients not being of first-order influence (ref. 22).

The next aspect to be considered is the effect of finite extent of the plasma (as contrasted to the semi-infinite plasma) on the reflection properties of the plasma. Since it was just shown that gradients having dimensions greater than  $1/10$  wavelength or so reduced the reflection significantly, there would naturally be the

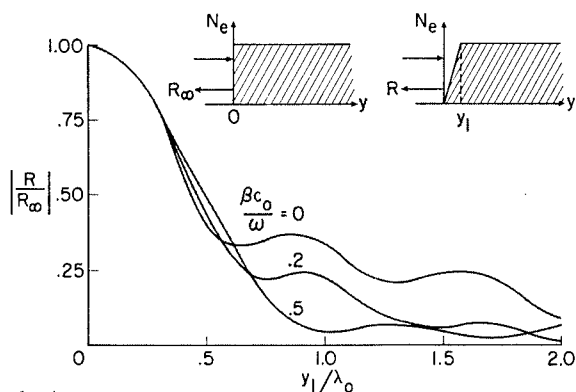


FIGURE 61-8.—Effect of plasma gradient on the semi-infinite plasma reflection.  $n=0.5$ .

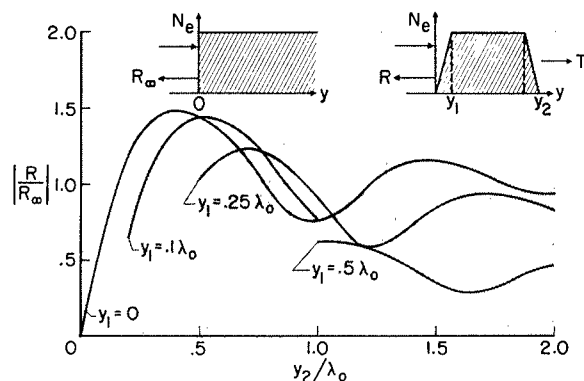


FIGURE 61-9.—Effect of finite extent of plasma on the reflection.  $n=0.5$ ;  $\frac{\beta c_0}{\omega}=0.1$ .

question of what happens when the plasma thickness is comparable to the wavelength of the signal. Figure 61-9 shows the effect of plasma extent (i.e., layer or slab thickness) on reflection for two types of plasma boundaries—a discontinuous jump and a linear ramp gradient, each type occurring at both the forward and rearward plasma boundaries. Although the interferometer effect—that is, interference and reinforcement at fractional wavelength multiples—might be expected, the fact that the plasma absorptivity can be high also when the refractivity is high would generally tend it toward the highly damped case. However, to illustrate most simply the effect of plasma extent on reflection, a weakly absorbing plasma is shown here. It is seen for this plasma that the reflectivity of the layer indeed varies periodically with the plasma extent measured in multiples of the signal wavelength. (The wavelength in the plasma is not equal to the free-space wavelength.) For high absorptivity, such as the more usual reentry plasma case, the wave cannot penetrate very far (i.e., fraction of a wavelength) into the plasma before much of its strength is dissipated, and the interferometer effect is then masked.

#### SIMPLIFIED ATTENUATION CONCEPT APPLIED TO FLIGHT RESULTS

Since the plasma model at least grossly resembles the actual plasma problem (compare figs. 61-3 and 61-9) the situation for plane-

wave RF transmission at normal incidence can now be briefly summarized. When the plasma is thick and  $\omega < \omega_p$ , the effects of gradients on reflection are unimportant, since the signal will be nearly all lost by absorption anyway. When the plasma is thin and  $\omega < \omega_p$ , the reflection problem may be the determining one, and the signal losses will not be as high as those predicted by the semi-infinite, discontinuous model. When  $\omega > \omega_p$ , there is no problem for any thickness; when  $\omega \approx \omega_p$ , the magnitude of the problem for both reflection and absorption depends furthermore on the value of  $\nu$ —that is, depends on altitude as well as thickness. Of course,  $\omega_p$ , which is always the prime parameter, depends on both velocity and altitude. To illustrate the possible range of variation of the plasma parameters  $N_e$  and  $\nu$  during reentry, plots of the normal shock and equilibrium far-wake values calculated at the Langley Research Center are shown in figure 61-10 for a blunt-body trajectory such as Mercury. Note the strong increase in plasma parameters in the early reentry period. The cases shown should be representative of the most extreme and least extreme values likely to occur in the shock layer. Since rather large bodies will generally be used for the manned space missions—that is, plasmas of the thick variety—the problem can be reduced to the simple question of when is the maximum value of plasma frequency in the shock layer higher than the signal frequency. In order to assess the value of such an attenuation yardstick, a study of figure 61-11 is of interest. In this figure are shown, on a velocity-

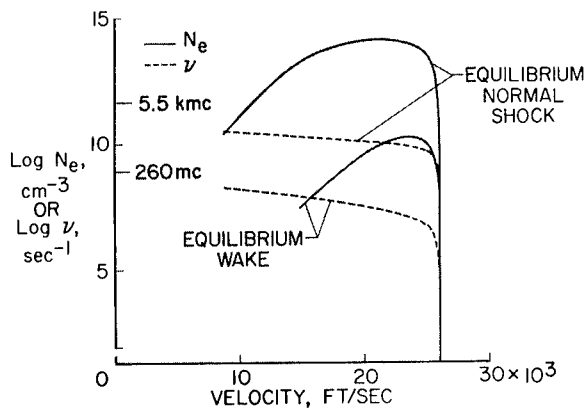
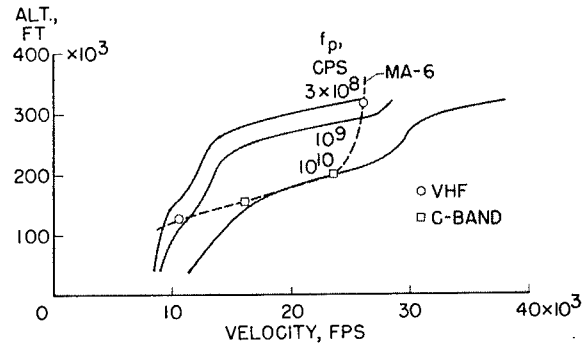

 FIGURE 61-10.—Variation of  $N_e$  and  $\nu$  during reentry.


FIGURE 61-11.—Comparison of flight blackout data with simplified concept.

altitude map, the contours of plasma frequency which might be characteristic of maximum shock-layer values occurring at an aft location on a large blunt body. These values were computed at the Langley Research Center according to the following simplified aerothermodynamic flow model for a frozen flow, far wake. It was assumed that the stagnation (or normal shock) flow streamline reached a condition of thermochemical equilibrium in the nose region (all the reaction and relaxation rates infinite) and then was expanded very suddenly (as around the corner and into the afterbody region) to ambient pressure. In the expansion, no chemical recombination was assumed to occur, which means the composition was frozen at the nose value (internal energy was allowed to follow the expansion) and is analogous to a flow model of very slow reaction rates. Such a flow model is a gross oversimplification of the actual finite rate, three-dimensional flow case but is certainly more appropriate than other simplified conceptual models—for example, the normal-shock flow or equilibrium-wake flow values shown in figure 61-10. (Note the ticks at 260 mc and 5.5 kmc.) It is seen that, fortuitously or not, the points in the MA-6 flight between which blackout occurred ( $>53$ -db attenuation) correspond very closely to the points at which the signal frequency equaled the computed plasma frequency. For the C-band beacon signal, actual blackout did not occur but the signal dropped to nearly the noise level of the receivers and was, in fact, highly attenuated (approximately 37 db). It would, of course, be dangerous, at this point, to consider

such agreement as being indicative of general applicability of such a concept to other bodies or to other flight trajectories.

### OTHER INTERACTION MODELS

Propagation at oblique incidence to the plasma layer should be considered in the RF attenuation problem since the look angle of the wave path will not always be normal or near normal, as for the models discussed so far. Oblique propagation has not yet, however, been worked out for the case of a dissipative nonuniform plasma of small extent—that is, where gradients occur in small parts of a wavelength, as appropriate to the reentry plasma. The magneto-ionic (propagation through the ionosphere) theories treat the oblique propagation from the standpoint of geometric optics, in which the nonuniformities are assumed to occur very gradually with respect to signal wavelengths. (See ref. 23.) To illustrate the qualitative nature of the actual problem, some results obtained for a thin, lossy, uniform plasma applied to propagation at oblique incidence are presented in figure 61-12. These results are from a program developed for the IBM 7090 electronic data processing system by Calvin Swift of the Langley Research Center. For the oblique case, the wave propagation must be shown in two modes,  $T_{\parallel}$  and  $T_{\perp}$ , since the two modes will behave differently due to polarization effects. The  $T_{\parallel}$  mode is that part

of the transmitted  $E$  vector which is parallel to the plane of incidence and the  $T_{\perp}$  mode is that part which is perpendicular to the incidence plane, as shown in the figure. The periodic nature of the transmitted power ratio  $|T|^2$  as a function of incidence angle is also seen in the figure and is due to multiple reflections occurring at the two interfaces (indicated in the sketch on the left). For the dissipative case, this effect is washed out by wave absorption. The important result is that, as in the case of optical refraction at oblique incidence, there is a critical angle of incidence beyond which no transmission through the medium is possible because of complete reflection of the wave.

The other interaction model which has not as yet been discussed is propagation in the presence of an imposed magnetic field. This is a very important problem, since it offers the possibility of providing "transmission windows" in parts of the wave frequency spectrum which would otherwise be opaque to RF transmission (ref. 24). The effect may be briefly explained as follows. In the presence of a static magnetic field, a free electron describes a circular motion about the field lines at a frequency (the gyrofrequency) which is proportional to the strength of the magnetic field and with a radius of gyration which decreases as the field increases. Since the electron motion in the plane transverse to the magnetic field is thereby altered, new propagation modes may be introduced, depending upon the orientation of the electromagnetic wave. For example, if a wave is propagated parallel to the field lines and the field is infinitely strong, then no electron motion can occur in the plane transverse to the propagation direction and, hence, there can be no interaction even when  $\omega < \omega_p$ . This problem has been studied for the model of a lossy, uniform, semi-infinite plasma for normal incidence of circularly polarized waves propagating parallel to the field lines and for propagation of electromagnetic waves transverse to the field lines. The first case is of particular interest since the location of the window is not dependent upon the value of the plasma frequency but only upon the strength of the magnetic field for a collisionless plasma. For a

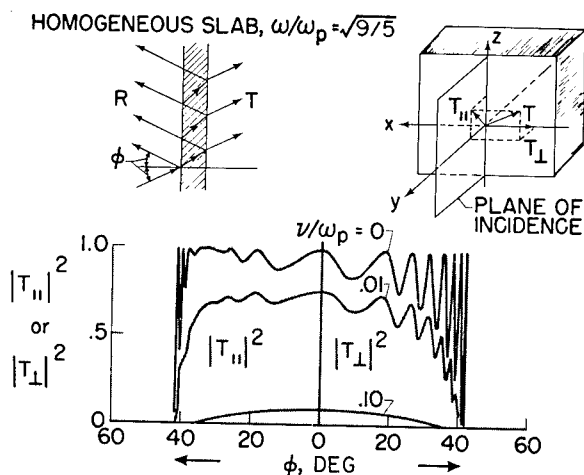


FIGURE 61-12.—Effect on transmission of signal incidence angle.

plasma with collisions the reduction of attenuation becomes less significant as the collision frequency increases. Figure 61-13 shows the effects of varying magnetic-field strength and collision frequency on the absorption properties, and figure 61-14 shows the effects on the reflection properties (in normalized form) of a semi-infinite, uniform plasma for normal incidence of right-hand circularly polarized waves when the field lines are parallel to the propagation direction. No results are yet available for nonuniform, finite-thickness plasmas.

There are a number of other interaction problems which may be of importance in certain situations, and they are only mentioned since there is considerable complexity and uncertainty involved in their formulation and assessment. (1) The near-field propagation problem involves alteration of the field of the antenna due to proximity of the plasma and, near the antenna, the wave is not like a plane wave, as was assumed for all the models considered. (2) Mismatch of impedance and detuning of the antenna, due to proximity of the plasma, have the effect of reducing the efficiency of the radiating system, and hence a signal degradation. (3) Voltage breakdown of the antenna elements may occur for high-power levels or low-density plasmas (resulting from field ionization near the antenna) and may greatly re-

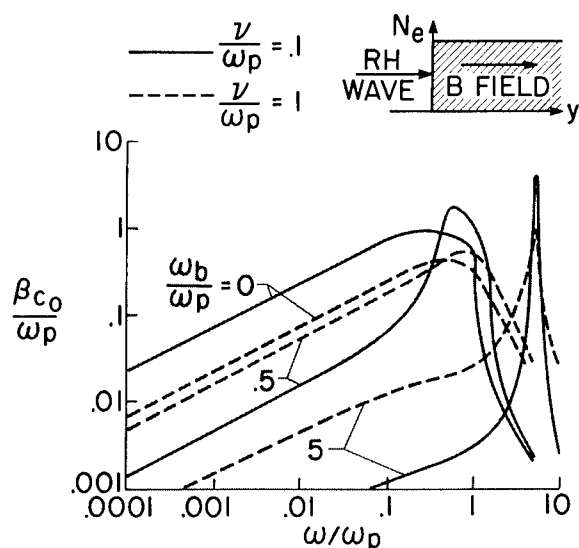


FIGURE 61-13.—Effect of magnetic field on wave-plasma absorption.

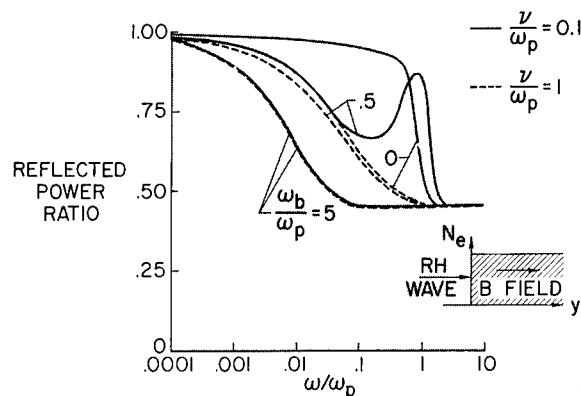


FIGURE 61-14.—Effect of magnetic field on reflected power ratio.

duce the signal. (4) A nonplane plasma layer (radius of curvature less than wavelength) may introduce deviations from the plane-wave-slab model.

#### MEANS FOR ACCOMPLISHING RADIO-FREQUENCY FLIGHT COMMUNICATION

From the discussion of the wave interaction problem for a plasma of the type to be expected in flight, some feeling for the parametric dependence of the problem has now been obtained. It would be well then to enumerate and assess the possible schemes which might be considered for maintaining transmission through the plasma during the critical part of the flight.

##### (1) Selection of signal frequency:

It has been shown that, for signal frequencies higher than the plasma frequency, transmission is possible. (See also ref. 25.) It can also be shown that in some cases (depends also on  $\nu$ ) very low frequencies will permit transmission. Because of the large investment in worldwide communications systems, as well as other problems, selection of frequency is not practicable outside of rather narrow limits. However, if such was possible, the Mercury spacecraft would require the X-band and the Appollo spacecraft would require at least the K<sub>a</sub>-band for continuous transmission (see figs. 61-2 and 61-11), if the concept in figure 61-11 applies. This, in turn, introduces acquisition problems and atmospheric absorption problems, but neither of these is insurmountable. Selection of very low frequencies entails problems with atmospheric noise and antennas and is of inconclusive value, based on present knowledge.

(2) Use of applied magnetic fields:

This scheme was, of course, not evaluated for the actual reentry-type plasma model, but by basing an estimate on the numbers from the uniform semi-infinite case and using peak shock-layer plasma properties, required magnetic-field strengths can be estimated. It would appear from such an assessment that the scheme requires magnetic-field producing systems of impracticably large size for the large manned vehicles, even considering the cryogenic superconductors. For small vehicles, however, the scheme offers very promising possibilities, since the field strengths can still be high at the smaller absolute distance out from the body surface where peak  $\omega_p$  occurs.

(3) Aerodynamic shaping:

This scheme involves the use of small bodies which might be mounted on the larger body to protrude outside of the main plasma layer. If the small body is the RF radiator, then the layer obstructing transmission will be relatively thin. It is certain that the absorption losses will be reduced in such a scheme, but the change in reflection loss is inconclusive lacking numerical evaluation of the actual case (scaling problem). The scheme is certainly an attractive one, provided that the cooling problems associated with the small probe and its mount are not too restrictive.

(4) Material injection:

This scheme might be referred to as the brute force scheme, since the material injection is for the purpose of cooling and/or neutralizing the plasma, as a means for reduction of the ionization. The injection of material may act as a heat sink (to lower the thermal state and, hence, ionization) and/or be electrophilic (to reduce the free-electron concentration by attachment). (See ref. 26.) The result is, hopefully, to open up a hole in the plasma layer for signal transmission or, in the case of small-body nose injection, to eliminate the ionization layer entirely. Also, selection of proper ablation products may act to reduce attenuation if the mixing and diffusion processes are great enough. On the other hand, ablation may work against the scheme, if the ablation products are easily ionizable.

(5) Miscellaneous schemes:

Other schemes which might be mentioned but are not discussed due to the uncertainty in-

involved in the formulation and evaluation of the ideas are as follows: (a) Use of the plasma layer as an electromagnetic radiator by some means of coupling the transmitter to the sheath; (b) use of modulated electron beams to introduce new propagation modes into the plasma; (c) modulation of the plasma properties from within to accomplish a modulation on a reflected continuous-wave signal from the ground (similar to, or a variation of, the Luxemburg effect); (d) use of modulated laser; and (e) finally, if there is no other resort or if real-time telemetry is not absolutely required, the storage and playback, or storage and recovery, type of systems may be used for the various flight data. This is not a very happy solution for manned flight.

#### OTHER FLIGHT RADIO-FREQUENCY PROPAGATION PROBLEMS

A problem of much interest with regards to tracking, detection, and discrimination of hypersonic vehicles during reentry is that of radar scattering from the vehicle and its plasma layer, including primarily the wake or trail plasma. (See refs. 2 and 27.) It has been observed that the signal may be at times absorbed by the gas cap (strong plasma layer around the nose) of the vehicle or that the reflected signal may actually be enhanced due to an apparent increase in the vehicle size, which is actually an increase in the radar cross section due to the growth of the plasma into the wake. This wake plasma may be very extensive at times and depends on many uncertain factors, such as ionization of ablation products in the wake, frozen recombination of the body flow-field plasma when expanded into the wake, and action of diffusion and mixing processes in the wake and ambient atmosphere (refs. 28 to 31). This is analogous to the meteor trail phenomena to a large extent but occurs at velocities lower than the usual meteor atmospheric entry.

Another interesting problem which is of great concern to communications and tracking from the launch site is that of rocket plume attenuation. In such a phenomenon, there is ionization in the rocket exhaust products or at the plume-air interface (again, due to the action of some uncertain factors) which results in a per-

turbation of the signal propagation through the plume (ref. 32). These uncertain factors may include chemi-ionization (nonequilibrium ionization in a combustion process) in the plume or at the interface, nonequilibrium expansion of the rocket combustion products, or seeding of the plume with ablated rocket-nozzle material. A much less likely factor is that of equilibrium ionization in the plume or plume-air mixture.

Another currently perplexing problem is that of signal propagation during the entry of a space vehicle into a planetary atmosphere, such as Venus or Mars, in order to effect telemetry of information about the planetary properties before a hard landing. The primary difference between this problem and an earth reentry communications problem is in the definition of the flow-field plasma properties resulting from the different chemistry involved (different atmospheric constituency). Once the electromagnetic properties of the plasma layer can be specified, the wave propagation problem should be no less tenable than another.

Finally, the problem of plasma noise should be mentioned, since this source of incoherent RF radiation may be troublesome over a wide frequency range. This radiation originates from within the plasma and may be due to processes known as *Bremsstrahlung* (free-free transitions) recombination, or from unstable plasma oscillations due to electron density gradients. In any case, a plasma noise level is added to the communications system noise level, and this is not desirable.

#### LABORATORY AND FLIGHT RADIO-FREQUENCY ATTENUATION STUDIES

Generally, the type of tests which may be carried out in the study of the RF wave-plasma attenuation problem falls into one of the following categories: (1) Diagnostic studies aimed at the experimental determination of electromagnetic plasma properties in reentry plasma layers, rocket plumes, and others, or the study and development of techniques and equipment for this purpose. Such techniques may be direct or passive and may involve probes, reflectometers, optical devices, and others. (2) Interaction studies aimed at understanding the basic nature of particular wave-

plasma interaction mechanisms by comparison of experimental determinations with theoretically evaluated results of tenable models (ref. 33). (3) Simulated flight tests in which conditions are produced in laboratory configurations which largely reconstruct or simulate the particular flight communications problem and thereby allow for bulk experimental data (attenuation, VSWR, etc.) which might be representative of the actual flight situation. Some of the main difficulties in this idea are: (a) production of very high kinetic energy air flow at proper ambient conditions, (b) wave reflection problems from the walls of the facility, (c) interference from electrical equipment used in the production of the flow or for equipment power, and (d) the problem of scaling the results from small models to the full-size vehicle (ref. 34). Involved primarily in the scaling problem are the separate aspects of viscous-flow scaling and scaling of the reflection effects, the latter being very uncertain due to the opposing aspects of electron density gradients ( $dN_e/dy$ ) and extent of the plasma ( $\lambda/\text{Body scale}$ ) which are in turn dependent also upon the viscous scaling. (4) Actual flight communications tests using models or portions of the space vehicle under the flight conditions expected for the vehicle. This technique is, of course, not usually economical but may be necessary to establish necessary criteria otherwise indeterminate, or for expediency. The cost can certainly be far less than the actual space mission cost since the payload, range, and so forth, need not be nearly as large. For small flight models, the same scaling problems exist as for laboratory models.

Various experimental programs are underway at a number of laboratories, which involve one or more of the aforementioned approaches. A shock tunnel program at Cornell Aeronautical Laboratory (ref. 4) is used for simulated flight studies and employs a fiber-glass nozzle to permit microwave transmission to models in the test section. At the Langley Research Center a comprehensive program known as RAM (radio attenuation measurement) is underway which involves portions of each of the foregoing categories (refs. 20 and 35) with flight tests serving as verifications of the concepts

developed from theoretical and experimental ground studies.

### CONCLUDING REMARKS

The problem of radio-frequency attenuation due to the interaction of an electromagnetic wave and a plasma layer has been reviewed with particular attention to that aspect dealing with communications during the reentry phase of space-flight missions. The electromagnetic plasma parameters have been discussed in rela-

tion to their influence on the wave propagation properties. It has been shown that theoretical models of wave-plasma interaction (absorption and reflection) can be synthesized to approximate the reentry plasma-layer problem; a comparison of flight results with those obtained with a simplified conceptual model was presented. Also, various means by which the attenuation problem may be alleviated or circumvented have been reviewed and the capabilities for laboratory and flight model tests have been discussed.

### REFERENCES

1. ANON.: Results of the First U.S. Manned Orbital Space Flight February 20, 1962. Manned Spacecraft Center, NASA.
2. ROTHMAN, WALTER, and MELTZ, GERALD, eds.: Electromagnetic Effects of Re-Entry. Planetary and Space Sci., vol. 6, June 1961.
3. MARSHALL, L. A., and GIRAGOSIAN, P. A.: Hypersonic Aerodynamic Characteristics of Blunt Faced Lifting Reentry Vehicles. Paper No. 62-169, Inst. Aerospace Sci., June 1962.
4. ESCHENROEDER, A. Q., DAIBER, J. W., GOLIAN, T. C., and HERTZBERG, A.: Shock Tunnel Studies of High-Enthalpy Ionized Airflows. Rep. No. AF-1500-A-1 (AFOSR 3025), Cornell Aero. Lab., Inc., July 1962.
5. EDSALL, ROBERT H.: Calculation of Flow Fields About Blunt Bodies of Revolution Traveling at Escape Velocity. [Preprint] 2492-62, American Rocket Soc., July 1962.
6. PIPPERT, G. F., and EDELBERG, S.: The Electrical Properties of the Air Around a Re-entering Body. Paper No. 61-40, Inst. Aerospace Sci., Jan. 1961.
7. BOWHILL, SIDNEY A.: The Ionosphere. Astronautics, vol. 7, no. 10, Oct. 1962, pp. 80-84.
8. MITRA, S. K.: The Upper Atmosphere. Second ed., The Asiatic Society (Calcutta, India), 1952. (Available from Hafner Pub. Co., New York.)
9. RATCLIFFE, J. A., ed.: Physics of the Upper Atmosphere. Academic Press, Inc. (New York), 1960.
10. RATCLIFFE, J. A.: The Magneto-Ionic Theory and Its Applications to the Ionosphere. Cambridge Univ. Press, 1959.
11. MARGENAU, H.: Conduction and Dispersion of Ionized Gases at High Frequencies. Phys. Rev., Second ser., vol. 69, nos. 9 and 10, May 1 and 15, 1946, pp. 508-513.
12. LINHART, J. G.: Plasma Physics. Second rev. ed., Interscience Publ., Inc., 1961.
13. STRATTON, JULIUS ADAMS: Electromagnetic Theory. McGraw-Hill Book Co., Inc., 1941.
14. CHAPMAN, SYDNEY, and COWLING, T. G.: The Mathematical Theory of Non-Uniform Gases. Cambridge Univ. Press, 1939, pp. 319-358.
15. MASSEY, H. S. W., and BURHOP, E. H. S.: Electronic and Ionic Impact Phenomena. The Clarendon Press (Oxford), 1952.
16. HAMMERLING, P., SHINE, W. W., and KIVEL, B.: Low Energy Elastic Scattering of Electrons by Oxygen and Nitrogen. Jour. Appl. Phys., vol. 28, no. 7, July 1957, pp. 760-764.
17. PENG, T. C., and PINDROH, A. L.: An Improved Calculation of Gas Properties at High Temperatures. Doc. No. D2-11722, Boeing Airplane Co., Feb. 23, 1962.
18. SCHULTZ, D. L.: Research at the National Physical Laboratory on the Ionization Properties of Gases at High Temperatures. NPL/Aero/378, British A.R.C., June 1959.
19. ELLIS, MACON C., Jr., and HUBER, PAUL W.: Real Gas Flow Conditions About Hypersonic Vehicles. Reentry Dynamics. Bull. of Virginia Polytechnic Inst., Eng. Exp. Station Ser. No. 150, vol. LV, no. 10, Aug. 1962, pp. 120-154.
20. HUBER, PAUL W., and EVANS, JOHN S.: Theoretical Shock-Layer Plasma Flow Properties for the Slender Probe and Comparison With the Flight Results. NASA paper presented at Second Symposium on the Plasma Sheath (Boston, Mass.), Apr. 10-12, 1962.



# PLASMA PHYSICS AND MAGNETOHYDRODYNAMICS

21. ALBINI, FRANK A., and JAHN, ROBERT G.: Reflection and Transmission of Electromagnetic Waves at Electron Density Gradients. *Jour. Appl. Phys.*, vol. 32, no. 1, Jan. 1961, pp. 75-82.
22. HERRMANN, G. F.: The Absorption of Microwave Radiation in a Plasma Whose Electron Density Varies Linearly With Distance. Tech. Rep. No. 2 (RADC-TDR-62-87), Gen. Telephone and Electronics Labs., Inc., Feb. 1, 1962. (Available from ASTIA as AD No. 274126.)
23. GINZBURG, V. L. (Royer and Roger, trans.): Propagation of Electromagnetic Waves in Plasma. Gordon and Breach, Sci. Publ., Inc. (New York), c. 1961.
24. HODARA, H.: The Use of Magnetic Fields in the Elimination of the Re-Entry Radio Blackout. *Proc. IRE*, vol. 49, no. 12, Dec. 1961, pp. 1825-1830.
25. BALDWIN, K. M., BASSETT, O. E., HAWTHORNE, E. I., and LANGBERG, E.: Telecommunications During Re-Entry. *Planetary and Space Sci.*, vol. 6, June 1961, pp. 207-218.
26. PAGE, F. M., and SUGDEN, T. M.: The Reduction of Attenuation of Microwave Radiation in Hydrogen/Air Flames Containing Alkali Metals by Chlorine, Bromine, and Iodine. Dept. Phys. Chem., Univ. of Cambridge, 1953. (Available as ASTIA Doc. AD 221440.)
27. LIN, S. C., GOLDBERG, W. P., and JANNEY, R. B.: Radio Echoes From the Ionized Trails Generated by a Manned Satellite During Re-Entry. Res. Rep. 127 (BSD-TDR-62-54), Avco-Everett Res. Lab., Apr. 1962.
28. FELDMAN, SAUL: Trails of Axi-Symmetric Hypersonic Blunt Bodies Flying Through the Atmosphere. Res. Rep. 82 (Contract No. DA-19-020-ORD-4765), Avco-Everett Res. Lab., Dec. 1959.
29. GOULARD, M., and GOULARD, R.: The Aerothermodynamics of Reentry Trails. Preprint 1145-60, American Rocket Soc., May 1960.
30. BLOOM, M. H., and STEIGER, MARTIN H.: Viscous Reacting Wake Flow—Symmetric and Axi-Symmetric. PIBAL Rep. No. 544, Polytechnic Inst., Brooklyn, 1960.
31. LEES, LESTER, and HROMAS, LESLIE: Turbulent Diffusion in the Wake of a Blunt-Nosed Body at Hypersonic Speeds. Aero. Dept. Rep. No. 50 (Contract AF 04(694)-1), Space Tech. Labs., Inc., July 1961.
32. SIMS, THEO E., and JONES, ROBERT F.: Rocket Exhaust Effects on Radio Frequency Propagation From a Scout Vehicle and Signal Recovery During the Injection of Decomposed Hydrogen Peroxide. NASA TM X-529, 1961.
33. HUBER, PAUL W., and GOODERUM, PAUL B. (With appendix A by THEO E. SIMS and DUNCAN E. McIVER, JR., and appendix B by JOSEPH BURLOCK and WILLIAM L. GRANTHAM): Experiments With Plasmas Produced by Potassium-Seeded Cyanogen Oxygen Flames for Study of Radio Transmission at Simulated Reentry Vehicle Plasma Conditions. NASA TN D-627, 1961.
34. BEISER, A., and RAAB, B.: Hydromagnetic and Plasma Scaling Laws. *The Physics of Fluids*, vol. 4, no. 2, Feb. 1961, pp. 177-181.
35. SIMS, THEO E.: Measurement of VHF Signal Attenuation and Antenna Impedance During the Ascending Flight of a Slender Probe at Velocities up to 17,800 Feet per Second. NASA paper presented at Second Symposium on the Plasma Sheath (Boston, Mass.), Apr. 10-12, 1962.

## 62. Survey of Plasma Accelerator Research

By Macon C. Ellis, Jr.

MACON C. ELLIS, JR., *Head, Magnetoplasmodynamics Branch, Aero-Physics Division, NASA Langley Research Center, received his Bachelor of Science degree in aeronautical engineering from Alabama Polytechnic Institute in May 1939. Ellis joined the Langley Staff in November 1939 as an aeronautical engineer. He does research and exploration into the basic nature and mechanism of the fundamental physical processes involved in ionized gases interacting with magnetic and electrical fields. He successfully developed one of the first supersonic wind tunnels in this country (the Langley 9-inch supersonic tunnel); he conducted early jet propulsion studies and made the first objective study of supersonic ram jets and supersonic wind-tunnel experiments, leading to the proposal of a supersonic airplane in 1945; he conducted the first supersonic-tunnel test of the X-2 airplane configuration. He is a member of the American Rocket Society, the British Interplanetary Society, the American Geophysical Union, the Engineers' Club of the Virginia Peninsula, and an Associate Fellow in the Institute of the Aerospace Sciences. He serves as a member on a number of technical committees at Langley and presently is a member of the NASA Research Advisory Committee on Electrical Energy Systems.*

### SUMMARY

A brief summary is given of the role of plasma acceleration in modern technology, including space exploration. The various types of plasma accelerators which are described and for which the current research status and problems are discussed include continuous-flow, direct-current, crossed-field accelerators; continuous-flow accelerators utilizing Hall currents; accelerators utilizing traveling-wave concepts; and pulsed, coaxial plasma guns.

### INTRODUCTION

Modern technology continues to seek, for numerous objectives, means to accelerate gaseous media of greater density to higher and higher velocities. Since this effort has mostly concentrated on the conversion of thermal energy to kinetic energy, containment of the hot gas and survival of the container has related progress primarily to advances in high-temper-

ature and high-strength materials and to advances in wall-cooling techniques. Eventually, however, radiation to the container walls from the hot gas at values of density desirable for many applications poses an upper limit on storage of thermal energy. It is obviously desirable then to seek means of adding directed energy to the gas by means which minimize the thermal energy added; use of electromagnetic forces on charged particles offers this possibility. An electromagnetic plasma accelerator avoids the necessity of containing a gas at its full stagnation temperature and pressure and alleviates the nozzle-throat heat-transfer problem.

The use of electric fields to accelerate ion and electron beams to velocities approaching that of light is a well-developed and documented science and art of the physicist; however, the

density of these beams is very low due to space-charge limitations. Hence, the interest here is in the possibilities of accelerating neutral plasmas where, in principle, no such space-charge limitations exist. Possible applications of high-velocity plasma streams are as follows:

- Efficient, high-exhaust-velocity thrusters for distant space missions
- Laboratory simulation of hypersonic flight (with quenched ionization in test flow)
- Plasma injectors in controlled thermonuclear fusion research
- Laboratory simulation of astrophysical phenomena
- Possible conversion of kinetic energy to radio-frequency energy
- Produce high-velocity plasma for other magnetoplasmadynamics, (MPD) research (e.g., MPD generators)
- Plasma acceleration studies increase basic MPD knowledge
- Furnishes primary exploitation of breakthrough in superconducting magnets

As related to the primary and continuing objectives of NASA space exploration, electric propulsion systems offer the promise of much greater payloads than do chemical or nuclear systems for the more distant space missions.

In the continuing effort to simulate, in the laboratory, hypersonic flight or reentry from orbital, lunar, and planetary flight, the attainable flight conditions are far in advance of the simulation capabilities. Inherent limitations of conversion of thermal to kinetic energy have already been mentioned; Mach numbers in the range of 15 to 18 appear as upper limits although radio-frequency (RF) or inductive heating of the supersonic stream may take this somewhat higher. Shock tubes have provided a wealth of data at real-gas conditions but simulate for very short times the flow only for blunt bodies or near the stagnation point, whereas study of flow around and behind the body is becoming increasingly more important. Use of electric body forces for acceleration thus appears as an attractive means of attaining high-velocity flows in the range of 26,000 to 60,000 feet per second. In contrast to plasma propulsion, where the efficiency of the thrust system directly affects the power system weight, efficiency

for the flow simulator is of secondary importance and running or test time need not be more than seconds or minutes.

The other applications listed are self-explanatory except, perhaps, generation of high-power RF energy. Most present means for converting electrical energy to RF energy involve electron streams in one way or another and their energy-density is low, requiring large volumes of apparatus for high power. High-velocity plasma streams offer several possibilities for resonant excitation and extraction of RF radiation and, in addition, plasma instabilities, which are a troublesome problem in both controlled thermonuclear fusion (CTNF) and plasma acceleration efforts, might be trained to give up their "losses" as controlled RF energy.

The first application of plasma accelerators was listed as electric propulsion so a word more on this is in order to get an idea of the "fit" of plasma systems into the mission picture. In the analysis of reference 1, comparison has been made among chemical, nuclear, and electric propulsion systems for some distant missions. One aspect of this analysis is shown in figure 62-1. The missions shown at the left are in approximate order of increasing difficulty or characteristic vehicle velocity increment required. The gross payload shown is that delivered at the mission objective, and it is considered that minimum useful payloads are in the range of 1,500 to 2,000 pounds. Without going into such details as trip times and weights in earth orbit, the analysis shows that for the more distant missions only the electric propulsion systems will do the job. (The analysis of ref. 1 assumes ion

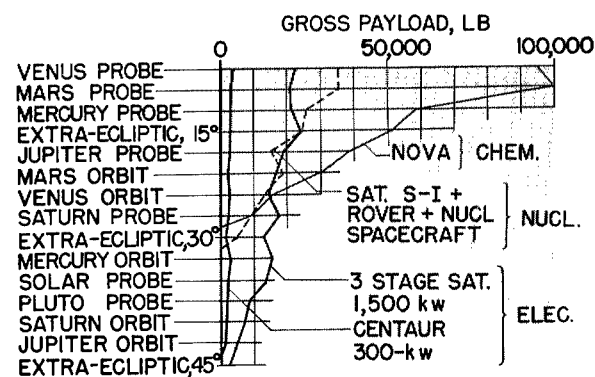


FIGURE 62-1.—Performance comparison of chemical, nuclear, and electric systems. (From ref. 1.)

## SURVEY OF PLASMA ACCELERATOR RESEARCH

thrust systems.) The final point is that tripling the output of the electric power system gives large gains in payload capabilities; therefore, the necessity for development of large space power systems is emphasized. These larger powers will be necessary if the potential advantage of higher thrust and shorter mission times for the plasma systems is to be realized. Furthermore, certain space missions call for variable specific impulse during flight, for example, from 2,000 to 40,000 seconds. (See refs. 2 and 3.) Magnetoplasmadynamic devices, at this time, appear to have no fundamental limitations on ability to vary exhaust velocity; thus, such devices potentially can encompass this specific-impulse range and at the same time offer high thrusts per unit area.

### SYMBOLS

$B$	magnetic induction
$E$	electric field strength
$j$	current density
$M$	Mach number
$p$	static pressure
$p_t$	total pressure
$T$	temperature
$u, v, V$	velocity
$x, z$	distance in axial direction
$y$	distance in vertical direction
$\gamma$	ratio of specific heats
$\rho$	mass density
$\sigma$	scalar electrical conductivity
$\tau$	mean free time between collisions
$\omega$	cyclotron frequency
<i>Subscripts:</i>	
$i, +$	ion
$e, -$	electron
$in$	ion neutral
$\phi$	angle from $x$ -axis
$\theta$	angle between ion and $E/B$ direction or azimuthal direction
$n$	neutral particle
$z$	longitudinal or axial direction
$R$	radial direction
$rot$	rotational
$trans$	translational
$cath$	cathode

Bar over symbol indicates vector.

### PLASMA-ACCELERATOR CATEGORIES

Many possibilities exist for the compounding of pieces and plasma principles to devise a plasma accelerator. In any attempt to categorize those that have been conceived or worked on,

one faces the dilemma that is illustrated in the following list:

A given accelerator might be

- (a) Continuous or
- (b) Pulsed.

The device may use

- (a) Electrodes or
- (b) No electrodes.

The plasma may be generated

- (a) Separate from accelerating region or
- (b) As integral or initial part of acceleration process.

Basic acceleration process may utilize

- (a) Self-magnetic fields or
- (b) Applied magnetic fields

Coupled with

- (c) Applied current or
- (d) Hall current.

Basic containment of plasma may be

- (a) Magnetic or
- (b) Aerodynamic.

Plasma may be closer to

- (a) Collisionless or
- (b) Collision dominated.

A given accelerator scheme or device might be of the continuous-flow variety in the sense that a steady source of gas (or propellant) is fed in and accelerated in a continuum sense or it may be pulsed in several ways. If the pulse rate is sufficiently high to provide only small fluctuations with time in the resulting flow momentum, then it would be continuous. The device may utilize electrodes to feed the electrical energy in and the cathodes may be thermionic emitters or field- or photo-emitters or ion-bombardment emitters. Many forms of electrodes are possible—for example, the hollow cathode. If electrodeless, the accelerator may take numerous forms, depending on the detailed magnetic-field configurations and their variation with time. The plasma to be accelerated may be generated separately from the primary accelerating region, as in a seeded arc jet, or the generation may be inseparable, in principle, from the process of imposing directed electromagnetic forces on the plasma. The basic acceleration process may utilize, for the magnetic component of the driving force, either the field of the driving current or an applied magnetic field, or both. The primary driving

current can be the applied current or a Hall current or both may be utilized. The plasma containment may be either aerodynamic or magnetic. Aerodynamic containment depends upon collisions to restrict the diffusion rate of particles toward the walls and magnetic containment depends upon the absence of collisions to restrain the motion of charged particles to magnetic field lines, hence, away from the walls. The mean free time between collisions or inversely the mean free path of the electrons or ions, coupled with the velocity of the particles and the magnetic-field strength, may define an  $\omega\tau$  domain of operation of a given acceleration scheme. Although not listed, RF energy may be used rather directly in the acceleration process or for plasma heating or may be combined in numerous fashions with other combinations of items shown. Plasma conditions and MPD principles force or restrict certain combinations; therefore, the choice of combinations is limited but still large. The subsequent discussion is thus restricted to those types of plasma accelerators which have been studied most extensively and which are hopefully farthest along toward their goals.

### PLASMA ACCELERATION

The following table shows the general types of accelerators to be discussed briefly:

	<i>Approximate number under study</i>
Continuous-flow, d-c, linear, crossed-field accelerator .....	13
Continuous-flow accelerators utilizing Hall currents .....	8
Accelerators utilizing traveling-wave concepts .....	9
Pulsed, coaxial plasma guns .....	24
TOTAL .....	54

A search of the literature on the subject of plasma acceleration reveals the relatively large number of devices under study as shown. Each of these represents at least some experimental as well as analytical effort and it is probable that the list is not complete; it is obvious, however, from the numbers that there exists considerable interest and competition toward achievement of the apparent potentialities of such devices. The engineer seeks to attain the high velocities for his own uses whereas the scientist is fascinated with an application for

this exploding science of magnetoplasma dynamics.

### CONTINUOUS-FLOW, LINEAR, CROSSED-FIELD PLASMA ACCELERATORS

The basic concept of a continuous-flow, linear type of crossed-field, direct current (d-c) plasma accelerator is shown schematically in figure 62-2. The cathodes are shown in the upper wall, the anodes in the lower wall, and an externally imposed magnetic field is normal to and out of the plane of the paper; the electric field is in the plane of the paper and directed upward, perhaps at a slight angle for reasons to be discussed subsequently. Since the gas flow is ionized and is an electrical conductor, the elements of an electric motor are evident, and the electric-motor or Lorentz force per unit volume on the current is

$$\vec{F} = \vec{j} \times \vec{B}$$

that is, the cross product of the current density and the magnetic induction. The device may be considered analogous to a shunt-wound, d-c motor, but the deceptive simplicity of the concept fades as one begins to examine the details of the acceleration process and the particle motions. The concepts of operation, together with results of analysis and experiments for the accelerator as carried out by George P. Wood and associates at the Langely Research Center (refs. 4, 5, 6, and 7) are outlined in the following comments.

As stated previously, the accelerator incorporates a magnetic field normal to the electric field and uses the Lorentz force. Since the force exerted by a magnetic field on a moving charged particle is normal to the velocity of the particle, no work is done on the particle by a stationary magnetic field. The magnetic field

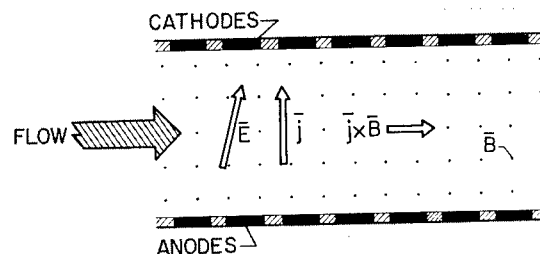


FIGURE 62-2.—Schematic of crossed-field accelerator.

simply determines in part the direction of the particle velocity. For the collisionless case, the two-dimensional projection of the ion and electron paths would be cycloids that lie along equipotential lines in a direction normal to both electric and magnetic fields. Because of the mass difference, the radii of gyration of the ions and electrons differ and the sense of rotation is opposite due to opposite sign of charge; however, the average drift direction and velocity are the same, and the drift velocity is  $E/B$ .

In the present instance, there is no interest in the low-density collisionless case, and the effects and results of collisions must be considered. From the macroscopic point of view, the driving force is the Lorentz force on a current in a magnetic field,  $\bar{j} \times \bar{B}$  per unit volume, where the current consists principally of a flow of electrons. In the microscopic picture, it is desired that the ions be accelerated in the electric field, and then, by collisions, drive the neutral particles along the channel. The microscopic method is used to provide insight into the physics of the process and the macroscopic method is used to provide quantitative results for use in designing accelerators.

#### QUALITATIVE ANALYSIS FROM MICROSCOPIC POINT OF VIEW

Because of the large difference in the masses of electrons and ions, these two species behave differently in crossed fields in a three-component plasma; that is, they have different mean free times, different cyclotron frequencies, and different velocity directions and magnitudes. The desirable behavior on the part of each is discussed first.

Because of its comparatively small mass, an electron cannot impart much momentum at a collision with a neutral particle. It is therefore not undesirable that the electron make many cycles between collisions with neutral particles and thus have its velocity vector directed essentially at random just before collision. On the other hand, the ion should make, on the average, just a portion of a cycloid between collisions with neutral particles. It is perhaps well to reiterate here that the basic acceleration process is considered to be first the acquisition of additional momentum from the electric field

by the ion, then the transfer of this additional momentum to a neutral particle by collision, and then the equal distribution, on the average, of this additional momentum over the more numerous neutral particles. The portion of the cycloid that it is desirable for the ion to traverse is one for which, on the average, three conditions are satisfied.

The first of these conditions is that, on the average, at collision the ion velocity is a specified amount greater than the average forward velocity of the neutral particle. Satisfying this condition allows additional momentum to be imparted to the neutral particle at a specified rate. Part of this additional momentum goes into random motion of the particle and tends to raise the temperature of the gas. On the other hand, the cooling effect associated with acceleration of the plasma tends to lower the temperature; thus satisfying this condition results in a partial control over temperature.

The second condition is that the collision occurs when, on the average, the instantaneous direction of motion of the ion is in the direction of the axis of the channel. The reason for this condition is that it is desirable to drive the neutral particles axially along the channel and not toward a wall.

The third condition is that the ion travels on the average along the axial direction—that is, in addition to moving axially at the time of collision, the average velocity of the ion should lie along the direction of the axis and not be directed toward a wall where on contact with an electrode the ion would be neutralized.

Some of these conditions are mutually contradictory, but usually not seriously so. As illustrated in figure 62-3, the ion path without collisions is cycloidal; however, the wish is that, on the average, the ion path will repeat a small section of this cycloid (the section between the two dashed lines), and that the initial and final directions will be nearly the same and will approximate a straight line.

In Wood's analysis (ref. 4), the first condition has been adopted that, on the average, at collision the ion velocity is a specified amount greater than the average forward velocity of the neutral particle; further, constant static temperature is assumed, so that the acceleration

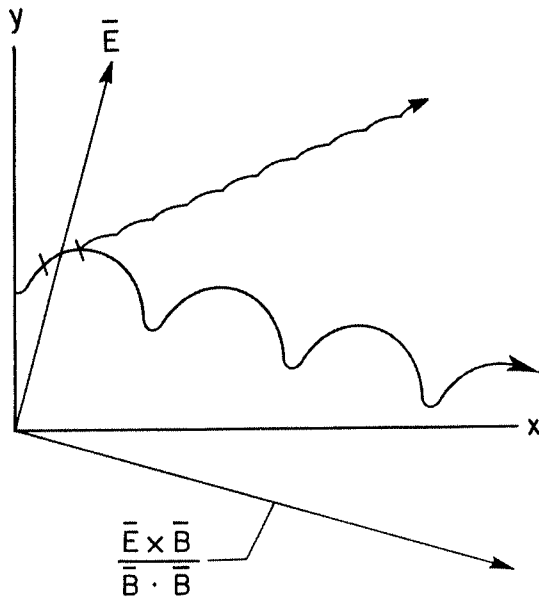


FIGURE 62-3.—Ion path with and without collisions.

rate is specified to be such that the decrease in temperature due to acceleration is just compensated by the increase in temperature due to Joule heating. The second condition is adopted in order that the driving force on the neutrals may be directed parallel to the axis of the channel. A choice can be made between the second and third conditions, that is, the ions or the

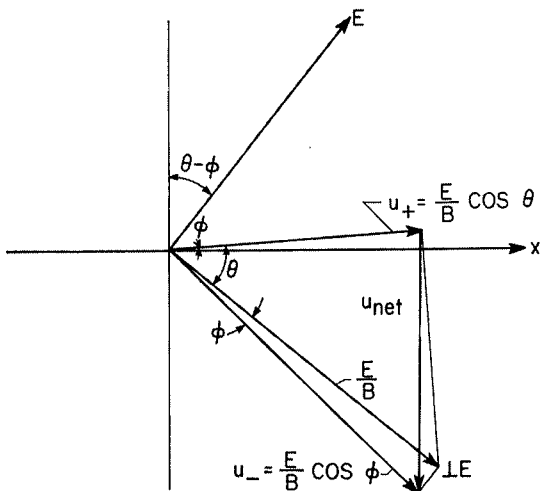


FIGURE 62-4.—Orientation of ion and electron velocities.

neutrals may be directed along the axis. If it is desired to direct the neutrals along the axis, then the electric field may be tilted in such a way that the x-components of ion and electron velocities are equal as shown in figure 62-4, thereby making the axial current zero. The direction of the ions is tilted but the angle for practical cases is extremely small.

#### QUANTITATIVE RESULTS FROM ANALYSIS FROM MACROSCOPIC POINT OF VIEW

At this point then, what do the results of macroscopic analyses show in terms of geometry and operating characteristics of such an accelerator? Figure 62-5 shows the Mach number as a function of normalized length for the conditions of constant cross-sectional area, constant static temperature, constant applied magnetic field, Lorentz force directed along the channel axis, small degree of ionization, no friction and heat transfer, and  $\gamma M^2$  greater than unity. The

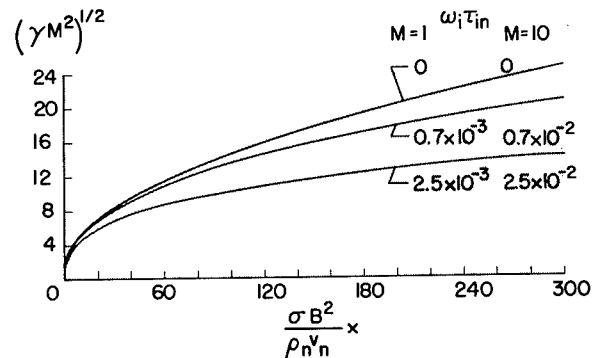


FIGURE 62-5.—Mach number as function of length.

curves show essentially the Mach number at a given longitudinal distance  $x$  from the  $M=1$  station as a function of the distance normalized by the parameter  $\frac{\sigma B^2}{\rho_n V_n}$ . Reference 4 takes into account the Joule heating due to ion slip as well as the conventional Joule heating due to resistance and the three curves show the effect in terms of  $\omega_i \tau_{in}$  where  $\omega_i$  is for the ions and  $\tau_{in}$  is for the ion-neutral collisions. Increasing  $\omega_i \tau_{in}$  corresponds to increasing the heating due to ion slip. The current, hence the acceleration, must correspondingly be decreased at a given  $x$ -station to preserve the balance between heating and cooling due to acceleration; the accelerator

length is then greater in order to reach a given Mach number. The detrimental effects of ion-slip heating on accelerator length can, however, be overcome by the cooling effect of a slight area expansion of the accelerator channel. Typical values of  $\omega_i \tau_{in}$  for the following experiments are approximately  $10^{-3}$  radian.

### CROSSED-FIELD ACCELERATOR EXPERIMENTS

The elements of the early experimental apparatus used at Langley to study crossed-field accelerators are shown schematically in figure 62-6. The source of plasma is a seeded arc jet, wherein the arc is magnetically rotated by the coils shown around the outer chamber wall. A typical mass flow of  $N_2$  is 2.6 g/sec with final enthalpy of 8,860 Btu/lb and corresponding temperature of 6,900° K. Cesium is fed at constant rate through a resistance-heated vaporizer to the hot nitrogen flow after the arc. The resulting plasma emerges from a Mach 2 nozzle at the entrance to the EM acceleration region at a temperature of 5,500° K with ionization levels of 1- to 4-percent mole fraction corresponding to nearly complete ionization of the cesium seed. The accelerator channel, shown in the low-pressure chamber, is 1 cm  $\times$  1 cm  $\times$  8 cm. Magnetic fields up to 11,000 gauss are imposed across the channel through pole faces contacting non-magnetic walls of the channel. As shown in the schematic, a total-pressure tube is shown at the flow exit. Static-pressure orifices are also incorporated along the channel walls. Figure 62-7 shows a cross section through the accelerator indicating the components and the seg-

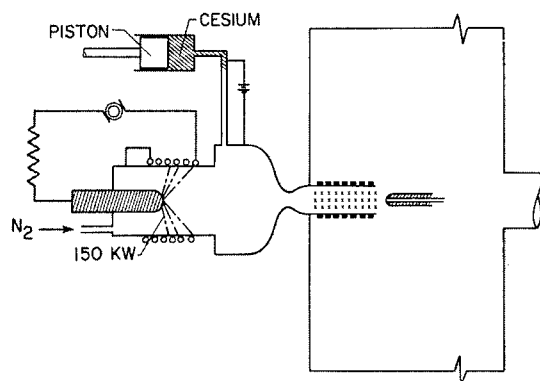


FIGURE 62-6.—Schematic of apparatus.

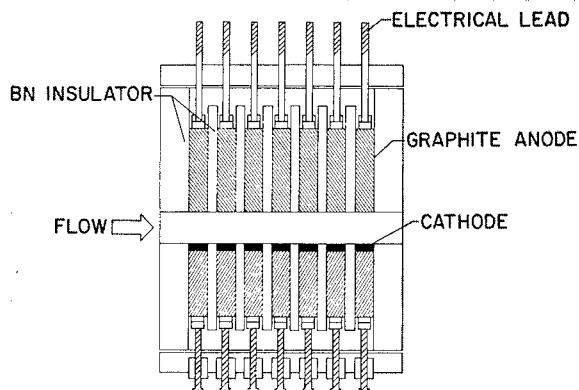


FIGURE 62-7.—Longitudinal section through accelerator.

mented electrodes. Cathodes used have mostly been of thoriated tungsten. The current loop through the gas between opposing electrodes is closed separately for each pair through external batteries, and voltage and current may be controlled separately for independent pairs.

The significance of the pressure measurements is indicated from the following equations:

$$\frac{\Delta p_t}{p_t} = \frac{2\gamma M^2}{[2 + (\gamma - 1)M^2]\rho u^2} \left[ jB - \frac{(\gamma - 1)M^2 j^2}{2\sigma u} \right] \Delta x$$

$$\frac{\Delta p}{p} = -\frac{\gamma M^2}{(M^2 - 1)\rho u^2} \left[ jB - \frac{(\gamma - 1)M^2 j^2}{\sigma u} \right] \Delta x$$

The equations show the relative change in total pressure  $p_t$  and in static pressure  $p$ . For the two terms in the brackets of each equation, the first is the effect of the Lorentz accelerating force and the second is the effect of Joule heating; therefore, an increase in total pressure and a decrease in static pressure (note negative sign of static-pressure equation) indicates a win for the accelerating force.

Typical results of several tests are shown in table 62-I. The column headings show mass flow, total current flow across the channel, and total pressures at the accelerator channel exit for the cases of current flowing and no current flowing. By sensing the change in total and static pressure (latter not shown) due to switching on the current flow, the fact that the accelerator was truly accelerating could be easily and directly observed. Typical runs are shown for two sets of pressure or density in the



TABLE 62-I.—Representative Data for  
1 cm × 1 cm × 8 cm Accelerator

Mass flow, g/sec	Accelerator current, amp	$p_t$ , mm Hg		$(\Delta p_t)_{on}$ $(p_t)_{off}$
		Current off	Current on	
1.37	66	143	214	0.50
1.37	110	145	245	.69
1.37	114	136	260	.91
2.74	160	342	520	.52
2.74	125	325	460	.42
2.74	144	357	501	.40

channel and it is seen that for all cases an increase in total pressure occurs; this increase indicates that the Lorentz force exceeds the effects of Joule heating in diminishing this force. By using the equations with known values of  $x$ ,  $B$ ,  $\rho u$  and  $M$ , estimated values of  $\gamma$ , and calculated values of  $\sigma$ , a calculated value of the total-pressure change can be made. The experimental values average between 50 and 60 percent of the calculated values and corresponding velocity increases implied from the measurements are about 30 percent. For this small accelerator, efficiencies from measurements are misleading mainly because of the losses associated with the large voltage drop through the cathode and anode sheaths. For larger accelerators this loss would be a far smaller fraction of the total losses. If these losses are ignored, efficiencies of conversion of electrical to kinetic energy of about 70 percent are indicated. Many other detailed measurements have been made with the use of this small accelerator and much has been learned concerning, for example, electrode materials, insulator materials, seeding techniques, temperature measurements, accelerator construction, and many other details. It is obvious that the small size of the apparatus greatly exaggerates wall losses and limits many measurements, especially probing-type measurements, and that a larger accelerator with higher power and greater acceleration is the desirable next step. A larger accelerator has been built at the Langley Research Center and operation has just started; the principal features of this larger facility are shown in the

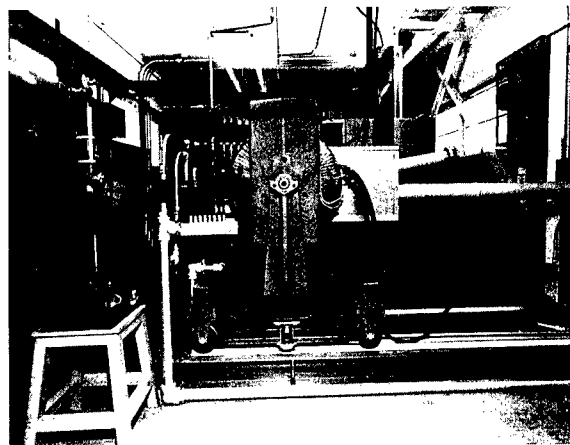


FIGURE 62-8.—Langley 1-inch-square plasma accelerator.

photograph of figure 62-8. Unfortunately, the accelerator channel and many details of the arc chamber are hidden behind the large electromagnet. The arc is at the left and the low-pressure discharge pipe is at the right.

The characteristics of the arc plasma source and estimated performance of the accelerator are shown in table 62-II. In the table, a con-

TABLE 62-II.—Langley 1-Inch-Square  
Plasma Accelerator*Arc plasma source:*

Arc potential and current.....	200 v, 2,500 amps
Arc-chamber pressure.....	1 atm
Gas flow rate.....	7 g/sec
Gas enthalpy.....	8,000 Btu/lb
Gas temperature.....	7,000° K
Gas ionization (Cs seed).....	≈ 2 percent

*Accelerator:*

Dimensions.....	1 in. × 1 in. × 12 in.
Number of electrodes.....	24 pairs
Magnetic field.....	10,000 gauss
Power source.....	400, 12-v battery
Potential across electrodes.....	135 to 225 v
Current through plasma.....	1,700 amps
Power into Joule heat.....	70 kw
Power into Lorentz force.....	180 kw
Pressure.....	70 mm Hg
Velocity at entrance.....	2,000 m/sec
Velocity at exit.....	4,000 m/sec

sistent set of nominal operating conditions are given; however, it is emphasized that the potential of the primary apparatus will permit still greater velocity increases than are shown (2,000 to 4,000 m/sec) as research progresses.

### Other Investigations of Crossed-Field Accelerators

Other experimental work on crossed-field accelerators is included in references 8 to 12. The experiments of Demetriades (ref. 8) are noteworthy in that he has achieved the highest thrust and velocity increase due to the Lorentz force and has reached an efficiency of 54 percent. His accelerator incorporates three pairs of electrodes, and the whole assembly of channel, electrodes, and magnet is mounted on a thrust stand, separate from the arc-jet plasma source; thus, direct measurements of thrust due to electromagnetic forces can be made. He reports thrusts up to 3.6 pounds at an acceleration efficiency of 54 percent. The specific impulse increment due to the plasma accelerator was reported to be 1,200 seconds, corresponding to an addition of 300 percent to the specific impulse of the arc jet used. In his experiments, he has made systematic variation in the electric parameters; for example, in tests where the voltage and current were held constant and thrust measured as a function of magnetic-field strength, he shows linear increase as expected up to a peak where the back electromotive force and Hall current predominate and cause a decrease. He has also made extensive study of electrode configurations, both flush and protruding. All his experiments are fairly short-time tests; thus, problems such as electrode erosion and so forth still remain.

Hellund and Blackman and their group have carried out experiments on crossed-field accelerators and have concentrated on properties of gases for use in such devices, especially as influencing choice of propellant and use of their nonequilibrium characteristics. (See ref. 9.)

Hogan (ref. 10) has carried out short-duration experiments at high-power and high-magnetic induction levels by the ingenious combination of an ionized shock-tube flow, a transverse magnetic field generated by the discharge of capacitor through a coil, and a transverse electric field supplied by another capacitor system. He obtained results which, although for a small 1½-inch channel, are for power inputs to the gas up to 5 megawatts and show that, for his range of conditions, deceleration due to eddy currents in the gas as it leaves the magnetic field

were small, electrical energy chargeable as loss to the boundary layer was relatively small (smaller with increase in power), and that overall efficiencies up to 70 percent were realizable.

### Problems and Future Research on Crossed-Field Accelerators

For the crossed-field accelerator, the detail problems and loss mechanisms deserving attention are numerous and have been elaborated recently by several authors. Janes has discussed the various loss mechanisms in an accelerator channel which he believes to be crucial (ref. 13) and implies from his summary and later comments (ref. 14) that because of wall loss and heating limitations of such aerodynamically contained accelerators, magnetically contained arrangements hold greater promise for the highest possible exhaust velocities. He has made approximate analyses (ref. 13), considered separately, of thermal-leaving losses, frozen-flow losses, electrical conductivity, propellant choice, eddy-current effects, Hall current limitations, ion-slip heat losses, wall effects, transport coefficients in a magnetic field, electronic heat conduction and thermal equilibrium, electrode boundary layers, insulator boundary layers, and Joule field coil losses. Obviously numbers of these effects are so interrelated that they must be considered simultaneously as pointed out in reference 15; consequently, as pointed out in reference 9, there is considerable doubt as to the accuracy of such analyses in that, at best, only trends can be indicated. One very important technological development subsequent to most of these discussions of problems is that of the superconducting magnet; Joule field coil losses will be nearly nonexistent and magnet weight will be very small.

In any case, it is safe to conclude that much more fundamental work, both theoretical and experimental, is needed to study

- (1) both macroscopic and particle characteristics of basic gas and acceleration processes,
- (2) nonequilibrium gas effects for a variety of gases that are potential propellants,
- (3) highest possible velocities to uncover limitations,
- (4) electrode characteristics,
- (5) insulator characteristics.

A number of groups including Langley Research Center are pursuing these studies with optimism, at this stage, for the future of the crossed-field accelerator.

### Continuous-Flow Accelerators Utilizing Hall Currents

The rectangular plasma accelerator discussed in the previous section used, as its plasma source, the seeded, high-temperature gas from an arc jet. This arc jet was a coaxial device in which an externally imposed axial magnetic field  $B_z$  and a radial current density  $j_r$  combined to exert a  $j_r B_z$  force/volume in the azimuthal direction as shown schematically at the lower left of figure 62-9. This force rotates a radial arc sector or disk as shown. In the arc jet used as a high-temperature gas or plasma generator, rotation of the arc serves to distribute the Joule heating of the gas and inhibit electrode erosion by avoiding stationary arc spots (or moving arc spots when a disk is formed). The question naturally arises as to whether it would be possible to use  $j_r B_z$  to put work into rotation of the gas and to convert rotational energy directly to translational energy. Such conversion can take place in a nozzle, as shown in the figure, into which the rotating gas moves and the centrifugal forces are balanced by the wall reaction, converting angular to axial momentum. In order to put the plasma into rotation, it is generally more efficient to use a uniformly distributed force derived from a current distributed over an arc disk interact-

ing with the axial magnetic field, rather than the "line force" derived from the current concentrated in an arc spoke. Such a view then gives a picture of a continuous azimuthal or Hall current. The differential motion of electrons and ions due to their different drift velocities in the azimuthal direction normal to both the radial electric field and the axial magnetic field constitutes a circular drift current mainly caused by the motion of the lighter electrons relative to heavier ions. It should be emphasized that even for the arc spoke covering a sector between the coaxial electrodes, a Hall current can exist within the spoke since the current follows the streamlines formed by the azimuthal components of the curved particle motion. Such components can then exist if  $\omega\tau > 0$ ; however, the primary point of interest for application to accelerators is to determine all the conditions necessary for a uniformly distributed discharge and continuous Hall current and these include not only the  $\omega\tau$  values but other conditions such as emission from the cathode.

Shown at the upper left of figure 62-9 is a schematic of an experimental apparatus at Langley Research Center for producing plasma rotation and conversion to translation. If the magnetic-field coil is slid back, as shown at the right, the magnetic field is no longer purely axial in the region of the discharge, but is divergent so that a radial component  $B_r$  exists. The second mode of operation of the accelerator is then evident whereby the azimuthal Hall current  $j_\theta$  and the radial component of the magnetic field  $B_r$  produce a  $j_\theta B_r$  force/volume which acts in the longitudinal direction. Conversion of residual rotational energy to translation can again utilize a mechanical nozzle and, in addition, the diverging magnetic-field lines can be used for magnetic guiding or containment. Both of these concepts of operation of this coaxial scheme, that is, conversion of rotation energy and Hall current operation, were first described in references 16 and 17. Both modes of operation have been the object of research at Langley for the past 2 years. Results of this research and those from studies of similar devices at other laboratories will be discussed in subsequent sections.

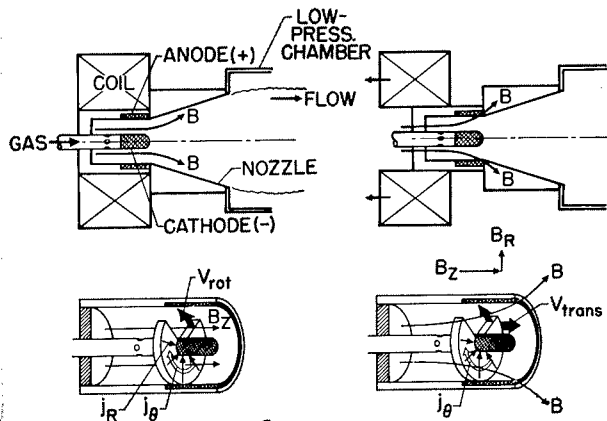


FIGURE 62-9.—Plasma rotation and Hall current acceleration.

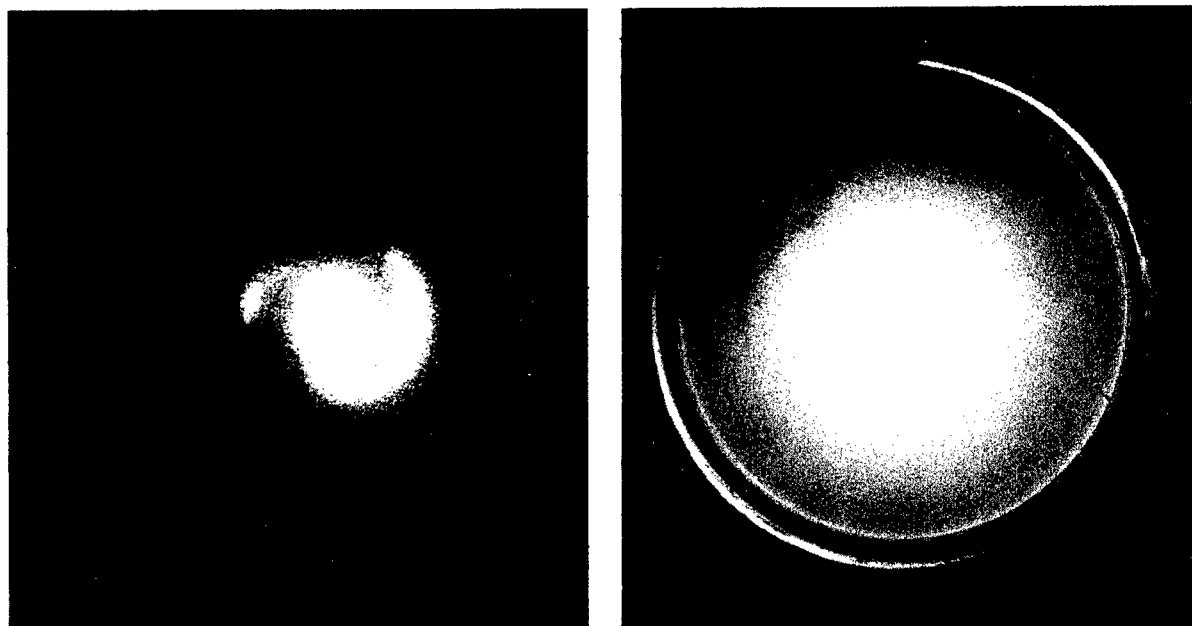
### Experiments With Coaxial Hall Current Devices

An experiment can be devised to show the Hall current operation of this coaxial device. For Hall current operation, the direction of acceleration changes with the polarity of the electric field which changes the direction of the Hall current. For a given direction, the magnetic field enters as the second power; thus, its direction does not affect the direction of acceleration. Experiments using an apparatus similar to that shown in the upper right-hand sketch (fig. 62-9) were made in which the electric field was reversed. These early experiments showed that the coaxial device can act in a diamagnetic fashion (pushing the plasma toward the weaker magnetic field) or in a paramagnetic fashion (pushing the plasma toward the stronger magnetic field).

One of the first objectives of study obviously is to determine the nature of the discharge in some detail, especially the conditions for a disk or uniform discharge. Patrick and Powers find experimentally that when  $\omega_e \tau_e > 1$ , the discharge is stable and the arc is uniform through the channel (refs. 18 and 19). Experiments at Langley in this range also give uniform dis-

charges; however, it has also been found that the cathode temperature has a primary effect on the discharge. The two photographs of figure 62-10 indicate the effect of cathode temperature, where all other conditions are the same. The photograph in figure 62-10(a) is from a film sequence taken at 4,000 frames per second and is for a relatively cold cathode. For this condition, the spokes (and possibly retrograde motion) are evident. As the cathode is heated to the conditions shown for the photograph in figure 62-10(b), the discharge is uniform, since at the Kerr cell shutter speed of 0.1 microsecond for this photograph, any probable spoke motion would be resolved if spokes existed. It is to be noted that at the temperature shown for the tungsten cathode, thermionic emission is very small but, even at this low value, is very effective in uniformizing the discharge. Further experiments on cathode conditions and materials are in progress, including gas and alkali-metal injection through the cathode.

Experiments on both modes of operation have been made and are still in progress at both Langley and Avco-Everett Research Laboratory. At Langley, concentration has been on



(a) Rotating spokes. Cold cathode. (b) Uniform discharge.  $T_{\text{cath}} = 2,360^\circ \text{ K}$ ; exposure time, 0.1  $\mu\text{sec}$ .

FIGURE 62-10.—Effect of cathode temperature on coaxial discharge in  $B_z$  field.

the discharge itself (refs. 20 and 21) as well as the means of feeding lithium into the system in such a fashion that it is vaporized in one step (without contacting the walls) and enters the accelerating region in a second step. Lithium is a desirable propellant because of the low frozen-ionization losses in the density range in which these devices operate and because it will permit higher power inputs. A Hall current acceleration device with a 50,000-gauss solenoid is nearing completion at the Langley Research Center.

Results of detailed measurements at Avco-Everett Research Laboratory for both modes of operation of the coaxial accelerator are given in reference 19. For the case in which rotation is converted to translation by means of a shallow nozzle ( $20^\circ$ ), a thrust of 0.7 pound was produced with an overall efficiency of 15 to 20 percent. These results led the investigators to a wide angle ( $50^\circ$ ) nozzle seeking to convert azimuthal motion more rapidly to axial motion. Figure 62-11 (taken from ref. 19) shows schematically the geometry and configurations of fields and currents that might be expected. Since a magnetic field with a large radial component could be produced in this nozzle, full advantage could be taken of the possible large Hall currents to produce additional body forces in the axial direction. In such a configuration, for  $\omega\tau > 1$ , current lines are pushed out of the annulus and are forced downstream by the Hall effect. In the arrangement shown, the interac-

tion of the Hall currents and both components of the magnetic field provide both acceleration and containment; that is the  $j \times B$  forces can be largely in a direction which accelerates the plasma away from the channel walls and in the thrust direction. They made very detailed pressure, mass-flow rate, velocity, and electric-probe surveys of the flow field for both the shallow and wide angle nozzles and found that the basic concepts were realized; however, large plasma-swirl effects were predominant, more so for the narrow nozzle. An average exhaust velocity corresponding to a specific impulse of 600 seconds was attained with an overall thrust efficiency of 25 percent for the  $50^\circ$  nozzle.

In general, for these coaxial devices in the "high-density plasma" range, principles have been proven and much progress has been made in studies of detail flows and mechanisms. The primary advantages this coaxial arrangement has in comparison with other devices are its combination of arc jet with the accelerator portion and the possibilities of magnetic containment of the plasma. The principal problems that must be studied arise from the nonuniformities in the flow which stem from the rotation of the jet. It appears that rational choices or compromises must be made between the requirements for best conditions for MPD acceleration and magnetic containment or nozzle requirements. For example, in figure 62-11, the current lines close back almost along magnetic field lines, this case being ideal for containment; however, these conditions are dissipative as far as acceleration is concerned. For best MPD acceleration, the desire is to cut the current lines with the magnetic field lines as near normal as possible. One way of doing this is to provide a series of segmented electrodes in the center cathode and the outer wall. In the latter case, however, the magnetic nozzle is lost. Another advantageous factor in these accelerators stems from the fact that the azimuthal driving current is larger than the radial current between electrodes; the direct losses to the electrodes because of the lesser thermionic emission required should thus be smaller than in the linear crossed-field accelerator. In continuing studies to improve these coaxial devices, it is desired to have available large variations in magnetic-

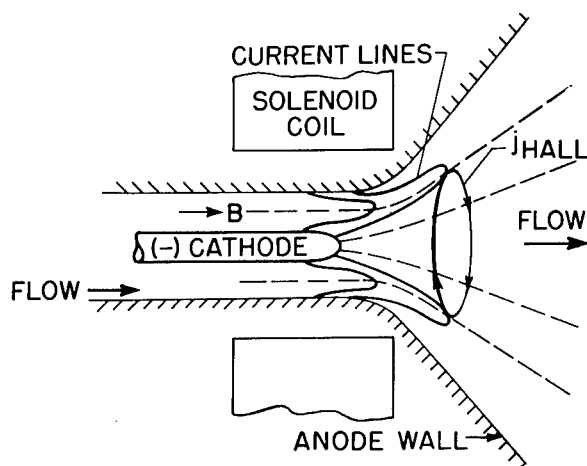


FIGURE 62-11.—Magnetic annular arc. (From ref. 19.)

field configurations. The solenoidal coil is readily adaptable to produce wide variations in field geometry; however, most important are the high field strengths that can conveniently be obtained with superconducting solenoids.

#### Low-Density Longitudinal Electric-Field Hall Current Accelerators

Several investigators have studied coaxial arrangements incorporating radial magnetic fields and longitudinal electric fields. (See refs. 22 to 27.) A class of these low-density devices may be considered to be nonspace-charge limited ion accelerators, wherein by a suitable choice of electric and magnetic fields, ions are electrostatically accelerated in a plasma in the presence of trapped electrons.

The apparatus described in reference 26 was designed at the Langley Research Center to study the basic phenomena in an axial electric field or discharge and a predominantly radial magnetic field. A cross-sectional view of this apparatus is shown in figure 62-12. Note the iron core which concentrates the field lines from the solenoid to make a predominantly radial magnetic field where the field strengths are highest. The iron core is laminated to prevent radical distortion of the electric field and is insulated from the discharge by an enclosing glass tube. The experiments with this apparatus covered a range of pressures from 15 to 150 microns of mercury, arc voltages to 700, currents to 80 amperes and average radial magnetic-field strengths to 450 gauss. The important distinction of these conditions from those of the Hall accelerator of the previous section is that it operated at high-density, small ion-

slip, and low ionization. In this case operation is at low density, small ion-slip and high ionization. In terms of the pertinent plasma parameters in the experiments here, both the ion gyro radius and ion mean-free path are large compared with the apparatus size, the electron gyro radius is small compared with the apparatus size and the electron mean-free path. Under these conditions, the ions may be accelerated in the electric field in the presence of electrons trapped in rotary  $E/B$  motion about the axis with small drift in the axial direction. As mentioned in reference 27 the  $j \times B$  force/volume is produced by the azimuthal Hall current and the radial magnetic field. For low density, highly ionized plasmas having few collisions, the  $j \times B$  force equals the electrostatic force from the electric field on the ions.

The apparatus shown represents an element of such an accelerator wherein studies of the plasma conditions have been made in terms of arc voltage and current, charge particle distribution and density, potential distribution, and Hall current. These experiments have generally indicated that the device operates as expected, but have, of course, brought out many problems requiring further study. Briefly the experiments gave the following results:

- (1) A positive slope volt-ampere characteristic was observed; the slope increased with increasing magnetic field or decreasing pressure.
- (2) Approximate values of the Hall current were observed by using a technique wherein a ballistic galvanometer sensed the Hall current by switching off the discharge with the magnetic field left on. Hall current values agreed "order-of-magnitude-wise" with those predicted. Ratios of Hall current densities to axial-current densities in the range of 10 to 15 were observed.
- (3) The pressure at the cathode was observed to increase depending on the direction of the electric field or ion motion.
- (4) At the lower pressures, anomalous diffusion effects became more pronounced, as expected, for fewer collisions.

An apparatus using the same principles as just outlined has been investigated by Janes, Dotson,

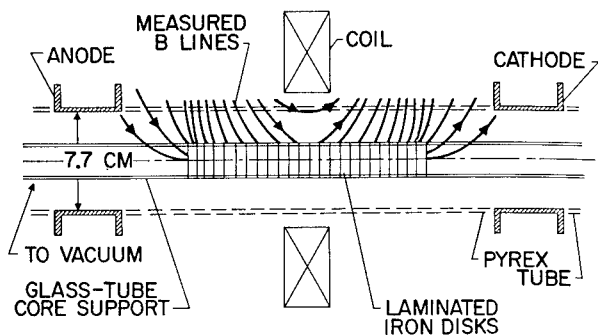


FIGURE 62-12.—Ion acceleration in a plasma using Hall currents.

and Wilson (ref. 22). Their accelerator shown in figure 62-13 does not have the oppositely rotating Hall currents that are in the apparatus at Langley. In their apparatus, ionization is produced by a Phillips Ionization Gage (P.I.G.) type discharge occurring between the ionizer filament and anode. Ion acceleration takes place in an electrically neutral region immediately below. The filament at the exit only serves to release electrons which are necessary to neutralize the outgoing plasma. Results with this apparatus have not yet been reported; however, extensive measurements using a cusped-field arrangement with predominantly radical fields have been made. A device similar to the one shown in figure 62-13 but smaller has been used in reference 28. Also, in this accelerator, no ionizer filament was included so that ionization had to be provided by the normal collision mechanism resulting from axial leakage of electrons. In all of these devices it is intended that the axial mobility of electrons will be sufficiently restricted by the magnetic fields to permit the plasma to sustain a significant voltage associated with the electric fields necessary to accelerate the ions as current carriers. Electrons produced near the anode are carried to the exit through an external circuit and there emitted from a hot filament to obtain an electrically neutral plasma-exit beam. The cusped-field apparatus shown in figure 62-14 has been used in the experiments of reference 22. For moderate magnetic fields (and specific impulse values) it was found (ref. 22) that specific impulse  $I_{sp}$  first increased linearly as a function of  $B$  but flattened out at a value of  $I_{sp}$

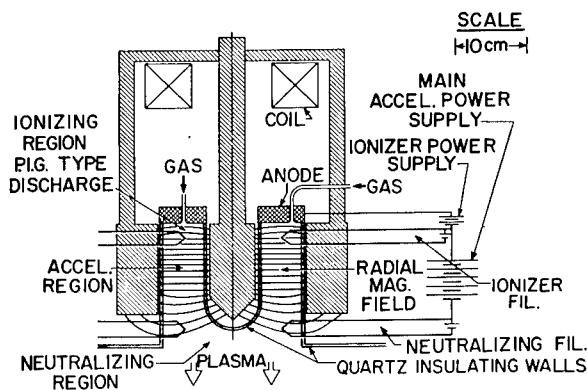


FIGURE 62-13.—Annular two-stage E.M. region d-c plasma accelerator. (From ref. 22.)

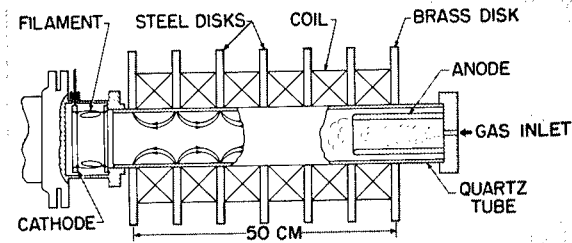


FIGURE 62-14.—E.M. region d-c cusp plasma accelerator. (From ref. 22.)

of 1,200 at the highest magnetic fields. This apparent saturation in the observable specific impulse was probably associated with decrease in ratio of ion gyro radius to tube radius well below a value of 1.0. The use of stronger magnetic fields to produce greater  $I_{sp}$  produced difficulties in detachment of the plasma from the magnetic field at the exit; this difficulty was partially circumvented by sloping the magnetic field at the exit to provide a gradual decrease in strength—that is, a magnetic nozzle. (See ref. 22.) Also, at the higher magnetic-field strengths, high localized wall heating was observed at the radial cusp points. At high values of the magnetic-field strength, large oscillations appeared in the anode to cathode voltage, of order 100 kc and of amplitudes exceeding several hundred volts. This experiment was modified to include a plug in the center of the tube in order to separate electron leakage arising as a result of the null point in the magnetic field from electron leakage associated with diffusion of electrons across magnetic-field lines. The plug greatly reduced the backstreaming of electrons.

On the basis of the experiments of references 22 and 28, it was concluded that electron diffusion rates were 100 to 1,000 times the currents predicted by classical diffusion theory but obeyed fairly well the anomalous diffusion law of Bohm as discussed in reference 27. Furthermore, the voltage across the discharge is proportional to  $B$  rather than  $B^2$ . The turbulence responsible for the enhanced diffusion observed is not well understood, and the large voltage oscillation observed may be associated with this turbulence. Similar oscillations were observed and the diffusion mechanism was discussed in some detail in connection with the studies of the Hall accelerator discussed in reference 17.

## SURVEY OF PLASMA ACCELERATOR RESEARCH

The potential engineering advantages of "EM region" d-c plasma accelerators are listed by Janes as follows (ref. 22) :

- (1) Freedom from space-charge limitations of conventional ion rockets
- (2) Magnetic containment possibilities.
- (3) High acceleration voltages which depend only upon the specific impulse rather than upon the instantaneous power level, thereby minimizing arc-voltage-drop problems
- (4) A readily variable specific impulse and power level
- (5) Extreme simplicity in the associated electrical circuitry
- (6) Convenient physical size together with moderate power levels, electrostatic voltage gradients, magnetic-field strengths, and heat-transfer rates

The principal study on these devices at the present time is directed toward an understanding of electron-diffusion mechanisms. If means cannot be found to reduce or circumvent the high diffusion rates indicated thus far by the experiments, the overall performance of these devices will be limited.

### PULSED PLASMA GUNS

Perhaps the most extensively studied of all plasma acceleration ideas is that of impulsively creating and accelerating a blob of plasma using simple geometric devices such as a pair of rail electrodes or a coaxial arrangement of electrodes. The problems and progress of such devices can be conveniently discussed by confining oneself to the coaxial arrangement. Lovberg has recently written an excellent summary paper (ref. 29) on his views and experiences in research with coaxial plasma guns and some of the following remarks and illustrations are drawn from his presentation.

The simplest embodiment of an impulsive plasma accelerator is the "rail gun," shown schematically in figure 62-15. It is nothing more than a pair of parallel conductors enclosed in a low-pressure system connected to a charged capacitor. When a gas is admitted to the region between the rails, electrical breakdown occurs, and current is conducted around the closed contour. Since it is a general prop-

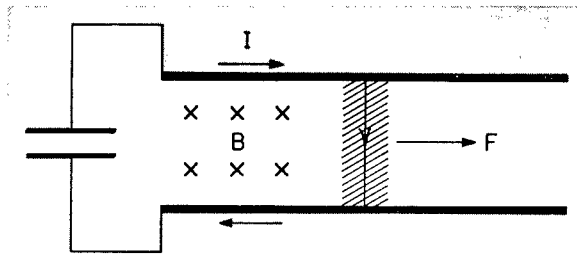


FIGURE 62-15.—Rail-gun plasma-accelerator concept.

erty of unconstrained inductive circuits to move toward larger inductance and particularly of current loops to expand, this particular current loop will seek to expand through a motion of the conducting plasma toward the gun muzzle at the right. In perhaps more fundamental terms, the plasma current interacts with its self-field to produce a  $j \times B$  force toward the right. In figure 62-16 the two rails have become a pair of coaxial cylinders in order that complications associated with the side forces on the plasma arising from the free edge interacting with the magnetic field may be avoided. Such essentially simple devices show fair promise as efficient propulsion units.

The development problems associated with making a plasma gun into an efficient propulsive device fall into two categories; those having to do with the physical processes in an accelerated plasma and those concerned with engineering questions involving components such as capacitors, switches, valves, insulators, electrodes, and so forth. Lovberg has said that a long road of fairly fundamental plasma physics still lies ahead before the plasma engine has reached the state of development of ion engines.

Some of the problems in coaxial plasma-gun development and requirements that may be

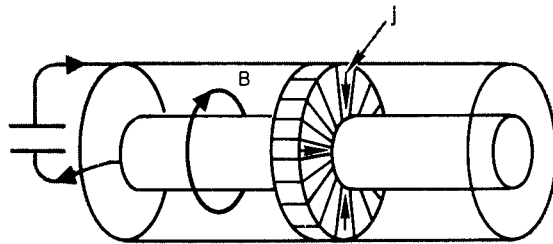


FIGURE 62-16.—Evolution of rail gun into coaxial accelerator. (From ref. 29.)



dictated by certain of these problems might be as follows:

(1) Fairly high electron temperatures, although a nonpropulsive energy loss, might be tolerated; however, high ion temperatures mean transverse thermal speeds which can be very effective in moving ions into electrodes where they lose their entire kinetic energy. Ordinarily, the presence of magnetic fields inhibits these thermal drifts; nevertheless, for long narrow accelerating channels, the electrode loss for even slow transverse speeds can be intolerable. The requirement is thus made that the channel be limited in length compared to diameter so that the acceleration is over before the ions have had time to move transversely a significant amount. (At Langley, analysis has been made of the role of the attainable or limiting velocity of a plasma gun and it is indicated that a primary factor may be the axial component of momentum lost at the electrodes by the ions associated with the current.)

(2) Instabilities of the plasma configuration arise from the previously stated theorem that if any part of a circuit is unconstrained, it will seek out the configuration of highest possible inductance. The propulsion purpose is achieved if the fluid can be coerced to move smoothly along only one possible avenue of inductance-increase toward the muzzle of a coaxial gun. The system, however, usually finds all such avenues, most of which are destructive to the goal. The discharge in a coaxial system not only moves axially, but tends to lose its initial azimuthal symmetry and gather up into a single spoke on one side of the tube as shown in figure 62-17. When this occurs, the discharge is no longer effective in imparting axial momentum to the gas. The spoke also develops violent instabilities of its own, and absorbs field energy, much like a resistor. Recognizing these instabilities (which occur also in a wide variety of accelerators), the requirement is made that conditions be found, if possible, to avoid them or to provide conditions such that their growth rate is small compared with the linear acceleration rate.

(3) The beam energy should be as close as possible to stored energy in the capacitors and the plasma should have absorbed this energy

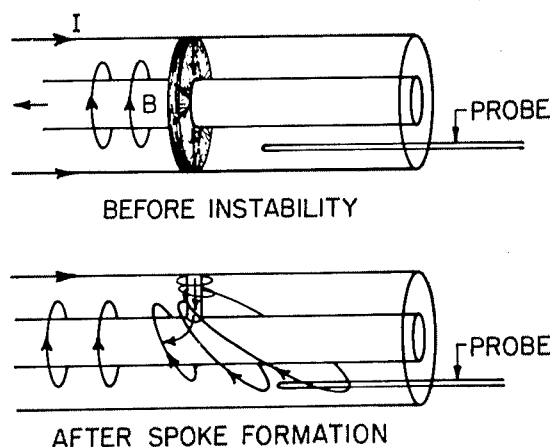


FIGURE 62-17.—Symmetric and spoked current distribution in pulsed coaxial accelerator. (From ref. 29.)

by the time it emerges from the gun. It can be shown that very low inductance energy sources will correspondingly be required for efficient engines.

Lovberg and his associates have built and carried out experiments with a number of coaxial plasma-gun arrangements. They have made extensive interior diagnostics of the discharge with probes which measure the electric and magnetic fields inside the plasma. Through data obtained with these probes they are able to make inferences of several important parameters, for example, ion density and directed ion velocity. Highlights of their observations (ref. 29) are briefed as follows:

(1) A distinct layer of radial current was accelerated toward the gun muzzle at about  $10^7$  cm/ $\mu$  sec ( $I_{sp}=10^4$  sec); however, the plasma ions were not accelerated to anything like the current layer speed. It was concluded that the accelerating current layer does not necessarily act as a piston as has been generally supposed. It has the character of a strong ionizing shock which does impart momentum to the propellant but at a speed which has to be determined by other means. They found, by using time-of-flight techniques that in some cases, the plasma and current layer move nearly together.

(2) A primary source of losses was attributed to a tendency of the gun to "crowbar," that is, set up a secondary discharge near the insulator after about one-half cycle of the oscillating gun current. This energy is sealed off

from the plasma and lost. Efforts to overcome this problem have not yet been successful and it continues to be a source of worry.

(3) The efficiency of transfer of field energy to the plasma was good, that is to say, losses associated with drift into the electrodes or plasma radiation do not appear to be ruinous.

(4) Heat transfer from electrons to ions is slow, that is, over the time of the total gun pulse, ion heating is small.

(5) Extensive surveys of conditions under which spoke instabilities are troublesome are not conclusive, however, "good" conditions to avoid these can be met. However, small departures of pressure, propellant, and voltage from values giving "good" condition could re-establish detrimental instabilities.

(6) Distribution of propellant gas in the barrel just prior to breakdown has a major influence on crowbaring at the insulator.

At Langley, extensive experiments have been made with various coaxial plasma-gun arrangements, and one development that has been made in reference 30 is schematically shown in figure 62-18. The gun is connected directly to a 50-kilojoule capacitor bank without a switch in the line; however, the gas pressure in the gun is sufficiently low that, for the standoff voltage and electrode spacing, breakdown does not occur. When the coil is switched on, an axial magnetic field is imposed between the electrodes, and for the desired electric and magnetic conditions, a breakdown occurs in a very short time interval. Part of the conditions are that the ion cyclotron radius is much larger than the electrode spacing, as indicated in the lower sketch, the elec-

tron cyclotron radius is smaller than the spacing and smaller than the mean-free path. The electrons will perform cycloidal motions in the crossed fields between collisions and, at each collision, the electron takes up a new cycloid closer to the anode by about one cyclotron radius. The avalanche progresses by the production of enough ion pairs on collisions with neutrals so that breakdown occurs very rapidly. Another view is that the electron transit distance is too small to produce collisions in the electric field alone and that the greatly increased transit distance in the crossed fields makes enough collisions possible. The theory for this breakdown process has been developed and experimentally proven. With a 36-microfarad bank charged to 48,000 volts, a peak current of 1,300,000 amperes was achieved with a current rise time of only 2 microseconds. Advantages of magnetic-ignition are: losses associated with external switching are avoided, the high rate of discharge generally means efficient energy transfer to the plasma, and the gun can be operated at very low pressures where many difficulties are avoided.

It may be somewhat puzzling that low-pressure operation is listed as an advantage for the coaxial plasma gun; however, many problems encountered at higher pressures can, in fact, be avoided. At Langley, a coaxial plasma gun was operated in this low-pressure region ( $10^{-5}$  mm Hg) with magnetic switching, and the following general findings were noted: conversion efficiency of electrical to beam energy of 50 percent was attained, no crowbaring or instability was observed, and the plasma is almost entirely electrode material; however, it is not inconceivable that a propulsion device could utilize consumable electrodes.

Other research at Langley has included development of a new approach to determination of the limiting velocity of plasma guns wherein the primary factor is that the axial component of the ion current is lost at the electrode (ref. 31). Estimates based on this approach check experimental values; however, the detail mechanisms at the electrodes require much further research. Also, spectrographic observations of the plasma show large contamination by electrode material; thus, a study of electrode conditions is being made. In all experimental

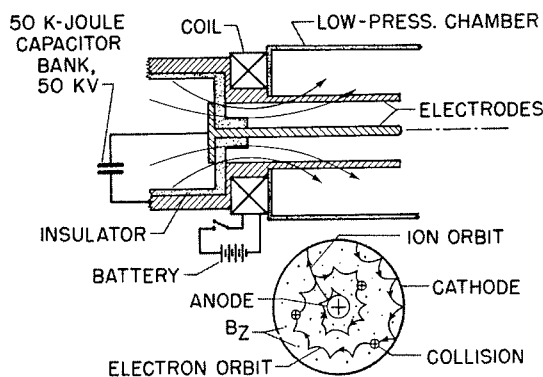


FIGURE 62-18.—Magnetically ignited coaxial discharge.

studies of plasma guns, the short duration of observation demands ever improved diagnostic techniques; at Langley a new type of magnetic probe has been developed recently (ref. 32).

### TRAVELING-WAVE ACCELERATORS

There is great attraction, in principle, to acceleration schemes which avoid electrodes, since in all the devices so far discussed electrodes are used and present energy-loss or survival problems to varying degrees—worst probably for the plasma guns with their very high initial current concentration at the electrodes. Characteristically, the electrodeless devices make use of time-varying magnetic fields which induce currents in the plasma; these in turn interact with the magnetic field to produce acceleration. Invariably, one is led to the idea of traveling magnetic fields or magnetic “traveling waves” so that the plasma may be effectively continuously accelerated or accelerated in magnetically contained plasma “bunches.” Reduction of wall losses by magnetic containment is also a desirable advantage offered by these concepts. A fairly large variety of traveling-wave schemes have been conceived and studied extensively (see bibliographies of refs. 33 and 34 and ref. 35). Description and distinction of the schemes from each other can become exceedingly involved in detail; thus, this brief summary seeks only to point out some broad categories.

Probably the simplest concept of an induction accelerator, which might constitute one stage of a traveling-wave scheme, is the so-called ring accelerator. In one form of this scheme, a capacitor discharge (or RF) is fed into a single loop of conductor around a tube containing low-pressure gas. The varying magnetic field associated with this loop induces an azimuthal electric field in the gas of sufficient intensity to ionize the gas. The resulting azimuthal current in the gas interacts with the magnetic field to produce a Lorentz force radially inward and axially away from the coil. This single-coil scheme can provide large instantaneous forces, but the short range of magnetic forces makes it inefficient. One is led immediately to a phased string of coils down the tube as shown in the lower part of figure 62-19. These coils might be single turns with properly

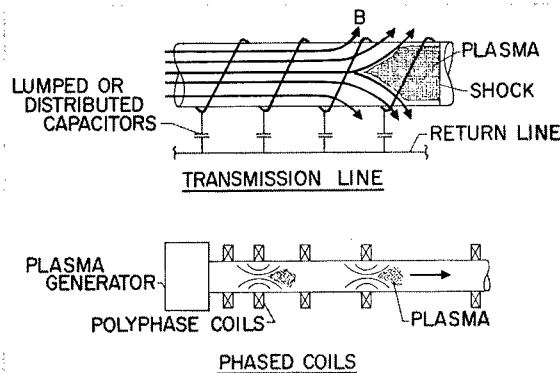


FIGURE 62-19.—Traveling-wave plasma-accelerator concepts.

timed discharges from a series of capacitors fed to each coil, or multiturn coils properly phased with the plasma velocity or with the coil spacing increasing with plasma velocity as shown. For these staged arrangements, the coils are not inductively independent and are effectively a transmission line. This arrangement has been called a timed-sequenced device in which it is sought to synchronize the driving currents with the plasma position.

The upper part of figure 62-19 shows a transmission line arrangement which gives more regular fields. A traveling magnetic piston drives the plasma down the tube; the shock wave preceding this piston ionizes the gas. With lumped capacitors, large amounts of energy can be stored for pulsed operation. However, repetitive operations imposes switching and capacitor problems. Another variation of the arrangement shown is to provide an RF generator instead of the switched pulses, and the device becomes a continuously operating transmission line; thus the high voltages and currents of the pulsed device are circumvented.

A number of persons have studied a variety of traveling-wave schemes. For the single-coil arrangements, very high velocities have been obtained, but at efficiencies of only a few percent. Penfold (ref. 36) has studied and operated a pulsed device which accelerates plasma toroids by means of an arrangement incorporating 19 one-turn coils spaced 1 inch apart along a 6-inch-diameter pyrex vacuum tube. The velocity of the magnetic field at the end of this sequenced array of coils was 11 cm/ $\mu$ sec and experimental observations with microwave

and photomultiplier techniques indicated that the toroids were, in fact, achieving this velocity. He has made extensive diagnostic measurements with the device.

One of the most extensive investigations of a traveling-wave device has been made by Janes (ref. 22) and is shown schematically in figure 62-20. The conditions of his operation are

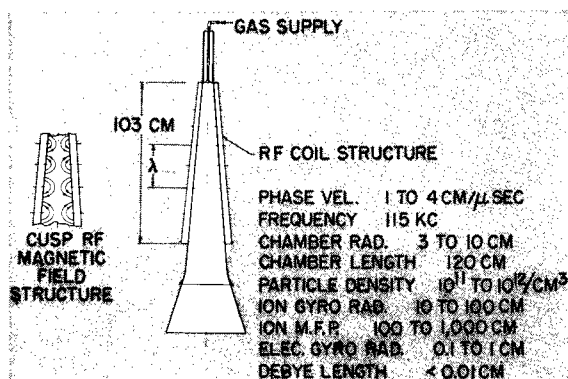


FIGURE 62-20.—E.M. region RF traveling-wave plasma accelerator. (From ref. 22.)

shown in the figure. With this apparatus, he has made measurements of mass-flow rate, RF power absorption in the plasma, local and integrated wall heat-transfer rates, and integrated axial voltage gradients. He also measured distribution of the local momentum flow with a quartz thrust plate. From these and extensive Langmuir probe measurements of ion flux, plasma potential and electron temperatures he found that the E.M. region accelerating mechanism was remarkably effective, the most striking feature being the appearance of strong electrostatic fields which were closely correlated with the ion accelerations. Specific impulses of 2,600 were computed from the measurements corresponding to two-thirds of the phase velocity of the cusps. His observation suggested that an external axial voltage be applied and experiments with such an axial field indicated the mean plasma velocity could be about doubled. His experience with this device led him to stud-

ies with the E.M. region steady-flow plasma accelerators previously mentioned.

Most of the traveling-wave schemes considered operate at high conductivities because of the moderate magnetic fields available, and at low densities, implying low thrusts. At low densities, diffusion losses to the walls are important; these could be reduced by longitudinal bias magnetic fields, but it has been found that this decouples the driving fields from the plasma and prevents acceleration.

It has been questioned whether traveling-wave devices can ever reach reasonable efficiency unless some way of using magnetic fields or other means to reduce losses are found. Even if this were so, their use as a laboratory device such as a hypersonic wind tunnel would still be attractive, especially if seeding could be avoided and exiting ionization quenched.

#### CONCLUDING REMARKS

It is emphasized that in this presentation, it has not been possible to cite all the important contributions to plasma accelerator research, which field has now reached such proportions that one type of accelerator alone has recently been the subject of a several-day meeting. The purpose here has been to show the broad possibilities of plasma acceleration schemes and to mention a few of the problems arising from active research. Accomplishments in the field of sufficient dramatic impact to impress those outside are few; however, the growing bulk of knowledge from many detailed findings lends increasing encouragement and full expectation that practical plasma-acceleration devices will be a reality in the very near future. Perhaps the greatest encouragement stems from the fact that a large number of outstanding scientists are working in the field. These numbers include those working toward controlled thermonuclear fusion, which research effort feeds much basic plasma physics information into the plasma acceleration efforts and vice versa.

#### REFERENCES

1. JAFFE, LEONARD D., LUCAS, JOHN W., MERRILL, OWEN S., SHAFER, JOHN I., and SPENCER, DWAIN F.: Nuclear Electric Spacecraft for Unmanned Planetary and Interplanetary Missions. [Preprint] 2389-62, American Rocket Soc., Mar. 1962.
2. SPEISER, E. W.: A Preliminary Study of Advanced Propulsion Spacecraft Payload

# SURVEY OF PLASMA ACCELERATOR RESEARCH

- Discharge Crossed With a Magnetic Field at Elevated Pressures. Presented at the Summer Meeting, American Phys. Soc. (Seattle, Wash.), Aug. 27, 1962.
22. JAMES, G. S., DOTSON, J., and WILSON, T.: Electrostatic Acceleration of Neutral Plasmas—Momentum Transfer Through Magnetic Fields. Presented at Third Symposium on Advanced Propulsion Concepts (Cincinnati, Ohio), Oct. 2-4, 1962. (Sponsored by U.S. Air Force and Gen. Elec. Co.)
23. LARY, E. C., MEYERAND, R. G., Jr., and SALZ, F.: Ion Acceleration in a Gyro-Dominated Neutral Plasma—Theory. Bull. American Phys. Soc., ser. II, vol. 7, no. 7, Aug. 27, 1962, p. 441.
24. SEIKEL, G. R., and RESHOTKO, E.: Hall Current Ion Accelerator. Bull. American Phys. Soc., ser. II, vol. 7, no. 6, June 19, 1962, p. 414.
25. CANN, G. L., TEEM, J. M., BUHLER, R. D., and BRANSON, L. K.: Magnetogasdynamics Accelerator Techniques. AEDC-TDR-62-145 (Contract No. AF 40(600)-939), Arnold Eng. Dev. Center, July 1962.
26. RIGBY, ROBERT NORRIS: Some Physical Properties of an Axial Electric Arc in a Radial Magnetic Field. M. S. Thesis, The College of William and Mary in Virginia, 1962.
27. HESS, ROBERT V.: Fundamentals of Plasma Interaction With Electric and Magnetic Fields. NASA University Conference, 1962. (Paper no. 62 of present compilation.)
28. SALZ, F., MEYERAND, R. G., Jr., and LARY, E. C.: Ion Acceleration in a Gyro-Dominated Neutral Plasma—Experiment. Bull. American Phys. Soc., ser. II, vol. 7, no. 7, Aug. 27, 1962, p. 441.
29. LOVBERG, R. H.: Impulsive MHD Devices as Space Engines. Presented at Third Symposium on Advanced Propulsion Concepts (Cincinnati, Ohio), Oct. 2-4, 1962. (Sponsored by U.S. Air Force and Gen. Elec. Co.)
30. THOM, KARLHEINZ, and NORWOOD, JOSEPH, Jr.: Magnetic Ignition of Pulsed Gas Discharges in Air of Low Pressure in a Coaxial Plasma Gun. NASA TN D-910, 1961.
31. THOM, K., NORWOOD, J., and JALUFKA, N.: Velocity Limitation of a Coaxial Plasma Gun. NASA Paper presented at the International Symposium on Coaxial Plasma Gun (Cleveland, Ohio), Sept. 6-7, 1962.
32. THOM, KARLHEINZ, and NORWOOD, JOSEPH, Jr.: Novel Method for Measuring the Electrical Conductivity of a Moving Conductor. Bull. American Phys. Soc., ser. II, vol. 7, no. 7, Aug. 27, 1962, p. 432.
33. BREWER, G. R., CURRIE, M. R., and KNECHTLI, R. C.: Ionic and Plasma Propulsion for Space Vehicles. Proc. IRE, vol. 49, no. 12, Dec. 1961, pp. 1789-1821.
34. GOURDINE, MEREDITH C.: Recent Advances in Magnetohydrodynamic Propulsion. ARS Jour., vol. 31, no. 12, Dec. 1961, pp. 1670-1677.
35. ANON.: Third Symposium on the Engineering Aspects of Magnetohydrodynamics. Univ. of Rochester, Mar. 28-30, 1962.
36. PENFOLD, ALAN S.: Estimating the Mass of a Fast Plasma Toroid. Ion and Plasma Propulsion Research, AFOSR 3-62, U.S. Air Force, Mar. 1962, pp. 28-29.

# PLASMA PHYSICS AND MAGNETOHYDRODYNAMICS

- Capabilities. Tech. Memo. No. 33-42 (Contract No. NASw-6), Jet Propulsion Lab., C.I.T., May 10, 1961.
3. SPEISER, EVELYN W.: Performance of Nuclear-Electric Propulsion Systems in Space Exploration. Tech. Rep. No. 32-159 (Contract No. NASw-6), Jet Propulsion Lab., C.I.T., Dec. 15, 1961.
4. WOOD, GEORGE P., CARTER, ARLEN F., LINTZ, HUBERT K., and PENNINGTON, J. BYRON: A Theoretical Treatment of the Steady-Flow, Linear, Crossed-Field, Direct-Current Plasma Accelerator for Inviscid, Adiabatic, Isothermal, Constant-Area Flow. NASA TR R-114, 1961.
5. WOOD, GEORGE P., and CARTER, ARLEN F.: Considerations in the Design of a Steady DC Plasma Accelerator. Dynamics of Conducting Gases, Ali Bulent Cambel and John B. Fenn, eds., Northwestern Univ. Press (Evanston, Ill.), c.1960, pp. 201-212.
6. CARTER, ARLEN F., WOOD, GEORGE P., SABOL, ALEXANDER P., and WEINSTEIN, RICHARD H.: Experiments in Steady-State High-Density Plasma Acceleration. Engineering Aspects of Magnetohydrodynamics, Clifford Mannal and Norman W. Mather, eds., Columbia Univ. Press, 1962, pp. 45-55.
7. WOOD, GEORGE P., CARTER, ARLEN F., SABOL, ALEXANDER P., and WEINSTEIN, RICHARD H.: Experiments in Steady State Crossed-Field Acceleration of Plasma. The Physics of Fluids (Letters to the Editor), vol. 4, no. 5, May 1961, pp. 652-653.
8. DEMETRIADES, STERGE T.: Experimental Magnetogasdynamic Engine for Argon, Nitrogen, and Air. Engineering Aspects of Magnetohydrodynamics, Clifford Mannal and Norman W. Mather, eds., Columbia Univ. Press, 1962, pp. 19-44.
9. HELLUND, EMIL J., and BLACKMAN, VERNON H.: Crossed Field Accelerators. [Preprint] 2128-61, American Rocket Soc., Oct. 1961.
10. HOGAN, WILLIAM T.: Experiments With a Transient D.C. Crossed-Field Accelerator at High Power Levels. Third Symposium on Engineering Aspects of Magnetohydrodynamics, Univ. of Rochester, Mar. 28-30, 1962.
11. RAGUSA, DOMENICO, and BAKER, JEROME: Experimental Results With a Direct Current Electromagnetic Plasma Accelerator. Engineering Aspects of Magnetohydrodynamics, Clifford Mannal and Norman W. Mather, eds., Columbia Univ. Press, 1962, pp. 56-63.
12. RAUSA, G. J., and GEARHART, L. M.: Plasma Acceleration Studies. Engineering Aspects of Magnetohydrodynamics, Clifford Mannal and Norman W. Mather, eds., Columbia Univ. Press, 1962, pp. 64-80.
13. JANES, G. SARGENT: Magnetohydrodynamic Propulsion. Res. Rep. 90 (AFOSR TN 60-955), Avco-Everett Res. Lab., Aug. 1960.
14. JANES, G. SARGENT: Introduction. Engineering Aspects of Magnetohydrodynamics, Clifford Mannal and Norman W. Mather, eds., Columbia Univ. Press, 1962, pp. 3-4.
15. SUTTON, GEORGE W., and GLOERSEN, PER: Magnetohydrodynamic Power and Propulsion. Magnetohydrodynamics, Ali Bulent Cambel, Thomas P. Anderson, and Milton M. Slawsky, eds., Northwestern Univ. Press (Evanston, Ill.), c.1962, pp. 243-268.
16. HESS, ROBERT V.: Experiments and Theory for Continuous Steady Acceleration of Low Density Plasmas. Vol I of Proc XIth Int. Astronautical, Carl W. P. Reuterswärd, ed., Springer-Verlag (Vienna), 1961, pp. 404-411.
17. HESS, R. V., BURLOCK, J., SEVIER, J. R., and BROCKMAN, P.: Theory and Experiments for the Role of Space-Charge in Plasma Acceleration. Electromagnetics and Fluid Dynamics of Gaseous Plasma, Vol. XI of Microwave Res. Inst. Symposia Ser., Polytechnic Press of Polytechnic Inst. of Brooklyn, c.1962, pp. 269-305.
18. POWERS, WILLIAM E., and PATRICK, RICHARD M.: Magnetic Annular Arc. The Physics of Fluids, vol. 5, no. 10, Oct. 1962, pp. 1196-1206. (Also, available as Avco-Everett Res. Rep. 129.)
19. PATRICK, R. M., and POWERS, W. E.: Plasma Flow in a Magnetic Annular Arc Nozzle. Presented at Third Symposium on Advanced Propulsion Concepts (Cincinnati, Ohio), Oct. 2-4, 1962. (Sponsored by U.S. Air Force and Gen. Elec. Co.)
20. WEINSTEIN, RICHARD H., and HESS, ROBERT V.: New Experiments With Hollow Cathode Discharges (For Application to Plasma Accelerators). Third Symposium on Engineering Aspects on Magnetohydrodynamics, Univ. of Rochester, Mar. 28-30, 1962.
21. GROSSMANN, WILLIAM, JR., and HESS, ROBERT V.: Existence of a Voltage Plateau for a

**SESSION T**

**Laboratory Techniques**

***Chairman,* LEONARD D JAFFE**

---

DR. LEONARD D. JAFFE, *Chief of Materials Research, Jet Propulsion Laboratory, was born in Brooklyn, New York. He was graduated with a B.S. in Electrochemical Engineering from Massachusetts Institute of Technology in 1939, and received the M.S. in Metallurgy at MIT in 1940. Harvard University conferred the Sc.D. in Metallurgy upon him in 1947. Author of a text and numerous technical papers, Dr. Jaffe is a member of AIME, ASM, AAAS, ARS, APS, and Sigma Xi.*



## 63. Techniques for Achieving Steady-State Temperatures Above 1500° C

By Howard E. Martens

HOWARD E. MARTENS is an Assistant Section Chief in the Materials and Research Section of Jet Propulsion Laboratory. Born in Bloomington, Illinois, he graduated with a B.S. in Mechanical Engineering from the California Institute of Technology in 1942.

### ABSTRACT

A description is given of various types of equipment used to reach steady-state temperatures above 1500° C. Applications and limitations of the equipment are reviewed. Among the types of equipment to be considered are resistance heating, induction heating, electron beam heating, and arc imaging heating.

### INTRODUCTION

The rate of advance of our modern technology, as demonstrated throughout this conference, has been greatly accelerated by our entering the missile and rocket age, the atomic age, and now the space age. The advancements in these areas have certainly taxed the ingenuity of the engineer and the scientist. One area in which the rate of advance has been particularly rapid is that of high-temperature technology. Here, problems which have arisen are many and varied. Some of these problems are of interest primarily to the metallurgist; others relate to the ceramist, or to the chemist, or to the physicist, etc.

Since university representatives are likely to cover all possible fields of interest and since the amount of material which can be presented is limited by the space available, this presentation will have to be of a general nature. As such, it is likely that it may prove to be disappointing to some individuals; however, it is hoped that

what is presented will meet the needs of the majority group interested in the field of high-temperature technology.

First, as indicated by the title, this presentation is to give consideration only to those techniques which are used to achieve steady-state temperatures as opposed to transient or short-time temperatures. Second, consideration is to be limited to temperatures above 1500°C. These limitations are in no way intended to evaluate the importance of the other areas, but are merely used as a means of restricting the area to be covered to some reasonable size.

Why are temperatures above 1500°C needed? If this question had been asked twenty-five years ago, many engineers and scientists might have strongly indicated that such temperatures would not be required, except for very special studies, for many many years to come. However, this has not proven to be the case. Rapid advancements made in the working fluid temperatures of the energy units now in use have quickly moved from the 500–1000°C temperature range of the steam and internal combustion engines, through the gas turbine, the rocket and the nuclear engine, and it is now commonplace to consider steady-state temperatures of 2500°C and above. The problems involved in consideration of such temperatures relate mainly to the fact that they are well above the

useful temperature of the commonly available engineering structural materials, and in many cases are above the melting point of any known materials. This is where the ingenuity mentioned earlier comes into the picture.

#### APPLICATIONS OF STEADY-STATE TEMPERATURES

Aside from the important fact that efficiency of energy conversion units can be improved by increasing the operating temperature, steady-state temperatures above 1500°C must be attained for other applications. Some of the more important applications are shown in Table 63-I.

TABLE 63-I.—*Applications of Steady-State Temperatures*

Material Production-----	Melting. Sintering. Hot pressing.
Material Fabrication-----	Forming. Joining. Heat treating.
Material Evaluation-----	Testing. Simulating.

Since very small percentages of the currently used materials are found in usable condition in nature, it is necessary that most materials be produced by chemical processes. Until a few years ago nearly all materials were produced by a process which involved melting or a liquid phase. As the desired usable temperature of engineering materials increased, so did the melting point. In those cases where melting was not a reasonable method of production, the cold pressing and sintering process was developed and used. In this process also, the most desirable temperature for the sintering process is generally near the melting point and thus requires steady-state high temperatures. Attempts to improve the results of the cold pressing and sintering process led to the development of the hot pressing technique, which again requires high temperatures.

The ability to produce materials which are useful at temperatures above 1500°C is of value

only if such materials can then be fabricated into usable shapes. Unfortunately, it has been found that most materials with high useful temperatures also require fabrication at high temperature. This has meant that forming processes such as forging, extruding, spinning, etc., are now being carried on at temperatures above 1500°C. The complications of our present technology have dictated the need for joining of materials, which has led to the development of high-temperature brazing and welding techniques. To achieve the maximum efficiency from engineering structural materials some type of heat treating process is normally required. Here again, high temperatures are needed.

It is obvious, of course, that production and fabrication are only a part of the problem of using materials at temperatures above 1500°C. A third factor, and an important reason for needing to reach these temperatures under steady-state conditions, is to allow evaluation of the materials. It is perhaps in this area that laboratory techniques for obtaining high temperatures have been most widely used. In many instances materials which cannot be produced or fabricated on an acceptable commercial basis are put through a series of tests so as to determine engineering properties, the idea being that the results of such tests can be used to justify the development of production or fabrication processes. Closely allied to the high-temperature testing needs is the need to achieve high temperatures for the purpose of simulating an actual use condition. In general, this is more difficult to attain because of the competing processes involved. It is, however, an important laboratory technique because of the savings which result if it is successful.

#### METHODS OF ACHIEVING HIGH TEMPERATURES

These, then, are some of the more important uses of steady-state temperatures above 1500°C. As might be expected, the methods which can be used to achieve these temperatures are varied and complicated. Table 63-II lists the general types of equipment which can be used. The combustion types, which use gas, liquid, or solid fuel, or some mixture thereof, were among the

# ACHIEVING STEADY-STATE TEMPERATURES ABOVE 1,500° C.

earliest developed, but in many applications have been replaced by more efficient methods, especially for temperatures above 1500°C.

TABLE 63-II.—*Methods of Achieving High Temperatures*

Combustion.....	Gas. Liquid. Solid.
Electrical.....	Resistance. Induction. Arc. Imaging. Electron beam.
Nuclear.....	

The most generally used type of equipment is, of course, electrical, and although its variations and combinations are far too numerous to be considered in detail in a presentation such as this, some of the more widely used types are listed in Table 63-II and will be discussed. (Although nuclear methods are not now fully developed, we are certainly not far from the time when it will be possible to use controlled nuclear processes as a source for steady-state high temperatures.)

Resistance heating is perhaps the most widely used of the several electrical types listed. For this equipment an element in the form of wire, ribbon, rod, or tube is heated by passing an electric current through it. The maximum temperature which can be achieved depends on the material from which the element is made, as well as the material used as insulation. Figure 63-1 shows a particular type of resistance furnace in which oxide elements are used as the primary source of temperature. It is necessary that such elements be preheated to a temperature at which they become conductive. To accomplish this, secondary heating elements are used. If the primary elements are made from materials such as metals or carbides which are conductive at room temperature, then the secondary elements can be eliminated.

There is, of course, a wide variety of materials which can be used for heating elements. However, for temperatures above 1500°C the number is quite limited. The refractory metals or al-

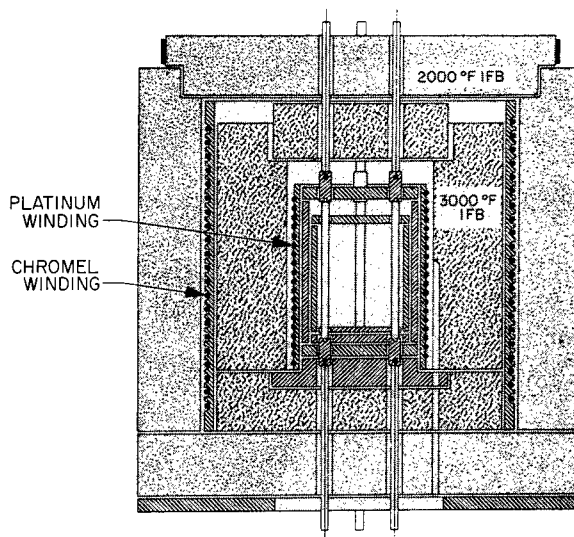


FIGURE 63-1.—Oxide resistor furnace.

loys, the conductive oxides of zirconium, and carbon are about the only suitable materials for this temperature range.

Among the limitations of resistance-type equipment is the melting point of the heating element and the supporting material. The lifetime of the heating element is also a limitation. In some instances heating elements can only be operated satisfactorily in atmospheres which are undesirable as far as the work piece is concerned. This means that an atmosphere barrier has to be placed between the heating element and the work. Those materials which can be used for the higher ranges of temperature are in many cases not available in a variety of shapes and sizes, so that problems of getting temperature uniformity are among the limitations. The versatility and the simplicity of this method are its major advantages and the reasons for its widespread use at all temperature ranges.

Induction heating is really one particular type of resistance heating. However, because of some basic differences it is generally classed separately. Figure 63-2 shows one type of induction heating equipment. High-temperature induction heating is attractive because (1) no electrical connections are required into the hot zone, (2) the primary coil can be operated at high-voltage—low current condition, and (3) one power supply can be readily adapted to many heating applications. Since this method also depends on the heating of a susceptor which

# LABORATORY TECHNIQUES

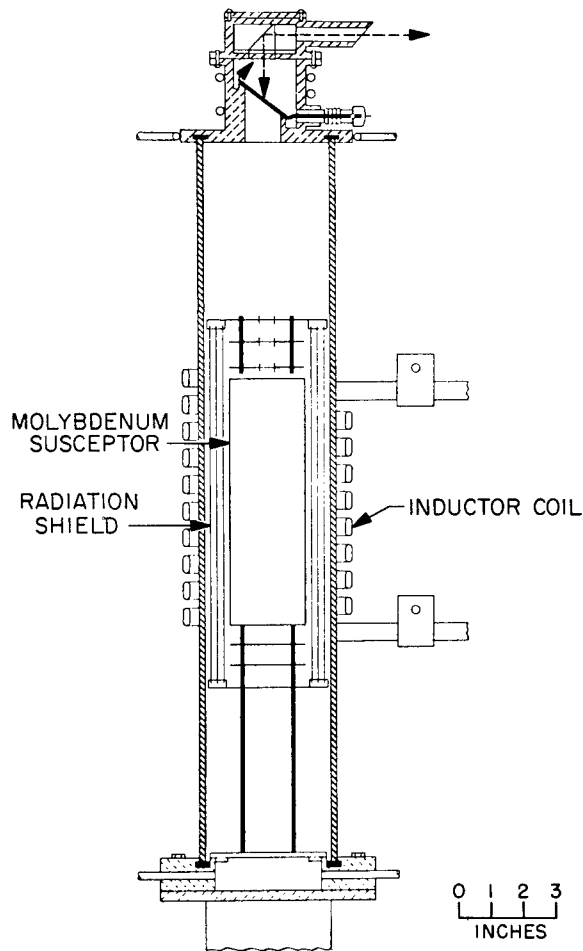


FIGURE 63-2.—Induction furnace.

then reradiates to the work, the limitations mentioned for the resistance heating also apply here.

Electric arcs were at one time the main source of high temperatures for laboratory techniques. But this method now finds its major use in the area of melting operations. Figure 63-3 is a simple schematic drawing of an arc melting unit. Obtaining temperature control and uniformity are two major problems which have limited the application of this method to areas such as melting. Recently, the arc heating method has received a major application in heating gas streams at high velocities. The so-called stabilized arc or plasma arc heating of gas streams to temperatures of 3000°C and above at supersonic velocities has been advanced to a high degree of utilization during the past few years.

In an attempt to overcome some of the limita-

tions caused by the atmosphere in all of the previously mentioned heating methods, the imaging technique has been used for some applications. Figure 63-4 shows some imaging methods. In general, two sources have been used. One of these sources is the Sun, and the imaging method would be as shown in either (a) or (b) of Figure 63-4. The other widely used source is a carbon arc used with the imaging methods shown in (c), (d), and (e) of Figure 63-4. While the use of the Sun has the advantages of high temperature, ready availability, and long-time operation, it is limited by clouds, atmospheric absorption, and the need for solar tracking devices. In general, the main disadvantage of imaging equipment is that the heated area is small and concentrated, with rather severe thermal gradients. Techniques for reducing these gradients have been developed, but usually at the expense of temperature and total heat flux. For systems requiring atmospheric variation, the imaging technique has much to offer.

Electron bombardment is a recently developed technique for obtaining temperatures

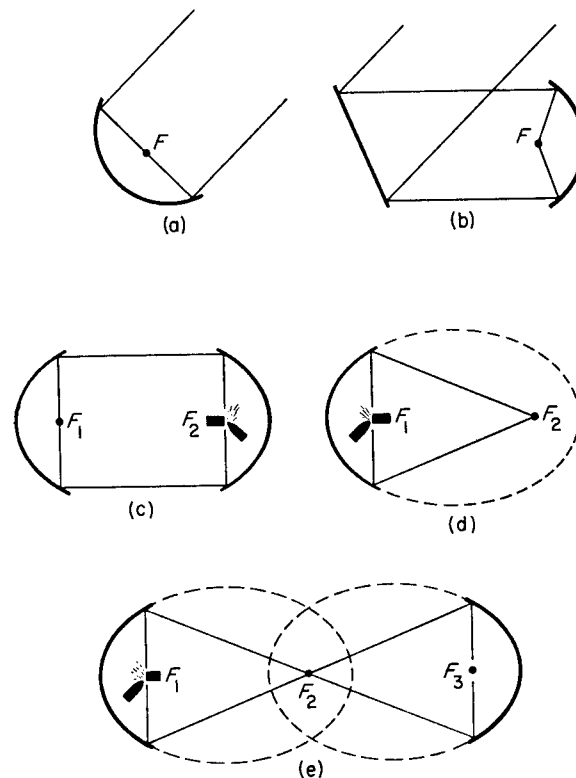


FIGURE 63-3.—Arc melting furnace.

# ACHIEVING STEADY-STATE TEMPERATURES ABOVE 1,500° C.

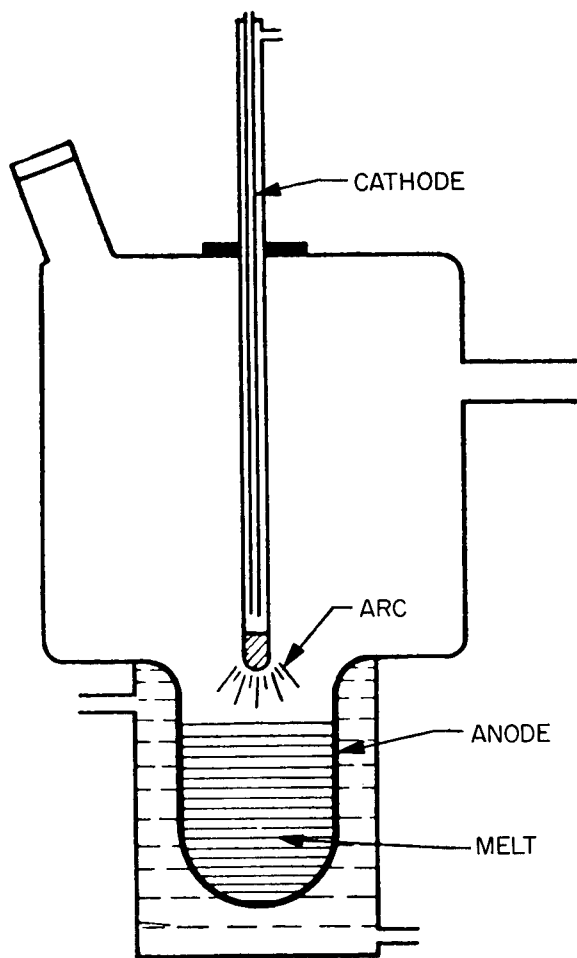


FIGURE 63-4.—Methods of imaging high-temperature sources.

above 1500°C. Figure 63-5 shows three applications of this method, the principle characteristics of which is that electrons emitted from

a heated filament are accelerated toward an anode under high voltage. Under these conditions the main energy release is at the anode, which is heated. The major advantages of this method are that the currents required are in the range below one ampere and the electron beam can be restricted as to size and shape by various focusing methods. One major disadvantage is the fact that an evacuated chamber is required. However, this problem has now been partly overcome by the development of electron beam guns which can be separated from the work anode. Further improvements will no doubt be made in this method of heating which will make it a valuable laboratory technique.

## LABORATORY USES OF HIGH TEMPERATURES

As indicated earlier, one of the major laboratory uses of steady-state high-temperature environments is the evaluation of materials as carried out in a testing program. Table 63-III lists some of the major laboratory uses in this specific area.

Design data and an understanding of the behavior of engineering structural material are best obtained from the various types of mechanical properties tests which have been standardized to a certain extent at approximately room temperature. It should be pointed out that extending these test procedures to temperatures above 1500°C can lead to difficulties which, in many cases, can be overcome only by compromise. It is perhaps in this particular area that workers in university laboratories

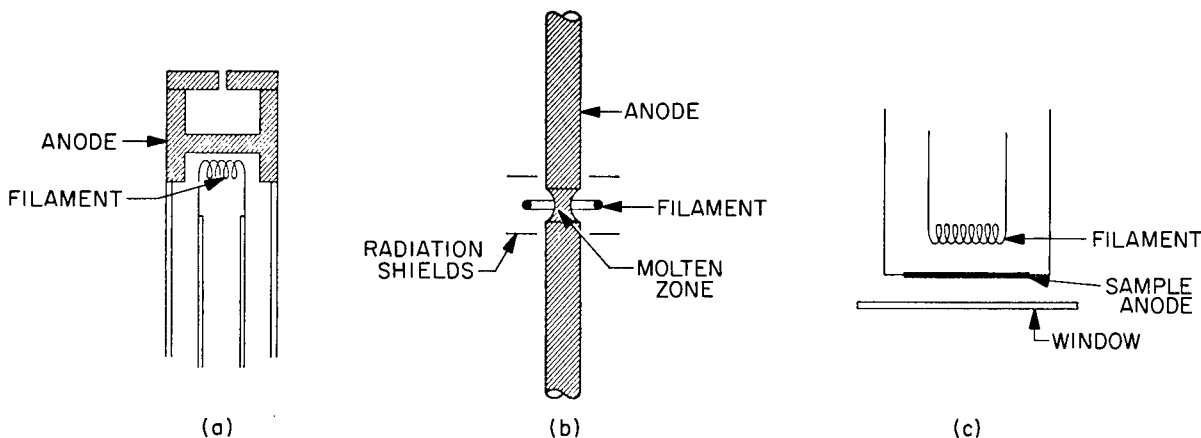


FIGURE 63-5.—Methods of using electron beam heating.

# LABORATORY TECHNIQUES

TABLE 63-III.—*Laboratory Uses of High Temperatures*

Evaluating mechanical properties of materials.	Tension. Compression. Torsion. Creep. Hardness.
Evaluating physical properties of materials.	Melting point. Vapor pressure. Phase equilibrium. Reactivity.
Special techniques	Microscopy. X-ray diffraction.

can make a much needed contribution. An evaluation of the effects of the various compromises on the high-temperature mechanical behavior of engineering structural materials is certainly an area where complete knowledge is lacking.

The university laboratories have been a major source of information in the area of material physical properties (see Table 63-III). One possible reason for this is that in many cases the information thus obtained is not of direct application to the engineering use of the material but is used mainly to understand and explain a particular behavior. The difficulties

encountered in making these property determinations at temperatures above 1500°C are often greater than those indicated earlier. This is partly due to the fact that these properties are more sensitive to small variations in the material, and careful experimental techniques are therefore a necessity.

There is also an area of special laboratory techniques in which steady-state temperatures are used. The two techniques which are given in table 63-III are intended to serve only as an example and are not to be considered a complete listing. These techniques are also utilized largely in university laboratories. However, at the present time there is a very limited amount of work done above 1500°C and there is certainly a need for an expansion of this activity.

As indicated previously, a presentation of this type has to be general in nature and therefore cannot consider specific problem areas. It is hoped, however, that the need has been demonstrated for university laboratories to develop rather widespread use of steady-state temperatures above 1500°C so that the research necessary for our advancing technology can be carried out in the highly desirable academic surroundings. While there are problems to be solved in the development of such capabilities, a good start has been made toward the solutions.

## 64. High-Vacuum Techniques for Research

By Jack L. Taylor

JACK L. TAYLOR is a Research Specialist in the Materials Research Section of Jet Propulsion Laboratory. He is conducting research on the mechanical properties of refractory metals at very high temperatures. Mr. Taylor was born in Montpelier, Idaho. He received his B.S. in Metallurgy from the University of California (Berkeley) in 1939, and his M.S. in Metallurgy from the Montana School of Mines in 1941. He is a member of AIME, ASM, Sigma Xi, and the American Vacuum Society.

### INTRODUCTION

The purpose of this paper is to discuss vacuum—what it is, how it is obtained, how it is used in research, and finally to conjecture about its future.

Man has already achieved a pressure so low as to be equivalent to one helium atom in a space sixteen times larger than our observable universe, that is, in a sphere whose radius is  $10^{79}$  light years. This unusable vacuum was attained in a very small volume by the adiabatic demagnetization of a paramagnetic salt which was used to lower the temperature of helium vapor to  $0.01^\circ\text{K}$ . At this temperature, physicist Russell Scott (Ref. 1) estimates the vapor pressure of helium to be  $0.3 \times 10^{-316}$  torr<sup>1</sup> or about  $10^{300}$  times lower than the vacuum of interplanetary space, estimated to be  $10^{-16}$  torr.

The magnitude of these numbers is beyond comprehension. However, some concept of vac-

uum may be grasped by examining table 64-I (Ref. 2), in which pressure is described in terms of molecular density and mean free path. At the beginning of the high-vacuum region ( $10^{-3}$  torr), the mean free path of one molecule between collisions with other molecules is 5 cm, and there are  $3 \times 10^{13}$  molecules/cm<sup>3</sup>. In the ultra-high region ( $10^{-12}$  torr) the mean free path is  $5 \times 10^9$  cm or 31,000 mi, and the molecular density is 30,000 molecules/cm<sup>3</sup>.

Before discussing the techniques for reaching the low pressures of  $10^{-3}$  to  $10^{-12}$  torr, it is appropriate to ask why these techniques were developed. The vacuum-tube electronics industry furnished the first practical lure to the development of high-vacuum techniques. Fundamental and applied research in the chemistry and physics of solids gave further impetus to

<sup>1</sup> After Evangelista Torricelli; equivalent to 1 mm of Hg.

TABLE 64-I.—Characteristics of Vacuum

	Atmospheric pressure	Start of high-vacuum region	Intermediate vacuum	Ultra-high vacuum region		
Pressure (Torr)-----	760	$10^{-3}$	$10^{-6}$	$10^{-8}$	$10^{-10}$	$10^{-12}$
Mean Free Path of One Molecule between Collisions with other Molecules, cm.	$6.5 \times 10^{-6}$	5	$5 \times 10^2$	$5 \times 10^5$	$5 \times 10^7$	$5 \times 10^9$
Number of Molecules per cm. <sup>3</sup> ---	$2 \times 10^{19}$	$3 \times 10^{13}$	$3 \times 10^{10}$	$3 \times 10^8$	$3 \times 10^6$	$3 \times 10^4$

## LABORATORY TECHNIQUES

this technology. The first large vacuum chambers, other than those used for coating astronomical mirrors, were required by nuclear physicists. Finally, space exploration problems have heightened the interest in the production and use of high and ultra-high vacuums.

### HIGH-VACUUM TECHNIQUES

The first problem confronting the vacuum technologist is to produce and maintain the desired order of vacuum. In every case, the vacuum attained represents a balance between the pumping capacity and the system gas-load. The gas-load results from gases adsorbed and

absorbed on system walls and components, plus in-leakage through seals. An additional gas-load, significant in the ultra-high region, comes from the permeability of glass to helium and of metals to hydrogen. Successful solutions result when each gas source is minimized. Besides pumping, two other methods are often required to produce high vacuum, namely, baking to hasten outgassing, and trapping to prevent pump-fluid backstreaming.

Figure 64-1, a bar-graph, indicates the order of vacuum pressure achieved with various types of pumping. Pumping means which are novel or rarely used for research, such as catalytic

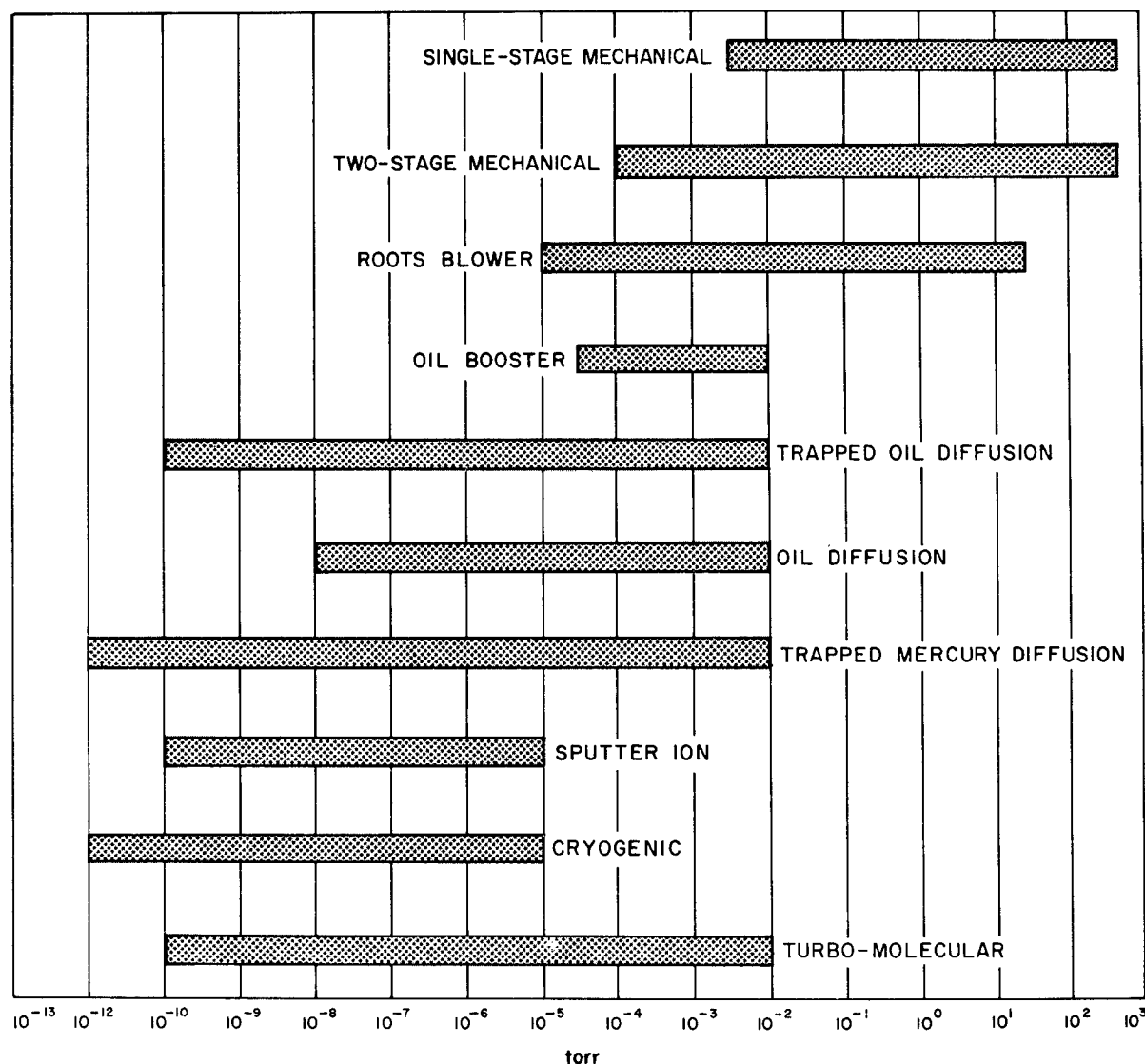


FIGURE 64-1.—Range chart for various types of vacuum pumping.



conversion, sorption pumping, and gettering, are not included. From this chart it is apparent that the high-vacuum region can be reached with a two-stage mechanical pump. This region can also be attained by a Roots blower backed by a mechanical pump, or an oil booster pump backed by a mechanical pump. To reach into the very high- and ultra-high-vacuum ranges, the diffusion pump is used, as are three more recently developed types of pump, namely sputter ion, cryogenic, and turbo-molecular drag pumps.

### Diffusion Pump

In spite of the many different methods available to reach very low man-made pressures, the diffusion pump is the most widely used. Invented by Gaede in 1915, it used mercury as the pump fluid. The diffusion pump, usually with oil as the pump fluid, has continued to be improved in pumping speed and efficiency and is available in sizes ranging from less than 1 in. to 48 in. in diameter. Liquid-nitrogen cold traps and molecular sieve traps have extended its capability into the ultra-high vacuum range. The ultimate vacuum attainable by a diffusion pump alone can never be better than the vapor pressure of the pump fluid above the pump inlet. In practice, effective trapping can suppress the back diffusion of pump fluid vapor so efficiently that the pressure is lowered by two orders of magnitude.

Mercury diffusion pumps are capable of producing a vacuum on the order of  $10^{-12}$  torr, approximately two orders of vacuum better than achieved with the best oil diffusion pumps. In addition, mercury in a diffusion pump is slightly more effective for hydrogen than any of the commonly used oils (Ref. 3). The vapor pressure of mercury at  $90^\circ\text{K}$ , attained with a liquid-nitrogen cold trap, is  $3.5 \times 10^{-29}$  torr (Ref. 4). With a well-trapped mercury diffusion pump, a system which is started clean stays clean, particularly if metal gasketing is used. Improvements in trap design, automatic equipment for controlling the flow of liquid gases, and the availability of liquid gases have served to revive interest in large mercury diffusion pumps.

### Ion Pump

Ion pumps are also used where a very clean vacuum is needed and where the processes carried out in the vacuum chamber do not produce large volumes of gas. The function of a sputter ion pump is illustrated schematically in Fig. 64-2. Electrons are emitted from the cathode plates and are accelerated toward the anode. The electrons are made to spiral by a magnetic field to enhance the probability of collision with gas molecules. Gas molecules struck by electrons are ionized and attracted to the negative collector plates where they are held by adsorption and in some cases react chemically with the material of the collector. The material of the collector plates is usually titanium. The bombardment of ions "sputters" the surface to provide fresh layers of metal with which chemically active gases combine.

It is apparent that the ion pump immobilizes gases within the system instead of removing them. Hence, its capacity is limited by saturation of the collecting surfaces. Another characteristic of the ion pump is that it removes chemically active gases faster than inert gases,

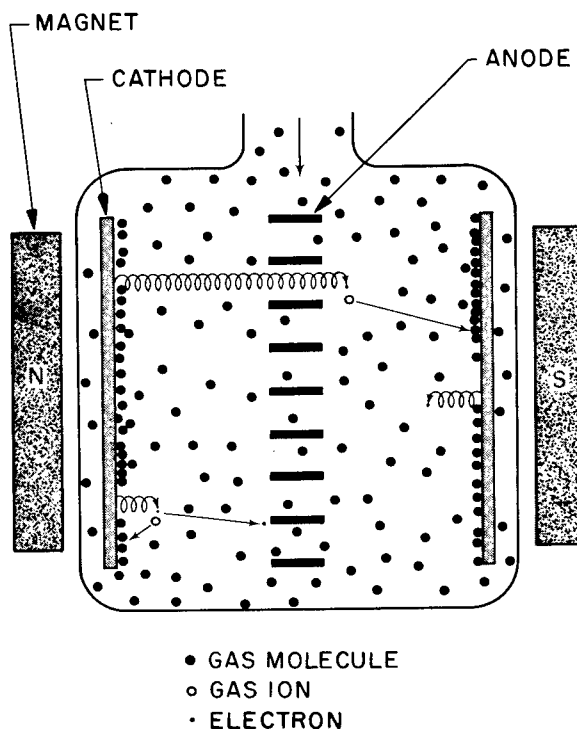


FIGURE 64-2.—Sputter ion pump (after Steinherz and Redhead).

because it pumps the active gases by both adsorption and chemical reaction. Furthermore, ion pumps re-emit a small fraction of the gases previously pumped because the ions reaching the collector surfaces dislodge some molecules which were already adsorbed. Ion pumping essentially ceases at  $10^{-10}$  torr.

### Cryogenic Pump

Cryogenic pumping can create a vacuum below  $10^{-12}$  torr, even in large chambers. This process simply immobilizes gas by condensation on a very cold surface. As shown in Fig. 64-3, a liquid gas (usually helium) is used to cool the condensing surface. Liquid-nitrogen cooled radiation barriers limit heat transfer from the experimental process in the chamber to the cold wall. The V-shaped baffle-form of the upper barrier allows molecules to pass. Cryogenic pumping requires back-up forms of pumping such as mechanical pumps, blowers, and diffusion pumps, which may or may not be valved off, depending on the experiment.

Cold-wall temperatures necessary to produce a vapor pressure of  $10^{-7}$  torr for various gases to be pumped are shown in Table 64-II (Ref. 5). It is interesting that even a cold wall at  $4^\circ\text{K}$ , attainable with liquid helium, will reduce the vapor pressure of hydrogen to only  $10^{-7}$  torr.

TABLE 64-II.—*Approximate Cold Wall Temperature Necessary to Attain a Vapor Pressure of  $10^{-7}$  torr for Various Gases*

	Boiling point $^\circ\text{K}$	Cold wall temperature $^\circ\text{K}$
Hydrogen.....	20. 39	4
Neon.....	27. 3	8
Nitrogen.....	77. 34	24
Carbon Monoxide...	81. 66	25
Oxygen.....	90. 19	27
Carbon Dioxide.....	194. 68	82
	(sublimes)	
Water.....	373. 2	175

The availability of cheap liquid gases has made cryogenic pumping practicable. This type of pumping may be advantageous for very large systems because the pumping speed is directly proportional to the area of the cold

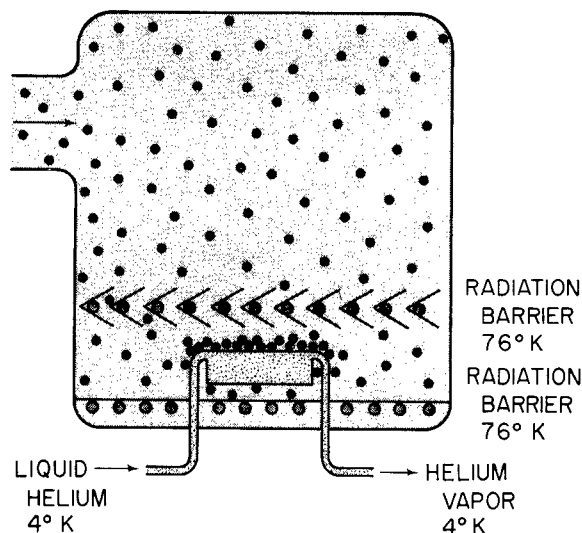


FIGURE 64-3.—Cryogenic pump (after Steinherz and Redhead).

wall and is not affected by the conductance of connecting piping.

### Turbo-Molecular Drag Pump

The turbo-molecular drag pump (Fig. 64-4), a strictly mechanical device capable of producing a very clean vacuum on the order of  $10^{-10}$  torr, has recently become available commercially in this country. It is based on the principle of providing a high probability of molecular flow in one direction by means of small clearances and proper rotor-stator relation. The pumping speed for air is virtually independent of pressure down to  $10^{-10}$  torr. It has a good pumping speed for hydrogen to a pressure on the order of  $10^{-6}$  torr. The development of this pump bears watching, although its usefulness may be limited because it is a high speed mechanical device and because of its (present) low capacity.

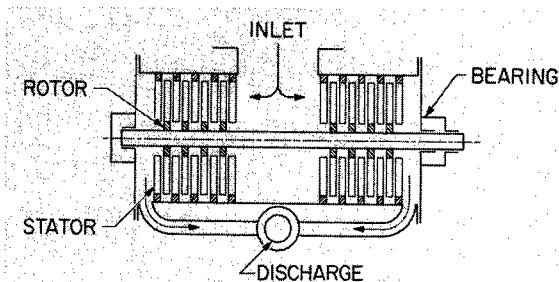


FIGURE 64-4.—Turbo-molecular drag pump.

### Traps, Seals, and Baking

Liquid-nitrogen traps of various designs have been commercially available for some time. Another form of trapping, now commercially available, is the molecular sieve trap. It utilizes stable materials having very low vapor pressures, such as the artificial zeolites or activated alumina. These materials, which are produced in porous form with minute pore structures, are capable of trapping large quantities of gaseous impurities, although they do not readily absorb argon and hydrogen. They also provide a difficult path for surface migration through the trap. The trap can be reactivated by baking and pumping. The molecular sieve trap has become increasingly popular for use in the foreline piping to reduce backstreaming of mechanical pump oil into the vacuum chamber during preliminary evacuation or roughing.

Seal design and gasket materials have a major influence on the degree of vacuum reached and maintained. Thermal outgassing studies, coupled with mass spectrometry for gas species identification, have led to the selection of elastomeric materials for seals which allow the ultra-high-vacuum region to be reached. One such material, Viton, a fluoro-elastomer has low permeability, low outgassing, and allows baking to 200° C.

The process of baking is often combined with trapped diffusion pumping to break the barrier between high and ultra-high vacuum when the process under investigation can withstand the application of heat. Effective sealing for bake-out in the range above 200° C., is accomplished with gold and aluminum wire between stainless steel flanges bolted together, with conical spring washers under the bolt heads.

### Conductance

It is especially important for a vacuum system to have interconnecting plumbing, valves, baffles, and traps with sufficient conductance to match the speed of the pumping components. Conductance refers to the capacity of a tube, orifice, or component for carrying gas. The conductance,  $C$ , is the proportionality constant in the expression

$$C = \frac{Q}{(P_1 - P_2)}$$

where  $Q$  is the quantity of gas flowing through the component, measured in units of pressure times units of volume/unit of time; and  $P_1 = P_2$  is the pressure drop across the component. The pressure unit in  $Q$  cancels the pressure unit in the denominator, leaving  $C$  expressed in units of volume/units of time (e.g., liters/sec).

The net conductance,  $C$ , of conductances  $C_1$ ,  $C_2$ ,  $C_3$ , etc., of components connected in series is

$$\frac{1}{C} = \frac{1}{C_1} + \frac{1}{C_2} + \frac{1}{C_3} + \dots$$

If these same components are connected in parallel, the resultant conductance is

$$C = C_1 + C_2 + C_3 + \dots$$

In the high-vacuum region, the mean free paths of the molecules are so long that the molecules collide much more often with the piping walls than with each other. This condition of gas flow, called free molecular flow, can be assumed for practical purposes to exist when the pressure is such that the mean free path is half the diameter of the pipe or greater. In the free molecular flow region, conductance is independent of pressure and reaches its lowest value. It is dependent upon the molecular weight of the gas, the temperature of the gas, and the diameter and length of the pipe.

The net pumping speed,  $S'$ , of the system is related to the speed of the pump,  $S$ , and conductance,  $C$ , by

$$\frac{1}{S'} = \frac{1}{S} + \frac{1}{C}$$

Thus,  $C$  must be considerably larger than  $S$  if  $S'$  is to remain a high percentage of  $S$ . A comprehensive treatment of vacuum system analysis is given in Refs. 4 and 6.

### Gauging

The second problem confronting the vacuum technologist is the need to measure vacuum accurately. Until the Bayard and Alpert experiments of 1950, which led to improvement of the hot filament ion gauge, it was not possible to measure vacuum below  $10^{-8}$  torr because of the X-ray effect suggested by Nottingham. In Fig. 64-5, a chart is shown indicating the range of pressures in which various gauges work. The

# LABORATORY TECHNIQUES

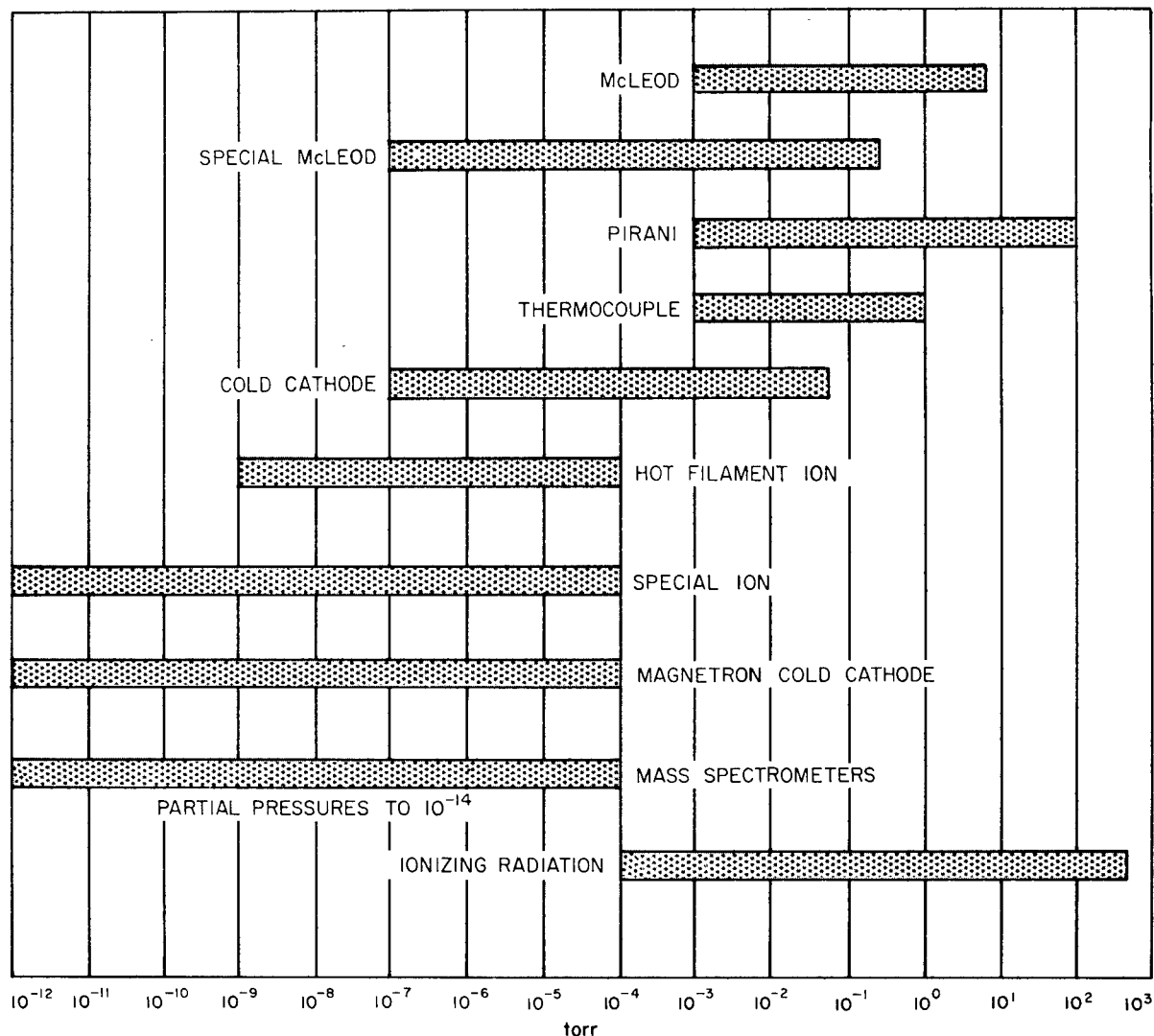


FIGURE 64-5.—Range chart for various types of vacuum gages.

improved cold cathode gauge is called the Magnetron, and the improved Bayard and Alpert hot filament ion gauge is designated the special ion gauge.

The hot filament ion gauge is the most widely used. Some of the factors which can cause errors at any pressure within its operating range are discussed by Redhead (Ref. 7). These factors are (a) pumping action of the gauge, (b) Barkhausen-Kurtz oscillations, (c) chemical effects at the hot filament and the bulb, and (d) variation of the residual current.

At 8 mA electron current and 250 v electron energy, the Bayard-Alpert gauge has a total pumping speed for nitrogen of 2 liters/sec when

first operated. Chemical pumping accounts for 75% of the pumping speed, electron pumping the remainder. Tubulation with a conductance of 40 liters/sec must be used when the pumping speed of the gauge is 2 liters/sec, in order to keep the partial pressure of nitrogen in the gauge less than 5% of that in the chamber. For nitrogen, a 3-cm diameter, 5-cm long tube has a conductance of 40 liters/sec. The usual tubulation on the gauge has a conductance on the order of 2 liters/sec, which gives rise to an error of 100% in pressure measurement. Hence, the gauge pumping action can be offset by providing high conductance tubulation between the gauge and the chamber. The Barkhausen-

Kurtz oscillations, which cause sudden discontinuous pressure sensitivity at critical amplitudes, can be minimized by a transparent conducting coating (e.g., tin oxide) inside the bulb. The chief chemical effect at the hot filament is the dissociation of hydrogen, water, and hydrocarbons to give spurious ion currents. This effect can be reduced by pre-heating the filament in  $10^{-7}$  torr of oxygen at  $2000^{\circ}\text{K}$  to lower the carbon impurity content, and by using low work-function coatings to lower the operating temperature of the filament. At very low pressures, the residual current due to X-ray effects and ultraviolet radiation from the filament is of the same magnitude as the ion current. One method of determining the residual current involves adding a modulator electrode to the usual Bayard-Alpert gauge design. A modulator factor is determined by measurements at high pressure where the residual current is negligible. With this information, the true ion current can be found by a difference method.

From the discussion above, it is obvious that a single ion gauge design will not have constant sensitivity across the pressure range from  $10^{-5}$  to  $10^{-12}$  torr. Furthermore, total pressure measurements below  $10^{-9}$  torr lose significance when differential pumping action takes place in the gauge; partial pressure measurements are preferable. Partial pressure measurements in the ultra-high-vacuum range are made with specialized mass spectrometers, such as the Omegatron, which identify the gas species. A recently developed modification of a 90-deg sector mass spectrometer by Davis and Vanderslice of the General Electric Company can measure partial pressures as low as  $10^{-14}$  torr. New developments in gauge design promise measurements down to  $10^{-18}$  torr.

### APPLICATION OF TECHNIQUES

Several examples have been prepared to illustrate how vacuum, once achieved and measured, is put to use in research.

#### High-Temperature Tensile Furnace

In the tensile furnace illustrated in Fig. 64-6, vacuum provides a protective atmosphere. The furnace is used to measure the deformation

behavior of refractory metals in tension at temperatures up to  $2980^{\circ}\text{C}$ . A vacuum atmosphere is required because of the high reactivity of the refractory metals with air gases at temperatures as low as  $500^{\circ}\text{C}$ . The elements, oxygen, nitrogen, carbon, and hydrogen, which dissolve interstitially, influence markedly the mechanical properties of the refractory metals at low and intermediate temperatures even when present in a few parts per million. The degree of vacuum can change the impurity level during testing, depending upon the temperature and the particular metal being tested. For commercially pure tungsten, having total interstitial element impurity levels of 50 ppm or less, a vacuum of  $10^{-5}$  torr and a temperature of  $2900^{\circ}\text{C}$  maintained for 10 min appear to leave the composition relatively unchanged.

The furnace has a hot zone  $2\frac{1}{2}$  in. in diameter by 8 in. long provided by a heater assembly consisting of a thick-walled tungsten susceptor surrounded by very thin, split, tungsten radiation-shields. The assembly is supported within an induction coil by tungsten rods resting on an insulating zirconia cylinder. Power is supplied by a 50-kw, 10,000-cycle motor generator set. The grips and specimen are entirely surrounded by the hot zone, insuring a uniform temperature in the specimen.

The vacuum in the  $10^{-5}$  torr range is provided by two baffled and cold-trapped 4-in. diffusion pumps backed by an 80-cfm mechanical pump. A 7-cfm holding pump in conjunction with high-vacuum valves above the diffusion pumps adds convenience and flexibility to the system. After conductance losses in trapping and piping, the two diffusion pumps have pumping speeds of between 400 and 500 liters/sec at the furnace port. The conductance of the furnace port is 430 liters/sec. The full capacity of the pumping system is required to maintain  $10^{-5}$  torr against the outgassing load at the higher heating rates. Typically, a tensile test at  $2980^{\circ}\text{C}$  takes  $2\frac{1}{2}$  hr to reach temperature, 10 min holding time, and 20 to 30 sec testing time at a strain rate of 2.0 in./in./min.

#### Cryogenic Gyro

The cryogenic gyro is a device which may provide inertial guidance systems for spacecraft.

# LABORATORY TECHNIQUES

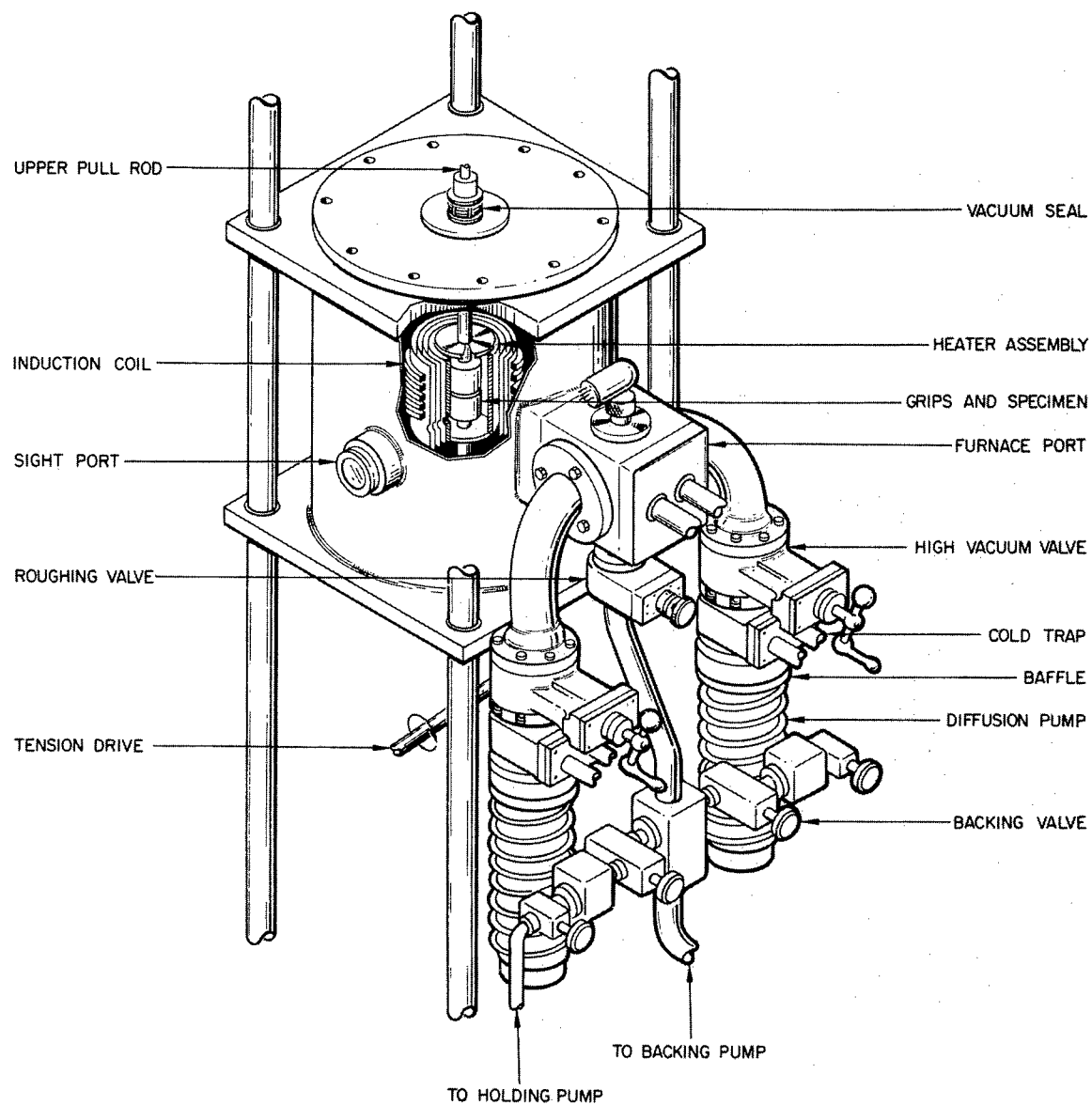


FIGURE 64-6.—High-temperature tensile furnace.

It depends on vacuum and extremely low temperature for its operation and is made possible by the fact that the magnetic forces on a superconductor are normal to its surface.



FIGURE 64-7.—Photograph of cryogenic gyro.

Figure 64-7 shows a photograph of the gyro (Ref. 8), with a  $\frac{1}{2}$ -in. niobium sphere levitated in a liquid helium bath. The gyro is shown schematically in Fig. 64-8. The starting coils are used to induce a current to flow in the "normal" coils in the direction indicated by the arrows. This current is then trapped in the coils by introducing liquid helium, which quickly cools the coils and rotor to superconducting temperature. The trapped current provides a magnetic field whose forces are normal to the superconducting rotor, causing levitation. After superconducting temperature is attained, the helium is pumped away. At the same time, a small jet of helium gas sets the levitated rotor in rotation, and the multiwalled Dewar operates to maintain the superconducting temperature. The rotor should continue to rotate on its magnetic suspension indefinitely, if the superconducting temperature is maintained.

Pumping proceeds until a vacuum on the order of  $10^{-7}$  torr is reached in the chamber. This order of vacuum is a compromise requirement. The vacuum must be such that there are enough molecules to transfer heat by conductance from the cold walls to the coils and sphere to keep them superconducting, yet not so many molecules as to slow the rotation of the sphere by molecular drag. Pumping of the chamber and the Dewar chambers is done with a 4-in. diffusion pump, backed by another 4-in. diffusion pump, in turn backed by a small mechanical forepump. It is thought that this series arrangement gives better helium pumping by providing a lower pressure drop across the first diffusion pump.

#### Bacteria Survival

An exceptional use of ultrahigh vacuum is made in a biological experiment to determine the ability of microorganisms to withstand space environment. A study of *Bacillus subtilis*, variety *niger*, required that a vacuum of  $10^{-8}$  torr or better be maintained for a period of at least 30 days (Ref. 9). It was necessary that the vacuum chamber be completely clean and sterile before introduction of the microorganisms, and during the period of vacuum exposure contamination had to be held to a minimum. No pump fluid gases could be allowed in the chamber. Furthermore, the vacuum had to be achieved without bake-out which might injure the microorganisms.

The apparatus used for the experiment is shown schematically in Fig. 64-9. The microorganisms were placed in the test tubes in the vacuum chamber, and a vacuum was pumped with a three-stage mercury diffusion-pump backed by a small mechanical forepump. Backstreaming of mercury vapor was controlled by a liquid-nitrogen cold finger placed over the top jet of the diffusion pump and by a separate liquid-nitrogen cold trap. A final barrier against back diffusion of mercury was provided by a gold film evaporated on the elbow connection to the chamber. Any mercury molecules travelling this far would hit the elbow wall and be immobilized by amalgamation with the gold.

Outgassing from the glassware in the ultrahigh-vacuum region was minimized by careful

## LABORATORY TECHNIQUES

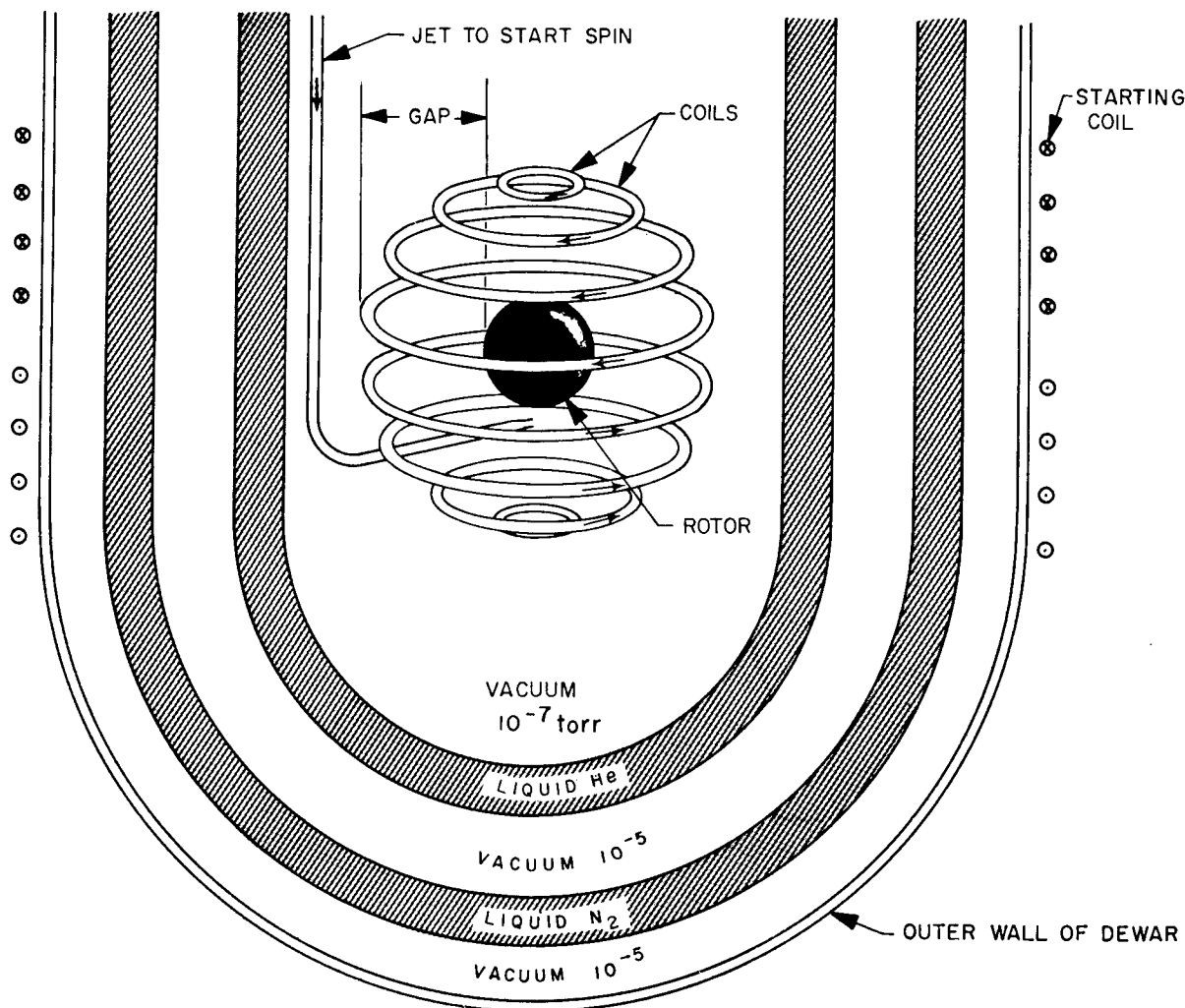


FIGURE 64-8.—Cryogenic gyro.

cleaning before assembly. Seven steps of degreasing, washing with bases, washing with acid, and alternate rinsings were performed.

The system functioned, as designed, between  $3 \times 10^{-8}$  and  $6 \times 10^{-9}$  torr for a period of 35 days. A Bayard-Alpert type hot filament ionization gauge remained in continuous operation throughout the experiment. The experiment showed that *bacillus subtilis*, variety *niger*, will survive an ultra-high vacuum of  $10^{-8}$  torr for a period of 35 days.

### FRICTION AND WEAR

A complicated ultra-high-vacuum system is that used in the friction and wear apparatus shown in Fig. 64-10. Buckley and Johnson (Ref. 10) are using the apparatus to measure

the lubrication properties of gallium-rich films in a vacuum of  $10^{-10}$  torr. This is a surface physics problem which sets stringent requirements upon the degree and cleanliness of the vacuum. At  $10^{-6}$  torr, it is known (Ref. 11) that a clean metal surface is contaminated by a monolayer of gas in a few seconds. At  $10^{-9}$  torr, it is estimated that a monolayer forms in approximately 17 min.

To achieve desired conditions, the procedure is the following: The entire apparatus is covered with a bake-out oven and hood while being pumped with a vane-type pump backed with an oil-sealed rotary pump of 13-cfm capacity. A liquid-nitrogen cold trap and a molecular sieve trap are placed in series in the piping between the vane-type pump and the vacuum



# HIGH-VACUUM TECHNIQUES FOR RESEARCH

chamber. The two mechanical pumps first mentioned continuously pump the forechamber, which contains the driven part of the magnetic drive, to preclude contamination of the main chamber with bearing lubricant. These pumps are valved off the main chamber when it reaches  $10^{-4}$  torr, and a 400-liter/sec ion pump is started. Baking proceeds during ion pumping, until the chamber reaches the  $10^{-8}$ -torr range. The hood and bake-out oven are removed, and an electron-beam heater is focussed on the disk and rider specimen area to further degas that area. The electron-beam heat source is also used to maintain temperatures to  $1000^{\circ}\text{F}$  during the friction experiment.

Although ion pumping is continued, the final pressure in the low  $10^{-10}$  torr range is achieved when the cold trap at the top of the chamber is filled with liquid helium. Occasionally, dry nitrogen purging and repumping is used after the oven bake-out.

For the friction measurements the rider specimen is loaded by the lever and weight principle with the gimbal assembly acting as the fulcrum. The disk specimen, rotated by the magnetic drive, rubs against the rider specimen, applying a torque to its holder shaft. The friction is proportional to the torque, which is measured with strain gauges. A photo-

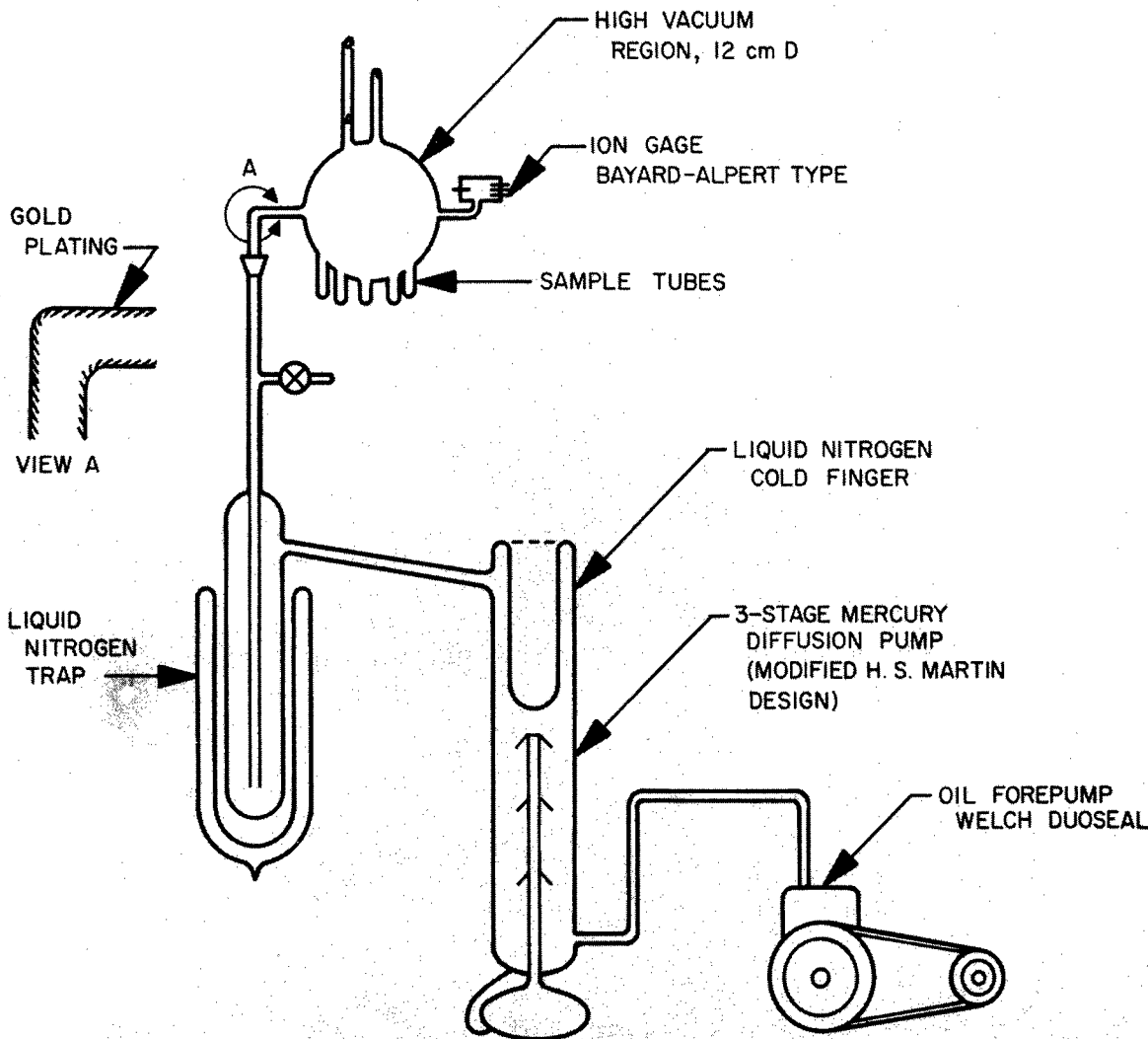


FIGURE 64-9.—Vacuum environment apparatus for bacteria survival test.

# LABORATORY TECHNIQUES

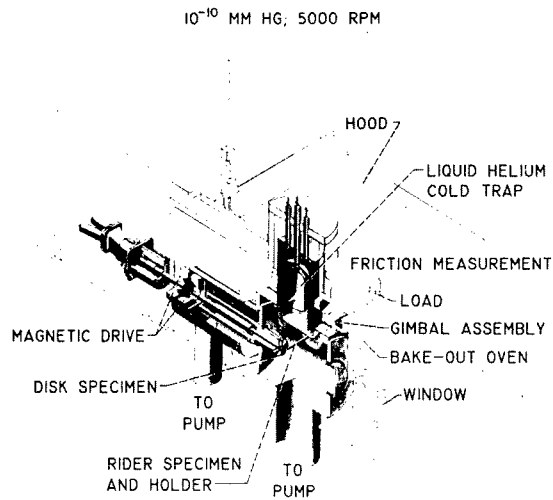


FIGURE 64-10.—Friction-and-wear apparatus (Buckley and Johnson, NASA Lewis).

graph of the equipment, viewed from the magnetic-drive end, is shown in Fig. 64-11.

This ingenious experimental apparatus combines two types of mechanical pumping, fore-line trapping, and ion and cryogenic pumping with oven bake-out and electron-beam heating to meet the vacuum requirements.

## Ion Propulsion Engine

The ion propulsion engine (Ref. 12) is designed for long-duration missions in space and will only operate in a vacuum. It depends for its thrust upon ions accelerated away from the spacecraft. The amount of thrust is proportional to the mass flow rate and the velocity of the ions.

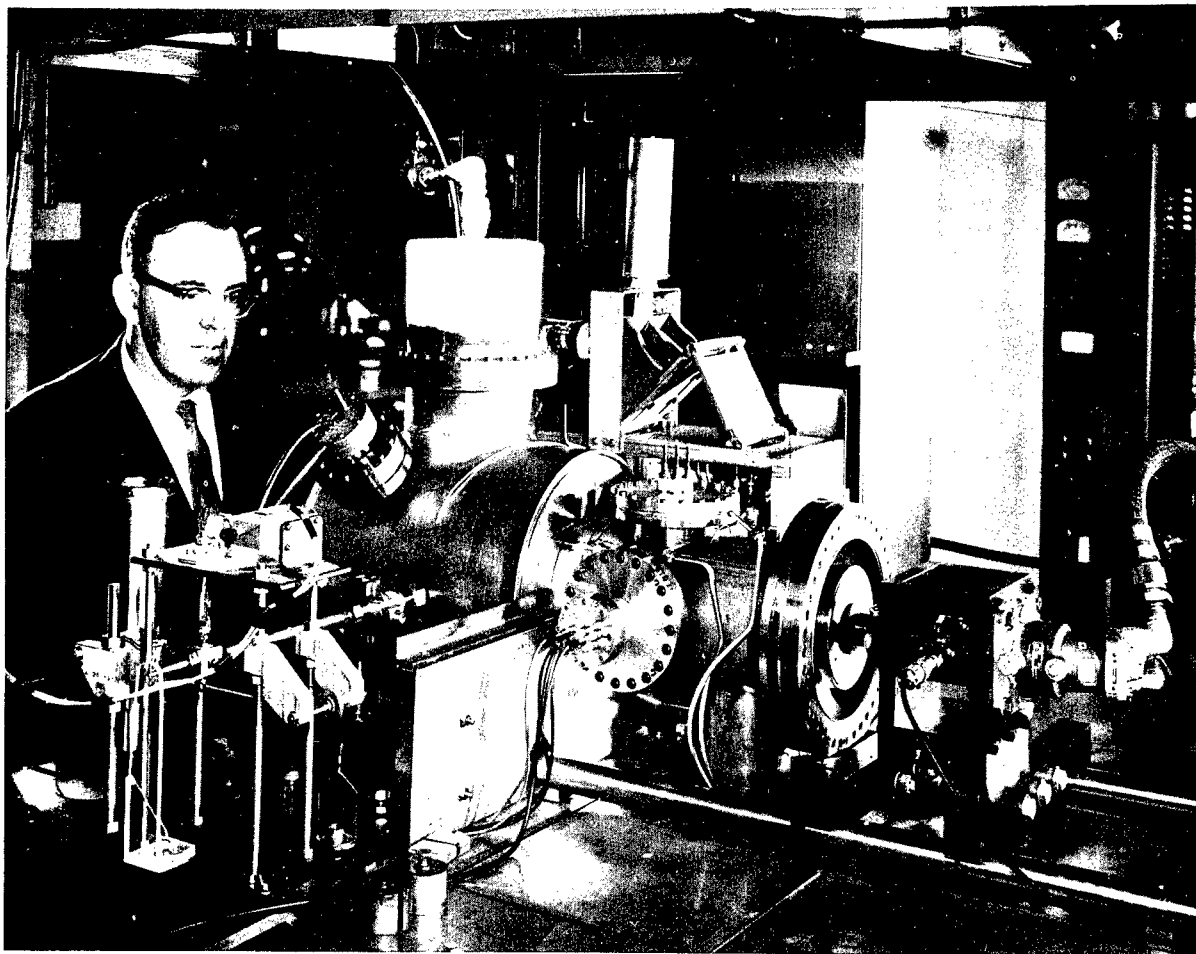


FIGURE 64-11.—Photograph of friction-and-wear equipment.

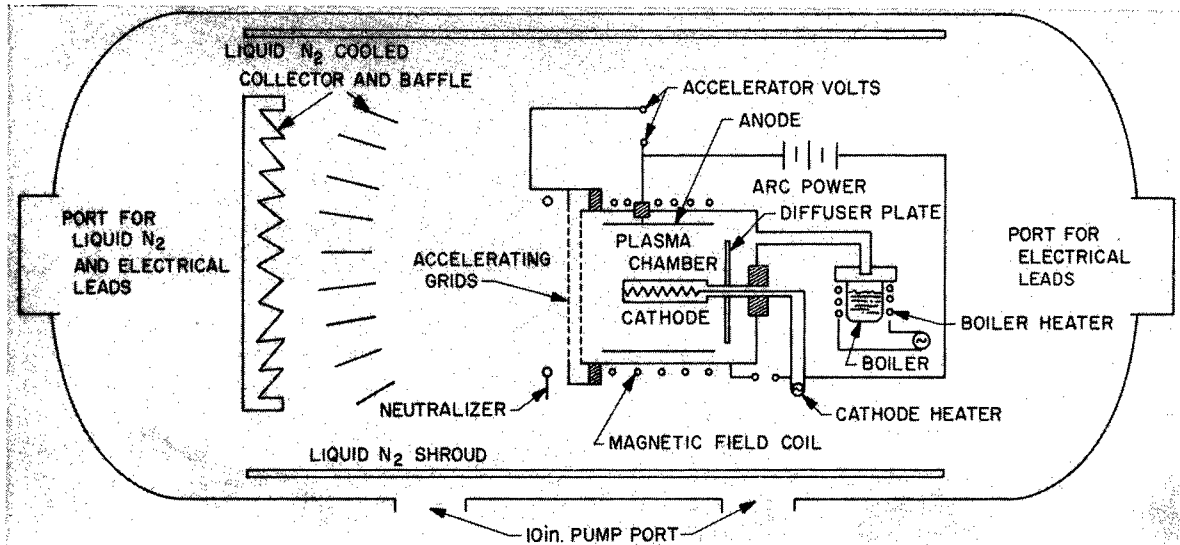


FIGURE 64-12.—Ion propulsion engine and chamber.

The engine is illustrated schematically in Fig. 64-12. The metal used for engine fuel, usually mercury or cesium, is vaporized in the boiler and diffused into the plasma chamber. Electrons are accelerated from the hot cathode toward the anode by means of a potential difference and are forced to take cyclotron orbits a few millimeters in diameter in the magnetic field introduced by the magnetic field coil. This path enhances the probability of the electrons colliding with the metal vapor atoms to produce ions before the electrons reach the anode. Ions migrating in the field gradient which reach the accelerating grids are accelerated away from the engine by the high potential between the grids. Surplus electrons from the ionizing process, upon reaching the anode, are pumped to the neutralizer and allowed to leak out, emerging with the ion beam. The neutralizer insures that the spacecraft will not become increasingly negatively charged and the engine cease to function. A photograph of the ion engine on its mount is shown in Fig. 64-13.

The optimum vacuum range for an efficient production of metal ions in the plasma chamber seems to lie between  $10^{-3}$  and  $10^{-4}$  torr. In the external environment, a higher vacuum, at least  $10^{-6}$  torr, is necessary to allow the ions

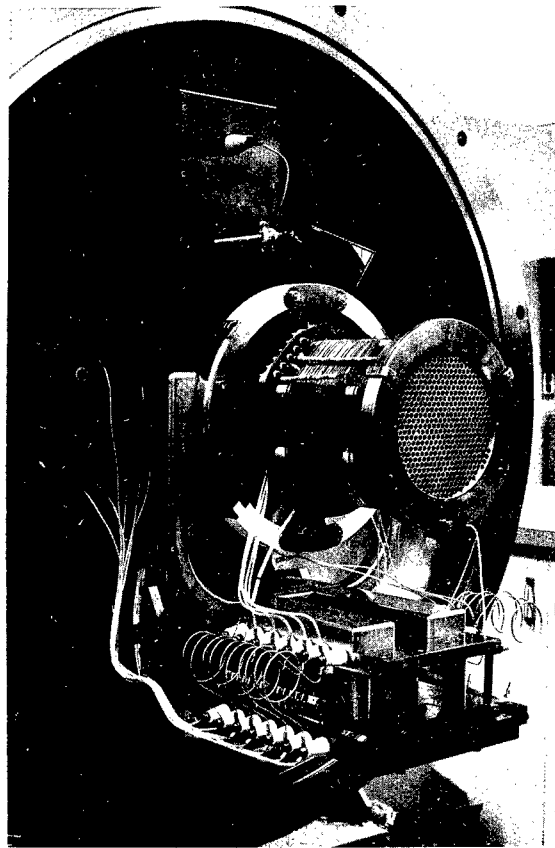


FIGURE 64-13.—Photograph of ion propulsion engine on its mount.

#### LABORATORY TECHNIQUES

to escape from the engine without excessive collisions between the residual gas and the directed ion beam (which would cause ion deflection and charge exchange). Furthermore, the condition of space which allows the ions to stay away and not return to the engine or bounce back into the beam must be simulated in laboratory testing.

These vacuum requirements are met by placing a liquid-nitrogen baffle and collector in front of the ion beam, as shown in the schematic of Fig. 64-12. The condensing surfaces of the baffle and collector are arranged in an optical trapping configuration. Stray metal atoms which escape the baffle and collector are immobilized on a liquid-nitrogen cold shroud. In practice, the vacuum facility is taken initially into the  $10^{-6}$  torr range using two 10-in. liquid-nitrogen-trapped diffusion pumps.

With the engine in operation at a fuel flow rate of 5 grams of mercury/hr, the baffle, trap, and shroud must pump mercury vapor at the rate of 100,000 liters/sec to maintain the initial pressure. In fact, the cryogenic pumping, with a surface area of about 30 ft<sup>2</sup>, is so effective that the chamber pressure continues to drop even with the engine operating and the diffusion pumps valved off.

A photograph of the over-all installation is shown in Fig. 64-14. Measurements of the engine's thrust are made on a thrust mount having a sensitivity of 2  $\mu$  lb. The vacuum tank is bolted to a 28,000-lb block to insure that resonance frequencies are too low to interfere with the measurements. Two 130-cfm mechanical pumps which back the diffusion pumps are mounted 50 ft away, with the connecting piping vibration damped.

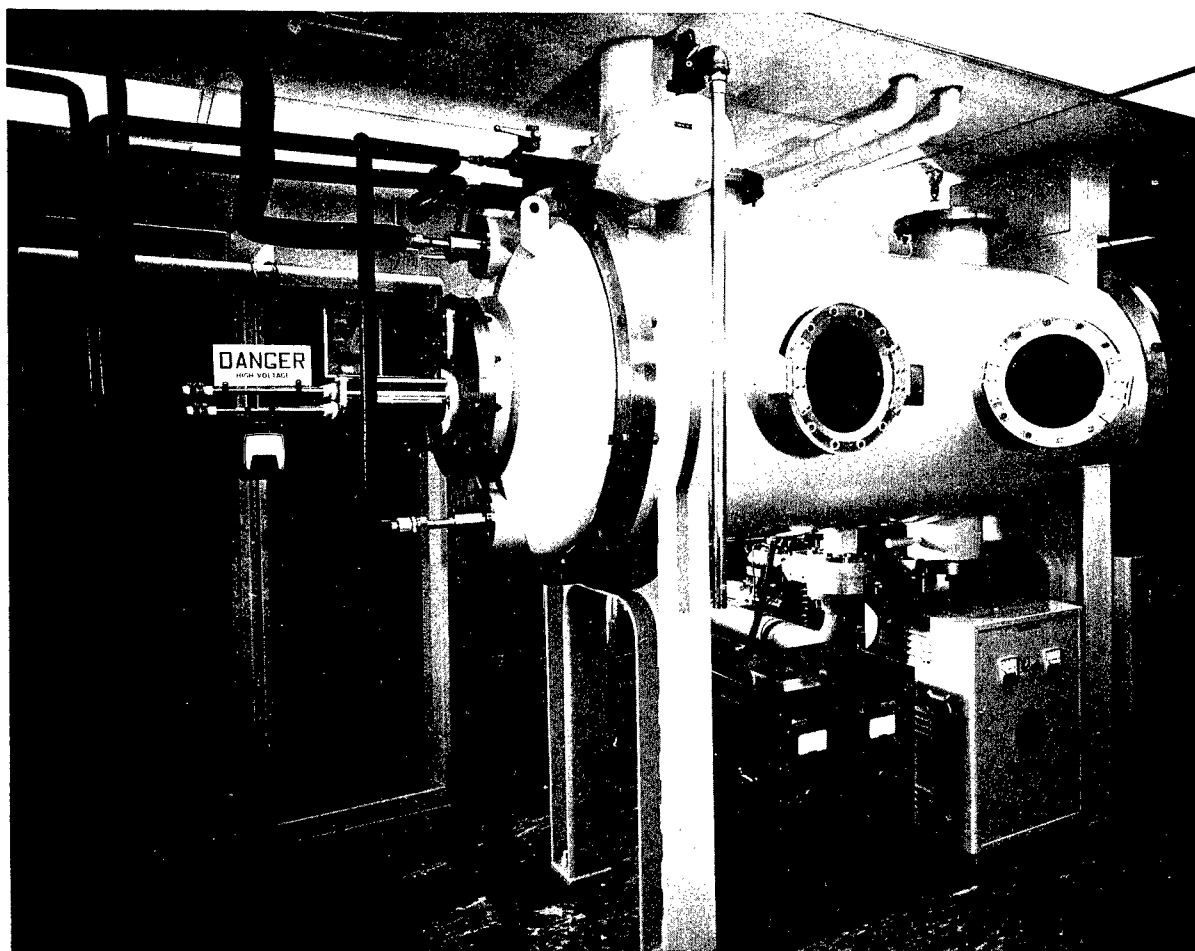


FIGURE 64-14.—Photograph of installation for testing ion engine.

### Fission Electric Cell

In a discussion of ion propulsion, it is natural to ask what source might be used to provide the high-voltage, low-current power the engine needs during space flight. One possibility is the fission electric cell (Ref. 13) shown in Fig. 64-15. The cell converts nuclear energy di-

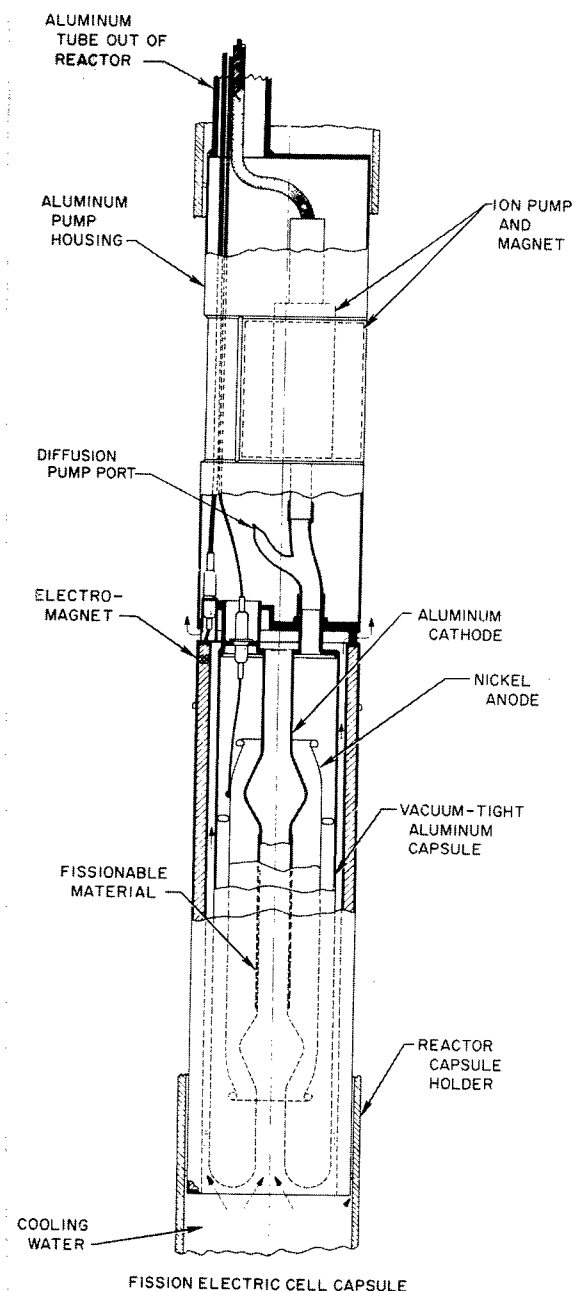


FIGURE 64-15.—Fission electric cell.

rectly to electrical energy in the following way: fragments from fissionable material coating the cathode traverse the vacuum space to the anode with energy levels of about 80 Mev and a net charge of  $+20 e$ . A potential of 4,000,000 v between the cathode and anode is theoretically possible. However, knock-on and follow-out electrons emerge with the fission fragments and interfere with the available electrical energy. An electromagnet is used to repress the electrons and realize a useful voltage across the cell. Vacuum environment allows the fission fragments to carry energy without wasting it by colliding with an ionizing gas molecules. It also prevents high voltage breakdown in the presence of the ionizing source.

The experimental cell, an all-welded aluminum construction 3 in. in diameter, is tested in a neutron flux 25 ft under water. Since the cell is out of reach during operation, dynamically pumping it to maintain a satisfactory vacuum presents a problem. The initial vacuum in the cell is achieved by diffusion pumping and bake-out, limited to  $100^{\circ} \text{C}$  by the aluminum construction. After pumping to approximately  $10^{-6}$  torr, the diffusion-pump port to the cell is pinched off, and the cell is placed in the reactor. The vacuum is maintained with a 1 liter/sec ion pump incorporated in the cell. The gases to be pumped are principally xenon and krypton, the fission fragments, which limit the efficiency of the cell when the pressure is too high. Gamma radiation plus Compton-effect electrons ionize the adsorbed and absorbed gases not previously removed by the bake-out, thereby adding to the gas load on the ion pump.

### Space Simulator

The Jet Propulsion Laboratory space simulator (Ref. 14) which has a vacuum chamber 25 ft in diameter by 25 ft high, is an example of the application of vacuum technique applied on a very large scale. A photograph of the simulator with the door open and the spacecraft Mariner in view is shown in Fig. 64-16. The simulator is designed to test spacecraft under simulated interplanetary conditions of intense solar radiation, radiation heat sink, and high vacuum. The vacuum is achieved by cold-trapped diffusion pumping. The radiation heat

sink of outer space is simulated by a liquid-nitrogen cold shroud with a coated surface having an emissivity of at least 0.9 for both ultraviolet and infrared radiation. The solar radiation is simulated by an array of 131 mercury-xenon arc lamps, which produce a design solar flux intensity of 200 w/ft<sup>2</sup>.

Figure 64-17 shows the solar-simulator optics. The light from the mercury-xenon arc lamp source array is reflected from flat circular mirrors arranged as facets on a parabola to a pseudo-hyperbolic reflector, thence through a quartz lens into the chamber. The virtual source, consisting of multifaceted pebbles, reflects light to spherical mirrors which, arranged as facets on a parabola, provide the even distribution of solar radiation. The primary virtual source casts a shadow into the working volume. This is filled in by a lens in the primary virtual source, an auxiliary pebble bed, and a parabolic reflector. The optical system has a collimation requirement of  $\pm 5$  deg for the extreme ray. The mercury-xenon arc lamp, which does not match the solar spectral distribution curve as well as a carbon arc lamp, has

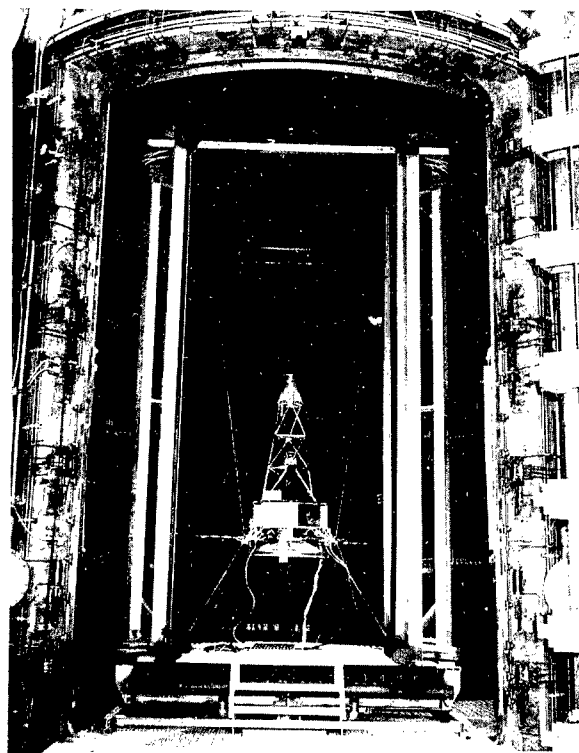


FIGURE 64-16.—Photograph of space simulator.

less fluctuation and can be controlled more closely. A further departure from the solar spectral distribution is caused by the aluminum reflecting surfaces. However, meaningful tests can be conducted by correcting the observed spacecraft temperature for spectral reflectance and absorptency.

A vacuum on the order of  $10^{-4}$  torr is sufficient to insure that heat transfer by radiation is 99% of the total heat transfer, conductance accounting for less than 1%. However, the design pressure for the clean, empty, outgassed chamber is  $5 \times 10^{-6}$  torr, which allows some margin for the unknown gas load of future spacecraft under solar heat flux. The pumping schematic for the chamber is shown in Fig. 64-18. Compressors in a nearby wind tunnel are used to rough the chamber to less than  $2 \times 10^{-4}$  torr, after which two 5000-cfm blowers (Stokes 1713), backed by a combination 1200-cfm blower and 300-cfm mechanical pump (Stokes 1711), further reduce the chamber pressure to  $10^{-2}$  torr. At this pressure, ten 36-in. oil diffusion pumps, which are held by a 130-cfm pump (KDH 130) during roughing, are valved in to reduce the chamber to the desired operating pressure. The diffusion pumps are liquid-nitrogen trapped to preclude contamination of the optics with pump oil films, which would gradually reduce the light intensity. When the system is at operating pressure, the shroud is filled with liquid nitrogen. Approximately 5000 gal are required to bring the piping and shroud system down to liquid nitrogen temperature. The 9500 ft<sup>2</sup> of shroud, in addition to simulating the radiation heat sink of outer space, also provide extra pumping capacity to handle outgassing from the spacecraft.

A vacuum system of this size is a major achievement, considering the myriad of weld joints, braze joints, and seals which must be leak-free, the thermal expansion in the liquid-nitrogen shroud and plumbing, and the huge-size pumping and its control. When the large complex optical system is considered as an integral part of the vacuum chamber, the achievement is even greater.

The examples discussed here are but a few of the many ways in which research projects utilize vacuum. Some examples of research highly

# HIGH-VACUUM TECHNIQUES FOR RESEARCH

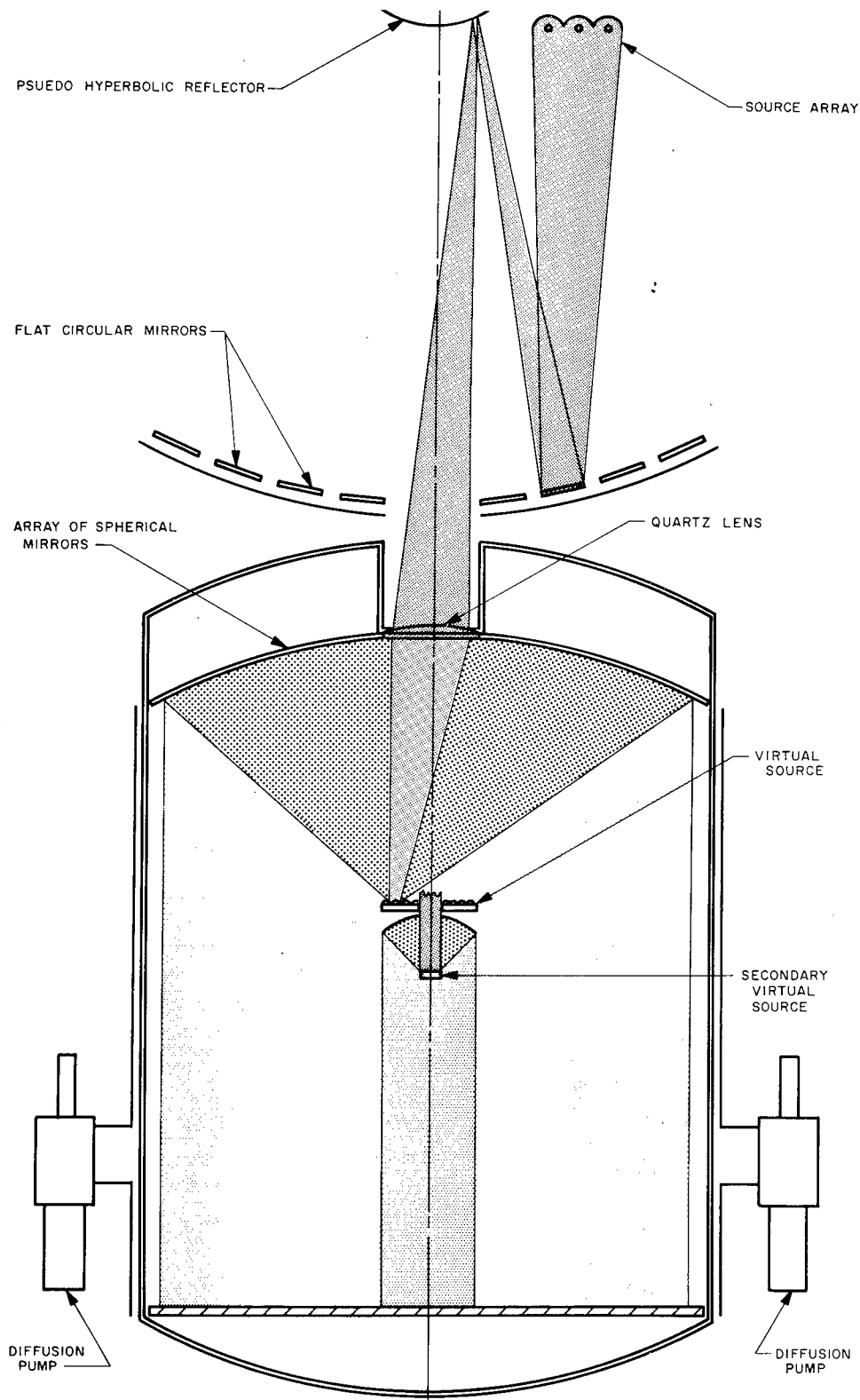


FIGURE 64-17.—Solar simulator optical arrangement.

## LABORATORY TECHNIQUES

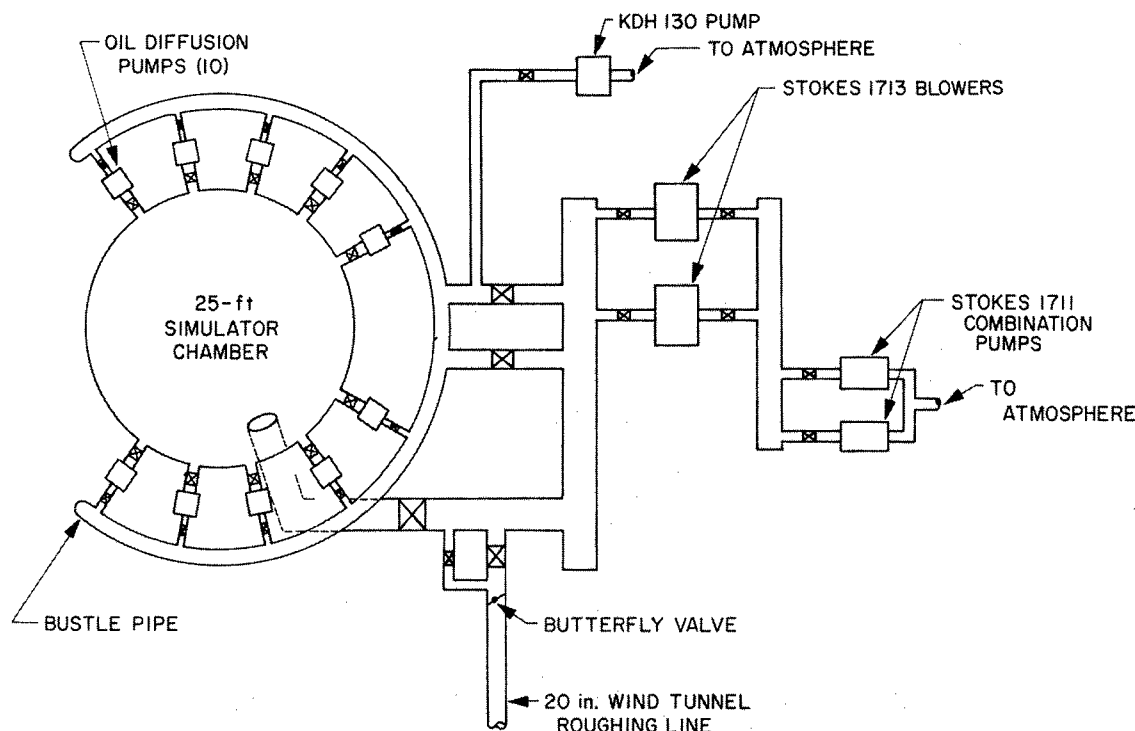


FIGURE 64-18.—Vacuum pumping schematic for solar simulator.

dependent of vacuum technology are investigations of vacuum deposition of thin films for optical, semiconducting and superconducting purposes; the degradation of polymers; zone refining of metals; and instrumentation for space exploration, such as gas chromatography and ultraviolet spectrometry.

### FUTURE OF VACUUM

What is the future of vacuum technology? For those who would build large ultra-high-vacuum systems, Balwanz (Ref. 5) has made an estimate of the relative operating costs of pumping by cryogenic means and by diffusion pump methods. In Fig. 64-19, three types of cryogenic pumping are shown. These are a one-stage pump consisting simply of a liquid-helium cold wall, a two-stage pump with liquid-

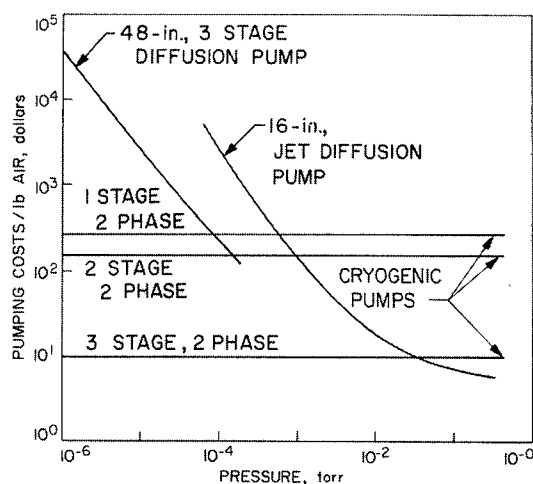


FIGURE 64-19.—Comparative operating costs of cryogenic and diffusion pumping.



helium and liquid-nitrogen cold walls, and a three-stage pump, the most complicated and efficient form of cryogenic pump, involving a liquid-helium cold wall, guarded by a liquid-hydrogen radiation baffle, which in turn is guarded by a liquid-nitrogen radiation baffle. The comparison indicates that cryogenic pumping, even in its simplest form, is cheaper than diffusion pumping for very large systems.

One nationally known vacuum equipment manufacturer claims in a news bulletin (Ref.

15) of August 1962 to have created a vacuum of  $10^{-15}$  torr in a volume of approximately 6 ft<sup>3</sup>. This pressure is at the limit of sensitivity of the best gauges and even the best mass spectrometers. The capability for achieving vacuum appears to have surpassed again the capability for measuring it. The degree of vacuum already produced will serve a great percentage of research needs. However, man will continue seeking higher and higher vacuum and the methods for measuring it.

### REFERENCES

1. SCOTT, RUSSELL B., *Cryogenic Engineering*, D. Van Nostrand Co., Inc., Princeton, New Jersey, 1959.
2. STEINHERZ, H. A., and P. A. REDHEAD, "Ultrahigh Vacuum," *Scientific American*, Vol. 206, No. 3, 1962, pp. 78-90.
3. YARWOOD, J., *Symposium on Some Aspects of Vacuum Science and Technology, London, January, 1962*. British Journal of Applied Physics, Vol. 13, No. 7, 1962, p. 304.
4. DUSHMAN, SAUL, *Scientific Foundation of Vacuum Techniques*, John Wiley and Sons, Inc., New York, 1949, p. 782.
5. BALWANZ, W. W., J. R. SINGER, and N. P. FRANDSEN, *High Pumping Rate Vacuum Systems*, Seventh National Symposium on Vacuum Technology Transactions, Pergamon Press, New York, 1961, pp. 182-186.
6. GUTHRIC, A., and R. K. WAKERING, *Vacuum Equipment and Techniques*, McGraw-Hill Book Co., Inc., New York, 1949.
7. REDHEAD, P. A., *Errors in the Measurement of Pressure With Ionization Gages*, 1960 Seventh National Symposium on Vacuum Technology Transactions, Pergamon Press, New York, 1961, pp. 108-111.
8. HARDING, JOHN T., and ROBERT H. TUFFIAS, *The Cryogenic Gyro*, Technical Release No. 34-100, Jet Propulsion Laboratory, Pasadena, California, August 1, 1960.
9. MORELLI, F. A., F. P. FEHLNER, and C. H. STEMBRIDGE, *Effects of Ultrahigh Vacuum on "Bacillus Subtilis Variety Niger"*, Research Summary No. 36-14, Jet Propulsion Laboratory, Pasadena, California, May 1, 1962, pp. 1-4.
10. BUCKLEY, D. H., and R. L. JOHNSON, *Gallium Rich Films as Boundary Lubricants in Air and in Vacuum to  $10^{-9}$  mm Hg*, prepared for ASLE-ASME Lubrication Conference, Pittsburgh, Pennsylvania, October, 1962.
11. BRYANT, PAUL J., *Vacuum Technology—Present and Future*, Vacuum Technology, September, 1962.
12. Space Programs Summary 37-17, Vol. IV, for the period August 1-October 1, 1962, Jet Propulsion Laboratory, Pasadena, California.
13. KRIEVE, W. F., "Fission Electric Cells," *Research Summary No. 36-8*, pp. 80-81, Jet Propulsion Laboratory, Pasadena, California, May 1, 1961.
14. WILSON, MELVIN N., JR., FRANCIS L. BALDWIN, and ERIC G. LAUE, *The JPL 25-Ft. Diameter Space Simulator*. Institute of Environmental Sciences 1962 Proceeding, Chicago, Illinois, pp. 105-118.
15. *Major Space Breakthrough by National Research Corp.*, News Release, National Research Corp., Cambridge, Massachusetts, August 23, 1962.

# 65. Techniques for Laboratory Studies of Modern Magnetism

By Floyd B. Humphrey

DR. FLOYD B. HUMPHREY is Research Group Supervisor in Guidance and Control Research Section of the Jet Propulsion Laboratory. In addition, Dr. Humphrey is a Senior Research Fellow on the California Institute of Technology Electrical Engineering Faculty. He was graduated with a B.S. in Chemistry from California Institute of Technology in 1950, and received an M.S. in Physics and Chemistry from the University of Minnesota in 1950-1951, and a Ph.D. in Chemistry from California Institute of Technology in 1956. A native of Greeley, Colorado, he is a member of the American Physical Society, Institute of Radio Engineers, and the AIEE.

## INTRODUCTION

The challenge of introducing modern electronics into space has opened a multitude of new problems and is, in many instances, breeding a new type of electronics. The influence is felt mainly in computer electronics, where computers are asked to make the many instantaneous decisions associated with all facets of a space mission. For unmanned missions, the problems are particularly severe since here missions lasting many years are contemplated. Magnetic devices are used as one of the main approaches for meeting this longevity challenge. They are particularly desirable for those missions of the future where a nuclear reactor is aboard the spacecraft, causing the associated high temperatures and radiation.

Thin magnetic films have been a fruitful vehicle for the investigation of this new type of magnetism. Compared to other magnetic structures, they require very little sample preparation and are generally ready for investigation immediately after fabrication. The equipment necessary for research is of moderate cost, and even the academic researcher can participate—in striking contrast to older types of magnetic research that required furnaces, roll-

ing mills, and hours of sample preparation. This paper will be confined to a discussion of those techniques and instruments used in research into the magnetic character of thin films. From such investigations, the magnetic character of other structures can be inferred.

## PREPARATION

The films are made by vacuum evaporation from permalloy. The useful compositions are from 15% iron, 85% nickel to 45% iron, 55% nickel. The thicknesses considered are from 100 to 5000 Å, with most consideration given to those of approximately 2000 Å. Usually the films are in the form of spots on a glass substrate. They are mirror-like and remain so for months without protection. When thicker than 150 Å, their electrical conductivity is as would be expected from bulk material before annealing (Ref. 1).

The evaporation technique most commonly used has been described by Blois (Ref. 2) and others (Ref. 3 and 4). A schematic diagram of the setup can be seen in Figure 65-1. Usually a zirconium or aluminum crucible is used to contain the melt. A charge of a few grams of either vacuum cast alloy or the proper propor-

tion of vacuum cast nickel and iron can be used. When heated to approximately  $1725^{\circ}\text{C}$  by either a resistance or an induction heater, evaporation takes place at such a rate that condensation onto a substrate 10 cm away occurs at approximately  $4000\text{ \AA}/\text{min}$ . The magnetic characteristics of the final film depend upon evaporation rate. A shutter system, shown in Figure 65-2, is generally used to shield the substrate while the melt is heating to temperature. It is desirable to maintain constant melt temperature during the time the film is actually being formed. It is also possible to evaporate directly from a filament of tungsten, although most investigations use induction heating. Soft glass is the most common substrate, and microscope slides are generally used. They must be cleaned and kept free from dust. Optimum films are obtained when the substrate is heated to approximately  $300^{\circ}\text{C}$ . Usually a mask is placed in front of the substrate to limit the area of the film, as can be seen in Figure 65-2.

The entire system indicated in Figure 65-1 is contained inside a vacuum system, usually a standard system as shown in Figure 65-3. The

pressure must be low enough to assure that the mean free path of the evaporated metal atom is long compared to the distance between the crucible and the substrate. Pressures between  $10^{-3}$  and  $10^{-6}$  mm Hg have been used.

One requirement peculiar to magnetic thin films is the necessity of establishing the direction of uniaxial magnetic anisotropy in the film by having a magnetic field in the plane of the substrate during evaporation and any subsequent anneal. The field in our system is provided by a pair of Helmholtz coils mounted outside the bell-jar. These are capable of supplying a field in excess of 50 Oe for an extended period of time.

The thickness of the film can be monitored by resistance which indicates the approximate thickness during evaporation. To obtain more detailed information about the evaporation, it is possible to use a micro-balance inside the vacuum system (Ref. 5). With the balance, the rate of evaporation and thickness can be determined and the temperature of the melt indicated. After the film is made, the thickness is usually measured optically or by X-ray fluorescence.

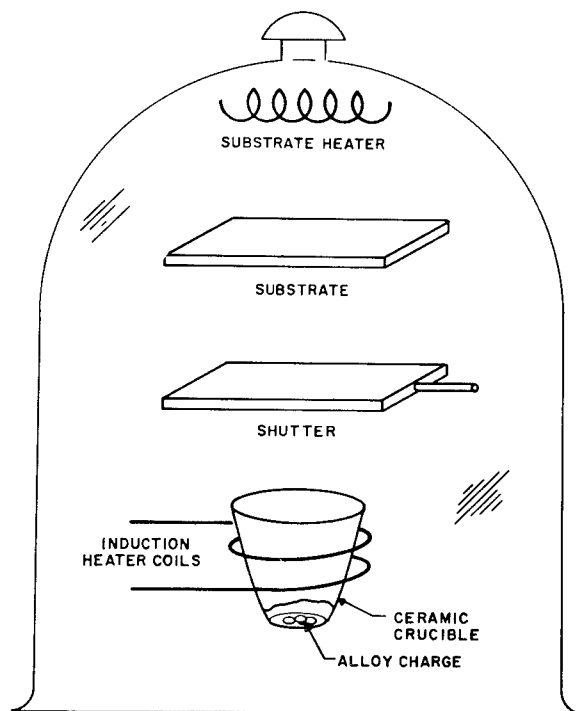


FIGURE 65-1.—Schematic of evaporation stand.

## HYSTERESIS LOOP

The most common magnetic measurement is the magnetization hysteresis loop. Instruments such as the one described by Crittenden, et al (Ref. 6), and Oguey (Ref. 7) are very useful and have the magnetic sensitivity necessary to operate with extremely thin films. The loop is usually presented directly on the screen of a cathode ray oscilloscope at the rate of 60 cps or less. A typical loop can be seen in Figure 65-4. On the abscissa the magnetic induction  $H$ , which is proportional to the current through the driving coil, is plotted. The ordinate is the flux density  $B$ . The value of  $B$  for a very large drive, either positive or negative, is the saturation flux density  $B_s$ . The value of  $B$  for zero drive is the remanent flux density  $B_r$ . The squareness may be defined as  $B_r/B_s$ . The value of  $H$  for zero magnetization; that is, the value of the drive that will just demagnetize the sample, is called the coercive force  $H_c$ .

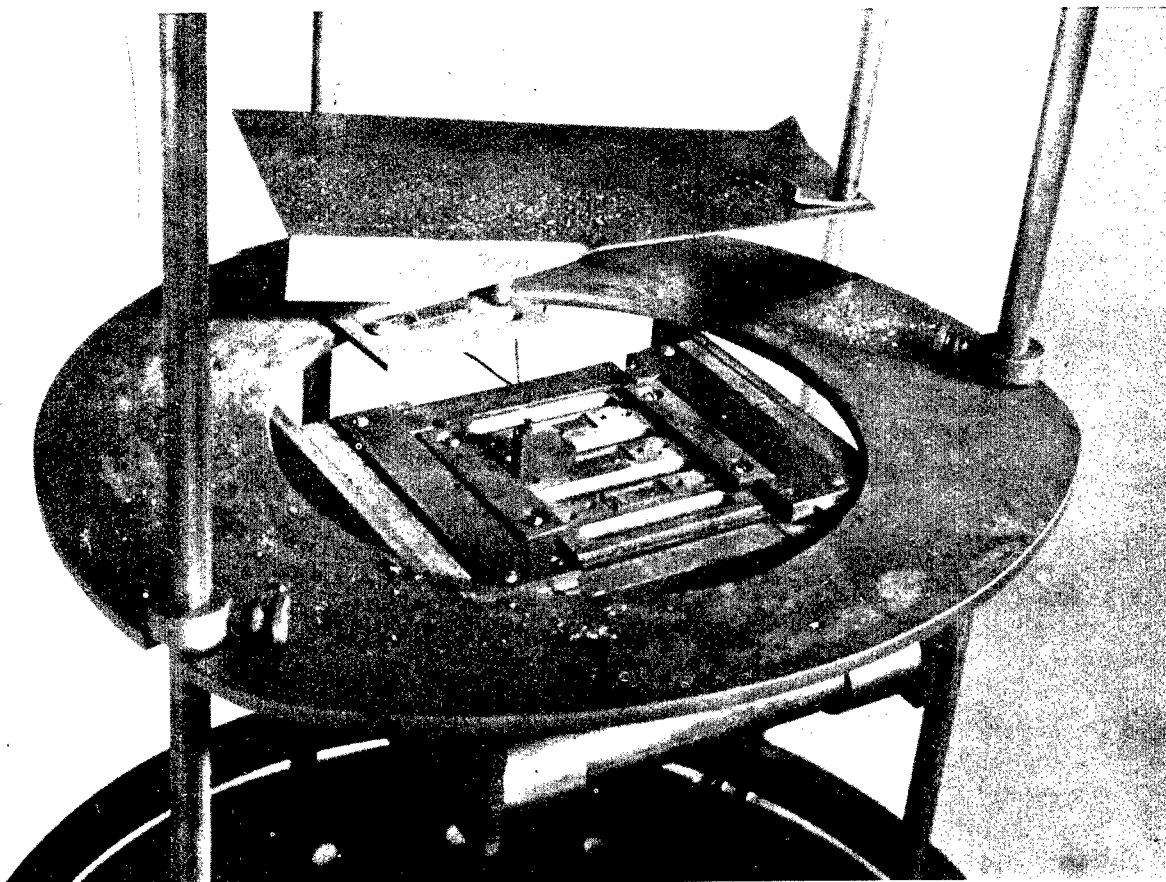


FIGURE 65-2.—Shutter system.

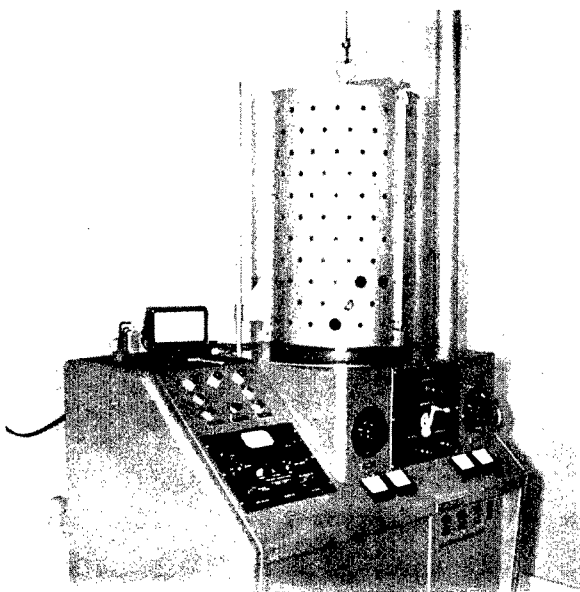


FIGURE 65-3.—Standard vacuum stand.

A photograph of our loop tracer is shown in Figure 65-5. The large coil pair cancel stray fields at the sample, a necessary procedure when working with thin films. The drive coils and pickup coils are smaller and can be seen in Figure 65-6. An operational amplifier provides the necessary integration. With a 1500 turn pickup loop and an open loop gain in the

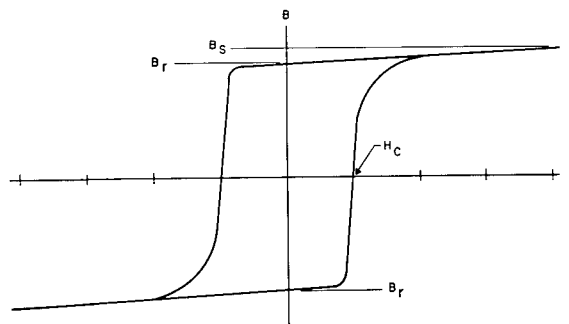


FIGURE 65-4.—Typical hysteresis loop.

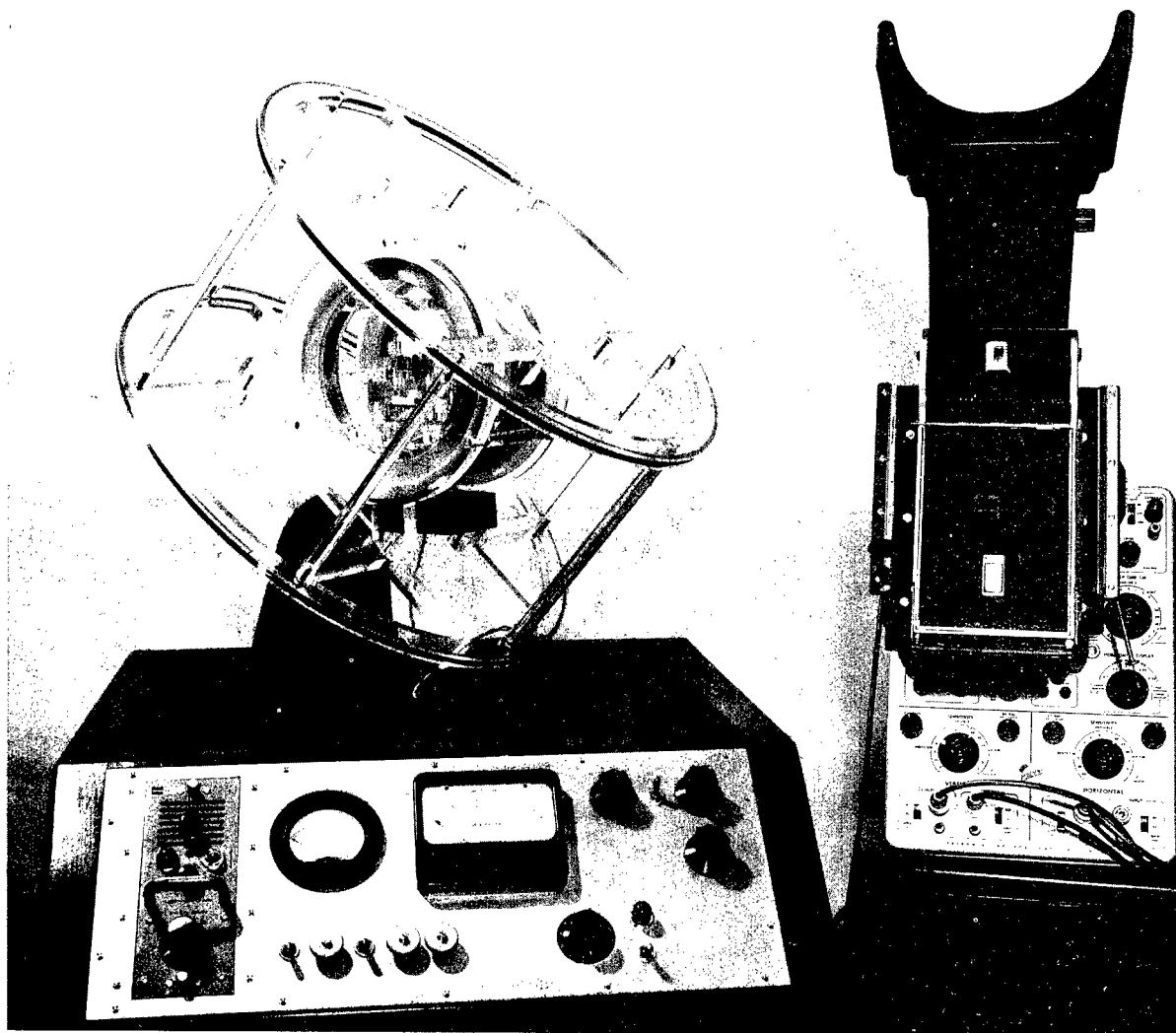


FIGURE 65-5.—Loop tracer.

amplifier of about  $10^7$ , the minimum flux detectable is  $10^{-3}$  maxwell. Trinagular drive is normally used at 17 cps. Manual control is also provided so that the field can be changed very slowly when the loops are steep.

A hysteresis loop taken along the easy axis of magnetization can be seen at the top of Figure 65-7. This figure was taken from a photograph of the oscilloscope face while sweeping the field very slowly. The Barkhausen pulses can be observed. Films typically have loops which are much squarer than those of ordinary magnetic material. In the center of Figure 68-7, taken as a double exposure, is the hard direction loop or transverse loop. The charac-

ter of the loop is considerably changed when the drive and pickup are perpendicular to the easy direction of magnetization. The typical loops of Figure 65-8 were taken with increasing drive in this perpendicular condition. As mentioned previously these films all contain a uniaxial anisotropy. The mechanism for this anisotropy is not well understood. The effect of this, however, can be characterized by measuring the quantity usually called the anisotropy field  $H_k$ . With the film such that drive and pickup perpendicular to the easy axis, the drive current is adjusted to be so small that a single sloping line is seen on the oscilloscope, as in the upper loop of Figure 65-8. The slope of this

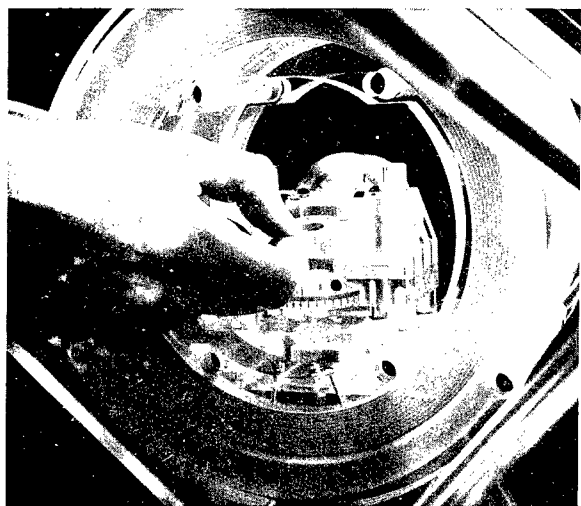


FIGURE 65-6.—Inner coils of loop tracer.

line is noted. The drive is then increased until the same is saturated as in the next loop of the Figure. The value of  $B_s$  for the sample is noted.  $H_k$  is defined as the field for which the extrapolated low drive slope intersects the value of  $B_s$ .

#### Torque Balance

For many years the magnetic torque balance has been an important instrument in the investigation of magnetic characteristics of materials. In 1937 H. J. Williams (Ref. 8) surveyed the usefulness of such an instrument for measuring the anisotropy constant, coercive force, and rotational hysteresis losses in magnetic materials. The evolution of the instrument continued gradually for over 20 years until R. F. Penoyer

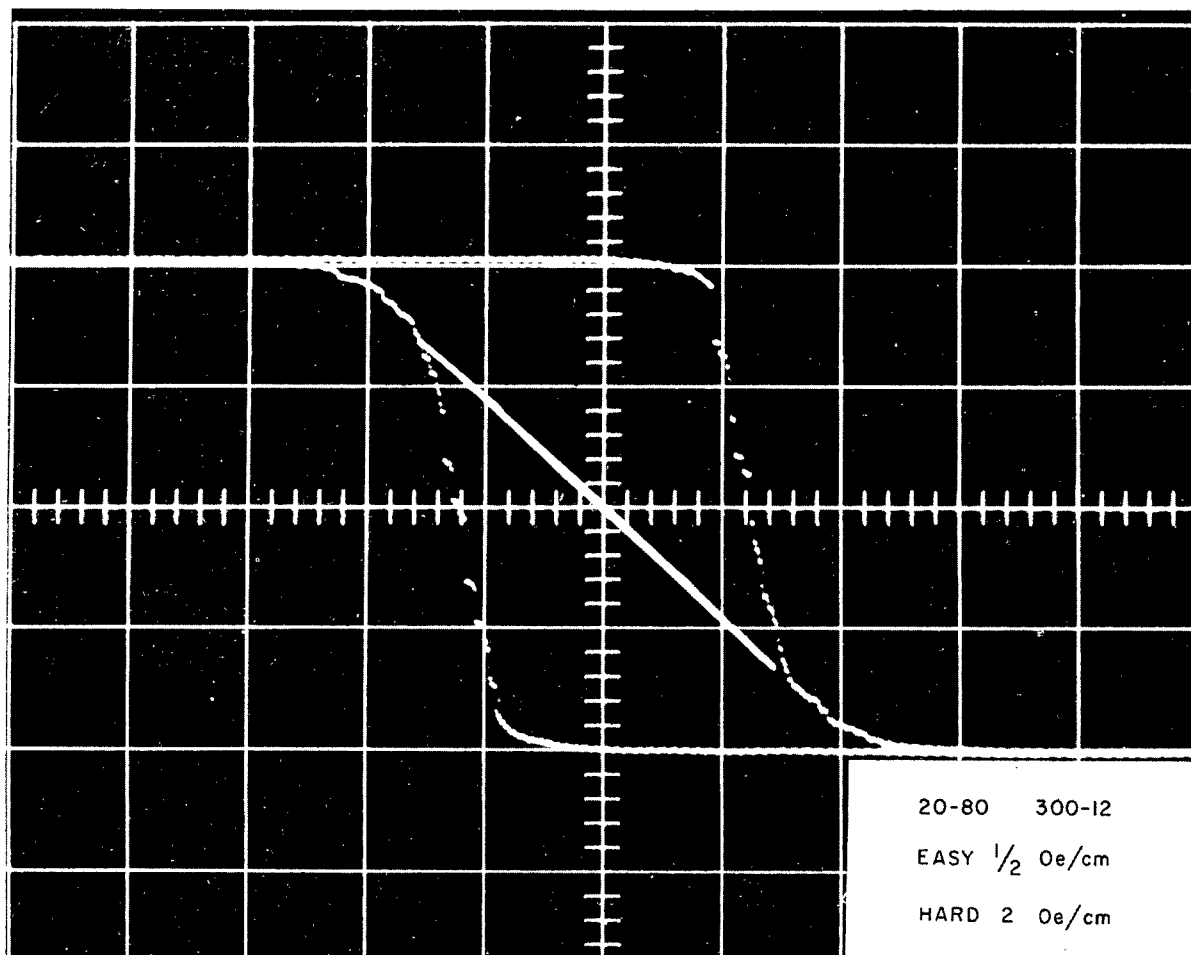


FIGURE 65-7.—Hysteresis loop.

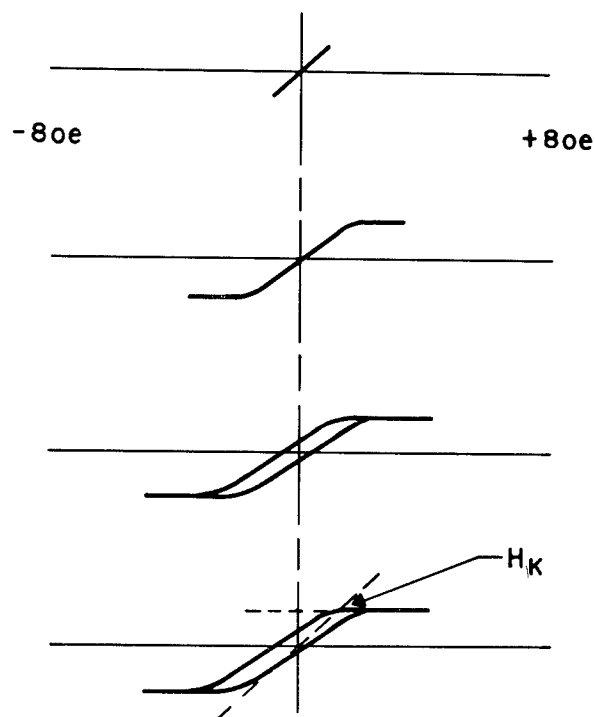


FIGURE 65-8.—Typical transverse loops.

(Ref. 9) incorporated electronics into the instrument to make it automatically self-balancing. E. L. Boyd (Ref. 10) increased the sensitivity of the automatic model and adapted it to the investigation of thin magnetic films as did W. D. Doyle (Ref. 11). Several others have adapted the manually-balanced torque meter for thin films (Ref. 12-16).

The instrument described here uses (Ref. 17) the principle of the Penoyer and Boyd instruments, but has a unique fused-silica suspension and servo-system that allows an increase in the sensitivity of about three orders of magnitude to  $10^{-6}$  dyn/cm, with a resolving time of a fraction of a second. It is designed principally for the investigation of thin permalloy films and can measure the torque either perpendicular or parallel to the surface of the film. The saturation magnetization  $M_s$ , remanent magnetization  $M_r$ , anisotropy constant  $K$ , and coercive force  $H_c$  can be measured directly, allowing calculation of the anisotropy field  $H_K$  and the squareness.

The measurements of anisotropy field are of particular interest because the anomalous uniaxial anisotropy has continued to be an interest-

ing and baffling phenomenon (Ref. 18). It is generally assumed, as was first thought by Smith (Ref. 19), that the classic Stoner-Wohlfarth model (Ref. 20) which was formulated to describe small single-domain particles, also describes the anisotropy in thin films. For a field in the plane of the film, the anisotropy can be defined in terms of energy (per unit volume) of the sample in the presence of a magnetic field as follows:

$$E = K \sin^2 \varphi - HM \cos (\alpha - \varphi)$$

where  $K$  is the anisotropy constant assuming uniaxial anisotropy,  $H$  is the magnetic field at some angle  $\alpha$  from anisotropy axis, and  $M$  is the magnetization (per unit volume) of the sample at some angle  $\varphi$  from the anisotropy axis. At equilibrium  $dE/d\varphi = 0$  so that

$$MH \sin (\alpha - \varphi) = K \sin 2\varphi \quad (2)$$

The torque ( $L = \vec{M} \times \vec{H}$ ) per unit volume for this case is equal to

$$L = -MH \sin (\alpha - \varphi) = -K \sin 2\varphi \quad (3)$$

where the minus sign indicates that the torque is in a direction of decreasing  $\alpha$ . Depending upon the particular circumstances, as will be discussed below, the torque perpendicular to the plane of the film is a sensitive indication of the remanent magnetization or of the anisotropy.

For fields small compared to  $4\pi M$  (so that the magnetization is in the plane of the film), another configuration is useful to measure the torque parallel to the plane of the substrate. For this case

$$L = -MH \sin \alpha \quad (4)$$

where  $\alpha$  is now the angle between the field and the substrate, and the torque is parallel to the plane of the film and perpendicular to the easy axis. If the easy axis is rotated so that it is parallel to the torsion axis (i.e., perpendicular to the field), Eq. (4) is applicable only for fields where  $H \cos \alpha$  is greater than  $2K/M$ . For  $(H \cos \alpha)$  less than  $2K/M$ , the torque along the easy axis ( $z$ -axis) can be calculated in similar manner to be

$$L_z = \frac{M^2 H^2}{4K} \sin 2\alpha \quad (5)$$

Depending upon the particular situation, the torque observed parallel to the plane of the

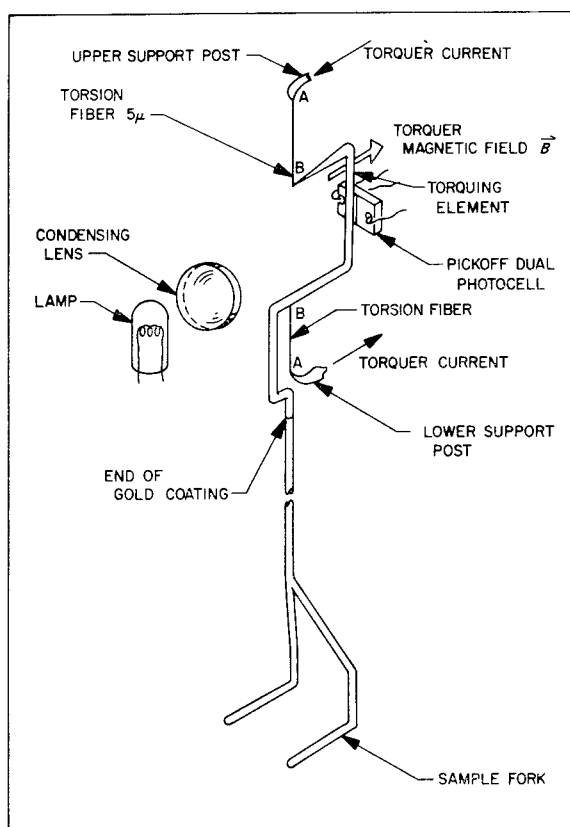


FIGURE 65-9.—Schematic of torque meter.

film when a field is applied at some angle to the plane may be a sensitive measure of the magnetization  $M$ , the anisotropy field  $H_K$ , and the coercive force  $H$ .

The operation of torque balance can best be understood by referring to Figure 65-9. The shadow of the torquing element (B-B) caused by the lamp and condensing system falls on the dual photocell. The torquing element is in a uniform magnetic field as indicated, so that current through the element causes a torque about the axis defined by the torsion fibers. The output of the photocell is connected, through a high-gain servo amplifier, to the current through the torquing element, so that this output remains centered on the photo pickoff. The current is proportional to torque and can be measured as indicated in Figure 65-10. An auxiliary hanger, shown in Figure 65-11, allows measurement of torque along a torsion axis parallel to the plane of the substrate. For torques perpendicular to the plane, the sample

is placed directly on the sample-carrying fork indicated in Figure 65-9. A photograph of completed assembly is shown in Figure 65-12. The earth-bucking cube coils and the rotating field coil can be seen.

Figure 65-13 shows a typical set of torque curves taken perpendicular to the plane of the film. These curves are from a film 40 Å thick, deposited in about 2 sec onto a glass substrate at 300° C. The composing is 76.2% nickel and 23.8% iron. A typical measurement parallel to the plane of the film using the auxiliary hanger is shown in Figure 65-14. Here the coercive force is measured. The details of these and other measurements made with the torque balance can be found in Ref. 17-21.

### MAGNETIC DOMAINS

One of the more exciting static observations in magnetism is the direct observation of magnetic domains. The three methods that are in general use are the Bitter technique, the Kerr technique and the Faraday technique. The Bitter powder pattern technique (Ref. 22) consists of placing a colloidal solution of magnetite in water upon the carefully-prepared surface of the specimen. There are high field gradients at the wall caused by a divergence of the magnetization which attract the ferromagnetic magnetite. Using dark field or oblique illumination, the concentration of colloidal particles can be observed defining the walls. A thin film is a fine specimen for this experiment since its surface needs no preparation. This technique has been used extensively by Williams and Sherwood (Ref. 23). A sample of their results can be seen in Figure 65-15.

Another technique, utilizing the longitudinal magneto Kerr effect, was first used for films by Fowler, et al. (Ref. 24). This scheme allows optical observation of the domain rather than the walls. The arrangement can be most easily understood by considering Figure 65-16. Polarized white light is used to illuminate the sample at about a 60-deg angle of incidence. The reflected light passes through an analyzer and then through a simple lens system to the eye or a TV camera. The plane of polarization of the reflected light can be rotated a few degrees depending upon the direction of the field



# LABORATORY TECHNIQUES

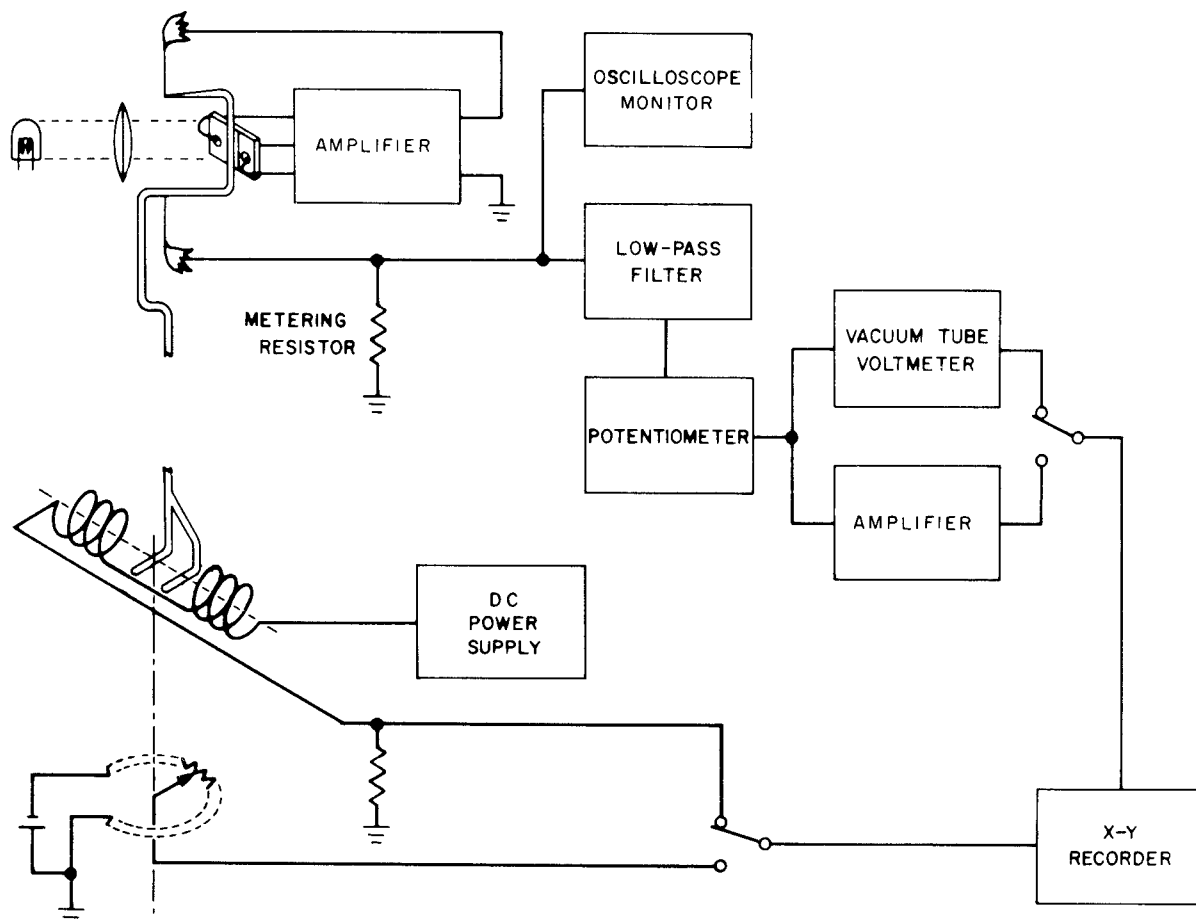


FIGURE 65-10.—Block diagram.

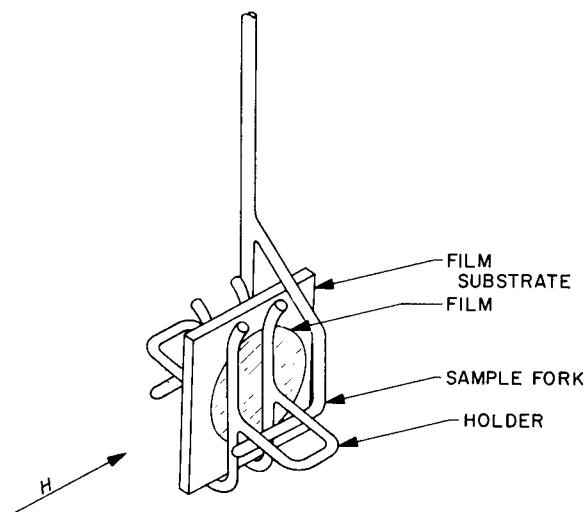


FIGURE 65-11.—Auxiliary hanger.

in the sample. Again nickel-iron films require no surface preparation, making this technique the most popular one for magnetic films.

A photograph of our equipment can be seen in Figure 65-17. It uses an Osram high-pressure mercury arc for illumination, Oland-Thompson prisms for polarization, and closed circuit television for observation. The television not only facilitates observation but increases contrast electronically. The cube coil system shown nullifies stray fields and establishes the necessary working fields used during the investigations. A photograph of some typical domain patterns is shown in Figure 65-18.

For very detailed observation where high magnifications are required, the Kerr effect loses

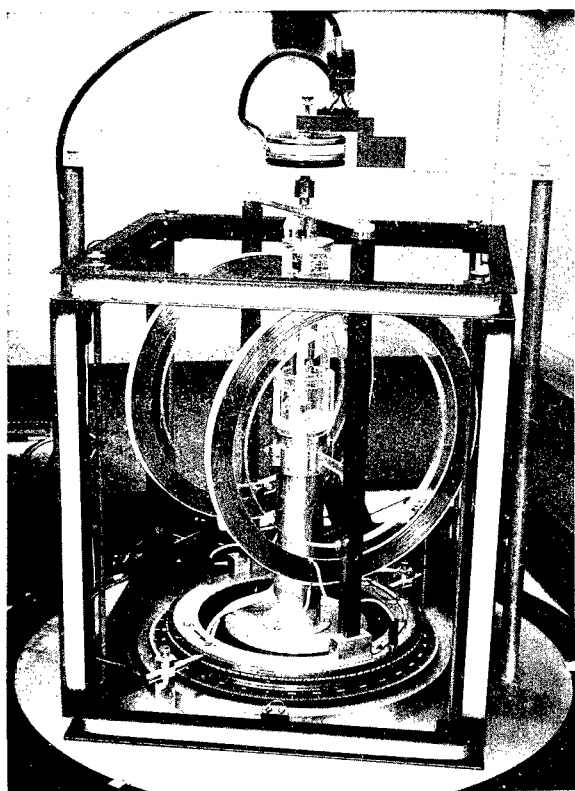


FIGURE 65-12.—Automatic torque balance.

contrast because of the very slight rotation. Either the Bitter technique must be used or, for films thinner than 700 Å, the Faraday effect can be utilized. The principle is essentially the same as before, except that now the light goes completely through the film at some angle, usually 45 deg. Interesting domain patterns result (Ref. 25), as can be seen in Figure 65-19.

### DYNAMIC FLUX REVERSAL

The usual pulse experiment consists of saturating the sample with a field of about ten times the coercive force, and then reversing the magnetization by applying a step field pulse in the opposite direction. The reversal time  $\tau_s$  is defined as the interval between the time when 10% of the total flux has reversed and the time when 90% of the total flux has reversed. The inverse of this reversal time can then be plotted as a function of the drive field  $H_c$ , as seen in Figure 65-20. It is possible to change the initial conditions by applying a dc field in the plane of the film and perpendicular to the drive

field and, hence perpendicular to the easy axis of uniaxial anisotropy. Such a transverse field changes the reversal time for a given drive as is noted in Figure 65-20, where the transverse field  $H_T$  is included as a parameter. This behavior is unique for thin films made as described.

The equipment used for such a given experiment involves a number of compromises which depend on the specific requirements for the experiment. The general character of all the pulse equipment is the same, however. A drive field is required. The amplitude of the field must be constant and the same over the entire sample compared to the shortest time measured in the experiment. It must be possible to conveniently adjust the amplitude from point to point. The duration of the pulse does not matter as long as it is longer than the time being measured. The detection equipment must have a response time that is shorter than the times being measured and a sensitivity capable of detecting the very small flux changes associated with thin films. It is usually necessary to integrate since the flux rather than rate of change of flux is of interest.

Two types of field generation equipment are in general use. The first is the stripline pulser used when the ultimate field rise time is desired. Such a system is indicated schematically in Figure 65-21. A high-voltage power supply charges a length of coaxial cable to twice the voltage of the pulse desired through a series charging resistor. A relay with mercury wetted contacts discharges the line through a length of cable, hence through a stripline section to a termination. Generally, the relay is operated at 60 cps. The length of the cable has delay one-half the time length of the desired pulse. It should also have a center conductor with a resistance small compared to the impedance of the system or compatible with the voltage drop that can be tolerated. The value of the series charging resistor is a compromise between charging the cable completely and having the dc current through the relay small. Although the relay will close and allow a very high current (thousands of amperes), it will open only a few hundred milliamperes.

# LABORATORY TECHNIQUES

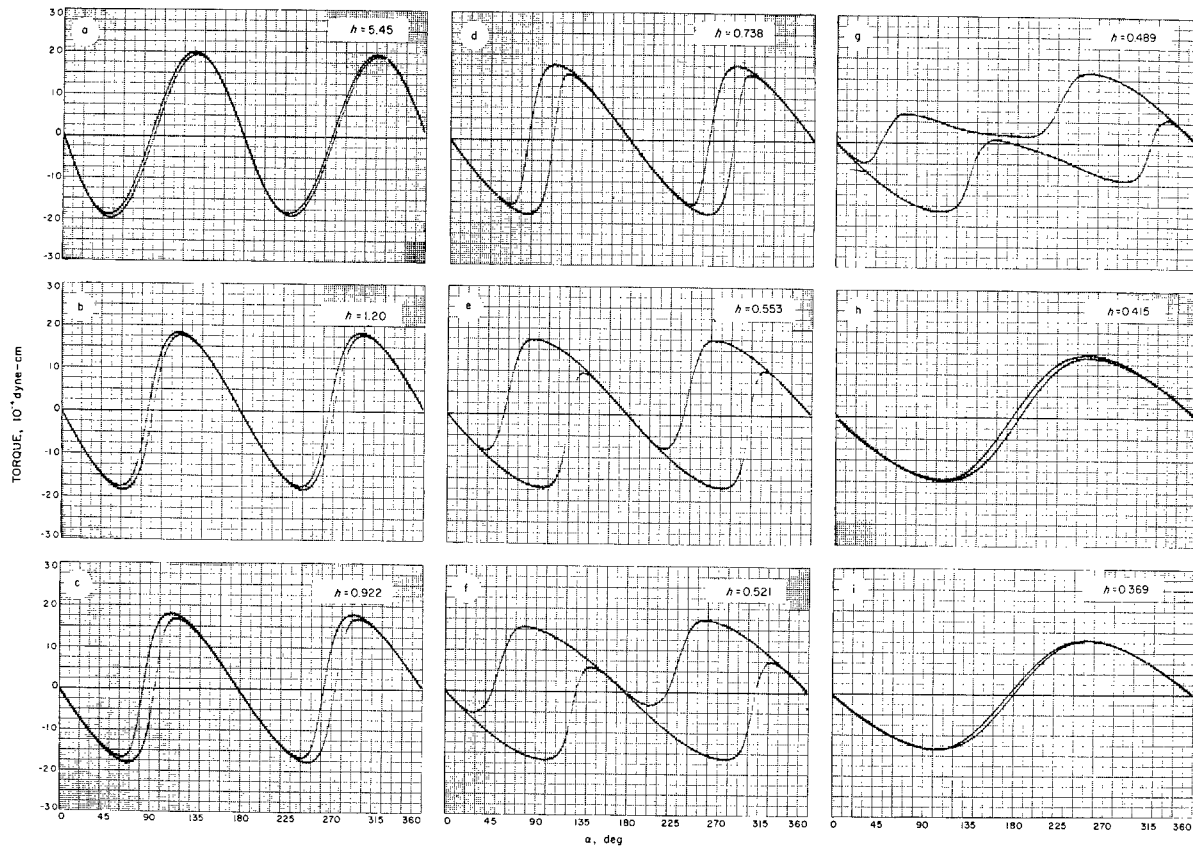


FIGURE 65-13.—Typical set of torque curves.

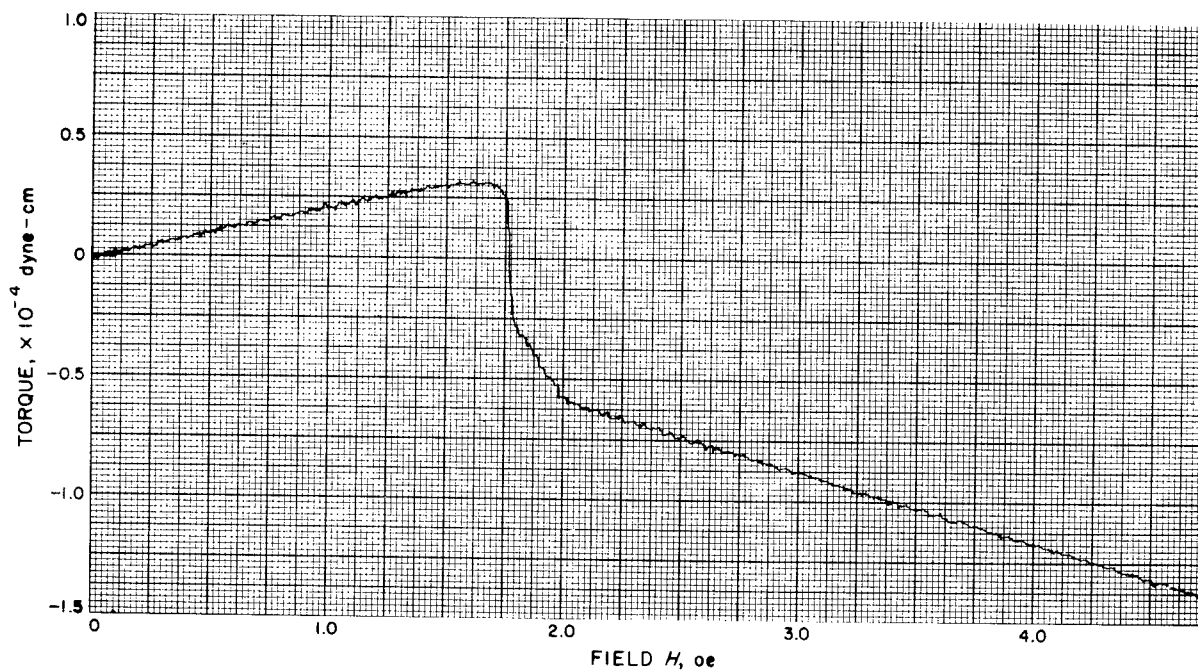
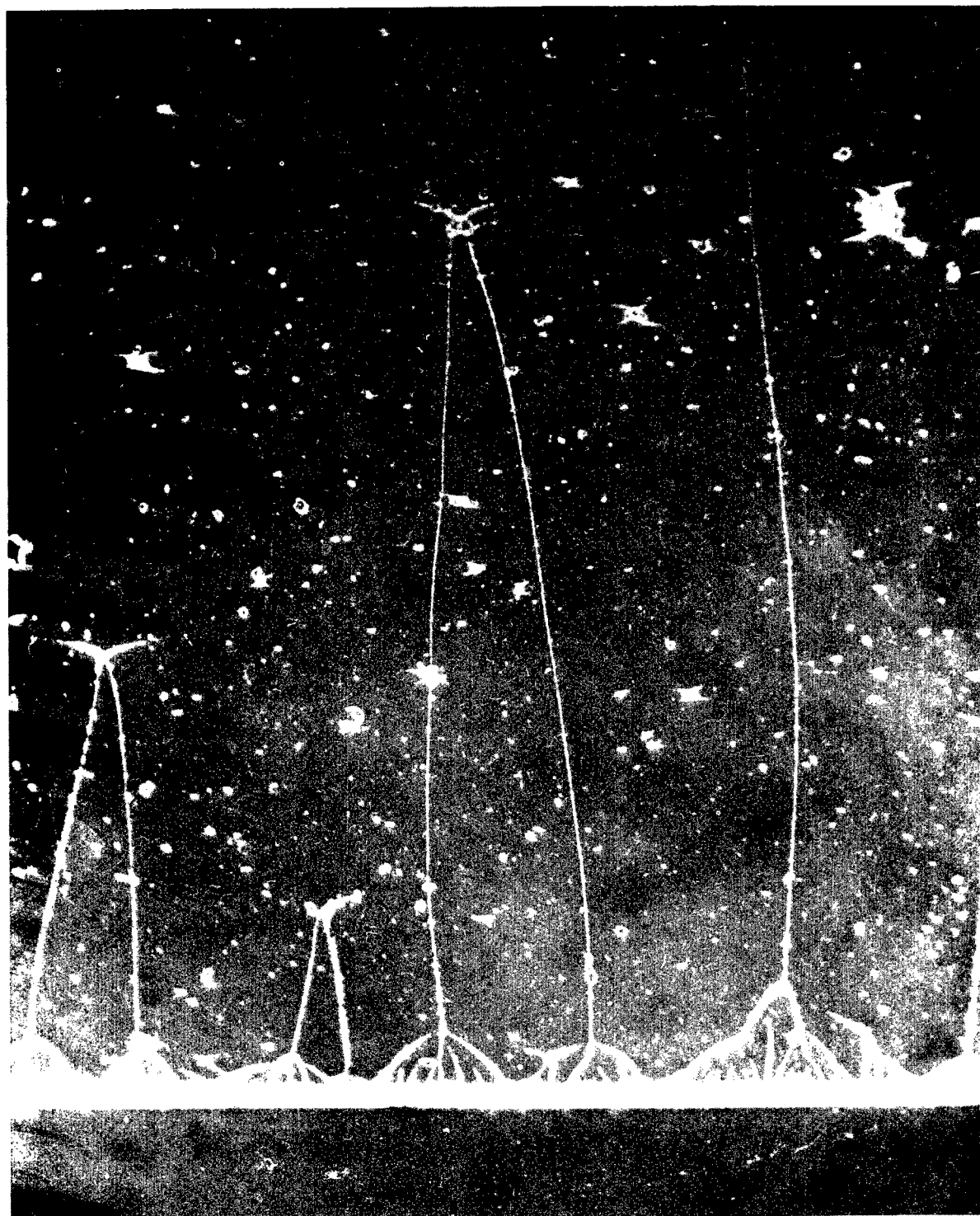


FIGURE 65-14.—Measurement of the coercive force.



0.1 MM

1300 Å FILM OF Fe-Ni-Mo

FIGURE 65-15.—Bitter powder pattern.

# LABORATORY TECHNIQUES

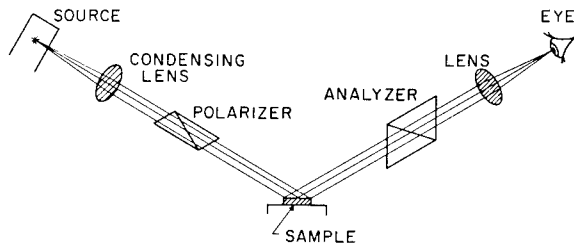


FIGURE 65-16.—Schematic of Kerr effect apparatus.

The relay is usually in a coaxial holder which can be fabricated in a number of straightforward ways. The relay body is a commercial item. It will generally hold off approximately 4000 v. Operating at 60 cps is within the capabilities of most relays.

The stripline affords a convenient transmission line section of the type where the magnetic field is uniform and accessible. A typical section is shown in Figure 65-22. The dimensions used depend upon the impedance in a straightforward way (Ref. 26). The pickup must be insensitive to the change in field brought on by the onset of the pulse. Generally two loops are used connected in series opposition, as shown in Figure 65-23. Since the use of the stripline pre-

supposes interest in fast events, normally only single turn coils are used, connected as in Figure 65-23. The series resistors prevent the loops from being a shorted turn.

It is usually most convenient to integrate immediately with either an RC integrator or an electronic integrator. Since again frequency response is presumed to be important, the RC integrator is the easiest. The voltage out is very small, however, putting a severe sensitivity requirement upon the rest of the detection equipment. A transistorized Miller integrator has been constructed (Ref. 27) which considerably simplifies the matter. It has a response time of 3 nsec and a decay time of 10 microsec with a capacity of 30 mv-microsec.

The rest of the detection system depends upon film thickness. Distributed amplifiers (HP 460 A and B) can be used or transistorized amplifiers with slightly better response time. The voltage rise can then be observed on a sampling oscilloscope. The ultimate in sophistication can be obtained by using the Tektronix 567 digital readout where the rise time is automatically recorded with nixie tubes.

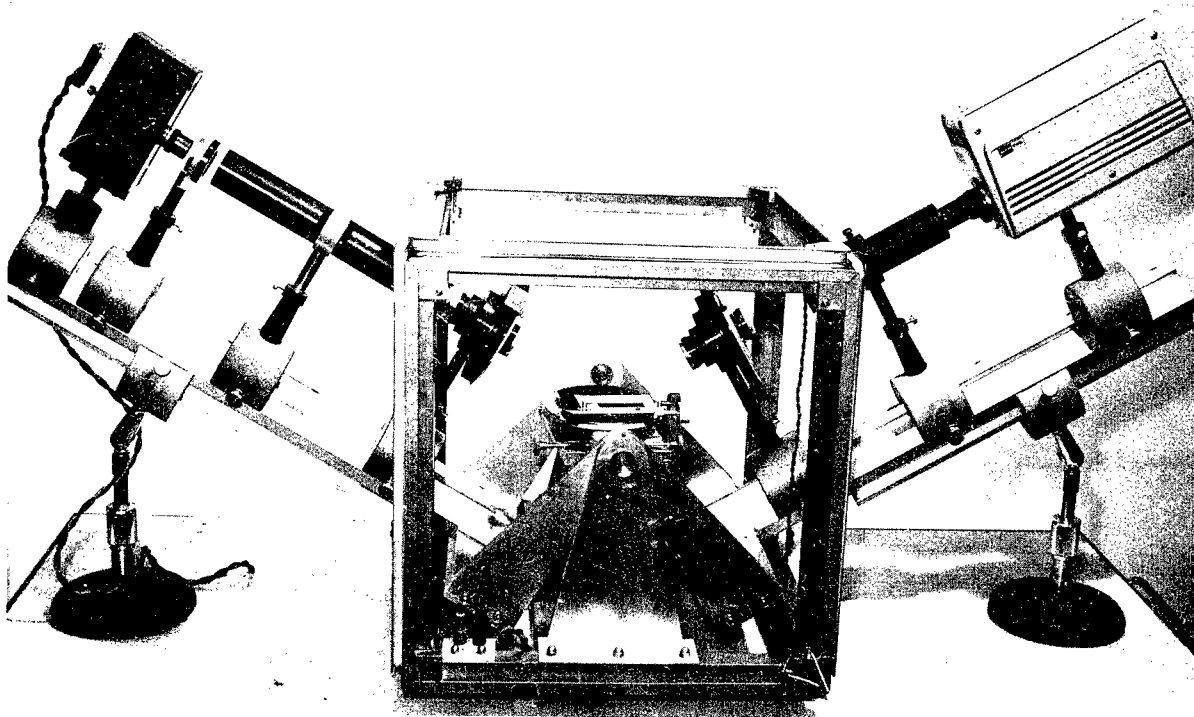


FIGURE 65-17.—Kerr magneto optic domain viewer.

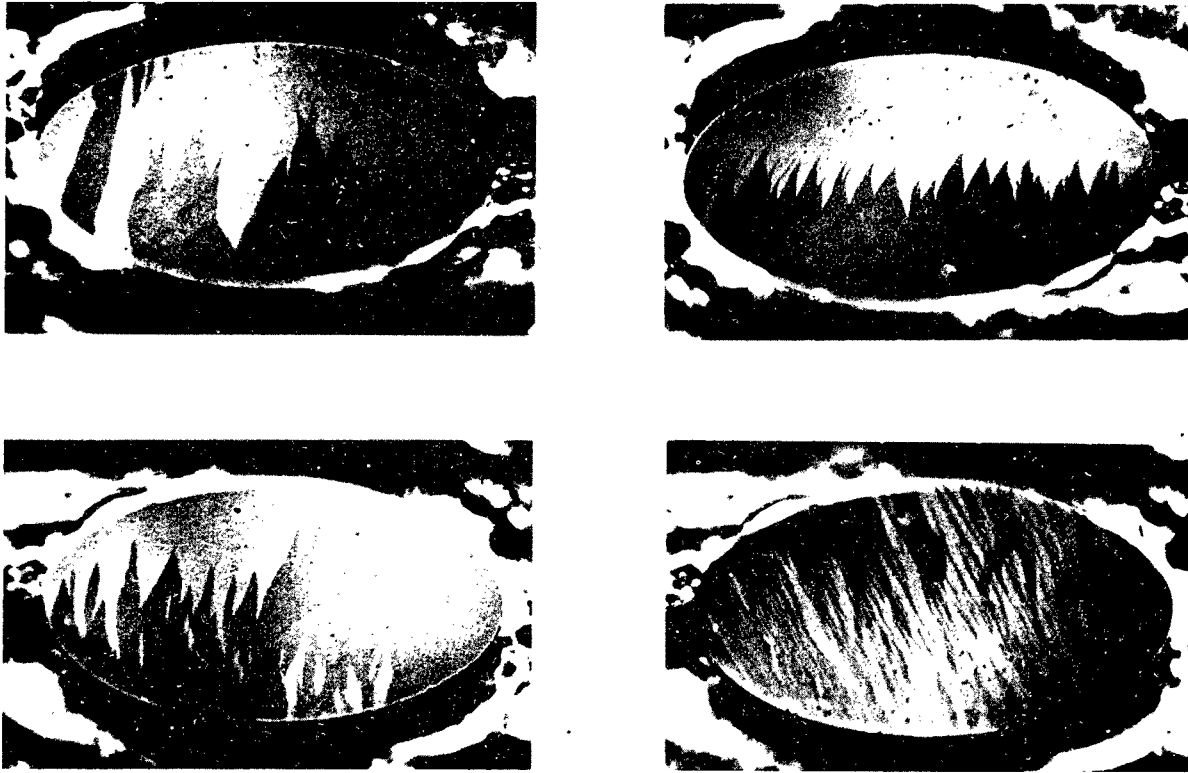


FIGURE 65-18.—Typical domain patterns.

A photograph of the stripline and setting coils is shown in Figure 65-24. Various other coils provide the logical fields for nullifying stray fields, providing the transverse fields, etc.

By not demanding the fastest system, the detection problem can be eased. Multiturn pickup loops can be used relieving the amplifier problem. Standard vacuum tube pulsers can feed distributed transmission lines to give the field. One such setup can be seen in Figure 65-25. The 20-turn pickup and distributed solenoid can be used for films as thin as 100 Å to investigate the velocity of Néel walls (Ref. 28). The entire electronics setup is illustrated in Figure 65-26.

Of course, in the investigation of the dynamics of flux reversal, it is not enough to just measure the switching time. There are many pulse experiments that can be used to infer the

reversal mechanism. The interrupted pulse experiment (Ref. 29) is a particularly important one to identify domain wall motion. The simultaneous observation of the longitudinal and transverse loops (Ref. 30) is particularly important in the identification of uniform rotations. These experiments, however, are all performed using the same type of equipment as discussed previously.

#### CONCLUDING REMARKS

In summary, it is proposed that investigations in modern magnetism are both interesting and timely. Participation can be achieved with a limited budget. The most important instruments in a laboratory devoted to such a study are a loop tracer, a torque balance, a Kerr domain viewer, and a pulse flux reverser.

LABORATORY TECHNIQUES

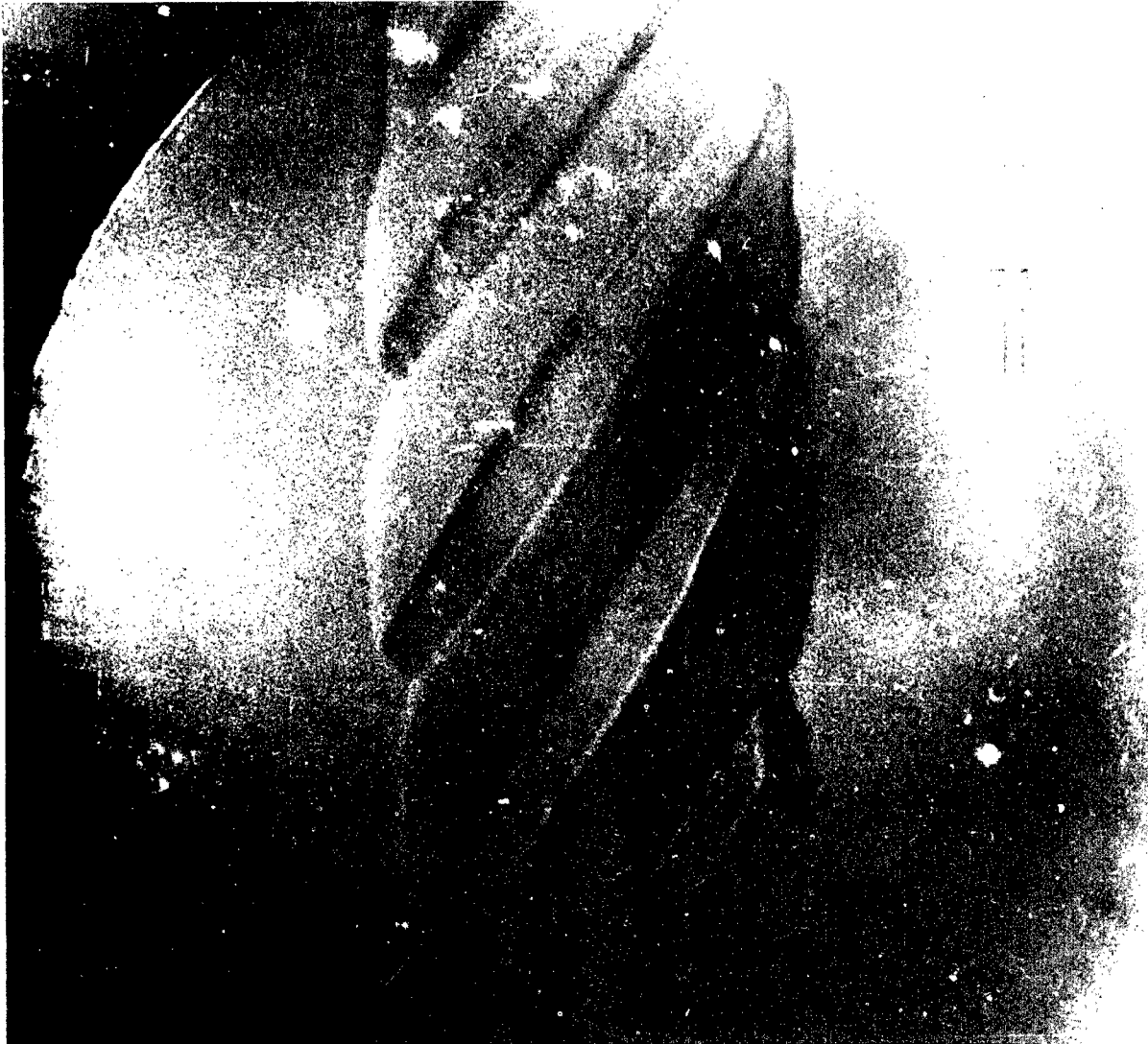


FIGURE 65-19.—Faraday effect patterns.

# LABORATORY STUDIES OF MODERN MAGNETISM

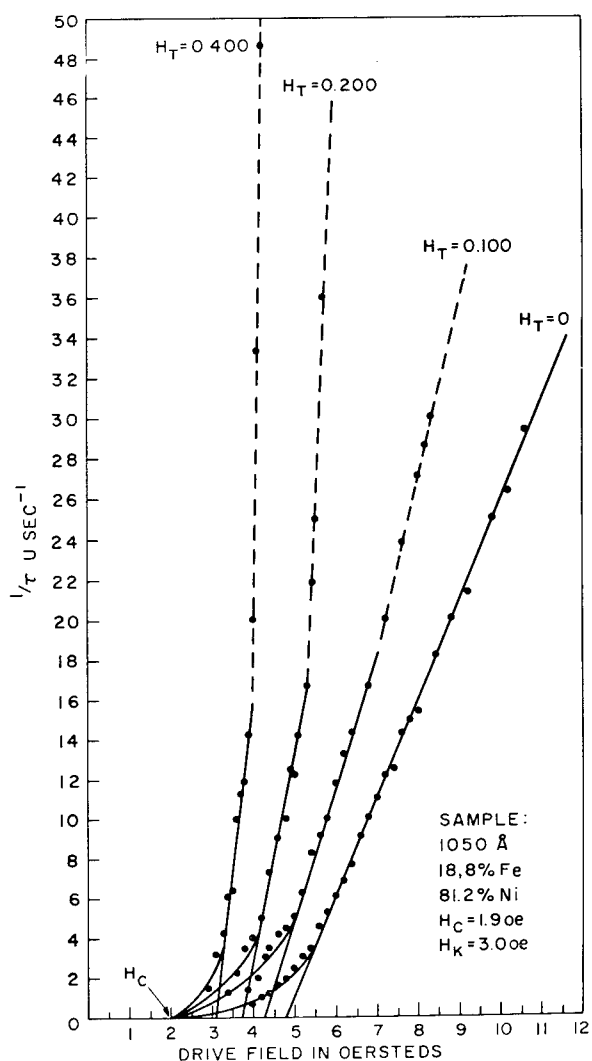


FIGURE 65-20.— $1/\tau$  vs.  $H$ .

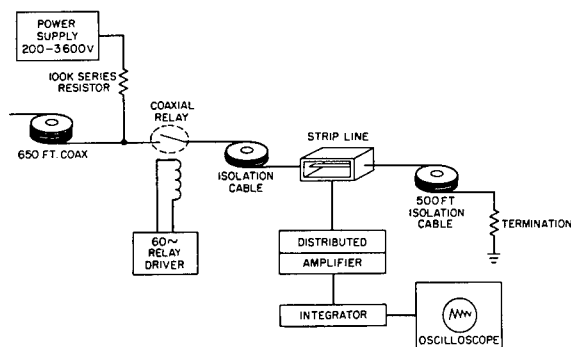


FIGURE 65-21.—Block diagram of stripline pulser.

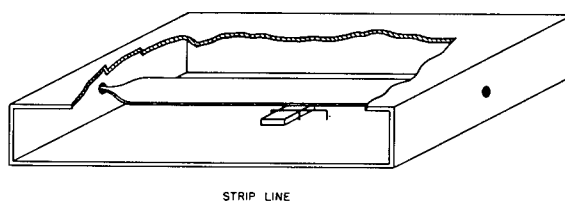


FIGURE 65-22.—Stripline cutaway.

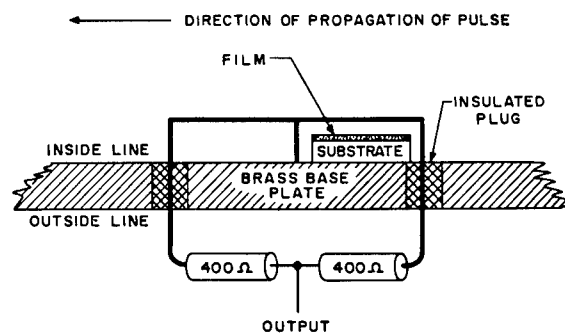


FIGURE 65-23.—Loops in stripline.



LABORATORY TECHNIQUES

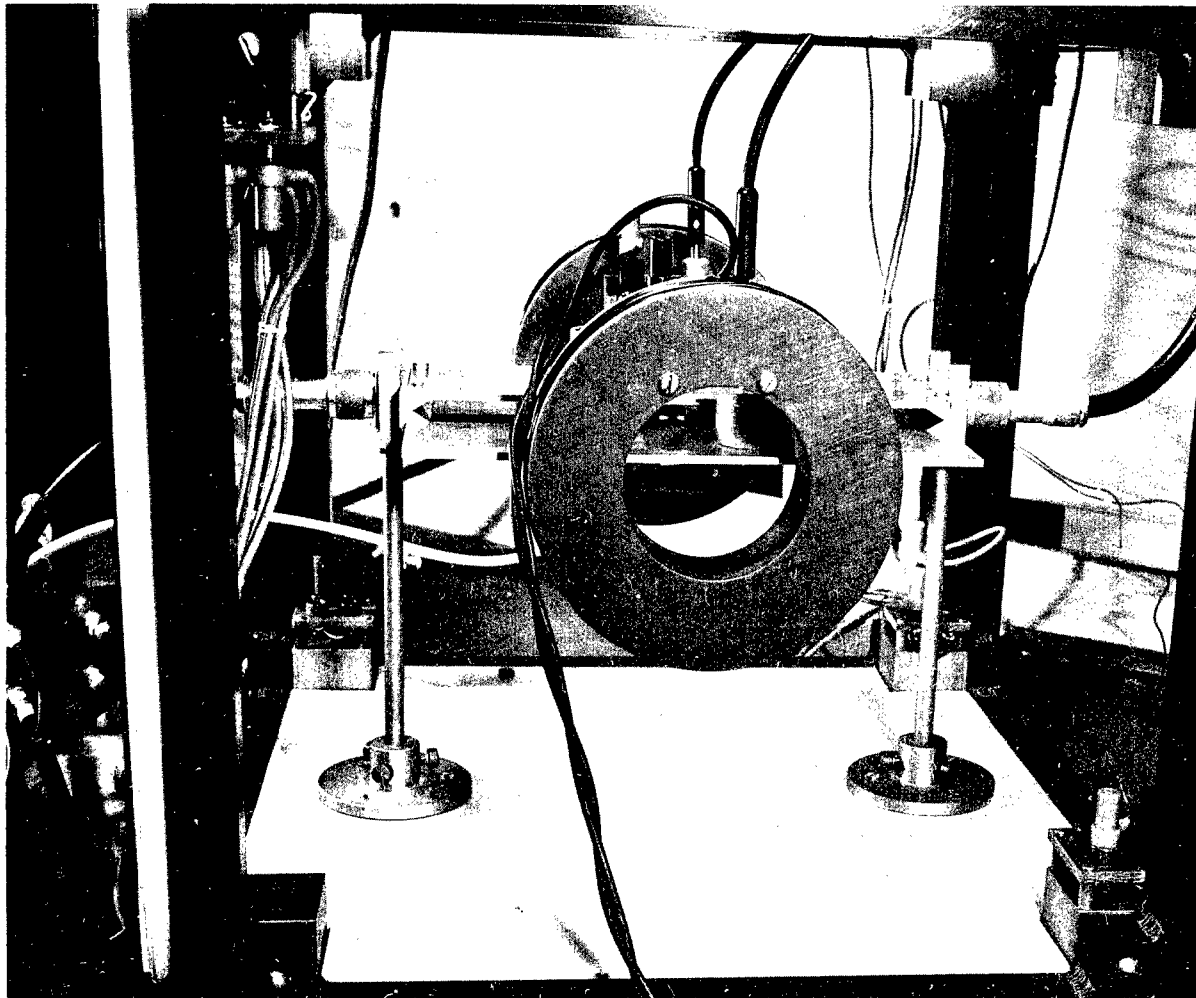


FIGURE 65-24.—Stripline.

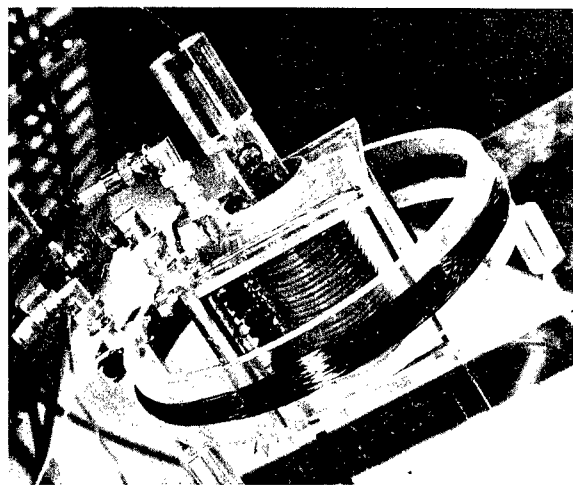


FIGURE 65-25.—Multiturn pickup and distributor solenoid.

# LABORATORY STUDIES OF MODERN MAGNETISM

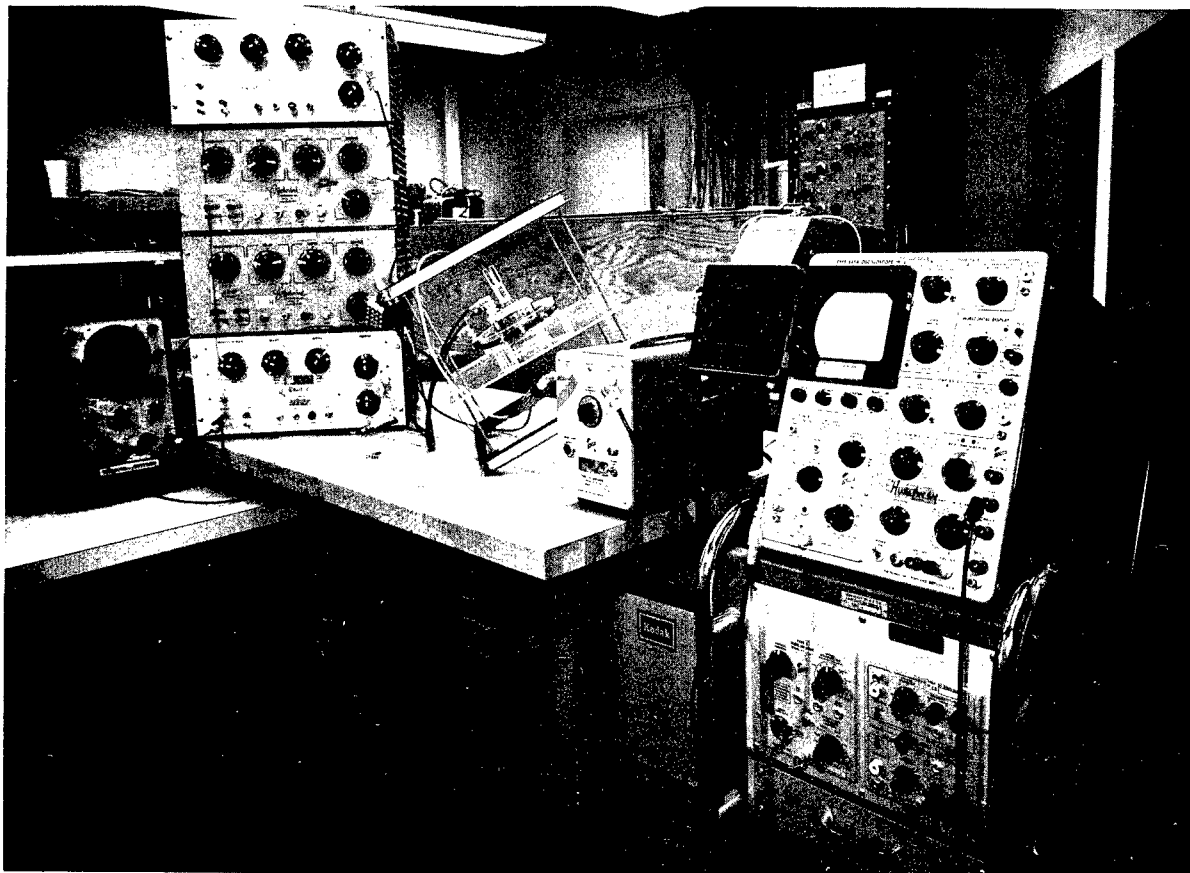


FIGURE 65-26.—Electronics for observing very thin films.

## REFERENCES

1. HUMPHREY, F. B., F. W. REYNOLDS and G. R. STILLWELL, Transactions Vacuum Society Symposium 1958, Pergamon Press, p. 204.
2. BLOIS, M. S., JR., J. Apply. Phys., 975 (1955).
3. CRITTENDEN, JR., E. C., and R. W. HOFFMAN, Rev. Mod. Phys. 25, 310 (1953).
4. CONGER, R. L., and F. C. ESSIG, Phy. Rev. 104, 915 (1956).
5. HOEDE, A. L., Proceedings of Third Symposium on Vacuum Balance Techniques, Los Angeles, Oct. 31, 1962, to be published.
6. CRITTENDEN, E. C., A. A. HUDIMAC and I. R. STROUGH, Rev. Sci. Instru. 22, 872 (1951).
7. OGUEY, H. J., Review of Scientific Instruments 31, 701.
8. WILLIAMS, H. J., Rev. Sci. Instru. 8, 56 (1937).
9. PENOYER, R. F., Rev. Sci. Instru. 30, 711 (1959).
10. BOYD, E. L., IBM J. Res. Devel. 4, 116 (1960).
11. DOYLE, W. D., J. E. RUDISILL, and S. SHTRIKMAN, J. Appl. Phys. 32, 1795 (1961).
12. TAKAHASHI, M., et al., J. Phys. Soc. Japan 14, 1959 (1959).
13. NEUGEBAUER, C. A., Phys. Rev. 116, 1441 (1959).
14. GRAHAM, JR., C. D., and J. M. LOMMEL, Proc. Int. Conf. on Magnetism, Koyoto, 1961.
15. ANDRA, W., et al, Naturwissenschaften 46, 257 (1959).
16. REINCKE, W., Z. Physik 137, 169 (1954).
17. HUMPHREY, F. B., and A. R. JOHNSTON, Technical Report No. 32-321, Jet Propulsion Laboratory, Aug. 1962.
18. TAKAHASHI, M., J. Appl. Phys. 33, 110 (1962).

#### LABORATORY TECHNIQUES

19. SMITH, D. O., Conference on Magnetism and Magnetic Materials, Boston, 1956. (AIEE Special Publication, Feb. 1957) p. 625.
20. STONER, E. D., and E. P. WOHLFARTH, Phil. Trans. Roy Soc., London, *240A*, 599 (1948).
21. HUMPHREY, F. B., and A. R. JOHNSTON, Rev. Sci. Instru. in press.
22. WILLIAMS, BOZORTH, and SHOCKLEY, Phys. Rev. *75*, 155 (1949).
23. WILLIAMS, H. J., and R. C. SHERWOOD, J. Appl. Phys. *28*, 548 (1957).
24. FOWLER, JR., C. A., E. M. FRYER and J. R. STEVENS, Phys. Rev. *104*, 645 (1956).
25. HOUE, A. L., J. Appl. Phys. *32*, 1234 (1961).
26. Symposium on Microwave Strip Circuits, IRE Transactions, Vol. MTT-3 No. 2, March 1955.
27. MARSHALL, J. H., Space Programs Summary No. 37-17, Vol. IV, Jet Propulsion Laboratory, Oct. 1962.
28. COPELAND, J. A., and F. B. HUMPHREY, J. Appl. Phys. in press. (1962 Magnetism Conference Supplement.)
29. HAGEDORN, F. B., J. Appl. Phys. *30*, 254S (1959).
30. DIETRICH, W., W. E. PROEBSTER and P. WOLF, IBM J. of Res. and Devel. *4*, 189 (1960).

# 66. Generation of Magnetic Fields by Flux Compression in Superconductors

By Daniel D. Elleman

DR. DANIEL D. ELLEMAN, *Senior Scientist in the Physics Section of Jet Propulsion Laboratory, was born in Lancaster, Ohio. A graduate of Ohio State University, he received the B.S. in Engineering Physics and the M.S. in Physics in 1955 and the Ph. D. in Physics in 1959. Dr. Elleman holds membership in the American Physical Society and Sigma Xi.*

## INTRODUCTION

The possibility of producing and carrying intense magnetic fields in space probes offers a solution to many problems encountered in space flight. A few of the obvious applications of magnetic fields are: plasma confinement for power generation and propulsion systems, magnetic shielding of astronauts, particle analyzers, bubble and cloud chambers, and magnetic resonance experiments. The utilization of these devices is feasible only if the power consumption and weight of the device are of a reasonable size for space probes.

The discovery (Ref. 1-4) of high critical field superconductors such as  $\text{Nb}_3\text{Sn}$  and  $\text{Nb}_2\text{Zr}$  has greatly stimulated interest in the possible production of very high field, large volume, superconducting solenoids (Ref. 5-7). Unfortunately, these high critical field superconductors do not have exceptionally high critical current density characteristics,  $J \approx 10^5$  amp/cm<sup>2</sup>. Furthermore, the manufactured superconducting wires must be rather small in diameter, 10-20 mil, because of the metallurgical properties of the superconductor. Another problem in wire wound solenoids arises from the introduction of heavy copper bus leads into the helium bath which produces a large heat leak into the

helium bath. These difficulties make it necessary to construct the superconducting solenoid with small diameter wire which results in small energizing currents, 10-20 amps, for the solenoid. Therefore, a many turn solenoid must be wound in order to obtain the large ampere turns required for the intense magnetic field. It is immediately obvious that to produce magnetic fields of even intermediate sizes, such as 1 liter, would require many thousand meters of superconducting wire. In this paper, we describe an alternate method in which persistent currents are induced in a block of superconducting material so as to trap and then compress a large magnetic field within holes in the superconductor.

## Flux Compression

It is a well known fact that when a multiply connected superconductor is cooled below its critical temperature in the presence of an external magnetic field the flux inclosed by the superconductor is trapped and remains constant even when the external magnetic field is reduced to zero (Ref. 8). Thus, if a superconducting cylindrical shell were placed in a magnetic field  $B_0$ , with the field parallel to the axis of the shell, then cooled below the critical temperature, the field  $B_0$  would be trapped in the

volume inclosed by the shell, and the field would remain trapped for an indefinite length of time (Ref. 9). In speaking of such a system, it is best to mention that the total magnetic flux trapped,  $\phi_0$ , and the magnetic field remain constant only so long as the cross sectional area normal to the field does not change. It is easy to see that if it were possible to decrease the cross section available to the trapped flux the magnetic field would correspondingly be increased.

Figure 66-1 shows a block of  $\text{Nb}_3\text{Sn}$  6.0 cm in diameter, 2.60 cm thick, and with two holes 2.30 cm diameter and 1.00 cm diameter drilled through the block. As an experiment to test the feasibility of compressing magnetic flux, this block was placed in the magnetic field of a copper wound solenoid 12 in. diam and 36 in. long, with the axis of the cylindrical holes in the block parallel to the magnetic field of the solenoid. A dewar system was constructed to cool the block below its critical temperature, 18° K, with liquid helium. In the experiment, the magnetic field was first turned on to a value  $B_0$ , and then the superconducting block was cooled with liquid helium and the magnetic field of the solenoid reduced to zero. Thus the field  $B_0$  or the flux  $\phi_0$  was trapped in the two holes in the block; next the superconducting cylindrical piston, 2.220 cm in diameter, shown in Fig. 69-1, was inserted into the larger hole, hole A, in the block. The insertion of the piston compressed the flux  $\phi_0$  into a smaller cross sectional area and thus gave an increase in the magnetic field measured in the small hole, hole B (Ref. 10 and 11).

If one assumes that the total trapped flux  $\phi_0$  in the superconducting holes remains constant both before and after the piston is inserted into hole B, then

$$B_a = B_0 \left[ \frac{A_a + A_b}{A_a + (A_b - A_p)} \right] \quad (1)$$

where  $B_a$  is the final field measured in hole A,  $A_a$  is the cross sectional area of hole A,  $A_b$  is the cross sectional area of hole B, and  $A_p$  is the cross sectional area of the piston. It is obvious from Eq. (1) that a very large magnetic field may be produced from a relatively small initial field merely by building a flux compressor with

both hole B and the piston very large compared to hole A.

It is of course advantageous to trap as large an initial flux as possible. Making the field  $B_0$  of the copper solenoid larger will accomplish this, but can become very difficult for larger fields. A more convenient method of trapping a large flux is to place soft iron rods through holes A and B while the solenoid is on and before the superconducting block is cooled below its critical temperature. The iron rods give a low reluctance path for the flux and thus increase the total flux through the holes in the block. After the superconducting block is cooled, the magnetic field of the solenoid can be turned off, then the iron rods can be withdrawn and the superconducting piston inserted into hole B. Using a technique similar to this, fields of 23.5 Kgauss have been produced with superconductors made of  $\text{Nb}_3\text{Sn}$ . If attempts are made to compress magnetic fields larger than 23.5 Kgauss, the superconductor goes normal, the magnetic flux leaks out of the holes in the block, and the field decays very rapidly to a value of only 2 to 5 Kgauss.

### A Cyclic Flux Pump

As was shown above, the compression ratio obtained by flux compression is the ratio of the cross-sectional area available to the trapped flux before the superconducting piston is inserted, to the cross-sectional area available to the trapped flux after the piston is inserted. Therefore, in order to produce a high field in a large working area, it is necessary to have a very large compression chamber and piston. It is obvious that this arrangement can become extremely cumbersome. This troublesome requirement can be alleviated, however, by the addition of two superconducting valves to a compressor similar to the one described above. This makes it possible to obtain a large increase in the magnetic field without a very large compression chamber.

Figure 66-2 shows a picture of a cyclic superconducting flux pump fitted with two superconducting valves. The flux pump is constructed from a block of 99.6% niobium, 1.90 cm thick and 4.14 cm in diameter. There are two large cylindrical holes drilled through the block, one of 0.96 cm diameter, the compression chamber,

# GENERATION OF MAGNETIC FIELDS BY FLUX COMPRESSION

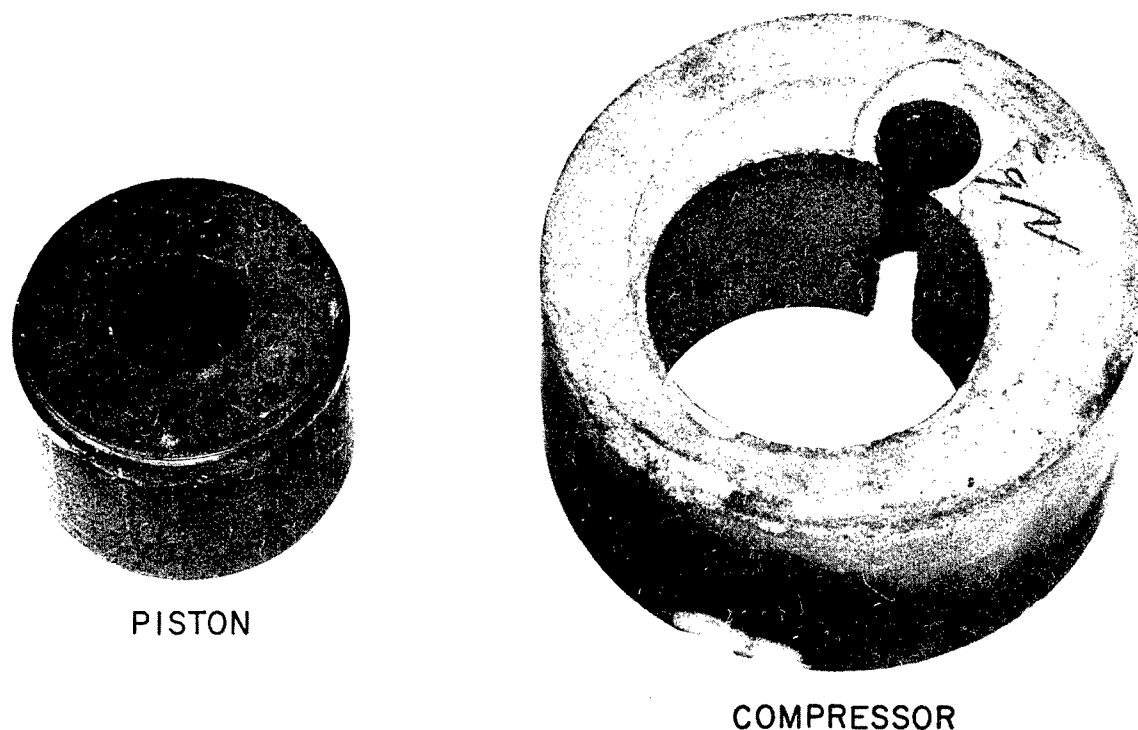


FIGURE 66-1.—A Nb<sub>3</sub>Sn superconducting flux compressor and piston.

and the other hole 2.38 cm diam, the experimental or probe chamber. In addition, very small holes are drilled into the wall which separates the two chambers, and also in the outside wall of the compression chamber. Nichrome heating wires are placed in these small holes.

When a small voltage is applied to these heating wires, the temperature of the niobium is raised above the critical temperature and the niobium cylinder 2.12 cm long and 0.89 cm diam changes from the superconducting state to the normal state. The two superconducting valves can, therefore, be open or closed to let magnetic flux into or out of a particular chamber. A niobium cylinder 2.12 cm long and 0.98 cm diam is used as a superconducting piston to compress the flux in the compression chamber. The sequence of operation of the valves and the piston

is the following: the entire system is brought to the superconducting state with liquid helium in the presence of an external field  $B_o$ , with both valves closed (superconducting), and the piston withdrawn from the compression chamber. The superconducting piston is then inserted into the compression chamber and the flux which was trapped in the compression chamber is compressed into the narrow annular region between the walls of the chamber and the piston to produce the resulting magnetic field

$$B = B_o \left( \frac{1}{1 - \frac{A_p}{A_c}} \right)$$

where  $A_p$  is the cross-sectional area of the piston and  $A_c$  is the cross-sectional area of the

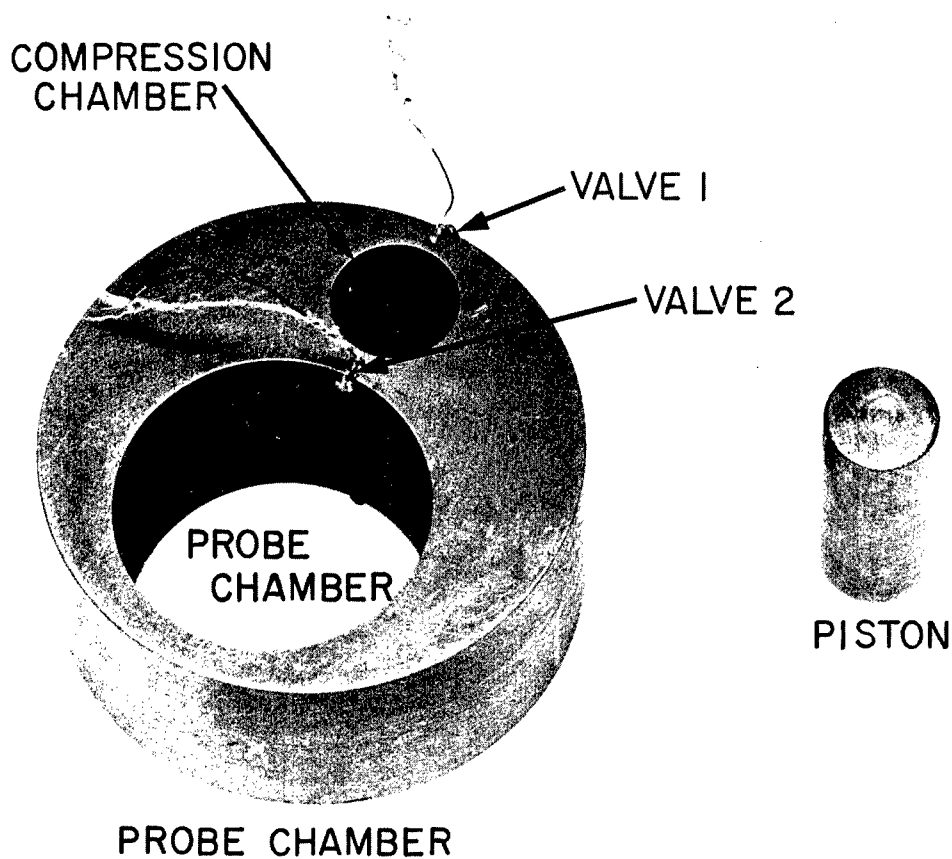


FIGURE 66-2.—A niobium superconducting cyclic flux pump and piston.

compression chamber. Valve 2 is then opened to enable the compressed flux to enter the probe or experimental chamber. (Actually, the flux is shared by the probe chamber and the annular region between the compressor wall and the piston). Valve 2 is then closed, isolating the two chambers, the piston is withdrawn from the compression chamber, and valve 1 is then opened. When valve 1 is opened, more magnetic flux from the ambient field enters the compression chamber; valve 1 is then closed, trapping this flux in the compression chamber. The piston is again inserted and the cyclic operation is repeated. With the completion of each cycle,

the flux within the probe chamber increases until the magnetic field within the probe chamber is identical to that in the compression chamber during the compression phase. Thus, the maximum field that can be produced in the probe chamber is given by Eq. (2).

Figure 66-3 shows the results for several such experiments carried out in different external fields with the 99.6% niobium flux pump. Additional experiments have been performed with cyclic  $\text{Nb}_3\text{Sn}$  flux pumps, which obtained a field of 10 Kgauss. This field is less than was anticipated because of flux penetration into the walls of the superconductor.

# GENERATION OF MAGNETIC FIELDS BY FLUX COMPRESSION

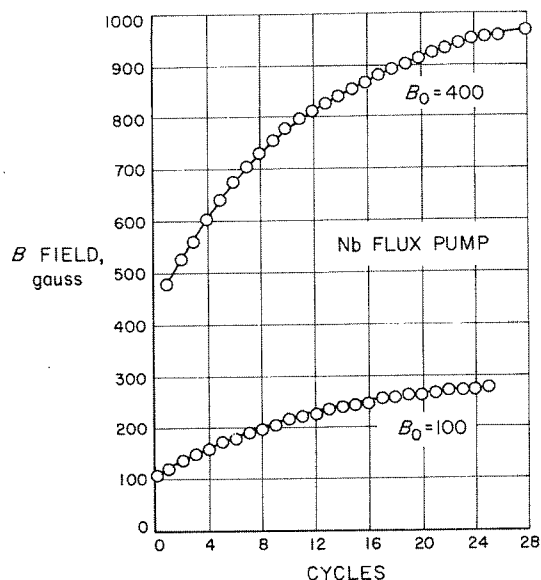


FIGURE 66-3.—A plot of magnetic field in probe chamber vs. cycles of operation for niobium flux pump.

A flux pump was also constructed out of two coils of 10 mil  $Nb_3Zr$  wire as is shown in Fig. 66-4. The coils were 1.2 cm in diameter and 4 cm in length, the superconducting piston was a 1.0 cm diam niobium cylinder 5 cm long. This flux pump was operated in a manner similar to the block of niobium pump. The results are shown in Fig. 66-5.

The  $Nb_3Zr$  flux pump has been operated as a "magnetic vacuum pump", that is, to pump magnetic flux out of the probe chamber. This was accomplished by merely changing the sequence of opening and closing the valves. The

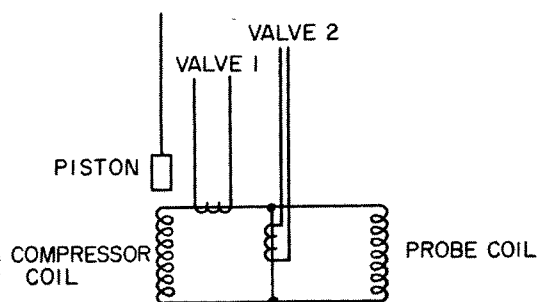


FIGURE 66-4.—A  $Nb_3Zr$  coil cyclic flux pump.

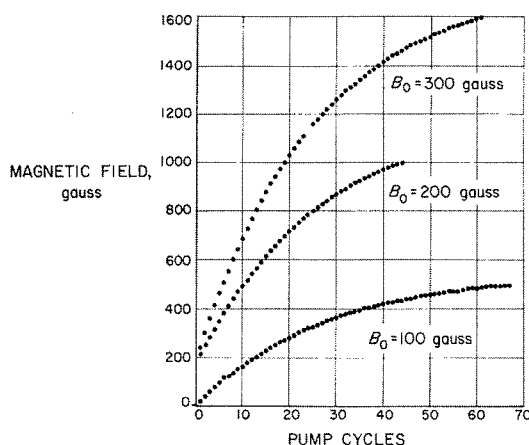


FIGURE 66-5.—A plot of magnetic field in probe coil vs. cycles of operation for  $Nb_3Zr$  flux pump.

Z component of the trapped field (the component along the axis of the coil) was pumped down from approximately 600 milligauss (the Earth's field in the laboratory) to 0.2 milligauss. Figure 66-6 shows a plot of Z component of the magnetic field vs. cycles of operation. The 0.2 milligauss field was extremely stable and showed changes of less than  $10^{-3}$  milligauss when the field external to the coil was varied several gauss.

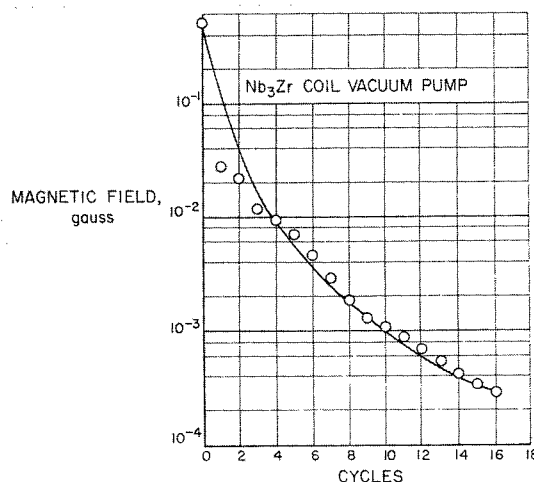


FIGURE 66-6.—A plot of magnetic field in probe coil vs. cycles of operation for  $Nb_3Zr$  "vacuum pump."



### Penetration of Magnetic Flux Into Nb<sub>3</sub>Sn

A superconducting flux compressor, similar to the one described above, has been used to measure the penetration of magnetic flux into the superconductor Nb<sub>3</sub>Sn (Ref. 12 and 13).

The compression ratio  $\alpha$  is defined as the ratio of the magnetic field measured in the probe chamber after compression to the original magnetic field trapped in the flux compressor. If the magnetic flux trapped in the two connected holes in the superconductor is conserved during compression, and if the flux does not penetrate the walls of the superconductor, then an ideal compression ratio  $\alpha_0$  can be calculated from the known dimensions of the two holes and the piston:

$$\alpha_0 = \frac{R_1^2 + R_2^2}{R_1^2 + R_2^2 - R_p^2} \quad (3)$$

where  $R_1$  and  $R_2$  are the radii of the compression hole and probe hole respectively, and  $R$  is the radius of the piston. The flux pump used in the experiment has the dimensions: compression hole 1.650 cm radius, piston 1.610 cm radius, and the probe hole 0.500 cm radius. A compression ratio  $\alpha_0 = 7.94$  is obtained when these dimensions are used in Eq. 3.

Figure 66-7 shows a plot of the experimental compressor ratio  $\alpha$  versus the magnetic field compressed into the probe hole. It is observed

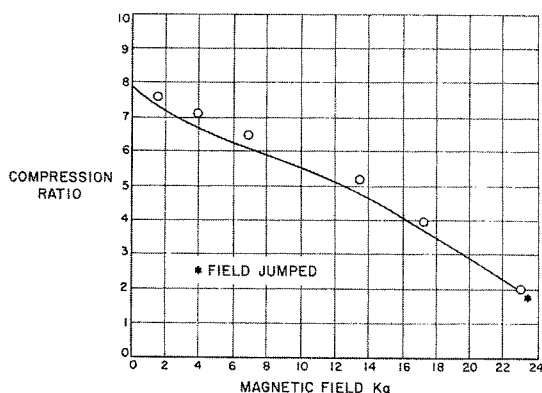


FIGURE 66-7.—A plot of compression ratio of flux compressor vs. compressed magnetic field.

that a compression ratio of 7.5 is obtained at low fields which compare favorably to the calculated compression ratio  $\alpha_0$ . However, at larger fields the compression ratio decreases steadily and is only 2.06 at 23.1 Kg.

It is observed that when the piston is removed from the compression hole the magnetic field returns to approximately the initial value trapped in the two holes. This indicates that the flux does not escape from the compressor. The decrease in compression ratio with increasing magnetic field does indicate that the magnetic flux penetrates a small distance into the walls of the compressor and the piston, and that this penetration is field dependent.

If it is assumed that the magnetic field penetrates a distance  $\delta$  into the superconducting material, that is

$$\begin{aligned} B_{int} &= B & \delta > r > r_0 \\ B_{int} &= 0 & r > \delta \end{aligned} \quad (4)$$

where  $B_{int}$  is the field in the superconducting material,  $B$  is the field compressed in the holes, and  $r$  is the distance along the radius of the hole ( $r = r_0$  at the interface), then the penetration depth  $\delta$  and the experimentally measured compression ratio  $\alpha$  are related by

$$\alpha = \frac{R_1^2 + R_2^2}{R_1^2 + R_2^2 - R_p^2 + \delta^2 + 2\delta(R_1 + R_2 + R_p)} \quad (5)$$

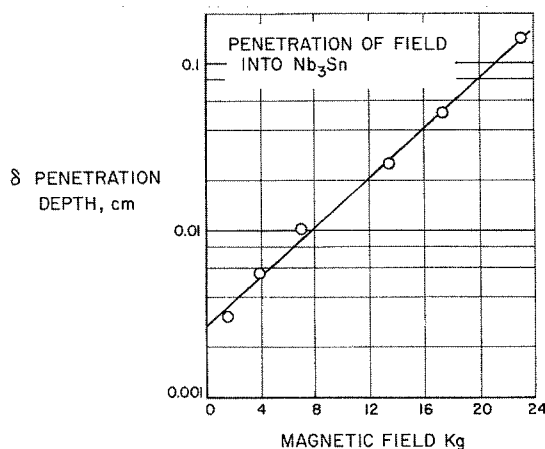


FIGURE 66-8.—A plot of penetration depth in Nb<sub>3</sub>Sn vs. magnetic field.

# GENERATION OF MAGNETIC FIELDS BY FLUX COMPRESSION

Figure 66-8 shows a plot of the penetration parameter  $\delta$  computed from Eq. (5) vs. the magnetic field compressed into the probe hole. For the Nb<sub>3</sub>Sn used in the experiment the equation

$$\delta(b) = ae^{bB} \quad (6)$$

where  $a = 2.8 \times 10^{-3}$  cm and  $b = 1.7 \times 10^{-4}$  gauss<sup>-1</sup>, gives a good approximation to the experimental data.

## REFERENCES

1. KUNZLER, J. E., E. BUEHLER, F. S. L. HSU, and J. H. WERNICK, Phys. Rev., Letters 6, 89 (1961).
2. BERLINCOURT, T. G., R. R. HAKE, and D. H. LESLIE, Phys. Rev. Letters 6, 671 (1961).
3. BERLINCOURT, T. G., R. R. HAKE, Phys. Rev. Letters 9, 293 (1962).
4. BERLINCOURT, T. G., VIII International Conference on Low Temperature Physics, September 17-21, 1962, London, England.
5. AUTLER, S. H., High Magnetic Fields, MIT Press and John Wiley and Sons, Inc., New York, (1962), p. 324.
6. DONADIEU, L. J., and D. J. ROSE, High Magnetic Fields MIT Press and John Wiley and Sons, Inc., New York (1962), p. 356.
7. HULM, J. K., VIII International Conference on Low Temperature Physics, September 17-21, 1962, London, England.
8. LONDON, F., Superfluids I, John Wiley and Sons, Inc., New York, (1950), p. 27.
9. HILDEBRANDT, A. F., D. D. ELLEMAN, Bull. Am. Phys. Soc. 5, 111 (1960).
10. HILDEBRANDT, A. F., D. D. ELLEMAN, F. C. WHITMORE, R. SIMPKINS, J. Appl. Phys. 33, 2375 (1962).
11. ELLEMAN, D. D., A. F. HILDEBRANDT, R. SIMPKINS, F. C. WHITMORE, Bull. Am. Phys. Soc. 7, 309 (1962).
12. ELLEMAN, D. D., A. F. HILDEBRANDT, JPL Space Program Summary 37-15, 4, (1962).
13. HILDEBRANDT, A. F., D. D. ELLEMAN, Bull. Am. Phys. Soc. 7, 473 (1962).

**SESSION U**

**Materials**

***Chairman, JOHN E. DUBERG***

---

DR. JOHN E. DUBERG, *Technical Assistant to the Associate Director of the NASA Langley Research Center*, received his B.S. degree in Engineering from Manhattan College in 1938. He received a fellowship to Virginia Polytechnic Institute in 1939-40 and earned the M.S. degree in Engineering. He was awarded his Doctorate in Engineering by the University of Illinois in 1948. Dr. Duberg returned to the University of Illinois in 1957 as a professor and conducted and reported original research. He is a recognized authority in the field of structural analysis, and has served on several technical committees at Langley. Dr. Duberg is a member of Tau Beta Pi, Phi Kappa Phi, Sigma Xi, Institute of the Aerospace Sciences, Society for Industrial and Applied Mathematics, and Scientific Research Society of America.



50235

## 67. Space Environment and Its Effects on Materials

By Don D. Davis, Jr.

DON D. DAVIS, JR., Assistant Head, High Temperature Materials Branch, Applied Materials and Physics Division, NASA Langley Research Center, received his Bachelor of Science degree in electrical engineering with distinction from the University of Nebraska in May 1944 and joined the Langley staff the following month in the Full-Scale Research Division. He earned his Master of Science degree in aeronautical engineering from the University of Virginia through Langley's graduate study program in June 1952.

Davis directs research in ablation and transpiration cooling, kinetics of chemical oxidation, protective coatings for refractory materials, physics of meteoroid impact, satellite instrumentation for meteoroid detection, effect of space radiation on solar cells and on materials for such satellites as A-12 (Echo II), and shielding of spacecraft components from the effects of radiation. He will also direct a new 1.5-million-dollar space-vacuum laboratory that is now under construction at Langley to study the effects of the ultra-high vacuum of space on spacecraft materials and structural components. He pioneered the successful development of specialized transonic wind tunnels and directed loads research which resulted in rapid and substantial progress in understanding the factors that control aerodynamic loads at transonic speeds. His scholarly contribution of a complete and rational system for the design of acoustic filters has gained international recognition. Davis is Chairman of the local section of the Institute of the Aerospace Sciences, and is a member of the American Rocket Society, the Engineers' Club of the Virginia Peninsula, Sigma Tau and Pi Mu Epsilon honorary fraternities.

### SUMMARY

Three aspects of the space environment that influence the selection of materials for use in spacecraft are considered: namely, vacuum, particle radiation, and meteoroids. To the best of our knowledge, vacuum effects have not so far been a serious problem for spacecraft. On the other hand, several spacecraft failures have been attributed to radiation, and confirmation of the suspected effects has been obtained in the laboratory. The extent of the hazard from meteoroids is uncertain. The most urgent need here is for reliable and accurate direct measurements of damage.

### INTRODUCTION

This paper considers three aspects of the space environment which influence the selection of materials for use in spacecraft. These aspects are the scarcity of atoms (vacuum), the presence of charged particles (particle radiation), and the presence of interplanetary debris (meteoroids). In each case the most significant features of the environment will be mentioned, and then a few selected examples of the effect of this environment on engineering materials will be given.

## SYMBOLS

$d$	diameter of projectile
$E$	energy
$e$	electron (used in figs.)
$P$	depth of penetration
$p$	pressure in reference to vacuum effects
$p$	proton in reference to radiation environment and effects (fig. 67-5)
$T$	temperature

## VACUUM

Space vehicles and their materials will be subjected to the vacuum environment for extended periods of time—months or even years. This environment is characterized by extremely low density, with a corresponding low pressure, and by a composition radically different from that at the earth's surface. Figure 67-1 shows the pressure as a function of altitude to 3,000 kilometers. (See ref. 1.) The width of the band indicates the variation in pressure from night to day. Pressure is used as the abscissa because there has been a tendency to define the space vacuum in terms of the pressure level. Actually, from the structural standpoint, the pressure forces in space are negligibly small. The physical phenomena of interest in connection with vacuum effects in space depend, instead, on the number of particles that come in contact with an exposed surface. Thus it is more meaningful to speak in terms of the number of particles in

a unit volume rather than the pressure force exerted by those particles. Therefore, a scale has been added at the top of figure 67-1 to show the number density of the particles. At 3,000 kilometers there are one or two thousand particles per cubic centimeter, and farther outward from the earth it has been estimated that in interplanetary space there may be only about 10 particles per cubic centimeter. Thus the environment in which spacecraft components and materials must function contains only from perhaps ten to a few thousand particles per cubic centimeter.

In the few years since space exploration has become a reality, much effort has been directed toward simulation of the space vacuum environment in ground facilities. A few years ago the state of the art dictated number densities of about  $10^9$  particles per cubic centimeter (about  $10^{-7}$  torr) in sizable vacuum chambers; today facilities are available to operate at number densities around  $10^6$  particles per cubic centimeter (about  $10^{-10}$  torr). These facilities, however, still fall far short of the number densities in space of a few to a few thousand particles per cubic centimeter. Facility development is still progressing rapidly; therefore, it is possible that the space vacuum can be simulated in the future.

In the meantime, studies have been undertaken in currently available facilities to determine vacuum effects on spacecraft materials and components at the vacuum levels presently available. Many measurable effects have already been found, several of which would be detrimental to the accomplishment of a mission.

Perhaps the first problem area that comes to mind is material loss due to evaporation or sublimation into the space vacuum. Preliminary studies indicate that structural materials such as steel and aluminum alloys will not sublime at a rate so fast as to deteriorate significantly their load-carrying ability, even at moderate temperatures. (See ref. 2.) On the other hand, where the materials are applied as thin coatings, such as those used for thermal control, the sublimation is more serious. Figure 67-2 shows the effect of a vacuum environment on three thermal-control coatings that are intended for use on the

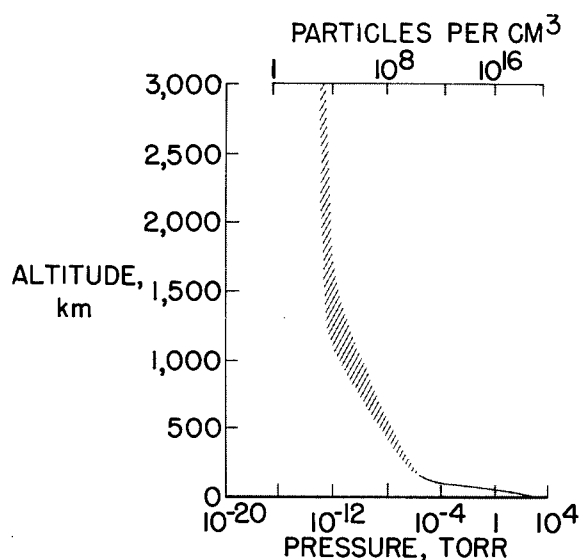


FIGURE 67-1.—Atmospheric pressure and number density of particles at altitudes to 3,000 km.

# SPACE ENVIRONMENT AND ITS EFFECTS ON MATERIALS

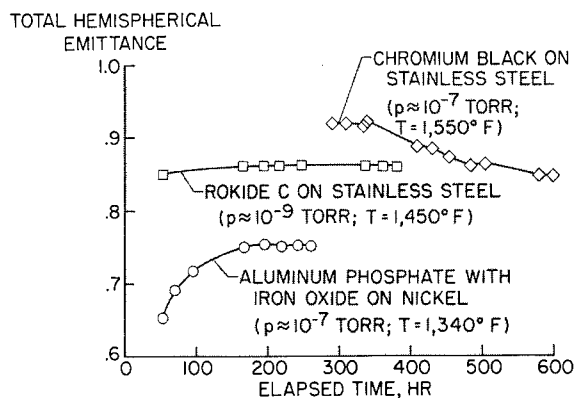


FIGURE 67-2.—Effects of exposure to vacuum on total hemispherical emittance at elevated temperatures for three coated materials intended for use as space radiators.

radiator of a space power plant. (See refs. 3 to 5.) The total hemispherical emittance is plotted as a function of the elapsed time in vacuum. The tests were conducted at elevated temperatures in the radiator operating range. The results show that the emittance can increase, can remain approximately the same, or can decrease because of exposure to vacuum. The cause of the observed changes in emittance has not yet been determined.

A second problem area arises because of the loss of adsorbed gas layers that are normally present on the surface of all materials. After prolonged exposure to the space-vacuum environment, a surface will lose all the surface adsorbed gases and will become "clean." As a result, it will behave differently when put in contact with another clean surface. Recent studies (ref. 6) have shown that cohesion or cold welding takes place. The studies were made by breaking a specimen in vacuum and then by placing the broken faces into contact again. The following table shows representative results from this study for 1018 steel.

Temperature, °C	Maximum cohesion, percent
500	96.0
150	35.9
25	18.5

The primary variable is the temperature. The maximum cohesion shown in the column on the right is the percentage of the initial breaking force that was required to break the specimen the second time. These studies indicate that very significant cohesion, up to 96 percent, can take place under certain conditions. As the temperature is reduced, the cohesion is significantly reduced. The time that the broken faces were held apart was short enough in the last two cases to prevent significant contamination by the gas in the vacuum chamber; therefore, it is clear that the reduction in cohesion with decreasing temperature is not due to contamination. The occurrence of this cold-welding phenomenon could seriously affect the operation of spacecraft in the vacuum environment.

Studies of some mechanical properties of metals have indicated that the vacuum environment is not always detrimental. Creep-rupture and fatigue experiments indicate that under certain conditions metals are stronger in the nonreactive vacuum environment than in air at normal atmospheric pressure. (See ref. 7.) Figure 67-3 shows some fatigue data for type 316 stainless steel in vacuum and in air. The amplitude of the vibration is plotted against the number of cycles to failure. At a constant amplitude of vibration the material exhibited a substantially longer life in vacuum than in air. Data which indicate similar trends for creep rupture are also available. (See ref. 7.)

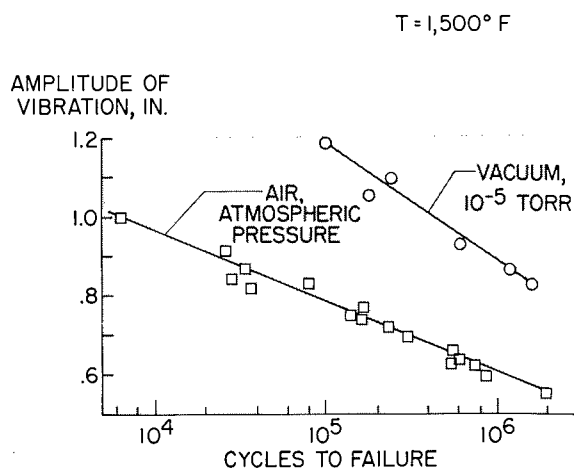


FIGURE 67-3.—Effects of exposure to vacuum on fatigue life of type 316 stainless steel.

# **PARTICLE RADIATION** → 446

The particle radiation in space may be divided into several different categories as shown in figure 67-4. The primary galactic cosmic radiation (refs. 8 and 9) consists of positively charged particles of very high energy. The particles are primarily protons (85 percent) and alpha particles (13 percent), and the remainder consists of completely stripped nuclei with masses up to that of tin. As an overall average in free space, the flux is on the order of 2.5 particles/cm<sup>2</sup>-sec. Even with generous allowances for the high relative biological effectiveness of the heavy particles, the estimated dose delivered to an unprotected man in space would be on the order of only 1/2 rem (roentgen equivalent man) per week. Thus, even for man this radiation is of negligible effect, except on journeys of several years. For materials there should be essentially no effect from the galactic cosmic radiation, except perhaps on some photographic emulsions.

A second source of particle radiation in space is the solar cosmic radiation, or solar flare. (See refs. 8 to 12.) Solar flares originate in chromospheric disturbances of the sun, and their frequency is directly related to the period of the solar activity cycle. Low-energy events (with particles up to 400 Mev) and medium-energy events (with particles up to a few Bev) occurred with frequencies between 5 and 13 times a year in the period from 1935 to 1959. During the same period, high-energy events (with particles up to 20 Bev) occurred once or twice every 4 or 5 years.

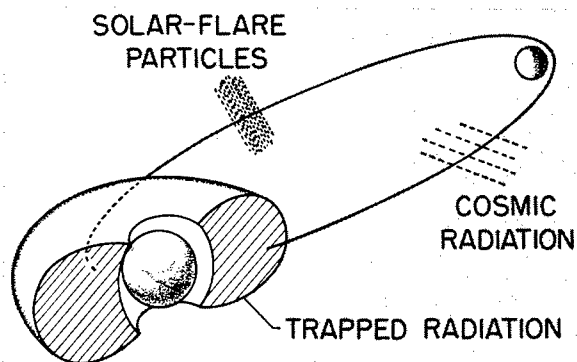


FIGURE 67-4.—Schematic diagram of space radiation.

The primary danger in this case is to man because some of these flares can deliver large radiation doses. Basic research is being conducted at present along two lines: shielding studies, including studies of the secondary particles within the shield as well as preliminary work on systems of magnetic shielding, and studies leading toward the ability to predict solar flares a week or more in advance of their occurrence.

The presently available prediction criterion, when applied to a 3 1/2-year period beginning in 1957 (ref. 11) would have allowed 117 four-day trips, only two of which would have encountered solar flares. During this same period, 77 seven-day trips would have been allowed with the unacceptably large number of 5 solar-flare encounters. A successful extension of prediction time to a period of 7 to 10 days would greatly relieve the shielding requirements for many lunar missions.

With regard to materials, the solar flare by itself may present problems for some of the more sensitive materials. Because of the sporadic nature of the solar flare, however, the time-averaged flux of particles will be relatively light. Thus, protection of materials from radiation damage due to flares may properly be considered as a subcase of protection from the natural trapped radiation near the earth.

The discovery and definition of this trapped radiation (refs. 8, 9, 13, and 14) shown schematically in figure 67-4 was one of our first scientific accomplishments with artificial satellites. The damaging potential of this radiation is such that the selection and protection of materials for satellites which will orbit for long periods of time in this region is our most pressing radiation damage problem.

Recent satellite measurements indicate that the older concept of two or more radiation belts is inadequate and misleading. A more appropriate concept is that the trapped radiation occupies one large and continuous region around the earth and that the intensity, energy, and type of radiation vary almost continuously throughout this region. The contours in figure 67-5 indicate the approximate spatial distribution of the trapped radiation. These contours are labeled with the counting rate that would



# SPACE ENVIRONMENT AND ITS EFFECTS ON MATERIALS

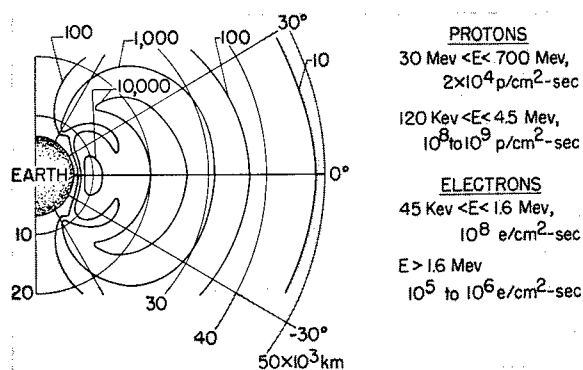


FIGURE 67-5.—Equal counting-rate contours of natural trapped radiation surrounding the earth.

be seen by a suitably shielded Geiger-tube and are useful only as a qualitative indication of those portions of the region which pose the most severe radiation problems.

Since the particles are trapped in the magnetic field of the earth, the intensities are highest near the equatorial plane and are substantially lower near the polar regions. The minimum altitude for significant counting rates varies around the earth because the magnetic and geometric axes of the earth are substantially offset from each other. Over the South Atlantic, counting rates begin to increase at an altitude of about 400 kilometers, whereas on the opposite side of the earth the corresponding altitude is about 1,300 kilometers. Thus it is possible, when allowed by the mission requirements, to orbit below this radiation. Estimates of the outermost extent of the trapped radiation range as high as 10 earth radii.

The maximum fluxes of the particles are shown at the right in figure 67-5. The high-energy protons are the most spectacular portion of the flux and are largely confined to the small inner high-flux contour. The maximum flux between 30 Mev and 700 Mev is on the order of  $2 \times 10^4$  protons/cm<sup>2</sup>-sec. Low-energy protons are found almost throughout the entire region. The measured fluxes between 120 Kev and 4.5 Mev range on the order of  $10^8$  to  $10^9$  protons/cm<sup>2</sup>-sec. There is also a substantial flux of low- and medium-energy electrons (45 Kev to 1.6 Mev) on the order of  $10^8$  electrons/cm<sup>2</sup>-sec throughout most of the region shown. The higher energy electrons are largely confined

to the outer high-flux contour with fluxes on the order of  $10^5$  to  $10^6$  electrons/cm<sup>2</sup>-sec.

More recently, an additional component of space radiation has been added by the high-altitude nuclear explosion of July 9, 1962. (See ref. 15.) This explosion created a new belt of electron radiation around the earth. The new belt is shown schematically in figure 67-6. It is somewhat smaller in extent and lower than the natural belt. Large fluxes are observed at only 200 kilometers above the earth over the South Atlantic; on the opposite side of the earth the minimum altitude is about 650 kilometers. These low altitudes are significant since it is at present almost impossible to escape radiation exposure by means of low-altitude orbits. Although the flux decay rate in the heart of the new belt seems negligibly small, some decay has been observed at the lowest altitudes. This decay will eventually ease the problem; however, it will be several years before radiation resistance can again be neglected for orbits sufficiently high to achieve long lifetimes. The new belt extends out to about 25,000 kilometers from the center of the earth. Maximum fluxes on the order of  $10^8$  electrons/cm<sup>2</sup>-sec have been observed. In contrast to the natural radiation, where over 99 percent of the electrons occur with energies of less than 1.6 Mev, the electrons of the new belt seem to occur with a typical fission energy spectrum. A breakdown of this spectrum by energy is given in the table on the right of the figure.

The large flux and higher energy of the electrons in the new belt means that adequate

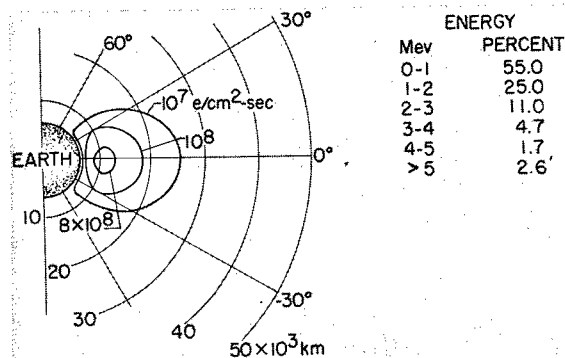


FIGURE 67-6.—Equal flux contours of new artificial electron belt.

heavy shielding must be provided for many radiation-sensitive devices. In many cases this shielding will be very heavy, and it will be needed where either no shielding or only minimal shielding was previously required. The need is best illustrated by the fact that, of those satellites in orbit at the time of the blast, three were inactivated by radiation damage to their solar cells within about a month; indeed, one failed in only three days.

Even before the new belt was formed, it was evident that space radiation possessed a severe damaging potential insofar as materials such as semiconductors and plastics are concerned. (The new belt has only increased the urgency of the need for data in these areas.) Consequently, the NASA has installed or is preparing to install a number of accelerators ranging from 1.0-Mev electron accelerators to a 600-Mev proton synchrocyclotron in order to study the problem. In addition, a substantial amount of contract research with private industry, universities, and other government organizations is already under way. Three examples have been selected for discussion in this paper. These examples are intended only to illustrate some of the work already in progress; the interests of the NASA in this area are far broader than these examples alone might indicate.

The first example concerns transistors. The sensitivity of many solid-state devices to radiation has led to a major program in which a number of available accelerators have been utilized to study the effect of proton irradiation on transistors. (See ref. 16.) Energies from 22 Mev to 440 Mev have been utilized to date. The data shown in figure 67-7 are typical and

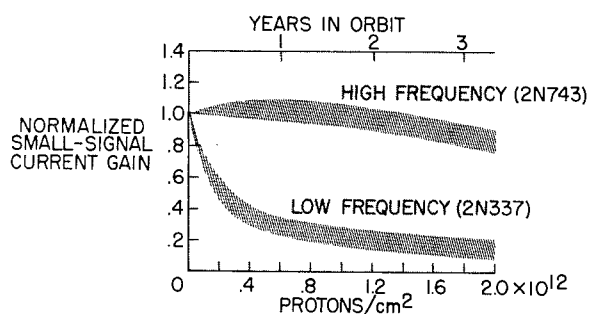


FIGURE 67-7.—Effect of exposure to 40-Mev protons on current gain of two transistors.

were obtained by using the 40-Mev linear proton accelerator at the University of Minnesota. Here the small-signal current gain, or essentially, the transistor's ability to operate as an amplifier, is plotted against the total dose in protons per square centimeter. The scale at the top shows the approximate time equivalent in terms of years in orbit in the worst part of the radiation belt. The two broad bands show the degradation of two different NPN silicon transistors, the 2N743 and the 2N337. The width of the bands indicates the scatter among the data for approximately a half-dozen samples of each type. The dramatic decrease in current gain for the 2N337 is typical of the lower frequency transistors tested; the negligible degradation of the 2N743 is typical of the highest frequency transistors tested. The lesser degradation of the higher frequency units is consistent in other types of construction. Indeed, the increased radiation resistance of the higher frequency units led to one of the design choices that was made in the case of the Telstar satellite.

The solar cell is an example of a solid-state device that is extremely sensitive to radiation (refs. 16 and 17) and at the same time difficult to shield from radiation when operating in space. Substantial additional interest in the solar-cell problem has been engendered by the aforementioned recent loss of three satellites to the new artificial radiation belt because of solar-cell damage. Figure 67-8 shows the spectral variation of short-circuit current for a P on N silicon solar cell before and after electron irradiation. The energy of the electrons was 0.65 Mev. The total dose is approximately that which might be encountered in a year in a practical orbit within the new belt. Immediately evident is the large loss of output in the infrared region where the output of the undamaged cell was highest. On the other hand, there is little or no degradation at the shorter wavelengths. The long wavelengths penetrate deeply in the cell, whereas the short wavelengths are absorbed at or near the surface. Thus the changes shown in figure 67-8 indicate that most of the damage is done in the base material well below the actual junction, which is about 1 micron deep.

# SPACE ENVIRONMENT AND ITS EFFECTS ON MATERIALS

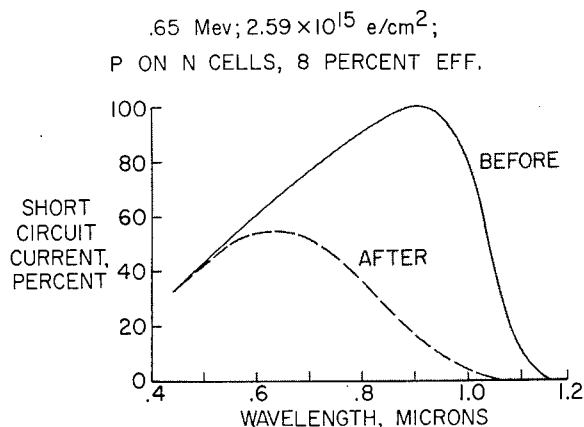


FIGURE 67-8.—Effect of exposure to 0.65-Mev electrons on spectral variation of short-circuit current for a P on N silicon solar cell.

One approach to improved radiation resistance in a solar cell is obvious from figure 67-8, that is, to improve the response in the short-wavelength region where the radiation has little effect. This is precisely what is done in the so-called blue-sensitive shallow-diffused cells which are indeed more radiation resistant. Far greater improvements are to be had in the use of N on P cells rather than the P on N cells shown here. (See ref. 17.) The radiation resistance of the N on P cells is so intrinsically superior that these cells are the presently preferred type and their use is indicated whenever permitted by the presently small but rapidly increasing production rate.

The NASA is currently sponsoring a substantial amount of research in industry, not only on silicon solar cells, but also on newer cells such as gallium arsenide, and even on vapor-deposited cells which could be deposited directly over large areas of a space vehicle.

Another approach to radiation resistance is to shield the item of concern with a thickness of some material which is adequate to stop all or most of the particles incident upon the item. In the case of solar cells and other light-sensitive or optical systems, this shield must not only be transparent, but it must also remain transparent under radiation. Most glasses do color under radiation. (See refs. 18 and 19.) The mechanism in most cases is described as the combination of displaced electrons with negative-ion sites (or vacancies) to form color centers. Such coloration may mean that the

shield, by stopping a major portion of the light, does more harm in some cases than the radiation would have done if no shielding had been provided.

Recently, this phenomenon has been studied at the Langley Research Center of the NASA in connection with providing shielding for the solar cells of a specific orbital spacecraft. This spacecraft will orbit well within the artificial belt and the major hazard will be from high-energy electrons. Many glasses were irradiated with 1.2-Mev electrons in this program. The results for three quartzes are shown in figure 67-9. Here the relative transmission of the glass, averaged over the solar-cell response spectrum, is plotted as a function of the total dose in electrons per square centimeter. The end point corresponds to one year in orbit for the particular payload. Results are shown for three different quartz samples, two fused and one vapor deposited. The vapor-deposited sample shows essentially no decrease in transmission. Of the two fused samples, one shows about a 10-percent loss and the other, about a 40-percent loss in transmission after a year's time. In the worst case, most of the coloration came very early, so that the solar-cell output behind this shield would have been reduced to a critical level within a very few weeks.

The actual differences in the materials shown here are presently believed to be related to the degree of impurity. The poorest quartz had 50 to 70 parts per million of impurities; the best had less than 1 part per million. The practical conclusion to be drawn from these results is that extreme care is essential in the selection of transparent radiation shielding and that

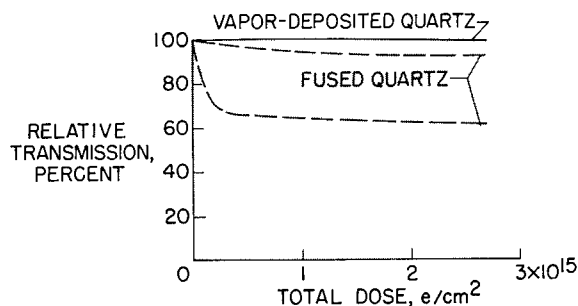


FIGURE 67-9.—Effect of exposure to 1.2-Mev electrons on solar-energy transmission for three types of quartz windows.

## MATERIALS

this care should extend to the point of actually exposing samples to radiation as a quality control check.

### [METEOROIDS] →

The discussion will turn now to the meteoritic debris in space. Damage to spacecraft that would result in danger to the occupants or that would prevent the fulfillment of the mission must not be allowed to occur. This is a difficult problem for the space-vehicle designer, because at the present time there is a large uncertainty with regard to the size and weight of meteoroids that will be encountered and with regard to the damage that they will do. The examination of the status of this particular problem will begin with a review of our knowledge of the space environment.

The available information on the meteoroid environment in space is illustrated in figure 67-10 (adapted from ref. 20). The cumulative influx rate in particles per square meter per second is plotted as a function of the particle mass in grams. The cumulative influx rate corresponding to a mass  $x$  is the total number of particles of mass  $x$ , or less, that pass through one square meter in one second. Logarithmic scales are used on both axes. The solid lines at the lower right show estimates of the meteoroid environment that are derived from astronomical observations of meteors in the earth's atmosphere. The observable quantities are the influx rate and the light intensity. By making

certain assumptions, it is possible to derive a relationship between the light intensity and the particle mass. With this relationship in hand it is possible to plot the astronomical observations in the form that they are shown in this figure. There is a very large difference between the two solid lines that are shown. This difference stems from a difference in the estimates of the astronomers for the relationship between the light intensity and the particle mass. At a cumulative influx rate of  $10^{-12}$  particles per square meter per second, a particle mass of about  $10^{-2}$  grams is indicated by the lower curve and a mass of about 2 grams by the upper curve. These estimates of the mass differ by a factor of 200 to 1, and thereby produce an extremely large uncertainty in the flux-mass relationship. The particles of most interest with regard to spacecraft damage are smaller than the observed meteors. Estimates of the flux of these particles have been obtained by straight-line extrapolation from the observed data. These extrapolations are shown by the dashed lines extending to the left from the solid lines that were derived from meteor observations. At the other end of the scale there are data points representing actual flight measurements of micrometeoroid impact rates. Most of these measurements were obtained by using a microphone type of dust-particle sensor; the slope of the line faired through these points is considerably greater than the slope of the lines that were derived from astronomical observations. The range of most interest to the spacecraft designer lies between the small particles observed in the dust measurements and the meteors observed from the ground. In this range there is at the present time much uncertainty both with regard to the level of the distribution curve and with regard to the slope of this curve.

The data and estimates shown in this figure apply in the immediate vicinity of the earth. The meteoroid hazard in other regions of space is also of concern to the NASA. In the Apollo program, for example, the meteoroid hazard in the vicinity of the moon and on the surface of the moon must be considered. In an attempt to get a feel for this problem in the absence of actual measurements, Gault, Shoemaker, and Moore have recently studied the problem of

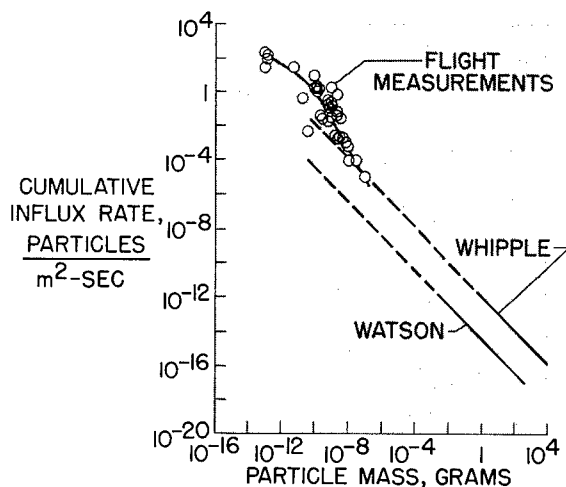


FIGURE 67-10.—Cumulative influx rate of meteoroids in vicinity of earth as a function of mass.

hypervelocity impact of a projectile on a basalt-rock surface. The results of their analysis (which are unpublished) suggest a heavy flux of debris in the vicinity of the moon due to meteoroid collisions with the moon, but they do not provide numerical values for use in spacecraft design. If there is, in fact, a heavy concentration of particles in the mass range that might be expected to puncture spacecraft, it would, of course, constitute a serious problem in the Apollo program.

In addition to the uncertainty as to the mass of the particles that will be encountered, there is a further uncertainty as to the damage that will be caused by a particle of known mass and velocity. This is illustrated in figure 67-11, which presents plots of penetration as a function of velocity as estimated by three of the many formulas that have been proposed. The symbols  $P$  and  $d$  are defined by the sketch at the right. The curves labeled Huth et al. and Charters and Summers are based on experimental data obtained at velocities well below those that are typical of meteoroids. (See refs. 21 and 22.) Bjork's curve is strictly theoretical. (See refs. 23 and 24.) At a velocity of 30,000 to 40,000 kilometers per second, which is typical of meteoroids, the penetration appears to be uncertain by a factor of about 10. There is a pressing need for the development of an adequate penetration theory.

The combined effect of the two uncertainties that have been discussed is such that, at the present time, if a spacecraft designer is faced with the problem of insuring that the number

of penetrations does not exceed a given value, he is faced with an uncertainty of about 20 to 1 in the thickness of material that he must use.

[A considerable amount of effort has been devoted to systems designed to protect a spacecraft from penetration by meteoroids. One of the most promising devices is the meteoroid bumper, which is simply a thin sheet of material that is placed outside and at a distance from the structural wall of a spacecraft with the object of providing protection from damage by meteoroids.] Figure 67-12 is a sequence of photographs that show the mechanism by which a meteoroid bumper provides protection. (See ref. 24.) In the first photograph, the vertical dark line at the left is a thin plate which has been impacted by a spherical projectile coming from the left. The projectile is in the dark area to the right of the plate. Some of the material from the plate can be seen flying back to the left. The two vertical lines to the right of the projectile are not in its path. They are simply markers which have been used to provide a length reference in the photographs. The first photograph was taken 6.5 microseconds after the initial impact. In the next photograph, at 9.8 microseconds, some light is visible through the debris at the right of the plate. The projectile has been broken into many small fragments in passing through the plate and the rest of the photographs show that these fragments disperse as they travel away from the plate. The impact of these many small particles dispersed over a wide area, of course, produces a great deal less damage than would the original projectile. Reference 25 also presents information on the influence of the geometrical arrangement on the effectiveness of bumpers.

### CONCLUDING REMARKS

A brief account of the state of our knowledge of the effects of the space environment on engineering materials will be attempted in conclusion. With regard to vacuum, a few problems have turned up in the laboratory, but the effects of the extreme vacuum of space are largely unexplored and therefore unknown. To the best of our knowledge (and in this area

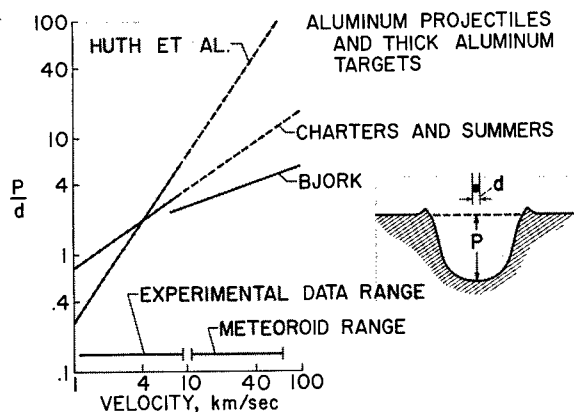


FIGURE 67-11.—Three estimates of penetration depth as a function of velocity for high-velocity aluminum projectiles impacting thick aluminum targets.

## MATERIALS

### TIME ELAPSED SINCE IMPACT

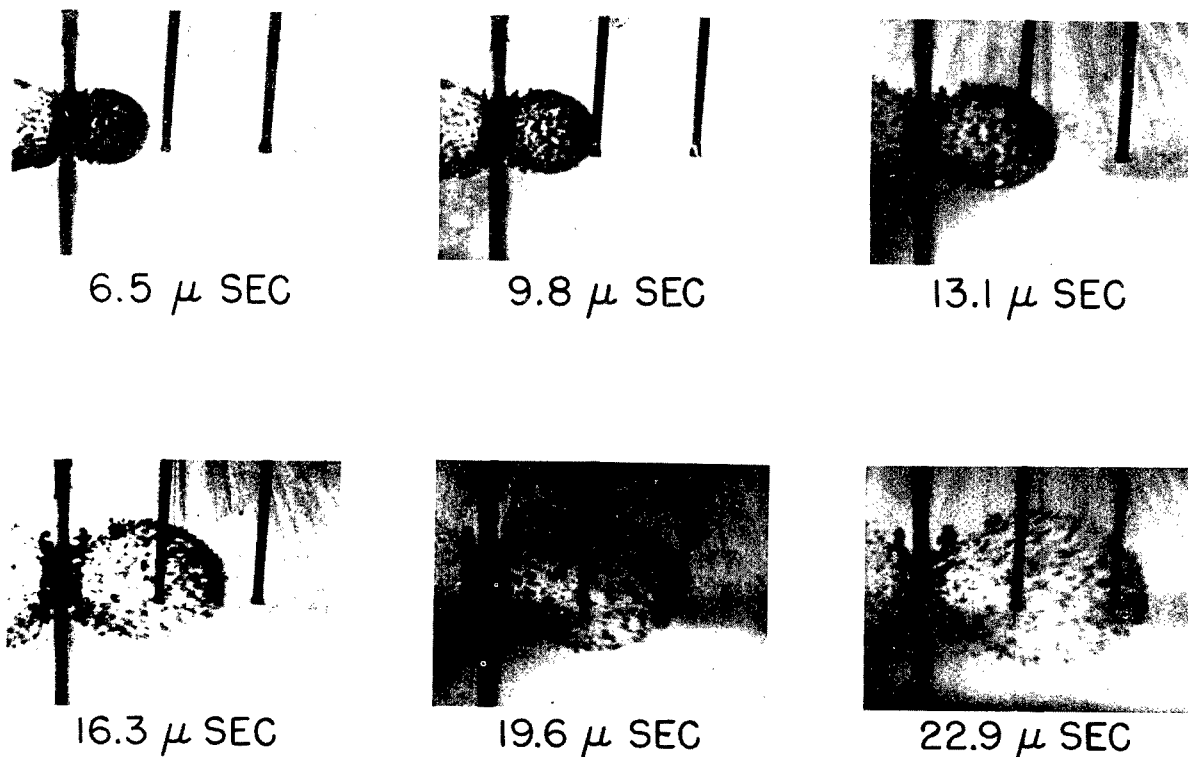


FIGURE 67-12.—Sequence of photographs showing breakup and dispersion of a high-velocity projectile by a meteoroid bumper.

the best is not good), vacuum effects have not so far been a serious problem for spacecraft.

The situation with regard to radiation is entirely different. Several spacecraft failures have been attributed to radiation, and confirmation of the suspected effects has been obtained in the laboratory. Because these effects have been so detrimental, it is obvious that there will be a great demand upon the operators of charged particle accelerators to produce engineering results and to evaluate engineering developments in this area.

With regard to the meteoroid environment, the status is clear, but the hazard is not. In other words, it is perfectly obvious that the extent of the hazard is not known—not even within an order of magnitude. The most urgent need here is for some reliable and accurate direct measurements of damage that can be used as a check on the work of both the theoreticians and the design engineers. Rapid progress would follow the establishment of even a single point of this nature in which real confidence could be placed.

## REFERENCES

1. JASTROW, R., and KYLE, H.: The Earth Atmosphere. Sec. 2.1 of Handbook of Astronautical Engineering, First ed., Heinz Hermann Koelle, ed., McGraw-Hill Book Co., Inc., 1961, pp. 2-2—2-13.
2. JAFFE, LEONARD D., and RITTENHOUSE, JOHN B.: Behavior of Materials in Space Environments. ARS Jour., vol. 32, no. 3, Mar. 1962, pp. 320-346.
3. ANON.: Measurement of Spectral and Total Emittance of Materials and Surfaces Under Simulated Space Conditions. Rep. No. PWA-1863 (Contract No. NASW-104), Pratt & Whitney Aircraft, 1960.

# SPACE ENVIRONMENT AND ITS EFFECTS ON MATERIALS

4. ANON.: Progress Report on the Determination of the Emissivity of Materials During the Period From July 1, 1960, Through September 30, 1960. Rep. No. PWA-1877 (Contract NASW-104), Pratt & Whitney Aircraft, 1960.
5. ASKWYTH, WILLIAM H.: Progress Report—Determination of the Emissivity of Materials. Rep. No. PWA-2043 (Contract NASw-104), Pratt & Whitney Aircraft, 1961.
6. HAM, JOHN L.: Investigation of Adhesion and Cohesion of Metals in Ultrahigh Vacuum. NRC Proj. No. 42-1-0121 (Contract No. NASr-48), Nat. Res. Corp. (Cambridge, Mass.), Dec. 15, 1961–Mar. 15, 1962.
7. ACHTER, M. R.: Effects of High Vacuum on Mechanical Properties. First Symposium—Surface Effects on Spacecraft Materials, Francis J. Clauss, ed., John Wiley & Sons, Inc., c.1960, pp. 286–306.
8. FOELSCH, TRUTZ: Current Estimates of Radiation Doses in Space. NASA TN D-1267, 1962.
9. VOSTEEN, LOUIS F.: Environmental Problems of Space Flight Structures. I. Ionizing Radiation in Space and Its Influence on Spacecraft Design. NASA TN D-1474, 1962.
10. ANDERSON, KINSEY A., and FICHTEL, CARL E.: Discussions of Solar Proton Events and Manned Space Flight. NASA TN D-671, 1961.
11. ANDERSON, KINSEY A.: Preliminary Study of Prediction Aspects of Solar Cosmic Ray Events. NASA TN D-700, 1961.
12. OGILVIE, KEITH W.: Solar Protons. NASA TN D-1139, 1962.
13. VAN ALLEN, J. A.: The Earth and Near Space. Bull. Atomic Scientists, vol. XVII, no. 5-6, May-June 1961, pp. 218-222.
14. KOLCUM, EDWARD H.: Research Challenge Encompasses Galaxy. Aviation Week and Space Technology, vol. 77, no. 15, Oct. 8, 1962, pp. 54-67.
15. HESS, W. N., and NAKADA, PAUL: Artificial Radiation Belt Discussed in Symposium at Goddard Space Center. Science, vol. 138, no. 3536, Oct. 5, 1962, pp. 53-54.
16. HULTEN, W. C., HONAKER, W. C., and PATTERSON, JOHN L.: Irradiation Effects of 22 and 240 Mev Protons on Several Transistors and Solar Cells. NASA TN D-718, 1961.
17. AUKERMAN, L. W.: Proton and Electron Damage to Solar Cells. REIC Rep. No. 23 (Contract No. AF 33(616)-7375), Battelle Memorial Inst., Apr. 1, 1962.
18. RILEY, W. C., COPPINS, W. G., and DUCKWORTH, W. H.: The Effect of Nuclear Radiation on Glass. REIC Tech. Memo. 9 (Contract No. AF 33(616)-5171), Battelle Memorial Inst., Nov. 30, 1958.
19. LEVY, PAUL W.: Radiation Effects in Glass and Other Materials. Physics Today, vol. 15, no. 9, Sept. 1962, pp. 19-23.
20. ALEXANDER, W. M., MCCracken, C. W., SECRETAN, L., and BERG, O. E.: Review of Direct Measurements of Interplanetary Dust From Satellites and Probes. X-613-62-25, Goddard Space Flight Center, NASA, 1962.
21. HUTH, J. H., THOMPSON, J. S., and VAN VALKENBURG, M. E.: Some New Data on High-Speed Impact Phenomena. Jour. Appl. Mech., vol. 24, no. 1, Mar. 1957, pp. 65-68.
22. SUMMERS, JAMES L.: Investigation of High-Speed Impact: Regions of Impact and Impact at Oblique Angles. NASA TN D-94, 1959.
23. BJORK, R. L.: Numerical Solutions of the Axially Symmetric Hypervelocity Impact Process Involving Iron. U.S. Air Force Project RAND S-103 (ASTIA Doc. No. AD 305657), The RAND Corp., Dec. 16, 1958.
24. BJORK, R. L.: Meteoroids Versus Space Vehicles. ARS Jour., vol. 31, no. 6, June 1961, pp. 803-807.
25. HUMES, DON, HOPKO, R. N., and KINARD, WILLIAM H.: An Experimental Investigation of Single Aluminum "Meteor Bumpers." Proc. of the Fifth Symposium on Hypervelocity Impact (Denver), vol. 1, pt. 2, Apr. 1962, pp. 567-580. (Sponsored by U.S. Navy, U.S. Army, and U.S. Air Force.)

~~50220~~  
dept of  
50609

## 68. Nonmetallic Materials for Spacecraft

By George F. Pezdirtz

DR. GEORGE F. PEZDIRTZ, Head, Spacecraft Materials Section, Applied Materials and Physics Division, NASA Langley Research Center, received his Bachelor of Science degree in Chemistry and his Doctorate in Organic Chemistry from the University of Notre Dame in 1955 and 1960, respectively. The W. W. Barton Research Fellowship was awarded to him in 1956 by the University. His thesis was on "The Effects of High Energy Electrons on a Series of Saturated Polyesters." During 1955 and 1956, he was a chemistry laboratory instructor at Notre Dame. He was a special lecturer in physics and chemistry for Indiana University Extension (South Bend) in 1956-1957. Dr. Pezdirtz carried out basic research on heterogeneous polymerization catalysts for polyolefins at the Texaco Research Center, Beacon, New York during 1958-1960. Dr. Pezdirtz, who joined the Langley staff in November 1960 as an Aero-Space Technologist, has specialized in radiation chemistry of polymers, heterogeneous polymerization catalysts, and thermal control surfaces. He is responsible for the ultrathin inorganic coating for thermal control of the 135-foot-diameter A-12 (Echo II) passive communications balloon scheduled to be launched into orbit next year. Dr. Pezdirtz has 15 patent applications on heterogeneous polymerization catalysts for Texaco research; he is author of several NASA publications and has presented papers before technical societies on erectable space structures. He is a member of the American Chemical Society, Research Society of America, and American Association for Advancement of Science.

### SUMMARY

Nonmetallic materials have many unusual and desirable properties for use in spacecraft applications, but their sensitivities to the ultraviolet and high-energy ionizing radiation of space have created problems—some as yet unsolved. The problems of thermal control coatings, polymers, and composites in space applications are discussed. The need for new nonmetallic materials with unusual properties such as inorganic polymers is also examined.

### INTRODUCTION

The unusual and highly advantageous properties of polymers have made these materials very desirable for use in aerospace programs. Polymers, which include plastics, rubbers, and most adhesives, have yielded significant reduc-

tions in the overall cost of aerospace systems. This reduction in cost may be expressed in terms of money, energy, weight, or time. It is the purpose of this paper to review some of the properties of polymers which are responsible for these savings and which have further resulted in many unique applications.

In aerospace projects, one of the ever-increasing needs is for materials with high strength-to-weight ratios, good temperature properties, availability, and ease of fabrication. Although the development of polymeric and other nonmetallic materials is not yet commensurate with the need, these materials have such fundamental advantages that they have already made substantial contributions to the space program.



## SYMBOLS

- |                    |  |
|--------------------|--|
| $p$                | pressure                               |
| $T$                | temperature                            |
| $t$                | thickness                              |
| $\alpha_s$         | absorptance of solar radiation         |
| $\epsilon$         | emittance of solar radiation           |
| $\epsilon_\lambda$ | emittance as a function of wave length |
| $\lambda$          | wave length                            |

## SOME RELATIVE PROPERTIES OF POLYMERS AND METALS

Some of the relative physical properties of metals and polymers are shown in figure 68-1.

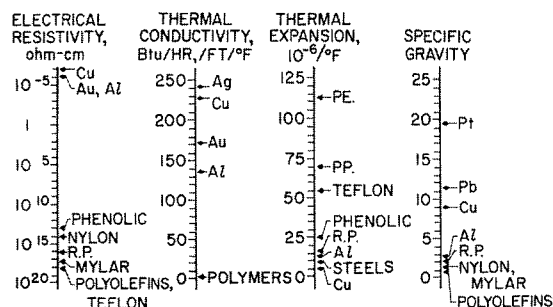


FIGURE 68-1.—Relative physical properties of metals and nonmetals. R.P. denotes reinforced plastics; PE., polyethylenes; PP., polypropylenes.

(See ref. 1.) One of the greatest differences in the properties of these two classes of materials is the electrical resistivity: metals are at the low end of the scale, and polymers are at the high end. Concurrent with the low electrical conductivity of polymers is low thermal conductivity. The higher coefficient of thermal expansion for polymers is another variable which can obviously lead to problems when the two materials are joined in composite form; however, in some instances, the lower modulus of elasticity and higher permissible strain of the polymers can alleviate this difference.

Some of the relative mechanical properties of metals and polymers are illustrated in figure 68-2. In general, polymers have a lower spectrum of tensile strength and a lower modulus of elasticity than metals, although it should be noted that the epoxy-glass composite does have a relatively high modulus of elasticity and one of the highest strength-to-weight ratios of the structural materials. The service temperature of polymers is also considerably lower than that

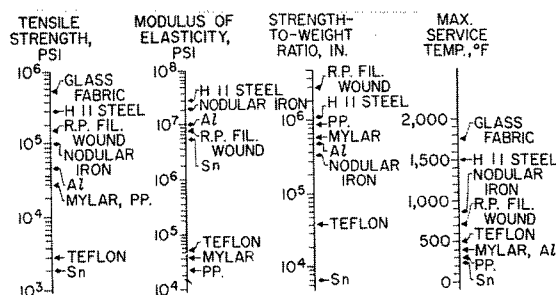


FIGURE 68-2.—Relative mechanical properties of metals and nonmetals. PP. denotes polypropylenes; R.P., reinforced plastics.

of metals, primarily as a result of the weaker organic carbon-to-carbon bonds in contrast to the strong metallic bonds of the metals and alloys. At present this low service temperature presents a severe limitation in some structural uses of polymers and represents a problem area which is discussed subsequently.

## AEROSPACE APPLICATIONS OF POLYMERS AND COMPOSITES

One of the largest materials research efforts on nonmetallic materials is in the field of composite materials, such as the epoxy-glass fibers for filament-wound structures. See references 2, 3, and 4.

Filament-wound structures offer a strength-to-weight ratio which is three times as efficient as that for titanium and four times as high as that for aluminum. In aerospace applications, this strength-to-weight ratio can lead to significant increases in final velocity and in payload weight. Filament-wound structures are considerably more efficient than metals because of the high directional strength of the glass fiber which can be applied in the direction of the load. Metals have isotropic strength properties and require additional weight in the structure to satisfy the maximum unidirectional loads while only part of the strength is used for lesser loads in other directions.

The materials presently used for filament-wound structures are high-strength continuous filaments of E glass held in an epoxy matrix. The resins used in the majority of cases are conventional bisphenol A - epichlorohydrin epoxies. Generally, these resins are cross-linked or cured by addition of an amine

## NONMETALLIC MATERIALS FOR SPACECRAFT

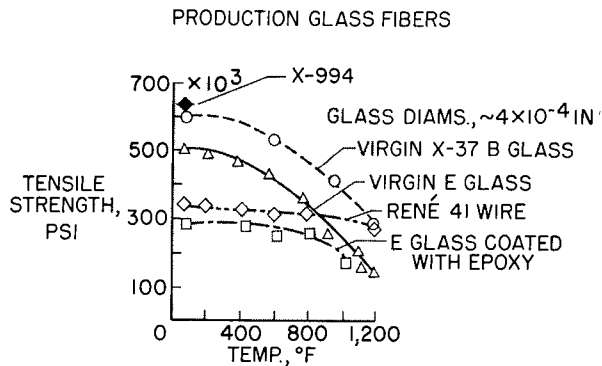


FIGURE 68-3.—Tensile strength as a function of temperature.

hardener. The effect of temperature on the tensile properties of E glass and on an experimental high-temperature glass X-37 B are shown in figure 68-3. (See ref. 2.) The top two curves refer to the glasses alone and the lowest curve applies to the glass-epoxy composite which has a lower service temperature because of the presence of the plastic. René, a superalloy of nickel and cobalt is included for comparison. The highest point (at 650,000 psi) is for a very new high-strength glass, X-994, which holds great promise for future applications.

Research at the NASA Langley Research Center (ref. 5) and in industry (ref. 6) on the isotenoid concept of filament winding has resulted in extremely efficient high strength-to-weight ratio rocket-motor cases. The isotenoid design is based on the concept of designing an equal and uniform tension in each fiber. An example of the isotenoid design is shown in figure 68-4. This case had a burst pressure of 710 psig which represents an overall skin stress of 185,000 psi, or more than twice the usual values for glass-fiber-reinforced cases. Even this advance could be improved upon by using some of the remarkable new glasses, such as X-994, and improved resin systems which would make possible skin stresses as high as 300,000 psi.

The properties of these kinds of materials are at least pragmatically understood for terrestrial applications. Even in the unusual environment experienced by a vehicle during transport into space, our knowledge of materials

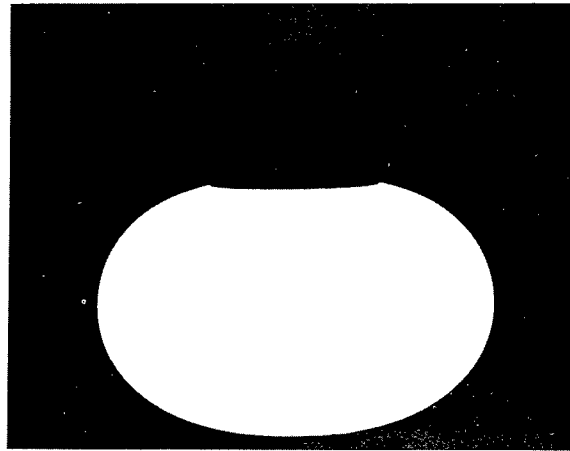


FIGURE 68-4.—Isotenoid filament-wound rocket case.

properties is adequate because of the short transit time. However, the knowledge of their extended life in space, under the combined influence of the ultravacuum, and ultraviolet, and ionizing radiation is by no means adequate.

### ERECTABLE SPACECRAFT

Future programs require knowledge of the long-time effects of the space environment on nonmetallic structural materials. Such projects as erectable space structures and space-storable fuel tanks might be cited as examples. Various designs and materials requirements were discussed at a recent conference on manned space stations (refs. 7 and 8). One space-station design is shown in figure 68-5. This concept calls for the use of an 80-mil Dacron filament-wound torus with an 8-mil butyl-impregnated nylon liner. Such a structure could be easily folded into 2 percent of its inflated volume external to the hub of transport into orbit where it could then be erected pneumatically. This design essentially uses only polymeric materials.

In another space-station design, polymeric materials were used in combination with metals because of their desirable low density and low thermal conductivity. Figure 68-6 shows a cross section of this composite shell in which a foamed polyurethane would serve several purposes, namely, to provide thermal insulation and structural rigidity, and to act as a micro-

## MATERIALS

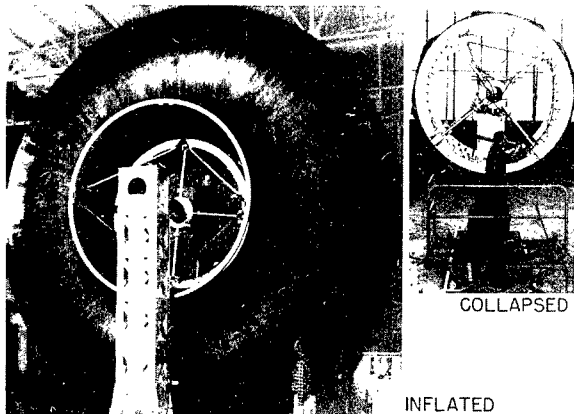


FIGURE 68-5.—24-foot erectable space station.

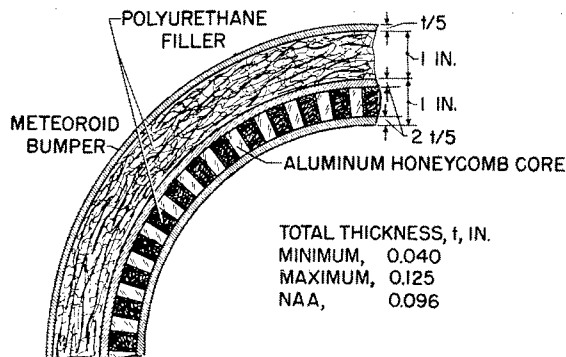


FIGURE 68-6.—Basic structure of module shell for rigid space station.

meteoroid bumper (see ref. 8). The density of a typical foam in this application is approximately 1.5 lb/cu ft.

Another example of the use of polymeric materials in spacecraft design is the giant Echo I sphere which has been in orbit for over 2 years. Echo I was the first passive communications satellite and had a diameter of 100 feet with a skin thickness of  $5 \times 10^{-4}$  inch. This large sphere was made almost entirely of polyethylene terephthalate (Mylar). This polymer is known to be highly resistant to the effects of high-energy ionizing radiation but is rather susceptible to damage from ultraviolet radiation. It was largely protected from the ultraviolet by a 2,200 Å coating of vapor-deposited aluminum. This thin layer of aluminum served several purposes: (1) it provided a radar-reflective surface for the communications experiments; (2) it protected the Mylar from extensive ultraviolet damage; and (3) it acted

as a thermal control surface to reduce the equilibrium temperature of the sphere.

## THERMAL CONTROL SURFACES

Another use of polymers and other nonmetallic materials in space is as thermal control coatings. The ratio  $\alpha_s/\epsilon$ , that is, the absorptance of solar radiation divided by the emittance of thermal radiation, is the prime surface parameter which determines surface equilibrium temperature. Figure 68-7 shows the relationship between  $\alpha_s/\epsilon$  and temperature. Nonmetallic mixtures such as paints have been used to provide the proper optical properties for previous spacecraft surfaces. In this instance, the polymeric vehicle is exposed, virtually unprotected, to the harsh space environment. This exposure has created some problems in the past and a considerable effort has been underway for the past few years to produce stable paints for thermal control coatings. It is generally recognized that inorganic surfaces are inherently more stable than organic surfaces as a result of the nature of the chemical bonds involved.

The NASA Langley Research Center has recently studied an unusually thin, stable inorganic coating known as Alodine 401 for use on A-12 (Echo II), a larger rigidized version of Echo I. This 135-foot sphere required a very light and thin surface coating to cover its nearly 60,000 sq ft of surface. Clemmons and Camp (ref. 9) have reported on the range of the  $\alpha_s/\epsilon$

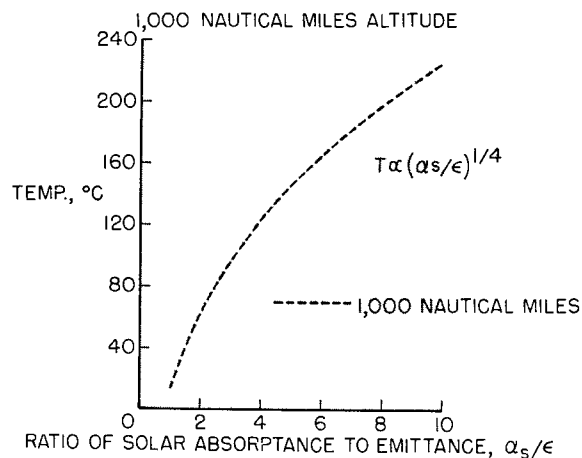


FIGURE 68-7.—Temperature as a function of the ratio of solar absorptance to emittance.

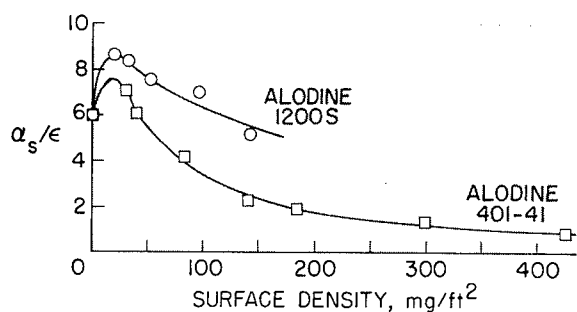


FIGURE 68-8.—Variation of  $\alpha_s/\epsilon$  with surface density for Alodine coatings.

ratios that can be obtained as a function of surface density of the inorganic Alodine coating; this is illustrated in figure 68-8. The Alodine surface is an amorphous mixture of aluminum and chromium phosphates which is formed by reacting pure aluminum foil with mixed acids in an aqueous dip process. In addition to its very desirable optical properties, Alodine can be applied easily to a surface, and the surface density can be controlled to within  $\pm 3$  mg/sq ft.

These have been but a few examples of the uses of polymers and other nonmetallic materials in aerospace applications. There are numerous other uses such as solid-fuel binders, electrical wire insulators, gaskets, and lubricants.

### EFFECTS OF SPACE ENVIRONMENT ON POLYMERS

During long-term exposure to the space environment, polymers can undergo many changes in their chemical and resultant mechanical properties. The chemical effects of the space environment on polymers can be classified into three major energy ranges which can act separately or in conjunction with each other. Figure 68-9 illustrates these three energy ranges—the ultravacuum-thermal range, the photochemistry range, and the radiation chemistry range. In the past, engineers have designed around the undesirable effects produced by each of these energy ranges. In the near and long-term future, this luxury will no longer be permitted. Each design must be optimum, and to do this effectively, a better understanding

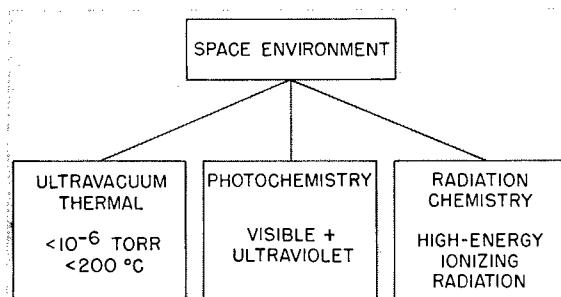


FIGURE 68-9.—Effects of space environment on polymers.

of the properties of materials and their interaction with the space environment must be reached. The recent state of knowledge with regard to the specific qualities and quantities of the high- and low-energy ranges in space is discussed in paper no. 67. The curve in figure 68-10 represents the solar spectrum at one astronomical unit from the sun. The general mechanism of the interaction of radiation with matter will now be considered.

Figure 68-11 represents the spectrum of energies from infrared to high-energy particles; the energy ranges included in thermal chemistry, photochemistry, and radiation chemistry are indicated.

In the infrared region, the energies are associated with vibrational, rotational, and translational motions of molecules, with no alteration of primary chemical bonds—simply an increase in temperature. On the other hand,

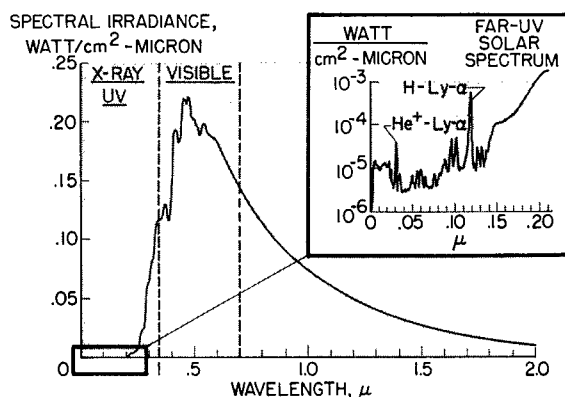


FIGURE 68-10.—Solar spectral irradiance at Earth's mean distance from the Sun.

## MATERIALS

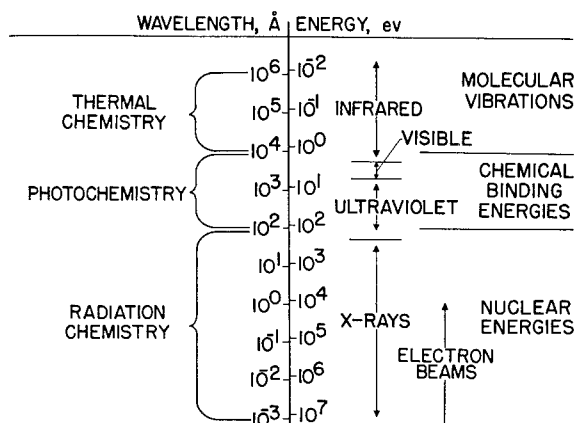


FIGURE 68-11.—Energy spectrum.

in the visible and ultraviolet region, there is considerable making and breaking of bonds, for here the energies involved are of the same order as the energies holding the molecules together. As a consequence, if small amounts of energy are absorbed from this region, they produce significant changes primarily at the surface of the material as this radiation is not very penetrating.

Beyond the ultraviolet range the high-energy ionizing radiation may be corpuscular or electromagnetic in form. These energies are generally much higher than molecular bonding energies and are not limited to surface effects but can penetrate to various depths of the structural material depending on the mass and energy of the radiation.

### Ultravacuum-Thermal Region

In the ultravacuum-thermal region, molecular distillation or outgassing is the main effect observed. The gases evolved may come from absorbed molecules or dissociation products produced by higher energies. Jaffee and Rittenhouse (ref. 10) have reviewed the research in this area. A controversy has been developing in the literature for some time with regard to the effects of the ultravacuum-thermal region on polymers. Most of the past data were obtained over relatively short time periods—on the order of days. There is some evidence by Osborne and Goodman (ref. 7) that the experiment should be continued for very long time periods—for weeks and months. This is

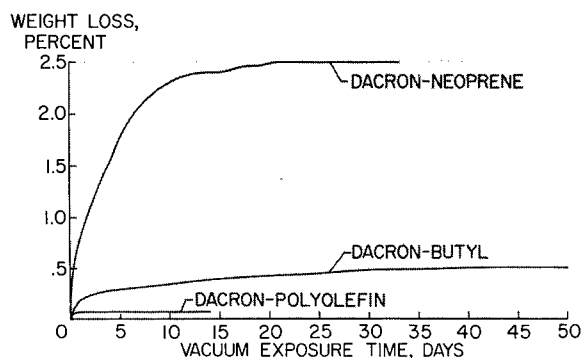


FIGURE 68-12.—Effects of vacuum on weight loss of flexible fabric.  
 $p=5 \times 10^{-7}$  mm Hg;  $T=25^\circ$  C.

illustrated in figure 68-12 which is a plot of percent weight loss as a function of exposure time for several different materials. Note that the Dacron-Neoprene case requires almost 2 weeks to level off. For the most part, the effects in this low-energy range are of concern primarily from the standpoint of contamination of man and instruments by volatile components.

### Visible-Ultraviolet Effects

The effects of the intermediate energies, the visible and ultraviolet radiation, while not highly penetrating, are of particular concern with regard to surface coatings. As mentioned previously, most satellites have some type of thermal control coating on their exterior surfaces. For those satellites which generate heat internally from onboard equipment, it is necessary to have very stable, thermally white surfaces. Here on earth the yellowing of white paints with age is a very familiar phenomenon. In space, this effect is accelerated because there is no atmosphere to filter out the ultraviolet radiation below 3,000 Å. One very stable surface which was discussed previously is the Alodine coating.

Figure 68-13 shows the effect of ultraviolet radiation on this Alodine surface. There is an initial small rise in its  $\alpha_s/\epsilon$  ratio and then a surprising decrease in this property. This is the reverse of the normal behavior of most thermal control surfaces and means that the equilibrium temperature should decrease somewhat rather than increase with age. Within limits this is desirable.

# NONMETALLIC MATERIALS FOR SPACECRAFT

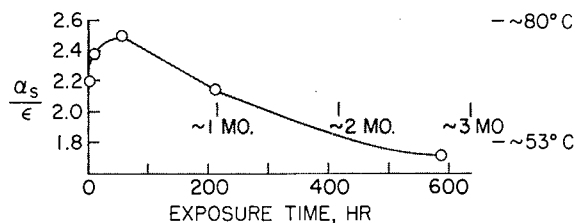


FIGURE 68-13.—Effect of ultraviolet on Alodine 401-41.

The  $\alpha_s/\epsilon$  ratio is a rather gross property, and to attempt to understand the mechanism of thermal control surfaces, such as Alodine, a more careful examination of basic optical properties must be made. This coating is essentially transparent to solar radiation and, as a result, the shiny opaque substrate of aluminum foil acts to reflect most of this energy away from the spacecraft. However, in the infrared region where the surface radiates away the small amount of energy which is not reflected, the Alodine coating is not transparent to the radiation. This is illustrated in figure 68-14 which shows the percent emittance as a function of wavelength. Note the very low emittance for the uncoated aluminum foil. While there are two major peaks at about  $3\mu$  and  $9.5\mu$ , respectively, they are not of equal importance. The ideal curve for a  $350^\circ\text{K}$  blackbody has its peak at about  $9\mu$  and about one-third of the energy is in the  $8\mu$  to  $12\mu$  region, whereas only a few percent of the total energy of a  $350^\circ\text{K}$  blackbody falls around  $3\mu$ . Hence, small changes in the  $9\mu$  region are much more significant than in the  $3\mu$  region. The large peak at  $9.5\mu$  for the Alodine 401 is probably due to the molecular vibrations of the phosphate

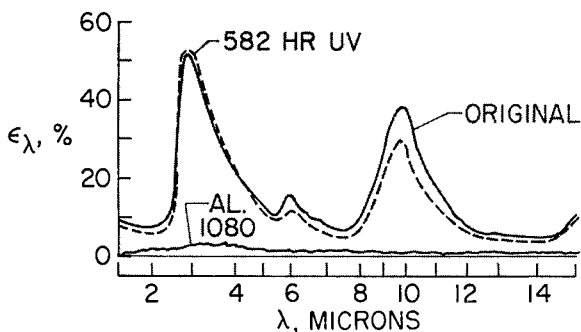


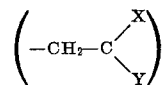
FIGURE 68-14.—Effect of ultraviolet on emittance of Alodine 401-41.

group. Note that after over 500 hours exposure to ultraviolet radiation there is little change in this property. The ultraviolet effects on structural polymers can be largely eliminated by such techniques as using an external opaque surface, for example, the vapor-deposited aluminum coating of Echo I.

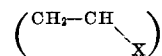
## Effects of Ionizing Radiation on Polymers

In contrast to photochemical effects, the effects of high-energy ionizing radiations found in space cannot be so easily shielded. These are the effects of the high-energy electrons and protons whose energies and fluxes were discussed in paper no. 67. The radiation chemistry of polymers became an area of intense activity shortly after World War II, and in recent years several review and reference texts have been published in this field (see refs. 11 to 14). The Radiation Effects Information Center at Battelle Memorial Institute maintains abstracts of current information in this field. Most of the past work in radiation effects on polymers has been oriented toward their use here on earth in and near nuclear reactors. As a consequence, many of these studies have been conducted in air and many polymers have been classified as sensitive to radiation. Several principles have been developed during the last decade which indicate some general trends in the effects of radiation on polymers. Some of these are shown in figure 68-15.

In general, addition polymers which have a 1,1 disubstituted repeating unit



have been shown to degrade under the influence of ionizing radiation. Those addition polymers which have only a single substitution



on alternate carbons generally cross-link under irradiation. It is also recognized that polymers with benzene rings such as polystyrene and Mylar are resistant to radiation effects because the unsaturated ring acts as an energy sink and absorbs energy without degrading the polymer. While these are general rules, they

## MATERIALS

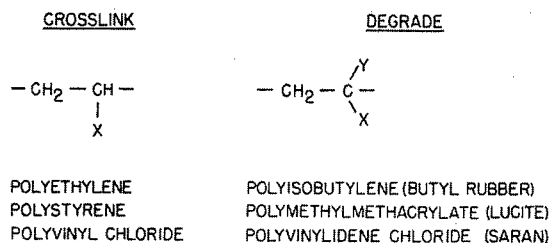


FIGURE 68-15.—Radiation effects on polymers.

do not cover a large number of other polymers such as the polycarbonates, polyacetals, and epoxies. It has been necessary therefore to treat these others as separate cases and to determine their behavior directly. One must exercise extreme caution so as not to misapply the wealth of background in radiation effects on polymers in air to their reactions in space. This is also true even for reported work in vacuo inasmuch as the degree of vacuum can play an important role. Vacuum work should be carried out at a continuous pressure of  $10^{-5}$  or  $10^{-6}$  torr as a maximum in order to reduce the concentration of oxygen and other reactive gases. Figures 68-16 and 68-17 illustrate the drastic difference between irradiation in air and in vacuo for some polyfluorocarbons (see ref. 15).

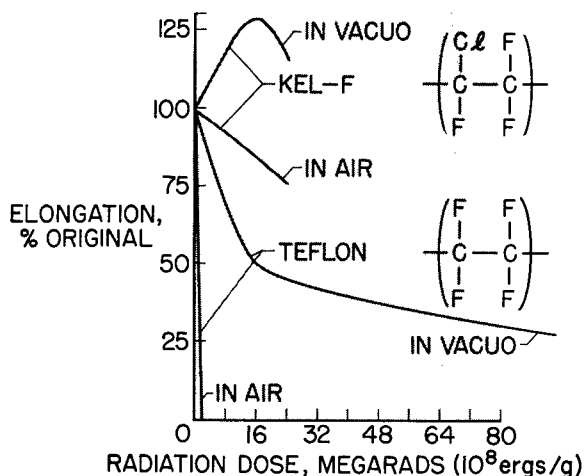


FIGURE 68-16.—Effect of  $\gamma$  irradiation on the elongation of fluorocarbon plastics.

### NEW MATERIALS RESEARCH

High-temperature environments represent another problem area which calls for increased research effort. Some of the details of one

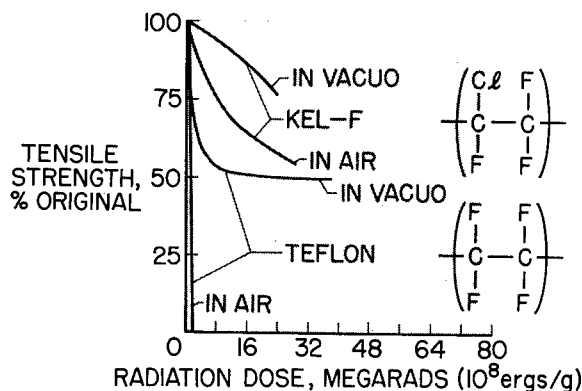
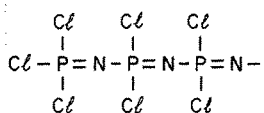


FIGURE 68-17.—Effect of  $\gamma$  irradiation on the tensile strength of fluorocarbon plastics.

high-temperature problem area, namely, reentry, are discussed in paper no. 69. There are many cases which require materials with high-temperature stability. In synthesizing polymeric materials, it is often possible to design specific properties into the molecular structure. This is readily apparent by recalling the dozens of new polymers with a wide range of properties, which reach production each year. One property design, thermal stability, is the goal of extensive polymer research which is now in progress in various university and government laboratories. This work is oriented toward tailor-making high temperature polymers. This research no longer deals with classical organic molecules as building blocks but reaches out to include inorganic materials. This work is still in the very early stages of development. The materials can be classed as inorganic polymers and compound organic-inorganic polymers.

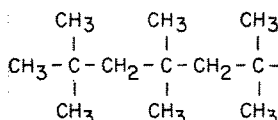
Probably one of the most notable inorganic polymers is the whole family of high-temperature silicone resins which have an Si-O-Si-O backbone in the main chain, though they do contain carbon in side groups. Most of the familiar organic polymers have relatively simple repeating units making up the molecular chain. This is the case with a few inorganic polymers but, in general, the repeating units are somewhat more complex. One example of a simple inorganic polymer is the phosphonitric linear polymer made up of P, N, and Cl. Its structure is shown in figure 68-18 and is somewhat reminiscent of the polyisobutylene

## NONMETALLIC MATERIALS FOR SPACECRAFT



- + HIGH TEMP. PROPERTIES (300° C)
- + ELASTOMER
- CHEMICAL STABILITY (HYDROLYSIS)

PHOSPHONITRILIC LINEAR POLYMER



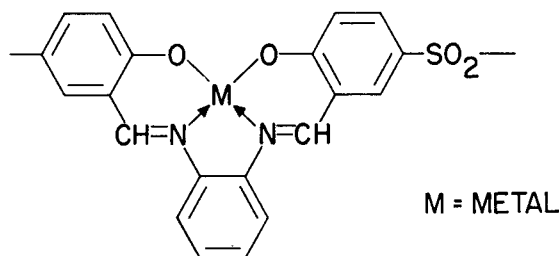
- HIGH TEMP. PROPERTIES
- + ELASTOMER
- ++ CHEMICAL STABILITY

POLYISOBUTYLENE (BUTYL RUBBER)

FIGURE 68-18.—Organic vs. inorganic elastomers.

structure of butyl rubber. The P, N, Cl polymer has been made in the form of oils, waxes, elastomers, and infusible solids. The elastomer has been of special interest as a thermally stable rubber at temperatures on the order of 300° C. Molecular weights from 20,000 to 80,000 have been reported. However, physical and thermal stability are only a part of the picture, chemical stability is also an important factor. The polymer cannot be used here on earth because of its susceptibility to hydrolysis, although in spacecraft applications, where likelihood of hydrolysis is greatly reduced, it may find some specialized use.

Another example of some work on high-temperature polymers is that of C. S. Marvel at the University of Arizona who has prepared a number of complex chelate polymers, one of which is shown in figure 68-19. These are stable from 300° C to 500° C in air and have been made with molecular weights of over 10,000. Many serious problems still exist before this family of polymers will find application. One of the most severe problems is difficulty of processing



CHELATE POLYMER

GOOD THERMAL STABILITY IN AIR

MOLECULAR WEIGHTS OVER 10,000

FIGURE 68-19.—Metal-organic polymer.

or fabrication. Often these materials are like a fine glass powder when formed in the reactor and cannot be processed. At present this is one of the unresolved, though not necessarily insurmountable, problems.

## CONCLUDING REMARKS

Nonmetallic materials, particularly polymers, have many unusual and desirable properties for use in spacecraft applications, but their sensitivities to ultraviolet and high-energy ionizing radiation of space have created problems—some as yet unsolved. The interaction of the space environment with these materials used in composite form and for thermal control surfaces has been discussed with relation to the present state of knowledge. The need for new nonmetallic materials with properties such as those of inorganic polymers has been discussed. In view of these desirable properties, it has been predicted (ref. 16) that by 1970, one-half of the structural weight of all aerospace vehicles will be fabricated of some form of polymers.

## REFERENCES

1. PECKNER, D., and RILEY, M. W.: Metals vs Plastics. *Materials in Design Engineering*, vol. 55, no. 3, Mar. 1962, pp. 131-142.
2. LAYTON, PAUL: Review of Various Glass Filaments. *Filament Winding Conference*, March 28-30, 1961, Soc. Aerospace Material and Process Eng., 1961, pp. 197-204.
3. ANON.: Seventeenth Annual Technical and Management Conference (Chicago), Feb. 1962. Secs. 1-A—1-E and Secs. 10—10-E. Sponsored by Soc. Plastics Ind., Inc.
4. PETERSON, GEORGE P.: High Modulus Glass Fibers For Reinforced Plastics. WADD Tech. Rep. 60-735, U.S. Air Force, Sept. 1961. (Available from ASTIA as AD 268902.)



## MATERIALS

5. LEWIS, D. J., MODISSETTE, J. L., and THIBODAUX, J. G.: High Mass Fraction Solid-Propellant Rocket Design Concept. Bulletin of the 18th Meeting—JANAF-ARPA-NASA Solid Propellant Group, Vol. 1, Appl. Phys. Lab., Johns Hopkins Univ., June 1962, pp. 237-260.
6. LEVENETZ, BORIS: Development of an Ultralight Rocket Motor Case. Bulletin of the 18th Meeting—JANAF-ARPA-NASA Solid Propellant Group, Vol. 1, Appl. Phys. Lab., John Hopkins Univ., June 1962, pp. 277-287.
7. OSBORNE, ROBERT S., and GOODMAN, GEORGE P.: Materials and Fabrication Techniques for Manned Space Stations. A Report on the Research and Technological Problems of Manned Rotating Spacecraft. NASA TN D-1504, 1962, pp. 45-58.
8. ZENDER, GEORGE W., and DAVIDSON, JOHN R.: Structural Requirements of Large Manned Space Stations. A Report on the Research and Technological Problems of Manned Rotating Spacecraft. NASA TN D-1504, 1962, pp. 33-44.
9. CLEMMONS, DEWEY L., JR., and CAMP, JOHN D.: Amorphous Phosphate Coatings For Thermal Control of Echo II. Paper presented at the Multilayer Systems Symposium of the Electrochemical Society Meeting (Los Angeles, Calif.), May 6-10, 1962.
10. JAFFEE, L. D., and RITTENHOUSE, J. B.: Behavior of Materials in Space Environments. Tech. Rep. No. 32-150 (Contract No. NASw-6), Jet Propulsion Lab., C.I.T., Nov. 1, 1961.
11. CHARLESBY, A.: Atomic Radiation and Polymers. Pergamon Press (New York), 1960.
12. BOVEY, FRANK A.: The Effects of Ionizing Radiation on Natural and Synthetic Polymers. Interscience Publ., Inc. (New York), 1958.
13. CHAPIRO, ADOLPHE: Radiation Chemistry of Polymeric Systems. Interscience Publ. Inc. (New York), 1962.
14. LIND, SAMUEL C.: Radiation Chemistry of Gases. Reinhold Publ. Corp. (New York), 1961.
15. BRINGER, ROBERT P.: Fluorocarbon Plastics Under the Influence of Unusual Environmental Conditions. Symposium on Effects of Space Environment on Materials. Soc. Aerospace Materials and Process Eng., May 1962.
16. ANON.: Aerospace Age: Plastics in Orbit. Modern Plastics, vol. 139, no. 6, Feb. 1962, pp. 74-79, 152-164.

## 69. Ablation Materials for Atmospheric Entry

By Leonard Roberts

DR. LEONARD ROBERTS, *Head, Mathematical Physics Branch, Theoretical Mechanics Division, NASA Langley Research Center*, received his Bachelor of Science and Doctorate degrees in the fields of aerodynamics, fluid mechanics, and applied mathematics from the University of Manchester, England, in 1952 and 1955, respectively. From 1955 to 1957 he performed post-doctorate research at the Massachusetts Institute of Technology on problems of heat transfer and mass ablation from bodies in extremely high temperature flows.

Dr. Roberts joined the Langley staff in June 1957, and has become one of the leading experts in this country in the complex area of analysis of reentry heat shielding by mass ablation. His report prepared while at Massachusetts Institute of Technology on a study of aerodynamic melting is considered a pioneer effort in this subject. In the field of aerodynamic cooling by means of boundary-layer injection and material ablation, Dr. Roberts has published many original papers and has served as a consultant to industry and government agencies. He presented a paper "Radiation and Ablation Cooling for Manned Reentry Vehicles" in Zurich, Switzerland, in September 1960, before the Second International Congress of the Institute of the Aerospace Sciences. His most recent efforts concern the problem of rocket-exhaust—dust-layer interaction during a lunar landing and he presented a paper entitled "Exhaust Jet-Dust Layer Interaction During a Lunar Landing" at the Thirteenth Congress of International Astronautical Federation at Varna, Bulgaria, in September 1962. He has served on several technical committees at Langley and is the author of several NASA publications and other documents.

### SUMMARY

Some of the more important concepts of thermal protection by ablation are described and the extent of our progress in ablation materials research is discussed.

A short summary of the thermal environment is given, followed by a discussion of the several ablation processes with particular emphasis on charring ablation. The problem of environment simulation is then discussed and examples of typical facilities presented. Finally, some of the materials that have been successfully flight tested are reviewed.

### INTRODUCTION

When a vehicle enters the earth's atmosphere, it has a large amount of kinetic energy which

must be disposed in a controlled manner if the vehicle is to survive. A large fraction of this energy is transferred to the atmosphere (as kinetic and heat energy); nevertheless, the remainder, which appears as the aerodynamic heat input to the vehicle, is of such magnitude that its disposal constitutes a major problem.

The limited capability of metals to absorb or to radiate this heat has led to the use of ablation materials—materials which continue to perform in a satisfactory way under conditions of extreme heating. In the 7 years since the use of ablation materials was first given serious consideration as a means of protecting vehicles entering the atmosphere, a large research and

## MATERIALS

development effort has been applied to the problem of producing, testing, and proving these materials for use in flight.

This paper will describe some of the more important concepts of thermal protection by ablation and at the same time relate the extent of progress in ablation materials research.

### THE THERMAL ENVIRONMENT

The motion and heating of vehicles entering the earth's atmosphere has been the subject of continued study for many years and a large amount of information on the flight environment is available. (See, for example, refs. 1 to 5.) The magnitude of the heating problem for vehicles entering the atmosphere is illustrated in figure 69-1.

During entry, the vehicle experiences a heating rate which increases (as the atmospheric density increases) to a maximum value and then decreases as the vehicle is slowed down by atmospheric drag. This maximum value is plotted as the abscissa (fig. 69-1) from  $10^1$  to  $10^4$  Btu/sq ft/sec. The total heat flux experienced by the vehicle during the entry is plotted as the ordinate from  $10^3$  to  $10^6$  Btu/sq ft. The hatched line indicates the limits to which metallic heat shields can operate: a molybdenum shield can radiate about 40 Btu/sq ft/sec and a copper heat shield, such as that used on the early ballistic missiles, becomes so heavy that it is unfeasible for heat inputs greater than 10,000 Btu/sq ft. The broad arrow shows the thermal region in which the present and future entry vehicles will operate—the upper half of the arrow corresponds to manned vehicles, the lower

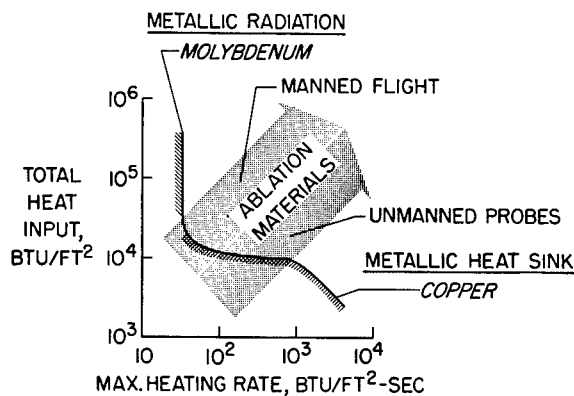


FIGURE 69-1.—Entry-vehicle heating environment.

half, to unmanned vehicles which experience a shorter duration of heating. The direction of the arrow is that of increasing entry velocity. It is clear from figure 69-1 that ablation materials play an extremely important role in the protection of vehicles returning from space.

### ABLATION CONCEPTS

The success of the ablation shield results first from the fact that it is not heating-rate limited, and second from its ability to dispose of a large amount of heat for a small amount of material loss. In general, the material may undergo sublimation or depolymerization (as is the case with most thermoplastic materials) or melting and vaporization (quartz is a good example of this). Analytical and experimental studies of these forms of ablation are to be found in references 6 to 10. Alternatively, pyrolysis may take place as with thermosetting plastics such as the phenolic resins. (See, for example, refs. 11 to 18.) Examples of the process of heat disposal by some of these materials are shown in figure 69-2.

A ceramic ablation shield is illustrated on the left of this figure. Aerodynamic heating of the virgin material causes it to flow as a liquid near the surface and part of this liquid layer is subsequently vaporized and is transported away by the airstream over the vehicle surface. The quartz ablation shield, presently used on the ICBM nose cone (ref. 19), behaves in this way. During ablation, heat is dissipated as latent heat in the phase change and is also transported away from the surface by convection in the liquid and gas layers.

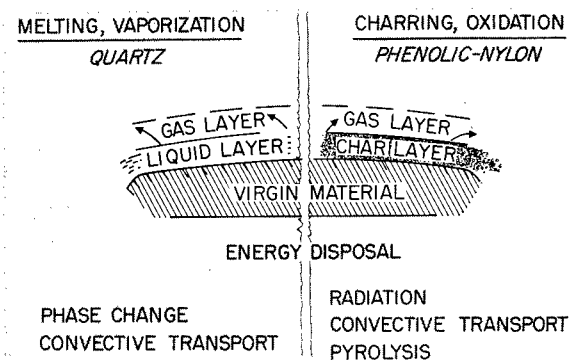


FIGURE 69-2.—Ablation concepts for two types of material.

# ABLATION MATERIALS FOR ATMOSPHERIC ENTRY

On the right of figure 69-2 is illustrated a charring ablation shield. In this case the shield may comprise a resinous material reinforced with glass or nylon. Pyrolysis of the virgin material produces a carbonaceous char which can sustain high surface temperatures. Heat energy is disposed by radiation from the surface, by convective transport, and by pyrolysis within the material.

The capability of the ablation material to dispose of heat cannot be defined without reference to the conditions of heating. The enthalpy of the airstream and the type of heating encountered (whether convective or radiative heating) may play an important part in the response of the material. Radiative heating (refs. 20 to 22) becomes important when the air passing over the vehicle is sufficiently hot to radiate heat energy.

The effects of these environmental conditions are illustrated in figure 69-3. On the left is shown the variation, with the stream enthalpy, of a heat-disposal parameter  $H$  measured in Btu/lb for two materials, quartz and Teflon, under conditions of negligible radiation. It is seen that the relation is approximately linear. For example, the intercept on the Teflon curve at  $H=1,000$  Btu/lb represents the latent heat of depolymerization of the material. The subsequent increase in  $H$  above this value with increase in stream enthalpy represents the additional heat absorbed by the gaseous products as they are transported away from the surface. It is evident that the material behaves very efficiently when the stream enthalpy is large, or equivalently, when the vehicle is traveling at high speed (since the stream enthalpy is an indication of the vehicle kinetic energy).

The right-hand side of figure 69-3 shows the additional effect of radiation. The broken line is the basic curve for no radiation, the upper line shows the enhanced performance when radiative cooling occurs, and the lower line shows the poorer response of the material to radiative heating. The hatched areas indicate the experimental results on each of these curves.

From figure 69-3 one would conclude that the high-temperature materials which allow the benefits of radiation cooling are superior. This

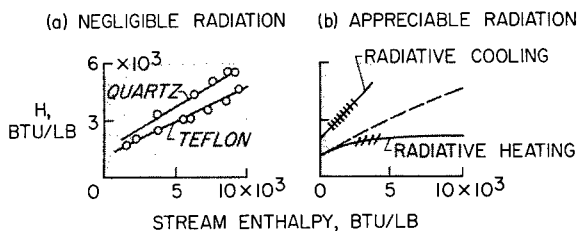


FIGURE 69-3.—Effects of environmental conditions on heat-disposal capability.

is not always the case, however, since the high-temperature materials also encourage conduction of heat to the cool structure and therefore introduce a severe insulation problem. This problem is especially important for manned vehicles since they tend to endure longer periods of heating. Therefore, the characteristic conduction time for the material must be considered since this time provides an indication of the insulative quality of the material.

The surface temperature of the material and the characteristic heat conduction time are the two quantities which determine its insulative capability; these two quantities are plotted along the ordinate and the abscissa, respectively, of figure 69-4. For the purposes of this paper, the characteristic conduction time is the time required for the temperature at the back surface of a slab, 5 lb/sq ft in thickness, to increase by 300° F when the front surface is raised to the indicated temperature. The characteristic conduction times for various types of material are presented in this figure.

The first noticeable result is that the high-temperature materials have low characteristic conduction times. Graphite, for example, is capable of sustaining very high temperatures and can dispose of large amounts of heat under

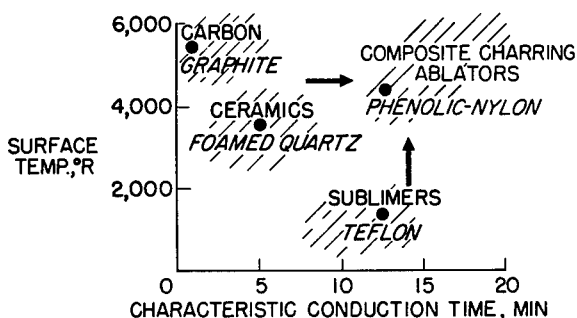


FIGURE 69-4.—Insulation capability of various materials.

severe heating conditions. Its characteristic conduction time, however, is extremely low; thus, it cannot be used when it is necessary for the vehicle to remain cool for a long period of time, although it may be used at isolated locations far removed from the cool structure.

The low-temperature subliming materials, on the other hand, have a much longer characteristic conduction time and thus reduce the problem of insulation. However, they cannot radiate appreciably and may suffer a large amount of ablation over long heating periods. Ceramics, as a class, tend to fall between these two extremes.

Evidently, the ideal material is capable of radiating at high surface temperatures and at the same time has a long characteristic conduction time so that heat penetrates through the material very slowly. The ideal material has not yet been found, of course, but some progress in this direction has been made in recent years in the development of composite charring materials. These materials, in the virgin state, have good insulative properties but during ablation produce a carbonaceous char which attains a high surface temperature and therefore radiates an appreciable amount of heat.

### CHARRING ABLATION

A typical composite ablation material consists of a phenolic or an epoxy resin reinforced with fiberglass or asbestos in the form of random or oriented fibers or in the form of a cloth. The ablation shield used on the Mercury spacecraft, for example, was a combination phenolic-fiberglass material. Figure 69-5 illustrates the sev-

PHENOLIC-NYLON; PHENOLIC-ASBESTOS; PHENOLIC-GLASS

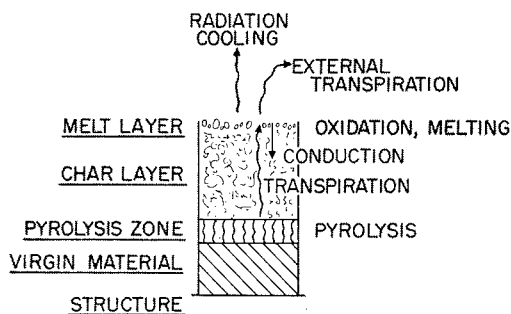


FIGURE 69-5.—Composite charring ablation phenomena.

eral phenomena that take place simultaneously during the ablation of such a material. The material is shown in several layers; at the lower part of the figure is the virgin material which is attached to the structure. Above the virgin material is a pyrolysis zone in which the phenolic resin starts to pyrolyze and form a char which accumulates to form a thick layer supported by the reinforcing material. The exposed surface of this reinforced char undergoes melting and oxidation and these two effects, together with aerodynamic shear and pressure forces, limit the growth of the char layer. Within the char, conduction of heat inwards to the pyrolysis zone is partly canceled by the transpiration of gases outward to the surface, and the subsequent introduction of these gases into the external flow provides further cooling. Since the char has a high carbon content, it sustains high surface temperatures and radiates an appreciable amount of heat. However, since pyrolysis takes place at a relatively low temperature, little conduction of heat takes place within the virgin material. This type of ablation has been investigated both experimentally and theoretically and appears to promise the solution to the heating problem encountered by manned entry vehicles. (See refs. 23 and 24.)

The evaluation of charring materials is made particularly difficult by the fact that several effects take place simultaneously, and a thorough understanding of the effects of extreme heating requires both experimental and theoretical research on the ablation mechanism. There are three major areas of research that require attention.

First, more complete information is needed on the chemistry that describes char formation. It is known experimentally that hydrogen and oxygen atoms are stripped from the phenolic structure at high temperatures, but there is still room for a more complete quantitative description of the reactions that take place throughout the char and of the way in which the internal transport of heat and chemical species affect these reactions. Second, information on char-layer properties is required, especially at high temperatures. Such properties as the surface emissivity, the thermal conductivity, porosity,

and resistance to shear and pressure forces are all important in determining its response to the environment of atmospheric entry. Last, information on the interaction of the products of ablation with the aerodynamic flow over the surface of the vehicle is needed. Chemical reactions at the surface and in the gas boundary layer may change the chemical and physical character of the flow to such an extent that appreciable changes in the heating rate may result, and these changes will then feed back and modify the response of the material.

Although these problems do not involve new concepts, they are nevertheless complex and are of such a nature that the researcher requires a background in two or three disciplines.

### SIMULATION OF THE HEATING ENVIRONMENT

Since the behavior of ablation materials depends so much on the environmental inputs, the heating rate, stream enthalpy, shear stress, and so forth, it is not always easy to extrapolate from laboratory experiments up to flight conditions, and it is rarely possible to simulate the several environmental effects which control the ablation process. Accordingly, in the planning of experimental tests, the primary inputs must be determined and provision made for their proper simulation while the less important ones must be abandoned. The environmental factors of most importance in one kind of ablation, however, are not necessarily important in another.

For materials that sublime or depolymerize, the stream enthalpy and the percentage radiative heating are important. For materials which melt at a high temperature, however, the total heat input, which determines the rate of production of the melt, and the shear stress, which governs the rate of removal of the melt, are the primary inputs. The stream enthalpy continues to be important. When ablation by charring takes place, char is produced by heating and removed by oxidation and by shear and pressure forces; therefore, these quantities must be simulated.

Experimental research on such materials has been carried out in a variety of facilities. (See refs. 12 and 25 to 30.) These facilities include the relatively simple oxyacetylene torch which

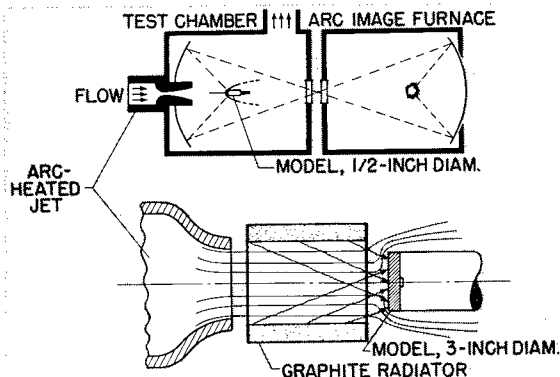


FIGURE 69-6.—Two types of reentry heating simulator.

has been used primarily as a means of screening materials, the rocket-motor exhaust, electric-arc tunnels, and the graphite furnace and arc-image furnace which produce a radiation-heating environment.

Figure 69-6 shows two facilities which simulate both the convective and radiative heating environment associated with high-speed entry into the atmosphere. In the upper half of the figure is shown a schematic diagram of the combined convective-radiative heating facility at the NASA Ames Research Center. (See ref. 30.) An arc-type heater supplies the hot air which passes through the nozzle and over the model to provide convective heating. Radiative heating is supplied by a carbon-arc lamp whose radiation is focused on the face of the model by the use of two elliptical mirrors as shown. The convective heater produces a heating rate up to 600 Btu/sq ft/sec (on a model with a nose radius of  $\frac{3}{8}$  inch) and a stream enthalpy up to 7,000 Btu/lb. The arc-image furnace produces heating rates up to 750 Btu/sq ft/sec when operating on a power source of 300 amperes at 75 volts.

The lower half of the figure shows a reentry heating facility at the Langley Research Center. (See ref. 28.) Again convective heating is supplied by an arc-heated airstream, but the radiative heating is supplied by a graphite radiator. In this facility 3-inch-diameter specimens have been subjected simultaneously to convective heating rates of 200 Btu/sq ft/sec at a stream enthalpy of 3,500 Btu/lb and varying radiative heating rates up to 200 Btu/sq ft/sec. The experimental results obtained from these facilities, together with some ana-

## MATERIALS

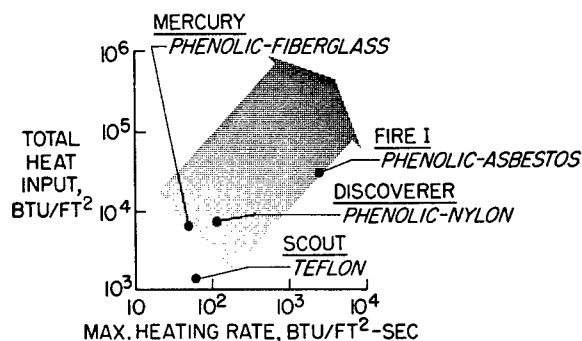


FIGURE 69-7.—Flight-tested ablation materials.

lytical work, have provided a better understanding of the ablation of charring materials under conditions of extreme heating.

## FLIGHT TESTS

Despite the large experimental efforts applied to the evaluation of ablation materials in ground facilities, it is never possible to duplicate the complete flight environment, and flight testing is always necessary before the material can be approved for operational use. During the last few years, an increasing amount of information has been obtained from recovered entry vehicles. Figure 69-7 shows some of the materials that have been tested and the vehicles used. The variables are those used in figure 69-1, the total heat input per unit area and the maximum heating rate per unit area. It is seen that the flight tests fall generally within the broad arrow that was shown in figure 69-1.

The Scout vehicle has been used to determine the flight performance of Teflon on a short-duration suborbital entry. The Mercury spacecraft has demonstrated the flight worthiness of the phenolic-fiberglass charring ablation shield. Similarly, the unmanned Discoverer satellite entered the atmosphere successfully with a phenolic-nylon ablation shield and a melting ceramic shield has also proved successful on the

Titan ICBM nose cone. Future flight plans by NASA include Project Fire which will investigate aerodynamic conditions at speeds up to 40,000 ft/sec and will probably use a phenolic-asbestos charring ablation shield. Much of this information will be useful in deciding the type of ablation shield to be used on future spacecraft.

There is still a large area within the arrow that has not yet been covered by flight tests; this region corresponds to flights of relatively long duration (20 to 40 minutes) and such flights cannot be made with a simple ballistic vehicle but require a more sophisticated vehicle having aerodynamic lift. In view of the importance of this longer duration heating environment to manned atmospheric entry, it is likely that this area will receive increased attention in future flight tests.

## CONCLUDING REMARKS

Considerable advances have been made in the technology of ablation in a relatively short period of time. This is not to say, however, that all the answers have been obtained, and there is a large continuing effort in this field. The need to produce lightweight versatile ablation materials still exists and future research and development will be directed toward materials that have a high heat-disposal capability and, at the same time, good insulative qualities and mechanical strength. Further, these materials must be easily applied to large surface areas if they are to protect vehicles having aerodynamic lift capability.

Clearly, the progress already made has been significant and, in view of the operational success of ablation materials on the Mercury spacecraft and other vehicles, the ablation approach appears to be the most satisfactory one for the protection of future vehicles returning from space.

REFERENCES

1. ALLEN, H. JULIAN, and EGGERS, A. J., JR.: A Study of the Motion and Aerodynamic Heating of Ballistic Missiles Entering the Earth's Atmosphere at High Supersonic Speeds. NACA Rep. 1381, 1958. (Supersedes NACA TN 4047.)
2. CHAPMAN, DEAN R.: An Approximate Analytical Method for Studying Entry Into Planetary Atmospheres. NASA TR R-11, 1959. (Supersedes NACA TN 4276.)
3. GAZLEY, CARL, JR.: Deceleration and Heating of a Body Entering a Planetary Atmosphere From Space. Vol. I of Vistas in Astronautics, Morton Alperin, Marvin Stern, and Harold Wooster, eds., Pergamon Press, c. 1958, pp. 8-32.
4. LOH, W. H. T.: Dynamics and Thermodynamics of Re-Entry. Jour. Aerospace Sci., vol. 27, no. 10, Oct. 1960, pp. 748-762.
5. GOODWIN, GLEN, and CHUNG, PAUL M.: Effect of Nonequilibrium Flows on Aerodynamic Heating During Entry Into the Earth's Atmosphere From Parabolic Orbits. Advances in Aero. Sci., vols. 3-4, Pergamon Press (New York), 1961.
6. SUTTON, GEORGE W.: The Hydrodynamics and Heat Conduction of a Melting Surface. Jour. Aero. Sci., vol. 25, no. 1, Jan. 1958, pp. 29-32, 36.
7. ROBERTS, LEONARD: On the Melting of a Semi-Infinite Body of Ice Placed in a Hot Stream of Air. Jour. Fluid Mech., vol. 4, pt. 5, Sept. 1958, pp. 505-528.
8. LEES, LESTER: Similarity Parameters for Surface Melting of a Blunt Nosed Body in a High Velocity Gas Stream. ARS Jour., vol. 29, no. 5, May 1959, pp. 345-354.
9. BETHE, HANS A., and ADAMS, MAC C.: A Theory for the Ablation of Glassy Materials. Jour. Aero/Space Sci., vol. 26, no. 6, June 1959, pp. 321-328, 350.
10. ROBERTS, LEONARD: Stagnation-Point Shielding by Melting and Vaporization. NASA TR R-10, 1959.
11. ADAMS, MAC C.: Recent Advances in Ablation. ARS Jour., vol. 29, no. 9, Sept. 1959, pp. 625-632.
12. LEES, LESTER: Convective Heat Transfer With Mass Addition and Chemical Reactions. Presented at Third Combustion and Propulsion Colloquium of AGARD (Palermo, Sicily), Mar. 17-21, 1958.
13. GRUNTZEST, I. J., and SHENKER, L. H.: Behavior of Reinforced Plastics at Very High Temperatures. Modern Plastics, vol. 35, no. 6, June 1958, p. 55.
14. BARRIAULT, R. J., and Yos, J.: Analysis of the Ablation of Plastic Heat Shields That Form a Charred Surface Layer. ARS Jour., vol. 30, no. 9, Sept. 1960, pp. 823-829.
15. SWANN, ROBERT T., and PITTMAN, CLAUD M.: Numerical Analysis of the Transient Response of Advanced Thermal Protection Systems for Atmospheric Entry. NASA TN D-1370, 1962.
16. SCALA, SINCLAIRE M., and GILBERT, LEON M.: The Thermal Degradation of a Char-Forming Plastic During Hypersonic Flights. ARS Jour., vol. 32, no. 6, June 1962, pp. 917-924.
17. BROOKS, WILLIAM A., JR., SWANN, ROBERT T., and WADLIN, KENNETH L.: Thermal Protection for Spacecraft Entering at Escape Velocity. [Preprint] 513F, Soc. Automotive Eng., Apr. 1962.
18. SCHMIDT, DONALD L.: Ablation of Plastics. ASD-TR-61-650, U.S. Air Force, Feb. 1962.
19. YAFFEE, M.: Ablation Wins Missile Performance Gain. Aviation Week and Space Technology, vol. 73, no. 3, 1960, pp. 54-55, 57, 59-61, 65.
20. MEYEROTT, R. E.: Radiation Heat Transfer to Hypersonic Vehicles. Lockheed Rep. LMSD 2264, Lockheed Aircraft Corp., Nov. 1957.
21. KIVEL, B., and BAILEY, K.: Tables of Radiation From High Temperature Air. Res. Rep. 21 (Contracts AF 04(645)-18 and AF 49(638)-61), AVCO Res. Lab., Dec. 1957.
22. TEARE, J. D., GEORGIEV, S., and ALLEN, R. A.: Radiation From the Non-Equilibrium Shock Front. Res. Rep. 112 (Contract AF 19(604)-7458), AVCO Res. Lab., Oct. 1961.
23. ROBERTS, LEONARD: Radiation and Ablation Cooling For Manned Re-Entry Vehicles. Advances in Aero. Sci., vols. 3-4, Pergamon Press (New York), 1961, pp. 1019-1044.
24. STEG, LEO: Materials for Re-Entry Heat Protection of Satellites. ARS Jour., vol. 30, no. 9, Sept. 1960, pp. 815-822.
25. LUCAS, WILLIAM R., and HUSTON, MYRON E.: Planning a Re-Entry and Recovery Test Program. Astronautics, vol. 4, no. 3, Mar. 1959, pp. 30-31.
26. ANON.: Determination of Factors Governing Selection and Application of Materials for Ablation Cooling of Hypervelocity Vehicles. CML-TN-M131-11 (Contract No. AF 33(616)-5436), Chicago Midway Labs., Univ. of Chicago, 1958.



#### MATERIALS

27. GEORGIEV, STEVEN, HIDALGO, HENRY, and ADAMS, MAC C.: On Ablation for the Recovery of Satellites. Res. Rep. 47 (Contract AF 04(647)-278), AVCO Res. Lab., Mar. 6, 1959.
28. WADLIN, KENNETH L., and KOTANCHIK, JOSEPH N.: The Use of Ablators for Achieving Protection Against High Thermal Flux. [Preprint] 417C, Soc. Automotive Eng., Oct. 1961.
29. SAVIN, RAYMOND C., GLORIA, HERMILO R., and DAHMS, RICHARD G.: The Determination of Ablative Properties of Materials in Free-Flight Ranges. NASA TN D-1330, 1962.
30. LUNDELL, JOHN, WINOVICH, WARREN, and WAKEFIELD, ROY: Simulation of Convective and Radiative Entry Heating. Presented at Second National Symposium on Hypervelocity Techniques (Denver, Colorado), Mar. 19-20, 1962.

## 70. Flow and Fracture Problems in Aerospace Vehicles

By Richard H. Kemp



**RICHARD H. KEMP**, *Head of the Powerplant Structures Section of the NASA Lewis Research Center, has specialized in stress and vibration research in propulsion structures. A native of Genoa, Ohio, Mr. Kemp is a graduate of the University of Toledo where he received his bachelor of engineering degree in 1943. He is a member of the Society for Experimental Stress Analysis, a member of the American Rocket Society, and a licensed Professional Engineer of the State of Ohio.*

### INTRODUCTION

Critical weight requirements for aerospace vehicles make it mandatory that each structural component bear its share of the imposed loads and operate at stress levels very close to the strength limits of the material. Such operation requires working with safety factors that are considerably smaller than those usually used. For example, a safety factor of 1.2 on the yield strength is not uncommon in the design departments of major space vehicle manufacturers. The use of such low safety factors requires, first, that the loads on the vehicle be precisely known, and, second, that the reaction of the material to a given situation of loading and environment be known or predictable. For the purposes of this discussion, it is assumed that the loads and stress distribution have been satisfactorily determined. (They can not always be determined, though, primarily because of unknown dynamic loads.) It remains to establish the capability of the given material in some component form to carry this load and stress distribution in the most efficient manner, despite the fact that materials are never perfect and will generally contain flaws or defects that establish some limit to their use.

As a result of utilizing materials at stress levels close to their maximum capability, it becomes exceedingly important to arrive at an under-

standing of their basic behavior when loaded. In conducting basic research leading to such an understanding, it is recognized that materials in their final use state (in the form of polycrystalline conglomerates) contain many imperfections. It has been shown, for example, that pure single crystal whiskers of sapphire prepared very carefully can attain a strength of as much as 1,800,000 pounds per square inch. Strengths such as this are not obtained in the engineering materials available at the present time, however, because of the presence of dislocations and defects within the crystal lattice that permit flow and fracture to occur at stress levels far below the cohesive strengths of the perfect lattice.

Materials research is, therefore, proceeding along several different lines to cope with this immediate problem. Some groups, for example, are attempting an explanation of the flow and fracture behavior of materials on an atomic level that will ultimately lead to a better understanding of the processes involved and possibly lead eventually to better engineering design concepts. Other groups are attempting empirical or semiempirical approaches, rather than exact theoretical explanations, in an effort to provide the designer with some badly needed guidance.

Research using both of these approaches is being carried on at the Lewis Research Center. Particular emphasis in the work is being placed on the environment that will be encountered in

## MATERIALS

space travel. For example, cryogenic temperatures down to that of liquid hydrogen will be encountered; corrosive media may influence fracture propagation; high-velocity meteoroid particles may transfer tremendous local energies to the material; and the type of stress field imposed may change the fracture characteristics.

### FLOW AND FRACTURE CHARACTERISTICS AT THE ATOMIC LEVEL

Essential to any mechanistic study of flow and fracture in solids is the study of the properties, interactions, and motions of crystal imperfections. These are largely responsible for the departure of the mechanical properties from ideal or theoretical behavior predicted by interatomic force laws. Plastic deformation or flow is always accompanied by dislocation motion, which in turn produces point defects such as lattice vacancies, interstitials, and various agglomerates of these. These point defects along with impurities may then markedly affect the motion of dislocations and flow behavior. In order to study these phenomena, single crystals of sodium chloride and magnesium oxide were carefully prepared and tested to determine their strength characteristics (ref. 1). The experiments show that these materials possess a fair degree of inherent ductility at room temperature and that the ductility and strength are extremely dependent on the mode of specimen preparation. Also, many of the findings indicate that the nature of the surface is a prime factor in the flow behavior of the crystals. For example, the ductility of crystals of sodium chloride has been substantially increased by treatments such as surface dissolution with water, coating with a 25-angstrom layer of silver, or coating with a thin film of stearic acid. Typical results of water treatment are shown in figure 70-1. The crystals were approximately the same size and were tested in bending. Specimen A was tested in the as-cleaved condition and is shown for reference purposes. The significant point to be noted in this figure is the variation in the amount of deflection obtained prior to failure as a function of the differences in the surface treatment. (The end points of the curves signify failures.) When only the com-

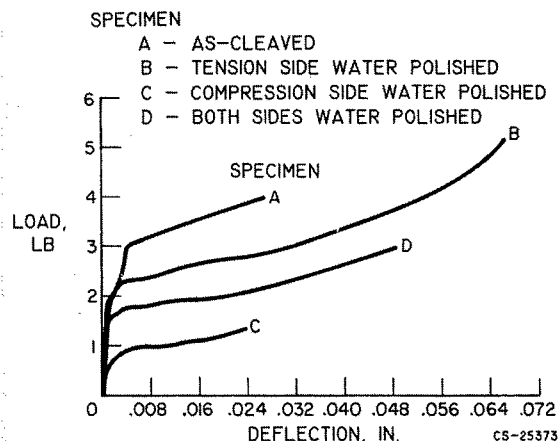


FIGURE 70-1.—Effect of surface treatment on ductility of sodium chloride single crystals.

pression side of the specimen was water polished, the ductility was roughly the same as for the as-cleaved crystal. When only the tension side was treated, however, the ductility was more than twice that of the as-cleaved crystal. The crystal polished on both sides had an intermediate ductility value. It is believed that the effect of the increased ductility obtained when the tension side was water polished is a result of the removal of surface flaws and defects. These flaws and defects provide the initiation site for the crack that ultimately propagates to produce the failure. The importance of the flaws and defects on the tension side as compared with the compression side would normally be expected. The differences in the actual load values at failure have not been satisfactorily explained.

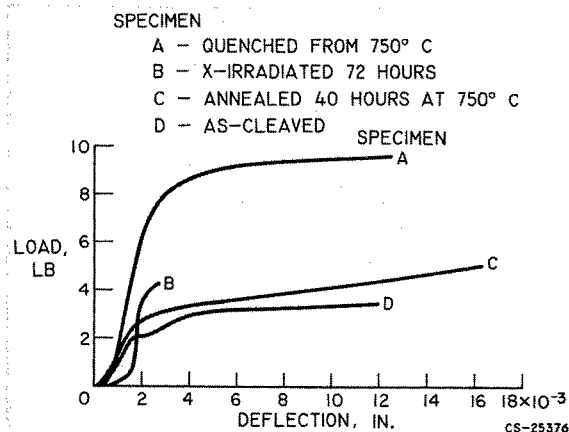


FIGURE 70-2.—Effect of bulk treatment on ductility of sodium chloride single crystals.

Figure 70-2 shows the effect of various bulk treatments as compared with the as-cleaved condition. These treatments are quenching from 750° C, X-irradiation for 72 hours, and annealing for 40 hours at 750° C. The point of primary interest in this figure is the very low ductility of the X-irradiated crystal compared with the other conditions, particularly the annealed condition. The irradiation effectively pins the dislocations and prevents them from moving as required for plastic flow. This phenomenon is also apparent in metals and is the subject of intense research in the consideration of materials for nuclear reactors for space vehicles. The difference in ductilities between the as-cleaved crystal of figure 70-1 and the as-cleaved crystal in figure 70-2 is indicative of the amount of scatter obtained. Despite this scatter, however, the effects of the various treatments on ductility were shown to be significant in repeated tests.

Aside from the marked changes in ductility, it is interesting to note the peculiar S-shape of the load-deflection curves. The initial portion of the curves, before the inflection point, is an anelastic region. In fact, at no point in the curves does the value of the slope approach the theoretical modulus for this single-crystal material. This behavior, originally thought to be unique with ionic crystals, has recently been found to occur in single crystalline metals at several other laboratories.

Although considerable progress has been made in the understanding of flow and fracture phenomena on the atomic level, the present state of the science does not permit the prediction of the performance of the polycrystalline conglomerates that must be dealt with in space engineering problems. For this reason, a number of empirical and semiempirical approaches have been proposed for predicting the strength of structures on the basis of certain parameters determined from test specimens of the material in question.

#### FRACTURE MECHANICS OF HIGH-STRENGTH MATERIALS

As a polycrystalline material is loaded or stressed, distortion of the crystal lattices occurs, and the bulk effect is a period during which the

strain is approximately linearly proportional to the stress. As the stress increases, however, the dislocations move and produce the effect called plastic flow as the atom layers slip past each other. The imperfections or dislocations accumulate at various points within the crystal until they may be considered as voids. When a sufficient number of these voids appear, they may interconnect to produce a microscopic flaw or crack. After the appearance of these cracks, a question remains as to how much higher the material can be stressed without propagating the cracks to the point where cataclysmic failure of the structure occurs. The empirical or semiempirical approaches in general assume that the material already contains voids of a size that can be considered as cracks and would be visible to the eye if the specimen were sectioned and examined. These approaches then ignore the steps in the process prior to the formation of the cracks and attempt to predict the growth pattern of the existing cracks as the material is loaded.

One such approach is that proposed by Griffith in 1920 when he published his paper on the brittle fracture of glass (ref. 2). He postulated that the crack becomes unstable when, for a given increase in crack length, the energy decrease in the surrounding stress field exceeds the energy required to create the new crack-surface area. The suggestion was made that, for a given material, the stress  $\sigma$  and half the crack length  $a$  should be related as follows:

$$K = \sigma \sqrt{\pi a}$$

As the stress is increased, the constant  $K$  approaches a limiting value  $K_c$  for the given material, and the crack immediately changes from a slow growth rate to a speed near the velocity of sound in the material. The  $K_c$  parameter, therefore, is a measure of the fracture toughness of the material, and by its use the critical crack length can be calculated for a given stress. This relatively simple approach appeared to satisfy the requirements to a large degree for the completely brittle materials such as glass, but did not work well when applied to the modern high-strength alloys. Many of these alloys fail in a brittle fashion, particularly at cryogenic temperatures, and it had been hoped that the same

concept could be used. Actually, considerable plastic flow is involved at the tip of the crack, and this suggests that the crack surface energy should be augmented by the work of plastic deformation in the volume of material adjacent to the crack tip (ref. 3). Definition and measurement of this plastic work are very difficult, however. The size of the plastic zone, and, therefore, the inelastic energy it absorbs, changes with crack length and with specimen dimensions generally, as well as with the material. Measurement of the rate of energy absorption with crack growth thus requires the measurement of a variable quantity that is not a characteristic constant of material toughness.

In considerations of the stress field surrounding the crack tip, it was suggested that the plastic zone appears to the stress field as a region of somewhat relieved normal stress and is roughly comparable with an extra extension of the existing crack. This approach resulted in the following equation:

$$K_c = \sigma \sqrt{\pi \left( a + \frac{K_c^2}{2\pi\sigma_{ys}^2} \right)}$$

where the term  $K_c^2/2\pi\sigma_{ys}^2$  is the required addition to the crack length to account for the plastic zone. The factor  $\sigma_{ys}$  is the yield strength of the material. This equation applies only to cases in which the ratio of crack length to specimen width is very small. For finite-width specimens, the equations are somewhat more complex, and a treatment of this problem is given in reference 4.

Research in the field of fracture mechanics is being carried out at the Lewis Research Center, with both uniaxial tensile specimens and biaxially stressed cylinders, as shown in figure 70-3. Cracks are simulated by machining central notches in the specimens with notch root radii as low as 0.0002 inch and determining the fracture toughness parameter  $K_c$ . The central notches are placed in the specimens by hand broaching the edges of a 0.080-inch drilled hole on a diameter of that hole perpendicular to the maximum principal stress. A photograph of these specimens is shown in figure 70-4. The test temperatures are those of primary interest in the space program because they occur in vehicle propellant tanks and life support struc-

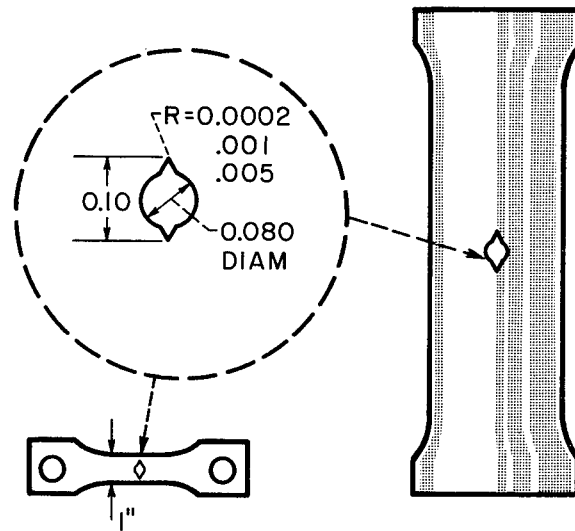


FIGURE 70-3.—Notch configuration and orientation in uniaxial and biaxial stress specimens.

tures. These temperatures range from 400° F for solid-propellant tanks to -423° F for cryogenic-propellant tanks. Considerable emphasis on the use of liquid hydrogen as a propellant in both chemical and nuclear propulsion engines centers much attention on the material properties at -423° F. The minimum weight requirements also involve the use of the highest possible strength-to-weight-ratio materials, and, in general, at -423° F the strength of notched specimens of these materials is below the yield point. Vehicle designs can not be made, therefore, on the basis of yield strength, because it must be assumed that at least one flaw or crack is probably present that escaped detection during the inspection process. This one flaw could prove disastrous if the fracture toughness of the material is not commensurate with the working stresses.

Attempts to use the uniaxial fracture toughness parameter  $K_c$  in the prediction of the fracture in the biaxial stress state of pressurized tanks have shown some signs of success, as is illustrated in figure 70-5. In this figure, the hoop burst stress for the cylinders is plotted as a function of the root radius of the notches machined in the cylinders. The material used was 2014-T6 aluminum, and the tests were conducted at two temperature levels, room temperature and -423° F. The notch radii were varied from 0.005 to 0.0002 inch. Tests re-

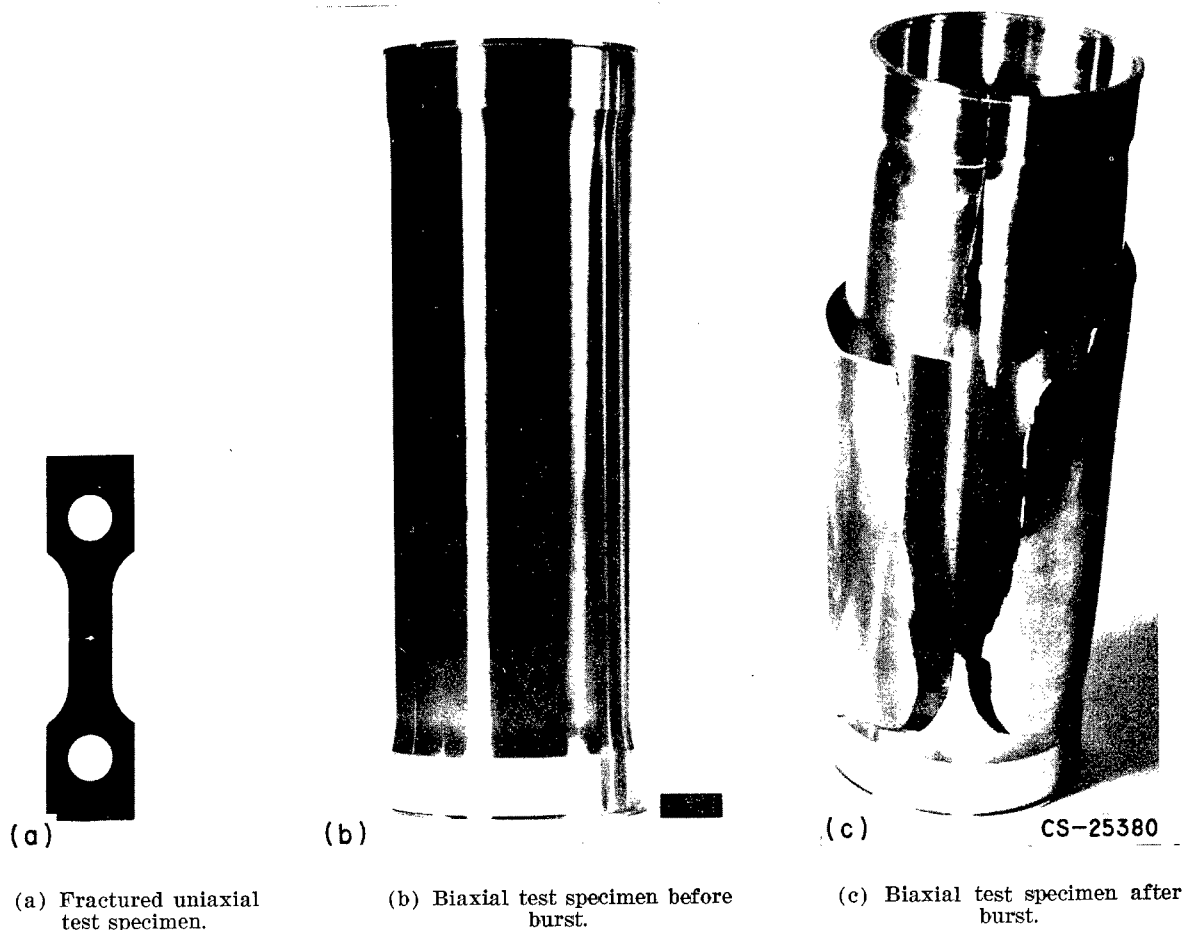


FIGURE 70-4.—Typical uniaxial and biaxial test specimens.

ported in reference 5 indicate that the 0.0002-inch-radius notch represents quite closely the performance of specimens having an actual crack. The data for less sharp notches were obtained to determine their effect on the cylinder strengths. The solid lines represent the predicted strength of the cylinders based on  $K_c$  values determined from tensile specimens having the same type of notches. In addition, it was necessary to make a correction to the size of the plastic zone at the tip of the crack in the cylinders in order to get the good agreement shown in figure 70-5. At  $-423^\circ\text{F}$  it was necessary to reduce the plastic zone size correction to a value of 46 percent of that required for uniaxial tensile specimens. At room temperature, the required reduction was 68 percent.

Figure 70-5 also shows the computed hoop

stress where yielding would occur in the cylinders based on the equivalent stress being equal to the uniaxial yield stress. For a notch root radius of 0.0002 inch, the failure stress of the cylinders was approximately 80 percent of the computed yield strength for both room temper-

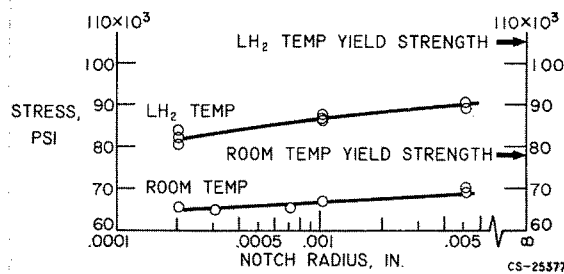


FIGURE 70-5.—Correlation of burst strength of notched 2014-T6 cylinders with modified Griffith-Irwin theory.

## MATERIALS

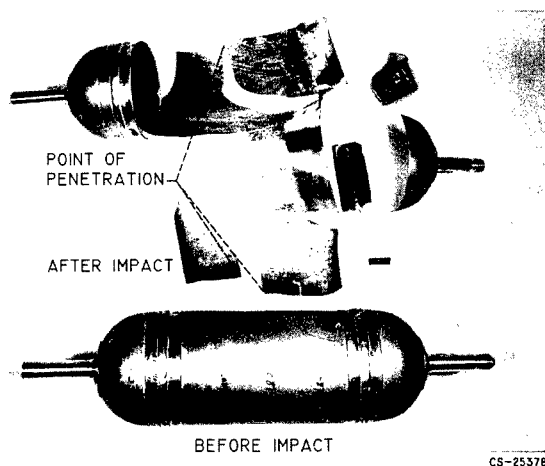


FIGURE 70-6.—Effect of high-speed particle impact on 2014-T6 aluminum tank filled with water.

ature and liquid-hydrogen temperature, which illustrates the danger of basing the design on yield strength for the case where there can be a small defect and the material shows a notch sensitivity.

### FLOW AND FRACTURE ASSOCIATED WITH HYPERVELOCITY IMPACT

Another interesting facet of the problem of flow and fracture of the high-strength materials used for propellant tanks lies in the area of hypervelocity impact. This problem is, of course, associated with the impact of meteoroids with space vehicles. These particles can be traveling at velocities from about 36,000 to 200,000 feet per second relative to the spacecraft.

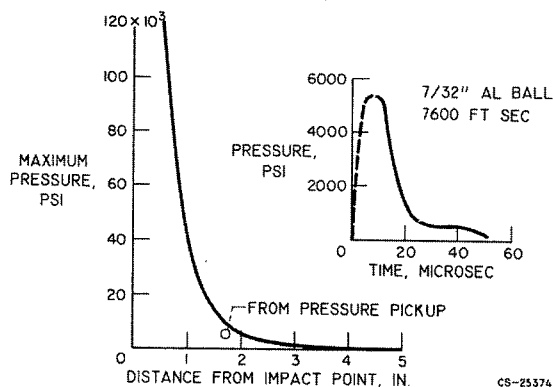


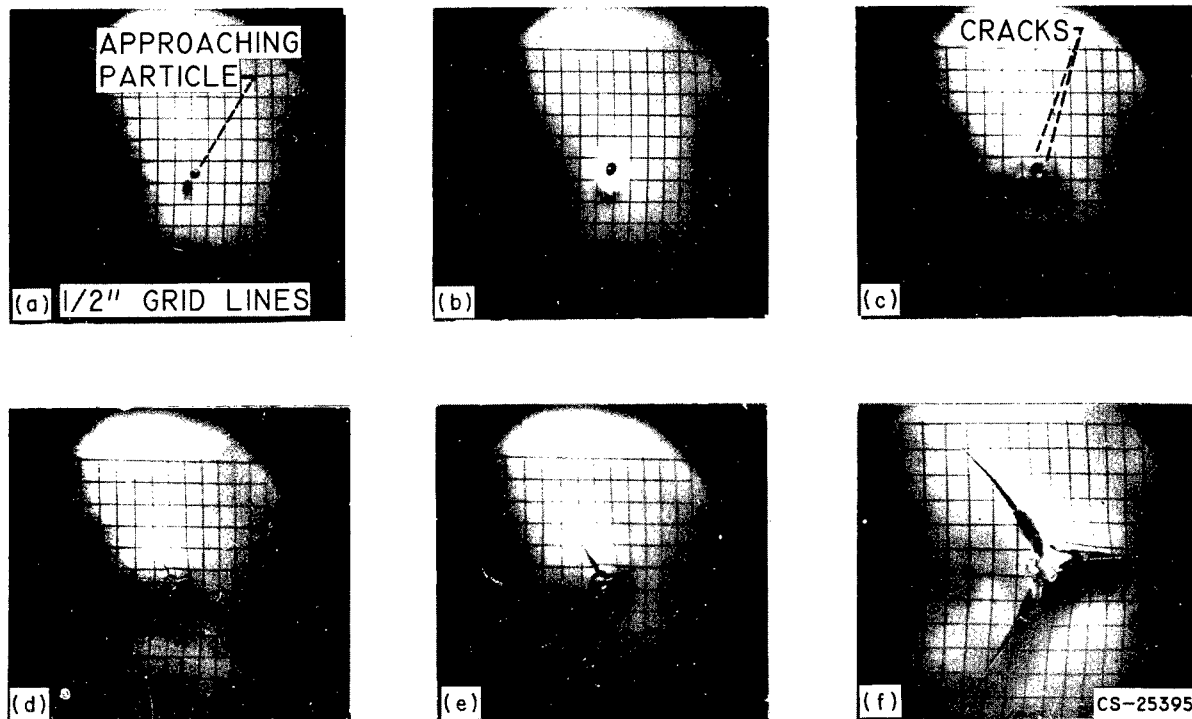
FIGURE 70-7.—Pressure generated in water-filled tank by high-speed particle impact.

If there is no liquid in contact with the wall that is impacted, the worst that will result is probably a clean hole that has some possibility of being patched or self-sealed in some fashion. If a liquid is in contact with the impacted tank wall, shock waves will be created in the liquid and will produce very high pressure forces. Figure 70-6 shows the results of firing a small aluminum pellet at about 7000 feet per second into a pressurized tank containing water. Similar experiments in which only a pressurized gas was contained in the tank resulted in a simple hole without the catastrophic damage illustrated.

An example of the pressures generated in the contained liquid at impact is illustrated in figure 70-7. These pressures were measured by means of high-speed photographs of shock waves traveling in water away from the point of impact. It can be seen that pressures well in excess of 100,000 pounds per square inch can be generated. These pressures are localized and result in a local initial failure, but the stored energy from pressurization within the tank can result in complete tank failure. Such a failure would immediately terminate the mission of a space vehicle and must be avoided at all costs.

The pressure pulse causing the failure is of short duration, as illustrated in the inset of figure 70-7. The pressure rapidly decays a few inches away from the point of impact. In order to be sure that the failure was occurring as a result of this initial high-pressure pulse, and not from a reflected shock wave, high-speed photographs were taken of the failure. A picture sequence of the failure is shown in figure 70-8. It can be noted that the first crack radiating from the point of impact was visible only 28 microseconds after impact. During the first 28 microseconds the shock wave in the water had a chance to travel less than 2 inches from the point of impact, and the shock wave in the metal only  $5\frac{1}{2}$  inches. It is thus clearly illustrated that the initial failure mechanism was local in nature.

The results shown were for tanks containing water. From analytical studies, the compressibility of the liquid is believed to have a significant effect on the impacting energy required to cause catastrophic failure. In addition, the



(a) Before impact.  
(b) Impact.

(c) At 28 microseconds.  
(d) At 50 microseconds.

(e) At 83 microseconds.  
(f) At 210 microseconds.

FIGURE 70-8.—Crack propagation as a result of high-speed particle impact on water-filled tank. Impacting particle,  $\frac{1}{32}$ -inch-diameter aluminum sphere; particle velocity, 5780 feet per second.

temperature of the fluid will be important because of its effect on the material properties of the tank wall. Cryogenic propellants will make the walls more susceptible to brittle fracture. Liquid oxygen, because of lower compressibility, may present more of a problem than liquid hydrogen. Future research programs will concentrate on studying the failure mechanism with these liquids.

As a matter of general interest, some preliminary results have also been obtained on reactions that occur when high-speed impacts occur on tanks containing liquid oxygen. For tanks made of aluminum or stainless steel containing liquid oxygen, impacts at velocities up to about 7500 feet per second resulted in rupture of the tanks, but there was no burning of the tank material due to the presence of liquid oxygen. When the tank wall was made of titanium alloy (5 percent aluminum, 21½ percent tin), a very violent reaction occurred. After impact, a series of detonations occurred, and

the subsequent burning consumed the titanium wall. A photograph of the impact in figure 70-9, taken from a single frame of a 16-millimeter movie, shows one of the detonations that occurred. It is obvious, therefore, that, even though titanium may have weight advantages for use in lightweight propellant tanks, there is a question as to whether to use it in oxidant tanks because of its high reactivity.

#### SUMMARY

The problem of flow and fracture in high-strength space vehicle materials has been shown to be very complex. It was indicated in particular how the problem can be influenced by environmental factors such as cryogenic temperatures and extremely high impact velocities of meteoroids. Investigations range from the atomic to the macroscopic level. It is hoped that eventually, when sufficient knowledge has been acquired, it will be possible to merge the seemingly divergent approaches now be-



## MATERIALS

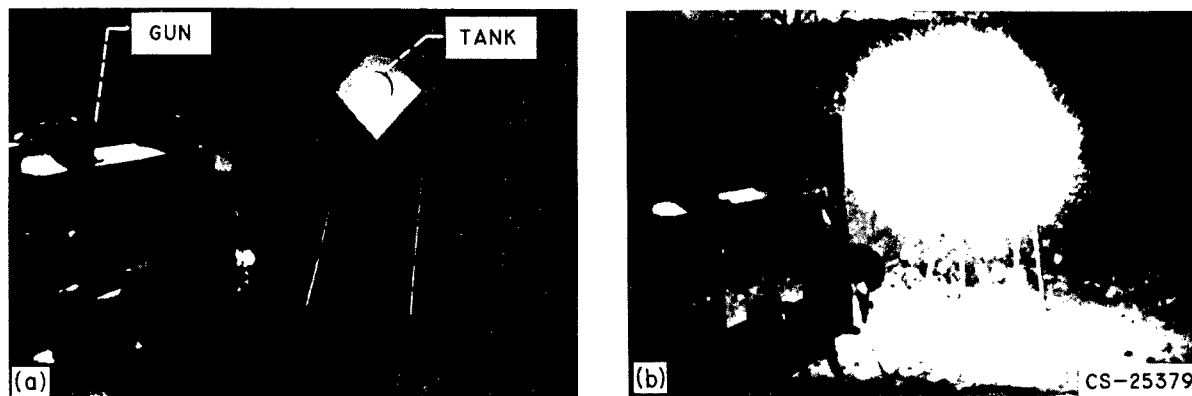


FIGURE 70-9.—Effect of impact of high-speed particle on titanium tank containing liquid oxygen.

ing used into one basic concept that will enable the designer of a vehicle to arrive at a satisfactory design with an exceedingly high degree of

reliability. It is obvious that much additional research is, therefore, required to attain this goal.

## REFERENCES

1. STEARNS, CARL A., PACK, ANN E., and LAD, ROBERT A.: Ductile Ceramics. I—Factors Affecting the Plasticity of Sodium Chloride, Lithium Fluoride, and Magnesium Oxide Single Crystals. NASA TN D-75, 1959.
2. GRIFFITH, A. A.: The Phenomena of Rupture and Flow in Solids. Phil. Trans. Roy. Soc. (London), ser. A, vol. 221, Mar. 1921, pp. 163-198.
3. IRWIN, G. R.: Fracture Dynamics. Fracturing of Metals, ASM, 1948.
4. First Report of a Special ASTM Committee: Fracture Testing of High-Strength Sheet Materials. ASTM Bull., Feb. 1960.
5. Third Report of a Special ASTM Committee: Fracture Testing of High-Strength Sheet Materials. Materials Res. Standards, vol. 1, no. 11, Nov. 1961.

## 71. High-Strength Materials Research

By Hubert B. Probst

DR. HUBERT B. PROBST, who is currently working on the properties of high-temperature nonmetallics, is Head of the Refractory Compounds Section of the NASA Lewis Research Center. He earned his B.S. in Metallurgy from the University of Notre Dame in 1953, his M.S. from the University of Michigan in 1954, and his Ph. D. from Case Institute of Technology in 1959. Dr. Probst is a member of the American Society for Metals and Sigma Xi.

The need for high-strength materials in aircraft and space applications stems from two necessities. First is that of weight savings; a high-strength material is able to sustain a given stress with a minimal cross section. Second is the need to combat the loss of strength that generally accompanies increased temperatures; many applications, particularly in powerplants, require stressed members to operate at high temperatures—thus the need for retention of strength to high use temperatures.

Some of the research that is in progress at the Lewis Research Center and that is devoted to improved strength characteristics of materials is reviewed herein. The review is made according to temperature ranges and covers many areas of vastly different materials and applications. The common thread in all these programs is improved strength.

When it is considered that the cost to orbit 1 pound of material about the Earth is in excess of \$1,000, the savings attendant to weight reductions by the use of high-strength materials is evident.

Figure 71-1 (ref. 1) compares a number of materials on a basis of strength-to-density ratio. The more conventional materials such as steels, titanium alloys, and aluminum alloys offer ratios of the order of 1 to 2 million. Beryllium shows some improvement over these. The fiber materials give the next step in improved strength-to-density ratios; however, they are

directional and must be oriented in the direction of the principal stresses and must be held together by a binder. Glass-reinforced plastics are present-day examples that utilize fiber strengths. In the field of propellant tanks, an attempt has been made to capitalize on the strength of a directional material by filament winding. The extremely strong whisker materials with ratios in the 12 to 24 million range hold promise for the future; however, there is much progress yet to be made toward quantity production and fabrication. The subject of whiskers is discussed later. Although alloys do not offer ultra high strength-to-density ratios, they are the materials in use today, and their shortcomings must be considered.

Consider first the room-temperature strength

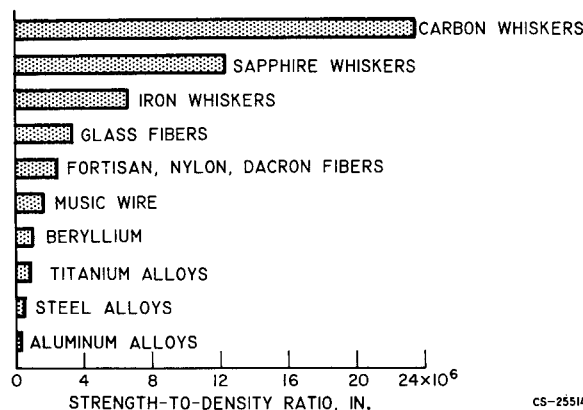


FIGURE 71-1.—Material strength-to-density ratios.

## MATERIALS

characteristics of alloys. An example of a quite serious problem in this temperature range is given in figure 71-2, which shows a solid-pro-

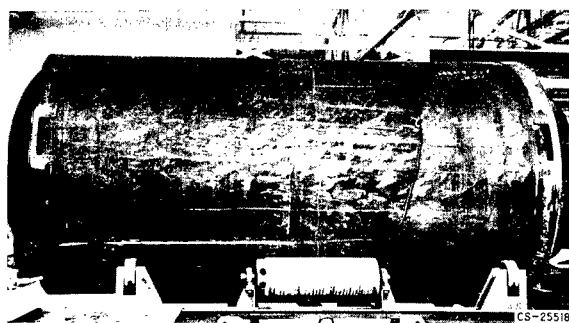


FIGURE 71-2.—Brittle fracture of large rocket motor case.

pellant motor case that failed during room-temperature pressure testing (photograph obtained from W. F. Brown, Jr. of Lewis). The failure is catastrophic and occurred at a stress level of only about 50 percent of the normal yield strength. Such a failure is attributed to the presence of small yet highly damaging cracks usually in the areas of welds. Such a crack can propagate unstably through otherwise sound material resulting in the catastrophic failure shown. Further insight into this problem is gained from figure 71-3 (ref. 2) in which the conventional tensile strength of smooth bar specimens is plotted against tempering temperature for a steel similar to that used in the rocket motor case. The material was heat treated in the 800° to 900° F range to give maximum tensile strength; however, a determination of strength for sharp-notched specimens gave the

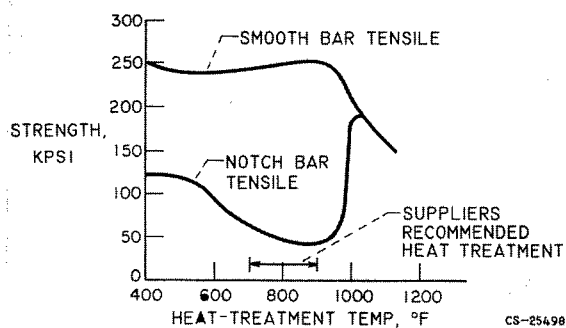


FIGURE 71-3.—Comparison of strength of smooth and notched specimens of steel at room temperature.

lower curve. It is apparent that the recommended tempering temperature has resulted in a minimum in notch strength, which accounts for the failure that occurred at a stress level far below the conventional tensile strength. This situation has, of course, been greatly improved by altering the heat treatment to one that results in higher notch strengths.

With this room-temperature behavior in mind, consider the effect of lowering temperature to the cryogenic range. In this range, the main concern for high-strength materials is for rocket cases and propellant tanks. Since these components represent a large portion of the total vehicle weight, significant weight reductions are possible by the use of thinner walls of higher-strength material. It is generally true that lower temperature results in increased strength, so that a lessening of problems stemming from material-strength considerations might be anticipated as lower temperatures are approached. Specifically, an improvement in the situation in progressing from present-day vehicles using liquid oxygen at -297° F to future systems requiring liquid hydrogen at -423° F is desired. Figure 71-4 (ref. 3) compares data for AISI-301 stainless steel and an alpha titanium alloy and shows the anticipated gains in strength; however, the problems are by no means lessened, because the presence of defects again is of major concern. This is illustrated in the curves plotted for sharp-notch strengths, which decrease below a certain tem-

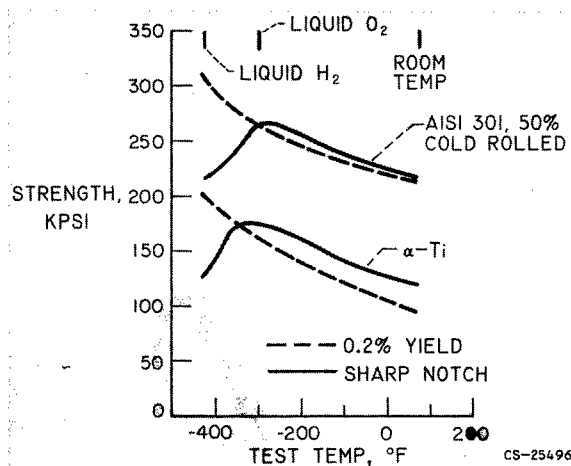


FIGURE 71-4.—Effect of cracks on strength of alloys tested at various temperatures.

perature. This increased sensitivity to the embrittling effects of notches renders the material vulnerable to catastrophic failure, as already illustrated in the failure of the motor case at room temperature.

Since the tanks of space vehicles will be large structures in which detection or elimination of all flaws introduced during the various fabrication processes is impossible, the behavior of materials with flaws or notches at cryogenic temperatures becomes of utmost importance to the designer. Along these lines, work at the Lewis Research Center is continuing in the development of testing methods to evaluate resistance to catastrophic failure and formulation of suitable criteria for rating materials for thin-walled cryogenic-pressure-vessel service. Significant contributions have already been made in this area. With these newly developed test methods, such variables as heat treatment, composition, and melting and fabrication practices are being investigated.

At elevated temperatures, the need for high-strength materials arises from the weight-savings consideration but primarily from the desire to increase operating temperatures of powerplants. The maximum operating temperature of a powerplant is usually set by the materials available. Thus, the quest for superior material is made to allow operating temperatures to increase.

One effective means of strengthening a metal or an alloy is to disperse fine particles throughout the matrix which serve to inhibit dislocation glide (slip) and creep and generally allow for higher strengths at higher temperatures. This effect was observed in 1919 (ref. 4) in the age hardening of an aluminum alloy and is attributed to a precipitation reaction. About 15 years ago, strengthening of extruded aluminum powder was observed (ref. 5) and attributed to thin oxide layers (aluminum oxide), which were broken into fine particles during the extrusion process and inhibited flow of the aluminum. This material, generally referred to as SAP (sintered aluminum powder), gave considerably improved strengths and use temperatures to aluminum, as shown in figure 71-5 (ref. 6). The higher use temperature of SAP is a result of the fact that it is a nonequilibrium structure.

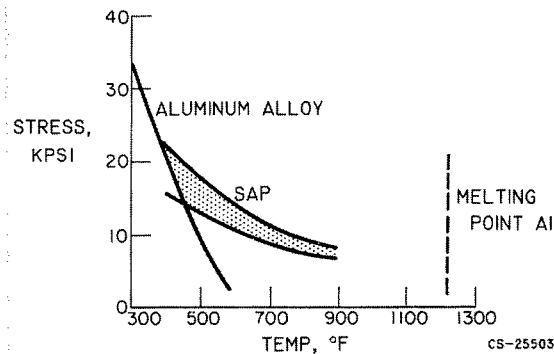


FIGURE 71-5.—Stress-temperature curves for rapture in 1000 hours (ref. 6).

Compared with an equilibrium structure, such as a precipitation-hardened aluminum alloy whose strength is lost at elevated temperatures because of complete dissolution of the strengthening precipitate, the oxide particles in SAP remain stable at such temperatures and continue to strengthen. Since the introduction of SAP, great effort has been put forth to apply such principles to higher melting metals in the hope of increasing use temperatures.

The oxide particles in SAP are spaced approximately 0.3 micron apart, and it is felt that such a submicron spacing is necessary to achieve the full potential strengthening benefits of the dispersed particles. Of the several methods by which fine dispersions may be produced, the approach taken at Lewis has been to mix directly powders of dispersant and matrix. This, of course, requires powders of submicron size. The production of such metal powders by normal attrition methods is difficult because of particle agglomeration that occurs before the submicron range is reached. Submicron powders have resulted from a study at Lewis (ref. 7) in which various grinding aids were used to prevent agglomeration. It is believed that such aids prevent agglomeration by reducing electrostatic attraction and by reducing the tendency of the particles to weld together. The effect of one such aid, potassium ferriocyanide ( $K_3Fe(CN)_6$ ), is shown in figure 71-6 (ref. 7). For a number of metal powders with starting sizes as large as 30 microns, final particle sizes less than 1 micron have been achieved in conventional ball mills.

With such powders, structures quite similar to

## MATERIALS

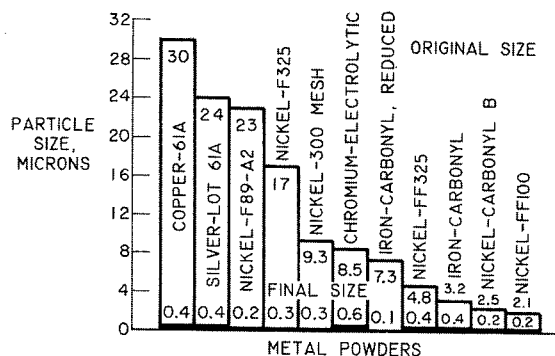
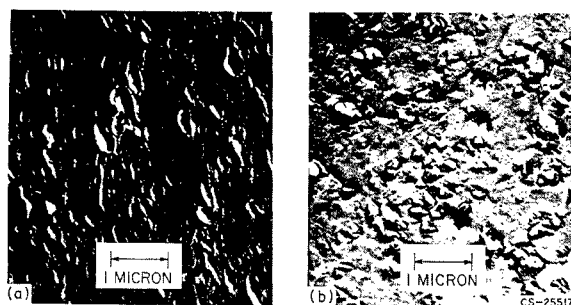


FIGURE 71-6.—Use of potassium ferricyanide to grind various metal powders. Milled for 15 days in 200-proof ethyl alcohol.



(a) Aluminum oxide in nickel.  
(b) SAP.

FIGURE 71-7.—Comparison of microstructures of aluminum oxide dispersed in nickel and SAP.  $\times 20,000$ .

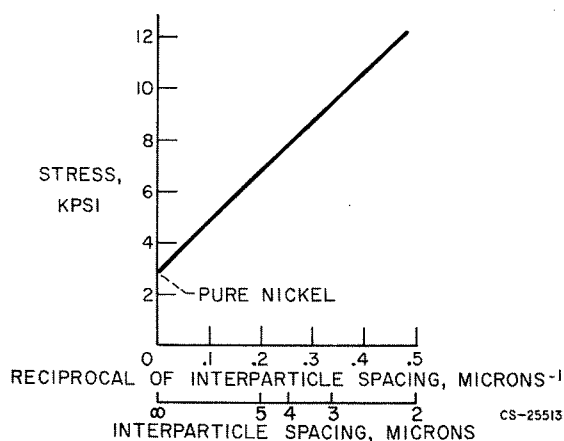


FIGURE 71-8.—Stress to cause rupture in 10 hours at 1500° F against reciprocal of measured interparticle spacing for nickel-aluminum oxide system (ref. 8).

those of SAP have been produced as shown in figure 71-7 (unpublished data of J. W. Weeton of Lewis). Here, finely dispersed aluminum oxide in nickel is compared with a typical SAP structure. The  $\text{Ni-Al}_2\text{O}_3$  structure was prepared by direct mixing of the two powders followed by extrusion. With such materials, the basic effects of particle sizes and interparticle spacing are now being studied in a variety of systems. Past results with the  $\text{Ni-Al}_2\text{O}_3$  system show a strong effect of particle spacing on strength as shown in figure 71-8 (ref. 8). The stress required to cause failure in 10 hours at 1500° F is shown to vary directly as the reciprocal of the interparticle spacing. Also, note the strengthening over pure nickel.

Another means of attaining improved strength is the conventional alloying approach. In this method an attempt is made to strengthen existing phases and produce new phases that will contribute to strength; these effects are brought about by judicious control of composition. Such a program has been in progress at the Lewis Research Center for several years (refs. 9, 10, and 11). The basic composition in weight percent of the experimental alloy is as follows:

Mo	Cr	Al	Zr	Ni
8	6	6	1	Bal.

The major additions to the basic alloy were  
Carbon  
Titanium  
Titanium plus carbon  
Vanadium plus carbon  
Tungsten plus vanadium plus carbon  
Tantalum plus tungsten plus vanadium plus carbon

Chromium and aluminum have been added primarily for oxidation resistance and molybdenum for solid-solution strengthening. Zirconium is believed to stabilize the composition against diffusion losses (ref. 12). Modifications to the base composition were made in attempts to get dispersed phases and strengthening.

The resulting strengthening is shown in figure 71-9 (ref. 11). The more complex tantalum-tungsten-vanadium-carbon modification has led to the greatest improvement. Increased stress-rupture lives are dramatic at 1800° F, for example. Also of importance is the improve-

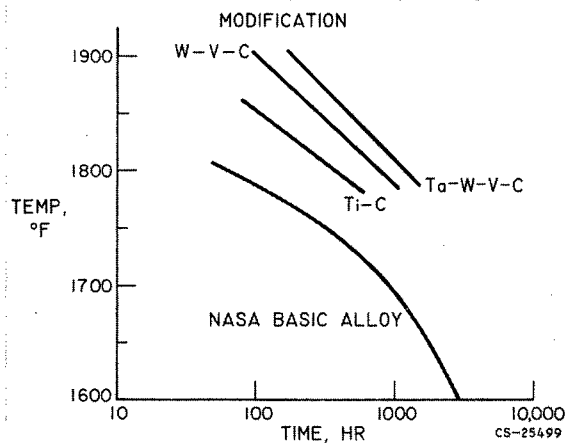


FIGURE 71-9.—Stress-rupture comparison at 15,000 psi stress of nickel-base alloy series.

ment in use temperature; for example, for a 200-hour life at 15,000 psi, the use temperature has been increased from 1760° to 1900° F.

Admittedly, with such complex compositions, it is difficult to define a singular strengthening mechanism; however, in the case of the Ta-W-V-C modification, electron diffraction has identified the  $\text{Ni}_3\text{Al}$  intermetallic and the carbides  $\text{TaC}$  and  $\text{MoC}$ . The presence of a nickel-aluminum-vanadium intermetallic and complex carbides is also suspected.

Of major importance to such highly alloyed compositions is workability, that is, the avoidance of complete embrittlement by the strengthening additions. The workability of the Ta-W-V-C-modification is illustrated in figure 71-10. The upper portion of the figure shows cross sections of a  $\frac{3}{4}$ -inch cylinder before and after forging at room temperature. The lower portion shows cross sections after various reductions. No cracking occurred, and no intermediate stress relief anneals were used. The maximum reduction in diameter is 29 percent; however, with the use of intermediate anneals, diameter reductions as high as 50 percent can now be obtained.

Work with this basic alloy is continuing both at Lewis and in industry. At Lewis, new efforts are under way to apply similar principles to cobalt-base alloys.

A dramatic approach to high-strength materials is to capitalize on the high strengths of fibers and whiskers. Figure 71-11 (ref. 13)

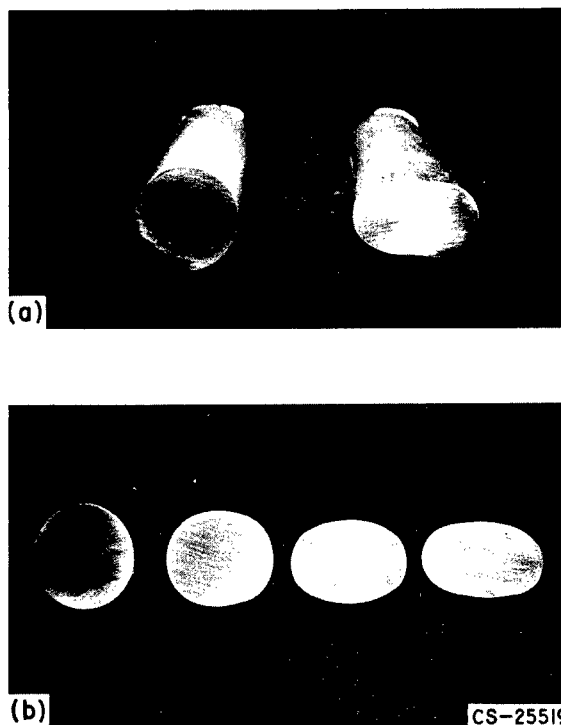


FIGURE 71-10.—Deformation of cold-forged bars of strongest tantalum-modified alloy.

shows the relation between strength and material size. This effect is believed to be a result of the attainment of more perfect structures at smaller sizes with extreme strengths being reached at the dimensions of whiskers of 1 to 10 microns, which have been shown to contain very few defects; in some cases, only one screw dislocation.

Past efforts at Lewis have sought to make practical use of the high strength of tungsten fibers by embedding them in a copper matrix.

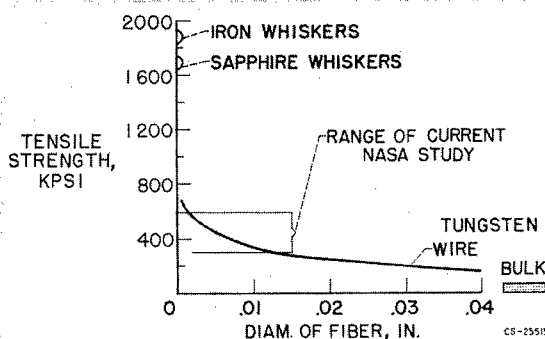


FIGURE 71-11.—Strength of whiskers and fibers at room temperature.

## MATERIALS

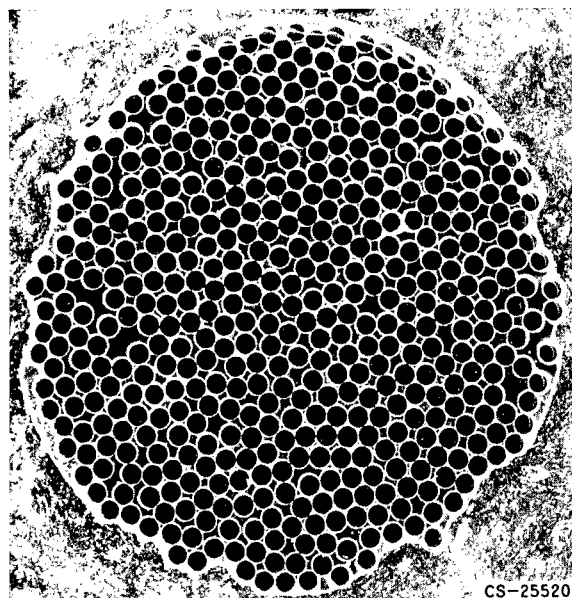


FIGURE 71-12.—Transverse section of tungsten-reinforced-copper composite; 483 wires of 5-mil diameter.  $\times 50$ .

This is done by infiltrating liquid copper into a bundle of tungsten wires, resulting in the structure shown in figure 71-12 (ref. 13). Such composites have been prepared at various wire-to-matrix volume ratios and strengths measured.

Figure 71-13 (ref. 13) shows some of the results. The strengths of bulk copper and tungsten fiber are shown along with two composite compositions. The strength of the composite increases directly with the number of fibers present. These data are for composites containing continuous tungsten fibers; that is, the fibers run the entire length of the tensile speci-

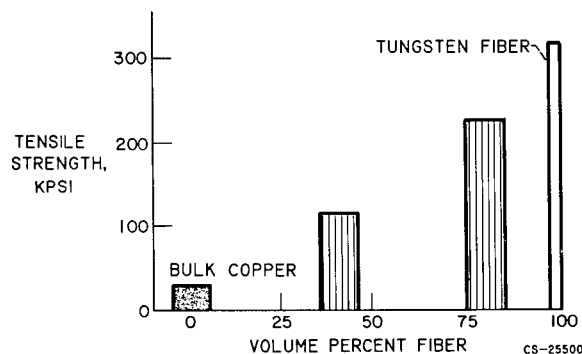


FIGURE 71-13.—Tensile strength of tungsten-copper composites with continuous tungsten fibers.

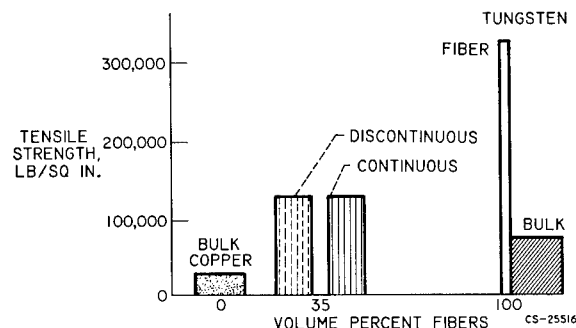


FIGURE 71-14.—Tensile strength of tungsten-copper composite with continuous and discontinuous tungsten fibers.

men. This brings up the immediate question, Would the tungsten fibers contribute to the composite strength if they were not continuous? This question has been answered by preparing composites in which the tungsten fibers were present as short discontinuous lengths. Some of the results are shown in figure 71-14 (ref. 13). This particular figure for 35 volume percent fiber shows the discontinuous fiber to be just as effective in strengthening as the continuous fiber. The strength of bulk tungsten is also shown for comparison.

The fact having been established that discontinuous fibers are effective strengtheners, the possibility of replacing wire and fibers with short lengths of whiskers becomes intriguing. This would make possible the achievement of ultra high strengths approaching those of whiskers in useful bodies of reasonable size.

Work in this field is continuing at Lewis. A complete understanding of the mechanism by which discontinuous fibers contribute to strengthening is being sought along with a description and understanding of the elastic and plastic behavior of such composites. Copper, iron, and alumina whiskers are also being produced and used in studies of true whisker composites.

At higher temperatures, those beyond the range of the nickel or cobalt superalloys, refractory metals (W, Mo, Cb, Ta) become of interest. Figure 71-15 (refs. 14 and 15) shows high-temperature-strength curves for molybdenum, two commercial molybdenum alloys, and tungsten. Tungsten is superior at all temperatures and retains useful strength even at 4400° F.

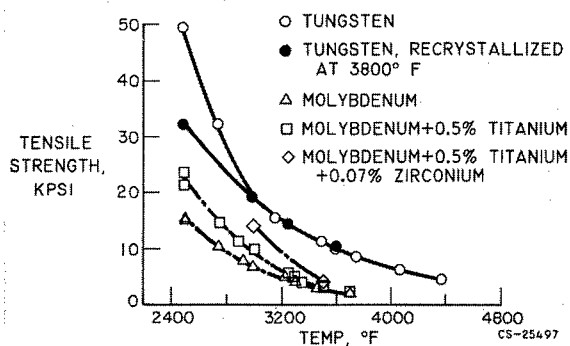


FIGURE 71-15.—Tensile strength of tungsten, molybdenum, and molybdenum alloys at high temperatures.

Since tungsten has the highest melting point of all metals ( $6170^{\circ}\text{F}$ ) and appears to offer the most potential for higher use temperatures, the major portion of the refractory metals program at Lewis is devoted to tungsten. Tungsten-alloy compositions of improved strength are being sought by both powder-metallurgy and arc-melting techniques. Strengths of some of the better alloys produced to date are shown in figure 71-16 (from unpublished data of P. Raffo of Lewis). These data are for arc-melted alloys after extrusion. The improvements offered by these binary compositions are encouraging. It is thought that the tantalum and columbium additions are resulting in solid-solution strengthening, while the boron addition gives grain refinement, which contributes to strengthening. More recent results predict that still further improvements can be expected by ternary and more complex compositions.

Tungsten as well as other body-centered cubic metals exhibits a transition temperature, that is, a temperature below which the metal behaves in a brittle manner and above which it possesses plasticity and exhibits some ductility before fracture. The transition temperature of tungsten in structural sizes is usually in the range of  $200^{\circ}$  to  $500^{\circ}\text{F}$ , which, of course, places room temperature, where tungsten parts must be handled, in the brittle range. Research into this transition behavior and attempts to lower the transition temperature are therefore of extreme importance. The transition behavior, as well as strength characteristics, has long been thought to be associated with and controlled by interstitial impurities, primarily carbon and

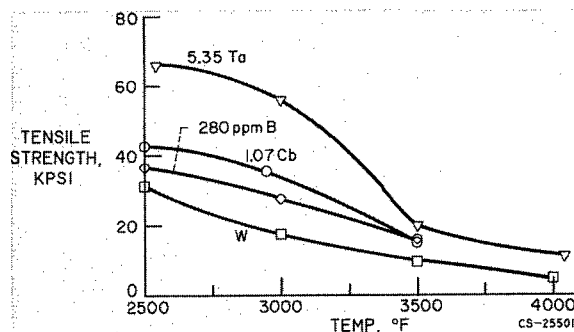


FIGURE 71-16.—High-temperature tensile strengths of tungsten-base alloys.

oxygen. In recent work at Lewis (ref. 16) in which controlled amounts of these impurities were introduced separately into high-purity polycrystalline and single-crystal tungsten, the role of each impurity has been elucidated. The results are too involved to cover here; however, they do show different effects of the two interstitials studied. The effect of carbon is believed to be one restricted to the lattice, possibly a Cottrell dislocation-locking mechanism, while the effect of oxygen appears to be isolated to high-angle grain boundaries.

For certain high-temperature applications beyond the range of refractory metals, the so-called hard metals or interstitial compounds are of interest. As part of this group, the refractory carbides are of particular interest since they represent the highest melting materials known. For example, hafnium carbide and tantalum carbide are the highest melting simple carbides with melting temperatures of approximately  $7000^{\circ}\text{F}$ .

Such materials are consolidated by powder-metallurgy techniques and are subject to some degree of porosity. Strengths of these materials are related to porosity and grain size. A determination of how each of these factors effects the strength of hafnium carbide and, consequently, the development of optimum combinations for maximum strength, are the goals of a current project at Lewis.

In summary, some of the research at the Lewis Research Center devoted to high-strength materials has been reviewed. A great variety of materials with use temperatures ranging from  $-423^{\circ}$  to over  $5000^{\circ}\text{F}$  are being studied, and it is hoped that the reader's interest has been stimulated in some of these areas.



## MATERIALS

### REFERENCES

1. ESGAR, JACK B.: Cryogenic Propellant Tank Structures. Aviation Conf., ASME (Wash., D.C.), June 26-28, 1962.
2. ESPEY, G. B., JONES, M. H., and BROWN, W. F., JR.: A Preliminary Report on Sharp Notch and Smooth Tensile Characteristics for a Number of Ultra High Strength Sheet Alloys. Proc. ASTM, vol. 59, 1959, pp. 837-871.
3. ESPEY, G. B., JONES, M. H., and BROWN, W. F., JR.: Factors Influencing Fracture Toughness of Sheet Alloys for Use in Lightweight Cryogenic Tankage. Symposium on Evaluation of Metallic Materials in Design for Low-Temperature Service, Spec. Tech. Pub. 302, ASTM, 1961.
4. MERICA, P. D., WALTEBERG, R. C., and SCOTT, H.: Heat Treatment of Duralumin. Bull. AIME, 150, 1919, pp. 913-949.
5. ILMANN, R.: Sintered Aluminum with High Strength at Elevated Temperatures. Metallurgia, vol. 46, no. 275, Sept. 1952, pp. 125-132.
6. CROSS, H. C., and SIMONS, W. F.: Alloys and Their Properties for Elevated Temperature Service. Utilization of Heat Resistance Alloys, ASM, 1954.
7. QUATINETZ, MAX, SCHAFER, ROBERT J., and Smeal, CHARLES: The Production of Sub-micron Metal Powders by Ball-Milling with Grinding Aids. Trans. AIME, vol. 221, Dec. 1961.
8. CREMENS, W. S., and GRANT, N.J.: Preparation and High Temperature Properties of Nickel-Al<sub>2</sub>O<sub>3</sub> Alloys. Proc. ASTM, vol. 58, 1958, p. 714.
9. FRECHE, JOHN C., RILEY, THOMAS J., and WATERS, WILLIAM J.: Continued Study of Advanced-Temperature Nickel-Base Alloys to Investigate Vanadium Additives. NASA TN D-260, 1960.
10. FRECHE, JOHN C., WATERS, WILLIAM J., and RILEY, THOMAS J.: A New Series of Nickel Base Alloys for Advanced-Temperature Applications. Trans. ASM, Spring, 1961.
11. FRECHE, JOHN C., WATERS, WILLIAM J., and RILEY, THOMAS J.: A New Series of Advanced-Temperature Nickel-Base Alloys. High Temperature Materials Symposium, AIME, Cleveland (Ohio), Apr. 1961.
12. DECKER, ROWE, and FREEMAN: Physical Metallurgy of Nickel-Base Super-alloys. DMIC Rep. 153, May 5, 1961.
13. MCDANIELS, D. L., JECH, R. W., and WEETON, J. W.: Metals Reinforced with Fibers. Metals Progress, December 1960.
14. HALL, ROBERT W., and SIKORA, PAUL F.: Tensile Properties of Molybdenum and Tungsten from 2500° to 3700° F. NASA Memo 3-9-59E, 1959.
15. SIKORA, PAUL F., and HALL, ROBERT W.: High-Temperature Tensile Properties of Wrought Sintered Tungsten. NASA TN D-79, 1959.
16. STEPHENS, J. R.: Effects of Interstitial Impurities on the Ductility of Tungsten. Paper Presented at AIME Meeting, New York (N.Y.), Oct. 1962.

**SESSION V**

## **Structures**

***Chairman,* RICHARD R. HELDENFELS**

**RICHARD R. HELDENFELS**, *Chief, Structures Research Division, NASA Langley Research Center, received his B.S. degree in Aeronautical Engineering from the Massachusetts Institute of Technology in 1942. He is an authority in structural analysis and testing and has served on many advisory panels and groups. He has been particularly active in the development of structures test facilities such as quartz-tube radiant heaters, true-temperature supersonic and hypersonic wind tunnels, and arc-heated air jets, that simulate or duplicate the high speed flight environment. Mr. Heldenfels is an Associate Fellow of the Institute of the Aerospace Sciences and a member of the American Rocket Society.*

## 72. Research, Design Considerations, and Technological Problems of Structures for Launch Vehicles

By Harry L. Runyan and Robert W. Leonard

HARRY L. RUNYAN, *Head of the Structural Dynamics Branch, Dynamic Loads Division, NASA Langley Research Center*, received his Bachelor of Science degree in Mechanical Engineering from Rutgers University in 1939. He joined the Langley staff in December 1945. He was one of the first to obtain his Master of Science degree in Aeronautical Engineering from the University of Virginia through Langley's graduate study program in 1951. Runyan is a renowned authority in the fields of flight loads, structural dynamics, and flutter and vibration of missiles and aircraft. He has achieved national and international recognition for fundamental research in such areas as analytical technique for determining oscillating air forces on a wing of arbitrary planform, flutter at hypersonic speeds, launch vehicle dynamics, and others. He is frequently called upon to present important papers before technical conferences and symposiums. Runyan is an Associate Fellow of the Institute of the Aerospace Sciences, a member of the American Geophysical Union, and a member of the Engineers' Club of the Virginia Peninsula.

DR. ROBERT W. LEONARD, *Head of the Structural Mechanics Branch, Structures Research Division, NASA Langley Research Center*, received his Bachelor of Science degree in Naval Technology from the University of Minnesota in February 1946. He received his Master of Science and Doctorate in Engineering Mechanics from the University of Nebraska and Virginia Polytechnic Institute in 1949 and 1961, respectively. Dr. Leonard joined the Langley staff in August 1949 and has specialized in research on response of continuous structures to transient loads, panel flutter, analysis of expandable structures, and thin shell and membrane theory. He has also undertaken the solution of certain structural problems arising in the development of the Echo II passive communications satellite. Dr. Leonard is currently a member of the Structures Criteria Subcommittee of the NASA Design Criteria Steering Committee of the ASME (serving on Spacecraft and Structures Committee of the Aviation and Space Division), and of Sigma Xi honorary fraternity.

### SUMMARY

Some of the branches of the technology needed in the reliable and efficient design of launch-vehicle structures are discussed. Included are shell buckling, stress analysis, panel flutter, noise, vehicle response to hori-

zontal winds, vibrations, dynamic modeling, and the study of new configuration concepts as complete systems. Examples are shown to indicate the state of the art and numerous problems, which require solution, are indicated.

## INTRODUCTION

A launch vehicle is one of the most efficient structures that has been devised for transportation. In table 72-I are shown weights of various major components of a launch vehicle compared with those of other means of transportation. As can be seen, the relative weight

TABLE 72-I.—*Relative-Weight Breakdown for Various Forms of Transportation*

	Propellant	Propulsion	Payload	Structure
Launch Vehicle-----	88	4	6	2
Airplane (Jet)-----	43	7	10	40
Ship-----	15	10	25	50
Automobile-----	3	22	25	50
Train (75-Car)-----	1	3	77	19

of the structure of the launch vehicle is exceedingly small compared with other transport structures. This small relative weight of structure is required to contain the propellant, support the engine, and support and protect the payload in the presence of very severe environments. The margin of safety is, consequently, exceedingly small.

The environment which this structure must resist includes many static and dynamic factors as illustrated in figure 72-1.

Before engine ignition, but after the gantry has been removed, ground winds can induce rather severe loads—both a steady drag load and a dynamic response in a direction mainly normal to the wind direction.

At engine ignition and launcher release, longitudinal transients are induced which can be rather severe and are important, not only from

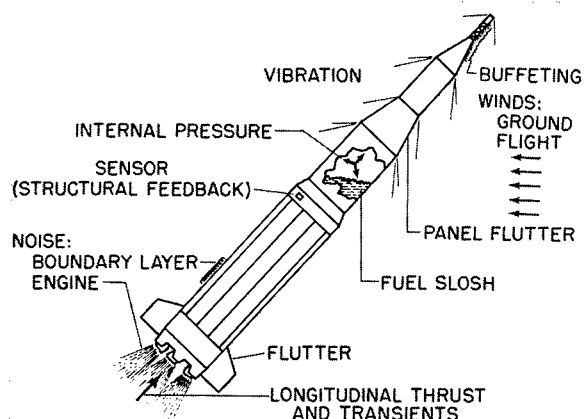


FIGURE 72-1.—Launch-vehicle problem areas.

the standpoint of basic structural strength, but also with regard to effects on smaller components. Also, the engine noise in the presence of the ground is of high intensity and, for the larger vehicles, new problems are being uncovered.

During flight through the transonic to the maximum-dynamic-pressure flight regime, the thrust and various steady-state and oscillating aerodynamic loads become important. These inputs include high steady-state acceleration, boundary-layer noise, winds and wind shear, and static high-pressure peaks around geometric discontinuities at transonic speeds upon which are superposed buffeting loads. In this same flight regime, consideration must be given to the vehicle control in the presence of high-velocity horizontal winds such as the jet stream as well as the stability and the coupling of the control sensor with the flexibility of the vehicle. Another stability problem involves flutter, either of the components such as fins or of a localized area involving thin panels.

Finally, stresses from internal pressure are also present during the launch period.

The principal load-carrying element of large launch vehicles is the thin-walled circular cylinder. A question of primary importance, therefore, is how to construct cylinder walls most efficiently for a given launch-vehicle design. Clearly, the best wall type will depend on the relative magnitudes of the loads shown in figure 72-1. Figure 72-2 illustrates this point for a hypothetical case where the only loads considered are two of the primary steady-state loads—internal pressure and bending moment.

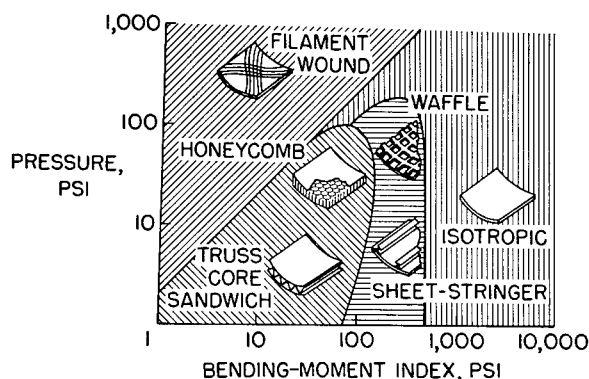


FIGURE 72-2.—Minimum-weight wall construction for bending of pressurized cylinders.

The plot in figure 72-2 shows the lightest form of construction which will carry pressure and bending loads without cylinder buckling or material yielding. The forms considered are filament wound, sandwich, stiffened skin, and simple isotropic walls. Note that, for high internal pressures as in solid-propellant launch vehicles, filament-wound construction is superior to the other types unless the applied bending-moment index is also large; then, the conventional, isotropic shell is lighter. For lower or zero internal pressures, as in liquid-propellant tanks or interstage structures, all types of wall construction have a range of efficient application, depending on the magnitude of the moment index.

Information of the type shown in figure 72-2 could obviously be very helpful in guiding the design of launch-vehicle structures. However, in deriving this figure, a very simple idealized structure has been assumed—a cylinder unobstructed by ends, cutouts, or other irregularities, and obeying simplified laws of behavior. Hence, the given boundaries must be modified or augmented for practical application. Further, other configurations and the many other static and dynamic loads must be taken into account. Thus, reliable and efficient design of launch-vehicle structures requires a wide knowledge of structural response to load plus an accurate knowledge of launch loads. This paper will touch briefly on some of these areas of necessary knowledge, their current state of development, and problems the solutions of which would contribute to their advancement.

### SYMBOLS

$EI_{sc}$ , $EI_{cyl}$	bending stiffeners for scalloped and cylindrical tanks, respectively
$K$	stress-concentration factor
$L$	length
$R$	tank radius
$r$	scallop radius
$T$	filament tension
$T_{MAX}$	maximum filament tension
$t$	thickness

### SHELL BUCKLING

A prime requirement in launch-vehicle design is a shell-buckling criterion. Yet the designer's ability to predict buckling strengths of cylinders

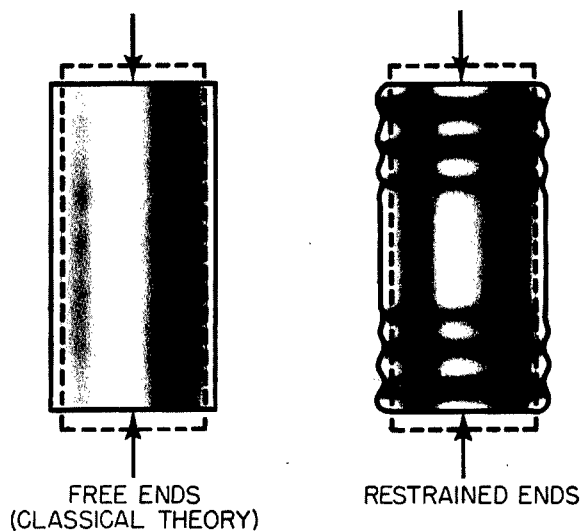


FIGURE 72-3.—Prebuckling state of axially compressed cylinders.

in axial compression or bending—loads of principal importance to launch vehicles—has been inadequate; there have continued to be large discrepancies between theory and experiment in spite of years of research effort. (See, for example, ref. 1.) Only very recently has there been uncovered what may be the chief cause of these discrepancies in the axial-compression case (ref. 2); this is illustrated in figure 72-3.

Consider for a moment, the illustration at the left in figure 72-3. In the classical linear theory and all other past theories, the cylinder is assumed to remain perfectly cylindrical with only uniform membrane stresses prior to buckling. Since an axially compressed cylinder tends to expand laterally, this assumption implies that, before buckling, the ends are free. But this condition is rarely found in practice; instead, the ends are restricted from lateral expansion by rings, bulkheads, or perhaps by the platens of a testing machine. This restraint induces prebuckling conditions that are widely different from those assumed in the classical theory; as illustrated at the right in figure 72-3 an axisymmetric, nonuniform deformation arises, accompanied by nonuniform stresses including bending stresses.

The importance of this nonuniform prebuckling state is illustrated by the example in figure

## STRUCTURES

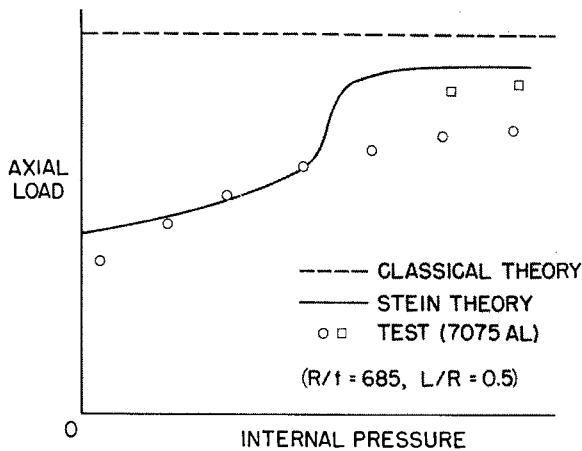


FIGURE 72-4.—Buckling of pressurized cylinders in axial compression.

72-4. In this figure are plotted combinations of axial load and internal pressure corresponding to buckling of a typical isotropic cylinder. The dashed line at the top is the prediction of classical theory whereas the solid curve is the prediction of a theory—termed here the “Stein theory” after its author—which takes account of the prebuckling state induced by simply supported ends. (See ref. 2.) The circles and squares represent test data from reference 3, which were obtained on two large cylinders of 7075 aluminum alloy.

Note that, at zero pressure, the Stein theory predicts buckling at approximately one-half of the load predicted by classical theory. This reduction is typical and corresponds roughly to the difference between classical theory and experiment. Although it differs in detail, the variation with pressure is also in general agreement with experiment.

The Stein approach to cylinder-buckling analysis begins with nonlinear cylinder equations and is, thus, quite complex. Nevertheless, additional calculations of this kind, extended to a wider range of parameters and to different boundary conditions, loading conditions, and configurations, would be well worthwhile.

While there is an evident need to improve the designer's ability to handle shell buckling problems of long standing, at the same time a variety of new problems important for launch-vehicle structures must be considered. Two examples are shown in figure 72-5.

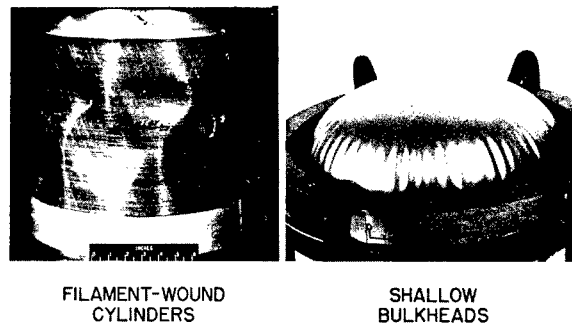


FIGURE 72-5.—New shell buckling problems of launch-vehicle structures.

Shown on the left in figure 72-5 is a filament-wound cylinder buckled by axial compression. This problem arises in upper stage motor cases before they are pressurized by ignition of their solid propellant. Surprisingly, almost no information on this problem seems to have been published. The cylinder shown is a test specimen from a current program of experiment and analysis. It consists of glass filaments in an epoxy matrix and is typical of construction in an upper stage motor case of the Scout launch vehicle. Preliminary results from this program are available (ref. 4), but much additional work is needed. For example, the calculation of wall stiffness properties from the properties of elastic fibers and an elastic-plastic matrix needs further study.

Another new and unique buckling problem involves the end bulkheads of fuel tanks. To minimize the length of interstage sections of launch vehicles, it is often desirable to utilize torispherical, Cassinian, or other shallow bulkhead shapes. In many practical cases, such bulkheads are put in a state of circumferential compression near their outer edges by internal pressurization. Thus, internal pressure can cause buckling of the bulkhead as shown by the photograph at the right in figure 72-5. As in axial compression of cylinders, the analysis of this buckling problem is complicated by the need for careful consideration of the prebuckling state. The torispherical bulkhead has been treated comprehensively in reference 5, but many shapes remain to be investigated.

# STRESS ANALYSIS

The designer of launch vehicles cannot confine his attention to the primary steady loads and their gross effects. Many localized phenomena must also be taken into account. Examples are local variations in stress near openings, near tank end closures, and in the vicinity of concentrated forces. Most past theoretical research on such problems has been confined to linear analyses with lateral deflections of the shell wall assumed to be small compared with the shell thickness. Unfortunately, launch-vehicle shell structures are often very thin and the loads very large so that many of these problems need to be reconsidered on the basis of nonlinear, large-deflection shell theory.

Furthermore, there are problems of this type which have only been touched. Consider, for example, stresses in filament-wound structures. There is the problem of optimum design of motor-case end closures—the calculation of the proper shape and filament orientation to achieve uniform filament stress. (See, for example, ref. 6.) This problem has been explored for symmetrical shapes with central openings, but work is needed, for example, on optimum design of unsymmetrical end closures with multiple openings. There is also the problem of stress concentrations caused by broken filaments; this problem is illustrated in figure 72-6.

Figure 72-6 contains results of a basic study of a single flat layer of filaments embedded in a matrix. This filament sheet is assumed to have one or more broken fibers and to be loaded so that, far from the break, the tension on each filament is  $T$ . The maximum tension occurs adjacent to the break in the first unbroken fiber. Thus, the stress-concentration factor  $K$  is the ratio of  $T_{MAX}$  to  $T$ . This factor is plotted in figure 72-6 against the number of broken fibers up to a total of 6. The solid curve has been drawn through values obtained theoretically by assuming the sheet to be infinite, the materials elastic, and the matrix capable of transmitting only shear. (See ref. 7.)

To evaluate this theory, a brief series of tests has recently been run by George W. Zender and Jerry W. Deaton of the Langley Research Center on strips of dacron filaments in a foam rubber and Mylar matrix. Stress-concentration

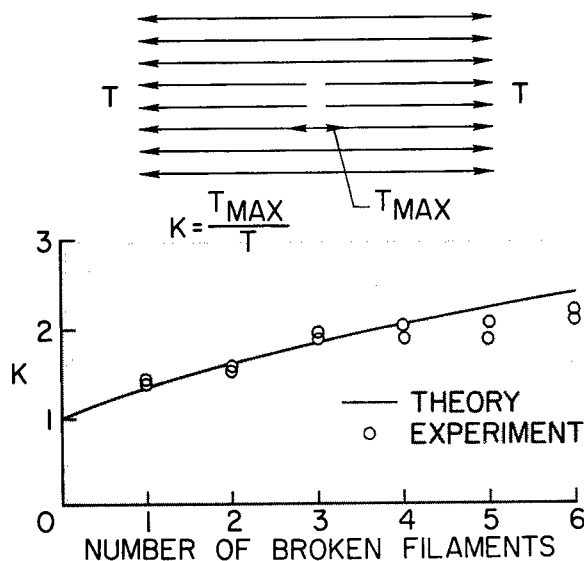


FIGURE 72-6.—Stress concentration in a filament sheet.

factors for the test strips were taken as the ratio of the fiber ultimate strengths with all fibers intact to the fiber strengths with one or more fibers broken. Two tests were run at each condition with the results shown by the circles in figure 72-6. The agreement with theory is good; one implication is that elastic stress concentrations must be seriously considered in design of filamentary structures with no careless reliance on plasticity to alleviate the effects.

This investigation represents a good beginning, but further studies are obviously needed if the consequences of broken fibers in a filament-wound motor case are to be fully understood. Such factors as multiple layers at different orientations and inelasticity of the matrix have not yet been studied. These complications pose a formidable challenge to the analyst.

## PANEL FLUTTER

The local phenomena which influence launch-vehicle design may also include certain dynamic effects. For example, calculations indicate that panel flutter may be a matter of concern, but the issue is somewhat in doubt because experiments on cylinders and curved panels have so far failed to confirm theory. (See, for example, ref. 8.) On the other hand, a practical type of interstage structure, already in use in some of today's large launch vehicles, is the stiffened cylinder with thin skin designed to buckle early in flight. The





FIGURE 72-7.—Launch-vehicle interstage structure.

skin panels of such interstage structures might well be especially susceptible to flutter. This possibility is currently being explored by tests on the structure shown in figure 72-7.

The photograph shows a quarter segment of a full-scale launch-vehicle interstage structure installed in the Langley 9- by 6-foot thermal structures tunnel. The structure is a stiffened cylindrical shell with rings on the inside and stringers on the outside. While data from these tests are not yet available, flutter has been observed in preliminary runs with the panels in a buckled condition. Thus it appears that more work is warranted on panel flutter, especially of buckled flat and curved panels.

### NOISE

It is appropriate at this point to direct attention to another local dynamic problem—the effect of noise. The two major sources of noise are the propulsion system, particularly at lift-off, and aerodynamic noise during flight due to boundary-layer buildup and flow around corners and blunt objects. (See ref. 9.) The spectra of aerodynamic noise peak at a relatively high frequency and are important with regard to local panels and small-equipment response. This topic is important to reentry vehicles as well as launch vehicles and is discussed in more detail in reference 10. The present paper will concentrate on new problems which are connected with the increasing size of launch vehicles.

Noise is important at the time of launch, particularly for the larger vehicles now in the

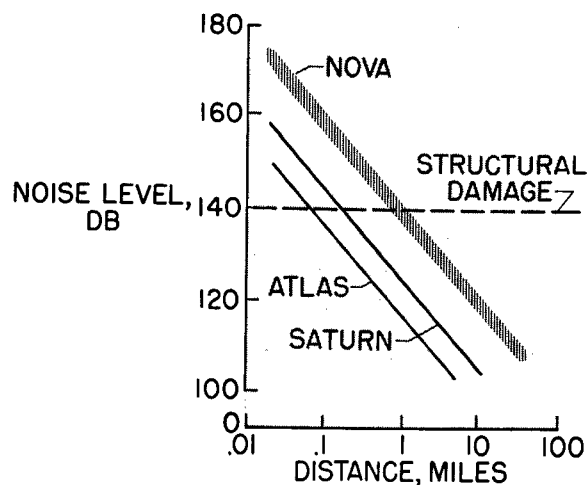


FIGURE 72-8.—Launch noise levels.

planning stages for manned space exploration. Because of the high thrust ratings, very intense noise fields will be generated and will extend to large distances from the launch complex. There are two major implications: the first is the impingement of this noise field on the vehicle itself and on launch vehicles installed in adjacent launch towers for later flight; and the second is the effect on the surrounding buildings and community. In figure 72-8, noise levels are plotted as a function of distance from the launch site for the Atlas, Saturn, and Nova classes of vehicles (ref. 11). Also shown is a horizontal line corresponding to noise levels at which damage has occurred. The position of this line is the subject of research and more work will have to be done to establish its location for various types of structures. It can be seen from figure 72-8 that damaging noise levels may extend outward as much as a mile from a Nova launch site; incidentally, it is this consideration that has determined to a large extent the amount of additional property purchased adjacent to launch sites in the Cape Canaveral area.

Another significant feature of the launch-vehicle noise problem is its frequency spectra; these are a function of the size of the vehicle as illustrated in figure 72-9. The noise generated has a continuous spectrum with a single broad peak as indicated in the sketch at the upper right. The frequency at which the spectrum peaks is plotted on the vertical scale against launch-vehicle thrust on the horizontal

## PROBLEMS OF STRUCTURES FOR LAUNCH VEHICLES

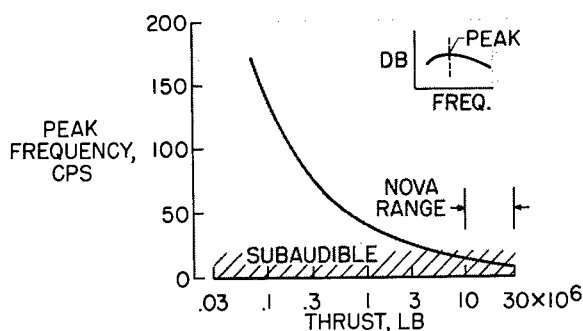


FIGURE 72-9.—Launch-vehicle noise spectra.

scale. It can be seen that the vehicles having higher thrust have noise spectra which peak at low frequencies and, in fact, much of the noise may be in the subaudible frequency range as indicated by the cross-hatched area. These low frequencies—of the order of 10 cps—are in the range of the response frequencies of launch-vehicle structures as well as many building structures. For this reason, a large, low-frequency-noise test facility is being constructed at the Langley Research Center to extend the knowledge of this area.

### WIND VELOCITY AND VEHICLE RESPONSE

The preceding sections of the present paper have been concerned with phenomena that affect launch-vehicle components. Attention will now be directed to some inputs and responses which involve the complete vehicle.

The horizontal wind through which the vertically rising vehicle must fly constitutes one of the largest sources of loads that the structure must resist. This is because maximum wind velocities and flight maximum dynamic pressure occur at very nearly the same altitude. Thus, the product of the dynamic pressure and the increased angle of attack resulting from these high winds induces very large bending moments on the vehicle.

For the most part, launch vehicles have been designed on the basis of the so-called "synthetic wind profile." This is a wind-velocity profile that has been generated from weather-balloon soundings and which represents the most severe wind and shear conditions to be expected in some given large percentage of cases, such as 99 percent.

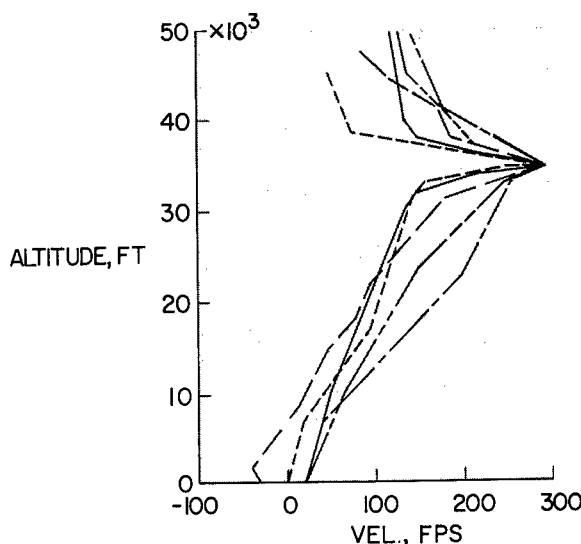


FIGURE 72-10.—Synthetic wind profiles.

An illustration of the multiplicity of some of these design profiles is shown in figure 72-10 where wind speed is plotted as the abscissa and the altitude is plotted as the ordinate. Note the large variations between these various design profiles. The control and load response of a vehicle is determined by "flying" the simulated vehicle on a computer through these design winds. Some designers also fly the simulated vehicle through a one-minus-cosine gust and add this loading to that determined by flying through the synthetic profile. Neglected in this process is the real finer grained wind-velocity structure to which the vehicle could dynamically respond.

In an attempt to fill the gap in knowledge of the fine-grain wind structure, a smoke-rocket technique has been developed. (See ref. 12.) This procedure is based on the near-vertical launching of a small rocket which has as its payload a smoke-producing agent. Photographs of the trail are taken every few seconds from 2 or 3 locations, usually about 10 miles from the launch site. The velocity may then be determined from the measurements of space variation of the trail with time. Two components of a typical profile, as determined from a trail, are shown in figure 72-11. Note in particular the fine-grain structure of the velocity distribution. Measurements are now being made at both the NASA Wallops Station

## STRUCTURES

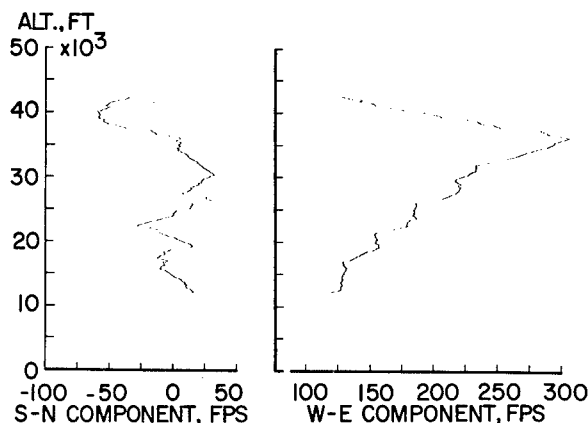


FIGURE 72-11.—Smoke-trail wind velocities.

launching site and at the Atlantic Missile Range, where about 100 smoke-trail firings are planned. In addition, recent advances in the balloon technique will provide additional statistical information.

The question arises: How does the designer use this new data? One procedure would be to fly the vehicle on a computer through each of the measured winds, from which motion and load response would be obtained. Thus, the probability of exceeding a certain level of a response such as bending moment could be obtained. This procedure would require a large amount of computer time and other approaches should be sought. The most obvious technique would be the use of random-process theory.

Aircraft dynamic response is being successfully treated as essentially a stationary random process. Launch-vehicle flight, on the other hand, is definitely a nonstationary process since such factors as vehicle mass, atmospheric density, and Mach number are rapidly changing. Thus, while the detailed wind velocities now being measured by the smoke-trail method will provide the basic input data, the numerical labor will be very great in utilizing these data with the present limited knowledge of nonstationary random processes. Attempts should be made to review the present techniques with a view toward reducing the numerical labor and providing a practical design tool.

### VIBRATIONS AND DYNAMIC MODELING

Before dynamic loads and responses can be predicted, or the control system designed, the

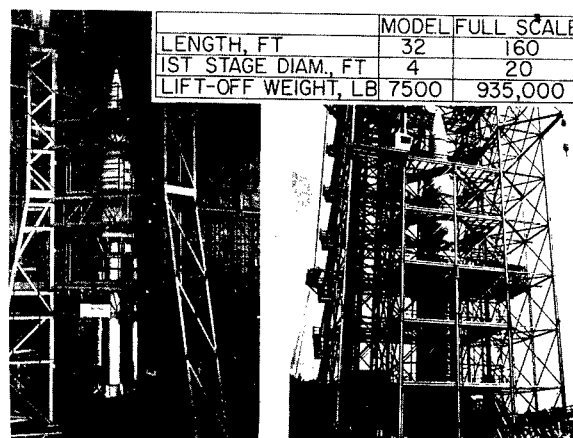


FIGURE 72-12.—Saturn vibration-test vehicles.

lateral vibration modes and frequencies of a complete launch vehicle must be known. Some of the newer configurations are quite unconventional and exhibit unusual vibration characteristics which are extremely difficult to predict analytically. The difficulties of determining these vibration characteristics experimentally, on full-scale hardware in simulated flight, are obvious when vehicles the size of Saturn are considered. These considerations have led to the concept of replica modeling as a tool for launch-vehicle design.

The Langley Research Center has designed, constructed, and tested a  $\frac{1}{5}$ -scale replica model of the Saturn SA-1 launch vehicle in an attempt to develop a technology for launch-vehicle dynamic models as well as to investigate the vibration characteristics of clustered configurations. (See ref. 13.) The  $\frac{1}{5}$ -scale model is shown on the left in figure 72-12. A full-scale Saturn (SAD-1), suspended in a test tower to simulate free-free boundary conditions, is shown on the right. The model is 32 feet tall and weighs 7,500 pounds, compared to 160 feet and almost 1,000,000 pounds for the full-scale vehicle. The model was designed by using replica scaling techniques which required that joints, cutouts, fittings, and so forth—with stiffnesses that could not be accurately predicted—be duplicated by dimensional scaling.

An example of the vibration-test results and a comparison with full-scale results are shown in figure 72-13. Results shown are for the first free-free bending mode, at a weight condition

# PROBLEMS OF STRUCTURES FOR LAUNCH VEHICLES

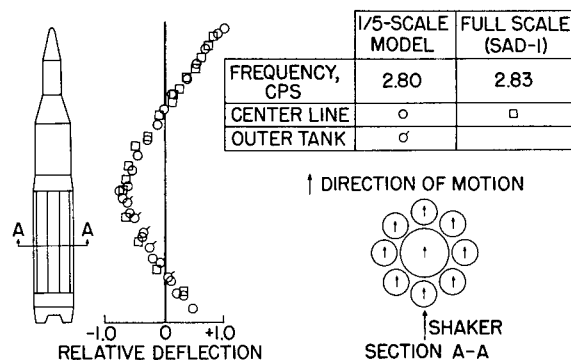


FIGURE 72-13.—First vibration mode at maximum dynamic pressure.

corresponding to the maximum-dynamic-pressure point in the launch trajectory. A scaled frequency of 2.80 cps was measured on the model, compared with 2.83 cps on the full-scale vehicle. The mode shapes measured on the model and on the full-scale vehicle agree very well as indicated by the circles and squares plotted in the figure. The flagged circles in the area of the first stage represent points measured along an outer tank in the cluster and indicate that these outer tanks follow the center-line motion. This tank motion is further illustrated by the cross-sectional sketch of the first stage, where the arrows indicate the motion of the various tanks within the cluster. All the tanks are seen to move together, with a resulting mode shape very similar to a beam bending mode.

A more complicated vibratory response is illustrated in figure 72-14. This is the mode shape at the second resonant frequency of the vehicle. The model frequency was 5.20 cps com-

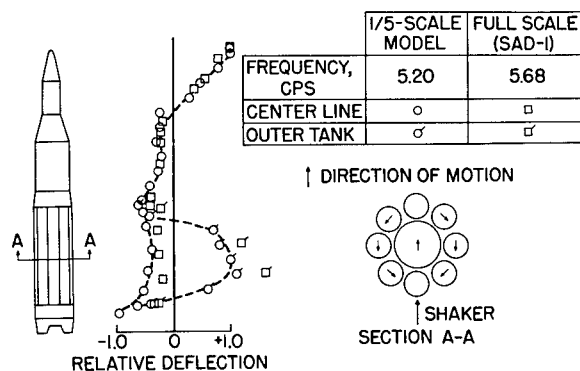


FIGURE 72-14.—Second vibration mode at maximum dynamic pressure.

pared with 5.68 cps for the full-scale vehicle—less than a 10-percent variation. Again, circles represent model data, squares represent full-scale data, and flagged symbols indicate deflections measured on an outer tank. Note the different behavior of the outer and inner tanks within the cluster. This is shown better by the arrows on the first-stage cross section at the right. The center tank is seen to deflect in one direction while the outer tanks tend to move tangentially, but predominantly opposite to the motion of the center tank. This unconventional mode, which results from the clustered-tank construction of the first stage, has been termed a "cluster" mode. Notice that, when circles and squares are compared, model behavior is essentially the same as that of the full-scale vehicle.

The results in figures 72-13 and 72-14 indicate that dynamic models can be used to determine the vibration characteristics of complex launch vehicles. The unusual vibration characteristics of a particular clustered-booster arrangement are also illustrated. As new configurations evolve, it is anticipated that dynamic modeling techniques may be used to great advantage to study their dynamic structural properties.

## CONCEPTS AND SYSTEM

This final topic will require an expanded viewpoint including more elements of the vehicle system—specifically, fuel slosh, control frequency, and their relationship to the lateral vibration modes. Attention will be focused on a promising new configuration—the scalloped tank—and the change in frequency spectrum from a cylindrical-tank vehicle to this new configuration will be indicated. A cross section of the scalloped tank is shown in figure 72-15; it consists essentially of a series of sectors of circles tied together by radial webs.

The primary and overriding reason for considering this configuration is the problem of fuel slosh. Since about 90 percent of the weight of a launch vehicle may be liquid, the stabilization of this large mass in cylindrical tanks by conventional means—for instance, by annular baffles connected to the outer walls of the cylindrical tank—imposes a rather severe weight penalty. Therefore, attempts should be

# STRUCTURES

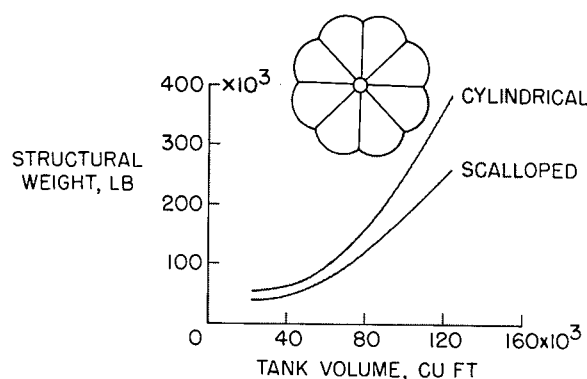


FIGURE 72-15.—Comparison of scalloped- and cylindrical-tank weights.

made to utilize this baffle material so that it will provide structural strength as well as reduce the fuel slosh effects. The scalloped-tank concept provides baffling by means of the radial webs which act also as structural tension members. On a two-dimensional basis (neglecting end effects and cylindrical-tank baffling), the weight of a cylindrical tank and a scalloped tank is the same if the same volume is enclosed and if the same internal pressure and material stress level is maintained in both tanks. A more realistic estimate of the weight of the two configurations (from ref. 14) is shown in figure 72-15 in which the tank ends have been accounted for as well as the required baffling in the cylindrical tanks. The cylindrical tank weighs about 25 percent more than the scalloped tank at smaller tank volumes and about 33 percent more for the largest volume considered.

Important aspects of the scalloped tank from the fuel-slosh viewpoint are the reduction of the effective fuel mass and, particularly, the elimination of any possibility of a swirling or rotary motion of the fluid which can be a dangerous and insidious fuel motion.

These advantages are, of course, not without certain penalties. First, fabrication of the tank becomes a much greater problem, that is, the complexity may increase the cost of manufacture. Also, the bending stiffness of the scalloped tank is decreased relative to that of the cylindrical tank as shown in figure 72-16 for several scalloped arrangements, including 4-, 6-, 8-, and 12-segmented tanks. The stiffness relative to that of a cylinder is plotted against the ratio of the scallop radius to the tank

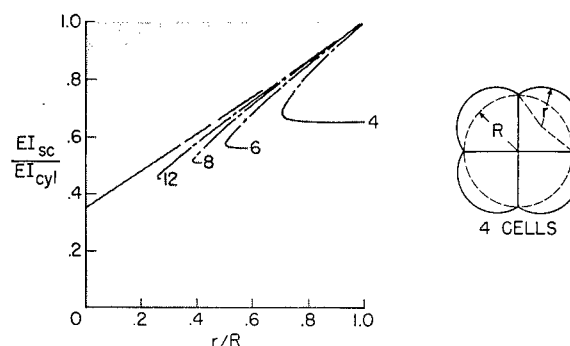


FIGURE 72-16.—Ratio of scalloped- to cylindrical-tank stiffness.

radius. As the number of segments increases, the stiffness is reduced. This reduction in stiffness results in a reduction in the frequency of the lateral modes and has an impact on both control-system design and the dynamic response due to gusts.

At the left of figure 72-17 is shown the variation in frequency of several important factors for a cylindrical tank plotted against flight time—for example, pitch (this compares with the more familiar airplane short-period frequency), fuel slosh, and first bending for a typical large launch vehicle. Baffling is required for stabilization in this case where the slosh and pitch frequency are very close.

Now, consider what happens to these frequencies for an 8-segmented scalloped tank. The results for this hypothetical configuration appear as shown on the right of figure 72-17. Note that the frequency curve for fuel slosh has been raised considerably (see ref. 15) and from a rigid-body control standpoint results in a more desirable situation, since the fuel-slosh

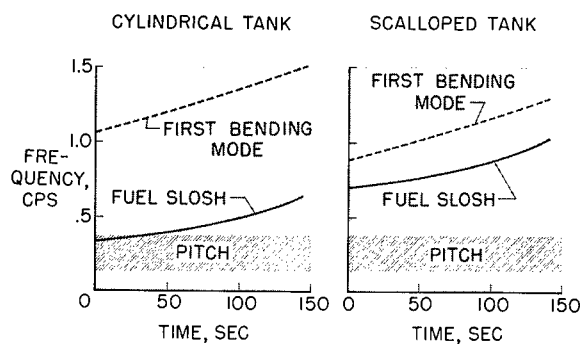


FIGURE 72-17.—Variation of frequency with flight time.

frequency is beginning to uncouple from the pitch frequency. At the same time the reduced stiffness has resulted in a reduced first bending frequency as indicated by the lowering of the frequency curve on the right side and thus introduces the possibility of a coupling between fuel slosh and the lateral vibration mode; this constitutes an area requiring research.

This exercise on the scalloped configuration has been made to indicate the type of thinking that must be pursued in investigating any particular configuration; that is, the complete system must be examined and the coupling of apparently unrelated elements must be sought out and evaluated.

### CONCLUDING REMARKS

In this paper some of the branches of the technology needed in reliable and efficient design of launch-vehicle structures have been considered. Examples have been given to indicate the current state of the art and various problems for which solutions are needed have

been mentioned; for the most part work more of an analytical than of an experimental nature has been indicated.

Among the problems considered were shell buckling and areas where analyses are needed of new shell configurations which have become important in launch-vehicle design. New and important problems of stress analysis—for example, stress concentrations in filamentary structures—have been pointed out, and the need for further studies of flutter of curved panels—especially in a buckled state—has been indicated. For the noise problem, work is needed involving the response of structures to the predominantly low-frequency noise of the largest launch vehicles and, for the determination of vehicle response to winds, a principal need is the development of a practical procedure for application of nonstationary random-process theory. Vibration analysis of clustered structures is needed, and finally, so is the conception and study of new configurations for application to the next generation of launch vehicles.

### REFERENCES

1. FUNG, Y. C., and SECHLER, E. E.: Instability of Thin Elastic Shells. *Structural Mechanics*, J. Norman Goodier and Nicholas J. Hoff, eds., Pergamon Press (New York), 1960, pp. 115-168.
2. STEIN, MANUEL: The Effect on the Buckling of Perfect Cylinders of Prebuckling Deformations and Stresses Induced by Edge Support. *Collected Papers on Instability of Shell Structures—1962*. NASA TN D-1510, 1962, pp. 217-227.
3. DOW, MARVIN B., and PETERSON, JAMES P.: Bending and Compression Tests of Pressurized Ring-Stiffened Cylinders. NASA TN D-360, 1960.
4. CARD, MICHAEL F., and PETERSON, JAMES P.: On the Instability of Orthotropic Cylinders. *Collected Papers on Instability of Shell Structures—1962*. NASA TN D-1510, 1962, pp. 297-308.
5. MESCALL, JOHN: Stability of Thin Torispherical Shells Under Uniform Internal Pressure. *Collected Papers on Instability of Shell Structures—1962*. NASA TN D-1510, 1962, pp. 671-692.
6. ZICKEL, JOHN: Isotenoid Pressure Vessels. *ARS Jour.*, vol. 32, no. 6, June 1962, pp. 950-951.
7. HEDGEPEETH, JOHN M.: Stress Concentrations in Filamentary Structures. NASA TN D-882, 1961.
8. STEARMAN, R., and FUNG, Y. C.: Experiments on the Stability of Circular Cylindrical Shells in a Supersonic Flow. *GALCIT SM 62-36*, 1962.
9. HILTON, DAVID A., MAYES, WILLIAM H., and HUBBARD, HARVEY H.: Noise Considerations for Manned Reentry Vehicles. NASA TN D-450, 1960.
10. MATHAUSER, ELDON E.: Research, Design Considerations, and Technological Problems of Structures for Winged Aerospace Vehicles. NASA University Conference, 1962. (Paper no. 73 of present compilation.)
11. REGIER, ARTHUR A., MAYES, WILLIAM H., and EDGE, PHILLIP M., Jr.: Some Noise Problems Associated With the Launching of Large Space Vehicles. Presented at Annual Meeting of Armed Forces-National Research Council Committee on Hearing

## STRUCTURES

- and Bio-Acoustics (Washington, D.C.), Nov. 3, 1961. (To be published in Sound, Nov.-Dec. 1962.)
12. HENRY, ROBERT M., BRANDON, GEORGE W., TOLEFSON, HAROLD B., and LANFORD, WADE E.: The Smoke-Trail Method for Obtaining Detailed Measurements of the Vertical Wind Profile for Application to Missile-Dynamic-Response Problems. NASA TN D-976, 1961.
  13. MIXSON, J. S., and CATHERINE, J. J.: Investigation of Vibration Characteristics of a 1/5-Scale Model of Saturn SA-1. Shock, Vibration and Associated Environments—Pt. IV. Bull. No. 30, Office of Sec. of Defense, Apr. 1962, pp. 30-39.
  14. STERETT, JAMES B., JR.: Shell Stability Problems in the Design of Large Space Vehicle Boosters. Collected Papers on Instability of Shell Structures—1962. NASA TN D-1510, 1962, pp. 57-66.
  15. ABRAMSON, H. NORMAN, GARZA, LUIS R., and KANA, DANIEL D.: Liquid Sloshing in Compartmented Cylindrical Tanks. ARS Jour., vol. 32, no. 6, June 1962, pp. 978-980.

# 73. Research, Design Considerations, and Technological Problems of Structures for Winged Aerospace Vehicles

By Eldon E. Mathauser

ELDON E. MATHAUSER, *Head of the Structural Materials Branch, Structures Research Division, NASA Langley Research Center, received his Bachelor of Science degree in civil engineering in 1944 and his Master of Science degree in engineering mechanics in 1950, both from the University of Nebraska.*

*Mathauser was an instructor in the Department of Engineering Mechanics at the University of Nebraska from 1946 to 1951. Since joining Langley in July 1951, he has specialized in research on structures and materials for high temperature applications. He is author of approximately 20 NASA technical papers on structures and materials with emphasis on behavior and performance at high temperatures. He is a member of the Institute of the Aerospace Sciences, Sigma XI honorary scientific society, and Sigma Tau honorary engineering society, and is a registered professional engineer in the state of Nebraska.*

## SUMMARY

Research, design considerations, and technological problems of structures for winged aerospace vehicles are discussed and areas in need of further research are explored. The presentation includes structural approaches required to cope with the high nonuniform temperatures and the influence of such factors as flutter, acoustic fatigue, and materials selection on the structural design.

## INTRODUCTION

Considerable interest is being displayed at the present time in winged aerospace vehicles. These vehicles possess various desirable operating characteristics such as high lift-drag ratio, maneuverability, and horizontal landing capability. In this paper structural concepts appropriate for winged aerospace vehicles will be discussed. The presentation will include structural approaches required to cope with the high nonuniform temperatures and the influence of several factors, such as flutter, fatigue,

and materials selection, on structural design will be indicated.

## DESIGN BASIS

### Winged Aerospace Vehicle Configurations

Three types of winged aerospace vehicles that will be considered are shown in figure 73-1. A research airplane characterized by the X-15 (ref. 1) is shown at the upper left, a reentry glider representative of the X-20 Dyna-Soar (ref. 2) is shown in the upper right, and a large hypersonic airplane (ref. 3) that may be capable of sustained flight at hypersonic speeds or may have orbital capability is shown in the lower view. The structural approaches for these vehicles have many common features. All experience moderate to severe aerodynamic heating and utilize radiation-cooled structural designs. All structures are essentially metallic and are intended for reuse with minimum refurbishment.



## STRUCTURES

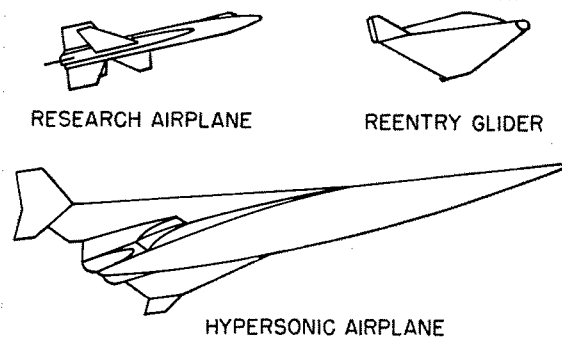


FIGURE 73-1.—Winged aerospace vehicles.

The operational characteristics of these vehicles are significantly different. The research airplane is carried aloft by another airplane and launched at altitude. The reentry glider may be launched with a ground-based booster. The hypersonic airplane carries its own fuel and possesses conventional horizontal take-off capabilities.

### Flight Corridors for Winged Aerospace Vehicles

Before a discussion of structural problems is undertaken, a brief look will be taken at the flight corridors for these vehicles. Figure 73-2 indicates the flight corridors in terms of altitude and velocity. The shaded area indicates the region that can be explored by the X-15 research airplane. (See ref. 4.) The glider is launched along an exit trajectory as shown and returns within the indicated reentry corridor. The lower limits of the reentry corridor are defined partly by temperature and dynamic pressure. The 4000° F temperature line defines a

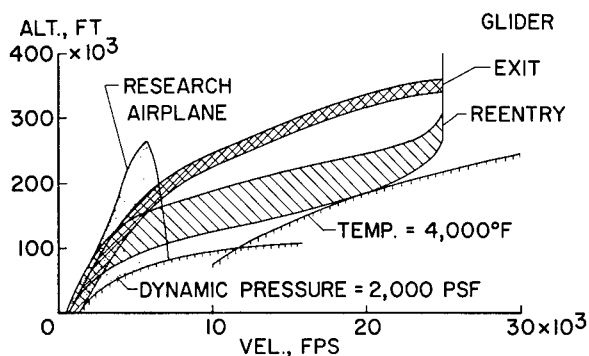


FIGURE 73-2.—Flight corridors for winged aerospace vehicles.

radiation equilibrium temperature for a 1-foot-diameter nose with an emissivity of 0.8. Note that the reentry glider does not experience severe heating during exit because the exit corridor does not appear close to the indicated temperature line. It is significant to note that the exit corridor is near the curve for 2,000 pounds per square foot dynamic pressure. This fact suggests the possibility that flutter may be a problem during exit. The highest structural temperatures occur at the point of tangency between the flight corridor and the temperature curve.

No specific flight corridor is indicated for the hypersonic airplane. It is expected that the hypersonic airplane will operate along a dynamic pressure curve and along a temperature line. If the vehicle possesses orbital capability, reentry with a hypersonic airplane would be made in approximately the same corridor as that for the glider.

### Structural Temperatures

The most pressing structural problems arising from operations in the indicated flight corridors come about because of the serious aerodynamic heating. The magnitudes of the temperatures that can result are shown in figure 73-3. A reentry glider is shown with surface-radiation equilibrium temperatures indicated for several areas of the vehicle. The nose temperature may approach 4000° F, the leading edges 3000° F, the underside 2500° F, and the leeward side 1000° F to 1500° F. The high structural temperatures that may be achieved by aerospace vehicles produce signifi-

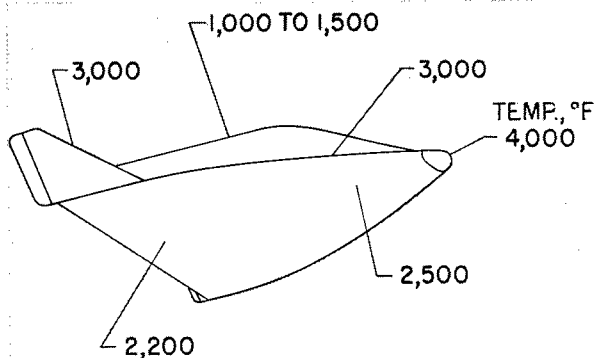


FIGURE 73-3.—Surface radiation equilibrium temperatures for a reentry glider.

## PROBLEMS OF STRUCTURES FOR WINGED AEROSPACE VEHICLES

cant design problems. Of equal significance is the fact that highly nonuniform temperatures occur that produce severe structural deformations and introduce thermal stresses. Temperature differences of over  $1000^{\circ}\text{F}$  are indicated between the lower and upper areas of the body. Because of such large temperature differences, new design approaches and special construction concepts are required. This paper is primarily devoted to design concepts required for structures subjected to severe nonuniform temperatures.

### DESIGN CONCEPTS

#### Design Concepts for Primary Structure

As may be expected, no single structural concept is applicable for the various types of winged aerospace vehicles of concern here. Figure 73-4 indicates two general approaches on which the structural design may be based. (See ref. 5.) Shown at the left is the hot-structure concept in which the structure operates near the equilibrium temperature and supports applied loads adequately. The other concept labeled "protected structure" consists of a thermal protection system that maintains low structural temperatures so that the imposed loads are carried by a relatively cold primary structure. The hot structure avoids the difficult design problems associated with the thermal protection system on the protected structure; however, other significant difficulties including materials and thermoelastic problems are introduced. The primary load-carrying structure associated with the protected-structure concept can be designed largely on the basis of existing technology associated with structures for current aircraft. For this reason no further atten-

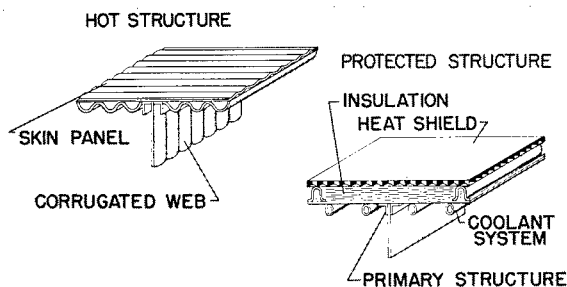


FIGURE 73-4.—Structural concepts for winged aerospace vehicles.

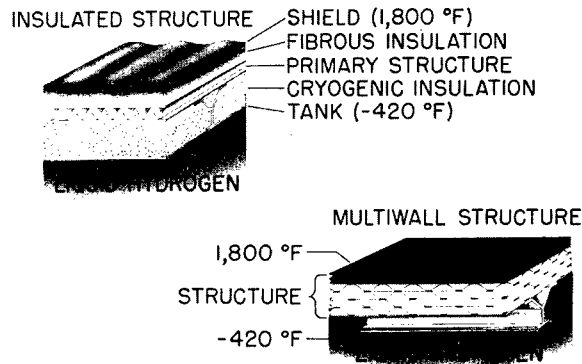


FIGURE 73-5.—Structural concepts for hypersonic airplane. Cryogenic fuel tank area.

tion to the cold primary structure design is given. Further considerations of thermal-protection systems with emphasis on heat-shield design will be presented subsequently.

The advantages and limitations of these two approaches have been the subject of numerous studies. (See ref. 6.) No clear choice exists between the two design concepts. The resulting designs are generally competitive weightwise and both concepts appear to be feasible.

#### Structural Concepts for Cryogenic Fueled Vehicles

Because vehicles that utilize cryogenic fuels pose unusual structural requirements, special considerations will be given here to possible design concepts. Two such concepts are indicated in figure 73-5. An insulated type of structural concept indicated in the left-hand view consists of a heat shield that may be a superalloy for temperatures up to  $1800^{\circ}\text{F}$  and refractory metal for higher temperatures, fibrous high-temperature insulation, primary structure, cryogenic insulation, and, lastly, the tank containing cryogenic fuel which is assumed in this case to be liquid hydrogen. The temperature of the primary structure is dependent in part on the relative thicknesses of the cryogenic and fibrous insulation utilized. A low primary-structure temperature appears desirable to take advantage of favorable material properties and to minimize thermal-expansion problems. This type of construction requires essentially three leak-tight shells including the internal hydrogen tank, the primary structure to preclude

## STRUCTURES

liquification of air that enters the cryogenic insulation area, and lastly, the heat shield to prevent trapping and freezing of moisture within the fibrous insulation area.

In the right-hand view a multiwall design approach is indicated. This design is unique because the thermal-protection and load-carrying functions are combined into one integral component. The design consists of alternate layers of flat and dimpled sheets joined together by welding. The insulating effect is produced by the multiple-layer reflective sheets. This structural concept possesses several advantages over other approaches including effective utilization of different sheet materials to give optimum strength-weight ratios, possible improvement in structural reliability through integration of the thermal-protection and load-carrying functions, improved resistance to dynamic pressures, and good protection against meteoroid penetration.

The full potential of the multiwall concept has not been established. It is anticipated that thermal stresses associated with the large temperature differences through the wall thickness may be a major problem. Development of appropriate methods of analysis are required, as well as experimental investigations to verify the analytical methods.

### Leading-Edge Approaches

Various types of designs that are representative of thermal-protection systems for leading edges of winged aerospace vehicles are indicated in figure 73-6. The nonmelting heat sink where some of the stagnation-region heat load is transferred rearward and then radiated represents one of the important leading-edge concepts. Its characteristics are readily amenable to analysis (ref. 5) and this approach has received extensive theoretical study. The leading edge of the X-15 research airplane is based on this approach. In the radiation approach, both metallic and ceramic designs are indicated. Recent advances in both coated refractory metals and in oxide ceramics indicate that the radiation approach to leading edges is feasible. The leading edge of the X-20 Dyna-Soar is based on the metallic radiation approach.

The internal cooling approach and the tran-

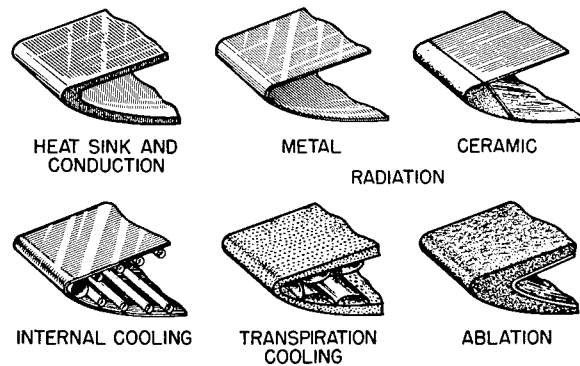


FIGURE 73-6.—Leading-edge approaches for winged aerospace vehicles.

spiration and film cooling approach may be expected to find application in some flight vehicles in which the shape of the edge must be accurately maintained during flight to achieve desired vehicle performance. Both of these concepts appear very promising; however, neither concept is in an advanced stage of development. Further efforts will be required to permit their utilization in flight vehicles. The ablation approach is of considerable interest and may also be utilized. The change in shape that accompanies the ablation process however may lead to undesirable vehicle performance in some cases. All of these leading-edge approaches appear to be feasible and are of current interest. No attempt will be made to compare these various concepts on a weight basis. In many cases, factors such as reusability, simplicity, and reliability will have important bearing on the type of approach utilized.

### Application of Construction Concepts for Nonuniformly Heated Structures

Numerous construction concepts have been proposed to cope with severe nonuniform temperatures. These include corrugations, beads, and expansion joints. All of these approaches have been incorporated in a large structural model representative of a forward portion of a reentry glider. The model was fabricated at the Langley Research Center and was subjected to an extensive experimental investigation. (See ref. 7.) Figures 73-7 and 73-8 show the interior and exterior details of the model.

Figure 73-7 shows the internal structure of a model 12 feet long. The structure consists

of an approximately orthogonal arrangement of longitudinal beams and transverse frames. The loads from the exterior skin panels are transmitted to the transverse frames and the frames in turn transmit the loads to the two longitudinal beams. Corrugated shear webs are used in both transverse frames and longitudinal beams to resist shear loads and to permit differential thermal expansion between the top and bottom spar caps. Two different types of corrugations are utilized as shown. A conventional 60° corrugation was selected for the longitudinal beams and a special corrugation that permitted large flexibility at right angles to the transverse frames was selected for the transverse frames.

An external view of the model showing the skin panels attached is presented in figure 73-8. The skin panels are attached to the outside flanges of the transverse frames. Expansion joints can be seen extending around the model at approximately 2-foot intervals. These expansion joints as indicated consist of an omega-shaped metal strip that permits differential expansion between adjacent panels and also provides a tie between the panels so that their shear stiffness can be utilized to provide torsional stiffness for the model.

The skin panels as shown consist of two thin sheets seam-welded together. The external sheet is beaded lightly to stiffen it against local buckling and to preset a pattern for uniform deformation when thermal expansion is restrained across the corrugations. The inner sheet consists of 1/2-inch flat 60° corrugations.

This model has been subjected to numerous

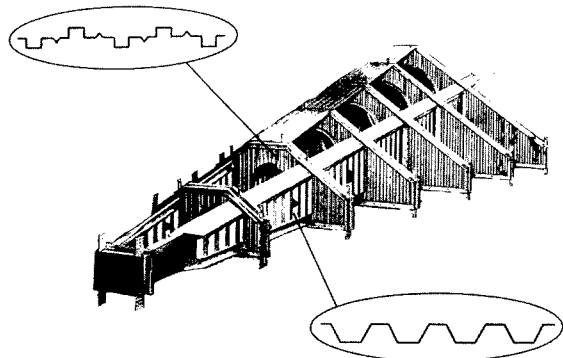


FIGURE 73-7.—Interior view of structural model.

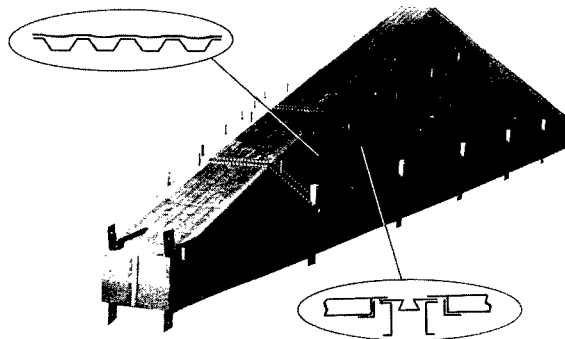


FIGURE 73-8.—Exterior view of structural model.

loading and heating tests with test temperatures ranging up to 1600° F. No significant structural damage was observed. It thus appears that the various structural concepts utilized in the model are practical for coping with both loads and high nonuniform temperatures.

#### Insulating Heat-Shield Concept

If the anticipated temperatures for the skin panels exceed the desired use temperatures, a possible method for coping with the high external temperatures is to provide a nonload-carrying insulating heat shield over the structural panels. With the proper amount of insulation, the load-carrying structure can be maintained within the useful temperature range for the material. Many different heat-shield concepts have been proposed. In this paper one typical design concept is described. (See ref. 8.) This typical design is indicated in figure 73-9. The shield consists of a lightly corrugated outer skin and then a layer of insulation. The primary structure is shown below the insulation. In the outer skin, nonuniform expansion is permitted to occur across the corruga-

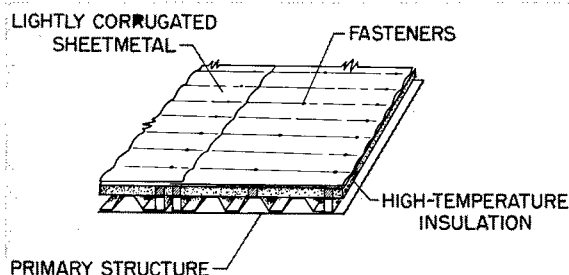


FIGURE 73-9.—Heat-shield concept.

## STRUCTURES

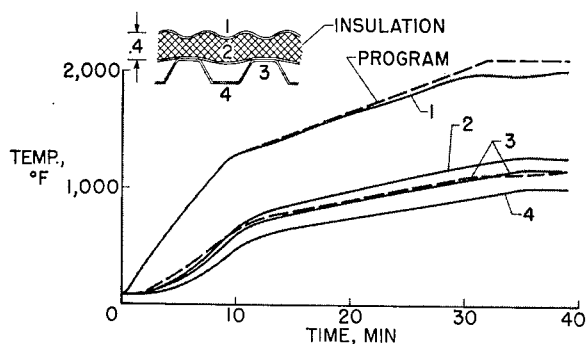


FIGURE 73-10.—Temperature-time history for heat shield.

tions by an increase or decrease in the amplitude or depth of the corrugations. In the other direction, expansion is permitted through the use of flexible supports at the ends of the corrugated outer sheet. The problem that must be coped with satisfactorily is to support the outer skin adequately so that it will survive in the airstream and will accommodate the thermal expansion resulting from the large temperature differences between the shield and structure. The aerothermoelastic environment imposed on the heat shield is usually very severe, and stiffness requirements to prevent panel flutter may generally dictate the design. (See ref. 4.) Adequate and properly spaced fasteners between the shield and primary structure must be provided.

The performance of a typical heat shield is shown in figure 73-10. The temperature-time history for the shield is shown. The upper dashed line (labeled "program") indicates a calculated temperature-time history for a point on the heat shield of a reentry glider. The experimentally applied temperature was obtained by program-controlled quartz-lamp radiators that heated the 2-foot-square panel. The response of the underlying structure is indicated by the solid curves and the predicted response by the dashed curve. Methods for predicting structural temperatures under conditions such as these are well established and have received extensive theoretical study. The adequacy of the theoretical methods is evidenced by the satisfactory correlation between theory and experiment.

This shield consisting of the outer corrugated sheet and attachment clips weighed approximately 1 pound per square foot. The insulation

was quartz fiber 0.4 inch thick. Note that a temperature difference of approximately 1000° F existed between the shield and the internal structure during the period of maximum shield temperature. It is of interest to note that similar shields have been subjected to supersonic airflow with dynamic pressures up to 3,000 pounds per square foot and to noise environment ranging up to approximately 160 decibels. The shields have withstood these environments successfully.

## OTHER FACTORS THAT INFLUENCE STRUCTURAL DESIGN

The discussion thus far has focused on structural designs for coping with the nonuniformly and highly heated vehicles. Several other factors that have a pronounced effect on the structural design will now be considered. These include flutter, fatigue, and materials selection.

### Flutter

Because it has an important bearing on structural integrity, flutter is presently recognized as a critical problem area for winged aerospace vehicles. In this paper attention will be devoted to only one aspect of the general problem of flutter, namely, panel flutter. Panel flutter is of particular significance for structural surfaces of winged aerospace vehicles that are fabricated from thin sheets of high-strength high-density materials and are designed to carry small structural loads. It is recognized as a supersonic phenomenon, and several present-day aircraft have recently encountered panel flutter in flight at supersonic speeds. Let us consider the X-15 research airplane for a specific example. (See fig. 73-11.) The shaded areas, including the fairing panels along the sides of the fuselage and the vertical tail, have been affected and modified by considerations of flutter. (See ref. 4.) It was found that many of these panels required reinforcements as high dynamic pressures were explored in flight. Panels with corrugations normal to the airflow were particularly prone to flutter. In view of the importance of corrugations for exterior surface panels of aerospace vehicles, the first consideration is the influence of corrugation orientation relative to airflow on panel flutter.

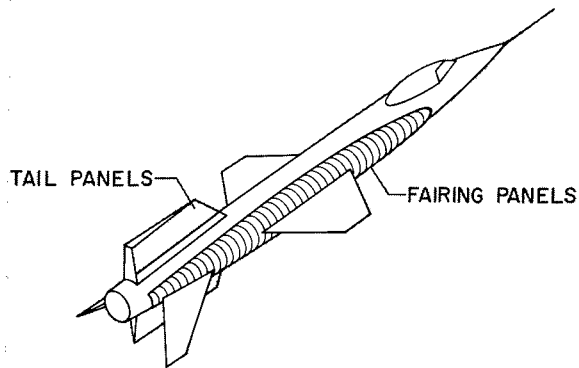


FIGURE 73-11.—Flutter areas on X-15 research airplane.

In figure 73-12 the panel-flutter parameter is plotted against the flow angularity. In this figure,

- $L$  panel length
- $t_{eff}$  effective panel thickness
- $q$  dynamic pressure
- $M$  Mach number
- $E$  Young's modulus for panel material
- $A$  flow angle measured in plane of panel relative to corrugation axes

The predicted flutter boundary is indicated by the curve and several experimental results are shown by the symbols. When compared with theory, the experimental data are low. The predicted flutter boundary was obtained from a four-mode solution of the orthotropic plate equation by assuming two modes in each of the orthogonal directions. (See ref. 9.)

Figure 73-12 demonstrates the strong influence of flow direction on orthotropic panel flutter. A particularly large decrease in resistance to flutter is indicated by the theory for small changes in flow direction from the corrugation axis. For example, for a  $15^\circ$  deviation in the flow direction the dynamic pressure estimated to produce panel flutter is approximately one-eighth of the magnitude indicated for zero flow angularity. This sensitivity to small variations in flow angularity would be of concern for vehicles that operate through large attitude changes with accompanying large variations in flow direction over the structural panels.

Attention will now be directed at two additional parameters that have significant influence on panel flutter. These parameters are

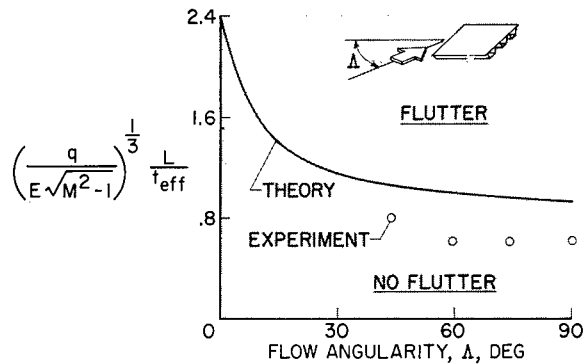


FIGURE 73-12.—Effect of flow angularity on flutter of orthotropic panels.

panel midplane stress and pressure difference across the panel. The influence of these parameters will be discussed with the aid of figure 73-13. The ordinate is essentially the same panel-flutter parameter shown in figure 73-12, and the abscissa is a differential temperature ratio. The temperature increase in the panel due to aerodynamic heating is denoted by  $\Delta T$  and a reference temperature that is proportional to the buckling temperature for the panel is denoted by  $\Delta T_R$ . The parameter on the abscissa gives an indication of the magnitude of the midplane stress in the panel. The symbols represent flutter points obtained from a series of similar isotropic panels tested in a supersonic wind tunnel. The open symbols establish the flutter boundary for the panels in a flat and unbuckled condition, and the solid symbols define the flutter behavior when the panels were buckled. Note that it is possible for a panel to

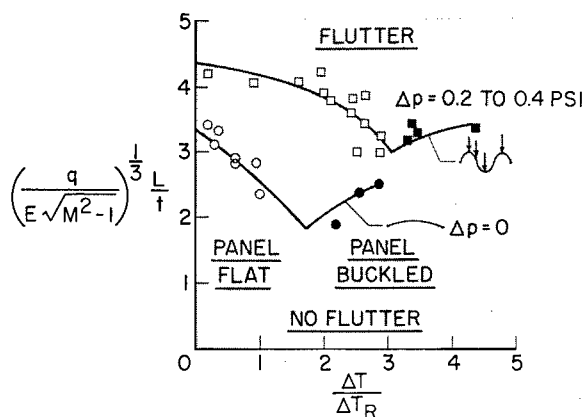


FIGURE 73-13.—Effects of midplane stress and differential pressure on panel flutter.

## STRUCTURES

remain flat and flutter free until some midplane stress is developed during the aerodynamic heating. The panel then flutters, and eventually flutter may stop when the panel is in a buckled condition. The data shown by the lower curve correspond to a pressure difference across the panel  $\Delta p$  equal to zero. The upper curve indicates test data for similar panels that experience a pressure differential of 0.2 to 0.4 pound per square inch acting inward on the panels. This magnitude of pressure difference was sufficient to change the flutter boundary from the lower to the upper curve. In addition, the flutter mode changed from a standing-wave type for the lower boundary to a traveling-wave type for the upper boundary. Thus, a small pressure differential of approximately 0.2- to 0.4-pound per square inch was sufficient to produce a considerable change in the flutter mode and a change in the flutter boundary.

Figures 73-12 and 73-13 have identified three factors that have significant effect on panel flutter. Theoretical predictions of panel flutter to date do not generally show close correlation with experimental results; however, valuable analytical contributions are being made at the present time. It is hoped that present studies will be continued to improve our understanding of the panel-flutter problem.

### Fatigue Aspects of Winged Aerospace Vehicles

Fatigue is recognized as a potentially important factor in the design of all modern lightweight flight vehicles. The specific role of fatigue in the design approach for winged aerospace vehicles is not clear although it appears that certain aspects such as acoustic fatigue will be of major concern. Acoustic fatigue problems may arise from either powerplant or aerodynamic boundary-layer noise. Attention will be devoted to the latter. Very little information is available at the present time to characterize the boundary-layer noise associated with hypersonic flight. On the basis of a large number of experiments, it appears that boundary-layer-noise pressures on a vehicle are generally proportional to the local dynamic pressures. (See ref. 10.) Figure 73-14 indicates the surface pressure level of the boundary-layer noise in

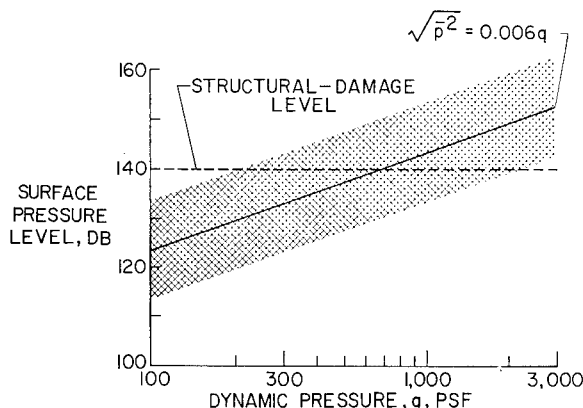


FIGURE 73-14.—Boundary-layer noise pressure levels.

decibels plotted against dynamic pressures that are of interest for winged aerospace vehicles. The solid line is given by the indicated equation in which the term  $\sqrt{p^2}$  is the mean-square value of fluctuating pressure and  $q$  is the dynamic pressure. A structural-damage level line is indicated at 140 decibels by the dashed line. The location of this line on the ordinate depends on the type of structural design, the duration of the noise pressure, and other factors.

The solid curve is derived mainly from experimental data at subsonic speeds. Recent wind-tunnel and flight tests at supersonic speeds have indicated that the surface pressure level may be either higher or lower as indicated by the cross-hatched band. (See ref. 11.) Insufficient experimental data exist, particularly at hypersonic speeds, to aid in establishing the proper relationship between these parameters; however, it is clear that boundary-layer noise increases with increasing dynamic pressure. It also appears that acoustic fatigue will become an increasingly severe problem for winged aerospace vehicles because of the use of high-strength thin-gage materials coupled with construction that will utilize large numbers of tiny weld joints that are potential sources for fatigue cracks.

The second aspect of the boundary-layer-noise problem is associated with determination of the structural response and estimation of fatigue life or damage. Studies in this area are based largely on experimental data. An example of structural fatigue damage that is determined experimentally (ref. 12) is given in figure 73-

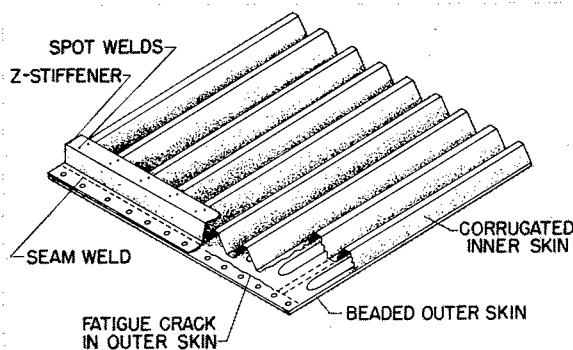


FIGURE 73-15.—Acoustic fatigue failure of corrugation-stiffened panel.

15. This figure shows a corrugation-stiffened panel utilized in an acoustic fatigue study to establish weaknesses in the panel design. This particular panel consisted of a lightly beaded outer skin, a corrugated inner skin seam-welded to the outer skin, and Z-stiffeners seam-welded to the outer skin and spot-welded to the corrugations. Acoustic fatigue tests were conducted at high noise levels for the purpose of determining the locations and types of failures. The tests determined that initial failure occurred in the spotwelds attaching the inner skin to the Z-stiffeners. Skin cracks were also observed near the end of the panel in the vicinity of the seam welds attaching the outer skin to the Z-stiffener. The results indicated were obtained at room temperature.

Figure 73-16 shows the results of a systematic series of acoustic fatigue tests that were made on corrugated-core sandwich panels fabricated from stainless steel. Sound pressure level is plotted against time to failure. Test temperatures of 450° F and 750° F are indicated on the

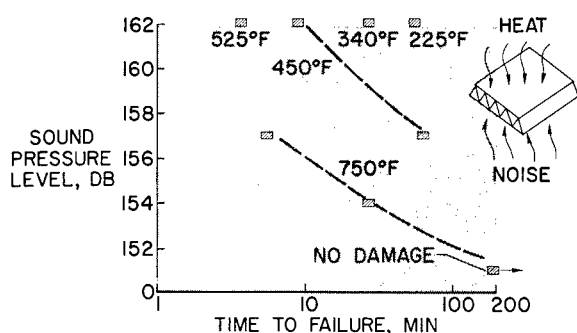


FIGURE 73-16.—Effect of noise level and temperature on time to failure of truss-core sandwich panel.

dashed curves. The panels were approximately 15 inches square and were subjected to simultaneous heating and noise environment. The width of the small horizontal bars indicates the uncertainty in the actual failure time of the panels. The test temperatures noted adjacent to the bars at the top of the figure indicate lifetime results obtained at different temperatures at 162 decibels. These results show that the life of the sandwich panels, as expected, was influenced by the magnitude of the sound pressure level as well as by the temperature. The ability to predict life of complex structural components does not exist at the present time and considerably more effort will be required to bring about a better understanding of this problem.

#### Materials Influence on Structural Design

Attention will now be directed to materials to indicate their influence on vehicle design. It is recognized that progress in materials has substantial influence on design and performance of flight vehicles. Materials limitations are instrumental in establishing temperature limits as well as strength and stiffness capabilities. Some of the materials problems that have direct bearing on structural vehicle performance will be reviewed.

In figure 73-17 the variations of materials strength with temperature are indicated for several classes of structural materials of interest for winged aerospace vehicles. The data shown on the left apply to tensile strengths obtained from smooth specimens and the data on the right were obtained from specimens

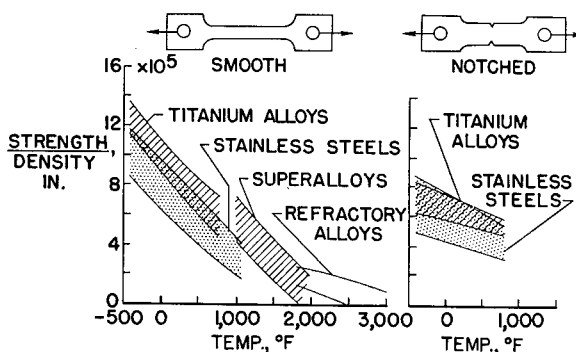


FIGURE 73-17.—Strength of structural materials determined from smooth or notched tensile specimens.



## STRUCTURES

with external notches. (See, for example, refs. 13 to 15.) The strength-density ratio is plotted against temperatures ranging from liquid hydrogen temperatures to 3000° F. Titanium alloys, stainless steels, superalloys, and refractory metal alloys are shown. The shaded areas corresponding to each class of materials indicate the spread in tensile strength for various alloys within each class of materials. It appears that the most efficient structural design is obtained at liquid hydrogen temperatures, provided that it is possible to realize such high strength-density values. The indicated strength-density values will not be realized, however, because of the notch sensitivity of the material.

The shaded areas on the right indicate the sharp notch strength which is a measure of the sensitivity of the material to high stress concentrations or cracks. Data are shown only for titanium alloys and stainless steels. Note that at liquid hydrogen temperatures the sharp notch strength is approximately one-half of the smooth specimen strength. Information of this type on the superalloys and refractory metal alloys above 1000° F is practically nonexistent at present. The large decrease in strength attributed to sharp notches emphasizes the fact that high strengths of many materials cannot always be realized. It should be noted that strength data obtained from notched specimens appear useful for comparison purposes among various materials; however, the methods for utilization of this information in vehicle design are not established at the present time. Further study of this problem appears to be warranted.

A generally large materials effort is underway at the present time to determine the potential of refractory metals for aerospace vehicle applications. Among the many problems that must be overcome, oxidation of the refractory metals at their desired use temperatures above 2000° F is perhaps one of the most serious. Figure 73-18 indicates the progress that has been made in this direction. The times that coatings will protect refractory metals from oxidation under constant temperature conditions are indicated by the solid curves and under cyclic temperatures by the dashed curves. (See, for exam-

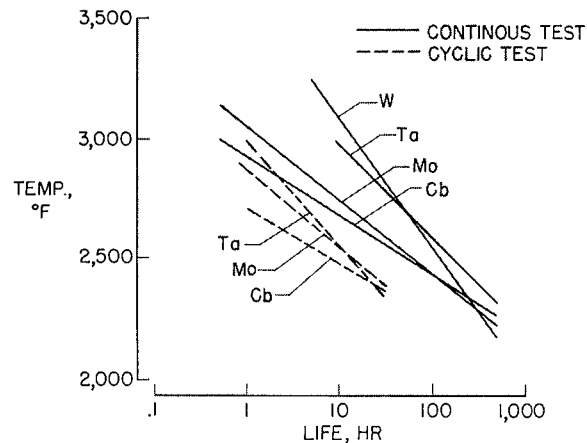


FIGURE 73-18.—Life of coated refractory metal sheet under continuous or cyclic temperatures.

ple, refs. 16 to 19.) Results are given for alloys of the four important refractory metals of interest, namely, tungsten, tantalum, molybdenum, and columbium. The curves represent a generally optimistic average of test information for several coatings including silicic, metallic or intermetallic, and ceramic types. With the exception of coatings for tungsten, several commercially available coatings will yield the type of results shown here. Coatings for tungsten are generally in the laboratory development stage at the present time.

These results indicate that present-day coatings can provide continuous protection of at least 1 hour at 3000° F to 100 hours at 2500° F and that an order of magnitude or greater decrease in coating life is obtained under cyclic exposure conditions. The serious degradation that is obtained under cyclic temperature exposure has direct bearing on the reusability of refractory metal components in aerospace vehicles. Further efforts to improve coating performance, particularly under cyclic temperatures, appear to be warranted.

One item of concern regarding utilization of coatings on refractory metals is based on the fact that the life of large complex structural components will generally be less than the life obtained from small materials coupons. This problem is indicated in figure 73-19. Figure 73-19 indicates the test temperatures and corresponding life for coated molybdenum coupons and coated corrugated-core sandwich panels.

# PROBLEMS OF STRUCTURES FOR WINGED AEROSPACE VEHICLES

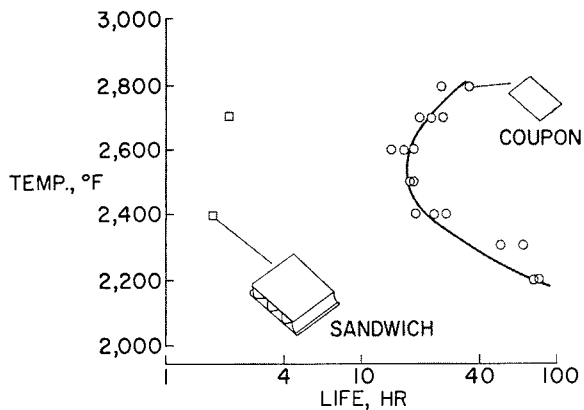


FIGURE 73-19.—Comparison between life of coated molybdenum coupons and life of coated molybdenum sandwich panels.

(See ref. 20.) The coating is a commercially available disilicide type. Life is defined as the time at test temperature during which the coating protected the metal with no measurable evidence of oxidation. The circle symbols indicate test results from small square sheet coupons tested continuously in slowly moving air in an electrically heated furnace. In the temperature range from 2400° F to 2700° F, a coating life of approximately 20 hours was obtained. The square test symbols indicate the life of two coated structural specimens under similar test conditions. The structural specimens consisted of corrugated-core sandwich plates. The difference in lifetime may be attributed to the difficulty of coating the sharp corners and recessed areas and to nonuniform expansion of various parts that may cause defects in the coating.

Several other factors have an important bearing on the performance and reliability of coated

refractory metals. These include protection afforded by the coating under dynamic airflow, the performance of the coating under low pressure simulating high-altitude environment accompanied by high temperatures, and a better understanding of the protective mechanism and the modes of failure of the various types of coatings.

## CONCLUDING REMARKS

To conclude this presentation, several research areas of particular importance to winged aerospace vehicles are noted and special problems in these areas that require further work are indicated. Under structural concepts, further attention should be devoted to formulation of new concepts and to analytical study of structural systems that incorporate thermal-protection and load-carrying functions into a single component. Further study of methods for application of transpiration cooling to winged aerospace vehicles should also be pursued. With reference to aerothermoelasticity, analytical studies are required to bring about a better understanding of flutter of orthotropic panels under aerodynamic heating. Two problems are noted under acoustic fatigue. These include characterization of boundary-layer noise at hypersonic speeds and development of approaches for establishing structural response and fatigue life. Under materials, the development of methods for application of notch-strength information to vehicles design, the improvement of coatings, and better understanding of protective mechanism and modes of failure of the coatings are of particular importance.

## REFERENCES

1. MELLINGER, GEORGE R.: The X-15. *Aerospace Engineering*, vol. 20, no. 8, Aug. 1961, pp. 12-13, 26, 28-30, 32, 34-36, 38.
2. YOLER, YUSUF A.: Dyna-Soar—A Review of the Technology. *Aerospace Engineering*, vol. 20, no. 8, Aug. 1961, pp. 8-9, 56-67.
3. FRICK, C. W., and STRAND, T.: Recoverable Air-Breathing Boosters—Analysis of Their Potentialities. *Aerospace Engineering*, vol. 20, no. 2, Feb. 1961, pp. 22-23, 66-70.
4. GARRICK I. E., and CUNNINGHAM, HERBERT J.: Problems and Developments in Aero-thermoelasticity. *Proceedings of Symposium on Aerothermoelasticity*, ASD Tech. Rep. 61-645, U.S. Air Force, 1961, pp. 12-60.
5. HELDENFELS, RICHARD R.: *Frontiers of Flight Structures Design*. Aeronautics and Astronautics, Nicholas John Hoff and Walter Guido Vincenti, eds., AFOSR TR 59-108, Pergamon Press, Inc. (New York), 1960, pp. 29-51.
6. GLASER, PETER E., ed.: *Aerodynamically Heated Structures*. Prentice-Hall, Inc., 1962.

## STRUCTURES

7. PRIDE, RICHARD A., ROYSTER, DICK M., and HELMS, BOBBIE F.: Experimental Study of a Hot Structure for a Reentry Vehicle. NASA TM X-314, 1960.
8. ANDERSON, MELVIN S., and STROUD, C. W.: Experimental Observations of Aerodynamic and Heating Tests on Insulating Heat Shields. NASA TN D-1237, 1962.
9. GUY, LAWRENCE D., and DIXON, SIDNEY C.: A Critical Review of Experiment and Theory for Flutter of Aerodynamically Heated Panels. Presented at Symposium on Dynamics of Manned Lifting Planetary Entry (Philadelphia, Pa.), Oct. 29-31, 1962.
10. HUBBARD, HARVEY H., and MAGLIERI, DOMENIC J.: Supersonic Transport Noise Problems. Presented to International Air Transport Association (Montreal, Canada), Apr. 17-28, 1961.
11. HILTON, DAVID A., MAYES, WILLIAM H., and HUBBARD, HARVEY H.: Noise Considerations for Manned Reentry Vehicles. NASA TN D-450, 1960.
12. EDGE, PHILIP M., JR.: Acoustic Fatigue Tests Relating to the Design of Structures for Elevated Temperatures. Presented at ONR/AIA Symposium on Structural Dynamics of High Speed Flight (Los Angeles, Calif.), Apr. 24-26, 1961.
13. SACHS, G., and PRAY, R. FORD, III, eds.: Air Weapons Materials Applications Handbook Metals and Alloys. ARDC TR 59-66, U.S. Air Force, Dec. 1959.
14. WEISS, V., SELL, R., and CHAVE, C.: Material Evaluation for a Supersonic Transport Plane. Rep. No. MET. E. 873-626-F (Contract No. NASr-43), Syracuse Univ. Res. Inst., June 1962.
15. NEFF, C. W., FRANK, R. G., and LUFT, L.: Refractory Metals Structural Development Program. Vol. II—Refractory Alloy and Coating Development. ASD Tech. Rep. 61-392, U.S. Air Force, Oct. 1961.
16. KRIER, C. A.: Coatings for the Protection of Refractory Metals From Oxidation. DMIC Rep. No. 162, Battelle Memorial Inst., Nov. 24, 1961.
17. NICHOLAS, M. G., PRANATIS, A. L., DICKINSON, C. D., and WHITMAN, C. I.: The Analysis of the Basic Factors Involved in the Protection of Tungsten Against Oxidation. ASD-TDR-62-205, U.S. Air Force, June 1962.
18. LAWTHERS, DEAN D., and SAMA, L.: High Temperature Oxidation Resistant Coatings for Tantalum Base Alloys. ASD Tech. Rep. 61-233 (Contract AF 33(616)-7462), U.S. Air Force, 1961.
19. RUMMLER, D. R., STEIN, B. A., and PRIDE, R. A.: Preliminary Results of a Comparative Study of Several Commercially Available Oxidation Resistant Coatings on Mo-0.5 Ti Alloy Sheet. Presented at Sixth Meeting of the Refractory Composites Working Group (Dayton, Ohio), June 16-19, 1962.
20. MATHAUSER, ELTON E., STEIN, BLAND A., and RUMMLER, DONALD R.: Investigation of Problems Associated With the Use of Alloyed Molybdenum Sheet in Structures at Elevated Temperatures. NASA TN D-447, 1960.

# 74. Research, Design Considerations, and Technological Problems of Structures for Planetary Entry Vehicles

By Roger A. Anderson

ROGER A. ANDERSON, *Assistant Chief, Structures Research Division, NASA Langley Research Center, received his Bachelor of Science degree in Civil Engineering from Northwestern University in 1944.*

*Anderson joined the Langley staff as a structural engineer in June 1944. With the emergence of reentry as a dominant problem in space structures and materials, Anderson has taken special interest in the problems of thermal protection systems ranging from analysis and evaluation of present capabilities to projected requirements for accomplishment of future manned and unmanned space missions. Anderson has served as a member of the evaluation boards for the Dyna-Soar glider, the Mercury spacecraft, and the Apollo System. He has served on several technical committees at Langley and other national organizations and currently serves on the Structures and Materials Committee of the American Rocket Society. He is the author of numerous technical papers in the field of aerospace structures.*

## SUMMARY

The technology for structural design of manned and unmanned planetary-entry vehicles is reviewed. Emphasis is placed on the important features of these vehicles—the thermal shield and the landing system. Basic structural and material concepts are discussed in the light of applicable environmental conditions, and areas for further research are suggested.

## INTRODUCTION

The technology for structural design of space vehicles whose mission includes a successful high-speed entry into a planet's atmosphere has had a relatively short but eventful history of development. Knowledge has accumulated rapidly through the practical experience gained in the design and successful flights of vehicles such as the Mercury spacecraft and a number of smaller vehicles which preceded it. Flight requirements continue to expand in the direction of higher speeds and longer and more complex missions; consequently, new materials

and concepts of construction are still needed.

In this review the primary emphasis will be placed on the unique feature of the entry vehicle—the thermal shield and its integration with structure—inasmuch as it accounts for an important fraction of the weight and of the problems in vehicle design. Because entry is not completed for most vehicles until a soft landing on a planet's surface has been made, current thinking regarding final letdown and impact will also be briefly reviewed.

## SYMBOLS

$A$	frontal area of vehicle
$C_D$	drag coefficient
$g_E$	acceleration due to Earth's gravity
$q$	heating rate
$Q$	heat load per unit area
$t$	time
$W$	total weight or weight per unit area
$W_{SYS}$	system weight
$W_{VEH}$	vehicle weight
$\rho$	density

## STRUCTURES

### GENERAL DESIGN CONSIDERATIONS

Entry vehicles are conveniently divided into two basic types—the unmanned vehicle designed for a specific research purpose, and the considerably larger vehicle utilized for manned missions. The structural approach for each class varies because of differences in size, shape, and degree to which the internal environment needs to be controlled.

Features of the unmanned class are shown in figure 74-1. Characteristically, they are ballistic bodies of relatively simple shape. The primary structure usually conforms to the aerodynamic outline and a layer of ablative material is bonded directly to it. In this manner internal volume is maximized and structural weight is held to a minimum. The principal structural complication is in the form of sensor and telemeter antenna installations. Windows which maintain transparency at specific optical and radio wave frequencies must be installed and are not always located in regions of low heat transfer. Such installations give rise to localized heating problems and require detailed thermal and stress analysis.

With the vehicle for manned missions (fig. 74-2), a much wider variation in aerodynamic configuration is encountered. They include the ballistic as well as the lifting shapes which provide a wider entry corridor and a horizontal-landing capability. For this class of vehicles the primary pressure shell forming the cabin does not differ substantially from current aero-

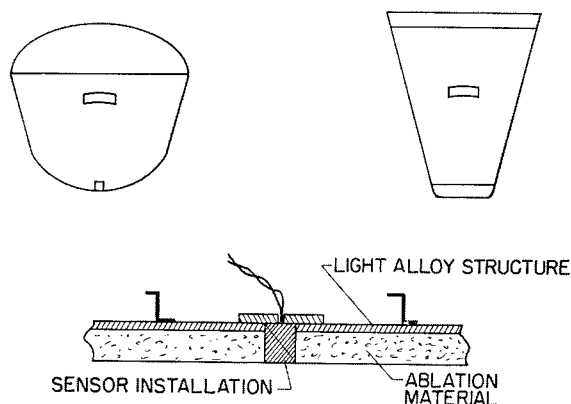


FIGURE 74-1.—Construction of unmanned entry vehicle.

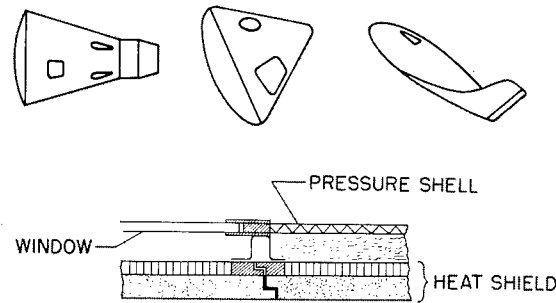


FIGURE 74-2.—Construction of manned entry vehicle.

nautical practice except for the precautions taken to maintain leak tightness. It usually does not conform to the external lines and is protected against entry heating by a separate structural component commonly referred to as a heat shield. The space between the cabin and the heat shield is occupied by insulation, connecting structure, and items of equipment which do not require storage in the controlled environment of the pressure cabin. The hatch and window openings in the cabin require doors in the heat shield. These cutouts in turn must be fitted with hatches which can be opened and closed during a mission. The associated interruptions in shield continuity are of concern during the entry phase. In addition, large sections of the shield may serve as a part of the landing-impact absorption system. Because of such features the heat shield can account for more than one-half the total structural weight of the vehicle.

In the selection of materials and design criteria for these structures, consideration is given to a wide spectrum of environmental conditions from initial assembly to final impact. These considerations are illustrated in figure 74-3. Assembly and disassembly operations must be considered in the basic design concept because of the demonstrated need for ease of access through the structure for repair and replacement of internal components. Repair of damage associated with ground-handling operations is a consideration in the choice of materials, especially those used for the heat shield.

The launch phase subjects the structure to a variety of vibratory and acoustic loadings. A review of these loadings may be found in ref-

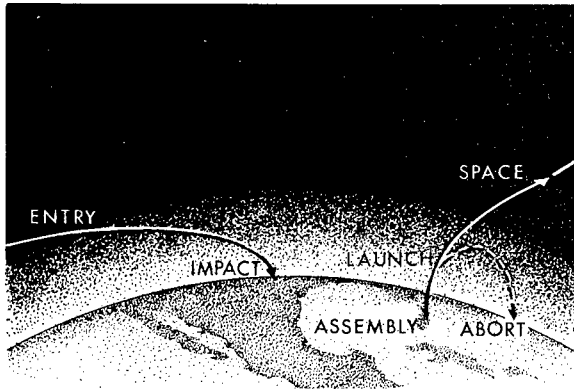


FIGURE 74-3.—Vehicle design considerations.

erence 1. The critical design values of aerodynamic load are likely to be encountered during launch. This is particularly true for manned vehicles which are designed for safe abort during any portion of the launch phase. Possible degradation of the surface of the heat shield due to heating during ascent requires attention.

An exposure to space environment for extended periods places a number of constraints on material selection. (See ref. 2.) Of most concern is the response of the heat shield to micrometeoroid impact and its subsequent performance during entry. At least for missions of short duration, the heat shield is called upon to serve as the meteoroid bumper and its construction must reflect this requirement. For longer missions, an additional consideration in selection of materials will be the shielding they afford against ionizing radiation.

The heat shield performs its primary design function during the entry phase. The severity and duration of heating and loading varies widely with vehicle type and trajectory (see ref. 3); consequently, a large number of material and structural concepts have evolved (refs. 4, 5, and 6). Proper selection of materials and prediction of their performance as mission times and entry speeds increase is a large and challenging research task.

After conclusion of the high-heating and deceleration phase, vehicle terminal velocity is generally too high for a survivable impact on a planet's surface. Loads associated with deployment of a suitable letdown system and sup-

port of an impact energy absorber contribute significantly to structural weight and to final structural arrangement.

Integration of the design inputs arising from this sequence of environments has resulted in structural weights that currently range from 30 to 55 percent of vehicle gross weight depending on the mission. These percentages are approximately twice those associated with aeronautical structures and primarily reflect the penalty of the thermal shield required during the entry phase.

### HEAT-SHIELD PERFORMANCE

A broad picture of the role that the thermal shield plays in determining the feasibility of future entry vehicles is presented in figure 74-4. Vehicle kinetic energy, heat-shield capability, and vehicle heat load, all expressed in Btu/lb, are shown as a function of entry velocity. The range of velocity shown must be considered if exploration of nearby planets is to be carried out. (See ref. 7.) Of the tens of thousands of Btu's of kinetic energy possessed by each pound of the entering vehicle, the major portion is dissipated in heating the atmosphere with only a small fraction returning as a heat load on the vehicle surface. At the lower velocities heat transfer to the vehicle is primarily by convection, whereas at the higher velocities radiative transfer from the highly heated shock wave contributes importantly. (See refs. 8, 9, and 10.)

The width of the heat-load band at a given velocity reflects differences in vehicle configuration and entry trajectory. Vehicles entering

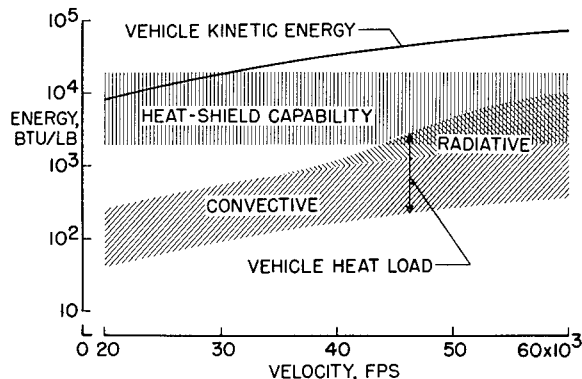


FIGURE 74-4.—Kinetic-energy dissipation.

## STRUCTURES

on ballistic trajectories encounter heat loads near the lower edge of the band, whereas vehicles flying lifting trajectories move higher in the band. Detailed knowledge of the heat load to be encountered by a given vehicle at the higher speeds is admittedly sketchy because of currently unresolved uncertainties in heat-transfer mechanisms.

Heat-shield capability can be represented by a broad band encompassing the range from 2,000 to 20,000 Btu/lb. That is, with currently known materials, each pound of heat shield can be expected to dispose of a certain amount of heat energy within this range while maintaining an acceptably cool vehicle interior for the duration of the entry maneuver. The diminishing separation between the bands of heat-shield capability and vehicle heat load suggests an increasing degree of difficulty in preserving a useful payload margin as entry speed increases. Observations of meteors in the Earth's atmosphere reveal a greatly diminished chance for survival at speeds in excess of 55,000 fps. (See ref. 7.) Clearly, at the higher speeds, vehicles designed for minimum total heat transfer and utilizing the most advanced heat-shield technology will be required if reasonable payload margins are to be preserved.

Because of wide variations in the time histories of heat transfer to various vehicle types, it may be helpful to examine figure 74-5. The stagnation-area heating histories shown are typical for a research vehicle entering the Earth's atmosphere on a fairly steep ballistic trajectory and for manned vehicles making

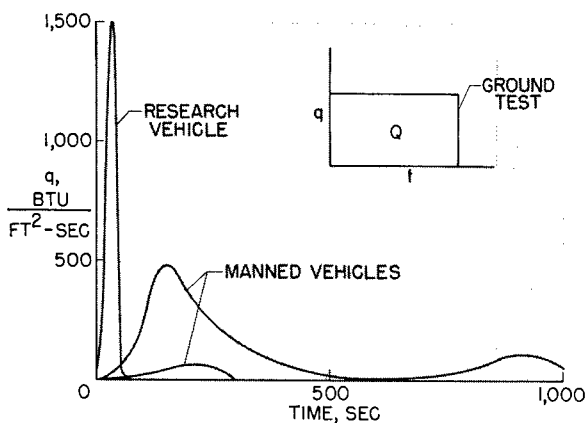


FIGURE 74-5.—Typical heating histories.

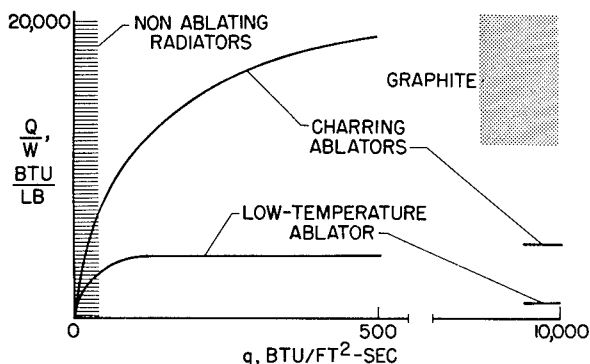


FIGURE 74-6.—Relative performance of thermal shields.

shallow-angle entries at orbital and escape velocity. The associated differences in heating rate and heating time have a substantial influence on the choice of shield material.

In the process of screening applicable materials and shield concepts for a given vehicle, a constant heating-rate pulse is usually employed. A desired constant total heat input  $Q$  can be obtained by varying the heating rate  $q$  and time  $t$ . The weight of material required to dispose of a given value of  $Q$  without significant penetration of heat to the shield interior side becomes a measure of shield performance.

The relative performance of several shield materials (at constant stream enthalpy) is shown in figure 74-6. An inverse measure of shield weight  $Q/W$  is plotted as a function of the imposed heating rate  $q$ . A break in scale is introduced to permit inclusion of the extreme heating rates associated with the higher speed entry problem.

At heating rates below about 40 Btu/ft<sup>2</sup>-sec, the current limit of serviceability for nonablating metallic surfaces, an insulating shield which disposes of heat by reradiation provides the best performance. (See ref. 11.) Because of fixed items of weight associated with construction of metallic-surfaced heat shields, the efficiency of the system depends to a large extent upon the total heat load. In vehicle areas where low heating rates permit utilization of this type of shield, a performance of the order of 20,000 Btu/lb can be achieved in a gliding entry of long duration.

In the intermediate heating-rate range, a class of materials known as charring ablators

has proven to provide a highly efficient thermal shield. (See refs. 12 and 13.) The improvement in their performance over a low-temperature ablator, such as Teflon, stems from the fact that their surfaces are forced to a high temperature by the insulating char layer formed during material pyrolysis. Thus, in addition to benefiting from the transpiration cooling provided by the gaseous products of pyrolysis, they dispose of a substantial fraction of the imposed heat load by reradiation from the hot surface.

At extreme values of heating rates, a degradation in performance is estimated for both the charring and low-temperature ablators as shown by the extension of their respective curves in figure 74-6. A qualitative explanation for this reduction is that, at the entry conditions which generate these high rates, a large fraction of the heating is presumed to be by radiation from the incandescent gas cap surrounding the vehicle. Under these conditions transpiration is less effective as a cooling mechanism. (See ref. 14.) In addition, high aerodynamic shear forces and thermal stresses may inhibit buildup of an insulative char layer on the charring ablators and thereby lead to mass loss rates more comparable to those for the low-temperature ablator.

A promising candidate material for the high-heating-rate regime is graphite. (See ref. 15.) Its high latent heat of vaporization can be used to advantage without too great concern for its relatively high thermal conductivity which hinders application at lower heating rates. A number of uncertainties remain regarding the performance of graphite under high rates of radiant and convective heating, among which is possible mechanical removal of material by spalling from thermal stresses associated with extremely steep thermal gradients. Data on the actual values of the heat of vaporization over the applicable ranges of temperature and pressure also appear to be incomplete. (An analysis of the available data is given in ref. 16.) For these reasons, the performance of graphite can only be estimated and is indicated by the shaded area shown in figure 74-6.

A particular range of heating rates in which marked advances in heat-shield performance

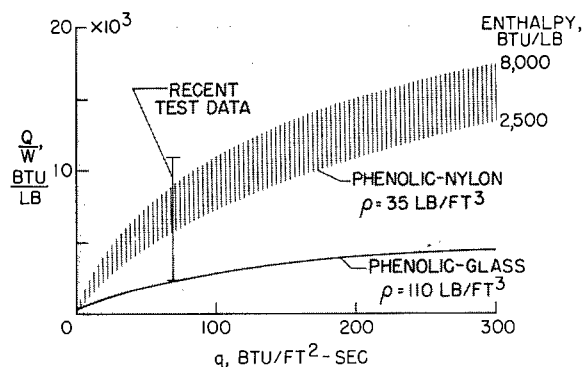


FIGURE 74-7.—Performance of charring ablators.

have been obtained in recent research is at the low end of the scale where conduction of heat through the shield to the interior is primarily responsible for the indicated dropoff in performance. This area is shown in more detail in figure 74-7. Available test data for low-density phenolic-nylon material were used to construct the indicated band. A sensitivity to stream enthalpy is noted with this charring ablator because of the high degree of vaporization obtained with nylon.

In contrast, a high-density phenolic-glass shield showed negligible enthalpy sensitivity in the same tests and provided markedly shorter protection times because of its relatively high thermal conductivity. Recent data gathered at one heating rate have revealed low-density shield compositions which show substantially higher performance. There is no reason to believe that an end point in improvement has yet been reached. In this connection, it should be noted that large surface areas of manned entry vehicles are subject to heating rates in this low range where shielding performance depends greatly on the material's ability to perform as an insulator.

A cross-sectional view of a high-performance shield is provided in figure 74-8. Here the ablative component of the shield is seen to possess a cellular structure which provides a high resistance to heat flow through the thickness. Materials of this type have low strength and stiffness and are therefore confined in a fiberglass honeycomb matrix for local reinforcement. Adequate bending stiffness is provided by attachment to a conventional honeycomb



## STRUCTURES

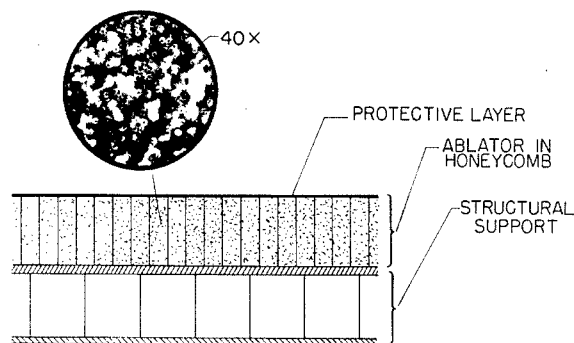


FIGURE 74-8.—Advanced shield design (low heating rates).

sandwich panel. The panel material and gage may be determined by the meteoroid impact problem as well as by stiffness or strength criteria. The indicated protective layer at the surface may be necessary to provide resistance to abrasion during ground handling and launch, and may be required in space to obtain desired values of reflectivity and emissivity. Investigation of variations of the general design concept illustrated in figure 74-8 is a subject of current research.

### GROUND RESEARCH

The bulk of ground research performed on heat-shield structures to date has of necessity been rather narrowly oriented to direct support of specific vehicle projects. The situation is changing, but with few exceptions little data can yet be assembled from the open literature for general engineering design use. The type of work underway, however, is of interest, and some of it is indicated in figure 74-9.

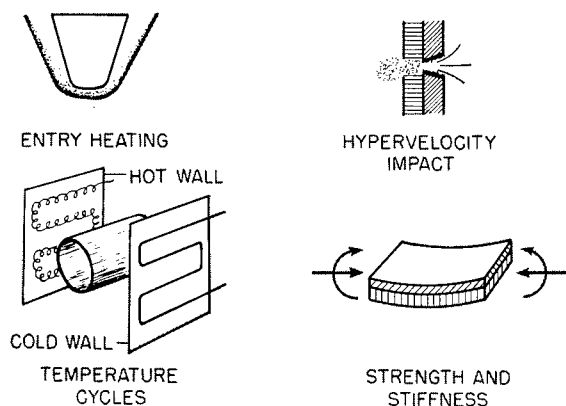


FIGURE 74-9.—Ground research.

Numerous organizations are conducting tests of materials and small structural samples in simulated entry environments. The electric arc-heated air jet in the power range of 1 to 10 megawatts is the principal facility used for this simulation. Numerous problems remain in developing this facility to its full capability, but steady advances are being made in the areas of increased stream enthalpy, Mach number, running time, model size, and control of stream chemistry. Facilities capable of combined convective and radiative heating simulation over certain ranges of heating rates are available at NASA Ames and Langley Research Centers. (See ref. 17.)

Space environmental tests in which fabricated sections of heat-shield structure are subjected to the temperature distributions and cycles expected during a space journey are being made. Radial and circumferential thermal gradients are varied to expose areas of failure due to thermal stresses. Adequate stress analysis is usually hindered by a lack of physical-property data for new shield materials and by the difficulty in accurately specifying the restraints offered by attachments between structural elements.

Some work has been accomplished on the response of shield structures to hypervelocity impact. Such tests need to be carried out at various temperature levels because of marked variations in the properties of polymeric materials with temperature. Ground facilities for this purpose are still limited in the attainable impact velocity and maximum particle size.

Inasmuch as the heat-shield structure can be required to transmit loads over considerable spans, the usual strength and stiffness tests and analysis must be performed. Again, the temperature level at which tests are carried out is important.

In addition to the work illustrated, there are numerous research investigations (see refs. 18 and 19 as examples) concerned with obtaining a basic understanding of these composite materials in the many environments of concern. These investigations, however, still leave the designer short of a final proof test on a full-scale structure with rather complete environmental simulation. Because of test-facility limitations,

# PROBLEMS OF STRUCTURES FOR PLANETARY ENTRY VEHICLES

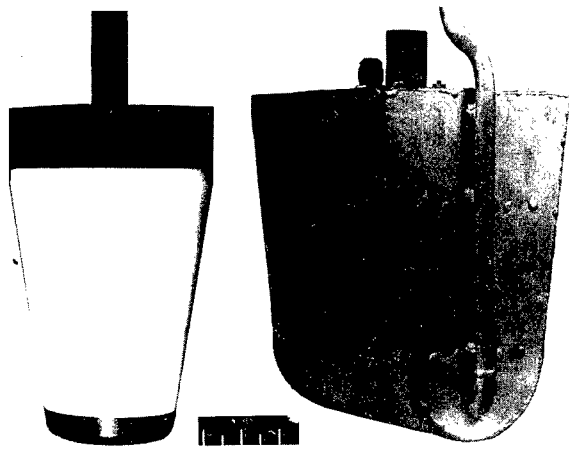


FIGURE 74-10.—Structural test specimens.

completely satisfactory proof tests on the ground cannot yet be made, but a step in this direction has been taken in tests of small structural models in arc-jet facilities. Two such models are shown in figure 74-10.

The blunted cone is a one-third-scale model of a flight research payload. With this model the conical surface is the primary test area. This area is of sufficient size to study failure mechanisms associated with differential thermal expansion as well as the effect of discontinuities and joints in the ablative shield. The round-nose wedge is a water-cooled holder for a 5-inch-square test panel. The flat panel affords some economy in specimen preparation. Currently, such specimens are tested in a large-diameter subsonic arc jet.

Views of 5-inch-square specimens tested to determine performance of charring ablators at very low heating rates are shown in figure 74-11. Characteristic problems revealed are various forms of char defects, gross dimensional changes due to thermal expansion, formation of blisters during escape of pyrolysis products, and destruction of the bond between the ablative layer and its supporting structure prior to complete pyrolysis of the ablator. The samples displayed here illustrate the after-test appearance of two materials—one without a reinforcement, and one reinforced with a honeycomb. Among other benefits of reinforcement, it is seen that fissures in the char layer are confined to the honeycomb cell dimension.

- CHAR DEFECTS
- DIMENSIONAL CHANGES
- BLISTERING
- BOND INTEGRITY

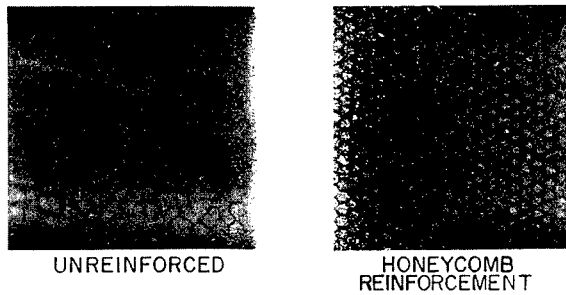


FIGURE 74-11.—Low-heating-rate problems.

Figure 74-12 shows typical results of tests designed to explore the effects of various types of discontinuities in shield materials. The result on the left illustrates the behavior of a ring of a noncharring low-temperature ablator inserted as an antenna window through a char-forming shield. The undercutting that was exhibited was considered undesirable in the full-scale flight vehicle, and a decision was made to use a heavier weight of the noncharring material for protection of the entire afterbody.

A pattern of holes similar to that shown on the face of the smaller specimen in figure 74-12 can arise from a need for electrical connections through the heat shield. Limited tests on a charring ablator have indicated that small holes are permissible, at least when located in areas

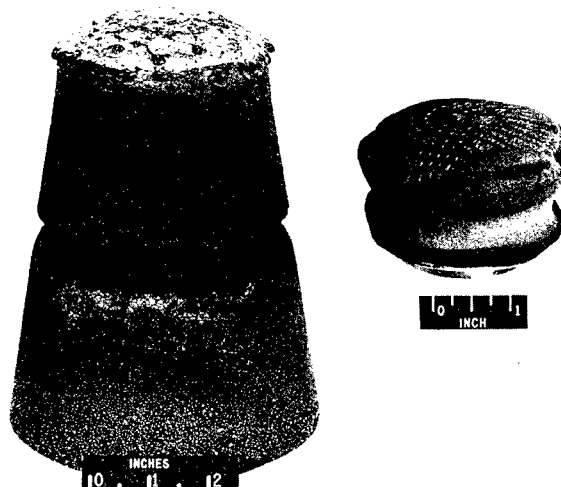


FIGURE 74-12.—Shield discontinuities.

of low dynamic pressure and shear force. However, the general problem of defining the tolerance limits for a given shield material to discontinuities of various types, including damage caused by micrometeoroid impact, is one warranting much more detailed investigation.

### FINAL LETDOWN SYSTEMS

After an entry vehicle has passed through the primary deceleration and heating phase and a speed near the terminal value in a particular atmosphere has been reached, there remains the problem of decelerating to a safe touchdown speed. The horizontal landing mode, of course, implies an aerodynamically suitable design and some preparation of the landing site. For arbitrary landing terrain conditions, and for the unmanned class of vehicles, a vertical descent will continue to find favor. For this type of descent both the parachute and the rocket landing systems have been studied, and a comparison of their weights is shown in figure 74-13. Weight of these systems as a percentage of vehicle weight is given as a function of planetary characteristics which determine the terminal velocity of freely falling bodies. Values of this ratio for Venus and Mars are indicated along with the value for Earth. The "greenhouse model" atmosphere (ref. 20) for Venus was chosen. A final impact velocity of 30 fps was assumed for this comparison.

Inasmuch as parachute-system weight (ref. 21) is not entirely independent of vehicle size

and weight, a 7,000-pound vehicle was arbitrarily chosen for the calculation of parachute-system weight. As would be anticipated, parachute-system weight is highly sensitive to variations in planetary characteristics. Rocket-system weight depends in somewhat greater detail upon the exact kinetic and potential energy to be dissipated and the maximum deceleration level. These considerations lead to a weight band for vehicles lying within the specified limits of the aerodynamic drag parameter  $W/C_D A$  and subject to a maximum deceleration of 10 Earth  $g$ 's.

The weight of letdown systems is seen to represent a significant percentage of vehicle weight on planets such as Earth and Mars. For planets like Mars with a low atmospheric density, it appears that a braking rocket could lead to the least weight system. For celestial bodies without an atmosphere, of course, it is the only choice.

After deceleration to 30 fps prior to contact, a formidable problem in landing-gear design still remains when large differences in surface terrain are considered. Variations in landing-gear geometry is a subject by itself and cannot be adequately treated here, but it may be instructive at least to look at the capability of those materials which either have been used, or have possibilities for use, as the energy-absorption medium in various gear designs. Such a comparison is presented in figure 74-14. (See refs. 22 to 25.)

Energy-dissipation capability is again presented as Btu/lb with the energy absorbed in

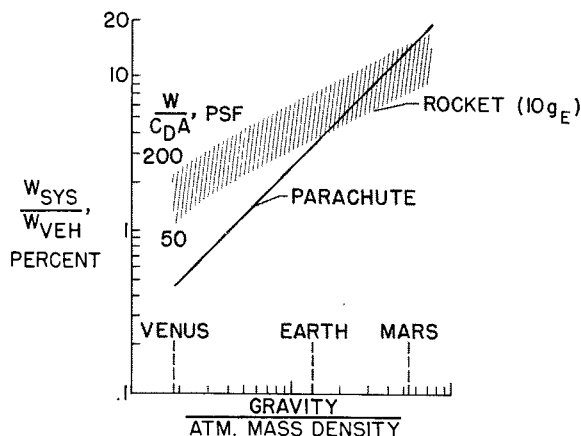


FIGURE 74-13.—Letdown system weight. Impact velocity, 30 fps.

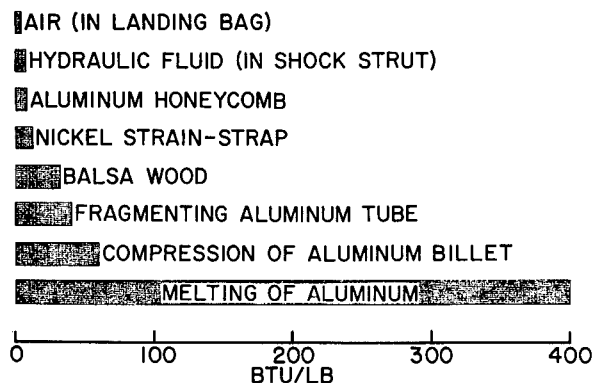


FIGURE 74-14.—Energy-dissipation capabilities of materials.

heating aluminum to its melting point used as a yardstick. The energy absorbed by the common working media, air and hydraulic fluids in their confining structures, is seen to be quite small in relation to the work done in crushing or deforming solid materials. Honeycomb, strain-straps, and balsa wood have already been incorporated in vehicle-impact absorption systems. The work done in fragmenting an aluminum tube begins to approach that done in straight compression of an aluminum billet, and offers controllable values of decelerating force. Simple devices which give controlled fragmentation at predictable force levels have been developed. In view of the disparity between current capability and that which may be achievable, further research on impact absorption appears to be warranted.

#### CONCLUDING REMARKS

For heat shields, new concepts in materials, fabrication process, and integration with structure are needed to cope with the wide variety of environmental conditions encountered in an extended flight mission. Ultimately, ease of refurbishment for successive missions will become an important requirement.

Along with advances in concepts more attention needs to be given to stress-analysis methods appropriate to shield materials and configurations. The problem becomes more difficult when

thermal degradation of material properties accompanying the heating is included in the analysis.

Research on space environmental effects on a variety of materials has been proceeding for some time but little information is yet available on the materials of particular interest in heat-shield construction.

Response of materials to extreme rates of radiative heating needs to be explored in much greater detail. Also, shield design concepts which are effective in either reflecting or absorbing high radiant rates must be sought.

Testing methodology for heat shields is developing slowly. Research on techniques leading to reproducible and more generally usable engineering data are needed. The source of this problem probably can be traced to the fact that standardization of test methods is difficult in a technology with rapidly changing requirements.

With respect to landing systems, concepts other than some form of parachute may be appropriate if a letdown to the surface of planets with lower atmospheric density is to be made efficiently. The use of braking rockets appears promising for manned vehicles but would pose numerous problems in unmanned missions. For these missions, more promise may lie in the development of highly efficient techniques for absorbing the energy of higher velocity landing impacts.

#### REFERENCES

1. RUNYAN, HARRY L., and LEONARD, ROBERT W.: Research, Design Considerations, and Technological Problems of Structures for Launch Vehicles. NASA University Conference, 1962. (Paper no. 72 of present compilation.)
2. JAFFE, LEONARD D., and RITTENHOUSE, JOHN B.: Behaviour of Materials in Space Environments. ARS Jour., vol. 32, no. 3, Mar. 1962, pp. 320-346.
3. LOVE, EUGENE S.: Reentry Vehicles: General Concepts and Operational Modes. Reentry Dynamics. Bull. of Virginia Polytechnic Inst., Eng. Exp. Station Ser. No. 150, vol. LV, no. 10, Aug. 1962, pp. 16-52.
4. SWANN, ROBERT T.: Composite Thermal Protection Systems for Manned Re-Entry Vehicles. ARS Jour., vol. 32, no. 2, Feb. 1962, pp. 221-226.
5. GLASER, PETER E., ED.: Aerodynamically Heated Structures. Prentice-Hall, Inc., 1962.
6. ANDERSON, ROGER A.: Thermal Protection Systems and Structures for Reentry Vehicles. Reentry Dynamics. Bull. of Virginia Polytechnic Inst., Eng. Exp. Station Ser. No. 150, vol. LV, no. 10, Aug. 1962, pp. 207-230.
7. RIDDELL, FREDERICK R., and WINKLER, HOWARD B.: Meteorites and Re-Entry of Space Vehicles at Meteor Velocities. ARS Jour., vol. 32, no. 10, Oct. 1962, pp. 1523-1530.
8. TEARE, J. D., GEORGIEV, S., and ALLEN, R. A.: Radiation From the Non-Equilibrium Shock Front. Res. Rep. 112 (AFCLR 937), Avco-Everett Res. Lab., Oct. 1961.

## STRUCTURES

9. ROSE, P. H.: Radiation and Ionization Problems in Re-Entry. Reentry Dynamics. Bull. of Virginia Polytechnic Inst., Eng. Exp. Station Ser. No. 150, vol. LV, no. 10, Aug. 1962, pp. 156-206.
10. SCALA, SINCLAIRE M., and WARREN, WALTER R.: Hypervelocity Stagnation Point Heat Transfer. ARS Jour. (Tech Notes), vol. 32, no. 1, Jan. 1962, pp. 101-102.
11. ANDERSON, ROGER A., and SWANN, ROBERT T.: Structures for Reentry Heating. NASA TM X-313, 1960.
12. WADLIN, KENNETH L., and KOTANCHIK, JOSEPH N.: The Use of Ablators for Achieving Protection Against High Thermal Flux. [Preprint] 417C, Soc. Automotive Eng., Oct. 1961.
13. BROOKS, WILLIAM A., JR., SWANN, ROBERT T., and WADLIN, KENNETH L.: Thermal Protection for Spacecraft Entering at Escape Velocity. [Preprint] 513F, Soc. Automotive Eng., Apr. 1962.
14. SWANN, ROBERT T.: Effect of Thermal Radiation From a Hot Gas Layer on Heat of Ablation. Jour. Aerospace Sci. (Readers' Forum), vol. 28, no. 7, July 1961, pp. 582-583.
15. NOLAN, EDWARD J., and SCALA, SINCLAIRE M.: Aerothermodynamic Behaviour of Pyrolytic Graphite During Sustained Hypersonic Flight. ARS Jour., vol. 32, no. 1, Jan. 1962, pp. 26-35.
16. GLOCKER, GEORGE: Heat of Sublimation of Graphite and the Composition of Carbon Vapor. Jour. Chem. Phys., vol. 22, no. 2, Feb. 1954, pp. 159-161.
17. HELDENFELS, R. R.: Ground Facilities for Testing Reentry Structures and Materials. Reentry Dynamics. Bull. of Virginia Polytechnic Inst., Eng. Exp. Station Ser. No. 150, vol. LV, no. 10, Aug. 1962, pp. 314-338.
18. SCALA, SINCLAIRE M., and GILBERT, LEON M.: Thermal Degradation of a Char-Forming Plastic During Hypersonic Flight. ARS Jour., vol. 32, no. 6, June 1962, pp. 917-924.
19. STEG, L., and LEW H.: Hypersonic Ablation. Tech. Inf. Series No. R62SD55—Class I, Missile and Space Vehicle Dept., Gen. Elec. Co., May 1962.
20. KELLOGG, WILLIAM W., and SAGAN, CARL: The Atmospheres of Mars and Venus. Pub. 944, Nat. Res. Council, Nat. Aca. Sci., 1961.
21. PARACHUTE BRANCH, DIRECTORATE OF DEVELOPMENT: United States Air Force Parachute Handbook. WADC Tech. Rep. 55-265, ASTIA Doc. No. AD 118036, U.S. Air Force, Dec. 1956.
22. BROOKS, GEORGE W., and CARDEN, HUEY D.: A Versatile Drop Test Procedure for the Simulation of Impact Environments. Noise Control Shock and Vibration, vol. 7, no. 5, Sept.-Oct. 1961, pp. 4-8.
23. McGEHEE, JOHN R.: A Preliminary Experimental Investigation of an Energy-Absorption Process Employing Frangible Metal Tubing. NASA TN D-1477, 1962.
24. FISHER, LLOYD J., JR.: Landing-Impact-Dissipation Systems. NASA TN D-975, 1961.
25. ESGAR, JACK B.: Survey of Energy-Absorption Devices for Soft Landing of Space Vehicles. NASA TN D-1308, 1962.

# 75. Research, Design Considerations, and Technological Problems of Structures for Spacecraft

By George W. Brooks

DR. GEORGE W. BROOKS, *Head, Vibration and Dynamics Branch, NASA Langley Research Center*, completed his undergraduate and graduate work at Princeton University. He received his Bachelor of Science in Engineering in 1947, his Master of Science in Engineering in 1949, and his Ph.D. in 1962. He is an instructor in advanced mathematics, teaching in the graduate study program conducted by Langley.

Since joining the Langley staff in March 1949, he has specialized in helicopter dynamics, vibration analysis, dynamic modeling, spacecraft environments, planetology, and spacecraft design. Dr. Brooks supervised the design and research of the first flyable model for detailed dynamics studies of helicopters and has performed basic research in several areas of applied mechanics. His designs and concepts for a lunar and planetary gravitational simulator for impact research and a penetrometer system for measuring the hardness of the lunar and planetary surfaces are now under development. He is the author or co-author of numerous NASA publications on a variety of subjects in applied mechanics. He is a member of Phi Beta Kappa and RESA.

## SUMMARY

The factors which influence the selection of the configuration and design features of spacecraft are reviewed. The multiplicity of configurations which result for the various mission objectives are exemplified by selected vehicles representative of compact, deployable, and inflatable structures. Problems unique to the design of these configuration types and general problems associated with the launch environment and space hazards such as vibrations, micro-meteoroids, and thermal balance are discussed. The paper concludes with a discussion of techniques for achieving sterilization, and summarizes the problem areas where further research appears timely and appropriate.

## INTRODUCTION

During the past 5 years great strides have been made in space flight, and to date nearly 100 spacecraft have been placed into orbit. The spacecraft launched during these flights varied

substantially in mission, configuration, and size. All of them, however, had a common purpose—to furnish more and better information on the nature of the earth, the extraterrestrial bodies which surround it, and the hostile regions of space in between.

Another thing in common among all these spacecraft is the fact that they represent the state of the art in man's capability to build efficient lightweight manned and unmanned structures which have a high probability of withstanding the launch environment and yielding useful scientific data. It is the purpose of this paper to summarize this state of the art by reviewing some of the more important factors which influence the selection of spacecraft configurations and their structures, and to indicate problem areas in need of further study.

### FACTORS WHICH INFLUENCE THE SELECTION OF SPACECRAFT CONFIGURATIONS

The primary factor in the selection of the configuration of a spacecraft is its mission, and the complexity of the mission usually dictates the complexity of the spacecraft. As an example, Echo I, the 100-foot-diameter balloon shown in figure 75-1, is relatively simple since it was designed primarily to serve as a passive communications satellite and therefore needed only to provide a reflective surface for radio waves. The balloon was constructed of a thin Mylar film coated with vapor-deposited aluminum. It was launched on August 12, 1960, and is still in orbit. During launch it was packaged in a sphere which had a diameter of 28 inches.

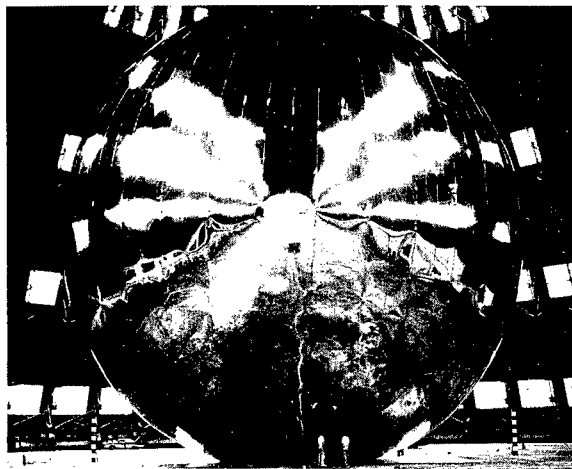


FIGURE 75-1.—Echo I (100-foot-diameter Mylar balloon).

The Apollo lunar excursion module, illustrated by the mockup shown in figure 75-2, is perhaps the best example of a complex spacecraft. A vehicle such as this must provide man with transportation to and from the lunar surface. Consequently it must incorporate the necessary life support systems to protect him from the extreme vacuum and temperature environment, and it must be designed to land and take off from a surface having poorly defined properties. In the latter respect, the design of the landing gear is a critical factor.

There are many other factors which have great influence on the selection of the configura-

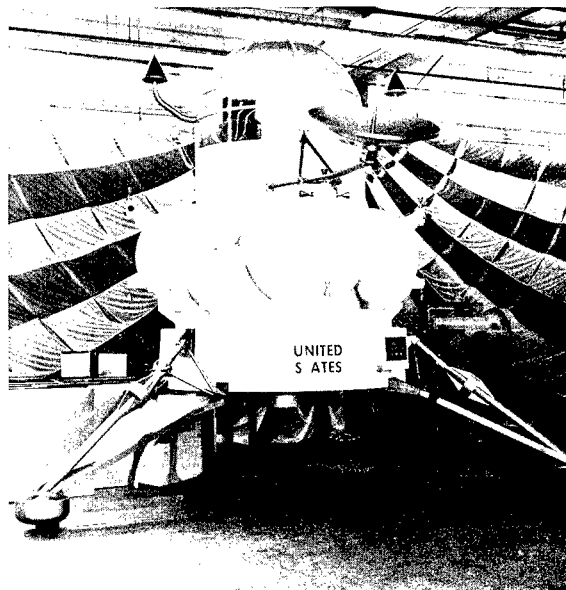


FIGURE 75-2.—Apollo lunar excursion module.

tion, such as launch-vehicle capability, on-board power requirements, communication requirements, and thermal protection for those spacecraft which are designed to reenter the earth's atmosphere.

### MULTIPLICITY OF CONFIGURATIONS

The aforementioned requirements as well as the designer's preference result in a host of spacecraft configurations. Each of these configurations has its own advantages and inherent problem areas. It is possible, however, to classify spacecraft as they now exist into three rather broad types: compact, deployable, and inflatable. An attempt will be made in the following paragraphs to point out some of the pertinent characteristics and problem areas of each type.

#### Compact Spacecraft

It is possible to design many spacecraft as compact units. Examples of such vehicles are Vanguard, Explorer, Tiros, and the Telstar spacecraft shown in figure 75-3. From the dynamicist's viewpoint, such designs are highly desirable because it is much easier to control their structural response during the launch phase.

One of the more difficult problems with compact spacecraft is the provision of adequate

## PROBLEMS OF STRUCTURES FOR SPACECRAFT

power in the allotted space for long-term operation of scientific instruments. Another important factor is thermal balance.

### Deployable Spacecraft

The term "deployable spacecraft," as used herein, denotes those whose major components remain folded or constrained during launching and then are deployed to enable the spacecraft to perform its mission. There is little doubt that this class of vehicles represents those which have both the greatest versatility and the most difficult design problems. The Surveyor spacecraft shown in figure 75-4 is a typical example.

A brief look at such a spacecraft readily reveals a complex structure which consists of a combination of trusses, panels, hinges, plates, and so forth, and which is surely unlike any conventional airborne vehicle. In order to analyze such a structure to obtain its static and dynamic stresses and motions, one must resort to the fundamental concepts and develop the theory for each such vehicle. It is apparent

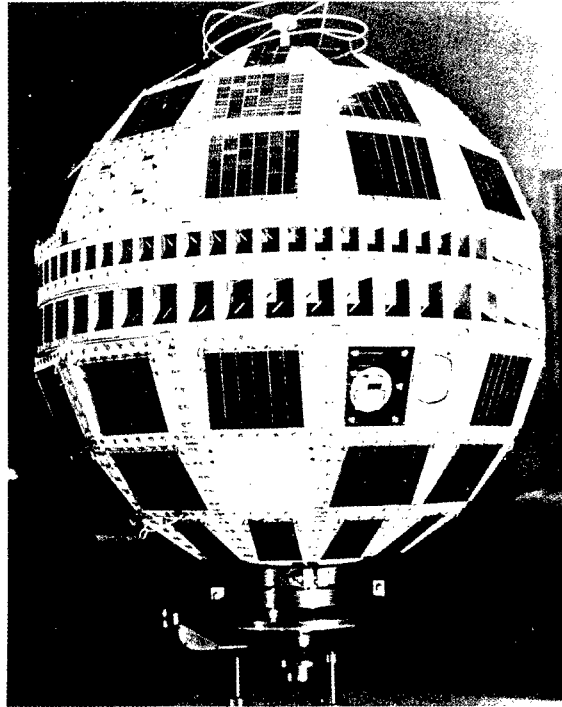


FIGURE 75-3.—Telstar spacecraft.

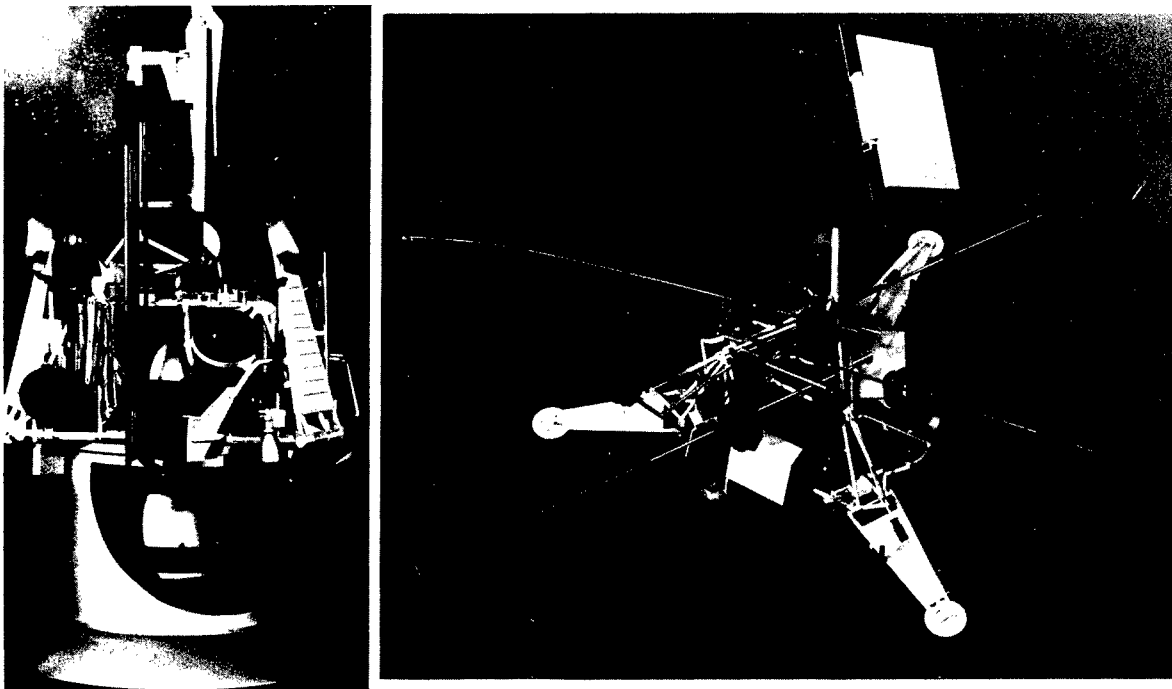


FIGURE 75-4.—Surveyor spacecraft.



## STRUCTURES

that such structures are highly redundant and contain many degrees of freedom, a combination which makes dynamic analysis a difficult task.

Another good example of a deployable spacecraft is Nimbus, shown in figure 75-5. This spacecraft can be used to illustrate several key

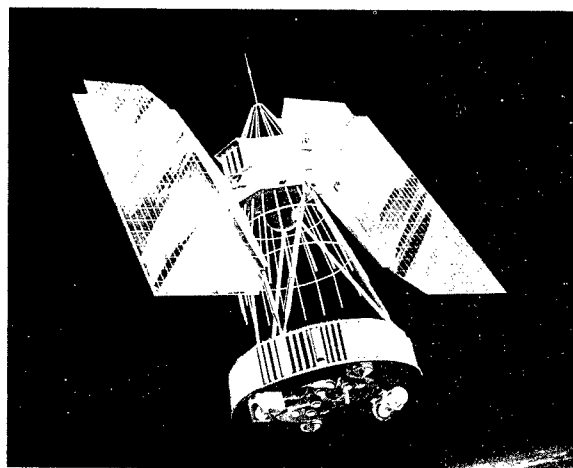


FIGURE 75-5.—Nimbus spacecraft.

structural design problems. The first of these is associated with the large solar panels which are necessary to provide the on-board power required. Whereas some spacecraft, such as those used to measure cosmic dust and radiation, may be space oriented, others designed to continually monitor a target must be oriented toward the earth or the planets. Nimbus, which is designed to photograph the earth's surface and cloud cover, is earth oriented, and consequently the solar panels are rotated relative to the remainder of the spacecraft once during each orbit in order to remain essentially perpendicular to the sun. This is necessary to maximize the absorption of solar energy by the panels. The need for panel rotations, together with the need to fold the panels for launch, introduces moving parts and associated mechanisms which inherently reduce spacecraft reliability.

Nimbus may also be used to illustrate the application of closed-cycle pneumatic shutters for temperature control of critical instrumentation components—in this case the instrumentation in the sensor ring at the base of the spacecraft. As the temperature in the compartments increases above the desired levels, the shutters

open automatically and the heat is radiated to space.

### Inflatable Spacecraft

Perhaps the best known example of an inflatable spacecraft is Echo I (shown in fig. 75-1). Currently NASA is in the process of developing a so-called rigidized balloon which will be 135 feet in diameter. This balloon, known as Echo A-12, is shown in figure 75-6. The skin is a soft-aluminum Mylar sandwich. The rigidization

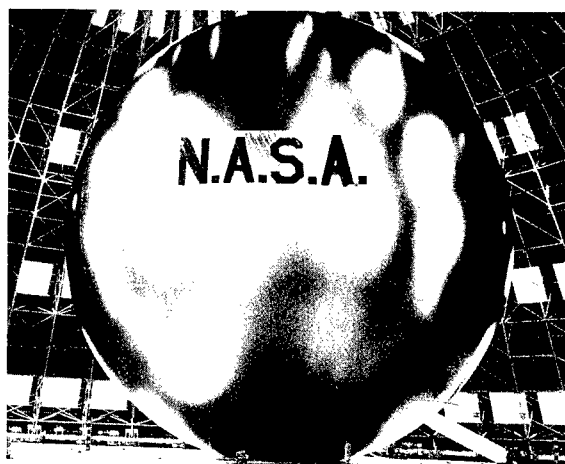


FIGURE 75-6.—Echo A-12 (135-foot-diameter rigidized balloon).

process consists of stressing the aluminum in the shell beyond the yield point during inflation so that the wrinkles formed during the manufacturing and folding process (it is stored during launch in a spheroid having a maximum diameter of 40 inches) are permanently removed. Such techniques require careful control of the pressures involved and necessitate the use of sublimating materials such as benzoic acid.

### DESIGN CONSIDERATIONS AND PROBLEM AREAS

Previous sections of this paper have presented a general discussion of some of the factors which influence the selection of spacecraft configurations and indicated some of the general problem areas. Subsequent sections are devoted to a more detailed study of problem areas and some of the design concepts which have been used or proposed for their solution. The first item to be discussed is inflation.

### Inflation

During the first vertical test shot of the 135-foot balloon, it failed during the unfolding process. Subsequent analyses indicated that the rate of inflation was probably too high to allow the thin skin to carry the inertia loads imposed by the unfolded portions and the attached beacon and solar-cell modules during inflation. The analysis and associated tests also indicated that, had the balloon withstood the initial unfolding conditions, it probably would have failed during the final phase of inflation when the skin had to arrest the 6-pound beacon assembly, which would then have been traveling at a velocity estimated at about 70 feet per second.

As a result of these analyses, which involved the solution of transient stresses in a highly nonlinear membrane, and the associated tests, a system of patching reinforcements was evolved and applied to the balloon. These reinforcements, plus a reduction in the rate of inflation to achieve a final velocity of about 40 feet per second during the final phase of inflation, resulted in a spacecraft which inflated satisfactorily during the second vertical test shot.

Additional research is necessary to improve inflation techniques and to define adequately the dynamics and associated forces during the inflation process.

### Lightweight Structural Components

The continued development of materials and fabrication techniques which possess high strength-to-weight ratios and can withstand the space environment is necessary to maximize spacecraft capabilities. The need for high-strength lightweight structural panels for support of solar cells is illustrated by inspection of any of the current types of spacecraft, particularly the deployable configurations such as Surveyor and Nimbus. In the construction of solar panels, for example, it is extremely desirable to have high rigidity per unit weight to provide adequate support for solar cells. As a result these structures are being constructed of honeycomb sandwiches. Although the current technology for the construction of uniform sandwich panels is good, the technology for constructing tapered panels with various joints and

cutouts leaves much to be desired as evidenced by joint and bonding failures in recently constructed hardware. Both joint formation and bonding are subject to improvement by further study. As an example, the weights of adhesives in some recently constructed sandwich beams and panels constituted from 2 to 14 percent of the total weight.

In recent years, considerable attention has been given to the development of waffle-stiffened panels which are formed by chem-milling, machining, rolling, and forging processes. Figure 75-7, taken from reference 1, shows the rela-

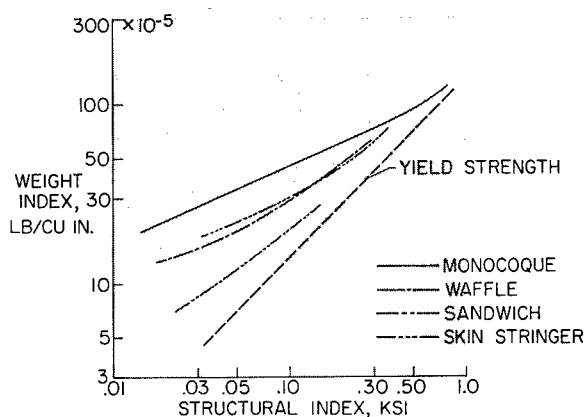


FIGURE 75-7.—Weight-strength comparisons for aluminum-alloy shells in bending.

tive weights of such structures when used as cylinders to carry bending loads. The specific-weight index is shown as a function of a structural index which is proportional to the bending moment divided by the third power of the radius. The object, of course, is to design a cylinder so that the allowable bending strength approaches the compressive yield strength. The results of the theoretical study shown in figure 75-7 indicate that the sandwich is substantially superior to the waffle as well as to other types for low values of the stress index. However, recent experimental results indicate that shells with skin-stringer stiffeners may be designed to be more competitive than indicated by the figure.

### Launch Environment

All types of spacecraft are subject to the severe shock and vibration environment imposed during the handling and launch phases.

## STRUCTURES

The general problem is discussed in some detail in the literature, reference 2 for example.

The major sources of vibratory forces during launch are as follows:

- Engine-ignition shocks
- Pulsations of engine thrust
- Turbine chugging
- Rocket-engine acoustic pressures
- Boundary-layer noise
- Fuel sloshing
- Control forces
- Nonstationary aerodynamic forces
- Unbalance of spinning components
- Engine burnout and staging shocks

These nonstationary forces generally have a more pronounced effect on deployable spacecraft because of the fact that the effective lengths of the structural elements between supports for these vehicles are such that the natural frequencies of the spacecraft generally correspond to the high-energy input frequencies. The conditions of resonance which result lead to high-amplitude structural responses, high stresses, and excessive accelerations of the on-board scientific instruments.

An example of the complexity of the problem is shown by figure 75-8, which presents the frequency responses of a  $\frac{1}{2}$ -scale dynamic model of the Nimbus spacecraft. The curves show the amplification factor, which is the ratio of the motion at the bottom of the paddle to the motion provided by the exciter to the base of the spacecraft, as a function of excitation frequency. The upper curve is for paddles which

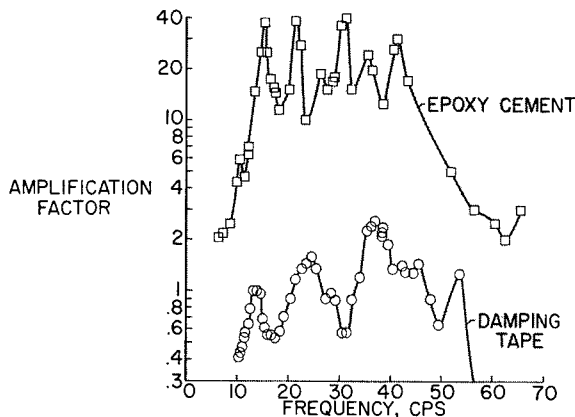


FIGURE 75-8.—Frequency response of Nimbus solar panels ( $\frac{1}{2}$ -scale dynamic model).

are formed by bonding aluminum sheets to a balsa filler by use of conventional epoxy cement. The lower curve is for the same basic type of construction except that the bonding material was replaced by a viscoelastic damping tape. The data emphasize three significant points. The first is that very high amplifications do often exist for such structures. The second is the existence of many structural resonances over a narrow frequency spectrum which extends to quite low frequencies. The third is that the response of such structures to nonstationary forces can be substantially improved by use of damping materials wherever possible.

The excitation forces are generally random functions of time with associated wide-band frequency spectrums as illustrated by the estimated sound pressure levels in the vicinity of the payload of the C-5 launch vehicle. Figure 75-9 shows the sound pressure levels outside the payload shroud as a function of frequency in octave bands. These fluctuating pressures, which result from boundary-layer buildup and flow breakdown around the shroud, have estimated peak values of approximately 157 decibels and result in an overall noise level of about 162 decibels.

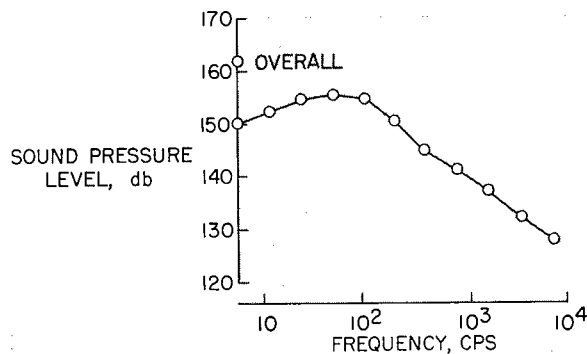


FIGURE 75-9.—Estimated aerodynamic noise pressure levels around payload of C-5 at maximum dynamic pressure.

The estimated maximum sonic-induced vibrations of a C-5 payload which would result from the acoustic pressures in figure 75-9 are shown in figure 75-10. These vibrations, which may be considered to be applied to the mounting base of the spacecraft, are of the order of 8g at frequencies above 100 cps. This is also the order of magnitude of the vibration levels imposed on spacecraft by other launch vehicles.

# PROBLEMS OF STRUCTURES FOR SPACECRAFT

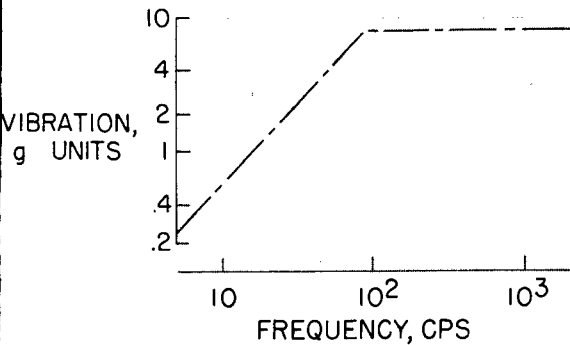


FIGURE 75-10.—Estimated maximum sonic-induced vibration around payload of C-5 at maximum dynamic pressure.

The design of a complex spacecraft to withstand the vibration environment is definitely not an easy task, but certain basic ground rules may be employed to good advantage. The first objective should be to isolate the spacecraft, or the critical components thereof, from the launch vehicle to minimize resonant responses of the spacecraft to high-frequency input motions. It is significant, in this respect, that the inputs to the spacecraft are primarily motion inputs and not force inputs.

The second objective is to introduce adequate damping into the structure by use of structural members which are inherently damped by incorporation of viscoelastic materials. Additional damping may then be applied as required by the use of discrete dampers.

The third objective, which should be started early in the spacecraft design phase, should be to determine the general dynamic or frequency response of the spacecraft by tests of simplified dynamic models, and to determine the frequencies and mode shapes of the principal natural modes. A knowledge of the mode shapes will indicate areas where distributed and concentrated damping forces may be applied to best advantage. It will also indicate nodal points where sensitive components may be installed for minimum response at critical frequencies. Dynamic-model tests have been employed to advantage for studying aircraft dynamics for many years and there is good reason to believe that they are equally applicable to spacecraft.

Several research areas which appear fruitful suggest themselves. These include the devel-

opment of efficient lightweight structural materials having high fatigue resistance and structural damping, the development of analytical procedures for analysis of complex structures, and—perhaps of greatest importance—the development of highly compact and reliable instrumentation for the acquisition of in-flight vibration and acoustic environmental data.

## Micrometeoroids

Any spacecraft which is designed to operate outside the earth's atmosphere for an appreciable length of time is subject to damage by micrometeoroids. The magnitude of the problem in terms of the flux and associated energies is presented by Davis in paper no. 67 of this compilation (ref. 3). During the past few years three general lines of research activity have been followed to obtain solutions to the micrometeoroid problem. The first consists of measurements of the flux by placing impact sensors on spacecraft. The second consists of the determination of the magnitude of the hazard associated with this flux by laboratory impact experiments with hypervelocity guns. The third, related to the second, consists of studies to evolve spacecraft structures which have a high probability of surviving anticipated micrometeoroid impacts.

The state of the art for solutions to the micrometeoroid problem is perhaps best illustrated by examining methods proposed recently for constructing a possible manned space station, shown in figure 75-11. This space station, in its deployed configuration shown on the left,

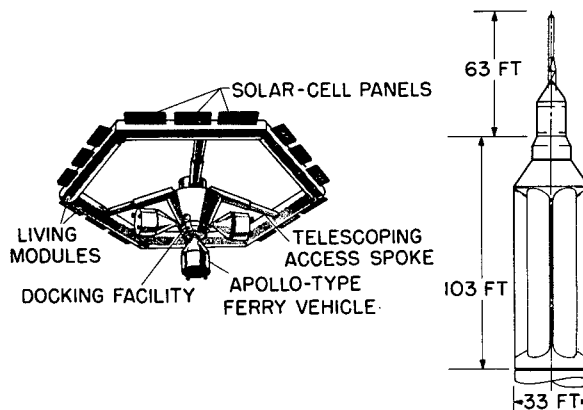


FIGURE 75-11.—Proposed manned space station. Diameter, 150 feet; area, 17,000 square feet.

## STRUCTURES

has a diameter of 150 feet, an exposed area of about 17,000 square feet, and an assumed launch weight of about 170,000 pounds. (See ref. 4.) As a result of basic research studies, which show the desirability of utilizing a micrometeoroid bumper, Zender and Davidson (ref. 5) have suggested the structure shown in figure 75-12 for the tubular modules of the space station. The fundamental feature of this structure is the apportionment of basic structural materials in three layers, the outermost layer having a

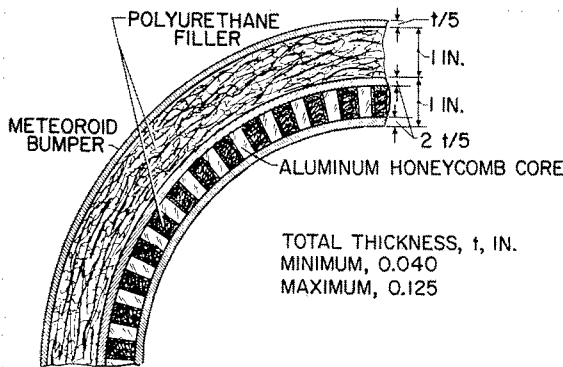


FIGURE 75-12.—Basic structure of space-station module.

thickness of  $t/5$  and the other two layers each having a thickness of  $2t/5$ . With this arrangement, the outer skin and filler serve as an impact bumper which breaks up the impacting body into smaller parts and effectively disperses the material over an area sufficient to reduce substantially the pointwise impact loads on the honeycomb sandwich, which is the primary load-carrying structure. The two thicknesses required are those which would yield a 50-percent probability of no penetrations per year of the entire space station according to the current low and high estimates of the flux.

The importance of developing adequate techniques for sealing micrometeoroid punctures in manned spacecraft is illustrated by figure 75-13, which shows the relative weight of the shell of the space station under discussion as a function of the probability of exceeding  $N$  punctures per year. Note that for a given probability of exceeding  $N$  punctures in a year, the weight drops sharply as the number is increased from 0 to 5. Note also that if the design is such that there is a 50-percent probability that no

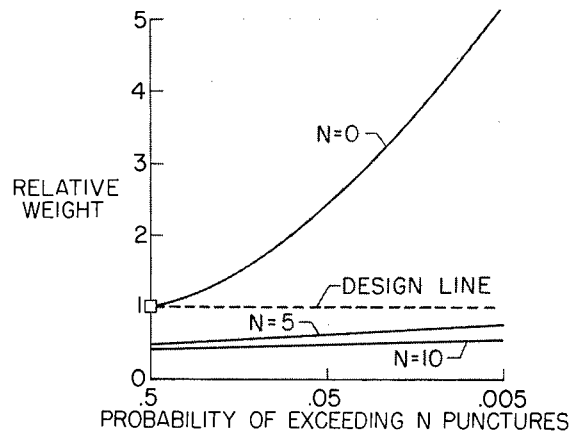


FIGURE 75-13.—Effect of allowed number of punctures per year.

punctures will occur in a year, the probability of exceeding 5 punctures per year will be very small.

Thus it appears that research in several areas needs to be continued to optimize solutions to the micrometeoroid problem. These include better definition of the flux, development of techniques for accelerating particles to micrometeoroid velocities for laboratory impact tests (current laboratory techniques yield velocities which approximate only the lower threshold of micrometeoroid velocities), and the development of reliable techniques for sealing punctures.

### Life Support

A great deal of study is now being given to the establishment of the necessities for supporting man in space and to the development of necessary hardware. The basic areas of concern are summarized in reference 6. These include carbon dioxide removal, oxygen supply, water reclamation, food supply, and waste disposal. Since the problem areas are not primarily structural design, the discussion of the problem is limited here to the observation that the life support systems which meet these requirements must also endure the severe shock and vibration environments during launch.

### Thermal Balance

The maintenance of spacecraft structures at approximately earth ambient temperatures during flight is currently achieved by two princi-

pal methods. The first consists of applying various types of coatings such as gold leaf, gold plate, or corrosion-resistant paints to the surface to control the ratio of the heat absorbed by the structure to the heat rejected or reradiated to space. This is the reason for the spots on the 12-foot balloon shown in figure 75-14. This balloon, known as Project Beacon, was launched into orbit to measure atmospheric density in the ionosphere.

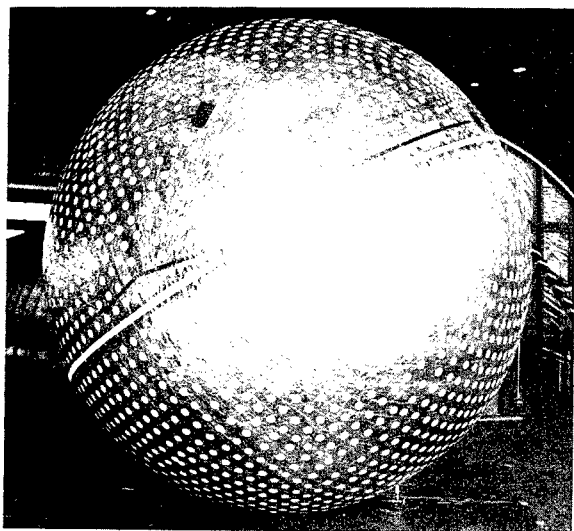


FIGURE 75-14.—Project Beacon (12-foot-diameter Mylar balloon).

The second method, which consists of providing shutters over critical temperature areas, was described in connection with Nimbus.

From the research point of view, one of the most interesting aspects of thermal control is the development of materials which become thermal radiation absorbers at low temperatures and thermal radiation reflectors at high temperatures. The coating of a reflective surface with paraffin is an example. When the temperature of the surface is below the melting point of the paraffin, the surface is opaque and absorbs radiation. However, when the paraffin melts, it becomes clear and the incident radiation passes through the film and is reflected by the subsurface. The development of better lightweight, reliable coatings or other adequate simple procedures for thermal balance is surely a matter of high priority.

### Spacecraft Power Systems

There are several ways to obtain power for operation of on-board spacecraft systems. The literature (refs. 7 to 9, for example) contains summaries of the potential capabilities of various systems.

Battery systems may be considered competitive for spacecraft power requirements measured in terms of hours, and for orbital vehicles which operate while in the earth's shadow rechargeable batteries may be necessary to supply a continuous source of power. However, for spacecraft operation times measured in terms of months or years, either a means must be provided to absorb energy from solar radiation and convert it into electricity, or some form of nuclear system must be considered. The solar-cell system is the only one which is advanced to the point of being readily available. This is the reason for the dominant arrangement of solar panels on current spacecraft. A number of small solar-cell systems have been employed with good success in spacecraft, and systems having a capacity of about 500 watts are now under development.

The current state of the art in the development of spacecraft power systems may be summarized by the fact that, for an earth-orbiting spacecraft, an average of about 200 square feet and 200 pounds of solar panels are required for the generation of 1 kilowatt of power. Nickel-cadmium batteries for electrical storage average about 250 pounds per kilowatt-hour.

The lightweight concentrator concept looks promising for future long-range spacecraft such as those to go to Venus and Mars. Figure 75-15 shows five of the many types of solar col-

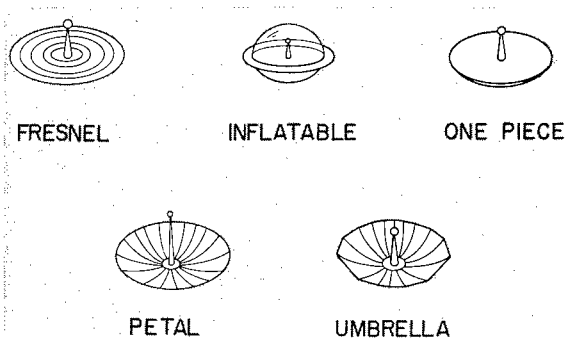


FIGURE 75-15.—Types of solar collectors.

lectors which are now being considered. All of these employ aluminum reflector surfaces and have been developed to the point where quantitative data are available to evaluate their capabilities. (See ref. 10.) Figure 75-16 shows the specific power, measured in watts per pound, for the models which have been constructed and tested to date, and the umbrella and inflatable collectors appear substantially better than other types in this respect. There are other factors such as absorber temperature, however, which are also significant.

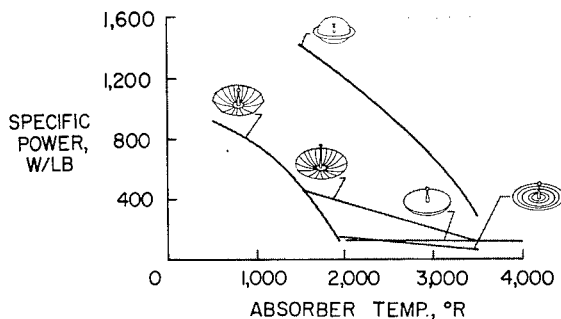


FIGURE 75-16.—Characteristics of solar collectors.

All of these collectors pose problems in packaging for launch and deployment in space to maintain the desired geometry for efficient energy absorption. Much work in this area remains to be done.

### Radiation

During the past few years a great deal of study has been given to the free-space and trapped radiation which surrounds the earth. This subject is presented in some detail in reference 3. Since this is primarily a materials problem, the reader is referred to that paper for a summary of the state of the art on the subject. It should be pointed out, however, that the high weight of shielding necessary to protect man from the radiation in the Van Allen belts or from major solar-flare radiations is a difficult problem. Other means for shielding the spacecraft, such as the establishment of strong electromagnetic fields to deflect the radiation, have not progressed to the point where they appear promising. The better approach currently is to avoid the radiation belts and

select flight times which correspond to minimum solar-flare activity.

### Lubrication in Space Environment

Another problem area, particularly pertinent to deployable spacecraft, is lubrication. Since common lubricants which have hydrocarbon bases are highly volatile and tend to oxidize or freeze in the space environment, other types must be employed (ref. 11). In general, liquids which will stand up in space are poor lubricants.

One of the better methods of lubricating ball bearings is to encase them in a retainer ring of fiber-glass-reinforced Teflon, impregnated with molybdenum disulfide, and let them run dry. (See refs. 12 and 13.) Reference 14 presents a good summary and bibliography on the use and limitations of inorganic dry lubricants.

Another method of achieving dry lubrication consists of metal plating. Reference 14 indicates that good results have been obtained for ball bearings plated with either gold or silver in that lifetimes of several hundred hours have been achieved at vacuum levels of the order of  $10^{-7}$  torr.

Another related problem for flights involving long exposure to the space vacuum is the possibility that the oxides and nitrides which prohibit seizure during contact of mating parts during atmospheric exposure may boil off in space and permit vacuum welding to take place. The results of studies presented in reference 15 and elsewhere indicate that this is a definite possibility and should be further investigated to assure the possibility of achieving separation of spacecraft components as required.

### STERILIZATION

The NASA has a policy which requires that any spacecraft having a significant probability of encountering an extraterrestrial body be sterilized to a level of severity and length of time necessary to kill all living entities. This policy is maintained because of concern over the possibility of contaminating extraterrestrial bodies with earth life or prelife forms and the contamination of earth with extraterrestrial life forms. Although it is not expected that life will be found on the moon, there is the possibility that the scientific opportunities for study

of cosmic materials may be substantially compromised by pollution of the lunar atmosphere and surface. In the case of Mars and Venus, there is a possibility that a nutrient environment adequate for the support of biological life exists, which could result in an exponential growth of transplanted organisms. The implications of such contamination are certainly a matter of concern to United States scientists and, according to reference 16, are also of concern to Soviet scientists. Further consideration of these implications is beyond the scope of this paper; however, appropriate discussions may be found in references 17 to 19. The primary objective here is to point out the requirement for sterilization, to enumerate methods for its achievement, and to indicate some of the associated problem areas.

It may be thought that the extreme environments of flight to the moon or planets, such as ultraviolet radiation from the sun, the high vacuum of space, and the extreme temperatures and gas environments of the surface, are such that adequate sterilization is inherent. As pointed out in reference 17, such is not necessarily the case and positive steps to achieve preflight sterilization are indicated.

Procedures for sterilizing spacecraft may be summarized as follows:

- (1) Heat soak at 125° C for 24 hours
- (2) Expose to  $\gamma$  radiation at  $10^7$  roentgens
- (3) Use liquid sterilizing additives to non-metallic components
- (4) Use surface sterilizing agents
- (5) Conduct assembly operations in sterile environment
- (6) Expose to mixtures of ethylene oxide and Freon-12 gases

Each of these methods suggests compromises which must be considered in the selection of spacecraft materials and techniques of fabrication and assembly.

All known living organisms are destroyed by exposure to dry steam at 160° C for 20 minutes. Since structural deficiencies of many spacecraft materials occur under these conditions, a compromise to 125° C for 24 hours is selected, which still may be too severe for many materials employed in bonding agents, seals, semiconductors, and batteries.

A second approach is to subject the spacecraft components to  $\gamma$  radiation dosages of  $10^7$  roentgens. Such radiation dosages, however, are known to be destructive to some plastics.

In the construction of spacecraft structures, it is particularly desirable to use substances such as sporicidal resins and to avoid substances of biological origin such as casein glue and shellac.

The addition of liquid sterilizing agents to nonmetallic components can be used to prevent the entrapment of live microorganisms during potting and molding processes. Similarly, liquid sterilizing agents may be used in local assembly areas such as bolt and rivet holes which may be sealed during the assembly process and therefore not be reached during the final overall sterilization process. During impact on the lunar and planetary surfaces, such areas may be exposed by structural failures which may have no destructive effects on living microorganisms.

Among the more effective and readily applied means of sterilization is the conduction of assembly operations in a sterile environment, followed by exposure to ethylene oxide and Freon-12 gas mixtures for a period of about 6 hours. After the sterilization process, the spacecraft or its components may be stored in metallic or plastic containers under continuous partial pressures to preserve sterility until launch. This technique is discussed in detail in reference 20 and the appendix of reference 19.

#### CONCLUDING REMARKS

Several factors which influence the design of spacecraft have been pointed out and some of the problems have been discussed. The major areas in which basic and applied research would be particularly timely and appropriate are as follows:

- (1) Advanced configurations
- (2) Inflation dynamics
- (3) Dynamic response during launch
- (4) Micrometeoroid flux and shielding requirements
- (5) Thermal balance
- (6) Radiation
- (7) Lubrication and vacuum welding



## STRUCTURES

### (8) Sterilization

It should be noted that these problems include the need for additional and better facilities for simulation and study of space hazards such as

radiation and micrometeoroids. Particular attention should be given to a more accurate evaluation of the natural levels of these hazards in the space environment.

## REFERENCES

1. PETERSON, JAMES P.: Weight-Strength Studies of Structures Representative of Fuselage Construction. NACA TN 4114, 1957.
2. CLEVENSON, SHERMAN A., and BROOKS, GEORGE W.: Considerations of Vibration Environments in Space Flight Systems. 1960 Proc. Inst. Environmental Sci., Apr. 1960, pp. 81-90.
3. DAVIS, DON D., JR.: Space Environment and Its Effect on Materials. NASA University Conference, 1962. (Paper no. 67 of present compilation.)
4. BERGLUND, RENE A.: Space-Station Research Configurations. A Report on the Research and Technological Problems of Manned Rotating Spacecraft. NASA TN D-1504, 1962, pp. 9-20.
5. ZENDER, GEORGE W., and DAVIDSON, JOHN R.: Structural Requirements of Large Manned Space Stations. A Report on the Research and Technological Problems of Manned Rotating Spacecraft. NASA TN D-1504, 1962, pp. 33-44.
6. POPMA, DAN C., WILSON, CHARLES H., and BOOTH, FRANKLIN W.: Life Support Research for Manned Space Stations. A Report on the Research and Technological Problems of Manned Rotating Spacecraft. NASA TN D-1504, 1962, pp. 107-120.
7. DAWSON, JOHN R., and HEATH, ATWOOD R.: Space-Station Power Systems. A Report on the Research and Technological Problems of Manned Rotating Spacecraft. NASA TN D-1504, 1962, pp. 59-70.
8. ZWICK, EUGENE B., and ZIMMERMAN, ROBERT L.: Space Vehicle Power Systems. [Preprint] 867-59, American Rocket Soc., June 1959.
9. ROSS, DANIEL P.: Space Power Trends. [Preprint] 61-191-1885, American Rocket Soc., June 1961.
10. HEATH, ATWOOD R., JR.: Status of Solar Energy Collector Technology. [Preprint] 2531-62, American Rocket Soc., Sept. 1962.
11. FREUNDLICH, MARTIN M., and ROBERTSON, ARTHUR D.: Lubrication Problems in Space Vehicles. Preprint No. 58-53, American Astronautical Soc., Dec. 1958.
12. ANON.: Dry Film Proves Best as Space Lubricant. Machine Design, vol. 34, no. 21, Sept. 13, 1962, p. 14.
13. VAN VLIET, R. M.: A Molecular Approach to Dry Film Lubrication in a Vacuum (Space) Environment. WADC Tech. Rep. 59-127, U.S. Air Force, July 1960.
14. EVANS, HAROLD E., and FLATLEY, THOMAS W.: Bearings for Vacuum Operation. Phase I. NASA TN D-1339, 1962.
15. BOWDEN, F. P., and YOUNG, J. E.: Friction of Clean Metals and the Influence of Adsorbed Films. Proc. Roy. Soc. (London), ser. A, vol. 208, no. 1092, Sept. 7, 1951, pp. 311-325.
16. ZYGIELBAUM, JOSEPH L., trans.: Soviet News Coverage of the Flight of the Second Cosmic Rocket Toward the Moon. Astronautics Information Trans. No. 10 (Contract No. NASw-6), Jet Propulsion Lab., C.I.T., Oct. 5, 1959.
17. DAVIES, R. W., and COMUNTZIS, M.: The Sterilization of Space Vehicles To Prevent Extraterrestrial Biological Contamination. Ext. Pub. No. 689 (Contract No. NASw-6), Jet Propulsion Lab., C.I.T., 1959.
18. JACOBSON, N. F.: The Operations Problem of Sterilization. [Preprint] 1771-61, American Rocket Soc., Mar. 1961.
19. POSNER, JACK, ed. (With appendix by Charles R. Phillips and Robert K. Hoffman): Proceedings of Meeting on Problems and Techniques Associated With the Decontamination and Sterilization of Spacecraft. NASA TN D-771, 1961.
20. PHILLIPS, CHARLES R., and HOFFMAN, ROBERT K.: Sterilization of Interplanetary Vehicles. Science, vol. 132, no. 3433, Oct. 14, 1960, pp. 991-995.